AD-A267 032

AGARD-CP-514

AGARD-CP-514

AGARD

ADVISORY GROUP FOR AEROSPACE RESEARCH & DEVELOPMENT
7 RUE ANCELLE 92200 NEUILLY SUR SEINE FRANCE

AGARD CONFERENCE PROCEEDINGS 514

DTIC
ELECTE
JUL 14 1993
S A D

Theoretical and Experimental Methods in Hypersonic Flows

(Les Méthodes Théoriques et Expérimentales pour l'Etude des Ecoulements Hypersoniques)

Papers presented and discussions held at the Fluid Dynamics Panel Symposium held in Torino, Italy, from 4th—8th May 1992.

This document has been approved for public release and sale; its distribution is unlimited.

NORTH ATLANTIC TREATY ORGANIZATION

Published April 1993

Distribution and Availability on Back Cover

AGARD-CP-514

AGARD

ADVISORY GROUP FOR AEROSPACE RESEARCH & DEVELOPMENT

7 RUE ANCELLE 92200 NEUILLY SUR SEINE FRANCE

AGARD CONFERENCE PROCEEDINGS 514

Theoretical and Experimental Methods in Hypersonic Flows

(Les Méthodes Théoriques et
Expérimentales pour l'Etude
des Ecoulements Hypersoniques)

Accesion For
NTIS CRA&I ✓
DTIC TAB ☐
Unannounced ☐
Justification
By
Distribution /
Availability Codes
Dist | Avail and / or Special
A-1

Papers presented and discussions held at the Fluid Dynamics Panel Symposium
held in Torino, Italy, from 4th—8th May 1992.

North Atlantic Treaty Organization
Organisation du Traité de l'Atlantique Nord

93-15932

The Mission of AGARD

According to its Charter, the mission of AGARD is to bring together the leading personalities of the NATO nations in the fields of science and technology relating to aerospace for the following purposes:

- Recommending effective ways for the member nations to use their research and development capabilities for the common benefit of the NATO community;
- Providing scientific and technical advice and assistance to the Military Committee in the field of aerospace research and development (with particular regard to its military application);
- Continuously stimulating advances in the aerospace sciences relevant to strengthening the common defence posture;
- Improving the co-operation among member nations in aerospace research and development;
- Exchange of scientific and technical information;
- Providing assistance to member nations for the purpose of increasing their scientific and technical potential;
- Rendering scientific and technical assistance, as requested, to other NATO bodies and to member nations in connection with research and development problems in the aerospace field.

The highest authority within AGARD is the National Delegates Board consisting of officially appointed senior representatives from each member nation. The mission of AGARD is carried out through the Panels which are composed of experts appointed by the National Delegates, the Consultant and Exchange Programme and the Aerospace Applications Studies Programme. The results of AGARD work are reported to the member nations and the NATO Authorities through the AGARD series of publications of which this is one.

Participation in AGARD activities is by invitation only and is normally limited to citizens of the NATO nations.

The content of this publication has been reproduced
directly from material supplied by AGARD or the authors.

Published April 1993

Copyright © AGARD 1993
All Rights Reserved

ISBN 92-835-0694-4

SPS

Printed by Specialised Printing Services Limited
40 Chigwell Lane, Loughton, Essex IG10 3TZ

Recent Publications of the Fluid Dynamics Panel

AGARDOGRAPHS (AG)

Design and Testing of High-Performance Parachutes
AGARD AG-319, November 1991

Experimental Techniques in the Field of Low Density Aerodynamics
AGARD AG-318 (E), April 1991

Techniques Expérimentales Liées à l'Aérodynamique à Basse Densité
AGARD AG-318 (FR), April 1990

A Survey of Measurements and Measuring Techniques in Rapidly Distorted Compressible Turbulent Boundary Layers
AGARD AG-315, May 1989

Reynolds Number Effects in Transonic Flows
AGARD AG-303, December 1988

REPORTS (R)

Unstructured Grid Methods for Advection Dominated Flows
AGARD R-787, Special Course Notes, May 1992

Skin Friction Drag Reduction
AGARD R-786, Special Course Notes, March 1992

Engineering Methods in Aerodynamic Analysis and Design of Aircraft
AGARD R-783, Special Course Notes, January 1992

Aircraft Dynamics at High Angles of Attack: Experiments and Modelling
AGARD R-776, Special Course Notes, March 1991

Inverse Methods in Airfoil Design for Aeronautical and Turbomachinery Applications
AGARD R-780, Special Course Notes, November 1990

ADVISORY REPORTS (AR)

Air Intakes for High Speed Vehicles
AGARD AR-270, Report of WG 13, September 1991

Appraisal of the Suitability of Turbulence Models in Flow Calculations
AGARD AR-291, Technical Status Review, July 1991

Rotary-Balance Testing for Aircraft Dynamics
AGARD AR-265, Report of WG 11, December 1990

Calculation of 3D Separated Turbulent Flows in Boundary Layer Limit
AGARD AR-255, Report of WG10, May 1990

Adaptive Wind Tunnel Walls: Technology and Applications
AGARD AR-269, Report of WG12, April 1990

CONFERENCE PROCEEDINGS (CP)

Aerodynamic Engine/Airframe Integration for High Performance Aircraft and Missiles
AGARD CP-498, September 1992

Effects of Adverse Weather on Aerodynamics
AGARD CP-496, December 1991

Manoeuvring Aerodynamics
AGARD CP-497, November 1991

Vortex Flow Aerodynamics
AGARD CP-494, July 1991

Missile Aerodynamics
AGARD CP-493, October 1990

Aerodynamics of Combat Aircraft Controls and of Ground Effects
AGARD CP-465, April 1990

Computational Methods for Aerodynamic Design (Inverse) and Optimization
AGARD-CP-463, March 1990

Applications of Mesh Generation to Complex 3-D Configurations
AGARD CP-464, March 1990

Fluid Dynamics of Three-Dimensional Turbulent Shear Flows and Transition
AGARD CP-438, April 1989

Validation of Computational Fluid Dynamics
AGARD CP-437, December 1988

Aerodynamic Data Accuracy and Quality: Requirements and Capabilities in Wind Tunnel Testing
AGARD CP-429, July 1988

Aerodynamics of Hypersonic Lifting Vehicles
AGARD CP-428, November 1987

Aerodynamic and Related Hydrodynamic Studies Using Water Facilities
AGARD CP-413, June 1987

Applications of Computational Fluid Dynamics in Aeronautics
AGARD CP-412, November 1986

Store Airframe Aerodynamics
AGARD CP-389, August 1986

Unsteady Aerodynamics — *Fundamentals and Applications to Aircraft Dynamics*
AGARD CP-386, November 1985

Aerodynamics and Acoustics of Propellers
AGARD CP-366, February 1985

Improvement of Aerodynamic Performance through Boundary Layer Control and High Lift Systems
AGARD CP-365, August 1984

Wind Tunnels and Testing Techniques
AGARD CP-348, February 1984

Aerodynamics of Vortical Type Flows in Three Dimensions
AGARD CP-342, July 1983

Missile Aerodynamics
AGARD CP-336, February 1983

Prediction of Aerodynamic Loads on Rotorcraft
AGARD CP-334, September 1982

Wall Interference in Wind Tunnels
AGARD CP-335, September 1982

Fluid Dynamics of Jets with Applications to V/STOL
AGARD CP-308, January 1982

Aerodynamics of Power Plant Installation
AGARD CP-301, September 1981

Computation of Viscous-Inviscid Interactions
AGARD CP-291, February 1981

Subsonic/Transonic Configuration Aerodynamics
AGARD CP-285, September 1980

Turbulent Boundary Layers Experiments, Theory and Modelling
AGARD CP-271, January 1980

Foreword

The previous AGARD Fluid Dynamics Panel Symposium to deal specifically with very high-speed flows (AGARD Conference Proceedings 428) took place in Bristol, UK in April 1987 when the subject addressed was the aerodynamics of hypersonic lifting vehicles. Since that time, considerable effort has been and is continuing to be devoted within many of the NATO Countries to a range of hypersonic transport vehicles and their associated research and enabling technology programmes. It was therefore considered appropriate for the FDP to hold another meeting on hypersonics in order to (i) report and assess the advances being made by the AGARD community on the development and application of theoretical methods and experimental techniques for simulating hypersonic flows over aerospace vehicles, (ii) highlight outstanding problem areas and (iii) establish pointers to aid in the planning and implementation of future research programmes.

Major topics covered by the Symposium were testing techniques and instrumentation, computational methods and physical modelling, and validation and accuracy assessment. Forty-two papers were presented in eight separate sessions. An additional paper, which the author was unable to present, is now included in the proceedings. The sessions were:

- — Design of Hypersonic Vehicles (7 papers)
- — Facilities (4 papers)
- — Instrumentation (5 papers)
- — CFD Validation and Data Accuracy (7 papers)
- — Rarefied Gas; Real Gas; Chemistry (4 papers)
- — Boundary Layer Transition (5 papers)
- — High Enthalpy Nozzle Computation (4 papers)
- — Development and Application of Codes (6 papers + 1 additional).

The session on Instrumentation consisted of five review papers which summarise the outcome of an Advanced Research Workshop on New Trends in Instrumentation for Hypersonic Research, organised by ONERA, DLR, NASA and VKI and held at ONERA, Le Fauga-Mauzac, France from 27th April to 1st May 1992.

The Symposium was concluded with a worthwhile discussion period which began with a preliminary assessment given by the Technical Evaluator, Professor E. Reshotko. The discussion helped to give additional prospective to the technical content of the meeting. These proceedings include a record of the discussion and also the Technical Evaluation Report.

P.R. Bignell and C. Dujarric
Programme Committee Co-Chairmen

Avant-Propos

Le dernier symposium organisé par le Panel AGARD de la dynamique des fluides sur le thème des écoulements à très grande vitesse (compte rendu de conférence AGARD 428) a eu lieu à Bristol au Royaume-Uni en avril 1987. Le symposium avait pour titre "Les véhicules hypersustentateurs". Depuis cette époque, des efforts considérables ont été consacrés, et le sont toujours, par un certain nombre de pays de l'OTAN, à l'étude de l'aérodynamique des véhicules hypersustentateurs et aux programmes de recherche et développement des technologies y associées.

Le Panel a donc jugé opportun de tenir une autre réunion sur le thème de l'hypersonique afin de (i) rendre compte et d'évaluer les progrès qui ont été réalisés par la communauté de l'AGARD dans le développement et les applications des méthodes théoriques et des techniques expérimentales pour la simulation des écoulements hypersoniques sur les véhicules aérospatiaux (ii) mettre en lumière les problèmes et (iii) établir des indications pour la planification et la mise en oeuvre de futurs programmes de recherche.

Les principales questions couvertes par le symposium ont été les techniques d'essai et l'instrumentation, les méthodes de calcul, la modélisation physique, la validation et l'évaluation de la précision. En tout, 42 communications ont été lors des huit sessions. Une communication supplémentaire qui n'a pas pu être présentée est incluse au compte rendu de conférence. Le programme des différentes sessions s'établit comme suit:

- La conception des véhicules hypersoniques (7 communications)
- Les installations (4 communications)
- L'instrumentation (5 communications)
- La validation de l'aérodynamique numérique et la précision des données (7 communications)
- Le gaz raréfié; la gaz réel; la chimie (4 communications)
- La transition de la couche limite (5 communications)
- Le calcul des tuyères à haute enthalpie (5 communications)
- L'élaboration et la mise en application des codes (6 communications + 1 supplémentaire).

Cinq communications ont été présentées lors de la session sur l'instrumentation. Elles résumaient les résultats d'un atelier de recherche avancée, organisé par l'ONERA, la NASA et le VKI à l'ONERA, Le Fauga-Mauzac, France, du 27 avril au 1er mai 1992, sur les nouvelles tendances en instrumentation pour la recherche hypersonique.

Le symposium a conclu par un débat très fructueux qui a commencé par une appréciation préliminaire donnée par l'évaluateur technique, le Professeur E. Reshotko. Le débat a donné une perspective supplémentaire au contenu technique de la réunion. Ce compte rendu comprend le texte des discussions ainsi que le rapport d'évaluation technique.

P.R. Bignell et C. Dujarric
Co-Présidents du Comité de Programme

Fluid Dynamics Panel

Chairman: Prof. Ir J.W. Slooff
National Aerospace Laboratory NLR
Anthony Fokkerweg 2
1059 CM Amsterdam
The Netherlands

Deputy Chairman: M.C. Dujarric
ASE-Programme HERMES
Bâtiment Copernic
18 Avenue Edouard Belin
31055 Toulouse Cedex — France

PROGRAMME COMMITTEE

Mr P.R. Bignell (Co-Chairman)
BAe PLC, Sowerby Research Centre
FPC 266, P.O. Box 5
Filton
Bristol BS12 7QW — UK

M.C. Dujarric (Co-Chairman)
ASE-Programme HERMES
Bâtiment Copernic
18 Avenue Edouard Belin
31055 Toulouse Cedex — France

Professor J.A. Essers
Université de Liège
Institut de Mécanique, Service
d'Aérodynamique Appliquée
rue Ernest Solvay 21
4000 Liège — Belgium

Mr J.M. Muylaert
ESTEC
Aerothermodynamic Section
Postbus 299
2200 AG Noordwijk — The Netherlands

Dr K.J. Orlik-Rückemann
Applied Aerodynamics Laboratory
Institute for Aerospace Research
NRC, Bldg M-10
Montreal Road
Ottawa K1A 0R6 — Canada

M. Ph. Vancamberg
Dept d'Aérodynamique Théorique
Dassault Aviation
78 Quai Marcel Dassault
92214 Saint-Cloud — France

Dr K. Kienappel
DLR
Forschungszentrum Göttingen
Bunsenstrasse 10
3400 Göttingen — Germany

Professor D. Papailiou
Lab. of Applied Thermodynamics
Dept of Mechanical Engineering
University of Patras
Kato Kostritsi
Patras 26500 — Greece

Dr Ing. G. Bucciantini
Alenia-Settore Aeronautica
Divisione Velivoli Difesa
C.P. 432
10100 Torino — Italy

Professor Dr Ir J.A. Steketee
Dept of Aerospace Engineering
Delft University of Technology
Kluyverweg 1
2629 HS Delft — The Netherlands

Professor Dr T. Ytrehus
Division of Applied Mechanics
The University of Trondheim
The Norwegian Inst of Technology
N-7034 Trondheim — NTH — Norway

Professor J. Jimenez
Escuela Tecnica Superior de
Ingenieros Aeronauticos
Departamento de Mecanica de Fluidos
Plaza del Cardenal Cisneros 3
28040 Madrid — Spain

Dr R.G. Bradley, Jr
Director, Flight Sciences Dept
Mail Zone 2888
General Dynamics, Fort Worth Div.
P.O. Box 748
Fort Worth, TX 76101-748 — United States

Professor W.S. Saric
Arizona State University
Mechanical & Aerospace Engineering
Tempe, AZ 85287-6106 — United States

PANEL EXECUTIVE

Dr W. Goodrich

Mail from Europe:
AGARD—OTAN
Attn: FDP Executive
7, rue Ancelle
F-92200 Neuilly-sur-Seine
France

Mail from US and Canada:
AGARD—NATO
Attn: FDP Executive
Unit 21551
APO AE 09777

Tel: 33(1)47 38 57 75
Telex: 610176 (France)
Telefax: 33 (1) 47 38 57 99

Contents

Page

Recent Publications of the Fluid Dynamics Panel iii

Foreword v

Avant-Propos vi

Fluid Dynamics Panel vii

Reference

Technical Evaluation Report T
by E. Reshotko

SESSION I – DESIGN OF HYPERSONIC VEHICLES

Chairman: C. Dujarric

CFD Analysis of Hypersonic, Chemically Reacting Flow Fields 1
by T.A. Edwards

Aerodynamic and Aerothermal Challenges for the Design of the Hermes Spaceplane 2
by P. Perrier

Experimental Results in Aerodynamic Stability and Control of a TSTO Configuration 3
by T. Gottman and G. Cucinelli

Numerical Simulation of the Flow through a Scramjet Engine 4
by V. Selmin

Control Effectiveness at Hypersonic Speeds 5
by J.L. Stollery, D. Kumar, P.A. Atcliffe and H. Babinsky

In-Flight Evaluation of Aerodynamic Predictions of an Air-Launched Space Booster 6
by R.E. Curry, M.R. Mendenhall and B. Moulton

Planetary Entry Vehicle Design for Planned and Potential ESA Missions to Titan, Mars and Earth Return (FGE TN 51/92) 7
by A.J. Smith

SESSION II – FACILITIES

Chairman: G. Bucciantini

Nouveaux Moyens d'Essais Hypersoniques Developpés à l'ONERA: Les Souffleries R5 et F4 8
par B. Chanetz et autres

The High Enthalpy Facilities HEG and TH 2 in Germany 9
by G. Eitelberg and H. Olivier

Design and Production of Insulated Wind Tunnel Models of the Hermes Shuttle for Heat Transfer Measurements at Hypersonic Speeds 10
by L. Visintini and C. Couedor

The Upgrading of the Arc Heated Wind Tunnel of the DLR (LBK) with Respect to its Effects on the Material Testing 11
by A. Gülhan and K. Kindler

Reference

SESSION III – INSTRUMENTATION

Chairman: J.A. Steketee

Recommendations for Future Research in Hypersonic Instrumentation 12A
by S.L. Ocheltree

Local Measurement of Temperatures and Concentrations: A Review for Hypersonic Flows 12B
by C. Dankert, R. Cattolica and W. Sellers

Pressure and Force Measurements on Models Set in Hypersonic Flows: A Review 13
by C.G. Miller

Velocity Measurements in Hypersonic Flows: A Review 14
by A. Boutier, W.J. Yanta and G. Smeets

Flow Visualization and Spectroscopy in Hypersonic Flows: New Trends 15
by J. Trolinger, G. Eitelberg and M. Rapuc

Thermal Flux Measurements in Hypersonic Flows: A Review 16
by J.F. Wendt, D. Balageas and R.D. Neumann

SESSION IV – CFD VALIDATION AND DATA ACCURACY

Chairman: D.L. Bowers

A CFD Validation Roadmap for Hypersonic Flows 17
by J.G. Marvin

Synthesis of the Workshop on Hypersonic Flows for Reentry Problems 18
by R. Abgrall et al.

Problems in the Validation of CFD Codes through Comparison with Experiment 19
by D.S. Dolling

Flow Development in a Circular Pipe in the UTIAS/RPI M = 8.3 Gun Tunnel 20
by J.D. Sislian, Z. He and R.L. Deschambault

Experimental and Computational Comparisons of Mach 6 High Reynolds Number Heat Transfer and Skin Friction 21
by L. Galassi and N.E. Scaggs

Experimental, Analytical, and Computational Methods Applied to Hypersonic Compression Ramp Flows 22
by G. Simeonides, W. Haase and M. Manna

Joint Computational and Experimental Aerodynamics Research on a Hypersonic Vehicle 23
by W.L. Oberkampf, D.P. Aeschliman and M. (McWherter) Walker

SESSION V – RAREFIED GAS; REAL GAS; CHEMISTRY

Chairman: K. Kienappel

Issues and Approach to Develop Validated Analysis Tools for Hypersonic Flows: One Perspective 24
by G.S. Deiwert

Comparison of Computation and Experiment for a High Enthalpy, Heated-Driver, Shock-Tube Environment 25
by S. Shahpar, A. Kennaugh, I.M. Hall and D.I.A. Poll

Reference

Thermodynamic Model of Air in Chemical Equilibrium 26
by D.Giordano and L.Marraffa

Three-Dimensional Hypersonic Rarefied Flow Calculations using Direct Simulation Monte Carlo Method 27
by M.C.Çelenligil and J.N.Moss

SESSION VI – BOUNDARY LAYER TRANSITION
Chairman: H.L.Reed

Stability of Hypersonic Flow over a Blunt Body 28
by T.Herbert and V.Esfahanian

Stability of Hypersonic Boundary-Layer Flows with Chemistry 29
by H.L.Reed, G.K.Stuckert and T.S.Haynes

Real Gas and Surface Transpiration Effects upon Swept Leading Edge High Speed Flow Including Transition 30
by D.I.A.Poll

On the Instability of Hypersonic Flow Past a Pointed Cone: Comparison of Theoretical and Experimental Results at Mach 8 31
by M.Simen and U.Dallmann

Studies of Hypersonic Viscous Flows 32
by R.Hillier, D.C.Kirk, M.Sell and S.Soltani

SESSION VII – HIGH ENTHALPY NOZZLE COMPUTATION
Chairman: J.Muylaert

Calculs d'Ecoulement Visqueux en Deséquilibre dans des Tuyères 33
par C.Marmignon, V.Joly et F.Coquel

Nonequilibrium Hypersonic Flow in a Wind-Tunnel Nozzle 34
by D.Zeitoun, E.Boccaccio, M.C.Druguet, M.Imbert and R.Brun

Some Experimental Study and Numerical Simulation in Wind Tunnel Flow 35
by S.Borrelli and E.Hettena

A CFD-Based Aerodynamic Design Procedure for Hypersonic Wind-Tunnel Nozzles 36
by J.J.Korte

SESSION VIII – DEVELOPMENT AND APPLICATIONS OF CODES
Chairman: P.R.Bignell

Numerical Methods for Aerothermodynamic Design of Hypersonic Space Transport Vehicles 37
by K.M.Wanie, A.Brenneis, A.Eberle and S.Heiss

Hypersonic Multi Block Flow Simulations around Space Vehicles Including Non-Equilibrium Chemistry 38
by J.B.Vos, A.W.Rizzi and C.M.Bergman

Hypersonic Flow Computations around Re-Entry Vehicles 39
by J.Peraire, J.Peirò, K.Morgan, M.Vahdati and R.C.Molina

On the Accuracy and Efficiency of CFD Methods in Real Gas Hypersonics 40
by D.Drikakis and S.Tsangaris

Reference

A Comparison of High Resolution Upwind Solvers on 3-D Inviscid Hypersonic Flows 41
by M.Manna, H.Deconinck, C.P.Li and E.Ma

Local Aerothermal Problems during HERMES Reentry 42
by A.Naim, M.Mallet, Ph.Rostand and J.M.Hasholder

Thermal and Chemical Non Equilibrium Hypersonic Flow Computations 43
by F.Grasso and V.Bellucci

General Discussion D

Technical Evaluation Report

by

Eli Reshotko
Department of Mechanical and Aerospace Engineering
Case Western Reserve University
Cleveland, Ohio 44106-7222, United States

ABSTRACT

The subject Symposium, "Theoretical and Experimental Methods in Hypersonic Flows," sponsored by the Fluid Dynamics Panel of AGARD took place in Torino, Italy during the period 4-8 May, 1992. The objectives of the Symposium were to report and assess advances within the AGARD community in the development and application of theoretical and experimental approaches for addressing hypersonic flows related to aerospace vehicles, to highlight particular problem areas, and to provide guidance for the planning and implementation of future research programs.

The meeting consisted of eight sessions, including a special session of review papers covering the various areas of modern instrumentation. This particular session was an outgrowth of the activity of the FDP Ad Hoc Study Group on Hypersonic Research and Technology. Each session is separately reviewed in this report. The comments on the sessions are drawn from those of all the Symposium participants as well as my own.

INTRODUCTION

This Symposium followed by five years an earlier FDP symposium on the "Aerodynamics of Hypersonic Lifting Vehicles" that took place in Bristol, UK in April 1987. At that time there was considerable excitement in the hypersonic community because of the vehicle development programs — NASP, HERMES, HOTOL and SANGER. After about a twenty year moratorium, hypersonics was being actively reconstructed using the modern developments in CFD and experimental techniques. The atmosphere at Bristol was one of great optimism.

In the five years since Bristol, the vehicle programs have been severely cut back if not suspended. The ambitions of those programs turned out to be beyond our technology base. It has become apparent that improvement in our technology base would be neither simple nor quick. The mood in Torino was more subdued and more sober. Concentration was more on methodology than on vehicles, on generating the technology base that would be needed for future vehicle development.

This report follows the format introduced by Dr Wolfgang Schmidt in his review of the immediately preceding AGARD-FDP Symposium (AGARD-CP-498). His was one of the first Technical Evaluators' Reports to be incorporated into the symposium proceedings volumes. He has set an excellent example and I am most appreciative.

Statistics

42 papers were presented. The presenting authors were from Belgium (2), Canada (1), France (8), Germany (7), Italy (3), the Netherlands (1), Sweden (1), Turkey (1), the United Kingdom (6) and the United States (12).

The Symposium was organized into the following eight sessions:

(I) Design of Hypersonic Vehicles
(II) Facilities
(III) Instrumentation
(IV) CFD Validation and Data Accuracy
(V) Rarefied Gas; Real Gas; Chemistry
(VI) Boundary Layer *Transition*
(VII) High Enthalpy Nozzle Computation
(VIII) Development and Application of Codes

Each session is reviewed separately. The conclusions and recommendations made reflect the comments and discussion that attended each of the papers as well as the concluding General Discussion. The papers cited in this review will be identified by their paper number as they appear in this volume.

SESSION I:
DESIGN OF HYPERSONIC VEHICLES

Of the seven papers in this session, one dealt with design methodology [2], two with computational technique [1][4], two with controls and control effectiveness [3][5], one with the Pegasus vehicle [6], and one with vehicle design for planetary entry [7].

Perrier's paper [2] notes that when considering a vehicle whose feasibility is not assured, the first phase of the design must be devoted to a determination of feasibility. Only when feasibility is demonstrated can one proceed with the more usual ("linear") design methodology. His paper emphasizes searching for "critical points", and resolving the critical issues that will determine the viability of a design. He proposes a "development triad" of CFD, ground-based experiment and flight experiment that is strongly based on CFD. This is a very thought-provoking paper. The Pegasus vehicle which is the subject of paper [6] was designed entirely by analytic techniques and CFD, and it has been successfully flown. The flight performance was within the tolerances of the design methodology. It would seem therefore that the Pegasus vehicle would be a very good test bed for the flight evaluation of critical design issues.

Papers [1] and [4] both profess to deal with real gas computations including finite rate chemistry. Neither is fully satisfactory. The first contains some ideal gas assumptions within a Reynolds averaged Navier-Stokes formulation. Paper [4] purports to calculate the flow through a scramjet engine — an internal flow — using Euler equations. However good the chemistry, an Euler method cannot correctly model the mixing processes and the boundary layer effects that are especially critical for internal flows. A rather complete description of real gas issues is given in the paper by Deiwert [24].

The experiments on controls and control effectiveness presented in papers [3] and [5] could be interpreted only qualitatively since the results were obtained at Reynolds numbers that were rather low compared to prospective flight Reynolds numbers. They did emphasize the sensitivity of control effectiveness to transition location, pointing out the need perhaps for a simulation methodology for hypersonic flow akin to that developed for transonic flow by FDP Working Group 09.

Paper [7] by Smith describes the design of a class of related ballistic entry probes for planned ESA/NASA missions to Mars, Titan (a moon of Saturn), and Earth-return after comet sampling. The study notes that some needed aerothermal data are non-existent while others require extension of existing data to higher temperatures. Such data are needed in order to come up with credible designs. Facilities for generating the additional data do not now exist.

SESSION II:
FACILITIES

Of the four papers in this session, three describe new high performance wind tunnels [8][9][11], while the fourth [10] discusses the problem of finding suitable model surface materials so that the models will not burn up.

Paper [8] describes two ONERA hypersonic tunnels, the R5 at Meudon, which became operational in 1989, and the arc-driven high-enthalpy F4 at Fauga-Mauzac which has been run but is still in the process of its qualification tests. Tunnel R5 is a Mach 10, To = 1100 K, low Reynolds number facility that operates entirely in laminar flow, simulating Earth entry at altitudes of about 60 km. Real gas effects are minimal and so the tunnel may also be useful for appropriate types of CFD validation experiments. Tunnel F4 is designed as a real gas facility with reduced stagnation enthalpies, Ho/RTa, up to 200. The static conditions in the test section are non-equilibrium, with running times of about 80 msec. At the higher enthalpy levels, the tunnel is troubled by erosion from the electrodes and the tunnel walls resulting in contamination of the flow. While solutions to these contamination problems are studied, the tunnel can be run with reasonably clean flow at reduced stagnation enthalpies up to 100.

Paper [9] describes two high enthalpy shock tunnels, the heated driver shock tunnel (TH2) in Aachen and the free-piston driven shock tunnel (HEG) in Göttingen. The TH2 which has been in operation for some years has a number of conical nozzles for the Mach number range from 6-15 as well as a Mach 7 contoured nozzle. Test section stagnation conditions are deduced from pitot probe and stagnation point heat transfer probe measurements taken in the test section. However the test section flow is not in equilibrium. The HEG tunnel has a contoured nozzle for Mach 7-9, depending on stagnation enthalpy, and is one of a number of Stalker inspired facilities now being built. It is expected to get to higher densities than the T5 at Caltech. At the time of the Symposium, the HEG facility was undergoing calibration runs.

For the high performance tunnels just described, models must be able to rapidly reach desired surface temperature levels without eroding, and tunnel component surface materials must be able to diffuse heat rapidly in order that they do not erode or melt. Paper [10] describes a study to develop model surface materials having a specified thermal product, $\sqrt{\rho c k}$. Two materials have been developed and will be tested in the ONERA F4 tunnel at Le Fauga: a polymer material for medium temperatures (400 C) and zirconia plasma sprayed onto stainless steel via an intermediate MCrAlY bond coat for temperatures in the 1000-1300 C range. The author cautions that different surface coatings may have different catalytic properties and that the issue of "catalytic similarity" will have to be addressed.

Paper [11] describes a proposed upgrading of the LBK low pressure arc tunnel at DLR-Köln that is used for high enthalpy tests of thermal protection systems for spacecraft. For the operating stagnation pressures, the flow is expected to be frozen downstream of the nozzle throat.

Most hypersonic tunnels except perhaps for the piston driven shock tunnels have non-equilibrium flow in the test section. I here reiterate my comment made at the Symposium that this might not be a problem for blunt configurations since their flowfields tend to be equilibrated behind the bow shock waves. For slender configurations, there may well be a simulation problem in testing in a non-equilibrium flow.

SESSION III
INSTRUMENTATION

This session consisted of five summary papers delivered by members of the Instrumentation Subgroup of the AGARD/FDP Ad Hoc Study Group on Hypersonic Research and Technology. Since these summary presentations were based on the deliberations of the subgroup at a meeting that took place at Le Fauga (Toulouse) the week before the Symposium, there were no written versions of the remarks available at the Symposium. The speakers deserve our thanks for very competently putting together their summaries in a very short time.

The papers covered principally many of the new instrumentation technologies, for example: measurements of temperature and concentration using EBF, LIF, and CARS, pressure measurements using piezoelectric and piezoresistive transducer technology and pressure sensitive paints, force measurements using six component balances that are not yet commercially available, velocity measurements by a number of non-instrusive techniques, holographic flow visualization, and liquid crystal and infra-red mapping of temperature and heat transfer rates.

A good number of these technologies were labeled as "mature" even though they are not commercially available. Perhaps the word mature has a different meaning to the instrument developer than to the user. It is my view that an instrumentation technology is mature when it can be purchased by the user together with a procedure manual so that the user is independent of the developer. Many of the new techniques are not yet at this stage.

Many of the non-intrusive optical techniques are developed and tested using free jet and mixing layer flows — flows without boundaries. Can they be used with wall bounded flows? If they cannot, then they are much less useful. Many existing wind tunnels do not have the optical accesses necessary for these technologies. Attention must therefore be given to ways of retrofitting existing tunnels to accommodate optical instrumentation or else to the design of new test sections and model supports expressly for optical instrumentation.

SESSION IV
CFD VALIDATION AND DATA ACCURACY

The five-step validation roadmap stated by Marvin [17] is worth repeating here so that it can help sort the remaining six papers of the session: "(1) Define what critical performance information is needed and establish the corresponding code requirements; (2) Establish the appropriate governing equations and the corresponding physical and/or chemistry modeling requirements; (3) Identify or develop the appropriate validation data (building block data to guide and validate modeling and benchmark data to validate complex flow computations); (4) Perform computations for exact experimental conditions and test their sensitivity to the numerical and modeling assumptions; and (5) Document the code including its validation to the extent necessary to provide users with knowledge of the code's sensitivity to internal numerical parameters, grid refinement effects, the code's accuracy and range of capabilities." The building block experiments involve simple shapes that are used to test a code's ability to model the physics. The benchmark experiments are done on representative component configurations to test the numerical performance of a code. Marvin identifies building block and benchmark configurations for various vehicle components (forebodies, inlets, nozzles, etc.), and also provides some validation examples.

Paper [18] by Abgrall et al. is a summary report of the first two INRIA/GAMNI Workshops that took place in Antibes, France in January 1990 and April 1991. In the workshops, a number of computational groups, principally European, addressed a selection of hypersonic building block and benchmark experiments that had been commissioned for the workshops. The first experimental results were not available until they were presented at the first workshop. The results at the first workshop were somewhat variable. However they highlighted some of the experimental inadequacies and identified any gross errors that emerged in the computations. Some of these inadequacies were addressed between workshops so that at the second workshop, there could be a good focus on how features of the numerical techniques affected the computed results. The work is not yet completed as attested to by the scheduling of a third workshop based on the same experimental set and scheduled for January 1993.

In paper [19], Dolling makes the argument, based on his experimental studies of turbulent shock-wave/boundary-layer interactions, that presenting experimental results in terms of mean flow measurements alone masks inherent unsteadinesses in the flow. Furthermore, "steady" (Reynolds averaged) turbulent flow computations cannot distinguish between turbulence and the flow unsteadiness. Hence it is important that both experiment and computation represent the correct physics if there is to be any hope of developing a validated code for this problem.

Paper [20] is not particularly interesting either as a building block experiment or as a benchmark experiment. The experiment needs considerable improvement if it is to be the paradigm of a hypersonic internal flow, say for example that in a scramjet combustor. Paper [21] presents measurements of skin friction and heat transfer on three building block shapes at M = 6. The quoted uncertainties and data scatter in Cf and Stanton number are too large for the experiments to be useful in validation. A similar comment applies to paper [22] except that the presented data are much less scattered.

In paper [23], Oberkampf et al. give a very nice example of a well-designed well-executed CFD validation exercise, one in which proper attention is given to the correct modeling of the physics.

SESSION V
RAREFIED GAS; REAL GAS; CHEMISTRY

A principal contribution of the lead paper by Deiwert [24] is its complete description of real gas issues — namely the thermal non-equilibrium, the non-equilibrium species composition and the need to continually compute the thermodynamic and transport properties for the local mixture. He makes the further point that the ballistic range is the only experimental facility that can correctly mimic the non-equilibrium hypersonic viscous interaction effects especially on slender shapes. While that may be absolutely correct, it does not make the ballistic range an attractive validation facility unless ways can be found to obtain at least surface pressure and heat transfer measurements. In any case, real gas CFD should be used in conjunction with work done in shock tunnels and other high temperature facilities.

The next two papers deal with issues of chemistry. Paper [25] by Shahpar et al., with the aid of shock-tube experiments on M = 7 flow past a circular cylinder, looks at effects of different assumptions in the non-equilibrium chemistry of air in the CFD modeling of such a flow. Although different sources give different rate coefficients for the reactions, the computed results do not show great sensitivity to be choice. So the authors opt for the set that is easiest to use. Some residual discrepancies in the agreement between computation and experiment may be due to the assumption of equilibrium flow in the shock tube ahead of the cylinder bow shock wave. Paper [26] by Giordano and Marraffa presents a thermodynamic model for air in chemical equilibrium involving 13 species components and 47 chemical reactions, only nine of which are independent. A FORTRAN program has been written to effect the calculations and the results from the presented formulation agree with most data in the literature. The authors note significant discrepancies in the literature for the specific heats above 6000 K of O2 and other molecules and molecular ions. These discrepancies have little effect on the results since those species have small to negligible concentrations at those temperatures in equilibrium air.

The last paper of the session [27] by Çelenligil and Moss looks at rarefied gas simulations of aerodynamic flows relevant to the early stages of planetary entry (transitional flow between free-molecule and continuum) using the authors' recently developed three-dimensional Direct Simulation Monte Carlo (DSMC) method. This method has a five-species non-equilibrium reacting gas model and accounts for rotational and vibrational internal energies. It uses a variable hard sphere collision model with full thermal accommodation and diffuse reflection at the solid boundaries. There is good agreement of aerodynamic and heat-transfer coefficients with experiment for a delta wing experiment conducted at DLR-Göttingen. In subsequent discussion, the authors noted also the application of DSMC to geometric features of a vehicle (cowl lips with very small radius for example) where the geometric size may be comparable to the local mean-free-path.

SESSION VI
BOUNDARY LAYER TRANSITION

This session had four theoretical-computational papers and one experimental paper addressing critical issues for hypersonic flow such as effects of bluntness, chemistry and cross-flow on stability.

In paper [28], Herbert et al. emphasize the need for a correct calculation of the basic laminar flow over a blunted cone as prerequisite for the subsequent stability calculations. Since

PNS methods are not reliable in the nose region, they use a Navier-Stokes method out to s/R = 5, and a PNS method downstream of that location. Care is given also to the accuracy of the derivatives of the flow profiles since stability calculations are sensitive to these derivatives. The stability calculations were still in process at the time of the Symposium. Early results for one case showed good agreement with a recent calculation of Malik but were only qualitatively reminiscent of the Stetson data. Not addressed is the relationship of the stability characteristics to features of the swallowing phenomenon.

Paper [29] by Reed et al. is one of the first to consider effects of non-equilibrium chemistry on boundary layer stability. The reported shift of the second mode to lower frequencies present for both equilibrium and non-equilibrium chemistry makes this mode even more dangerous than for ideal gases. The paper looks also at effects of three-dimensionality on stability using a rotating cone flow to simulate swept-wing boundary layers. The suggested crossflow transition correlation is suspect since the crossflow velocity appears in such a way that it cancels out of the correlation. This requires reexamination.

In paper [30], Poll develops expressions for equilibrium real-gas attachment-line heat transfer for swept leading edges in both laminar and turbulent flow, including effects of surface transpiration. These expressions contain a mixture of perfect gas factors (evaluated for $\gamma = 1.4$) and real gas factors. Some of the expressions do not seem to be dimensionally consistent. Transition is handled simply through an attachment line Reynolds number criterion taken from low speed flow. Calculations based on the presented expressions show that real gas heat transfer exceeds that for perfect gases and that this difference is much more pronounced for turbulent flow than for laminar.

Paper [31] by Simen and Dallman addresses past discrepancies between theory and Stetson's stability results for a pointed cone. They show that with careful attention to coordinate system and metric for both the basic flow profiles and the stability of those profiles, they can attain agreement with Stetson's growth rates for both first and second modes. This paper should help in clarifying some of the disputes in the literature regarding the correct inclusion of curvature effects for this particular flow.

Paper [32] by Hillier et al. describes experiments principally on blunted cones conducted in the M = 9 gun tunnel at Imperial College. The results show that the tunnel has full laminar to full turbulent capability and can produce reliable laminar and turbulent heat transfer data. The effect of nose bluntness on transition and the relation to entropy layer swallowing is nicely demonstrated. It is important however that the tunnel disturbances be measured and their spectra ascertained so that one can decide whether the tunnel is quiet enough for the presented transition data to be meaningful for flight in the atmosphere.

A disappointment in this session and in the Symposium in general is that the issue of transition estimation was almost totally ignored. The computational community should become more familiar with the present state of transition estimation toward inclusion of "transition modules" in CFD flowfield codes.

SESSION VII
HIGH ENTHALPY NOZZLE COMPUTATION

Of the four papers in this session, those of Marmignon et al. [33] and Zeitoun et al. [34] are distinguished in that they present fully non-equilibrium Navier-Stokes calculations. Furthermore, they have one example in common so that comparison between the two is facilitated. They both consider a five species model of air with 17 chemical reactions (but not the same set of reaction rates) and allow for vibrational non-equilibrium as well. The case that they treat in common is the Marseille wind tunnel conical nozzle which is also an Antibes Workshop test case. Zeitoun et al. find little difference in exit Mach number and translational temperature between their Navier-Stokes calculation and an Euler calculation for the same conditions. However, their exit Mach number of 11.1 to 11.3 is below the value of about 12.5 found by Marmignon et al. There are some differences in translational temperature and in the "frozen" vibrational temperature of nitrogen between the two groups. Both groups state that the boundary layer effects are slight. The differences in the computed results are due likely to the differences in the chemical models used. Marmignon et al. [33] complete their paper by a presentation of results for the ONERA F4 tunnel nozzle. While the exit velocity profile is quite uniform, the static temperature and therefore the Mach number are not. The Mach number varies from about 22.5 on the axis to about 16 at the edge of the wall boundary layer. It is assumed in both papers that the nozzle boundary layers are laminar. The validity of this assumption is not known. Early experiments in these tunnels may provide the answer. Neither group has addressed the issue of turbulent boundary layers on the nozzle walls.

Paper [35] presents the results of what is principally a one-dimensional non-equilibrium study of the Aérospatiale SIMOUN plasma wind tunnel nozzle in which several chemical models are tested. Boundary layer effects are mostly ignored. While the different non-equilibrium models give fair agreement for the exit pressure, the experimental results are higher and closer to the equilibrium values. Introducing a simple boundary layer correction into the calculation has the effect of restricting the expansion slightly and yielding non-equilibrium results that are close to experiment. In this case, even small boundary layer effects are significant.

Paper [36] presents a parabolized Navier-Stokes method coupled with a least-squares optimization procedure for hypersonic wind tunnel design. The technique is motivated by difficulties with method-of-characteristics coupled with boundary layer procedures at Mach numbers greater than 10. The new technique is applied to the design of helium tunnels and so does not test any non-equilibrium issues. The author does however demonstrate that the optimization technique helps in meeting flow uniformity objectives.

One may conclude from this session that viscous effects should be included in any hypersonic nozzle calculation, and that an optimization technique may be helpful in achieving greater flow uniformity. The various methods for handling non-equilibrium chemistry need further comparative study, and not least of all, the possibility of turbulent flow on the nozzle walls has to be considered.

SESSION VIII
DEVELOPMENT AND APPLICATION OF CODES

There were six papers in this session (paper [40] was withdrawn) each of them giving emphasis to some different aspect of code development.

Paper [37] by Wanie et al. tells of a set of codes in use at MBB going from geometry definition through grid generation to inviscid and viscous codes and finally a code for the postprocessing of results. Different levels of computation are used in the different stages of vehicle development. The paper concentrated on a Navier-Stokes code, NSFLEX, and a second order boundary layer code, SOBOL, used most often with an Euler code. These codes have non-equilibrium chemistry modules available. Transport coefficients seem to be simply determined without the use of mixture rules. Turbulent flows are handled using a Baldwin-Lomax model. There is no provision for estimating transition location. It was noted in response to a question that the SOBOL code gives better definition of boundary layer details than NSFLEX. Accordingly it was suggested that an NSFLEX solution could be followed by one postprocessing SOBOL run to obtain the boundary layer detail.

Paper [38] by Vos et al. emphasizes multi-block techniques that can be efficiently used by parallel computers. The codes to which the technique is applied are somewhat incomplete. The presented Euler code can handle non-equilibrium chemistry but of course ignores viscous effects. The presented Navier-Stokes code is for perfect gases and the transport coefficients are assumed constant, which is of course a gross oversimplification. Nevertheless, the efficiency of the presented multi-block solver for parallel computation was demonstrated.

The paper by Peraire et al. [39] deals with the Euler flow of a perfect gas. The paper extends an algorithm, originally developed for transonic flow, to the calculation of hypersonic flow on unstructured tetrahedral grids. The extension to hypersonic flow introduces some instabilities which are countered by increased numerical dissipation. A multigrid capability has also been developed.

Paper [41] is a direct comparison of independently developed high-resolution, three-dimensional upwind TVD Euler solvers. The paper is in a sense a progress report in that it expresses the belief that such schemes are the most reliable for handling the strong discontinuities experienced in high speed flows, however, the authors were not able to realize grid-converged solutions for their test cases.

Paper [42] describes a procedure wherein an overall computation of a configuration is done using an Euler plus boundary layer technique, then followed by local application of a Navier-Stokes solver in difficult regions such as those involving separation and recirculation. The primary example presented is that of the owl-like canopy of the HERMES vehicle. The scheme thus approaches the results of a full Navier-Stokes solver for complex configurations that could not be handled by a Navier-Stokes solver over the complete flowfield using present computers.

In paper [43], Grasso and Belluci present a finite-volume Navier-Stokes procedure based on a second order TVD formulation that encompasses thermal and chemical non-equilibrium and proper computation of transport coefficients. They apply the technique to two simple two-dimensional flows, the flow past a wedge and the flow over a cylinder whose axis is normal to the flow direction. It would be interesting to see how their technique applied to the Marseille and F4 nozzles would compare with the results of Marmignon et al. [33] and Zeitoun et al. [34].

All of the efforts reported in this session were undertaken with the conviction that a proper computation of flowfields is necessary to obtain correct aerodynamic information. It is known that non-equilibrium effects can influence moment coefficients of entry vehicles. Not unexpectedly, however, all of the presented codes are in some sense incomplete. The Euler codes omit viscous effects and aerodynamic heating considerations entirely. The viscous codes are predominantly for laminar flow. The few that include a turbulence model do so only in a very crude way. All the viscous codes share the deficiency of ignoring transition estimation. The next phase in code development requires increased attention to transition and to turbulent flow in order to have proper assessment of thermal protection needs.

CONCLUDING REMARKS

Many of my basic conclusions were given in my remarks that opened the General Discussion at the end of the Symposium and they can be found at the end of this document. Nevertheless a few more remarks are in order.

The objectives of the Symposium as listed in the Call for Papers are for the most part realized. Computational and experimental tools are noticably improved over where they were five years ago. But the improvements are not as much as we would have liked. Hypersonic internal flows and engine/airframe issues were not discussed. Radiative gasdynamics, turbulence and transition estimation were for the most part ignored. Flight testing was mentioned, but the problems of developing meaningful flight tests were not really addressed. We see much imagination in the development of improved CFD tools but the validated set of "production" codes has yet to appear.

The absence of a viable vehicle development program has clearly slowed the pace of technology development. In order to be ready for a resumption in vehicle development, it is important that facility and instrumentation programs underway be completed, and that the promising CFD codes continue in their development. As is evident from this report, I am a strong proponent of viscous codes for hypersonic flows, in order that viscous interactions and aerodynamic heating be properly treated.

While hypersonic vehicle development is again in a lull period, let us not despair. The interest of the world in activities in space is permanent, and therefore there will doubtless be continuing interest in the vehicle technology that will enable us to exploit the opportunities of space. Let us continue in a rational, continuous and sustained effort to provide the necessary technology base for this important activity.

CFD ANALYSIS OF HYPERSONIC, CHEMICALLY REACTING FLOW FIELDS

T. A. Edwards
NASA Ames Research Center
Moffett Field, California 94035
USA

1. SUMMARY

Design studies are underway for a variety of hypersonic flight vehicles. The National Aero-Space Plane will provide a reusable, single-stage-to-orbit capability for routine access to low earth orbit. Flight-capable satellites will dip into the atmosphere to maneuver to new orbits, while planetary probes will decelerate at their destination by atmospheric aerobraking. To supplement limited experimental capabilities in the hypersonic regime, computational fluid dynamics (CFD) is being used to analyze the flow about these configurations. The governing equations include fluid dynamic as well as chemical species equations, which are being solved with new, robust numerical algorithms. Examples of CFD applications to hypersonic vehicles suggest an important role this technology will play in the development of future aerospace systems. The computational resources needed to obtain solutions are large, but solution-adaptive grids, convergence acceleration, and parallel processing may make run times manageable.

2. LIST OF SYMBOLS

c	species mass fraction
e	specific total energy
p	pressure
u,v,w	Cartesian velocity components in x,y,z directions
$\dot{w}$	species production rate
A,B,C	flux vector Jacobians
D	multicomponent diffusion coefficient
E,F,G	dependent variable flux vectors in x,y,z directions
M	molecular weight
Pr	Prandtl number
Q	dependent variable vector
Re	Reynolds number
T	temperature
γ	specific heat ratio
$\tilde{\gamma}$	effective specific heat ratio
ε	specific internal energy
κ	thermal conductivity
μ	molecular viscosity
ρ	density
τ	shear stress tensor
$\Re$	universal gas constant

Subscripts

c	chemical species variables
f	fluid dynamic variables
i	chemical species counter, grid index counter
v	thin-layer viscous component

3. INTRODUCTION

The difference between supersonic and hypersonic flow is a rapid increase in the total energy of the flow as the freestream Mach number increases beyond about three. Kinetic energy is transformed to thermal energy when air passes through shock waves and is slowed near the body surface by viscous stresses. At moderate temperatures, air exhibits properties that are well predicted by kinetic theory for a diatomic gas. However, at sufficiently high temperatures, the molecules that comprise air (primarily diatomic molecules of oxygen and nitrogen) undergo chemical reactions that alter its thermodynamic properties. The high-temperature air transfers great amounts of heat to the vehicle. This thermal load must be predicted and managed to protect the structure of the vehicle. Chemical reactions also affect the aerodynamics of hypersonic vehicles, which in turn can impact propulsion system performance, vehicle forces and moments, and mission capabilities.

Proposed vehicles for the hypersonic regime have brought forth a need for more accurate modeling of the aerothermal environment. The National Aero-Space Plane (NASP), under development for the past several years, is a single-stage-to-orbit, conventional takeoff and landing vehicle for rapid, routine access to space. Flight-capable satellites of the future will dip into the atmosphere at hypersonic speeds to perform orbit-change maneuvers. Probes such as Galileo will dissipate kinetic energy by aerobraking in planetary atmospheres. For all of these vehicles, sustained flight at hypersonic speeds is a critical capability. Requirements go beyond merely surviving the passage through high Mach number conditions, but now demand efficient, routine operations at Mach 15 to 25.

The traditional process of analysis and experimentation to develop vehicle concepts is hampered by the limitations of ground-based facilities in reproducing hypersonic flight conditions. Continuous-flow tunnels require too much power to operate at high Mach numbers, while shock tunnels and ballistic ranges have short test duration. Thus, hypersonic flow research is relying heavily on computational fluid dynamics (CFD) to guide experimental activity and provide performance estimates of vehicle concepts.

Until recently, CFD had not been applied to hypervelocity flow problems. Extending CFD technology to the hypersonic regime required two major efforts: developing robust numerical algorithms, and modeling air chemistry effects. Conventional algorithms based on central differences can generate spurious pre- and post-shock oscillations that degrade the accuracy of solutions near flow discontinuities. For the strong shocks present in hypersonic flows, these oscillations can be destabilizing and cause solutions to diverge. Upwind algorithms have now demonstrated superior performance in solving hypersonic flows. Real gas models are available to model several approximations to the thermochemical state of air. These include the widely used perfect gas model, along with the more general equilibrium, nonequilibrium, and frozen chemistry assumptions.

This paper outlines the theory, implementation and application of hypersonic CFD. First, the governing equations for fluid motion and chemical species are described. Next, solution algorithms used for high-speed flows are presented. The problem of coupling the fluid and chemistry equations is addressed, and then some typical applications are presented. In light of the large computer resources needed for these solutions, some approaches to improving code efficiency are discussed.

4. GOVERNING EQUATIONS

Hypersonic flow predictions need to provide estimates of not only global vehicle performance parameters, such as forces and moments, but also parameters specific to particular systems or components, such as heat transfer rates, inlet mass capture, and kinetic energy efficiency. Accurately predicting these quantities requires a mathematical model with few simplifying assumptions. This section describes the partial differential equations that govern the motion of a fluid and the concentration of chemical species in a reacting gas. Coupling these two equation sets provides the capability to model the flow of a reacting gas.

4.1 Fluid Dynamic Equations

Navier and Stokes in the 1800's independently derived the general set of equations for the flow of a Newtonian fluid. Two important subsets of the Navier-Stokes equations are widely used for hypersonic flow computations: the thin-layer Reynolds-averaged Navier-Stokes equations, and the parabolized Navier-Stokes (PNS) equations. Within the limitations of their approximations, each of these equation sets yields a substantial reduction in the computational cost with little loss of accuracy.

4.1.1 Thin-Layer, Reynolds-Averaged Navier-Stokes Equations

For flight vehicle applications, the thin-layer approximation is usually invoked, because viscous effects are generally confined to a boundary layer near the surface. This approximation neglects viscous derivatives in the directions tangent to the body surface, simplifying the equations somewhat and alleviating grid resolution requirements substantially. The resulting equation set is the thin-layer Navier-Stokes equations, which in Cartesian coordinates is written

$$\frac{\partial Q}{\partial t}+\frac{\partial E}{\partial x}+\frac{\partial F}{\partial y}+\frac{\partial G}{\partial z}=\frac{\partial G_v}{\partial z} \tag{1}$$

where

$$Q=\begin{bmatrix}\rho\\ \rho u\\ \rho v\\ \rho w\\ e\end{bmatrix}\qquad E=\begin{bmatrix}\rho u\\ \rho u^2+p\\ \rho uv\\ \rho uw\\ u(e+p)\end{bmatrix} \tag{2}$$

$$F=\begin{bmatrix}\rho v\\ \rho uv\\ \rho v^2+p\\ \rho vw\\ v(e+p)\end{bmatrix}\qquad G=\begin{bmatrix}\rho w\\ \rho uw\\ \rho vw\\ \rho w^2+p\\ w(e+p)\end{bmatrix}\qquad G_v=Re^{-1}\begin{bmatrix}0\\ \tau_{xz}\\ \tau_{yz}\\ \tau_{zz}\\ \beta_z\end{bmatrix}$$

The viscous flux terms are given by

$$\begin{aligned}\tau_{xz}&=\mu(u_z+w_x)\\ \tau_{yz}&=\mu(v_z+w_y)\\ \tau_{zz}&=\frac{4}{3}\mu w_z-\frac{2}{3}\mu(u_x+v_y)\\ \beta_z&=\gamma\kappa Pr^{-1}\partial_z\varepsilon+u\tau_{xz}+v\tau_{yz}+w\tau_{zz}\end{aligned} \tag{3}$$

and the internal energy ε can be found from

$$\varepsilon=\frac{e}{\rho}-\frac{1}{2}(u^2+v^2+w^2) \tag{4}$$

These equations are written in nondimensional form by normalizing flow quantities by their freestream values. The Reynolds number and Prandtl number appear in the equations as a result. The viscosity, conductivity and specific heat ratio are material properties given by constitutive relations specific to the composition and thermodynamic state of the fluid.

Pressure is related to the conserved flow variables by the ideal gas equation of state

$$p = (\gamma - 1)[e - \frac{1}{2}\rho(u^2 + v^2 + w^2)] \qquad (5)$$

or in chemically-reacting flows by Dalton's law of partial pressures

$$p = \sum_{i=1}^{n} p_i = \sum_{i=1}^{n} \frac{\rho_i \Re T}{M_i} \qquad (6)$$

Usually, a coordinate transformation is applied to these equations so as to map an arbitrarily shaped body surface to a constant coordinate surface. This makes the thin-layer approximation possible for curved surfaces, at the expense of generating smooth grids about complex shapes.

The grid density and computer resources required to resolve a turbulent flow using the thin-layer Navier-Stokes equations would be prohibitive. Therefore, a final constitutive relation is needed for the turbulent scales of motion smaller than the grid. First, the equations are Reynolds-averaged, wherein turbulent fluctuations in the dependent variables are statistically averaged. As a result, the effect of turbulence appears in the Navier-Stokes equations in the same form as the stress tensor and the additional terms are referred to as Reynolds stresses. A model then defines the Reynolds stresses in terms of the dependent variables. The most straightforward of these is the algebraic turbulent eddy viscosity formulation (cf. Ref. 1), which augments the molecular viscosity μ. More sophisticated models have also been implemented that solve partial differential equations for the production and dissipation of turbulent kinetic energy (Ref. 2).

The phenomenon of boundary layer transition is even more difficult to model. Hypersonic flight conditions often occur at relatively low Reynolds numbers, so a large portion of the flow can be transitional. Accurately predicting the onset and development of turbulence is important to calculating aerodynamic and propulsion system performance parameters. A simple transition model that has shown promise in validation studies makes use of empirical correlations for the location of transition onset and the length of transitional flow, then modulates the eddy viscosity through the transition region (Ref. 3).

4.1.2 Parabolized Navier-Stokes Equations

If it is further assumed that the flow is steady, that it is supersonic outside the boundary layer, and that there is no streamwise separation, the Navier-Stokes equations become parabolic (except in the boundary layer). The PNS equations can be solved with a very efficient space-marching procedure that yields flow solutions one to two orders of magnitude faster than time-dependent formulations. Although the assumptions for the PNS equations are very restrictive, there is still a wide class of problems that can be addressed. For example, most hypersonic forebody and afterbody flows can be analyzed with this approach. PNS solutions for inlet and combustor flows may not be accurate, but nonetheless they could be useful for conceptual design studies. Lawrence et al. (Ref. 4) give a complete description of the theory, implementation and application of this approach.

4.2 Air Chemistry Equations

The chemical behavior of air depends on the flight conditions. Below about 2000 K, deviations from perfect gas behavior are small. In flight, this temperature is first reached behind normal shocks at a Mach number of about six. However, most ground test facilities have very low freestream temperatures and so real gas effects are difficult to obtain, even at very high Mach numbers. The perfect gas equation of state is thus sufficient for many hypersonic flows when the peak temperature is below this limit.

When the temperature in the flow is high enough to cause air to react, the density then comes into play in determining the character of the fluid/chemistry interaction. At relatively low altitudes, the density and intermolecular collision rate are very high, so reactions proceed to equilibrium very rapidly. In the hypothetical limit of infinite reaction rates, a universal state of chemical equilibrium exists. At higher altitudes, the chemical relaxation time increases and eventually becomes significant compared to the flow convection time. This creates a flow that is in a state of chemical nonequilibrium as it traverses the body. Opposite the equilibrium flow approximation is frozen flow, where reaction rates are set to zero. Invoking these approximations simplifies the solution procedure and reduces the computer time. The models and their implementations are described below.

4.2.1 Equilibrium Air

The equilibrium composition of air is a unique function of its thermodynamic state. Implementing the equilibrium model in a computer program can be accomplished by the table look-up approach or the curve-fit approach. In the table look-up approach, the equilibrium data are stored as a database in matrix form while the flow solution is advanced. When thermodynamic data are needed in the flow solver, the information is retrieved from the database. The efficiency of this approach suffers from high input/output overhead. In the curve-fit approach, the equilibrium data are approximated by splines (Ref. 5). The spline coefficients store the data much more compactly, and the splines are evaluated as needed while the flow solution advances. A recent enhancement of the curve-fit method involves generating spline coefficients using only a subset of the database that is applicable to the conditions for the current problem (Ref. 6).

The assumption of chemical equilibrium imposes only a small computational penalty, about 15%, over the perfect gas model. The penalty is small because no additional partial differential equations are solved. The perfect gas equation of state is modified by an "effective" specific heat ratio, γ, that is evaluated by the table look-up or curve fit method:

$$p = (\tilde{\gamma} - 1)[e - \frac{1}{2}\rho(u^2 + v^2 + w^2)] \qquad (7)$$

4.2.2 *Nonequilibrium Air Chemistry*

Simulating the properties of chemically reacting air requires knowing the concentration of all the species at all points in the flow field. This calls for solving transport equations for each of the species present in the flow. These equations are written as

$$\frac{\partial \rho_i}{\partial t} + \frac{\partial \rho_i u}{\partial x} + \frac{\partial \rho_i v}{\partial y} + \frac{\partial \rho_i w}{\partial z} = Re^{-1}\rho D\frac{\partial c_i}{\partial z} + \dot{w}_i \qquad (8)$$

The left hand side of the equation represents the convective terms. The first term on the right hand side accounts for the diffusion of species due to a concentration gradient. The second term, $\dot{w}_i$, accounts for the net production of species arising from chemical reactions. This term is dependent on the forward and backward rates of the reactions being modeled, which will differ with the gas species and reaction set of the gas model.

A five-species model is sufficient to model chemically reacting air over a wide range of conditions. These species are: atomic and molecular nitrogen (N_2 and N), atomic and molecular oxygen (O_2 and O) and nitric oxide (NO). The following six reactions govern the production and destruction of species:

$$\begin{array}{llcl}
(1) & O_2 + M & \rightleftarrows & 2O + M \\
(2) & N_2 + M & \rightleftarrows & 2N + M \\
(3) & N_2 + N & \rightleftarrows & 2N + N \\
(4) & NO + M & \rightleftarrows & N + O + M \\
(5) & NO + O & \rightleftarrows & O_2 + N \\
(6) & N_2 + O & \rightleftarrows & NO + N
\end{array} \qquad (9)$$

where M represents a catalytic third body. Rate constants have been determined for each of these reactions (Ref. 7), so the local thermodynamic state and gas composition determine the rate of production of each species. Thus, the nonequilibrium gas model requires solving an additional set of partial differential equations, the number of equations being dependent on the number of species in the model. In this instance, four species continuity equations are solved (the concentration of the fifth species is determined by requiring the concentrations to sum to unity) in conjunction with the five equations for the fluid dynamics. If the density is low enough, thermal nonequilibrium can become an important effect, requiring a multiple-temperature model.

4.2.3 *Frozen Flow*

If the temperature of a reacting flow drops below the activation temperature for reactions to continue, such as in a sudden expansion, the mixture will be "frozen" in a nonequilibrium state. It is often useful to assume that frozen flow is a limiting case to assess the sensitivity of the flow field to the reaction rates. This, along with the equilibrium flow approximation, bound the chemical kinetics and hence their effect on the overall flow field.

In the frozen flow approximation, reaction rates are set to zero. This model still allows for nonuniform mixtures and variable thermodynamic properties, though, so the species continuity equations are still needed. However, a computational saving arises by no longer needing to evaluate the reaction and species production rates. This reduces the computational effort in two ways: each time step requires fewer mathematical operations, and the equations are not as stiff as in reacting flows, so larger time steps are possible, yielding faster convergence.

4.3 Solution Algorithms

The most straightforward approach to discretizing the governing equations is to approximate derivatives by central differences, for example

$$\frac{\partial F}{\partial x} \approx \frac{F_{x+\Delta x} - F_{x-\Delta x}}{2\Delta x} \qquad (10)$$

At flow discontinuities such as shock waves, central differencing schemes generate spurious oscillations, which must be suppressed with artificial dissipation. For the strong shocks present in hypersonic flows, the artificial dissipation required to stabilize the numerical solution algorithm can be large enough to degrade the accuracy of the solution. New upwind algorithms are more robust and are tailored to the equations of gas dynamics, enabling accurate solutions of strong shocks. Two classes of schemes widely used for solving hypersonic flows are flux-split schemes and Riemann solvers.

4.3.1 Flux-Split Schemes

In the flux-splitting approach, the flux vector F in Eq. 1 is separated into the sum of two vectors, one associated with the positive eigenvalues of the flux Jacobian matrix $\partial F/\partial Q$, and the other with the negative values. Then appropriate one-sided differences are used on the split terms. Many splitting schemes are possible as long as the eigenvalues of the split flux Jacobians are positive or negative definite. For example, applying the Steger-Warming scheme (Ref. 8) to the flux vector F in Eq. (1) gives

$$F^{+} = \frac{1}{2}(I + \mathrm{sgn}\ A)F \qquad (11)$$
$$F^{-} = \frac{1}{2}(I - \mathrm{sgn}\ A)F$$

where A is the flux Jacobian associated with the flux vector F, and

$$\mathrm{sgn}\ A = R(\mathrm{sgn}\ \Lambda)R^{-1} \qquad (12)$$

where R^{-1} is the matrix whose rows are the left eigenvectors of A, and (sgn Λ) is the diagonal matrix having either 1 or -1 at the ith position according to the sign of the ith eigenvalue of A. Derivatives of the split fluxes are then discretized with a one-sided difference scheme. This is analogous to adding dissipation to a central difference scheme such that the dissipation automatically increases near flow discontinuities such as shock waves, yielding improved stability without an overall loss of accuracy.

4.3.2 Riemann Solvers

Riemann solvers are a class of schemes that solve local Riemann problems at each point in the computational grid. These schemes have the attributes of monotonicity, enabling sharp resolution of discontinuities, and robustness for capturing strong shocks. The Riemann problem for one-dimensional inviscid flow is written

$$\frac{\partial Q}{\partial t} + \frac{\partial F}{\partial x} = 0 \qquad (13)$$

Equation (13) can be solved exactly, but this requires an expensive iterative approach. Most schemes linearize the equation and solve an approximate Riemann problem to obtain a value for F:

$$\frac{\partial Q}{\partial t} + A\frac{\partial Q}{\partial x} = 0 \qquad (14)$$

where A is the flux Jacobian matrix. Then, the value of F at an interface between two nodes i and i+1, denoted by $F_{i+1/2}$, can be found from Roe's scheme (Ref. 9), for example, which gives

$$F_{i+1/2} = \frac{1}{2}\{F_i + F_{i+1}\} - \frac{1}{2}\left|A_{i+1/2}\right| \cdot (Q_i - Q_{i+1}) \quad (15)$$

Here $|A|$ denotes the matrix with the same eigenvectors as A, whose eigenvalues are the absolute values of the eigenvalues of A. The flux at the interface between nodes can then be used in forming the necessary differences.

4.4 Fluid/Chemistry Coupling

As noted above, the energy equation contains terms relating to the fluid dynamics and the chemical kinetics, and thus couples the Navier-Stokes equations to the species continuity equations. A fully implicit solution procedure therefore requires the simultaneous solution of all the equations. This increases the matrix bandwidth considerably. For example, the Navier-Stokes equations alone produce 5x5 block tridiagonal matrices. With the four species equations needed in the present air chemistry model, the coupled system produces 9x9 blocks. The form of the flux Jacobian in the strongly-coupled system can be written

$$A = \begin{bmatrix} A_{ff} & A_{fc} \\ A_{cf} & A_{cc} \end{bmatrix} = \begin{bmatrix} \frac{\partial F_f}{\partial Q_f} & \frac{\partial F_f}{\partial Q_c} \\ \frac{\partial F_c}{\partial Q_f} & \frac{\partial F_c}{\partial Q_c} \end{bmatrix} \qquad (16)$$

where Q_f signifies fluid dynamic variables and Q_c signifies chemical species, and similarly for the flux vector F (Ref. 10). The number of mathematical operations needed to solve block tridiagonal systems is proportional to the cube of the block dimension, so the additional cost is considerable even for this relatively simple model. Therefore, alternative means of coupling the fluids and chemistry are also under investigation.

Certain hypersonic flow problems suggest a loosely coupled approach. This is most effective when the energy associated with chemical reactions is small compared to the total energy. To take advantage of this, the two equation sets are solved in a loosely coupled procedure (Ref. 11). In this approach, the Navier-Stokes equations are solved separately from the species continuity equations, which presupposes a flux Jacobian of the form shown below:

$$A = \begin{bmatrix} A_{ff} & 0 \\ 0 & A_{cc} \end{bmatrix} = \begin{bmatrix} \frac{\partial F_f}{\partial Q_f} & 0 \\ 0 & \frac{\partial F_c}{\partial Q_c} \end{bmatrix} \qquad (17)$$

Invoking this assumption allows the implicit operator to be solved as separate 5x5 and 4x4 block tridiagonal systems, which is much more efficient than solving the 9x9 system. The coupling is achieved through an adjunct equation of state that provides thermodynamic variables needed in the Navier-Stokes equations, while the species continuity equations are solved assuming that the velocity and flow energy are temporarily fixed, as shown in Fig. 1. Additional source terms appear in the energy and momentum equations as a result of the chemical reactions. By alternating iterative updates between the two equation sets, the coupling mechanism is able to transfer information between the fluid dynamics and chemistry, retaining the physical interaction of the two phenomena.

The advantage to this approach is a large reduction in computational effort needed to perform an iteration of the solution algorithm. Weakening the coupling between the equation sets may reduce the convergence rate and stability bound, so the costs and benefits must be weighed to determine the superior approach in a particular application. The following examples demonstrate the viability of both approaches.

5. HYPERSONIC VEHICLE APPLICATIONS

NASA's hypersonic research program has tailored the development of CFD codes for promising hypersonic vehicle concepts. For example, a horizontal take-off and landing, single-stage-to-orbit vehicle derives its efficiency from an airbreathing hypersonic propulsion system called a scramjet (supersonic combustion ramjet). This propulsion system uses hydrogen fuel, which burns in a supersonic stream of high-pressure, high-temperature air flowing into the engine. Using atmospheric oxygen eliminates the need to carry an oxidizer and thus benefits the payload capacity and gross weight substantially. However, scramjet propulsion has yet to be demonstrated in flight and is difficult to test in ground-based facilities. Therefore, CFD is playing a major role in the analysis of scramjet propulsion.

Scramjet propulsion systems are highly integrated with the airframe. Figure 2 shows how the forebody serves the function of a compressor for air approaching the inlet. The internal portion of the flow consists of a combustor, where the fuel mixes and ignition occurs. Because of the short engine length, the fuel is still burning as it leaves the nozzle. The reacting mixture flows along the afterbody, where a significant amount of thrust results from high pressure on the backward-facing surface. Thus, scramjet propulsion systems begin at the nose of the vehicle and continue to the tail.

As a result of the highly integrated airframe/propulsion system, CFD analysis of this system must also be integrated. Codes must be capable of solving the external flow of air on the forebody, then the internal combusting hydrogen-air flow inside the scramjet, and finally the mixture of reacting flow leaving the nozzle and merging with the external flow along the afterbody. To meet this challenge, PNS and Navier-Stokes codes have been developed with air and hydrogen-air chemistry models to solve the nose-to-tail flow field. Figure 3 shows how these codes are applied to the nose-to-tail problem.

The Navier-Stokes codes use a zonal approach, where the solution domain is subdivided into several subdomains. This technique has several advantages. Small subdomains reduce the computer memory requirement and simplify grid generation for complex shapes. Also, the governing equations may vary from one zone to the next. For example, on the forebody, the PNS equations with an air chemistry model are sufficient. The scramjet module requires an internal flow capability with a hydrogen-air combustion model and an advanced turbulence model for mixing streams. Hence, for a given problem, these codes may be arranged and applied so as to give an accurate answer at the lowest cost of computer time and manpower. At NASA Ames Research Center, CFD code development in support of hypersonics has produced a set of Navier-Stokes and PNS codes using the strongly coupled approach (named TUFF and STUFF, respectively), and a set using the loosely coupled approach (named CNS and UPS, respectively).

To demonstrate fluid/chemistry modeling in these CFD codes, two applications are considered. The first, a generic hypersonic configuration, shows the importance of modeling nonequilibrium air chemistry effects in hypersonic propulsion systems. The second case simulates a ballistic range test to validate the accuracy of real-gas CFD predictions.

5.1 Hypersonic Body

The McDonnell-Douglas Generic Option Blended Wing-Body has been used extensively for code validation. This model incorporates many of the features of proposed hypersonic configurations: small nose radius, compression ramps on the forebody, and an afterbody expansion surface. Tests on the Generic Option have been conducted in shock tunnels at Mach numbers up to 19. However, because of the low total temperature of the flow, real gas effects were not present in the experiments. A numerical experiment was performed by solving the flow about the Generic Option forebody at freestream conditions expected to generate nonequilibrium effects (Ref. 12). The investigation centered on the impact real gas modeling has on the flow into the inlet.

Figure 4 shows the predicted concentration of atomic oxygen at several stations along the Generic Option forebody. Oxygen has a much lower dissociation energy than nitrogen, so it is the first atomic species present in reacting air flows. Outside the bow shock, the concentration is zero because the flow is unaffected by the presence of the body. The highest concentration of atomic oxygen is on the windward centerline. Here, the flow has traversed the bow shock and two additional shocks arising from the compression ramps, so it has undergone the most heating in the flow field. Figure 5 compares the thermal boundary layers predicted at the inlet centerline using perfect gas, nonequilibrium and equilibrium air models. Through most of the shock layer, the nonequilibrium model produces the lowest temperature. Whereas the equilibrium model causes rapid recombination of atomic species upstream of this body station, the nonequilibrium result indicates that energy absorption through recombination is still occurring at this station near the inlet. Near the wall, the temperature profiles for the equilibrium and nonequilibrium models cross.

The nonuniform gas composition entering the inlet reduces propulsion system efficiency. Furthermore, the results in Fig. 5 indicate that the perfect gas and equilibrium chemistry models are not necessarily limiting cases that bound the nonequilibrium flow characteristics. Hence, systems designed using simpler gas models need to verify performance estimates under nonequilibrium chemistry conditions.

5.2 Shock Generator

A shock generator shape tested in the NASA Ames Ballistic Range further exemplifies real-gas effects on hypersonic aerodynamics. The body is a five-degree sphere-cone with annular bumps whose purpose was to generate shock waves embedded in the bow shock layer. The fluid in the shock layer partially dissociates because of its passage through the strong bow shock. Therefore, predicting the location of embedded shocks requires modeling the nonequilibrium air chemistry. Figure 6 is a shadowgraph of the shock generator at a flight Mach number of 14.4 and an angle of attack of 0 deg. The computationally predicted shock pattern is superimposed on the photograph. The computation accurately predicts the bow shock and embedded shocks. This flow exhibited significant dissociation of oxygen and thus helps validate the accuracy of reacting flow computations.

Figure 7 shows the same body at 6 deg. incidence. The atomic oxygen concentration contours indicate significant dissociation. Atoms on the windward side convect around the body to the leeside, creating a thick layer of dissociated oxygen. Predicted values of the forces and moments on this projectile compared well with values deduced from the experiment. A perfect gas solution underpredicted the pitching moment by more than 25%.

6. COMPUTATIONAL ISSUES

The computational requirements of hypersonic calculations reach beyond the capabilities of current supercomputers. For example, to solve the reacting flow about a hypersonic vehicle in powered flight requires hundreds of hours of computing time on a Cray Y-MP. Timely analysis and design optimization require that this be reduced by at least two orders of magnitude. Advances are being sought in both CFD methods and computer technology to meet this challenging goal. Areas of research include interactive surface definition and grid generation, solution-adaptive grids, convergence acceleration, and parallel processing. The following section highlights two of these efforts.

6.1 Solution-Adaptive Grids

Solution-adaptive grids use a numerical algorithm to move grid points automatically toward regions of high flow gradients, such as shock waves and slip surfaces. Solution-adaptive grids enhance the efficiency and accuracy of numerical solutions in several ways. First, the grid adjusts as the solution progresses, reducing the initial effort of generating a suitable grid. This reduces the overall number of grid points as well, because fine grid resolution results only where it is needed, rather than throughout the domain. Because truncation error is proportional to grid spacing, solution-adaptive grids improve the accuracy of solutions by reducing numerical errors. Finally, the stability and convergence rate of the algorithm can benefit by improving grid resolution in high gradient regions, which are often a source of difficulty. These benefits result from a relatively low-overhead procedure to move grid points toward flow gradients.

A grid-adaption approach devised by Nakahashi and Deiwert (Ref. 13) conceptualizes flow gradients as tension springs located between the grid points. The value of the spring constant is proportional to the local flow gradient, causing a natural tendency for grid points to cluster near the high-gradient regions. The spring forces form a set of elliptic equations that determine the new equilibrium grid point locations. Adding torsion springs at crossing grid lines throughout the system helps minimize the skewness of the adapted grid. The flow solution is interpolated onto the new grid and the flow solution is advanced. While this procedure could be applied at every iteration of a flow solution, most often it is necessary to re-adapt the grid only occasionally.

This technique is demonstrated for the case of a two-dimensional hypersonic inlet problem (Ref. 14). The initial grid for this case was generated by algebraic interpolation between the upper and lower boundaries. Figure 8(a) shows the final adapted grid for this solution. The adaptation procedure has clustered grid points toward multiple shock waves. Figures 8(b) and 8(c) compare the pressure contours for solutions on the original and adapted grid, respectively. The original grid produced the correct compression ratio and located the primary shock waves accurately. However, the shock waves are spread over several grid points. The adapted grid clearly indicates the presence of two incident shock waves entering the inlet. The shock-shock and shock-boundary layer interactions are also more clearly defined. In this instance, grid adaptation yields a much better resolution of the flow structures, some of which were not evident using the original grid.

6.2 Parallel Processing

Massively parallel computer architectures offer another avenue for improvements in computing time. By dividing the work required to obtain a flow solution among hundreds or even thousands of processors, the time to complete a flow solution reduces dramatically. However, this is only possible if the work is balanced across all the processors and communication between them is kept to a minimum. A NASA research program is being undertaken to investigate the performance of CFD codes on massively parallel machines. This effort includes hardware development, systems software development, and mapping CFD applications codes onto massively parallel machines. CFD codes have been successfully mapped onto these machines, although realizing theoretical processing rates has yet to be demonstrated.

7. CONCLUSION

Simulating flows at hypersonic speeds requires the addition of real gas models to CFD codes. Robust algorithms must also be implemented to capture strong shocks accurately. Several levels of approximation for the fluid physics are available, each with a region of applicability and a simplification to the solution procedure made possible by its assumptions. The effects of real gas modeling on hypersonic fluid dynamics have been demonstrated through two examples. These examples showed real gas effects on boundary layer thickness, heat transfer and shock location. Hypersonic calculations about complex geometries require large amounts of computer resources. To make hypersonic CFD practical for design applications, several approaches to code efficiency are being explored. The most ambitious and potentially fruitful of these is massively parallel processing, which may someday reduce turnaround time from hundreds of hours to a few minutes.

8. REFERENCES

1. Baldwin, B.S., and Lomax, H., "Thin Layer Approximation and Algebraic Model for Separated Turbulent Flows," AIAA paper 78-257, January 1978.
2. Narayan, J.R., "A Two-Equation Turbulence Model for Compressible Reacting Flows," AIAA paper 91-0755, January 1991.
3. Kaul, U.K., "Laminar-Turbulent Transition Calculations of Heat Transfer at Hypersonic Mach Numbers over Sharp Cones," Collected Papers in Heat Transfer 1988 - HTD-Vol. 104, K.T. Yang ed.
4. Lawrence, S.L., Tannehill, J.C., and Chaussee, D.S., "An Upwind Algorithm for the Parabolized Navier-Stokes Equations," AIAA paper 86-1117, May 1986.
5. Srinivasan, S., Tannehill, J.C., and Weilmuenster, K.J., "Simplified Curve Fits for the Thermodynamic Properties of Equilibrium Air," ISU-ERI-Ames-86401, June 1986.
6. Vinokur, M. and Liu, Y., "Equilibrium Gas Flow Computations II. An Analysis of Numerical Formulations of Conservation Laws," AIAA paper 88-0127, January 1988.
7. Blottner, F.G., Johnson, M., and Ellis, M., "Chemically Reacting Viscous Flow Program for Multi-Component Gas Mixtures," Report No. SC-RR-70-754, Sandia Laboratories, Albuquerque NM, December 1971.
8. Steger, J.L., and Warming, R.F., "Flux Vector Splitting of the Inviscid Gasdynamic Equations with Application to Finite Difference Methods," NASA TM 78605, 1979.
9. Roe, P.L., "Approximate Riemann Solvers, Parameter Vectors, and Difference Schemes," Journal of Computational Physics, 43 (1983), pp.357-372.
10. Molvik, G.A., and Merkle, C.A., "A Set of Strongly Coupled, Upwind Algorithms for Computing Flows in Chemical Nonequilibrium," AIAA paper 89-0199, January 1989.
11. Edwards, T.A., and Flores, J., "Computational Fluid Dynamics Nose-to-Tail Capability: Hypersonic Unsteady Navier-Stokes Code Validation," Journal of Spacecraft and Rockets, Vol. 27, No. 2, March-April 1990, pp. 123-130.
12. Lawrence, S.L., "Numerical Performance Estimates for a Generic Hypersonic Forebody," AIAA paper 91-1695, June 1991.
13. Nakahashi, K., and Deiwert, G.S., "A Practical Adaptive-Grid Method for Complex Fluid-Flow Problems," NASA TM 85989, June 1984.
14. Harvey, A., Acharya, S., and Lawrence, S.L., "A Solution Adaptive Grid Procedure for the Three-Dimensional Parabolized Navier-Stokes Equations," AIAA paper 91-0104, January 1991.

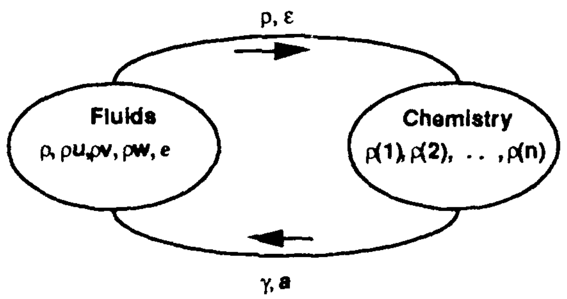
p, ε
Fluids
ρ, ρu, ρv, ρw, e
Chemistry
ρ(1), ρ(2), .. , ρ(n)
γ, a

Figure 1. Fluids/chemistry interaction mechanism for loosely coupled approach.

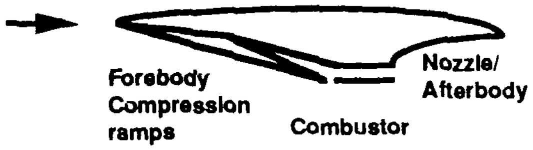
Forebody
Compression
ramps
Combustor
Nozzle/
Afterbody

Figure 2. Integrated airframe/propulsion system for airbreathing scramjet.

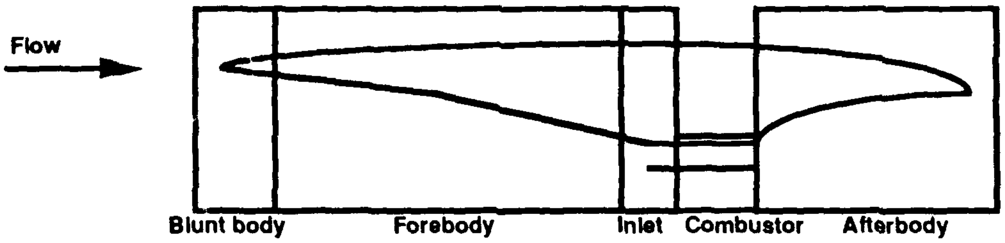
Flow
Blunt body
Forebody
Inlet
Combustor
Afterbody

Fluids	N-S	X		X	X	
	PNS		X			X
Chemistry	Air	X	X	X		
	H_2-air				X	X

Figure 3. Selection chart for fluid dynamic equations and gas models for nose-to-tail solution.

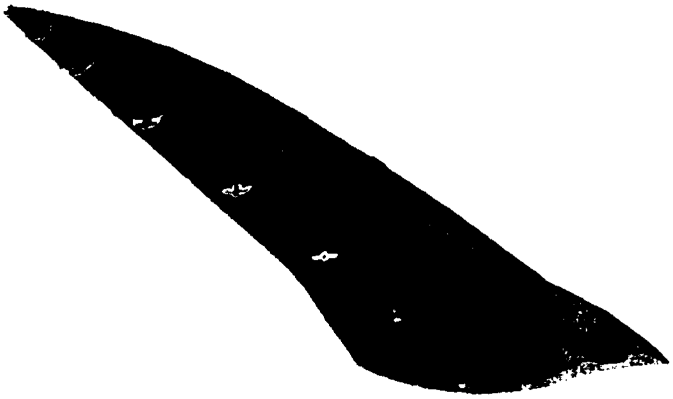

Figure 4. Forebody flow field of hypersonic body at Mach 19 showing atomic oxygen concentration.

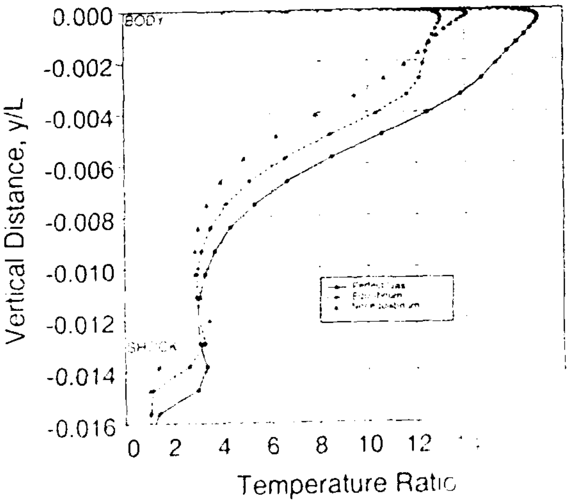

Figure 5. Thermal boundary layer at inlet centerline using perfect gas, equilibrium and nonequilibrium air chemistry models.

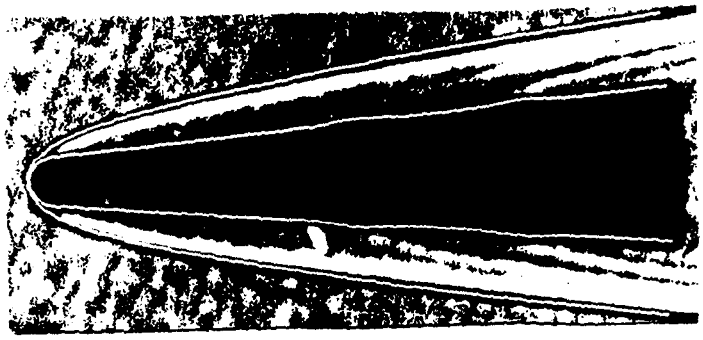

Figure 6. Shadowgraph of shock generator at Mach 14 and zero incidence with computationally predicted shock shape superimposed.

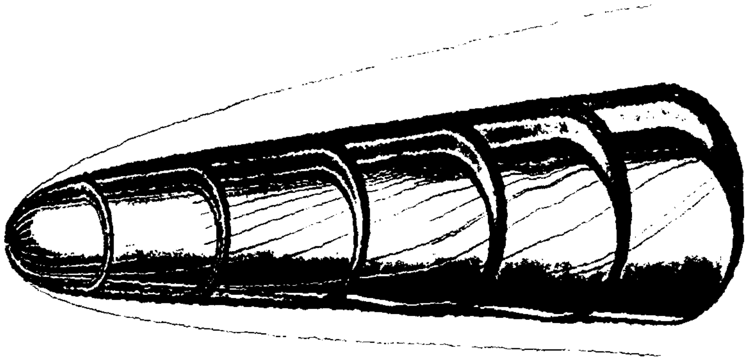

Figure 7. Flow field about shock generator at Mach 14 and 6.35 deg. incidence showing bow shock, atomic oxygen concentration, and simulated oil flow pattern.

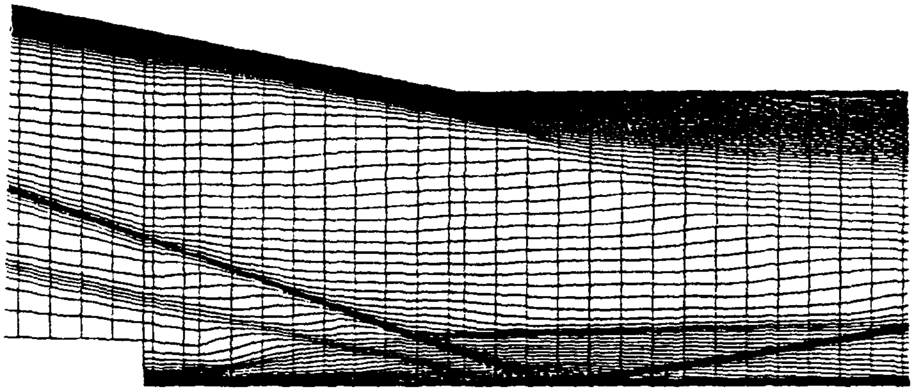

(a) Adapted grid

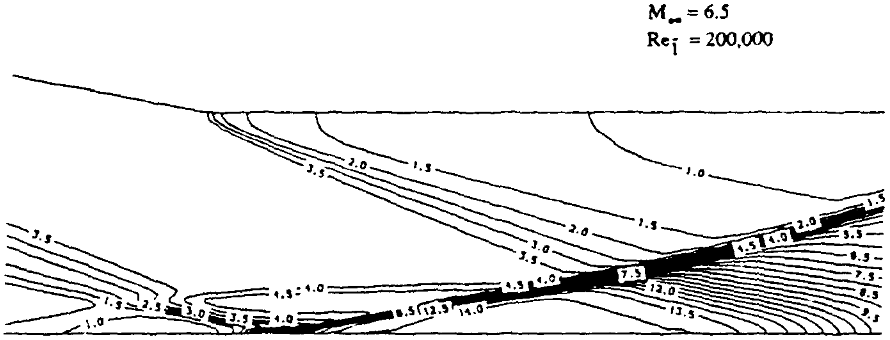

(b) Pressure contours on original grid

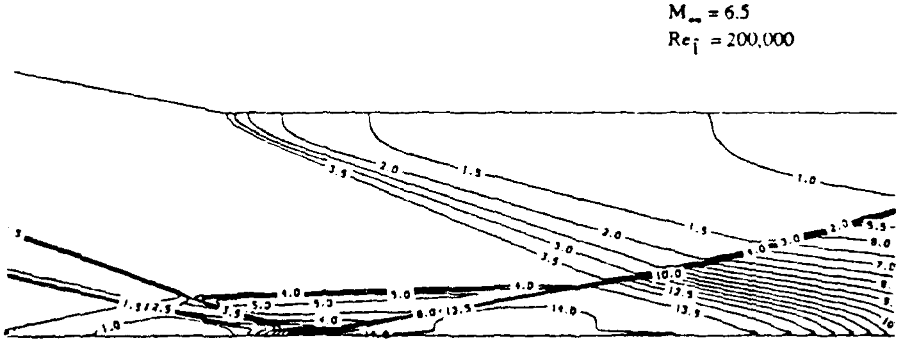

(c) Pressure contours on adapted grid

Figure 8. Solution of two-dimensional hypersonic inlet problem using solution-adaptive grid.

AERODYNAMIC AND AEROTHERMAL CHALLENGES FOR THE DESIGN OF THE HERMES SPACEPLANE

by

Pierre Perrier
Dassault Aviation
78 quai Marcel Dassault
92552 St Cloud, Cedex
France

1 - ABSTRACT

The Hermes spaceplane will represent a major step in the European space activities. It will be placed into orbit by the heavy-lift launcher Ariane 5. After completion of the mission, it will glide back from low earth orbit to its landing site.

In order to take the different problems linked to the ascent and the reentry phases, an aerodynamic strategy has been set up. A global review of this strategy will be made. It will contain elements on the available and necessary tools (experimental and theoretical) for the Hermes definition and qualification phases. Some aspects such as the design of the Hermes spaceplane will also be highlighted. It will review the different constraints that will be faced during the ascent and reentry phases.

Constraints may come from mission requirements such as crossrange capability or from technology limits such as thermal limits on the thermal protection system or from guidance and control requirements. A new methodology has been selected in order to take constraints and uncertainties into account in the design oriented towards qualification of the Hermes spaceplane. The main line of this methodology is the projection on a typical reentry trajectory of the uncertainties in the aerodynamic characteristics checked on control points.

2 - METHODOLOGY OF DESIGN OF HERMES SPACEPLANE

2.1 - Two methodologies

Systematically, a choice between two methodologies appears when feasibility of a project is either probable or unsecured.

Simple linear methodology is sufficient when it is probable that feasibility is not too difficult ; then the freezing of the design has to lead to better or lesser quality (in performances, cost...). The best selection of the major parameters, or of the technologies permits the desired achievements in performances and cost. Linear methodology consists of a selection of a first design followed by successive improvements of it without major technological changes ; in addition some initial loops may consist in the selection of different concepts and their evaluation using the knowledge of advantages and disadvantages for each of them ; for example civil aircraft like Airbus or Falcons need limited effort in the selection of general architecture like position of engines related to wing and fuselage, double slotted flaps versus simple slotted flaps... and major effort is required in better adjustment of parameters and improvement robustness of the shapes for variations of requirements or parameters.

When it is evident that feasibility is the main problem for a new aerospace design, the methodology has to rely on a two phase approach ; the first phase is oriented towards a demonstration of feasibility, the second one towards a refinement and is close to the above linear methodology but with a specific qualification process. For example as long as the specific thrust of jet engines does not guarantied a large number of feasible designs of Vertical-Take-Off And Landing aircraft, the first phase of V.T.O.L. feasibility demonstration is a long loop of convergence and requires adequate funding and careful methodology; the objective of the first phase is to demonstrate the existence of, at least, one viable concept of the future aircraft with adequate margins ; such adequacy asks for a sufficient knowledge of the technological constraints and of the physical background behind global performance evaluations.

In order to select the viable concepts, an unambiguous set of criteria is needed. Such set comes from a limited number of critical pointsȳ; they characterize the required performances in the flight envelope and they can be estimated with sufficient accuracy. As long as one viable concept does not exist (where the complete set of criteria is fulfilled, with positive margins), no confidence can be given to derivatives of the main parameters, because the derivative has to be expressed with regard to constrained variations but not to free variations. Fig. 1 gives for example the variation of mass of Hermes versus wing area parameter.

Figure 1

THE TWO METHODOLOGIES

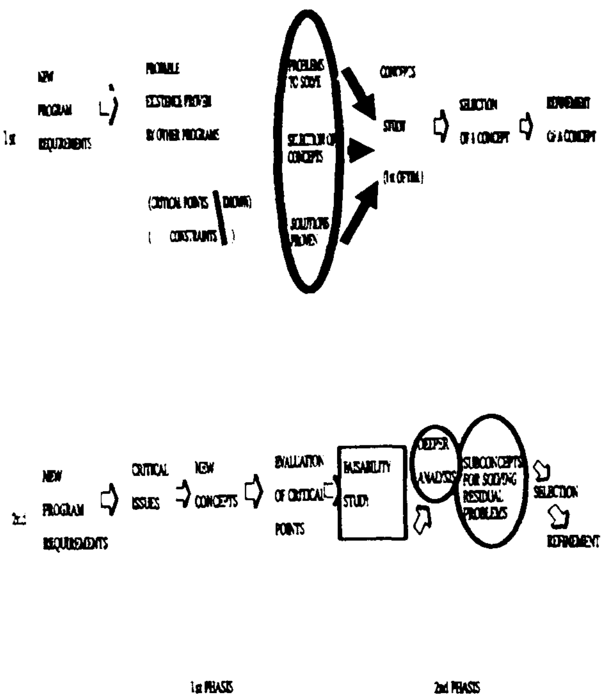
1st
NEW
PROGRAM
REQUIREMENTS
PROBABLE
EXISTENCE PROVEN
BY OTHER PROGRAMS
(CRITICAL POINTS KNOWN)
(CONSTRAINTS)
PROBLEMS
TO SOLVE
SELECTION OF
CONCEPTS
SOLUTIONS
PROVEN
CONCEPTS
STUDY
(1st OPTIM.)
SELECTION
OF A CONCEPT
REFINEMENT
OF A CONCEPT
2nd
NEW
PROGRAM
REQUIREMENTS
CRITICAL
ISSUES
NEW
CONCEPTS
EVALUATION
OF CRITICAL
POINTS
FEASABILITY
STUDY
DEEPER
ANALYSIS
SUBCONCEPTS
FOR SOLVING
RESIDUAL
PROBLEMS
SELECTION
REFINEMENT
1st PHASIS
2nd PHASIS

Figure 2

THE DESIGN - ANALYSIS LOOP

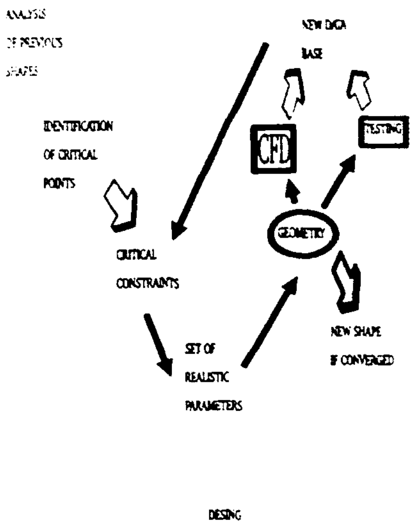
ANALYSIS
OF PREVIOUS
SHAPES
NEW DATA
BASE
IDENTIFICATION
OF CRITICAL
POINTS
CFD
TESTING
GEOMETRY
CRITICAL
CONSTRAINTS
SET OF
REALISTIC
PARAMETERS
NEW SHAPE
IF CONVERGED
DESING

Figure 3

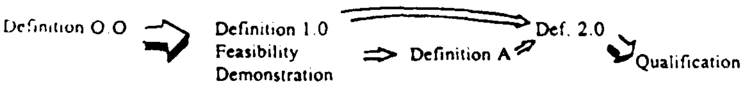
Definition O.O
Definition 1.0
Feasibility
Demonstration
Def. 2.0
Definition A
Qualification

Figure 4

CONSTRAINTS PERFORMANCES

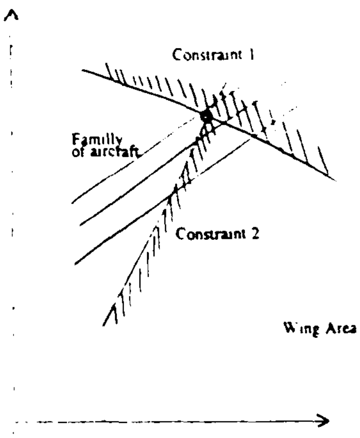

Figure 5

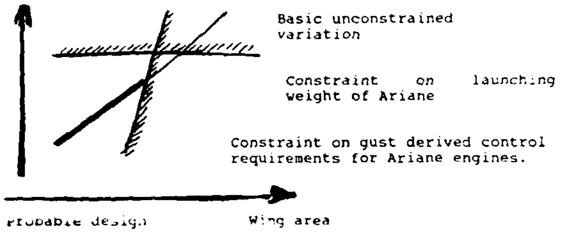
Basic unconstrained variation
Constraint on launching weight of Ariane
Constraint on gust derived control requirements for Ariane engines.
Probable design
Wing area

Obviously the basic unconstrained variation is interesting only if probable design parameters is not constrained (i.e. the lower one on the figure 1), otherwise such derivative is useless. However one may rely on an algebraïc parameter for variation analysis, so dropping one constraint too difficult to be fulfilled ; the existence of a design is obtained at the end of the interaction process. For example negative payloads may help to find a family of design concepts otherwise too sensitive to balance problems of the payload. Such an algebraïc process avoids to design aircraft (such a design cannot be done otherwise than in an explicit way) only if they are viable, that is to be demonstrated at the end.

2.2 - Methodology for Hermes

Major problems of Hermes came from technological constraints related to thermal properties of materials. The request was to limit the refurbishing activity when the thermal constraints were 200° higher than Orbiter due to scaling effect (ref. 1). Use of advanced materials has been retained for the major part of the skin ; but the hotter parts have to be constrained by carbon-carbon extreme properties so the nose cape and the wing leading edges are first to be concept-drivers in the general layout. It gives the characteristic shape of Hermes with a nose of large radius and the shielding of the wing in the bow-shock. The nose is a three-dimensional product of optimisation for shear-stress reduction constrained by visibility requirement giving the characteristic oblate shape of nose cape. The shielding of the wing avoids shear-layer to come on double sweep design by double shock surface intersection and its impingement on the leading edge. However the tip of the wing with a small chord needs an additive effort ; too high heat fluxes are reduced by an additive effect of upwards canting plus increase in sweep angle. High angle of attack of the reentry (larger than 30°) helps to minimize such needed sweep effect in combination with large canted angle, and gives the characteristic winglet shape of Hermes. So the main features of the Hermes concept are mandatory issues coming from aerothermal constraints. The existence of one feasible design remains to be proven because many other problems remain after a survey of other critical points along the trajectory, and adjustment of all parameters.

2.3 - Critical points

We have had to identify the main critical points of design of Hermes knowing that such points are linked along trajectories to various problems, some technological, some physical. So the best way to classify the critical points is to identify areas or phase domains where some phenomena are occurring.

Figure 6

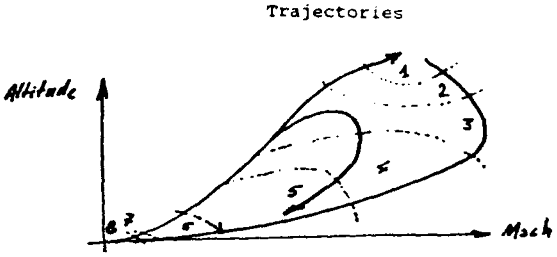

From the maximum altitude, at the beginning of reentry we can discriminate 8 domains :

1 - One orbital flight domain where major problems come from hazards of meteorites or space debris.

2 - One domain where major phenomena are in rarefied flow gas dynamics, continuous flow being a poor approximation of the modeling of phenomena occurred. This domain is reduced in importance in Hermes design outside the overall efficiency of jet control system.

3 - One domain where the flow is continuous but the low pressure involved does not allow thin layers of viscous flows and so no transition can occur. However this part of the trajectory gives a concern to efficiency of controls : in such low Reynolds number flow maximum of complexity of the chemistry and physics come from high enthalpy of incoming flow near orbital velocities.

4 - One domain where the flow is continuous, where the non-equilibrium properties come also from high enthalpy of incoming flow but the rear of the vehicle is at sufficient Reynolds number so that heating on the flaps can occur with turbulent reattaching flows.

5 - One domain where the flow is low hypersonic flows with almost no chemical effects nor thermodynamically non-equilibrium behaviour.

6 - One supersonic domain where the flowfield does not include hypersonic phenomena like entropy swallowing, very high ratio of skin temperature to stagnation temperature, complex shock-waves-wake-boundary-layer interactions...

7 - One transonic domain where the flowfields can be unstable due to the necessary oblate shape of Hermes.

8 - One subsonic domain where the round shapes of Hermes give large uncertainties in flow characteristics.

For each of these 8 domains some specific problems occur but at the end critical ones were limited to the following after a first loop of convergence.

Domain 8 : Low-speed lateral control at low angle of attack induced by the non conventional shape of the vehicle. Addition of a vertical fin would solve the problem but should increase the weight and moreover introduce a difficult transition for the flying control system when such vertical fin become operant in domain 6.

Domain 7 is the more critical issue for the unstable control of Hermes induced by forward shift of centre of pressures ; high lift in compressible low transonic flow and use of airbrakes on the rear of upper fuselage are the main sources of deterioration of stability : airbrakes on the fuselage need careful analysis of the interaction of the wake of airbrakes with the elevons. Intensity of pressure fluctuations is also a major concern.

Domain 6 with maximum rearward shift of centre of pressure is critical for efficiency of controls in up position ; main concern is balance of forward position of centre of gravity. Keeping lateral control effective in low angle of attack, for conteracting unstable forces in front fuselage, is also a critical issue.

Domain 5 is a classical low hypersonic domain. There lies the perfect gas reference for more complex phenomena influence. It is essential for evaluation of uncertainties and real gases and aerothermochemistry problems. Furthermore in that domain the phenomena of transition to turbulence on roughness is also to be evaluated ; some in flight and wind tunnel correlations (theoretical versus empirical predictions) can help.

Domain 4 introduces a large complexity in the phenomena, with coupling between chemistry at the wall or in the flowfield, real gases effects in flight, and transition phenomena. This domain is the most important for aerothermal design but unfortunately it adds all the difficulties in physical and chemical rebuilding. The shape of Hermes was selected in order to be robust to uncertainties on such phenomena by selection of a delta wing where the centre of pressure remains not far from the centroïd of the platform. However the peak transitional reattachment heating on flaps is unavoidable critical point : balance between efficiency and thermal overheating is the main concern.

Domain 3 with low Reynolds number is also not so critical by using such delta-wing. However the knowledge of flowfield on control is also mandatory when the experimental rebuilding is clearly poor and far from real flight conditions.

When a feasible concept was retained, after the loop of feasibility studies corresponding to the first phase of methodology (as explained in 2.1 before), the following list of critical points continues to be essential to the design constraints :

1 - Lateral control in low speed (domain 8)

2 - Transonic instability with airbrakes (domain 7) in forward position of the COG

3 - Transonic buffet induced fluctuation of pressure on front fuselage (domain 7).

4 - Supersonic lateral characteristics at low angle of attack (domain 6).

5 - Supersonic longitudinal balance in forward position of COG (domain 6).

6 - Hypersonic longitudinal balance in rearward position of COG with poorer correlation between overheating and efficiency (domains 3 - 4 - 5).

7 - Hypersonic windshield overheating in ascent trajectory at low angle of attack and in reentry at high angle of attack (domains 3 - 4 - 5).

8 - Hypersonic 1st tile junction overheating due to forced transition (domains 4 - 5).

9 - Hypersonic tip of wing overheating at the leading edge and on the flap deflected (domains 4 - 5).

10 - Hypersonic local overheating in gaps, holes and file junctions (domains 4 - 5).

11 - Hypersonic low Reynolds number efficiency with reduced dynamic pressure on all axis (domain 6).

These critical points defined each a constraint in design that is to be fulfilled by final careful adjustment of parameters.

It appeared that a design able to fulfil the critical points 1 - 2 - 4 - 5 - 8 - 9 needed a minimum size of wing and of controls and also needed careful design of front fuselage for avoiding excess of variation of centre of pressure with Mach number and angle of attack. So there exists anyway an Hermes design that will fulfil such requirements coming from these six critical points, at the expanse of a larger wing with larger controls.

However a critical point comes from the Ariane V launcher and was related to balance of maximum gust induced loads during ascent : it is clearly proportional to the gradient of lift with incidence qACLx of the aircraft on the tip of its launcher, and to the maximum arm lever of this destabilizing effect ; the control effectiveness comes on Ariane from the thrust deflection. For a given fuselage, increase of wing put more backward the C.G position and increase requirements from control and reduce the instability. So the following figure is kernel of wing size determination :

Figure 7 :

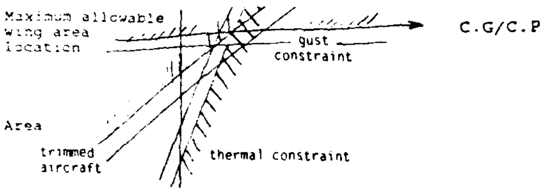

A feasible concept is possible only by reducing the size of the fuselage (and consequently of the wing), moving forward the Centre of gravity position (and consequently reducing the size of the control and of the wing). Such converged design was obtained in 1991 and so put an end to the first phase of the methodology demonstrating the existence of a viable design. However some refinements were needed to be done, particularly with account of the five remaining critical points plus some others coming from detailed design as the proof of flutter free design of the structure of winglets, or the robustness of design to holes coming from space hazards and losses of one element of the thermal protection system. The geometric definition of this design was named 1.0.

2.4 - Methodology for convergence

The methodology, now, when a solution exists (i.e, is feasible), is to rely upon an interpolation procedure rather than upor an extrapolation one. Due to the difficulty to express the multiple constrained fields of optimisation of Hermes, it appears that an interpolation process guarantees better final product than more open loop of optimisation. To have such an interpolation procedure need to design a shape that includes solutions to all critical points one by one.

For example, it appears that critical point n° 7 needed a careful study of the direct connexion between the length and the centre of gravity of fuselage and the detailed layout of the canopy with ejection-seat geometrical constraints. So any overheating on windshield that lead to major changes in the design may have catastrophic consequences on the existence of a converged geometry. It was proposed to the design office a set of modifications that cover with margins the reduction of transparencies overheating to a acceptable figure ; similarly on the other critical points, the shape that includes that set of modifications has been called "Shape A" and will furnish a basis with shape 1.0 to an interpolation procedure. Final shape will be shape 2.0 and such a methodology guarantees, with reasonable uncertainties, that this shape will also exist.

To summarize : from the first to the second phasis of work, the methodology moves from an open research of concepts or of basic shapes to the selection of related geometrical parameters (wing span, sweep angle, wing tip canted angle, ...). This first phasis leads to the shape 1.0 considered as feasible at the state of the knowledge of all critical problems, whereas the second phasis is an interpolation procedure. However, it is to be said that qualification of the final 2.0 shape needs much more efforts due to the long time for final design of all internal and external parts and checking of its adequation to local thermal and mechanical requirements and global function relevancy. The process of qualification will involve more detailed analysis and will only be able to begin when the interpolated 2.0 will be selected.

3 - TOOLS FOR DESIGN

3.1 - Complementary use of the different tools

It is unrealistic to minimize the difficulty of the design of a spaceplane like Hermes. Aerodynamic and aerothermal validation of the design are tremendous challenges. The present status of the cross validation of the triad CFD - ground based testing - flight testing is poor. That triad is in fact the present regular extension of an early approach relying only on prediction plus validation. Real flight is the unique complete validation of the design for near nominal trajectory. Comparisons of prediction and flight data are the main ingredients of the required confidence in the design. It is clear that such a validation not having the support of a large set of experience in hypersonic for various shapes and concepts is poor. Careful analysis of the quality of the prediction is the only way for improving confidence in any design. First unmanned flight oriented towards cost reduction by reduced equipment and flight envelope is the best graduated strategy.

However, the CFD progresses give new opportunities for a revised approach using all the tools available in a mix of theoretical and experimental approaches for a most important pre-flight qualification.

We can define two worlds : the real world that can only be tested in flight and the simulated world that has to be validated as a simulation tool of the real world. The simulated world has two levels : one is the flight simulator where the pilot can experiment, on a sensory approach, the rebuilding of external world and the behaviour of the final vehicle. The second level is the fine simulation experimental and/or numerical.

In fact small domains in the flight envelope can be simulated in experimental ground simulation ; so the impact of fine computer simulation is large on design, particularly when ground experimentation is limited, as for hypersonic aircraft. For Hermes the strategy of design was adjusted from the beginning to all the capabilities of CFD, in order to gain progressive confidence on the CFD approach as a tool for analysis of the problems (directly from partial experimental data) and as a tool for design by progressive improvement of basic shapes. CFD will be also a major tool for qualification and analysis of data extracted from first unmanned scale one flight (Hermes X 2000).

The methodology is given by the following development of the Triad.

Figure 8 :

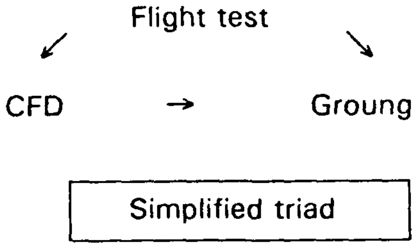
Flight test
CFD
Groung test
Simplified triad

Figure 9:

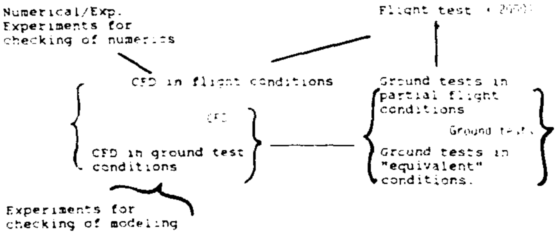
Numerical/Exp.
Experiments for
checking of numerics
Flight test (2000)
CFD in flight conditions
CFD
CFD in ground test conditions
Ground tests in partial flight conditions
Ground tests
Ground tests in "equivalent" conditions.
Experiments for checking of modeling

Extended triad

The complement in the triad comes from the incompleteness of each of the tools :

- Flight test cannot be done before the vehicle itself is identified so at a cost equivalent to the operational vehicle assembly and testing (prototype approach, or automatic first flight as on X 2000). However a reduced-sized vehicle could be the answer to the more critical problems at a reasonable cost. It was the target of "Maia" vehicles (scale > 1/4) on the first strategy for Hermes development, and the "Bor's" in the Russian approach to Buran ; however reduced size means no qualification of the complex unscalable devices like sealing or junctions.

- Ground test cannot cover the high enthalpy conditions in pressure temperatures and Mach number and Damkoeler number. In fact the real gas effect appears first in the expansion in the nozzle of the facility so thermodynamic equilibrium is regained from the bowshock on wind tunnel when it has to be recovered later in flight. Ground tests can, on the contrary, be the more correct and validated approach with low enthalpy wind tunnel in the more conventional test range of subsonic to low hypersonic ; so it is a source of reference data for any prediction, if calibration of facility is accurately done.

- Computational aerodynamic- aerothermodynamic cannot cover too fine description of phenomena if modeling does not allow it (e.g. in transitional and turbulent flow) and need careful checking of the mesh size effect as of the numerical viscosity added for stability of the solution. No large limitation exists presently on the rebuilding of Hermes in high enthalpy flow if validation can be done. So computational work is necessary for checking in-flight versus ground tests and for uncertainties analysis.

Figure 10 : DEVELOPMENT TRIAD

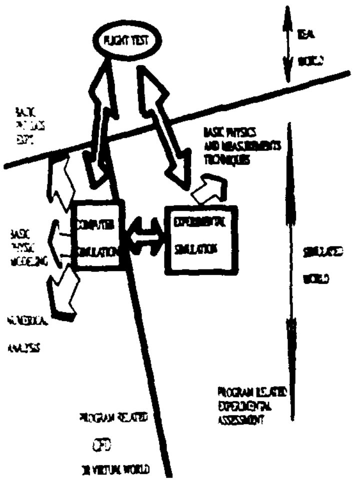
FLIGHT TEST
REAL
WORLD
BASIC
PHYSICS
EXPT.
BASIC PHYSICS
AND MEASUREMENTS
TECHNIQUES
COMPUTER
SIMULATION
EXPERIMENTAL
SIMULATION
BASIC
PHYSIC
MODELING
SIMULATED
WORLD
NUMERICAL
ANALYSIS
PROGRAM RELATED
EXPERIMENTAL
ASSESSMENT
PROGRAM RELATED
CFD
IN VIRTUAL WORLD

3.2 - Experimental tools

It is of major importance to add sufficient experimental data in all 9 phases of the trajectory.

If the 7 - 8 - 9 are classical aerodynamics, requiring classical wind tunnel, it is however to be emphasized that the Reynolds number effect is critical on the round shapes of HERMES, as Orbiter or Buran. Experimental data coming from flight remains useful or mandatory according to the critical points and the corresponding phases of the flight (mainly for stability or flying qualities).

In cold hypersonic regime, with low enthalpy and perfect gas modeling the need for a high quality experimental tool is mandatory because it will be the pivotal point for all adjustment of CFD extrapolation to flight. Selection of different wind tunnel is very useful and help to master the most probable aerodynamic aerothermic data. We selected German and French W.T. plus reference wind tunnel proven in USA (AEDC for Orbiter) and in Russia (T117 of TSAGI for Bouran).

High enthalpy and low Reynolds number wind tunnels exist, but such a range of low pressure is not critical for an aerospace vehicle.

For high enthalpy Germany and French proposed new facilities of different technology and performances : the high enthalpy facility in Göttingen (HEG) gives adequate dissociation but with very short duration, whereas arcjet facility in Toulouse (F4) gives longer duration (adequate for balance measurements). Both facilities are able to cover the highest pressures near the flight Reynolds number but on what level of flow field and data measurement quality ? Both facilities rebuild flow from frozen non-equilibrium expansion in a nozzle.

In fact such facilities (conventional, or low enthalpy or higher enthalpy) have two major characteristics : the first one is to be far from duplicating the flight conditions, more and more when the enthalpy increases ; the second one is to be far from supporting careful analysis of fundamental problems. Such analysis requires specific facilities and more specific instrumentations and equipments. So that, parallel to industrial testing (as defined in the above facilities), is needed research testing to produce reference data for workshops or for direct local analysis validated by high level of instrumentation (e.g. validation of chemical species by spectrometric measurements).

So we can classify the needed experimental tools in three groups :

- flight experiments on model of large size
- industrial experiments on model of small size
- research experiments on reference models.

For validation of the CFD (now continuously present in the design) specific tests have to be so instrumented that only research organisation would be able to support such a validation process. The same can be said for large material testing, where arc-jet facilities are to be duplicated by research facilities.

3.3 - CFD tools

The use of different wind tunnels relying on different physical strategy for heating or expanding flows are the necessary ingredient for complementary consolidation of data (what-so-ever the lack of true rebuilding of flight conditions). In the same way the use of different codes, with different mathematics and physics modeling, is the necessary ingredient for going from the validation of one method, to the evaluation of the global uncertainties of one code compared to another. So the European founding of Hermes program have helped to build the same variety of codes in the so-called "alternate approach" as of ground facilities. European cooperation was necessary for the support of Dassault and INRIA in organizing the first international workshops in hypersonic where uncertainties on both experimental and numerical were evaluated.

The alternate approach in CFD revealed itself as very efficient because differences in mesh, algorithm and physical modeling resulted in lower discrepancies than anticipated and allowed a rapid detection of major clues. Alternates algorithms, meshes, modelings in Hermes program are therefore playing an essential role in the European strategy, contributing to the reduction of uncertainties of Hermes.

3.4 - Cross validation

It is clear that pure adjustment to a family of reference experimental test cases is not a replacement to validation procedure. In fact it is on basic phenomena, and not on complex ones, that elementary errors can be identified.

Figure 11 :

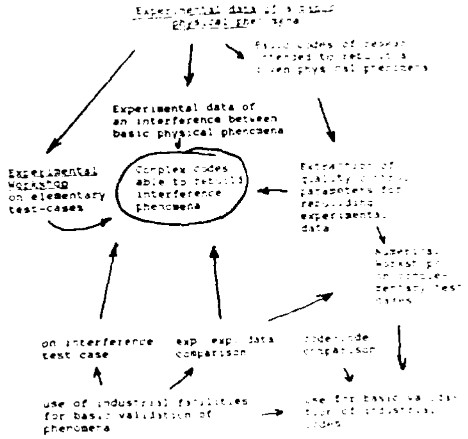
Experimental data of a single physical phenomena
Fluid codes of research intended to rebuild a given physical phenomena
Experimental data of an interference between basic physical phenomena
Experimental Workshop on elementary test-cases
Complex codes able to rebuild interference phenomena
Extraction of quality criteria parameters for rebuilding experimental data
Numerical workshop on simple elementary test cases
on interference test case
exp. exp. data comparison
code-code comparison
use of industrial facilities for basic validation of phenomena
use for basic validation of industrial codes

Multiplication of experimental and numerical workshops gives increased confidence in true phenomena rebuilding. Unique requirement is the variety of approaches retained in order that the agreement between CFD and experimental data don't come from hazardous coherence but from a better selection of the more probable but independent rebuilding of basic phenomena.

International cooperation is clearly of common interest due to the cost of alternate approach in experimental testing as in CFD rebuilding of experiments. Moreover independent results means independent teams !

4 - THE CHALLENGE OF UNCERTAINTIES EVALUATION

4.1 - General methodology

Conventional aircraft margins come from experimental tests and from past experiences of flight wind-tunnel correlation. Extrapolation in hypersonic not relies on same confidence in estimated data obtained by test data + CFD computations of the test ; it assumes that CFD code is validated by a set of experimental tests checking the sensitivities of computer code to :

1 - geometry changes,
2 - physical - chemical modeling
3 - discrete computation parameters, current number, size of mesh...).

Validation of this approach is not giving confidence because such a procedure does not guarantee that the sources of the errors are in one or another of the three terms. The only way for decreasing the uncertainties is to eliminate the basic errors by large variations of the parameters and of the tools.

Two approaches can be followed :

- the first one is the "building block" approach, that tries to cover the basic phenomena by rational surveyÿ; that leads to validation by CFD + experimental tests of the rebuilding of each phenomena or of interacting phenomena ; the number of blocks is quite large (see J. Marvin for such an approach) and question is open of completeness of the blocks.

- the second one is the "analysis approach", that tries to cover just the phenomena involved in a specific design. It assumes that the reduced building-block approach is well documented and validated (see the International Workshop in Antibes).

Whatever the approach retained (and the associated funding), the major problem is the data fusion : mixing errors in CFD rebuilding and experimental data acquisition is to be done in a proper way. The method that is described below seems the best one for reducing the uncertainties using a reduced number of dedicated experiments. Its assumes clear domains of physical modeling (or physical phases) selected as we have done for Hermes.

Assuming that we wish to rebuild probable value and uncertainties around probable value in one of the physical domain 1 to 9, we will identify all the phenomena involved and check that the uncertainty of the rebuilding of each is sufficiently low ; then the contribution of each phenomena is added and probable uncertainty of experimental data can be evaluated. For example the divergence of the flowfield in the nozzle of wind-tunnel due to variation in stagnation pressure induces such or such fluctuation of one useful parameter on Hermes model.

With CFD rebuilding of the distance between different wind tunnels has to be proven as repeatedly rebuild. Then the most probable data can be derived after elimination of the probable errors (as substantiated by large variation of the parameters). In fact, such strategy needs coverage of extreme variations of all available parameters plus the selection of the point where derivative is to be assessed. If large discrepancies in derivatives versus prediction without support of a rational explanation are obtained in a facility, such facility cannot be retained.

Taking into account a statistic of same data, probable mean values and experimental uncertainties can be assessed. It is an experiment - experiment assessment.

In the same way CFD codes can be assessed in a groups of codes with rational explanation for the discrepancies between codes and between numerical data for different parameters. It is a code - code assessment.

Now the problem is to follow the Hermes trajectory and to build the total uncertainties by mutual assessment of the coherence of errors in each phases of flight. Total sum-up of incertainties will be built using mathematical theory of control.

Assuming that the physical rebuilding of true physic of the hypersonic flight can be done with the convenient modeling, then we can associate to the flight trajectory n functions of time t ; the n functions are all the discrete local parameters (e.g. the variables at all control points of a computation) ; they are associated to integral values as total forces, moments or to local values as heat fluxes, temperature, species concentration... The functional dependency of a time t is valid, as all modelisation, if convenient scale of t is chosen in modeling approach (e.g. mean value for turbulent flows or collision integral on rarefied flow) as related to physical quantities (e.g. different temperatures...).

Applying the same modeling to the flight and ground testing, phase by phase, the rebuilding is to be done on same geometry (reduced scale of models or scale 1 vehicle). Between points of reference we can build a tree of connexion. Along the main trunk of the tree, the true flight trajectory is described as a function of true time of a normal tree t ; on the branches some parameters are supposed varying in the same physical phase and in the same way as true trajectories.

So we can associate a in family of trajectories as in a fire work with multiple fuses. We can then apply the same optimal prediction of the n functions knowing that the physics don't let them to be random, but that they are correlated at least by physical laws. We can then apply to PDE, or to linear part of PDE the same mathematical techniques as are used for LDE when a Kalman filtering help to minimize the predicted parameters of a trajectory. Such approach gives more probable mean value and variance of main parameters.

4.2 - Reference points for Hermes uncertainties evaluation

We take as a reference an hypersonic point of flight with cold flow (with perfect gas condition). We apply the procedure for assessment of each wind tunnel leading us to a mean value plus a law of probability of each experimental point for a set of parameters. With a set of numerical codes, for which a procedure has led us to the most probable value (with infinite discretisation convergence...) the projection is made to the reference point : shift estimated goes from true testing conditions to reference conditions (e.g in flight conditions). We can use all the experimental points for contributing to the building of the reference point with a law of probability relative to all experimental points translated to reference conditions ; it is the projection process, controlled as we have described in 4.1.

From this reference point we can check if the existing flight data can be rebuild in the same way for the Orbiter and AEDC facility, for the Buran and Tsagi T117 etc... with other smaller test articles.

From this reference point we can now follow the trajectories. Each of the codes can :

- estimate the values of aerodynamic-aerothermic data along the trajectory in nominal or extreme conditions.

- estimate in each physical phase the value to be obtained in other facilities like F4 or HEG

As large will be the variations of the parameters we will cover by experimental testing, as better will be the substantiation of the uncertainties by comparison to computational simulation. On the point on the trajectory will be done a "projection" of the errors coming from uncertainties on experimental as on theoretical data. Building a law of probability of typical data (in experimental as on theoretical side) it is then possible to balance the results and the uncertainties proportionally to the variance of the laws of these probabilities of experimental and theoretical data. If the numerical or experimental data are outside of the estimated range of validity, it is to be dropped in the ponderation as inconsistent. Otherwise each projected point contributes and reduces the uncertainties to the mean root square of the elementary addition and not to the pure addition as the initial formula implies.

It is an extension of the Kalman filter approach to the control of basic data along the trajectory. Such approach guarantees the optimal minimisation of uncertainties along the trajectory. It assumes a good modeling (random errors and no jump in bias on the projection paths), so a good rebuilding of physics and chemistry and of the flow field ; a parallel effort for validation of building blocks involves the same alternate computation and testing philosophy.

5 - FINAL REMARKS

Challenges for aerothermal and aerodynamic design of Hermes are very large ; but the diversity and the richness of the experimental and numerical data coming from the variety of the contributors in Europe will finally reduce the critical discrepancies at an acceptable level, taking advantage of all the knowledge included in the simulation process in each country. Cooperation in Hermes is an additive contribution to methodology ; that will increase the confidence in cooperative CFD-experiment approach and will reduce the uncertainties. From then the spaceplane is starting to be improved at a new standard of quality.

So Hermes will be designed in a very advanced way at the benefit of ESA European Man in Space Program.

Figure 12

PROJECTION PROCESS FOR UNCERTAINTIES ANALYSIS

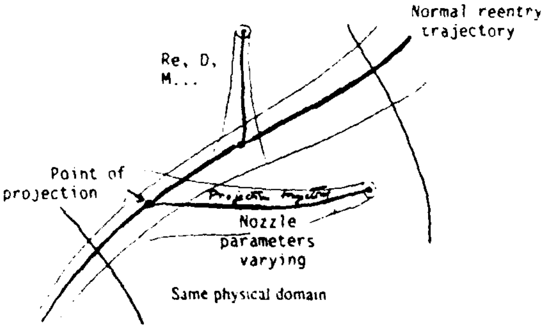

Figure 13

UNCERTAINTIES ADDITION

(Variance weighted)

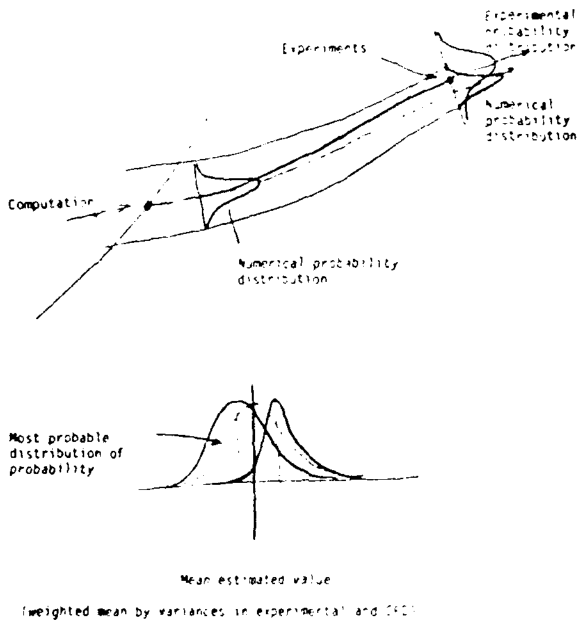
Experimental probability distribution
Experiments
Numerical probability distribution
Computation
Numerical probability distribution
Most probable distribution of probability
Mean estimated value
(weighted mean by variances in experimental and CFD)

REFERENCES

P. Perrier - Methodology for Hermes design. 1st Europe-US. hypersonic short course - Aachen 1987.

J.G. Marvin and T.L. Holst - CFD validation for Aerodynamic Flows - Challenge for the 90's - AIAA 8th Applied Aerodynamic Conference 1990.

J.G. Marvin - Accuracy requirements and benchmark experiments for CFD validation - AGARD Conference proceeding n° 437.1992.

Damköhler G. Zeitschrift Fur Electrochemie, vol 42, p.846, 1936.

Ruptash J. - Supersonic wind-tunnels - Theory, Design and Performances - University of Toronto, June 1992.

Moffatt R.J. - Contribution to the theory of uncertainty analysis for single sample experiments 1980-1981 - AFOSR / HTTM - Stanford Conference on complex flow.

Mehta U.B. - Some aspects of uncertainty in Computational Fluid Dynamics results, Vol. 113, N° 4, Dec. 1991.

Desideri J.A. et J. Periaux - Antibes - Workshop on Hypersonic Flows for reentry problems - Part I - Part II - Springer Verlag 1991 - 1992.

Jazwinski A.H. - Math. in science and engineering - Vol. 64 - pp. 266-286 - Academic Press 1970.

Experimental Results in Aerodynamic Stability and Control of a TSTO Configuration

T. Gottmann, G. Cucinelli

Messerschmitt-Bölkow-Blohm AG,
FE211, PO-Box 80 11 60,
8000 München 80, FRG

ABSTRACT

A Winged Launcher Configuration (WLC) in a Two Stage To Orbit (TSTO) version has to fly through a wide range of Angles-of-Attack and Mach numbers (roughly $-3^\circ \leq \alpha \leq 20^\circ$ and $0.2 \leq Ma \leq 7.0$). This and the requirements for horizontal take-off and landing in Central Europe, and the special separation manoeuvre at a hypersonic Mach number, causes a wide range of new aerodynamic and aerothermodynamic problems. Especially the problem of stability and control is increased by the wide α-Mach range and possibly strong engine effects. The main tasks of the experimental investigations of a TSTO configuration are to establish a data base to support the whole design process of Winged Launcher Configurations, to provide a validation base for CFD codes and to understand the very complicated problems which dominate stability, control, and stage separation aerodynamics. A generic baseline configuration of a TSTO has been developed at MBB (lower and upper stage), which satisfies all requirements so far. To be able to test this configuration in all occuring speed regimes, a titanium model (size 1:160) was manufactured with an acceptable size to fit into most windtunnels for sub-, super-, and hypersonic Mach numbers, especially at DLR in Germany and FFA in Sweden.

The main part of the presentation deals with trends of the TSTO configuration in aerodynamic stability and control over the entire Mach regime, showing that some aerodynamic characteristics change significantly with increasing Mach number. Because all aerodynamic forces and moments must be balanced by the engine or aerodynamic controls to obtain reasonable flight conditions, statements regarding absolute stability and control features cannot be set up within this investigation, but tendencies can be given.

Major emphasis is placed on the flap efficiency at high Mach numbers which exhibits a strongly nonlinear behaviour. The separation of the upper stage was investigated in a special test phase, which shows the enormous changes in longitudinal characteristics caused by interference effects in close proximities between upper and lower stage.

NOMENCLATURE

α	Angle-of-Attack
ε	Angle of incidence between upper and lower stage
β	Sideslip angle
η	Trailing-edge flap deflection angle
ς	Rudder deflection angle
ξ	Aileron deflection angle
Δz	Vertical distance between upper and lower stage during separation
L_{Body}	Total length of the lower stage
C_L	Lift coefficient
C_m	Pitching-moment coefficient
$C_{n\beta}$	Derivative of yawing moment due to sideslip angle β
$C_{l\beta}$	Rolling moment derivative due to sideslip angle β
$C_{L\eta}$	Flap efficiency due to lift
$C_{m\eta}$	Flap efficiency due to pitching-moment
$C_{n\varsigma}$	Efficiency of rudders, yawing moment
$C_{l\varsigma}$	-.- rolling moment
$C_{n\xi}$	Efficiency of ailerons, yawing moment
$C_{l\xi}$	-.- rolling moment
$\delta_{B.L.}$	Boundary-layer thickness
C_p	Pressure coefficient $(p-p_\infty)/q_\infty$

Abbreviations:

a.c.	Aerodynamic center
A.o.A.	Angle-of-Attack
Re	Reynolds number
L.S.	Lower stage
U.S.	Upper stage

1 INTRODUCTION

A spacecraft system has to be cost effective as well as environmentally acceptable already in the near future, in addition to the classical requirements of maximum payload fractions and safety. Therefore, the transportation system must be fully re-usable. One solution to these main requirements could be a Wing Launched Carrier (WLC), likely in a Two Stage To Orbit (TSTO) version. The WLC TSTO takes advantage of the staging principle and gains payload fraction by using the atmosphere twice: first as a lifting medium, and secondly by airbreathing propulsion. Especially a European Space Program has to look for geographical independent solutions, which means take-off and landing in Europe. Such a spacecraft program induces a number of new technical requirements (Fig.1):

- Range flight towards the equator (or latitude 28°) and different inclinations, (Range > 2•3000km)
- High number of cycles
- Acceleration and climb to max. possible speed and altitude
  (high energy level) with airbreathing propulsion:
  (Mach = 5...7, at Alt = 30...40 km, ramjet engine,
  Mach = 8...12, at Alt = 40...50 km, scramjet engine)
- A safe orbiter launch procedure at maximum Mach number
- Horizontal take-off and landing from existing conventional runways
- H_2 fuel handling
- Minimum ground support, short turnaround times

These general requirements themselves cause a wide range of new aerodynamic and aerothermodynamic problems. Especially the problems of stability and control, which are not completely understood yet, still need some effort to establish 'know how' and a good data base for design work. In order to identify the inherent problems of a WLC system and the tools required for the design process, a technology concept has been worked out, including a windtunnel model of a generic hypersonic TSTO. The present test campaign is primarily needed for validation of design methods, CFD codes, to establish error bounds, and to establish a database. This 'predesign TSTO' has run only through one design loop to assure that weight, propulsion and size are not diverging, so it is a non optimized configuration, designed to represent only the most important functional items.

The test campaign was planned and conducted by MBB and performed by DLR Germany, with facilities at Göttingen, Cologne and Braunschweig. Additional measurements were started at FFA in Sweden, but are not finished yet, so that control effectiveness in the Mach number range from 0.5 to 2.0 is not available at the moment.

2. PROBLEM DESCRIPTION

On the one hand there are some predominant problems and special effects of the operational configuration regarding stability and control which should be mentioned first, and on the other hand, there are problems of the windtunnel test campaign itself, which are described thereafter.

The lower stage of the present generic TSTO covers the wide range of Mach numbers from 0.2 to 7.0 and altitudes up to 40 km. Herewith four characteristic flow regimes are involved, i.e.: subsonic, transsonic supersonic and hypersonic. These different types of flow cause large changes in aerodynamics and in engine effects.

Within that Mach number range an aircraft typically has two extremes of static stability in longitudinals and in laterals: in transsonic flow it has maximum stability whereas at hypersonic speed stability decreases. But the center of gravity cannot be shifted in an arbitrary range, to overcome the FCS problems. The highest Mach number defines the limit of instability (i.e. the aft c.g. location). Thus the stability margin at supersonic speed is increased (which means trim losses). Also control surface effectiveness shows a dramatic change from supersonic to hypersonic speed: in low speed it is usually reducing at high deflection angles, but rises at hypersonic Mach numbers, caused by the nonlinear growth of precompression with increasing α, η and Mach.

These are important trends within the envisaged flight envelope, globally sketched. But in detail stability and control surface effectiveness in hypersonics are most critical to predict exactly, with windtunnel tests as well as with CFD codes, as the first shuttle re-entry demonstrated (the flap efficiency had been overestimated).

This is due to the environment of a hypersonic aircraft, given by the altitude in terms of temperature and density, which cause a great number of aerothermodynamic problems in high speed, such as temperature rise, real-gas effects, heat transfer effects, shock-boundary layer interactions etc., which have an influence on stability and control. The reason is the very low density at maximum altitude of only 0.3%, compared to 100% at sea level. The Reynolds number within the flight envelope therefore varies over almost a number of magnitude, from subsonic to the achieved hypersonic maximum speed.

In general, the design of a TSTO is affected by the propulsion integration (i.e. forebody and base shape), by the Mach cone, and by the integration of the upper stage. Figure 2 /1/ sketches the growing importance of the power plant with increasing Mach number. The propulsion package (4 to 6 turbo-/ramjet combinations) is mounted on the lower side of the fuselage in order to take advantage of the precompressed flow of the wing/fuselage lower side and to use the rear part of the fuselage as a half nozzle contour. As a consequence, the forces and moments of the power plant in certain regimes are of the same order as the global aerodynamic forces and moments. Because it is not possible to represent a functional intake of a turbo-/ramjet combination (with a variable geometry) on a small windtunnel model, the power plant area is totally omitted in the present windtunnel test campaign. The forces and moments resulting from intake and nozzle flow had been subject of a different working group at

MBB by CFD calculations. To obtain a realistic dataset for the flight configuration, the power plant and aerodynamic datasets have to be combined by an exact bookkeeping method. The consequences should be kept in mind watching Fig.3 /2/, where the importance of the lower side of specific lifting surfaces vs Mach number is shown.

Longitudinal control is provided by trailing-edge flaps which, in differential mode, operate as ailerons for the roll control. Double fins with integrated rudders provide directional stability within the entire α-Mach regime. The fins of the upper stage are located directly upstream of the fins of the lower stage to minimize drag. Due to this location of the wing tip mounted fins, a vortex interaction with the strong vortices of the lower stage wing was expected and had been one of the subjects of testing. The centres of gravity of both stages coincide in longitudinal direction, to minimize changes in pitching moment after upper stage launch.

Now some of the main problems of the present windtunnel test are described.

Short measurement times of the windtunnels cause dynamic difficulties and also heat transfer simulation is not possible. The blow-down type windtunnel induces an excessive amount of noise to the flow (which might cause boundary-layer transition). Tripping is uneffective at hypersonic Mach numbers so that the boundary-layer transition area could not be fixed. As already mentioned, the small model size causes problems not only with the power plant, but also does not allow pressure measurements on wings and fins, only on the center line of the lower side of the fuselage and at the base. Additionally, due to the size the Reynolds numbers in the used windtunnels were low. The windtunnel tests had been laid out to represent roughly the total Mach number range (up to Mach 6) of the typical mission, *employing four types of windtunnels.*

The Reynolds numbers (based on body length) along the trajectory are presented in Fig.4, together with those of each windtunnel test run. This figure shows differences between one and two numbers of magnitude in Reynolds number. Herewith the problems in understanding the aerothermodynamic phenomena dominated by viscous effects are aggravated.

The main problem areas (in particular respect to vortex interaction and upper stage influence) to be clarified are:

- o longitudinal stability
- o lateral stability
- o control surface effectiveness
- o stage separation (Mach > 6)

The presented results of the tested characteristics have the following structure:

- o stability of the baseline configuration (longitudinal/lateral)
- o control surface effectiveness (longitudinal/lateral)

- o stage separation (longitudinal interference effects)

3. DESCRIPTION OF THE WINDTUNNEL TEST CAMPAIGN

Facilities and Measurement Phases
(s. Fig. 4)

The present results of the test campaign are based on the windtunnel test runs in the following DLR facilities:

WT1: Niedergeschwindigkeits Kanal MUB,
Braunschweig
WT2: Transsonischer Windkanal TWG, Göttingen
WT3: Trisonikkanal TMK, Köln
WT4: Hyperschallkanal H2K, Köln

Type:

WT1: closed, continuous
WT2: closed, slotted, continuous
WT3: closed, (perforated), smooth blow-down
WT4: open, blow-down, suc-down

Some of the tests were realized by a contribution of the DLR budget, which is greatfully acknowledged.

Facilities Main Data:

	Mach range	A.o.A. [°]	Reynolds number (*10^6)
WT1	0.1 to 0.4	-5. to 20.	1.2 to 4.2
WT2	0.5 to 2.0	-2. to 12.	3.2 to 5.8
WT3	0.4 to 0.5	-2. to 12.	6.5 to 15.
	0.5 to 1.15	-2. to 12.	15. to 20.
	1.6 to 4.0	-2. to 12.	15. to 40.
WT4	6.0	-5. to 10.	0.5 to 3.4

Balance: 0.75" Task Able Strain gauge ('extended range')

Windtunnel Model

Size: 1:160
Material: Titanium
Controls: Flaps and rudders with fixed deflection angles

Model/flight configuration differences:

- o the base contour is filled in the nozzle area to allow conventional sting mounting

- o the power plant package (turbo-/ramjet combination) is completely omitted, except the engine side walls to provide an appropriate representation of the power plant in sideslip

A sketch of the model is given in Fig.5, including the separation measurement principle.

Tripping:

Measurement phases I:		generally none
II:		-"
Additional phases:		
	WT2	K1 Ballotini 0.3 mm ϕ (upper side)
	WT3	K2 Karborund 120 K3 Karborund 60 (K2/K3: upper- & lower side & nose)

4. RESULTS

4.1 MAJOR TRENDS AND EFFECTS ON STABILITY AND CONTROL:

Clean Configuration

- Longitudinals

A very prominent influence of the upper stage on the pitching moment behaviour was identified in windtunnel testing as well as in CFD-calculation. This influence depends strongly on the A.o.A. (Fig. 6): Comparing the pitching moment characteristics in the supersonic Mach regime for the configuration with and without the upper stage, one can observe a significant amount of pitch up, induced mostly by the compression in the rear part of the open bay. This area is located rearward of the moment reference point and therefore the pressure distribution yields a pitch-up. Additionally, a suction peak occurs forward of the a.c. due to the changed contour without upper stage. This influence of the open bay is clearly reduced with increasing A.o.A. and it nearly vanishes for hypersonic Mach numbers greater than 6 and $\alpha > 5^\circ$, where separation of the upper stage will take place (compare subsketch in Fig.6). For confirmation an additional figure is shown with the pressure coefficient on the center line on the upper and lower side of the configuration (Fig.7)., at $\alpha > 5^\circ$ and Mach 2, /3/. The pressure distributions only show a small difference on the lower side at the rear part of the fuselage, whereas the upper side C_p-distribution demonstrates the reason for the positive pitching moment increment for the configuration without upper stage: A relatively broad suction peak in front of the a.c. and a positive C_p behind, acting both as pitch-up increment.

The difference in stability margin is not that dramatically influenced by the upper stage (Fig.8): at subsonic speed the configuration without upper stage is only 0.3% less stable and in supersonic regime above Ma 1.5 it is about 0.7% more stable. The configuration with the upper stage is neutrally stable at Mach 3.2 at zero A.o.A., but stability increases above Mach 4 with increasing A.o.A..

- Laterals

Directional stability decreases with increasing Mach number, as expected, very similar due to the behaviour of $C_{L\alpha}$ and $C_{m\alpha}$ related to Mach number, the fins acting as wings in terms of β. Therefore the maximum Mach number of the flight envelope determins the size of the vertical fins (Fig.9). This figure also shows a well known behaviour of $C_{n\beta}$ vs A.o.A.: In subsonic speed, the flow on the upper side of the wing is accelerated with increasing A.o.A. so that the efficiency of the fins is augmented. In the supersonic speed regime the shock shaded parts of the fins naturally grow with A.o.A. and efficiency is linearily reduced. It is supposed that the divergence tendency in hypersonic Mach regime above Mach 5 is somewhat recovered by the side walls of the engine package, which have about 30% of the area of the fins in lateral projection and, therefore, have the effect of dorsal fins. Together with the lower side of the wing they produce a corner flow in sideslip, which may either reduce its stability by flow separation or amplify it by a small precompression effect at high Mach numbers at a combination of A.o.A. and sideslip angle (both in the order of 5°).

There is a surprising influence of the upper stage on directional stability: Within the whole tested speed range the upper stage reduces stability. This means that the amount of stability produced by the fins of the lower stage alone is greater than that of the fins of both stages. (The influence of the upper stage obviously diminishes at maximum Mach number near 6 or slightly above (and $\alpha > 5^\circ$), where the configuration becomes unstable.) This result was quite opposite from what was predicted, though interference effects were taken into account for a first estimate. The upper stage as well as the lower stage on their own were designed to be stable. So globaly only interference effects might cause the reduction. Two reasons are considered so far: Probably the upper stage forebody (incl. the coverage) produces more destabilizing effects by interfering with the forebody of the lower stage than expected. A second assumption is a strong flow straightening effect by the upper stage fins on the lower stage fins located in the same plane. All these effects act together. Despite these considerations, natural directional stability is attainable by a configuration of the investigated TSTO type with a back mounted second stage.

In general, $C_{l\beta}$ is mostly dependent on the wing planform and therefore coupled with the lift slope of the wing (Fig.10). The measurements confirmed the expected linear behaviour of $C_{l\beta}$ vs α, so this coefficient can be separated into a Mach dependent and an α-Mach dependent contribution, i.e.: $C_{l\beta} + C_{l\beta\alpha} \cdot \alpha$. The characteristics of the first term (vs Mach) was estimated very well by handbook methods, but the measurements did not meet the predicted values. The above mentioned additional stabilizing effect of the power plant sidewalls on directional stability would have the opposite effect on $C_{l\beta}$. Unfortunately the configuration was not measured without the engine side walls to state this. Again the configuration with the upper stage demonstrates less stability in comparison to the lower stage solo. The reasons are assumed to be mostly the same as for $C_{n\beta}$. On the other hand, the A.o.A. dependent part, i.e. $C_{l\beta\alpha}$, gains more with increasing A.o.A. than predicted. In the supersonic region above Mach 2 (with the upper stage) at zero angle, the behaviour is indifferent, which means, that the surfaces above and below the a.c. point are facing the side flow in equivalent portions and/or compensation of all stabilizing and destabilizing effects takes place (compare for example the small anhedral of the wing and the fins working against each other). A note should be given at that point: The measurements with sideslip angle β were carried out without any tripping, so that transition was not fixed and Reynolds number effects are possible. Compare the presented curves of $C_{l\beta}$ (Ma) (Fig.10) and the Reynolds number curves vs Mach number (Fig.4). A Reynolds number difference by factor 3 from WT2 to WT3 results in an A.o.A. dependent gap in the $Cl\beta$-curve. $C_{L\alpha}$ shows the same (but rather weak) tendancy, so mostly this effect is attributed to the wing lift. The difference of $\Delta Re \approx 10^7$ occurs in a critical transitional range, concerning boundary-layer flow and therefore may have an influence on separation. Additionally, in the low supersonic speed range the wing produces a very well established system of vortices along the leading edge ($\alpha > 4°$). The higher Reynolds number of the WT3 allows the vortex generation only at higher A.o.A., but then it is located further outboard of the wing and produces more rolling moment power than the low Reynolds number vortex. This might be an additional α-Re dependent effect.

General Remarks on Flap Efficiency at Hypersonic Speed

The efficiency of any kind of controls at hypersonic speed is influenced by viscous effects. In general the Reynolds number of the involved boundary-layer of a TSTO, as already mentioned, is by about a number of magnitude lower at high speed compared to low speed. Additionally, very strong shock waves exist on and near deflected flaps. In those regions also strong shock boundary-layer interactions occur and the induced flow separation (in this case i.e. mostly boundary-layer separation) may increase, reduce or completely delete the control surface effectiveness. The pressure distribution, for example, along a deflected flap can have remarkable jumps at separation lines and also in the reattachment areas.

Generally the separated flow is affected by the state of the boundary-layer, i.e. laminar, transitional or turbulent. Separation characteristics of main interest are flap effectiveness, pressure rise and the extension of the separation region. But the separation phenomena are very difficult to predict and also to find experimentally. Future measurements should focus on this problem and infrared measurement techniques could probably give answers to details.

The sketch in Fig.11, taken from DATCOM /4/, gives a two-dimensional scheme of the mechanism of separation and the correlated global pressure rises in laminar and turbulent flow. Laminar flow separates earlier, caused by adverse pressure gradient along the surface, than the turbulent one. The laminar separation zone may extend 10 times further than the turbulent one. This is due to the higher compatability of adverse pressure gradients of the turbulent boundary. The turbulent pressure rise is able to reach twice the value of the laminar one. The long separated region of the laminar flow reduces control power of the deflected flap.

Flaps & Rudders

- Longitudinals

Figure 12 illustrates the typical change in the behaviour of trailing-edge flap efficiency in the transition region between super- and hypersonic Mach numbers: Increasing the Mach number in the supersonic regime up to Mach 2+, efficiency decreases with increasing flap deflection angle in a well known manner. Further increase in Mach number causes a characteristical change in the following way: with positive A.o.A. and positive deflection angle efficiency is increased nonlinearly by precompression of the lower side of the wing. It is a function of A.o.A., flap deflection angle η and Mach number, and was detected to start above Mach 2 in the measurements.

In the case of the measurements in WT4 it is assumed that most parts of the model boundary-layer were laminar. The selected combinations of A.o.A. and flap deflection angle, presented in Fig.12 vs Mach number, therefore probably exhibit an exaggerated reduction in efficiency at Mach 6. The reasons are assumed to be either the described separation influence or boundary-layer thickness: between Mach 4 in WT3 and Mach 6 in WT4 there is a Reynolds number reduction by a factor of 10. Even if at both Mach numbers the boundary-layer in the flap area was turbulent, the boundary layer at Mach 6 is thicker ($\delta_{BL} \sim (Re)^{1/5}$), which reduces the efficiency as well. The dependance of the flap efficiency $C_{m\eta}$ vs Mach and A.o.A is sketched in Fig. 13. A transitional line with the described change in the behaviour of the efficiency is presented, dependent on A.o.A. and Mach number. This result is preliminary, because especially on the flight configuration some more reducing and also amplifying effects must be taken into account. Also investigations concerning the state of the boundary-layer in the flap area should be carried out next.

Fig.14 offers an example of the measured values of $C_{L\eta}$ and $C_{m\eta}$ at Mach 2, which demonstrates a strong interference effect at -10° flap deflection angle. This interference effect is attributed to a flap-vortex interaction as the vortex core is located directly above the flap. This tendency was also seen at lower or higher Mach numbers in the supersonic speed regime.

- Laterals

Rudders: $C_{n\varsigma}$, $C_{l\varsigma}$

The rudder effectiveness was determined at a deflection angle of ς=10° (Fig. 15). At zero A.o.A. the prediction for $C_{n\varsigma}$ (configuration with upper stage) in supersonic speed coincides with measurement. Usually the interference between upper and lower stage is more difficult to predict, especially at higher A.o.A., because of flow separation and wake impingement on the rudders. Both, the direct and the coupled derivatives are reduced by the presence of the upper stage, very similar for example to the directional stability behaviour. The part of the balance, which is responsible for the coupled derivative $C_{l\varsigma}$ (rolling moment coefficient) was at its lowest sensitivity limit, the absolute values in hypersonics for example only reach 10^{-5}. At an A.o.A. of 10° and ς=10° the upper stage interference may cause a change in sign in $C_{l\varsigma}$ at Mach numbers above 2.5 (Fig.15). This case should be carefully investigated.

4.2 OTHER EFFECTS

- Separation of Upper Stage

The nominal separation procedure (s. Fig. 16) is supposed to take place at a Mach number between 6 and 7 and an altitude between 35 and 40 km in a pull-up zero-g procedure. For a safe stage separation it might be necessary to support the procedure by a lifting holder mechanism, to avoid an uncontrolable pitching moment behaviour of the upper stage by interference effects. The windtunnel test was performed in WT4 at Mach 6.0 with two different balances for the upper and the lower stage (s. Fig. 5). The actual Reynolds numbers were $1.8 * 10^6$ and $3.4 * 10^6$ in two test campaigns. At this fixed Mach number the longitudinal behaviour of both stages was investigated by variing three parameters: A.o.A., incidence angle $\varepsilon = \Delta\alpha$ between both stages and the vertical distance, related to the body length ($\Delta z/l_{Body}$). The kinematics of the upper stage during separation are described by rotation and translation ($\varepsilon + \Delta z$). In Fig. 17 and 18 the most outstanding interference effects are summarized. The lift increments of the upper stage resulted in always positive, upward directed values. The lift of the lower stage is affected only marginally. The pitching moments of both stages demonstrate a strong dependance on all parameters, i.e. versus A.o.A., ε, Δz. At $\varepsilon \geq 4°$ a nose down tendency in C_m occured at a small value of Δz (i.e. very close proximity). Therefore the holder mechanism might be necessary.

When Δz is increased and the upper stage is still connected by the holder, lift and drag components of the upper stage (and pitching moment) cause an additional pitching moment contribution on the lower stage (s. Fig. 19). The maximum possible Δz and ε values therefore are limited by the lower stage flap efficiency of the positively deflected flaps and its heat load resistance. The gap between lower and upper stage during separation produces a lot of interference effects by shock boundary-layer interactions, similar to a nozzle flow, which only can be investigated in detail by high sophisticated CFD calculations. No more interaction is possible above a distance of $\Delta z/l_{Body} \sim 0.2$ and $\varepsilon \leq 8°$, due to the narrow Mach cones at Mach 6. The DLR is preparing further measurements for WT4 with the possibility of continuously variing α, ε and Δz, and additionally with a second hypersonic windtunnel nozzle at Mach 7. Fig.20 offers a Schlieren picture series at α=0°, ε = 2° and different Δz, from which interference areas of both stages are easy to identify.

- Comparison to Approximative Methods

Most of the longitudinal and lateral characteristics have been determined by handbook methods (total Mach range) and by the HYP3 code (Mach > 2) /5/ during the very first design phase. Fig.21 shows the panel model of the TSTO that was used in the calculation with HYP3. The code was developped at MBB and is based on different impact methods. Fig.21 also includes the plotted values of pitching moment, as calculated by HYP3 and, for comparison, as measured in WT3 at Mach numbers 2, 3, and 4.5. Tendencies are predicted well, but absolute values in some cases are not reliable. This is due to the simplified methods which calculate pressure and coefficients of the entire configuration well and only locations with strong interactions are not represented correctly.

5. CONCLUSIONS

A windtunnel investigation has been performed at DLR facilities with a generic WLC-TSTO wind tunnel model, designed at MBB, within a Mach number range from 0.2 to 6.0 and an A.o.A. range from -2° to 12°. Major emphasis was placed on stability and control in the super- and hypersonic Mach range up to Mach 6. Additionally, the separation procedure was investigated in a first step. Due to the differences between the wind tunnel model and the flight configuration, above all in Reynolds number, and also some substantial shortcomings of the model and the involved facilities, only tendencies could be given.

Based on the results of this investigation the following conclusions were made:

1. The wide Mach number range (0.2 to 7.0) and the requirement for horizontal takeoff and landing causes a substantial shift of the aerodynamic center with maximum stability at Mach 1.2 and minimum stability at Mach number 7. The total difference between these extremes is about 10%, based on body length. A retractable canard might therefore be necessary to compensate in low speed and in the transsonic Mach range.

2. The upper stage in most cases reduces stability in longitudinals and in laterals. This is due to the interference effects between upper and lower stage, caused by flow separation and vortex interactions on the upper side of the configuration with increasing A.o.A. In total, natural stability is achieved within the concerned α-Mach range (longitudinal/lateral), except some extreme combinations of α, η, ς and Mach, which should be subject of further investigations.

3. The flap/aileron efficiency turned out to be a complicated function of α, η, and Mach: From low speed to supersonic speed, flap efficiency generally decreases with α or η, but in hypersonic Mach regime it increases with positive α, η-values and with Mach number. Additionally, the Reynolds number affects the flap efficiency in a noticeable manner by separation effects at hypersonic Mach numbers, which are *different between* laminar and turbulent flow. Additional measurements should focus on this problem involving infrared measurement techniques.

4. The separation procedure at Mach number 6 demonstrated a strong influence on the upper stage, resulting in lift increments always directed away from the lower stage, but in a nose down pitching moment, dependent on vertical distance to the lower stage and on the incidence of the upper stage with respect to the lower stage. The lower stage receives an additional increment of positive pitching moment by induction of the upper stage lift, drag and moment when both stages are connected by a holder within the first separation phase. Flap efficiency of the lower stage and heat load to the holder play the limiting role to the maximum allowable vertical distance in connected mode.

5. Handbook methods and the involved predesign code HYP3 were considered adequate for preliminary estimation of longitudinal and lateral coefficients and derivatives, as far as the characteristics stay within the linear range and no extreme combinations of A.o.A. and positive flap deflection angles at high Mach numbers are concerned. Interference effects generally are very difficult to predict and in some cases the measurement resulted in just the opposite behaviour to the prediction.

REFERENCES

/1/ C.L.W. Edwards,W.J. Small, J.P.Weidner
Studies of Scramjet/Airframe Integration Techniques for Hypersonic Aircraft
AIAA-Paper 75-58, 1975

/2/ R. Ceresuela
Stability and Control Problems of Hypersonic Aircraft
ICAS-Paper 70-17, 1970

/3/ Eberle A.
Enhanced Numerical Inviscid and Viscous Fluxes for Cell Centered Finite Volume Schemes, paper selected for publication in 'Computers and Fluids', Editor Stanley Rubin, 1992

/4/ USAF Stability and Control DATCOM
MCDonnel Douglas Corporation
Douglas Aircraft Division

/5/ Cucinelli, G.; Kämpf,P.
Hyperschall-Aerothermodynamik:
Eine approximative Beiwertmethode
für den Vorentwurf
MBB-FE211-AERO-MT-825
Dezember 1988

FIGURES

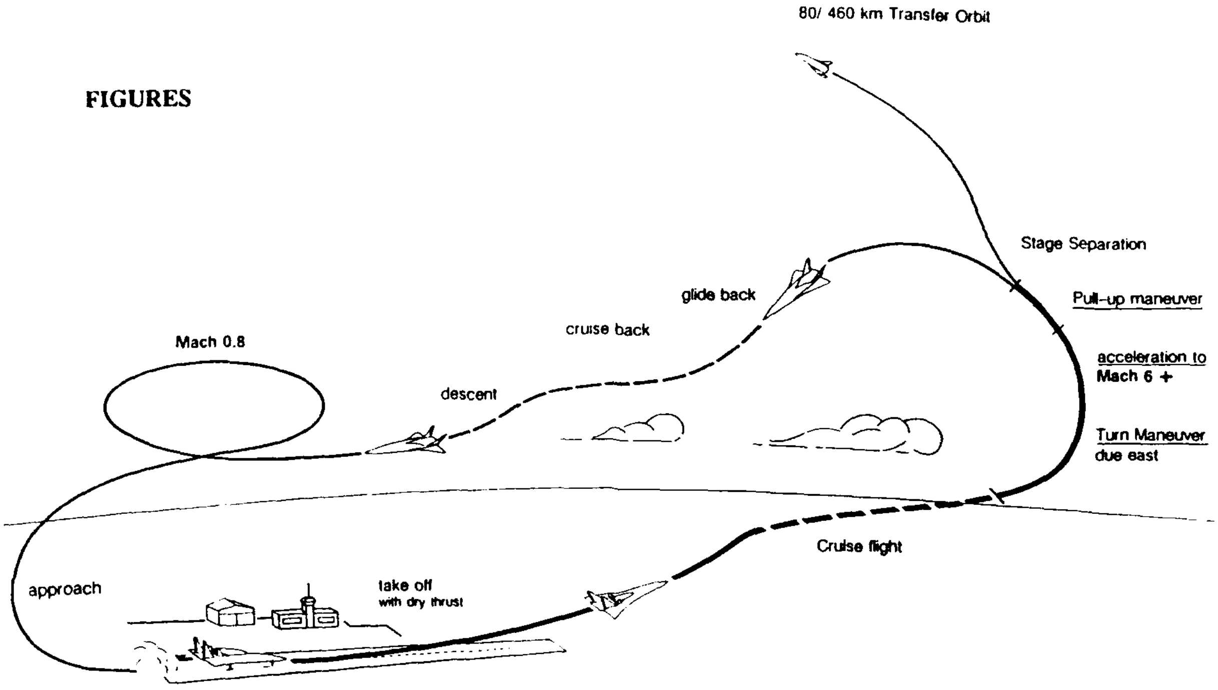
80/ 460 km Transfer Orbit
Stage Separation
Pull-up maneuver
acceleration to Mach 6 +
Turn Maneuver due east
Cruise flight
glide back
cruise back
descent
Mach 0.8
approach
take off with dry thrust

Fig.1 Mission Profile of a TSTO Configuration

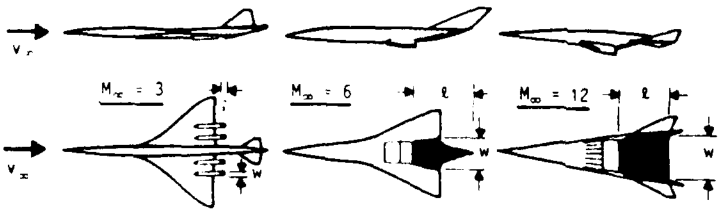
V_∞
$M_\infty = 3$
$M_\infty = 6$
$M_\infty = 12$
ℓ
w
V_∞

Fig.2 Importance of Power Plant with Increasing Mach Number, after /1/

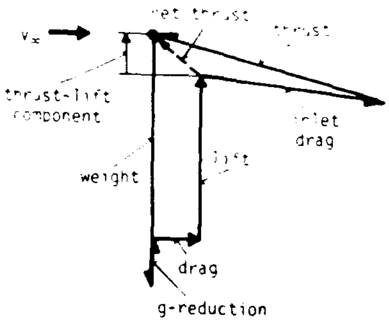
V_∞
net thrust
thrust
thrust-lift component
inlet drag
lift
weight
drag
g-reduction

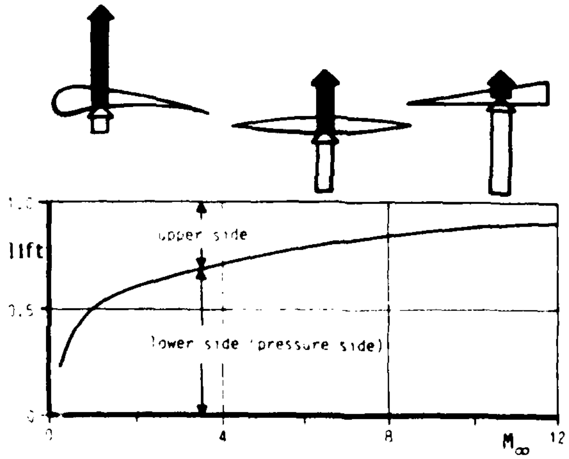

Fig.3 Lift Contributions of Lower & Upper Side of Lifting Surfaces vs Mach Number, after /2/

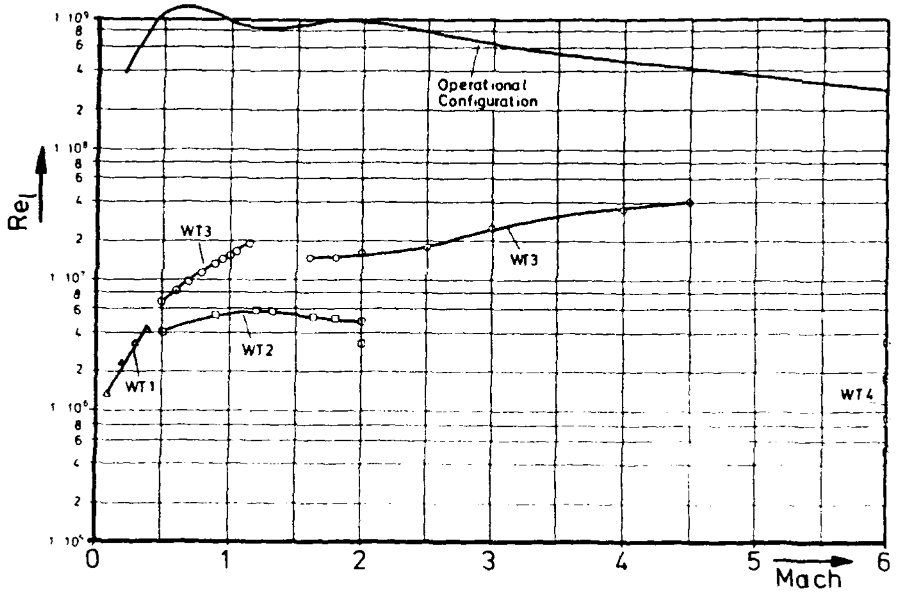

Fig.4 Reynolds Numbers of the Flight Configuration and of the Model in Different Windtunnels

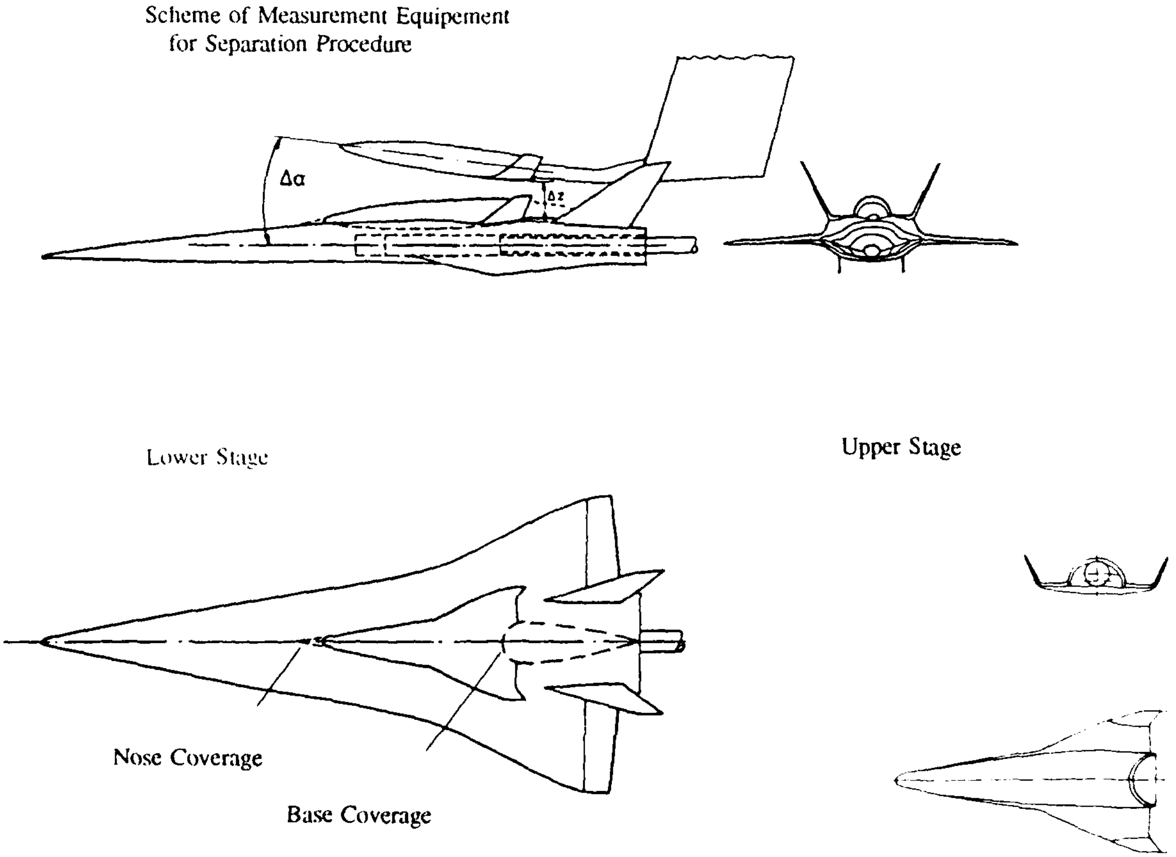
Scheme of Measurement Equipement for Separation Procedure
Δα
Δz
Lower Stage
Upper Stage
Nose Coverage
Base Coverage

Fig.5 Sketch of Windtunnel Model

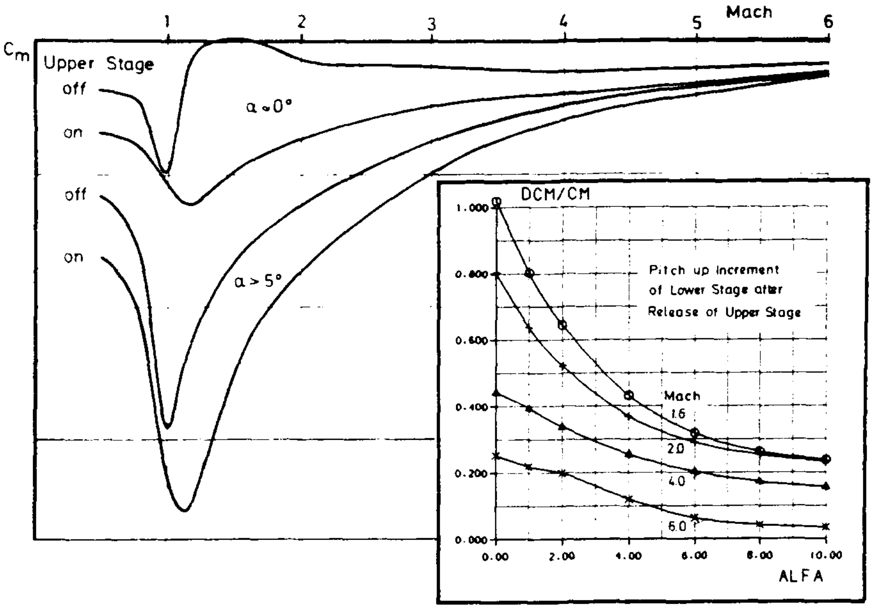

Fig.6 Basic Pitching Moment Characteristics, With and Without Upper Stage

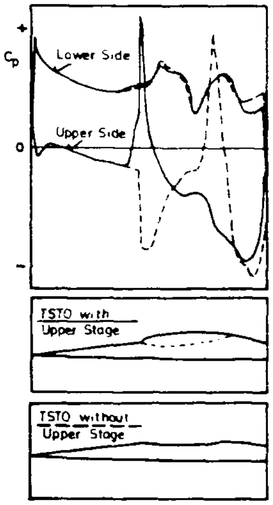

Fig.7 C_p on C.L., Lower Stage, 'EUFLEX'Code /3/

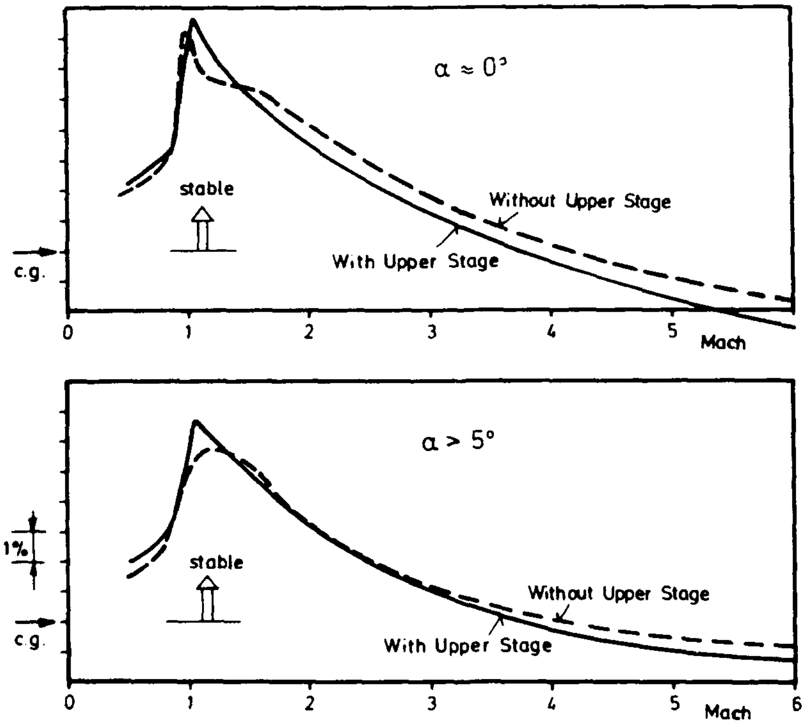

Fig.8 Location of A.C., With and Without Upper Stage

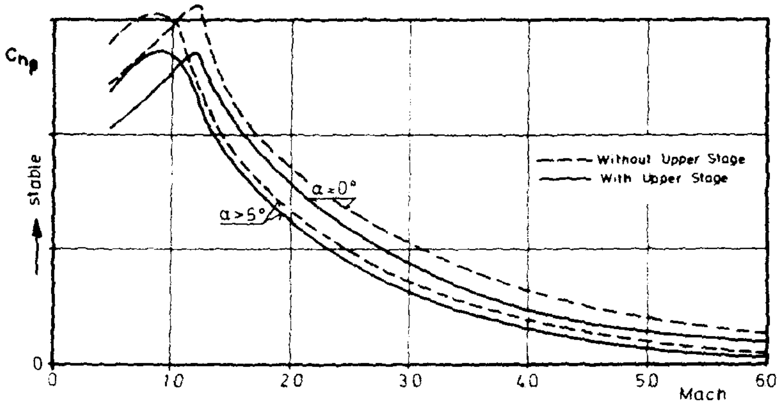

Fig.9 Directional Stability $C_{n\beta}$, Influence of A.o.A and Upper Stage

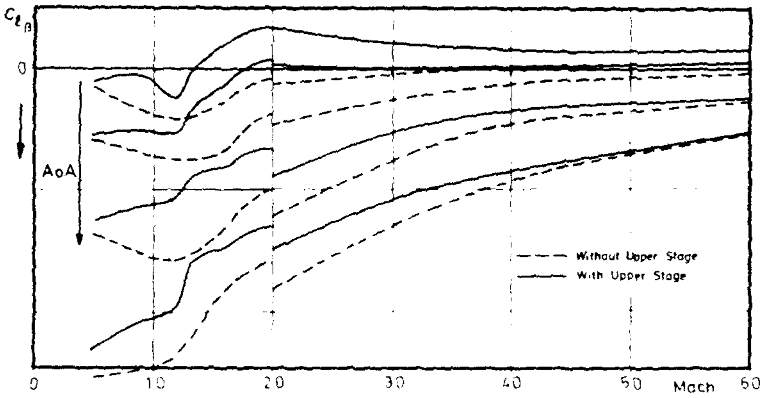

Fig.10 $C_{\ell\beta}$, Influence of A.o.A. and Upper Stage

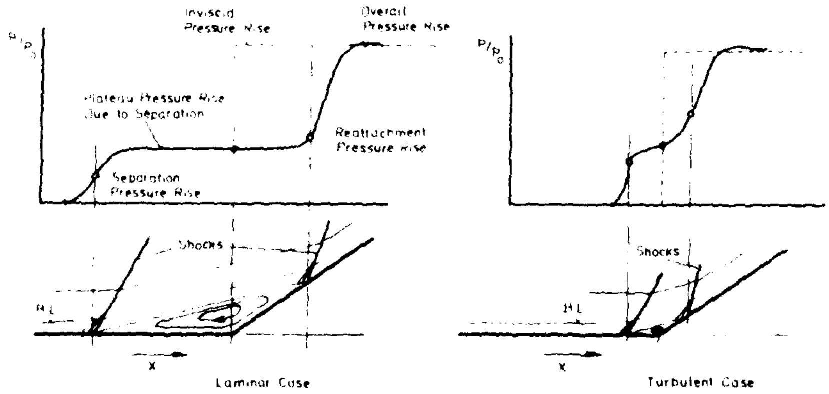
P/P₀
Inviscid Pressure Rise
Overall Pressure Rise
Plateau Pressure Rise Due to Separation
Reattachment Pressure Rise
Separation Pressure Rise
Shocks
H L
x
Laminar Case
P/P₀
Shocks
H L
x
Turbulent Case

Fig.11 General Boundary Layer Influence on Flap Efficiency /4/

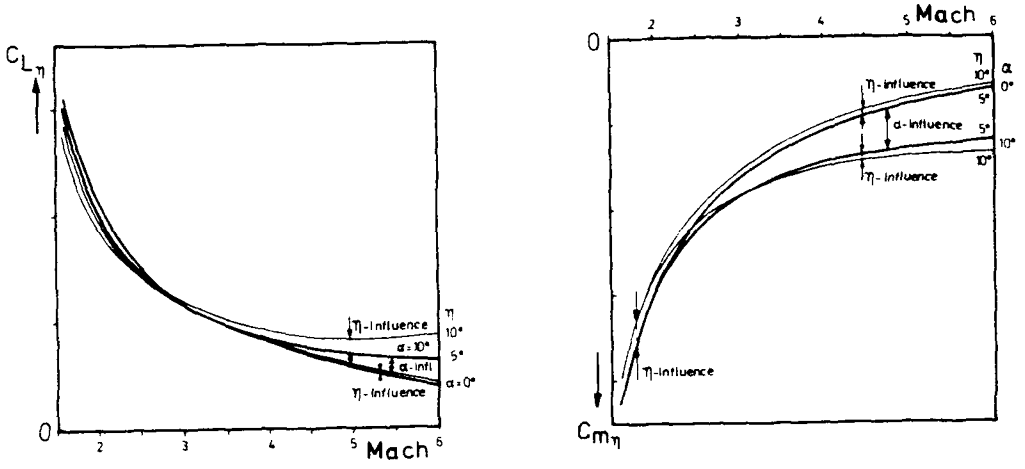

Fig.12 Flap Efficiency on Lift and Pitching Moment Coefficients

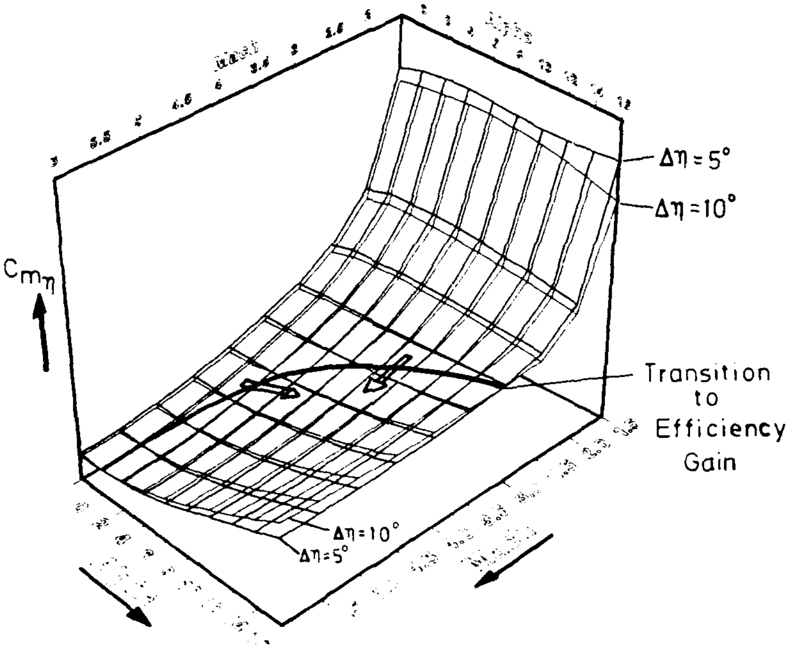

Fig.13 $C_{m\eta}$ vs Mach and Alfa

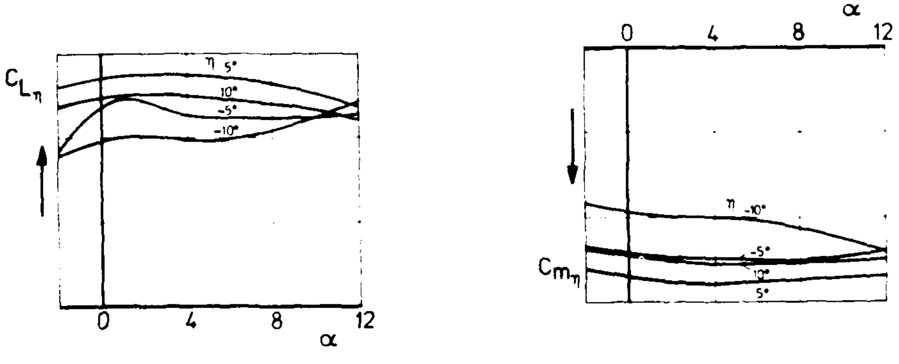

Fig.14 Influence of A.o.A. on $C_{L\eta}$ and $C_{m\eta}$ at Mach 2, TSTO with Upper Stage (Vortex Interaction Example)

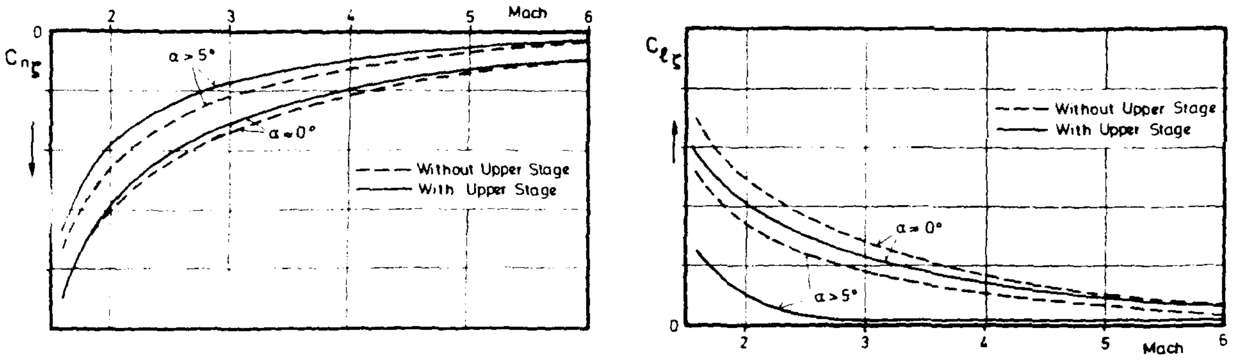

Fig.15 Effectiveness of Rudders, C_{n_ζ} and C_{l_ζ}, $\zeta_L = \zeta_R = -10°$

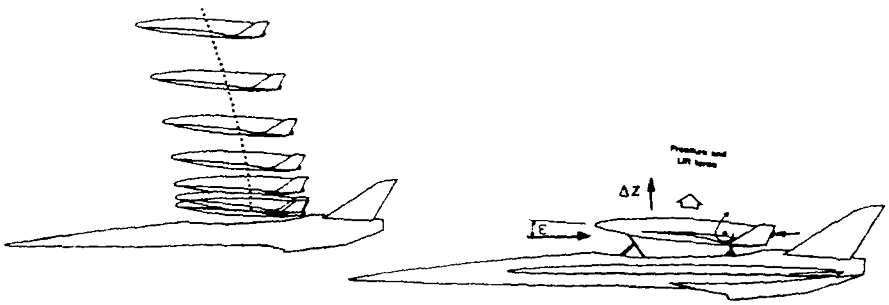

Fig.16 Stage Separation Scheme

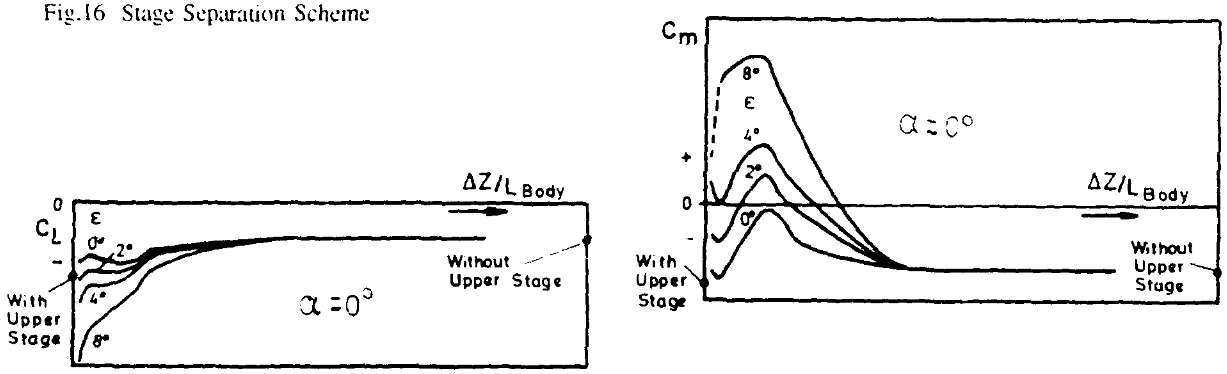

Fig.17 Interference Effects on Longitudinals vs Δz (Lower Stage)

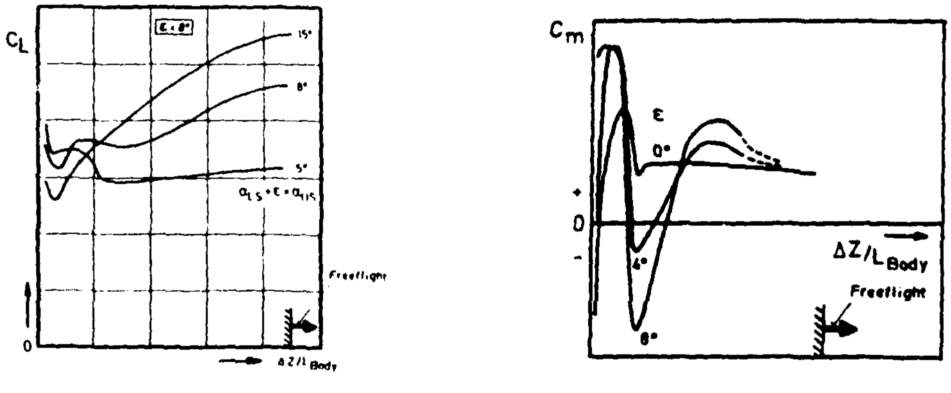

Fig.18 Interference Effects on Longitudinals vs Δz (Upper Stage)

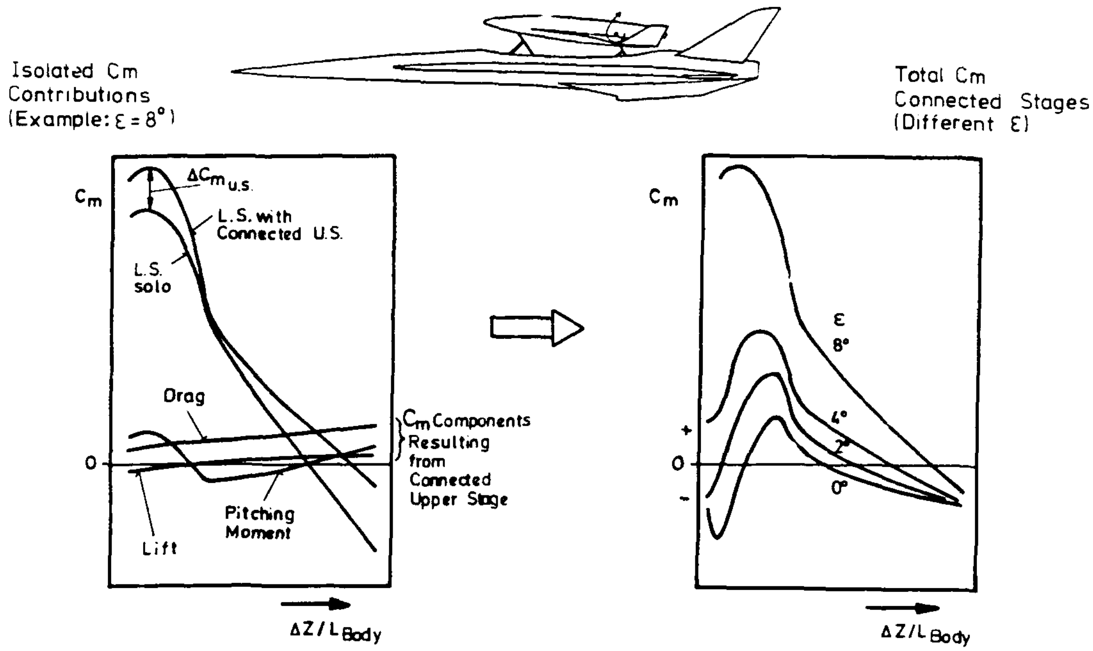

Fig.19 Total Pitching Moment of the Connected Configuration During Separation α=0°

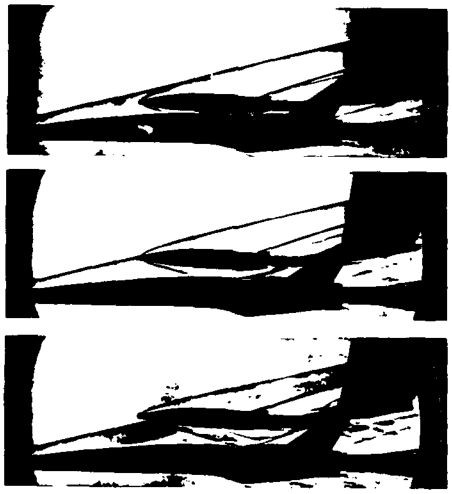

Fig.20 Schlieren Pictures of the Separation Procedure (ε= α=0°, Re=1.8•10^6, Different Δz)

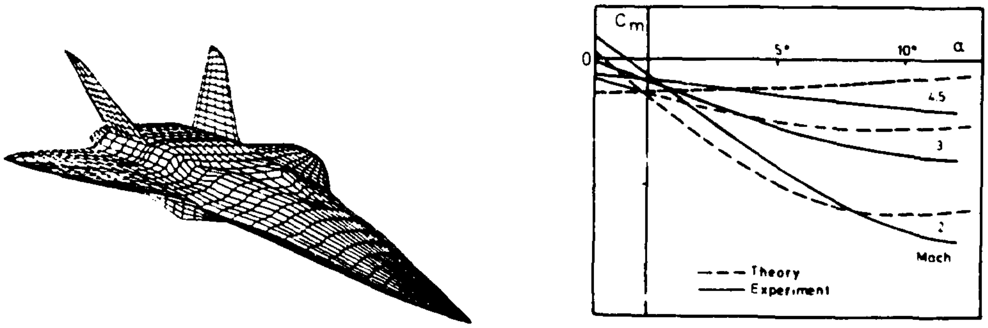

Fig.21 Comparison of Measurement and Calculation (Approx. Method HYP3) in Pitching Moment at Supersonic Mach Numbers /5/

NUMERICAL SIMULATION OF THE FLOW THROUGH A SCRAMJET ENGINE

V. Selmin
Alenia Aeronautica D.V.D.
TEVT–Metodi Fluidodinamici
C.so Marche 41, 10146 Torino, Italy

ABSTRACT

In this paper, an inviscid numerical method has been developed to simulate the flow through each component of a scramjet engine. We will emphasize the effects due to non ideal gas assumption and to H_2/air chemistry on the performance of air intakes and nozzles.

1. INTRODUCTION

The exponential growth of computer speed and storage capacity as well as algorithm sophistication has allowed the application of advanced numerical methods to practical design problems in many engineering disciplines such as fluid dynamics. More and more use is being made of numerical methods in analysing complex flow fields than has been possible in the past. The recent resurgence of interest in developing hypersonic airbreathing aircraft and missiles has resulted in a significantly increased effort focused on the development of supersonic combustion ramjet(scramjet) engines. A scramjet engine consists of an air inlet, a combustion chamber and an exhaust nozzle. Of vital importance to engine propulsive efficiency, and hence vehicle payload capacity, is the precise optimization of the aerodynamic design of the scramjet engine and its components. Modern computational methods allow the direct simulation of the flow field in a reasonably efficient way. Intelligent use of such capability can be very helpful in eliminating the poorer designs and allowing promising configurations to be developed with less reliance on extensive wind tunnel testing.

In this paper, we will deal particularly with a discussion of the effect due to non ideal gas assumption and to H_2/air chemistry on the performance of air intakes and nozzles. Our purpose is to understand qualitatively the role that chemistry plays in a hypersonic engine rather that to obtain quantitative predictions of actual scramjet performance. Consequently, we have decided in favour of an inviscid numerical method to simulate the flow through each components of a scramjet engine and evaluate its performance.

For an ideal gas (calorically perfect gas), the efficiency parameters of the air intake (total pressure recovery, kinetic energy efficiency, etc.) can be expressed by the usual relations taking into account the Mach number and the specific heats ratio. But, the design of an inlet for hypersonic application will require the consideration of deceleration and compression induced temperature effects that are beyond the range of validity of the ideal gas model. A sound theoretical assessment of inlet performance must therefore take into account for caloric imperfections, such as the vibrational molecular motion. In particular, we show that the complexity of the calorically imperfect gas model does not lend itself to the same explicit equations as the ideal gas model.

At last, a sensitivity analysis on parameters which influence the combustion of H_2+air is performed. This analysis examines the effects on combustion efficiencies by varying various flow parameters in order to help identify conditions for maximum chemical yield and thrust.

2. FLOW MODELIZATION

2.1 Euler equations

The two-dimensional inviscid gas dynamic equations can be expressed in conservation law form as:

$$\frac{\partial W}{\partial t} + \vec{\nabla} \cdot \vec{F}(W) = 0 \qquad (1)$$

where the unknown W and the flux vector $\vec{F} \equiv (F, G)$ are given by

$$W = \begin{pmatrix} \rho \\ \rho u \\ \rho v \\ \rho e_t \end{pmatrix}, F = \begin{pmatrix} \rho u \\ \rho u^2 + p \\ \rho u v \\ \rho u h_t \end{pmatrix}, G = \begin{pmatrix} \rho v \\ \rho u v \\ \rho v^2 + p \\ \rho v h_t \end{pmatrix}$$

respectively. Here ρ, $\vec{w} \equiv (u, v)$, e_t, p and h_t denote the mass density, the velocity vector, the total energy per unit mass, the pressure and the total enthalpy per unit mass. The total enthalpy is expressed as

$$h_t = e_t + \frac{p}{\rho} \qquad (2)$$

The pressure is in general related to the flow variables by an equation of state of the type:

$$p = f(\rho, e) \qquad (3)$$

where $e \equiv e_t - \frac{1}{2}\|\vec{w}\|^2$ is the internal energy per unit mass.

2.2 State equation

We can describe the modelization of a real gas as a mixture of perfect gases which are subject to chemical reactions. The state law must take into account, on one hand, the species composition and, on the other hand, the excitation of internal degrees of freedom of atoms and molecules (translation, rotation, vibration).

The internal energy takes then the form

$$e \equiv \sum_{i=1}^{ns} Y_i e_i = \sum_{i=1}^{ns} Y_i C_{vi} T + \sum_{i=1}^{ns} Y_i h_i^0 + \sum_{i=1}^{ns} Y_i e_i^{vib} \quad (4)$$

In this formula, h_i^0, Y_i, and C_{vi} represent the energy of formation, the mass fraction and the specific heat at constant volume of species i, respectively. Note, that

$$C_{vi} = \begin{cases} (3/2)R_i & \text{for atoms} \\ (5/2)R_i & \text{for diatomic molecules} \\ (7/2)R_i & \text{for triatomic molecules} \end{cases}$$

where $R_i = \mathcal{R}/m_i$ is the gas constant for species i; $\mathcal{R}$ is the universal gas constant and m_i is the molar mass of the species i. Moreover, e_i^{vib} represents the vibrational energy for molecules which, if we assume a gas in vibrational equilibrium takes, the form

$$e_i^{vib}(T) = \sum_{j=1}^{nli} \frac{\theta_i^j R_i}{\exp(\theta_i^j/T) - 1} \quad (5)$$

where θ_i^j is the characteristic vibrational temperature of the jth vibrational degree of freedom of the molecular species i and nli represents the number of these degrees of freedom. Using *Dalton*'s law, the pressure is given by

$$p = \rho T \sum_{i=1}^{ns} Y_i R_i \quad (6)$$

Eqs. (4) and (6) lead to the following expression for the specific enthalpy

$$h \equiv \sum_{i=1}^{ns} Y_i h_i = \sum_{i=1}^{ns} Y_i C_{pi} T + \sum_{i=1}^{ns} Y_i h_i^0 + \sum_{i=1}^{ns} Y_i e_i^{vib} \quad (7)$$

where $C_{pi} = C_{vi} + R_i$.

We can finally introduce the following alternatives for the definition of the ratio of specific heats:

1. $\gamma \equiv \frac{C_p}{C_v} = \frac{(\partial h/\partial T)_p}{(\partial e/\partial T)_v}$ which is the true ratio of specific heats (definition).
2. $\bar{\gamma} = 1 + \frac{p}{\rho e}$ which is an "equivalent-γ" relating pressure to internal energy and density.
3. $\tilde{\gamma} = \frac{\rho c^2}{p}$ which is an "equivalent-γ" relating sound velocity to pressure and density.
4. $\hat{\gamma} = \frac{\sum_{i=1}^{ns} Y_i (dh_i/dT)}{\sum_{i=1}^{ns} Y_i (de_i/dT)}$ which represents the ratio of specific heats of the frozen flow.

For an ideal gas (calorically perfect gas), all these definitions leads to the same value for the specific heats ratio. In particular, for air,

$$\gamma = \bar{\gamma} = \tilde{\gamma} = \hat{\gamma} = 1.4$$

But, in the case of a general reactive mixture, these values can be very different from each other.

2.3 Finite rate chemical model

The chemical model adopted considers nine species, namely O, N, NO, O_2, N_2, H, OH H_2O and H_2 (which will be characterised by the subscripts 1 to 9), and 33 chemical reactions:

N_2/O_2 Mechanism

$$\begin{aligned} O_2 + M &\rightleftharpoons O + O + M \\ N_2 + M &\rightleftharpoons N + N + M \\ NO + M &\rightleftharpoons N + O + M \\ N_2 + O &\rightleftharpoons NO + N \\ NO + O &\rightleftharpoons N + O_2 \end{aligned} \quad (8)$$

where $M = O, N, NO, O_2, N_2$.

H_2/O_2 Mechanism

$$\begin{aligned} OH + H_2 &\rightleftharpoons H_2O + H \\ H + O_2 &\rightleftharpoons OH + O \\ O + H_2 &\rightleftharpoons OH + H \\ OH + OH &\rightleftharpoons O + H_2O \\ H + H + M &\rightleftharpoons H_2 + M \\ H + O + M &\rightleftharpoons OH + M \\ H + OH + M &\rightleftharpoons H_2O + M \end{aligned} \quad (9)$$

where $M = H_2, O_2, N_2, H_2O$.

The composition of the mixture is defined by the values of the mass fractions Y_i. Because of the assumption of a mixture in thermodynamic non-equilibrium, the mass fractions are inferred from the conservation of mass for each species i which is expressed by

$$\frac{\partial}{\partial t}(\rho Y_i) + \vec{\nabla} \cdot (\rho Y_i \vec{w}) = \Omega_i \quad (10)$$

where Ω_i is the mass production rate of species i (production term). We note that if the lengthscale characteristic of chemical relaxation phenomena is smaller than the geometrical lenghtscale, or equivalently, if the characteristic timescale of chemistry is much smaller than the characteristic timescale of fluid motion, Eq. (10) reduces to the algebraic system

$$\Omega_i = 0$$

which define the equilibrium state. The inverse situation corresponds to the limit, for which the effect of the production rate Ω_i is negligible in the flow field, so that the species are simply convected. This evidentiates the different behaviours that may assume a flow in chemical nonequilibrium.

For each of the 33 reactions listed in (8) and (9), the forward sense is indicated by the left-to-right arrow, and the net rate is the difference, $R_{\text{net}} = (R_f - R_r)$, between individual forward and reverse rates, R_f and R_r, respectively. The coefficients that multiply the corresponding concentrations in these terms are k_f and k_r which are represented by highly nonlinear functions of the temperature. These coefficients have been taken from [1] for the N_2/O_2 mechanism and from [2] for the H_2/O_2 mechanism.

For *inviscid flow*, species diffusion is normally neglected. As a consequence, we may write the equations of conservation for oxygen, nitrogen and hydrogen nuclei as

$$
\begin{aligned}
\frac{2Y_4}{m_4} + \frac{Y_1}{m_1} + \frac{Y_3}{m_3} + \frac{Y_7}{m_7} + \frac{Y_8}{m_8} &= \frac{2Y_4^*}{m_4} \\
\frac{2Y_5}{m_5} + \frac{Y_2}{m_2} + \frac{Y_3}{m_3} &= \frac{2Y_5^*}{m_5} \qquad (11) \\
\frac{2Y_9}{m_9} + \frac{Y_6}{m_6} + \frac{Y_7}{m_7} + \frac{2Y_8}{m_8} &= \frac{2Y_9^*}{m_9}
\end{aligned}
$$

where Y_4^*, Y_5^*, Y_9^* represent the value of Y_4, Y_5 and Y_9 when *no dissociation* occurs. Instead of the nine partial differential equations (10), the finite rate chemistry can then be described by six partial differential equations and three algebraic ones.

A useful parameter in characterizing the combustion of H_2+air is the equivalence ratio ϕ:

$$
\phi = \frac{\text{Fuel to Air Ratio}}{\text{Stoichiometric Fuel to Air Ratio}} \qquad (12)
$$

which characterize the amount of fuel we add to air to perform combustion. For $\phi = 1$, we have a stoichiometric mixture of hydrogen and air, while for $\phi = 0$, the chemistry of hydrogen does not occur anymore. Moreover, if the mass fractions of the air components are freezed to their undisturbed values, the non ideal gas behaviour reduces to the effect due to vibrational molecules motion. Thus acting on few parameters, we can take into account only frozen air with vibrational molecules motion, or air in chemical nonequilibrium, or the complete H_2+air chemistry.

2.4 Link between fluid motion and chemistry

In brief, we have two kinds of set of equations for the computation of an inviscid flow in thermodynamic non-equilibrium. On one hand, the Euler equations which provide the so-called "fluid motion quantities" (ρ, $\overrightarrow{w}$, e_t) and, on the other hand, the finite rate equations which give the chemical composition of the mixture (Y_i). In addition, we need a closure relation for the determination of the state equation which is performed through the computation of the temperature. This equation is obtained by expressing the identity of the internal specific energy written in terms of "fluid motion quantities" and "chemical ones". From Eq. (4), we have

$$
\sum_{i=1}^{ns} Y_i C_{v_i} T + \sum_{i=1}^{ns} Y_i h_i^0 + \sum_{i=1}^{ns} Y_i e_i^{vib} = e_t - \frac{1}{2}\|\overrightarrow{w}\|^2 \qquad (13)
$$

3. DISCRETIZATION PROCEDURE

The numerical scheme is based on a node-centered finite volume formulation and operates on completely unstructured grids. The main motivation for using unstructured triangular grids is the relative ease with which complex geometries can be treated. Furthermore, unstructured grids provide a natural framework for the use of adaptive mesh refinement, which may allow to place points exactly where needed, thus resulting in a better control on the global number of mesh points and, consequently, computational costs.

The spatial discretization of the Euler equations is obtained from the integral equation for conservation of mass, momentum and energy in a polygonal control volume which is constructed surrounding each vertex of the grid. A flux vector splitting decomposition, which makes use of Hänel flux vector splitting [3], has been chosen for the evaluation of the inviscid fluxes between adjacent cells. This decomposition is expressed only in function of density, components of the velocity vector, pressure, sound speed and total enthalpy, and it is not restricted to any particular formulation for the equation of state. The basic scheme is first-order accurate and satisfies at steady state the condition of constant total enthalpy for isoenergetic flows. Second-order accuracy in space is obtained by the introduction of a linear distribution of variables in each control volume, such as in the MUSCL approach [4]. The use of limiters on these distributions is necessary for stability reasons and to limit spurious oscillations near discontinuities. The spatial approximation of the finite rate chemistry equations is carried out in a way similar to the continuity equation.

The time discretization is performed using a multistage algorithm, where the flow variables and the chemical ones are advanced together at each stage. In particular, the source term present in the finite rate equations is treated implicitly to avoid the use of prohibitively reduced timesteps. The process is continued until steady state is achieved.

We refer to [5] and [6] for a more detailed description of the numerical procedure here adopted, which can be easily extended to 3-D flows.

4. AIR INLET

In aircraft propulsion systems, the inlet provides the means of channeling freestream air into the engine for the use of its oxygen content for combustion with injected fuel. In so doing, it also reduces the Mach number thus allowing a more efficient heat addition in the combustion chamber. This deceleration generates inviscid and viscous losses through boundary layer and shock waves formation. Several different measures of efficiency have been applied to the scramjet inlet; all of which in some way give a measure of the entropy production.

4.1 Inlet performance

The inlet performance is often characterized by air capture ratio (ACR), total pressure recovery (η_{pt}), kinetic energy efficiency (η_{ke}) and exergy efficiency (η_x). For a quasi-one-dimensional inlet delimited by stations 1 (inflow) and 2 (outflow), the performance can be defined as follows:

$$ACR = \frac{\dot{m}_2}{\dot{m}_1} \tag{14}$$

$$\eta_{pt} = \frac{p_{t2}}{p_{t1}} \tag{15}$$

$$\eta_{ke} = \frac{V_{2*}^2}{V_1^2} \tag{16}$$

$$\eta_x = \frac{h_{t2}}{h_{t1}} - \frac{T_1(s_2 - s_1)}{h_{t1}} \tag{17}$$

where $\dot{m}$ is the mass flow rate, V the velocity, p_t the total pressure and s the specific entropy. The subscripts denote the station. The velocity V_{2*} is the velocity that the flow at the station 2 would obtain if it is isentropically expanded to the inflow pressure (station 1).

For an ideal gas (calorically perfect gas), the efficiency parameters can be expressed by the usual relations taking into account the Mach number and the specific heats ratio. However, the design of an inlet for hypersonic application requires to consider a temperature range well beyond that corresponding to the validity of the ideal gas model. Higher temperature causes vibrational molecular motion that will change the value of C_p, C_v and their ratio γ. The complexity of the calorically imperfect gas model does not allow a straightforward explicit treatment as in the ideal gas model.

We describe here a way to evaluate the inlet performance using the calorically imperfect gas model. We assume that the flow is frozen, so that the composition of the mixture remains constant. This assumption is valid for inlets for which the temperature remains below 3000 K. Beyond this temperature, thermal imperfections and molecular dissociation effects take place, and the following formulas are no more valid.

Total pressure recovery, kinetic efficiency and exergy efficiency are determined from the expression of the total enthalpy h_t and the entropy s. Total enthalpy can be expressed as

$$h_t = h(T) + \frac{1}{2}\|\overrightarrow{w}\|^2 \tag{18}$$

$$ = h(T_t) \tag{19}$$

where specific enthalpy h is given by Eq. (7) and T_t represent the stagnation temperature. For isoenergetic flows (as in our case), $h_t = h_{t1} = h_{t2}$ and the stagnation temperature is a constant which can be determined solving the nonlinear equation

$$h(T_t) = h_{t1} \tag{20}$$

For a frozen flow, the specific entropy takes the form[7]:

$$s = \sum_{i=1}^{ns} Y_i C_{pi} \ln T - \sum_{i=1}^{ns} Y_i R_i \ln p + \sum_{i=1}^{ns} Y_i s_i^{vib} + s_0 \tag{21}$$

where s_0 is a constant and s_i^{vib} represents the specific vibrational entropy of the species i which is given by

$$s_i^{vib} = R_i \sum_{j=1}^{nli} \left(\frac{\theta_i^j/T}{\exp(\theta_i^j/T) - 1} - \ln(1 - \exp(-\theta_i^j/T)) \right) \tag{22}$$

Eq. (21) can be rewritten in the following way:

$$\Delta s \equiv s - s_0 = s_a(T) - s_b(p) \tag{23}$$

which shows that the entropy is essentially formed by two terms, s_a and s_b, which are only a function of the temperature and of the pressure, respectively. Note that, if the vibration of the molecules is not excited, we obtain the classical formula for entropy:

$$s = C_v \ln \frac{p}{\rho^\gamma} + s_0^* \tag{24}$$

where $C_v = \sum Y_i C_{vi}$, $\gamma = \frac{\sum Y_i C_{pi}}{\sum Y_i C_{vi}}$, and s_0^* is a constant.

Total pressure recovery

The total pressure recovery is expressed as the ratio of total pressures at stations 2 and 1, respectively. The discretization procedure described in section 3 is a so-called shock-capturing method and do not need any special treatment across shocks. As a consequence, the numerical solution satisfies the Rankine-Hugoniot relations for discontinuities and predicts the entropy jump across them.

The total pressure can then be computed from the knowledge of the numerical solution using the following identity

$$s_a(T_t) - s_b(p_t) = s_a(T) - s_b(p) \tag{25}$$

which is derived from two different ways to write the entropy: the first uses total quantities and the second static ones. As temperature and pressure are evaluated from the numerics and stagnation temperature is determinated solving Eq. (20), the total pressure is obtained at stations 1 and 2 by the solution of the following equations

$$s_b(p_{t1}) = s_a(T_t) - s_a(T_1) + s_b(p_1) \tag{26}$$

$$s_b(p_{t2}) = s_a(T_t) - s_a(T_2) + s_b(p_2) \tag{27}$$

Kinetic energy efficiency

The kinetic energy efficiency is defined by Eq. (16). We recall that, in that formula, the velocity V_{2*} is the velocity that the flow at station 2 would obtain if it is isentropically expanded to the inflow pressure (station 1). The quantity V_{2*} is evaluated using the following procedure.

In first place, the entropy at station 2 is computed:

$$\Delta s_2 = s_a(T_t) - s_b(p_{t2}) = s_a(T_2) - s_b(p_2) \quad (28)$$

Secondly, the static temperature T_{2*}, which the flow at station 2 would reach if it were isentropically expanded to the pressure p_1, is evaluted by solving the nonlinear equation:

$$s_a(T_{2*}) = \Delta s_2 + s_b(p_1) \quad (29)$$

At last, V_{2*}^2 is determined using the conservation of total enthalpy:

$$V_{2*}^2 = 2\,(h_{t1} - h(T_{2*})) \quad (30)$$

For an ideal gas, kinetic energy efficiency can be shown to be a function of total pressure ratio through

$$\eta_{ke} = 1 + \frac{1 - (1/\eta_{pt})^{\frac{\gamma-1}{\gamma}}}{\frac{\gamma-1}{2} M_1^2} \quad (31)$$

This equation demonstrates a disadvantages of the kinetic energy efficiency term. Values approaching unity are incurred not only as η_{pt} approaches one but also as the Mach number increases. Thus it gives misleadingly high values at high hypersonic conditions.

Exergy efficiency

The exergy efficiency is defined by Eq. (17) in the general case. We note that since it deals with total enthalpies then it must be sensitive to heat addition or removal between the state 1 and 2 as well as to losses measured by the entropy change $s_2 - s_1$. For adiabatic flow (it is our case), the exergy efficiency becomes

$$\eta_x = 1 - \frac{T_1(s_2 - s_1)}{h_{t1}} \quad (32)$$

For an ideal gas, exergy efficiency can be shown to be a function of total pressure ratio through

$$\eta_x = 1 + \frac{\frac{\gamma-1}{\gamma}}{1 + \frac{\gamma-1}{2} M_1^2} \ln \eta_{pt} \quad (33)$$

Like the kinetic energy efficiency, it gives misleadingly high values at high hypersonic conditions.

4.2 Numerical test

The air inlet we have considered for our computations is illustrated in Fig. 1. This very simple geometry, used only for tests, is composed by two compression surface, one on the wall which simulate the aircraft fuselage and one on the cowl. The starting conditions are interpolated(extrapolated) from values tabulated in [8] and are summarized in Tab. 1. In this table, M_∞ corresponds to flight Mach number and the subscript 1 characterizes quantities obtained after the forebody compression. We recall that, in this section, we assume frozen conditions, so that the non ideal gas effect is only due to molecules vibrational mode.

M_∞	M_1	p_1,KPa	T_1,K
4.6	4.0	7.5	327
5.8	5.0	4.9	329
7.0	6.0	3.55	335
8.2	7.0	2.7	345

Table 1: Flow conditions for the air inlet.

The computation has been performed at the different flight conditions using both the ideal and non ideal gas assumptions. The corresponding iso-temperature contours are illustrated in Fig. 2 which evidentiate shock reflexions, and complex shock/shock and shock/expansion interactions. Local values of the efficiency parameters at the outflow station are presented in Fig. 3. In this figure, we have also reproduced the case when the efficiency parameters are calculated from the knowledge of the imperfect gas model solution, but using the formulas corresponding to the ideal gas ($\gamma = 1.4$). The values obtained are much higher. Thus, we must avoid to use incorrect formulations or approximate formulas when evaluating the efficiency parameters. We note that even for the lowest Mach number the temperature reached at outflow station is high due to the multiple shock reflexions. The difference between ideal and non ideal gas assumptions is small as long as the temperature is not too high ($T \leq 900$K). Beyond this temperature, the effects due to the vibrational mode are no more negligible and influence both the characteristics of the flow (the locations of the shocks are different) than the values of temperature, pressure and parameters efficiency.

M_1	4	5	6	7.0
ACR	0.89	0.99	1.0	1.0

Table 2: Air capture ratio.

The efficiency parameters are summarized in Tabs. (3) to (6) using two kinds of averaging procedure. The first procedure leads to area-averaged quantities which are computed from the local knowledge of the parameters. The second one uses quasi 1-D quantities evaluated as follows. First the density is averaged using the area-averaging technique. The 1-D velocity is then computed assuming mass flow rate conservation. At last, the 1-D temperature is calculated from the conservation of total enthalpy. With these three quantities, it is easy to compute the efficiency parameter using the equations described in

M_1	η_{pt}	η_{ke}	η_x
4.0	.7730	.9761	.9825
5.0	.6918	.9777	.9824
6.0	.6625	.9822	.9854
7.0	.6300	.9843	.9868

Table 3: Area-averaged efficiency parameters for ideal gas model.

M_1	η_{pt}	η_{ke}	η_x
4.0	.7746	.9763	.9826
5.0	.6933	.9778	.9825
6.0	.6653	.9824	.9855
7.0	.6283	.9841	.9867

Table 4: Area-averaged efficiency parameters for gas model with vibration.

M_1	η_{pt}	η_{ke}	η_x
4.0	.7118	.9681	.9769
5.0	.6181	.9705	.9771
6.0	.5243	.9719	.9775
7.0	.5085	.9769	.9811

Table 5: Quasi 1-D efficiency parameters for ideal gas model.

the previous paragraphs. We note that these two procedures of averaging leads to values of the efficiency parameters which are a little different. This is due to the high variation of flow quantities on the outflow section.

5. COMBUSTOR AND NOZZLE

A key factor for the interpretation of H_2/air chemistry is the energy yield, or completeness of combustion at an intermediate or exit station of the combustor and/or nozzle. This is defined as the fraction Q_h of the ideal enthalpy of reaction. The initial gas mixture consists of only H_2, O_2 and N_2, whose enthalpy of formation are all zero. Thus, only final-state terms appear in the energy yield expression

$$Q_h = \frac{1}{Y_{H_2O} h^0_{H_2O}} \sum_i Y_i h_i^0 \qquad (34)$$

The index i in the numerator includes all the product species produced with a mass fraction Y_i and with a specific enthalpy of formation h_i^0 The final product in an ideal reaction is just water and, for nonstoichiometric mixtures, residual reactants. The only nonzero term in the denominator is for H_2O. Its ideal yield is denoted Y_{H_2O}.

At the fuel inlet of the combustor, the assumptions of instantaneous mixing and noninteracting streamlines (no diffusion, convection or conduction) are made, and the chemistry is not allowed to alter the upstream flow pattern. Our purpose is to understand qualitatively the role chemistry plays in a supersonic engine, rather than to obtain quantitative predictions of actual scramjet performance. Our calculations in the combustor represent only a limiting case of a realistic engine because turbulent mixing and other factors may strongly influence the chemistry in this region. However, these calculations should be adequatly representative of actual nozzle performance. To model a realistic engine at particular Mach numbers, we consider approximate starting conditions from the case tabulated by Billig [9]. The effects on combustion efficiency by changing pressure and temperature in the combustion region (implemented through changes in contraction ratio), by different area expansions in the nozzle (which allow to control temperature), and by various equivalence ratios, are examined in order to help identifying the conditions for maximum chemical yield and thrust. The thrust is evaluated as the integral of the absolute pressure forces on the surfaces washed by the capture flow of the engine projected along the flight direction. A more complete study, which includes a sensitivity analysis on the individual rates of the H_2/air combustion mechanism and the chemistry involving HO_2 and H_2O_2 can be found in [10] for a quasi-one-dimensional simulation.

M_1	η_{pt}	η_{ke}	η_x
4.0	.7175	.9689	.9774
5.0	.6104	.9697	.9765
6.0	.5235	.9718	.9774
7.0	.5172	.9776	.9816

Table 6: Quasi 1-D efficiency parameters for gas model with vibration.

Equilibrium vs finite-rate chemistry

The first calculations performed consider the differences between combustors constrained to maintain equilibrium and combustors with the full finite-rate chemistry included. The equilibrium calculation is obtained by increasing the individual rates of a subset of the whole mechanism to a point at which the kinetics are no longer the limiting factor. Both calculations are for stoichiometric mixture of hydrogen and air. The combustor is straight-walled to 100 cm and has an height Δz_0 of 10 cm. The lower wall of the nozzle is an extension of the combustor wall and its upper wall is described by the following equation

$$\Delta z = \Delta z_0 \sqrt{1 + \frac{x - 100}{10}}$$

which is valid only for $x \geq 100$. The unstructured grid used to perform calculations is represented in Fig. 4.

The initial combustor inlet conditions are

$$T = 1463\,\mathrm{K}\ ,\ p = 60\,\mathrm{KPa}\ ,\ M = 5$$

which corresponds to a flight Mach number of about 15 [9]. Plots of energy yield, temperature and pressure along the walls are presented in Fig. 5. It is evident that the non equilibrium flow do not reach equilibrium at the end of the combustor. From the *inlet to the end of the combustor*, the temperature has risen from the initial 1463K to approximatively 2850K. This high temperature limits the maximum possible energy yield attainable to 51% at the end of the combustor. In the nozzle region, the difference of heat releases between the equilibrium constrained case and the kinetics limited case is very high, in particular on the lower part of the nozzle. The effect of finite rate dissociation-recombination chemistry is to lower the energy yield below that expected for equilibrium chemistry and the available thrust as indicated in Tab. 7. It is clear that nonequilibrium chemistry plays a significant role in high-Mach-number scramjets compared to a more conventional engine where the chemistry is fast enough to maintain equilibrium.

	Non equilibrium	Equilibrium
Thrust	1.08	1.20

Table 7: Thrust($\times 10^{-4}$) for non equilibrium and *equilibrium assumptions.*

Effects of changing compression ratios

Changing the compression ratio of the air to the combustor can affect the chemistry in the engine by altering temperature, density and velocity of the gas flow. To obtain an intuitive feel for what happens to the chemistry and, consequently, to the energy output, the initial temperature and pressure have been systematically varied at the combustor inlet. These results are presented in Fig. 6, where the initial starting pressure is varied ±20% from the basic value by changing the initial starting species densities (a unity equivalence ratio is maintained) and keeping the starting temperature constant. The energy yield is highest at higher temperature because of increased recombination rates. The percent change from the base case at the nozzle end is +5% and -10%. The influence on the thrust is +23% and -24%, respectively, as shown in Tab. 8.

	$p = 60$KPa	$p = 48$KPa	$p = 72$KPa
Thrust	1.08	0.82	1.33

Table 8: Thrust($\times 10^{-4}$) for different starting conditions (T = 1463K).

In Fig. 7, the effect of changing the initial temperature by ±20% is examined. The initial pressure is kept constant by allowing the species density to change in accordance with the temperature change. The most obvious effect of changing temperature is to alter dramatically the relative ignition times. The lowest-temperature case produces the highest yield. A lower temperature is accompanied by a higher value of density, both of which favor recombination. The effects of changing temperature cannot be completely decoupled from pressure or density changes, but it is apparent that an inlet designed to produce higher densities with lower temperatures will give a more efficient engine. The percent change from the base case is +16% for energy yield at nozzle end and +25% for thrust.

	$T = 1463$K	$T = 1174$K	$T = 1757$K
Thrust	1.08	1.35	0.87

Table 9: Thrust($\times 10^{-4}$) for different starting conditions (p = 60KPa).

Effect of changing the equivalence ratio

Tab. 10 indicates that the maximum thrust is obtained by a value of the equivalence ratio slighly higher than unity.

	$\phi = 0.5$	$\phi = 1.2$	$\phi = 1.5$	$\phi = 2.0$
Thrust	0.85	1.10	1.11	1.08

Table 10: Thrust($\times 10^{-4}$) for different values of the equivalence ratio.

Changes in nozzle contours

As a final point of analysis, the effects of different nozzle contours on heat release and thrust are compared. Fig. 8 depicts the different profiles used for this comparison. Case I is the base case to all previous calculations shown. Case II started with a rapid flare-out at the beginning of the nozzle and is then straight-walled to the end of the nozzle. In case III, the nozzle starts with a slight expansion and flared quickly to the end. Finally, case IV essentially extends the combustor until it again flares out at the same rate as in the case II. All shapes cames to the same end nozzle section, so that the only effect on chemistry is one of changing paths, not overall area expansion.

The best heat release is provided by case III, but it does not correspond to the maximum thrust as indicated in Tab. 11.

	Case I	Case II	Case III	Case IV
Thrust	1.08	0.51	0.77	0.54

Table 11: Thrust($\times 10^{-4}$) for different nozzle contours.

If we compare it with case I, which gives the maximum thrust, the favourable level of pressure reached during the slight expansion is followed by a dramatic decrease of pressure in the region which should greatly contribute to thrust because of the larger projected area. At last, we note that, in case II, the shock reduce greatly the energy yield and the associated increase in pressure does not contribute to thrust because of the straight wall.

Care in nozzle contouring can play an important role in attaining the maximum possible thrust. Some works have been performed in this direction by using optimum design techniques[11].

CONCLUSIONS

In this paper, an inviscid method has been developed to evaluate the performance of a scramjet engine. From the results of the study, several conclusions can be drawn on the effect non ideal gas assumption and H_2/air chemistry have on the performance of air intakes and nozzles.

For the air intake, the effect of non ideal gas assumption is to reduce both temperature and pressure at the inlet of the combustor and to modify the characteristics of the flow (the position of the shocks is different from the prediction obtained using an ideal gas model). The inlet efficiency parameters are not altered by the molecules vibration as far as the temperature is not too high ($T \leq 900K$). Beyond this limit, we note a reduction of the value of the efficiency parameters.

For combustor and nozzle, we have shown that a realistic code must incorporate finite-rate chemistry in order to account properly for chemical energy yield at the termination of the hypersonic engine, i.e., equilibrium cannot be assumed. Changes in inlet design that increase density and decrease temperature enhance scramjet energy yield and thrust. Finally, the design of the nozzle contour plays an important role in the thrust production.

References

[1] Rakich,J.V., Bailey,H.E., and Park,H.C., "Computational of Non equilibrium Three Dimensional Inviscid Flow over Blunt Nosed Bodies Flying at Supersonic Speeds", AIAA Paper 75-835 (1975).

[2] Dixon-Lewis,G., "Structure and Extinction Limits of Some Strained Premixed Flames", in Dynamics of Reactive Systems, Part I: Flames, A.L. Kuhl, J.R. Bowen, J.-C. Leyer and A. Borisov Editors, Progress in Astronautics and Aeronautics, 113 (1988).

[3] Hänel,D., Schwane,R., and Seider,G., "On the Accuracy of Upwind Schemes for the Solution of the Navier-Stokes Equations", AIAA Paper 87-1105, 1987.

[4] Anderson,W.K., Thomas,J.L., and van Leer,B., "A Comparison of Finite Volume Flux Vector Splittings for the Euler Equations", AIAA Paper 85-0122, 1985.

[5] Selmin,V., and Formaggia,L., "Simulation of Hypersonic Flows on Unstructured Grids", Int. J. Numer. Methods Engng., **34**, pp. 569-606 (1992).

[6] Desideri,J.-A., Glinsky N., and Hettena,E., "Hypersonic Reactive Flow Computations", Comp. Fluids, **18**, 151-182 (1990).

[7] Vincenti,W.G., and Kruger,C.H., "Introduction to Physical Gas Dynamics", R.E. Krieger Publishing Co., Malabar Florida, 1982.

[8] Kumar,A.,"Numerical Analysis of Flow through Scramjet Engine Inlets", AGARD CP 428, November 1987, Paper 15.

[9] Billig,F.S., "Combustion Process in Supersonic Flow", Journal of Propulsion and Power, **4**, pp. 209-216 (1988).

[10] Harradine,D.M., Lyman,J.L., Oldenborg,R.C., Schott,G.L., and Watanabe,H.H., "Hydrogen/Air Combustion Calculations: The Chemical Basis of Efficiency in Hypersonic Flows", AIAA Journal, **28**, pp. 1740-1744 (1989).

[11] Van Wie,D.M., White,M.E. and Waltrup,P.J., "Application of Computational Design Techniques to the Development of Scramjet Engines", AIAA Paper 87-1420 (1987).

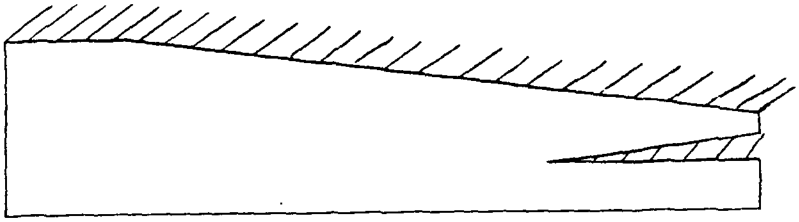

Fig. 1: Air intake geometry.

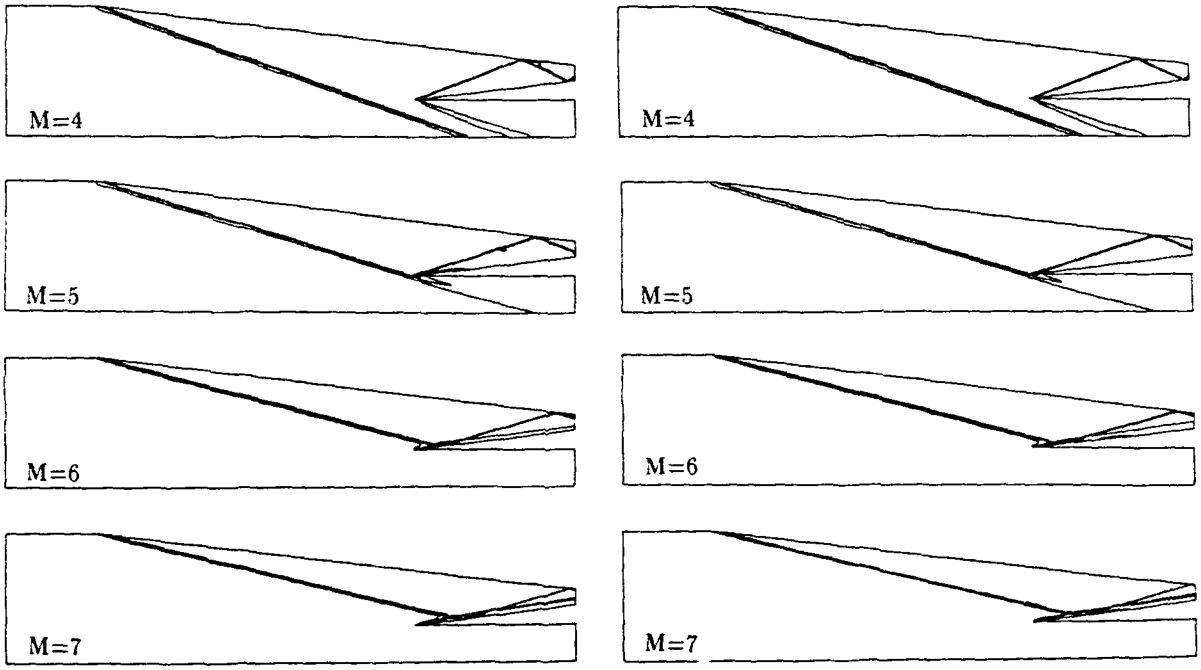

Fig. 2: Iso-temperature contours of the flow through an air intake assuming calorically perfect(left) and calorically imperfect(right) gas models.

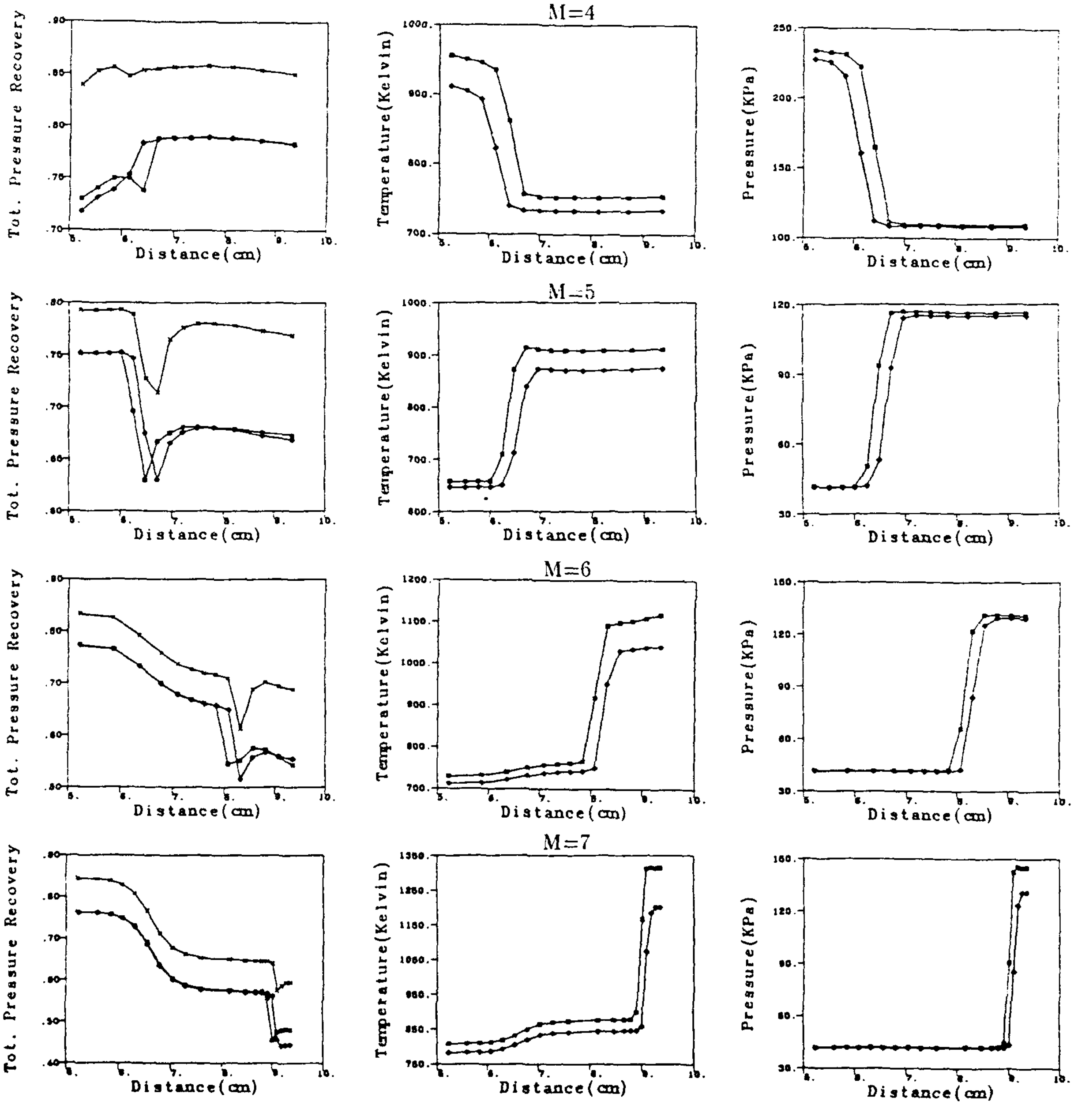

Fig. 3: Local values of efficiency parameters and flow quantities at the outflow station.
□ Ideal gas model. ◇ Non ideal gas model. × Hybrid formulation.

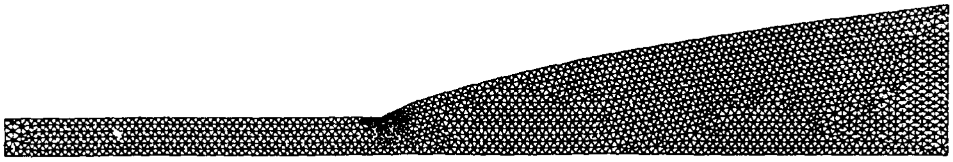

Fig. 4: Grid for the computation of the flow through combustor+nozzle configuration.

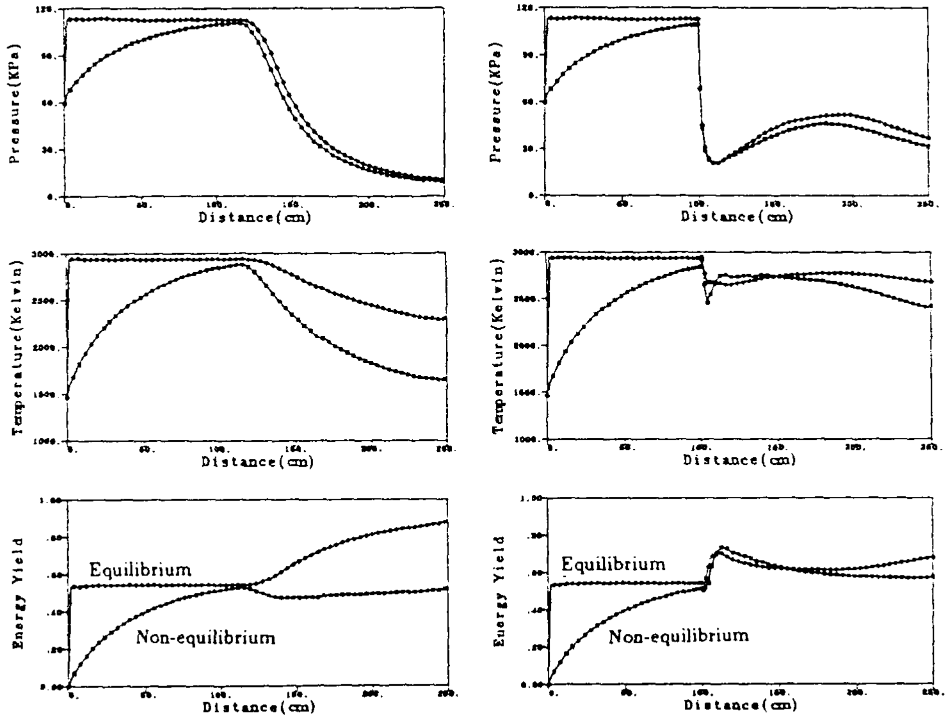

Fig. 5: Equilibrium vs finite-rate kinetics. Left: bottom wall. Right: upper wall.

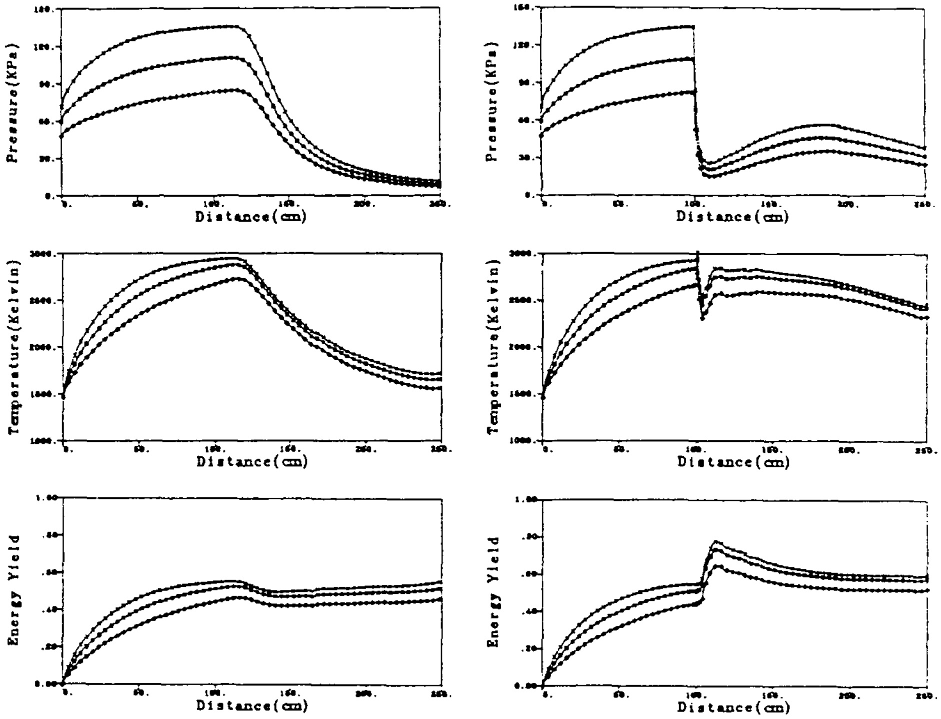

Fig. 6: Effects on energy release with 20% changes in pressure at 1463K inlet temperature. Left: bottom wall. Right: upper wall.

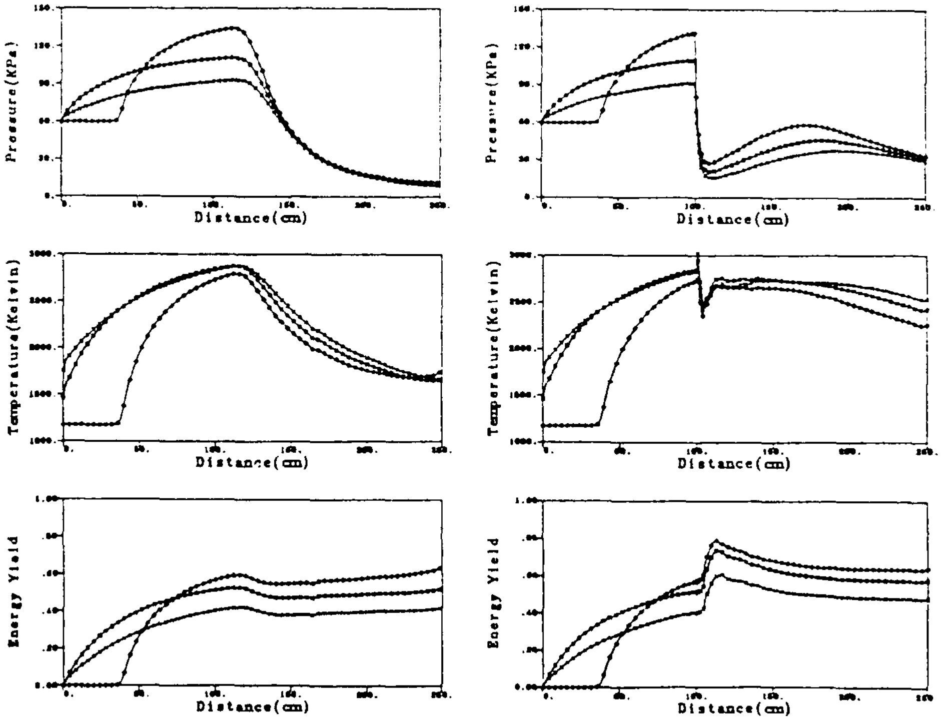

Fig. 7: Effects on energy release with 20% changes in temperature at 60KPa inlet pressure. Left: bottom wall. Right: upper wall.

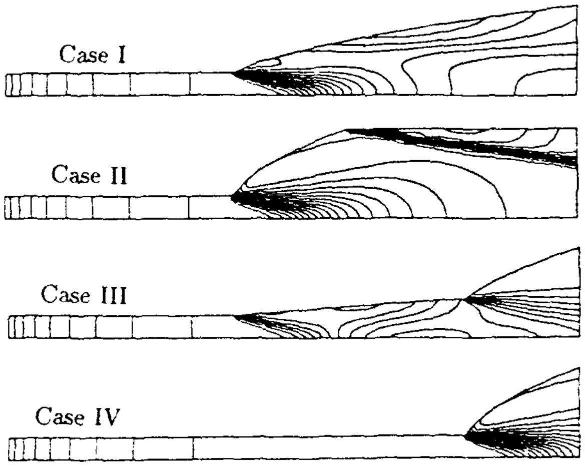
Case I
Case II
Case III
Case IV

Fig. 8: Iso-pressure contours for different nozzle profiles.

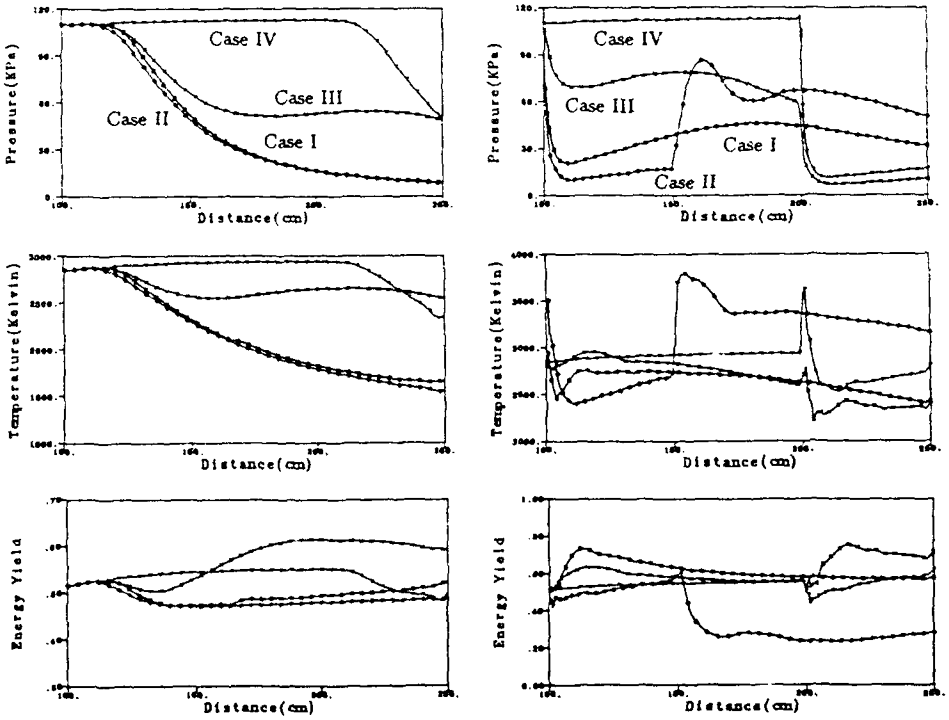

Fig. 9: Variations on energy release for different nozzle contours. Left: bottom wall. Right: upper wall.

CONTROL EFFECTIVENESS AT HYPERSONIC SPEEDS

by
J.L.Stollery
D.Kumar
P.A.Atcliffe
H.Babinsky

College of Aeronautics
Cranfield Institute of Technology
Cranfield. Bedford, MK43 0AL
United Kingdom

SUMMARY

Two models equipped with trailing edge flaps have been tested at a Mach number of 8.2. A simple flat plate model has been used to understand how control effectiveness is influenced by transition, bluntness and incidence, whilst a cropped-delta- wing spaceplane configuration has emphasised the important three-dimensional effects arising from the geometry chosen. Schlieren photographs were used to visualise the flow, and pressure measurements on the windward surface of the spaceplane model showed any regions of separation. Encapsulated liquid crystals were used to obtain an overall picture of the heat transfer distribution and to highlight the three-dimensional structure of the flow.

LIST OF SYMBOLS

C	Chapman-Rubesin constant
d	Diameter of the leading edge
L	Distance from leading edge to hinge line
M	Mach number
P	Pressure
Re	Reynolds number
t	Flat plate thickness
T	Temperature
α	Angle of incidence
β	Flap deflection angle
$\bar{\chi}$	Viscous interaction parameter $M^3/(C/Re)^{1/2}$

Subscripts

4	Driver conditions
1	Initial barrel conditions
o	Stagnation conditions
∞	Freestream conditions
e	Local inviscid flow conditions

1. INTRODUCTION

Hypersonic vehicles operate over a considerable altitude and Mach number range. As a consequence, the boundary layer flow may be laminar, transitional or turbulent. Since laminar flows are far more sensitive to separation than turbulent ones, it is important to be able to predict the onset and extent of transition. However, boundary layer transition is affected by geometric shape, roughness, noise and vibration as well as the usual aerodynamic parameters such as Mach number, Reynolds number and wall temperature ratio.

The Cranfield hypersonic gun tunnel generates conditions in which transition occurs naturally and studies are being conducted on a number of different models in order to investigate the effects of transition on separation using surface pressure distributions and local heat transfer rate measurements.

One recent programme studied plume effects at the base of a spherically blunted cone. Heat transfer measurements indicated that in the absence of a base plume, the boundary layer was laminar and attached along the length of the body. A small plume induced separation over the rear of the cone, but the separated shear layer remained laminar with a consequent reduction in the local heat transfer rate. A larger plume caused separation over most of the length of the cone and transition to turbulent flow occurred in the shear layer. The result was an increase in the heat transfer rate over the rear part of the cone to values above those for fully attached laminar flow. This work is reported in ref. 1.

The present investigation is to explore whether similar effects occur over trailing edge flaps fitted to a simple, low-aspect-ratio flat plate and to a more representative spaceplane configuration with a cropped delta wing.

2. EXPERIMENTAL STUDIES

2.1 Facility

All the experiments were carried out in the Cranfield hypersonic gun tunnel. This is an intermittent, free-piston, blow-down tunnel with a typical running time of 25 ms. A contoured nozzle with an exit diameter of 20 cm provides uniform flow at $M_\infty = 8.2$ in the open jet test section. The freestream Reynolds number was varied by changing the driver pressure, and the various test conditions are given in table 1.

2.2 Models

The two types of models used are shown in figure 1. Type A is a family of flat plates of aspect ratio 0.5 with various degrees of hemi-cylindrical leading edge bluntness, as shown by figure 1(a). The effective hinge line was at 78% chord with flaps simulated by fixed wedges.

The type B model is a wing-body configuration with a sharp leading edge, cropped delta wing swept at 54° and equipped with a constant-chord trailing edge flap. Pressures on the lower surface of the model were measured using Kulite LQ-057 and LQ-080 transducers mounted either on the sting or inside the body. The model and the position of the pressure ports are illustrated in figure 1(b).

In order to gain more information about the structure of the lower surface boundary layer, both models were painted black and covered with a thin layer, estimated to be approximately 10 μm thick, of TCF 552 liquid crystals[1]. By recording their colour response during the run with a high speed video camera, qualitative information regarding the surface temperature history was obtained. Further details of this technique are given in refs. 2-4.

---

[1] Manufactured by the British Drug House Company

Recently, Babinsky has used a sharp leading edge flat plate model machined from black plastic, thus eliminating the potentially uneven surface structure due to the black paint and allowing for a more accurate estimation of the substrate properties. Automatic scanning and digitising of the resulting colour-temperature history has resulted in quantitative estimates of the surface heat transfer rates. Preliminary results are reported in ref. 5.

3. DISCUSSION OF RESULTS

3.1 Sharp Flat Plate with Trailing Edge Flap

3.1.1 Tests at zero incidence

With a flap angle of 5°, schlieren photographs, shown in figure 2(a), indicate an attached laminar boundary layer over the whole model with a single shockwave located near the hinge line. However, with a flap angle of 10°, the boundary ~~layer,~~ although still laminar, has separated ahead of the hinge line, resulting in the formation of separation and reattachment shockwaves.

A correlation based on simple dimensional arguments (ref. 6) suggests that for laminar boundary layers, the incipient separation flap angle β_i is given by

$$M_\infty \, . \, \beta_i = 80(\bar{\chi}_{\infty L})^{1/2} \qquad (1)$$

where β_i is in degrees. For our test conditions, this correlation predicts a value for β_i of 6.6°, which agrees with the above results. As the flap angle is further increased, the length of the separated shear layer increases. With a flap angle of 20°, there are indications of transition in the separated layer, and with 30° of flap, transition occurs soon after separation.

3.1.2 Tests at 5° incidence

With the plate at an incidence of 5°, the local inviscid flow Mach number, M_e, is reduced to 7.0 and the corresponding value of Re_{eL} is increased to 2.1×10^6. For these hinge line conditions, the laminar correlation predicts an incipient separation flap angle of 5.5°. With a flap angle of 5°, the flow is laminar and attached, but at $\beta = 10°$, the characteristic indications of separation are present. At larger flap angles, the separated region appears to be considerably smaller than the corresponding test at zero incidence.

3.1.3 Tests at 10° incidence

At 10° incidence, the local conditions are $M_e = 5.8$ and $Re_{eL} = 2.4 \times 10^6$. The schlieren pictures (figure 2(c)) show no conclusive signs of transition and the laminar incipient separation angle calculated from

$$M_e \, . \, \beta_i = 80(\bar{\chi}_{eL})^{1/2} \qquad (2)$$

is 4.9°. The photograph of the flow with the 5° flap is consistent with incipient conditions, and there are clear signs of a separated region ahead of the hinge line at $\beta = 10°$. What is interesting is the behaviour with 15° of flap: here the length of the separated region has *decreased* rather than expanding further as expected (and as was seen at zero and 5° incidence). There are no obvious signs of transition, so the cause of this unexpected behaviour may be the three-dimensional nature of the flow. It must be remembered that this is a low-aspect-ratio flat plate and, at 10° of incidence with a trailing edge flap deflected 15°, the spanwise flow at the edges of the model ~~must be~~ considerable.

The liquid crystal tests, though only qualitative so far, were useful in indicating the planform curvature of any separation and reattachment lines.

3.2 Effects of Leading Edge Bluntness

The effects of bluntness on the incipient separation angle and the length of the separated region can be dramatic. In those of our tests where we believe the flow to be entirely laminar (e.g., $\alpha = 0°$, $\beta = 10°$), the separation length is significantly reduced as bluntness is increased. Holden (ref. 7) found the same tendency, but he also found that bluntness decreased β_i, though the trend was weak. By contrast, in our tests β_i seems to increase with bluntness. Admittedly it is sometimes hard to detect incipient separation when the leading edge is very blunt since bluntness creates an entropy layer under which the boundary layer grows. Both layers have temperature and density gradients which interact, so that it is often difficult to detect signs of separation and/or transition in schlieren pictures. Figure 3 shows the dramatic reduction of separated length with bluntness for plates at zero incidence with a flap angle of 30°.

The sharp leading edge model in figure 3 has a separated shear layer which is transitional. In our tests it is not clear whether bluntness promotes or delays transition. Stetson (ref. 8) has studied transition on blunted cones, and found that a small amount of bluntness delayed transition but an optimum was reached and further increases in nose diameter moved transition forward again.

Future quantitative heat transfer and pressure measurements on type A models will detect whether bluntness inhibits separation by promoting transition to turbulent flow ahead of the hinge line, or just changes the local values of Mach number and Reynolds number so that, although the boundary layer remains laminar, the incipient separation angle is increased.

3.3 Delta Winged Vehicle (Model B) with Trailing Edge Flap

Following earlier work reported in reference 9, tests have been made with a single flap angle of 20° at four incidences (0, 5, 10 and 15°). Schlieren photographs indicate a separated region around the flap hinge line. In addition, the shock from the sharp conical nose strikes the wing leading edge at about mid semi-span, as shown by figure 4.

Pressure measurements on the lower surface enable chordwise distributions to be plotted at various spanwise stations, (e.g., figure 5) and isobar maps (e.g., figure 6) to be drawn. These figures show that the separated region has a complex three-dimensional shape. Along the centreline, where the distance to the hinge line is greatest, we believe that the boundary layer undergoes transition, and consequently the length of the separated region is small. On the wing, the distance to the hinge line is less, the boundary layer remains laminar with early separation, and the separated region is considerably longer.

A further complication is indicated by the liquid crystal pictures, which suggest that the nose shock impinging on the wing leading edge promotes a highly localised thin wedge of transitional or turbulent flow. With a turbulent wedge, the local extent of the separated region would be reduced. The pattern of heating recorded, shown by figure 7, is consistent with this view. Comparison of isobar maps produced at different incidences indicates that the effects of the nose shock impingement decreases with increasing angle of attack.

From the pressure and liquid crystal tests, a possible shape for the separated region may be drawn, as shown in figure 8. Confirmation must await quantitative heat transfer measurements using thin-film gauges and further development of the liquid crystal technique.

4. CONCLUSIONS

The gun tunnel facility operating at a freestream Mach number of 8.2 is capable of generating transitional flow conditions. It is particularly useful for emphasising the importance of transition and for demonstrating the complex nature of the pressure and heat transfer distributions which can result.

Increasing the flap angle on a flat plate model can either increase or decrease the length of the separated region, depending upon the incidence. It is not yet clear whether decreasing separated length results from transitional or spanwise spillage effects.

Leading edge bluntness leads to a significant reduction in the extent of the separated flow region ahead of the trailing edge flap on the flat plate model.

The effects of transition on a hypersonic vehicle can produce separated flow regions of complex shape.

5. REFERENCES

1. Atcliffe, P.A., Kumar, D. and Stollery, J.L. Plume effects on the flow around a blunted cone at hypersonic speeds; 5th Symposium on Numerical and Physical Aspects of Aerodynamic Flows, California State University, Long Beach, 1992.

2. Scholer, H. Application of encapsulated liquid crystals on heat transfer measurements in the fin body interaction region at hypersonic speed; AIAA Paper 78-0777, 1978.

3. Jones, T.V. and Hippensteele. High resolution heat transfer coefficient maps applicable to compound-curve surfaces using liquid crystals in a transient wind tunnel; ASME Heat Transfer Division Vol.71., 1987.

4. Smith, A.J.D., & Baxter, D.R.J. Liquid crystal thermography for aerodynamic heating measurements in short duration hypersonic facilities; Proc. 13th ICIASF, Gottingen, 1989.

5. Babinsky, H. and Edwards, J.A. Application of liquid crystal thermography in short duration hypersonic wind tunnels; Conference on Optical Methods and Data Processing for Heat and Fluid Flows, City Univ., London, 1992

6. Needham, D.A. and Stollery J.L. Boundary layer separation in hypersonic flow; AIAA Paper 66-455, 1966.

7. Holden, M.S. Leading edge bluntness and boundary layer displacement effects on attached and separated laminar boundary layers in a compression corners; AIAA Paper 68-68, 1968.

8. Stetson, K.F. Effects of bluntness and angle of attack on boundary layer transition on cones and biconic configurations; AIAA Paper 79-0269, 1979.

9. Stollery, J.L. and Babinsky, H. Flow over a delta wing at hypersonic speeds; 1st European Symposium on Hypersonic Flow, ESTEC, 1991

Driver Pressure P_4 (bar)	Driven Pressure P_1 (bar)	Stagnation Pressure P_o (bar)	Reservoir Temperature T_o (K)	Re_∞/cm 10^4
34.5	1.0	28.0	820	4.56
69.0	1.0	55.2	1030	6.39
103.5	1.0	78.9	1160	8.00
138.0	1.0	109.6	1290	9.05

Table 1 : Freestream Conditions for a given driver pressure

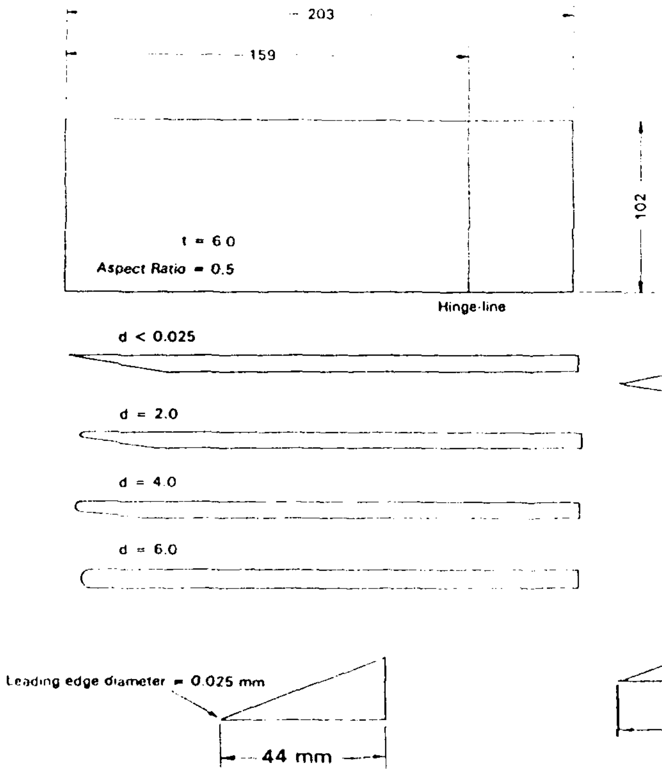
203
159
102
t = 6.0
Aspect Ratio = 0.5
Hinge-line
d < 0.025
d = 2.0
d = 4.0
d = 6.0
Leading edge diameter = 0.025 mm
44 mm

Simulated Flap Angles: 5, 10, 15, 20, 25 and 30°

Figure 1(a): FLAT PLATE MODEL GEOMETRY

All dimensions in mm

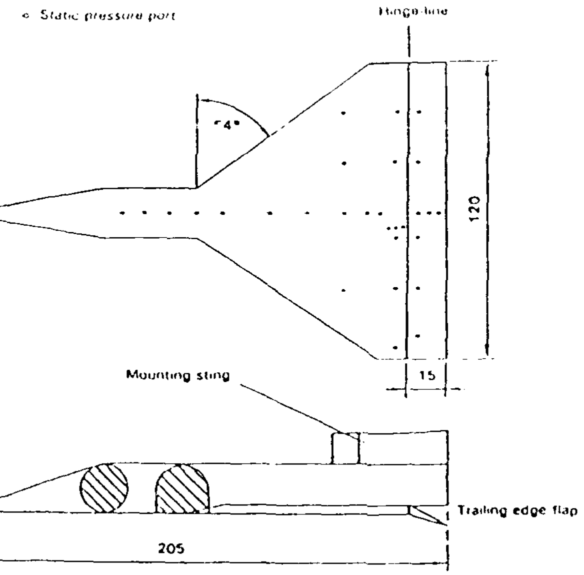
○ Static pressure port
Hinge-line
54°
120
15
Mounting sting
Trailing edge flap
205

Figure 1(b): DELTA-WINGED MODEL GEOMETRY AND PRESSURE TAPPING POSITIONS

All dimensions in mm

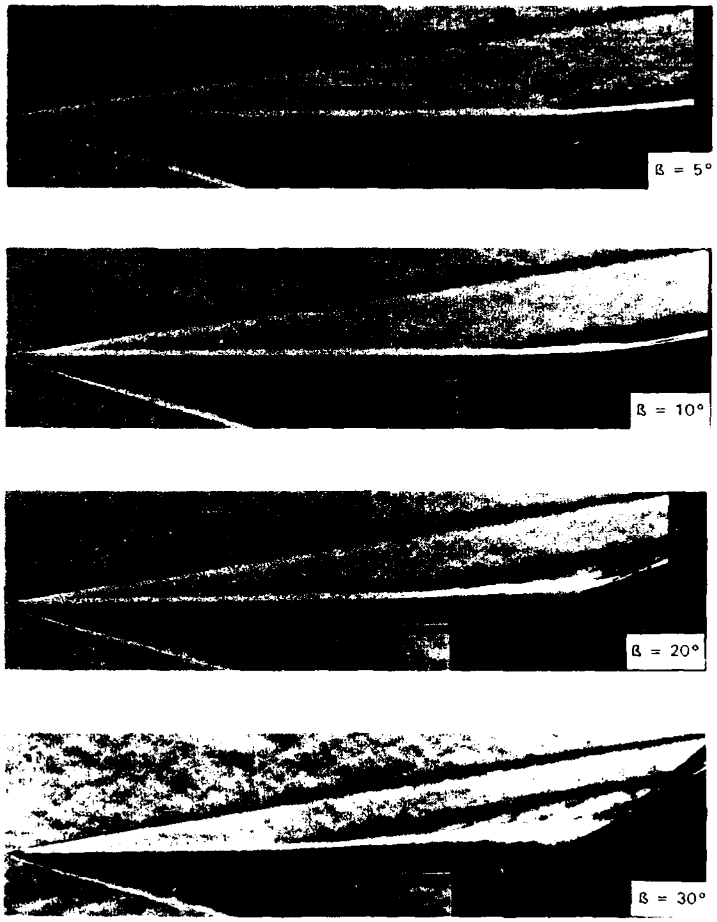
β = 5°
β = 10°
β = 20°
β = 30°

Figure 2(a): TESTS AT ZERO INCIDENCE
$M_\infty = 8.2$, $Re_\infty/cm = 9.05 \times 10^4$

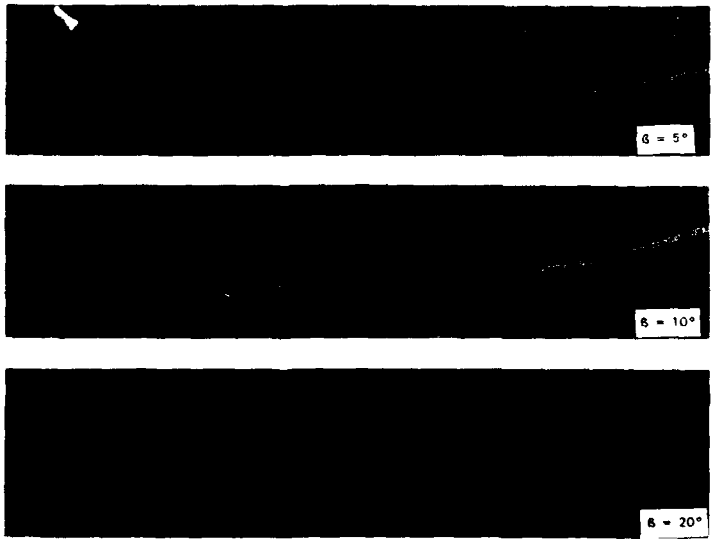

Figure 2(b): TESTS AT 5° INCIDENCE
$M_\infty = 8.2$, $Re_\infty/cm = 9.05 \times 10^4$

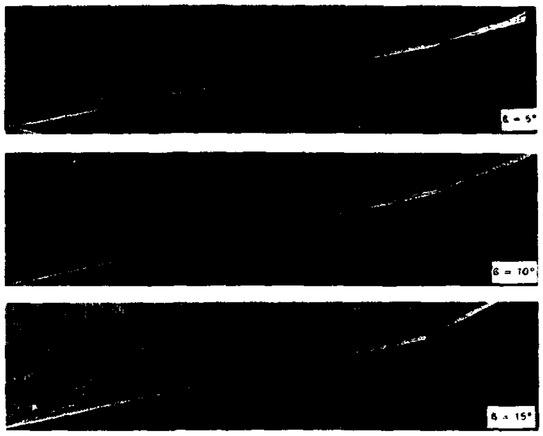

Figure 2(c): TESTS AT 10° INCIDENCE
$M_\infty = 8.2$, $Re_\infty/cm = 9.05 \times 10^4$

d/t = 0.004

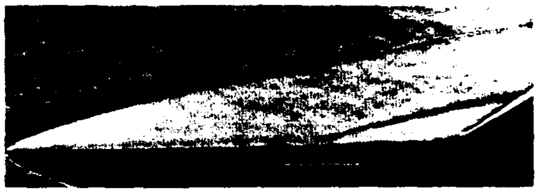

d/t = 0.33

d/t = 0.66

d/t = 1

Figure 3: EFFECTS OF LEADING-EDGE BLUNTNESS ON SEPARATION
$M_\infty = 8.2$, $Re_\infty/cm = 9.05 \times 10^4$

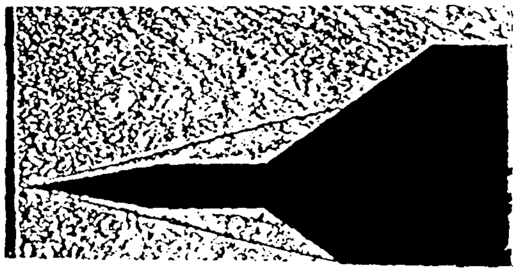

Figure 4: SCHLIEREN PICTURE SHOWING NOSE SHOCK IMPINGEMENT ON WING LEADING EDGE

$\alpha = 0$, $\beta = 20°$

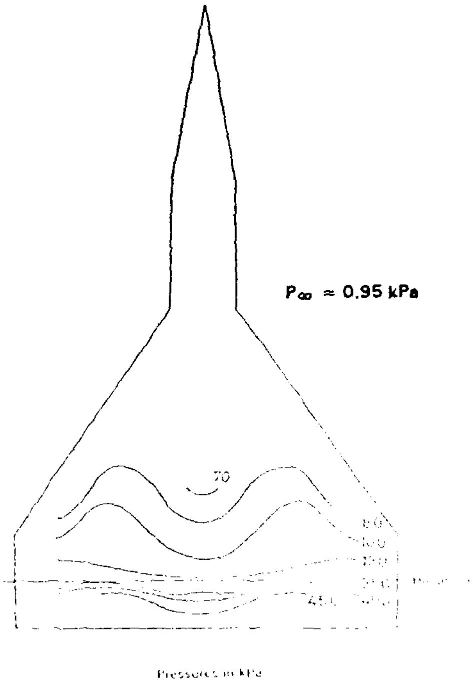

Figure 6: ISOBAR MAP ON WINDWARD SURFACE OF THE WING

$\alpha = 15°$, $\beta = 20°$

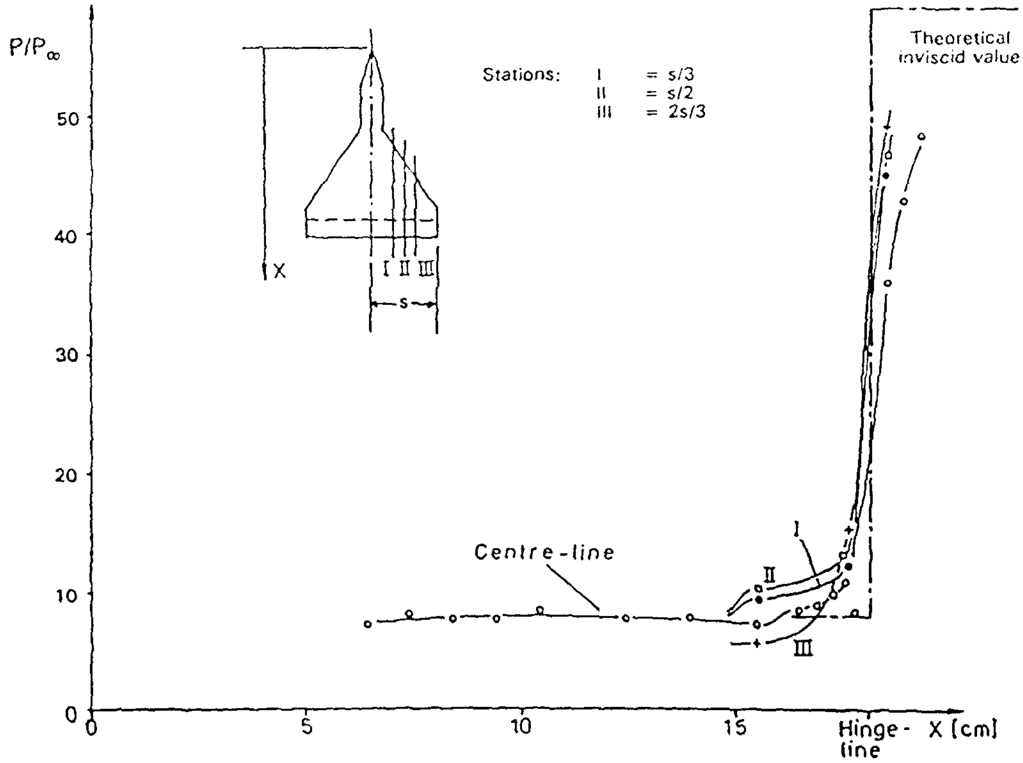

Figure 5: CHORDWISE PRESSURE DISTRIBUTIONS ALONG MODEL LOWER SURFACE AT VARIOUS SPANWISE STATIONS

$M_\infty = 8.2$, $Re = 9.3 \times 10^4\ cm^{-1}$

$\alpha = 15°$, $\beta = 20°$

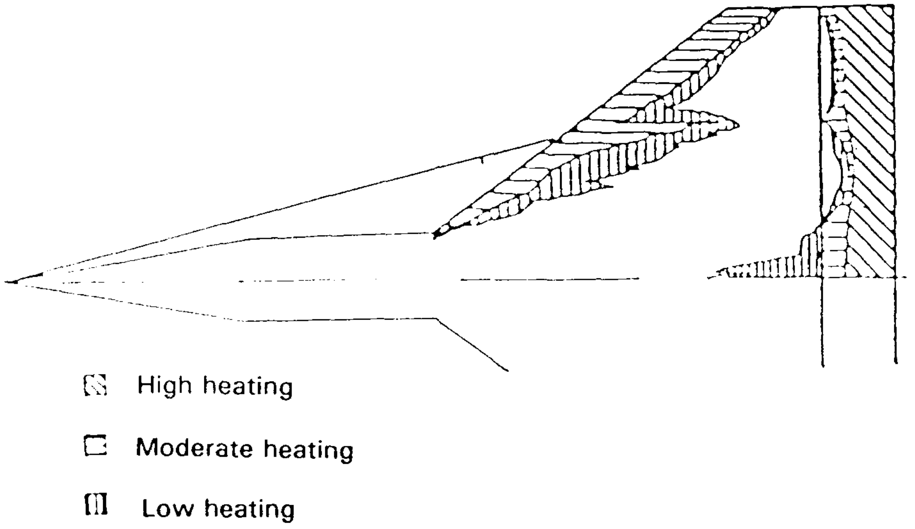
High heating
Moderate heating
Low heating

Figure 7: QUALITATIVE DISTRIBUTION OF AERODYNAMIC HEATING FROM LIQUID CRYSTAL PICTURES

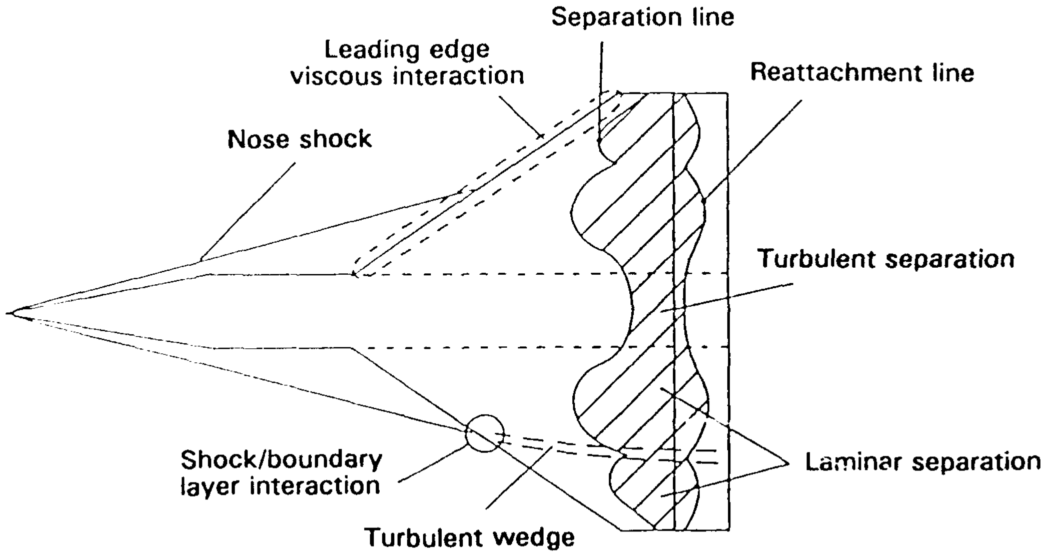
Separation line
Leading edge viscous interaction
Reattachment line
Nose shock
Turbulent separation
Shock/boundary layer interaction
Laminar separation
Turbulent wedge

Figure 8: PROPOSED FORM OF SEPARATED FLOW REGION

IN-FLIGHT EVALUATION OF AERODYNAMIC PREDICTIONS OF AN AIR-LAUNCHED SPACE BOOSTER

Robert E. Curry
NASA Dryden Flight Research Facility
P.O. Box 273
Edwards, CA 93523 - 0273, USA

Michael R. Mendenhall
Nielsen Engineering & Research, Inc.
510 Clyde Avenue
Mountain View, CA 94043, USA

Bryan Moulton
PRC Inc.
Edwards, CA 93523-0273 USA

SUMMARY

Several analytical aerodynamic design tools that were applied to the Pegasus® air-launched space booster were evaluated using flight measurements. The study was limited to existing codes and was conducted with limited computational resources. The flight instrumentation was constrained to have minimal impact on the primary Pegasus missions.

Where appropriate, the flight measurements were compared with computational data. Aerodynamic performance and trim data from the first two flights were correlated with predictions. Local measurements in the wing and wing-body interference region were correlated with analytical data. This complex flow region includes the effect of aerothermal heating magnification caused by the presence of a corner vortex and interaction of the wing leading edge shock and fuselage boundary layer.

The operation of the first two missions indicates that the aerodynamic design approach for Pegasus was adequate, and data show that acceptable margins were available. Additionally, the correlations provide insight into the capabilities of these analytical tools for more complex vehicles in which design margins may be more stringent.

NOMENCLATURE

C_D	drag coefficient
C_L	lift coefficient
C_m	pitching moment coefficient
CFD	computational fluid dynamics
c.g.	center of gravity
FS	fuselage station, measured in forward direction, in.
h_p	pressure altitude, ft (m)
HRSI	high-temperature reusable surface insulation
M	Mach number
$\frac{p}{p_R}$	local pressure divided by pressure measured at reference location (FS = 288.4 in., z = 17 in.)
$\bar{q}$	dynamic pressure, lb/ft^2 (kPa)
$\frac{q}{q_R}$	local convective heating rate divided by rate measured at reference location (FS = 288.4 in., z = 17 in.)
Re	unit Reynolds number, ft^{-1} (m^{-1})
T	temperature, °F (°C)
TPS	thermal protection system
y	lateral coordinate measured from vehicle centerline, in.
z	vertical coordinate measured from vehicle centerline, in.
α	angle of attack, deg
β	angle of sideslip, deg
Δ	incremental change
δR	rudder deflection, deg

® Pegasus is a registered trademark of Orbital Sciences Corp., Fairfax, VA.

INTRODUCTION

In recent years, computational aerodynamic methods have played a more significant role in developing hypersonic flight vehicles. Two reasons are the potential cost savings from reduced ground test requirements and the need for design data at conditions which cannot be fully simulated in wind-tunnel facilities. The usefulness of such methods depends on two issues: their ability to represent important physical phenomena and their practicality (i.e., application effort and resource requirements) in the design process. To assess the first issue, the code validation process, requires a series of highly controlled experiments with extensive measurement surveys as discussed in Ref. 1. The issue of the practical nature of such methods, however, must be assessed with respect to the design of actual flight vehicles. Few opportunities have arisen for this type of evaluation.

The Pegasus® air-launched space booster system offered an opportunity to conduct such an evaluation. This vehicle was developed as a commercial joint venture by Orbital Sciences Corp., Fairfax, VA, and Hercules Aerospace Corp., Magna, UT, to deliver small payloads into orbit. In addition to the primary payload, some limited additional instrumentation was installed on the first two flights for research. This instrumentation had minimal impact on the orbital delivery mission and, therefore, was accommodated at low cost.

Several features of the Pegasus vehicle made it attractive for this research approach. Pegasus uses wing and tail surfaces for lift, stability, and control at speeds up to Mach 8. These surfaces generate interesting hypersonic flow fields for analysis and provide convenient locations for instrumentation. Because of the multistage design, the weight of additional research hardware on the first stage had small impact on the payload performance of the overall system (the ratio of additional first-stage weight to reduced payload capability was about 18:1).

In addition to these benefits, a significant analytical database existed for the Pegasus. The original aerodynamic design was developed exclusively through computational design tools by Nielsen Engineering & Research, Inc., Mountain View, CA. This approach and the resulting data are described in detail in Ref. 2. The resulting database was obtained from existing codes and methods which could be applied within the cost and manpower constraints of the project. The design effort concentrated on the requirements for vehicle development and not with the intent to develop codes or theory.

In addition to the design effort, some postflight computations were conducted to enhance the value of the flight data. All analytical results discussed in this report, however, represent a level of sophistication and application effort typical of the privately funded Pegasus design effort.

The objective of this study was to evaluate certain aspects of code performance with measurements from the first two flights. Specifically, this includes correlations of first-stage vehicle aerodynamics (performance and trim) at high speeds and local aerodynamics on the wing and in the wing root interference region. The evaluation includes analytical data from both the preflight and follow-on computational efforts. Many aspects of the extensive analytical design process (such as launch dynamics, exhaust-plume-induced separation studies, fin actuator heating, etc) could not be assessed with the available flight data and, therefore, will not be addressed in this paper.

This paper will describe the various flight and analytical data sources and their limitations. The correlations will be considered with respect to the relatively conservative Pegasus requirements and also with respect to more complex vehicles which may have less design margin.

A series of more sophisticated hypersonic flight experiments to be conducted using the Pegasus is under development. The series will use a stand-alone data acquisition system and an aerodynamically smooth wing test panel. These experiments will build on the minimal-impact, add-on, flight-research approach developed in the current research.

BASELINE VEHICLE DESCRIPTION AND OPERATION

The Pegasus is a three-stage, solid-rocket space launch vehicle designed to insert small payloads, 600 to 1000 lb (270 to 450 kg), into orbit, (Ref. 3). Figure 1 shows the configuration. The configuration has a cylindrical fuselage and high wing with clipped-delta planform. A large fairing, referred to as the fillet, extends along the wing-body intersection. The wing and tail surfaces are part of the first stage. The aerodynamic surfaces are fabricated primarily from graphite-epoxy structures and covered with thermal protection materials. The thermal protection system (TPS) includes layers of insulating material and ablatives. The vehicle has an autonomous onboard guidance and control system. The flight 1 and 2 vehicles had virtually identical external configurations. Key physical characteristics of Pegasus follow:

Wing reference area	145.4 ft^2 (13.51 m^2)
Span	22 ft (6.7 m)
Mean aerodynamic chord	8.14 ft (2.48 m)
Root chord	12.11 ft (3.69 m)
Tip chord	1.11 ft (0.338 m)
Aspect ratio	3.33
Wing leading edge sweep	45°
Wing leading edge radius	1 in. (0.0254 m)
Fuselage length overall	49.34 ft (15.0 m)
Fuselage nominal diameter	4.17 ft (1.27 m)

The Pegasus vehicle is carried aloft under the wing of a B-52 aircraft, and is air-launched at an altitude of about 42,000 ft (12.8 km) and Mach 0.8. Approximately 5 sec after release, the first-stage motor is ignited and the vehicle accelerates to a Mach number of about 8 and an altitude of about 210,000 ft (64 km). During this first-stage operation, which lasts about 80 sec, the vehicle is aerodynamically controlled by all-moving tail surfaces. A 2.5-g pull-up is initiated early in the flight to achieve the desired flightpath angle. The g-level is gradually reduced so that the vehicle is nominally at 0° angle of attack at Mach numbers of 5 and above. During the final seconds of the first-stage flight, small solid-rocket motors in the movable tail surfaces are ignited to augment control at low-dynamic pressure conditions. After burnout, the vehicle coasts for several seconds before stage separation. After separation, the stages are not recovered.

FLIGHT TEST DATA

Data from the first two flights of the Pegasus were used in this study. The intent to have minimal impact on the primary satellite deployment missions was a significant challenge to the research effort. The sensors were constrained to have little structural design impact, data were acquired through the baseline Pegasus systems which had additional limitations, and the trajectories were fixed by the requirements of the primary mission payloads. More information about the flight test procedures and data can be obtained from Refs. 4 through 6 and a later publication.*

Instrumentation

Flight data were derived from the baseline Pegasus flight instrumentation as well as from additional research instrumentation. The baseline flight instrumentation included onboard control surface position and inertial navigation system data, ground-based radar data, and weather observations.

Additional research instrumentation on flight 1 included conventional thermocouples which were installed on nonablating plugs and thin-foil thermocouples. The 1-in. diameter nonablating plugs were fabricated from high-temperature reusable surface insulation (HRSI) material with a high-emissivity coating. The HRSI plug surface temperatures were significantly different from the surrounding structure but were highly responsive to changes in the local flow characteristics. Ten HRSI plugs were installed on the right fillet sidewall. Seventy-six foil gauges were distributed in two rows on the right wing lower surface and leading edge, and at various locations on the right fillet sidewall. These foils were approximately 0.006-in. thick and were inserted between layers of the TPS during fabrication. Certain locations had more than one gauge inserted at different depths of the TPS. The TPS consisted of layers of insulative material and a spray-on ablative and in these regions had a nominal thickness of about 0.06 in. (1.5 mm). The foil-gauge installation resulted in only minor distortion of the thermal properties of the surrounding structure. On the other hand, these gauges were covered by a low-temperature ablative and not directly exposed to the flow. As a result, they were of limited value in studying local flow phenomena. Figures 2(a) and 2(b) show a layout of the flight-1 instrumentation.

The flight-2 vehicle accommodated 8 IRSI plugs, 8 surface pressures, 7 commercially available calorimeters, and 14 foil thermocouples. The flush pressure measurement ports were installed on selected HRSI plugs. All flight-2 instrumentation was located on the right fillet sidewall, as shown in Fig. 2(c).

All onboard measurements were obtained through the baseline Pegasus data processing system. In addition to data acquisition, this 8-bit system provided all flight-control, guidance, and vehicle-management functions. For both flights, the research instrumentation bandwidth portion of this system was limited to approximately 3000 bit/sec. The system had fixed frame rates with a maximum of 25 samples/sec. All onboard data were telemetered to ground stations as a pulse-code-modulated signal.

---

*Proposed NASA Technical Memorandum by Noffz, Moes, Haering, and Kolodziej.

Data Reduction

Flight conditions along the trajectory were estimated from a combination of radar tracking from up to eight sites and the onboard inertial measurements using a weighted least-squares method and an atmospheric model. The atmospheric model was determined from a combination of weather observations including balloon data, launch aircraft measurements, stratospheric charts, and climatological databases. This model was also used to correct for radar refraction. The trajectory analysis was adversely affected by the low radar tracking angles (which resulted in high sensitivity to atmospheric refraction modeling) and the large geographic range covered during the first-stage flight.

The vehicle aerodynamic forces and moments were derived by balancing the measured body axis accelerations with vehicle properties. The mass and inertias were estimated from preflight measurements and the expected propellant loss during rocket motor burn. Thrust was modeled as a function of time using data from ground tests corrected for ambient pressure at altitude. Fin rocket thrust was also modeled as a function of time. Total rocket thrust was assumed to be longitudinally aligned and subtracted from the net axial force to determine the aerodynamic component of axial force. Lift and drag were determined from the normal and axial force components and the derived angle of attack. The lift, drag, and pitching moments were converted to coefficient form using wing reference dimensions and dynamic pressure. The pitching moment was referenced to the modeled flight center-of-gravity (c.g.) location. The accuracy of these terms is largely dependent on the accuracy of the estimated trajectory and meteorological reconstruction which may vary from flight to flight. The repeatability of results over a series of future flight dates should identify any significant errors if they exist.

At high altitudes, as dynamic pressure diminishes, small misalignment errors in the thrust axis result in large surface trim requirements. Since these trim requirements are primarily thrust related and not aerodynamic, moment data at these times cannot be expected to correlate well with aerodynamic predictions. This effect can be identified by elevator and rudder deflections (rudder data are shown in Fig. 3) which vary proportionately to the reduction in free-stream dynamic pressure and end with motor burn-out. The orientation and magnitude of the thrust misalignment vary between vehicles. As a result, moment measurements were limited to Mach numbers of about 5 or below. A control-system-induced oscillation occurred on flight 1 which contaminated the linear acceleration measurements. This limited the usable range of lift and drag data to Mach numbers less than 4.5. This problem was eliminated on flight 2.

Convective heat-flux estimates were derived postflight from the various thermocouple installations. The foil thermocouples located in the leading edge TPS were analyzed using an inverse analysis method, Ref. 7. In this study, the results are only considered as an indication of relative heating rate distribution. This approach is only valid prior to the onset of ablation. Convective heat flux was derived from the HRSI plug temperatures using a one-dimensional model and finite element thermal resistance analogy method. These computations are sensitive to the modeling of material properties, sensor installation, and emissivity. No attempt was made to account for the local surface temperature perturbations caused by the plugs or for ablation products in the boundary layer. As a result, the absolute value of heating rate from this derivation is not considered representative of Pegasus surface heating; however, the data are indicative of relative heating characteristics. Relative heating rates in the fillet region are defined as the local value divided by the value obtained on the lower, forward region of the fillet, as shown on Fig. 2. As noted in Ref. 4, this location is expected to be forward of the intersecting wing shock location and is, therefore, felt to represent a suitable reference condition.

Trajectories

Figure 4 shows flight-trajectory parameters for the two flights. Differences in the trajectories were primarily caused by requirements of the satellite payloads. Both flights achieved a maximum angle of attack of about 20°; flight 1 then stabilized briefly at about 7.5°, and flight 2 stabilized at about 2.5°. The angle of attack for both vehicles was about 0° for Mach numbers of 5 and higher. Flight 2 experienced higher dynamic pressures, but both were generally in the ideal gas flight regime.

ANALYTIC DATA

Force and Moment Aero Models

A six-degree-of-freedom model of the vehicle forces and moments was developed for conditions throughout the flight envelope. The coefficient data include the effects of Mach, angles of attack and sideslip, control surface deflection, and angular rates. Development of this aero model was a major accomplishment of the

Pegasus development effort and is described in detail in Ref. 2. It relied primarily on a variety of semi-empirical database and panel methods; however, advanced computational methods (for example, Euler and Navier-Stokes) were used for selected studies throughout the design and analysis. The computational resources for this effort were not severe by modern standards, but the overall size of the data sets (504 longitudinal and 918 lateral flow conditions) indicates the level of analysis effort required. Approximately four times this number of flow conditions were studied because of design iterations and configuration changes. This data set was used to support preliminary design, performance studies, structural loading predictions, and guidance and control law simulation and development.

The aero model data shown in this report were obtained by applying the flight-estimated altitude, angle of attack, dynamic pressure, and control surface time histories to the database and correcting for modeled c.g. position. The resulting lift, drag, and pitching moment coefficients, therefore, can be directly correlated with flight values.

Computational Fluid Dynamics (CFD)

Flow-field solutions for the Pegasus configuration were obtained at a selected set of flight conditions as shown in Fig. 5.

The F3D code was utilized by Nielsen Engineering & Research, Inc., during the design effort prior to flight 1 to assess flow quality in the vicinity of the fillet and to corroborate aero load predictions. Additional F3D solutions were obtained after flight 1 at specific free-stream conditions encountered on the flight. The code solves the compressible three-dimensional, thin-layer Navier-Stokes equations as described in Ref. 8; details of the current application are provided in Ref. 9. The initial grid was developed during the Pegasus design effort. Solutions of this grid required approximately 40 hr of computer time per case on a Cray-2 (Cray Research, Inc., Minneapolis, MN) computer. The grid for the postflight analysis was modified to concentrate on data in the fillet region. During the postflight analysis the surface temperatures were set to values estimated from the foil thermocouple sensors.

In a similar CFD effort, Ref. 10, the PARC code was applied to the Pegasus configuration by researchers at the University of California at Los Angeles. This code was applied at selected conditions from flights 1 and 2. A different grid system was used, although it was tailored again to emphasize the fillet region. Solutions required approximately 50 hr of computer time per case on an IBM-9000^{TM} (IBM Corp., Armonk, NY) computer. Details of this effort can be found in Ref. 11.

The computational solutions provided data at all locations in the flow field, and the PLOT3D interactive graphics program, Ref. 12, was used to interpret the results. Convective surface heating rates were determined from the CFD solutions using the temperature gradient between the surface and the first grid point away from the surface. The wing leading edge relative heating rates shown in this report are the temperature gradient multiplied by a constant. The relative heating rates on the fillet sidewall were divided by the value obtained at a location on the lower, forward corner of the fillet. This allows direct correlation of the data with the flight-measured relative heating rates.

RESULTS AND DISCUSSION

Vehicle Forces and Moments

The measured lift, drag, and pitching moment coefficients are shown in Fig. 6 along with the corresponding values derived from the preflight database. The overall agreement between flight and prediction is good. The incremental differences for both flights are shown to be consistent in Fig. 7.

At the lower Mach numbers, lift is lower than predicted and drag is higher than predicted. The largest discrepancies occur at the higher angles of attack at transonic speeds, where the error in lift is about 10 percent of the total. The corresponding error in drag is about 20 percent of the total. These conditions are only encountered for a few seconds and, therefore, have minimal impact on the payload performance of the Pegasus system as a whole. At higher speeds, the lift biases (flight minus predicted) are slightly positive on flight 2 and nonexistent on flight 1. The drag biases are slightly positive at all speeds.

The pitching moment flight data indicate more nose-down moment than the prediction. The errors vary during the most dynamic portions of the flight (Mach less than 2.5), which may indicate the limits of this quasi-steady analysis. At higher speeds the error is a constant level of about 0.035 which corresponds to a center of pressure bias of about 0.4 times the fuselage diameter. In turn, this corresponds to an elevator trim error of about 3°, which is within acceptable margins.

Local Aerodynamics

An example of two temperature measurements at varying depths in the wing leading edge is shown in Fig. 8. The lag between the two curves indicates the effect of the TPS in delaying the transfer of heat to the primary structure. The TPS on the wing leading edge, wing surfaces, and fillet was designed through coupled boundary layer and thermostructural analysis methods. Although the flight data indicate that the layer of ablative material was completely removed by aerothermal heating in some regions of the wing, the temperature of the primary structure was kept within its design limit of 170 °F (77 °C) until the final seconds of flight (at which point aerodynamic loads were minimal).

The relative heating rates on the leading edge at Mach 4 derived from such data are shown in Fig. 9, along with results from the F3D analysis, Ref. 9. The flight data analysis indicates that significant ablation has not begun at this flight condition. The scatter in the measured data is expected to be the result of the sensor installation. As previously discussed, the sensors were inserted during the application of thin layers of spray-on ablative, and precise control of sensor depth was not possible. The overall trend of the data indicates higher heating rates near the wing tip which would be expected because of the nature of the curved bow shock. The F3D computational solution indicates the same relative variation in heating rates, even though the modeling of the leading edge itself was very sparse.

In comparison with the wing and leading edge regions, the fillet flow field under the wing is very complex. The flow along the flat sidewall of the fillet is intersected by a shock wave generated by the wing leading edge. In addition, the flow is conditioned by the three-dimensional geometry of the circular cylinder and the transition into the flat sidewall of the fillet. The relative significance of these effects varies with the angle of attack, Mach number, and Reynolds number range encountered throughout the Pegasus flight trajectories.

During the preflight design effort, CFD methods were used to check for potential flow separation problems in this region and to provide pressure distributions for follow-on boundary-layer and TPS design methods. Flight data were used to assess other details of the CFD analysis in this region which will be discussed next.

Although the computational solutions provided data at all points on the surface and in the flow field, the flight data are available at only discrete locations. On the other hand, the CFD data were only available at discrete times in the trajectory, whereas the flight testing provided a continuous time history of data. The combination of the two sets of data was very useful in interpreting the actual characteristics of the flow.

Figure 10 shows the relative heating rate distributions at several fuselage stations for selected flight and CFD analysis conditions. All local heating rate data have been divided by the corresponding values at the reference location shown. Typical computational distributions, such as those in Fig. 10(a), consist of two vertically separated heating rate maximums (spikes) at the forward fuselage stations (FS = 288.4 and 280.6). These appear to blend together by the most aft location shown (FS = 253.1). Computed pressure coefficients in the flow field (Fig. 11) indicate that this upper heat-flux spike is associated with the wing compression region and leading edge shock. It is felt that the lower spike is associated with the turning of the flow from the cylindrical fuselage to the flat sidewall.

The flight data for the flight 1 conditions generally confirm the location and approximate magnitude of the upper heat-flux spike at the forward fuselage stations. Agreement between the flight and computational data at the aft-most station is not consistent.

Comparison of Figs. 10(a) and 10(b), at similar Mach numbers, shows that more pronounced spikes occur in the PARC solution. This difference could be related to the differences in flight condition, the codes, or the analysis grids. At Mach 5 (Figs. 10(c) and 10(d)), the two computational solutions differ more significantly. The only difference in free-stream conditions for these cases is the Reynolds number. The available flight data are not adequate to assess the relative effectiveness of the two codes.

The pressure data also indicate that a suction region exists aft of the wing shock, that is, in the corner of the fillet sidewall and wing lower surface (Fig. 11). This suction in the computational data is associated with a corner vortex and becomes stronger at lower angles of attack. Figure 12 shows the limited flight-pressure measurements, also referenced to the forward location on the fillet, along with computational results. Both data sets show lower pressures near the wing lower surface ($z = 28$), which tends to support the existence of a corner vortex. The flight measurements show greater levels of suction that the computations at Mach 5.

CONCLUDING REMARKS

Flight measurements from the Pegasus air-launched space booster were obtained and correlated with computational data. The flight instrumentation was accommodated with minimal impact to the flight operation, and the computational results were obtained from the actual preflight design effort and a limited amount of follow-on analysis. The follow-on studies were conducted with the same level of sophistication as the design effort, relying on available codes and limited computer resources.

The correlation of vehicle forces and moments from flight and prediction was acceptable. Aerodynamic performance was slightly lower than predicted, and pitching moment was more nose-down than predicted; but these errors were within the design margins of the Pegasus system. Similarly, the aerothermal characteristics on the wing and fillet were found to be within Pegasus design limits.

Additionally, the correlations provide insight into the capabilities of the computational fluid dynamics techniques for more complex applications. Relative heating rate and pressure distributions in the complex wing body interference flow region indicate that key features were identified, despite the limitations of the computational methods (no modeling of ablation, constant wall temperatures, limited computational grid size, etc). In particular, the location and approximate magnitude of the wing shock interference heating and presence of a corner vortex were consistent in both the flight and computational fluid dynamics data. The correlations are better on the forward edge of the fillet and degrade further aft, as the flow characteristics merge. The flight data were too sparse to assess the relative effectiveness of the two codes.

ACKNOWLEDGEMENT

The authors acknowledge the Defense Advanced Research Project Agency and Orbital Sciences Corp. for their support of this research.

REFERENCES

1. Marvin, Joseph G, *Accuracy Requirements and Benchmark Experiments for CFD Validation*, NASA TM-100087, May 1988.
2. Mendenhall, Michael R., Daniel J. Lesieutre, Steven C. Caruso, Marnix F.E. Dillenius, and Gary D. Kuhn, "Aerodynamic Design of Pegasus^{TM}—Concept to Flight with CFD," *in Missile Aerodynamics*, AGARD-CP-493, 1990 (also available as AIAA 91-0190).
3. Covault, Craig, "Commercial Winged Booster to Launch Satellites from B-52," *Aviation Week and Space Technology*, vol. 128, no. 23, June 6, 1988, pp. 14–16.
4. Noffz, Gregory K, Robert E. Curry, Edward A. Haering, Jr., and Paul Kolodziej, *Aerothermal Test Results from the First Flight of the Pegasus Air-Launched Space Booster*, NASA TM-4330, 1991.
5. Noffz, Gregory K. and Robert E. Curry, "Summary of Aerothermal Test Results from the First Flight of the Pegasus Air-Launched Space Booster," AIAA-91-5046, presented at the AIAA Third International Aerospace Planes Conference, Orlando, FL, Dec. 3–5, 1991.
6. Kolodziej, Paul and Gregory K. Noffz, "Aerothermal Heating Measurements on the Pegasus Air Launched Booster," 38th International Symposium, Instrumentation Society of America, Las Vegas, NV, Apr. 1992.
7. Blackwell, B.F., R.W. Douglass, H. Wolf, and Raymond F. Giffels, "A User's Manual for the Sandia One-Dimensional Direct and Inverse Thermal (SODDIT) Code," SAND85-2478, Sandia National Laboratories, Albuquerque, NM, May 1987.
8. Ying, S.X., D. Baganoff, J.L. Steger, and L.B. Schiff, "Numerical Simulation of Unsteady, Viscous, High-Angle-of-Attack Flows Using a Partially Flux-Split Algorithm," AIAA 86-2179, Aug. 1986.
9. Kuhn, Gary D., *Postflight Aerothermodynamic Analysis of Pegasus® Using Computational Fluid Dynamics Techniques*, NASA CR-186017, March 1992.
10. Cooper, G.K. and J.R. Sirbaugh, "The PARC Code: Theory and Usage," AEDC-TR-89-15, Arnold Engineering and Development Center, Arnold AFB, TN, ~~Dec. 1989~~.

11. Fricker, Darren, John Mendoza, and Ivan Catton, *A Computational Fluid Dynamics Analysis of the Hypersonic Flights of the Pegasus*, NASA CR-186023, 1992.

12. Walatka, Pamela, and Pieter G. Buning, *PLOT3D User's Manual*, NASA TM-101067, 1989.

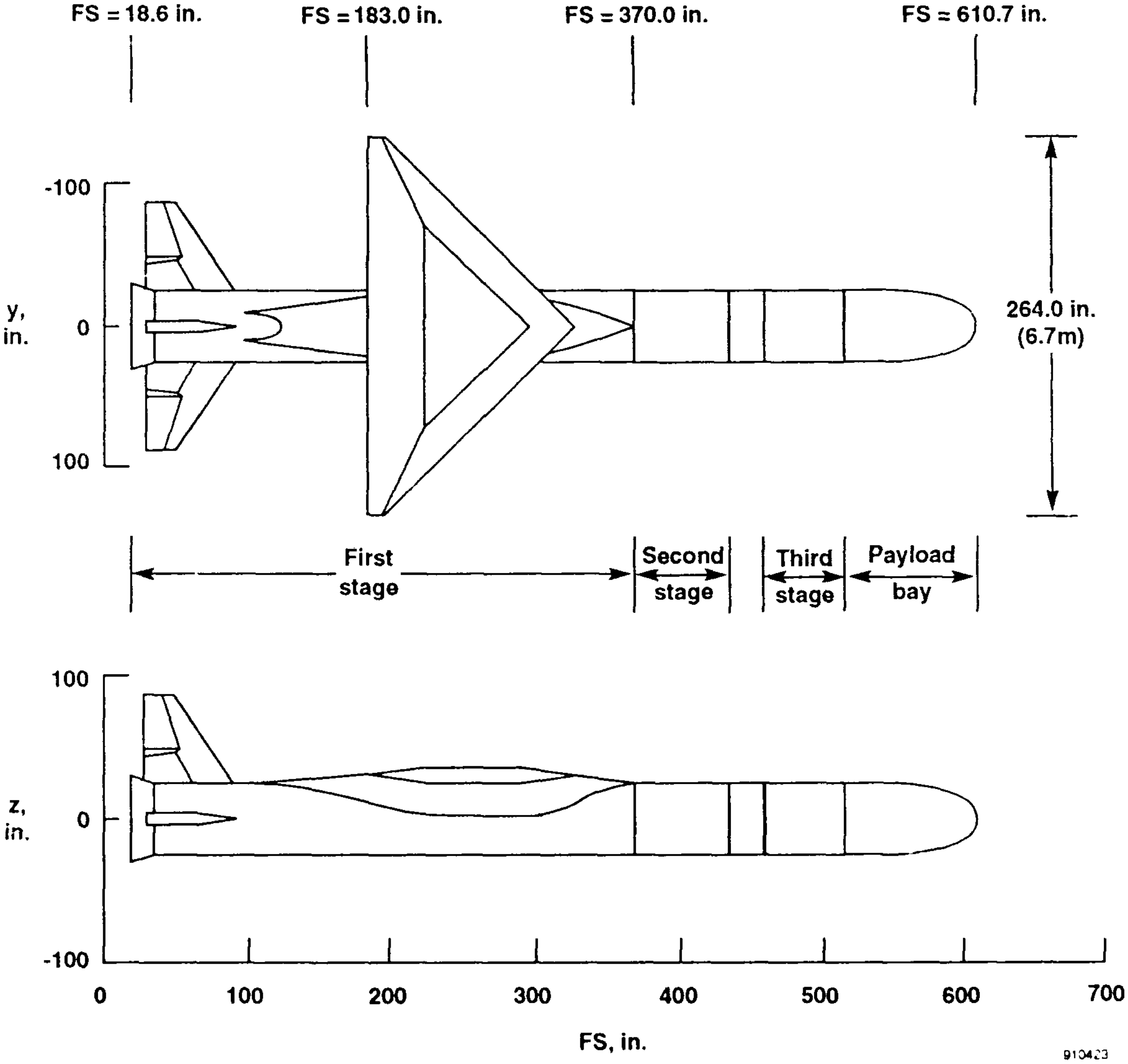
FS = 18.6 in.
FS = 183.0 in.
FS = 370.0 in.
FS = 610.7 in.
-100
y, in.
0
100
264.0 in. (6.7m)
First stage
Second stage
Third stage
Payload bay
100
z, in.
0
-100
0
100
200
300
400
500
600
700
FS, in.
910423

Fig. 1. Pegasus launch configuration.

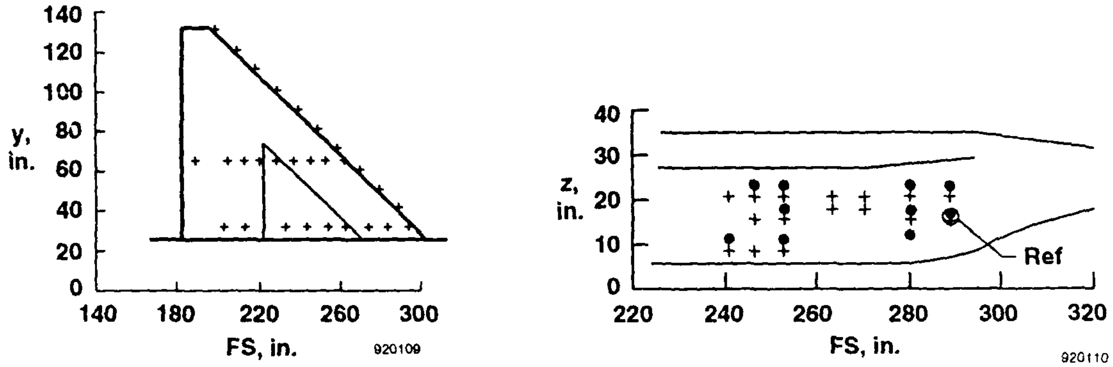

(a) Flight 1, right wing lower surface.

(b) Flight 1, right fillet sidewall.

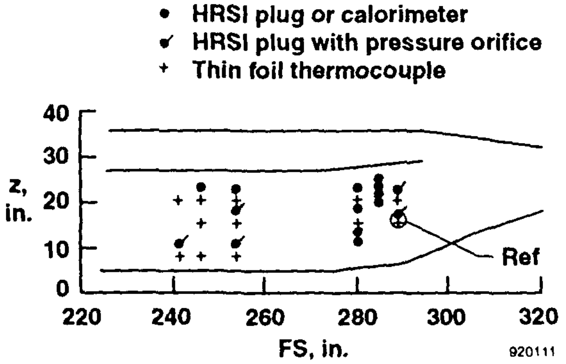

(c) Flight 2, right fillet sidewall.

Fig. 2. Flight instrumentation.

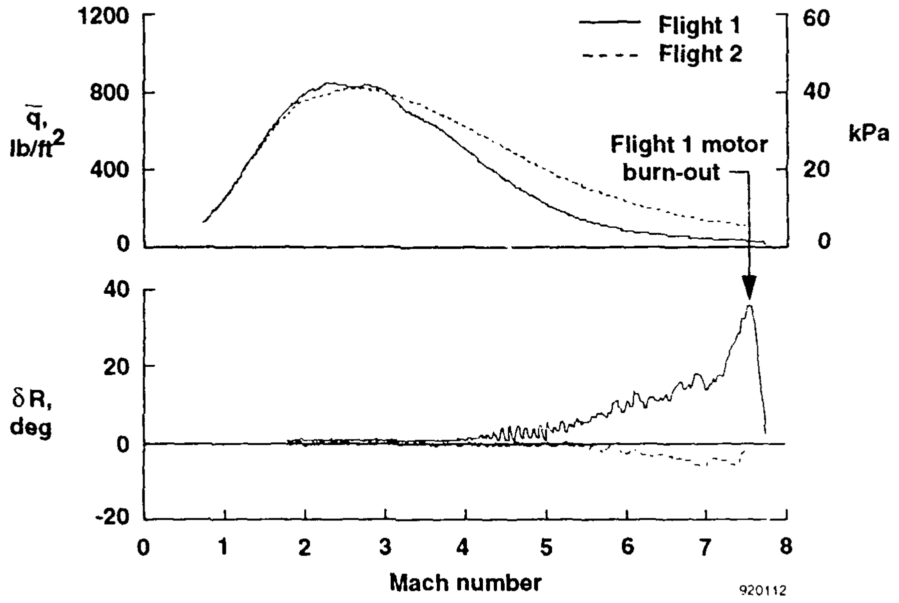

Fig. 3. Identification of thrust misalignment effects.

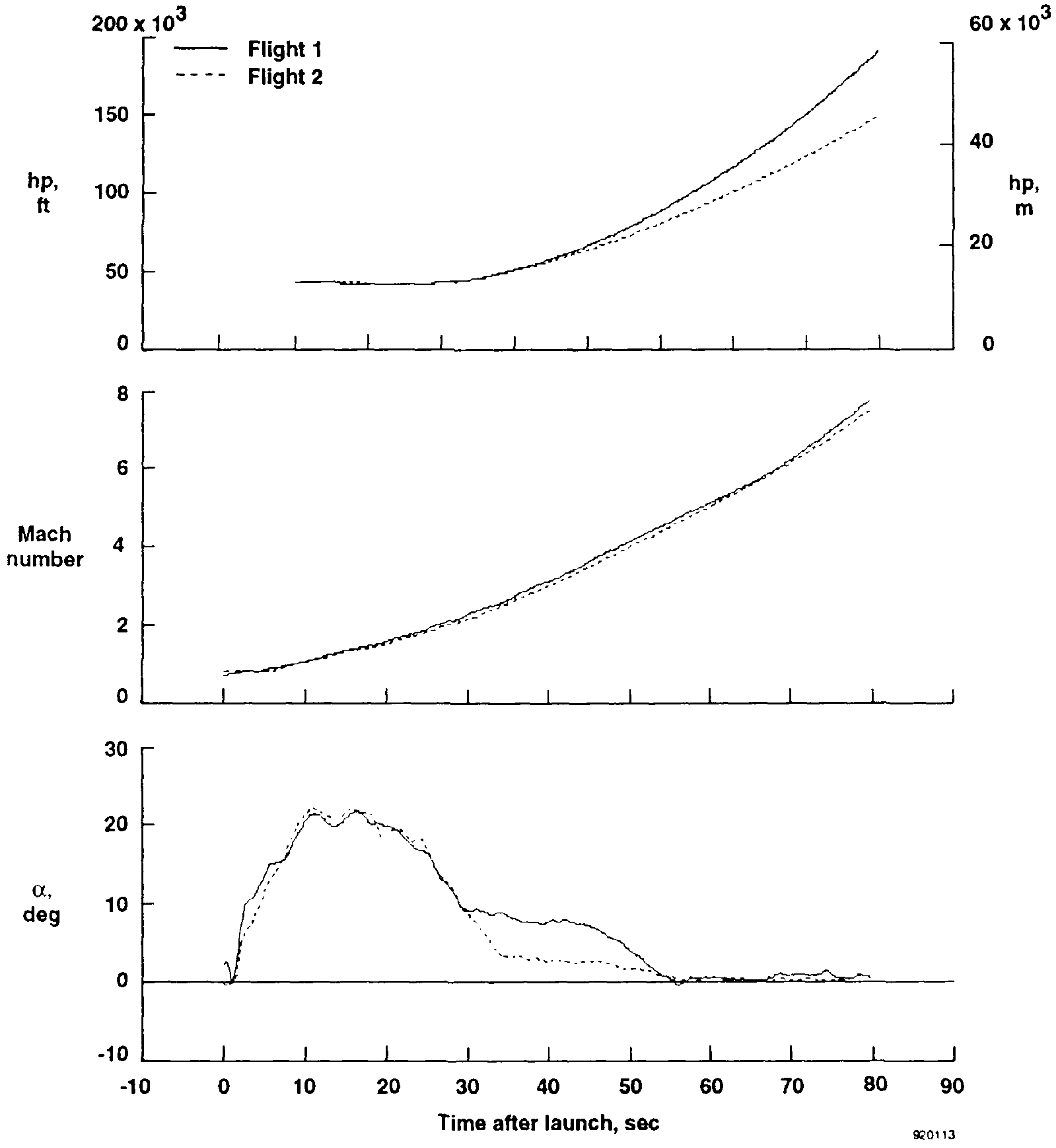

Fig. 4. Trajectory flight conditions.

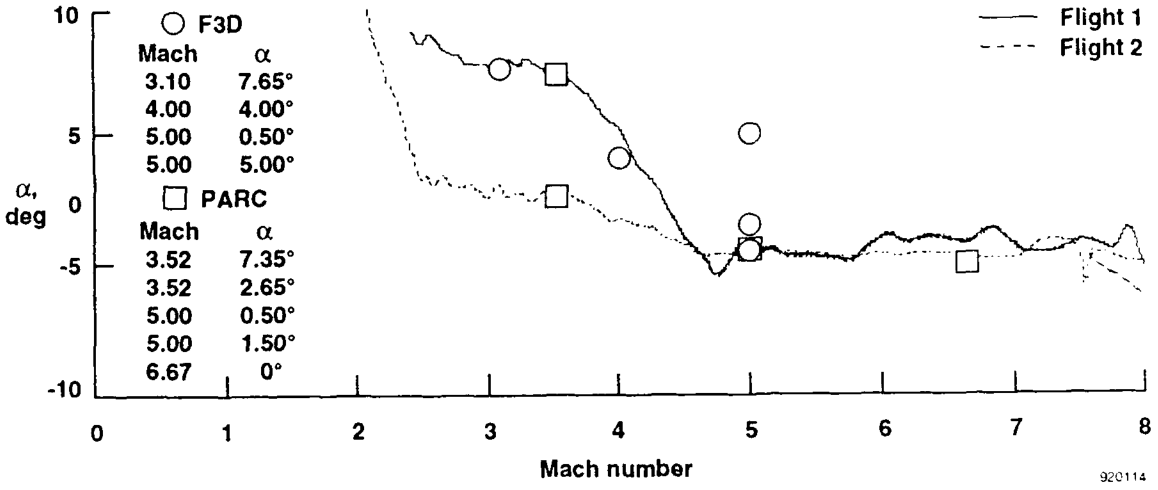

Fig. 5. High-speed computational fluid dynamics analysis flight conditions.

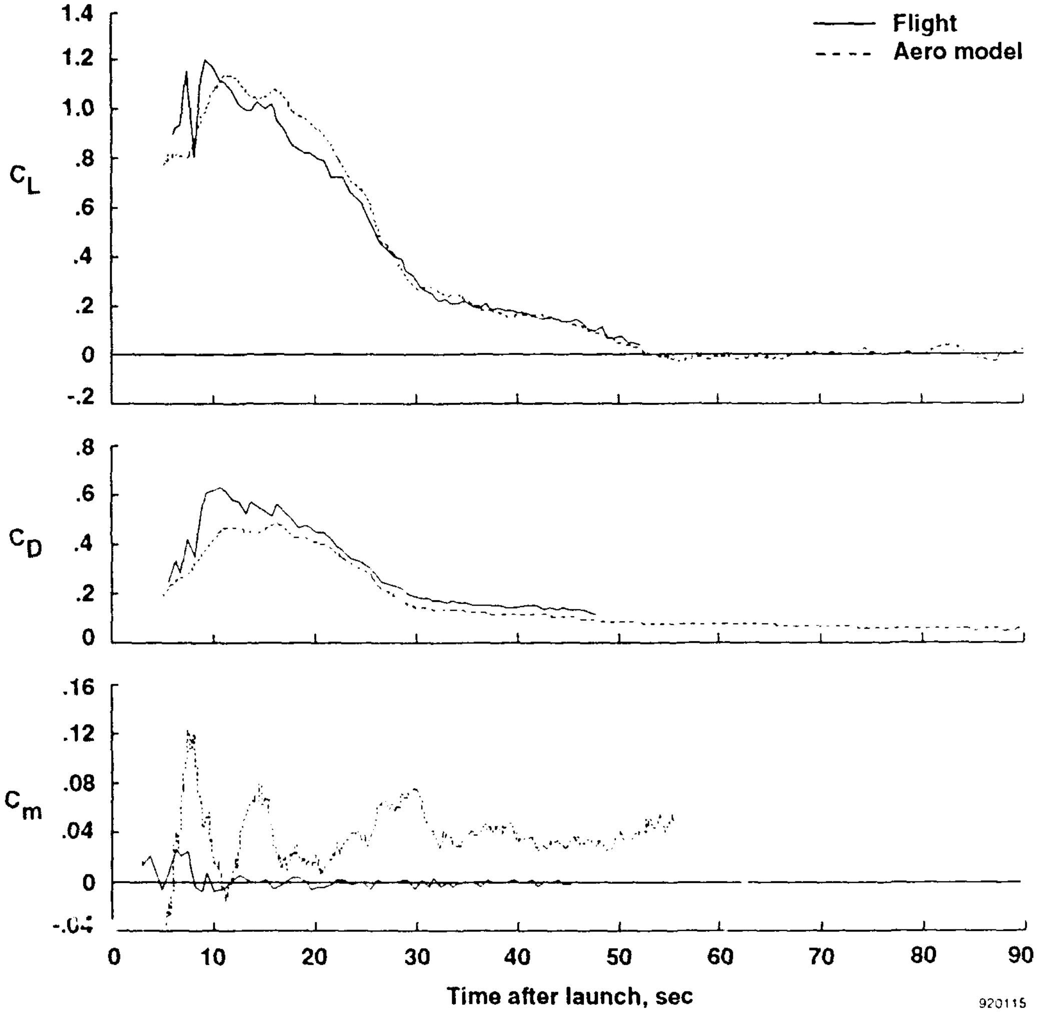

(a) Flight 1.

Fig. 6. Vehicle forces and moments.

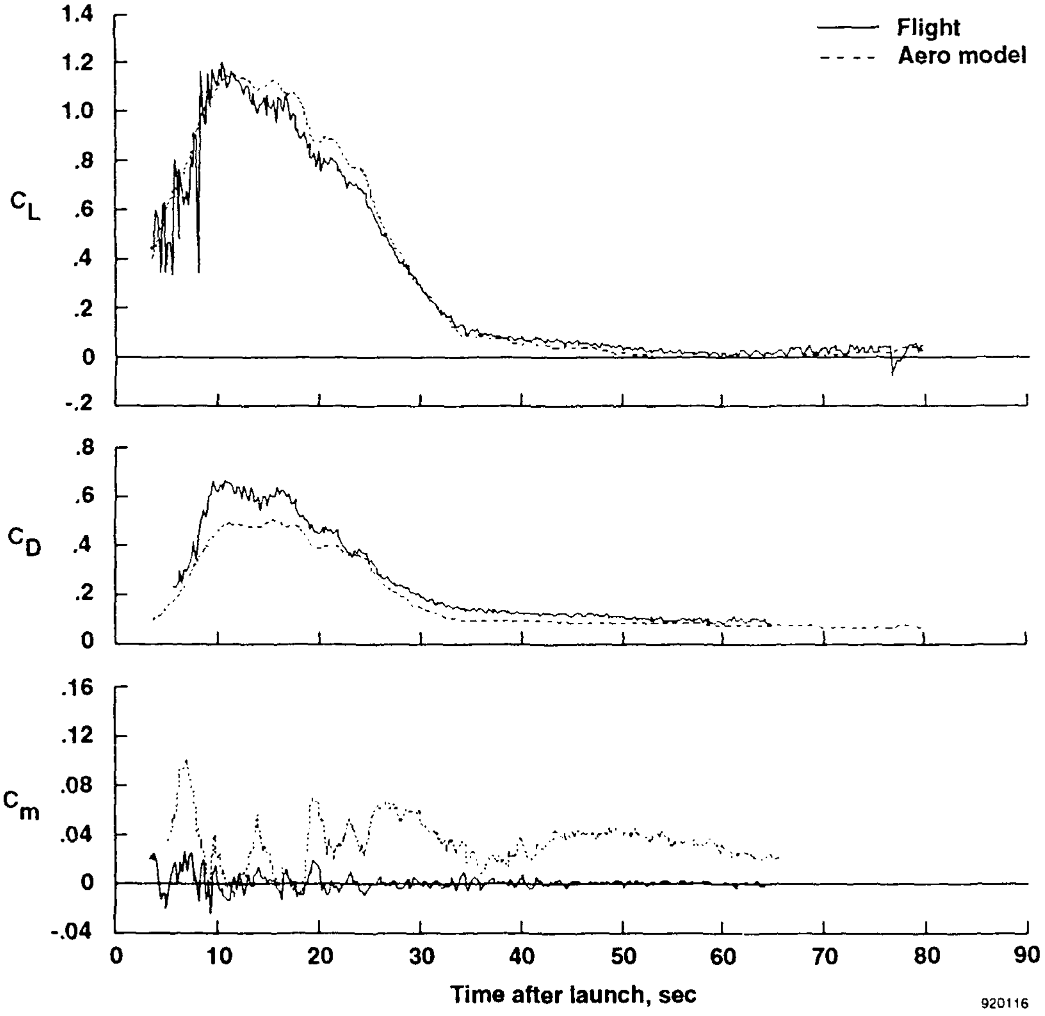

(b) Flight 2.

Fig. 6. Concluded.

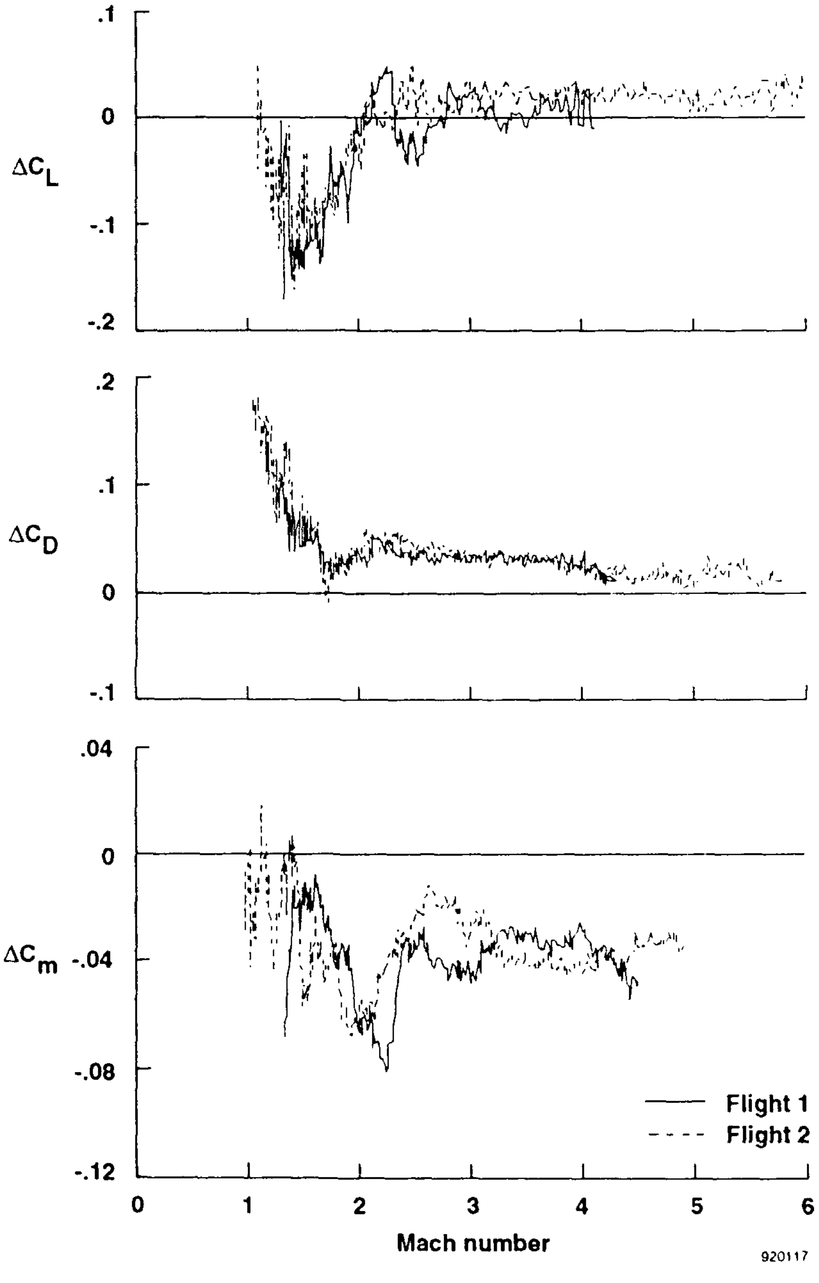

Fig. 7. Biases in vehicle aerodynamics (flight minus prediction).

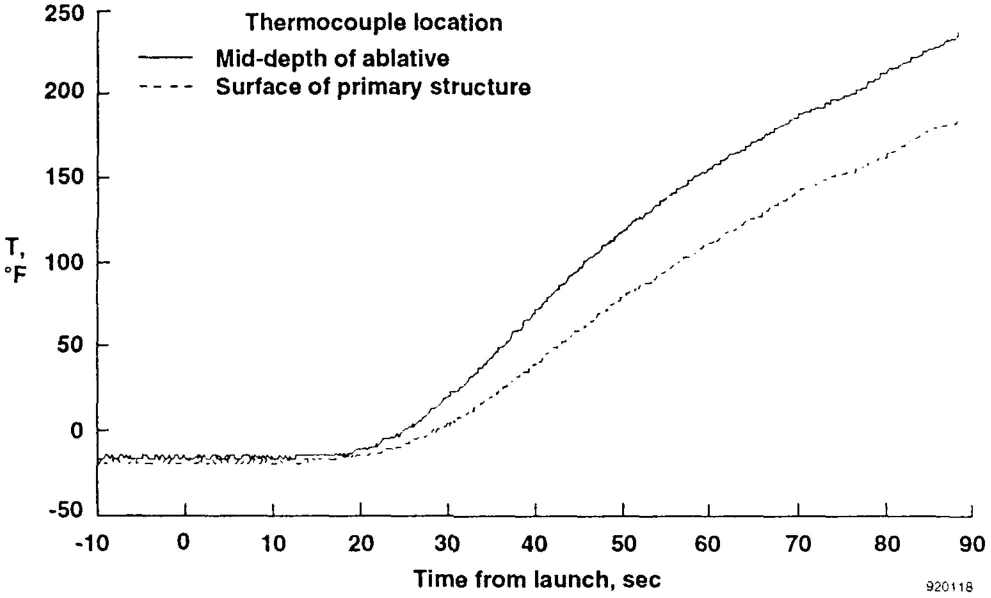

Fig. 8. Leading edge temperature time histories, $y = 65$ in.

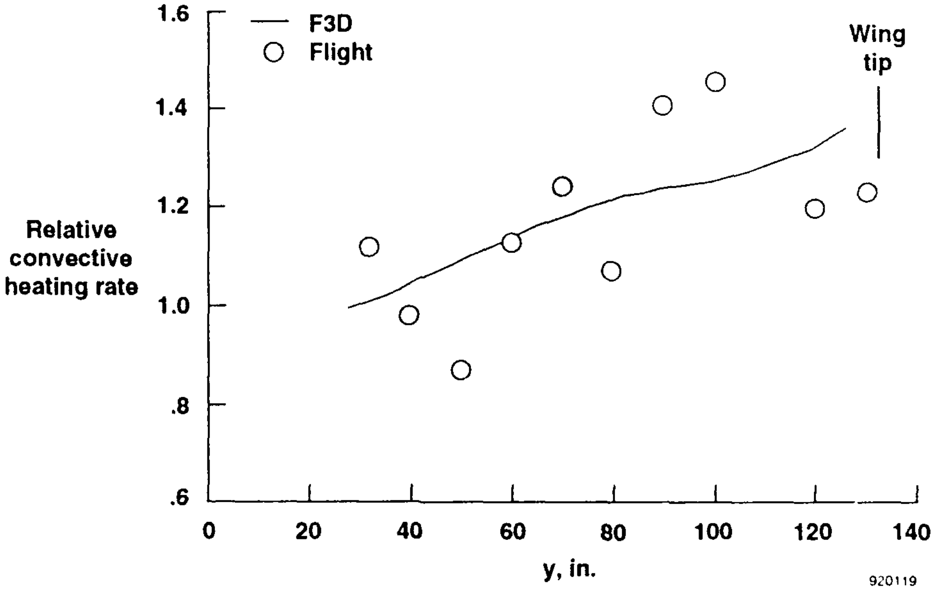

Fig. 9. Spanwise leading edge relative heating rates, Mach 4.

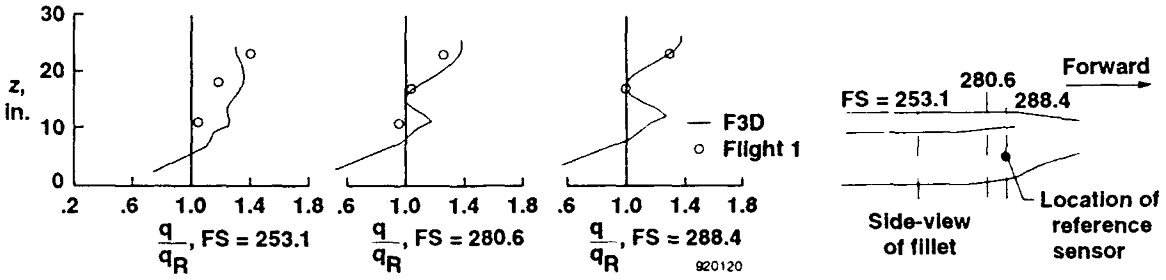

(a) $M = 3.1$, $\alpha = 7.65°$, and Re = 2.08 million/ft (6.82 million/m).

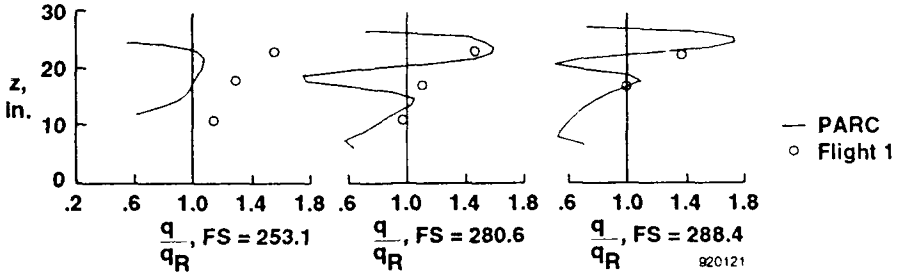

(b) $M = 3.52$, $\alpha = 7.35°$, and Re = 1.56 million/ft (5.12 million/m).

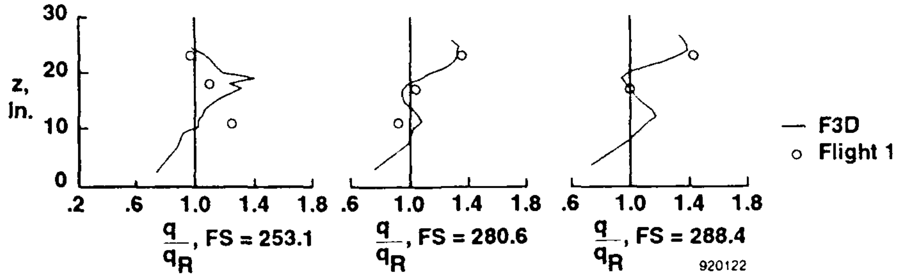

(c) $M = 5$, $\alpha = 0.5°$, and Re = 0.215 million/ft (0.705 million/m).

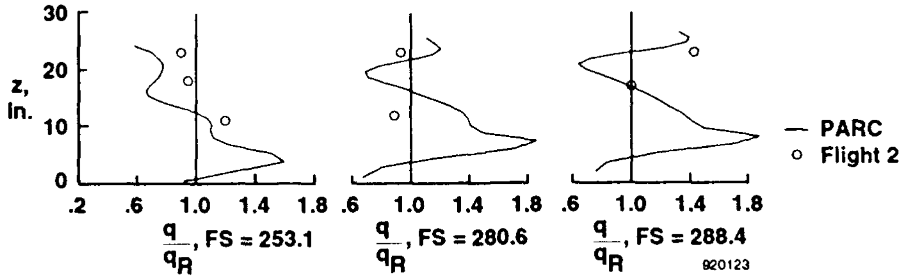

(d) $M = 5$, $\alpha = 0.5°$, and Re = 0.404 million/ft (1.32 million/m).

Fig. 10. Relative heating rates on the fillet sidewall.

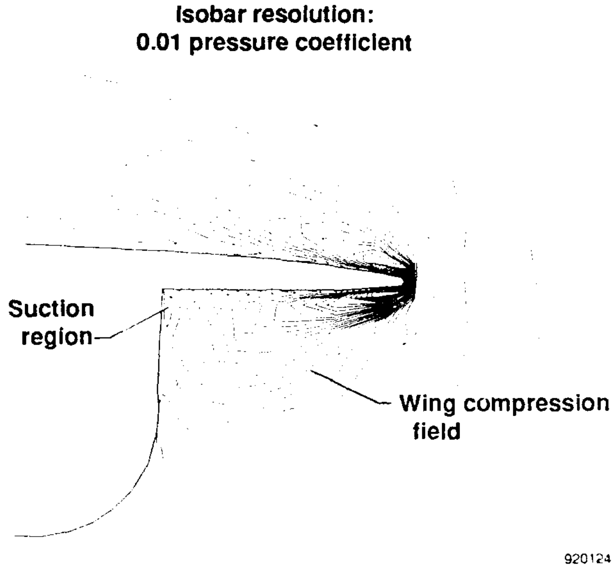
Isobar resolution:
0.01 pressure coefficient
Suction region
Wing compression field
920124

Fig. 11. Off-surface pressure field, $M = 4$, $\alpha = 4°$, and Re = 0.171 million/ft (0.561 million/m). F3D computations, FS = 253.1 in.

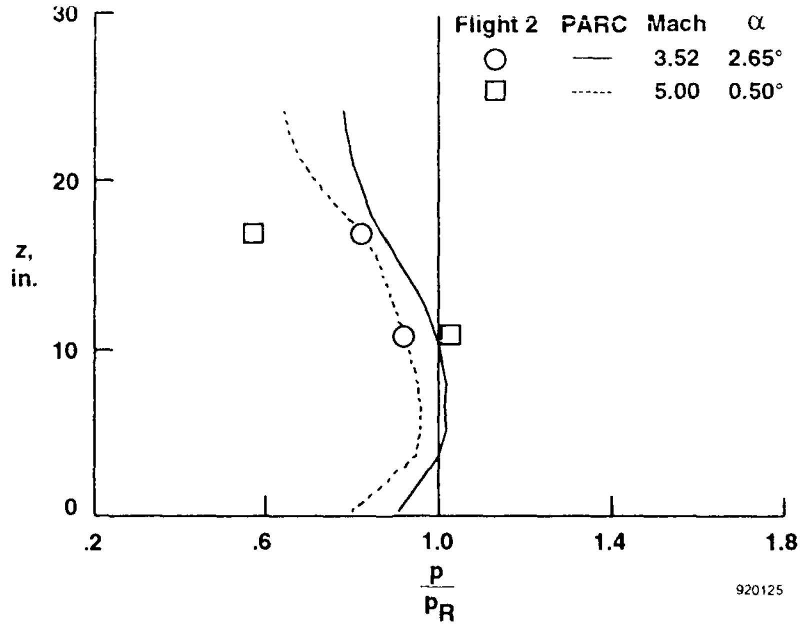

Fig. 12. Correlation of flight and computational pressure data, FS = 253.1 in.

PLANETARY ENTRY VEHICLE DESIGN FOR PLANNED AND POTENTIAL ESA MISSIONS TO TITAN, MARS AND EARTH RETURN (FGE TN 51/92)

by

Arthur Smith

Fluid Gravity Engineering Ltd
Miltons, Petworth Road
Witley, Godalming
Surrey, GU8 5LH, UK

SUMMARY

Design of ballistic planetary entry probes for planned ESA/NASA Titan, Mars and Earth-Return missions is discussed with emphasis on the common design constraints. The choice of aeroshell configuration and some of the simple design rules are outlined which are used initially at pre-feasibility stages. These include the influence of body dynamics, conventional aerodynamics and aerothermodynamics. Prediction of the aerothermodyanmic environment and influence of uncertainties in the basic physics and chemistry are seen to dominate. Analysis methodology and some of the ESA sponsored experimental programme which has been initiated to tackle the lack of basic chemistry data is discussed.

1 INTRODUCTION

The European Space Agency in partnership with NASA is engaged on an exciting and demanding exploration of the solar system, which includes missions to Saturn's moon Titan (Cassini-Huygens), Mars (Mars Network) and Comets (CNSR-Rosetta). These missions have as a common requirement to enter (or re-enter) a planetary atmosphere with scientific instruments or material and aerobrake to the surface.

FGE has been closely involved in the preliminary studies of these planetary entries and has produced initial entry vehicle configurations with the common themes of high reliability, low cost and well characterised aerodynamic performance to enable more detailed mission and system studies to begin.

This paper outlines the entry environments and vehicle design, together with the design methodology and draws common conclusions among the unresolved problems which mainly relate to non-equilibrium thermo chemistry effects for shock layer and thermal protection system (TPS) surface. The strategies for resolution of the problems involving combined computattional fluid dynamics (cfd) and testing are also outlined.

1.1 Mission Overviews

All three missions require a direct aerobraking entry into differing atmospheres, but the mission objectives and constraints lead to very similar entry vehicle concepts. These result in ballistic entries using low ballistic coefficient large angle sphere cones. (Figure 1 shows the three vehicle forward aeroshell configurations.)

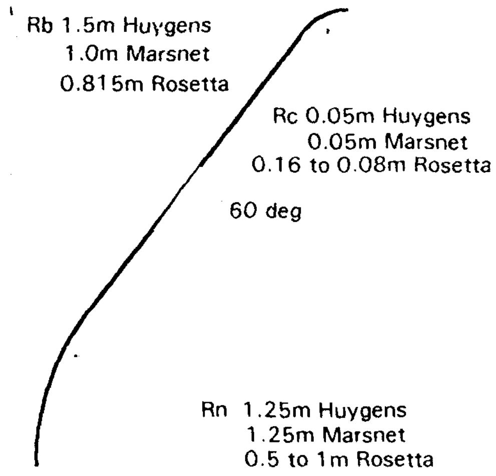

Figure 1 Forward Aeroshell Configuration

1.1.1 Cassini-Huygens

After approximately a 6 year interplanetary cruise the Huygens Titan probe will be separated from the Mariner Mk2 (MM2) several days prior to a direct entry into Titans atmosphere. The hypersonic entry at about 6 km/s and with a steep entry angle of between -60 and -90 degrees will be completed in about three minutes allowing a descent under parachute to the surface in a further three hours during which time the atmosphere experiments will be performed. Finally the module will touch-down or splash-down onto the Titan surface.

Titans atmosphere is composed mainly of N_2 with up to about 20% CH_4 and small quantities of other hydrocarbons, argon may also be present. The convective and radiative fluxes which peak at about $50W/cm^2$ lead to the adoption of a radiative or low density ablative heat-shield. The dissociation of CH_4 and formation of CN leads to potentially high radiative heat flux even at the low entry velocity planned.
The radiative flux is highly sensitive to the non-equilibrium chemistry and thermodynamics in the shock layer

Another potential problem is contamination of the probe surface by dissociation products which later during descent may contaminate instrumentation. Carbon has been shown to be deposited on the TPS during the hypersonic entry.

1.1.2 Mars Network

The Mars Network scenario involves several landers and penetrators, dispersed to provide a ground network for observation of the Martian surface, subsurface and atmosphere. A direct ballistic entry probably at less than 6 km/s for the landers/penetrators will prove more mass efficient than braking the whole spacecraft and its attendant landers/penetrators into orbit first. The thin Martian atmosphere requires shallow entry angles to achieve acceptable deceleration prior to final descent. Using an entry velocity of 5.8 km/s results in a shallow entry angle of about -15 degrees.

Convective fluxes are slightly lower but similar to the Titan entry, but the low N_2 content and large amount of CO_2 dissociation lowering the shock layer temperature leads to negligible thermal radiation. The magnitude of the fluxes again lead to the conclusion that a radiative/heatsink or low density ablative heatshield is appropriate. The thermochemical database dates largely from Viking with a few recent studies, and now requires extending, particularly as the entry is largely in thermo-chemical non equilibrium.

1.1.3 Rosetta

After sample acquisition from the surface of the selected comet the Spacecraft with attached entry capsule will return towards Earth. The entry capsule will be separated from the Spacecraft which may then flyby Earth while the capsule with samples on board performs the atmospheric entry, parachute descent, and splash-down. Return from the current range of possible comets results in an entry velocity of about 16 km/s and due to limiting entry deceleration of 100g for sample integrity and low dispersion requirement, leaves a narrow entry corridor for ballistic entry around -13 degrees.

This is the highest entry velocity for Earth and beyond the range of current thermo chemical databases. Significant thermal radiation has a large impact on the entry geometry optimisation. Non-equilibrium effects on the radiative flux are seen as critical at present.

The low entry angle results in a long heat pulse, and heat fluxes are also very high at several kW/cm^2 requiring a new heatshield concept to give acceptable mass. A hot substructure with outer high density charring ablator is foreseen.

1.2 Common Problems.

Some of the common problems in the design of optimum performance low cost ballistic entry vehicles include:

- Construction of thermochemical and radiation models for the shock layer and thermochemical models for surface activity.
- Availability of test facilities to validate or develop thermochemical models, radiation transport models, and to investigate TPS materials response and surface catalytic activity.
- Validation and application of cfd methods to support the aeroshell optimisation and TPS design.
- Development of supporting computational tools for parametric studies.
- Availability of test facilities for the construction of the aerodynamic database including dynamic terms and investigation of the dynamic behaviour.

2 VEHICLE DESIGN PHILOSOPHY

The design of the entry vehicle needs to fulfil the demanding requirements of the mission. The mission environment consists usually of the following phases.

- Assembly and Test
- Transport and Integration
- Launch
- Inter-planetary Cruise
- Hypersonic Entry
- Supersonic/Subsonic Descent
- Landing/Impact
- On-surface performance

The environment effectively imposes engineering constraints on the overall design, and possibly of greatest interest is the hypersonic entry which lasts only a few minutes but can dictate most of the aeroshell configuration and a large proportion of the mass budget.

As well as the environment the remaining engineering constraints are provided by timescales, both launch opportunity and mission lengths, and most importantly in these times, costs.

The cost driver has become predominant for these tightly budgeted missions and has had a great influence on the designs.

This influence has been subjective at early stages of the projects and has resulted in the adoption of the following philosophy which should allow the maximum confidence in performance at the earliest possible time. This is particularly important at pre-feasibility stage.

- Adoption of ballistic entry where possible (no guidance)
- Simple generic shape to take maximum advantage of existing aerodynamic data, and to simplify analysis.
- Interpolation within the existing data where possible rather than extrapolation. This may lead to sub-optimal design, but higher confidence
- Maximum commonalty in geometry between missions, such that the confidence in performance is

built up and common problems are more likely to be discovered.

3 ENTRY DYNAMICS

Before considering the aerothermodynamic problems, it is instructive to look at the simple rules which contribute to the commonalty in entry design.

Consider the ballistic entry vehicles so far defined for the three missions. All are separated on direct approach to the planet, and to preserve their attitude for entry are spun slowly at separation.

Since the separation can occur several days prior to entry, nutation of the motion is to be avoided, and as such the principal inertial axis should be arranged to be the spin axis.

The vehicle enters the atmosphere at an angle of attack which is a combination of exoatmospheric coning motion and the inclination of the coning axis to the trajectory velocity vector. The coning motion is caused by the separation tip-off errors from the spacecraft at spin eject time, combined with the mass characteristics of the body, principally the dynamic imbalance. During entry as the body experiences atmospheric forces, an aerodynamic moment is generated which acts to decrease the angle of attack. The motion becomes gradually more dominated by the aerodynamic forces and less by gyroscopic effects. The entry vehicle begins to respond in a pitching motion. As the aerodynamic stiffness increases, the angle of attack envelope is reduced. This motion is damped by the dynamically induced aerodynamic force generated called the pitch damping force. After peak dynamic pressure the angle of attack envelope would again increase, however due to the damping of the pitching motion, the angle of attack continues to reduce and becomes asymptotic to the static trim angle of attack.

Blunt cones exhibit a pitching reinforcing (positive) damping force in the transonic to low supersonic regime and while this does not effect the hypersonic entry phase, it is important to note that the destabilising coefficients are maximum for the blunter configurations, and the effect must be considered for the supersonic-transonic motion which may include parachute deployment or aeroshell/decelerator jettison sequences. Also of note is that the destabilising coefficients reduce with increasing angle of attack, such that by 20 degrees incidence the damping coefficients again act to reduce the pitching motion.

Structural modes should be well clear of the pitch or spin frequency to prevent any aeroelastic coupling. For the high atmosphere deceleration, low spin rate entries, the frequencies are of order a few Hz, and major structural modes are well above these, for the current designs.

On entering the atmosphere, it can be arranged that the spin axis is aligned with the velocity vector, however a small angle of attack is allowable, 15 degrees maximum has been used for all three missions. This is chosen for several reasons :

- The vehicle aerodynamics are not well characterised above 30 degrees incidence.
- Allowance has been included for exoatmospheric coning motion.
- Large lateral forces are not desirable.
- Cyclic heat flux variations are not desirable.
- Large pitch angles are not desirable for atmosphere analysis from trajectory data.

3.1 Effect Of Asymmetries On Vehicle Motion

3.1.1 Centre Of Gravity Lateral Offset

A centre of gravity (cg) lateral offset from the geometric central (spin) axis is normally due to the accuracy of the static balance and leads to both the offset of the principle rotation axis from the geometric centreline and to the generation of a trim angle of attack during atmospheric entry. With the very statically stable entry vehicles considered, (the static margin is about 50-60% of the base diameter) the consequences of cg offset on the trajectory are small and any initial angle of attack is quickly damped to the trim angle of attack. The main consequence of cg offset alone is lateral accelerations which have been shown to be very small, and as a small roll damping effect which always acts to reduce the spin rate. The resultant static trim angle of attack for the Huygens Probe for example is under four degrees for every centimetre lateral cg offset, such that a very small trim should be achievable with a balance within 5mm.

A much larger maximum cg offset was used in Monte-Carlo six degree-of-freedom trajectory stability studies of this vehicle, such that the probe is shown to be statically and dynamically stable during entry.

For Rosetta, sample density and load asymmetry where shown to have a small overall effect on trim.

3.1.2 Aeroshell Asymmetry

During manufacture, assembly and flight the aeroshell or decelerator will gain some degree of distortion.
The distortion may be in both hoop and axial modes.

Axial symmetric distortions and even harmonic hoop distortions of even large magnitude will have very little effect on the trajectory or entry vehicle (apart from roll moments) and will be well within the predicted accuracy of the ballistic coefficient. However odd harmonic hoop distortions and axial body bending modes could produce significant trim moments. These again in isolation produce a trim angle of attack which will act the same as a centre of gravity offset discussed above.

The first harmonic hoop mode on the aeroshell or decelerator (equivalent in effect to first body bending 'shuttlecock' mode) produces the largest trim moment for a given deviation from the nominal shape as may be expected since the higher harmonics are closer to the limiting symmetry. Figure 2 shows the static trim angle of attack resultant from first harmonic radial distortion of the decelerator on the Huygens Probe. The distortion is assumed to be zero at the decelerator/probe joint station and linearly increasing to the maximum at the decelerator rear. Also shown in Figure 2 are the cg offset eeffects on trim. The figures for Rosetta are shown for comparison.

Figure 2 Static Trim from Asymmetries

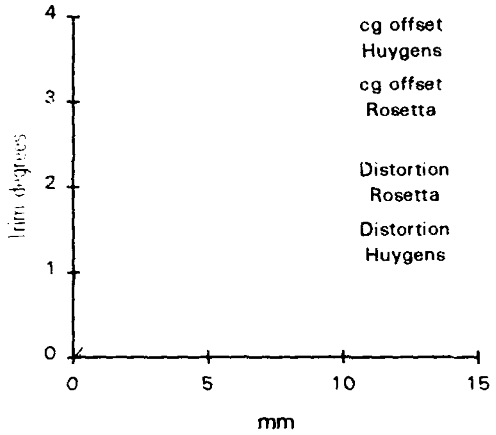

In addition where there is a large amount of surface recession due to ablation, similar asymmetries may occur. For the Rosetta entry vehicle the effect was estimated by allowing the carbon phenolic char layer to 'strip' from one side of the vehicle only, although in practice this is unlikely with the shear forces predicted. The resultant trim was very small (less than one degree).

3.1.3 Combined Asymmetries- Spin Rate Limitation.

Mass and geometric asymmetries in combination and depending on their angular relationship can produce significant roll torque's which may either spin the entry vehicle up or down (and through zero roll rate). The angular relationship is critical but for low spin rates an out of plane (90 degree) relationship is close to the worst case. Six degree-of-freedom entry simulations with varying asymmetries are used to produce spin rate histories. Figure 3 shows contours of spin rate excursions from the spin rate at the start of the entry phase to Mach 1 for a typical Huygens entry. While these will vary with trajectory, this type of figure serves as a design guide-line for geometric and mass tolerancing. The heatshield roll damping due to skin friction has not been included. The effect is likely to be small for these classes of entry but always acts to reduce the spin rate.

The choice of an adequately low initial spin rate (initially 60 deg/s) ensures that the spin rate at the start of the descent phase is in the desired range for Huygens (i.e. the limiting spin up case), and may be a consideration for Rosetta and Mars entry for parachute deployment.

Only sufficient spin to ensure low exoatmospheric 'wobble' is necessary. The entry vehicles do not require spin for entry stability, and even spin excursions through zero roll rate do not contribute significantly to 'ground' disperions when compared with initial trjectory alignment errors and atmopshere density variations.

Figure 3 Change in Huygens Probe Spin to Mach 1

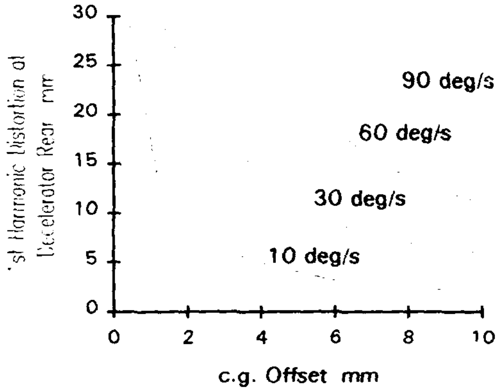

3.1.4 Moments Of Inertia

To avoid nutation and consequent tumble during coast, pitching/spin resonance problems during entry, and to relax the tip off error rotation rates budget, the spin or polar moment of inertia Ixx should be larger than the lateral moments of inertia Iyy and Izz. This should also be observed for the Huygens Probe without decelerator as the Probe pitching frequency is quite low after decelerator jettison and should the probe spin rate have increased during entry then a resonance could occur.

The possibility of a resonance is removed (and the need for analysis) if Ixx remains greater than Iyy & Izz. The Huygens Probe for example has accaepatble inertia ratios of about 1.4 : 1.

Asymmetry of Iyy and Izz is of little consequence during entry, resulting only in sine squared variation in the spin rate during 'coning' motion. For the missions considered it is desirable to measure roll acceleration to examine the aerodynamic performance and therefore Iyy and Izz should be close.

Non zero products of inertia Ixz and Ixy cause the principal polar axis to be at an inclination to the geometric axis. During exoatmospheric flight this leads to a coning motion even in the absence of pitch and yaw impulses during spin up and separation from the spacecraft. During the entry phase so long as the entry vehicle spins then an additional 'trim' angle of attack is induced which is dependent both on the spin rate and the aerodynamic pitching frequency. This effect together with c.g offset and trim asymmetries may increase or reduce the roll rate depending again on the phasing, however the effect is small as when the entry vehicle is close to peak dynamic pressure the aerodynamic pitching frequency is highest and the roll rate low even for large asymmetrics. Therefore products of inertia are only limited by the initial angle of attack generated by the exoatmospheric coning motion. The coning motion angle must be added to the inclination of the coning axis to the trajectory to form the total angle of attack. The practical limit of products of inertia are recommended to be less than 2% of the difference between the polar and lateral moments of inertia. This may be relaxed considerably once the mission trajectories become more firmly established in post feasibility stages of the project.

3.2 Dynamic Instability

There are several possible causes of dynamic instability:

- Roll Resonance's. If the spin frequency becomes equal to the aerodynamic pitch frequency then a resonant lock in can occur. This may case large pitch angle increases and large lateral loads and perhaps failure. Lock in can occur twice, initially as the pitching frequency increases prior to peak dynamic pressure, and then as the pitching frequency decreases after peak dynamic pressure. Usually first resonance occurs at high altitude where aerodynamic forces are low, and usually no problem occurs, however at low altitude especially if the vehicle has an increasing roll rate due to asymmetry, a problem can occur. The resonant phenomena is entirely avoided if the vehicle spin axis is the major inertial axis. This has been the design goal for all three vehicles.

- Pitch Damping. Instability can occur if there is positive pitch damping. This commonly occurs with bluff vehicles at low supersonic and transonic speeds. Axi-symmetric vehicles have this characteristic at zero or small angle of attack and the bluffer the vehicle the worse the problem. It is therefore avoided by one of 3 methods:

  1. Avoid flying through this flight domain. Supersonic parachute deployment is a possibility but can impose additional problems for the parachute design.

  2. Adapt the geometry to a less bluff shape. This is the common route and is a performance trade-off

  3. Fly at angle of attack where the effect is minimised. A lifting entry requires a guidance system and can increase complexity and costs significantly. This is therefore to be rejected if adequate performance in terms of deceleration/altitude can be achieved with an aerobraking ballistic entry.

- 'Unsteady' Aerodynamic Effects. For example unsteady flows in separated regions can lock in with the vehicle motion. Similarly re-attachment points can move with the vehicle motion, again resonance can occur. Base flows for the vehicles presented here are of concern, and re-attachment is avoided by ensuring that the base aeroshell is within the shear layer up to maximum expected angle of attack. Blowing from ablation is an example where forebody aerodynamics can be effected adversely. The lag in ablation product formation is caused by the heat soak time constant of the material to react and produce pyrolysis gases. This can occur if there is a significant coning motion where the windward meridian is rotating in body co-ordinates. This is avoided by ensuring a low initial angle of attack and low coning motion for Rosetta.

- Aeroelastic effects. Although not strictly dynamic instabilities, a structure - flowfield coupling can occur, for example panel flutter. No aeroelastic analysis has been carried out in the early stages, but natural structural modes have been checked against aerodynamic frequencies.

  For example the decelerator natural frequencies are well above the Probe pitch and spin frequencies, base flow pressure oscillations have been assessed as very low, and forebody acoustic excitation is avoided with a laminar boundary layer, step size minima and roughness criteria being set.

3.3 Conclusions From Entry Dynamics Discussion.

The entry vehicle should ideally have the following features :

- Geometric axi-symmetry.

- Inertial axi-symmetry about the geometric symmetry axis (statically and dynamically balanced).

- Spin axis as the major inertial axis.

- Arrange major structural modes away from Aerodynamic modes.

- Small initial angle of attack.

4 ENTRY AERODYNAMICS

4.1 Aerodynamic Configuration

The primary mission requirement which drives the aeroshell geometry is for deceleration at the highest altitude. For Huygens this is so that atmosphere experiments can begin at the highest possible altitude, 170 km is the target, whilst for Mars the atmosphere density is so low that maximum deceleration is required to provide sufficient altitude for parachute deployment at some of the chosen higher altitude sites. For Rosetta the requirement is to provide minimum mass, at a sufficiently steep entry angle to provide acceptable downrange dispersion for recovery, thus the trade-off is between heat flux and TPS thickness and area.

The aerobraking scenario uses a low ballistic coefficient vehicle for a 'direct' entry and aims to lose sufficient energy in the upper atmosphere to achieve the desired velocity and altitude conditions for the later mission phases. For a non lifting ballistic entry no guidance or control is necessary provided that dispersions are acceptable. The aerobraking concept is therefore less costly than its aerocapture equivalent but places emphasis on the design of an acceptably low ballistic coefficient stable aeroshell.

To achieve a low ballistic coefficient, a large area, high drag coefficient, low mass vehicle is required. For all of the missions considered, the mass is critical and the scope for mass reductions below the provisional budget allowable was small. Therefore the design drivers are for a large area and high drag coefficient entry vehicles.

Large drag coefficients are achieved usually at the expense of stability, and since the mass and cost budgets can not provide an onboard stability and control system, the geometric configuration must be sufficiently stable in free flight.

The philosophy of the studies undertaken was to provide a minimum cost solution and the adoption of a simple sphere cone with large half cone angle and sufficient stability can make use of a large amount of existing aerodynamic data and is therefore the natural choice.

4.1.1 Cone Angle

Previous studies have covered the range of half cone angles, 30 degrees 45 degrees and between 56 and 75 degrees. A cone angle of 70 degrees as used on Viking produced a near maximum drag coefficient, further increasing the cone angle has little effect on drag coefficient. Stability of the large angle cones however is lower and therefore to achieve a nominal zero angle of attack through peak heat flux and peak dynamic pressure during entry, 60 degrees was chosen for Huygens.

This configuration has an acceptably large drag coefficient (only 4% less than the 70 degree cone) but a higher static stability. Low supersonic/transonic dynamic stability is also greatly improved.

Figure 4 Typical Drag and Moment Coefficients Varying Cone Angle (Experimental Results at Mach 9.5

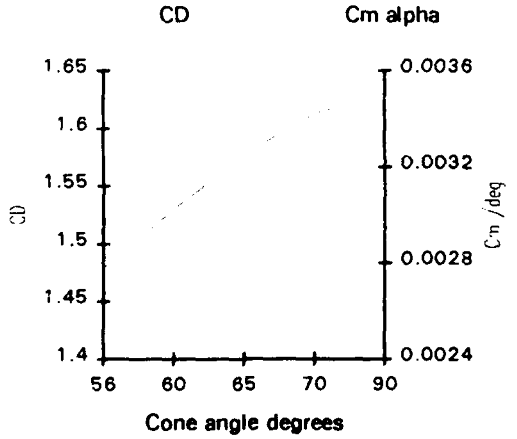

Figure 4 shows pitching moment coefficient about the stagnation point and the drag coefficient for a range of cone angles taken from Walker and Weaver (1) together with the flat disk limit.

4.1.2 Base Diameter

The maximum base diameter vehicle is utilised with Mars entry for three landers and the single Huygens probe, consistent with the space envelope available on the Spacecraft. Deployable decelerators were rejected in initial studies on grounds of complexity. The base diameter is the single largest contributor to a low ballistic coefficient for these missions. The lowest ballistic coefficient also provides the lowest heat flux.

For Rosetta the choice was complicated by the high heat fluxes which required a dense charring ablator. With a heavy heatshield which is the most massive part of the vehicle, increasing the area increases the mass proportionally since the ablator thickness is only marginally reduced, and thus the performance driver is minimising the mass. A changeover point in TPS material to a lower density may alleviate the situation as the fluxes reduce with decreasing ballistic coefficient. However even increasing the base diameter to the maximum allowable (3m) in the space envelope did not produce a lower mass even with a TPS material change. Therefore given the high drag shape to give lowest fluxes, the total mass may be minimised by reducing the volume to the minimum required for the payload by reducing the diameter, this of course increases the ballistic coefficient. Further optimisation involving the rear TPS is yet to be carried out.

4.1.3 Nose Radius

The nose radius has been chosen as a near optimum for minimum heatshield mass, ease of fitment in the spacecraft and launch envelope, and for maximum drag coefficient.

Although the effect of nose radius on drag coefficient is small a large radius gives a slightly larger drag coefficient and less mass per unit base area.

Huygens. For Huygens phase A with a Carbon TPS, the decelerator and forward heatshield have adequate thermal margins, and thus the mass is governed by the structural loading and by the thermal insulation requirement, therefore the smallest area will give the lowest mass, as the insulation mass is secondary. An instrument cover nose cap had a mass fixed by the ballistic separation requirement, and was independent of the nose radius to a first order.

Therefore the largest nose radius consistent with aerodynamic stability and existing data availability (i.e. certainty in aerodynamic coefficients) should provide minimum insulation thickness for a radiative heatshield concept (given the low radiative heating content). The maximum geometric value was 1.5m allowing the decelerator to be conical.

A Beryllium forward TPS was rejected for lack of thermal margin, while a low density ablative design was also rejected due to excess mass.

Boundary layer heat transfer analysis shows that the total convective heat load to the Probe forebody (i.e. less decelerator) reduces with increasing nose radius, this is a combination of reducing stagnation heat transfer and reducing total area. This is achieved despite the fact that the conical section has lower heat transfer rates than the spherical section.

The 1.25m radius chosen consistent with the limit of bluntness ratio where transonic aerodynamic data is readily available for the Probe less decelerator.
This ensures maximum confidence in the design by using computational methods to interpolate between experimental data rather than relying on extrapolation beyond the available range of data.

Marsnet. No optimisation was carried out in the early studies, the initial geometry was chosen as identical to Huygens in order to utilise the same aerodynamics (factored as necessary for atmosphere differences). Reductions in base diameter have been made for Spacecraft envelope fitment purposes with three landers each with reduced mass. However the maximum nose radius produces the lowest convective coefficient and highest drag and the nose radius remains large at 1.25m. Radiative fluxes were found to be negligible with the low entry velocity and relatively low shock layer temperatures. The current ratio of nose radius to base radius is still within the existing aerodynamic databases for bluntness ratio, and therefore there is room for optimisation in later studies.

Rosetta. For Rosetta since the radiative fluxes are significant, the nose radius was optimised for minimum total radiative plus convective heat load. Two distinct designs evolved, 'Iteration 1' is a steep entry providing close to the maximum deceleration load allowable for the payload of 100g. 'Iteration 2' is a shallower entry designed to give the payload an easier ride at 45-55g and is the shallowest entry with acceptable downrange dispersion. The steep entry has a shorter duration heat pulse and even though the heat fluxes are higher this leads to a thinner heatshield and is the FGE preferred solution. The nose radius is 0.5m for this case, although the uncertainty about the magnitude of the radiative fluxes may lead to a reduction. The shallower entry is preferred by the project team since all structural and payload loadings are the smallest practicable. The nose radius for this case is increased to 1.0m but again there is uncertainty over the radiative fluxes and a reduction may be made.

4.1.4 Aeroshell or Decelerator Corner Radius

The final geometric feature is a radius to limit heating in the expansion corner region of the decelerator due to flow acceleration. For Huygens, and Marsnet, the provisional Carbon-Carbon (C-C) and Ceramic (C-SiC) decelerators of the entry vehicles had a large thermal margin, however the corner heating, similar to the nose convective heating, increases as the corner radius decreases.

For a sharp corner the calculated heat transfer at the corner is very large value. At angle of attack, test data show that the corner heating is further increased, and even the high temperature ability of the Carbon and SiC may be exceeded locally.

Introducing a progressively larger corner radius to the rear of the decelerator produces a lowering heat flux at the corner which at zero angle of attack becomes less than the stagnation heating. This is the criteria used and a 5 cm corner radius has been selected representing a corner to base radius ratio of 0.03 for Huygens.
Analysis shows that even at large angle of attack (20^0) the heat flux should be limited to less than twice the zero angle of attack stagnation value. This increase in heat flux only increases the surface equilibrium temperature by about 20% and therefore is easily within the TPS capability.

6dof trajectory studies show that angle of attack excursions near peak heating are small, consequently the design assumptions are adequate. A secondary effect of a corner radius is a contribution to hoop stiffness where it is most required, and therefore mass penalties should not accrue from this feature.

Introducing a corner radius reduces the drag coefficient while the centre of pressure is moved forward, static stability is increased by the compensating increase in normal force producing an increase in the moment coefficient. The 5 cm corner radius selection reduces the drag coefficient by about 2.5% over a sharp corner, again the wind tunnel data is scaled by Newtonian aerodynamics. The corner radius should be reduced to the minimum in later project phases to allow the maximum drag coefficient. The adoption of an elliptic corner profile is expected to prove more efficient but is outside existing databases. The same corner radius is provisionally selected for Marsnet.

For Rosetta the situation is similar even with a different TPS, here the TPS is ablating and whilst the reduction in drag coefficient is important with increasing corner radius, it was judged more important to preserve a nearly constant thickness of forward TPS in order to lessen manufacturing complexity. A smaller radius thicker TPS may be lower in mass however, but shape change and consequent aerodynamic effects would be larger.
The corner radius is thus sized to give a total heat flux equal to the stagnation value at zero angle of attack. Radiative flux uncertainties are also taken into account for this computation. The resulting corner radii are much larger than for the radiative TPS of Huygens and Marsnet at 8 cm for the Iteration 2 geometry and 16 cm for the Iteration 1 geometry.

4.2 Conclusions from the Aeroshell Geometry Discussion

The entry vehicle geometric features are determined by:

- Minimum ballistic coefficient
- Availability of existing aerodynamic databases
- High drag shapes consistent with stability constraints and existing databases. This leads to the choice of large angle sphere cones.
- Nose radii based on minimum mass, maximum drag. This leads to maximum radius for large margin C-C and C-SiC TPS limited only by Bluntness ratios in Aerodynamic databases. The minimum heat load is the criteria for ablators, with equal radiative and convective components.

- Corner radii minimum for maximum drag based on thermo-structural limit for C-C and C-SiC radiator and constant thickness for an ablator.
- Base diameter maximum for minimum ballistic coefficient for maximum altitude missions, limited by minimum mass constraints for Rosetta.
  Non-deployable decelerators chosen for low cost and complexity.

5 ENTRY AEROTHERMODYNAMICS

5.1 'Computational Tool Set' Requirements

So far the shape of the entry vehicles has generally been defined by simple laws and can be accomplished with relatively simple tool set which is adequate in the very early project stages. This may be designated the 'level one' analysis, using :

- 3dof and 6dof trajectory codes with planetary atmosphere models
- Newtonian aerodynamic code to interpolate existing aerodynamic databases
- Free-molecule aerodynamic code and suitable empirical drag and flux bridging functions
- Heat flux correlation's for convective and radiative fluxes.
- Heatshield sizing algorithms.

However in all but the trajectory codes, detailed knowledge is required to develop or confirm the basis of the engineering solutions.

The determination of accurate aerodynamic coefficients is very important since the atmosphere composition can be determined from the vehicle performance for Mars and Titan, while stability is always a consideration whatever the mission.

The heat flux distribution and history determine the choice of TPS and geometric ratios.

The first essential analysis is to determine the aerodynamic and aerothermal flight regimes through which the vehicle will pass. This will give the engineer a clear perception of where in the entry particular analysis methods should be used. In the preliminary stages the classical regimes will have become evident from the trajectory analysis which should use both free molecule and continuum drag coefficients with a suitable bridging function. A simple Knudsen based bridge is most common for drag coefficient.

The formal analysis should consolidate the classical regimes and should investigate the thermal and chemical regimes. Most commonly the latter are expressed in terms of the Dahmkohler number.

To carry out this investigation a chemically reacting shock layer simulation is most useful, and since the whole entry parameter space needs to be investigated the method should be fast.

In this respect FGE use a loosely coupled suite consisting of an inverse Euler code for the shock layer, followed by streamtube tracing and chemistry computation along the streamtube. Chemical source terms are then fed back to the Euler energy equation. The Euler iterations take a few seconds and the chemistry a few minutes for each trajectory point. Shock stand-off is used as the convergence criteria. This code is designated PMSSR.

Boundary layer edge conditions are taken as a post process of the PMSSR solutions for convective heat flux analysis using usually an integral code with frozen or equilibrium chemistry assumptions. Radiation calculations are also performed from the shock layer results as a post process. Both the boundary layer and radiation codes takes a few minutes to compute the solutions for the whole trajectory.

The radiation source terms can also be fed back to the Euler solution, as can boundary layer thickness. However for regime scoping studies an uncoupled procedure is usually used.

Wall conditions can be accommodated in the boundary layer solution in a simple manner blowing is accommodated with a correlation within the integral boundary layer code, whilst for the frozen boundary layer solution, a 'catalytic' wall can be introduced by substituting the wall enthalpy for equilibrium wall enthalpy at the same temperature.

Parametric investigations using these methods have been carried out to varying degrees in the early stages of all three missions discussed. In general the results are acceptably accurate excepting radiation in highly non-equilibrium flow at present.

Such a suite also allows rapid comparison of the sensitivity of differing thermochemical mechanisms, and allows rapid construction of a viable set prior to more complex computations. These 'level two' results can be used to calibrate the engineering correlations in the level one analysis. The level two codes are therefore :

- Fast inviscid shock layer solution.
- Loosely coupled chemistry solution
- Boundary layer codes.
- Uncoupled or loosely coupled slab radiative solution.
- Charring material ablation code

Once the thermochemical data has been assembled and tested with the level two codes, and the results validated as far as practicable a more sophisticated analysis again must be carried out to verify the simpler results in areas beyond the validation. (here verification is defined as being correct numerical implementation of the physics and chemistry, while validation is the comparison of the models with the real world). For continuum regimes this verification is by a full or thin layer thermo-chemical nonequilibrium Navier Stokes solution. Due to the lack of other suitable methodologies the Navier Stokes codes are used well into the transitional regime, and account can be taken of slip effects. Direct Simulation Monte-Carlo should be used to confirm bridging functions between continuum and free-molecular but this has not yet been carried out for this class of vehicle.

Figure 5 shows the comparison between the fast solution from PMSSR and the full Navier Stokes solution using FGE's TINA code for a Marsnet vehicle at peak heat flux. PMSSR uses a 6 by 5 Euler grid with 50 points on each streamline for the thermo-chemical solution, while TINA uses a 60 by 50 grid for the whole forebody. Reducing the chemistry to the stagnation streamline only, the PMSSR solution is produced in 3 minutes on a 386 PC, whereas the point-implicit TINA requires an overnight run on an IBM RS/6000.

Figure 5 Navier Sokes code TINA Comparison with Inverse Euler code PMSSR

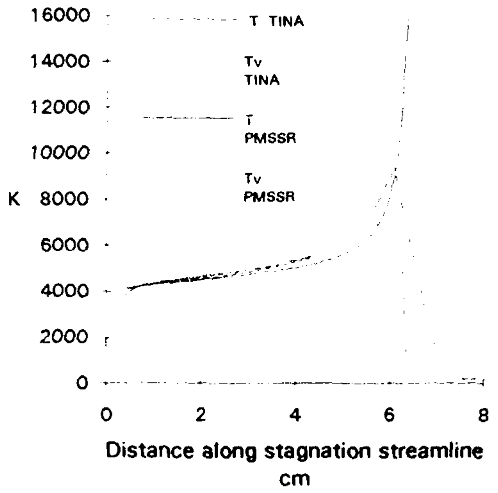

The agreement is very good considering the simplicity of the PMSSR scheme, and shows that regime determination and initial sensitivity studies can be quite accurate with the level two codes. The Navier Stokes solutions also require more operator expertise in obtaining a reliable solution. (Note the high initial Translational temperature from the shock fitting PMSSR).

The level three codes are :

- Thermo-chemical non-equilibrium Navier Stokes.
- Direct Simulation Monte Carlo with suitable chemistry and radiation models.
- Full 2D radiation code.

Full thermo-chemical non-equilibrium Navier Stokes code solutions for Rosetta and Marsnet have been computed by FGE, and other workers have produced solutions for Huygens. The level three codes are used sparingly in the early stages due to the costs involved, but must be used in development phases to confirm design viability, whilst experiments provide validation data for these codes. These codes are often the only way to investigate the entry phenomena where no flight data is available, and ground tests are impractical.

5.1.1 Conclusions From The Methods Discussion.

- A three level set of codes is time and cost efficient for vehicle design studies.
- Level one codes are readily available but require careful calibration.
- Level two codes have been widely developed in the past, and are shown still to be very useful.
- Level three codes can simulate many situations, but the required level of expertise and time required for use can be underestimated by customers.

5.2 Boundary Layer Transition.

Boundary layer transition for all the bluff vehicles is based on the Viking assessments of a boundary layer momentum thickness Reynolds number of 140 as being pessimistic. Using this value, Huygens and Marsnet maintain a laminar boundary layer throughout the entry, whilst on Rosetta the boundary layer becomes turbulent after peak convective flux, such that the total heat load is not greatly affected. This is fortunate for all vehicles since transition uncertainty prior or close to peak heat flux significantly effects the TPS sizing.

No attempt was made to utilise a more sophisticated transition 'law' developed for other vehicles or flow types since extrapolation to this type of vehicle would be dubious considering the small database available.

Conclusions from the Transition discussion

- Lack of suitable transition data specific to this class of vehicle leads to pessimistic assumptions.

5.2 Base Flow

Base flow effects on these class of vehicle need analysis for two main areas :

- Shear layer impingement on the rear cover can cause local heat flux increases, plus re-attached flow can cause stability problems if the attachment point 'locks in' with the dynamic motion.
- The base convective heat fluxes determine the rear TPS design and mass.

For Huygens the rear cover is well clear of any impingement and therefore only recirculation region heating is of interest. Using a thin C-C decelerator TPS also produces a radiant heat flux to the rear.

For Rosetta the rear conical heatshield was designed to be inside the shear layer based on flat base computations and a k-ε turbulent model with perfect gas (frozen) flow. The forebody boundary layer input to the shear layer was included, but the large base radius to boundary layer thickness means that the boundary layer state has little effect on the base flow.

For Marsnet the rear cover is also expected to be within the shear layer, and Navier Stokes computations are underway at present to confirm this and while the base heating is particularly difficult to accurately predict, an estimate will also be made.

The base convective fluxes are generally estimated from flight correlations. Those from Viking being used for Marsnet giving about 4% of stagnation. For Rosetta with its conical rear TPS, Apollo correlations for the separated regions were used at about 1% of stagnation, and for Huygens 2% of stagnation was used as an estimate from other bluff body correlations.

Conclusions from the discussion of base flow :

- Differing base flow heat flux correlations seem appropriate in differing regions and atmospheres for very bluff vehicles. Further analysis is still required.
- Base impingement and reattachment needs to be assessed with Navier Stokes codes.
- Accurate predictions of the base convective fluxes are elusive.

5.3 Catalytic Wall Effects

Catalytic wall effects are expected for both Huygens and Marsnet where non-equilibrium flows are encountered. Fully catalytic walls were assumed in the early analysis, but boundary layer solutions for Huygens and Navier Stokes Solutions for Marsnet show that significant reductions in convective fluxes can occur for non-catalytic TPS surfaces. However before advantage can be taken of this, the catalytic behaviour of the atmosphere gases on the TPS wall must be known with some certainty, especially if the TPS has been exposed to space environments for example radiation, debris impact, thruster plume impingement and thermal cycling. The reactions for O_2 and N_2 recombination have been studied for some Earth entry TPS, but the data still exhibit large scatter. For Mars the CO_2 recombination is very important to assess. Similarly for Huygens N_2 and CH_X recombination appear very important.

Conclusions from the discussion of catalytic effects :

- Catalytic wall reactions are important for Marsnet and Huygens
- TPS lifetime needs certain assessment before advantage can be taken.
- Catalytic reaction experiments for the Mars entry are planned in current ESA sponsored research, as part of the 'Aerochemistry in Hypersonic Flows' contract.
- Catalytic wall boundary condition has been incorporated into the Navier Stokes code TINA.

5.4 Ablation Effects

Ablation is significant for the Rosetta entry where heat fluxes are high and dictate the use of a high density charring ablator such as carbon phenolic. The relatively shallow entry to protect the sample payload leads to a long heat pulse and therefore a thick single layer heatshield to keep the sub-structure cool. A new technology hot structure / hot bond concept is being developed by SEP (2) for this TPS to reduce the heatshield mass.

Since the shock layer is close to thermochemical equilibrium during the heat pulse, existing chemical equilibrium ablation codes such as CMA are used to predict the in-depth response. The ablation code also provides the blowing boundary condition for the Navier Stokes and boundary layer codes. This is important since the blowing reduces the wall gradients and therefore reduces the convective flux. The cool carbon laden blowing gases can also absorb some of the radiative flux to the wall, the resulting heated boundary layer gases increasing the convective flux again. Convective blockage of about 20% for Rosetta is estimated from the boundary layer and ablation codes, and this is currently being assessed using a full Navier Stokes code. Radiative blockage has not yet been assessed, but is part of current studies.

- Ablator response is fully coupled to the flowfield and thus TPS sizing.
- Ablation and thermal characteristics of candidate carbon phenolic is to be investigated in the current phase of the ESA sponsored 'Aerochemistry effects Hypersonic Flows' contract. This will provide validation data for prediction codes to be used for Rosetta.
- Ablative boundary conditions have been incorporated into the Navier Stokes code TINA.

5.5 Contamination

TPS contamination can occur when atmospheric gases dissociate to form potential condensates or absorbants. Such is the case for Huygens where carbon is formed from the cracking of CH_4. Analysis and experiment have shown that the carbon is driven towards the cool wall by diffusion, and condenses on the wall. Since the wall temperature is low compared to the carbon sublimation temperature, it is supposed that the carbon is supercooled and gives up its latent heat on touching the surface. A significant build up of carbon deposits is expected from analysis and experiment for Huygens amounting to 0.3 mg/cm^2. Other hydrocarbons may be absorbed or formed in the deposit or TPS surface.

Absorbents may outgas during descent, and particulates may shear off if the TPS is present. To date it has not been possible to distinguish between particulate and gaseous material removed, but it has been shown that circumstances could exist where the contaminant removed from the heatshield could enter the instruments if the TPS is present. While this is a worst-on-worst analysis, total TPS removal was selected for the Phase B baseline.

- Contamination remains an open issue for Huygens
- TPS contaminant absorption models no not exist.
- Outgassing models need specific experimental investigation.

6 AEROTHERMAL DATABASE

From the level 2 parametric studies, the extent of the required aerothermal database is determined. All three entries require some extension of existing data to higher temperatures, and in some cases the data are sparse or non-existent.

Sensitivity studies of the Titan atmosphere chemical mechanism indicated that a reduction in the set could be made but that this differed throughout the entry regime, thus while a reduction for the time consuming Navier Stokes computations could be made, the full set is retained for parametric studies. Generally extension and validation of the thermodynamic properties to 15000K is necessary for the Huygens entry. Although the dissociation of CH_4 occurs very rapidly, initial studies at FGE have only used diatomic vibrational relaxation equations, and there is a lack of high temperature polyatomic relaxation data.

For Mars, initial studies show very low ionisation levels. However there is a variation in the chemical kinetics data and high temperature data for CO_2 is lacking. The low level of N_2 in the atmosphere can lead to a small proportion of CN and this may make the radiative heating significant should entry velocities increase. At present the radiative fluxes are negligibly small.

The Rosetta entry gives equilibrium shock layer temperatures of about 14000K, with substantially higher temperatures just inside the shock. A large amount of ionisation is also predicted at these temperatures. At present the database takes advantage of the large amount of recent activity in Earth entry for AFE and Mars return up to about 12 km/s. The Rosetta entry at 16 km/s presents a significant increase over current Earth entry knowledge.

Radiative fluxes for the Rosetta entry are large and have influenced the geometry of the entry capsule significantly. Prior to these missions radiative flux predictions in Europe were not required, and now development of these techniques is necessary.

- The Huygens thermochemical database responsibility has passed to the project prime contractor, but it seems likely that the chemical mechanism and radiation databases will need validation.
- The establishment of a high temperature thermochemical database for Mars entry is planned at Universite de Provence (SETT) free piston tunnel with Professor Brun under the present 'Aerochemistry Effects in Hypersonic Flows' contract.
- An initial validation of the air thermochemical model for Rosetta is also planned at the same facility under the same contract..
- Development of a non-equilibrium radiation code is underway at University of Stuttgart (IRS) with Professor Messerschmid under the same contract activity.

7 FACILITY REQUIREMENTS

The development of high enthalpy facilities is essential for the understanding of, and database generation for aerothermodynamic problems for planetary entry.
The trend towards increasing cfd analysis to support design is only sustainable if the databases are made available, which means development of the necessary facilities. It appears that project funding is too late for this effort since both facility development and experimental programmes are time consuming.

Facilities need to be upgraded to enable investigation of the highly ionised flows applicable to Rosetta. Marsnet and Huygens are not so much of a problem with the modern free piston facilities being developed, but the higher temperature ranges may not be reached even for these class of entries in an undisturbed flow.

Catalytic wall studies are most important, but clean experiments to produce consistent results seem elusive. Further effort is needed here.

Ablation studies are being carried out for Rosetta, but the pressure and heat flux conditions are difficult to match with existing European plasma arc or solar furnace facilities. A significant upgrade in arc jet facilities and further effort on plasma characterisation is required.

8 CONCLUSIONS

An overview of some aspects of the preliminary design of ballistic entry vehicles for planned and potential ESA/NASA missions to Titan, Mars and Earth return has been presented. The historical development of the designs from the early studies has been shown, where mostly low level design tools were used.
The designs tend to change little in later phases where the most sophisticated methods are brought to bear for fine tuning and confirmation.

Apart from the need for continued development of computational tools at all levels, the greatest need is seen to be for thermochemical and radiation data without which the tools are useless, and therefore the facilities to gather such data are equally important to support the long term design requirements. The timescales for code development, fundamental experimental programmes and facilities development are comparable to project development times. The tools and data need to be available very early in the project, and early planning is essential.

REFERENCES

1. Walker B, Weaver R W. Static Aerodynamic Characteristics of Blunted Cones in the Mach Number range from 2.2 to 9.5. NASA TR 32-1213, December 1967.

2. Eiden M, Desnoyer D, Chiarelli C, Smith A, Heatshield Concepts for the Rosetta Aerocasule. 4th European Symposium on Space Environmental Control Systems. Florence Italy, 21-25 October 1991.

NOUVEAUX MOYENS D'ESSAIS HYPERSONIQUES DEVELOPPES A L'O.N.E.R.A. : LES SOUFFLERIES R5 ET F4

par

B. Chanetz, M.-C. Coët, D. Nicout, T. Pot, P. Broussaud, G. François, A. Masson
Office National d'Etudes et de Recherches Aérospatiales

et

D. Vennemann
ESA/CNES Joint Team

18 Avenue Edouard Belin
31055 Toulouse
France

RESUME

Les souffleries R5 et F4 constituent deux moyens complémentaires pour l'étude des phénomènes de rentrée atmosphérique de véhicules spatiaux.
La soufflerie R5 a été conçue pour simuler des écoulements hypersoniques à faible nombre de Reynolds en régime continu. Depuis sa mise en service en 1989, sa mission a d'abord consisté en la qualification de méthodes de mesures en basse densité destinées à la soufflerie à haute enthalpie F4. Son activité s'est orientée ensuite vers l'étude des phénomènes d'interaction visqueuse dans une optique de validation de codes de calcul résolvant les équations de Navier-Stokes.
La soufflerie à arc bref F4 est en cours de mise en service. Construite dans le cadre du programme d'avion spatial Hermès, elle est destinée à l'étude des effets de gaz réel et notamment des effets liés à la cinétique chimique au cours de la rentrée dans l'atmosphère.
Les performances, le principe et la description de l'installation sont rappelés ainsi que le déroulement des premiers essais de mise en service.

1. INTRODUCTION

Avec les souffleries hypersoniques R5 et F4, l'ONERA s'est doté de moyens d'essais d'importance capitale pour l'étude des phénomènes aérothermodynamiques liés à la rentrée atmosphérique d'engins spatiaux.
Destinée à l'étude des phénomènes aérodynamiques dominés par les effets simultanés des grands nombres de Mach et des faibles nombres de Reynolds (qui conduisent au développement de couches limites très épaisses), la soufflerie hypersonique à basse densité R5 est particulièrement bien adaptée à l'étude des interactions visqueuses fortes. Elle a été conçue et en grande partie réalisée en 1968/1969 sur le centre ONERA de Chalais-Meudon, mais en raison de la baisse d'activité dans le domaine hypersonique dans les années 1970, sa mise en service a été différée.
A la suite du regain d'intérêt pour les études hypersoniques suscité par le programme Hermès, il fut décidé, en 1989, de rendre la soufflerie R5 opérationnelle [1], d'une part pour y mener un programme de recherches fondamentales sur les interactions onde de choc-couche limite (dans le but, notamment, de valider des codes de calcul), d'autre part pour y développer des méthodes de mesure destinées à la soufflerie à haute enthalpie F4 [2].
La décision de construire la soufflerie à haute enthalpie F4 au centre d'essai ONERA du Fauga-Mauzac, près de Toulouse, a été prise en 1988 dans le cadre du programme Hermès.
La définition de l'installation a fait appel à l'expérience acquise par l'ONERA avec les souffleries ARC de Fontenay aux Roses, qui ont fonctionné jusqu'en 1975.
Ce type de soufflerie se caractérise par une durée de rafale de plusieurs dizaines de millisecondes appréciable, notamment, pour les mesures d'efforts. F4 complète donc d'autres moyens d'essais utilisés pour étudier les effets de gaz réel pour le programme Hermès. Elle permet d'atteindre des enthalpies réduites et des pressions génératrices significatives : ses composantes sont dimensionnées pour atteindre $H_i/RT_a = 200$ et $p_i = 2000$ 10^5 Pa à l'air. La mise en service, commencée au deuxième trimestre 1991 jusqu'à $H_i/RT_a = 100$, nécessite des mises au point visant à améliorer la tenue de la chambre à arc et à réduire la pollution liée au chauffage du gaz d'essai.
La mise au point des moyens de mesure (sonde d'enthalpie et de flux massique ρV, balances à compensation d'inertie) est également effectuée avant les premiers essais industriels.

2. LA SOUFFLERIE R5

2.1 Présentation de la soufflerie

2.1.1 Domaine de simulation et intérêt de ce moyen d'essai

Dans les conditions de vol hypersonique à haute altitude, les effets visqueux tendent à prendre une importance primordiale en raison de l'épaississement rapide des couches limites et de la grande sensibilité de la pression à l'égard de la variation locale de direction induite par la couche limite elle-même. Ce phénomène est connu sous le nom "d'interaction visqueuse" [3] et ses répercussions sur le champ aérodynamique sont qualifiées, pour les coefficients globaux, par le paramètre d'interaction visqueuse $\bar{\chi} = M/\sqrt{Re_L}$, où M et Re_L sont respectivement le nombre de Mach et le nombre de Reynolds. Au cours de la rentrée atmosphérique d'un engin d'une longueur de 10 m, ce paramètre $\bar{\chi}$ varie de 0,1 à 0,01 lorsque l'altitude passe de 75 à 50 km, comme le montre la figure 1. La soufflerie R5 simule ce domaine de valeur de $\bar{\chi}$. Elle répond à un besoin majeur rencontré en hypersonique, les souffleries en service jusqu'alors à l'ONERA ne permettant pas de simuler des valeurs de $\bar{\chi}$ supérieures à 0,008.
De plus, du fait des faibles nombres de Reynolds, il est possible de réaliser des écoulements entièrement laminaires sur des maquettes de dimension importante, ce qui présente

un grand intérêt pour valider les codes Navier-Stokes, en s'affranchissant des problèmes liés à la modélisation de la turbulence. Par ailleurs, la faible masse spécifique ($\rho_0 = 3{,}9\ 10^{-4}$ kg/m^3) de l'écoulement dans cette soufflerie en fait un moyen d'essai privilégié pour la mise au point des méthodes de mesures optiques en basse densité.

2.1.2 Description et fonctionnement

La figure 2 représente l'ensemble du circuit aérodynamique de la soufflerie. En amont l'air est chauffé jusqu'à une température génératrice T_i voisine de 1100 K par passage à travers un réchauffeur électrique à effet Joule d'une puissance de 100 kW. Il s'agit donc d'une soufflerie hypersonique "froide", le niveau de température génératrice étant juste suffisant pour éviter la liquéfaction de l'air en cours de détente dans la tuyère. A la sortie du réchauffeur est disposée une vanne à trois voies à action rapide qui permet de réaliser un amorçage de l'écoulement en un temps de l'ordre d'un centième de seconde.

La tuyère réalisée en acier a une longueur totale de 1,7 m. C'est une tuyère de révolution profilée "tronquée" dont le contour a été calculé [4] pour donner dans le plan de sortie un écoulement uniforme de nombre de Mach égal à 10 pour les conditions nominales suivantes : pression génératrice $p_i = 2{,}5\ 10^5$ Pa et température génératrice $T_i = 1100$ K. Le col de la tuyère a un rayon $r_c = 5{,}279\ 10^{-3}$ m. Le rapport $\mathcal{R}/r_c$ du rayon de courbure de la méridienne au col ($\mathcal{R}$) au rayon du col (r_c) vaut 80, ce qui assure une grande progressivité de la détente dans la première partie de la tuyère. Le diamètre en sortie de tuyère est 0,355 m. La tuyère débouche dans un caisson d'essai de vastes dimensions identique à celui adopté pour toutes les autres souffleries à rafales de l'établissement de Chalais-Meudon.

La veine d'essai est du type à jet libre, la distance entre le plan de sortie tuyère et l'entrée de la reprise du diffuseur étant de 0,47 m (voir figure 3).

L'ensemble diffuseur est constitué d'une reprise tronconique convergente suivie d'un mélangeur cylindrique prolongé par une partie diffusante divergente venant se raccorder à une canalisation qui aboutit à la sphère à vide. La mise au point de l'ensemble diffuseur a été réalisée en bénéficiant des installations du Laboratoire d'Aérothermique du CNRS de Meudon. Une étude fine d'une famille de diffuseurs pour souffleries hypersoniques à faible nombre de Reynolds a ainsi été effectuée [5]. Cette étude mettait l'accent sur les avantages que l'on peut tirer d'une recompression naturelle de l'écoulement dans le diffuseur. En effet, plus longtemps l'écoulement dans le diffuseur conserve une pression supérieure à la pression dans le réservoir aval - laquelle augmente au fur et à mesure que celui-ci se remplit - plus le désamorçage est retardé, ce qui prolonge bien évidemment la durée utile de la rafale. Le rapport de compression de l'ensemble reprise plus mélangeur est ici de l'ordre de 68, ce qui est très satisfaisant et autorise des durées de rafales comprises entre 60 et 90 secondes selon la maquette placée dans la veine d'essai.

Le diffuseur, dans lequel s'effectue la recompression, est raccordé à une sphère à vide d'une capacité de 500 m^3 et dont la pression est de l'ordre de quelques Pascal en début de rafale.

On trouvera rappelées en Annexe les conditions nominales de fonctionnement de l'installation et les caractéristiques qui en résultent pour l'écoulement

2.1.3 Qualification de la veine d'essai

L'écoulement produit par la tuyère a été qualifié de manière expérimentale et théorique.

Le sondage de l'écoulement a été effectué au moyen d'un tube de Pitot fixé à l'extrémité du sabre d'un explorateur. Les explorations ont été exécutées en adoptant le repère défini sur la figure 3, qui montre également la position des profils présentés sur la figure 4.
Il s'agit des distributions radiales du nombre de Mach dans les sections X = 0,005 m (très proche du plan de sortie tuyère), X = 0,1 m et X = 0,2 m. Pour la région isentropique (écoulement sain) ces valeurs sont calculées directement à partir du rapport entre la pression d'arrêt isentropique p'_i donnée par le tube de Pitot et la pression génératrice p_i. Au sein de la zone dissipative (couche limite et zone de mélange), le nombre de Mach est calculé en supposant la pression statique p transversalement constante et égale à la valeur déduite du nombre de Mach donné sur la frontière de cette région. On distingue très nettement la partie d'écoulement sain et la couche de mélange entourant le noyau fluide parfait. La couche limite en sortie de tuyère a une épaisseur δ pratiquement égale à 0,08 m, ce qui réduit le noyau de l'écoulement utile à un cercle de diamètre 0,195 m. Il est à noter que ce diamètre est presque constant sur l'étendue axiale explorée, la zone de mélange se développant depuis la sortie de la tuyère en continuation de la couche limite ayant un taux d'épanouissement faible en raison de son caractère laminaire.
Si l'on considère la totalité des lignes explorées (8 lignes, de X = 0,05 à X = 0,3 m), le nombre de Mach moyen de l'écoulement isentropique a la valeur M = 9,918 ± 0,07. Ces explorations ont permis de qualifier expérimentalement l'écoulement en démontrant l'absence, d'une part de pertubations notables du type onde de choc, d'autre part de gradient axial appréciable.

Par ailleurs, l'écoulement a été calculé par résolution numérique des équations de Navier-Stokes [6] grâce au code HOMARD2 mis au point à l'ONERA par Hollanders et Marmignon [7,8]. Ce code repose sur une méthode de type volumes finis implicite et suppose que l'air se comporte comme un gaz parfait pour lequel $\gamma = 1{,}4$ et $Pr = 0{,}72$.
La figure 5 présente une comparaison entre la répartition de nombre de Mach sur l'axe de la tuyère issue du calcul et celle qui a été imposée lors de la conception de la tuyère [1]. Cette comparaison conduit à d'excellents résultats compte tenu du faible raffinement du maillage utilisé (7300 noeuds) pour réaliser le calcul.
La figure 6 compare le profil de vitesse réduite u/u_e issu du calcul en sortie de tuyère à celui déduit des mesures effectuées dans la section X = 0,005 m. Les deux distributions coïncident bien, sauf dans la région où se situe la frontière entre la couche limite et le noyau d'écoulement isentropique où le calcul surestime la vitesse, reflétant ainsi le fait que l'épaisseur de la couche limite se développant le long de la paroi de la tuyère est légèrement sous-estimée, ce qui est peut-être dû au manque de finesse du maillage.

2.2 Domaine d'activité

2.2.1 Qualification de méthodes optiques pour des écoulements de basse densité

Le niveau de masse volumique dans la soufflerie à haute enthalpie F4 est, pour certains régimes de fonctionnement, le même que celui de la soufflerie R5 (ρ = 3,9 10^{-4} kg/m^3). Aussi, en raison de sa souplesse d'emploi (une rafale d'au moins 60 secondes par heure) et de son faible coût de fonctionnement, la soufflerie R5 est utilisée pour la qualification de méthodes de visualisation : strioscopie classique et à contraste de phase [9], interférométrie holographique [10], fluorescence induite par faisceau d'électrons [11]. La figure 7 illustre ces techniques. Il s'agit de visualisations réalisées autour d'un barreau cylindrique disposé transversalement à l'écoulement, de diamètre 15 10^{-3} m et de longueur 150 10^{-3} m. La figure 7a est relative à une vue strioscopique éclair de l'écoulement. La figure 7b présente un interférogramme holographique avec franges de fond horizontales. Il est obtenu par un montage dit "à multiple traversées", ici 2 aller-retours, soient 4 traversées, ce qui permet d'augmenter d'autant la sensibilité par rapport à un montage à simple traversée. La déformation de l'image du cylindre est probablement due à une mauvaise orientation du cylindre vis à vis du champ lumineux d'étude.
La figure 7c présente une visualisation du même écoulement au moyen de la Fluorescence par Faisceau d'Electrons (FFE). La photo réalisée a été prise avec un temps de pose de 30 secondes pendant lequel le faisceau d'électrons balaie angulairement le domaine, de manière à créer un plan de visualisation. Cette visualisation matérialise nettement l'onde de choc détachée qui se produit en amont du cylindre. Ce procédé ne permet pas seulement de réaliser des images, mais donne aussi des renseignements quantitatifs sur l'écoulement traversé : vitesse, masse spécifique, températures de vibration et de rotation. Cette technique est du plus haut intérêt pour l'analyse des écoulements en gaz raréfié.

La distance de détachement du choc (Δ) mesurée sur les vues strioscopiques et par fluorescence par faisceau d'electrons vaut Δ/R = 0,36. Ce résultat est en bon accord avec les formules empiriques [11] comme avec les résultats de calcul [12] qui donnent 0,4.

2.2.2 Validation de code de calcul

Le code de calcul HOMARD2, employé pour calculer l'écoulement dans la tuyère a, par ailleurs, été utilisé pour le calcul de configurations de type rampe bidimensionnelle dans les conditions de la soufflerie R5 en vue de comparer les résultats obtenus aux mesures effectuées par les différentes techniques expérimentales mises en oeuvre sur des configurations semblables [14,15].
La figure 8 présente les maquettes étudiées. Il s'agit d'une plaque à bord d'attaque aigu, suivie d'une rampe bidimensionnelle d'angle β = 15° ou 25°. Le nombre de Reynolds basé sur la longueur de référence L = 0,179 m séparant le bord d'attaque de la charnière de l'élevon vaut dans les deux cas Re_L = 30000.
La figure 9 montre les lignes de courant obtenues par calcul dans les deux cas considérés. L'interaction se développant sur le dièdre de 15° (Fig.9a) ne conduit pas au décollement de la couche limite. Le choc de tête est courbe près du bord d'attaque, région siège de phénomènes d'interactions fortes [16]. L'interaction engendrée par le dièdre d'angle 25° (Fig. 9b) entraine la formation d'un décollement étendu.

Rampe d'angle β = 15°

Sur la figure 10 le champ de masse volumique calculé est confronté à une visualisation obtenue au moyen de la FFE, cette technique étant sensible aux variations de densité de l'écoulement [17]. Cette comparaison met en évidence un excellent accord calcul-expérience. Les positions de l'onde de choc de tête et celle due au dièdre sont correctement déterminées par le calcul.
Dans le cas de cette rampe, des pressions pariétales ont été mesurées [18] à l'aide de capteurs différentiels à self. Lors de ces essais, les capteurs étaient situés dans le caisson d'essai et reliés aux orifices de pression par l'intermédiaire de conduits en caoutchouc. Les mesures réalisées sont présentées sur la figure 11 sous la forme du coefficient de pression $C_p = (p - p_0) / 0{,}5\ \rho_0 U_0^2$, où p est la pression à la paroi et p_0, ρ_0, U_0 sont les grandeurs de l'écoulement libre précisées en Annexe. Ces mesures sont comparées à l'évolution longitudinale calculée par le code HOMARD2. L'accord est satisfaisant. L'impossibilité d'implanter des prises de pression dans le biseau de la maquette ne permet pas d'obtenir des valeurs expérimentales dans le domaine proche du bord d'attaque. Néamoins à partir de X/L = 0,363, l'expérience rend compte de la décroissance de C_p sur la plaque plane suivant le mécanisme de l'interaction visqueuse forte [3]. Le coefficient de pression C_p croît ensuite de manière quasi-linéaire le long de la rampe reflétant ainsi la compression de l'écoulement provoquée par la rampe. Cette courbe est typique d'une interaction sans décollement [19].

Rampe d'angle β = 25°

Afin de s'affranchir d'effets de bord mis en évidence sur cette configuration [20], les expériences avec un angle de dièdre de 25° ont été exécutées sur une maquette munie de barrières latérales ou "fences".
La figure 12 compare une visualisation obtenue par FFE avec les lignes d'égales valeurs de la masse volumique calculée. Elle fait ressortir un excellent accord aussi bien au niveau de la position des ondes de choc que de la frontière de la couche limite. Les chocs dus au décollement et au recollement de la couche limite sont particulièrement bien mis en évidence par la visualisation et recoupent parfaitement le calcul. La ligne oblique qui apparaît sur cette vue est la trace de la barrière latérale en verre disposée pour éviter les effets tridimensionnels.
La figure 13 présente une comparaison entre l'évolution longitudinale du coefficient de frottement pariétal C_f et une visualisation par enduit visqueux. La ligne de décollement est clairement matérialisée sur la plaque en amont de l'élevon à l'abscisse X/L = 0,75 , ce qui coïncide remarquablement avec l'abscisse où le coefficient de frottement s'annule en changeant de signe. La position de la ligne de recollement sur l'élevon est moins précisément identifiable et fait apparaître des effets tridimensionnels notables. Toutefois, elle coïncide approximativement avec l'abscisse à partir de laquelle le coefficient de frottement redevient positif [20].

Des profils de température et de masse volumique ont été mesurés en cinq abscisses (X/L = 0,4 ; 0,6 ; 0,8 ; 1,0 et 1,2) au moyen de la Diffusion Raman Anti-Stokes Cohérente (DRASC) multi-raies [21]. Cette technique permet la mesure de la température de rotation de la molécule d'azote, qui est assimilable à la température de translation, moyennant l'hypothèse justifiée qu'il n'y a pas de déséquilibre rotationnel dans la soufflerie R5. Cette méthode permet en outre la mesure de la masse volumique.

La figure 14 montre des comparaisons entre les profils de température mesurés et ceux issus du calcul [22]. Les profils à X/L = 0,4 et 0,6 sont situés en amont de la région de recirculation, ceux à X/L = 0,8 ; 1. et 1,2 concernent des stations situées dans la partie décollée. L'accord calcul-expérience au niveau des températures est remarquable. En revanche les densités diffèrent sensiblement pour les deux profils situés les plus en aval. Ce désaccord est peut-être dû aux effets tridimensionnels qui affectent sensiblement l'écoulement dans cette zone.

3. LA SOUFFLERIE F4

3.1. Domaine de fonctionnement

La figure 15 présente une trajectoire de rentrée d'Hermès dans le plan (altitude, vitesse). Les courbes de température d'arrêt derrière le choc (calculées en supposant que l'équilibre thermodynamique est atteint), ainsi que les limites approximatives des domaines de dissociation de l'oxygène et de l'azote sont aussi représentées.

On sait que dans ces conditions d'écoulement, il n'y a plus de loi de similitude exacte et qu'il est impossible, dans le cas général, de reproduire, sur une maquette à échelle réduite, l'écoulement du vol. La prévision de ce qui se passera en vol doit être faite par le calcul, après validation de la méthode utilisée par des expériences sur maquette, réalisées dans des conditions bien connues, mettant en jeu des phénomènes physico-chimiques de même nature que ceux qui sont attendus, ces conditions étant bien entendu aussi proches que possible de celles du vol.

Les phénomènes de gaz réel sont liés au niveau d'énergie du gaz atteint derrière le choc, c'est à dire en fait à la vitesse de rentrée de l'avion spatial, et pour la soufflerie, au niveau d'enthalpie totale H_i. L'objectif de F4 est d'atteindre des enthalpies génératrices réduites H_i/RT_a de l'ordre de 200 à l'azote et de 180 à l'air, correspondant à des vitesses d'écoulement, après détente dans la tuyère, dépassant 5000 m/s.

Même si la similitude complète n'existe plus, on peut s'intéresser à des similitudes partielles. Si l'on s'intéresse particulièrement à la cinétique chimique, des paramètres importants sont la vitesse (c'est à dire l'énergie du gaz) et $\rho_\infty L_R$ (ρ_∞ masse volumique, L_R longueur de référence), dont l'égalité en vol et sur maquette assure, si les chocs binaires sont prépondérants, que les distances caractéristiques de dissociation sont bien dans le rapport des longueurs de référence. La figure 16 présente les possibilités de simulation de F4 en ce domaine.

La soufflerie R5 permet une étude approfondie des effets d'interaction visqueuse. Un des objectifs de F4 est de permettre de compléter ces études, lorsque des effets importants de gaz réel sont présents. La figure 17 présente les possibilités de F4 en ce domaine : les grandes valeurs de $\bar{\chi}$ rencontrées dans la phase initiale de la rentrée pourront être atteintes, à des vitesses qui, bien qu'elles soient inférieures à celles du vol, s'accompagneront d'effets de gaz réel importants.

3.2. Description de la soufflerie (Figs. 18 et 19)

Le gaz d'essai enfermé dans la chambre à arc, est chauffé et mis en pression, à densité constante (7 à 200 kg/m^3), au moyen d'un arc électrique de plusieurs dizaines de millisecondes, alimenté par un générateur impulsionnel. Lorsque la pression visée est atteinte en fin d'arc le gaz est fortement détendu dans une tuyère. L'expulsion d'un bouchon placé au col de la tuyère marque le début de la rafale (Fig.20).

La maquette instrumentée est placée dans un caisson. L'écoulement en jet libre est repris à l'aval par un diffuseur jusqu'à un réservoir mis à un vide de 2 Pa avec le caisson d'essai et la tuyère avant le tir.

La rafale est interrompue par ouverture d'un clapet pyrotechnique entre la chambre à arc et un réservoir tampon, recevant l'excès de gaz lorsque la chute de pression ne permet plus l'écoulement souhaité.

3.2.1. Générateur impulsionnel

Il est constitué d'un volant d'inertie de 15 tonnes couplé à un alternateur de 150 MW. L'alternateur fonctionne en moteur synchrone à fréquence variable pour lancer le volant à 6000 tr/mn ce qui représente un stockage d'énergie de 400 MJ. Le circuit électrique moteur est alors déconnecté, le rotor est excité et l'alternateur alimente la chambre à arc en courant continu par l'intermédiaire d'un pont redresseur à diodes et d'un contacteur rapide C1. L'arc est initié entre les électrodes par un fil conducteur fusible. Le contacteur C2 interrompt l'arc.

3.2.2. Chambre à arc

La chambre est constituée d'une enveloppe cylindrique résistante à la pression et comportant une chemise amovible en acier. A chaque extrémité les porte-électrodes ferment la chambre. Leur position relative est réglable pour ajuster le volume jusqu'à 15 litres (l'essentiel des essais a été effectué à 10 litres). Les électrodes de forme spiralée produisent un champ magnétique qui entraîne l'arc en rotation sur leur périphérie afin de réduire l'érosion. Un "liner" métallique d'épaisseur 5 mm, garnit l'intérieur de la chambre et protège la chemise en acier.

Le remplissage, air ou azote purs, se fait par un orifice et comporte un cycle de purge. La pression dans la chambre est mesurée par plusieurs capteurs de pression. L'enthalpie génératrice moyenne est calculée au moyen du diagramme de Mollier à partir de la densité initiale (pression et température de remplissage) et de la pression mesurée.

3.2.3. Caisson d'essai

La sphère constituant le caisson d'essai est située entre l'extrémité de la tuyère et la pièce de reprise du diffuseur. Un premier support, réglable en incidence et dérapage par positions discrètes, reçoit les montages de maquette en dard. Un second support motorisé permet une variation d'incidence de 20° en 50 ms.

Le système de fixation des supports de maquette permet également l'accrochage de supports de sondes et d'instruments divers. Des balances dard à 3 et 6 composantes, à compensation d'inertie, ont été développées pour les pesées des maquette Hermès. Ces balances et la méthode de restitution des efforts sont en cours de qualification après étalonnage (lâchers dynamiques).

3.2.4. Système de commande et de surveillance

Les divers lots de l'installation sont commandés et contrôlés par des automates placés eux-mêmes sous le contrôle d'un système de supervision qui assure le déroulement des séquences pendant la préparation et l'exécution des tirs. Un tel système est indispensable compte tenu de la durée des tirs. Il délivre les ordres successifs avec une précision de 0,5 ms. Les informations d'état sont transmises à l'opérateur par l'intermédiaire de synoptiques sur écran vidéo.

3.2.5. Chaîne d'acquisition et dépouillement

La chaîne d'acquisition comporte 72 voies de mesures, autonomes jusqu'au stockage numérique des informations.
La cadence d'acquisition peut atteindre 50 KHz par voie et la mémoire rapide permet de stocker 64000 mots de 16 bits par voie.
Chaque voie de mesure comporte des dispositifs de calibration automatiques. Un ordinateur Micro Vax assure l'exploitation des rafales.

3.3. Essais de mise en service

La mise en service de F4 a été retardée par un accident survenu en juillet 1990 au volant d'inertie et consécutif à un défaut de graissage des paliers lors des essais de réception par le fournisseur.
Après remplacement du volant, une première série de tirs a été effectuée au deuxième trimestre 1991 en utilisant une chambre atmosphérique puis une chambre ARC2, récupérée et adaptée, de la soufflerie de Fontenay.
Les lots constituant l'installation (machine impulsionnelle, système de vide, remplissage, supervision, moyens d'acquisition) ont été mis au point.
La chambre à arc F4 a alors été installée et mise en service fin juin 1991 avec remplissage à l'azote, jusqu'à novembre 1991. $H_i/RT_a = 118$ et p_i maximale 875 10^5 Pa ont été atteints.
Sur cette chambre de conception nouvelle des mises au point technologiques ont été nécessaires. D'abord un problème d'isolants entre électrodes et porte-électrodes. Puis une modification de circuit d'alimentation pour éviter l'arrêt de l'arc par une protection du générateur placée sur le circuit de masse commun et sensible aux courants parasites au niveau de la chambre à arc. Avant d'aboutir à une solution définitive il a été nécessaire d'isoler le "liner" métallique avec un dépôt de pâte silastène (Rhodorsil CAF4) avant chaque tir (Azote) ou un chemisage nylon (début des essais à l'air).
Au cours des essais à l'azote quelques essais de variation de paramètres ont été faits pour optimiser la forme et la distance des électrodes, la nature des isolants, les matériaux et la protection du "liner", le dimensionnement des bouchons "passifs" pour obtenir leur expulsion à la pression souhaitée, les réglages de la machine impulsionnelle.
Sous la pression des futurs utilisateurs, les essais à l'air ont été abordés dès novembre 1991 et se poursuivent. Quelques essais à l'azote sont cependant intercalés, par exemple lors d'essais par la Direction de la Physique pour identifier l'écoulement en veine et mettre en évidence des différences azote-air (Fig. 21).

Les essais à l'air ont essentiellement comporté 3 phases à ce jour :

- des essais pour l'amélioration de la configuration de la chambre pour augmenter la pression et l'enthalpie avec un minimum de dégradations des surfaces en contact avec le gaz et un minimum de pollution solide, évaluée par pesée d'un impacteur dans la veine.
Actuellement le "liner" cuivre donne les meilleurs résultats pour les valeurs d'enthalpie réduite de 100 atteintes.
Des essais sont encore effectués pour tester les meilleurs isolants autour des électrodes.

- des essais de développement de différentes techniques de qualification de l'écoulement par la Direction de la Physique : strioscopie, tomographie par plan de lumière laser, spectrométrie d'émission, vélocimétrie laser, sondes de Langmuir, fluorescence excitée par électron (FFE).

- Le début des essais de qualification de la tuyère n° 2 en mars 1992.

L'objectif à court terme est d'identifier et d'améliorer l'écoulement pour ces conditions avant d'étendre le domaine. Des améliorations technologiques pour le domaine ouvert sont d'ailleurs déjà étudiées : chambre intermédiaire, "baffles"....

4.CONCLUSION

La soufflerie R5 permet de simuler des écoulements hypersoniques à faible nombre de Reynolds, correspondant à des conditions de rentrée rencontrées à des altitudes voisines de 60 km.
Elle permet de reproduire des paramètres d'interaction visqueuse globaux $\overline{\chi}$ proches de 0,05 pour un nombre de Mach de 10 et de réaliser des écoulements entièrement laminaires sur des maquettes de dimension importante.
Cette installation constitue donc un moyen particulièrement précieux pour la qualification de méthodes de mesure optiques et la réalisation de cas tests permettant la validation de codes de calcul.
Ainsi les essais qui ont été menés dans cette soufflerie selon ce double point de vue ont conduit à une validation mutuelle des méthodes de mesure et de calcul.

La soufflerie F4 est actuellement en cours de mise au point et constitue un important outil d'investigation des effets de gaz réel, parallèlement à d'autres installations européennes et notamment HEG.
Le domaine visé permet une large exploration de conditions d'essais différentes, pendant des temps de rafale relativement longs, de plusieurs dizaines de millisecondes.
Le problème essentiel de ce type de soufflerie à arc est celui de la pollution du gaz d'essai par les produits venant de l'érosion des electrodes et des surfaces en contact avec le gaz. Des dispositions particulières ont été prises, lors de la conception de la chambre à arc, pour minimiser ces pollutions, notamment pour la mise en rotation très rapide de l'arc electrique. L'analyse de la qualité des écoulements obtenus vient de commencer et des améliorations technologiques visant à éliminer le plus possible les particules métalliques trouvées dans l'écoulement, sont en cours d'étude et pourront être apportées à la chambre. Il reste évidemment beaucoup de travail pour atteindre tous

les objectifs assignés à F4, mais son utilisation jusqu'à des conditions d'essai d'enthalpie réduite moyenne, de l'ordre de 100, devrait pouvoir commencer prochainement.

Remerciements : Les auteurs tiennent à remercier M. Claude Marmignon pour le code de calcul HOMARD2 ainsi que leurs collègues de la Direction de la Physique Générale pour la mise en oeuvre des moyens de mesure optique dans les souffleries R5 et F4 : MM. Bouchardy, Boutier, Dunet, Faleni, Girard, Grisch, Mohamed, Péalat, Philbert, Surget et Taran.

ANNEXE

Conditions nominales de fonctionnement de la soufflerie R5

L'ensemble de l'installation (réchauffeur, tuyère, diffuseur) a été défini pour des conditions nominales rappelées ici :

pression génératrice $p_{i0} = 2,5\ 10^5$ Pa
température génératrice $T_{i0} = 1100$ K
nombre de Mach $M_0 = 10$
vitesse de l'écoulement amont $U_0 = 1450$ m/s

Il en résulte les conditions statiques suivantes dans la veine d'essai calculées en supposant $\gamma = 1,4$

$$p_0 = 5,9 \text{ Pa}$$
$$T_0 = 52,5 \text{ K}$$
$$\rho_0 = 3,9\ 10^{-4} \text{ kg/m}^3$$

ce qui conduit aux valeurs suivantes :
nombre de Reynolds unitaire $Re_u = 167000$ m^{-1}

nombre de Reynolds
(calculé avec L = 0,2 m) $Re_L = 33600$
paramètre global d'interaction visqueuse
(calculé avec L = 0,2 m) $\bar{\chi} = 0,059$

Le libre parcours moléculaire moyen vaut $\lambda = 0,514\ 10^{-3}$ m d'où pour une longueur L = 0,2 m, un nombre de Knudsen $K_n = \lambda/L = 2,57\ 10^{-3}$.

Réferences

[1] CHANETZ B., DELERY J., NICOUT D., POT T. et QUELIN C., "La soufflerie hypersonique à faible nombre de Reynolds R5Ch". ONERA RT n° 11/4362AN.

[2] BERTRAND C., BROUSSAUD P., CHRISTOPHE J. et FRANCOIS G. "Note de présentation de la soufflerie F4". ONERA RT n° 06/3164 GN.

[3] HAYES W.D. et PROBSTEIN R.F. Hypersonic Flow Theory, Academic Press, New York and London, 1959.

[4] MONNERIE B. et PACOU C. "The design of low density hypersonic nozzle". 38th Supersonic Tunnel Association Meeting, San Diego, 11-12 Septembre 1972.

[5] MONNERIE B. "Etude d'une famille de diffuseurs pour soufflerie hypersonique à faible nombre de Reynolds". La Recherche Aérospatiale, n° 114, Septembre-Octobre 1966.

[6] COET M.-C. et BAILLY P."Validation de l'écoulement dans la tuyère de la soufflerie R5Ch par résolution numérique des équations de Navier-Stokes".ONERA RT n°18/4362 AN 000 A, Novembre 1990.

[7] HOLLANDERS H. et MARMIGNON C. "Navier-Stokes high speed flow calculations by an implicit non-centered method".27th AIAA Aerospace Sciences Meeting,Reno (Nevada), January 8-12 1989.

[8] MARMIGNON C., HOLLANDERS H. et COQUEL F. "Navier-Stokes calculations of hypersonic flow configurations with large separation by an implicit non-centered method.
12th ICNMFD, Oxford (GB), July 9-13 1990.

[9] GIRARD A., BOUTIER A., BARBE S., DAIGNE B., FRANCOIS G., GODEFROY J.C., LASGORCEIX P., LEFEBVRE M., MOHAMED A., PEALAT M., PHILBERT M., SAGNIER P., SURGET J. et TOBELI J.P. "Développement des moyens de mesures adaptés aux souffleries hypersoniques, état des travaux au 31 décembre 1989". ONERA RT n° 24/3409 PN, Janvier 1990.

[10] SURGET, J. and DUNET, G. "Multipass holographic interferometry for low density gas flow analysis"
19th International Congress on High Speed Photography and Photonics, Cambridge (G.B.), September 16-22, 1990.(ONERA TP n° 1990-122)

[11] MOHAMED, A.K. "Sondage par faisceau d'electrons des écoulements hypersoniques en rafales brèves"
Thèse de Doctorat de la Faculté des Sciences d'Orsay - 17 décembre 1991.

[12] LENGRAND J.C."Le Problème du corps emoussé dans un écoulement supersonique raréfié". Laboratoire d'Aérothermique du CNRS Meudon-Bellevue, Octobre 1975.

[13] COET M.-C et CHANETZ B."Calcul par résolution des équations de Navier-Stokes de l'écoulement autour d'obstacles emoussés cylindre et sphère dans les conditions de la soufflerie R5Ch". ONERA RT n° 24/4362 AN (à paraître).

[14] CHANETZ B. et COET M.-C."Calcul par résolution des équations de Navier-Stokes de l'interaction choc-couche limite produite par une rampe bidimensionnelle dans les conditions de la soufflerie R5Ch".ONERA RT n° 19/4362 AN, Janvier 1992.

[15] JOULOT A."Contribution of ONERA to problem III : 2D Laminar Ramp Flows" Second Workshop on Hypersonic Flows for Reentry Problems. Antibes, April 15-19 1991.

[16] DELERY J. "Shock/shock and shock-wave boundary layer interactions in hypersonic flows. AGARD-FDP-VKI Special course on Aerothermodynamics of Hypersonic Vehicles", 30 May-3 June 1988. AGARD REPORT N°761.

[17] MOHAMED A.K."Electron beam probing of hypersonic flows" New trends in Instrumentation for hypersonic research. April 27th-May 1st 1992 ONERA Le Fauga-Mauzac (France.)

[18] NICOUT D., POT T. et CHANETZ B."Mesures de pressions pariétales sur des rampes bidimensionnelles dans la soufflerie R5Ch". ONERA RT n°25/4362 AN (à paraître)

[19] DELERY J.M. et MARVIN J.G. "Turbulent shock-wave/boundary-layer interaction" AGARDograph n° 280 (February 1986)

[20] CHANETZ B., POT T. et COET M.-C. "Visualisations pariétales dans la soufflerie R5Ch : Essais de mise au point". ONERA RT n°20/4362.

[21] PEALAT M. and LEFEBVRE M. "Temperature measurement by single-shot dual-line CARS in low-pressure flows" Appl. Phys. B 53,23-29, (Springer-Verlag, 1991)

[22] GRISCH F., BOUCHARDY P., PEALAT M., CHANETZ B., POT T. et COET M.-C., "Rotational temperature and density measurements in a hypersonic flow by dual-line CARS" New trends in Instrumentation for hypersonic research. April 27th-May 1st 1992 ONERA Le Fauga-Mauzac (France).

[23] LEYNAERT J. "Les moyens d'essais en hypersonique" ONERA TP n°1991-47.

[24] CARRIERE P., CHEVALLIER J.P. "Recent progress in ONERA Hot shot wind tunnels" ONERA TP n° 1967-447.

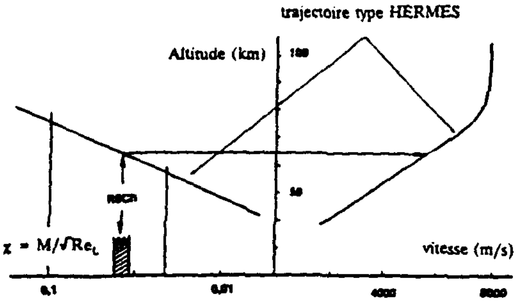

Fig.1 : Domaine de simulation de la soufflerie R5

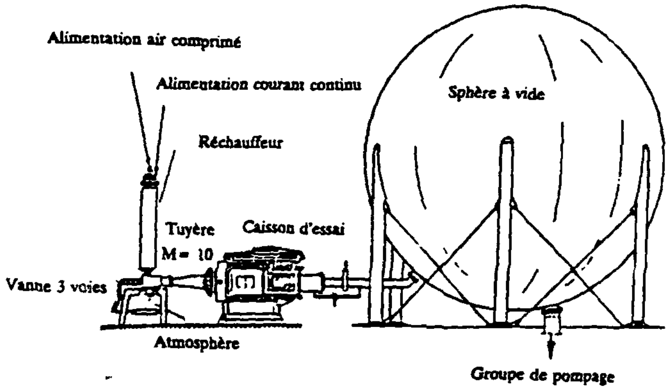
Alimentation air comprimé
Alimentation courant continu
Réchauffeur
Tuyère
M= 10
Caisson d'essai
Sphère à vide
Vanne 3 voies
Atmosphère
Groupe de pompage

Fig.2 : Circuit aérodynamique de la soufflerie R5

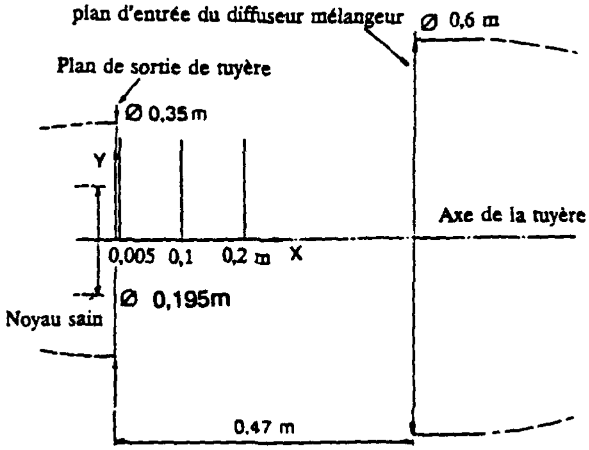
plan d'entrée du diffuseur mélangeur
Ø 0,6 m
Plan de sortie de tuyère
Ø 0,35 m
Y
Axe de la tuyère
0,005
0,1
0,2 m
X
Ø 0,195m
Noyau sain
0,47 m

Fig.3 : Schéma de la veine d'essai R5

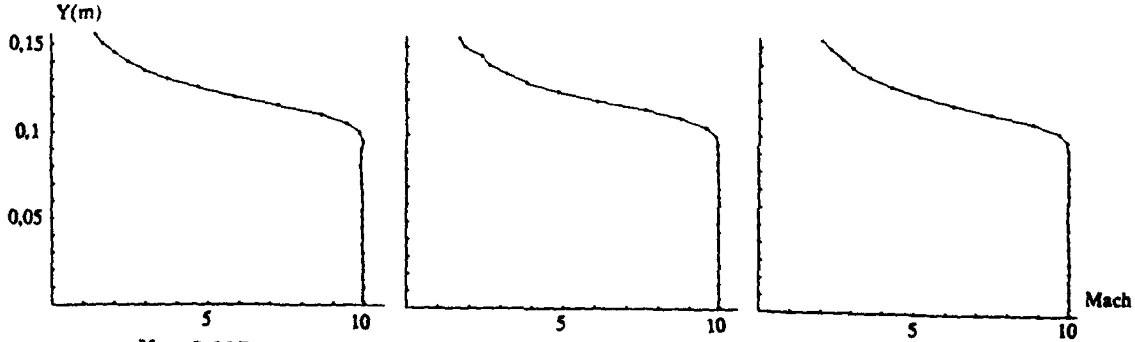

X = 0,005 m

X = 0,1 m

X = 0,2 m

Fig.4 : Profils de nombre de Mach selon la direction radiale Y(R5)

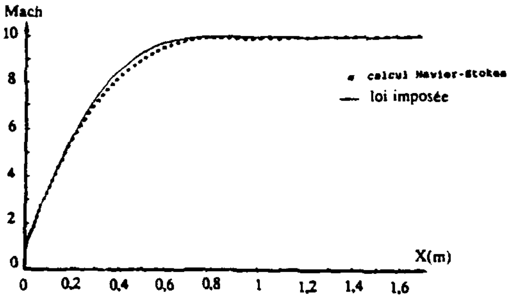

Fig.5 : Comparaison entre la loi de Mach théorique sur l'axe et la répartition calculée (R5)

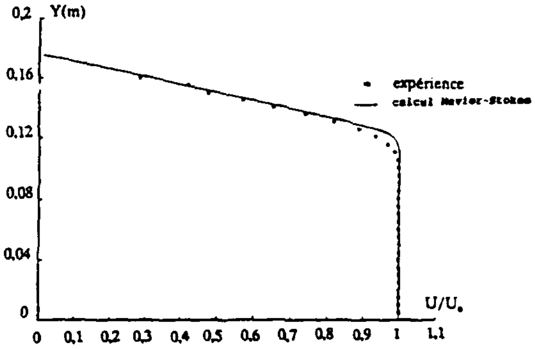

Fig.6 : Comparaison des profils de vitesse calculés et mesurés en sortie de tuyère (R5)

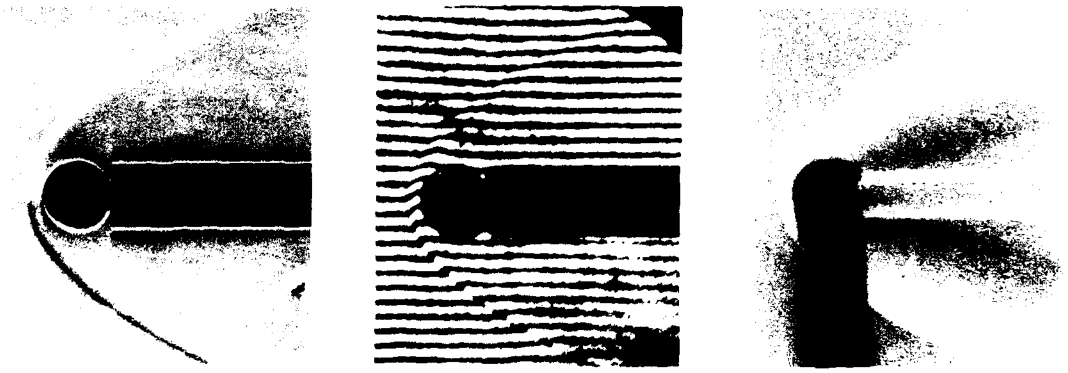

a) vue strioscopique

b) interférogramme holographique

c) visualisation par fluorescence par faisceau d'électrons

Fig.7 : Visualisation de l'onde de choc détachée devant un barreau cylindique (R5)

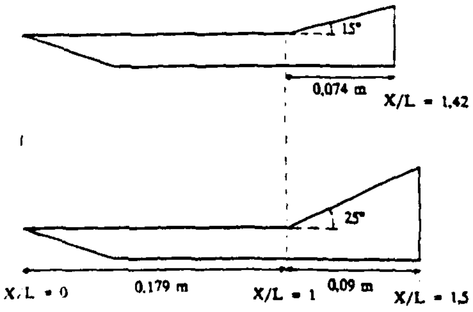

Fig.8 : Schéma des maquettes de rampe bidimensionnelles

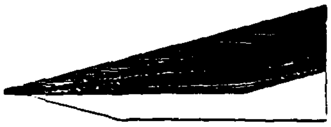

a) β = 15°

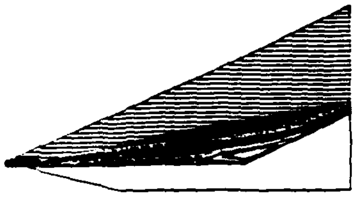

b) β = 25°

Fig.9 : Lignes de courant calculées par resolution des équations Navier-Stokes

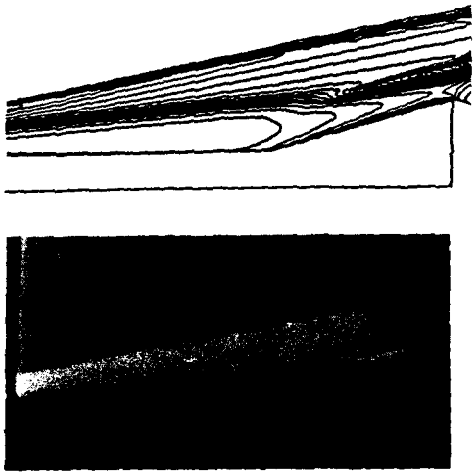

Fig.10 : Comparaison des lignes d'égales valeurs de la masse volumique calculée et d'une visualisation FFE sur la rampe β = 15° (R5)

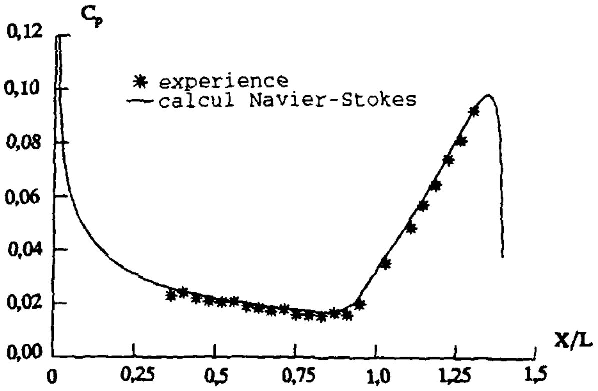

Fig.11 : Comparaison de l'évolution longitudinale de la pression pariétale calculée et mesurée sur la rampe β = 15°

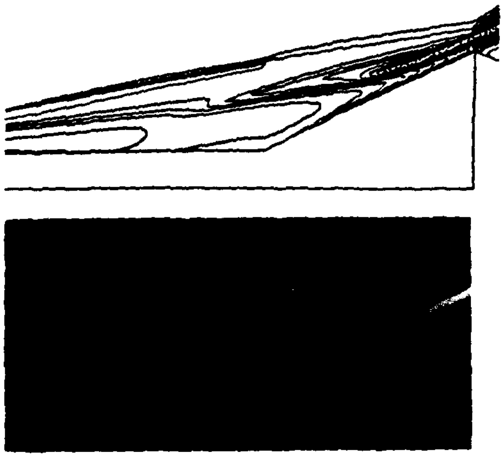

Fig.12 : Comparaison des lignes d'égales valeurs de la masse volumique calculée et d'une visualisation FFE sur la rampe β = 25° (R5)

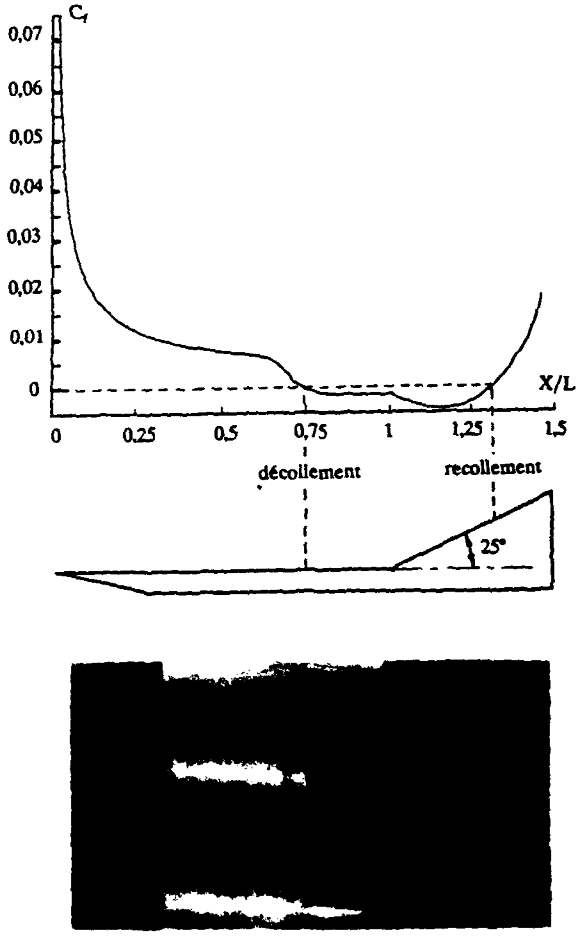

Fig.13 : Evolution longitudinale du coefficient de frottement calculé C_f et lignes de frottement pariétales sur la rampe β = 25° (R5)

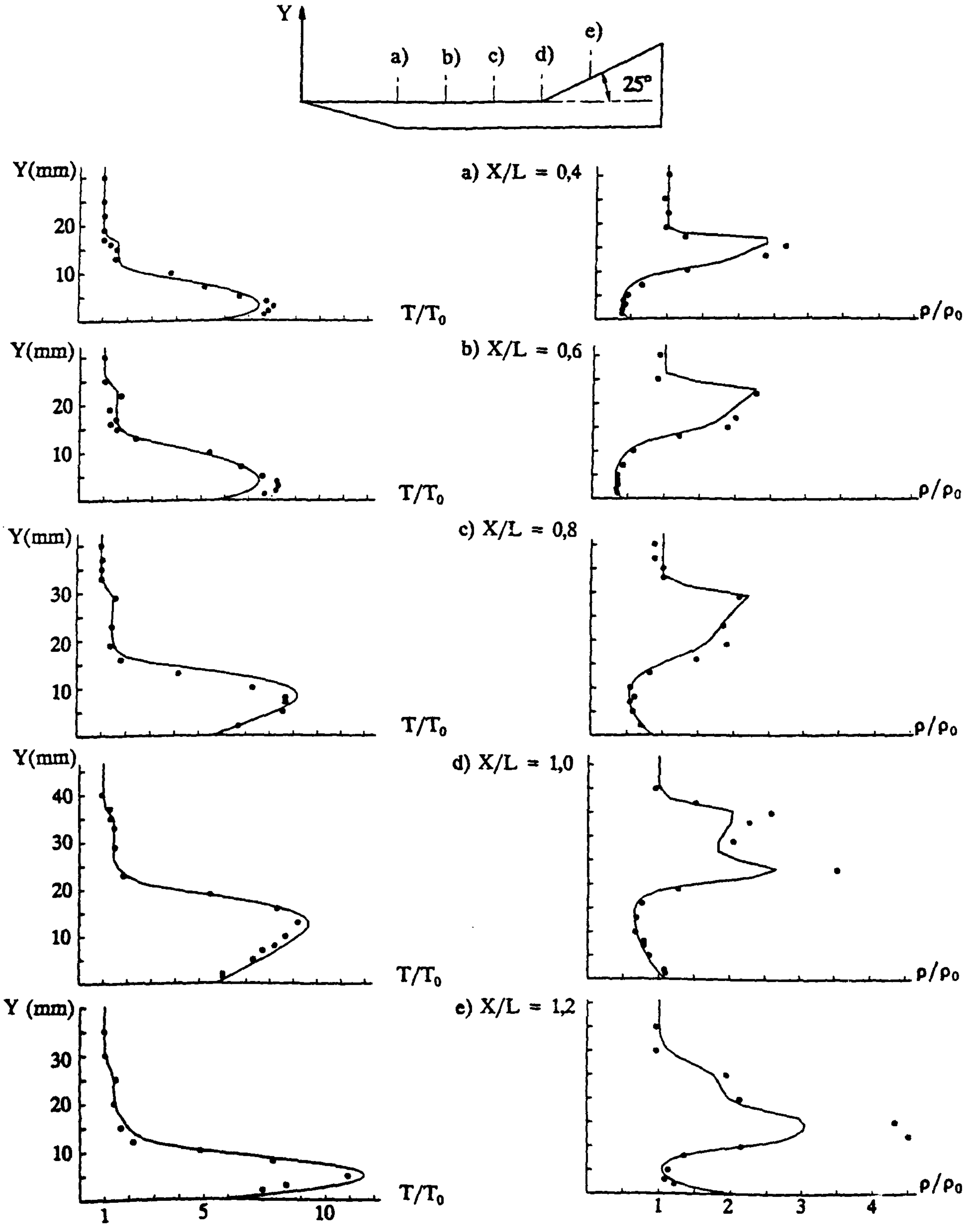

Fig. 14 : **Comparaison des profils de température et de masse volumique calculées et mesurées par Diffusion Raman Anti-Stokes Cohérentes (DRASC)**

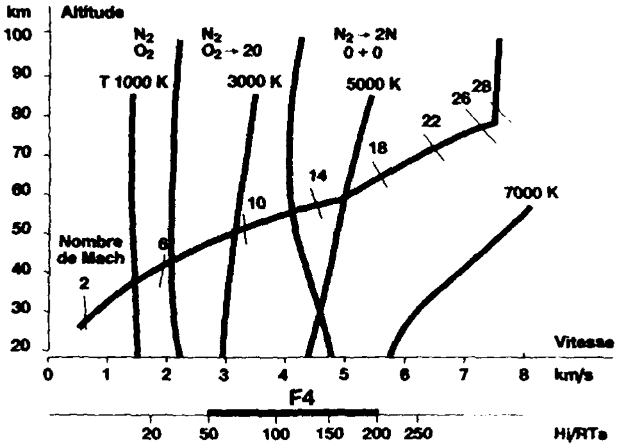

Fig.15 : Hermès - Trajectoire de rentrée (F4)

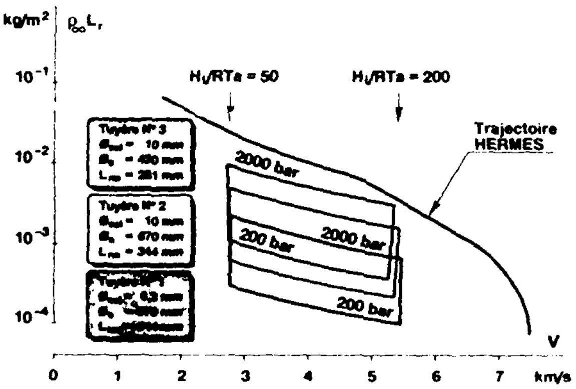

Fig.16 : Domaine ρL(V) (F4)

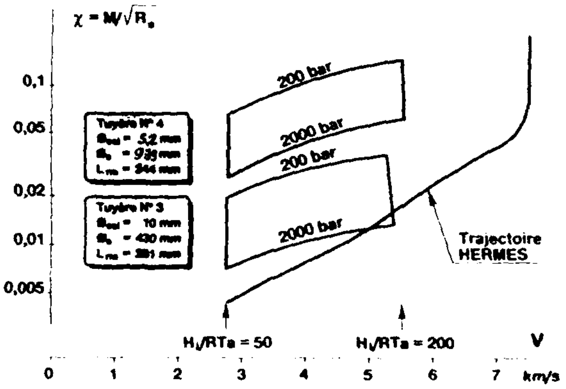

Fig.17 : Domaine $\overline{\chi}$(V) (F4)

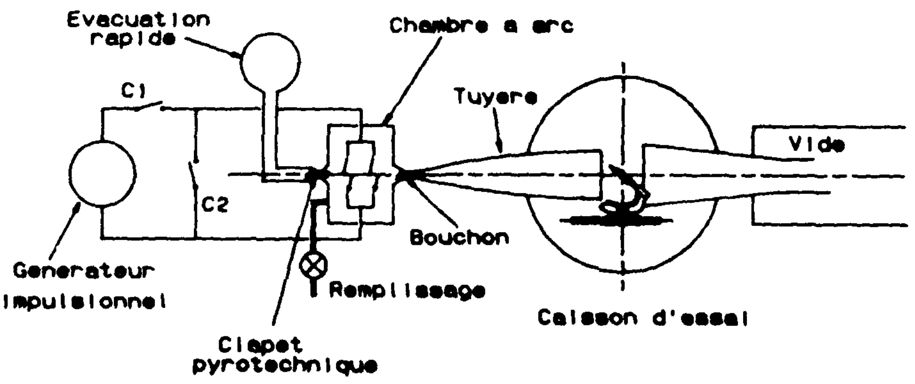
Evacuation rapide
Chambre a arc
C1
C2
Tuyere
Vide
Bouchon
Generateur impulsionnel
Remplissage
Caisson d'essai
Clapet pyrotechnique

Fig.18 : Principe de la soufflerie F4

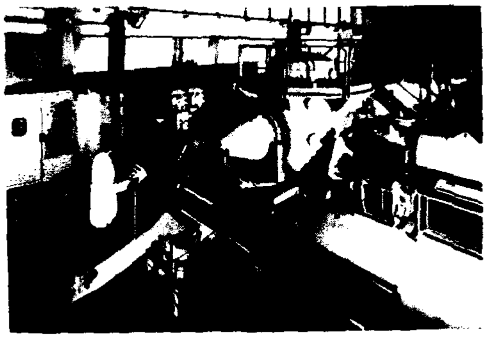

Fig.19 : Vue de la soufflerie F4

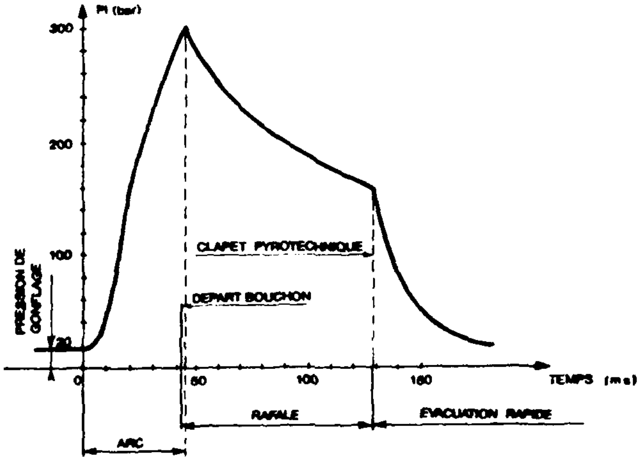

Fig.20 : Evolution de la pression génératrice - Air - (H_i/RT_a = 100 , p_i = 300 bar) (F4)

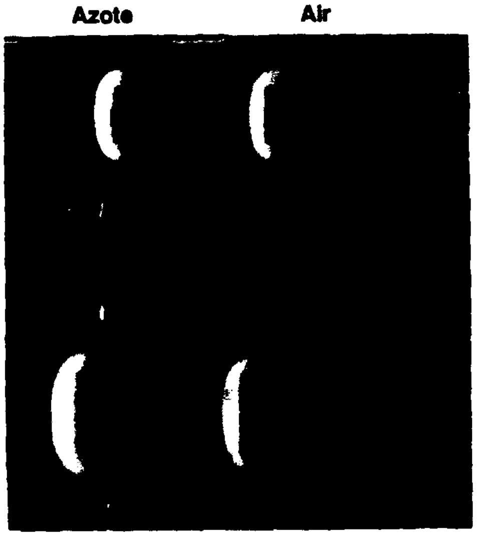

Fig.21 : Strioscopies Air et Azote (H_i/RT_a = 100, p_i = 300 bar) (F4)

The High Enthalpy Facilities HEG and TH 2 in Germany

G. Eitelberg1) and H. Olivier2)
1)DLR, Bunsenstr. 10, D - 3400 Göttingen and 2)RWTH Aachen,
Stoßwellenlabor, Templergraben 55, D - 5100 Aachen
Germany

SUMMARY

The two high enthalpy shock tunnels in Aachen and Göttingen, both Germany, are described. Both of these are shock tunnels operating in the reflected mode. The Aachen tunnel has a heated driver and the Göttingen tunnel has a free piston driver. The Aachen tunnel has been in operation for a number of years already and the characteristic operating conditions of this tunnel are described. The tunnel in Göttingen (HEG) is currently being established. In this paper the first commissioning results of this tunnel are being described. The Aachen tunnel TH2 covers a testing range in air from perfect gas behaviour to real gas behaviour with significant oxygen dissociation effects. The HEG was designed to operate in the flow regimes were also significant nitrogen dissociation dominates.

1. SHOCK TUNNEL OPERATING PRINCIPLES

The elementary shock tube performance is well documented in a number of text books (e.g. Ref. 1). It will thus be sufficient to bring into attention the usual notations of the different flow fields.

A shock tunnel consists of a driver, driven section, nozzle, and dump tank with test section (see Fig. 1). Detailed characteristics of the Aachen shock tunnel may be found in (Ref. 2), the Göttingen tunnel HEG is described in (Ref. 3). Driver and driven section are separated by the main diaphragm. The driver section is filled with the so-called driver gas, usually helium, at an initial pressure p_4 and temperature T_4. In the HEG, the burst conditions p_4 and T_4 are achieved by a fast adiabatic compression of the driver gas with a free flying piston. The driven section contains the test gas, usually air, at an initial pressure p_1 and temperature T_1. Before the test starts the dump tank is evacuated. It is separated from the driven section by another, thin diaphragm to avoid the inflow of the test gas into the dump tank before the test starts. Figure 1 shows schematically the setup of the tunnel and the pressure distribution within the shock tube for various times during the run. To start the operation, the diaphragm between driver and driven section is allowed to burst. Then a shock wave forms into the test gas (1) increasing its pressure and temperature to p_2 and T_2 in the region (2). Behind this shock wave the contact surface follows which separates the driver and driven gas. The driver gas acts like a piston which compresses the test gas rapidly.

A few milliseconds after the bursting of the diaphragm the incident shock wave arrives at the end wall of the driven section. The Aachen and the Göttingen shock tunnels operate in the reflected mode, i.e., the incident shock wave is reflected at the end wall and thereafter propagates upstream. During this reflection process the second diaphragm between driven secton and nozzle burst and the nozzle flow starts. The flow velocity behind the reflected shock is zero to a first approximation if the outflow into the nozzle is neglected. The complete kinetic energy of the shock heated gas in region (2) is thus converted to high temperature and pressure of the stagnant region (5) behind the reflected shock. The compressed test gas having a termperature of a few thousand degrees centigrade expands subsequently through the nozzle. The high stagnation enthalpy is thus converted to a high free stream velocity in the test section.

In the following a summary description of the Aachen shock tunnel TH 2 is given. The second part of the paper gives a brief discussion of the distinguishing characteristics of the HEG.

2. THE AACHEN SHOCK TUNNEL TH2

2.1 Typical Air Flow Data and Calibration of the Aachen Shock Tunnel TH 2

During the last years the tunnel was mainly operated under test conditions which are listed in Tab. 1. The main purpose of these conditions is to study the influence of real gas effects on hypersonic aerodynamics. Therefore the stagnation temperature is varied between 1500 K and 4700 K, which covers at the lower limit perfect gas behaviour and at the upper limit real gas behaviour with significant oxygen dissociation behind the bow shock. Of course not only these test conditions can be generated but also all other possible test section flows which are within the operating characteristics of the shock tunnel.

The calibration of the test flow is performed by measuring the Pitot pressure distribution in streamwise and crosswise directions and by stagnation point heat flux measurements to determine the stagnant enthalpy (Ref.2)

To get a first knowledge of the thermal and chemical free stream properties, calculations of the nozzle flow have been performed, which take into account vibrational and chemical relaxation processes of a five component air model (Ref. 4). The high nozzle reservoir pressure prohibits the evolution of big amounts of dissociated species in the flow.

Therefore at the nozzle exit for test condition IV (see Tab. 1) only 0.2 % atomic oxygen and 3 % NO are expected so that the chemical composition of the free stream in front of the model even at this high nozzle supply temperature can be regarded as atmospheric air.

2.2 Operating procedure to determine the flow conditions of TH 2

To determine the actual flow performances the shock tunnel is equipped with several measuring gauges. In the driver section the supply pressure p_4 of the driver gas as well as the gas temperature T_4 are measured. The speed of the incident shock is deduced from the signals of three pressure gauges which are installed at different axial positions near the end wall. The last of these three gauges also gives the nozzle reservoir pressure. Within the test section a Pitot pressure gauge and a shpere with a thermocouple at its stagnation point are mounted (see Fig. 1). For the determination of the flow conditons these two gauges give the most important informations. The measured Pitot pressure and stagnation point heat flux of the sphere are used to deduce the stagnation enthalpy h_0, the specific free stream mass flux $\rho_\infty u_\infty$ and the dynamic pressure $1/2\rho_\infty u_\infty^2$. Of course in this case the free stream density and velocity are also known. The knowledge of the total enthalpy, specific mass flux and dynamic pressure is necessary to determine pressure coefficients (Eq. 1) and simplified Stanton numbers (Eq. 2) from surface pressure and heat flux measurements around a model:

$$c_p = \frac{p - p_\infty}{\frac{p_\infty}{2} u_\infty^2} \qquad (1)$$

$$St = \frac{\dot{q}}{\rho_\infty u_\infty (h_o - h_w)} \qquad (2) .$$

Of course the accuracy of the achieved pressure coefficients and Stanton numbers also depend on the knowledge of the considered free stream conditions. From the experimental point of view it makes no sense to try to increase the accuracy of the measured model surface values, like the pressure p or the heat flux q, unless the knowledge of the free stream conditions is adequate.

The procedure to determine the free stream conditions is as follows: The formula of Fay and Riddell (Ref. 5) (see Eq. 3) gives an implicit equation for the stagnation temperature T_s at the stagnation point behind a normal shock. The stagnation point heat flux q_{sph} is measured during the test:

$$\dot{q}_{sph} = 0.94\,(\rho_w \mu_w)^{0.1}\,(\rho_s \mu_s)^{0.4} \cdot$$

$$\left[1 + (Le^{0.52} - 1)\,\frac{h_D}{h_s}\right](h_s - h_w)\cdot\sqrt{\frac{du}{dx}\Big|_s} \qquad (3) .$$

The subscript w indicates the wall conditions and the subscript s the flow conditions at an imaginary stagnation point of the external flow. Le indicates the Lewis number and $du/dx|_s$ is the tangential velocity gradient at the stagnation point. All stagnation values at the right hand side ot Eq. (3) are computed as function of the Pitot pressure and the stagnation temperature, where an equilibrium flow between shock and stagnation point is assumed. During the routine use of this formula, it turned out, that to achieve a high accuracy of the stagnation temperature it is necessary to employ a more accurate flow model for the computation of the velocity gradient (Ref. 6) than it was proposed by Fay and Riddell (Ref. 5) and others. Using this more accurate flow model for the stagnation point region, the accuracy of the deduced stagnation temperatures, achieved from Eq. (3) could be increased by approximately 10 % (Ref. 6).

To compute the free stream values ρ_∞, u_∞ and p_∞ simple normal shock relations are applied, where the conditions behind the shock are reduced to the measured and computed stagnation values. Between the shock and the stagnation point a constant density flow is assumed. This leads to very simple equations for the free stream values. As it has been shown by Stalker (Ref. 7) for blunt bodies this assumption is even valid for high enthalpy flows with real gas effects. The solution of this set of equations for the considered mass fluxand dynamic pressure is (Ref.9):

$$\rho_\infty u_\infty = \frac{p_s}{RT_S} \sqrt{2\,(h_s - h_\infty)}.$$

$$[1 - \sqrt{1 - \frac{RT_s}{p_s}\frac{p_s - p_{\propto}0}{h_S - h_{\propto}}}] \quad (4)$$

and

$$\rho_\infty u^2_\infty = \frac{2\,p_s}{RT_s}(h_s - h_\infty).$$

$$\left[1 - \sqrt{1 - f(RT_s;p_s)\frac{p_s - p_\infty}{h_s - h_\infty}}\right]. \quad (5)$$

A complete description of the method will be given in (Ref. 6).

The accuracy of these expressions have been tested, comparing the values given by Eqs. (4) and (5) with corresponding ones found by a complete nozzle calculation for equilibrium air and frozen flow (Ref. 8). At 5000 K stagnation temperature the difference between the mass flux given by Eq. (4) and the nozzle calculation only amounts to 1 % (Ref. 9). The same holds for the dynamic pressure.

But the main advantage of the described method is, that it only uses values which are measured within the test section. In short duration facilities, free stream conditions in particular are sometimes hard to determine. The general recommendation is to deduce these values from the nozzle reservoir conditions behind the reflected shock, where the pressure is usually recorded and the temperature calculated from the measured values of the initial driven section temperature T_1 and the shock Mach number. With these values a nozzle calculation is performed which gives the desired free stream conditions. However, using the recommended method a lot of uncertainties enter the problem. These arise due to several problems:

- due to complex reflected shock shapes at the shock tube end wall, a reliable computation of the reservoir temperature is not possible, also due to unknown influence of heat losses caused by radiation and driver gas contamination;

- the computation of the nozzle flow is not very reliable due to uncertain chemical and thermal models of the nozzle flow, and also due to uncertain description of the transitional and turbulent nozzle boundary layer;

- using the measured nozzle reservoir and Pitot pressure for a nozzle flow calculation, in short duration facilities the time delay caused by the finite signal travelling speed between the signals of the reservoir and the test section has to be taken into account. This time delay can not be predicted very precisely.

All these problems are avoided, if, as it is described, the free stream conditions are determined without referring to the nozzle reservoir conditions. Figure 2 shows typical time histories of the stagnation temperature, as they are achieved from the measured stagnation point heat flux and the described method. For comparison there are also shown theoretical values of the stagnation temperature which have been computed from the nozzle reservoir condition assuming both an equilibrium flow along the nozzle up to the stagnation point and a frozen flow. The nozzle reservoir temperature has been computed from the measured reservoir pressure.

For the highest stagnation temperature in Fig. 2, the deviation from the equilibrium value is due to the fact, that for this flow condition the free stream is not fully in equilibrium. A quasi 1 D-nonequilibrium computation for the stagnation point streamline yielded the stagnation temperaure $T_{s,noneq.}$ (see Fig. 2), which is in excellent agreement with the experimental value. This example shows, that the used method is also valid for nonequilibrium free stream conditions, provided that between shock and stagnation point the flow comes to equilibrium (Ref.6).

In Fig. 2 it is seen that during the flow starting process, $t \leq 2$ ms, obviously the stagnation temperature develops from a very high value, which is remarkably higher than that of the stationary flow phase. This is an unphysical phenomenon, therefore in this region the time history is marked as broken line. The reason for this is given by the relatively long rise time of the Pitot pressure compared to that of the stagnation point heat flux (Ref. 6).

2.3 Typical results of pressure and heat flux measurements

As a typical result of pressure and heat flux measurements and the following data reduction of these values to pressure coefficients and Stanton numbers, Fig. 3 shows the results of 4 tests with a double ellipsoid model, which was used as test case of the Antibes Workshop Part I, II (Ref. 10). Tests with other models and at other flow conditions have also been performed (Ref. [illegible]). Since the results of these 4 tests are achieved at the same flow condition, Fig. 3 also gives typical repeatability margins for this case.

It is seen that in general the repeatability is good, even in critical region of strong pressure and heat flux gradients it is still satisfactory. As expected the deviations of the pressure coefficient are smaller than those of the

Stanton number, because the pressure is not so sensitive to changes of the free stream properties as the heat flux. In general, the repeatability of the considered parameters depend on the free stream Mach number, Reynolds number, etc. On the other hand, for a fixed nozzle geometry these values depend on the nozzle reservoir conditions. Of course, with some similarity laws deviations of the Mach and Reynolds number from one test to each other can be accounted for . But these laws are often only valid for simple shapes, like a flat plate, and for laminar boundary layers. Therefore to achieve a high repeatability it is necessary to reproduce the nozzle reservoir conditions as well as possible. For the tests of Fig. 3 the maximum deviation of the nozzle reservoir pressure for *all 4 tests was 4,6 %*, which gave a maximum repeatability margin of 7 % for the Pitot pressure. Therefore the free stream deviations were so small, that a Mach and Reynolds number correction were not applied to the results shown in Fig. 3.

3. THE HEG

3.1 Description of the HEG

Like all free piston driven shock tunnels, the HEG is used to provide simulation capability for the dissociation effects in both oxygen and also nitrogen. The arrangement of the free piston driven shock tunnel HEG consists of three main sections: the driver section including the air buffer for piston acceleration; the driven tube; and the nozzle and test section. The driver section consists of a 33m long compression tube of internal diameter 0.55m within which the free flying piston compresses the driver gas (usually helium). At the downstream end of the compression tube the primary diaphragm is located.

The shock tube has a length of 17 m and an internal diameter of 0.15 m. The downstream end of the shock tube acts as the reservoir for the nozzle.

The HEG nozzle is contoured to provide parallel flow in the test section at Mach 7 -9 depending on the reservoir enthalpy achieved. The nozzle has a length of 3.75 m, throat diameter of 22 mm and exit diameter of .88 m. The Mach number decreases with increasing reservoir enthalpy due to the increase of the free stream temperature.

The piston is accelerated with air from the wrap-around secondary buffer at the upstream end of the compression tube. The fill pressures for the compression tube are selected such that the designed burst pressures for the primary diaphragm are achieved with the compression ratio of $\lambda = 60$, which yields a driver gas temperature of approximately $T_5 = 4200$ K (the driver gas is initially at ambient temperature). When the piston, through its inertia, has compressed the driver gas to the required pressure level, the primary diaphragm bursts, starting the shock tube operation.

As the aim is to produce high enough enthalpies for nitrogen dissociation simulation, very strong shocks are required in the driven tube. The characteristic dissociation energy of nitrogen is $E_d = 34$ MJ/kg . Through adiabatic heating of the driver gas with the help of a heavy piston, specific enthalpies h, comparable with the above value can be achieved in combination with high densities. The high densities are required in order to obtain sufficiently short dissociation lengths. The dissociation energy of nitrogen is also comparable with the specific energy of an orbital flight vehicle $E = v^2/2$.

3.2 Calibration Status of the HEG

Calibration of HEG is performed by measuring parameters at various positions within the facility and then making comparisons with currently available modelling. Of principal importance is the characterization of the flow at the exit ot the HEG nozzle (free-stream conditions). Here parameters are required when making comparisons with computer modelling of reentry conditions as experienced by, for example, Hermes. It is also important to establish the uniformity of the flow for each of the operating conditions.

As well as calibration measurements in the nozzle, flow upstream is to be measured as it influences both the free-stream conditions and the safety and lifetime of the facility. Measurements in the shock tube section provide input data on the entry conditions of the nozzle while measurements in the compression tube will monitor the piston motion which can influence the operating time of the facility.

3.2.1 Driver Section

The driver section of HEG consists of a free-moving piston which is accelerated along the tube by high pressure air currently at pressures up to 50 bar. In front of the piston is the driver gas (normally helium) which has currently been compressed up to 500 bars, at which point a diaphragm ruptures initiating the shock tube flow. A summary of conditions tested in the HEG so far is given in Table 2. Parameters and methods of measuring were:

- *Piston trajectory*. Sensors located at 5 positions along the compression tube monitor the time at which the piston passes from which the piston trajectory as a function of position and time has been determined. The main part of the trajectory agrees with the prediction within the resolution of the modelling. The prediction method is described by McIntyre and Atcitty (Ref. 12).

- *Driver gas pressure*.Two Kistler piezo-electric pressure gauges mounted at the end of the compression tube monitore the driver gas pressure (helium) as a function of time. A comparison of an experimental result with a numerical prediction from (Ref.12) is given in Figure 4.

- *Holding time*. The holding time (the time during which the driver gas pressure remains within 10% of its peak value starting after the diaphragm rupture) can be inferred from the helium pressure trace. The diaphragm burst time is determined from the signal at the first shock registration sensor which is positioned in the shock tube right behind the diaphragm. The holding times achieved are of the order of 1.8 ms

- *Brake deformation*. Measurement of the brake (used to bring the piston to rest) before and after the shot have been used to provide an indication of the final stages of the piston trajectory. The brake deformation has been in the expected range.

3.2.2 Shock Tube

After diaphragm rupture, a shock wave is generated which propagates along the shock tube, heating and compressing the test gas, normally air, in the experiments so far, nitrogen. After reaching the end of the tube, the shock reflects and propagates back upstream. Behind the reflected shock, the gas is stationary and at a high temperature and pressure. This region serves as the reservoir for the nozzle.

Parameters and methods of measuring are (cf. Table 2):

- *Initial shock tube pressure.*

- *Shock velocity*. Five ionization gauges situated at various points along the shock tube record the passing of the initial shock. These, together with a pressure measurement at the end of the shock tube, provide six measurement locations giving five shock velocities.

- *Nozzle reservoir pressure*. Two Kistler pressure gauges at the end of the shock tube record the time history of the reservoir pressure. The positioning of the pressure transducers in the end wall of the shock tube is novel in shock tunnel applications.

Modelling of the above parameters is performed by using the equilibruim shock tunnel program (ESTC) developed by McIntosh (Ref.13). Input parameters are the initial shock tube pressure and the shock wave velocity. Predicted are the conditions behind the reflected shock. To account for non-tailored conditions (an expansion or compression of the reservoir gas), an isentropic expansion or compression is used to arrive at the measured reservoir pressure (see Morgan et al(Ref. 14)).

Results:

Four nozzle reservoir pressure traces are shown, filtered, in Figure 5. These were obtained at identical burst pressures with varying shock tube fill pressure. The analysis of these results leads to a tailoring condition of $p_{\text{shock tube}} \cong 0.33$ bar for $p_{\text{burst}} \cong$ 500 bar. A summary of the operated shock tube conditions is given in Table 2. From Figure 5 it can be seen, that at the $p_{\text{burst}} \cong 500$ bar conditions constant reservoir conditions are achievable for nearly 2 ms. The reservoir pressures obtained are considerably higher than the predicted values using the Page-Stalker correlation (Ref. 15).

3.2.3 Test Section

The contoured nozzle designed by Hannemann(Ref. 16) has been used. Flow duration is limited because of the drainage of the reservoir and because of contamination of the test gas by the driver gas.

Measurements:

- *Pitot pressure.* Pitot pressure has been measured currently at one location only. This together with a hemispherical probe for stagnation point heat transfer, similar to the arrangement shown in Figure 1. For the $P_{burst} \cong 500$ bar condition a characteristic pressure trace is shown in Figure 6. For a duration of $t_m \cong 1.5$ ms an approximately constant pressure level of $p_t \cong 450$ mbar is obtained. This agrees reasonably with the result predicted by the quasi-1D-calculation using STUBE (Ref. 18).

- *Static pressure.* The static pressure of the gas has not been measured yet.

- *Stagnation point heat transfer.* The stagnation point heat transfer has also been measured at one location only. The evaluation of the heat transfer gauge output is currently at a preliminary stage only. The results of such a preliminary evaluation, as performed by Grauer-Carstensen (Ref.17) are encouraging.

- *Flow visualization.* Holographic interferometry was used to provide measurements of the shock stand-off distance on an oblique cylinder, which is indicative of the density and therefore the degree of dissociation of the flow. A comparison of the measured shock standoff distance with various theoretical predictions is shown in Figure 7 for two different experiments. The flow luminosity photographs were also evaluated in respect to the shock stand-off distance. Both evaluations yield a bow shock which is closer than the predictions for perfect gas yield. The density jump across the shock along the stagnation streamline can be estimated at approximately $\rho/\rho_\infty \cong 10$, where the test gas used is nitrogen. This means that considerable dissociation occurs behind the shock. An average degree of dissociation behind the shock along the stagnation streamline can be estimated to be $\alpha \cong 0.3$.

Acknowledgement

The financial support by the European Space Agency through the ESA/CNES joint HERMES Team and by the German State of Lower-Saxony for the development of the HEG is gratefully acknowledged. The contributions of numerous collaborators also are gratefully acknowledged.

References

1. Liepmann, H. W. & Roshko, A.: Elements of Gasdynamics, John Wiley & Sons, New York, 1960, *Section 3.2.*

2. Anonymous: Description of the Aachen Shock Tunnel TH 2, Shock Wave Laboratory, Rheinisch Westfälische Technische Hochschule, Aachen, Germany, 1991

3. Beck, W.H., Eitelberg, G., McIntyre, T.J., Baird, J.P., Lacey, J., Simon, H., The High Enthalpy Shock Tunnel in Göttingen (HEG). *In: Proc. 18th ISSW, Sendai, July* 1991

4. Ritzerfeld, E.: Stationäre Nichtgleichgewichtsströmung, 4th STAB-Workshop, DLR Göttingen, 1989.

5. Fay, J.R. & Riddell, F. R.: Theory of Stagnation Point Heat Transfer in Dissociated Air, J. of the Aeron. Sci., Vol. 25, 1958, pp. 73 - 85.

6. Olivier, H.: An improved method to determine the free stream conditions in hypersonic facilities, to be submitted to Shock Waves.

7. Stalker, R.J.: Some Real Gas Shock Tunnel Experiments at Australian Universities, Workshop on Hypersonic Flows for Reentry Problems, Part II, INRIA, GAMNI-SMAI, Antibes, France, 1991.

8. Esser, B. & Grönig, H.: Equilibrium Shock Tube Flow of Real Gases, Grönig, H. (Ed.), Proc. of the 16th Int. Symp. on Shock Tubes and Waves, VCH-Verlagsgesellschaft, Weinheim, Germany, 1988, pp. 663 - 669.

9. Olivier, H. & Vetter, M. & Grönig, H.: High Enthalpy Testing in the Aachen Shock Tunnel TH 2, In: Proc. of the First Europ. Symp. on Aerothermodynamics for Space Vehicles, ESA SP - 318, Noordwijk, Netherlands, 1991, pp. 377 - 384.

10. Vetter, M. & Olivier, H. & Grönig, H.: Flow over Double Ellipsoid and Sphere - Experimental Results, Workshop on Hypersonic Flows for Reentry Problems, Part II, INRIA, GAMNI- SMAI, Antibes, France, 1991.

11. Sawley, H.L. & Wütrich, S.: Nonequilibrium Hypersonic Flow Simulation using a Coupled Euler/Boundary Layer Method, In: Proc. of the First Europ. Symp. on Aerothermodynamics for Space Vehicles, ESA SP - 318 , Noordwijk, Netherlands, 1991, pp. 387 - 392.

12. McIntyre, T.J. & Atcitty, C.: Pistons and Compression Tubes - Piston motion in the high enthalpy shock tunnel (HEG), DLR IB 222 - 90 A 20, 1990.

13. McIntosh, M.K.: Computer program for the numerical calculation of frozen and equilibrium conditions in shock tunnels, Australian National University, 1968.

14. Morgan, R.G., Paull, A., Stalker, R.J., Jacobs, P., Morris, N., Stringer,I. & Brescianini, C.: Shock tunnel studies of scramjet phenomena, NASA-CR-181721.

15. Page, M.W., Stalker, R.J.: Pressure losses in free piston driven shock tubes, Proc. 14th Int. Symp. on Shock Tubes and Shock Waves, Sydney, 1983.

16. Hannemann, K,: Design of an axisymmetric, contoured nozzle for the HEG, DLR FB 90-04, 1990.

17. Grauer-Carstensen, H.: Comments on results of the 1st heat flux measurements in the HEG. HEG-Project Meeting, 04.03.1992, Göttingen.

18. Vardavas, I.M.: Modelling reactive gas flows within shock tunnels, Australian J. Phys. 37,157-177, 1984.

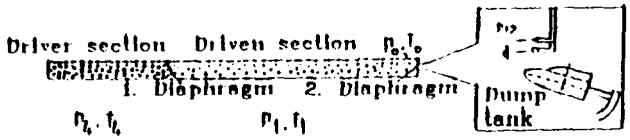
Driver section
Driven section
p_0, T_0
1. Diaphragm
2. Diaphragm
Dump tank
p_4, T_4
p_1, T_1

Condition	p_4	T_4	p_1	p_0	T_0	h_0	M_∞	$Re_{\infty l}$	u_∞
	bar	K	bar	bar	K	MJ/kg	–	10^6/m	m/s
I	100	293	1	66	1500	1.7	7.0	3.6	1740
II	350	600	1	190	2700	3.3	7.3	3.7	2490
III	650	600	0.7	360	3800	6.1	6.9	3.4	3050
IV	1100	620	0.6	650	4700	8.8	6.7	3.2	3470
V	100	293	0.9	63	1500	1.7	11.3	1.3	1763
VI	460	600	1.2	230	2700	3.3	11.3	1.3	2480
VII	1300	620	0.7	630	4600	6.6	12.1	0.8	3560

Tab. 1: Some typical test conditions of Shock Tunnel TH 2.

Shot #	Burst Pressure (bar)	Comp. Ratio	Shock Tube Pressure (bar)	Shock Speed (km/s)	Reservoir Pressure (bar)	Reservoir Temperature (K)
3	91	36.1	0.20	2.92	66	5930
4	109	40.1	0.20	2.89	47	5540
5	119	42.2	0.20	3.09	73	6320
6	539	65.0	0.20	4.76	420	9710
7	557	64.8	0.17	4.79	380	9700
8	496	58.1	0.26	4.57	430	9450
9	476	56.6	0.31	4.41	455	9270
10	516	59.1	0.35	4.34	490	9210
11	508	58.6	0.17	4.09	480	9290
12	529	60.4	0.47	4.04	510	8860
13	495	58.0	0.33	4.44	470	9300

Table 2: *Summary of the HEG calibration conditions.*

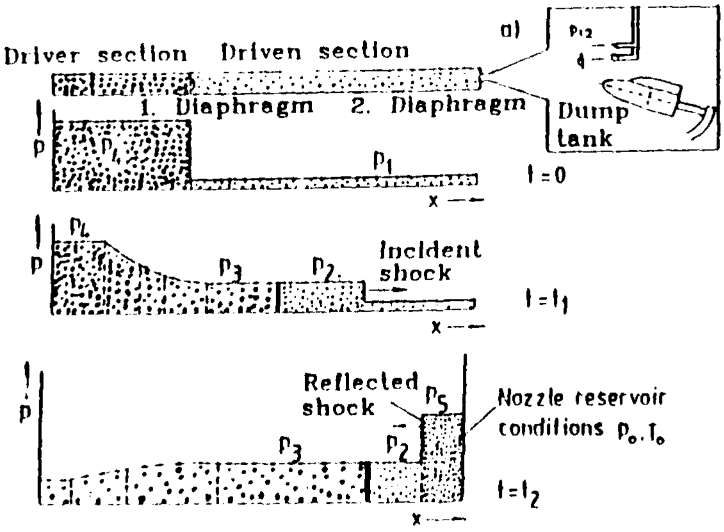
a)
p_{12}
Driver section
Driven section
1. Diaphragm
2. Diaphragm
Dump tank
p
p_4
p_1
t = 0
x
p
p_4
p_3
p_2
Incident shock
t = t_1
x
p
Reflected shock
p_5
p_3
p_2
Nozzle reservoir conditions p_0, T_0
t = t_2
x

Fig. 1: Schematic setup and operating principle of a shock tunnel.

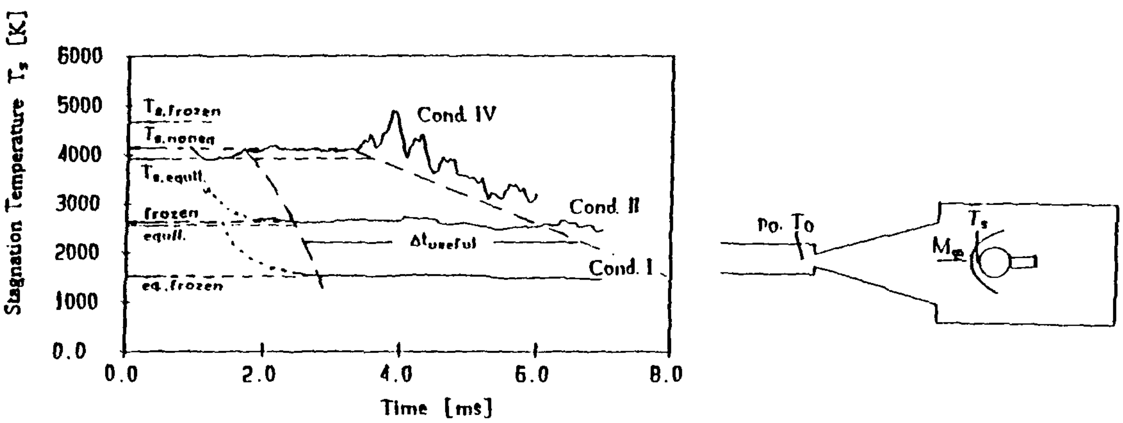

Fig. 2: Time histories of stagnation temperatures for different test conditions.

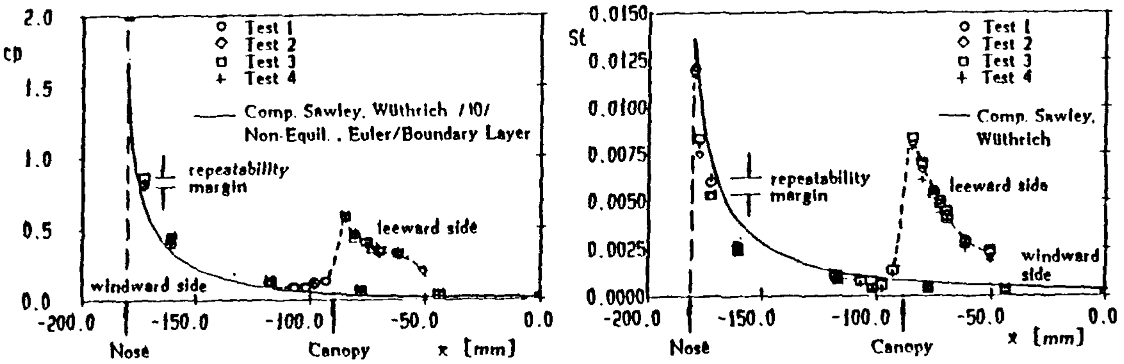

Fig. 3:
Pressure and Stanton number
distribution around double ellipsoid
model, flow cond. IV.

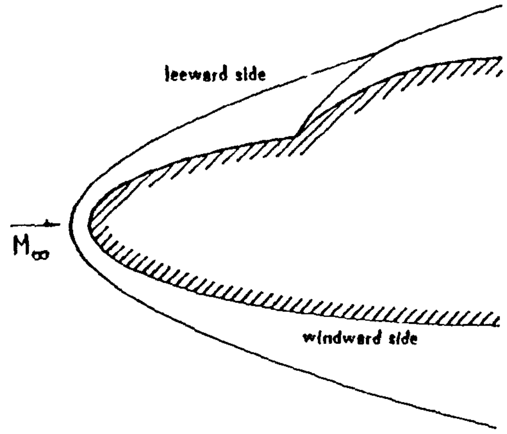
leeward side
M_∞
windward side

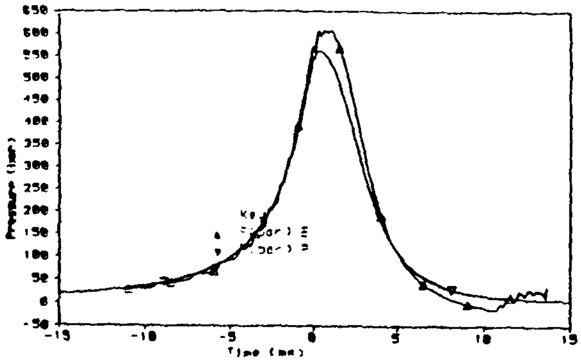

Figure 4: The experimental driver gas pressure overshoots the predicted pressure.

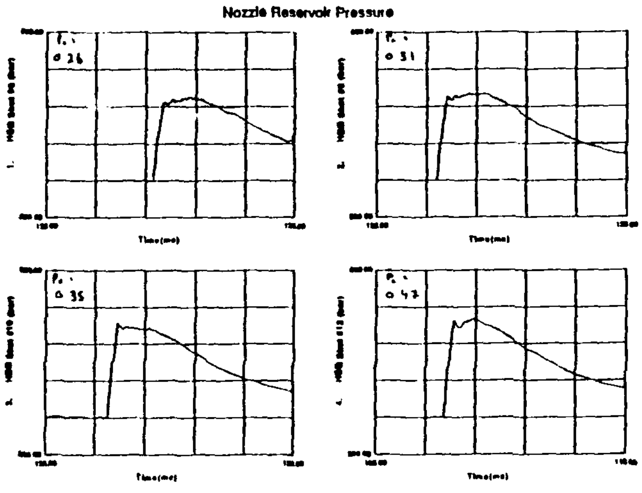

Figure 5: Nozzle reservoir pressures at different tayloring conditions

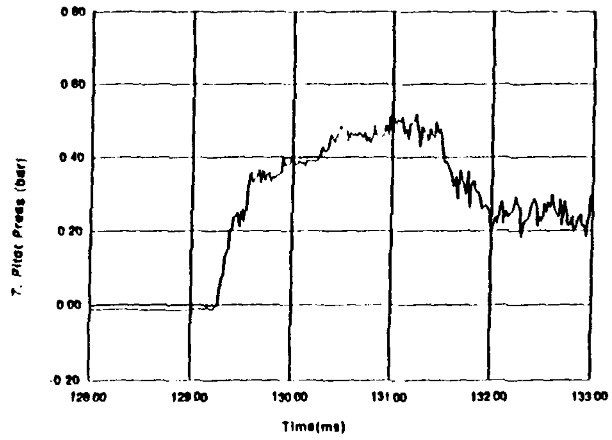

Figure 6: Measured pitot pressure trace

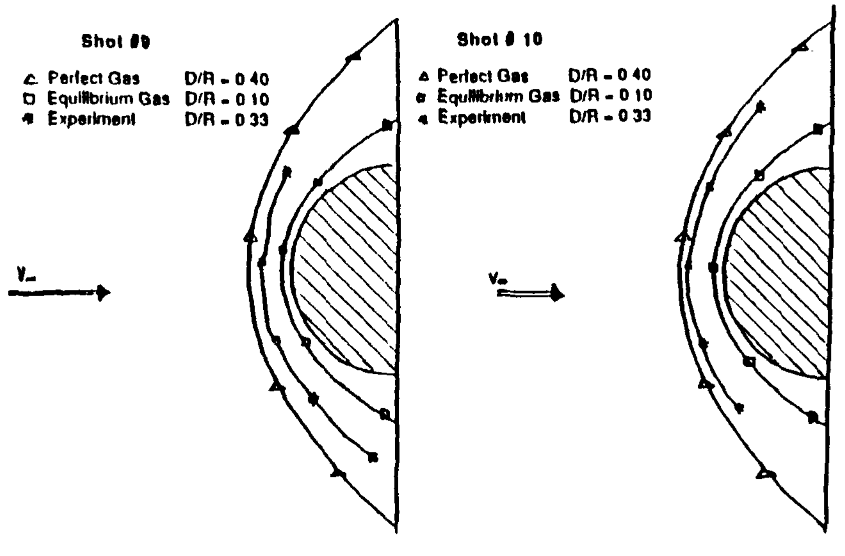
Shot #9
△ Perfect Gas D/R = 0.40
□ Equilibrium Gas D/R = 0.10
◄ Experiment D/R = 0.33
V∞
Shot # 10
△ Perfect Gas D/R = 0.40
□ Equilibrium Gas D/R = 0.10
◄ Experiment D/R = 0.33
V∞

Figure 7: Measured and calculated shock shapes on a cylinder.

DESIGN AND PRODUCTION OF INSULATED WIND TUNNEL MODELS OF THE HERMES SHUTTLE FOR HEAT TRANSFER MEASUREMENTS AT HYPERSONIC SPEEDS

L. Visintini
Chief Aerodynamics Department - AerMacchi S.p.A.
Via Sanvito 80 - 21100 VARESE - Italy

C. Couedor
Dept. Aérodynamique Expérimentale - Dassault Aviation
Avenue de l'Europe - 78140 VELIZY - France

SUMMARY

Among all kind of wind tunnel experiments undertaken up to now by Dassault Aviation to develop the European HERMES shuttle, those relative to heat transfer measurements could be the last to be fully accomplished.

To some extent, one could say that difficulties came from sensors themselves, from their integration conditions, and finally from additional similitude parameters not considered before.

The paper introduces to Dassault Aviation so-called "insulated models" and describes the ongoing activity developed with the collaboration of AerMacchi.

The models have the purpose of making heat transfer measurements with correct simulation of surface temperatures due to its demonstrated effect on boundary layer transition.

A number of pathfinder models have been developed for this purpose: after a first attempt made by using a machinable ceramic, the second one was intended for surface temperatures up to 400 °C and was made in a temperature resistant composite material, and the third one, able to sustain skin temperatures above 1000 °C, is made by an insulating ceramic coating on a steel core.

The fluid-dynamic and technological aspects related with the design and manufacture of these models are described.

LIST OF SYMBOLS

c	specific heat (J/Kg/°K)
h	depth (m)
k	thermal conductivity (W/m/°K)
t	time (sec)
T_w	wall temperature (°K)
T'_i	flow temperature after bow shock (°K)
α	thermal diffusivity $= k/\rho c$
ρ	density (Kg/m^3)

1. INTRODUCTION

Heat transfer measurements have a large importance in the design of high speed and re-entry vehicles and must still be considered an area of technical risk requiring development of the experimental techniques.

The uncertainties in the experimental data are still very large and no reliance can be given to CFD tools until experimental data of high quality are available in order to support code validation.

Also, the correct simulation of the full scale flow conditions is of key importance for the correctness of the heat transfer measurements as much as for force or pressure results.

Dassault Aviation began hypersonic heat transfer measurements for the european Hermes space shuttle by the end of 1986 with the available methodologies in several European facilities.
The tests could be classified in the following way:

- for local measurements, "thick wall" techniques on steel high conductivity models, using platinum thin film sensors on insulating inserts or co-axial thermocouples;
- for global measurements "thick wall" mapping techniques using thermosensitive paints on low conductivity models ("Silastène" siliconic rubber).

By 1989 it was clearly demonstrated that results obtained on identical scale models tested in the same cold hypersonic blow-down wind tunnel were not consistent.
The typical test result (Fig. 1) shows what looks like an anticipated transition at $\alpha = 40°$ on the insulated Silastène model.

After careful roughness checks, such trends were attributed to skin temperature differences. In the specific test conditions the two procedures led to very different ratios of T_w/T'_i, being respectively in the order of 0.3 for the metallic model and 0.5 for the Silastène one.
Due to the critical importance of having the correct boundary layer transition and associated heat fluxes, it became necessary to develop a new family of models by which to make heat transfer measurements with correct skin temperature.

The present paper summarizes the work done up to now in this respect.

2. FLUID-DYNAMIC REQUIREMENTS

Wall temperature may effect hypersonic flowfields and related heat transfer rates through a variety of mechanisms.
In "cold" (i.e. perfect gas) hypersonic flows wall temperature affects [1-5,10]:

- local skin friction and Stanton number in laminar and turbulent boundary layers;
- boundary layer thickness and related viscous interaction phenomena;
- mostly important, boundary layer stability and transition;
- shock-wave/boundary layer interactions and related separated flows.

The topic of wall temperature effect on transition at hypersonic speed is discussed in detail in refs. 4-5, but is still unclear. For moderate cooling transition is delayed, just as for subsonic flow, while for highly cooled walls there is evidence of reversal of such a trend.

In high temperature hypersonic flows further effects come in, related to:

- the non-linear behaviour of heat transfer, since Stanton number depends on fluid properties at the wall;
- the change in the level of gas dissociation with temperature (for equilibrium flows or in presence of wall catalycity).

All of the above arguments stress the importance of making hypersonic tests in general, and heat transfer measurements in particular, on models having the correct temperature ratio T_w/T'_i (for "cold" flows) and correct surface temperatures (for "hot" flows).

3. THE CONCEPT OF THE MODELS

The models are partial models whose geometry is representative of the front part of an early Hermes shape at 1/30 scale. Their purpose is to develop and prove the technology of model manufacture and instrumentation and the related experimental procedures.

Dassault Aviation built a first pathfinder model in 1990. The model was composed of an upper steel part including attachment to the sting and a removable windward part made of machinable MACOR ceramic. The equipment essentially consisted in platinum thin film sensors produced by ONERA (Fig. 2).

The major difficulties encountered during both machining and thin film equipment of this simplified model have cancelled any hope to build complete Hermes models (including removable control surfaces) in such brittle materials.

Only few tests could be performed with this model in a narrow temperature range, which did not allow to draw any conclusion about the influence of the wall temperature on heat transfer measurements.

At this stage AerMacchi was chosen to carry on with this kind of models.

A first version (Model 3036.1, Fig. 3) was produced during 1991 by using an advanced temperature resistant composite material. A body flap was added to the basic nose in order to include a typical control surface component with its associated high loads and small thicknesses.

This model is equipped with chromel/constantan co-axial thermocouples developed and integrated by ONERA and is suitable for short test times and surface temperatures up to 400° C.

It was initially meant for tests in the "cold" hypersonic regime at ONERA S4MA (M=6.4 and 10) and R3Ch (M=10) blow down wind tunnels.

Later shift of the emphasis to higher temperature flows brougth to the decision to use the model as a first step in heat transfer measurements in the new high enthalpy tunnels ONERA F4 in Toulouse [7] and DLR RWTH2 in Aachen [6] (Fig. 4) .

Postponed for reasons without relation with the model, the tests are now scheduled for early autumn 1992.

In the meantime a new specification was issued by September 1991, focusing on the need to reach flight temperature ratios (T_w/T'_i = 0.3 to 0.35) in the same high temperature flow conditions (Model 3036.2).

The following parts of this paper will focus on the description of the design and technological, choices related with the design and manufacture of these two models.

4. MEDIUM TEMPERATURES: Model 3036.1

4.1 The requirement

After the difficulties encountered by the first ceramic model, the 1990 requirement aimed mainly at obtaining a model made in a tougher material and using a technology that could be extended to the manufacture of a complete model, even at the expense of the maximum allowable skin temperature.

It called for a material:

- able to withstand a continuous service temperature of 250 °C with local surface temperature peaks of 400 °C for periods up to 15 secs;
- having a low thermal conductivity so that the required surface temperatures could be achieved during the available running time.
  This requirement called for limits in the so called "thermal product" $\sqrt{\rho c k}$ which had to satisfy the following relationship:
  $$750 < \sqrt{\rho c k} < 1050 \quad (J/m^2/°C/sec^{0.5})$$
- being thermally isotropic as much as possible;
- having an ultimate bending strength of 15 Kg/mm^2 or more up to the service temperature of 250 °C;
- having enough toughness and resistance to thermal stresses;
- being machinable or formable to precise (surface tolerance of ±.05 mm) and complex shapes and small thicknesses (few mm);
- allowing a good surface finish (order of 1 μm).

4.2 Choice of the material

The search for the appropriate material was conducted on a broad spectrum of options. Of course any conventional metallic material is ruled out by its high thermal conductivity and even "low conductivity" stainless steels have a thermal product as high as 7500.

The following classes of materials have been examined:

- advanced ceramics
- refractory materials (fused bonded silica)
- graphites
- high temperature plastics and composites.

Graphites have been quickly ruled out by their low mechanical strength and high conductivity, and refractory materials because of their low strength.

A range of advanced ceramics, promising high toughness and resistance to thermal shocks, was examined (see Table 1), but very few of them were found to have or approach the required properties. Ceramics were finally dropped because of the difficulty in the production of precise shapes and in the fastening of components.

Plastics have had in recent years a rapid evolution towards higher temperature resistance, this evolution being driven mainly by the manufacture of engine cowlings for civil and military aviation.

A panorama of advanced polymers is reported in Table 2, which was limited to commercially available materials, thus excluding laboratory or "new" materials which could not be procured within the planned time frame.

The table shows poly-imides as the family of polymers with the highest temperature resistance. Among this large family there is still a variety of products from the different manufacturers and with different properties.

The final choice was based on the following priority criteria:

1- highest temperature resistance, which, for a termosetting polymer, is measured by its glass transition temperature;

2- availability as a reinforced composite in order to achieve the required strength;

3- availability in the form of machinable plates and blocks, reinforced with "short" fibers in order to achieve a macroscopically isotrope structure.

The choice fell on the resin system called PMR-15, originally developed by NASA Lewis Research Center, having a declared glass transition temperature in excess of 400 °C and commercially available from different manufacturers. This choice satisfied criteria 1) and 2) above but not criterion 3), since the composite, at the time, was only available in the form of glass and carbon fibre pre-pregs for the preparation of laminates.

4.3 Production process

The production process envisaged for the manufacture of the model required:

a) polymerization of the cloth pre-pregs in the form of thick plates; cloths are stacked in the form a symmetrical and balanced laminate so that a macroscopic isotropy is achieved at least in the plane of the layers;

b) bonding of such plates in blocks of the required thickness;

c) machining of the blocks to the final shape by using special tools on conventional N/C milling machines.

The technological difficulties of the process were mainly related to the difficulties in the polymerization of the pre-pregs since:

a) the resin contains carcinogenic substances which may be harmful and require safety precautions;

b) poly-imides release a large amount of volatiles during polymerization. This limits the maximum thickness of the plates and calls for special evacuation procedures;

c) polymerization requires a temperature of 300 °C and pressures of 15 bar which is above what normally required for conventional composites. A heated platen press was used.

From the point of view of the wind tunnel model requirements the main drawback of the approach was related to the layered structure of the final blocks which raised concern about its degree of isotropy.

4.4 Qualification tests

The following qualification tests were performed in order to verify the achievement of the original specification:

a) inspection of the composite laminate by ultrasonic technique in order to guarantee the absence of blisters within the layers;

b) measurement of the glass transition temperature, which was shown to be about 330 °C. This guarantees a service temperature (at low stresses) up to 300 °C and can be exceeded locally for short periods since the resin is a termoset and its transition temperature is actually raised by heating to 300 °C.

c) measurement of the mechanical characteristics, which showed a tensile strength of 48 Kg/mm^2 up to 250 °C for the simmetrical and balanced laminate.

d) measurement of the thermal characteristics in terms of heat capacity and conductivity. Such measurements showed that the degree of nonisotropy of the laminate is in fact much less than expected and that final values of the thermal product fall exactly within the required boundary (Fig. 5).

e) geometrical and surface roughness inspection.

4.5 Simulated behaviour

The behaviour of the model during wind tunnel tests was simulated for the model stagnation point by one dimensional finite volume solution of the Fourier heat transfer equation using the actual temperature dependent material properties and the estimated heat fluxes. Heat radiation from the model surface was also taken into account.

Simulations have been made for the case of ONERA S4 wind tunnel at M=10 where tests were initially planned. The estimated initial stagnation point heat flux by using conventional semi-empirical approximations (e.g. see ref. 1) in this case is about 0.4 MW/m^2. Figs. 6 and 7 show that the limit skin temperature is reached after less than 10 secs of running time. Also shows the desired large increase in surface temperatures compared to a conventional steel model. The model heating is limited to a depth of less than 5 mm and falls down rapidly after the end of the blow.

The running time of the ONERA F4 arc-jet tunnel now considered for tests is only 10 msec. Free stream conditions and stagnation point heat fluxes have been estimated from the published nominal operationg points[6] by assuming equilibrium flow expansion in the tunnel nozzle and the well known Fay-Riddel correlation[9] (Fig. 8).

Figs 9 to 11 show that the model characteristics are well balanced for testing at the low density boundary of the tunnel performance (nozzle 1, min pressure) where the heat flux is about 5 MW/m^2. Again a surface temperature above 500 °C is reached before the end of the run. A higher temperature resistance is required for the higher density cases.

4.6 Heat flux instrumentation

Twelve standard ONERA coaxial thermocouples* are distributed along the windward certerline, including the flap. The metallic deposit which makes electrical surface contact between chromel and constantan is less than one micron thick, thus ensuring measurement of the temperature at the model surface. Its ability to withstand erosion is very high and, in case of need, repair is quick and easy, directly in the wind tunnel.

Having an external diameter of 2.7 mm, one can verify that the thermal wave is contained within the boundaries of the thermocouple for the expected runtime of the high enthalpy facilities. This enables simplified data processing without any interference from the thermal characteristics of the surrounding model material.

5. HIGH TEMPERATURES: Model 3036.2

5.1 The requirement

Following the increasing emphasis in high temperature hypersonics the new requirement issued in september 1991 called for a model able to allow testing in the full operational envelope of the F4 and RWTH2 wind tunnels with representative skin temperatures.

In particular the specification asked for:

a) the capability to reach surface temperatures in excess of 1000 °C, preferably as high as 1300 °C;

b) the lowest possible heat conductivity (thermal product $\sqrt{\rho c k} < 2500$), so that the model can reach the desired skin temperatures within the 10 msec running time;

c) again, that material and processes shall permit to build complex complete models instrumented with about 100 thermocouples. In order to demonstrate this possibility a number of representative model components is to be manufactured and qualified.

A look to the properties of ceramic materials (Table 1) shows that very few of them have a value of thermal product low enough to satisfy requirement a). Also, a little thermal analysis[8] shows that the penetration depth of a heat pulse is $h = 4\sqrt{at}$, so that a thickness of only 0.5 mm is involved in the heating process.

5.2 Selection of the coating

After a first review of the new requirement the concept of a model made by bulk ceramic material was again ruled out on the basis of considerations similar to the earlier ones. The thermal shock stresses in this case are much larger, thus raising the risk of brittle fracture, the mechanical strength requirement would ask for very hard materials which are very difficult to shape and almost impossible to machine and finally the problem of fastening different model components would be a very tough one.

The fact that only a thin layer of insulation is sufficient to achieve the desired temperatures creates the possibility of making a ceramic coating to an otherwise conventional metallic model, which is a much more attractive option.

Two processes have been evaluated:

a) a glass ceramic coating achieved by electrophoretic techniques;

b) a zirconia (ZrO_2) coating applied via an intermediate MCrAlY bond coat by the plasma spray technique.

Option a) required a fairly long and expensive development program in order to find the appropriate glass/metal combination having matched expansion coefficients, the required temperature resistance and thermal properties.

Option b) is a technology which was developed for the thermal protection of engine turbine blades and is considered to be a more "mature" technology.

Its main advantages are:

- very good resistance to thermal shock;
- possibility to use different ceramics, with varying thermal properties and toughness on almost any metal core;
- the coating contains approx 10% porosity which helps increase the thermal insulation further. In fact the average thermal conductivity of the coating as sprayed is only 1.3 W/m °K.

Its limits are:

- the need to test the spraying procedure on several specimens of each component in order to achieve a uniform thickness;
- the high roughness of the deposited layer (about 2 μm), which requires some kind of polishing of a very hard surface;
- the difficulty of obtaining and mantaining sharp corners.

5.3 Production process

The following production process has been devised:

- metal core pieces are produced and geometrically inspected as for a conventional model; three specimens are required for each final model component;
- pieces are coated by plasma spray technique and coating thickness is controlled and inspected by an eddy current machine;
- surface is finished by hand using special tools for hard materials in order to achieve the required surface finish.

5.4 Qualification tests

In order to asses the capability of the selected coating to withstand the wind tunnel environment a number of qualification tests are performed.

These include:

a) mechanical tests, for the presence and growth of cracks in the coating during repeated mechanical load;

b) thermal resistance tests, by exposing specimens of the coating to heat pulses of 10 msec with a thermal flux of increasing intensity and examining the presence of damage by metallographic techniques;

c) thermal "fatigue" tests, by again exposing specimens to repeated thermal shocks at intensity level and number of exposures representative of wind tunnel model usage.

The heat flux for the thermal tests is generated by a de-focused high power CO_2 laser pulse (20 KW).

5.5 Simulated behaviour

Temperature distributions in the coating at the model stagnation point have been simulated by using the same software and heat flux estimates described above. Only room temperature material properties are available at the moment.
Figures 12 to 14 show that:

- for the reference high enthalpy condition with nozzle 2 (case E) a local surface temperature of 1050 °C can be reached;
- the whole heating process is concentrated in the coating layer and the steel is not heated above 60 °C;
- temperatures above 1000 °C last for less than 1 msec and for a thickness of less than .01 mm.

5.6 Heat flux measurements

The model will be initially instrumented with the same ONERA coaxial thermocouples already described for model 3036.1.
Infrared thermal mapping will also be considered as a back up possibility.

5.7 Special issues related to high temperature tests

It is well known that high temperature flows are characterized by chemical reactions of dissociation and recombination and that surface heat fluxes in such conditions include a component due to atom diffusion. Under such conditions and especially with a hot surface, the catalytic properties of the wall play a role in the actual heat fluxes.

Possible effects of wall catalycity on heat fluxes at stagnation point in ONERA F4 have been estimated by using again the Fay-Riddel formula[9] and are shown in Fig. 12. Up to now the topic of catalytic "similarity" of wind tunnel models for high temperature wind tunnel tests has not been addressed yet.

[illegible] can be made:

- the available information show that the catalytic properties of zirconia are not very different from silica which is a typical material for the heat shield "tiles" or "shingles";
- in any case the ceramic powders used for the plasma spaying can be varied and their chemical composition adjusted, to some extent, in order to fit requirements in this sense. In particular different metallic oxides (MgO, Y_2O_3 or CeO_2) may be added to ZrO_2 for stabilization;
- both zirconia and silica are low catalicity materials. There is therefore a risk of contamination, scatter of results and increasing catalycity with model wear, particularly in the high enthalpy corner of the tunnel envelope.

6. CONCLUSIONS

Early heat tranfer tests of the HERMES shuttle have shown the importance of having the correct simulation of model surface temperatures. This evidence has started a technological research activity for the development of appropriate materials, instrumentation and manufacturing processes for the production of wind tunnel models able to satisfy this requirement. Two pathfinder models have been produced up to now covering skin temperatures up to 400 °C and 1000 °C respectively. Testing of these models in ONERA F4, now planned in the fall of 1992, will demonstrate the technique and will open the way to complete models which will help filling up the experimental aerothermodynamic data set of the HERMES shuttle.

ACKNOWLEDGEMENTS

Special thanks to Dr. V. Wagner, Materials Science Specialist, Dr. A.M. Colombo, New Technologies Dept., Mr. F. Pacori, Wind Tunnel and Model Workshop Manager and Dr. A. Masciocchi, Laboratory Specialist of AerMacchi for their continuing support in this project and to Mr. Gallazzi of Monfrini S.p.A. for his assistance in the production of PMR-15 laminates.

REFERENCES

1. Anderson J.D., "Hypersonic and High Temperature Gas Dynamics", McGraw Hill, 1989
2. Van Driest E.R., "Investigation of Laminar Boundary Layer in Compressible Fluids using the Crocco Method", NACA TN 2579, Jan 1952
3. Delery J.M., "Shock Interference Phenomena in Hypersonic Flows", in 3rd Joint Europe/US Short Course in Hypersonics, Aachen, 1990
4. Stetson K.F., "Hypersonic Boundary Layer Transition", in 3rd Joint Europe/US Short Course in Hypersonics, Aachen, 1990
5. Arnal D., Aupoix B., "Hypersonic Boundary Layer Transition and Turbulence Effects", in Proceedings of the 1st European Symposium on "Aerothermodynamics for Space Vehicles", Nordvijk, 1991
6. Muylaert J. et al., "Review of the European Hypersonic Wind Tunnel Performance and Simulation Requirements", in Proceedings of the 1st European Symposium on "Aerothermodynamics for Space Vehicles", Nordvijk, 1991

7. Chevallier J.P., Cristophe J., Girard A., "High enthalpy wind tunnel F4: general description and associated instrumentation", in DGLR meeting on "Measurement Techniques in Hypersonics", Goettingen, 1989

8. Schultz D.L., Jones T.V., "Heat-transfer Measurements in Short-duration Hypersonic Facilities", AGARDograph No. 165, 1973

9. Fay J.A., Riddell F.R., "Theory of Stagnation Point Heat Transfer in Dissociated Air", Journal of the Aeronautical Sciences, Vol. 25 No. 2 pp. 73-85 Feb. 1958.

10. Back L.H., Cuffel R.F., "Shock Wave/Turbulent Boundary Layer Interactions with and without Surface Cooling", AIAA Journal Vol. 14 No. 4 pp. 526-532 (Apr. 1976).

Table 1

ADVANCED CERAMIC MATERIALS

Thermal and mechanical data

	Components	Commercial name	Temp. max. °C	Density Kg/m3	Heat cap. J/Kg/°K	Heat cond. W/m/°K	Therm. prod. √ρck	Bend. strength Hbar
ZIRCONIA	ZrO2	ZN100	1000	6.000	400	2.5	2450	
		ZFCE	2500	5.700	670	1.9÷2.2	2690+2900	20+18
		ZFME	2500	5.800	680	1.9+2.2	2740+2950	50÷25
ALUMINE		AF950	1650	3.650	980	22.1+8.6	8890+5550	30+22
	96% Al2O3	V38	1200	3.700	900	20	8160	30
CORDIERITE	MgAlSi	--	--	2.900	700/900	2	2150	12
TIALITE	Ti/Al2O3	Ti20	950	3.650	1000	2.5	3020	6(?)
SILICA CARBIDE	SiC	CS102/107	1200	3.050	700	100	14600	30
SILICA NITRIDE	Si3N4	NR115	1400	2.400	700	11	4300	22
		KERNIT	1300	3.190	800	30+15	6190+8750	80(?)
GLASS-CERAMIC	SiO2/Al2O3/MgO	MACOR	1000	2.520	840	1.68	1690	10.5
GLASS	SiO2/CaO/Na2O	Common	750	2.200	720	1.3+1.5	1600	15
	SiO2/Na2O/B2O3	Pyrex	850	2.250	700	1.08+1.3	1500	15

All material properties at room temperature

Table 2

TEMPERATURE RESISTANT POLYMERS

Class	Manufacturer	Commercial name	Service temperature (°C)	Glass transition temperature (°C)
Adv. Epoxy	Various	--	180+200	--
Siliconic	Bayer	--	250	--
	Davidson	Ferobestos	300	--
	"	Feroform	350	--
	"	Etaling	450	--
Peek	ICI/Polypenco	PEEK 450	--	330
Polyetherimides	DuPont/GE	--	250	--
Polyimides	Rhône-Poulenc	Kinel	--	300
	DuPont	Vespel	--	360
	Polypenco	Envex	--	290
	Amoco	Torlon	--	280
	DuPont	Avimid	?	?
Addition Polyimides (PMR-15)	Ferro	--	300	--
	Cyanamid	Cycom 3006	310	--
	ICI	966C/D	300	up to 420

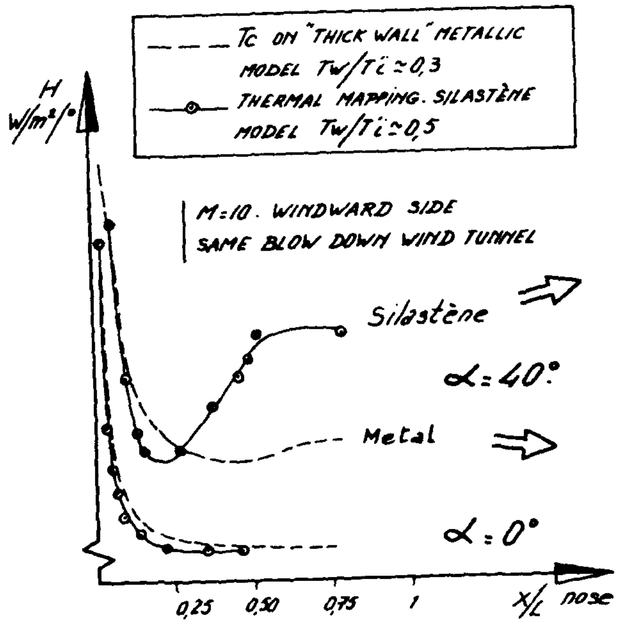

HERMES NOSE MODELS λ = 1/30 . 1989

Fig. 1 - HEAT TRANSFER MEASUREMENTS TYPICAL DISCREPANCY ATTRIBUTED TO SKIN TEMPERATURE

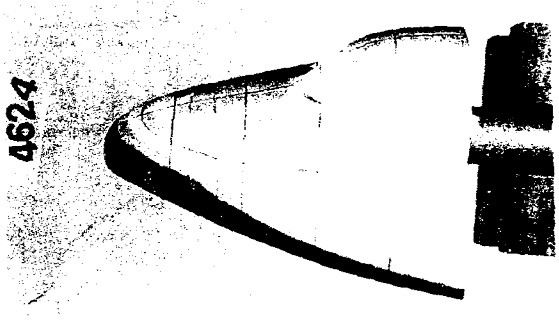

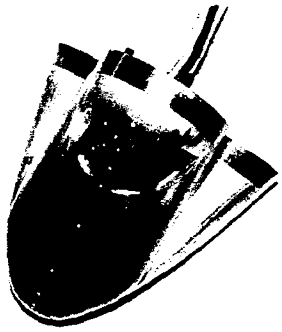

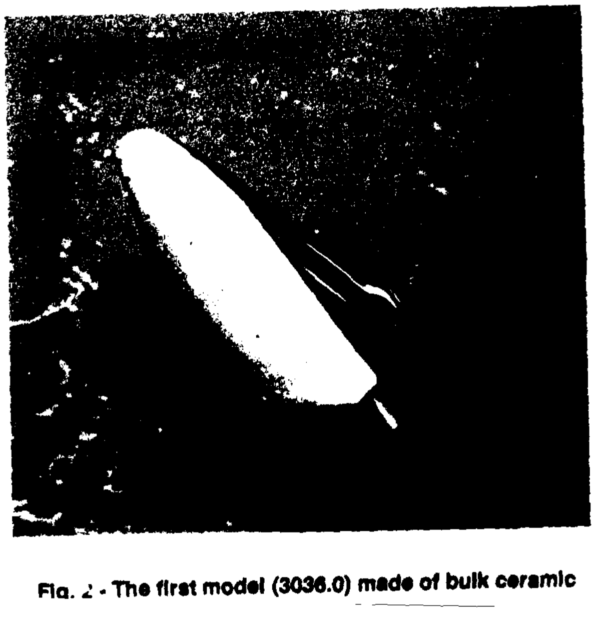

Fig. 2 - The first model (3036.0) made of bulk ceramic

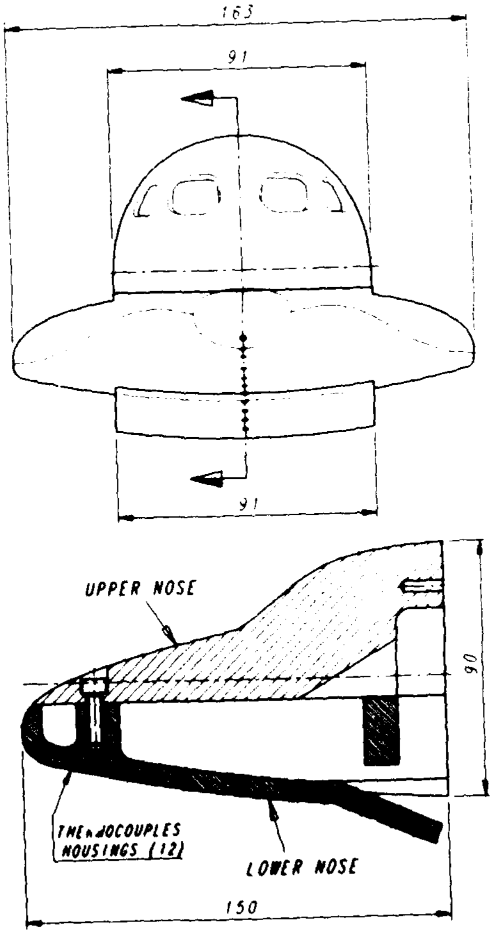
163
91
91
UPPER NOSE
90
THERMOCOUPLES HOUSINGS (12)
LOWER NOSE
150

Fig. 3 - Geometry of models 3036.1 and 3036.2

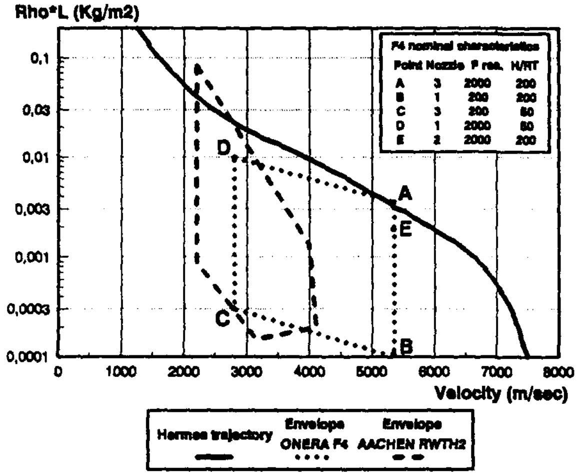

Fig. 4- European high entalpy facilities (ref.6)

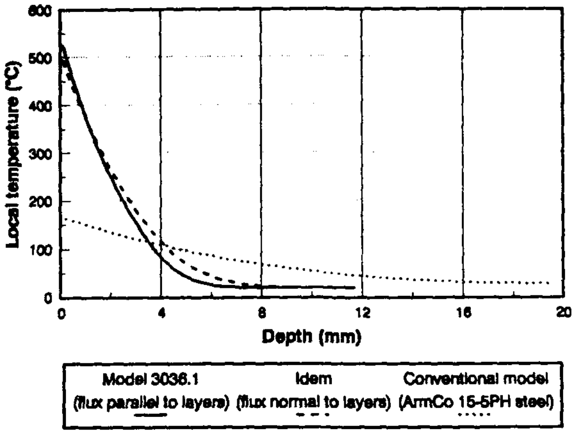

Fig. 7-Temperature distribution at end of blow
Stagnation point
Model 3036.1 in ONERA S4 (M=10.2, Pt=95 bar)

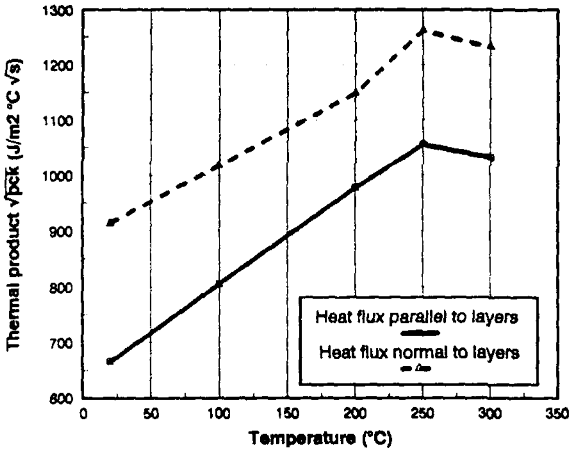

Fig. 5 - Thermal characteristics of Model 3036.2
carbon fiber/PMR-15 laminates

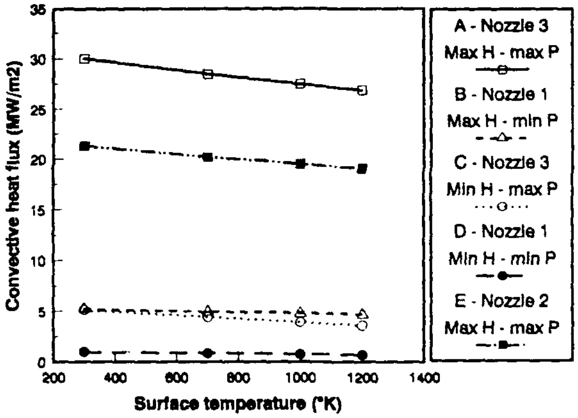

Fig. 8 - Estimated convective heat fluxes at
stagnation point for model 3036 in
ONERA F4 high enthalpy tunnel.

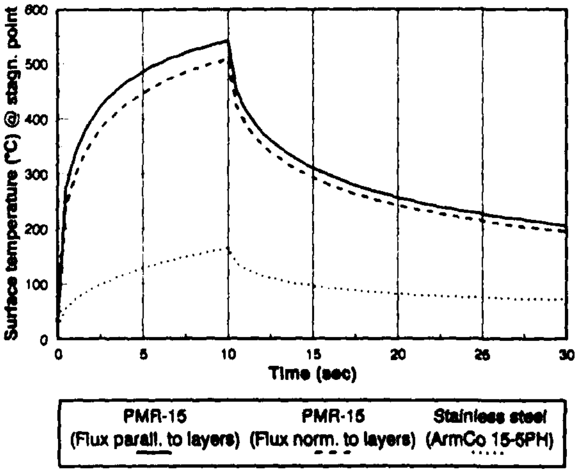

Fig. 6-Predicted surface temperature time history
Model 3036.1 in ONERA S4 (M=10.2, Pt=95 bar)

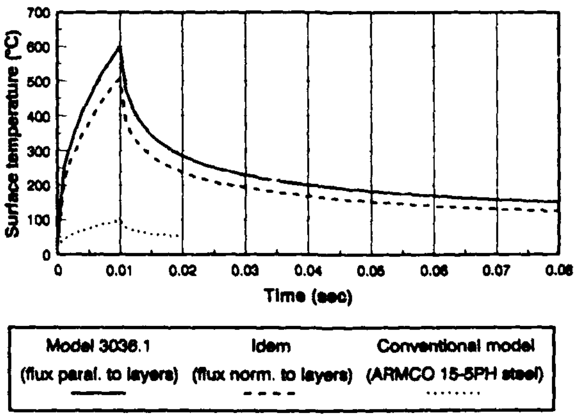

Fig. 9 - Surface temperature time history
Model 3036.1 stagnation point
ONERA F4 (point B, H/RT=200, P=200bar, nozzle 1)

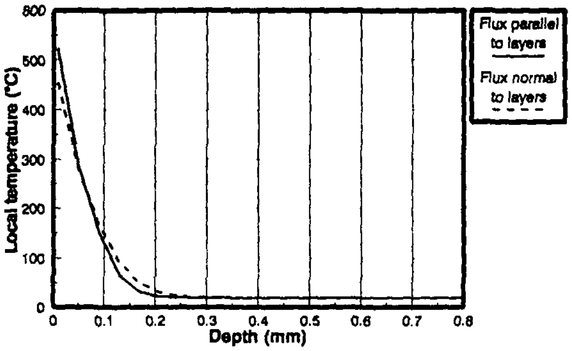

Fig. 10 - Temperature distribution at end of blow
Model 3036.1 stagnation point
ONERA F4 point B

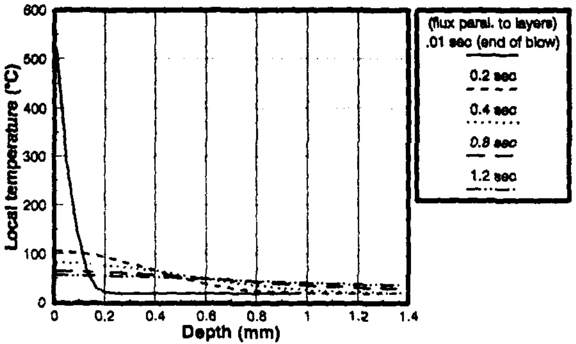

Fig. 11 - Temperature distribution after end of blow
Model 3036.1 stagnation point
ONERA F4 point B

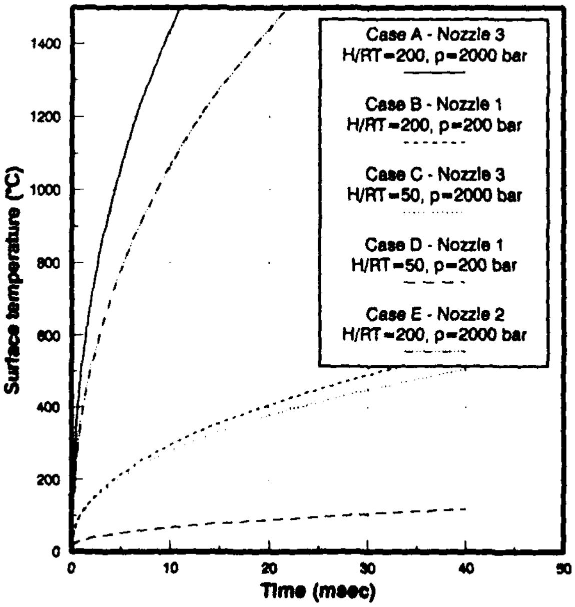

Fig. 12 - Estimated surface temperatures at stagnation point
Model 3036.2 in ONERA F4

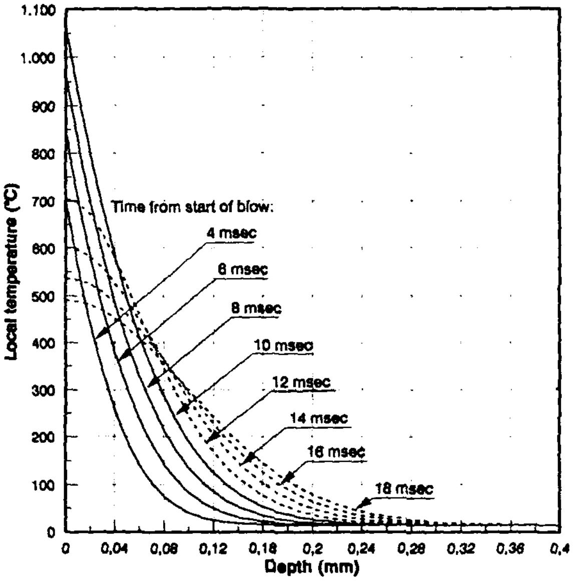

Fig. 13 - Estimated internal temperature distribution
Model 3036.2 in ONERA F4 - Point E

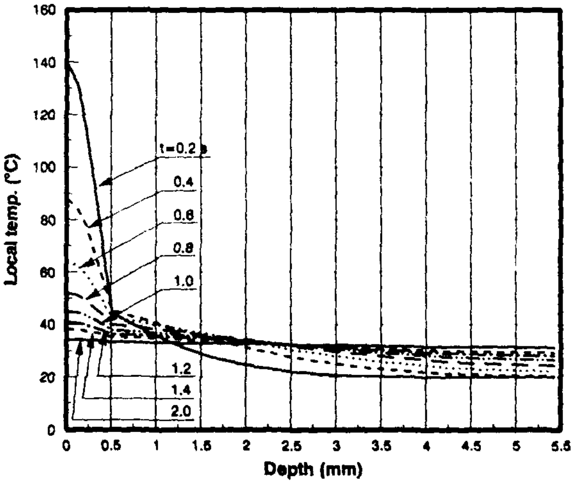

Fig. 14 - Internal temperature distribution
after end of blow at stagn. point
Model 3036.2 in ONERA F4 (Point E)

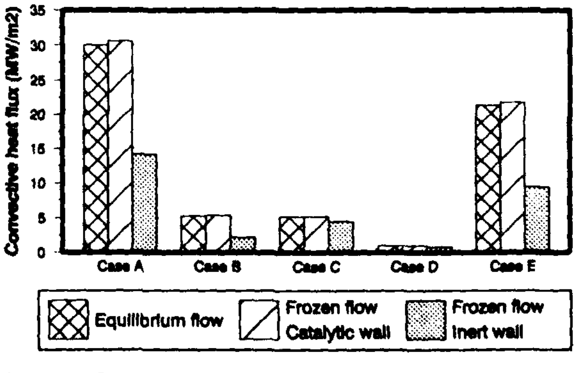

Fig. 15 - Estimated effect of surface chemical properties on stagnation point heat fluxes for model 3036.2 in ONERA F4

The Upgrading of the Arc Heated Wind Tunnel of the DLR (LBK) with Respect to its Effects on the Material Testing

A. Gülhan & K. Kindler
DLR Köln-Porz, WT-WK-KP
Linder Höhe, 5000 Köln-Porz
Germany

Summary

The arc heated wind tunnel (LBK) of the DLR is a useful device for high enthalpy tests of thermal protection systems of spacecrafts. The facility is described concerning its capability in simulation of the gas-surface interaction phenomena at the stagnation point of space vehicles. The working area of the tunnel resulting from tests on SiC-samples is discussed and compared with other arc heated wind tunnels.

To support experimental works on the LBK numerical computations including flow solutions based on chemical equilibrium, frozen chemistry and chemical nonequilibrium have been performed. It is shown that the flow field downstream the nozzle throat is nearly frozen.

Finally the upgrading concept and the proposed performance of the facility are discussed.

1. Introduction

During the reentry phase of space vehicles into the atmosphere the nose cap and wing leading edges are exposed to high thermal loads which are produced by shock waves heating the air up to temperatures at which real gas effects are important. At these high temperatures the simulation of reentry aerodynamics requires not only the duplication of Mach number and Reynolds number to consider the compressibility and viscous effects, but also setting the real gas similarity parameters [1].

In order to distinguish frozen, nonequilibrium and equilibrium flow regimes characteristic reaction and flow times should be compared. The characteristic flow time is determined by the ratio of a characteristic length L and flow velocity V_∞. The time scale to achieve the equilibrium depends on the thermal or chemical processes. While three-body collisions are necessary for recombination binary collisions lead to dissociation. Binary reactions are characterized by $\bar{C} \cdot \rho_\infty \cdot L/V_\infty$, where $\bar{C}$ and ρ_∞ are the reaction rate constant and the density of the free stream. Under the assumption that $\bar{C}$ is the same as in free flight, the binary scaling factor $\rho_\infty \cdot L$ must be duplicated in addition to the velocity, in order to achieve a simulation of the dissociation process. Because of the high density level of shock tunnels or other short time facilities it is possible to produce a nearly equilibrium flow field which can satisfy the above mentioned simulation requirements for a time duration of a few milliseconds [2].

The recombination reactions, which are mostly neglected, can be enhanced due to catalytic surfaces. The characteristic parameter for this process is the surface Damköhler number defined as the ratio of the characteristic particle diffusion time to the characteristic time for surface reaction [3]. Long duration high enthalpy tests must be carried out to investigate this phenomenon. Despite restrictions in simulation of flight environment arising from strong nonequilibrium phenomena in their flow field due to low stagnation pressures the arc heated wind tunnels are very useful tools to analyse the gas-surface interaction behind the shock wave. The development of various suitable materials for thermal protection systems requires such facilities with capability to investigate this phenomenon.

A continuous high enthalpy flow field can be produced by thermal or magnetoplasmadynamic generators, which mainly differ in their acceleration mechanism [4]. While in a thermal plasma generator the test gas is heated by an electric arc and usually accelerated through a nozzle, in a magnetoplasmadynamic generator additional electromagnetic forces are applied to supply the acceleration of the gas.

According to their electrode shape the arc heater can be classified in two groups: hollow electrode arc heater and tungsten rod cathode arc heater. In arc heaters with a rod-shaped cathode the gas is supplied along the cathode. Because of tungsten cathodes being highly sensitive to chemical reaction with oxygen only inert gases or nitrogen can be used. To change the gas composition oxygen or other gases are injected into the main flow downstream the nozzle throat [4]. This type of arc heater is mostly used for low mass flow rates up to 10 g/s, and allows to reach stagnation enthalpies up to 100 MJ/kg.

Most of the high power arc heaters consist of two hollow electrodes positioned either in series or in Y-form. The characteristic curve of these arc heaters is nearly the same despite different geometries [5].

The DC-arc heater of the arc heated wind tunnel (LBK) of DLR consists of two hollow electrodes and can be operated with mass flow rates up to 80 g/s. Operating the tunnel at low mass flow rates like 5 g/s and high current level specific stagnation enthalpies up to 20 MJ/kg can be achieved.

2. Experimental set-up

A high power (1.0 MW) DC-arc heater with hollow electrodes is connected to a thyristor controlled rectifier consisting of four units of 360 kW (600 A, 600 V), which can be operated in parallel or series mode. The test gas received from the DLR storage tanks with a volume of 1000 m³ and maximum pressure of 60 bar is injected tangentially into the injection chamber of the arc heater to force the rotation of the arc. The rotation of the arc foot points on the inner surface of electrodes reduces the erosion rate (8 ppm) and improves the flow quality. Rotation in the flow field is reduced by the expansion in the settling chamber and nozzle. Mass flow rates up to 100 g/s can be controlled by means of the mass flow controller based on the orifice method.

High quality flow conditions can be achieved through an optimization between current and mass flow rate. The voltage of the arc varies depending on the resistance of the gas between two foot points. A further parameter concerning the flow quality, i.e. small fluctuations in thermodynamics properties, is the voltage of the magnetic coil around the anode. The length of the arc and its stability can be controlled by means of this coil.

The LBK has two different test legs called L2K and L3K (Fig. 1). L2K has a cylindrical test chamber with a diameter of 2.6 m and a length of 2 m. The test chamber of the L3K has the shape of a cube of 1.5 · 1.5 · 2.0 m³. The inlet flanges of L2K and L3K have the same geometry, in order to use the same nozzle and arc heater.

The conical nozzles used have a half angle of 12 degree. The throat diameter of nozzles is 14 mm or 29 mm and the exit diameter can be varied between 100 mm, 200 mm, 300 mm, 400 mm and 600 mm. All nozzle parts are water cooled. The expansion part from 400 mm to 600 mm can be cooled with liquid nitrogen too.

Both test legs L2K and L3K have a separate cooling system, which is fed by the local low pressure water circuit. Arc heater, settling chamber and nozzles are cooled by coolant circuits fed by two high pressure water pumps with a capacity of 40 m³/h at 40 bar.

The test chambers can be disconnected from the pumping system consisting of three Root's blowers (R107, R87, WGK 12000), one rotary plunger vacuum pump S720 and one liquid seal pump using gate valves with an inner diameter of 1 m. Replacing the pump R57 by the WGK12000-pump the suction capacity of the pumping system has been improved (Fig. 2). The noxious gas NO produced during the operation of the LBK is decontaminated in the NO-absorption facility washing it with NaOH-solution. The facility can be operated with mass flow rates up to 300 g/s.

3. Measurement technique

The mass flow rate and the pressure in the settling chamber are continuously measured quantities during the tests. The nozzle flow field can be calculated completely using these two parameters and the nozzle geometry. The stagnation pressure is measured depending on the pressure level with a BHL-transducer with a measurement range of 0-10 bar or another BHL-transducer covering the range of 0-3.45 bar.

Pitot probe, model holder and heat flux probe are mounted on the same shaft and can be traversed into the flow field successively. The Pitot probe is water cooled and has an inner diameter of 3 mm, outside diameter of 15 mm and nose length of 150 mm.

The pressure is measured by means of a PV 111-transducer, which can measure pressures up to 1000 mbar with an accuracy of ±1 mbar. The surface temperature is measured using a spectral radiation or a two color pyrometer. The low temperature pyrometer measures the temperature between 80°C and 1000°C at the wave length range 2000-4500 nm. The other spectral radiation pyrometer is used for temperatures between

900°C and 2000°C and has a spectral range of 830-1030 nm. If the emissivity of the surface is not known, the two color pyrometer with a measurement range of 800-2000°C and two wave lengths of 920 nm and 1040 nm (20 nm half width) can be used. Temperature measurement with NiCr-Ni- or PtRh-Pt-Thermocouples is another common method. The heat flux probe consists of a water cooled copper cylinder with two embedded NiCr-Ni-Thermocouples (Fig. 3). The probe has the same geometry and outer diameter as the sample holder in order to achieve the same shock standoff distance. The heat flux can be evaluated solving the one dimensional heat flux equation with two measured temperature histories as its boundary conditions.

In Fig. 4 one can observe a strong correlation between the current, voltage and stagnation pressure. Increasing the current at a constant mass flow rate enhances the ionization, i.e. decreases the resistance and voltage, but increases the temperature leading to higher stagnation pressures in the settling chamber.

The operation range of the LBK with respect to the stagnation point tests on SiC-samples in connection with HERMES thermal protection systems is shown in Fig. 5. As this diagram shows, the main part of HERMES trajectories lies in the LBK-working area and the LBK closes the gap between operation ranges of two other european arc heated wind tunnels IRS and SIMOUN.

4. Numerical computation

To support experimental works on the LBK a computer program including options for flow solutions based on chemical equilibrium, frozen chemistry and chemical nonequilibrium has been used [6].

In the argon free air model used at low and moderate temperatures NO^+ is the only important ion among other species N_2, O_2, N, O, NO and the electron. At higher temperatures above 6000°K four additional ions like N_2^+, O_2^+, N^+ and O^+ are added to these species. The calculation of the thermal species properties has been performed under the assumption that the vibrational degrees of freedom of the molecules are in thermal equilibrium with the other degrees of freedom.

The computation of reservoir conditions is carried out for measured stagnation pressure in the settling chamber and mass flow rate using the temperature as iteration parameter until the calculated sonic mass flow rate is equal to the measured one. The gas composition is assumed to be the same as for an ideal gas mixture, but calculations of the enthalpy and density are based on the modified van der Waals equation.

In the frozen flow solution, the species concentrations are held constant at their reservoir conditions. In the equilibrium solution, the gas is assumed to be in a state of local equilibrium at each point in the nozzle. The non-equilibrium solution is obtained under the basic approximation of a quasi-one-dimensionality of the flow field. The species concentrations are assumed to be governed by chemical rate equations. The basic method of the solution consists in the numerical integration of these rate equations together with the differential equations of conservation of mass, momentum and energy. Such equation systems are mostly stiff. A stable solution can be achieved only for extremely small step sizes, especially when the flow is close to equilibrium. Because the flow starts from a state of equilibrium in the reservoir, the numerical integration technique there can not be used initially. Instead, the solution is started by treating the non-equilibrium flow as a perturbed equilibrium flow. The perturbation method is used until the departure from equilibrium has become large enough to allow the use of numerical integration.

An approximate laminar boundary layer calculation based on the integral method developed by Cohen and Reshotko is included. The boundary layer is assumed to start at a specified point upstream of the nozzle throat, and is computed step by step along with the inviscid flow solution. Beyond the throat, the inviscid flow is coupled with the boundary layer through the displacement thickness on the effective area ratio.

The calculations of the stagnation point conditions begin with Rankine-Hugoniot normal shock solution. The gas immediately behind the shock can be assumed to be frozen or in chemical equilibrium, regardless of the free stream flow regime. The stagnation pressure at a point on the stagnation streamline just outside the boundary layer on the model can be compared with the measured Pitot pressure. An isentropic relation between states just behind the shock and at the stagnation point is used for the computation of the stagnation point enthalpy. The incompressible Bernoulli equation, which is only an approximation to the compressible isentropic flow relation, can be used for the stagnation point pressure computation. For calculating other gas variables both equations of gas state are necessary.

The measured Pitot pressure under the stagnation conditions given in Fig. 4 was 75.6 mbar. The equilibrium shock solution coupled with a nonequilibrium flow solution provides a stagnation point pressure of 78 mbar. The small deviation can be caused by the underestimated boundary layer thickness. While the non-equilibrium solution in the nozzle part upstream of the nozzle throat deviates from the equilibrium solution only slightly, both solutions provide quite different species mole fraction in the supersonic part of the nozzle (Fig. 6). The temperature distribution along the nozzle (Fig. 7) shows only a weak difference in nonequilibrium and frozen solution. These two facts support the assumption that the flow after the nozzle throat is nearly frozen.

5. Upgrading of the LBK

The main purpose for upgrading the LBK facility is to increase the total enthalpy and the surface pressure of the test specimen, which requires higher electrical power and gas mass flow rate. In connection with this aim some components of the LBK have to be upgraded or adapted.

To obtain higher surface temperatures at different surface pressures the generation of total enthalpies beyond 15 MJ/kg is necessary. Such a value requires the increase of the electrical power up to 5-6 MW and subsequently a new arc heater.

In detail the technical upgrading of LBK requires the modification of the following tunnel components:

- gas mass flow rate control system
- heat exchanger of the test section L3K
- arc heater
- electrical power supply system
- wind tunnel control system.

Mass flow rates up to 300 g/s will be necessary to achieve conditions defined for the future research program. They cannot be controlled using the existing control system. Therefore a new mass flow controller with another measurement technique based on the Coriolis effect has been installed.

The walls of the test chamber of the test leg L3K are water cooled and designed for gas internal energy rates up to 4 MW. But the heat exchanger placed between the test section and pumping system can not be used for powers larger than 1 MW. A new heat exchanger with a cooling capacity of 3 MW will reduce total gas temperatures in the range of 7400 K to 320 K at pressure levels of 20 mbar. The flow has to cover the whole cross section of the heat exchanger. It seems to be necessary to use a two stage exchanger to reach the low entrance temperature in the pumping system.

The arc heater consists of multiple hollow electrodes with internally mounted magnetic coils, transition sections and column of segments with a smaller bore. The transition and column segments will be radiation-shielded and interlocked. Electrically insulated copper segments are water cooled and allow gas injection. It is anticipated that two electrode rings at each cathode and anode ensemble are required. Each electrode ring will require a water cooled ballast resistor.

Because of economical reasons, it is not intended to enlarge the existing rectifier but to install a new one. The new rectifier is a 6-MW, 24 pulse thyristor power supply, which can be switched in series or parallel from 2 to 4 modules (1000 A at 6000 V; 2000 A at 3000 V; 4000 A at 1500 V; 8000 A at 750 V). The regulator delivers a constant current with an accuracy of ±1% of full scale. The improvement of the total conditions of LBK with the new rectifier is shown in Fig. 7.

A computerized control system will supervise the operating conditions of the facility. The arc heater ignition and the setting of the desired mass flow rate will be performed by this system automatically. During the tests cooling circuits are watched and, if necessary, adjusted. In order to achieve constant operation conditions the values of mass flow rate and current will be optimized. All important parameters will be monitored and stored for further evaluations.

6. Concluding remarks

The arc heated wind tunnel LBK has been proved to be a valuable device for the qualification tests on thermal protection materials for space transportation systems. Because of its low pressure level in the settling chamber the flow in the tunnel is nearly chemically frozen and restricts a simulation in the aerodynamics sense.

The LBK covers a big number of points on the temperature-pressure field for surfaces which are exposed to high thermal loads during the reentry phase of HERMES. The gap between the working areas of the other european plasma wind tunnels IRS and SIMOUN can only be closed by means of the LBK.

Higher stagnation enthalpies and heat flux rates will be produced after performing upgrading, which will allow to reach higher surface temperatures and pressures.

7. References

1. Koppenwallner, G., "Low Density Facilities", the third joint Europe/US short course in hypersonics, Aachen, October 1990.

2. Olivier, H., Vetter, M. and Grönig, H., "High-Enthalpy Testing in the Aachen Shock Tunnel TH2", Proceedings of the first European Symposium on Aerothermodynamics for Space Vehicles, ESTEC, Noordwijk, May 1991.

3. Kindler, K., "Aerodynamic Simulation Conditions in Arc Heated Wind Tunnels", Proceedings of the 2nd European Aerospace Conference on Progress in Space Transportation, Bonn, May 1989.

4. Auweter-Kurtz, M., "Qualification of Thermal Protection Systems by Laboratory Simulation Techniques", Space Course on Low Earth Orbit Transportation and Orbital Systems, Aachen, February 1991.

5. Kindler, K., "Arc heated wind tunnel facilities", DLR-Report, IB-39113-87-C-24, 1987.

6. Bade, W.L., Yos, T.M., "The NATA Code", NASA CR-2547, 1975.

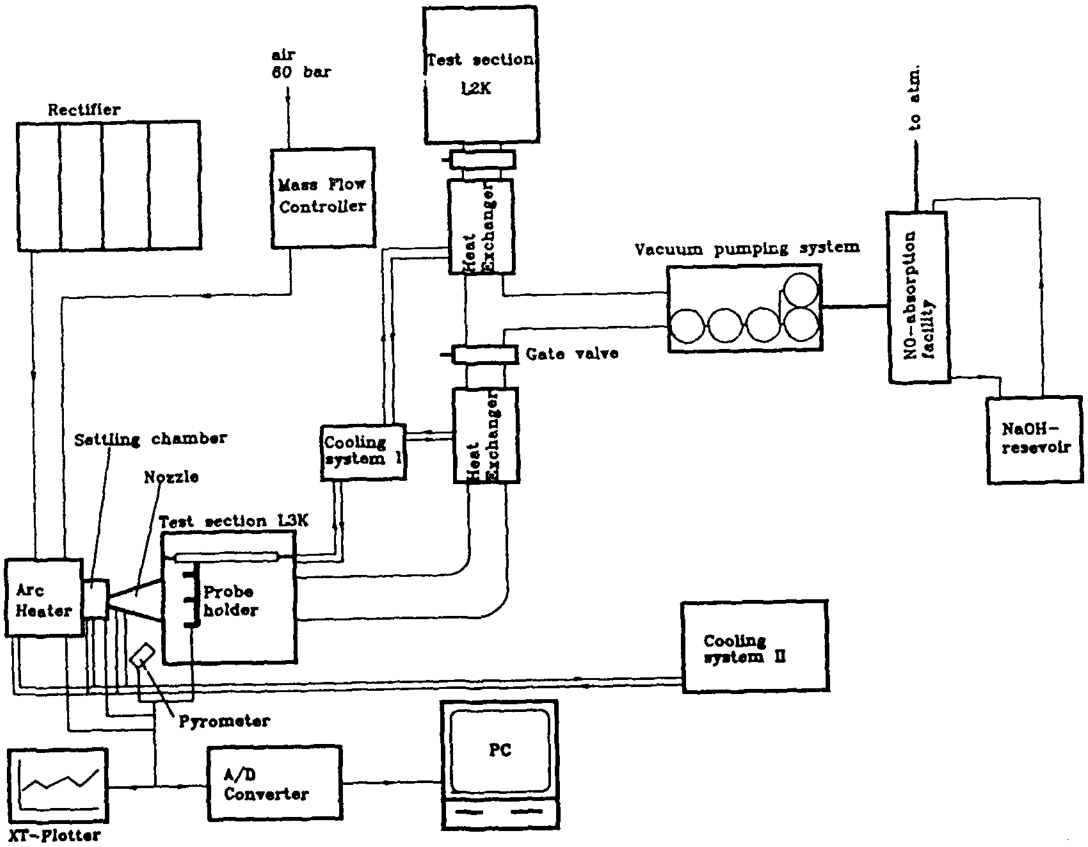
Test section L2K
air
60 bar
Rectifier
Mass Flow Controller
Heat Exchanger
to atm.
Vacuum pumping system
NO-absorption facility
Gate valve
NaOH-resevoir
Cooling system I
Heat Exchanger
Settling chamber
Nozzle
Test section L3K
Arc Heater
Probe holder
Cooling system II
Pyrometer
PC
A/D Converter
XT-Plotter

Fig. 1: Experimental set-up

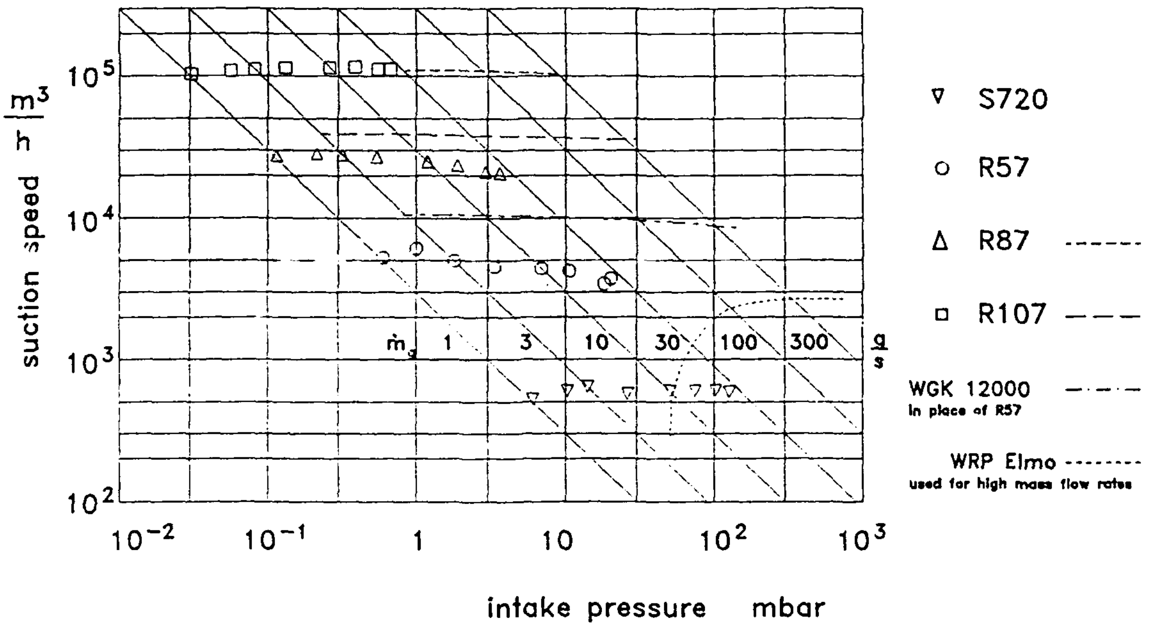

Fig. 2: Characteristics of Upgraded Vacuum Pumping System

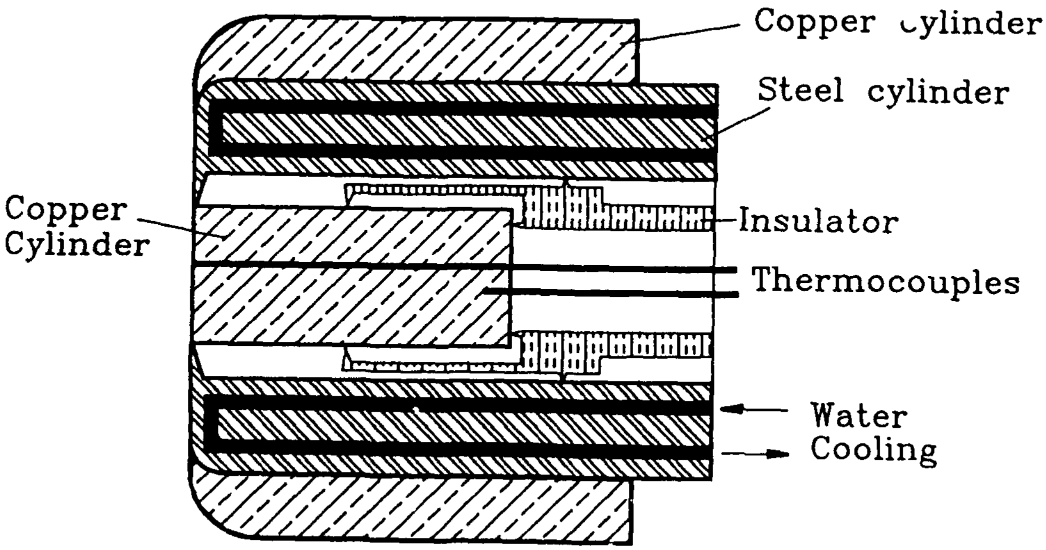
Copper Cylinder
Steel cylinder
Copper Cylinder
Insulator
Thermocouples
Water Cooling

Fig.3: Heat Flux Probe

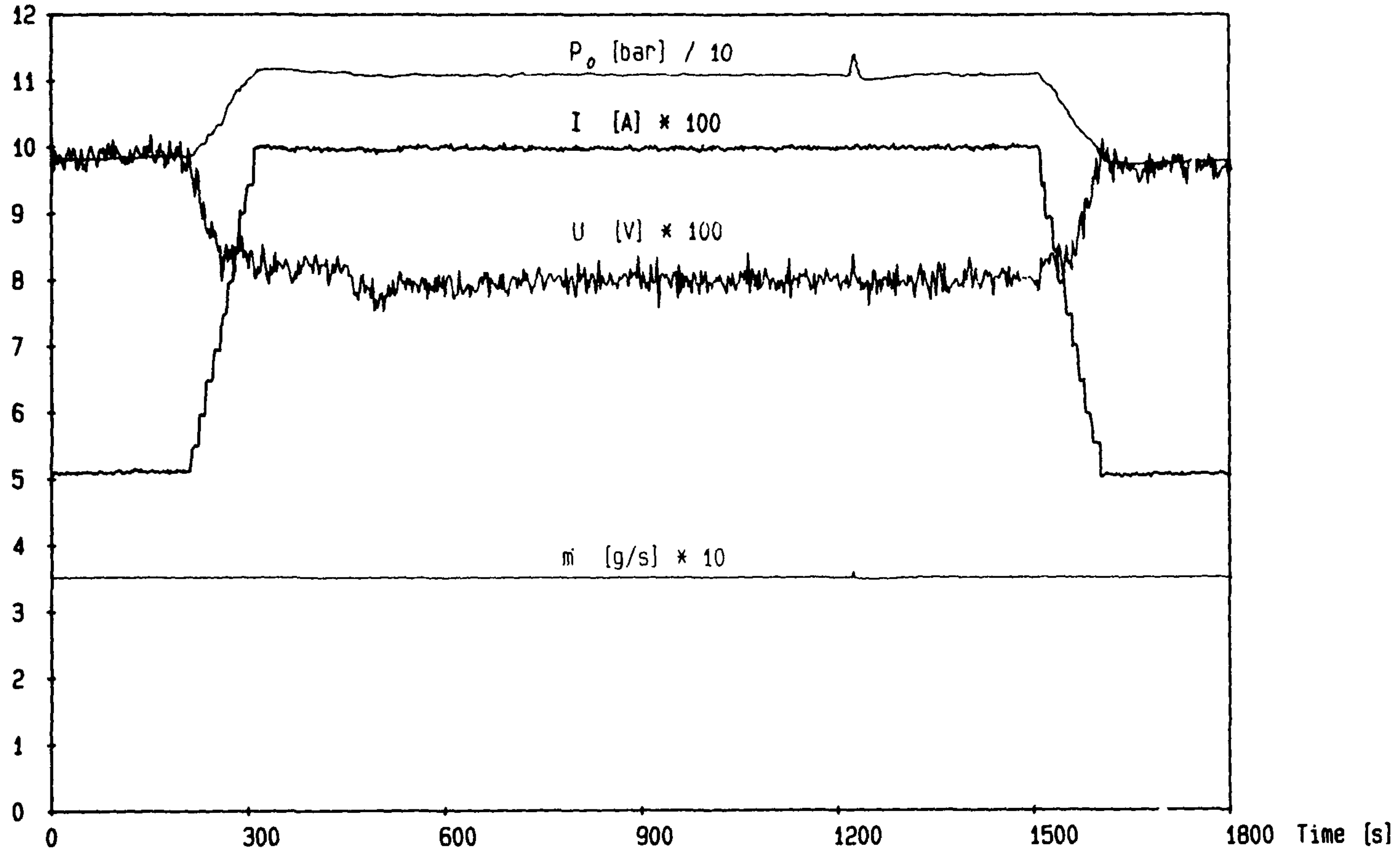

Fig.4: Stagnation conditions during an oxidation test at 1600 C and 75 mbar

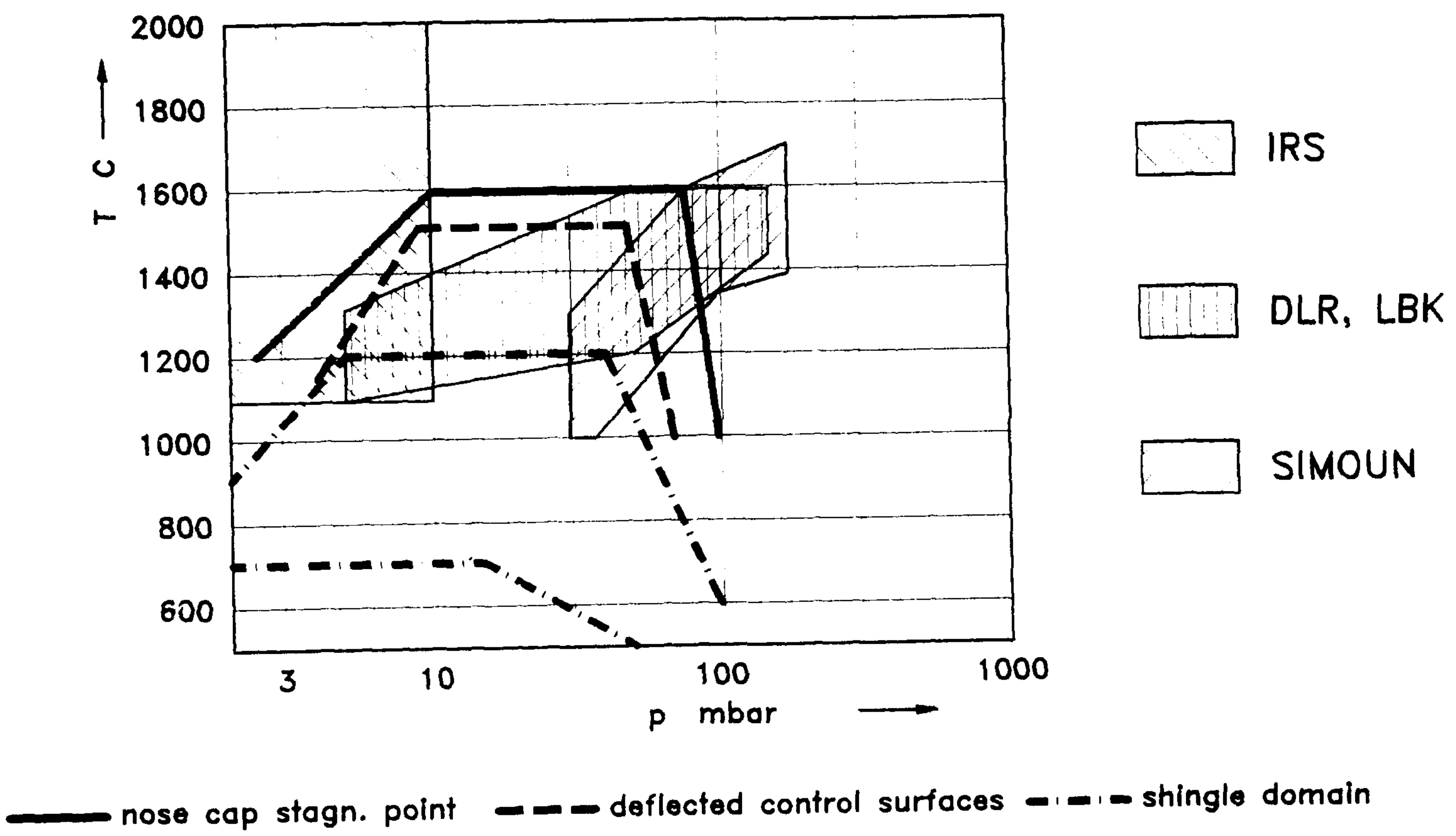

Fig. 5: Operating Range of European Wind Tunnels

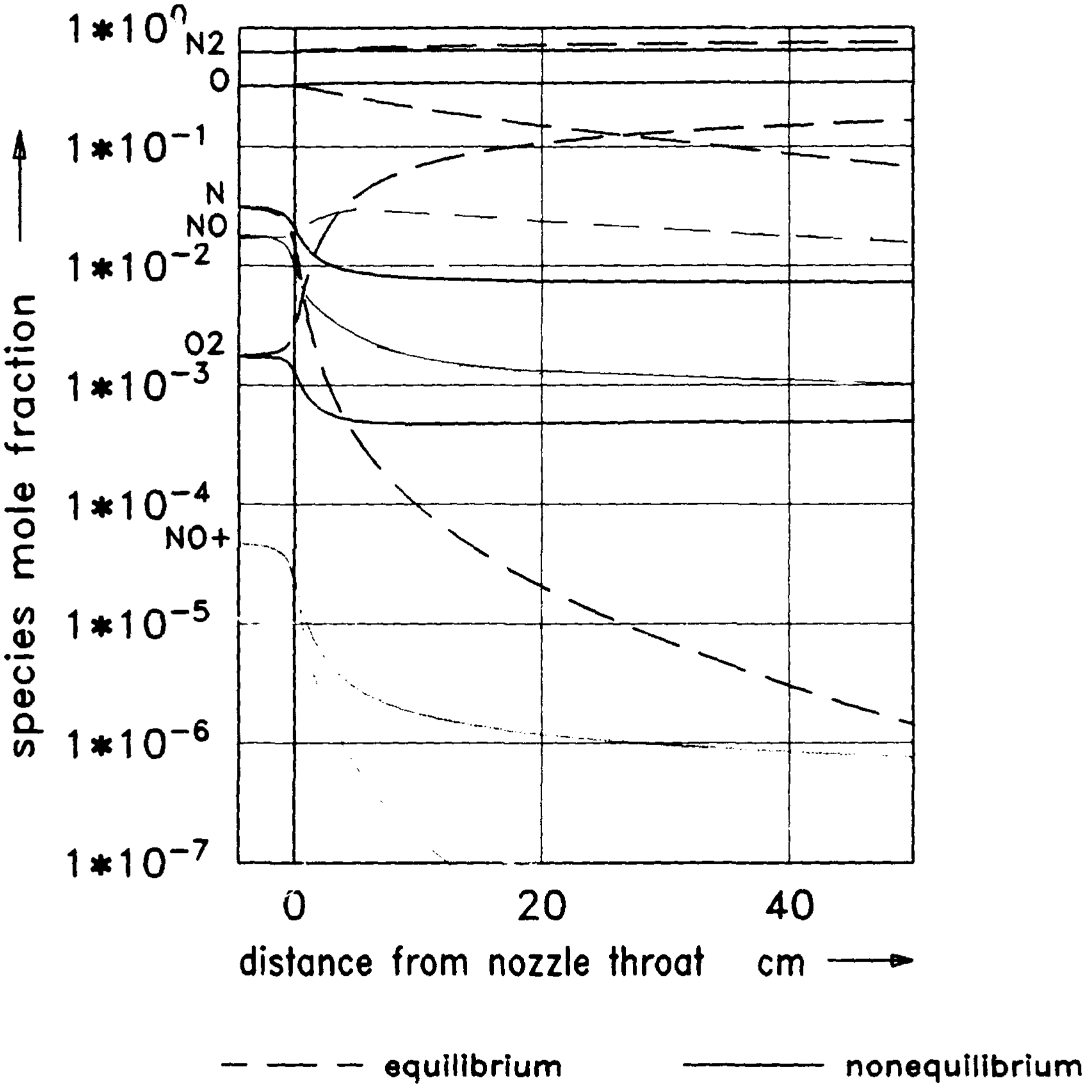

$H_o = 10.62 \ \frac{MJ}{kg}$ $p_o = 1.10$ bar

$T_o = 5110.$ K $\rho_o = 0.061 \ \frac{kg}{m^3}$

Fig. 6 : Axial mole fraction distribution in the nozzle

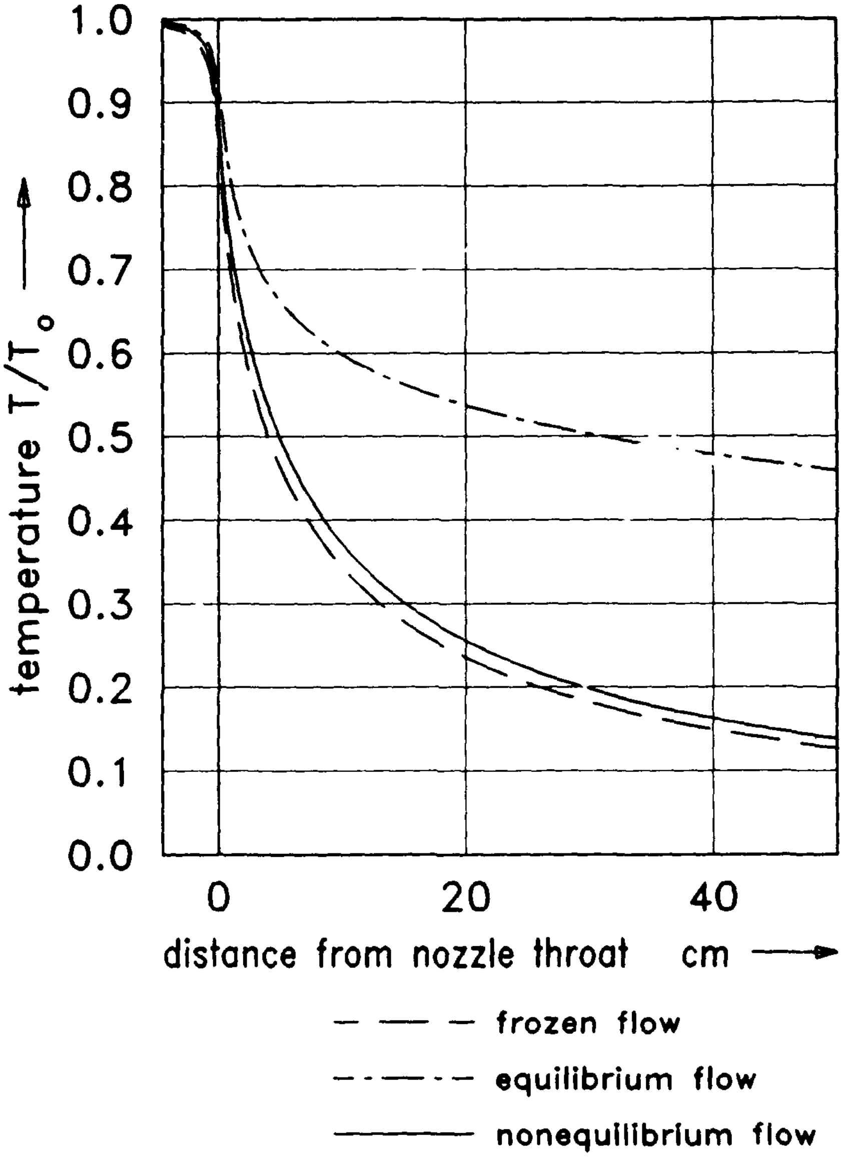

$H_o = 10.62 \frac{MJ}{kg}$ $p_o = 1.10$ bar

$T_o = 5110.$ K $\rho_o = 0.061 \frac{kg}{m^3}$

Fig. 7 : Axial temperature distribution in the nozzle

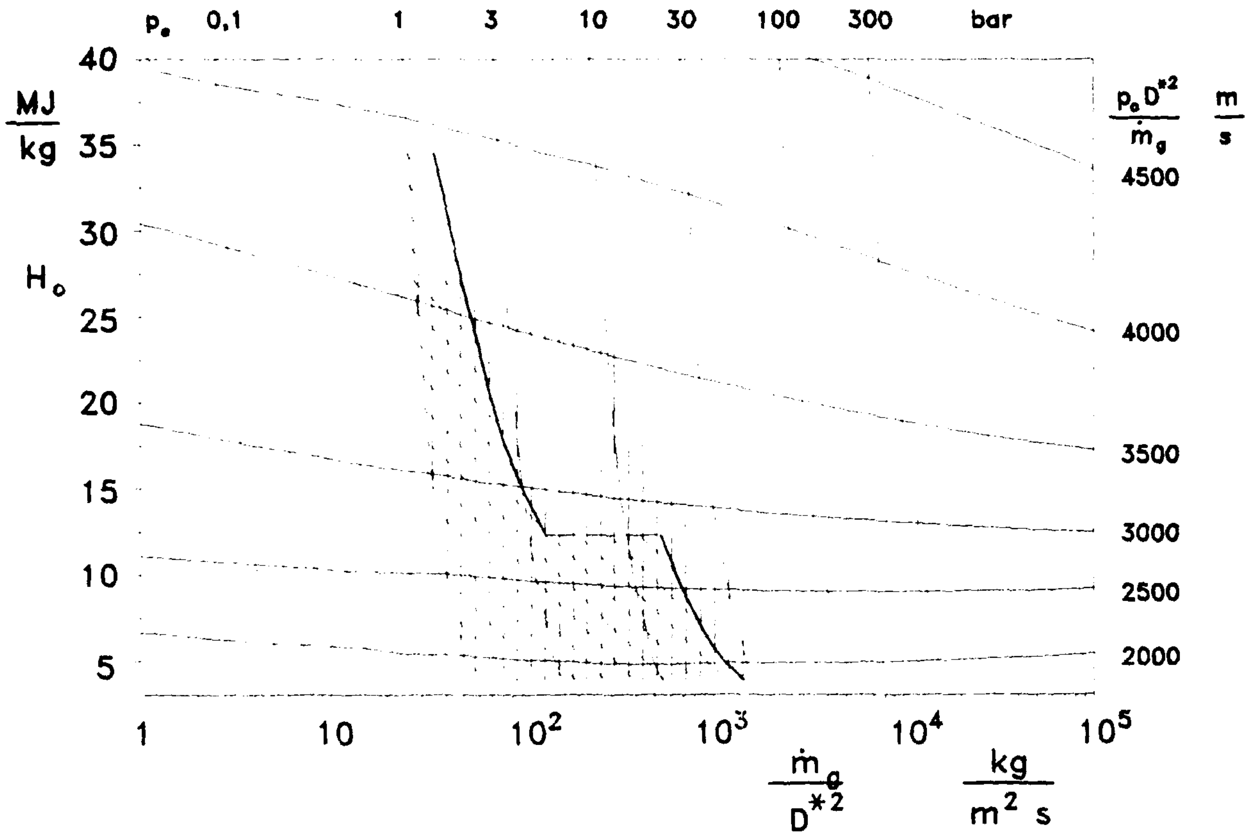

H_e: total enthalpy, p_e: total pressure, m_g: gas mass flow rate, D^*: nozzle throat diameter

LBK, low density tunnel LBK, upgraded for material tests

Fig. 8: Total enthalpy with respect to wind tunnel data

RECOMMENDATIONS FOR FUTURE RESEARCH IN HYPERSONIC INSTRUMENTATION

S. L. Ocheltree
National Aeronautics and Space Administration
Langley Research Center
Hampton, Virginia 23665-5225, USA

SUMMARY

An overview of the NATO Advanced Research Workshop Session 7 is presented. It describes the process followed to obtain a group consensus on the main technical recommendations for each of the five technical sessions of the Workshop and presents the general conclusions and recommendations for future research agreed upon by the workshop participants.

INTRODUCTION

Session 7, the last session of the NATO Advanced Research Workshop, was organized to provide an open forum for the workshop participants to reach a group consensus on the main conclusions of the workshop and to formulate a set of recommendations for future research in hypersonic instrumentation. The format of this last session was to have the five lead rapporteurs for each of the earlier five technical sessions present their draft summary reports and recommendations to the group. Each draft report was prepared by the three rapporteurs who led each of the earlier session group discussions and was based on both the technical papers presented in their sessions and the group discussions that followed. Following each draft report presentation to the workshop group in Session 7, there was a group discussion period where the final consensus position for the workshop participants was agreed upon. The session papers that follow are reports on the final conclusions and recommendations that resulted from the process just described.

The last part of Session 7 provided for a group discussion that led to the development of a set of general conclusions and recommendations for the Workshop as a whole. These latter overview comments were meant to capture the broader technical issues, concerns, and recommendations that were expressed by the group participants throughout the five technical sessions. There were eight general recommendations formulated and agreed upon by the workshop participants in this last session.

GENERAL CONCLUSIONS AND RECOMMENDATIONS

The eight general conclusions and recommendations produced at the Workshop were:

1. Advanced measurement technology is critical and enabling to the development of hypersonic flight vehicles and requires high level management attention and support. The group identified four classes of enabling hypersonic research experimental data that require advanced measurement technology development and instrumentation. These were:

a. Aerospace vehicle design data obtained from wind tunnel and propulsion test facilities. An advanced measurement capability in these test facilities is needed to acquire the fundamental experimental test data base to support vehicle design in the flight regimes that cannot be obtained through existing engineering or Computational Fluid Dynamics (CFD) predictive capabilities.

b. New test facility free stream characterization and calibration. The complete free stream flow field characterization of both new and an existing facilities is the essential first step to defining the "input conditions" that will provide a high quality hypersonic experimental data base for all future engineering design and CFD code validation testing. Hypersonic test facilities place the most extreme performance demands on advances in new instrumentation that must survive and perform measurements in their highly hostile environments, e.g., high temperature; vibration; micro- to millisecond test times; chemically-reacting, high-speed flows; and simultaneous, global multi-parameter data sets for both model surface and disturbance-free gas flow properties.

c. Fluid physics and CFD code development and validation. All future advances in the improved understanding of hypersonic fluid physics and CFD code development and validation must rely on a high quality experimental data base obtained either from ground-based test facilities or future flight test data. The development of new measurement technology is enabling to acquire this essential experimental data base.

d. Flight test data. Even with the most advanced and sophisticated ground test facilities, there are still significant flight test envelope conditions that cannot be adequately simulated in ground test facilities. Flight testing under extreme flight envelope conditions places the most stringent demands on instrumentation. These flight test constraints limit the domain of advanced measurement technologies to those that can survive the hostile flight environment and yet, can provide accurate measurements with the additional constraints of limited size, weight, power consumption, etc.

2. The diversity of hypersonic test requirements will demand the development and application of a broad spectrum of advanced measurement techniques and sensors. A common theme agreed upon throughout the workshop deliberations was that multiple solutions must be addressed to satisfy many of the advanced hypersonic measurement requirements because of the wide variety of experimental test conditions and requirements. Further, the high risk nature of the hypersonic advanced measurement technology R&D program will require pursuit of multiple approaches to the most critical measurement requirements in order to reduce risk in the experimental test program.

3. It is essential that a close collaboration be established between the research data user, test facility engineer, and the instrument developer beginning with experiment definition and continuing through final demonstration. The workshop group cited the importance of a thorough scientific definition of the experimental data requirements,

experimental test conditions and measurement accuracies as a necessary first step to successful hypersonics experiments. The instrument developer is a critical part of this initial experiment definition process. This is particularly true in hypersonic testing, since it is often found that the present state of the measurement technology will not support the test requirements. With this realization, and involvement of the instrument developer, an alternative experiment may be designed which is achievable or else an aggressive measurement technology development program must be defined and begun. The workshop participants felt that this early dialogue – which involves the data user, test engineer and instrument developer – and continues throughout the course of the experimental test program cannot be over emphasized.

4. Major extensions in the state of the art are needed in many areas (e.g., nonintrusive gas diagnostics, high temperature sensors) and will require a long-term (5-7 years) R&D investment to mature. As indicated earlier, major advances in measurement technology are needed to meet the needs of the hypersonic ground and flight test research program. Further, new fundamental scientific discoveries and technologies outside of the aerospace community must be aggressively monitored and considered for development and application to meet the new measurement technology requirements.

5. CFD code experimental validation will place the highest demands on facility data accuracy and on instrumentation with well-validated, low measurement uncertainties that must be supported. It was pointed out repeatedly during the workshop that the most demanding measurement requirements are dictated by CFD code validation tests which require well-calibrated test facility free stream input conditions, high-accuracy mean model surface conditions, and global multi-parameter gas flow field data with the highest spatial resolution. Further, to develop and test turbulence CFD models, these measurement requirements must be extended to include fluctuating quantities with wide measurement bandwidth--up to 100 kHz, turbulence power spectra and cross correlation functions of measured values. These sophisticated requirements combined with experimental uncertainties in the 1 to 10% range require significant advances in measurement technology to achieve.

6. A balanced near-term/long-term investment strategy is required that will address the following:

a. Extend mature technologies that have been successfully used in the past but which need to be reactivated or investigated for extension beyond the experimental test domain of their prior use. Examples cited in the workshop include electron beam fluorescence (former class) and laser Doppler velocimetry (latter class).

b. Exploit new emerging technologies in other disciplines. The workshop participants felt strongly that it was only through the adaption and extension of the latest emerging technologies -- e.g., lasers, fiber optics, electro-optic devices, laser spectroscopy, high-temperature sensor concepts and materials -- that the required quantum advances in hypersonic measurement technology can be achieved.

c. Develop advanced measurement and sensor concepts at university, industry, and federal laboratories. This element of the investment strategy, which was strongly endorsed by the workshop group, cites the essential managed coordination between the university, industry, and government laboratory research staffs to draw upon the strengths of each element in a synergistic way. Long-term support for university labs classed as "Centers of Excellence" and seed funding to small innovative private companies must be the cornerstones of this investment strategy.

7. New calibration techniques and facilities need to be identified and developed to satisfy measurement uncertainty requirements under both ground and flight test conditions. The issue of calibration techniques and facilities for new instrumentation technology was identified in the workshop as a significant issue that needs to be addressed along with new measurement techniques and sensors. The development of special calibration techniques and facilities for extreme test conditions – e.g., high heat flux levels and high temperature – can be as costly, time consuming, and technically challenging as the development of the new sensor or measurement technique itself and needs to be included as an integral part of the measurement technology R&D program.

8. Flight test measurement requirements should be identified and appropriate flight sensor development programs supported early in the program. Although the main thrust of this workshop addressed hypersonic ground facility instrumentation, the subject of extending new measurement techniques and sensors to flight testing was discussed. It was agreed that flight sensors are an evolutionary extension of those developed for ground testing which can be miniaturized and hardened for flight. As a consequence, potential flight sensor technologies should be identified and support begun early in the ground test development program so that there is a well-planned transition from ground test to flight.

CONCLUDING REMARKS

In summary, Session 7 of the NATO Advanced Research Workshop provided a forum for the workshop participants to develop a final consensus on the main conclusions of the workshop and to formulate a set of recommendations for future research in hypersonic instrumentation. The general conclusions and recommendations of the group are presented above while the final reports of the lead rapporteurs for each of the technical sessions are presented in the following papers.

LOCAL MEASUREMENT OF TEMPERATURES AND CONCENTRATIONS: A REVIEW FOR HYPERSONIC FLOWS

by

C. Dankert
DLR Göttingen
Germany

R. Cattolica
University of California at San Diego
United States

W. Sellers
NASA Langley Research Center
Hampton, Virginia 23665-5225
United States

SUMMARY

The quality of reentry simulation for Shuttle, HERMES, Sänger, and NASP systematically suffers from the strong non-equilibrium of rotational and vibrational temperature due to the rapid acceleration of the test gas in the nozzle. Therefore the determination of temperatures is necessary and, if possible, preferable by a non-intrusive technique. The specific interests of this review are optical techniques such as electron beam fluorescence, laser-induced fluorescence, and coherent anti-Stokes Raman scattering. The capabilities available for local measurements with temporal resolution and quantitative accuracy are discussed for velocity, temperature, density, species concentrations, and fluctuations due to turbulence. The applicability of these methods of measurement is presented and discussed for the coming topic in aerothermodynamics: experimental techniques of hot gases in high enthalpy flows.

1. INTRODUCTION AND SCOPE

The interest in hypersonic aerodynamic research is now increasing due to the new hypersonic space transport vehicles like the European HERMES, the German Sänger, and the U.S. NASP. The two classical major problems of such reentry vehicles are steering at high angle of attack with flaps or thrusters and the extreme heat loads in the nose area of the vehicle structure during aerodynamic breaking. Therefore the knowledge of gas- and wall-temperatures, wall-material characteristics, and species composition is essential. The latter point is also of interest for environmental studies of the upper atmosphere.

The design of hypersonic space vehicles depends on computational fluid dynamics codes (CFD) which simulate the hypersonic flow field. Another, somewhat historic, engineering tool is the wind tunnel with a flowing gas medium and a test model at rest.

Hypersonic research requires an integration between flight, CFD and wind tunnel methods:

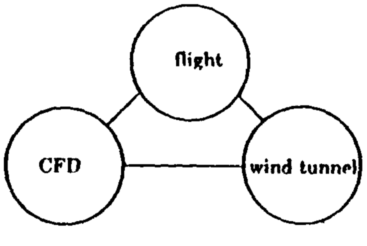

This paper focusses on wind tunnel aspects of this interaction, taking into account the different conditions in flight, and keeping in mind the validation of CFD codes.

Several optical methods are reviewed which are non-intrusive [1, 2] and have already been applied to hypersonic wind tunnel testing. These techniques are surveyed especially for possible use in two of the new European wind tunnels: the F4 at Le Fauga and the HEG at Göttingen. Both wind tunnels operate in intermittent modes at testing times of 100 ms in F4 and only 1 ms in HEG, which is very short compared to the low density hypersonic wind tunnels [5, 6] which run for some hours. The densities in the low density tunnels are $10^{12} - 10^{16}\ molecules/cm^3$ $(30\,K < T_{rot} < 2500\,K,\ 800\,K < T_{vib} < 2500\,K)$, and for the intermittent tunnels up to $10^{20}\ molecules/cm^3$ $(T_{vib},\ T_{rot} < 10\,000\ K)$.

The new tunnels use air as the test gas, and due to the high temperatures in the flow, the O_2 – and N_2 – molecules will dissociate and recombinate to NO. So we have to work with at least three molecular species (N_2, O_2, and NO) in a temperature range from 100 K to 10 000 K with non-equilibria in rotation, vibration and thermal dissociation. Furthermore, the state population distribution might not be of a Boltzmann type [3, 4] so the definition of temperatures becomes questionable.

2. ELECTRON-BEAM FLUORESCENCE DIAGNOSTICS

2.1 Description

The electron-beam technique is well established for hypersonic wind tunnel testing since more than 25 years [7, 8]. Also, for flight-research diagnostic for hypersonic boundary layer measurements this method can be used to probe nitrogen [2, 9 – 16]; eight previous flight experiments with optical detection of electron-beam fluorescence are summarized by Cattolica [2].

Limitations of the electron-beam technique at high density concern quenching of the signal, reduction of spatial resolution by gas scattering, and possible interference from background emission. Muntz et al. [24] proposed the Electron-Photon-Fluorescence, a combined electron beam ionization/laser-induced fluorescence detection approach. In addition Muntz [46] has also proposed a pulse electron-beam technique to overcome some of these limitations.

Many types of electron guns were used for wind tunnel applications, with energies ranging from 5 kV up to 300 kV and beam currents ranging from 1 µA up to 1 mA [17]. Most of the scientists probed the N_2^+-ion and measured rotational and vibrational temperatures [3, 5, 6, 7], *NO* [18, 19, 20], O_2 and *O* [21], *CO* [22], and CO_2 [23] were also investigated.

2.2 Application Regimes

The density range of the e⁻-beam fluorescence is, according to Lewis [17], 10^{13} to 10^{16} *molecules/cm³*. At higher densities quenching and beam scattering problems occur and make this technique difficult but not impossible; the pulsed e⁻-beam technique (10 ns) may extend the density range up to 10^{18} *molecules/cm³* [46]. In **Fig. 1** the application densities are listed and compared to some other optical methods [17] like LIF (laser-induced fluorescence), LIPF (laser-induced predissociative fluorescence), Rayleigh scattering, CARS (coherent anti-Stokes Raman scattering), and 2D-LIF (planar laser-induced fluorescence).

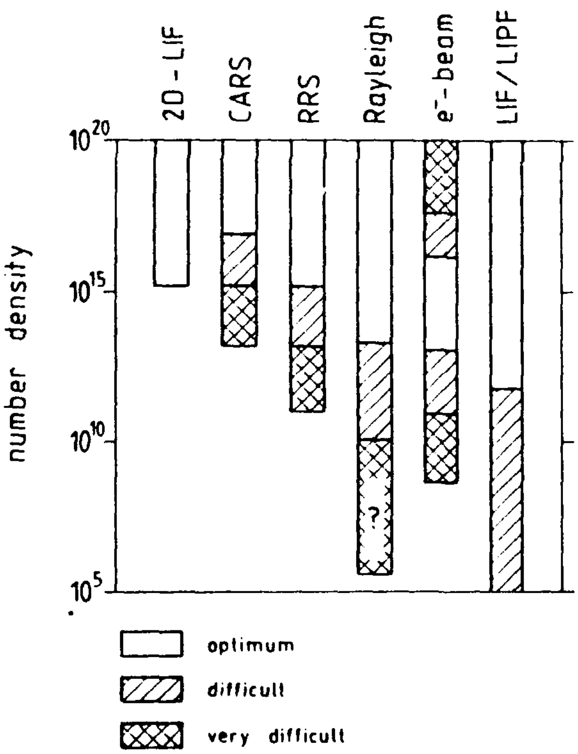

Fig. 1 Diagnostics application regimes [17]

2.3 Electron Beam and Wind Tunnel

The standard experimental set-up for temperature and density measurements is shown in **Fig. 2.** The electron gun is mounted in a separate chamber at low pressure (< 10^{-4} mbar) differentially pumped by turbomolecular pumps [25]. Older systems used oil-diffusion pumps [5, 6, 7]; hence the chamber must be cleaned from time to time. The electron beam in Fig. 2 is pulsed rectangular (1 kHz ... 50 kHz) to increase the signal-to-noise ratio by means of the lock-in-technique. The emitted light from $N_2^+(0,0)$ band (at $\lambda \approx 400$ *nm*) is focussed by a lens outside the wind tunnel on a monochromator and a photomultiplier. Therefore the wind tunnel must have either a window with a good transmission in the near ultraviolet or one can use a fiberoptic. The width of the entrance slit of the spectrograph is dependant on the optical resolution which is needed: for rotational spectra a resolution of $\Delta\lambda_{rot} = 0.05\,nm$, and for vibrational bands of $\Delta\lambda_{vib} = 0.5\,nm$. **Fig. 3** shows an unresolved N_2 fluorescence spectrum including bands from the first negative and second positive system. Usually, for temperature determination the N_2^+ (01) and N_2^+ (12) transitions are used.

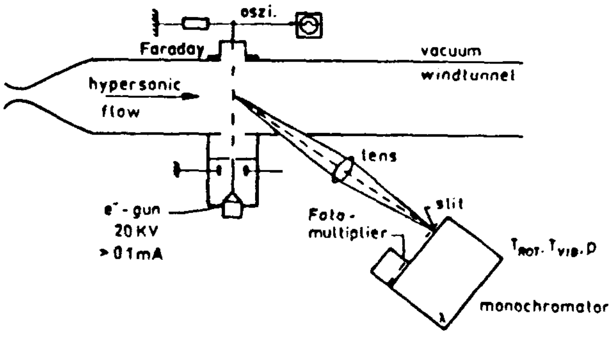

Fig. 2 Electron beam apparatus in a wind tunnel

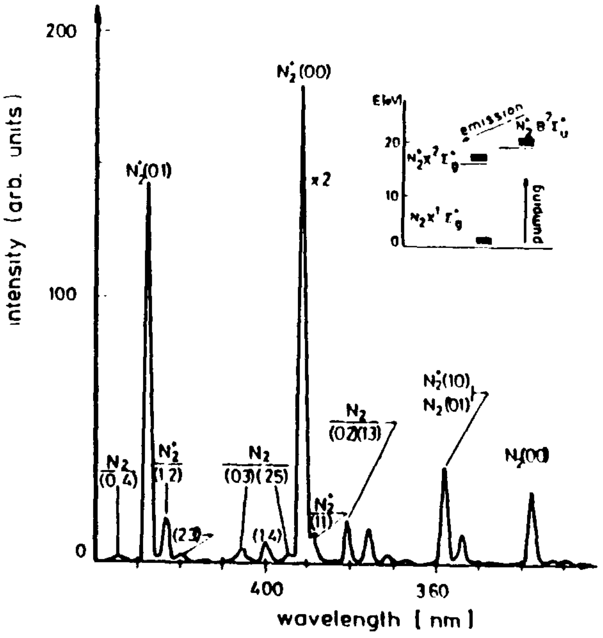

Fig. 3 Unresolved N_2 fluorescence spectrum including bands from the first negative and the second positive system. Most temperature measurements use the N_2^+ (01) and N_2^+ (12) transitions.

2.4 Results and Outlook

One example of applying the e^--beam technique to hypersonic flow is shown in **Fig. 4**. The density profile and the velocity gradient across a normal shock are measured [47] in a low density wind tunnel at a Mach number of 24. Both velocity and density show the expected change along the Rankine-Hugoniot relations by a factor of 6 known from continuum theory for high Mach numbers. The possibility of two-dimensional temperature-, density-, and velocity-fields is also given by this technique [18, 48, 49]. Some planar results taken in wind tunnels are published [47, 48].

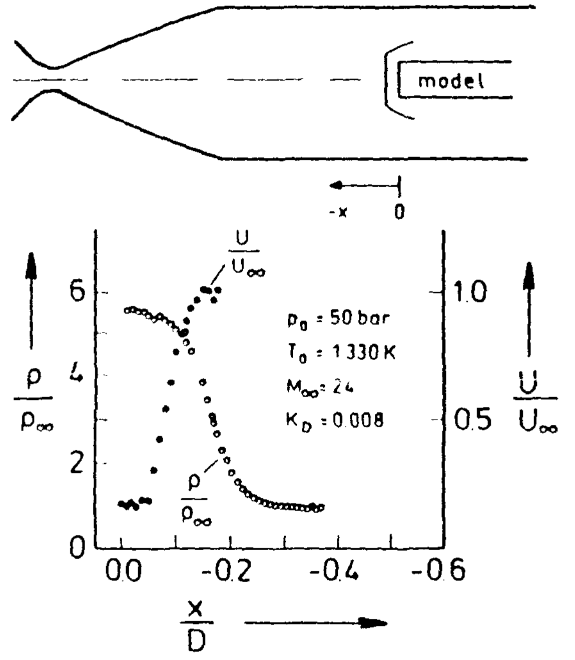

Fig. 4 Velocity measurements across a normal shock together with the corresponding density profile at $M_\infty = 24$ [47].

Focussing on the two new wind tunnels F4 and HEG, a gun of about 20 - 50 kV and variable current output (low current for point, high current (1 mA) for planar-measurement) is favoured. Such a gun can be pulsed up to 50 kHz [18] which will provide several e^--shots even during the 1 ms running time of the HEG. In F4 some problems will occur due to charged particles generated by the arc-heater system. At higher densities the electron beam fluorescence suffers from quenching problems. In gas mixtures one has to take into account direct ionization, Penning ionization via collisions between target molecules and metastable atoms, and charge-transfer reactions by collisions of ionized atoms with target molecules. Using metastable atoms as a high energy source gives us many suggestions to improve the conventional electron beam technique [47].

3. LASER-INDUCED FLUORESCENCE DIAGNOSTICS

3.1 Description

The principle of LIF is the use of laser-excited emission to provide local measures of the number density distribution functions [17]. The introduction of tunable lasers of high spectral power density has resulted in a manifold applicability of one-photon and multi-photon excitation processes of atoms and molecules. The LIF technique is on the way of becoming a standard tool for non-intrusive measurements in supersonic wind tunnel flow fields [26 - 30] in a wide density range. It can measure translational, vibrational and rotational temperatures by exciting selectively (in contrast to the electron beam) each molecular state even at very low densities. At higher densities quenching may occur [36, 37], but it is possible to modify this technique and detect predissociative molecular states [31] (LIPF). **Fig. 5** shows (in principle) the LIF- and LIPF-processes; of major interest is the repulsive curve crossing the potential curve on the upper right hand side: the laser excited molecule (O_2) can dissociate immediately after the stimulation process. This has the big advantage of very low quenching influence, but the disadvantage of low intensity compared to the conventional LIF-technique.

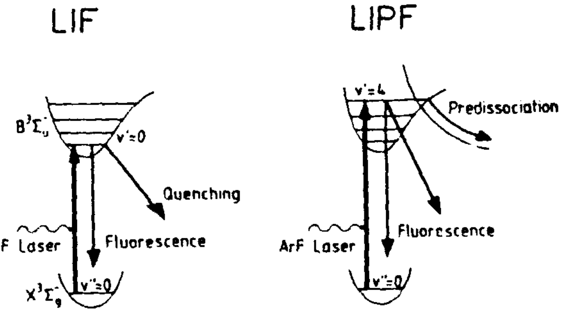

Fig. 5 Principle of LIF with laser excitation, fluorescence, quenching, and LIPF with the additional predissociation potential.

3.2 Application Regimes

The density range of the LIF-technique is enormous, see Fig. 1 [17], but one should point out that the LIF-sensitivity is strongly dependant on the molecule which is stimulated: *NO* has best sensitivity [27, 29, 50, 51, 52, 53, 54], *CO* and N_2 are extremely difficult [32, 33] (two-photon process in the vacuum ultra violet) but possible, O_2 is about two orders of magnitude less sensitive than *NO* but still a good candidate at higher densities [31, 34, 50, 53, 54]. Two-dimensional temperature fields can also be measured by LIF [27, 29, 30, 50, 55] and LIPF [31, 35] if powerful UV-lasers are used.

3.3 LIF-Apparatus and Wind Tunnel

The experimental set-up with a tunable ArF*-excimer laser in front of a supersonic vacuum wind tunnel is shown in **Fig. 6**. Three windows with a good transmission in UV (193 nm) are installed. For pointwise measurement the laser beam can be focused by a lens outside the tunnel [26]. The fluorescence light is collimated by two lenses on a photomultiplier. The maximum laser pulse energy of the ArF*-laser is 100 mJ at a pulse length of 13 ns and a maximum repetition rate of 250 Hz.

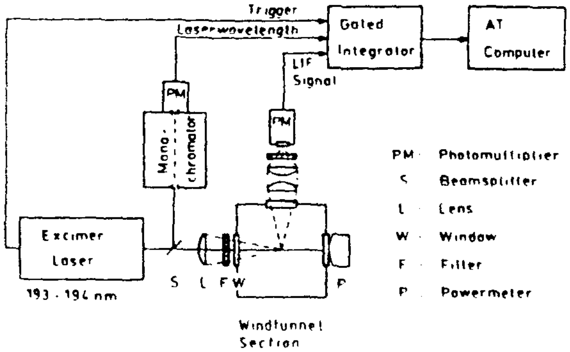

Fig. 6 LIF-apparatus installation in a wind tunnel.

Fig. 7 shows a static *NO* excitation spectrum at room temperature [52] with equilibrium of rotational and vibrational energies. The measured spectrum is compared to the computer calculation. The $B^2\Pi_r(v'=7) \leftarrow X^2\Pi_r(v''=0)$-band is the only one within the tuning range of the ArF*-excimer laser at $T = 300\,K$. Therefore the spectrum is very simple and easy to identify.

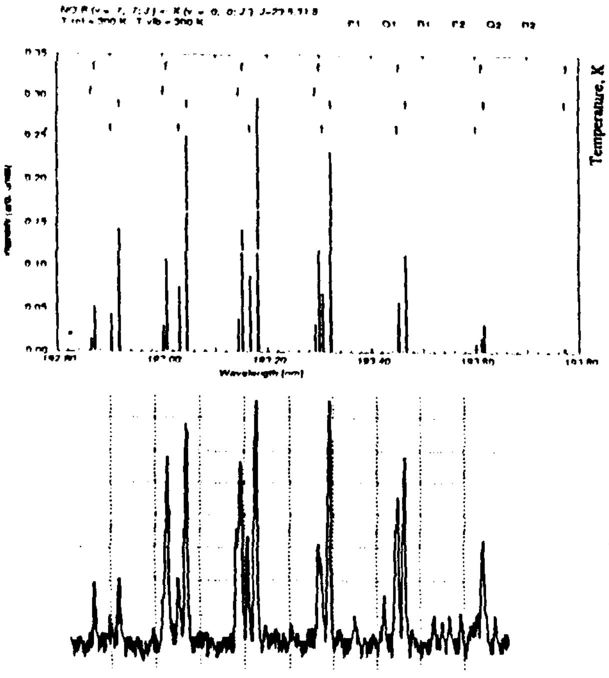

Fig. 7 Calibration measurement in comparison to calculated spectra at room temperature.

Planar images can be recorded by replacing the multiplier by a Newton telescope plus a CCD-camera and spreading the laser beam by a cylinder lens [27, 50].

3.4 Results and Outlook

A good demonstration for the high spatial resolution is given in **Fig. 8.** Along the center line of a supersonic free jet (orifice diameter D = 3.1 mm) single point measurements of rotational temperature were conducted by laser-induced fluorescence of *NO*, conducted with a rapid-tuning ring dye layer [50]. The agreement with the isentropic temperature distribution calculated along the center line is quite good except at x/D greater than 2 where rotational freezing appears to set in. Also the position of the Mach disc at $x/D = 3.2$ is measured clearly and a temperature increase from 80 K to 300 K is detected. It is interesting that such quantitative results can be obtained with only 1 mW laser power and that the measurements can be executed at a repetition rate of of 4 kHz!

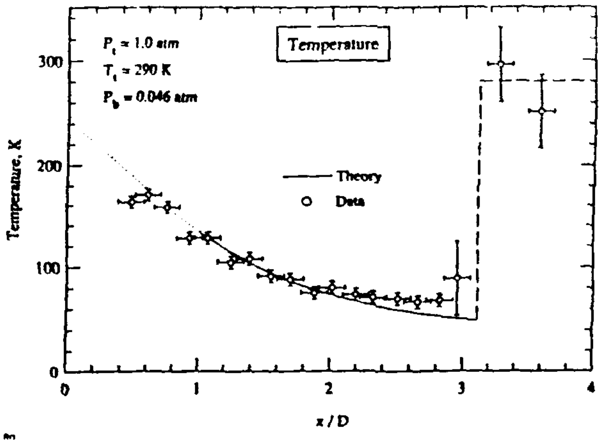

Fig. 8 Rotational temperature along free jet center line by LIF [50].

Another application of the LIF-technique to turbulent boundary layers can demonstrate the high temporal resolution when operating with laser pulses of 10 ns. **Fig. 9** shows a comparison of the root-mean-square (RMS) fluctuation amplitudes of temperature and density obtained by spectroscopic methods [54] and from hot wire data taken in a 12 mm thick, fully turbulent boundary layer that is adjointed by a relatively undisturbed flow of the same thickness, Mach number 2.

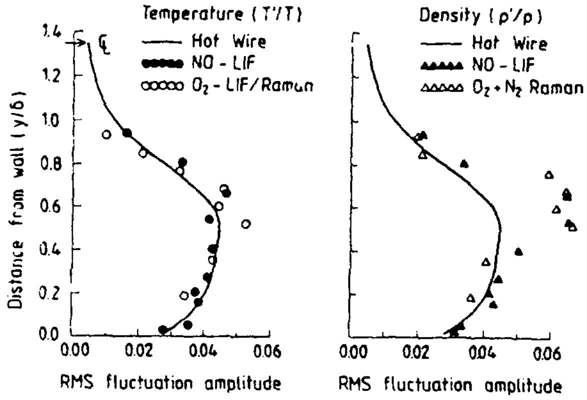

Fig. 9 Measurements of temperature and density fluctuation in turbulent Mach 2 channel flow [54].

The laser results, *NO*-LIF and O_2-LIF/Raman, are in agreement. They both show a region in the boundary layer near $y/\delta = 0.6$ where the density fluctuations are exceptionally large. A histogram of the *NO*-LIF fluctuations displays a bimodal character which suggests that a weak wave was oscillating across the sample volume. These comparisons demonstrate that the O_2-LIF/Raman technique can provide accurate measurements in air flows at the low temperatures and densities which are prevalent in high-speed wind tunnels.

Focussing on the F4- and HEG-wind tunnels the *NO*-LIF- and O_2-LIPF-methods are applicable, see Fig. 1, for planar measurements. Due to the short running time (1 ms) of HEG and the low laser repetition rate two separate excimer lasers will be used which are tuned to two selected transitions. These two lasers are fired one after the other, and two camera systems are installed, which are synchronized with the lasers.

4. CARS DIAGNOSTICS

4.1 Description

CARS has been shown to be a versatile and powerful technique for spectroscopic studies in supersonic flows [1, 38, 39, 56] and in hot gases [4, 37, 40, 41]. It is ideally suited to determine density and temperature profiles with high spatial resolution and to study rotational and vibrational relaxation processes. Many species have been studied: H_2, D_2, OH, O_2, NH_3, N_2, CO_2..., so all species in hypersonic wind tunnels can be detected. The multi-parameter dependancy of CARS performance makes the applicability region complex to define. Single shot experiments (20 ns) are possible.

4.2 Application Regimes

Fig. 1 shows the possible number density range for CARS-measurements having an optimum at 10^{17} to 10^{20} *molecules/cm*^{3} [17]. The spectroscopy experts from ONERA [42] checked the possible density range for 300 K and 3000 K:

multiline CARS $5 \cdot 10^{15}$ to $2 \cdot 10^{17}$ *molecules/cm*^{3}

multiplex CARS 10^{12} to $2 \cdot 10^{18}$ *molecules/cm*^{3}

4.3 CARS-Apparatus and Wind Tunnel

A standard set-up incorporates a frequency-doubled Nd: YAG laser at 532 nm [38]. Its output is split into two parts, see **Fig. 10**: one beam is used to pump a tunable dye laser, the other part provides the pump beam for the CARS process. Both laser beams are carefully aligned in time and space and focussed by a lens outside the wind tunnel. The two optical windows of the tunnel are not critical (visible light). The anti-Stokes photons are detected via monochromator and photomultiplier; an explain OMA-system with photodiodes is also possible. **Fig. 11** shows a measured N_2 CARS spectrum from a flame [45]. It was taken in the narrow-band mode and is well resolved. For single shot experiments it is possible to detect only two representative lines of the spectrum.

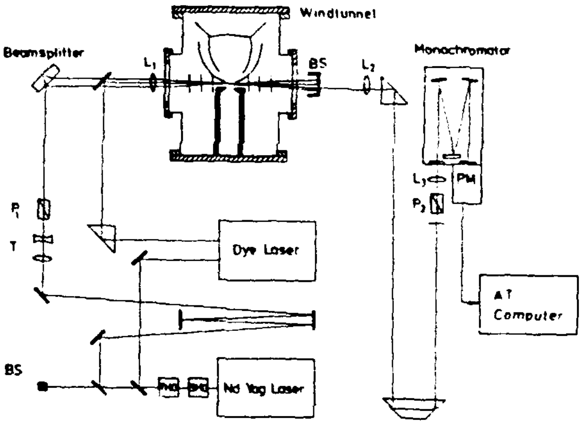

Fig. 10 CARS-apparatus installation in a wind tunnel.

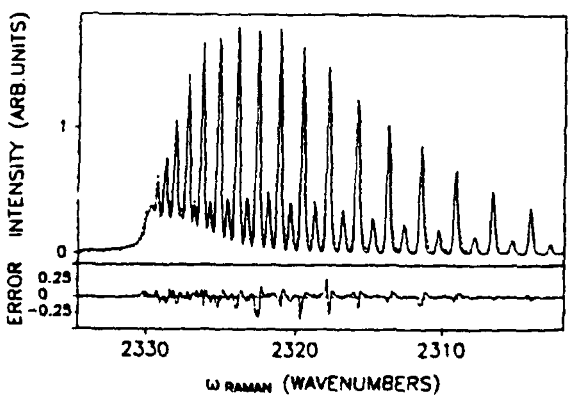

Fig. 11 Narrow-band N_2 CARS spectrum (Q-branch) from a propane/air flame above burner surface, flame center. Measurement (dashed), theoretical (full line), and error surve (lower track). Approximately 30 shots were averaged at each point; $T = 1983\,K$ [45].

4.4 Results and Outlook

In a Mach 10 hypersonic air flow of a blow-down wind tunnel temperatures and densities of nitrogen were measured [56]. The data were recorded using a non-linear optical technique named dual-line CARS which allows single laser-shot spatially-resolved measurements. The flow was probed from the free stream to the vicinity of a two-dimensional ramp model (25°). Averaged temperature and density profiles are shown in **Fig. 12**. The measurements are compared with those predicted by a Navier-Stokes solver and show good agreement.

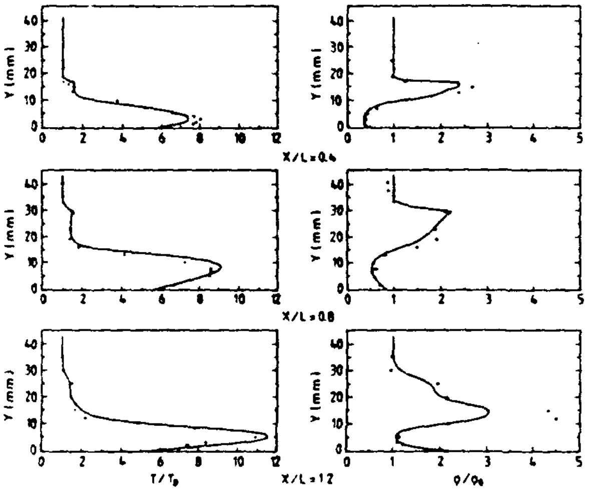

Fig. 12 Rotational temperature (left) and total density (right) profiles normalized by the free stream conditions at: a) X = 0.072 mm (X/L = 0.4), c) X = 0.144 m (X/L = 0.8), e) X = 0.214 m (X/L = 1.2): (-) HOMARD2 code; (+) experiment [56].

Dual-line CARS is a sensitive technique to probe molecules in hypersonic flow. Time-averaged temperature and density can be measured simultaneously in the vicinity of a two-dimensional model with a separation flow field region.

Focussing on the F4- and HEG-wind tunnels all scanning CARS methods are ruled out out due to a data acquisition time of several minutes. Single shot experiments remain [42]:

- dual-line CARS with high sensivity (10^{18} *molecules/cm*^{3})
- broad band CARS with minor sensivity (10^{17} *molecules/cm*^{3}).

The dual-line CARS-technique will be applied to the F4; it is also applicable to HEG.

5. ADDITIONAL NON-INTRUSIVE METHODS

Raman- and Rayleigh scattering are two additional candidates for use in supersonic flows. These techniques and some derivations are listed by Bonnet and Gressilon [1] and Miles [43]. A new method should be pointed out based on the combination of Raman Excitation and Laser-Induced Electronic Fluorescence (RELIEF). Two or three lasers are used [43, 44], tagging O_2-molecules. The method provides two-dimensional temperature- and density-surveys of the flow field, but is limited to temperatures below 800 K.

Absorption measurements of O_2 and H_2O with tunable semi-conductor diode lasers offer high potential for diagnostic applications at low prize and compact size [50, 57]. The latter point is of major importance for future flight experiments.

6. CONCLUSION

6.1 Discussion

Several non-intrusive techniques look promising for high-temperature hypersonic flows. These techniques include electron beam, LIF, laser absorption, and CARS. All four techniques suffer from the problem of spectrum overlapping at temperatures of 3000 K and above. This can be solved by spectra simulation and choice of transitions which are not influenced by other bands [26]. The expected results in F4 and HEG are planar temperature plots of *NO* and O_2 measured by LIF, temperature measurements at least pointwise and along a line at lower densities by electron beam fluorescence, and single laser-shot temperature measurements pointwise by CARS at higher densities. All three techniques have overlapping density ranges, see Fig. 1; the electron beam is (up to now) the only one providing continuous measurements during the tunnel running times.

A summary of the advanced optical diagnostic methods for temperature and density for hypersonic research is listed in **Table 1.**

The techniques listed above will provide temperature profiles near the nose of a reentry vehicle at high angle of attack and realistic flow velocities. This should help to validate CFD-data. The strong non-equilibrium of rotational and vibrational temperature is typical in hypersonic wind tunnels due to the rapid expansion in the nozzle. The chemical non-equilibrium (production of *NO*) is characteristic for wind tunnels with stagnation temperatures higher than 5000 K. Both effects will occur in F4 and HEG, and this is in strong contrast to the flight situation in a static atmosphere of a reentry vehicle. Therefore, flight experiments are necessary with an electron beam or a laser on board. Only flight data can simulate (because it is the flight reality) the true conditions to compare with CFD. Furthermore such flight data of temperatures and species concentrations are of great

Tab. 1 **Summary of Advanced Optical Diagnostic Methods for Temperature and Density for Hypersonic Research**

Technique	Flow Properties	Spatial Type	Temporal Resolution	Lab Experience	Wind Tunnel Experience	Flight Experience	Comments on Status
Electronic Beam Fluorescence	ρ_i, v, T_{trans}, T_{rot}, T_{vib}	point, 1D, 2D	high, continuous	extensive	moderate	some (8 flights)	Needs modernization in WT and can provide flight experiments within 3 years
Laser *Fluorescence*	ρ_i, v, T_{trans}, T_{rot}, T_{vib}	point, 1D, 2D	high, pulsed	moderate	some	none	Needs more utilization in WT for CFD validation
Laser Absorption	ρ_i, v, T_{trans}, T_{rot}, T_{vib}	line-of-sight	moderate, continous	moderate	some	none	Primarily for internal flows, line-of-sight method
Coherent Laser Raman (Cars)	ρ_i, v, T_{trans}, T_{rot}, T_{vib}	point	moderate, pulsed	moderate	some	none	More development, WT applications at high density
Laser Rayleigh Scattering	ρ, v, T_{trans}	point, 1D, 2D	low, pulsed	some	minimal	none	WT applications at high density, not species specific
Laser Raman Scattering	ρ_i	point	very low, pulsed	minimal	none	none	WT applications only at high density

importance for environment studies of the upper atmosphere.

Finally, it should be recognized that many of the diagnostic techniques are not only species specific, but, in addition, measure the internal state distribution of the probed molecules [57]. Thus the newer diagnostics present a revolution of sorts in that they are leading to an understanding of aerodynamic phenomena from the molecular level rather than from the traditional bulk properties approach.

6.2 Summary

1. The capabilities are available for local measurements with temporal resolution and quantitative accuracy of
   - velocity
   - temperature
   - density
   - species concentrations
   - fluctuations due to turbulence
2. Planar and point field measurements are demonstrated in laboratories for quantitative data.
3. Some techniques are now ready for wind tunnel application.
4. The potential for flight experiments is demonstrated for the electron beam for high altitudes; the laser systems require miniaturization.

6.3 Recommendations

Major funding is now required to move these techniques from the laboratory to the wind tunnels and to flight experiments. These techniques can supply data with resolution required for CFD development.

7. RERERENCES

[1] J.P. Bonnet, D. Gressilon, *Advanced Non-Intrusive Experimental Techniques in Fluid and Plasma Flows.* Experiments in Fluids, Springer Verlag 1991, 12, pp. 131-135.

[2] R.J. Cattolica, *Modern Development in Electron-Beam Fluorescence.* Rarefied Gas Dynamics, 1990, Aachen. Ed. A.E. Beylich. Weinheim: VCH, 1991, pp. 1581-1592.

[3] A.K. Rebrov, R.G. Sharenfutdinov, *Relaxation Process in a Jet in the Presence of Phase Transition.* Proceedings of the Fifteenth International Symposium on Rarefied Gas Dynamics, Vol. II, 1986, p. 109. Stuttgart: B.G. Teubner, 1986.

[4] N. Herlin, M. Pealat, M. Lefebore, P. Alnot, J. Perrin, *Rotational Energy Transfer on a Hot Surface in a Low-Pressure Flow Studied by CARS.* Surface Science 258, 1991, pp.381-388.

[5] J.-C. Lengrand, J. Allegre, M. Raffin, *Electron Beam Fluorescence Technique at Rarefied Dynamics.* Proceedings of the 14th International Symposium on Rarefied Gas Dynamics, Vol. I (1984), p. 423. Ed. H. Oguchi. Tokyo: University of Tokyo Press, 1984.

[6] C. Dankert, K.-A. Bütefisch, *Influence of Nozzle Geometry on Vibrational Relaxation in an Expansion Flow.* Proceedings of the 9th International Symposium on Rarefied Gas Dynamics, Göttingen 1974, Vol. I, p. B.20-1.

[7] E.P. Muntz, *The Electron Beam Fluorescence Technique.* AGARDograph, 132, 1965.

[8] K.A. Bütefisch, D. Vennemann, *The Electron Beam Technique in Hypersonic Rarefied Gas Dynamics.* Progress in Aerospace Science, Vol. 15, p. 217, 1974.

[9] R.J. Cattolica, R.L. Schmitt, R.E. Palmer, *Feasibility of Non-Intrusive Optical Diagnostic Measurements in Hypersonic Boundary Layers for Flight Experiments.* AIAA 28th Aerospace Science Meeting, AIAA-90-0627, Reno, Nevada/USA, 1990.

[10] J.H. De Leeuw, W.E.R. Davies, *Measurement of Temperature and Density in the Upper Atmosphere Using an Electron Beam.* Canadian Journal of Physics, 50 (1972), pp. 1044-1052.

[11] R. Grandal, E.V. Thrane, J. Troim, *Polar 5 - An Electron Accelerator Experiment within an Aurora. 4.Measurements of the 391.4 nm Light Produced by an Artificial Electron Beam in the Upper Atmosphere.* Planet Space Sci., 28 (1980), pp. 309-319.

[12] R.R. O'Neil, W.R. Pendleton, Jr., A.M. Hart, A.T. Stair, Jr., *Vibrational Temperature and Molecular Density of Thermospheric Nitrogen Measured by Rocket-Borne Electron Beam Induced Luminescence.* Journal Geophys. Res., 79 (1974), pp. 1942-1958.

[13] A.A. Haasz, J.H. De Leeuw, W.E.R. Davies, *Thermophysics* N_2 and O_2 *Concentration with Rocket-Borne Electron Beam Fluorescence Probes.* Journal Geophys. Res., 81 (1976), pp. 2382-2391.

[14] G. Israelson, J.R. Winckler, *Measurements of 3914 Å Light Production and Electron Scattering from Beams Artificially Injected into the Ionosphere.* Journal Geophys. Res., 80 (1975), pp. 3709-3712.

[15] R.R. O'Neil, F. Bein, D. Burt, J.A. Sandock, A.T. Stair, Jr., *Summarized Results of the Artificial Aurora Experiment, Precede.* Journal Geophys. Res., 83 (1978), pp. 3275-3280.

[16] P.M. Banks, W.J. Raitt, A.B. White, R.I. Bush, P.R. Williamson, *Results from the Vehicle Charging and Potential Experiment on STS-3.* J. Spacecraft, 24 (1987), pp. 138-149.

[17] J.W.L. Lewis, *Optical Diagnostics of Low-Density Flow Fields.* Rarefied Gas Dynamics, 16th Int. Symp., Pasadena/USA, 1988. Edited by E.P. Muntz, D.P. Weaver, D.H. Campbell. Progress in Astronautics and Aeronautics, Vol. 117 (1989), pp. 107-132.

[18] A. Mohammed, *Electron Beam Probing of Blow-Down Hypersonic Flow.* Ph.D. Thesis of University of Paris Sud, 17th Dec 1991.

[19] S.L. Petrie, J.J. Komr, *Application of the Electron Beam Fluorescence Technique to the Measurement of the Properties of NO in Non-Equilibrium Flows.* AFFDL-TR-72-144, Dec. 1972.

[20] R.J. Cattolica, *Electron Beam Fluorescence Measurements of Nitric Oxide.* Rarefied Gas Dynamics, 16th Int. Symp., Pasadena/USA, 1988. Edited by E.P. Muntz, D.P. Weaver, D.H. Campbell. Progress in Astronautics and Aeronautics, Vol. 117 (1989), pp. 133-139.

[21] S.L. Petrie, A.A. Boiarski, S.S. Lazdinis, *Electron Beam Studies of the Properties of Molecular and Atomic Oxygen in Non-Equilibrium Flows.* 6th Aerodynamic Testing Conference, AIAA 71-271, 1971.

[22] P.J. Dagdigian, J.P. Doering, *Electron Impact Ionization Excitation of CO in a Supersonic Beam.* Journal of Chemical Physics, Vol. 78, No. 4, Feb. 1983.

[23] A.E. Beylich, *Experimental Investigation of Carbon Dioxide Jet Plumes.* The Physics of Fluids, Vol. 14, No. 5, May 1971, pp. 898-905.

[24] E.P. Muntz, J.A. Kunc, D.A. Erwin, *A Pulsed Electron-Photon Technique for Temperature and Specie Concentration Measurements at Points in Relatively Dense, Unseeded Air Flows.* AIAA-87-1526, 22nd AIAA Thermophysics Conference, July 8-10, 1987.

[25] C. Dankert, G. Koppenwallner, *An Experimental Study of Nitrogen Condensation in a Free Jet Expansion.* Rarefied Gas Dynamics, Eleventh Symposium. Edited by R. Campargue, Vol. II, Paris 1979: Commissariat a l'Energie Atomique (CEA), pp. 1107-1118.

[26] C. Dankert, G. Gundlach, *Laser Induced Fluorescence Apparatus for Application in Rarefied Hypersonic Flow Fields. Part I: Static Cell Experiments with NO.* DLR-IB 222-91 A 11, DLR Göttingen/Germany, 1991.

[27] W.H. Beck, C. Dankert, G. Eitelberg, G. Gundlach, *Preliminary Laser Induced Fluorescence Measurements in Several Facilities in Preparation for Application to Studies in the High Enthalpy Shock Tunnel Göttingen.* 30th Aerospace Sciences Meeting, AIAA 92-0143, Reno, Nevada/USA, 1992.

[28] T. Niimi, T. Fujimoto, N. Shimizu, *Planar Measurements of Temperature in Rarefied Gas Flow by LIF Images.* Rarefied Gas Dynamics, Proceedings of the 17th International Symposium on Rarefied Gas Dynamics, Aachen 1990. Edited by A.E. Beylich. Weinheim: VCH, 1991.

[29] R.K. Hanson, A.T. Chang, J.M. Seitman, M.P. Lee, P.H. Paul, B.E. Battles, *Laser-Induced Fluorescence Diagnostics for Supersonic Flows*. 28th Aerospace Sciences Meeting, AIAA-90-0625, Reno, Nevada/USA, 1990.

[30] B.K. Mc Millin, J.L. Palmer, R.K. Hanson, *Two-Dimensional Temperature Measurements of Shock Tube Flows Using Planar Laser-Induced Fluorescence Imaging of Nitric Oxide*. AIAA 22nd Fluid Dynamics, Plasma Dynamics & Laser Conference, AIAA-91-1670, Honolulu, Hawaii, 1991.

[31] P. Andresen, A. Bath, W. Graeger, H.W. Luelf, G. Meijer, J.J. Meulen, *Laser-Induced Fluorescence with Tunable Excimerlasers as a Possible Method for Instantaneous Temperature Field Measurements at High Pressure: Checks with an Atmospheric Pressure Flame*. Appl. Opt. 27 (1988), pp. 365-378.

[32] F. Aguillon, A. Lebehot, J. Roussean, R. Campargue, *Two-Rotor Resonant Third Harmonic Generation in the XUV Range Reflecting Internal State Populations in CW CO Free Jets*. Proceedings of the Fifteenth International Symposium on Rarefied Gas Dynamics, Grado/Italy, Vol. II, 1986, pp. 565-574. Stuttgart: B.G. Teubner, 1986.

[33] O. Faucher, F. Aguillon, A. Lebehot, R. Campargue, *Two-Photon Third Harmonic Generation in a CW Nitrogen Free Jet Zone of Silence Reflecting Quantitatively Internal State Populations*. Proceedings of the 17th International Symposium on Rarefied Gas Dynamics, Aachen/Germany 1990. Edited by A.E. Beylich. Weinheim: VCH, 1991, pp. 1088-1095.

[34] G. Lauter, D. Fletcher, R. Mc Kentic, *A Method for Measuring Tempertures and Densities in Hypersonic Wind Tunnel Air Flows Using Laser-Induced O_2 Fluorescence*. 28th Aerospace Sciences Meeting, 1990, Reno, Nevada/USA, AIAA-90-0626.

[35] M.P. Lee, P.H. Paul, R.K. Hanson, *Quantitative Imaging of Temperature Fields in Air Using Planar Laser-Induced Fluorescence of O_2*. Optical Letter 12 (1987), 75.

[36] K. Shibuya, F. Stuhl, *Fluorescence Lifetime and Collisional Quenching of the Predissociative NO $B^2\Pi$ ($v' = 7$) State*. Chemical Physics 79, 1983, pp. 367-381.

[37] K. Kohse-Höinghaus, U. Meier, B. Attal-Tretout, *Laser-Induced Fluorescence Study of OH in Flat Flames of 1 - 10 bar Compared with Resonance CARS Experiments*. Appl. Opt. 29 (10), 1990, pp. 1560-1569.

[38] H.-D. Barth, C. Jackschath, T. Pertsch, F. Huisken, *CARS Spectroscopy of Molecules and Clusters in Supersonic Jets*. Appl. Phys. B45, 1988, pp. 205-214.

[39] H.-D. Barth, F. Huisken, A.A. Ilyokhin, *Coherent Raman Spectroscopy of Nitrogen Molecules and Clusters in Supersonic Jets*. Appl. Phys. B52, 1991, pp. 84-89.

[40] W. Stricker, M. Woyde, *CARS Temperature Measurements in High Pressure Flames*. Proceedings of the Joint Meeting of the German and Italian Section of the Combustion Institute, Ravelo/Italy, 1989, Paper 1.1.

[41] G. Marowsky, A. Slenczka, *Laser Spectroscopy VIII*. Edited by W. Persson and S. Scramberg, Springer Series Opt.Sci. 55, 1987, p. 334.

[42] J.P. Taran, M. Pealat, F. Grisch, *Private Communication*.

[43] R.B. Miles, D.M. Nosenchuck, *Three-Dimensional Quantitative Flow Diagnostics*. Lecture Notes in Engineering 45, M. Gad-el-Hak, Editor. Advances in Fluid Mechanics Measurements, Springer Verlag, 1969.

[44] R.B. Miles, J.J. Connors, E.C. Markovitz, P.J. Howard, G.J. Roth, *Instantaneous Profiles and Turbulence Statistics of Supersonic Free Shear Layers by Raman Excitation Plus Laser-Induced Electronic Fluorescence (Relief) Velocity Tagging of Oxygen*. Experiments in Fluids, 8, pp. 176-24, Springer Verlag 1989.

[45] W. Kreutner, W. Stricker, Th. Just, *Comparison of Spontaneous Raman and CARS Measurements in a Laminar Flame at Atmospheric Pressure*. Applied Spectroscopy, Vol. 41, No. 1, 1987, pp. 98-105.

[46] E.P. Muntz, D.A. Erwin, *Rapid Pulse Electron Beam Fluorescence for Flow Field Diagnostics*. Hypersonic ARW, Theoretical and Experimental Methods in Hypersonic Flows, 70th Fluid Dynamics Panel Meeting, ed. by Kluwer, 1992.

[47] E. Hirai, K.-A. Bütefisch, C. Dankert, *Velocity and Density Determination by Electron Beam Technique*. Hypersonic ARW, Theoretical and Experimental Methods in Hypersonic Flows, 70th Fluid Dynamics Panel Meeting, ed. by Kluwer, 1992.

[48] R.J. Cattolica, *Electron Beam Fluorescence Imaging for Hypersonic Research*. Hypersonic ARW, Theoretical and Experimental Methods in Hypersonic Flows, 70th Fluid Dynamics Panel Meeting, ed. by Kluwer, 1992.

[49] A.K. Mohammed, *Electron Beam Velocimetry*. Hypersonic ARW, Theoretical and Experimental Methods in Hypersonic Flows, 70th Fluid Dynamics Panel Meeting, ed. by Kluwer, 1992.

[50] R.K. Hanson, *Laser-Based Diagnostics for Hypersonic Flows.* Hypersonic ARW, Theoretical and Experimental Methods in Hypersonic Flows, 70th Fluid Dynamics Panel Meeting, ed. by Kluwer, 1992.

[51] G. Gundlach, C. Dankert, *Nonintrusive Temperature Determination by LIF in Hypersonic Wind Tunnels.* Hypersonic ARW, Theoretical and Experimental Methods in Hypersonic Flows, 70th Fluid Dynamics Panel Meeting, ed. by Kluwer, 1992.

[52] W.H. Beck, U. Koch, M. Müller, *Spectroscopic Diagnostic Techniques for the High Enthalpy Shock Tunnel in Göttingen (HEG): Preparatory LIF Studies on other Facilities.* Hypersonic ARW, Theoretical and Experimental Methods in Hypersonic Flows, 70th Fluid Dynamics Panel Meeting, ed. by Kluwer, 1992.

[53] F. Dionnet, J. Monard, D. Puechberty, *Broad Band Excimer Laser Induced Fluorescence Applied to Hypersonic and Supersonic Air Flows.* Hypersonic ARW, Theoretical and Experimental Methods in Hypersonic Flows, 70th Fluid Dynamics Panel Meeting, ed. by Kluwer, 1992.

[54] R.L. Mc Kenzie, D.G. Fletcher, *Laser-Spectroscopic Measurement Techniques for Hypersonic, Turbulent Wind Tunnel Flows.* Hypersonic ARW, Theoretical and Experimental Methods in Hypersonic Flows, 70th Fluid Dynamics Panel Meeting, ed. by Kluwer, 1992.

[55] U. Meier, I. Plath, K. Kohse-Höinghaus, *Determination of Minority Species Concentrations and Temperature in Combustion Systems by Laser-Induced Fluorescence.* Hypersonic ARW, Theoretical and Experimental Methods in Hypersonic Flows, 70th Fluid Dynamics Panel Meeting, ed. by Kluwer, 1992.

[56] F. Grisch, P. Bouchardy, M. Pealat, B. Chanetz, T. Pot, M.C. Coet, *Rotational Temperature and Density Measurements in a Hypersonic Flow by Dual-Line CARS.* Hypersonic ARW, Theoretical and Experimental Methods in Hypersonic Flows, 70th Fluid Dynamics Panel Meeting, ed. by Kluwer, 1992.

[57] R.J. Exton, *Absorption, Scattering, and Fluorescence Techniques for Hypersonic Flow Measurements.* Hypersonic ARW, Theoretical and Experimental Methods in Hypersonic Flows, 70th Fluid Dynamics Panel Meeting, ed. by Kluwer, 1992.

Pressure and Force Measurements on Models Set in Hypersonic Flows: A Review

Charles G. Miller
NASA Langley Research Center
16 Victory Street, MS 408
Hampton, VA 23665-5225 USA

ABSTRACT

A review of measurement techniques used to obtain aerodynamic forces and moments and surface/flow field pressures for models tested in impulse hypersonic-hypervelocity facilities and in conventional-type hypersonic wind tunnels is presented. Although force and moment measurement techniques presently used in hypersonic wind tunnels are relatively unchanged from the 1960's and 1970's, significant advances have recently been made for impulse facilities. For both hypersonic wind tunnels and impulse facilities, the state-of-the-art has advanced via refinements, improved test techniques, and advances in semiconductor technology, data acquisition systems and computers. The introduction of electronically scanned pressure systems over a decade ago "revolutionized" pressure measurements in hypersonic wind tunnels and a second "revolution" is impending with the development and application of optical, two-dimensional, global pressure measurement techniques. The development and continued refinement of miniature piezoresistive transducers has provided the capability to perform detailed surface pressure measurements on relatively small, complex models in impulse facilities; these transducers also provided the capability for intrusive flow field pressure measurements with miniature survey rakes.

PREFACE

The original intent of this paper, as indicated by its title, was to provide a review of force and moment and of pressure measurement techniques used in hypersonic facilities, both conventional-type hypersonic wind tunnels and impulse-type hypersonic-hypervelocity facilities. This review was to be based primarily on reports presented at the NATO Advanced Research Workshop entitled "New Trends in Instrumentation for Hypersonic Research" and held at ONERA Le Fauga-Mauzac, France, April 27 to May 1, 1992. Four papers were presented in session 4, which was entitled "Pressure-Forces", of the workshop and all addressed force and moment measurements in impulse facilities. The titles and authors of these papers are as follows:

(1) "Force Measurement in Hypervelocity Impulse Facilities" by J. M. Simmons, W. J. Daniel, D. J. Mee, and S. L. Tuttle, (paper 4A).

(2) "A Six Component Balance for Short Duration Hypersonic Facilities" by C. Jessen and H. Grönig (paper 4B).

(3) "Millisecond Aerodynamic Force Measurement Technique for High Enthalpy Test Facilities" by K. W. Naumann, H. Ende, and G. Mathieu (paper 4C).

(4) "Aerodynamic Force Measurements in the VKI LongShot Hypersonic Facility" by M. Carbonaro (paper 4D).

In the spirit of the original intent for this paper and for the sake of completeness, the synopses of the four papers presented at the workshop will be augmented by discussions on measurement techniques routinely used to: (1) obtain aerodynamic forces and moments and pressure distributions in conventional-type (i.e., relatively low enthalpy, blowdown-to-vacuum) hypersonic wind tunnels and (2) to obtain pressure measurements in impulse facilities.

INTRODUCTION

The contribution of hypersonic/hypervelocity ground-based facilities to the aerodynamic and aerothermodynamic assessment of proposed aerospace vehicle concepts over the past four decades is well recognized. Aerodynamic assessments are typically performed via the measurement of forces and moments and of pressure distributions on stationary models subjected to hypersonic/hypervelocity flow; similarly, aerothermodynamic assessments are performed via the measurement of heat transfer rate distributions. Models may be tested over a wide range of hypersonic simulation parameters (principally Mach number, Reynolds number, and normal shock density ratio or ratio of specific heats for continuum flow) and attitudes (angles of attack and sideslip) using conventional-type hypersonic wind tunnels and/or impulse facilities, some of which are capable of generating flow velocities representative of flight at high hypersonic Mach numbers. (A conventional-type hypersonic wind tunnel, referred to herein as hypersonic wind tunnel, is defined as: (1) operating at a relatively low enthalpy such that perfect or near-perfect gas behavior is achieved throughout the nozzle expansion process; (2) providing a given Mach number via a fixed nozzle area ratio; and (3) providing a range of Reynolds number via variation of reservoir pressure. The facility may be intermittent (i.e., blowdown to vacuum) or continuous, running for several hours. Impulse facilities may be of the shock tube family, such as shock tunnels (steady expansion process) and expansion tubes (unsteady expansion process), or hotshot type whereby electrical energy is provided directly to the test medium. (A collection of presentations made on impulse facilities, which include descriptions of facilities and instrumentation, was recently edited by Rodgers, 1990.) Test times for such impulse facilities typically range from 0.1 to 100 millisecond. (Ballistic ranges, whereby the model is launched and allowed to free flight or is tracked, are not considered herein. Although arc-heated wind tunnels are important contributors to the study of materials at high temperatures, they are not generally considered amenable for aerodynamic/aerothermodynamic testing and thus are also not considered herein.) Both types (i.e., conventional-type and impulse) of facilities provide challenges to experimental aerodynamicists in pursuit of credible aerodynamic data. From a simplistic viewpoint, three interdependent factors require consideration in the measurement of forces and moments and of pressure distributions irrespective of the type of hypersonic facility; they are (1) magnitude, (2) time, and (3) the influence of temperature change.

The magnitude of the aerodynamic forces and moments and the surface/flow field pressures during all phases of the facility flow sequence (i.e., flow establishment, testing period, and flow breakdown) will naturally influence the measurement approach selected. Care must be exercised so to not exceed the acceptable range of the instrumentation, nor damage it, and to provide acceptable signal-to-noise ratios. Most hypersonic wind tunnels and impulse facilities are capable of at least an order of magnitude variation in dynamic pressure. This variation coupled to variations in model shape (very blunt to very slender) and attitude generally precludes a single measurement device from covering the entire range of magnitude possible in most tests.

The time required to establish flow within the facility and the period of steady or quasi-steady flow is quite short for impulse facilities. Because of this short test time, impulse facilities are attractive from an aerothermodynamic testing viewpoint (e.g., Schultz and Jones, 1973). Generally, the heat transfer rate to models may be measured to a greater accuracy than surface pressures in such facilities. Force and moment measurements in impulse facilities, particularly for those having run times less than 3-5 millisecond, are quite challenging due primarily to the finite mass of the model (model inertia; infinite mass corresponds to no model movement whereby zero mass corresponds to instantaneous response to the flow) and the associated dynamics. On the other hand, with the possible exception of extremely low levels of surface pressure such as those encountered in the base region of blunt bodies and on very slender configurations at high hypersonic Mach numbers, model surface pressures may be more accurately measured than heat transfer rates in hypersonic wind tunnels. Primarily because of differences in run time, both types of hypersonic facilities challenge experimentalists in different ways. One common denominator, however, is the detrimental effect of temperature change on the instrumentation commonly used for force and moment and for pressure measurements.

The relatively long run times, hence model exposure times to the flow, of hypersonic wind tunnels often allow the model and the support system to become quite hot (e.g., Mach 10 air tunnels require stagnation temperatures around 1800°R to avoid liquefaction during expansion of the nozzle flow). Commonly used techniques to measure model forces and moments and pressure distributions in these tunnels are sensitive to temperature change. Thus steps must be taken to isolate the instrumentation from temperature effects (e.g., water cooled and/or ceramic coated model support systems, glass-ceramic models, etc.) and/or accurately compensate for such effects. One example of recent changes in methodology to minimize, if not eliminate, the effect of temperature on pressure measurements in hypersonic wind tunnels having an injection/retraction system is the incorporation of onboard, small volume transducers even for relatively small models. The short tubing lengths possible with onboard transducers significantly reduces the lag time, allowing steady-state values of pressure to be measured after only a few seconds of exposure to the flow. The model may then be retracted from the flow prior to the occurrence of appreciable temperature changes. Although the short model exposure times for impulse facilities generally precludes large temperature variations of the model, pressure instrumentation must often be flush mounted to achieve acceptable response. Any volume between the sensing element of a transducer, which is often protected by a screen, and the model surface will induce a finite lag as the volume is filled and may be viewed as a pneumatic filter (e.g., Moore, 1979). Commonly used piezoelectric and piezoresistive pressure transducers are quite sensitive to temperature; and when mounted in close proximity to the high enthalpy test medium, they must be thermally protected or compensated.

Because of the demise of interest in hypersonics in the 1970's and well into the 1980's, as resources and personnel were diverted into other disciplines and a major portion of the hypersonic wind tunnels were deactivated or terminated, force and moment measurements are currently performed much as they were in the 1960's and 1970's. Although refinements have been made in the materials and adhesives used in strain gage balances, improvements made in test techniques, and advances made in data acquisition and reduction, the basic technique is relatively unchanged over the past two decades. The lack of interest in hypersonics coupled with the relatively good performance of existing methods simply did not provide an incentive in the 1970's and 1980's to develop other techniques. This was not the case for pressure measurements, however. About a decade ago, electronically scanned pressure (ESP) systems became commercially available which essentially "revolutionized" pressure measurements in hypersonic wind tunnels. These systems significantly reduced the cost per channel compared to variable capacitance or reluctance transducers; were quite compact, with 16, 32, or 48 sensors being housed in a small module that could be mounted close to the model surface and often within the model; and could be calibrated *immediately prior to a test.* ESP systems have continued to be refined and presently are standard equipment for many hypersonic wind tunnels world wide.

Similar trends were experienced by the impulse facility community. Because impulse facilities are primarily used for aerothermodynamic and fluid dynamic studies, there was little incentive in the 1970's and early-to-mid 1980's to improve methods for force and moment measurements in the few facilities that remained operational. Advances were made, however, in the measurement of model surface and flow field pressures with the introduction of commercially available miniature piezoresistance pressure transducers around the mid 1970's. Employing silicon diaphragms, these transducers could be made quite small (typically to a diameter of 0.050 inch) thereby allowing detailed pressure distributions to be made on relatively small, complex models. As for hypersonic wind tunnels, impulse facilities benefitted greatly from advances in data acquisition systems (DAS) and computers. Gone were the days of large banks of oscilloscopes with cameras and the laborious digitation of traces from film. Today, data acquisition systems for impulse facilities provide essentially the same rapid data reduction as those for hypersonic wind tunnels.

The purpose of this paper is to provide a review of techniques presently used in hypersonic wind tunnels and in impulse facilities to measure model forces and moments and surface/flow field pressures. It is not intended to provide a comprehensive, indepth discussion of any one technique, but rather a synopsis.

MEASUREMENT TECHNIQUES

Model Surface Pressure

Impulse Facilities

Representative test times for shock tunnels and expansion tubes range from 0.1 to 10 millisecond. For such short times, model surface pressures are generally measured with transducers based on the piezoelectric or the piezoresistive principal. Such transducers may also be used for impulse facilities having longer run times such as hotshot tunnels (typically 20 to 100 milliseconds), as may other concepts such as small volume variable reluctance diaphragm transducers. Piezoelectric and piezoresistive pressure transducers are commercially available and cover a wide range of size, pressure range, and response time. Because of their wide spread utilization in impulse facilities world wide, these transducers are reviewed in this section.

Peizo is derived from the early Greek word meaning "to squeeze." For piezoelectric transducers, the surface of certain crystals is charged electrically when the crystal is loaded mechanically or "squeezed." The three basic components of such transducers are: (1) the sensor housing which hermetically encloses the quartz elements; (2) quartz elements, and (3) the diaphragm welded to the sensor housing and transmitting the pressure exerted onto the quartz elements. Piezoelectric transducers produce an output only when subjected to a change in pressure and thus are ideally suited for measuring dynamic events; since the electrical charge cannot be stored for an indefinite period of time, piezoelectric transducers cannot perform truly static measurements. High impedance piezoelectric systems (charge mode) require charge amplifiers for signal conditioning; low impedance piezoelectric systems have built-in charge-to-voltage converters and are referred to as the voltage mode. Acceleration compensation consists of a tuned accelerator system connected in series, with opposite polarity, to the pressure measuring system. Commonly used piezoelectric transducers (e.g., those manufactured by Kistler Instrument Corporation and PCB Piezotronics) have 0.1 or 0.22 inch diameter diaphragms, quoted rise times of one microsecond and resonant frequencies from about 150 kHz to up to 500 kHz. These transducers are quite sensitive to change in temperature; that is, the transducer output varies (generally, nonlinearly) with temperature. Elimination of temperature effects can be quite challenging, particularly for flush mounted units which are necessary for run times less than a millisecond, or so. A thin layer of RTV or layer of electrical tape fitted to the diaphragm help to isolate piezoelectric transducers from temperature effects.

The piezoresistance effect is defined as the change in electrical resistivity with applied stress; this change is relatively large in semiconductors. Piezoresistive transducers utilize a silicon pressure sensing diaphragm. Silicon is used primarily because the high sensitivity of this material allows very small diaphragms with high resonant frequencies; however, silicon is brittle and can crack or shatter on impact or under excessive loading. Newer transducers incorporate four piezoresistive silicon strain gages atomically diffused into the diaphragm. (Older designs used wire gages bonded to the thin diaphragm. Newer gages using silicon resistors are free of mechanical hysteresis and have greater sensitivity.) These strain gages serve as the arms of a Wheatstone Bridge. This fully active bridge converts the strain-induced resistance change of the gage to voltage changes which may be measured. The bridge is normally energized by applying a regulated voltage across two opposite corners; the output voltage is proportional to the product of the excitation voltage and the resistance changes of the strain gages. Piezoresistive transducers having outside diameters as small as 0.030 inch (e.g., Kulite Semiconductor Products, Inc. model CQ-030) are available, but diameters of 0.050 to 0.060 inch are more representative of commonly used transducers (e.g., those manufactured by Endevco Corporation, Entran International, and Kulite). As with piezoelectric gages, piezoresistive gages are temperature dependent. Temperature compensation is generally accomplished with simple circuit techniques using passive shunt or series resistor elements whose resistance is temperature independent. A protective coating of silicon rubber or RTV may be applied to the diaphragm for thermal protection and a screen is generally used to protect the diaphragm from particles incident upon the transducer. The rise time of a piezoresistive transducer is inversely proportional to the resonant frequency; this frequency for commonly used transducers having a diameter of 0.050 to 0.060 inch ranges from 100 to 1500 kHz depending on the pressure range (diaphragm resonant frequency increases with increasing pressure range). A resonant frequency of approximately 1200 kHz provides a rise time of one microsecond.

Piezoresistive transducers offer the advantage of dc (O Hz) operation, hence provide the capability to perform static measurements and yet have excellent dynamic behavior. This capability allows transducers installed in a model, which has been installed in the facility, to be calibrated in-place over the appropriate range of pressure. This calibration of the entire system (sensor, signal conditioning and recording) is usually performed by first evacuating the facility. The pressure level is increased in discrete increments and recorded via a precision pressure standard. The transducer output at each pressure level provides a calibration of the transducer. Because piezoresistive transducers are capable of static measurements, such transducers are used in both impulse facilities and hypersonic wind tunnels. Both absolute (i.e., with respect to vacuum) and differential (i.e., measured between two different levels) transducers are available.

To achieve accurate measurements, painstaking care must be exercised in the static and/or dynamic calibration and the installation. Caution must be exercised to avoid damage to the transducer; to avoid loading it such to influence its output; not providing adequate thermal or mechanical (vibration) protection; not providing a proper seal to avoid leaks around the gage; and maintaining a controlled and known reference pressure for differential transducers. With care and for pressure levels in excess of one psid, measurements accurate to within 5 percent are possible.

The miniaturization of piezoresistive pressure transducers provides the capability to measure detailed total pressure surveys in shock layers and in boundary/shear layers with survey rakes. The transducer is mounted, naturally, at or very close to the sensing end of the probe.

Hypersonic Wind Tunnels

Model surface pressures are measured in many hypersonic wind tunnels with either electronically scanned pressure (ESP) piezoresistive (silicon) sensors, or with high-volume, multi-range, variable-capacitance diaphragm-type transducers (e.g., Miller and Smith, 1986; Miller, 1990). ESP modules are commercially available with different pressure ranges and typically contain 16, 32, 48 or 64 sensors. The small size of the sensor modules allows for installation in the model or near the base of the strut to minimize tubing length (pressure lag) between the model surface and sensor. When installed externally to the model, modules are generally housed within an insulated box through which air may be passed to provide a thermally stable environment, if required. These modules combine pressure transducers, internal multiplexing, and amplification to provide a scanner for a high data rate. An integral, pneumatically controlled mechanism allows the transducers to be calibrated on-line. This on-line calibration consists of applying accurately known pressure (or vacuum) levels to the sensors (original ESP systems used a 3-point calibration whereas newer systems use 5 points); these levels are generally selected to cover the expected pressure levels for a run. Since calibration is performed using an absolute pressure standard, maintaining the same reference pressure between the calibration and the wind tunnel test will provide absolute pressure measurements. Such systems contain their own signal-processing and thus are interfaced directly to the controller (computer). Representative maximum sampling rates for the ESP systems are 10/sec for each of 128 channels, or 5/sec for 256 channels.

The primary advantages of the ESP system over the variable-capacitance system are significantly lower (by about 1/5) cost per channel, miniaturization, and faster response. The primary disadvantages are limited range of application for a given module and a higher uncertainty in the measurement of low pressure levels, for example less than 0.1 psid.

As one example, most hypersonic wind tunnels at NASA Langley (Miller, 1990) have Pressure System Incorporated (PSI) model 8400 systems having 256 channels. Provisions were provided at each tunnel to allow the rapid augmentation of an additional 256 channels. Such systems operate well in pressure ranges associated with low speed (subsonic and transonic) wind tunnels, but modifications are required to meet the low pressure (vacuum) requirements of hypersonic wind tunnels (e.g., Hutchinson, 1991). These modifications, which include improvements to the vacuum and pneumatic system used in the calibration procedure, and the calibration standard, are discussed by Hutchinson, 1991. Also, forty variable-capacitance transducers have been assembled into a "portable" system that may be moved from facility to facility. Most tunnels have 10 to 20 variable-capacitance transducers onsite. When using the ESP system, several tubes are often teed to variable-capacitance transducers to provide a check on the pressure level measured. Similarly, when using multiple ESP modules, transducers from different modules are teed together to determine the level of agreement (or disagreement) between modules.

As mentioned previously, piezoresistive pressure transducers provide the capability to perform static measurements and have good dynamic characteristics. Thus, the same pressure transducers used in impulse facilities are also used in hypersonic wind tunnels. (As a rule of thumb, manufacturers recommend the selection of a transducer having a resonant frequency that is five times the frequency of interest, i.e., the useful frequency range is linear (within ±5 percent) for 20 percent of the resonant frequency.) Their fast response characteristics are amenable to the study of hypersonic internal (e.g., inlets) and external flow separation phenomena, and these transducers are often used in traversing flow field survey probes.

Complex models tested over a range of Reynolds number and attitude provide a wide range of surface pressure. One disadvantage of ESP systems is they are not multi-ranged. Thus, to accommodate a large surface pressure range, modules must be changed or possibly teed together provided they can withstand the overloads. Primarily for this reason, a pressure measurement system has been developed that employs a number of miniature piezoresistive pressure transducers with different ranges to appear as a single transducer. The different range pressure transducers are connected to a comparator circuit which compares the output from the transducers, determines which gage is reading closest to full scale, biases the signals from the other transducers, and provides a continuous single output so to appear as a single transducer. This system, manufactured by Dynamic Engineering Incorporated and referred to as the ATS-1 Pressure Measurement System, is presently being evaluated in the NASA Langley Unitary Plan Wind Tunnel.

Heavily instrumented pressure models for conventional-type hypersonic wind tunnels require a relatively long time to design and fabricate (often in excess of 1 year), are thus quite expensive, challenging to fabricate to high fidelity primarily due to the tubing process, and often require considerable setup time in the wind tunnel (corresponding to considerable tunnel down time). Thus, it is not surprising that there is considerable interest in the hypersonic community concerning recent advancements in optical pressure measurement systems (OPMS) (e.g., DeMeis, 1992) based on photoluminescence which includes both phosphorescence (e.g., Kavandi, et al., 1990) and fluorescence (e.g., Morris, et al., 1992). Such systems avoid many of the previously mentioned disadvantages associated with conventional pressure model fabrication and tunnel setup while providing the significant advantage of global two-dimensional pressure mappings.

As discussed by Morris, et al., 1992, models are coated with a material that photoluminesce when excited by the appropriate light source. A probe molecule is excited via the absorption of a photon having the appropriate energy. Upon returning to the ground electronic state by emitting a lower energy photon, the molecule photoluminesce. (Fluorescence is the emission of light generally within a time on the order of 10^{-8} sec; in contrast, phosphorescence is a delayed emission generally within 10^{-3} to 100 sec.) An alternate transition to the ground state is provided by a collision with an oxygen molecule. Rather than emitting a photon, the excess energy of the molecule is absorbed by the oxygen during a collisional deactivation. As the number of oxygen molecules increases in a given volume, the frequency of collisional deactivation increases and lowers or quenches the luminescence. Thus, for a coated model, the greater the static air pressure (i.e., the greater the oxygen concentration), the less the phosphorescence or fluorescence. Advances in image processing hardware and computers now allow the concept of oxygen quenching to be extended to the quantitative measurement of pressure. Digital cameras with a scientific-grade CCD array having 16 bits of resolution and 4 million pixels can be used to measure luminescence. Computers can quickly reduce and store the large quantities of data generated by such cameras and image processors can be used to analyze and display the data.

The development and/or application of OPMS (e.g., University of Washington - NASA Ames Research Center (Kavandi, et al., 1990); McDonnell Douglas Research Laboratory (MDRL) (Morris, et al., 1992); and Central Aerohydrodynamics Institute (Ts AGI) of the Commonwealth of Independent States (marketed by Inteco, an Italian Software firm) (Vollon and Loreto 1991; and Engler, et al., 1992)) has provided new diagnostic capability to the lower speed (subsonic to supersonic) aerodynamic community via successful demonstrations in subsonic and supersonic wind tunnels and in flight. The extension of this technique to hypersonic wind tunnels using air as the test medium will require compensation for temperature effects. The oxygen quenching process is temperature dependent and the properties of the coating may also vary with temperature, hence time. The technique developed by MDRL has recently been tested in the NASA Langley 12-Inch Mach 6 High Pressure Tunnel and these data are presently being analyzed.

Forces and Moments

Impulse Facilities

A few general comments will be made prior to discussing the four papers presented at the subject workshop. Most force transducers have an elastic sensing element whose deformation provides a measure of the acting force. Aerodynamic forces in impulse facilities are generally measured with: (1) piezoelectric force transducers, where the sensing element is the same as the transduction element that produces the electrical output signal from the acting force, (2) piezoresistive or semiconductor strain gages, and/or (3) conventional foil strain gages. Generally, three component and six component balances are used in impulse facilities having useful run times of approximately 3 to 10 millisecond (i.e., excluding facility flow establishment time). These balances may employ one or a combination of the measurement techniques (i.e., piezoelectric, piezoresistive, or foil strain gage). Aerodynamic force measurements in impulse facilities are not straightforward and may require additional (typically 6) accelerometers on the model for inertial corrections (i.e., the effect of model vibration) to the balance output. The natural frequency of the model material is also an important consideration, and the model must be dynamically calibrated. Jessen and Gronig, 1992 provide an excellent discussion of the rationale for the design and construction of a balance for use in shock tunnels having run times of several milliseconds. A classical review of force and moment measurements in impulse facilities is provided by Bernstein, 1975.

A new technique that provides the capability to measure aerodynamic forces for sub-millisecond test times has been developed and demonstrated by Simmons, et al., 1992 for nonlifting bodies at zero incidence. This technique is based on the interpretation of transient stress waves propagating within the model and support. Sharp cones, having half angles of 5° and 15°, lengths of 7.9 and 16.7 inches respectively, and fabricated from *aluminum*, were attached to a relatively long (2 m) brass sting having an outside diameter of 1.5 inches. The sting, hence model, was suspended in the test section of the University of Queensland piston-driven Shock Tunnel T4 via two strings; hence the model was free to move axially although the actual movement is negligible during a run. To protect the sting from external forces due to shear layer impingement and the wake flow in general, it was enclosed in a shroud. Two strain gages were attached to the sting 180° apart. Upon establishment of the flow about the model and during the useful test period, a large number of stress wave reflections occur within the model. The period of these reflections is an order of magnitude less than the test time. The model reacts against the mass of the sting and stress waves propagate along the sting and reflect from the end. The resulting outputs of the strain gages mounted on the sting, which are sampled every 5 microseconds, are averaged to cancel bending effects and used to provide a time history of the drag. This time history of the drag is determined numerically via the deconvolution process (inverse dynamic problem) and follows the pitot pressure time history (i.e., decays with time). The rise time for this technique, which is shown to be insensitive to the assumed spatial and temporal loading distributions on the model, is approximately 100 microseconds. A technique that extends this capability to include measurements of lift and moment is under study and discussed by Simmons, et al., 1992. Future plans include the utilization of this suspended model technique to measure the thrust of a combustor. The exhaust of a combustor would be captured by a nozzle having parallel side walls and 11° diverging top and bottom walls. This nozzle would be attached to stings and suspended via strings as discussed previously, thus is free to move relative to the fixed-position combustor. The impulsive pressure loading on the inner walls of the nozzle will send stress waves along the stings where they are monitored by strain gages. A positive thrust will move the nozzle closer to the combustor.

An excellent discussion of the design rationale for a new geometry, six-component balance for use in a shock tunnel having a 4 millisecond flow duration is presented by Jessen and Gronig, 1992. The primary driving factors in the design of this balance, which utilized finite element analysis, were test time, balance natural frequency, and model moment of inertia. Based on a geometry involving connecting cross arms having quadratic cross sections and being conical as the arms extend outward from a center inner plug to a 1.65-inch-diameter outer shell, the resulting balance is quite short (length is 0.87 inch without the model mounting adaptor). Semiconductor strain gages are attached to each side of each arm, resulting in a total of 16 gages. Although challenging to fabricate, the balance is easy to handle, robust, and quite accurate. The *minimum natural* frequency of the balance without the model is 2.4 kHz and all six force and moment components are measured without acceleration compensation. A third-order static calibration involving 500 load cases was performed with the balance. (The minimum number of individual load cases required is 400. One thousand cases are required for good results and 1500 for excellent results.) This new balance has been successfully demonstrated via tests at Mach 8 in the RWTH Aachen Shock Tunnel for a 15° half angle sharp cone and a 30° half angle sharp cone with a cylindrical afterbody. Future plans include compensation for sting oscillation, testing in a contoured (as opposed to conical) nozzle that will provide uniform flow, and the design of an advanced prototype involving calibration with 1500 load cases.

A novel device for free-flight testing a model in a conventional-type shock tunnel is the subject of the paper by Naumann, et al., 1992. This technique is insensitive to disturbances resulting from the flow establishment process of the facility and compensates for variations in flow parameters during the useful test period. The model, instrumented with piezoelectric accelerometers, is positioned in the test section by a model support system consisting of a clamping device. This clamp is closed about the sting attached to the model thereby fixing the position of the model in the test section. Just prior to flow arrival at the test section, pyrotechnic charges are ignited to open the clamp, thereby allowing the model and sting to free flight. Following the useful test period, the clamp closes on the sting thereby securing the model. A minimum of 6 accelerometers (more for redundant information) are used to infer the forces and moments, and wires from these accelerometers are routed through the sting for protection. Aerodynamic coefficients are calculated directly from the measured accelerations and the pitot pressure time history. This technique has been demonstrated for a 30° half-angle sharp cone with cylindrical afterbody model having 8 symmetrically mounted accelerometers to provide 5 components. This "release-capture" force measurement technique has also been demonstrated with a body-plate model having side jets. The body houses two pyrotechnic charges, a settling chamber, and 1 to 3 parallel nozzles which may have different shapes. The pyrotechnic charges provide a maximum settling chamber pressure of about 7000 psi. All accelerometers are mounted on this body. The plate-wing, together with the upper surface of the body, provides a flat surface that is 5.5 inches in length and aligned with the oncoming flow; this plate-wing is exchangeable. The forces imparted to the body upon discharge of the pyrotechnics are measured via accelerometers for the case of no flow and for the test flow. These tests revealed that the 3 millisecond test time of the ISL Shock Tunnel was just sufficient to establish quasi-steady flow; i.e., the limiting factor is the establishment of the complex flow structure, not the dynamic response of the model. Future plans include testing with reservoir-supplied side jets and measurement of lateral force due to external combustion. Also planned are scramjet model tests with a built-in supply.

Although having a longer run time (10 to 20 milliseconds) than piston-driven or conventional-type shock tunnels, the VKI Longshot Hypersonic Facility nevertheless presents experimental aerodynamicists with a challenge in obtaining accurate measurements of forces and moments. The techniques developed for and used in the longshot facility at hypersonic Mach number of about 15 are discussed by Carbonaro 1992. In this report by Carbonaro, the techniques and problems associated with the measurement of model accelerations using piezoelectric or piezoresistive accelerometers, including calibration and transverse sensitivity aspects, are discussed. Inertial corrections are optimized taking into account accelerometer transverse sensitivity effects, time lags, signal filtering or smoothing, and tuning for the inertia of the vibrating masses. Low frequency oscillations due to sting vibration are well corrected, but high frequency oscillations must be damped by suitable numerical filtering or smoothing. The viability of the subject measurement technique is demonstrated via tests of the shuttle orbiter and Hermes configurations.

Hypersonic Wind Tunnels

Internal strain gage balances used most frequently in hypersonic wind tunnels are sting or blade strut supported, range in diameter from 0.56 to 0.85 inch, and cover a wide range of maximum design loads applicable to blunt, high drag models and to slender, high lift models (e.g., Miller, 1990). Most balances are six-component, water cooled, and the excitation voltage is typically

5 volts. The general procedure used in most tunnels is to calibrate all six-components, or as a minimum the axial-and-normal-force and pitching moment components, of the balance by loading the balance with weights and recording the output. These onsite data are compared to the formal calibration data to assure the balance is operating within acceptable tolerances. Tare runs with the model mounted to the balance are performed over the desired angle of attack range prior to and during the test series. Following the establishment of steady flow in the wind tunnel, the model is injected into the flow from a sheltered position, the angle of attack varied via the pitch-pause model of operation, and the model retracted prior to flow breakdown. The model injection, attitude variation, and retraction is generally controlled by a computer.

As mentioned previously, a major concern with force and moment tests in heated flows of relatively long duration is the potential conduction heating to the balances through the model wall and along the sting or strut; therefore, only water cooled balances are used in such facilities. Conduction of heat along the sting or blade strut is generally reduced via water cooling and/or ceramic coating; for severe heating problems, a water-cooled balance-to-sting adapter may also be used. Protecting the balance from conduction effects through the model wall is usually achieved with passive techniques such as insulated balance sleeves and air gaps. Whenever model weight is not a consideration, stainless steel is selected over aluminum as the model material so to reduce conduction effects. Force and moment models cast of ceramic or machined from Macor, a machinable glass ceramic manufactured by Corning Glass Incorporated, have been made to reduce conduction effects.

Data Acquisition Systems

Impulse Facilities

Significant advances have been made in the last decade in high frequency waveform recording systems. Commercially available analog-to-digital (A/D) systems typically are 12 bit, provide sample rates in excess of 2 MHz and have in excess of 16K of memory per channel. Such systems provide data acquisition and reduction capabilities for impulse facilities that are not unlike those for conventional-type hypersonic wind tunnels. The cost of such systems is relatively high, typically $5K to $10K per channel, depending on the capability (bit, sample rate, memory). Thus, the number of channels at various facilities may run from only a few channels to the 128 enjoyed by the Calspan Shock Tunnel.

Hypersonic Wind Tunnels

Again, as an example, all hypersonic wind tunnels at NASA Langley have stand-alone data acquisition systems. The heart of the system for most tunnels is a 256-channel, 15 bit, 50 kHz or 100 KHz through put rate, amplifier per channel, analog-to-digital (A/D) unit manufactured by the NEFF Instrument Corporation and having programmable gains and filters per channel and internal clock (NEFF system 620/series 600). These systems are controlled via a Hewlett Packard (HP) 9000 series model 375 computer networked to a central HP model 750 computer. Peripheral equipment for each DAS includes dual-disc and optical disc mass storage units, 9-track tape systems, and printers. The recent addition of a portable 20-channel NEFF system 490 having 12-bit A/D, up to 1 MHz sampling rate, programmable amplifiers and filters, and 2 megaword RAM provides the capability to routinely utilize fast response pressure transducers to examine unsteady surface flow phenomena.

REFERENCES

Bernstein, L., 1975, "Force Measurements in Short Duration Hypersonic Facilities," AGARDograph 214.

Carbonaro, M., 1992, "Aerodynamic Force Measurements in the VKI LongShot Hypersonic Facility." NATO Advanced Research Workshop, LeFauga, France.

DeMeis, R., 1992, "Paint Under Pressure" Aerospace America, pp. 40-41, March 1992.

Engler, R. H., et al., 1992, "Aerodynamic Assessment of an Optical Pressure Measurement System (OPMS) by Comparison with Conventional Pressure Measurements in a High Speed Wind Tunnel."

Hutchinson, M., 1991, "Langley Research Center's Hypersonic Wind Tunnel Pressure Instrumentation." Proceedings of the 37th International Instrumentation Symposium. Instrument Society of America paper 91-074.

Jessen, C.; and Gronig, H., 1992, "A Six Component Balance for Short Duration Hypersonic Facilities." NATO Advanced Research Workshop, LeFauga, France.

Kavandi, J., et al, 1990, "Luminescent Barometry in Wind Tunnels." Rev. Sci. Instr., Vol. 61, No. 11, pp. 3340-3347, November 1990.

Miller, C. G.; and Smith, F. M., 1986, "Langley Hypersonic Facilities Complex - Description and Application." AIAA 86-0741-CP.

Miller, C. G., 1990, "Langley Hypersonic Aerodynamic/Aerothermodynamic Testing Capability - Present and Future," AIAA 90-1376.

Moore, J. A., 1979, "A Study of Response Time of Pitot Pressure Probes Designed for Rapid Response and Protection of Transducer. NASA TM 80091.

Morris, M. J., et al, 1992, "Aerodynamic Applications of Pressure-Sensitive Paint," AIAA 92-0264.

Naumann, K. W.; Ende, H.; and Mathieu, G., 1992, "Millisecond Aerodynamic Force Measurement Technique for High Enthalpy Test Facilities." NATO Advanced Research Workshop, LeFauga, France.

Rogers, R. C. (edited by) 1990, "Workshop on the Application of Pulse Facilities to Hypervelocity Combustion Simulation," NASP Workshop Publication 1008. Restricted distribution.

Schultz, D. L.; Jones, T. V., 1973, "Heat-Transfer Measurements in Short-Duration Hypersonic Facilities" AGARD AG-163. February 1973.

Simmons, J. M.; Daniel, W. J.; Mee, D. J.; and Tuttle, S. L., 1992, "Force Measurement in Hypervelocity Impulse Facilities." NATO Advanced Research Workshop, LeFauga, France.

Vollon, A., and Loreto, A., 1991, "A New Optical Pressure Measurement System (OPMS)," 14th ICIASF Congress, Rockville, MD, USA, October 27-31, 1991.

VELOCITY MEASUREMENTS IN HYPERSONIC FLOWS: A REVIEW

Alain BOUTIER
ONERA - BP 72
92 322 - Châtillon CEDEX - FRANCE

William J. YANTA
NSWC - 10901 New Hampshire Avenue - White Oak
Silver Spring - Maryland 20903 - 5000 - USA

Gunter SMEETS
ISL - 5 rue de l'Industrie - BP 34
68 301 - Saint Louis - FRANCE

1. ABSTRACT

An analysis of the different means to measure the velocity is done; the relative merits of the particle based and the molecular based methods are evaluated, leading to a set of recommendations for future research.

2. INTRODUCTION

With the renewed interest in hypersonics, as seen by the large number of flight programs in the international community, there is a real need for accurate, detailed measurements of fluid flow and thermodynamic properties of high speed, high temperature flows. Since the last major hypersonic activities took place in the late 1960's, major strides have taken place both in computational fluid dynamics (CFD) and experimental measurements. For the CFD community these include large high speed computers with efficient algorithms. These new techniques now make it possible to make accurate predictions of very complex flows. This requires accurate global data for the calibration/verification of these complex codes. For the experimentalist, new tools include high powered lasers, miniature electron beams, fast digital cameras, high speed image processing hardware and software, fast desktop computers, paints that are temperature, pressure and shear sensitive. All of these techniques have provided the experimentalist with a vast assortment of means of obtaining nonintrusive measurements of a variety of fluid properties. These new diagnostics can either replace or complement the traditional physical probes which have numerous problems such as probe interference, lag corrections and the requirement for subsidiary cooling systems. This paper is concerned with the review and summary of the papers presented in Session 5 (Velocity Measurements) at the NATO Advanced Research Workshop [1]. Eight papers were presented ([2] to [9]) in that session. Although this paper will focus on the results from those papers, other results will be described for completeness.

3. BACKGROUND

The choice of velocity measurement systems is governed by a variety of parameters. These include: whether the experiment is a flight test or takes place in a ground test facility, is the test duration a few milliseconds or a few seconds, are real gas properties being measured, is the experiment carried out in a small research facility or is the test being made on a component of a full scale vehicle.

Velocity measurement techniques are generally broken down into two categories: particle based and molecular based. Both of these categories can be used to make either point or planar measurements; they can also be time-of-flight or Doppler shifted methods.

Particle based velocimetry has a 30 year history of development which has made it a very important diagnostics. Particle based systems generally depend upon micron size particles that have been placed in the flow and the Doppler shifted light scattered by these particles is measured to determine the velocity of the particle and, hence, the velocity of the fluid in which the particle is immersed. The Doppler shift has been directly got with optical spectrometers (Michelson and Fabry-Pérot) or through set-ups creating interference of two Doppler shifts yielding beat frequencies that can be detected by photomultiplier tubes and which are further processed with a "counter" type of electronics or the more recently developed FFT type of devices. These systems are generally referred to as Laser Doppler Velocimeters (LDV). Variants of this system measure the time for the particle to travel a known distance, two spot or two dash velocimeters sometimes called laser transit velocimeters; or, measure the distance the particles have gone in a known time, Particle Image Velocimetry (PIV). The problem of all the particle based systems is that the effect of the particle's inertia must be seriously considered. In low density flows or wherever there may be large velocity gradients, the particle's velocity may not accurately represent the flow velocity. The kind of particle chosen for the experiment is of vital importance. This will be described in more detail in the following section.

A spectrometric technique using a Michelson spectrometer is described in [10]. The velocity can be recorded in real time and with a μs time resolution provided the scattering particles are numerous enough for creating a continuous stream of scattered light from the measuring volume. As the Doppler shifted light is delivered by an ensemble of may be many particles, a good signal to noise ratio can be obtained also with rather small particles resulting in less problems from particle inertia. The technique is of special interest for impulse facilities.

Molecular based velocity measurements systems have not had the broad development efforts that the particle based systems have had. A small number of researchers have used the electron beam and laser systems to measure velocities. It is only in the last five years that molecular based systems have been developed to make accurate measurements in "lab-top" experiments. Again, these systems fall into two categories: time-of-flight and Doppler shifted. These will be discussed in more detail later.

4. SCATTERING PARTICLES

As was mentioned above, the choice of scattering particle for hypersonic measurements is very important. The 1985 conference held at NASA Langley [11] was devoted to various aspects of the use of aerosols for velocity measurements. In [4], which describes the application of the classical "fringe" type LDV system to several of ONERA's wind tunnels, a variety of particles have been used, including ZrO_2, SiO_2, alumina powder, and natural particles occurring in the flow system. The powders were generally fed through a cyclone generator to remove large particles or agglomerates. The nominal size for the ceramic powders was about 0.5 μm and their specific gravity varied from 2.2 to 5.5 g.cm^{-3}. Their melting temperatures vary from 1700°C to 2700°C, thus making them quite suitable for high temperature flows. Since these powders were maintained at the same pressure as the supply pressure of the wind tunnel, this generally required a complex plumbing system to introduce the aerosols into the flow. Tests were also carried out in an arc facility where naturally occurring particles were present. It is ascertained that the particles were probably copper or copper oxide particles with diameters between 15 and 30 μm. In [2], particles are used which when compared to predictions, appear to have a diameter of 0.5 μm and a specific gravity of 0.1 g.cm^{-3}. Results with these particles will be described later in this paper. No description is given as to the type of particles or the nature of the particle material. In [3] a fluidized bed was used to disperse Alumina (Al_2O_3) with a mean diameter of 0.3 μm into a Mach 6 wind tunnel supply system. All of the above systems were used in continuous running wind tunnels. For the case of impulse facilities, Avidor [12] used exploding aluminum wires in the supply section of a shock tunnel to generate aerosols. The wires were exploded shortly before the tunnel was run, providing a continuous source of scattering particles during the multi milli-second run. It was estimated that the particle size was less than 0.02 μm so this technique could not be used with a conventional LDV system for single particle scattering. If the gas temperatures are not significant (less than 250°C) then some of the organic aerosols such as polystyrene, latex, dioctylphthalate and other aerosols that have been in use over the years could be used.

5. PARTICLE BASED RESULTS

Some of the significant results from [2] to [9] will now be discussed. In [3], both laser transit anemometer and LDV measurements were made in a Mach 6 wind tunnel. Velocity measurements of the normal velocity component using agglomerate free 0.3 micron alumina normalized to free stream reference velocity, with theoretical predictions for different particle sizes as a function of position behind a 40.8° oblique shock are shown in Figure 1. The effects of particle lag are seen in the figure. The measured velocity values converge to within 8% of the expected 133 m/s 8 millimeters behind the shock. The values were within 5% of the 133 m/s 12 millimeters behind the shock. Shown in Figure 2 are the results from [2]. An oblique shock wave is generated by a flat plate model at -10° incidence in a Mach 12.5 air flow. The measurements, which were made above the plate, about 125 mm from the leading edge, are shown in Figure 3. The probability density measurements shown, clearly point out the shift from the dominant freestream peak ahead of the shock as the probe volume is traversed towards the plate. It was concluded that the measured particle response indicates a particle of 0.5 μm with a specific gravity of 0.1: theoretically these particles have a 95% response to velocity fluctuations up to 50kHz. In [4] velocity results from three of ONERA's wind tunnels are presented. Specifically, the results from S4 Modane are shown. The Mach number was 12 and three different electronic processing systems were used: a digital oscilloscope Lecroy 7200, a Dantec counter and the IFA 750 from TSI. The results are shown in Figure 4. The measured results lie between the calculated values for a perfect gas and a real gas. It is concluded in [4] that for these conditions, the results from the different processors correlated well with each other and that velocities up to 1 700 m/s could be measured with a good confidence level.

6. MOLECULAR BASED SYSTEMS

As was said above, molecular based velocity measurements can be categorized into two groups: time-of-flight and Doppler shift techniques. We will first discuss the time-of-flight methods.

A pulsing electron beam is utilized in [5] (shown schematically in Figure 5) to determine the velocity in a hypersonic flow. The electron beam generates ions with long lifetimes. One can then measure their time of flight during their travel downstream among the surrounding neutral molecules along a known distance. The beam is pulsed for 1 μsec at a repetition rate of 2-8 kHz. Downstream in the flow an ion collector acting like a Langmuir probe is positioned. From the time delay of the ion signal at the probe with respect to the corresponding electron beam pulse the time-of-flight of the ions is measured. When the probe is moved a well defined distance downstream or upstream the time-of-flight is measured again. The velocity may then be computed readily. Shown in Figure 6 are the results of measurements in a variety of gases at many different speeds. The results are compared with theoretical isentropic expansion velocities. One sees that the results are in good agreement. A slight variant of this velocity measurement technique was described in [6]. An electron beam was again used to excite the gas molecules in a low density, Mach 10 airflow. A lens (see Figure 7) forms the image of the flowfield on a high speed gated image intensifier. The final image is recorded on a 400 ASA sensitive photographic plate. The image intensifier has two purposes, the first one is to act as high speed shutter in order to freeze the movement of the plasma columns; the second is to use the high gain to amplify the low intensity light coming from the plasma columns. A photograph of the plasma is shown in Figure 8. One effectively knows the time-of-flight and one determines the distance from the scaled photograph; thus, one can deduce the velocity. It was concluded in [6] that the optical spatial imaging of luminous plasma columns induced by a pulsed electron beam can be a useful tool to measure the velocity of low density hypersonic flows. The last time-of-flight paper [8] describes results obtained with the RELIEF method. Air is tagged by vibrationally exciting oxygen molecules and interrogating at a later time by laser-induced electronic fluorescence. Lines can be instantaneously (10ns) written into the flowfield, and their displacement after an accurately measured time interval gives the flow velocity. If a cross is written into a flow, then the displacement of the cross gives an accurate measure of the mean flow velocity; rotation of the cross and distortion of the lines can be used to have access to vorticity and turbulence. Experiments have been carried out in flows up to Mach 4 and the results look very promising, but the technique requires a shorter wavelength laser source in order to generate high fluorescence intensities to low density hypersonic flows. For steady, nonreacting flows, planar velocity measurements can be made using planar laser-induced iodine fluorescence (PLIIF)[7]. Seeding the flow with iodine vapor and then exciting these molecules with a light sheet of the 514.5nm line of an argon laser with an air-spaced etalon, the resulting broadband planar fluorescence is imaged into a CCD camera (Fig. 9). Time averaged data (over 30 s) are then taken. By scanning the laser frequency of discrete frequencies, a series of images is obtained from which the Doppler shift is deduced. For application to high-speed reacting flows, velocity measurements can be made using planar laser-induced OH fluorescence. The same approaches that were used in PLIIF can be used for OH PLIF if a sufficiently narrow linewidth, tunable, UV laser is used. Pointwise measurements of velocity have been demonstrated in a small, combustor, jet facility. Planar velocity measurements have also been demonstrated in a reacting jet.

Velocities and temperature measurements in high speed flows which were based on spectrally resolved Rayleigh scattering were described in [9]. Time averaged measurements were carried out in a Mach 1.3 air jet. The experimental set-up is shown in Figure 10. The central item in the image processing system is a planar mirror Fabry-Pérot interferometer. The results are shown in Figure 11. The maximum velocity is about 422m/s with a maximum error of about 10-15m/s.

A new approach in time-domain CARS is proposed [13] to perform single shot measurements of the velocity (as well as of the static temperature) in low pressure supersonic flows. Instead of repetitive probing the macroscopic polarizibility coherently driven by short pump and Stokes pulses with variable delay times, the coherence is created with a long duration pump and a short duration Stokes pulse, and is continuously probed with the same pump pulse. The decay of the anti-Stokes signal reveals the static temperature; the beating between two signals which are created in opposite crossing directions with respect to the flow direction gives the flow velocity.

7. CONCLUSIONS AND RECOMMENDATIONS

The results from the papers presented in the Velocity session at the NATO workshop indicated that major strides have been made in being able to make velocity measurements in high speed, high temperature flows that may have chemical reactions present. It is also obvious that much work still remains to be carried out. Most of the experiments described in the above papers were carried out in carefully controlled, small scaled laboratory environments. Only a small number were attempted in large scaled test facilities; none were attempted in flight vehicles.

The following recommendations are offered for future research:

- Continued improvement in particle techniques for use with LDV systems. The development for particles with large aerodynamic diameters with low specific gravity, such as micro spheres, is important. The continued development of electronic processors capable of measuring frequencies with a range of 100's of megahertz is also important.
- A continued emphasis on molecular based techniques including both time-of-flight and Doppler techniques.
- Attempts to apply the Michelson spectrometer to molecular based Doppler measurements: recording the wavelengths of spectral lines stimulated by electron beam or laser radiation.
- The development of high powered, high repetition rate UV lasers.
- In order to supplement turbulence modeling, particularly in the analysis of high speed mixing, the density-velocity correlation should be emphasized. This will require multi-parameter measurements from such techniques as CARS velocimetry, LIF and the electron beam.
- Planar techniques in blow down facilities.

8. REFERENCES

[1] NATO Advanced Research Workshop - New trends in instrumentation for hypersonic research - ONERA Le Fauga-Mauzac - 27 April-1 May, 1992.

[2] F.K. Owen - Measurement of hypersonic flows [1].

[3] W.W. Hunter Jr., L.R. Gartrell, W.M.

Humphreys Jr., D.W. Witte, C.E. Nichols Jr.- Development and assessment of an LDV system for Mach 6 flow field measurements [1].

[4] A. Boutier, J. Lefèvre, F. Micheli - Laser velocimetry applied in hypersonics [1].

[5] E. Hiraï, K.A. Bütefisch, C. Dankert - Velocity and density determination by electron beam technique [1].

[6] A.K. Mohamed - Electron beam velocimetry [1].

[7] J.C. McDaniel, S.D. Hollo, K.G. Klavuhn - Planar velocimetry in high-speed aerodynamic and propulsion flowfields [1].

[8] R. Miles, W. Lempert, J. Forkey, B. Zhang, D. Zhou - Filtered Rayleigh and RELIEF imaging of velocity, temperature and density in hypersonic flows for the study of boundary layers, shock structures, mixing phenomena and the acquisition of in-flight air data [1].

[9] R.G. Seasholtz - 2D velocity and temperature measurements in high speed flows based on spectrally resolved Rayleigh scattering [1].

[10] G. Smeets, A. George _ Michelson spectrometer for instantaneous Doppler velocity measurements - J. Phys. E: Sci. Instrum.,Vol.14, 1981.

[11] W.W. Hunter, C.E. Nichols - Wind tunnel seeding systems for laser velocimeter - NASA Conference Publication 2393, Proceedings of a workshop held at NASA Langley research center, March 19-20, 1985.

[12] J.M. Avidor, A.M. Schneiderman - Experimental investigation of high Reynolds number compressible axisymmetric turbulent wakes - AIAA paper 74-576, presented at AIAA 7th Fluid and Plasma Dynamics Conference, Palo Alto, CA, June 17-19, 1974.

[13] M. Lefebvre, M. Péalat, J. Strempel - Single-shot Time-Domain CARS: application to temperature and velocity measurements in supersonic flows - Submitted to Optics Letters.

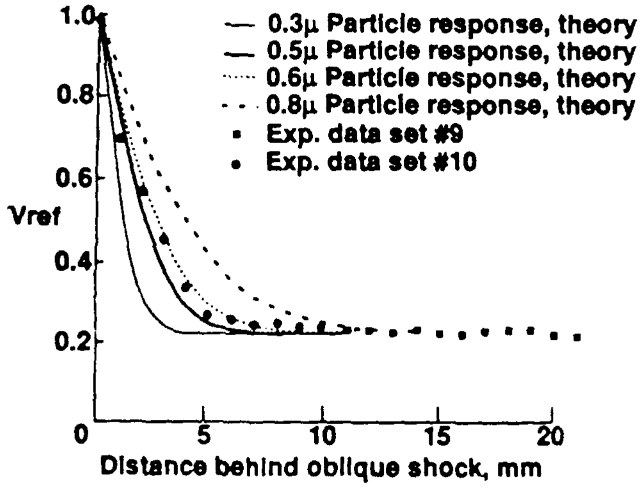

Fig.1: Comparison of LDV normal velocity component measurements using agglomerate free 0.3 μm Al_2O_3, normalized to freestream reference velocity, with theoretical predictions for different particle sizes as a function of position behind az 40.8° oblique shock [3].

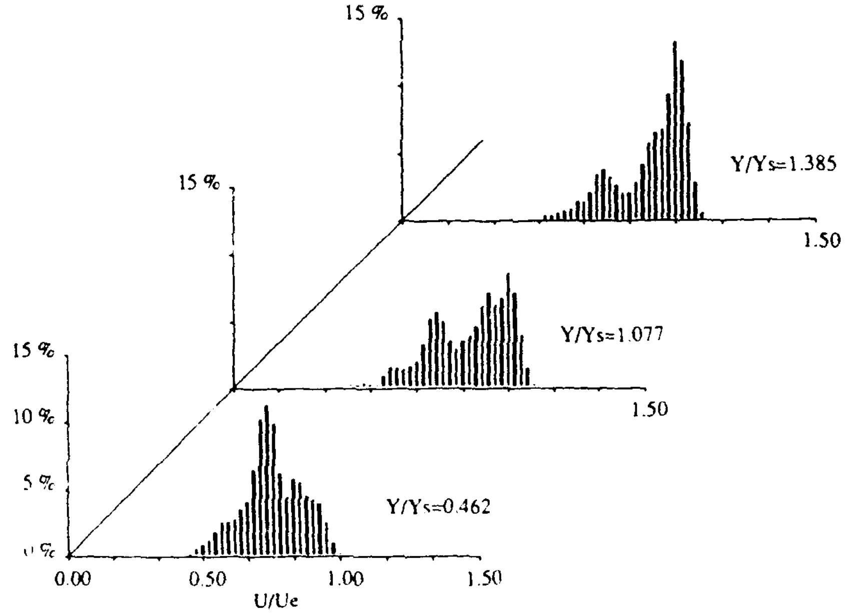

Fig.2: Particle response in hypersonic flow [2].

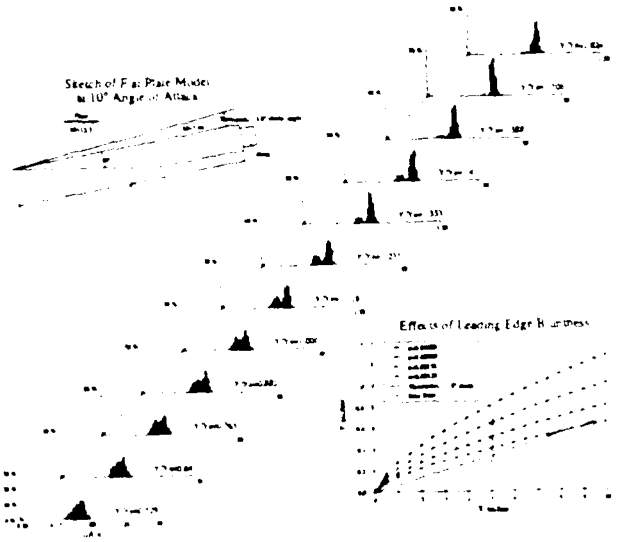

Fig.3. Particle response in the Wright Laboratory 20-inch hypersonic wind tunnel [2].

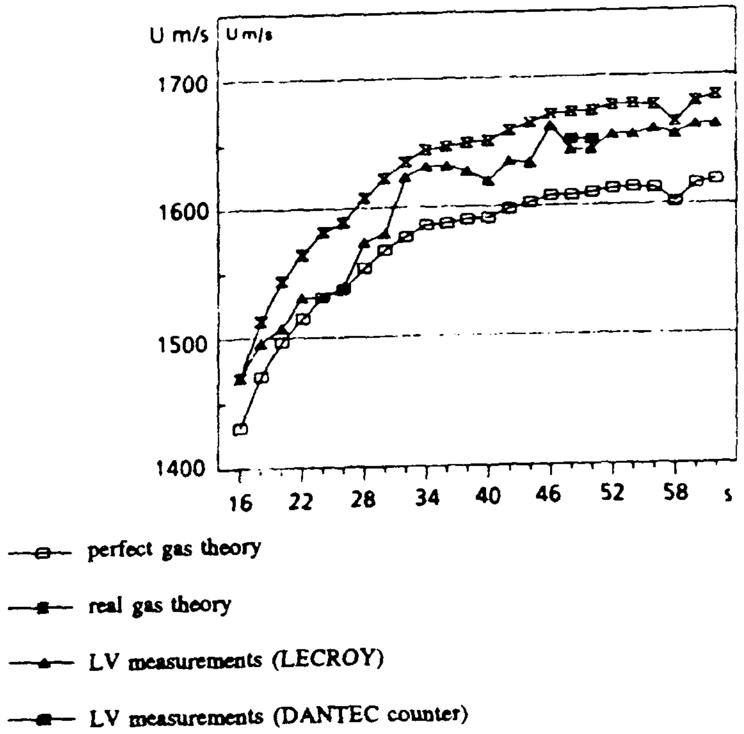

Fig.4: Velocity evolutions during run 1015 at S4 Modane [4].

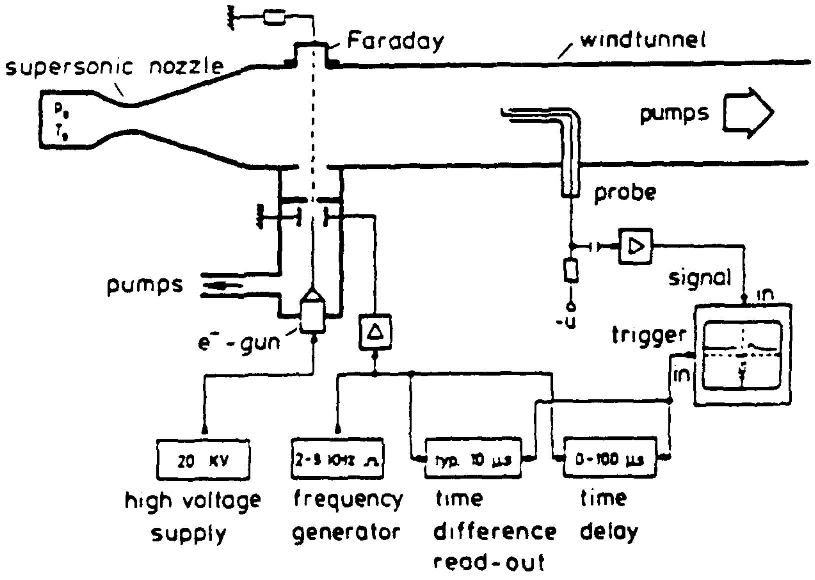
Faraday
windtunnel
supersonic nozzle
p_0
T_0
pumps
probe
pumps
signal
in
e⁻-gun
-u
trigger
in
20 KV
2-5 10Hz
typ. 10 µs
0-100 µs
high voltage supply
frequency generator
time difference read-out
time delay

Fig.5: Experimental set-up for velocity measurements by means of a pulsed electron beam [5].

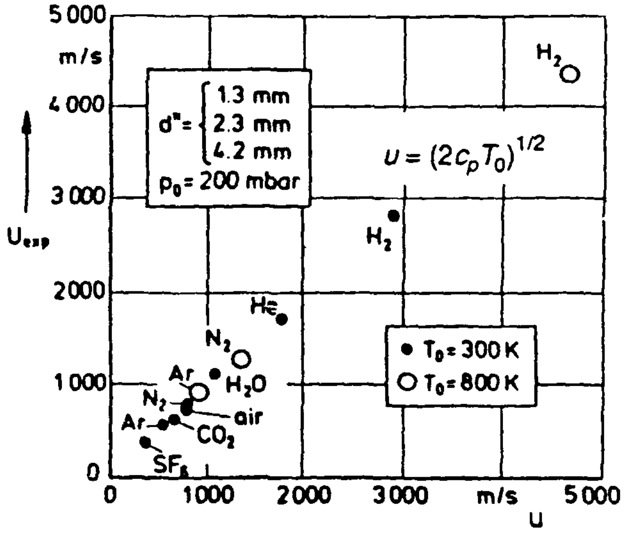

Fig.6: Measured flow velocities for different atoms and molecules; d* = orifice diameter [5].

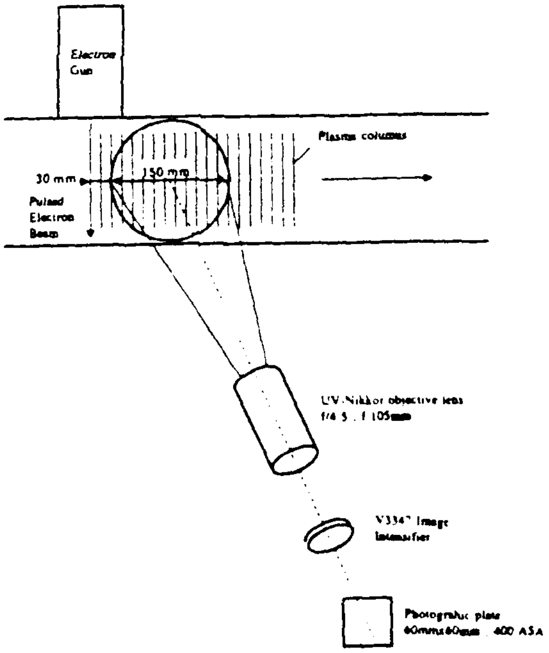
Electron Gun
Plasma columns
30 mm
150 mm
Pulsed Electron Beam
UV-Nikkor objective lens f/4.5 , f 105mm
V3347 Image intensifier
Photographic plate 60mmx60mm , 400 ASA

Fig.7: Experimental set-up [6].

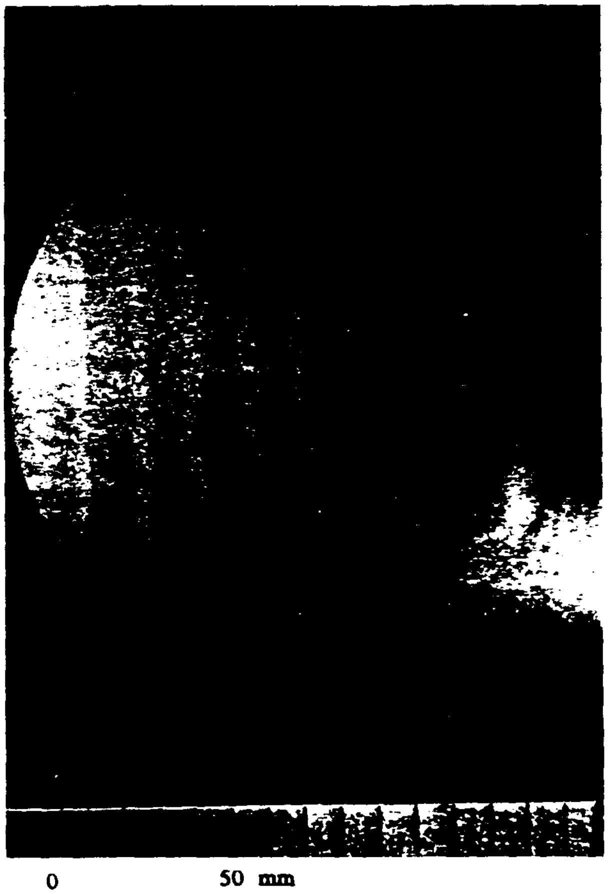

Fig.8: Plasma columns in the free flow [6].

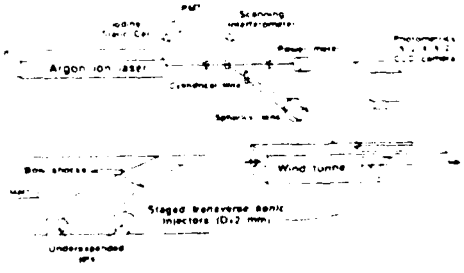
PMT
Scanning interferometer
Iodine Static Cell
Power meter
Photometrics CCD camera
Argon ion laser
Cylindrical lens
Spherical lens
Wind tunnel
Bow shocks
Staged transverse sonic injectors (D=2 mm)
Underexpanded jets

Fig.9: Experimental setup for PLIIF velocity measurements [7].

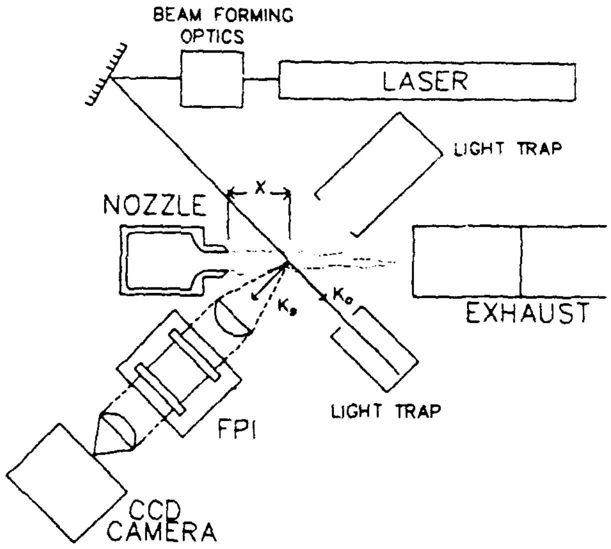
BEAM FORMING OPTICS
LASER
LIGHT TRAP
X
NOZZLE
EXHAUST
K_s
K_o
LIGHT TRAP
FPI
CCD CAMERA

Fig. 10: Experimental setup for measurement of velocity in Mach 1.3 free jet using imaging Fabry-Pérot interferometer [9].

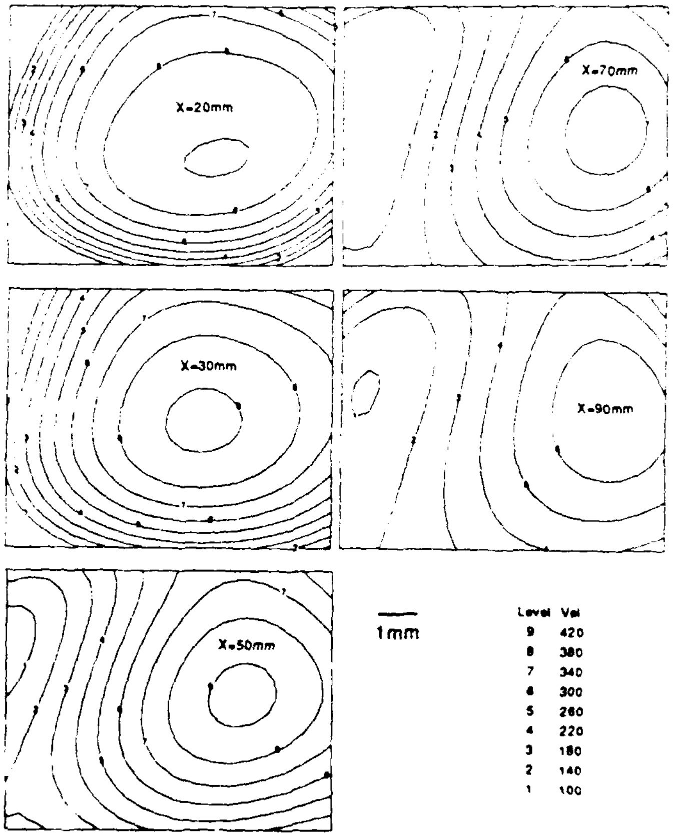

Fig. 11: **Measured constant axial velocity contours.**
Distances from nozzle exit are X = 20,30,50,70,90 mm. Isentropic velocity = 422 m/s [9].

FLOW VISUALIZATION AND SPECTROSCOPY IN HYPERSONIC FLOWS: NEW TRENDS

by

James Trolinger
MetroLaser
Irvine, California
United States

Georg Eitelberg
DLR
Göttingen
Germany

Marc Rapuc
Dassault Aviation
78 quai Marcel Dassault
92214, Saint Cloud
France

SUMMARY

This paper is based upon a session of the NATO Advanced Research Workshop, *New Trends in Instrumentation for Hypersonic Research* held at the ONERA La Fauga Facility in France during the week of April 27, 1992. The discussion includes some of the frontiers of the technology of flow visualization and spectroscopy as well as a discussion of the current development needs and trends. Included in the discussion are optical integrated measurements such as resonance absorption, schlieren, interferometry, and holographic methods. The discussion shows that while the technology is mature in a broad sense, a significant number of new development areas exist such as resonant holography and phase shifting holographic interferometry. The maturity of the technology makes it immediately applicable to many problems and the untapped potential offers considerable room for improvement of existing capability. The methods which are described can be used in harsh environments and have the potential for becoming flight test diagnostics for the measurement of temperature, density, constituency, and velocity.

1 INTRODUCTION

When an optical wave front traverses a gaseous medium, the wave front can be modulated in phase, direction, and intensity by the medium. The analysis of the integrated effect of the medium upon the wave can characterize the medium if enough information is recorded. At the simplest level, some aspects of the otherwise invisible flow field can be made visible through various optical processing procedures. At the highest level, some aspects of the flow can be accurately quantified. The fundamental principals underlying optical flow visualization techniques described herein are the following:

1. The refractive index changes in fluid mediums of varying density and/or constituency which means the wave fronts of optical waves propagating through these mediums are phase shifted and deflected. Gas density can be derived from refractive index if the constituency is known. Refraction can be measured directly with schlieren systems. Phase shift is usually measured with interferometry.

2. When the exciting wavelength is near the resonance of a gas, the complex refractive index changes radically such that absorption and refraction properties are strongly affected. The analysis of absorption and refraction at resonance can be done by either tuning the wavelength of a narrow band illuminating diagnostic beam through the resonances of the medium or by comparing the input and output spectra of a broad band illuminating beam.

Flow visualization as well as spectroscopic methods are information intensive diagnostics and have been limited in practical application for many years by the capability of affordable image processing hardware and software. In recent years, the availability of small powerful computers is fast removing such limitations. Also, new lasers are simplifying the application and interpretation of such methods. Miniaturization hardware such as fiber optics, diode lasers, and small electronics hardware are opening the way to the development of small, rugged, lightweight instrumentation. New methods such as phase shifting interferometry are improving the resolution and accuracy of interferometry. Holography is expanding the capability of both interferometry and spectroscopy by providing a convenient method of storing wave front information in a form which makes its processing simpler. So even though each of the methods under discussion here is already widely used, the field is extremely dynamic and the capabilities of these methods will be extended in future years as the supporting technologies are advanced.

These methods can provide quantitative density measurements of two dimensional and axisymmetrical fields since the integrated measurement can be solved to provide point information. When flow fields become more spatially complex, the method becomes semi quantitative. In some situations, the measurement of integrated data over a sufficient number of angles of view can lead to three dimensional analysis through the process of tomography (tomography is the determination of a spatial distribution when only the projections through the distribution are given).

In the study of aero-optical phenomena, the desired measurement is the total integrated affect on the wave front, so these methods are finding broad application in this area.

2. ADVANTAGES

This class of instrumentation possesses a number of advantages over most of the more recently emerging optical diagnostics such as laser induced fluorescence and Raman techniques. The instruments are essentially in a high state of maturity, some of them having been in routine use for many years. This makes their incorporation into hypersonic testing more straightforward since many test facilities are already equipped with the required optical access. The results are often easier to communicate to the end user since aerodynamacists are already familiar with their use and interpretation. The methods currently in use are relatively simple, employing well known recording materials and data reduction procedures. They are readily adaptable to electronic recording and data reduction methods which have evolved in recent years. The expansion potential is extremely promising, which means that the methods already in use can be retrofitted with advancements that will enhance the system capability. For example, facilities which are already equipped with schlieren systems can be upgraded to incorporate new holography methods. Holography methods can add interferometry capability to such a facility. Facilities already using holography will be expandable to incorporate phase shifting interferometry, on-line recording and reduction, and resonant holographic methods.

3. EMERGING TECHNOLOGY

A considerable effort is being made to extend the methods under discussion for use in hypersonics research. Hypersonic testing requires diagnostics at lower densities and higher velocities than the methods easily reach. Also, high temperatures result in dissociation and ionization with a resulting loss of knowledge of the gas state and constituency. The state of the gas can become an important factor in the simulation, so its measurement can become a major issue for modelers and for those desiring to simulate flight conditions.

In some instances, pulsed facilities are the only facilities that can simulate flight conditions. Accommodating short run times is another challenge being accepted by diagnostics technique developers. The environment in which such tests must be carried out offers still another challenge. For example, simply getting light in and out of the test facility without introducing spurious information on the light wave is not a simple task.

The following examples of emerging technology were presented in the workshop, illustrating some of the approaches being taken to deal with the problems of hypersonic testing.

3.1 Schlieren Methods

A good example of the refinement of a mature technology for application in hypersonic research was presented by Bize et al[1]. They have designed, constructed and tested a high sensitivity schlieren system for the ONERA La Fauga F4 Hotshot facility. This facility has been designed to cover the HERMES trajectory through gas densities ranging from 10^{-6} to 10^{-2} kg/m^3. The minimum detectable optical path difference is given by

$$\Delta s_{\min} = K L \Delta \rho_{\min}$$

Where K is the Dale/Gladstone constant, which for air is 2.27×10^{-4} (Kg/m^3)$^{-1}$, and L is the length of the gas flow. This requires the ability to measure an optical path length change from 2.3×10^{-2} to 2.3 micrometers per meter of path length or in terms of wavelength, a range from about $\lambda/20$ to 5λ per meter of optical path.

To extend the sensitivity to its maximum, the authors have employed long focal length (5 meter) mirrors (50 cm. diameter) polished to an accuracy of 0.1 arc seconds. Three major factors limit the achievable (in practice) sensitivity of schlieren systems: 1) vibration, 2) air current perturbations outside of the facility, and 3) distortions and noise caused by the windows of the facility. These have been minimized in the current design by 1) mounting the knife edge on a rapidly controllable mount with feedback to eliminate the effects of vibration on the knife edge, and vibrationally isolating the entire system, 2) placing the entire optical system in a vacuum chamber, and 3) removing the windows entirely, since the optics are all inside the vacuum of the test facility. Also, by using the phase contrast method instead of a normal knife edge, another factor of 10 is gained in sensitivity (the phase contrast method employs a phase shifting step instead of a knife edge). With these refinements the system can resolve a refraction as small as 0.01 arc seconds and can measure a step change in optical path of less than λ/500. This schlieren system is quite possibly the most sensitive schlieren system of its size in use for aerodynamics.

As an additional refinement, the authors plan to employ laser illumination to allow the high level of ambient light near the stagnation region of the models to be removed from the visualization.

3.2 Spectroscopic Methods

Bize et al[1] also describe a method that was employed for extending the use of emission spectroscopy to the La Fauga F4 facility by employing fiber optics to collect the light inside the facility and to conduct it to a high resolution grating spectrometer some distance away. Measurements were made of Cu, Fe, OH, O, and NH UV bands from 300 nm to 330 nm to evaluate various parameters in the flow. Temperature measurement is one of the primary objectives. This diagnostic also provides an evaluation of measures taken to reduce the metallic pollution of the flow.

Limbaugh[2] and McGregor[3] similarly described methods for adapting highly refined emission/absorption spectroscopic procedures to extremely harsh test conditions, specifically in the testing of propulsion systems. By employing a heated plate as an IR (1-3 Micrometers) source and measuring the transmission through the flow field, Limbaugh can deduce the temperature and species concentration in the exhaust of a propulsion system. A band model approach to solving the radiative transfer problem provides quantitative determination of these properties when the integral representing the measured illumination can be solved. Solution of the integral is straightforward only for symmetrical distributions of the field. By staying in the short wavelength band, Limbaugh shows how quartz fibers can be used to conduct the light in and out of a test facility to ruggedize the instrument. Primary candidates for measurement are the 4.3 μm band of CO_2 and the 2.7 μm band of H_2O. Work closer to the 1 μm bands would allow use of uncooled silicon or germanium detectors, but the method has not yet been extended to this regime to date. NO, OH, CO, and NO_x are also candidate molecules.

McGregor described the requirements and potential for applying resonance absorption methods in hypersonic flow using non laser illuminators. Typically, a source is produced with a discharge tube containing the species under study and the receiver is a high resolution spectrometer (Figure 1). The instrument can provide a measure of gas density and temperature if the integral representing the measurement can be solved and if broadening effects caused by Doppler shift or other effects can be incorporated. Considerable work is still needed in the physics of the process to make the method accurate. Ultimately, if rugged, low cost lasers in the correct wavelength become available, the method could be simplified. Figure 2 shows a candidate design for an in-flight diagnostic using the technique. Fiber optics conducts the light in and out of the rectangular combustor.

Smeets[4] reviewed a variety of interferometers specifically developed to view extremely weak phase objects (optical path length changes less than λ/500). Of special significance is the fact that these instruments were developed and used routinely over 20 years ago, and now they should be easily adaptable to meet some of the newly emerging requirements in present day hypersonic flow diagnostics. A Wollaston prism differential interferometer shown in Figure 3 provides a capability to quantify optical path length changes as small as 10^{-5} λ. Using the above formula, this leads to a minimum detectable density change of about 2×10^{-8} Kg/m^3 per meter of optical path which covers essentially the full range of ground testing for most hypervelocity aircraft. The method biases the interferometer into its most sensitive region and reduces optical noise by canceling out light which is not contributing to the measurement of changing refractive index. When the image can be divided into small regions probed by individual rays which are then sensed electronically, the frequency response of the interferometer is virtually unlimited, making it an excellent candidate for modern day hypervelocity testing in pulsed facilities. The device has actually been used to map the density profiles surrounding a ballistic projectile as it passed through the interferometer.

Variations of the Wollaston prism interferometer have been employed for different problems. One variation represents one of the precursors to modern optical image processing for enhancing the sensitivity of flow visualization. One interferogram is produced when the object is present using one polarization orientation, and a second exposure is made without the phase object being present with the other polarization. This procedure makes the second recording complementary to the first in intensity with respect to the fixed illumination. Adding the two recordings effectively smoothes out the constant information, enhancing the signal-to-noise ratio of the temporally changing information. A recording of a sound wave of phase strength less than λ/500, using the interferometer, vividly demonstrated the high sensitivity made possible through image processing and setting the interferometer in its most sensitive mode. This type of interferometer can be adapted directly into almost any conventional schlieren system. The chief drawback is the difficulty in quantifying the data, limiting present use of the method to flow visualization. Smeets states that the method can be characterized by a typical sensitivity of 10^{-7} Amagat/meter (An Amagat is the density of the gas normalized to its value at STP.)

Instrument sensitivity enhancement in flow visualization must always be accompanied by procedures to remove or account for the variations in the flow field outside of the region of interest, which can dominate the measurement. This is especially true in hypersonic testing where the test region can be relatively small. Removing the test chamber windows and the ambient air itself, as described in the schlieren system above, is one way of achieving this. In Smeets interferometer, this is accomplished essentially by subtracting off such effects in real time. Techniques described below offer still other ways to abate ambient effects.

3.3 Holographic Interferometry

Four presentations were given describing advanced holography developments and applications[5,6,7,8] representing what is probably the most dynamic area in flow diagnostics.

Since holography provides a technique to store optical wave fronts for later retrieval, holographic flow visualization and interferometry would appear to be an obvious application of holography. The modulated wave front can be stored in a hologram for later retrieval, at which time it can be reconstructed for processing with any of the conventional optical flow visualization procedures including schlieren, shadowgraph, moiré, and many types of interferometry; so the single recording can lead to a multitude of representations of the flow .

The primary features of holographic flow visualization are the following:

1. Information-carrying wave fronts of arbitrary complexity can be stored in holograms for later retrieval.
2. The holograms can be recorded in nanosecond or shorter time frames.
3. Data is stored in a narrow wavelength range.
4. Holograms can be recorded at high frequency (megahertz).
5. Many holograms can be superimposed on a single recording.
6. Data is stored in a format that is readily accessible to optical processing procedures.

Storing entire wave fronts allows a number of extremely important and unique direct and quantitative comparisons, additions, subtractions, correlation and filtering of wave fronts such as the following:

1. Wave fronts that existed at different times.
2. Extremely aberrated and complicated wave fronts that differ by a small amount.
3. Wave fronts of different wavelengths.
4. Multiple wave fronts existing simultaneously.

Table 1 summarizes some of the advanced holographic techniques that support flow diagnostics.

Improved data reduction hardware and software may be the single most important new development in flow visualization holography. In recent years, great strides have been made in improving the efficiency and use of holography data. The application of modern image analysis and enhancement procedures such as logarithmic detection, normalization, subtracting off the non uniform background, floating thresholds, bandpass filtering and others have greatly simplified automated data reduction. Only through the routine processing and use of the additional data made possible by holography can the methods compete with more established and accepted techniques which may offer less, but which require little data processing before use.

Phase shift interferometry is a relatively new interferometric procedure for producing a continuous phase map from a series of three or more interferograms of an object field. At any point in an interferogram, the intensity is given by

$$I = I_0\left(1+\gamma\cos\left[\phi+\theta\right]\right)$$

Where I_0 is the background (D.C.) intensity, γ is the fringe contrast, ϕ is the desired phase and θ is an adjustable constant phase shift over the interferogram. By measuring intensity for three different values of θ , three equations are produced which can then be solved for ϕ. The interferogram can be sampled by a detector array during the phase shifting operation and a phase map is produced almost instantaneously (with a 2π ambiguity). The features and benefits of using this procedure include using more of the data in the interferogram, filling in data between the fringes in the interferogram, removal of optical noise, improvement of sensitivity, and rendering the process more easily automated. This represents a significant improvement over more conventional methods of locating fringe centers.

Spring et al[6] describe a system and an application in the NSWC hypervelocity facilities which represent various edges of the state of the art in applied holographic flow diagnostics. The system employs double plate (sandwich) holography in which a reference wave front is recorded on one hologram, the test field wave front is recorded on a second hologram, then the two wave fronts are superimposed by placing the two holograms together and reconstructing both wave fronts simultaneously. The phase shift operation for phase shift interferometry can be implemented with the hologram "sandwich" in various ways, and was achieved in this system by moving one of the plates relative to the other during reconstruction. Automated image interferogram reduction using this process is one of the significant features of the system allowing large amounts of data to be quantified. Image processing systems and software which now are relatively inexpensive would have been prohibitive in cost for most users only a few years ago. The study illustrates the use of holographic interferometry to evaluate CFD codes. Comparisons of the interferometry results with CFD clearly illustrate where the codes fail to predict the flow about models in hypersonic flows. **Figure 4** shows such a comparison where the CFD solution predicted by a three dimensional Euler code breaks down in the turbulent boundary layer. Some of the weaknesses of the technique are illustrated in this figure which underlined the problem of refraction near strong density gradients, which makes the data analysis difficult near the shock wave.

Eitelberg et al[5] reported on the development of an advanced on-line holocamera for the HEG shock tunnel at DLR. The system employs a thermo-plastic recording device, which allows holograms to be recorded, developed electronically in place, and reconstructed within seconds after recording. The system also employs multiplex holography using two separate reference waves. When the two wave fronts are recorded with two different reference waves, they can be independently reconstructed. Consequently, a constant phase shift can be added independently to either of the two waves during reconstruction, providing a capability to use phase shift interferometry.

Surget and Dunet described holographic interferometry systems designed for use in two ONERA facilities, F4 at La Fauga and F5 at Chalais-Meudon. The density in these facilities ranges from about $4x10^{-3}$ to $6x10^{-5}$ kg/m^3. The change in optical path length for a typical model is much less than one wavelength. The authors' approach to sensitivity increase is to employ a multiple pass interferometer. Although this has been done before, previous methods for recording multipassed beams have led to almost intolerable noise caused by the difficulty in recording only the desired beams which make n passes through the facility. When a light beam passes back and forth through a test facility, some method must be devised to select only that beam which has passed through the facility the desired number of transits. This can be achieved holographically by path matching a relatively short coherence length reference wave with the object wave that has made the desired number of passes. The remaining light exposes the hologram but does not interfere with the reference wave. This method, called coherence filtering, works reasonably well for two passes, but results in lower quality data as the number of passes increases. A time filtering method was developed by these authors that actually gates the recording, electro-optically shuttering out all light except that which traverses the facility by the desired number of times. **Figure 5** illustrates the system capability of recording the flow field over a wedge in the F5 facility. The interference fringes are almost straight in the single pass case, whereas the three pass case shows the improved sensitivity. This configuration leads to quantifiable interferometry data with a sensitivity gain of three. The time filtering method could increase sensitivity by orders of magnitude. Once again, methods for eliminating ambient effects would almost certainly be required to maintain the useful sensitivity.

Trolinger et al[8] describe a series of experiments that demonstrate the use of resonant holographic interferometry spectroscopy (RHIS) in detecting OH in a flame. RHIS is a new type of flow diagnostics technique that combines the power of holography with the species selectivity of spectroscopy to provide three dimensional images of the density of selected species in complex flows. The technique is particularly suitable to study high speed mixing processes, to measure minor species in the presence of major species, and to observe major species in a heterogeneous low pressure environment. Both experiments and modeling are being conducted to establish the feasibility of RHIS in measuring the concentration of water vapor, oxygen, and OH in high speed propulsion applications. In addition to the species concentration, the resonant holographic technique has the potential of providing temperature, pressure, and flow velocity.

The potential benefits of producing holographic recordings at a wavelength near a resonance of one of the constituent gases or a seed gas, have been recognized for many years, but hardware and technology have only recently proven adequate for practical application. At resonance, the refractive index varies drastically resulting in a potential improvement in sensitivity with the attendant capability to apply interferometry at much lower pressure. Also, the measurement can be made selective to spectroscopically diagnose a specific constituent. The resulting data can lead to quantitative measurement of concentration, temperature, pressure, and velocity, producing an extremely powerful diagnostics capability which extends far beyond conventional holographic interferometry.

Species Concentration can be determined by producing a hologram of the field of interest with a beam of wavelength close to a spectral line, superimposed upon a hologram at a slightly different wavelength (see Figure 6), either far from the line or symmetrically separated from line center, and simultaneously with the first hologram. When these two wave fronts are interfered by reconstruction with a single beam of light, the resulting interferogram characterizes only the resonant species, since the effects of all other species are contained on both wave fronts. Sensitivities as high as ten parts per million (for NO, OH, and iodine) are detectable in principle. The authors also cited other studies[9] that conceptually compared RHIS with Raman and laser induced fluorescence, for measuring concentration, temperature, pressure, and velocity, which reached the conclusion that RHIS actually excels in several ways. Perhaps the greatest advantage lies in the fact that RHIS does not depend upon a knowledge of quenching and other radiative decay paths, which is probably the greatest of the practical problems limiting the accuracy of LIF.

4. CONCLUSIONS

Flow diagnostics and spectroscopy fill a vital need in hypersonics research. Mature technology already allows the global visualization of a flow field, clearly depicting properties of boundary layers, transition, and shock wave interactions. The spectroscopic methods make the measurement of constituents such as NO, OH, H_2, O, and O_2 possible, while also providing a mechanism for measuring temperature. The more advanced spectroscopic measurements can also measure velocity. Flow visualization and spectroscopy methods provide candidates for assisting in vehicle design, facility calibration, modeling, and flight testing.

Recommendations for required future efforts emerging from this session of the workshop include the following:

1. Characterize the methods from hypersonics prospective.
2. Additional comparisons with computation and other methods needed to check accuracy.
3. Insure that modelers, facility developers, and testers know capabilities and potential of the methods.
4. Refine methods for hypersonics application. Specific areas requiring attention are sensitivity, quantification, and adaptation to facilities, models, and aircraft.
5. Prepare some of the methods for flight applications.

TABLE 1
ADVANCED HOLOGRAPHIC TECHNIQUES SUPPORTING FLOW DIAGNOSTICS

TECHNIQUE	FEATURES
1. **Phase shift and heterodyne interferometry**	Improves sensitivity of interferometry and simplifies data reduction.
2. **Multiplex holography:**	Allows simultaneously storage and independent reconstruction of different types of wave front information by using different reference waves. Provides a method to implement phase shift and heterodyne interferometry, optical subtraction and correlation of two image conditions.
3. **Sandwich holography:**	Allows different wave fronts to be stored on separate recordings, reconstructed separately, and directly compared optically during reconstruction. Further simplifies phase shift and heterodyne interferometry, optical subtraction and correlation of two image conditions.
4. **Multiple wavelength recording:**	Allows additional information about the subject to be stored (i.e. different variables that affect the refractive index).
5. **Particle image displacement velocimetry:**	Provides three dimensional velocity fields and enhances flow diagnostics.
6. **On-line systems-Thermoplastic and TV holography:**	Provides quicker access to data.
7. **Fiber optic holography:**	Improves optical access, simplifies path matching, and ruggedizes the optical system.
8. **Resonant Interferometry**	Allows species identification and increases sensitivity.
9. **Holographic optical elements:**	Reduces weight and volume and simplifies optics.
10. **Automated Data Reduction**	Makes the handling of large quantities of data that are available in the hologram tractable.

5. REFERENCES

1. "Schlieren Device and Spectroscopic Measurements in F4" D. Bize, G. Dunet, M. Philbert, A. Roblin, J. Surget, Proceedings of the NATO Advanced Research Workshop, New Trends in Instrumentation for Hypersonic Research, Held at ONERA La Fauga, 27 April-1 May, (1992).

2. "Considerations for the Application of the Infrared Emission Absorption Technique to Hypersonic Propulsion Diagnostics", C.C. Limbaugh, Proceedings of the NATO Advanced Research Workshop, New Trends in Instrumentation for Hypersonic Research, Held at ONERA La Fauga, 27 April- 1 May, (1992).

3. "Molecular Electronic Resonance State Techniques" W.K. McGregor, Proceedings of the NATO Advanced Research Workshop, New Trends in Instrumentation for Hypersonic Research, Held at ONERA La Fauga, 27 April- 1 May, (1992).

4. "Interferometry in Rarefied Gas Flows", G. "meets, Proceedings of the NATO Advanced Research Workshop, New Trends in Instrumentation for Hypersonic Research, Held at ONERA La Fauga, 27 April- 1 May, (1992).

5. "Holographic Interferometry on the High Enthalpy Shock Tunnel in Gottingen (HEG), G. Eitelberg, B. Fleck, T. J. McIntyre, Proceedings of the NATO Advanced Research Workshop, New Trends in Instrumentation for Hypersonic Research, Held at ONERA La Fauga, 27 April- 1 May, (1992).

6. "The Use of Holographic Interferometry for Flow Diagnostics", W. C. Spring III, W. J. Yanta, K. Gross, and C. A. Lopez, Proceedings of the NATO Advanced Research Workshop, New Trends in Instrumentation for Hypersonic Research, Held at ONERA La Fauga, 27 April- 1 May, (1992).

7. "Multipass Holographic Interferometer for the High Enthalpy Hypersonic Wind Tunnel F4", J. Surget and G. Dunnet, Proceedings of the NATO Advanced Research Workshop, New Trends in Instrumentation for Hypersonic Research, Held at ONERA La Fauga, 27 April- 1 May, (1992).

8. "Resonant Holographic Interferometry; A Multipoint, Multiparameter Diagnostics Tool for Hypersonic Flow", J.D. Trolinger, R. K. Hanson, B. Yip, and B. Battles, Proceedings of the NATO Advanced Research Workshop, New Trends in Instrumentation for Hypersonic Research, Held at ONERA La Fauga, 27 April- 1 May, (1992).

9. "Flow Diagnostics By Resonant Holographic Interferometry," Sirota, J.M., and Christiansen, W.H., AIAA Paper 90-1550, AIAA 21st Fluid Dynamics, Plasma Dynamics and Lasers Conference, Seattle, WA, June, 1990.

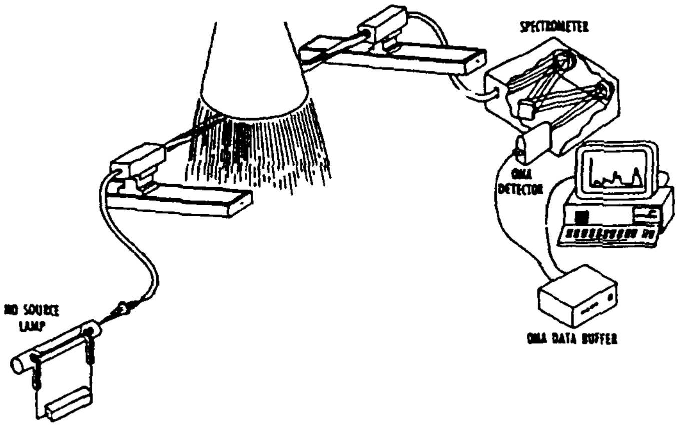
SPECTROMETER
OMA DETECTOR
OMA DATA BUFFER
NO SOURCE LAMP

Figure 1. Illustration of the NO Resonance Absorption Measurement System.

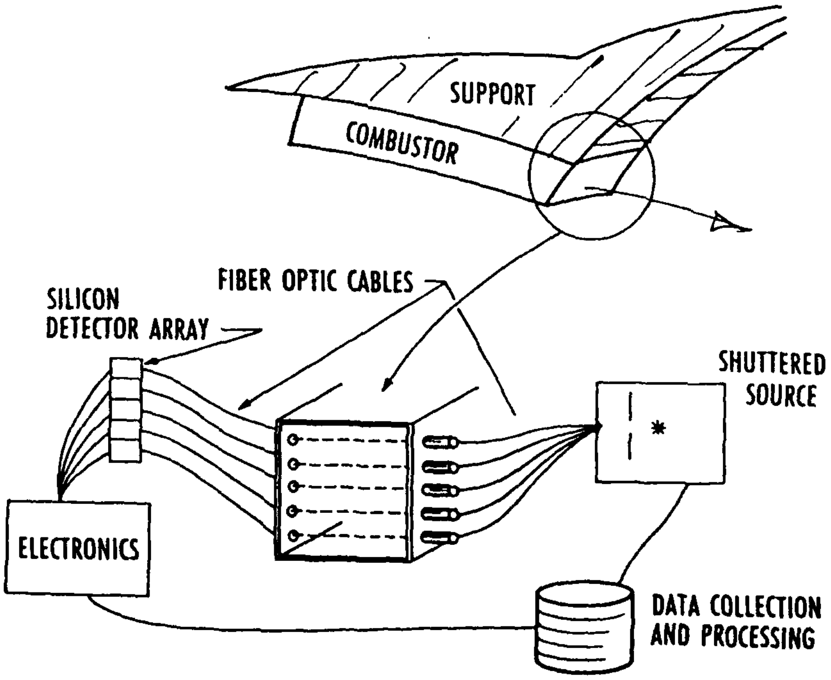
SUPPORT
COMBUSTOR
FIBER OPTIC CABLES
SILICON DETECTOR ARRAY
SHUTTERED SOURCE
ELECTRONICS
DATA COLLECTION AND PROCESSING

Figure 2. E/A Concept for Combustor Diagnostics

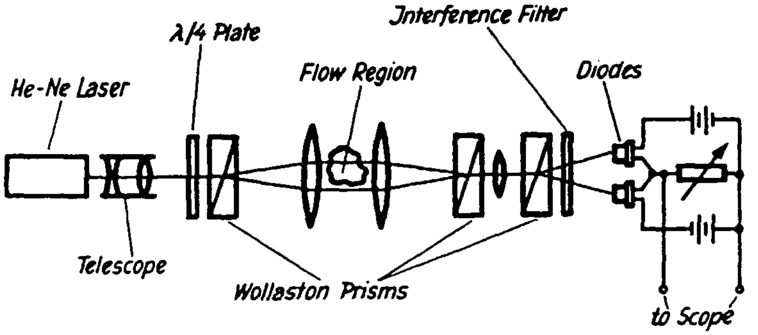
Jnterference Filter
λ/4 Plate
He-Ne Laser
Flow Region
Diodes
Telescope
Wollaston Prisms
to Scope

LDI using two separate diodes for complementary interference detection.

Figure 3. Laser Differential Interferometer

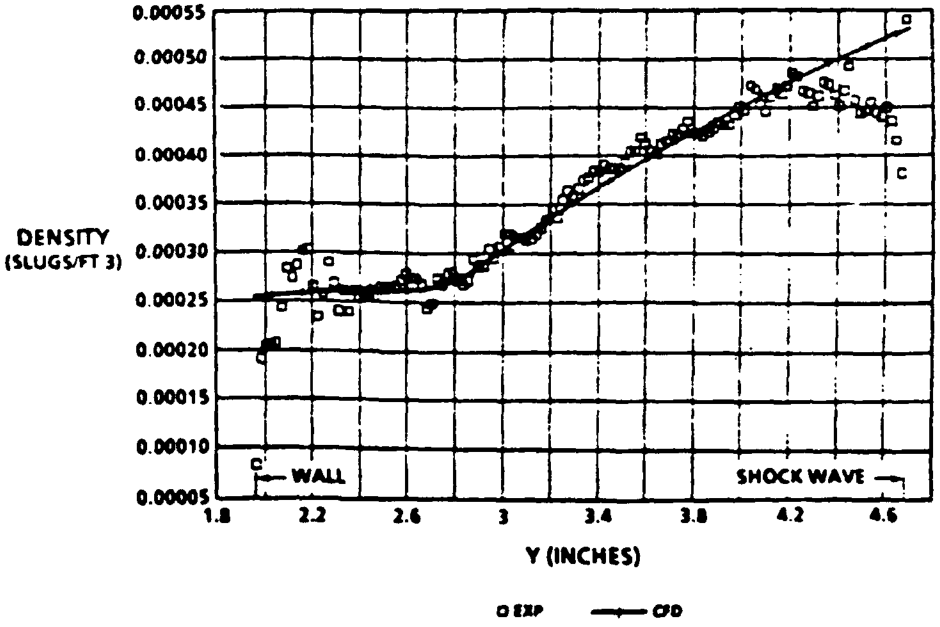

Figure 4. Measured Desnity Vs. CFD Solution for Blunt Cone.

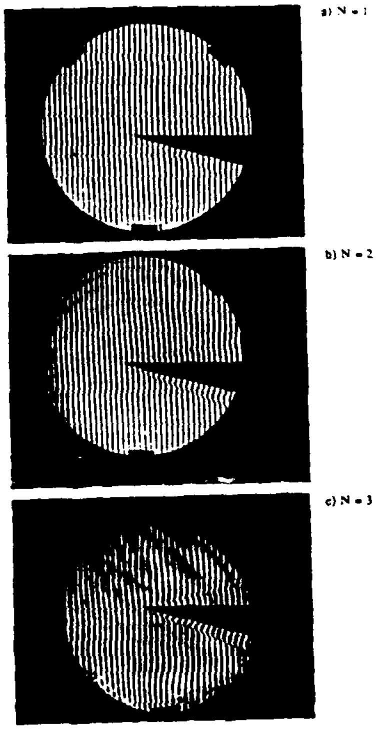

Figure 5. Finite fringe interferograms

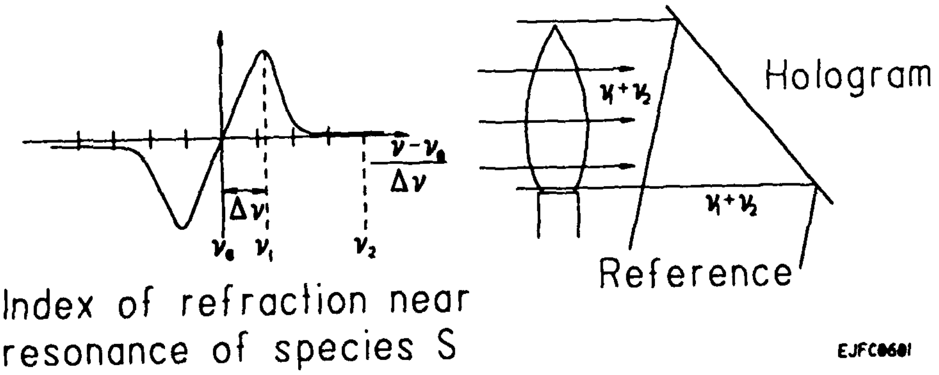
$\frac{\nu-\nu_0}{\Delta\nu}$
$\Delta\nu$
ν_0
ν_1
ν_2
Index of refraction near resonance of species S
$\nu_1+\nu_2$
Hologram
$\nu_1+\nu_2$
Reference
EJFC0601

Figure 6. Holographic recording at frequencies ν_1 (near resonance) and ν_2 (off resonance)

THERMAL FLUX MEASUREMENTS IN HYPERSONIC FLOWS
- A REVIEW -

J.F. Wendt
von Karman Institute
Chaussée de Waterloo, 72
B-1640 Rhode Saint Genèse-Belgium

D. Balageas
O.N.E.R.A.
BP 72
F-92322 Châtillon, Cedex-France

R.D. Neumann
The U. of Dayton Research Institute
300 College Park
Dayton, Ohio 45469, USA

ABSTRACT. This contribution reviews the papers presented in the Session on "Heat Flux" and "Thermography" at a NATO Advanced Research Workshop entitled "New Trends in Instrumentation for Hypersonic Research", 27 April-1 May, 1992, Le Fauga, France. The present status and problem areas associated with specific methods are discussed and recommendations for future research and development are presented.

Kluwer Academic Publisher will produce the complete proceedings as part of the NATO Advanced Study Institute Series.

1. INTRODUCTION

One of the authors (R.D.N.) opened this session with a paper (6A) containing a statement which summarizes the reality faced by the designers and users of instruments to determine heat flux :

"The fundamental problem is that you and I would like to hear broad, sweeping, universal truths about thermal sensors, but the subject is dominated by the details of the particular application".

The tone of the session having been set by the above remark, the remaining presentations from a number of large national aerospace laboratories as well as a few smaller establishments touched on virtually all techniques to measure heat flux on models in hypersonic flows; the sole exception was the liquid crystal technique.

Clearly, the choice of technique by the user will depend, among other requirements, on the objective of the experiment. Measurements are carried out in wind tunnels to provide detailed aerothermal design data where the need exists for a large quantity of data to be gathered on numerous complex shapes. Wind tunnel measurements are also carried out to validate or calibrate codes and in this case the spatial (and even temporal) resolution of the measurement technique is much more important than the quantity of data gathered. Flight measurements, likewise, generate or provide a check on design data; an equally important task on an operational vehicle may be "vehicle tending", i.e., monitoring certain flight parameters.

Once the objective as described above is clear, then the key parameters which will fix the choice of the instrument will be :

- the level of heat flux and surface temperature;
- the duration of the test;
- the material and geometry of the structure, i.e., the model or vehicle sub-element.

In earlier years, most if not all quantitative measurements of heat flux were performed with discrete gauges (thermocouples, thin films, etc.). Today, the user often has a choice between the discrete gauges which have developed, generally speaking, a certain maturity and survey techniques which provide an overall surface image (the equivalent of an infinite number of discrete gauges).

Our review is arranged according to the discrete or field nature of the technique. In each case, the present status, problem areas, and recommendations for future research and development are presented.

2. DISCRETE TECHNIQUES

2.1. Thermocouples and Thin Film Gauges

2.1.1. *Present Status.*

Thermocouples have been the active element in numerous heat flux techniques spanning many years of applications. The thin-skin method, which relies on an inner surface temperature measurement in conjunction with a mathematical model relating temperature, model geometry, and material properties to heat flux, seems to be less employed at present in wind tunnel applications in spite of the ease of fabrication. Surface thermocouples, which use the same mathematical model as thin-film gauges, find application in harsh environments and where heat fluxes and corresponding changes in surface temperature are large. Consigny et al [6B] described the use of a constantan jacket in which a series of chromel wires were embedded flush to the surface as a means of simplifying the thermal model. His paper also stressed the need to numerically simulate the data reduction process, particularly when materials of different thermal properties are employed.

Many specialized forms of gauges based on thermocouples and employing a suitable sub-surface model have found application in flight instruments [6A, 6D].

2.1.2. *Problem Areas.*

The major problem area appears to be an understanding of non-uniform heating effects and non-uniform substrates; this is a common issue with all of the following techniques as well and will be discussed in 5.0.

2.2. Thin-Film Gauges

These gauges, using the thick-skin technique as the model relating heat flux to the surface temperature, determined through the change in resistance of a thin metallic film, are in an advanced state of development. Miller [6C] concludes that with suitable care they present the most accurate means of measuring heat flux on wind tunnel models (~ 5 to 8 %).

2.2.1. *Problem Areas.*

Erosion of the gauges in harsh environments which characterize most high enthalpy wind tunnels has always been a problem. Olivier et al. [6E] describe their method of manufacture including protective coatings which seems to have produced a very durable gauge.

The trend is to manufacture the models, or large sections of the models, with a single insulating material, such as MACOR, a machinable ceramic, so as to eliminate thermal discontinuities. However, this is a costly process and the models are easily damaged.

2.2.2. *Recommendations.*

The development of more resistant coatings to protect thin film gauges from erosion and thermal shock should be accelerated. Better substrate materials which are easily machinable to high tolerances, characterized by nearly temperature-independent thermal properties, and are shock-resistant should be the object of research by materials specialists.

2.3. Gradient Heat Flux Gauges

2.3.1. *Present Status.*

Two examples of micro-machined gradient-type heat flux gauges were mentioned; one was developed at ONERA [6F] and the other is a commercial product of the Vatell Corporation in the U.S. Both gauges are fabricated by alternately stacking layers of insulator and thermocouples on a test article. While the two examples differ in detail, they both represent applications of integrated circuit fabrication technology to heat flux instruments and they both suggest a fundamental shift in philosophy from instruments that are inserted into existing structures to instruments that are fabricated on or with the structure. These examples of aerospace heat flux instruments join parallel developments in the measurement of heat transfer in rotating machinery.

2.3.2. *Problem Areas.*

The development problems for this class of heat gauges are somewhat different than traditional gauges. There still exist fabrication problems associated with the etching and deposition of films on a substrate. Gauge thickness is a problem that will be solved with more experience. The application of this class of thermal gauges to arbitrary model materials and calibration of the gauge at room and elevated surface temperatures are problem areas.

2.3.3. *Recommendations.*

Encourage development of this promising technology.

2.4. Gauge Calibration

2.4.1. *Present Status.*

There is a need for heat flux gauge calibration both at room temperature for aerodynamic ground test applications and at elevated temperatures for high temperature applications both on the ground and in flight. AEDC has developed very high heat flux calibration techniques which are essentially conducted at room temperature.

2.4.2. *Problem Areas.*

Corresponding high temperature calibration devices do not exist. In-situ, high temperature, high heat flux calibration devices are increasingly needed as the heat flux sensors become smaller and more complex and are increasingly integrated into the high temperature structure as previously discussed. There are several problem areas; e.g., controlling the errors due to surface radiation, producing convective and radiative calibration sources and developing portability within the calibration device.

2.4.3. *Recommendation.*

Develop a standardized, portable, thermal calibration device capable of calibration up to 1000°C at heating rates up to 1000 watts/cm^2.

3. SURVEY TECHNIQUES

3.1. Infrared

Infrared thermography is the survey technique which appears most often in the papers presented.

3.1.1. *Present status.*

Miller [6C] explains that due to recent advances providing high data acquisition rate radiometric measurements and computer based digitized image processors, infrared has received renewed interest at Langley. His group uses three single detector imagers with 6,25 and 30 frames per second in the 8-12 μm range. The models are viewed through ZnSe windows with antireflective coatings. The calibrations are made directly in the test section. Work is in progress for using emissivity calibration laws varying with angle of view (for three-dimensional models) and temperature. Curvature effects are taken into account by extrapolating to zero time the coefficient-time history.

Paper [6G], not orally presented, describes the application of infrared thermography to hypersonic blowdown wind tunnel tests using long-wave Agema cameras (782 and 880) with digitization by a microcomputer-based system. Original work is made which concerns image restoration for enhanced image resolution. This is obtained using an FFT inverse filter algorithm with a generalized system transfer function in which are cascaded an average sampled system modulation transfer function (imaging and sampling effect correction) and a temperature amplitude transfer function (lateral conduction effect correction). The corrections thus obtained in the case of Görtler vortex patterns are presented.

Paper [6H] presents the application of IR thermography in a low density hypersonic wind tunnel. The camera is an Agema 780 short wave (3-5 μm range) version. The calibration is also made in the test section using a model instrumented with thermocouples. The acquisition rate of the digitized images is rather low : 1 image/second.

Paper [6I] deals with a hot shot wind tunnel application with run durations as small as 20 to 100 ms (F4 wind tunnel). To follow the fast transients, two solutions are proposed :

i) line scanning using an Agema 880 long wave camera (one of the scanning movements is blocked) with 7°x7° objective. Through a ZnSe window, a line on the model is scanned 2500 times per second. A microcomputer system digitizes in real time, with 12 bits, 250 points per line.

ii) high frame rates (400 Hz) obtained by using a staring array camera built at ONERA. The camera is based on a 64x64 HgCdTe array working at 3-5 μm. A real-time system stores the digitized 12-bit data.

Paper [6K] presents results obtained with a long wave Agema 782 camera and a portable microcomputer-based system allowing analog-to-digital conversion (12 bits) and storage in real time of all the frames. As in paper [6G], the work presented deals with Görtler vortices. Here, the enhancement of the spatial resolution is obtained by a special arrangement using extra IR lenses. The Görtler phenomenon is taken as an illustration of the possibilities of IR survey techniques for identification of the governing parameters of the heat transfer : heat transfer coefficient and recovery temperature. This last parameter is rarely measured in spite of its importance, especially in an interaction zone where it can experience important variations. Use of spatial Fourier analysis is also presented for identification of the spanwise modulation of the heat transfer.

Most survey techniques, such as IR, will continue to use discrete gauges for continuous recalibration.

3.1.2. *Problem Areas.*

Neumann [6A] emphasizes the challenge of the technique : the ability to handle the data efficiently (density of information is 500 times higher than that of gauges).

For ground tests, there is a need :

i) to broaden the range of temperature response, for example, in shock-interaction regions (problem of peak heating where the peaks are chopped off).

ii) for transition location measurements by means of a survey technique such as IR thermography while the forces and moments are measured simultaneously.

In flight, the interaction regions must also to be studied but many difficulties are to be solved to successfully obtain infrared measurement surveys (see, for example, problems encountered with the Shuttle in-flight measurement).

In high enthalpy wind tunnels, energy emitted by hot parts of the facility (the throat, for instance) may perturb the measurements if reflection off the model is not avoided. High-emissivity diffuse surfaces are needed.

For many models, the three dimensional geometry is difficult to handle and must be taken into account when using a survey technique.

3.1.3. *Recommendations.*

For Miller [6C], in the 90's optical video-based infrared emission and relative intensity phosphor thermography systems will provide the vast majority of aerothermodynamic information from conventional hypersonic wind tunnels. They will provide quantitative, global three-dimensional heating distributions (multiple cameras and/or mirror systems). There will be an extension of the technique to impulse facilities (a few milliseconds) thanks to high speed video cameras with fast response phosphors and staring array cameras as in [6I].

Active infrared thermography with two main techniques which use uniform extended radiant heat flux stimulations combined with classical IR scanners or laser flying-spot cameras are to be evaluated since they can be useful for continuous flow experiments and for eliminating spurious radiation artefacts which can be encountered in high enthalpy facilities.

Two and three-dimensional conduction solvers must be used routinely allowing better identification of the heat transfer parameter in the presence of model curvature and high aerodynamic gradients. The three-dimensionality of models is also to be taken into account by procedures which establish correlations between the pixels of the infrared images and the surface elements of the model. A possibility is the inlay of these IR images with a calculated projection of the model 3-D mesh. This operation allows to take into account the variation of emissivity with the angle of view, to eliminate the pixels which are not on the model for computer time and memory saving, and to obtain a more meaningful presentation of results (iso-coordinate distribution in relation to aerodynamic phenomena in place of line or column distributions rarely interesting for the aerodynamicist).

3.2. Photoluminescence

3.2.1. *Present Status.*

The temperature sensitivity of various phosphor compounds has been known for many years; recent advances in imaging techniques and associated digital image processing algorithms have made this method a practical reality.

Reports were presented by three different laboratories, ONERA, NASA Langley and AEDC/Calspan, on their experiences with the phosphor technique [6B, 6C, 6D]. It seems that the so-called "two-color" or relative intensity method exhibits better accuracy; it has become "the most widely used heat transfer measurement technique at (NASA) Langley" [6C]. Developments were noted in the choice of phosphor compound and binder material, the coating thickness, and model construction (which seems to be moving toward slip casting techniques). Processing software is being further refined.

Miller [6C] described a new system that is undergoing acceptance tests at the time of this workshop (May 1992). It possesses the hardware and software for target recognition capability. A frame rate of 30 frames per second in possible and a calibration procedure which includes the response of each pixel is included. Provision for a second camera, synchronized with the first, is provided for three-dimensional analysis.

3.2.2. *Problem Areas.*

The temperature range for the application of phosphors is unduly narrow for some applications. Their use in impulse facilities will pose problems because of the need for a finite phosphor thickness which may result in a false indication of the model surface temperature; in addition, erosion of the phosphor coating will be a problem in some facilities. The phosphor surface tends to be too rough for certain applications. Finally, none of the authors commented on the spatial resolution of the technique.

3.2.3. *Recommendations.*

Efforts should be made to obtain mixtures of phosphors which will extend the useful temperature range and improve signal strength. The influence of phosphor thickness and binders on signal-to-noise ratio should be quantified. Model materials, discussed in 5.0, should be analyzed for ease of machining, although as mentioned above the ceramic slip-casting technique appears promising.

The limitations of phosphors in short duration facilities should be identified. Since the IR technique may not be usable in flows with hot particles emanating from the reservoir, the photoluminescence method may prove a good candidate in this more challenging flow environment.

3.3. Paints

Paints for heat transfer measurement were mentioned by two experimenters : thermosensitive paint presented by Consigny from ONERA [6B] and phase change paint presented by Matthews AEDC/Calspan [6D].

3.3.1. *Present Status.*

The thermosensitive paint used at ONERA, presenting three color changes, allows quantitative measurement of the heat transfer coefficient. The calibration procedure is detailed in the paper. The main advantages of the technique are the possible achievement of very detailed maps of heat transfer coefficient and the detection of possible hot spots.

The phase change paint is used at Calspan and also provides results in reasonable agreement with thin skin data.

3.3.2. *Problem Areas.*

One of the major problems with the thermosensitive paint is the tedious data reduction needed. Consigny [6B] presented a digital image processing method based on segmentation of two-dimensional histograms.

3.3.3. *Recommendations.*

No recommendations were formulated on this subject.

4. MODEL MATERIALS

4.1. Present Status

Three types of materials are used for models with survey techniques:

i) thin skin (0.5 mm) metallic models in stainless steel as in [6G,6H] or in nickel [6H] with black matte paint for high emissivity.
ii) very poor conductors such as Rhodorsil RTV 147 used for both thermosensitive paints and IR thermography in [6G] and Norcoat 4000 [6G,6K], which consists of hollow silica microspheres in a silicone elastomer, are used for small effusivity $(k\rho C)^{1/2}$ and high emissivity.
iii) ceramic materials like Macor used in [6B,6C] which are interesting because of their refractority and high emissivity.

4.2. *Problem Areas*

There is a need to obtain low effusivity, high emissivity, low-cost models; there is also a need to calibrate the emissivity dependence with temperature and angle of view (for angles higher than 60°). Finally, there is a need for the temperature dependence of the thermal properties (effusivity for semi-infinite models, conductivity and diffusivity for thin skin models). A step heating procedure is used for effusivity measurements at ONERA [6B].

4.3. *Recommendations*

Ceramic models will be the norm instead of the exception in the 90's [6C]. Sintered slip-cast ceramic techniques are needed.

5. NON-ISOTHERMAL SURFACE PHENOMENA

5.1. Present Status

Several authors discussed the effects of surface temperature discontinuities which may distort the level of inferred heat flux through temperature measurements. Temperature mismatches between the measurement device and the measured structure distort both the flow of heat within the structure as well as the convective heat transfer to the surface through boundary layer distortion. Non-isothermal effects are found both in wind tunnel studies and more dramatically in flight applications where heating rates can be changed by a factor of two. Correction methodology is available for more simple flows, but not for the more practical cases; for example, the presence of shock interactions.

5.2. Problem Areas

Correction methodology based on analytical methods is limited to classical plate flows. Corresponding CFD-based correction methodology is not validated for complex situations and probably suffers the same resolution errors of other thermal CFD applications. There are two problem areas : a lack of enduring sensitivity to the problem and perceived deficiencies in existing CFD correction methodology.

5.3. Recommendations

Develop a series of validating experiments based on thermal surface mismatch and shock interaction processes to challenge and encourage the CFD community.
Upgrade AGARDograph 165 to provide a mechanism of continuing education.

6. FLIGHT HEAT FLUX GAUGES

6.1. Present Status

Flight gauges differ from ground test gauges in several important ways; they are high temperature gauges, their fundamental measurement technique as well as construction materials are tied to ever-changing flight material systems and they must function in severe environments of long test duration or extremely complex material systems. The very character of these gauges, whether discrete sensors or sensors integrated into the structure at the time of fabrication creating a 'smart skin', is open.

6.2. Problem Areas

Since little was presented, there appears to be a lack of experience and/or perception within the instrumentation community.

6.3. Recommendations

Create increased awareness of the problems and possibilities through AGARD meetings or documentation.

7. FLIGHT MEASUREMENTS

7.1. Present Status

This workshop skirted the fringes of flight measurement technology. 'Making instruments that fly' was a common theme. The difficulty of flight measurements is both technical (high temperatures and the integration of sensors into complex structures) and cultural in that many diverse groups with very different perspectives come together in a flight test project. The 'no holes' criterion is a reflection of the difficulty that the measurement engineer has in discussing instrumentation with a structures engineer. This interaction is not the only one occurring in a flight test discussion. It is important that the instrumentation community develop the hardware to make instruments that fly and, as well, it is important that this community carefully develop and articulate the philosophy of why the proposed measurements are required in flight. For the thermal flux example, the measurement of temperature is easy. The inference of heat flux is far more complex. Whether heat flux is required in flight is an open issue that must be carefully articulated to the broader flight test community.

7.2. Problem Areas

Flight instrumentation is discussed in too narrow a technical setting. There is a need for broader dialog between instrumentation engineers and those who would design the flight vehicle; i.e., flight test systems engineers and structures engineers.

7.3. Recommendations

Focus a discussion on high temperature, high-heating-rate instrumentation appropriate for both flight and elevated temperature ground test facilities (such as arc tunnels).
At some point (perhaps after the instrumentation people have developed further among themselves), create a discussion format between the instrumentation engineers ('everything is measurable') and flight test systems engineers ('here are the constraints') to determine what is most useful to measure in flight, given practical constraints and how that data is used.

8. PRINCIPAL RECOMMENDATIONS

Heat flux instrumentation is an enabling technology, both in wind tunnels and in flight. A strong need exists today for greater accuracy due to code validation studies and for survey methods which can, e.g., illustrate transition front location with time. Future requirements indicate that surface temperatures and heat fluxes in flight may reach 2000 K and 10^4 to even 10^5 watts/cm^2, respectively. Modest investments in instrumentation development and in test planning at an early stage can reduce substantially future total vehicle costs.

Near-term actions which are recommended :
- exploration for phosphors with a larger temperature range;
- more emphasis on determination of recovery temperature for code

validation;
- a concerted look at "active" IR;
- an up-date of the classic AGARDograph 165 by Schultz & Jones, so as to set down in one source the recent developments in heat flux measurements;
- efforts must be devoted to techniques suitable for the accurate determination of the reservoir conditions of high enthalpy facilities;
- the special instrumentation problems of the newly-emerging arc-heated facilities need more attention. (They are more closely allied with flight instrumentation.)

Longer-term actions which are recommended :
- development of model materials with smaller temperature dependence on ρck and easier machinability;
- IR array cameras in the kilohertz range for unsteady flows;
- instrumentation techniques for surface temperatures to 2000 K and heat fluxes to 10^4 or even 10^5 watts/cm^2.

9. TITLES OF CONTRIBUTIONS

6A Neumann, R.D.: Temperature and heat flux measurement challenges for high temperature aerospace applications.
6B Consigny, H.; Le Sant, Y.; Bouvier, F.; Baumann, P.; Merienne, M.C.: Heat transfer measurement techniques used or in development at ONERA Chalais-Meudon.
6C Miller, C.G.: Aerothermodynamic measurement techniques employed in NASA Langley hypersonic facilities.
6D Matthews, R.K.: Aerothermal test methodology and techniques for the development of hypersonic vehicles.
6E Olivier, H.; Vetter, M.; Jessen, Gr\"onig, H.: Measurements on models for hypersonic real gas conditions.
6F Kayser, P.; Rodrigues, M.; Godefroy, J.C.: Thin gradient heat fluxmeters developed at ONERA.
6G Carlomagno, G.M.; De Luca, L.; Cardone, G.: Hypersonic aerodynamics research with an infrared imaging system.
6H Westby, M.F.: Heat transfer measurements using infrared thermography in rarefied flows.
6I Barbe, S.; Boscher, D.; Deschamps, J.; Gauffre, G.; Girard, A.: Infrared thermography for hot-shot wind-tunnel.
6J Gülhan, A.; Jöres, V.; Kindler, K.: Experiments on the catalytic efficiency of heat protection materials in the arc heated facility wind-tunnel (LBK) in Cologne.
6K Boscher, D.; Baudouy, B.; Deom, A.; Coet, M.C.; Delery, J.; Balageas, D.: Infrared thermography characterization of Görtler vortex type patterns in hypersonic flows.

A CFD Validation Roadmap For Hypersonic Flows

Joseph G. Marvin
NASA Ames Research Center
MS 229-1
Moffett Field, CA 94035-1000
U. S. A.

1. SUMMARY

A roadmap for CFD code validation is developed. The elements of the roadmap are consistent with air-breathing vehicle design requirements and related to the important flow path components: forebody, inlet, combustor, and nozzle. Building block and benchmark validation experiments are identified along with their test conditions and measurements. Based on an evaluation criteria, recommendations for an initial CFD validation data base are given and gaps identified where future experiments would provide the needed validation data.

2. INTRODUCTION

Computational Fluid Dynamics (CFD) must play a major role in the development of aerospace vehicles because ground test facilities are not able to fully simulate flight conditions. A CFD code's accuracy must be determined by a validation process, however, because of possible sources of error in the solutions. The process of validation involves two aspects: numerical and experimental. Numerical validation is necessary because CFD codes provide approximate solutions to the governing equations; they use discrete grids; they employ algorithms that contain numerical dissipation; and they may have nonconvergence errors. Validation of a code's physical modeling and its application to complex flows requires experiment to determine accuracy limits and range of applicability. Consequently, the pace of CFD's introduction and the extent of its reliability depends on validation.[1]

The second aspect of validation depends on comparisons with well-posed experiments. Since code applications are becoming more complex, it no longer suffices to use data from surface or integral quantities such as lift and drag to provide the validation. Two types of experiments are essential to the determination of CFD accuracy.[2] Building block experiments are necessary to validate physical and chemical modeling. Special attention must be given to measurements necessary to guide and validate the modeling. Benchmark experiments are necessary to validate CFD code prediction capabilities. Measurements illuminating the ability to predict engineering quantities are required.

Shortcomings in CFD validation exist at all flight regimes, but especially at hypersonic speeds. Gaps exist in the validation data base at true flight enthalpy due to facility and instrumentation limits. Nevertheless, there is a need to review the current data base to determine whether or not it can provide a basis for initiating a CFD validation process. Furthermore, much can be gained by assembling the data base and making CFD comparisons so that the inevitable pitfalls can be avoided in planning new validation activities.

The purpose of this paper is to propose a validation roadmap consisting of a series of steps that can establish a code's capabilities and associated accuracy. A series of appropriate experiments will be identified and cataloged. Selected validation experiments will be identified and cataloged according to the flow path for an air-breathing vehicle, e.g., forebody, inlet, combustor, and nozzle. Some examples taken from the data base will be used to clarify and demonstrate their utility and applicability.

3. VALIDATION ROADMAP

For the purposes of this paper, validation will be used to imply an established correspondence between actual flows and those produced by computation. The author, together with colleagues from various NASA Research Centers, developed the following five-step validation roadmap: (1) Define what critical performance information is needed and establish the corresponding code requirements; (2) Establish the appropriate governing equations and the corresponding physical and/or chemistry modeling requirements; (3) Identify or develop the appropriate validation data (building block data to guide and validate modeling and benchmark data to validate complex flow computations); (4) Perform computations for exact experimental conditions and test their sensitivity to the numerical and modeling assumptions; and (5) Document the code including its validation to the extent necessary to provide users with knowledge of the code's sensitivity to internal numerical parameters, grid refinement effects, the code's accuracy, and range of capabilities.

4. REQUIREMENTS

CFD performance estimates to support the design of an air-breathing vehicle can be accomplished with "nose to tail" computations using a series of codes identified with the air flow path, i.e., forebody, inlet, combustor, and nozzle codes. Following the first two steps in the roadmap, vehicle component performance, code, and modeling requirements are introduced.

4.1 Forebody

The design performance requirements are lift, drag, and heat load. To predict these, a code is required to compute surface pressures, skin friction, heat transfer rates, and provide inlet flow profile conditions required to initiate the inlet component code. Modeling requirements are subdivided into numerical and physical categories. Numerically, it is essential to preserve mass, momentum, and energy, to capture discontinuities such as shock waves, and to compute or admit flows developed by blunt noses or leading edges to capture any entropy layer development. Code sensitivity to grid refinement, numerical dissipation, lack of convergence, and any internal code parameters must be determined and specified. Physical and chemistry modeling is required for transition, turbulence, shock interactions, entropy layer swallowing, equilibrium, nonequilibrium air chemistry, wall catholicity, and low density flow at high altitudes. Mach number, Reynolds number, and forebody structural material will determine the modeling needs for air chemistry.

4.2 Inlet

The design performance requirements are mass capture, kinetic energy efficiency, pressure recovery, heat load, and spillage drag. To predict these the code is required to compute wall pressures, skin friction, heat transfer, mass flow, and provide exit profiles for the initial conditions of the combustor component code. Numerical, physical, and chemical modeling requirements are similar to those described previously for the forebody, but the code must additionally model cowl shock interactions and separation resulting from shock/boundary-layer interaction.

4.3 Combustor

Thrust, heat load, efficiency, pressure losses, and structural loads are the performance requirements of concern in the design. Codes are required to compute overall thrust, wall pressures, skin friction, heat transfer, and provide the flow exit profiles needed to initiate the nozzle component codes. Complex situations involving vortex and injector interactions with the main flow must be modeled in these codes. Numerical and mathematical modeling requirements are essentially the same as those listed previously, but it is essential that these codes handle finite rate chemistry, including air-fuel reactions, and that they model turbulence chemistry interactions.

4.4 Nozzle

Thrust, moments, and heat loads are the performance parameters required for design. The codes are required to predict net thrust, wall pressures, heat transfer, and skin friction. Physical and chemical modeling requirements include turbulence, shock interactions, shear layers, relaminarization, secondary flows, and finite rate chemistry for the air-fuel products of combustion.

5. VALIDATION DATA BASE

The next roadmap step is to identify or develop an appropriate data base. Candidate experiments for CFD validation were identified through literature searches and knowledge of recent validation activities within the U.S.A. They were divided into the building block and benchmark categories referred to previously and integrated into a matrix table. The tables were then used to show the range and completeness of the data, to identify gaps, and to select an initial validation data base.

A portion of the results are shown in tables 1–7 for each component category. The experiments, listed across the top of the table in numerical sequence according to reference number, were checked against the physical and chemical modeling requirements and performance requirements for the building block and benchmark experiments, respectively. (There is no significance attached to the numbering order.) Brief notations of test conditions and geometry are given. Measurements from the experiments were then checked to determine their match with the requirements.

Several important conclusions can be drawn from a study of the tabular results. The number of benchmark experiments is substantially fewer than the number of building block experiments, partly because component testing is often proprietary and not generally accessible. While the range of Mach numbers extends into the hypersonic regime, the enthalpy at which the experiments were conducted is mostly not commensurate with flight enthalpy and hence few "real gas" sets of data are available. The number of combustor and nozzle experiments lags considerably compared to the other categories and no combustor benchmark data are available to the general user. The types and variety of measurements for any single experiment and from experiment to experiment varies considerably, reflecting the fact that experiments performed in former decades were not planned to satisfy the needs of validation and that instrumentation and facilities, even today, limit our ability to perform complete validation experiments. Nevertheless, selected experiments from this data base provide the basis for initiating a focused validation effort.

5.1 Selection Criteria

The criteria for selecting the building block experiments were as follows: The data were required to be performed at conditions matching hypersonic flight Mach numbers (M > 3) for single flows associated with components of an air-breathing vehicle; they had to provide enough useful data to test specific physical or chemical modeling problems; they had to have boundary conditions defined sufficiently to initiate CFD solutions; and they had to have experimental errors identified and their specificity was desired. To the extent possible with today's status of instrumentation and facility development, measurements of flow field quantities and at least some measurement redundancy was desirable.

The selection of the benchmark experiments was made using a similar basis. Measurement details on flow modeling and chemistry, desirable for the building block data base, were not considered essential so long as the data reflected a measure of the actual physics and chemistry. However, test cases were sought that could test a code's ability to predict performance over a range of flow conditions. To the extent possible, measurements of flow field quantities in critical regions of the flow were desirable.

6. RECOMMENDED EXPERIMENTS

These are sketched in figs. 1–7 and listed by reference number. Although the experimental data base has shortcomings and gaps, it is assumed that code developers can use it collectively to provide a much needed validation baseline. Adhering to it can establish the physical and chemical modeling attributes of the codes, establish credibility regarding performance prediction, and establish important code-to-code comparisons for added confidence. Furthermore, code developers and experimentalists can use the information as a guide to improving and enhancing current experiments or for proposing additional ones.

6.1 Forebody

Transition, turbulence, and air chemistry are the most critical modeling issues. Selected building block experiments are given in fig. 1.

Transition onset and extent, influence of pressure gradient and bluntness, and influence of three-dimensional flow all must be modeled. At present, transition modeling is ad hoc and founded on experimental evidence influenced by uncertainties associated with free stream flight or wind tunnel conditions. Nevertheless, some experiments were selected in order to assess and compare current transition modeling. Experiment 3 is a flight experiment useful in assessing transition onset criteria for high Mach number real gas conditions. The remaining group of wind tunnel experiments are recommended for assessing the ability to model trends with bluntness and the influence of 3-D effects with the understanding that wind tunnel disturbances influence the actual locations of transition, if not the trends. NASA Langley Research Center's development of disturbance-free, quiet wind tunnels will provide much better validation data in the future. Experiment 6 was one of the first quiet wind tunnel demonstration experiments.

The validation experiments for attached flows selected for assessing turbulence modeling cover a range of Mach numbers, are limited in wall cooling range to 0.2, and the majority do not simulate flight enthalpies. (The latter may not present a major impediment as the influence of turbulence-chemistry interaction is not believed to be a first-order effect, except in combustor and nozzle flows.) Validation studies to date show turbulence modeling for attached hypersonic flows is reasonably in hand (see, e.g., ref. 60). Uncertainties remain in modeling the influence of pressure gradients, however, and a data base is only available at lower Mach numbers. One experiment on a conical configuration is available for assessing modeling for forebodies at angle of attack.

Air chemistry modeling is essential to numerical computations of hypersonic flows. Implementation of equilibrium air chemistry in CFD codes is straightforward and has a sound basis. Nonequilibrium air chemistry implementation in CFD codes is less advanced, e.g., decisions regarding strong or weak coupling of the species equations with the fluid dynamics equations and the choice of rate constants. Therefore, the recommended experiments involve conditions where nonequilibrium chemistry modeling is needed. The sharp and blunt cone data from a ballistic range test for laminar flow conditions in air provides a unique set of experiments conducted for this purpose. Other experiments in heated oxygen and nitrogen are also available. The paucity of detailed experimental profile data apropos to validation at flight enthalpies for both equilibrium and nonequilibrium flows suggests that code-to-code comparisons become an integral part of the validation process. With this objective in mind it is also recommended that code-to-code comparisons be made for the altitude and velocity conditions specified in cases 1 and 2 of ref. 61 for testing nonequilibrium modeling and case 2-b from ref. 62 for testing equilibrium modeling.

The recommended benchmark experiments are given in fig. 2. Only two experiments are recommended and they provide data on generic geometries at hypersonic Mach number and Reynolds number conditions leading to both laminar and turbulent flow. (The data from experiment no. 46 are currently restricted to U.S. citizens with access to NASP information.) The test conditions do not match flight enthalpies and corresponding air chemistry reactions. These experiments, however, will serve to validate 3-D algorithms, incorporation of transition and turbulence models in them, and performance predictions of aerodynamic parameters.

6.2 Inlet

Transition, turbulence, and air chemistry are also important modeling issues associated with developing inlet codes. In addition however, shock-wave/boundary-layer interaction modeling is crucial. The building block experiments selected for the validation data base are listed in fig. 3. In addition to those previously selected and discussed for transition, turbulence, and chemistry modeling for the forebody, the remainder deal with the shock-wave/boundary-layer interaction problem for laminar and turbulent flows. A comprehensive search for turbulent shock interaction validation experiments was conducted for NASA by Settles.[63] Most of those experiments were listed in the candidate data base shown previously and a few are recommended herein. Additionally, recent turbulent validation experiments performed at NASA Ames Research Center have been selected. They provide data on flows with compression ramps, impinging shocks, and swept and intersecting shocks. All of the selected experiments were performed in wind tunnels at enthalpies that do not match flight.

Inlet benchmark experiments selected for the validation data base are shown in fig. 4. The Mach number range is limited and flight enthalpy is not matched. Although more experiments have been performed recently, they could not be recommended because they were performed on proprietary geometries. Nevertheless, the experiments selected will serve to validate 3-D algorithms, incorporation of turbulence modeling, and provide some data to evaluate predictions of performance parameters.

6.3 Combustor

The critical modeling issues for supersonic combustors involve various mixing processes of chemically reacting constituents. The combustor building block experiments shown in fig. 5 can be useful in assessing modeling of various mixing processes with and without chemical reactions, although they are limited in many instances by the variety and accuracy of their data.

Experiment 34 provides supersonic data for 3 nonreacting ejector flows: jet-off, jet-on , and two streamwise-aligned jets-on. Experiment 37 provides subsonic data for a reacting flow case. Experiment 36 and the data correlation from ref. 39 provide data to assess turbulence modeling of single and two-stream shear layers, and experiments 35, 38, and 40 provide shear layer mixing data for hydrogen-air reacting flows.

No combustor component experiments were selected because of their proprietary nature. There is still, nevertheless, a serious gap in both the combustor building block and benchmark experimental data base adequate for CFD validation.

6.4 Nozzle

The nozzle building block experiments selected for assessing modeling issues are shown in fig. 6. Of the critical modeling issues, turbulent boundary layer development and the expansion of reacting hydrogen-air mixtures are addressed

Some of the flat plate flows from the forebody recommendations can be used to test implementation of turbulence models into nozzle codes. In addition, experiment 41 provides data on a turbulent boundary layer developing on a nozzle wall to a very high Mach number in helium. The data can be used to assess turbulence modeling for highly expanding nozzle flows. Experiments in nozzles with reacting air chemistry are lacking. Therefore a numerical test case developed recently and described in ref. 45 is recommended for code-to-code comparisons.

Only one nozzle benchmark experiment is recommended (see fig. 7). This particular experiment was designed with CFD Navier-Stokes codes under development at NASA Ames Research Center and was recently completed. Although it is a cold-air nozzle experiment, it can provide a basis for validation of 3-D algorithms, turbulence modeling, and the ability of the codes to predict some of the required performance parameters. Experiments with reacting air chemistry are needed.

7. RECENT VALIDATION ACTIVITIES

Some of the selected validation experiments were designed and carried out recently at the NASA Ames Research Center. Building block experiments at hypersonic Mach numbers were performed to guide and validate turbulence and real gas air chemistry modeling. Benchmark experiments were performed to validate 3-D forebody and nozzle codes. Each of the experiments was designed with validation as their primary purpose and some of the results are described next.

7.1 Physical and Chemical Modeling Experiments

Experiments designed to provide guidance and validation for the development of compressible turbulence models for various shock-wave/boundary-layer interactions have been accomplished in the Ames 3.5-Foot Hypersonic Wind Tunnel (3.5' HWT). Four experiments[21,30,33] were completed, providing surface measurements and mean-flow boundary layer profiles. Turbulence measurements will be obtained in the future with a laser anemometer and a laser-induced-fluorescence instrument developed for the facility.

One of these experiments consisted of a series of axisymmetric flares preceded by a cone-ogive-cylinder. The test geometry and conditions are shown in fig. 8. Beginning and end of transition occurred on the cone ahead of the cylinder. The measurements in the interaction zones included surface pressure, heat transfer, and surface oil streaks. A few mean flow velocity and density profiles were also obtained ahead of the interaction zone and on the 20° flare. The data are summarized and tabulated in ref. 21.

Experimental surface pressure and heat transfer distributions are shown in fig. 9 for the 35° flare. The separation locations determined from surface oil streaks are shown along with typical data error bars. The data are being used to validate turbulence model corrections for compressibility. They are compared with computations by Horstman[64] using a standard k-e eddy viscosity model and one corrected for compressibility. These solutions were obtained by solving the Reynolds-averaged Navier-Stokes equations. ITW refers to "integration to the wall" using low Reynolds number damping terms. For the modified model, which accounts for compressibility effects and limits the length scale in the vicinity of reattachment, significant improvements were obtained in predicting the measured pressure distribution, the predicted separation location, and the heat transfer.

Other tests were performed to guide turbulence modeling for impinging, swept, and intersecting swept shocks interacting with a turbulent boundary layer. A model sketch is shown in fig. 10. A sharp flat plate was used for these experiments. The plate was pitched at −2° angle of attack to increase the test Reynolds number and provide a uniform 2-D flow field on the plate. The plate was of a hollow frame construction, having interchangeable panels with several 20-cm-diameter holes in the center that accommodated surface pressure, heat transfer, pitot-static, yaw, and total temperature instrumentation ports. Tests were made with a wedge mounted above the test bed to generate a shock wave which impinged on the test bed. Pressure and heat transfer were measured throughout the interactions. In addition, to surface pressures and heat transfer, flow field surveys and skin friction were measured. Wedges with angles of 5°, 10°, and 15° were tested. In another configuration, fins were placed on the flat plate to generate a glancing shock-wave interaction. Fin angles of 5° to 15° were investigated. More recently a crossing shock interaction experiment was completed. In addition to surface pressure and heat transfer, flow field surveys and skin friction were obtained. Documented data are provided for each of these experiments.[30,33]

Typical data from the swept shock experiment are shown in fig. 11. Measured pressure and heat transfer, normalized by the upstream flat plate values, are plotted as a function of spanwise distances. Error bars are shown at two locations to indicate the variations in accuracy of the measurements. As the fin angle is increased, the corresponding increase in its shock strength causes the flow to separate, as observed from converging surface streamline patterns. Corresponding increases in heating and pressure were observed between 5 and 10 cm. As the fin wall is approached the pressures and heating continue to increase. On the fin the flow is laminar above the interaction and near the plate surface. Fin pressures (not shown) decrease rapidly at the intersection with the plate indicating the presence of a corner vortex.

Comparisons of the data on the plate with the 10° fin are compared with computations by Horstman[65] in fig. 12. Pressure, heat transfer, and skin friction data predicted with the Navier-Stokes code computations using a k-e model are in good agreement with the data. Although not shown here, comparisons of predictions with flow field profile data were also in good agreement. Evidently, for these flows, compressibility corrections needed for the strong 2-D interactions where large streamwise separations occurs are not required. Modeling studies on this flow are continuing, however.

Another building block experiment[10] has been carried out to obtain aerodynamic data at true flight enthalpy on sharp and blunt slender cones to assist in validating air chemistry modeling. It was carried out in the Ames Hypervelocity Ballistic Range at speeds in excess of 5 km/s. Reynolds numbers were between 10^5 and 10^6 and the flow was laminar. The resulting set of data is suitable for testing air chemistry modeling. Aerodynamic data for a 30% blunt 5° cone with conical ring shock generators were obtained and a summary of the important results taken from ref. 11 are shown in fig. 13. Aerodynamic data and a typical shadowgraph are shown and compared with computations by Molvik using a Navier-Stokes code with a strongly coupled 7-species air chemistry model and an ideal gas model. A histogram is shown for the number of data points used to deduce the aerodynamic coefficients. Confidence in the reported coefficients is greatest at moderate angles, where the number of data points is greatest. The top data figure shows the experimental and computed drag coefficient. The computed values of C_D using both perfect gas and real-gas chemistry models lie within the experimental error bars as one would expect, since the drag is mostly associated with the blunt nose. On the other hand, the pitching moment is quite sensitive to the gas modeling because the cone surface pressures resulting from the gas expansion are affected by gas composition. The reacting gas model calculations provide a good prediction of the results. The shadowgraph is compared with pressure contours, and the shocks from the ring generators, which are also sensitive to gas composition, compare nicely.

A finite fringe interferogram was obtained during one range firing of a smooth blunted cone to provide validation information on flow field density.[66] However, obtaining density was more difficult than first anticipated because of pitch and yaw orientations of the model, the test density level, and because of the index of refraction's implicit dependence on density. Rather, it is now proposed that optical path be computed from the computations using real gas modeling and subsequently compared with the measured optical path. In fig. 14 the infinite fringe interferogram and interpreted optical path through the model wake are shown. As can be seen, the optical path data may provide an alternative, more sensitive means of validating the computations.

7.2 Generic All-Body Hypersonic Benchmark Experiment

A model of a generic hypersonic vehicle was tested in the NASA Ames 3.5-Foot Hypersonic Wind Tunnel to establish a benchmark experimental data base for validation of forebody computer codes. Experimental data on flow visualization, surface pressures, surface convective heat transfer, and pitot-pressure flow-field surveys were obtained.[47] A sketch of the model showing the basic model geometry and dimensions is given in fig. 15. The model has a delta planform with leading-edge sweepback of 75° and total axial length, L, of 0.9144 m (3 ft). The forebody is an elliptic cone with a major-to-minor axis ratio of 4, and the afterbody has elliptical cross sections with a sharp straight-line trailing edge. The juncture between the forebody and afterbody occurs at 2/3 of the body length. The model nose was sharp.

Examples of the data showing windward centerline surface-pressure and heating distributions are given in figs. 16 and 17. Also shown are predictions of the windward pressures and heating from the Ames UPS code (an upwind parabolized Navier-Stokes solver) with the Baldwin-Lomax turbulence model. There is generally good agreement between the windward pressure and heating data and the predictions, with greater differences at the higher angles of attack where the forebody pressures and heating are underpredicted .

Experimental pitot-pressure profiles of the shock layer for the afterbody centerline at x/L = 0.8 are compared with computations in fig. 18 for various angles of attack. The predictions are considered in good agreement overall with experiment except near the bow wave because of grid resolution. On the windward side, the merging of the viscous and expansion regions of the flow are also captured by the code.

7.3 Generic Single Expansion Ramp Nozzle Experiment

This experiment was conducted in the Ames 3.5' HWT at Mach 7.3 and a Reynolds number of 150 million/ft. A photograph of the model is shown in fig. 19. CFD was applied to design the model. Pressures, 5-hole pitot probe surveys, and ramp boundary layer profiles are available along with flow visualization. Navier-Stokes solutions are now being performed. An example of the results showing a comparison of the measured and computed shock system taken from ref. 67 is given in fig. 20. Very good agreement is observed.

8. CONCLUDING REMARKS

A comprehensive data base for CFD code validation was reviewed and experiments selected that provide a focused basis for evaluating code development. Two types of experiments were selected for each major flow component: building block experiments for simple flows that can verify physics and chemistry modeling and benchmark experiments that can validate forebody, inlet, combustor, and nozzle codes. Major gaps in the data base exist for the real gas conditions associated with flight, for reacting combustor flows, and for reacting nozzle flows.

In spite of these gaps, data to assess physical modeling for turbulent boundary layers, shock interactions with laminar and turbulent boundary layers, and combustor injector interactions are available. Similarly, some data on chemistry modeling for simple external aerodynamic flows and internal flows involving mixing of hydrogen and air were identified that can provide partial validation of the real gas aspects of the codes. Benchmark experimental data, mostly at enthalpy conditions below those associated with hypersonic flight, are also available for assessing predictions of various 3-D algorithms and their associated physical modeling assumptions.

While most of the recommended experiments provide the essential information for initiating computations, it would be prudent to establish unified input conditions, data presentation format, and error analysis for each of them. Precedents for such undertakings have already been established (see, e.g., refs. 68-70). A team of experts, knowledgeable in CFD and EFD, could undertake the steps necessary to see that this is accomplished in a timely fashion.

9. REFERENCES

1. Marvin, J. G., "Accuracy Requirements and Benchmark Experiments for CFD Validation," Symposium on Validation of Computational Fluid Dynamics, AGARD CP-437, 1988.

2. Marvin, J. G. and Holst, T. L., "CFD Validation for Aerodynamic Flows - Challenge for the '90's,". AIAA Paper 90-2995, AIAA 8th Applied Aerodynamics Conference, August 20 - 22, 1990/Portland, Oregon.

3. Raper, J. L. Carter, H. S., Hinson, W. F., and Morris, W. O., "Basic Measurements from a Turbulent-Heating Flight Experiment on a 5° Half-Angle Cone at Mach 20 (Reentry F)," NASA TMX-2308, 1971. See also NASA TMX-2584, 1972 and NASA TMX-2282, 1977.

4. Sanator, R. J., De Carlo, J. P., and Torillo, D. T., "Hypersonic Boundary-Layer Transition Data for a Cold-Wall Slender Cone," AIAA J., Vol. 3, No. 4, April 1965, pp. 758-80.

5. DiCristina, V., "Three-Dimensional Laminar Boundary-Layer Transition on a Sharp Cone at Mach 10," AIAA J., Vol. 8, No. 5, May 1970, pp. 852-856.

6. Chen, F. J., Malik, M. R., and Beckwith, I. E., "Boundary-Layer Transition on a Cone and Flat Plate at Mach 3.5," AIAA J., Vol. 27, No. 6, June 1989.

7. Stetson, K. and Rushton, "Shock Tunnel Investigation of Boundary Layer Transition at M=5.5," AIAA J., Vol. 5, No. 5, May 1967, pp. 899-905.

8. Owen, F. K. and Horstman, C. C., "On the Structure of Hypersonic Turbulent Boundary Layers," JFM , Vol. 53, part 4, pp. 611-636, 1974. See also AIAA J., Vol. 10, No. 6, pp. 769-775, June 1972.

9. (Flow Case 8101,2), "The 1980-81 AFOSR/HTTM-Stanford Conference on Complex Turbulent Flows," Vols. I, II and III, Ed. S. J. Kline et al., 1982.

10. Strawa, A. W., Molvik, G., Yates, L., and Cornelison, C., "Experimental and Computational Results for 5 Degree Blunt Cones with Shock Generators at High Velocity," AIAA Atmospheric Flight Mechanics Conference, Boston, MA, Aug. 1989, AIAA Paper 89-3377.

11. Spurk, J. H., "Experimental and Numerical Nonequilibrium Flow Studies", AIAA J., Vol. 8, pp. 1039-1045, 1970.

12. Hornung, H. G., "Non-equilibrium Dissociating Nitrogen Flow Over Spheres and Circular Cylinders," JFM, Vol. 53, pp. 149-176, 1772.

13. Lewis, J. E., Gran, R. L., and Kubota, T., "An Experiment on the Adiabatic Compressible Turbulent Boundary Layer in Adverse and Favorable Pressure-Gradients," J. Fluid Mechanics, Vol. 51, pt. 4, 1972, pp. 657-672.

14. Taylor, M. W., "A Supersonic Turbulent Boundary Layer on Concavely Curved Surfaces," Princeton, Gas Dyn. Lab. Rep. MAE 1684, 1984.

15. Fernando, E. M. and Smits, A. J., "A Data Compilation for a Supersonic Turbulent Boundary Layer Under Conditions of an Adverse Pressure Gradient," Princeton, Gas Dynamics Lab. Rep. MAE 1746.

16. Jayaram, M., Taylor, M. W., and Smits, A. J., "The Response of a Compressible Turbulent Boundary Layer to Short Regions of Concave Surface Curvature," J. Fluid Mech., 175, pp. 343-362.

17. Carver, D. B., "Heat Transfer, Surface Pressure and Flow Field Surveys on Conic and Biconic Models with Boundary Layer Trips at Mach 8 - Phases IV and VI," Calspan/AEDC Div., AEDC-T5R-80-V14, 1980.

18. Christophel, R. G., Rockwell, W. A., and Neumann, R. D., "Tabulated Mach 6 3-D Shock Wave-Turbulent Boundary Layer Interaction Heat Transfer Data (Supplement)," AFFDL-TM-74-212-FXG-Supplement, 1975 and Law, C. H., "Two-Dimensional Compression Corner and Planar Shock Wave Interactions," AFFDL-TR-65-36, 1966.

19. Coleman, G. T. and Stollery, J. L., "Heat Transfer from Hypersonic Turbulent Flow at a Wedge Compression Corner," J. Fluid Mechanics, Vol. 56, 1972, pp. 741-752.

20. Holden, M. S., Havener, A. G., and Lee, C. H., "Shock Wave/Turbulent Boundary Layer Interaction in High-Reynolds-Number Hypersonic Flows," CUBRC-86681, 1986 and Holden, M. S., "Experimental Studies of Quasi-Two-Dimensional and Three-Dimensional Viscous Interaction Regions Induced by Skewed-Shock and Swept-Shock Boundary Layer Interaction," AIAA Paper 84-1677, 1984.

21. Kussoy, M. I. and Horstman, C. C., "Documen-tation of Two- and Three-Dimensional Hypersonic Shock Wave/Turbulent Boundary Layer Interaction Flows," NASA TM-101075, 1989.

22. Kussoy, M. I. and Horstman, C. C., "An Experimental Documentation of a Hypersonic Shock-Wave Turbulent Boundary Layer Interaction Flow - With and Without Separation," NASA TM X-62412, 1975.

23. Fernholz, H. H., Finley, P. J., Dussauge, J. P., and Smits, A. J., "A Survey of Measurements and Measuring Techniques in Rapidly Distorted Compressible Turbulent Boundary Layers," AGARDograph 315, 1989. and Smits, A. J., and Muck, K. C., "Experimental Study of Three Dimensional Shock Wave/Turbulent Boundary Layer Interactions," J. Fluid Mechanics, Vol. 182, Sept. 1987, pp. 291-314.

24. Zheltovodov, A. A., Zaylichny, E. G., Trofimov, V. M., and Yakovlev, V. N., "Investigation of Heat Transfer and Turbulence in Supersonic Separation," ITPM Preprint 22-87, 1987.

25. Knight, D. D., Horstman, C. C., Bogdonoff, S. M., and Shapey, B. L., "The Flowfield Structure of the 3-D Shock Wave-Boundary Layer Interaction Generated by a 20 deg. Sharp Fin at Mach 3," AIAA Paper 86-0343, 1986.

26. Kim, K. S., Lee, Y., Alvi, F. S., Settles, G. S., and Horstman, C. C., "Laser Skin Friction Measurements and CFD Comparison of Weak-to-Strong Swept Shock/Boundary-Layer Interactions," AIAA Paper 90-0378, 1990.

27. Brown, J. L., Kussoy, M. I., and Coakley, T. J., "Turbulent Properties of Axisymmetric Shock-Wave/Boundary-Layer Interaction Flows," Turbulent Shear-Layer/Shock-Wave Interactions, edited by Delery, J., Springer-Verlag, Berlin, 1986, pp. 137-148 and Dunagan, S. E., Brown, J. L., and Miles, J. B., "Interferometric Data for a Shock-Wave/Boundary-Layer Interaction," NASA TM-88227, 1986.

28. Brown, J. D., Brown, J. L., and Kussoy, M. I., "A Documentation of Two- and Three-Dimensional Shock-Separated Turbulent Boundary Layers," NASA TM-101008, July 1988.

29. Settles, G. S., Horstman, C. C., and McKenzie, T. M., "Flowfield Scaling of a Swept Compression Corner Interaction-A Comparison of Experiment and Computation," AIAA Paper 84-0096, 1984.

30. Kussoy, M. I. and Horstman, K. C., "Documentation of Two- and Three-Dimensional Shock-Wave/Turbulent-Boundary Layer Interaction Flows at Mach 8.2," NASA TM-103838, May 1991.

31. Wieting, A. R. and Holden, M. S., "Experimental Study of Shock Wave Interference Heating in Supersonic Flows," AIAA Paper 87-1511, 1987.

32. Holden, M. S. and Moselle, J. R., "Theoretical and Experimental Studies of Shock Wave-Boundary Layer Interaction on Compression Surfaces in Hypersonic Flows," ARL 70-0002, Jan. 1970.

33. Kussoy, M. I. and Horstman, K. C., "Intersecting Shock-Wave/Turbulent Boundary-Layer Interactions at Mach 8.3," NASA TM 103909, Feb. 1992.

34. McDaniel, J., Fletcher, D., Hartfield, R., Jr., and Hollo, S., "Staged Transverse Injection into Mach 2 Flow Behind a Rearward-Facing Step: A 3-D Compressible Flow Test Case for Hypersonic Combustor Code Validation," AIAA Paper 91-5071, AIAA Third International Aerospace Planes Conference, 3-5 December 1991.

35. Jarrett, O., Cutler, A. D., Antliff, P. R., Chitsomboom, F., Dancey, C. L., and Wang, J. A., "Measurements of Temperature, Density, and Velocity in Supersonic Reacting Flow for CFD Code Validation," Proc. of the 25th JANNIF Combustion Meeting, Huntsville, AL, 1988.

36. Cheng, T. S., Wehrmeyer, J. A., Pitz, R. W., Jarrett, O., and Northam, G. B., "Finite Rate Chemistry Effects in a Mach 2 Reacting Flow," AIAA 91-2320, June 1991. See also AIAA Paper 91-0181, Jan. 1991 and NASA CR-189544, 1991.

37. Marek, B., "Reacting Mixing Layer," NASA CP 10003, Vol. 5, 1988.

38. Peschke, W. T., "Hydrogen Fueled Scramjet Study," 26 JANNAF Combustion Meeting, CPIA, Oct. 1989.

39. (Flow Case 8500), "The 1980-81 AFOSR/HTTM-Stanford Conference on Complex Turbulent Flows,"Vols. I, II and III, Ed. S. J. Kline, et al., 1982.

40. Barrows, M. C. and Kurkov, A. P., "Supersonic Combustion of Hydrogen in Vitiated Air Steam Using Stepped-Wall Injections," AIAA Paper 71-721, AIAA/SAE 7th propulsion Joint Specialist Conference, June 1-18, 1971.

41. Kemp, H. and Owen, F. K., "Experimental Study of Nozzle Wall Boundary Layers at Mach No. 20-47," NASA TND-6965, October 1972.

42. "Hypersonic Research Engine Project-Phase IIA, Nozzle Program 3rd Interim Technical Data Report, Data Item No. 5555-3.02," December 14-March 13, 1967, NASA Contract No. NAS1-6666, Air Research Manufacturing Division of the Garrett Corp., Rpt. Ap-67-3129, January 11, 1988.

43. Lewis, L. and Carlson, D., "Normal Shock Location in Underexpanded Gas and Gas Particle Jets," AIAA J., Vol. 2, No. 4, April 1964, pp. 776-777.

44. "Report of the Working Group on Aerodynamics for Afterbodies," AIAA Advisory Report #226, June 1986.

45. (Problem VIII.2), "NonEquilibrium Flow in a Shock Tube," Workshop on Hypersonic Flows for Reentry Problem,. Part II co-organized by INRIA - Sophia Antipolis and GAMNI-SMAI, April 15-19, 1991, Antibes, France.

46. "Generic Option #2 Experimental Database/CFD Code Validation," Vol. 4, Blended Wing Body Aerothermal Model and Test Program, prepared by McDonnell Douglas, Sept. 1988. (Information Subject to Export Control Laws).

47. Lockman, W., Lawrence, S., and Cleary, J., "Experimental and Computational Surface and Flow-Field Results for an All-Body Hypersonic Aircraft," AIAA Paper 90-3067.

48. Wier, L. J., Reddy, D. R., and Rupp, G. D., "Mach 5 Inlet CFD and Experimental Results," AIAA Paper 89-2355, 25th Joint Propulsion Conference, 1989; see also Reddy, D. R., Benson, T. J., and Wier, L. J., "Computation of 3-D Viscous Flow Computation of Mach 5 Inlet with Experimental Data," AIAA Paper 90-0600.

49. Anderson, W. E. and Wong, N. D., "Experimental Investigation of a Large-Scale, Two-Dimensional, Mixed-Compression Inlet System," NASA TMX-2016, May 1970.

50. Mueller, J. N., Trexler, C. A., and Sounders, S. W., "Wind Tunnel Tests on a 3-Dimensional Fixed-Geometry Scramjet Inlet at M=2.30 to 4.60," NASA TMX-73933, March 1977.

51. Yanta, W. J., Collier, A. S., Spring, W. C., III, Boyd, C. F., and McArthur, J. C., "Experimental Measurements of the Flow in a Scramjet Inlet at Mach 4," AIAA Paper 88-01988.

52. Torrence, M. G., "Experimental Investigation of a Mach 6 Fixed-Geometry Inlet Featuring Swept External-Internal Compression Flow Field," NASA TN D-7998, October 1975.

53. Trexler, C. A. and Scuders, S. W., "Design and Performance at a Local Mach Number of 6 of an Inlet for an Integrated Scramjet Concept," NASA TN D-7944, August 1975.

54. Gnos, A. V., Watson, E. C., Seebaugh, W. R., Sanator, R. J., and DeCarlo, J. P., "Investigation of Flow Fields Within Large-Scale Hypersonic Inlet Models," NASA TN D-7150, April 1973.

55. "Generic Option #2 Experimental Database/CFD Code Validation," Vol. 6, Inlet Models and Test Programs, prepared by McDonnell Douglas, Sept. 1988. (Information Subject to Export Control laws).

56. Orth, R. C., Erdos, J. T., et. al., "Data Report for Parametric Scramjet Combustor Experiments Conducted in the Calspan Shock Tunnel - 3rd Entry," Vol. I, GASL TR-309, General Applied Science Laboratories, 1989.

57. Mikkelsen, K., McDonald, T., and Brasket, R., "Model Tests of NASP Generic Option 2 Exhaust Nozzle Configuration," Fluidyne Report 1570, May 1989.

58. Spaid, F. and Keener, E., "Experimental Results for a Hypersonic Nozzle/Afterbody Flowfield," paper to be presented at 17th AIAA Ground Testing Conf., July 6-8, 1992, Nashville, TN.

59. Cubbage, J. and Kirkham, F., "Investigation of Engine Exhaust Airframe Interference on a Cruise Vehicle at M=6," NASA TND-6060, January 1971.

60. Marvin, J. G. and Coakley, T. J., "Turbulence Modeling for Hypersonic Flows," NASA TM-1201079, June 1989.

61. Prabhu, D. K., Tannehill, J. G., and Marvin, J. G., "A New PNS Code for Chemical Nonequilibrium Flows," AIAA J., Vol. 26, No. 27, July 1988.

62. Bhutta, B. A., Lewis, C. H., and Cantz, F. A., "A Fast Fully Iterative Parabolized Navier Stokes Solver for Chemically Reacting Reentry Flows," AIAA Paper 85-926, June 1989.

63. Settles, G. S. and Dodson, L. J., "Hypersonic Shock/Boundary-Layer Interaction Database," NASA CR-177577, April 1991.

64. Horstman, C. C., "Hypersonic Shock-Wave Turbulent-Boundary-Layer Interaction Flows - Experiment and Comptutation," AIAA Paper 91-1760, Honolulu, HI, Jun. 1991.

65. Knight, D. D., Hortsman, C. C., and Monson, D. J., "The Hypersonic Shock Wave-Turbulent Boundary Layer Interaction Generated by a Sharp Fin at Mach 8.2," AIAA Paper 92-0747, 30th Aerospace Sciences Meeting, 1992.

66. Tam, T. C., Brock, N. J., Cavolowsky, J. A., and Yates, L. A., "Holographic Interferometry at the NASA-AMES Hypervelocity Free-Flight Aerodynamic Facility," AIAA Paper 91-0568, Jan. 1991.

67. Ruffin, S. M., Venkatapathy, E., Lee, S. H., Keener, E. R., and Spaid, F. W., "Single Expansion Ramp Nozzle Simulations," AIAA Paper 92-0387, 30th Aerospace Sciences Meeting, Jan. 1992.

68. Fluid Dynamics Panel Working Group 04: "Experimental Data Base for Computer Program Assessment". AGARD-AR-138, 1979.

69. "The 1980-81 AFOSR/HTTM Stanford Conference on Complex Turbulent Flows," Vol. I, Editors, Kline, et. al., 1992.

70. Fluid Dynamics Panel Working Group 07: "Test Cases for Inviscid Flow Field Methods," AGARD-AR-211, 1985.

Table 1 Forebody building block data base.

Experiment(ref. no.)	3	4	5	6	7	8	9	10	11	12	13	14	15	16	17
Mach No.	20	10	10	3	5.5	7	0~6	15	9~9.5	6	4	3	3	3	8
Re No.x(E-06)		2/ft	2/ft	12	2~8	25	-	.5~1	.05~.06	006~.01	5	63/m	63/m	63/m	3.7
2-d Geometry or Axisymmetric	✓	✓	✓	✓	✓	✓	✓	✓	✓	✓	✓	✓	✓	✓	✓
3-d Geometry															
Angle Of Attack(deg.)	0	0	0,4	0	0			0~20	0			0	0	0	0, 10
Physical And Chemical Modeling Req'mts															
Transition	✓	✓	✓	✓	✓										✓
Turbulence	✓					✓	✓				✓	✓	✓	✓	✓
Shock Boundary Layer Interactions*															
Entropy Layer Swallowing					✓			✓							✓
Equilibrium Chemistry	✓							✓							
Non equilibrium Chemistry								✓	✓	✓					
Wall catalysity									✓	✓					
Low Density Flow															
Adverse Press. Gradient											✓	✓	✓	✓	
Measurements															
Boundary Conditions	✓	✓	✓	✓	✓	✓	✓	✓	✓	✓	✓	✓	✓	✓	✓
Transition Location	✓	✓	✓	✓	✓	✓									
Wall Pressures	✓		✓			✓					✓	✓	✓	✓	✓
Heating Rates	✓	✓	✓	✓	✓	✓					✓				✓
Pitot Profiles						✓						✓	✓	✓	
Temperature Profiles						✓						✓	✓	✓	
Static Pressure Profiles						✓						✓	✓	✓	
Density Profiles						✓		✓		✓					
Velocity Profiles						✓					✓	✓	✓	✓	
Species Profiles															
Flow Visualization**								S		S					
Other(Specify)						cf,ch	cf,ch	Drag	standoff	standoff	cf	cf	cf	✓	
* See Inlet Unit Experiments															
** Shadowgraph															
Turbulece Measurements						✓								✓	

Table 2 Inlet building block data base.

Experiment(ref. no.)	18	19	20	21	22	23	24	25	26	27	28	29	30	31	32	33
Mach No.	6	9	11, 13	7	6.9	3	3	3	3	3	3	3	8.2	8	14	8.3
Re No.x(E-06)	10,30/f	25	3.7/ft	5.8/m	35.8	.8~7.6	32/m	700/m	6/m	18/m	18/m	63/m	4.9/m		0.072	4.9/m
2-d Geometry or Axisymmetric		✓	✓	✓	✓	✓	✓			✓			✓	✓	✓	
3-d Geometry	✓			✓				✓	✓		✓	✓	✓			✓
Physical And Chemical Modeling Req'mts																
Transition																
Turbulence	✓	✓	✓	✓	✓	✓	✓	✓	✓	✓	✓	✓	✓			✓
Shock Boundary Layer Interactions	✓	✓	✓	✓	✓	✓	✓	✓	✓	✓	✓	✓	✓	✓	✓	✓
Separation	✓	✓	✓	✓	✓	✓	✓	✓	✓	✓	✓	✓	✓	✓	✓	✓
Secondary/Corner Flows	✓														✓	
Mass Injection																
Bleed																
Equilibrium Chemistry																
Unsteady Flow																
Measurements																
Boundary Conditions	✓	✓	✓	✓	✓	✓	✓	✓	✓	✓	✓	✓	✓	✓	✓	✓
Transition Location				✓	✓											
Wall Pressures	✓	✓	✓	✓	✓	✓	✓	✓	✓	✓	✓	✓	✓	✓	✓	✓
Heating Rates	✓	✓	✓	✓	✓		✓						✓	✓	✓	✓
Pitot Profiles		✓	✓	✓	✓	✓	✓	✓	✓			✓	✓			✓
Temperature Profiles			✓	✓	✓	✓	✓						✓			✓
Static Pressure Profiles				✓	✓	✓	✓						✓			✓
Velocity Profiles				✓	✓	✓	✓			✓	✓					
Turbulence Quantities					✓	✓	✓			✓	✓					
*Flow Visualization**	S			OF					OF	OF		OF	S,OF	S	S	OF
Other(Specify)					cf	cf		yaw	cf	rho (y)		yaw	yaw, cf		cf	yaw
* S=Shadograph, OF=Oil Flow, SP= Structure Plot																

Table 3 Combustor building block data base.

Experiment(ref. no.)	34	35	36	37	38	39	40
Mach No. for Experiment	2	2.1	2	<1	3	0~6	2.4
Flight MachNo. Simulated***	6c	6h	6c		7h	N/A	6h
2-d Geometry or Axisymmetric		✓	✓	✓	✓	✓	✓
3-d Geometry	✓						
Scale(in.) d=Duct Ht.; L=Flow Length	0.75d	0.75d	0.75d	4x8d	3d	N/A	2x3.5d
Physical And Chemical Modeling Req'mts							
Turbulence		✓	✓			✓	
Shock Interactions	ltd.		✓		✓		
Shear Layers		✓	✓	✓	✓	✓	✓
Vortex/Shock Interaction							
Injector Interactions	✓	✓					
Finite Rate Chemistry		✓			✓		✓
Measurements							
Boundary Conditions	✓	✓			✓	✓	
Wall Pressures	✓			✓	✓		
Heating Rates					✓		
Skin Friction							
Pitot Profiles				✓			
Temperature Profiles		✓	✓	✓	✓		✓
Static Pressure Profiles	✓				✓		✓
Velocity Profiles	✓	✓	✓	✓			✓
Species Profiles	✓	✓		✓			✓
Turbulence Quantities	✓	✓	✓	✓	✓		✓
Flow Visualization*	LIF	✓	LIF	PLIF			
Other(Specify)						width	
* LIF= Laser Induced Fluorescence							
*** c=Cold Flow, Mc=1/3Mexp. ; h= Hot Flow, Flight Enthalpy Simulated							

Table 4 Nozzle building block data base.

Experiment(ref. no.)	41	42	43	44	45
Mach No. (Eqivalent Flight Or Test)	20~47	5~8		2.2	14
Mj		1~2.6	1.7~3	2	
Pj/Pfree stream			To 500	1.4	
2-d Geometry or Axisymmetric	✓	✓	✓	✓	✓
3-d Geometry					
Physical And Chemical Modeling Req'mts					
Turbulence	✓				
Shock Interactions			✓		
Shear Layers		✓		✓	
Secondary Flows					
Separation					
Relaminarization					
Finite Rate Chemistry		✓			✓
Measurements					none
Boundary Conditions		✓	✓	✓	✓
Transition/Relaminarization Location					
Thrust		✓			
Moments		✓			
Wall Pressures	✓	✓		✓	✓
Heating Rates					✓
Skin Friction					
Pitot Profiles	✓	✓			
Temperature Profiles	✓				✓
Static Pressure Profiles					✓
Velocity Profiles	✓				✓
Species Profiles					✓
Turbulence Quantities	✓				
Flow Visualization					
Other(Specify)		✓	Mach Disk	✓	

Table 5 Forebody benchmark data base.

Experiment(ref. no.)	17	46	47
Mach No.	8	11~20	7.4
Re No.x(E-06)	3.7	.3~32	5~25
2-d Geometry or Axisymmetric	✓		
3-d Geometry		✓	✓
Performance Requirements			
Lift		✓	
Drag		✓	
Heat Load		✓	
Inlet Profiles			
Flow Phenomena			
Transition	✓	✓	
Turbulence	✓	✓	
Shock Boundary Layer Interactions*			
Entropy Layer Swallowing	✓	✓	
Equilibrium Chemistry			
Non equilibrium Chemistry			
Wall Catalysity			
Low Density Flow			
Measurements			
Boundary Conditions	✓	✓	✓
Transition Location	✓	✓	
Lift		✓	
Drag		✓	
Wall Pressures	✓	✓	✓
Heating Rates	✓	✓	✓
Pitot Profiles		✓	✓
Temperature Profiles			
Static Pressure Profiles			
Velocity Profiles			
Species Profiles			
Flow Visualization**		S	S, OF
Other(Specify)			
* See Inlet Unit Experiments			
** S=Shadowgraph, OF=Oil Flow			

Table 6 Inlet benchmark data base.

Experiment(ref. no.)	48	49	50	51	52	53	54	55
Mach No.	3.5~4	3	2.3~4.6	4	6	6	7.4	11~16
Re No.x(E-06)/Ft	25	2.2	2.2	1.3	50.8	32.2	29.1	.2~10.5
2-d Geometry	✓	✓		✓			✓	✓
3-d Geometry	✓	✓	✓		✓	✓		✓
Performance Requirements								
Mass Capture	✓	✓	✓			✓		
Kinetic Energy Efficiency						✓		
Pressure Recovery	✓	✓	✓		✓	✓	✓	
Heat Load								
Spillage Drag								
Exit Profiles	✓	✓	✓	✓		✓	✓	
Flow Phenomena								
Transition							✓	✓
Turbulence	✓	✓	✓	✓	✓	✓	✓	
Shock Boundary Layer Interactions	✓	✓	✓	✓	✓	✓	✓	✓
Separation	✓	✓	✓	✓				✓
Secondary/Corner Flows	✓	✓	✓	✓				✓
Mass Injection								
Bleed	✓	✓		✓	✓			
Equilibrium Chemistry								
Unsteady Flow	✓	✓		✓				✓
Measurements								
Boundary Conditions	✓	✓	✓	✓	✓	✓	✓	✓
Transition Location							✓	✓
Wall Pressures	✓	✓	✓	✓	✓	✓	✓	✓
Heating Rates								✓
Pitot Profiles	✓	✓	✓	✓	✓	✓	✓	✓
Temperature Profiles							✓	
Static Pressure Profiles	✓	✓	✓		•	•		
Velocity Profiles								
Flow Visualization*				S	S	Oil	S,OF	S
Other(Specify)				cf, <u'>				
* S=Shadowgraph/Schlerin, OF=Oil Flow								

Table 7 Nozzle benchmark data base.

Experiment(ref. no.)	56	57	58	59
Estimated Date Available	Now	Now	'92	Now
Mach No. (Flight Equiv. Or Free Stream	10	1-16	7.4	6
Mj	1.5~2	2&4.4	1.5~3.4	3.5
Pj/P free stream	6~60	20~200	6~100	1~4
2-d Geometry or Axisymmetric	✓	✓		
3-d Geometry			✓	✓
Performance Requirements				
Thrust		✓		
Moments		✓		
Heat Loads	✓	✓		
Flow Phenomena				
Turbulence				✓
Shock Interactions				
Shear Layers	✓		✓	
Secondary Flows	✓			✓
Separation				
Relaminarization				
Finite Rate Chemistry	✓		✓	✓
Multiple Jets				✓
Measurements				
Boundary Conditions-Inflow	Mass Fl.	Mass Fl.		
	Pitot	Pitot		
	Species			Gamme Je
Transition/Relaminarization Location	✓			
Thrust		✓		✓
Moments				
Wall Pressures	✓	✓	✓	✓
Heating Rates or Wall Temperature	✓	✓	✓	
Skin Friction	✓		✓	
Pitot Profiles	✓	✓	✓	
Temperature Profiles				
Static Pressure Profiles	✓	✓	✓	
Velocity Profiles			✓	
Species Profiles	✓			
Flow Visualization	✓		✓	
Other(Specify)				

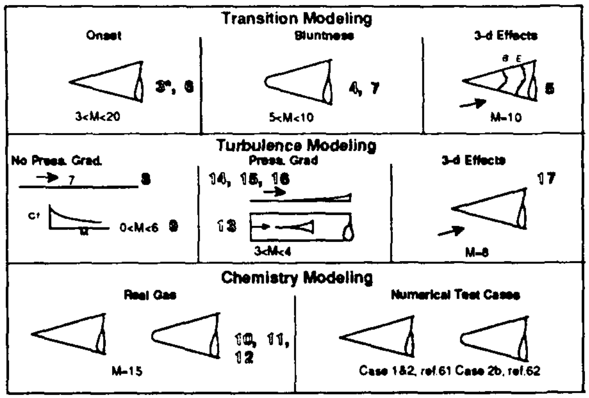
Transition Modeling
Onset
3*, 6
3<M<20
Bluntness
4, 7
5<M<10
3-d Effects
θ E
5
M=10
Turbulence Modeling
No Press. Grad.
7
8
Cf
x
0<M<6
9
Press. Grad
14, 15, 16
13
3<M<4
3-d Effects
17
M=8
Chemistry Modeling
Real Gas
10, 11, 12
M=15
Numerical Test Cases
Case 1&2, ref.61 Case 2b, ref.62

*Experiment Ref No.

Fig. 1 Recommended forebody building block validation experiments.

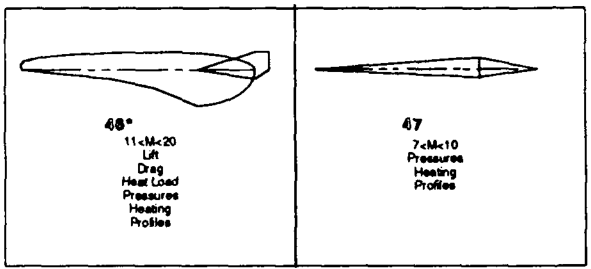
46*
11<M<20
Lift
Drag
Heat Load
Pressures
Heating
Profiles
47
7<M<10
Pressures
Heating
Profiles

*Experiment Ref. No.

Fig. 2 Recommended forebody benchmark validation experiments.

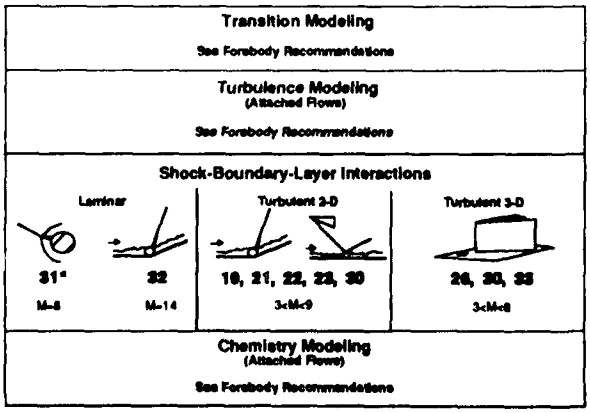
Transition Modeling
See Forebody Recommendations
Turbulence Modeling
(Attached Flows)
See Forebody Recommendations
Shock-Boundary-Layer Interactions
Laminar
31*
M=6
32
M=14
Turbulent 2-D
18, 21, 22, 23, 30
3<M<9
Turbulent 3-D
26, 28, 33
3<M<8
Chemistry Modeling
(Attached Flows)
See Forebody Recommendations

*Experiment Ref. No.

Fig. 3 Recommended inlet building block validation experiments.

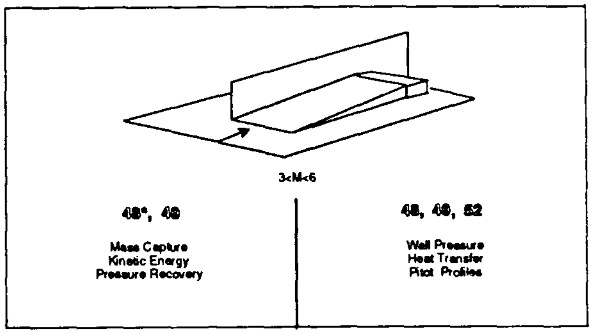
3<M<6
48*, 49
Mass Capture
Kinetic Energy
Pressure Recovery
48, 49, 52
Wall Pressure
Heat Transfer
Pitot Profiles

*Experiment Ref. No.

Fig. 4 Recommended inlet benchmark validation experiments.

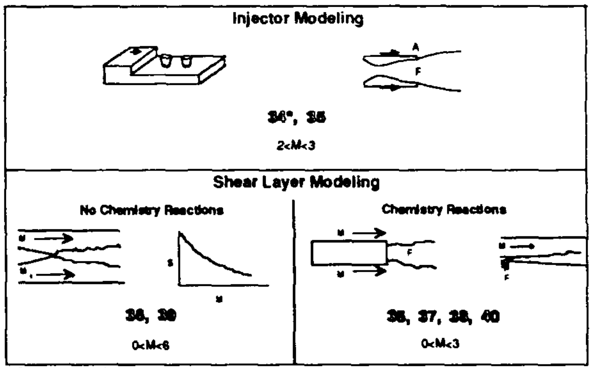
Injector Modeling
A
F
34*, 35
2<M<3
Shear Layer Modeling
No Chemistry Reactions
M
M
δ
M
36, 39
0<M<6
Chemistry Reactions
M
F
M
M
F
35, 37, 38, 40
0<M<3

*Experiment Ref. No.

Fig. 5 Recommended combustor building block validation experiments.

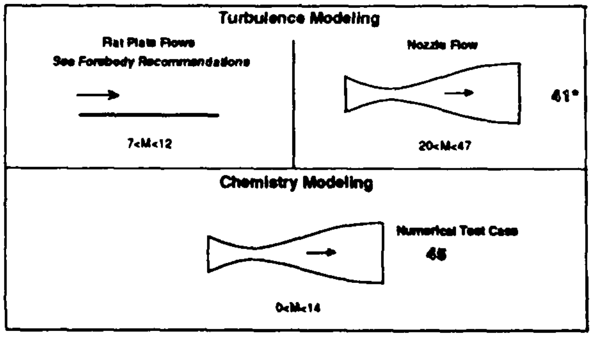
Turbulence Modeling
Flat Plate Flows
See Forebody Recommendations
7<M<12
Nozzle Flow
41*
20<M<47
Chemistry Modeling
Numerical Test Case
45
0<M<14

*Experiment Ref. No.

Fig. 6 Recommended nozzle building block validation experiments.

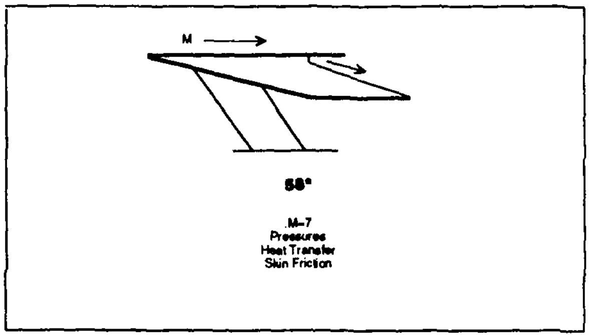
M
58*
.M-7
Pressures
Heat Transfer
Skin Friction

*Experiment Ref. No.

Fig. 7 Recommended nozzle benchmark validation experiments.

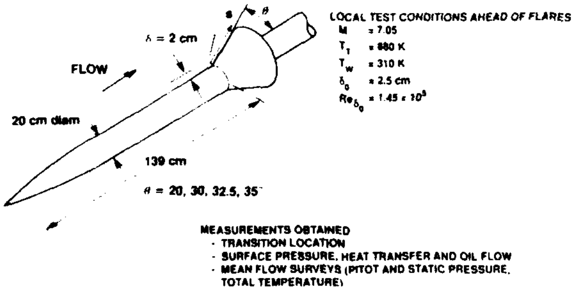
s
θ
δ = 2 cm
FLOW
20 cm diam
139 cm
θ = 20, 30, 32.5, 35°
LOCAL TEST CONDITIONS AHEAD OF FLARES
M = 7.05
T_T = 880 K
T_w = 310 K
δ_0 = 2.5 cm
Re_δ0 = 1.45 × 10^5
MEASUREMENTS OBTAINED
- TRANSITION LOCATION
- SURFACE PRESSURE, HEAT TRANSFER AND OIL FLOW
- MEAN FLOW SURVEYS (PITOT AND STATIC PRESSURE, TOTAL TEMPERATURE)

Fig. 8 Geometry and test conditions for an axisymmetric flare experiment.

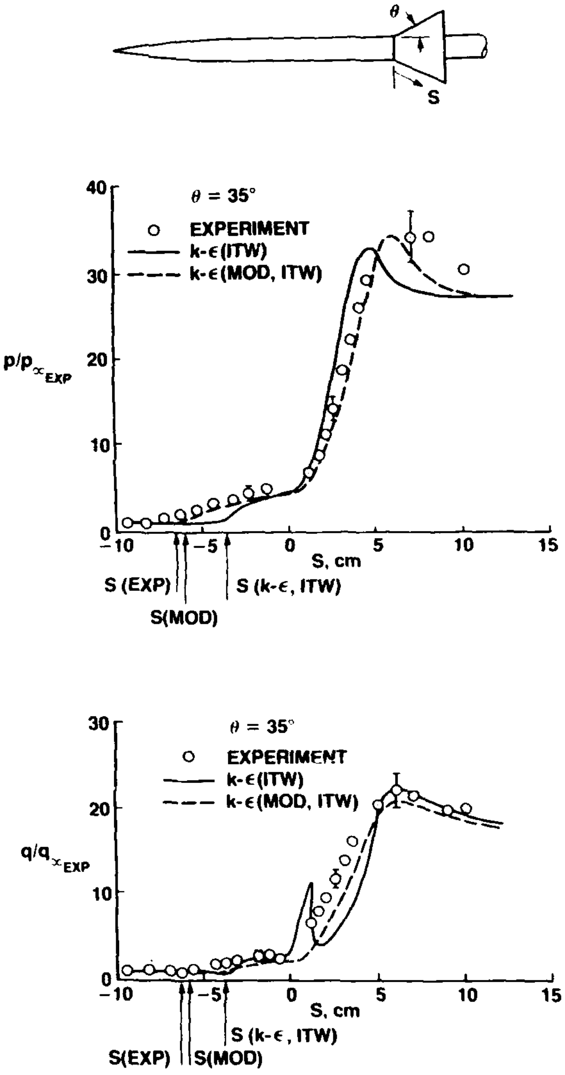

Fig. 9 Surface pressures and heating rates on an axisymmetric cylinder-flare.

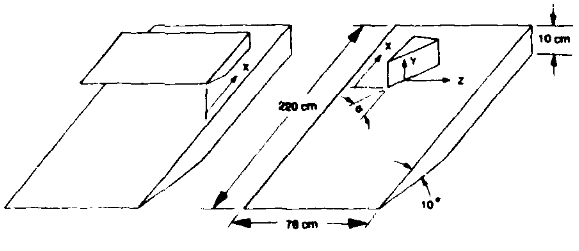
x
x
y
z
10 cm
220 cm
θ
10°
76 cm

Wedge Configuration

Fin Configuration

Fig. 10 Model geometries for impinging and swept shock interaction experiments.

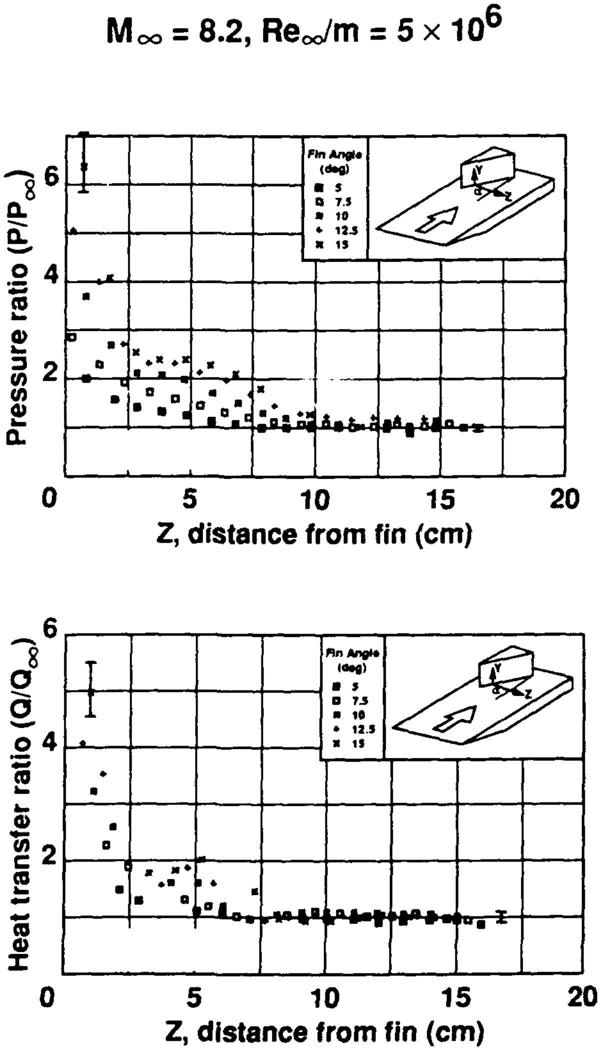

Fig. 11 Surface pressures and heating rates for a swept shock interaction.

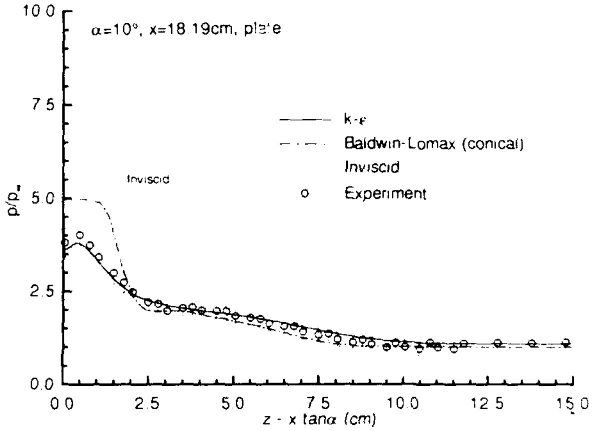

(a) Pressures

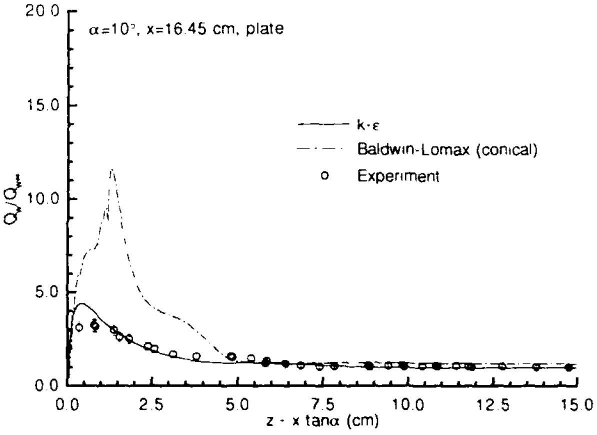

(b) Heat transfer

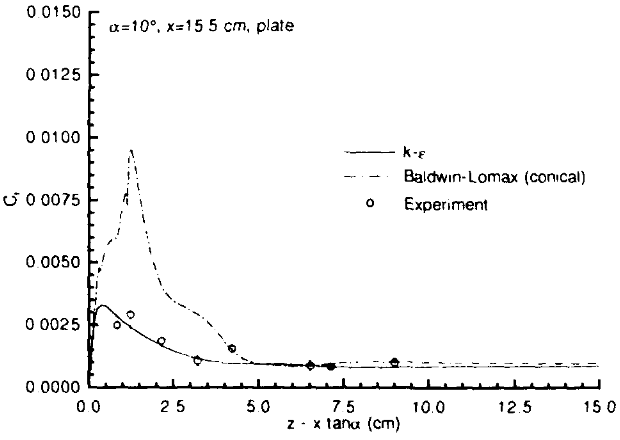

(c) Skin friction

Fig. 12 Comparisons of measurements and computations.

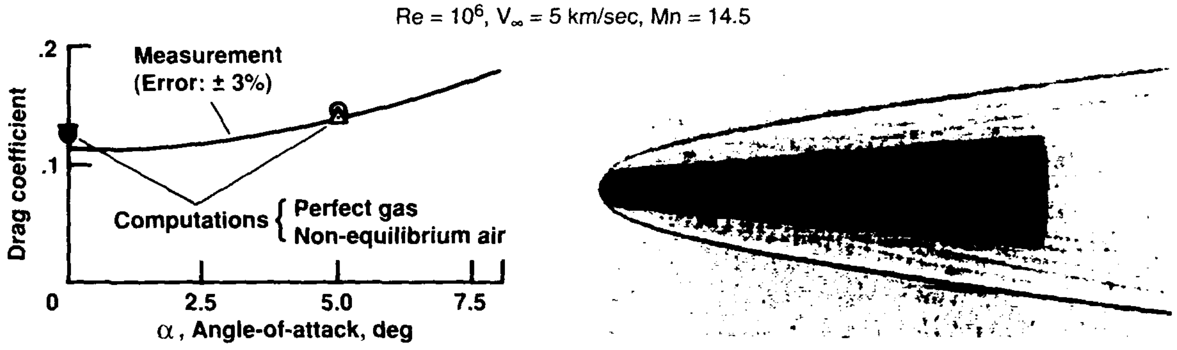

(a) Drag coefficient

(d) Shadowgraph

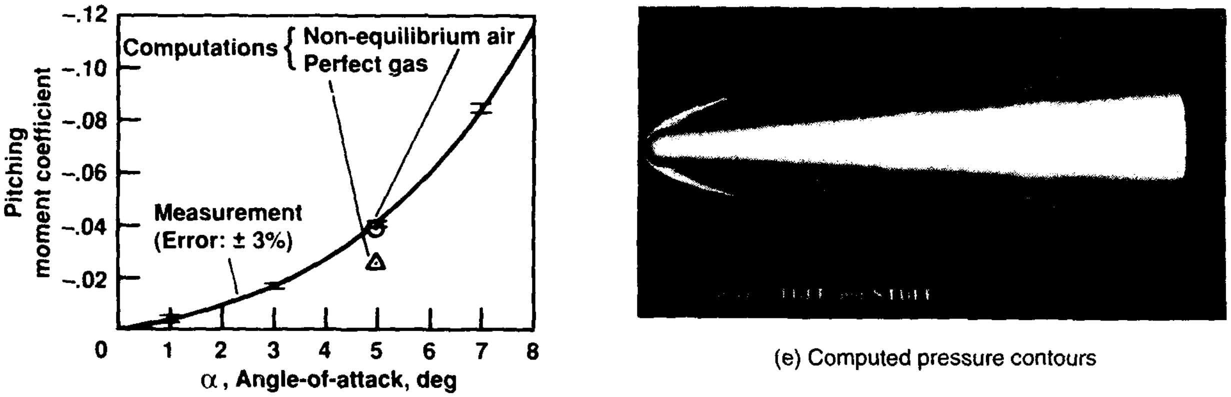

(b) Pitching moment

(e) Computed pressure contours

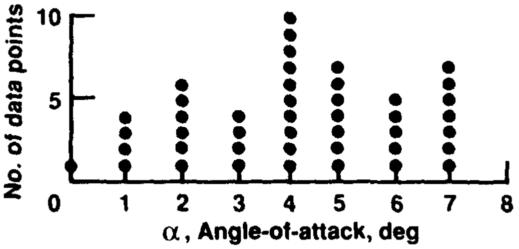

(c) Statistical data sample

Fig. 13 Comparisons of force and moment coefficients and shadowgraph from a ballistic range experiment with computations.

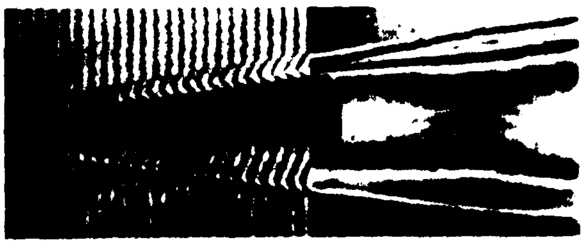

Fig. 14 Finite fringe interferogram and interpreted optical path from a ballistic range experiment.

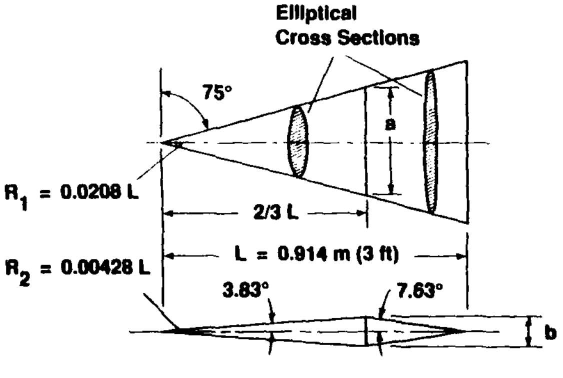
Elliptical
Cross Sections
75°
a
R_1 = 0.0208 L
2/3 L
R_2 = 0.00428 L
L = 0.914 m (3 ft)
3.83°
7.63°
b

Forebody – Elliptic Cone (a/b = 4) with Sharp or Blunt Nose Tip
Afterbody – Elliptical Cross Sections with Sharp Trailing Edge

Fig. 15 Hypersonic All-Body model geometry and dimensions.

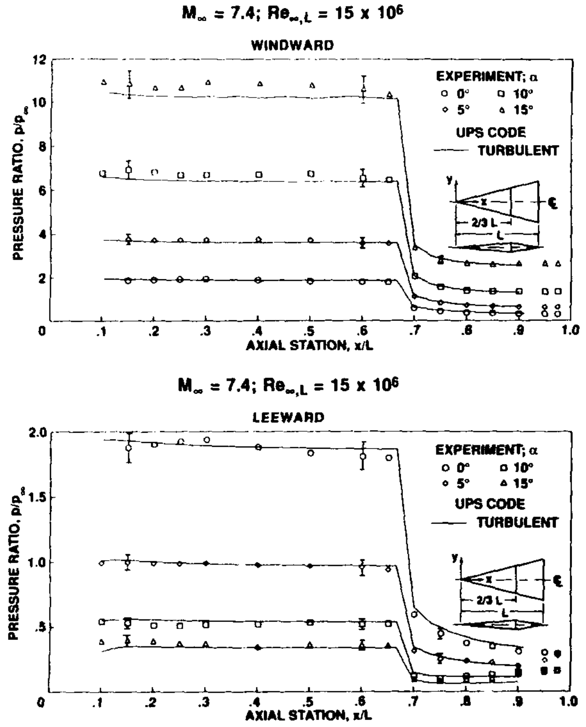

Fig. 16 Surface pressures on a hypersonic All-Body model.

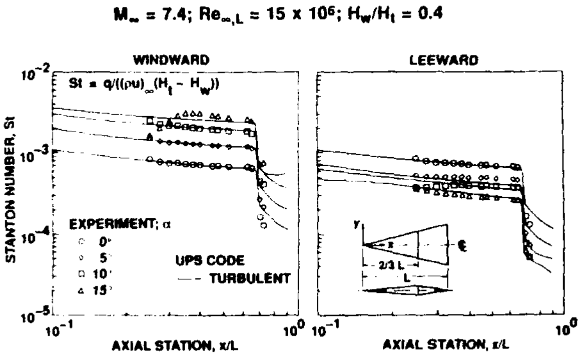

Fig. 17 Surface heat transfer on a hypersonic All-body model.

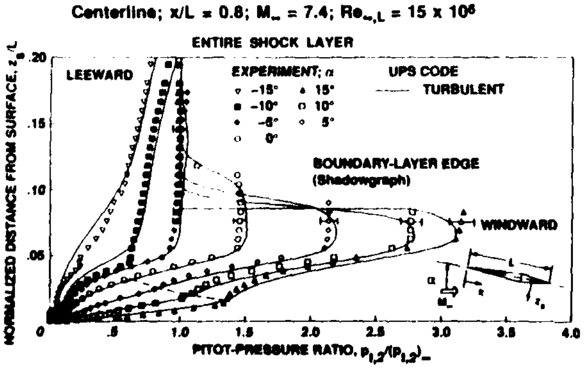

Fig. 18 Flow field pitot pressure profiles on a hypersonic All-Body model.

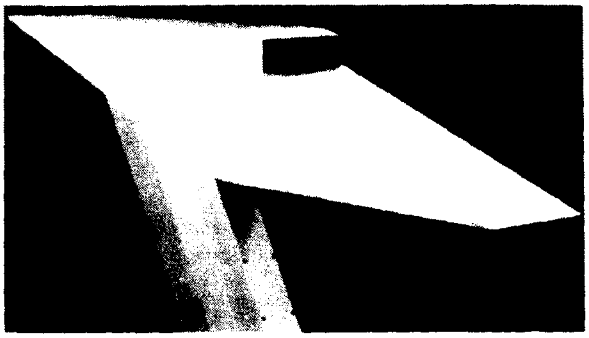

Fig. 19 Photograph of the SERN experiment.

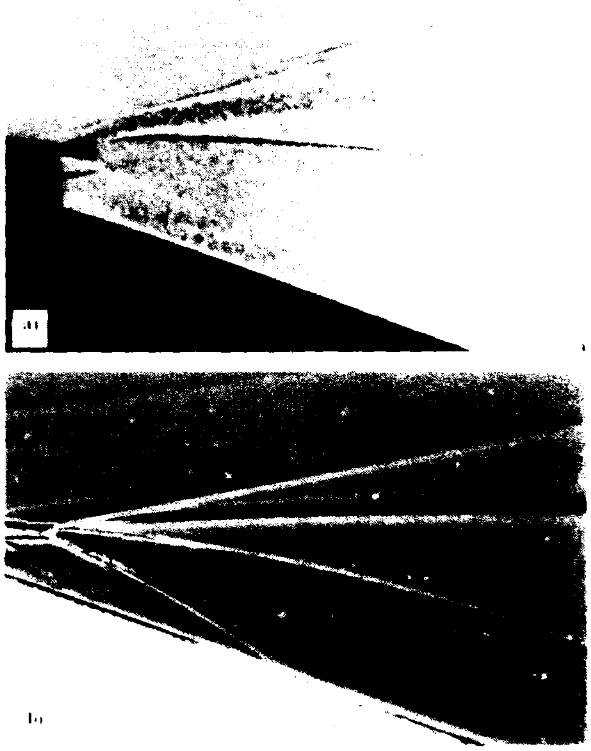

Fig. 20 Comparisons of nozzle shock patterns from experiment and a Navier-Stokes computation: (a) shadowgraph; (b) computation.

Synthesis of the Workshop on HYPERSONIC FLOWS FOR REENTRY PROBLEMS

held in Antibes, France, in January 1990 and April 1991

Rémi Abgrall, Jean-Antoine Désidéri, INRIA Sophia Antipolis,
B.P. 109, 2004 Route des Lucioles - 06561 Valbonne Cedex (FRANCE),

Michel Mallet, Jacques Périaux, Pierre Perrier and Bruno Stoufflet,
Dassault Aviation, 78 Quai Marcel Dassault - 92214 Saint-Cloud (FRANCE).

1 Motivations

One of the most challenging problems of modern aerospace engineering is undoubtedly the prediction of hypersonic flows around reentry vehicles. Indeed this challenge has many aspects : defining the appropriate physical model for these flows is the first difficulty since very complex physical and chemical phenomena take place during the reentry phase; moreover, temperature, velocity and enthalpy are very high, density very low, making the reentry conditions very difficult to reproduce in ground-based experiments.

Thus, in the past two decades, important efforts in Computational Fluid Dynamics have been made employing supercomputers to simulate these complex flows. However, most simulation tools were originally designed for transonic or supersonic flow applications and later extended; these usually contain imperfect models, and also still have to be improved to permit the accurate prediction of hypersonic flows.

This situation has motivated strong international cooperative efforts including three Europe / US Short Courses on Hypersonics [1] [2] and two sessions (Parts I and II) of the scientific workshop organized by INRIA and GAMNI [3] which took place in Antibes, France.

Part I brought together a group of experts active in Hypersonics, and promoted direct comparisons of codes and experiments. Eight critical test problems involving well-defined 2-D and 3-D steady flows governed by specified P.D.E.'s and boundary conditions were submitted to computation. CFD results have been compared altogether, and confronted to experiments when available. This led to a first estimation of CFD capabiliti~~es in~~ Hypersonics as reported in the workshop proceedings [3].

The motivation for a second session, Part II, of the same workshop was to propose a more thorough study of each test problem by reducing the test-cases to a representative subset, by improving the definition of some of them (e.g. when possible the description of the non-uniformity of the inflow in the experiment was provided to the CFD community), and also by adding a few novel test-cases associated with new experiments. In addition, computational contributors were urged to perform calculations on refined meshes, and to study grid refinement effects, and to control artificial diffusion.

In summary, the main objective of Part II was to improve the quality of both experimental and computational results, and evaluate numerical codes by code-to-code or code-to-experiment comparisons, and permit a better confidence in the prediction tools to be used in the design of hypersonic vehicles.

The presentation is aimed at reporting the main conclusions as they were expressed at the meeting by experts, including some of their recommendations regarding the validation of numerical codes.

2 Development of the meetings

Both sessions (Parts I and II) included ten invited lectures related to specialized issues in experimentation, modeling and computing in Hypersonics.

The rest of the workshop was developed around specific test problems. During reentry, three main types of flow are encountered :
- rarefied gas flow,
- reacting flow,
- non-reacting flow .

The governing equations to be solved are then respectively
- the Boltzmann equations,
- the Euler or Navier-Stokes equations (or other intermediate models such as the thin layer or parabolized, viscous shock layer or coupled Euler/Boundary layer models) augmented of a chemistry model,
- the Navier-Stokes equations possibly combined with a turbulence model.

The following eight critical problems were proposed for experimentation and computation :

Problem 1 : Flow over a slender cone
Problem 2 : Base flow
Problem 3 : Flow over a 2-D ramp
Problem 4 : Flow over a 3-D obstacle
Problem 5 : Corner flow
Problem 6 : Flow over a Double-Ellipse/Ellipsoid
Problem 7 : Flow over a delta wing
Problem 8 : Non-equilibrium flow in an arc-jet or a shock tube.

The themes of theses problems are turbulence transition (1 and 2), heat-transfer prediction (3, 4 and 5), real-gas effects (6), vortex or rarefaction effects (7), thermal non-equilibrium (8).

For each problem, computational contributions were presented following the presentation of experimental results, and preliminary critical analyses were made by experts during the program, which also included poster sessions.

In tables 1 and 2 below, are listed the number of experimental or computational contributions to the various test problems. The numbering of these problems was modified (to roman figures) for Part II to facilitate the suppression of certain test cases associated to given problems, and the introduction of novel ones. The details of the definition of the test cases can be found in the announcement brochures (Part I and II), and in the proceedings of the workshop [3].

Table 1 : Participation in Part I

		Pbs 1-2	3-4	5	6	7	8
Experiments	12	1	3	1	3	3	1
Computations:							
Europe	56	2	12	1	29	8	4
USA	22	3	4	2	7	4	2
Japan	3	1	-	-	2	-	-
Australia	2	-	1	-	1	-	-
TOTAL	95	7	20	4	42	15	7

Table 2 : Participation in Part II

		Pbs I-II	III-IV	V	VI	VII	VIII
Experiments	8	1	1	1	1	3	1
Computations:							
Europe	65	2	20	2	19	11	11
USA	8	-	3	-	1	4	-
Australia	2	-	1	-	-	1	-
TOTAL	83	3	25	3	21	19	12

It appears that if a substancial effort was made (mostly by the European Community) on the double-ellipse/ellipsoid problem for Part I, and to a lesser extent on the ramp problem, a noticeable shift of interest was observed for Part II on the delta wing and the high-enthalpy flow problems.

3 Invited talks

During each session, the technical presentation of test problem results were completed by invited lectures given by leading scientists on topics related to modeling experimental aspects and numerical simulations of hypersonic flows. The list of these talks is given below :

Part I :

- Inaugural Talk : Introduction to the Workshop, J. Carpentier (ONERA, France),
- Comments on experiments for computational validation for fluid dynamic predictions, S. M. Bogdonoff (Princeton, USA),
- Hypersonic Stability and Transition, E. Reshotko (Case Western Reserve University, USA),
- Scattering kernels for gas-surface interaction, C. Cercignani (Politecnico di Milano, Italy)
- CFD for hypersonic air-breathing aircraft, J. L. Thomas, D. L. Dwoyer, A. Kumar (NASA Langley, USA),
- Similitude in hypersonic aerodynamics, H. Viviand (ONERA, France),
- Gas-kinetical and Navier-Stokes simulations of reentry flows, H. Oertel Jr. (University of Braunschweig, Germany),
- Numerical simulation of Boltzmann flows of real gases - Accuracy of models used in the Monte-Carlo methods, K. Nanbu (NAL, Japan),
- Intrusive and non-intrusive measurements of flow properties in arc jets, C. D. Scott (NASA JSC Houston , USA),
- CFD for hypersonic propulsion, L. A. Povinelli (NASA Lewis, USA),
- Experimental simulation of high-enthalpy real-gas effects, H. Hornung (Cal'Tech, USA).

Part II :

- Inaugural talk : Fundamental and applied research in space applications, R. Pellat (CNRS and CNES, France),
- Experimental studies in shock-shock and shock-boundary-layer in laminar and turbulent hypersonic flows, M. S. Holden (Calspan, USA),
- Some viscous interactions affecting the design of hypersonic intakes and nozzles, J. L. Stollery (Cranfield Institute of Technology, UK),
- Reacting viscous flow and gas-surface interaction modeling, J. Warnatz (University of Stuttgart),
- Shock-tunnel experiments involving real-gas effects at Australian Universities, M. Stalker (University of Queensland, Australia),

- Numerical simulation of scramjet engine flowfield, A. Kumar (NASA Langley, USA),
- The role of applied mathematics in the numerical simulation of hypersonic flows, O. Pironneau (University of Paris VI, France),
- The German hypersonic technology program Sänger, H. A. Hertrich (Ministerialrat BMFT, Germany),
- Hypersonic reasearch at German universities, E. Krause (RWTH Aachen, Germany),
- CFD code validation experience, J. G. Marvin (NASA Ames, USA).

4 Analysis of Results

4.1 Synthesis of results for Problems I and II

4.1.1 Experiments

(Figure 1)

P. A. Denman, J. K. Harvey and R. Hillier (Imperial College, UK) provided stanton number, Mach number and pitot pressure along the cone and the base. They measured pitot pressure and velocity profiles at two different stations on the cone. The experiments were conducted in the Imperial College No. 2 gun tunnel.

Measurements exhibited a small streamwise gradient, a simple model of which was provided for computations for Part II.

The challenge in the first experimental test case was to reproduce a very simple conical flow.

4.1.2 Computations

One of the major problems for Part I relied in the location of transition. This transition was arbitrarily fixed for Part I, and specified by the experimentalists for Part II. Important discrepancy between computations and experiments despite sensitivity to grid, wall temperature, turbulence model had been studied. The Stanton number has been slightly over-estimated (of some 10 %) by certain computations.

The accurate calculation of the Stanton number in Problem II is critically dependent on the location of the reattachment point. Some 20 % discrepancy with the experiment in this parameter was observed in certain computations. The computed separation region was found too small and making a questionable angle with the wall at the edge of the base.

4.2 Synthesis of results for Problem III (flow over a 2D ramp)

4.2.1 Experiments

J. Delery and M. C. Coët conducted the tests in the R2Ch and R3Ch blow-down wind-tunnel of the ONERA Chalais-Meudon establishment. They provided Schlieren photographs, wall heat transfer and wall pressure distributions. The wedge-flow experiments were made at Mach number 5 and 10 to study the interaction pattern at both low and high Reynolds numbers.

G. Simeonides and J. F. Wendt (Von Karman Institute, Belgium) conducted experiments in the long-shot heavy-gun piston gun-tunnel at the VKI with a flat-plate/2-D 15° ramp model and provided pressure and heat transfer distribution along the centerline yielding an indication of the transition in the reattachment region.

4.2.2 Computations

(Figure 2)

Navier-Stokes computations of a hypersonic flow over a 2-D ramp are compared to one another and to experiments. The importance of grid density was clearly put into evidence as concerns the prediction of separation lengths. Difficulties in achieving well-defined experimental conditions, particularly fully laminar conditions at reattachment were discussed. Considerable variations in the predicted location of the reattachment region were observed, and one alleged explanation is that the experiment is characterized by a transitional reattachment. Some contributors showed that putting a switch to turn on the turbulence model resulted in a much better agreement with the experiment in the ramp region.

Four test cases were proposed:

- test cases III-1 and III-2 are characterized by a low value of the Reynolds number (Rey= 143800). This was chosen to make the test case less sensitive and to reduce the likelihood of transition at reattachment.

- test case III.3 was already proposed for Part I of the workshop (problem 3.5), a large amount of information is already available but improved results were expected.

- test case III.4 is chosen from a set of tests performed by Holden and has already been used extensively for validation.

24 numerical contributions were presented at the meeting, this is enough to get a good idea of how CFD tools can perform on this problem. Various numerical approaches were used including centered + artificial viscosity, upwind and Galerkin least squares methods.

Very good agreement is observed for problem III.1 which was easy because of the absence of recirculation.

Reasonably good agreement is observed for problem III.2 which was designed to be easier for numerical contributors (e.g. on skin-friction coefficient). It should be noted that the structure of the flow is quite different than what is observed for a standard (less viscous) case: the pressure skin friction and heat flux do not reach a maximum on the deflected plate. Results can be gathered into two groups that differ on the size of the recirculation.

Experimental results are not available at present to discriminate between both sets. Even though the overall agreement is good, it is somewhat disappointing to observe that for such a viscous case large differences still exist.

For problem III.3, a very large discrepancy is still observed. The most striking results of the computations is the prediction of an excessively large region of recirculation. A number of explanations can be considered:

- the thin layer Navier Stokes simplification may not be valid.
- the two dimensional character of the flow was questioned (however, the deflection angle is low and no experimental evidence of 3D flow was observed (influence of side plates).
- the proper choice of the grid is critical. This was not addressed in enough detail and it was not clear that the solutions presented were grid independent (in the sense that nodes should be added until addition of nodes does not affect the solution; better agreement would be observed if calculations were performed again on refined grids).
- transition near the reattachment point is a possibility.
- the presence of Görtler vortices on the ramp is still an open question.

4.2.3 Conclusions

The problem of the calculation of the flow over a ramp is more difficult than could be anticipated. Nevertheless, at the second meeting, we observed in certain contributions grid-converged solutions, convergence acceleration by Multigrid, and a more careful attention given to the grid density in the boundary layer. Provided that sufficient attention is given to the choice of a proper mesh, we still feel that accurate solutions can be obtained.

4.3 Synthesis of results for Problem IV (flow over a 3D ramp)

4.3.1 Experiments

An experiment was made at Mach number 10 by Delery et al. for a 30°-swept 3-D obstacle. They provided surface flow visualizations, wall heat transfer and pressure distributions illustrating very extended zone of separated flow.

Again, the authors indicate that reattachment may have been transitional rather than laminar.

4.3.2 Computations

(Figure 3)

Two results were available at the meeting.

The contribution by Jouet et al. uses a finite volume approach with Roe's fluxes and Van Leer's MUSCL approach. The grid includes 300000 nodes. Results are not fully converged and the initialization leads to an overprediction of the size of the recirculation.

Hassan et al use a Taylor Galerkin FEM and a mesh of 80000 nodes. The calculation slightly underpredicts the value of the Stanton number.

In addition, a contribution by Venkatapathy in which the full compressible Navier-Stokes equations were solved for a problem close to the workshop specification, indicated good qualitative features (separation line position, separation line curvature).

4.4 Synthesis of results for Problem V (corner flow)

4.4.1 Experiments

(Figure 4)

A. Henckels and F. Maurer (DLR Köln, Germany) measured the heat flux for the corner flow case at *the H2K hypersonic wind tunnel with an infrared* thermovision camera system in connection with image processing.

We note that the experimental data were very accurate and supported by a large amount of local measurements.

4.4.2 Computations

Two contributions only were available at the meeting.

Lacor et al. use a finite volume approach with central difference and artificial diffusion. The mesh consists of 31000 nodes.

Panaras et al. use an upwind finite difference scheme based on a TVD method. A good visualization of the leading edge shocks interaction is provided.

The agreement between the contributions is poor.

4.5 Synthesis of results for Problem VI.1 (Inert-gas flow over Double Ellipse/Ellipsoid)

4.5.1 Experiments

D. Aymer, T. Alziary (CEAT Poitiers, France) and L. De Luca, G. Carlomagno (Università di Napoli) provided Schlieren and wall streamline visualizations, wall pressure and heat flux measurements at the H210 wind-tunnel facility. The heat flux was measured by infrared thermocouple using the thick wall technique.

4.5.2 Computations

(Figure 5)

The 3-D double-ellipsoid shape has shown to be a very good test of complex flow in hypersonics (small nose radius, bow shock, secondary shock at the canopy, complex pattern of separated flow with angle of attack). A lack of detailed flowfield measurements did not permit a precise check of the topology of the flow away from the wall.

At the first meeting, all solutions exhibited a good performance with respect to the prediction of pressure concerning both the comparison between each other and with experimental data. As expected the inviscid flow simulations do predict well windward pressure distributions in hypersonic flows.

Concerning the prediction of the embedded shock, the shock seemed generally predicted detached.

Appreciable scatter was observed on boundary layer quantities such as skin-friction coefficient and Stanton number, probably due to differences in grid resolution and numerical diffusion terms. It is surprising to observe scatter not only in flows with embedded shocks but also in those along windward surfaces.

During Part II, the overall quality of the Navier-Stokes contributions improved due to efforts made in constructing better meshes : number of nodes in the boundary layer, first node close to the wall, better control of cell aspect ratio.

4.6 Synthesis of results for Problem VI.2/3 (Reacting-gas flow over Double Ellipse/Ellipsoid)

4.6.1 Experiments

(Figure 7)

M. Vetter, H. Olivier and H. Grönig (RWTH Aachen, Germany) measured Cp and Stanton number wall distributions along an 18-cm long double-ellipsoid subject to real-gas effects and catalytic wall.

They also provided Schlieren pictures of the reacting flow around a 50-mm radius sphere for $T_0 \approx 1500$ K and 4600 K.

4.6.2 Computations

(Figures 6 and 8)

Synthesizing the results of Part I, we concluded that several computations of reactive flows over the double ellipse (ellipsoid) had been proposed. They mostly dealt with inviscid flow in chemical equilibrium or non-equilibrium. For equilibrium flows, the agreement in shock locations between the various contributions was comparable with that of inert-gas computations with comparable meshes; the discrepancies between the various contributions were very small in temperature but somewhat larger in Mach number and composition. For non-equilibrium flow, some discrepancy in the main shock location had been observed in two shock fitting procedures. Conventional codes were observed to predict wall values of temperature and composition vastly different from equilibrium state because, in the theoretical inviscid solution, the gradient of temperature or composition normal to the wall is infinite ("chemical layer"). Two procedures had been shown to remedy this problem: one by mesh refinement, the other by post-processing of the conventional solution. Both essentially agreed.

Part II confirmed these facts. Nevertheless the agreement between the various computations of 2-D non-equilibrium inviscid flows were somewhat better in Part II due to the authors efforts in mesh-refinement studies. Concerning, 2-D viscous non-equilibrium flows, although flowfields are comparable, discrepancies with the experimental data are substancial in wall distributions; this is true even for the wall pressure distribution, traditionally less controversial. Mesh refinement near the wall was evidently found very critical, but naturally more importantly the treatment of the boundary condition (catalyticity). The latest results by Salvetti et al. are much closer to the experiment. A general observation concerning Navier-Stokes calculations, was that the scatter in the stagnation point heating possibly due different models was of the order of 25 %. A boundary-layer calculation for the double-ellipse case was also presented and appear to be a reasonable less costly alternative when applicable.

Concerning equilibrium-air flows, at least three Navier-Stokes solutions were presented and five dealing with inviscid flow. In addition, at the meeting was shown a 3-D boundary-layer calculation of non-equilibrium flow.

4.7 Synthesis of results for Problem VII (Delta Wing)

4.7.1 Experiments

M. Linde (FFA, Sweden) investigated the leeside flow over a sharp delta wing in terms of vortical features and shock induced separation test in the FFA HYP 500 hypersonic wind tunnel with surface oil flow and pressure measurements. The flow is conical at the forward part of the wing whereas on the rear part there is a separated region with recirculating flow.

J. Allègre, X. Hériard Dubreuilh and M. Raffin (CNRS/SESSIA, Laboratoire d'Aérothermique de Meudon) provided the density flowfield data and aerodynamic forces for the rarefied-flow case around the delta wing by the electron-beam technique. The experimental conditions were characterized by two rarefaction levels ($M_\infty = 20.2$, $Re_L = 2050$ and $M_\infty = 20$, $Re_L = 8380$).

Experiments were carried out in the hypersonic vacuum wind tunnel V2G in Göttingen by Ch. H. Chun (DLR Göttingen, Germany) around a different delta wing with the freestream conditions : $M_\infty = 24$, $Re_L = 2.9 \times 10^4$, at angles of attack α between 0° and 30° for the heat flux measurements, and α between 0° and 40° for the force measurements,

H. Legge (DLR Göttingen, Germany) provide force and heat transfer measurements of rarefied flow over a mini delta wing at large Knudsen number showing complete accommodation. The covered rarefaction range is especially useful for comparisons with Monte Carlo calculations. The rarefied flow on the delta wing was of high quality. For this reason, a duplication of the test did not seem necessary.

4.7.2 Computations

(Figures 9-10)

The understanding of vortex structures and leeside separations constitutes one of the major element in the analysis of hypersonic flows around reentry vehicles in atmosphere. As test case supporting this objective, the computation of the flow around a Delta Wing was proposed with two models (inviscid and viscous simulations).

For Part I, the geometry of a Delta Wing with a sharp nose was defined and a test case (VII.1 for inviscid flow and VII.2 for viscous one) based on experimental conditions was considered ($M_\infty = 7.15$ and $\alpha = 30^0$). In the second part, a blunt nosed Wing has been defined corresponding to a model tested at DLR at $M_\infty = 8.7$ and $\alpha = 30^0$ (test cases VII.3 and VII.4). A more thorough analysis of such problems was then possible with the two sets of solutions.

For the first geometry, we were concerned with a wedged windward side and a general shape close to a conical-like shape whereas the second one consisted in a curved windward side with a general shape far from being a conical-like one. Consequently, the flow solution is more or less autosimilar in x-planes for the first geometry whereas solution evolves with the space direction x for the second one. The sharp nose is good leeside vortex generator while no vortex sheet appears for the blunted nose wing. These remarks are illustrated by numerical results provided by ONERA.

For Part II, contributors concentrated much on the test cases VII.3 and VII.4. Eight computations wer performed for the inviscid case with meshes ranging from 110,000 to 2,000,000 nodes (this contribution can be considered as a reference solution) for structured grid approaches and of about 70,000 nodes for the two unstructured grid methods. Concerning test case VII.4 (viscous flow), seven contributors participated with meshes ranging from about 300,000 to 1,000,000 nodes.

4.7.3 Conclusions for the inviscid flow solutions

Although a good agreement was found in the evaluation of pressure coefficients, two families of solutions were obtained when considering Mach number distribution on the leeside. Some contributions show a large Mach number peak due to the very strong expansion at the leading edge. This peak was found in the ONERA computation with the very fine grid but no real conclusive interpretation has yet been given. A strong grid sensitivity on leeward was revealed for all approaches and in particular in the DASSAULT solutions. It has been noticed that a total temperature loss of about 3.5% was obtained among the most accurate solutions.

4.7.4 Conclusions for the viscous flow solutions

Comparisons of the numerical solutions with the experimental curves were available. Computed Stanton numbers have been found noticeably higher than the experimental values. A good qualitative agreement was however found.

This test case was computed with different flow modelizations (Euler solver with boundary layer analysis, Parabolized Navier-Stokes solver and Navier-Stokes solvers) and all the numerical results provide a remarkable numerical agreement for Stanton numbers.

4.7.5 Conclusions for the rarefied flow solutions

(Figure 11)

The classical Bird DSMC method and a variant, which is referred to as the Finite-Pointset Method (FPM) introduced by the University of Kaiserslautern, were employed to compute rarefied gas flow cases. It is evident that both of the computations are of very high standard and they yield almost identical results for the overall flux quantities. It has been demonstrated that these methods are capable of predicting complex flows in which molecular non-equilibrium effects are present.

4.8 Synthesis of results for Problem VIII (Arc Jet and Shock Tube)

4.8.1 Experiments

The purpose of this test case was to obtain a better understanding of the non-equilibrium flowfield of a high-enthalpy plasma tunnel which serves to study the thermal protection system of future spacecraft.

J. M. Léger, J. F. Coudert, A. Grimaud and P. Fauchais (University of Limoges, France) measured the temperature fields of d.c. nitrogen plasma jets in a controlled atmosphere chamber filled with nitrogen at pressure between 13 and 100 KPa by emission spectroscopy. Non-equilibrium effects were shown with significant differences between rotational, population and excitation temperatures. Recently, they provided the entrance velocity distribution near the axis for a better specification of the initial condition.

4.8.2 Computations

(Figure 12)

Arc Jet

The comparison between computational contributions could not be performed in sufficient details because of the differences in the assumed chemistry composition at the inlet cross section. Comparing the calculated values with the measurements, the trends were the following :
- the calculated values of T_{rot} and T_{ele} seem underestimated along the jet axis,
- the difference of this two variables was less in the computations than in the experiments.

The computational validation has recently been improved since additional velocity distribution in the plasma was made available from the experiments. CFD tools seem more powerful than anticipated for a so complex and difficult test case. A logical follow up of this test case would be an arc jet with air surrounded by expanding nozzle to better simulate industrial plasma tunnels.

Nozzle Flow

The purpose of this test case was to validate the computational tools which are mandatory for the correct interpretation of the measurements made on models in high enthalpy facilities.

As no experimental results are available, only code-to-code comparisons have been made. From the computations, it appeared that the results are mostly sensitive to :
- numerical approximation (scheme and mesh),
- inclusion of thermal non-equilibrium;

however, the following parameters seem to play a lesser role :
- choice of vibrational model,
- inclusion of V-T, V-V exchange models,
- 2-D approximation rather than 1-D.

Finally, it was noted that a systematic sensitivity study of the chemical model would be necessary.

5 Conclusion and Further Comments

The Antibes Workshop has permitted a better assessment of some of the performance and limits of modern CFD tools applied to hypersonic flow computations. The necessity of bringing together fluid mechanicists, specialists of physico-chemical modeling, numerical analysts, applied mathematicians is obvious since the full understanding of hypersonic flows cannot be achieved by either community alone. This type of scientific validation workshop contributes to reduce uncertainties in the design of spaceplanes [5]. Evidently, a limited number of experiments, or alternatively, an approach based solely on computations, would not permit a total confidence in hypersonic design tools.

By the number of participants, the quality of experimental and computational data obtained despite the difficulty involved, and the material presented, this first open workshop in Hypersonics has been a good achievement.

From a technical point of view, it appeared that the computation of Eulerian flows was now well achieved by current approximation methods provided sufficient efforts were devoted to the mesh quality in particular. However, the computation of complex viscous and/or rarefied flows, possibly turbulent or reactive, or both, is still a great challenge. These require good numerics, but also adequate models still under investigation, and experiments of high standard for the validation.

The validation process will continue using some the data collected at the occasion of this workshop. A *European Hypersonic Data Base* (EH) is currently being set up at INRIA Sophia Antipolis, France and will be accessible by networks. The objective is to offer experts in this field a means to evaluate novel CFD methodologies using existing data related to the workshop test problems.

The great challenge for the forthcoming years with available massively parallel computing facilities is to conduct experiments and computations of three-dimensional complex flows including transition, separation and real-gas effects [4]. This will undoubtedly be the focus of the future workshops.

Acknowledgements

The authors are grateful to invited speakers, experimentalists and computational contributors who made this workshop a success by their continuous and friendly assistance. We are particularly indebted to the experts who prepared the syntheses of Part I, and the Chairmen of Part II: their role was essential in the preparation of this article.

References

[1] J. J. Bertin, R. Glowinski, J. Périaux, Eds., *Proc. of the First Joint Europe / US Short Course in Hypersonics, Paris, France, December 1987, Vol. I and II, Progress in Scientific Computing, Birkhäuser, Boston, 1989.*

[2] J. Ballman, J. J. Bertin, J. Périaux, Eds., *Proc. of the Second and Third Joint Europe / US Short Course in Hypersonics, Colorado Springs U.S.A., January 1989, and Aachen Germany, October 1990, Progress in Scientific Computing, Birkhäuser, Boston, to appear.*

[3] J. A. Désidéri, R. Glowinski, J. Périaux, Eds., *Hypersonic Flows for Reentry Problems, Vol. I and II, Springer-Verlag, 1991, Vol. III in preparation.*

[4] T. L. Holst, M. D. Salas, R. W. Claus, The NASA Computational Aerosciences Program-Toward Teraflops Computing, AIAA 92-0558, Reno 1992.

[5] P. Perrier, Aerodynamic and Aerothermal Challenges for the design of the HERMES Spaceplane, *70th Fluid Dynamics AGARD Panel Meeting and Symposium on Theoretical and Experimental Methods in Hypersonic Flows, Torino, Italy, May 4-8, 1992.*

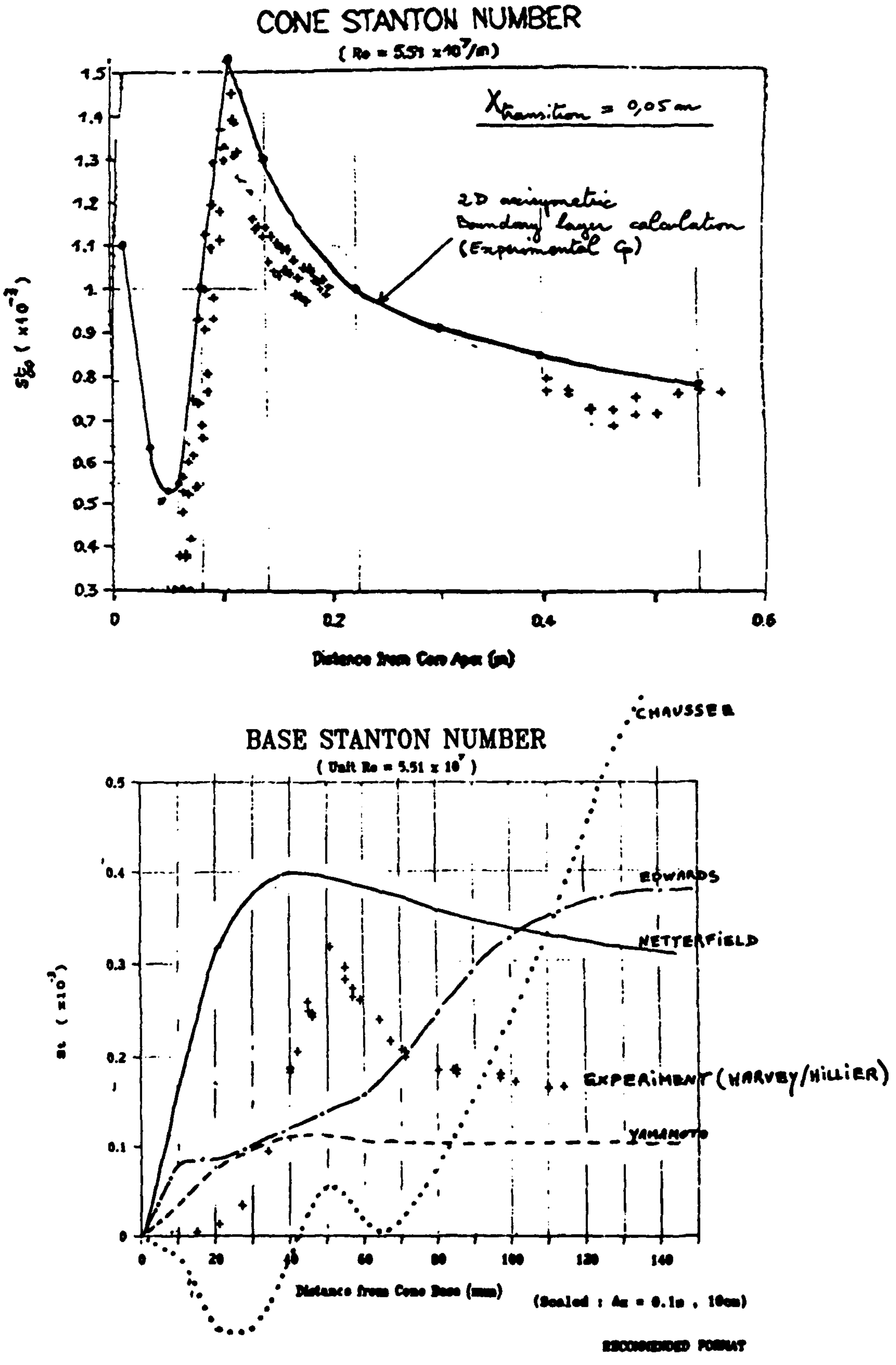

Figure 1 : Cone and Base Stanton number

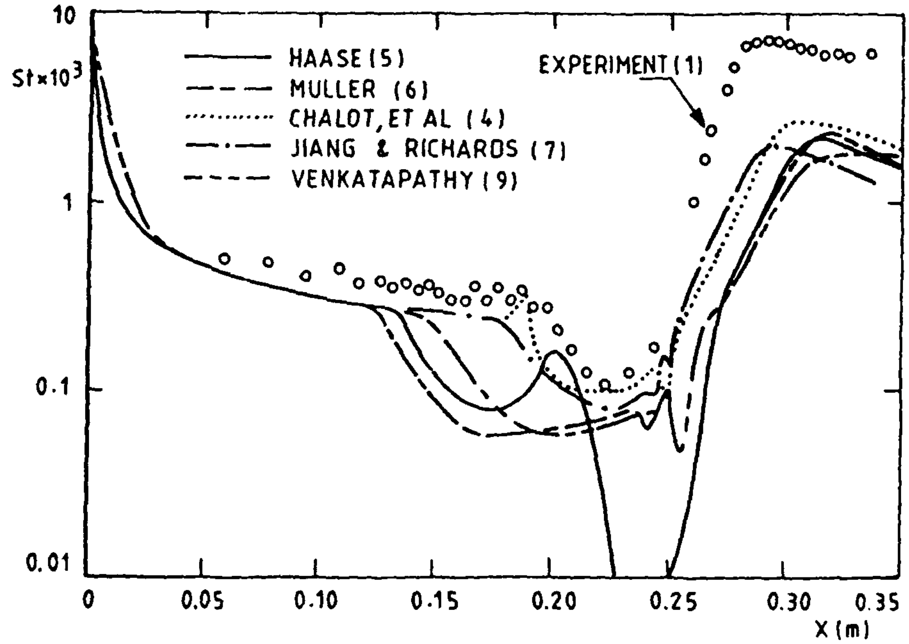

TEST CASE 3.5 - STANTON NUMBER

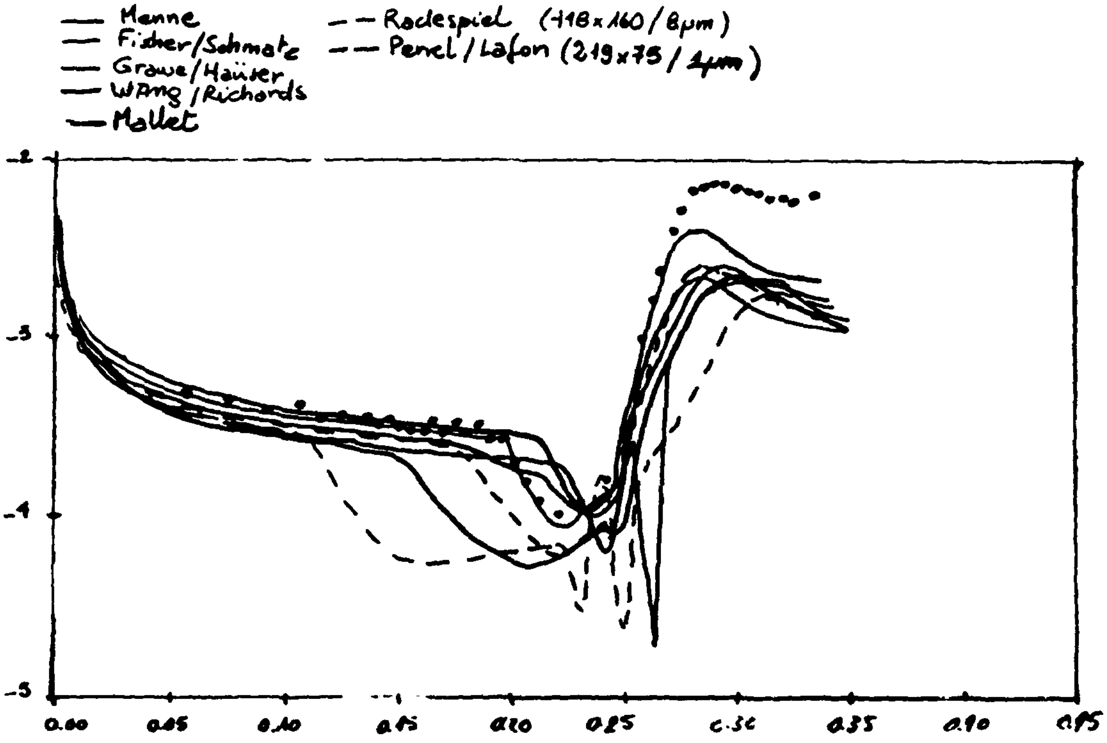

CASE III.3 ••• Measurements Delery.

Figure 2 : Stanton number (results from Part I, case 3.5, and Part II, case III.3).

test case 4.1: Mach = 10 ; Re = $9\ 10^6$; Tw = 290 K ; Tinf = 50 K

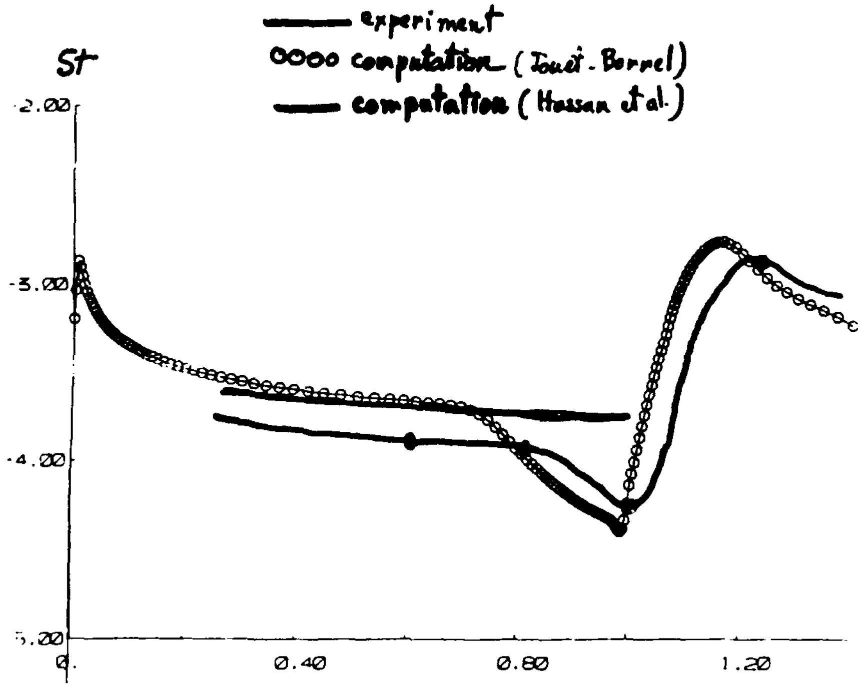

Distribution of Stanton number on section A

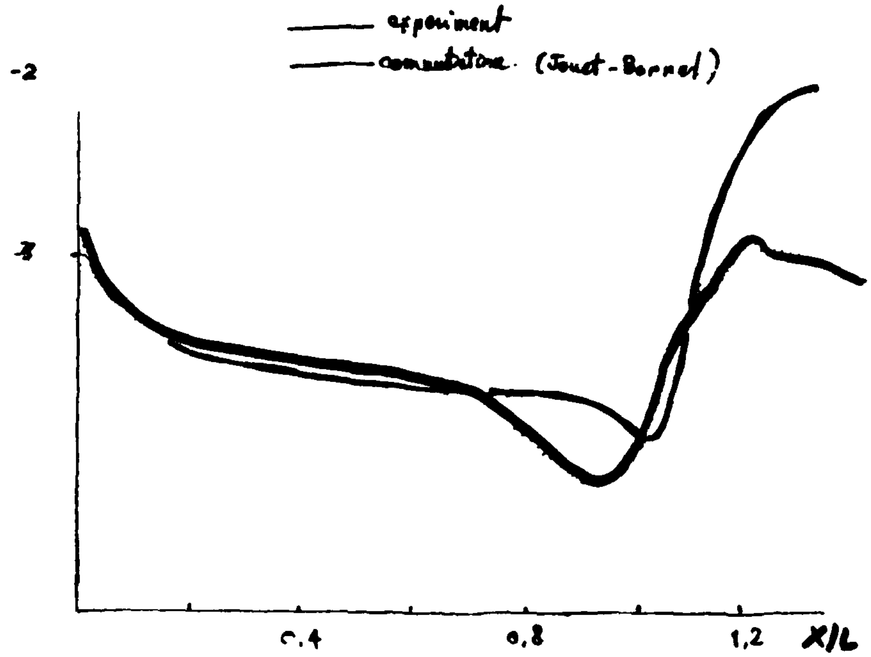

Distribution of Stanton number on section C

Figure 3 : Stanton number on sections A and C (test case IV.1)

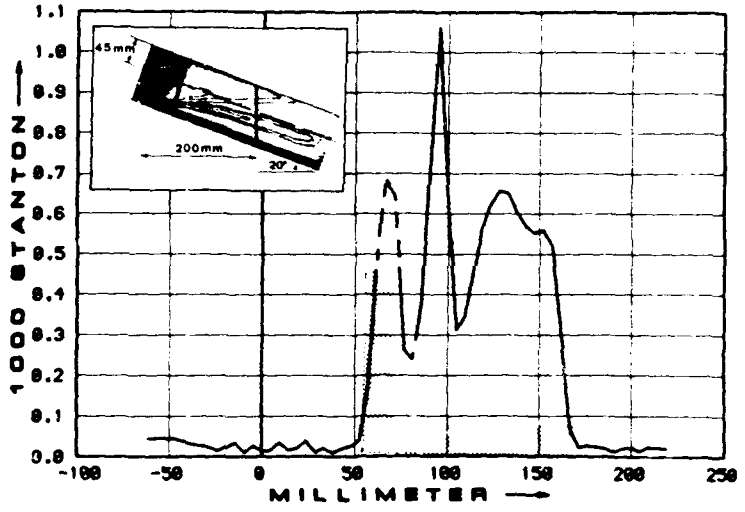

Stanton numbers in the sectional cut 0.2 m behind leading edge.

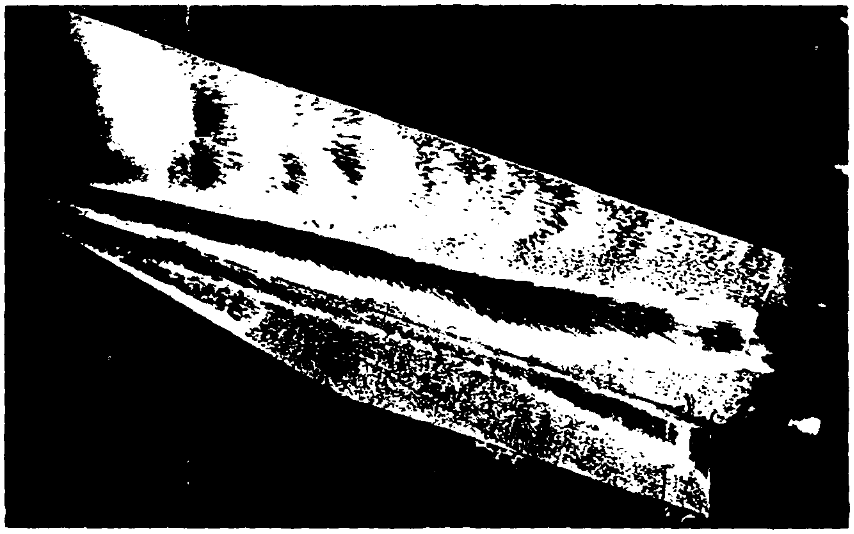

Oil flow visualisation technique applied to the corner flow.

Figure 4 : Stanton number in the sectional cut 0.2m behind leading edge; oil flow visualization (Henckels et al.).

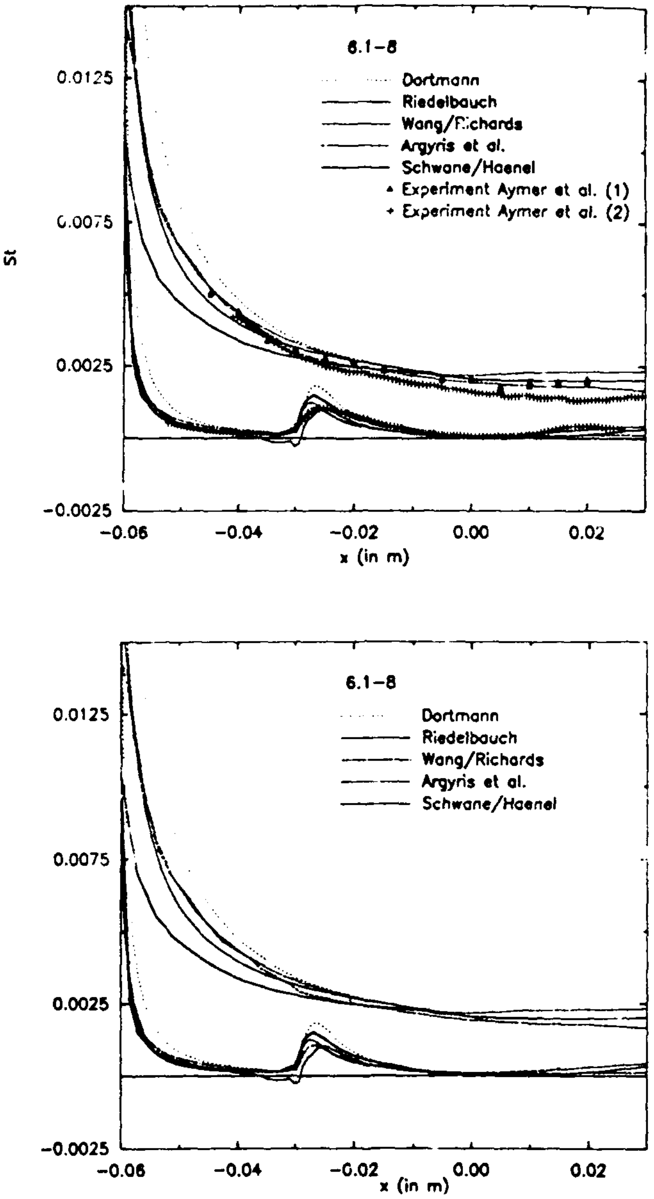

Skin-friction (bottom) and Stanton-number (top) distributions at the wall in the symmetry plane of the laminar flow past a double ellipsoid, test case 6.1-8.

Figure 5 : Wall Stanton number and skin friction coefficient in symmetry plane - Navier Stokes inert flow (from Part I).

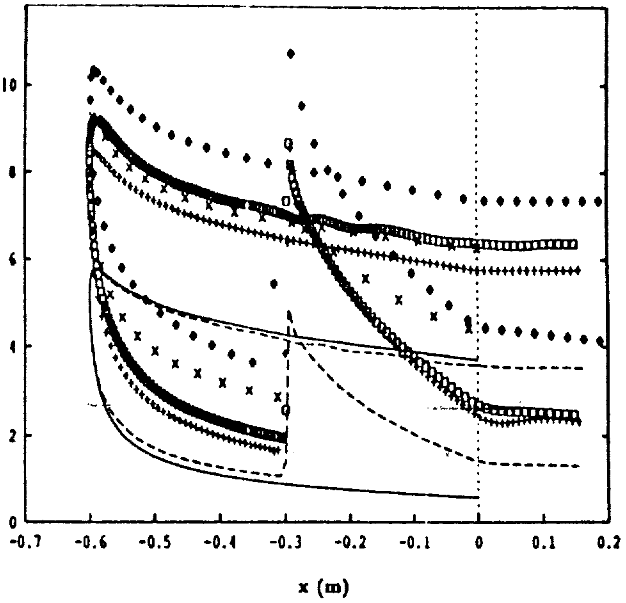

TEMPERATURE (× 1000 K) ON THE BODY SURFACE

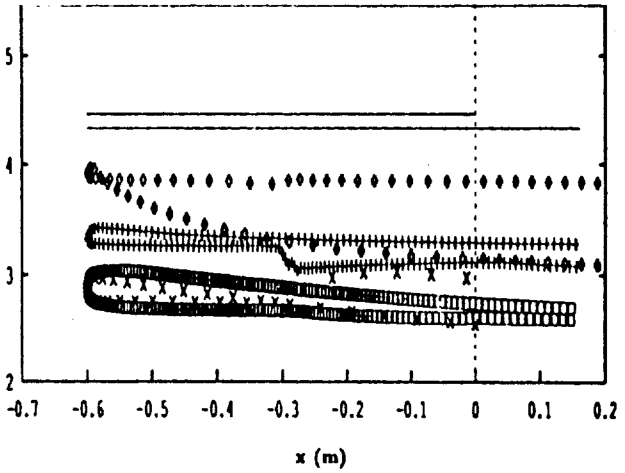

ATOMIC NITROGEN (Y_N × 10) ON THE BODY SURFACE

- **Fey et al. (5) (ETH Zentrum) (symbol: ◇)**
- **Vos et al. (8) (EPFL-CERFACS) (symbol: +)**
- **Botta et al. (36-A) (INRIA Sophia Antipolis) (symbol: □)**
- **Borelli et al. (87) (CIRA-Politecnico di Torino) (symbol: ×)**
- **Sabetta et al. (67) (Università di Roma) (Test Case 6.2-1) (solid line)**
- **Salvetti et al. (36-B) (dashed line).**

Figure 6 : 2-D non-equilibrium Eulerian flow computations (temperature and atomic nitrogen on body surface) (test case 6.2.3)

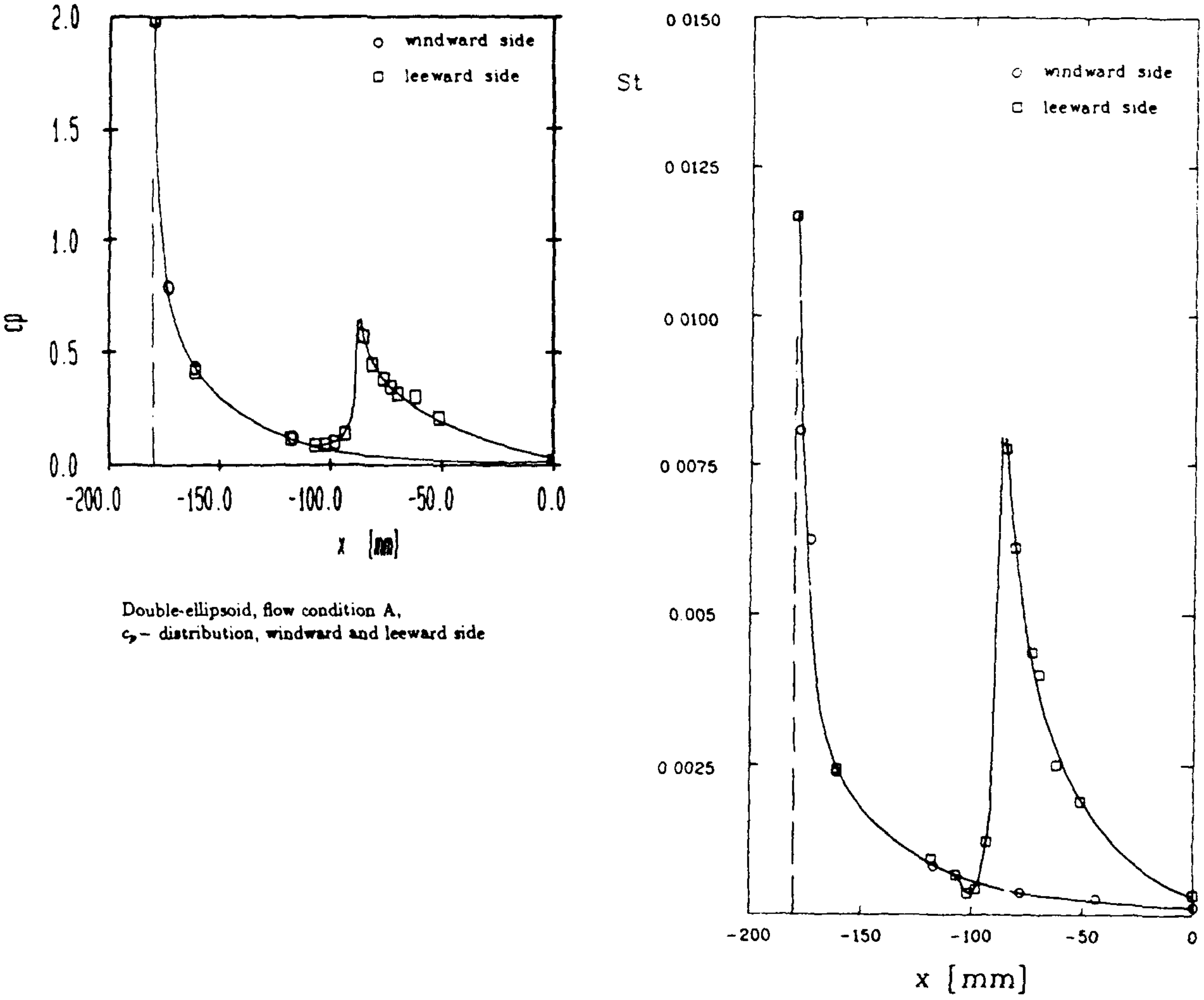

Double-ellipsoid, flow condition A,
c_p– distribution, windward and leeward side

Double-ellipsoid, flow condition A,
St– distribution, windward and leeward side

Figure 7 : Wall pressure coefficient and Stanton number in the symmetry plane (Vetter et al.).

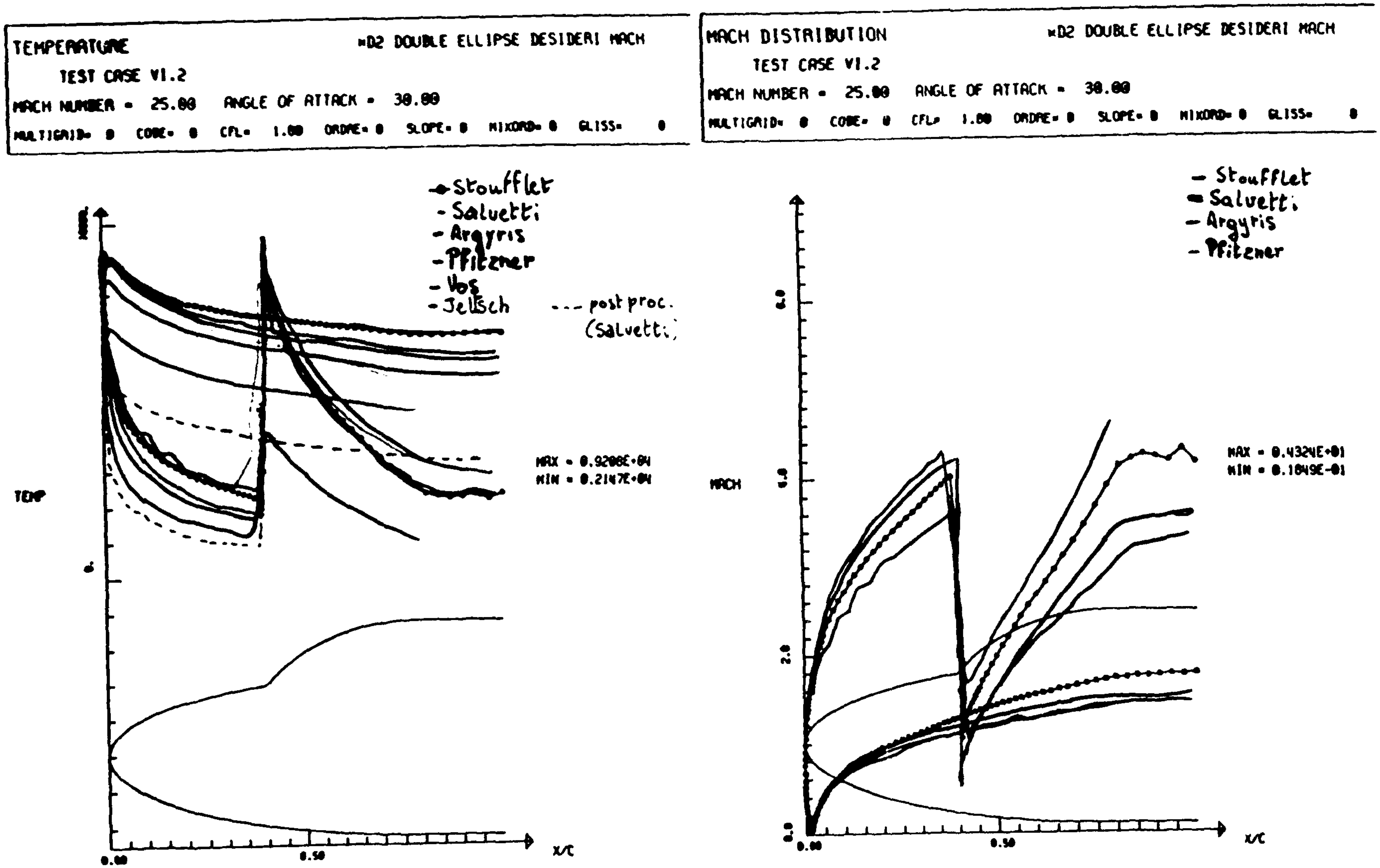

Figure 8 : 2-D non-equilibrium Eulerian flow computations (Mach number and temperature on body surface) (test case VI.2)

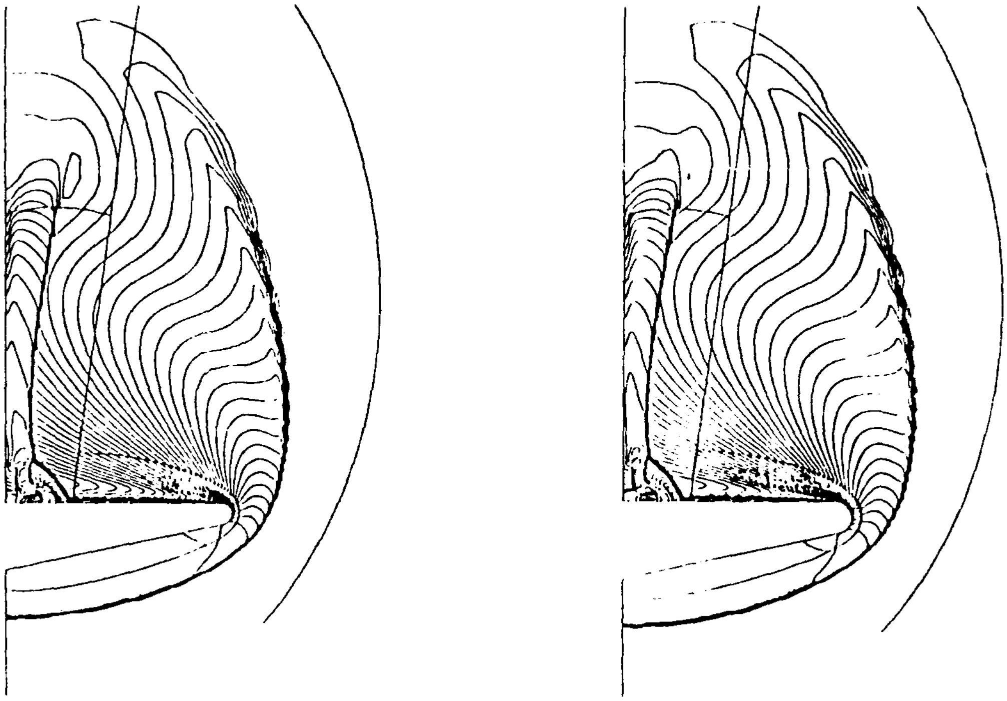

Mach contours in the cross section x/c = .8
(multidomain results).

Mach contours in the cross section x/c = .5
(multidomain results).

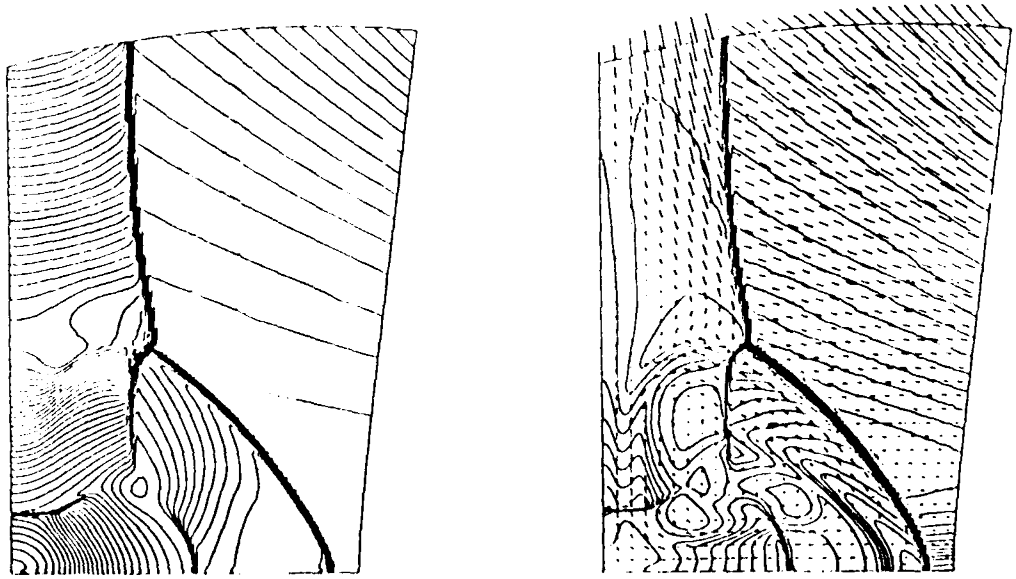

Cp contours in the cross section x/c = .5
(refined grid results).

Mach contours and cross velocity vectors
in the cross section x/c = .5
(refined grid results).

Figure 9 : Mach, Cp, cross velocity (refined grid results) contours at x/c = 0.5 and 0.8 of Eulerian flow around the sharp delta wing (test case VII.1) (Le Toullec et al.).

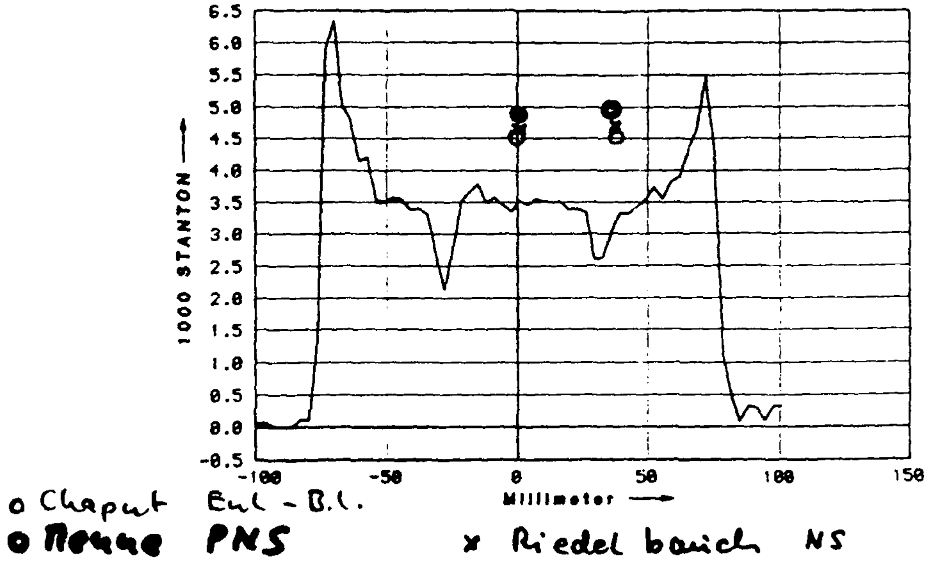

Sectional cut of Stanton number distribution in spanwise direction 180 mm behind tip

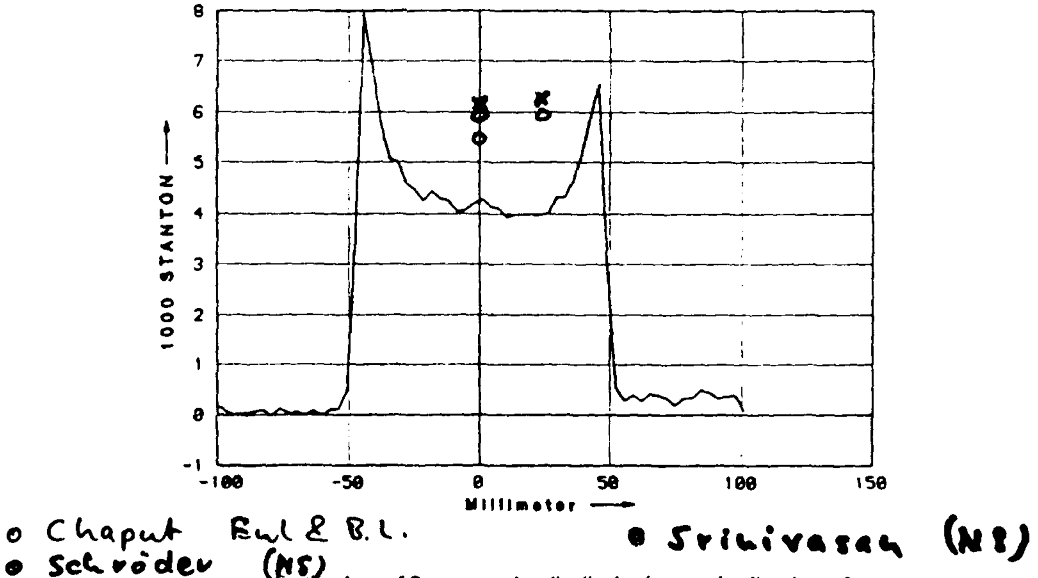

Sectional cut of Stanton number distribution in spanwise direction *110 mm* behind tip

Figure 10 : Comparison of Stanton number distributions in spanwise direction, 110 mm and 190 mm behind tip (test case VII.1) (Chaput et al., Menne, Riedelbauch; Chaput et al., Srinivasan et al., Schröder et al.).

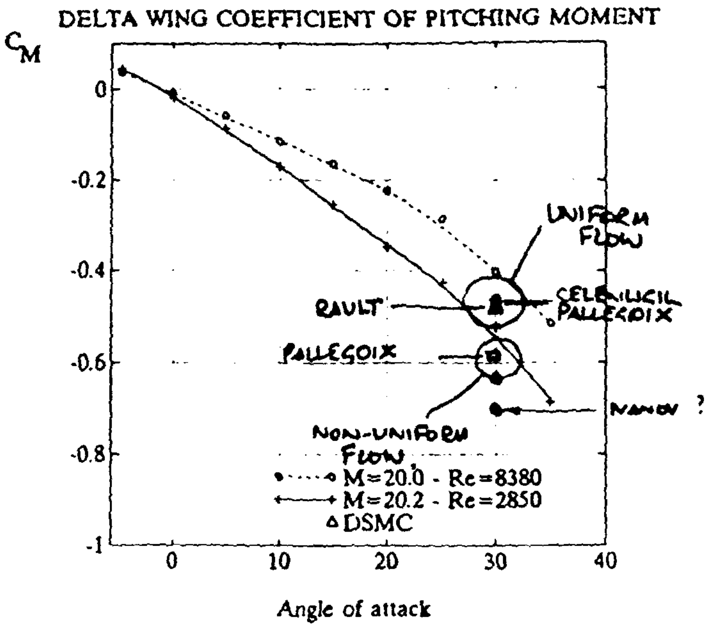

Experimental values of pitching moment

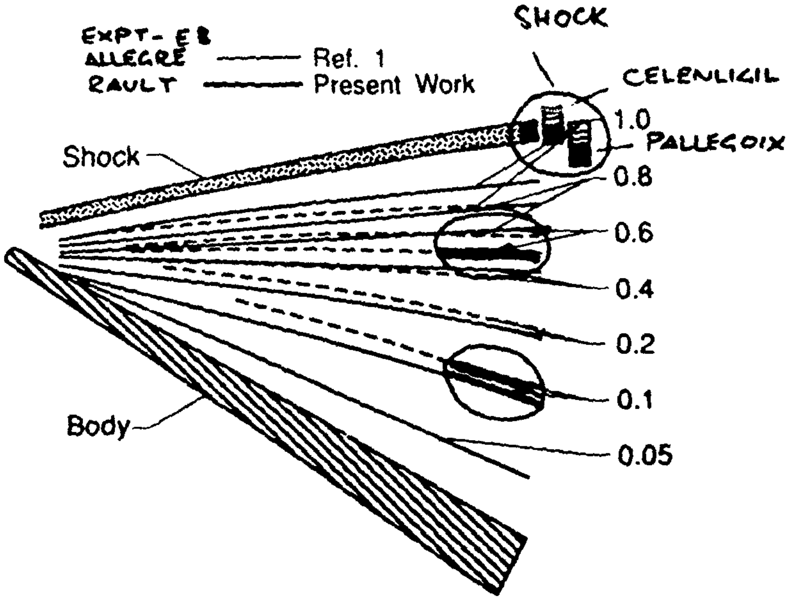
EXPT- ET ALLEGRE
RAULT
Ref. 1
Present Work
SHOCK
CELENLIGIL
PALLEGOIX
Shock
Body
1.0
0.8
0.6
0.4
0.2
0.1
0.05

Gas density distribution (ρ / ρ_∞) in the plane of symmetry of the delta wing at 30 °incidence angle.

Figure 11 : Pitching moment coefficient and density flowfield in the plane of symmetry at $\alpha = 30°$; calculated results compared with experimental data (test case VII.5).

Problem 8.1

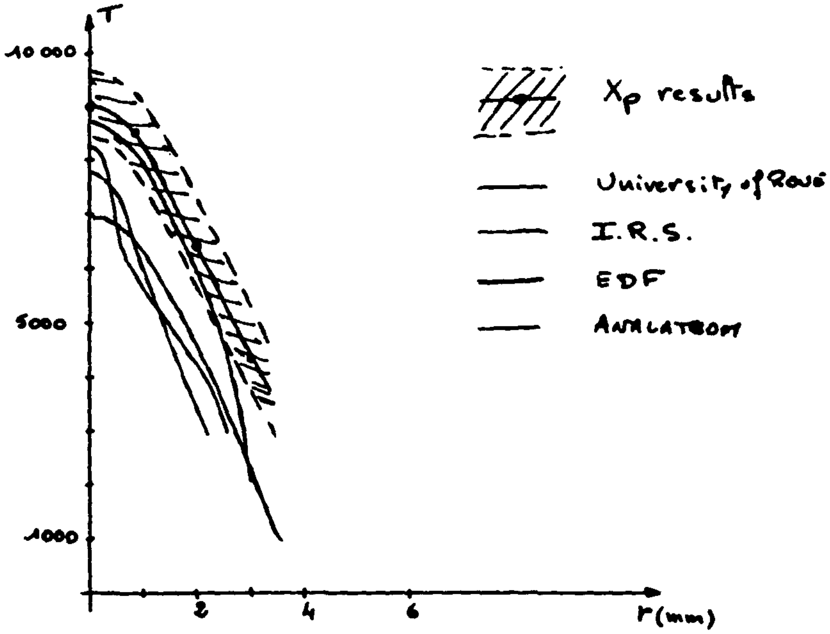

Translational temperature

at X = 0.013 m.

Problem 8.2: Non equilibrium Flow in a Shock Tube
Po = 1.53e+08 Pa, To = 6500 K
Temperatures along symmetry axis

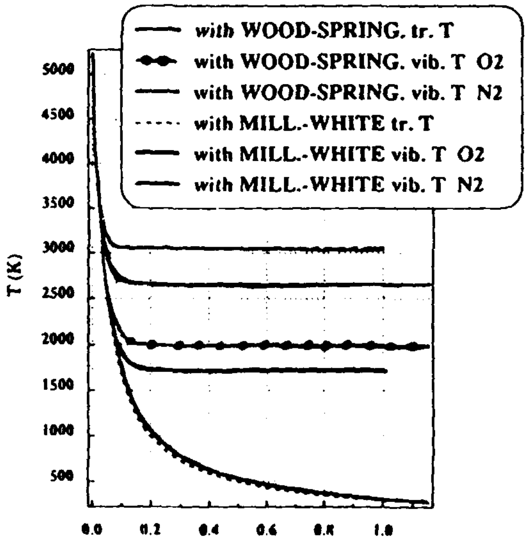

V. MULARD and G. MOULES

Figure 12 : Electronic concentration (x=3 mm); translational temperature (x=.013 m) (VIII.1); Temperatures along symmetry axis (Mulard et al.); 2-D viscous results (VIII.2).

Problems in the Validation of CFD Codes Through Comparison with Experiment

David S. Dolling
Professor
Center for Aeromechanics Research
W. R. Woolrich Laboratories, Room 220
The University of Texas at Austin
Austin, TX 78712-1085
U.S.A.

1. ABSTRACT

Accurate predictions of the effects of shock wave turbulent boundary layer interactions are of particular importance in the design of hypersonic vehicles. Such flows can generate intense heat transfer rates and pressure levels, complex large-scale unsteady separated flows, and large-amplitude fluctuating loads. With increased reliance on computation, it is critical that the predictions are accurate. Thus, it is imperative that such codes be validated and calibrated and deficiencies be identified and rectified.

Comparison of the predictions of CFD codes with experimental data is the key element of the validation process. However, drawing meaningful conclusions about the strengths and weaknesses of solution methodologies or of turbulence models from these comparisons is not a trivial task. As recently stated by Jameson, "Simply comparing experimental data with numerical results provides no way to distinguish the source of the discrepancies, whether they are due to faulty numerical approximation or programming, or to deviations between the math model and true physics." The conclusions drawn may be quite misleading if it is not clearly understood what the computations represent and what the experimental data represent. This paper discusses why it is important to know how experimental mean flowfield and surface data being used for comparison with CFD are generated. If the flowfields exhibit local or global large-scale unsteadiness, then such mean measurements, which form the bulk of the existing data base, may mask the underlying flow physics and be inappropriate for comparison with computation.

2. INTRODUCTION

The January and February 1992 editions of *Aerospace America* (a publication of the American Institute of Aeronautics and Astronautics) were largely devoted to "a perspective on aerospace computational fluid dynamics." Articles authored by both practitioners and program managers discussed the military, industrial, and academic perspectives of CFD, not only in terms of the technical challenges, but also in terms of the economic and political issues. The objective of the current paper can probably best be introduced by extracting a few sentences from one of these recent articles. The author is Professor A. Jameson of Princeton University, New Jersey, who writes:[1] "Code validation is increasingly being recognized as being vital to raising confidence in CFD use. In considering this requirement, it is important to distinguish between the correctness of the program and the suitability of the math model to the application. *Simply comparing experimental data with numerical results provides no way to distinguish the source of the discrepancies, whether they are due to faulty numerical approximation or programming, or to deviations between the math model and the true physics.*" (text italicized by current author) The difficulty of determining the deviation between the "math model and the true physics" is the topic of the current paper.

The emphasis in this paper is on high speed flows and shock wave turbulent boundary layer interactions in particular. A large fraction of the examples cited are drawn from studies of turbulent unswept compression ramp interactions. A schematic of the compression ramp geometry and the coordinate system employed in the paper are shown in Fig. 1. Such flows have been studied experimentally since the 1950's, and results from such experiments have been widely used for comparison with numerical work since the 1970's. The nominal two-dimensionality of such flows permits relatively rapid computations, at least compared to fully three-dimensional flows, and thus they would appear to be a suitable flowfield candidate to evaluate turbulence models and solution algorithms. In the next section, some examples are given of the comparison between experiment and computation for such flows. Some remarks are then offered which suggest that a "fundamental deviation between the math model and the true physics," namely the global unsteadiness of the experimental flowfield, which is not modelled numerically, may be the primary contributor to the discrepancies between computation and experiment.

3. UNSWEPT COMPRESSION RAMP INTERACTIONS

3.1 Hypersonic Flows

Figure 2 shows comparisons of the normalized wall pressure from computations and experiment for turbulent flow over a 34 deg. compression ramp at Mach 9.22. The data are those of Coleman[2] and Coleman and Stollery,[3] and the computations were made by Horstman[4] using the k-ϵ, Cebeci-Smith, and Baldwin-Lomax turbulence models. The computations employ the time-dependent, mass-weighted, Reynolds-averaged, Navier-Stokes equations for 2-D flow and are solved using the MacCormack explicit-implicit, second order predictor-corrector, finite volume method. The purpose of Horstman's study was to assess how well these turbulence models, which have been widely used in transonic and supersonic flows and have met with some success, fare in hypersonic flows. It was not assumed, *a priori*, that they were suitable for hypersonic flow. Indeed, as indicated on the figure, modifications were made to the k-ϵ model to include hypersonic effects. The modifications to the k-ϵ model, indicated in the legend of Fig. 2, are as follows: (i) Mod A – a correction to the ϵ equation to account for the effect of rapid compression on the turbulent length scale; (ii) Mod B – corrections to both the k and ϵ equations to model the additional terms which appear after mass-averaging; and (iii) Mod C – a correction to the turbulent stress terms for the density fluctuations. Details of each correction and its implementation are described in Ref. 4.

Before commenting on Fig. 2, one further set of comparisons is shown in Fig. 3. This figure shows comparisons of the same numerical approaches with the Mach 11.3 data of Holden.[5] In this case the flowfield is generated by an incident shock wave generated by a wedge. In both the Mach 9 and 11 experiments, the wall temperature ratios are similar ($T_w/T_0 = 0.28$ and 0.19, respectively) and the Reynolds numbers differ only by a factor of two. In both cases, it can be seen that the major discrepancies occur upstream of the ramp corner. In Fig. 2 the Cebeci-Smith model predicts the wall pressure distribution quite well. The k-ϵ model underpredicts the upstream influence, whereas with Mods A, B, and C it is overpredicted. In contrast, at Mach 11 (Fig. 3) the Cebeci-Smith (and k-ϵ) models are now the worst, and the k-ϵ with Mod C does the best. In fact, none of these predictions can be considered satisfactory upstream of the corner for the Mach 11 flow.

In Ref. 4 Horstman states, "Two features of shock wave boundary layer interaction flows which are probably of most interest to the designer are the maximum heat transfer near reattachment and the length of the separation zone." Comparisons of the measured and predicted values of (q_{max}/q_∞) and the separation locations are shown in Figs. 4 and 5, respectively, for the Mach 9.22 compression ramp experiment. Note that the vertical axis in Fig. 4 is logarithmic. The k-ϵ model and modifications do not even predict the right trend of (q_{max}/q_∞) with α. The algebraic models predict the trend with α better but underpredict the separated cases ($\alpha > 30$ deg.). Figure 5 shows that the trends for the separation location are generally correct for all models, but only the Cebeci-Smith model predicts the values quantitatively. That the latter result is probably fortuitous is evident in Fig. 6, which shows similar comparisons at Mach 11. In this case, the Cebeci-Smith model is the worst. It is not just the maximum heating rate in the compression ramp interaction that is inadequately captured by any of the codes. The shape of the heat transfer rate throughout the interaction is also poorly predicted (Fig. 7). The same remark applies to the heat transfer rate distribution in the incident shock wave experiment of Holden (Fig. 8).

In Ref. 4 Horstman also points out that: "Experimenters have observed large unsteadiness for separated supersonic shock wave turbulent boundary layer interaction flows. There is no reason to doubt that unsteadiness is also present for the hypersonic test flows considered here. These unsteady effects can at times dominate the flowfield." It was also pointed out that "the computations show no sign of unsteadiness. There is also no apparent mechanism in the present day eddy viscosity models for the observed unsteadiness. This may be an important factor that contributes to the discrepancies between the predicted and measured results."

The present author believes that the "may be" of the last sentence should be replaced by "is"; not only is the unsteadiness an important factor that contributes to the discrepancies between experiment and CFD but flowfields of this type cannot be understood in terms of mean measurements alone. Without an understanding of the dynamics of these flowfields, comparisons of mean surface and flowfield measurements with computations can lead to very misleading conclusions about a given algorithm or turbulence model. These statements are based on what is now known of the unsteadiness of similar interactions at lower Mach numbers. The considerable body of work done under those conditions has shown quite clearly how mean measurements in such unsteady flowfields are generated, what they represent physically, and why the comparisons of experiment and computation are poor. A brief description of some of this recent work is the focus of the remainder of this paper. For details, the reader is referred to the cited references.

3.2 Supersonic Flows

Numerous computations, using a variety of turbulence models, have been made of the 24 deg. Mach 3 unswept compression ramp experiment of Settles.[6] Four sets of computed wall pressure distributions for this flow are shown in Fig. 9. Similar to the hypersonic results of Figs. 2 and 3, the major discrepancies are upstream of the corner. Figure 9a shows those calculated by Viegas and Horstman[7] using turbulence models available in 1979; Fig. 9b shows these calculated by Viegas et al.[8] in 1985 using the k-ϵ model and employing both wall functions and integration to the wall (The experimental data of Dolling and Murphy[11] are also shown in Fig. 9b. These data are time-averages of fluctuating wall pressure signals rather than single value mean measurements from scani-valves, as obtained by Settles.); Fig. 9c shows the results of Champney,[9] presented in 1989, using more recent turbulence models; while Fig. 9d shows the most recent computations by Wilcox,[10] using his new "multi-scale" model and the k-ω model. Champney's work includes calculations made using the turbulence model of Mansour and Shih, which was derived from direct simulation data for a channel flow and applied for the first time to a compressible flow by Champney. Details are given in Ref. 9. The computations share certain common features—a generally steeper pressure gradient up through separation to the corner and a higher "plateau" level upstream of the corner than in the experiment. The k-ω model of Fig. 9d is an exception to the latter and predicts the plateau pressure fairly well, but the upstream influence is substantially underpredicted. Of all the computations, Wilcox's "multi-scale" model is superior; both upstream influence and plateau pressure levels are predicted quite well. The multi-scale model employs a physically more realistic description of the Reynolds stress tensor which is probably partly responsible for the overall improved comparison with the experiment. However, neither the multi-scale model nor any of the other methods model the low frequency unsteadiness of the separated flowfield. In this sense, as will be discussed later, the matching of the upstream influence by the multi-scale model can only be considered as fortuitous.

3.3 Physical Interpretation of Time-Averaged Wall Pressures

As noted above, the wall pressure distributions in Settles' experiment were measured using the standard technique of wall tappings connected to a scani-valve *via* several feet of plastic tubing. Such a system has essentially zero frequency response, and the corresponding wall pressures are mean values. Later measurements made using high frequency response wall pressure transducers in the same flowfield show that the distributions of the rms of the wall pressure fluctuations, σp_w, exhibit 2 peaks—one near separation, the other near reattachment[11] (Fig. 10). The rapid rise of rms upstream of separation is a common feature of 2-D and 3-D shock-induced turbulent separated flows.[12] The relative amplitude of the fluctuations in this region is extremely large, with the maximum value of σp_w being a significant fraction of the local mean value, $\bar{P}_w$. This large rise in rms is not due to turbulence amplification through the initial compression, but is directly attributable to unsteadiness of the separation shock wave. That the physical cause is the separation shock wave motion can be seen from the pressure signals. Two examples, at $X/\delta_0 = -2.1$ and -2.3, are shown in Fig. 11. In each case, the mean wall pressure, $\bar{P}_w$, is indicated and, for reference, the incoming boundary-layer wall pressure signature is also shown. The instantaneous wall pressure, P_w, is intermittent, jumping randomly back and forth from the range characteristic of the undisturbed boundary layer to a higher level corresponding to flow downstream of the separation shock. $\bar{P}_w$ is generated by the superposition of very large amplitude fluctuations on the undisturbed boundary layer pressure signal, and $\bar{P}_w$ increases in the downstream direction because the "intermittency" (i.e., the fraction of time the flowfield is disturbed) progressively increases.

At each station under the unsteady separation shock wave, the "intermittency" can be easily calculated. It is simply the fraction of the total time that the separation shock wave spends upstream of the given station. Figure 12 shows that the entire region upstream of the separation line 'S' is intermittent. Both curves have the same shape and are displaced from one another due to the change in interaction length scale with δ_0. The length of the intermittent region, L_i, is about 0.75–0.9δ_0 in both cases. Since long sampling times are needed to define γ accurately when it is less than about 0.02 to 0.03, a more accurate comparison of the two cases can be made by defining L_i as the distance over which γ increases from about 0.04 to 0.99. This gives 0.6δ_0 in both cases and represents the region over which $\bar{P}_w/\bar{P}_{w0}$ increases from about 1.03 to about 1.7.

Similar distributions of mean wall pressure and rms of the fluctuations have been measured by Erengil and Dolling (Fig. 13) in separated compression ramp interactions at Mach 5.[13] The corresponding intermittency distribution (fitted to the curve of the error function) is shown in Fig. 14. Similar to the Mach 3 results shown earlier, the entire flowfield upstream of the separation line is intermittent, with a length scale of approximately 1δ_0. Figure 14 also shows the zero-crossing frequency distribution. The zero-crossing frequency is defined simply as the frequency of shock crossings over a given transducer in the intermittent region. The maximum value in the Mach 5 flow, about 1 kHz, is typical of that measured in a wide variety of interactive flows under similar conditions.[12] Thus this region of the flowfield is characterized by an unsteady separation shock whose motion is large-scale and low frequency (i.e., low compared to the characteristic frequency of the incoming flow, U_∞/δ_0).

Erengil and Dolling also calculated ensemble-averaged pressures $\bar{P}_{E/A}$ from the shock foot to the ramp corner, generated by "freezing" the shock at various positions in the intermittent region. These are plotted vs. X/δ_0 in Fig. 15. In the schematic at the top of the figure, filled markers shown an example of four simultaneously sampled transducer positions. (The "crossed" markers indicate the other positions at which ensemble-averaged pressures were obtained.) The symbol n represents the position of the shock in the intermittent region, and i is used to indicate the distance from the foot of the separation shock to the position of interest. The solid line in the Fig. 15 is the mean pressure distribution, obtained by averaging at each station the pressure values shown in Fig. 13. Each one of the dashed-line curves was generated by freezing the shock at a given position in the intermittent region as it moved upstream and ensemble-averaging on each of the downstream channels.

Three features are evident. First, $\bar{P}_{E/A}$ in the separated flow within about $1\delta_0$ upstream of the ramp corner is relatively insensitive to the shock position in the intermittent region (i.e., the difference between the pressure values when shock is furthest upstream and when it is furthest downstream is only a few percent). Second, for the "shock-upstream" case, the ensemble-averaged pressure distribution has a well-defined plateau region, consistent with a large-scale separated flow. As the shock moves toward its most downstream position, the ensemble-averaged pressure distribution progressively changes, finally resembling that typical of a small-scale separated flow. The data presented are for upstream motion of the separation shock; similar results were obtained for downstream motion as well. Using similar ensemble-averaging methods, Erengil and Dolling also showed that (i) the separation shock wave strength was a function of its position in the intermittent region, (ii) the separation shock is followed by compression waves whose strength decreases with distance from the shock foot, and (iii) the compression following the shock becomes stronger as the shock moves downstream. The structure was independent of the direction of motion of the shock wave.

3.4 Implication for Computations of Flow Upstream of the Corner

The discussion above shows clearly how the time-averaged results are generated. It is the occasional presence of the unsteady shock at the upstream influence line (UI) which first increases the mean wall pressure above the undisturbed value. Most of the time the pressure at UI is within the undisturbed range typical of the incoming boundary layer. The mean pressure rises downstream of UI because the translating shock spends an increasing amount of time upstream of stations nearer the separation line. What is, in an instantaneous snapshot, an abrupt pressure rise across the separation shock, is smeared out from UI to S in the time-averaged picture by the shock motion.

Modeling the flowfield with a stationary separation shock **cannot** simultaneously generate the correct upstream influence (as usually defined) and the correct time-averaged wall pressure. Even if the upstream influence matches the experiment (as it does in several of the computations in Fig. 9), the pressure distribution is generally incorrect. This is because the stationary shock model essentially produces an instantaneous snapshot of the flowfield (i.e., one of the "shock frozen" distributions of Fig. 15). In the case just cited, the separation shock is close to the experimental upstream influence line. In the experiment, the mean pressure at any given point is the weighted average of a series of instantaneous flowfields, each for the separation shock at a different streamwise position. This is evident from Fig. 15, which showed ensemble-averaged streamwise pressures, $\bar{P}_{E/A}$, from the shock foot to the ramp corner, generated by "freezing" the separation shock at various positions in the intermittent region. Mean surface properties in an unsteady flowfield cannot be reproduced by a model in which the shock (even if successfully modeled as a discontinuity) is stationary. The only way in which both the correct upstream influence and pressure distribution can be generated is to include the translating shock front in the modeling. Time-averaging the computed wall pressures over many time steps (as is actually done in either digital or analog fashion in the experiment) should substantially improve the comparison with experiment, irrespective of the turbulence model.

3.5 Physical Meaning of Experimental *Separation Lines*

Surface tracer techniques such as the kerosene-lampblack method are widely used in high-speed flows to find "separation lines" or "lines of coalescence," particularly in shock-wave turbulent boundary-layer interactions. These methods are relatively easy to use and produce highly defined, repeatable "separation lines." In the case of the kerosene-lampblack method, in which the pattern is lifted off the surface on large sheets of transparent tape, full-scale undistorted records are obtained. Measurements of angles and length scales are easily made from these patterns and are widely used for comparison with numerical simulation results. The locations indicated by 'S' on Figs. 9–13 were obtained using this method.

In flows in which the separation shock is highly unsteady, the physical meaning of these surface tracer lines comes into question. Figure 16 shows a typical surface pattern in an interaction generated by a blunt fin together with wall pressure signals upstream of the separation line. It is quite evident that the shock moves well upstream of the separation line. Does intermittent backflow occur upstream of the surface tracer line? No information can be gleaned from the flow visualization since the surface tracer material has essentially zero frequency response and indicates only the mean-wall shear stress direction (which evidently acts in the downstream direction).

In Refs. 14 and 15, Gramann and Dolling used conditional cross-correlations of wall pressure fluctuations to show that, in the case of an interaction induced by a circular cylinder in a Mach 5 turbulent boundary layer, the instantaneous separation point is at or close to the instantaneous shock foot in the intermittent region. Hence the separation point itself also undergoes a large-scale, streamwise motion. The well-defined separation line from the kerosene-lampblack pattern, such as that in Fig. 16, is at or close to the downstream boundary of a region of intermittent separation.

The reason why the surface streak lines are in the downstream direction upstream of 'S' can be explained using a relatively simple model. Consider the flow on centerline. If the instantaneous surface shear stress in the intermittent region is modeled as a step function, then the mean wall shear, $\bar{\tau}_w$, which the surface streaks respond to, is given by

$$\bar{\tau}_w = (1-\gamma)\bar{\tau}_u + \gamma\bar{\tau}_d$$

where $\bar{\tau}_u$ and $\bar{\tau}_d$ are the average wall shear stresses in the upstream and downstream zones. The mean wall shear, $\bar{\tau}_w$, will equal zero when

$$\frac{1-\gamma}{\gamma} = \left|\frac{\bar{\tau}_d}{\bar{\tau}_u}\right|$$

Since $\bar{\tau}_u$ is the wall shear stress of the incoming supersonic boundary layer and $\bar{\tau}_d$ is at the upstream boundary of the separated flow, the ratio $|\bar{\tau}_u/\bar{\tau}_d|$ given by N, will be large. Hence, $\bar{\tau}_w = 0$ when

$$\gamma = \frac{N}{1+N}$$

For large values of N, γ is close to 1. Thus, the mean shear stress at the wall can be in the downstream direction even when the flow is separated for the major fraction of the time.

The same conditional cross-correlation technique has also been employed by Gramann and Dolling in the Mach 5 compression ramp interaction referred to earlier.[17] The same result was obtained. It was also shown that the separation bubble expands and contracts at the same frequencies as those of the separation shock wave, generating a bubble whose streamwise length varies from about $1.7\delta_0$ to about $4\delta_0$. Ensemble-averaged wall pressure distributions (for the separation shock close to its upstream and downstream limits), shown in Fig. 17, show how the interaction expands and contracts and how the overall time-averaged surface pressure distribution throughout the flowfield is actually generated.

Recent work by Erengil and Dolling (Ref. 19) shows that the physical interpretation of the line of coalescence of the surface streaks changes with interaction sweepback. In a study at Mach 5, wall pressure fluctuations were measured upstream of the ramp corner line in interactions generated by unswept, 10, 20, 25, 30, 40, and 50 deg. swept compression ramps. The streamwise angle was 28 deg. in all cases. Figure 18a shows the normalized length of the intermittent region, L_i/δ_0, as a horizontal line for the unswept and the moderately swept interactions ($\lambda_C \leq 20$ deg.). Since highly swept interactions ($\lambda_C \geq 25$ deg.) are quasi-conically symmetric, it is more appropriate to define the intermittent region length in terms of an angular increment rather than in terms of δ_0. Figure 18b shows the angular extent of the intermittent region by a vertical line drawn from λ_0 to λ_1. Here, λ_0 and λ_1 are the sweepback angles of rays along which the intermittency is about 0.02 and about 0.98, respectively. In this representation, each line forms a scale ranging from $\gamma \approx 0.98$ to $\gamma \approx 0.02$. The relative position of the separation line from the flow visualization is also indicated on each of these lines. The decreasing length of the horizontal lines (and the vertical ones in highly swept interactions) shows quite clearly the shrinking of the intermittent region as the interaction is progressively swept back. Furthermore, the changing position of the marker indicating the location of the separation line shows that the separation location from surface flow visualization moves upstream in the intermittent region towards lower and lower values of intermittency. A plausible explanation of why this forward motion of the separation line occurs was given by Dolling et al.[20] In brief, the line of coalescence in surface flow patterns, i.e., the separation line, occurs at a location where the time-averaged wall shear stress is zero. As noted earlier, in the unswept interaction, the wall shear stress in the downstream direction, $(\tau_w)_d$, is much greater than the wall shear stress in the upstream direction, $(\tau_w)_u$, such that the coalescence of surface streamlines occurs at the downstream end of the intermittent region. Whereas in the swept interactions, the upstream component of the wall shear stress increases appreciably, hence changing the relative position in the intermittent region where the time-averaged wall shear stress is zero. As a result, the line of coalescence of surface streamlines shifts progressively upstream in the intermittent region.

3.6 Outgoing Mean Velocity Profiles

In Ref. 10, Wilcox shows comparisons of the mean velocity profiles in the Mach 3, 24 deg. compression ramp interaction, with predictions from the k-ω and multiscale turbulence models. Examples are shown in Fig. 19. Downstream of the corner ($S/\delta_0 = 0.44$ to 6.18), the experimental data are much fuller than the computations below y/δ of about 0.4. Wilcox also computed the outgoing mean velocity profiles for Brown's experiment[21] of Mach 2.85 flow into a 30 deg. axisymmetric compression corner. These results are shown in Fig. 20. Again, below y/δ_0 of about 0.4, the measured profiles are much fuller than the computed profiles.

Viegas et al.[8] also computed outgoing velocity profiles for the 20 deg. compression ramp interaction of Settles at Mach 2.8. The k-ϵ model was used and results were presented based both on wall functions and integration to the wall. Profiles at four stations downstream of the corner are shown in Fig. 21. In this flowfield, which has a relatively small scale separated flow, experiments[22] show that the separation shock is also unsteady but with a smaller range of motion than the 24 deg. ramp under the same freestream conditions. Again, the experimental profiles near the wall are fuller than the computed profiles.

McClure and Dolling[23] have examined how the outgoing mean pitot pressure profiles are actually generated in a Mach 5, 28 deg. compression ramp interaction. Three cases were studied: (i) ramp with suction applied along a 6mm-long slot spanning the ramp near the reattachment; (ii) ramp with suction slot exposed to the flow but without suction applied; (iii) baseline case (i.e., no slot or suction). Measurements were made using (i) a conventional pitot probe with a flattened tip (0.64 mm × 2.1 mm) with about 50 cm of pressure tubing between the probe tip and the pressure transducer, and (ii) a pitot probe with a single Kulite Model XCQ-062-100A miniature pressure transducer projecting upstream of the tip. The frequency response of the Kulite probe was about 50 kHz.

First, mean pitot pressure surveys were made perpendicular to the ramp face using the conventional probe. Second, simultaneous measurements were made of fluctuating pitot pressures above the ramp and wall pressure fluctuations under the unsteady separation shock. Analysis of the fluctuating results confirmed earlier findings that the separated flowfield expanded and contracted in a "breathing" fashion, and the flowfield unsteadiness associated with the separation shock motion extended well downstream of the corner. While the slot-alone and slot-with-suction significantly altered the mean flowfield scale, the dynamics of the separation shock were largely unaltered.

Results from the mean and fluctuating pitot surveys at four stations downstream of the corner are shown in Fig. 22 for the baseline and suction cases. Note that z is measured perpendicular to the ramp face. The solid lines are the mean profiles from the conventional probe. The dashed lines are "frozen" pitot profiles. "Frozen" profiles were obtained by averaging pitot pressure values only for the condition when the upstream separation shock was located between two specified surface transducers. The intermittencies of the surface transducer pair used are indicated in the figure keys. The two positions correspond to the separation shock far "upstream" and "downstream." Also indicated is the mean value from the fluctuating measurements.

In both cases it can be seen that, as the separation shock moves downstream (to a location of higher intermittency), the downstream extent of the interaction shrinks, and vice versa. The qualitative behavior is the same in both cases. Only the mean scales differ. This "breathing" behavior is consistent with the conclusions of Kussoy et al.[24] based on conditional laser doppler measurements in a flared cylinder interaction and by Gramann and Dolling[17] based on conditional fluctuating surface pressure cross correlations on the face of a two-dimensional compression corner.

Comparison of the mean pitot pressure values obtained from the conventional pitot probe with mean values from the fluctuating pitot pressure signal shows differences at each station. The differences have three possible causes. First, slight shifts in survey position show up as differences in pitot pressure. These differences should vary from ramp station to station but would be consistent for a given station. It is estimated that streamwise probe placement for a given ramp position varied by less than 0.06δ between *conventional* and *fluctuating* runs, and so should contribute only very slightly to P_t discrepancies. This possibility can therefore be disregarded. Second, the diameter of the fluctuating probe "tip" was 2.5 times greater than the conventional probe height, which would tend to integrate P_t over a larger distance and hence contribute to differences, particularly in regions of large gradients.

It is probable that this integration has some effect. The third cause, which is almost certainly the major contributor, is the skewness of the fluctuating signal. Examination of the probability density distributions (pdd's) for the fluctuating pitot signals indicated that, close to the ramp surface ($< 0.6\delta_0$), the pdd's had positive skewness and, in some cases, exhibited a bimodal shape with very large separation between peak values ($\simeq$ 32 psi). Under conditions where the probability density values of these peaks were sufficiently different, *the conventional pitot reading was higher than the mean of the fluctuations*. Fig. 23 shows this effect for the data set with the largest disagreement, the suction survey at $Z/\delta_0 \simeq 1.45$. The accompanying probability distributions for the fluctuating pitot pressure clearly show that the conventional pitot probe measurement is biased toward the higher mode in the fluctuating pitot pressure data for $Z/\delta_0 \leq 0.43$. This behavior reverses, though, for $Z/\delta_0 = 0.58$, where the probability density of the lower mode is six times greater than that of the higher mode. The 50 cm of tubing between the orifice and pressure transducer for the conventional pitot probe behaves as a *pressure sensitive* filter with an output dependent on the nature of the fluctuations (i.e., frequency and amplitude content).

In the experiments used for comparison with computation in Figs. 19 through 21, the pitot profiles from which mean velocity profiles were calculated were obtained using conventional probes. It is almost certain that these profiles are fuller than would be obtained by time-averaging the corresponding fluctuating pitot pressure signals. If the mean velocity profile was computed using the mean of the fluctuating signal rather than the single time-averaged value from the conventional probe, the profiles would be much less full near the wall and would probably agree better with the computations.

4. SUMMARY

Experiments show that the separated interaction generated by an unswept compression ramp is characterized by a relatively low frequency expanding/contracting bubble whose effects are felt from the upstream influence line to at least 5-$6\delta_0$ downstream of reattachment. The change in length scale of the flowfield is large; when the bubble shrinks to its smallest size, the streamwise length (measured from the instantaneous upstream influence line to where the final inviscid pressure level is reached on the ramp) in the Mach 5 experiments reported here is about $4.5\delta_0$. At its largest extent, the scale is about 50% larger. The well-defined separation line seen in surface flow visualization is actually at, or very close to, the downstream boundary of a region of intermittent separation. It forms at this location because of the tracer material's response to a time varying wall stress.

It is clear that the measured mean surface and flowfield properties are controlled by the flowfield unsteadiness. The discrepancies between the predicted and measured properties are almost certainly not just due to inadequate turbulence modeling, but also due to neglect of the unsteadiness in the modeling. Without modeling the unsteadiness, it is unlikely that the codes can reproduce correct mean property distributions. For flows of this type, it is felt that equal emphasis should be placed on developing methods capable of modeling the unsteadiness as is placed on turbulence modeling.

5. REFERENCES

[1] Jameson, A., "Universities Foster CFD Growth," *Aerospace America*, Feb. 1992, pp. 42-47.

[2] Coleman, G. T., "A Study of Hypersonic Boundary Layers over a Family of Axisymmetric Bodies at Zero Incidence: Preliminary Report and Data Tabulation," Imperial College of Science and Technology Aero Report 73-06, London, Sep. 1973.

[3] Coleman, G. T. and Stollery, J. L., "Heat Transfer in Hypersonic Turbulent Separated Flow," Imperial College of Science and Technology Aero Report 72-05, London, Mar. 1972.

[4] Horstman, C. C., "Prediction of Hypersonic Shock Wave/Turbulent Boundary Layer Interaction Flows," AIAA Paper 87-1367, AIAA 19th Fluid Dynamics, Plasma Dynamics and Lasers Conference, Jun. 8-10, 1987, Honolulu, HI.

[5] Holden, M. S., "Experimental Studies of Quasi-Two-Dimensional and Three-Dimensional Viscous Interaction Regions Induced by Skewed-Shock and Swept-Shock Boundary Layer Interaction," AIAA Paper 84-1677, 1984, Snowmass, CO.

[6] Settles, G. S., "An Experimental Study of Compressible Turbulent Boundary Layer Separation at High Reynolds Numbers," Ph.D. Dissertation, Mechanical and Aerospace Engineering Department, Princeton University, Sep. 1975.

[7] Viegas, J. R. and Horstman, C. C., "Comparison of Multi-Equation Turbulence Models for Several Shock Boundary Layer Interaction Flows," *AIAA Journal*, Vol. 17, No. 8, 1979, pp. 811-820.

[8] Viegas, J. R., Rubesin, M. W., and Horstman, C. C., "On the Use of Wall Functions as Boundary Conditions for Two-Dimensional Separated Compressible Flows," AIAA Paper 85-0180, AIAA 23rd Aerospace Sciences Meeting, Jan. 1985, Reno, NV.

[9] Champney, J., "Modelling of Turbulence for Compression Corner Flows and Internal Flows," AIAA Paper 89-2344, AIAA/ASME/SAE/ASEE 25th Joint Propulsion Conference, Jul. 1989.

[10] Wilcox, D. D., "Supersonic Compression Corner Applications of a Multi-Scale Model for Turbulent Flows," *AIAA Journal,* Vol. 78, No. 7, Jul. 1990, pp. 1194–1198.

[11] Dolling, D. S. and Murphy, M. T., "Unsteadiness of the Separation Shock Wave Structure in a Supersonic Compression Ramp Flowfield," *AIAA Journal,* Vol. 21, Dec. 1983, pp. 1628–1634.

[12] Dolling, D. S. and Dussauge, J. P., "Fluctuating Wall Pressure Measurements," Chapter 8 of *A Survey of Measurements and Measuring Techniques in Rapidly Distorted Compressible Turbulent Boundary Layers,* Agardograph 315, May 1989.

[13] Erengil, M. E. and Dolling, D. S., "Separation Shock Motion and Ensemble-Averaged Wall Pressures in a Mach 5 Compression Ramp Interaction," *AIAA Journal,* Vol. 29, No. 5, May 1991, pp. 728–735.

[14] Gramann, R. A. and Dolling, D. S., "Detection of Turbulent Boundary Layer Separation Using Fluctuating Wall Pressure Signals," *AIAA Journal,* Vol. 28, No. 6, Jun. 1990, pp. 1052–1056.

[15] Gramann, R. A. and Dolling, D. S., "Interpretation of Separation Lines from Surface Tracers in Shock Induced Turbulent Flow," *AIAA Journal,* Vol. 25, No. 12, 1987, pp. 1545–1546.

[16] Gramann, R. A. and Dolling, D. S., "Unsteady Separation in Shock Wave Turbulent Boundary Layer Interaction," AIAA Paper 86-1033, AIAA/ASME 4th Joint Fluid Mechanics, Plasma Dynamics and Lasers Conference, May 1986, Atlanta, GA.

[17] Gramann, R. A. and Dolling, D. S., "Dynamics of Separation and Reattachment in a Mach 5 Unswept Compression Ramp Flow," AIAA Paper 90-0380, 28th Aerospace Sciences Meeting, Jan. 8–11, 1990, Reno, NV.

[18] Gramann, R. A., "Dynamics of Separation and Reattachment in a Mach 5 Unswept Compression Ramp Flow," Ph.D. Dissertation, Dept. of Aerospace Engineering and Engineering Mechanics, The University of Texas at Austin, Dec. 1989.

[19] Erengil, M. E. and Dolling, D. S., "Effects of Sweepback on Unsteady Separation in Mach 5 Compression Ramp Interactions," AIAA Paper 92-0430, *30th Aerospace Sciences Meeting,* Jan. 6–9, 1992, Reno, NV.

[20] Dolling, D. S., Boitnott T., Erengil, M. E., "Effects of Moderate Sweepback on the Separation Shock Wave Dynamics in a Mach 5 Compression Ramp Interaction," AIAA Paper 91-0254, AIAA 29th Aerospace Sciences Meeting, Jan. 7–10, 1991, Reno, NV.

[21] Brown, J. D., "Two Component LDV Investigation of Shock Related Turbulent Boundary Layer Separation with Increasing Three-Dimensionality," PH.D. Thesis, University of California at Berkeley, 1986.

[22] Dolling, D. S. and Or, C. T., "Unsteadiness of the Shock Wave Structure in Attached and Separated Compression Ramp Flows," *Experiments in Fluids,* Vol. 3, 1985, pp. 24–32.

[23] McClure, W. B. and Dolling, D. S., "Exploratory Study of Effects of Suction Near Reattachment on the Unsteadiness of a Mach 5 Compression Ramp Interaction," AIAA Paper 91-1767, AIAA 22nd Fluid Dynamics, Plasma Dynamics and Lasers Conference, Jun. 24–27, *1991, Honolulu, HI.*

[24] Kussoy, M. I., Brown, J. D., Brown, J. L., Lockman, W. K., and Horstman, C. C., "Fluctuations and Massive Separation in Three-Dimensional Shock-Wave/Boundary-Layer Interactions," 2nd International Symposium on Transport Phenomena in "Turbulent Flows," Tokyo, Japan, Oct. 25–29, 1987.

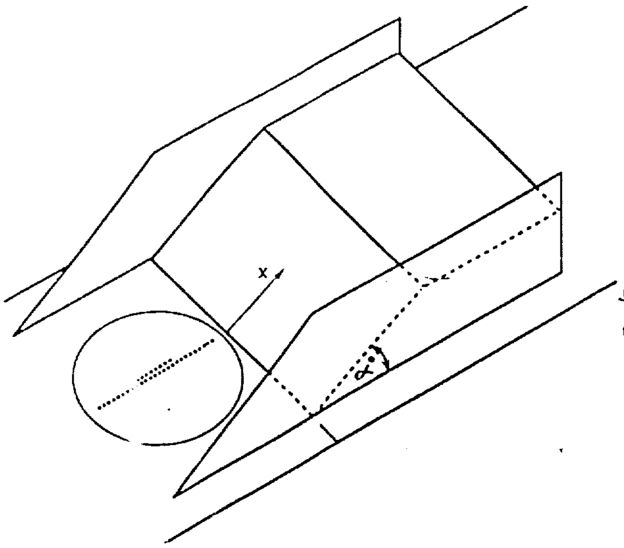

Fig. 1. Schematic of compression ramp geometry and coordinate system.

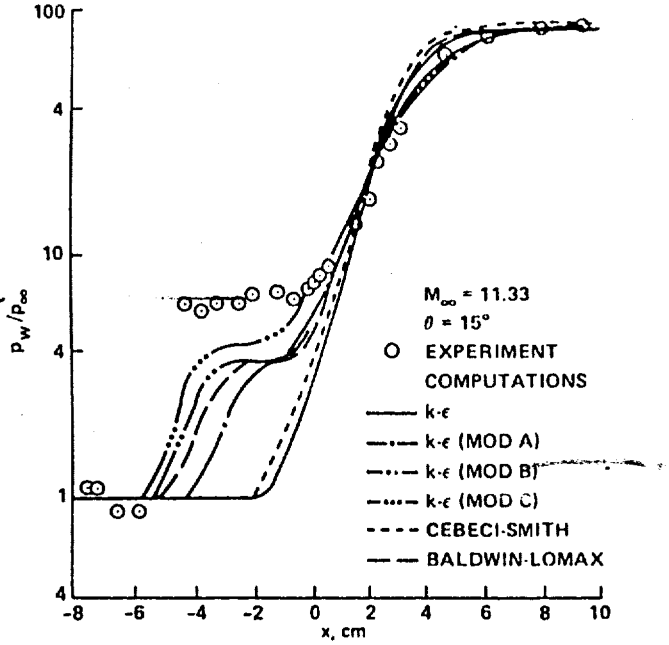

Fig. 3. Normalized wall pressure distributions in incident shock wave interaction ($M_\infty = 11.33$, $\theta = 15$ deg., data of Holden, Ref. 5). Figure from Horstman, Ref. 4.

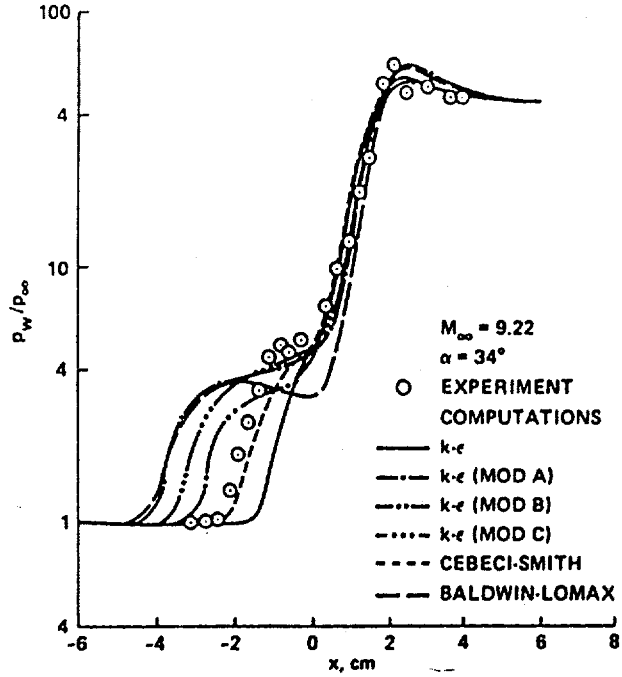

Fig. 2. Normalized wall pressure distributions in a compression ramp flow ($M_\infty = 9.22$, $\alpha = 34$ deg., data of Refs. 2 and 3). Figure from Horstman, Ref. 4.

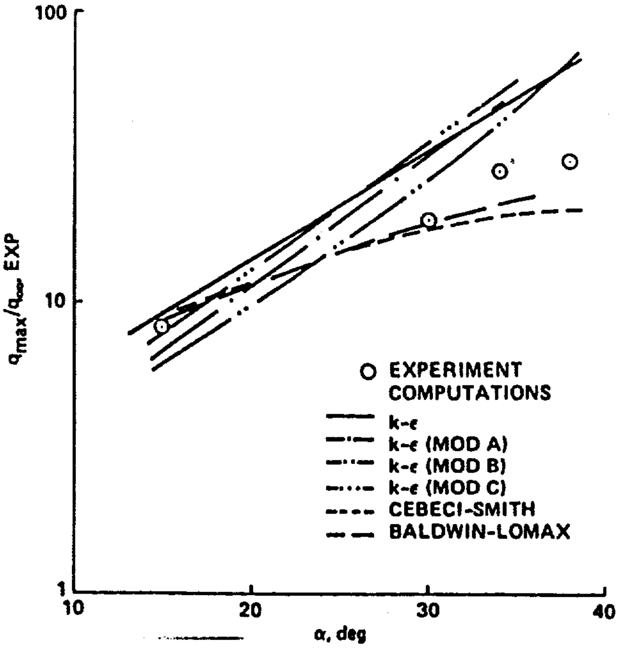

Fig. 4. Mach 9.22 compression ramp interaction: comparison of computed and experimental maximum heat transfer rates (from Horstman, Ref. 4).

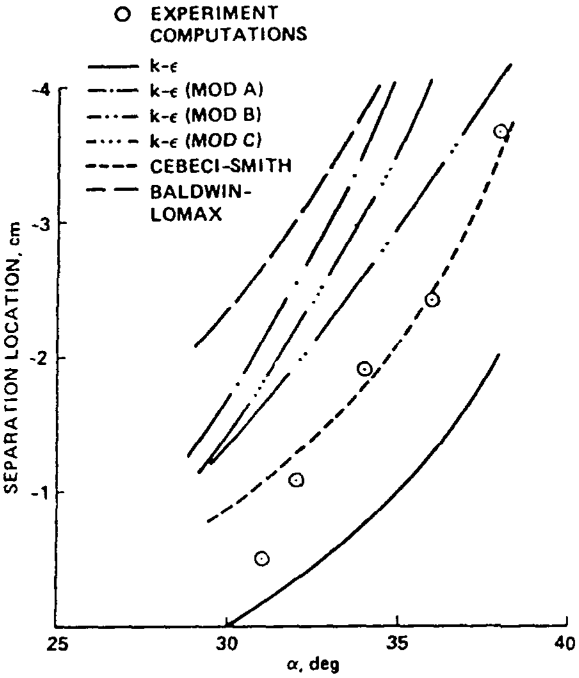

Fig. 5. Mach 9.22 compression ramp interaction: comparison of computed and experimental separation locations (from Horstman, Ref. 4).

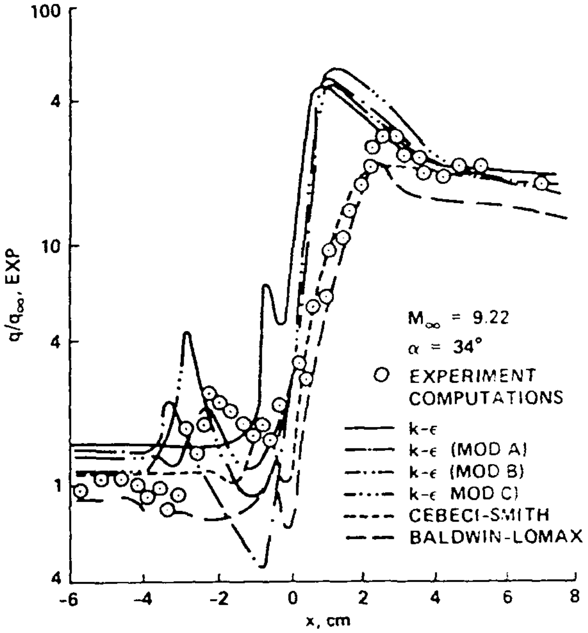

Fig. 7. Normalized heat transfer rate distributions in a compression ramp flow (M_∞ = 9.22, $\alpha = 34$ deg., data of Refs. 2 and 3). Figure from Horstman, Ref. 4.

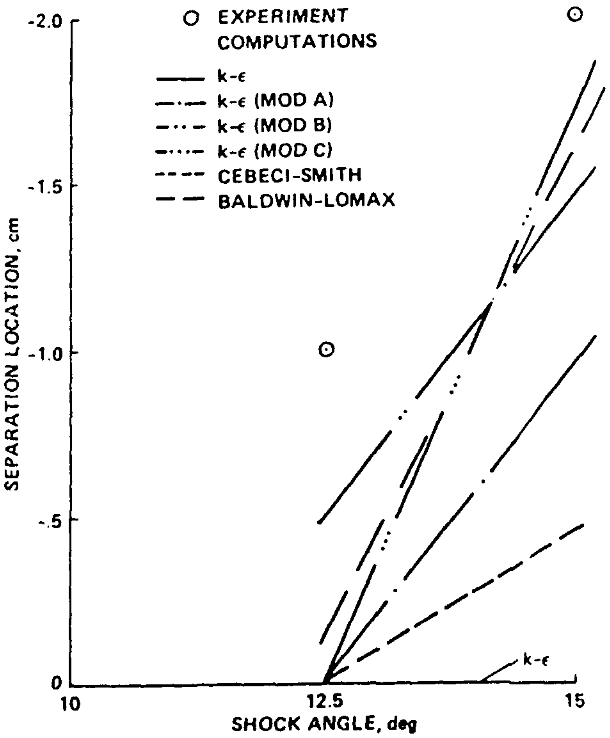

Fig. 6. Mach 11.3 incident shock wave interaction: comparison of computed and experimental separation locations (from Horstman, Ref. 4).

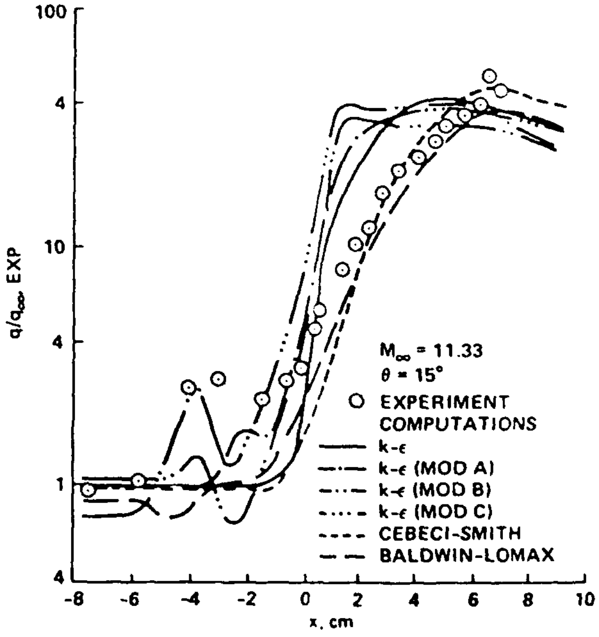

Fig. 8. Normalized heat transfer rate distributions in incident shock wave interaction (M_∞ = 11.33, θ = 15 deg., data of Holden, Ref. 5). Figure from Horstman, Ref. 4.

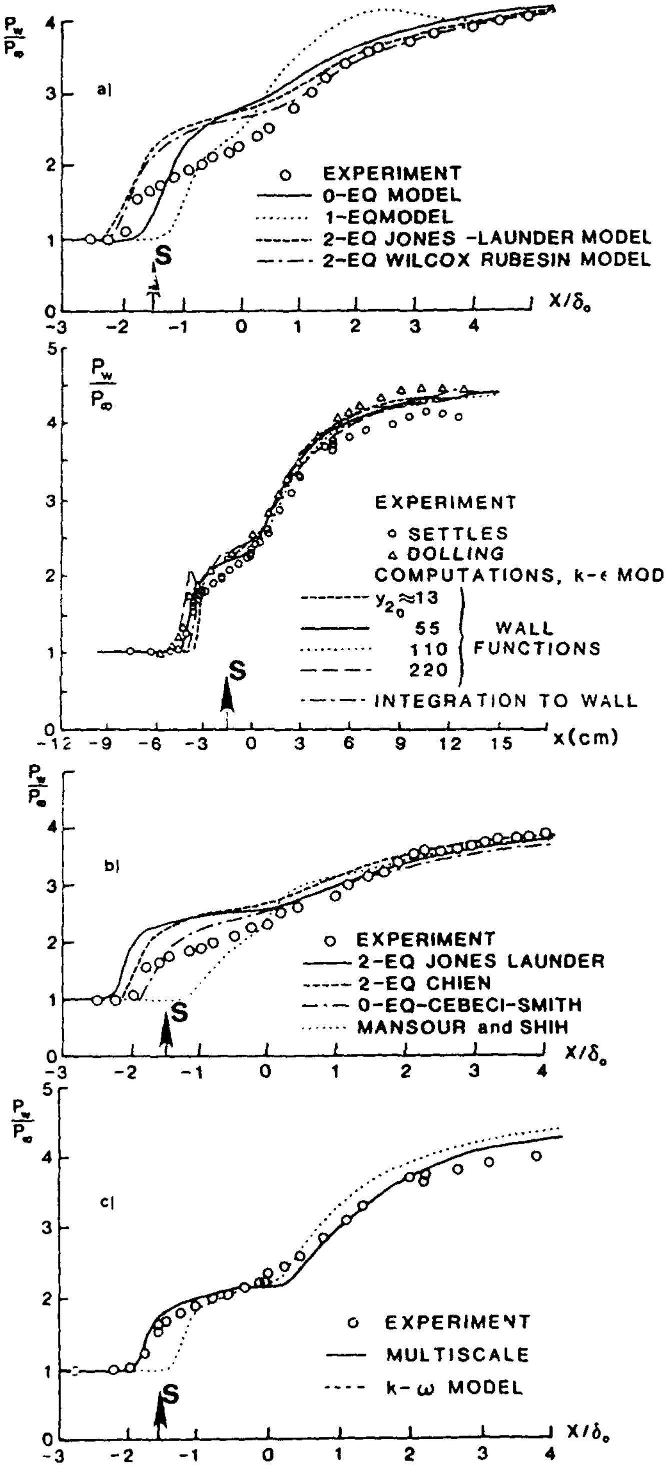

Fig. 9. Measured and computed wall pressure distributions in a 24 deg., Mach 3 compression ramp interaction: a) Viegas and Horstman, 1979 (Ref. 7); b) Viegas, Rubesin and Horstman, 1985 (Ref. 8); c) Champney, 1989 (Ref. 9); d) Wilcox, 1990 (Ref. 10).

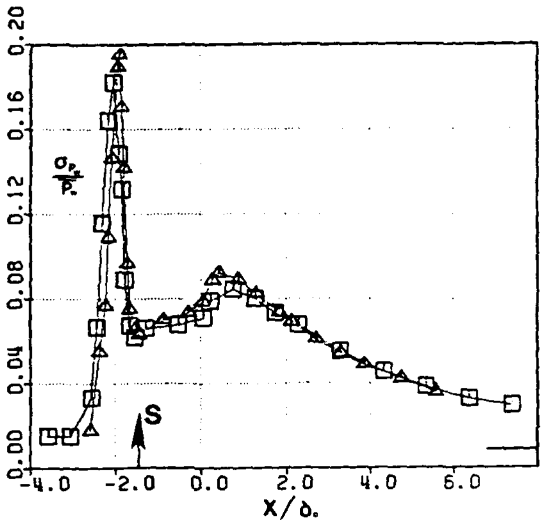

Fig. 10. Wall pressure standard deviation distributions in a 24 deg., Mach 3, compression ramp interaction (from Ref. 11).

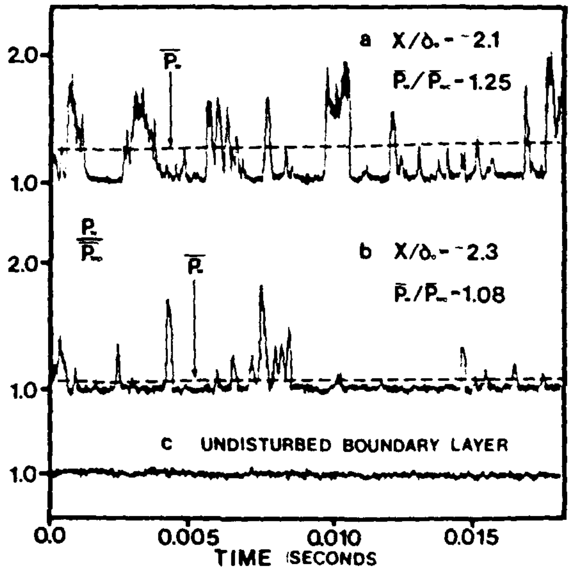

Fig. 11. Sample wall pressure signals upstream of separation in a 24 deg. Mach 3 compression ramp interaction (from Ref. 11).

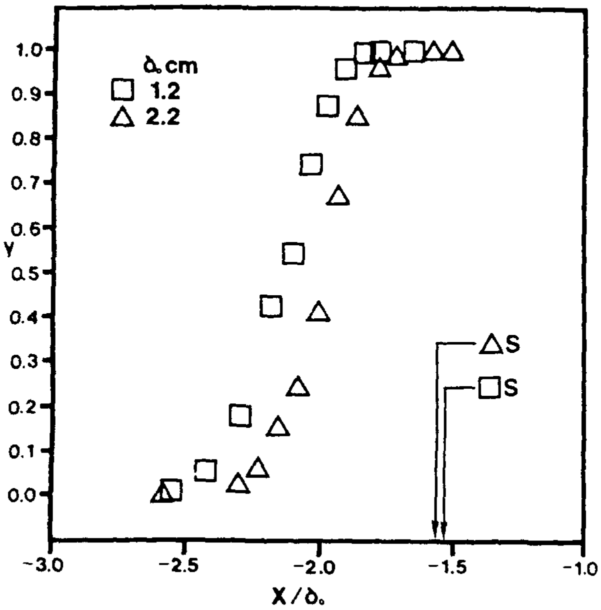

Fig. 12. Intermittency distributions in a 24 deg., Mach 3 compression ramp interaction (from Ref. 11).

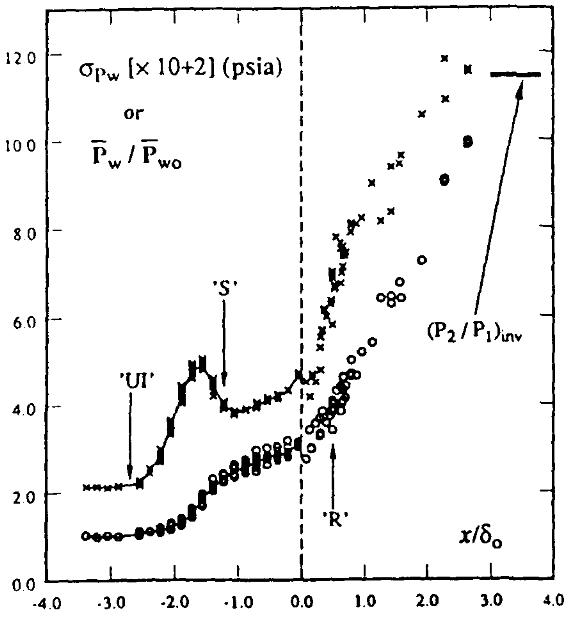

Fig. 13. Normalized mean wall pressure and standard deviation distributions in a 28 deg., Mach 5 compression ramp interaction (from Ref. 13).

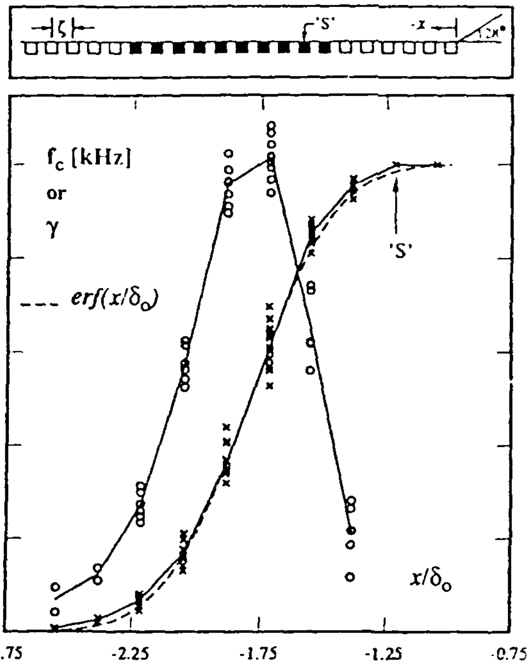

Fig. 14. Distributions of intermittency and zero crossing frequency in a 28 deg., Mach 5, compression ramp interaction (from Ref. 13).

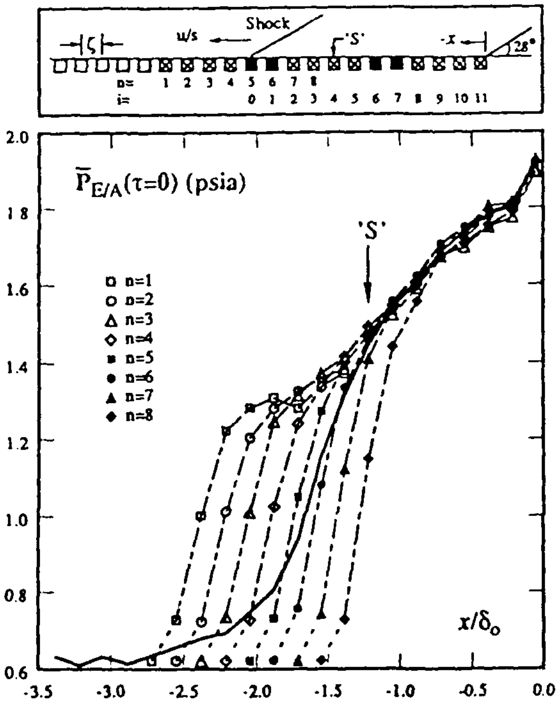

Fig. 15. Ensemble-averaged wall pressures upstream of the corner in a 28 deg., Mach 5 compression ramp interaction (from Ref. 13).

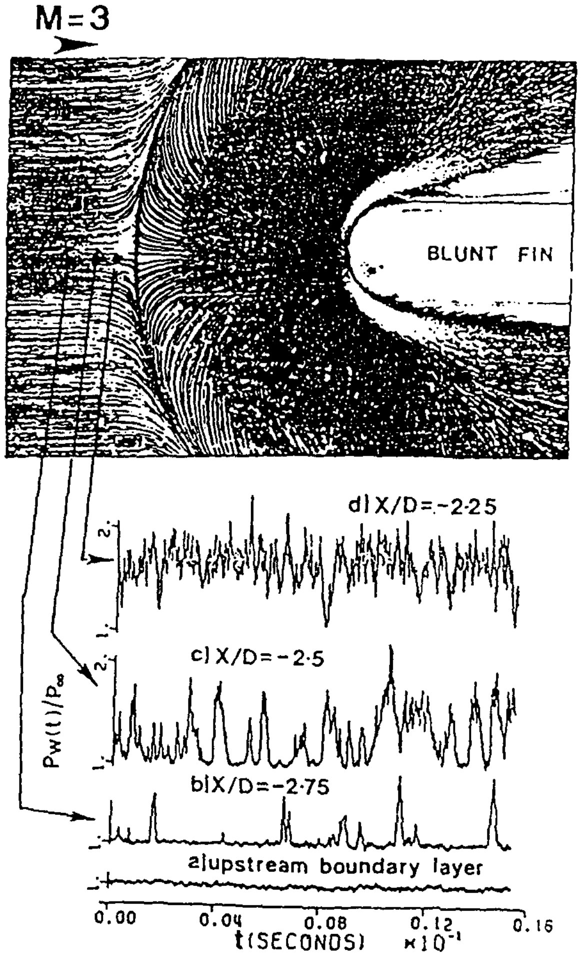

Fig. 16. Kerosene-lampblack surface flow visualization and wall pressure signals (from Ref. 14).

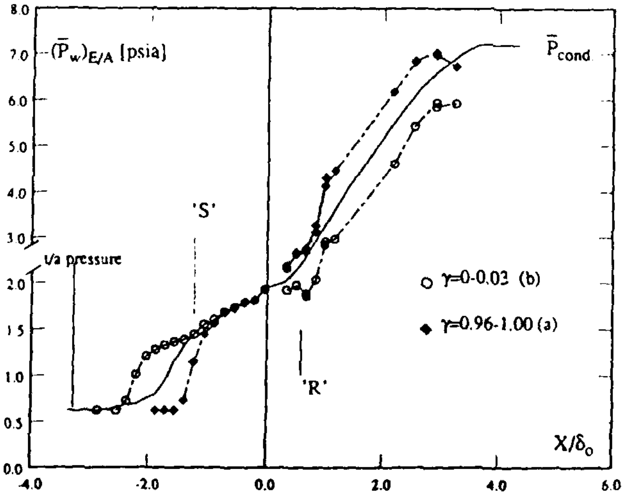

Fig. 17. Ensemble-averaged wall pressure distributions in a 28 deg., Mach 5 compression ramp interaction corresponding to "shock-upstream" and "shock-downstream." (From Ref. 18).

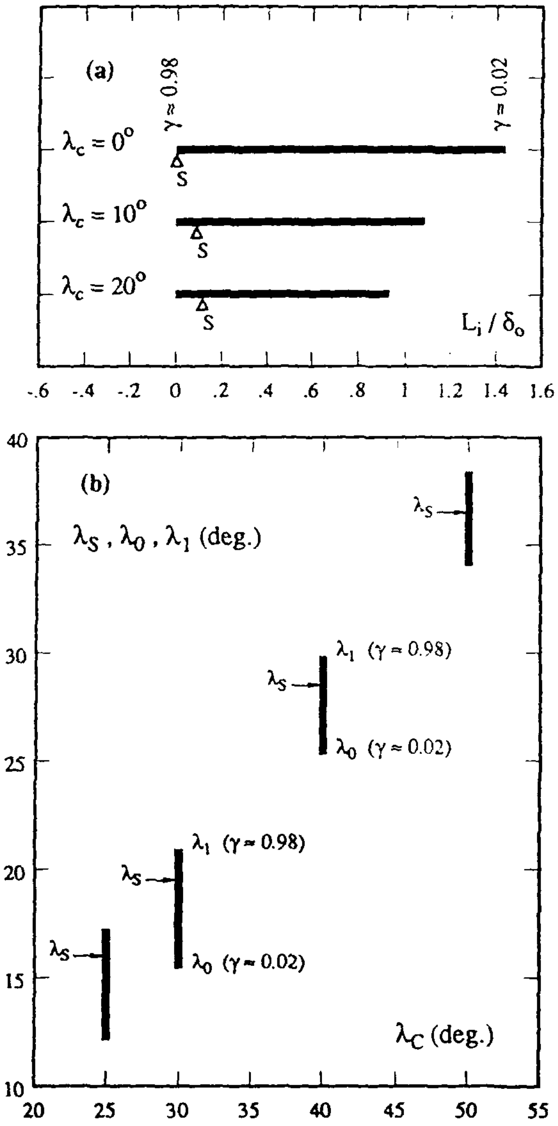

Fig. 18. Normalized length of the intermittent region in unswept and swept compression ramp interactions at Mach 5 (from Ref. 19).

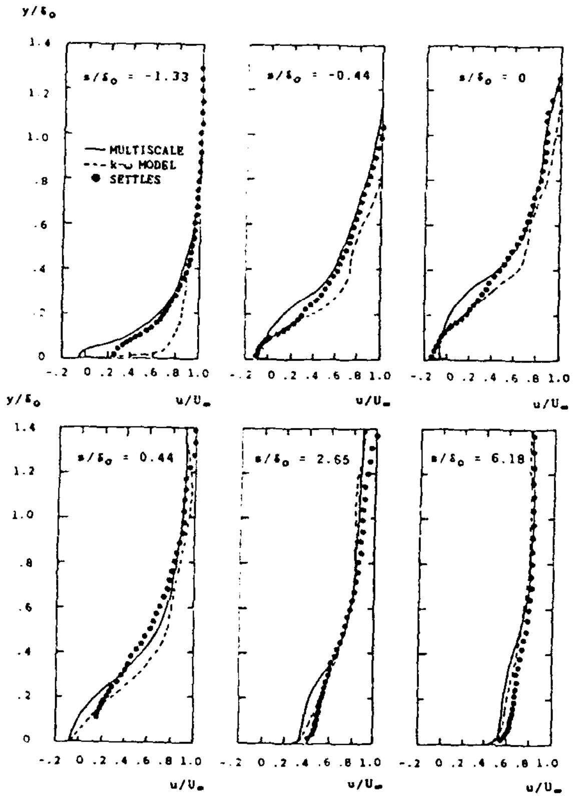

Fig. 19. Measured and computed mean velocity profiles downstream of the corner in a 24 deg., Mach 3 compression ramp interaction (from Ref. 10).

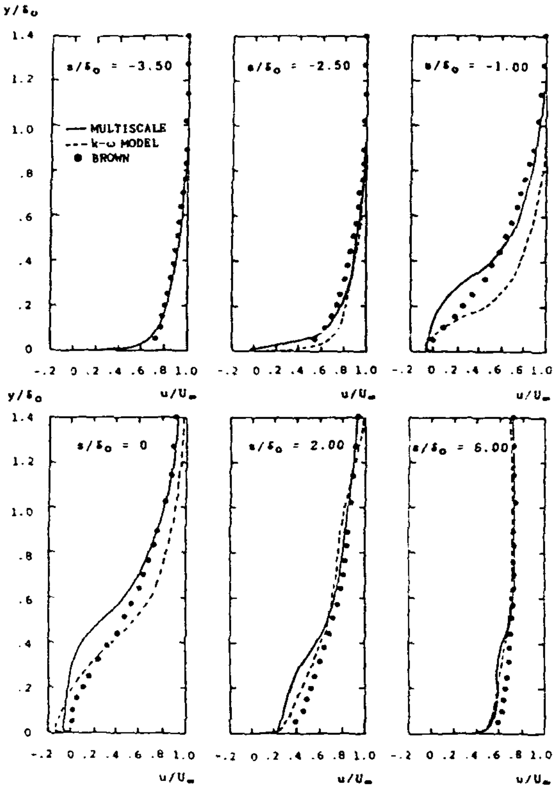

Fig. 20. Measured and computed mean velocity profiles downstream of the corner in a 30 deg., Mach 2.85, axisymmetric ramp flow (from Ref. 10).

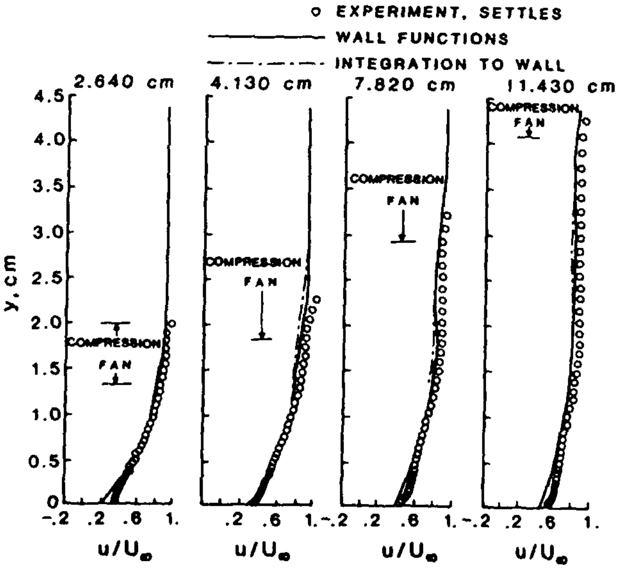

Fig. 21. Measured and computed mean velocity profiles downstream of the corner in a 20 deg., Mach 2.8 compression corner interaction (from Ref. 8).

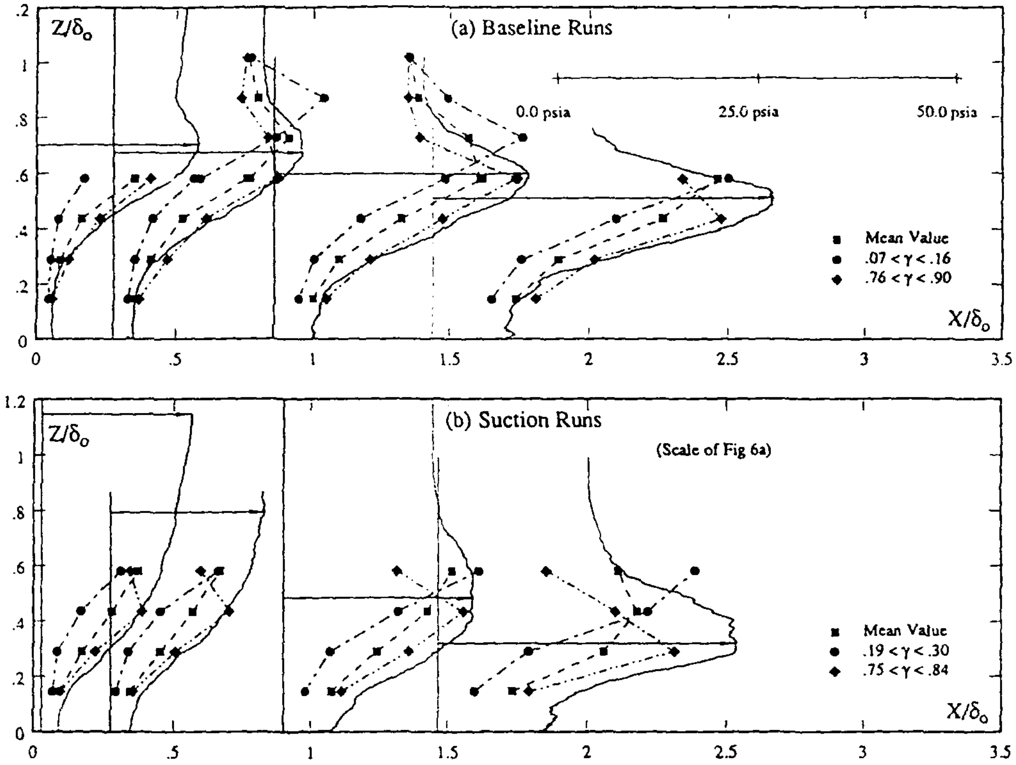

Fig. 22. Results from mean and fluctuating pitot surveys downstream of the corner in a 28 deg., Mach 5 compression ramp interaction: a) baseline; b) ramp with suction (from Ref. 22).

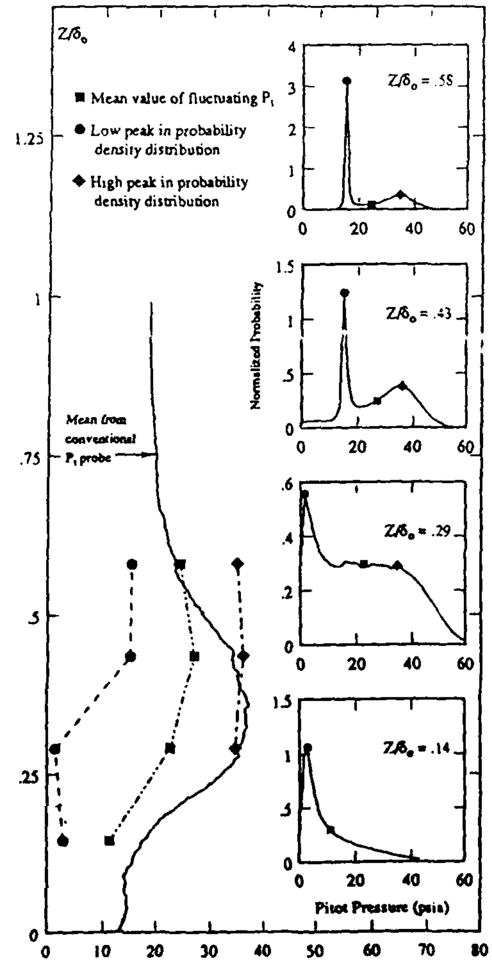

Fig. 23. Comparison of mean values from fluctuating and conventional mean pitot surveys (from Ref. 22).

FLOW DEVELOPMENT IN A CIRCULAR PIPE IN THE UTIAS/RPI M = 8.3 GUN TUNNEL

J. P. Sislian, Z. He* and R. L. Deschambault
University of Toronto Institute for Aerospace Studies
4925 Dufferin Street
Downsview, Ontario, Canada
M3H 5T6

SUMMARY

The present investigation is concerned with the understanding of the structure of the hypersonic flow developed in a circular pipe. The experiments were conducted in the University of Toronto Institute for Aerospace Studies (UTIAS)/Ryerson Polytechnical Institute (RPI) gun tunnel at a free-jet Mach number of 8.30 and Reynolds number based on the pipe diameter, Re = 2.44×10^6. Wall static pressure, as well as in-stream static and pitot pressure measurements at several sections in the pipe, shed some light into the physical nature of the considered flow. The measurements indicate that shocks generated in the pipe flow are primarily oblique. Measurements near the pipe axis and in wave structures presented some difficulties. Further work is needed to clarify certain features of the investigated flow. The presented results may guide the development of computational fluid dynamic codes applicable to hypersonic pipe flows.

1. INTRODUCTION

The structure of a supersonic flow in a duct has important implications in the design and operation of wind tunnel diffusers, inlets and induction systems of hypersonic airbreathing engines. There have been numerous experimental investigations of the viscous-inviscid interactions that occur in such confined flows. These have included the influence of such parameters as: the Mach number of the oncoming flow, pipe diameter and length, and the presence or absence of an upstream boundary layer. Depending on the thickness of the boundary layers present, various shock-wave configurations were observed. Boundary layers formed in these flows, as well as shock wave/boundary layer interactions have also been investigated. The free-stream Mach number considered in all of these investigations did not exceed four (see Refs. 1-12).

Wall pressure distributions in long circular ducts, L/D = 42-53, over a range of oncoming Mach numbers $1.8 \leq M_\infty \leq 4.2$, were measured in an early paper by Neumann and Lustwerk (Ref.1). The purpose of the investigation was to determine the optimum length for the design of the throat section of a wind tunnel diffuser. It was found that when shocks were generated in the ducts, the pressure rise extended over a length of 8-12 tube diameters. In a subsequent paper (Ref.2) Lustwerk studied the influence of the boundary-layer thickness at the beginning of the shock system formed in a sharp leading edge rectangular duct in a Mach 2.05 wind tunnel.

---

*Presently at the Nanjing Aeronautical Institute, Nanjing, People's Republic of China.

Schlieren pictures of the flow showed that with no upstream boundary layer, a plane normal shock wave was formed. As the boundary layer thickened, a series of plane or lambda shocks occurred. Further thickening of the boundary layer generated oblique shock waves. For a lower free-stream Mach number of 1.5, Richmond and Goldstein (Ref.3) measured streamwise wall static pressure and centreline total pressure distributions in an expanding rectangular duct in order to infer friction factor and heat transfer coefficients for a turbulent supersonic channel flow that develops at a nominally constant core-flow Mach number without shocks. The structure of shock waves generated in rectangular ducts at free-stream Mach numbers $M_\infty = 1.6\text{-}2.5$ was also studied in Ref.4. It was shown that various shock-wave structures with pressure jumps up nearly to normal shock value could be generated. In Ref. 5, shock stabilization in constant-area ducts, for Mach numbers of 1.76-2.51, was investigated as applied to the induction system for turbojet inlets.

Test results of supersonic combustion ramjets in hypersonic free jets and in direct-connect mode showed (see Ref.6) that combustion in a supersonic flow generates a shock train in the upstream flow and that an *isolator* duct of prescribed length is required to stabilize the wave train and prevent combustion-induced disturbances to affect the flow in the engine inlet. The flow structure in such isolator ducts was investigated in Refs.7-9. Wall static and in-stream pitot pressure distributions, as well as wall shear stress, were measured at free-stream Mach numbers of $1.13 \leq M_\infty \leq 2.72$ and at a Reynolds number based on upstream boundary-layer momentum thickness of $5\times10^3 \leq Re_\theta \leq 6\times10^4$ in a cylindrical duct. Based on an analysis of these measurements, the character of the shock-wave structure was shown to be oblique rather than normal, with the flow remaining supersonic downstream of the shock system. The influence of the Mach number, Reynolds number Re_θ, duct diameter and upstream boundary layer momentum thickness, θ, on pressure recovery was also studied. It was shown that for a given pressure ratio across the disturbance the distance over which the pressure rise is spread varies approximately directly with the product $\theta^{1/2}D^{1/2}$ and inversely with $(M_\infty^2-1)Re_\theta^{1/4}$.

In a more recent paper Om and Childs (Ref.10) have obtained detailed pitot, static and wall pressure measurements for multiple shock wave-turbulent boundary layer interactions in a circular duct at a freestream Mach number of 1.49 and at a unit Reynolds number of 4.90×10^6 per meter. Their results show the formation of a series of normal shock waves with successively decreasing strength and with decreasing distance between the successive shock waves. The overall pressure recovery is much lower than the single normal shock pressure recovery at the same free-stream Mach number. Lately, a detailed experimental study of the supersonic turbulent flow development in a square duct was reported in Refs.11 and 12, over a development length $0 \leq L/D \leq 20$ for a uniform flow with a Mach 3.9 condition at the duct inlet. Total pressure contours and local skin friction coefficient distributions showed that the flow develops in a manner similar to that observed for the incompressible case.

The objective of the present research effort is to gain a better understanding of the physical nature of the flow developing in a circular pipe at a flow Mach number $M = 8.30$. Data obtained provide a picture of the mean flow behaviour and the shock-wave system formed within a constant-area pipe, from essentially uniform mean flow conditions at the inlet, determine the boundary-layer development along the duct and may guide the development of computational fluid dynamic codes applicable to hypersonic pipe flows.

2. EXPERIMENTAL FACILITY

The experimental study was performed in the hypersonic gun tunnel setup at the University of Toronto Institute for Aerospace Studies. A schematic diagram of the major tunnel components is shown in Fig. 1. Air is stored at about 202.31 atm. in the driver (1), which has an internal diameter of 0.305 m and a length of 5.2 m. The driver is connected to the 76.2 mm internal diameter and 6.1 m long barrel (4) by a remotely actuated isolating ball valve (2) and a double diaphragm breech assembly (3). The barrel is connected by the nozzle breech (5) to a contoured hypersonic nozzle (6) which is 1.52 m long and has throat and exit diameters of 12.7 mm and 217 mm, respectively. A free-moving piston is accelerated down the barrel to compress and adiabatically heat the air which then flows through the nozzle. The nozzle, which has a design Mach number of 8.3, delivers the flow to an open jet test section (7) which is connected by a short receiving circular duct (8) to a 1.22 m diameter and 2.44 m long dump tank (9). Tunnel specifications are found in Table 1. A history of the barrel pressure just upstream of the throat of the nozzle is shown in Fig. 2. Due to the double diaphragm technique and accurate setting of initial conditions, it has been shown that these histories are highly repeatable. The double diaphragm technique allows the operator to choose when the tunnel is fired. The pressure history shows a small jump (first reflected shock from the nozzle throat) and then much larger spikes as the piston stops and actually reverses direction. The motion of the piston settles down and a relatively flat, slowly increasing pressure is observed until the run ends and the pressure drops. Typical running times are 10-40 ms, and the maximum effective reservoir pressure is 24 MPa and reservoir temperature can be up to 1300K. The free-stream pitot pressure profiles measured downstream of the nozzle exit show a well-defined inviscid core with excellent radial and axial uniformity. At 10 mm away from the nozzle exit plane, the core is about 140 mm in diameter, at a distance 195 mm from the nozzle exit plane, the core is only slightly smaller than that at 10 mm. The axial gradient of the pitot pressure in the test section core flow is negligible. For the present experiments a new 250 mm diameter viewport has been incorporated between the test section and the dump tank in order to visualize the pipe exit flow by schlieren photography.

The experiments were performed with a barrel pressure of 400 kPa. The test section flow parameters are given in Table 1.

3. THE EXPERIMENTAL MODEL

A 76.2 mm inside diameter and 762 mm long constant area brass pipe having a 2.8 mm wall thickness was used for the present investigation (Fig. 3). The length of the pipe was mainly determined from practical consideration by matching it to the overall test section size and from one-dimensional constant-area supersonic flow analysis for preventing choking in the pipe. In order to minimize leading edge effects on the flow within the pipe, shallow 3° angle wedge sections were used to form the pipe leading edge with a tip thickness of 0.127 mm. The brass provides for material strength and ease in forming the sharp leading edge.

The front end of the pipe is fixed to the test section floor via a support which can rotate around horizontal and vertical axes. The aft end is mounted through a similar support on a traversing mechanism which moves the aft end of the pipe in the vertical and lateral directions with a positioning accuracy of 0.4 mm. This traversing mechanism and two pairs of differential pressure transducers for four wall static pressure taps circumferentially located at 1.27 cm from the aft end of the pipe are used to align the pipe axis with the direction of the test section flow by changing its angles of attack and yaw.

4. INSTRUMENTATION

4.1 Pitot and Static Pressure Probes

Since visualization of the internal pipe flow is impossible, it is necessary to reconstruct the flow from pressure measurements. Therefore, the pipe is instrumented primarily for wall static pressure and in-stream static and pitot pressure measurements.

For wall static pressure distribution measurements the pipe was instrumented with 22 wall static pressure taps with hole ports of $d = 0.686$ mm. For a relatively accurate determination of the locations of shock waves that could be generated in the pipe, static pressure taps were placed at 2.54 cm intervals along the wall of the pipe. Their locations along the pipe are shown in Fig. 4.

A standard straight pitot probe and a curved axis pitot probe (for the boundary layer region) were used for in-stream pitot pressure measurements (see Fig. 5). The boundary layer probe is a flattened pitot stainless steel tube. The tip of the probe is approximately 0.1 mm and 0.89 mm wide. The performance of this probe was compared to the output of the straight pitot probe with a circular orifice (Fig. 5a) in the highly non-uniform and complex flow field at the aft test section of the gun tunnel (with the pipe removed). Although the responses were slightly different, the "steady state" portions of the traces agreed quite well. Since the orifice size of the boundary layer pitot probe is very small relative to the boundary layer thickness measured, $h/\delta << 0.05$ (see Fig. 5b), any influence of the probe size on the performed measurements can be neglected (Ref. 13).

For in-stream static pressure measurements three different designs were considered (Fig.6). A total of eight probes were fabricated: three based on design (a) with the static pressure holes located at 10, 15 and 20 external probe diameters downstream of the cone-cylinder junction; two based on design (b) with two holes located 16 probe diameters downstream of the cone-cylinder junction at angles $\omega = \pm 70^\circ$ and $\omega = \pm 90^\circ$ from the vertical plane; and three probes based on design (c) with three or two holes located 16 diameters downstream of the probe shoulder and at angles 120° for the three-hole case, and ±70° and ±90° for the two-hole case. All other relevant dimensions are given in Fig. 6. These probes were tested in the tunnel test section. Figure 7 depicts the best "steady" static pressure trace obtained by the static pressure probe of design (c) with three 120°-spaced holes, and also the corresponding reservoir and static-to-reservoir pressure ratios multiplied by 10 (which can be read on the right ordinate of the traces). The test section Mach number determined by using this static probe differed only by 0.5% from the test section Mach number of 8.3 measured by using a conventional pitot probe at the same location. Therefore this static probe was chosen for in-stream static pressure measurements in the pipe.

4.2 Measurements of Pitot and Static Pressure Distributions in the Duct

Assuming the flow inside the pipe to be perfectly axisymmetric, in-stream static and pitot pressure measurements were performed by inserting, at each measuring section, two static or two pitot pressure probes into the pipe (conventional straight probe and boundary layer probe) via two diametrically opposed slots in the vertical symmetry plane of the pipe. The probes were moved vertically by a traversing mechanism. The initial position of the boundary layer probe was determined by an electrical contact. Pitot and static pressure probes with distances from the probe stem centreline to the measuring orifices of 63.5 mm were constructed. Static or pitot pressure measurements were performed simultaneously at two points located in the upper and lower halves of the section. Seventeen such double measurements of static and pitot pressures were taken at each section (radial positions are given in Fig. 4). For measurements at the duct exit section, the probes were mounted on a probe holder attached to a vertical traverse.

4.3 Schlieren System

To visualize the fore and aft end flow of the pipe model a schlieren system was employed. The schlieren was set up in a standard two mirror arrangement with a shaped light source at the focus of the first mirror and a knife edge at the focus of the second mirror. Each mirror was 23 cm in diameter and had a focal length of approximately 1.83 m. The mirrors were approximately 7 m apart and the system could be adjusted to provide excellent sensitivity. A standard 10.2 x 12.7 cm view camera capable of holding sheet film or polaroid film was used to record the schlieren photographs. The light source used was a 4-pulse spark source discharging through argon gas. This provided spark stability and a duration of 750 ns. For this investigation only one spark was used.

5. DATA ACQUISITION AND PROCESSING SYSTEM

The pressure history in the gun barrel was measured with a PCB Model 113A22 piezoelectric pressure transducer with a range of 0 to 35 MPa. Pressure is measured with respect to the initial pressure seen by the transducer. The transducer has an excellent frequency response, a short rise time of 1 μs, and a resonant frequency of 500 kHz. The associated power supply, PCB Model 494A amplifier, also provided selectable filters to provide some signal conditioning. All barrel pressure histories in this investigation were filtered at a cutoff frequency of 20 kHz.

Static pressure histories along the wall were measured using primarily Endevco Model 8510B-5 piezoresistive transducers with a range of 0 to 5 psi (0 to 35 kPa). These transducers have excellent risetime response and a typical resonant frequency of 85 kHz. These transducers are differential in type, and reference tubes were attached to the test section via tygon tubing and clipped when the test section pressure stabilized to its lowest value, typically 50 Pa.

Endevco Model 8510-50 (0 to 350 kPa, resonant frequency of 270 kHz) and Model 8530-15 (0 to 100 kPa, resonant frequency of 120 kHz) were used to measure the pitot pressure at different points in the flowfield. Measurements of the static pressure surveys inside the pipe were accomplished with Endevco Model 8514-10 (0 to 70 kPa, resonant frequency of 140 kHz) transducers. The physical construction of these transducers allowed them to be placed very close to the static probes used in the survey.

All pressure histories were recorded by Pacific Transient Recorders Model 9830. In this study up to 10 channels were used to record the data. Each transient recorder had a resolution of 12 bits to ensure a high fidelity record of the signal. The recorders were capable of a maximum of 1 MHz sample rate. An AT class MS-DOS based microcomputer (AST Premium 286) was used to transfer data from the recorders.

The raw data files contained approximately 64,000 data points, each consisting of a 12-bit word representing a voltage at a particular time. For the present investigation, the time interval for each point after trigger was 4 μs or 250,000 samples/second. During the experiments, the various pressure histories started approximately 7 ms after trigger and ran for about 40 ms. Hence, over 12,000 data points were obtained during the time of interest. For the purposes of the present experiments, only every 20th point was used (over 600 data points) in the analysis. Averages were taken over a 10 ms span selected to be more or less constant for the duration of the run. This was sufficient for the majority of cases.

6. EXPERIMENTAL RESULTS

As mentioned above, the pipe was aligned with the nozzle free jet flow direction by changing its angles of attack and yaw and by monitoring the wall pressures at four circumferentially located pressure taps at the aft end of the pipe. The alignment of the pipe was further fine-tuned by comparing, at each measuring section, the pitot pressure magnitudes at two symmetrical points, with respect to the axis (along the vertical diameter). Schlieren photographs of the flow at the entrance and exit of the pipe show that flow has started properly. At the exit, the flow is relatively simple with no waves from the outside of the pipe being generated. Only two shock waves and a boundary layer are seen coming from the exit of the pipe.

Three gun tunnel runs were required to measure the entire wall pressure distribution. During each run, pressures at only eight locations were recorded, with at least pressures at one or two locations being repeatedly measured to check the reproducibility of the results. A typical measured wall pressure distribution is depicted in Fig.8. The wall pressure increases slowly but steadily from the pipe leading edge to a peak value of twice the free stream static pressure at x/D = 5.7, characteristic of a shock-boundary layer interaction. It then decreases rapidly after the interaction zone, and the flow seems to expand in this region. Thereafter it slowly decreases to its pre-interaction value. A slight increase in wall pressure occurs in the last 125 mm of the pipe. Measurements show that the alignment of the pipe axis with the oncoming flow direction has a significant effect on the wall pressure distribution, especially in the shock-wall interaction region, $0.533 < X/L < 7.0$ (Fig. 9). The peak pressure moves slightly upstream as the angle of attack α reaches 1.9°.

In-stream static and pitot pressures were measured at distances x/D = 2.38, 3.0, 5.0, 5.67, 6.33, 8.0, 8.65 and 9.83 from the pipe leading edge. Measurements proceeded from section x/D = 9.83 forward. Static pressure traces generated by the employed probe at certain locations in the pipe flow are shown in Fig. 10. In such instances, the probe was probably very close to a wave structure or in the transition region of the wave. A static pressure trace representative of this region is shown in Fig. 10(a). Moreover, pitot and/or static pressure traces obtained near the axis of symmetry at some sections depicted some flow unsteadiness [see Fig. 10(b)]. As it was not possible to obtain a meaningful average, values of static pressures in these regions of the flow are not reported.

The distributions of measured ratios of local static to (average constant) free stream static pressures and the local total pressure (determined from the Rayleigh pitot tube equations) to average, constant, free stream total pressure are presented in Figs. 11-18. Near the wall static pressure measurements at x/D = 5.0, 6.33, 8.0, 8.65 and 9.8 were within ±5% of the values obtained from wall pressure taps at these locations. Therefore, it was assumed that the static pressure is constant in those near wall regions (represented by white squares in these figures). It was not possible to obtain meaningful near wall static pressure measurements at all other sections.

A distinct pressure jump, characteristic of a shock, is clearly seen in all static and total pressure profiles. The pressure jump at section x/D = 2.4 is radially located in the vicinity of y/D ~ 0.23. At subsequent sections, it seems to move radially towards the wall up to the section x/D = 5.7, Fig. 14, where shock-boundary layer type interaction takes place (Fig. 8). Thereafter, it slowly but steadily moves away from the wall and exits from the pipe at y/D ≈ 0.24.. The shocks generated in the flow seem to be oblique, with possible normal shocks in central portions of the pipe where these oblique shocks reflect off the axis of symmetry. Also, total pressure profiles near the pipe wall give an insight into the boundary layer thickness which notably increases in the downstream portion of the pipe flow. Presented data exhibit some scatter in some regions of the flow which does not exceed ~10% (see, for example Figs. 13, 14 and 18). Mach number profiles in the vicinity of the shock-boundary layer interaction region, X/L = 0.5, 0.533 and 0.633, as well as at the pipe exit, are shown in Fig. 19. These profiles do not change appreciably near the interaction region, although the flow seems to be accelerating in its central "uniform" portion. At the exit the Mach number has reached approximately its free stream value. Figure 20 is a tentative reconstruction of the shock pattern in the pipe based on data presented in Figs. 11-18, if it is assumed that the shock is indicated by a sharp rise in static pressure. The leading "conical" shock wave forms a 9.8° angle with the pipe wall. It converges at an axial position X/L = 0.28 and continued further intersects with the pipe at X/L ≈ 0.57, i.e., where the wall pressure distribution exhibits a sharp increase (Fig. 8). The reflected shock angles calculated from the measured static pressure jump and determined Mach numbers before the jump is very close to 11°, which shows that the reflected shock angle is approximately equal to the incident shock angle. The schlieren photograph of the pipe aft end flow shows two shocks exiting at approximately the same angle and same radial position, as shown in Fig. 20, from the pipe axis. Measured data at sections X/L = 0.24 and 0.3 show that shocks are curved and stronger in the intersection region near X/L ≈ 0.78.

7. ACKNOWLEDGEMENTS

This research was financially supported by Johns Hopkins University Applied Physics Laboratory, the U.S. Air Force Wright Aeronautical Laboratories under Contract F33615-87-2748, and the Natural Sciences and Engineering Research Council Canada under Grant No. SEF8703. Their support is gratefully acknowledged.

REFERENCES

1. E. P. Neumann and F. Lustwerk, "Supersonic Diffusers for Wind Tunnels," J. Appl. Mech., No. 6, 1949, pp. 195-202.
2. F. Lustwerk, "The Influence of Boundary Layer on the Normal Shock Configuration," MIT, Cambridge, Massachusetts, Meteor Report No. 9661, Sept. 1950.
3. J. R. Kenneth and R. Goldstein, "Fully Developed Turbulent Supersonic Flow in a Rectangular Duct," AIAA J., No. 8, 1966, pp. 1331-1336.
4. A. A. Fejer, et al, "An Investigation of Constant Area Supersonic Flow Diffusion," ARL 64-81, Aerospace Research Labs., Wright-Patterson Air Force Base, Ohio, 1965.
5. G. H. McLafferty, E. L. Krasnoff, E. D. Ranard, W. G. Rose, and R. D. Vergara, "Investigation of Turbojet Inlet Design Parameters," United Aircraft Corp., East Hartford, Connecticut, Report R-0790-13, Dec. 1955.
6. F. S. Billig, G. L. Dugger, and P. J. Waltrup, "Inlet-Combustor Interface Problems in Scramjet Engines," 1st International Symposium on Air Breathing Engines, International Airbreathing Propulsion Committee, Marseilles, France, June 1972.
7. P. J. Waltrup and F. S. Billig, "Precombustion Shock Structure in Scramjet Engines," AIAA Paper 72-1181, New Orleans, Louisiana, 1972.
8. P. J. Waltrup and F. S. Billig, "Structure of Shock Waves in Cylindrical Ducts," AIAA J., Vol. 11, No. 10, 1973, pp. 1404-1408.
9. P. J Waltrup and J. M. Cameron, "Wall Shear and Boundary-Layer Measurements in Shock Separated Flow," AIAA J., Vol. 12, No. 6, June 1974, pp. 878-880.
10. D. Om and M. E. Childs, "An Experimental Investigation of Multiple Shock Wave/ Turbulent Boundary Layer Interactions in a Circular Duct," AIAA Preprint No. 83, 1744, 1983.
11. F. B. Gessner, S. D. Ferguson, and C. M. Lo, "Experiments on Supersonic Turbulent Flow Development in a Square Duct," AIAA J., 1987, 25, No. 5, pp. 690-697.
12. D. O. Davis and F. B. Gessner, "Furtgher Experiments on Supersonic Turbulent Flow Development in a Square Duct," AIAA J., 1989, Vol. 27, No. 8.
13. J. M. Allen, "Impact Probe Displacement in a Supersonic Turbulent Boundary Layer," AIAA J., Vol. 10, No. 4.

14. Wilhelm Behrens, "Viscous Interaction Effects on a Static Pressure Probe at M=6", AIAA J., Vol. 1, No. 12, pp. 2864-2866.

15. J. Don Gray, "Evaluation of Probes for Measuring Static Pressure in Spersonic and Hypersonic Flows," AEDC-TR-71-265.

16. M. J. Williams, "Static Pressure Probe at Mach Number 7.5," ARL/A.327, Australia.

17. S. H. Chue, "Pressure Probe for Fluid Measurement," Prog. Aerospace Sci., 1975, 16, No. 12, pp. 147-223.

Table 1. Hypersonic Gun Tunnel — Specifications

Physical Dimensions		
Tunnel length	16 m	
Gun barrel length	6.1 m	
Gun barrel ID	76.2 mm	
Test Section		
Width	635 mm	
Height	610 mm	
Length	610 mm	
Nozzle exit diameter	217 mm	
Piston material	Aluminum 7075-T6	
Piston mass	96 g	
Initial Tunnel Operating Conditions		
Reservoir pressure	20.5 ± 0.2 MPa	
Barrel pressure	100 to 800 kPa	
Test section pressure	50 ± 10 Pa	
Tunnel Flow Properties		
Freestream pitot pressure	183 kPa	
Freestream static pressure	2.06 kPa	
Stagnation pressure upstream of the throat	26.5 MPa (current nozzle)	
Usable Flow Test Time		
200 kPa in barrel	10 ms	
400 kPa in barrel	30 ms	
600 kPa in barrel	40 ms	
800 kPa in barrel	40 ms	
Total Temperatures and Reynolds Numbers (estimates)		
	T_t (K)	Re (per meter)
200 kPa in barrel	1220	23×10^6
400 kPa in barrel	970	3.378×10^7
600 kPa in barrel	890	39×10^6
800 kPa in barrel	830	44×10^6

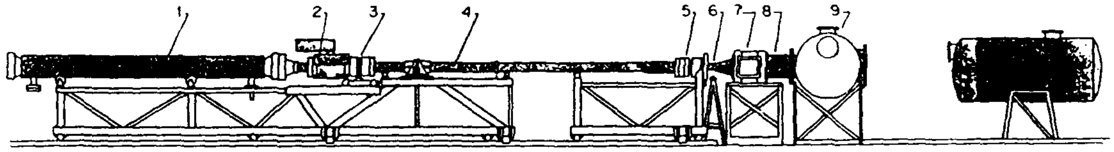

Fig. 1 Schematic diagram of the Hypersonic Gun Tunnel.

1. High pressure reservoir (driver)
2. Remote controlled isolating ball valve
3. Double-diaphragm station breech lock
4. 6.1m gun barrel
5. Nozzle throat station breech lock
6. Convergent-divergent nozzle
7. Test section
8. Diffuser
9. Dump tank

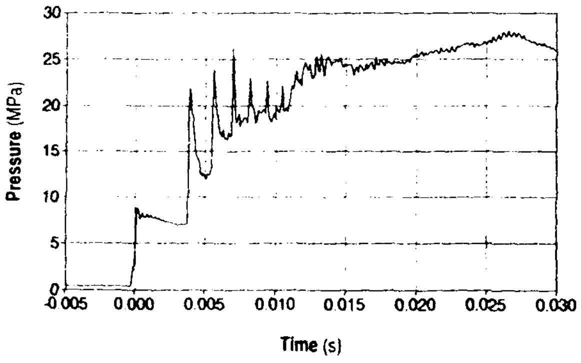

Fig 2 Typical barrel pressure history in the Hypersonic Gun Tunnel.
Initial barrel pressure of 400 kPa

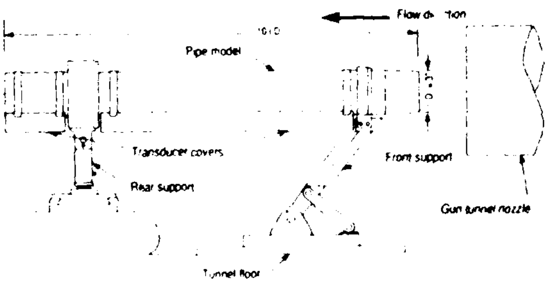
Flow direction
Pipe model
Transducer covers
Rear support
Front support
Gun tunnel nozzle
Tunnel floor

Fig 3 Schematic diagram of pipe model and mounting details

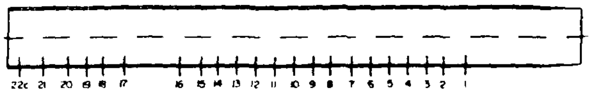
22c
21
20
19
18
17
16
15
14
13
12
11
10
9
8
7
6
5
4
3
2
1

Section	Position (mm)	Position (x/D)
1	152.4	2.00
2	181.0	2.38
3	203.2	2.67
4	228.6	3.00
5	254.0	3.33
6	279.4	3.67
7	304.8	4.00
8	333.4	4.38
9	355.6	4.67
10	381.0	5.00
11	406.4	5.33

Section	Position (mm)	Position (x/D)
12	431.8	5.67
13	457.2	6.00
14	482.6	6.33
15	504.8	6.63
16	533.4	7.00
17	608.0	7.98
18	636.6	8.35
19	658.0	8.65
20	684.2	8.98
21	717.6	9.42
22c	749.3	9.83

34 Position Radial Survey

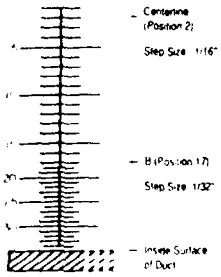
Centerline (Position 2)
Step Size 1/16"
B (Position 17)
Step Size 1/32"
Inside Surface of Duct

Position	(mm)	(x/D)
1	39.69	0.5208
2	38.10	0.5000
3	36.51	0.4792
4	34.90	0.4503
5	33.34	0.4375
6	31.75	0.4167
7	30.16	0.3958
8	28.58	0.3750
9	26.99	0.3542
10	25.40	0.3333
11	23.01	0.3125
12	22.23	0.2917
13	20.64	0.2708
14	19.05	0.2500
15	17.46	0.2292
16	15.08	0.2082
17	14.29	0.1875

Position	(mm)	(x/D)
18	13.49	0.1771
19	12.70	0.1667
20	11.91	0.1562
21	11.11	0.1458
22	10.32	0.1254
23	9.53	0.1250
24	8.73	0.1146
25	7.94	0.1042
26	7.14	0.0938
27	6.25	0.0833
28	5.56	0.0729
29	4.76	0.0625
30	3.97	0.0521
31	3.18	0.0417
32	2.38	0.0313
33	1.59	0.0208
34	0.79	0.0104

Fig 4 Locations of wall static pressure taps and radial positions
of in stream pressure probe at the same locations

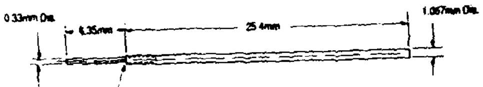
0.33mm Dia.
6.35mm
25.4mm
1.067mm Dia.
Silver Solder

(a)

Straight 2-section pitot probe

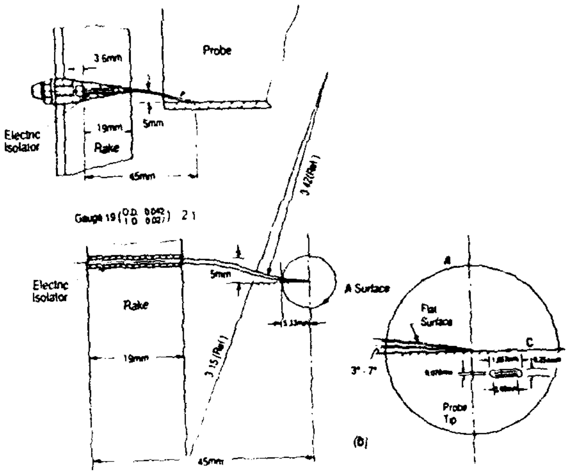
Probe
3.6mm
Electric Isolator
19mm
5mm
Rake
45mm
Gauge 19
2:1
3.42(Ref.)
Electric Isolator
Rake
5mm
A Surface
19mm
3.15(Ref.)
45mm
(b)
A
Flat Surface
C
3°-7°
Probe Tip

Fig 5 Geometrical dimensions of the Pitot Pressure Probe

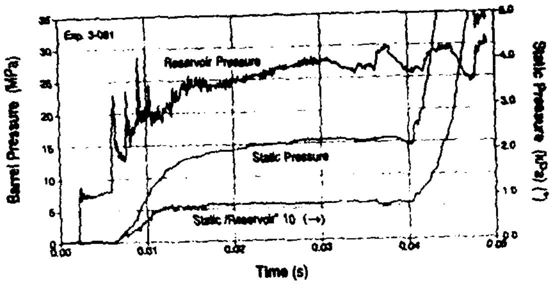

Fig. 7 Static pressure history in the tunnel test section
(Initial barrel pressure 400kPa.)

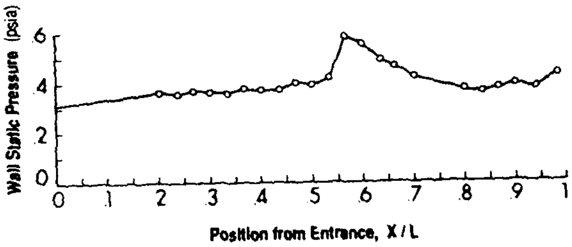

Fig. 8 Wall static pressure distribution in a constant area duct.

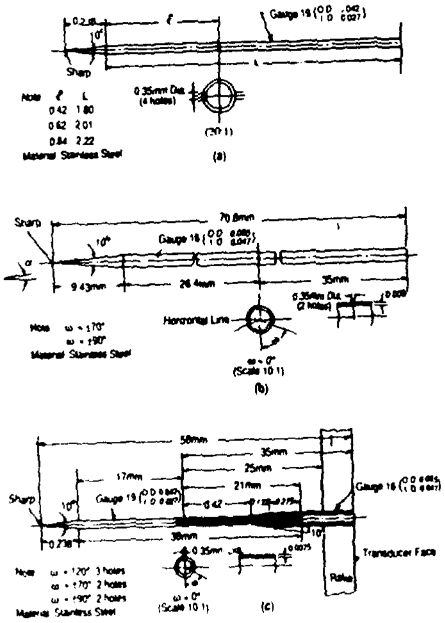
0.2
ℓ
Gauge 19 (O.D. .042 / I.D. 0.027)
10°
L
Sharp
0.35mm Dia. (4 holes)
Note ℓ L
0.42 1.80
0.62 2.01
0.84 2.22
Material Stainless Steel
(20:1)
(a)
Sharp
70.8mm
10°
Gauge 18 (O.D. 0.065 / I.D. 0.047)
α
9.43mm
26.4mm
35mm
0.35mm Dia. (2 holes)
Horizontal Line
Note ω = ±70°
ω = ±90°
Material Stainless Steel
ω = 0°
(Scale 10:1)
(b)
58mm
35mm
25mm
17mm
21mm
Sharp
10°
Gauge 19
Gauge 16
38mm
0.278
0.35mm
Transducer Face
Rake
Note ω = ±120° 3 holes
ω = ±70° 2 holes
ω = ±90° 2 holes
Material Stainless Steel
ω = 0°
(Scale 10:1)
(c)

Fig 6 Static pressure probe designs

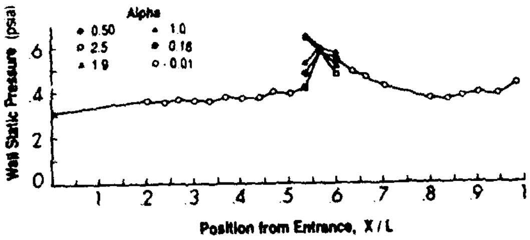

Fig. 9 Effect of angle of attack on wall pressure distribution.

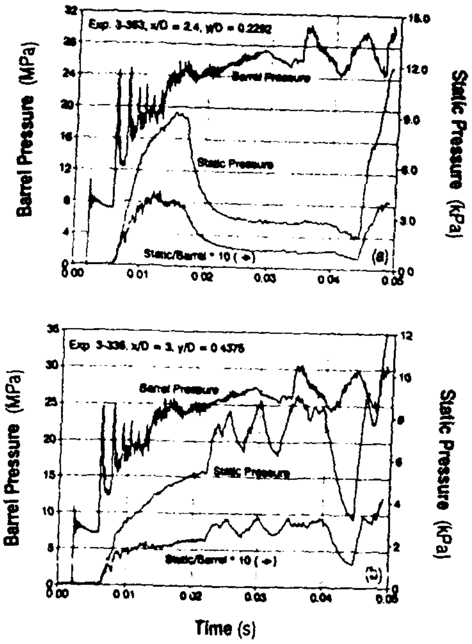

Fig. 10 Barrel pressure history P_0 and in-stream static pressure history.

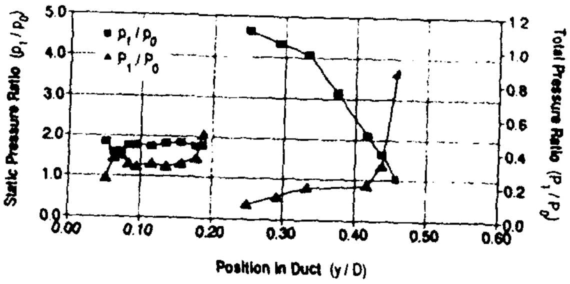

Fig 11 Static and total pressure ratio profiles at x/D = 2.4

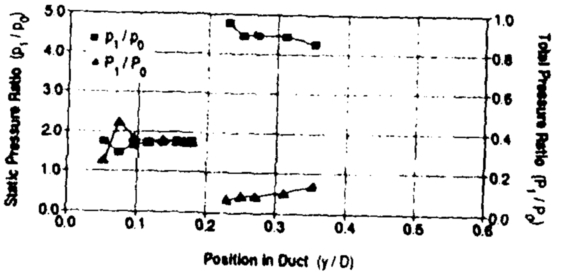

Fig 12 Static and total pressure ratio profiles at x/D = 3.0

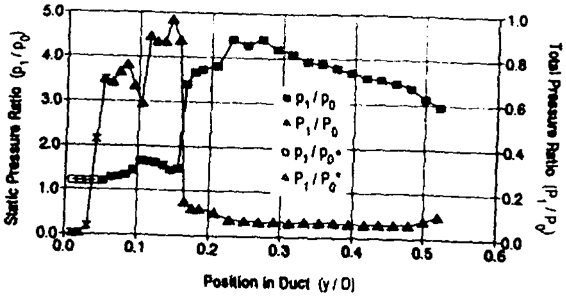

Fig. 13 Static and total pressure ratio profiles at x/D = 5.0 (*- projected values)

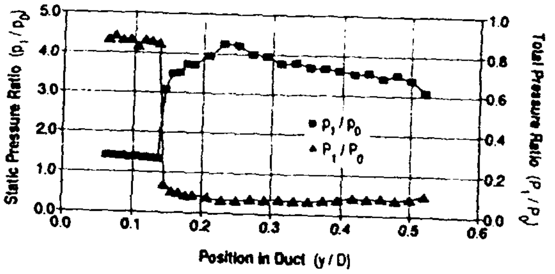

Fig. 14 Static and total pressure ratio profiles at x/D = 5.7

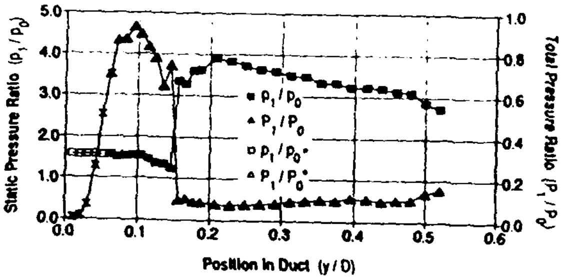

Fig. 15 Static and total pressure ratio profiles at x/D = 6.33 (* - projected values)

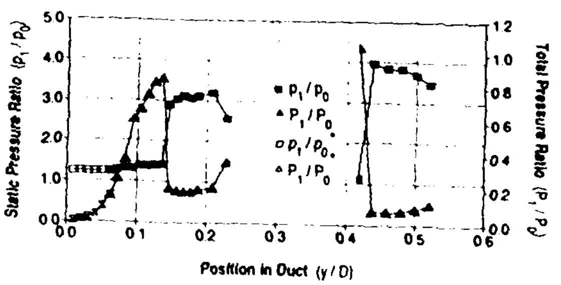

Fig 16 Static and total pressure ratio profiles at x/D = 8.0 (* - projected values)

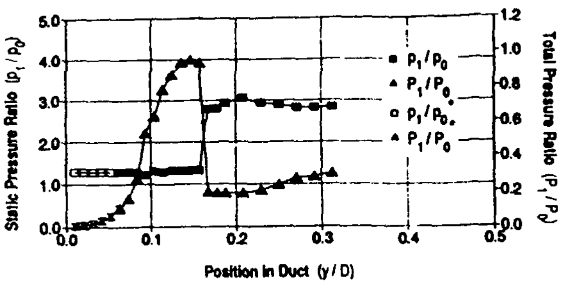

Fig. 17 Static and total pressure ratio profiles at x/D = 8.65 (* - projected values)

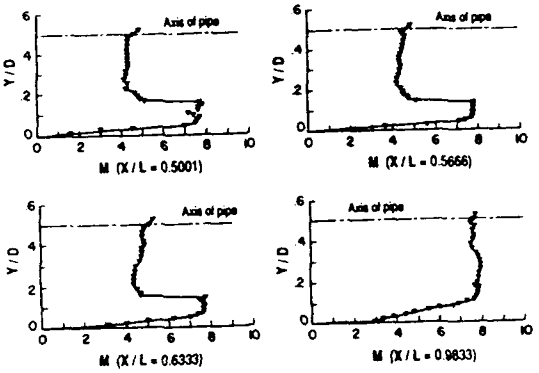

Fig. 19 Mach number profile.

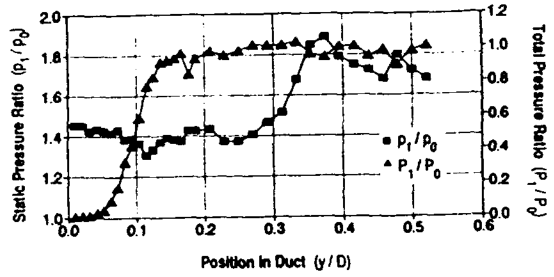

Fig. 18 Static and total pressure ratio profiles at x/D = 9.8

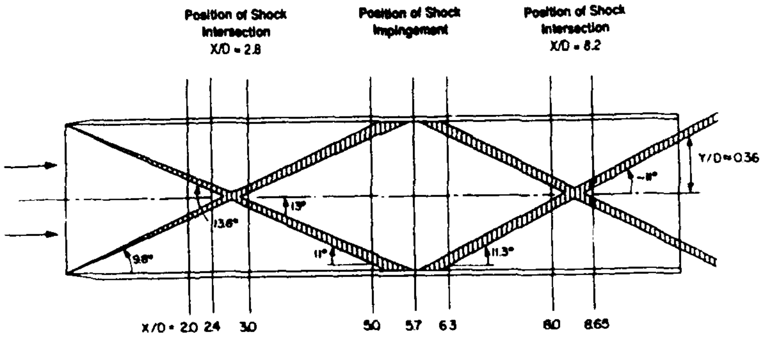
Position of Shock Intersection X/D = 2.8
Position of Shock Impingement
Position of Shock Intersection X/D = 8.2
Y/D≈0.36
~11°
13°
13.6°
9.8°
11°
11.3°
X/D = 2.0
2.4
3.0
5.0
5.7
6.3
8.0
8.65

Fig 20 Reconstructed shock pattern inside the pipe at M = 8.3

Experimental and Computational Comparisons of Mach 6 High Reynolds Number Heat Transfer and Skin Friction

Lello Galassi[1]
Norman E Scaggs[2]
Wright Laboratory
Wright-Patterson Air Force Base, Ohio 45433-6553
USA

Summary

Wind tunnel measurements on a flat plate, ogive cylinder and a compression ramp at zero angle-of-attack are compared to CFD predictions of the flow parameters. These models provide a zero-pressure gradient, favorable-pressure gradient, and an adverse-pressure gradient flow condition, respectively. Results are presented for surface pressure and temperature distributions, boundary layer surveys, heat transfer rates, and local skin friction coefficients. Test conditions were varied over a free-stream Reynolds number range of 0.45–9.1 (10^7) per meter, at a nominal Mach number of 6. Wind tunnel measurements on the three models were made using static pressure ports, embedded thermocouples, coaxial heat transfer gauges, slug calorimeters, Preston tube skin friction devices, and skin friction force balances. Boundary layer profiles were measured with total temperature and pitot pressure probes and with laser doppler velocimetry. Parabolized Navier-Stokes and full Navier-Stokes code predictions of the measured parameters are compared to experimental measurements.

Results indicate surface pressure distributions are easily predicted by the CFD codes used in this study and for the simple geometries modeled. For CFD codes which predict the surface heat transfer rate accurately, the local skin friction coefficient agrees to within 7–10 percent of the measured data for favorable-pressure gradient and zero-pressure gradient configurations. For adverse-pressure gradients, the code used in this study did not predict skin friction values accurately, although heat transfer predictions matched the data. Large gradients in the hypersonic boundary layer require dense grids near the model surface in order for CFD codes to accurately predict the surface heat transfer rate and the local skin friction coefficient. Additionally, dense grids in the streamwise direction are necessary to properly resolve the boundary layer for adverse-pressure gradients.

List of Symbols

C_f	Skin friction coefficient
C_p	Specific heat at constant pressure
d	Tube diameter (mm)
h	Convection heat transfer coefficient ($\frac{W}{m^2K}$)
M	Mach number
P	Surface static pressure (kPa)
P_{t2}	Probe stagnation pressure (kPa)
Pr	Free-stream Prandtl number
$\dot{q}$	Total heat flux (W/m^2)
$\dot{q}_{cond}$	Heat conduction (W/m^2)
$\dot{q}_{conv}$	Heat convection (W/m^2)
$\dot{q}_{rad}$	Heat radiation (W/m^2)
R	Universal gas constant (8.314 $\frac{J}{kg-molK}$)
Re_x	Reynolds number based on length
r_c	Reference temperature recovery factor
r_p	Temperature probe recovery factor
St	Stanton number
T_o	Local total temperature (K)
T_t	Measured total temperature (K)
U_∞	Free-stream velocity ($\frac{m}{s}$)
u	X-component velocity ($\frac{m}{s}$)
x	Distance along the reference X-axis (mm)
y	Distance along the reference Y-axis (mm)
z	Distance along the reference Z-axiz (mm)
δ	Boundary layer thickness (mm)
δ^*	Displacement thickness (mm)
γ	Ratio of specific heats (1.4)
μ	Dynamic viscosity coefficient ($\frac{kg}{ms}$)
ν	Local kinematic viscosity ($\frac{m^2}{s}$)
ρ	Static fluid density ($\frac{kg}{m^3}$)
θ	Momentum thickness (mm)

I. Introduction

The prediction of aerodynamic performance of hypersonic configurations will be accomplished, to a great extent, through utilization of various computational fluid dynamics (CFD) methods. In order to validate these CFD codes, their numerical predictions of the flight conditions must be evaluated at the conditions produced in ground test conditions and/or at conditions generated in flight test programs. There are three primary parameters that must be generated in flight test programs, namely, external surface pressure distributions, surface heat transfer rate distributions and local skin friction distributions. Measured values of these parameters are required for proper validation of a CFD code parameter predictions. Surface pressure distributions can be readily measured through ground tests or flight tests. Heat transfer rate distributions, although routinely measured during ground tests, are not so easily measured in flight tests. However, the measurement of skin friction coefficients on simple hypersonic configurations is not readily done during either ground tests or during flight tests. Complex hypersonic vehicle configurations pose even greater challenges for experimental measurement of the flow parameters. A procedure for the elimation or reduction of skin friction measurements is highly desirable.

---

[1] Hypersonic Aeromechanical Engineer, Wright Laboratory, United States Air Force Systems Command

[2] Hypersonic Engineering, Technical Manager, United States Air Force Systems Command

This experimental and numerical investigation tested the hypothesis of using CFD codes to accurately predict heat transfer and other state variables of the hypersonic flow around a body and extend the prediction to include skin friction for like conditions.

Three body configurations were tested at a nominal Mach number of 6 in a high-Reynolds number facility. Several numerical models were computed for comparison to experimental results. The numerical models include a flat plate, ogive cylinder, and an isentropic compression ramp, representing a zero, favorable and adverse pressure gradient, respectively.

II. Apparatus

Mach 6 High Reynolds Facility

The Mach 6 high Reynolds number test facility is an intermittent blowdown-type wind tunnel with an axisymmetric 31.4 cm exit diameter nozzle. Nozzle wall boundary layer effects reduce the actual diameter of the test core to approximately 25.4 cm. The test section is an open jet which can be adjusted from 43.2 to 71.1 cm. The air supply to the tunnel is heated to 500-611 K in order to prevent liquefaction of the air in the area of the test section. The tunnel reservoir pressure can be varied from 0.62-13.8 MPa, which produces a freestream Reynolds number of 0.45-9.8 (10^7) per meter. The tunnel is exhausted into a large vacuum sphere, below tunnel reservoir pressures of 4.2 MPa, otherwise, the flow is exhausted directly to the atmosphere. Laminar through fully-developed turbulent boundary layers can be produced on the models. The tunnel simulates flight conditions at Mach 6 from 15.24-36.58 kilometer altitude. A more complete description of this tunnel and its capabilities have been reported by Fiore [1].

Test models are injected into the open jet with a hydraulic model support system. Total temperature and stagnation pressure probes are moved throughout the tunnel test section on an x-y-z probe drive system. Side windows on each door of the tunnel test section are of schlieren quality, allowing visualization of the shock waves and boundary layers. Additionally, laser dopler velocimetry (LDV) is permissible through the windows.

Experimental Models

A photograph of the flat plate test model mounted in the wind tunnel is shown in Figure 1. The model is constructed of 17-4 PH stainless steel and is 47.0 cm long and 39.4 cm wide. There are 29 static pressure ports spaced 2.54 cm midspan along the chord of the model. The first pressure port is located 15.86 cm behind the model leading edge. Additionally, there are nine chromel-constantan (Type E) coaxial heat transfer gauges and seven Type-E thermocouples embedded within the model. Type-E heat transfer gauges and thermocouples were chosen in order to maintain electrical compatibility with the 17-4 PH stainless steel. A slug calorimeter, skin friction force balance, or Preston tube skin friction device may be mounted in a milled port midspan, centered 43.82 cm behind the leading edge.

Figure 2 shows the ogive cylinder test model. The model is 7.62 cm in diameter and 38.10 cm long and constructed of 17-4 PH stainless steel. There are 23 static pressure ports, 6 chromel-constantan coaxial heat transfer gauges, and 11 Type-E thermocouples within the model. Two ports were milled into the model centered x = 20.32 cm and x = 29.85 cm behind the model tip for mounting a slug calorimeter, skin friction force balance, or the Preston tube friction device.

Figure 3 shows the isentropic compression ramp test model. The model is constructed of 17-4 PH stainless steel and is 47.0 cm long, 39.37 cm wide, and has a compressive surface cut on a 349.3 cm radius. Two flow-directing fences are shown on either side of the compressive surface. The model is equipped with 29 static pressure ports, 9 chromel-constantan coaxial heat transfer gauges, and 7 Type-E thermocouples distributed midspan along the model's chord. A single port was milled 43.82 cm behind the leading edge of the model, midspan, in order to accept a slug calorimeter, skin friction force balance, or a Preston tube friction device.

Instrumentation

A schematic of the skin friction force balance is shown in Figure 4. The skin friction force balance is a self-contained unit with a model-mating surface to permit flush mounting with the model surface. The balance has a 0.94 cm diameter floating element and is self-nulling to the center with a 0.076 mm circumferential gap. The center element is statically balanced about the center of the support housing. Surface shear force is measured directly with the center element. The gauge was calibrated against known weights to within 0.3 percent of full-scale readings prior to each test.

A Preston tube skin friction device was used to measure local skin friction. The Preston tube is a pitot tube resting on the model surface and inline to the oncoming flow. The Preston tube unit was designed to fit into the milled port of each model. A #304 annealed stainless steel tube, 1.57 mm and 1.19 mm outside and inside diameter, respectively, was used to measure the local stagnation pressure. Local static pressure was measured using two static pressure ports. The local shear stress is determined from the measurement of the local stagnation pressure near the surface of the model, the surface static pressure and the model surface temperature in the region of the Preston tube device. The reader is referred to Preston's [2] work for an in-depth study of this skin friction device.

Probe stagnation pressure profiles in the boundary layer were measured using a pitot pressure probe. A total temperature probe similar to that designed by Winkler [3] was used to measure total temperature boundary layer profiles. On the compression ramp, a combined boundary layer probe was used. The combined probe used a Winkler probe with stagnation pressure probes attached to either side of the Winkler probe. A schematic of this probe is shown in Figure 5. Although this probe created a larger probe-model surface interference, the benefits of simultaneous pressure and temperature measurements at the same location were desirable.

III. Procedures

Experimental Procedures

The measured tunnel parameters were reservoir pressure and temperature, model surface pressures, model surface temperatures and model surface heat transfer rates. Corresponding surface shear forces were also measured. In the boundary layer, the total temperature and stagnation pressure were measured with total temperature and stagnation probes, respectively. Local velocities were measured using LDV. Throughout data reduction, the static pressure through the boundary layer was assumed to be constant in a direction normal to the model surface.

In the boundary layer, the Mach number profile was determined from the Rayleigh Pitot formula

$$\frac{P}{P_{t2}} = \frac{\left(\frac{2\gamma}{\gamma+1}M^2 - \frac{\gamma-1}{\gamma+1}\right)^{\frac{1}{\gamma-1}}}{\left(\frac{\gamma+1}{2}M^2\right)^{\frac{\gamma}{\gamma-1}}} \tag{1}$$

P_{t2} is the flow stagnation pressure measured behind two shocks; a weak oblique shock generated by the finite leading edge of the model and a normal shock generated at the entrance to the pitot probe. The Mach number is solved for iteratively.

The ratio of the local total tempearture to static temperature is given by

$$\frac{T_o}{T} = 1 + \frac{\gamma - 1}{2}M^2 \tag{2}$$

A temperature probe recovery factor is defined as

$$r_p = \frac{T_t - T}{T_o - T} \tag{3}$$

which is dependent on the design of the temperature probe. The total temperature probe was calibrated for all tunnel flow conditions in the free-stream. Probe recovery factors were measured as 0.94, 0.97, 0.98, 0.98 and 0.99 for 0.69 MPa, 2.07 MPa, 4.83 MPa, 9.65 MPa, and 13.65 MPa free-stream stagnation conditions, respectively.

With Equations 2 and 3 and the Mach number profile determined from Equation 1, the local total temperature through the boundary layer is formulated as

$$T_o = \frac{T_t}{r_p + \frac{(1-r_p)}{1+\frac{\gamma-1}{2}M^2}} \tag{4}$$

The static temperature distribution (T) is computed using Equation 2. The velocity profile is determined from the Mach number profile and the speed of sound profile which is based on the static temperature profile. Density profiles are determined from the ideal gas equation of state and static temperature profile.

The boundary layer momentum thickness is defined as

$$\theta = \int_0^\infty \frac{\rho u}{\rho_e u_e}\left(1 - \frac{u}{u_e}\right) dy \tag{5}$$

In discrete form Equation 5 becomes

$$\theta = \sum_{i=1}^{n} \frac{\rho_i u_i}{\rho_e u_\infty}\left(1 - \frac{u_i}{u_e}\right) \Delta y \tag{6}$$

In Equations 5 and 6, u_e is the streamwise component of velocity at the boundary layer edge and ρ_e, the corresponding fluid density. The boundary layer thickness (δ) is arbitrarily assigned as that height above the model surface where a negative normal pressure gradient ($\frac{-dp}{dz}$) is detected.

The displacement thickness (δ^*) is calculated in a similar method as the calculation of the momentum thickness

$$\delta^* = \int_0^\infty \left(1 - \frac{\rho u}{\rho_e u_e}\right) dy \tag{7}$$

which becomes in discrete form

$$\delta^* = \sum_{i=1}^{n} \left(1 - \frac{\rho_i u_i}{\rho_e u_e}\right) \Delta y \tag{8}$$

Skin friction (C_f) was measured using two types of instrumentation. The first method uses the pressure measurements from the Preston tube device. Skin friction is computed as the root-mean-square (rms) value of three methods of calulation using the Preston tube data. The first method of calulation uses the Yanta [4] equation.

$$C_{f_Y} = \frac{0.07361 \left(\frac{M_P}{M_e}\right)^{1.71233}}{\left[\frac{\rho_e}{\rho^*}\left(\frac{\rho^* u_e d}{\mu^*}\right)^2\right]^{0.14364}} \tag{9}$$

where ρ^* corresponds to the fluid density at the reference temperature, M_P is the Preston tube Mach number, M_e the edge Mach number, and d the inside diameter of the Preston tube.

The second method of computing the skin friction was developed by Hopkins and Keener [5] and is similar to Equation 9.

$$C_{f_{HK}} = \frac{0.0522 \left(\frac{M_P}{M_e}\right)^{1.75}}{\left[\frac{\rho_e}{\rho^*}\left(\frac{\rho^* u_e d}{\mu^*}\right)^2\right]^{0.125}} \tag{10}$$

The last method uses Allen's semi-empirical relationship [6]

$$C_{f_A} = \frac{\rho_e}{\rho^*}\left[\frac{10^{a \log_{10}^2 F_1 + b \log_{10} F_1 - c}}{\frac{\mu_e}{\mu^*}\frac{\rho_e u_e d}{\mu_e}}\right]^2 \tag{11}$$

where the value of the constants a, b, and c have been determined as 0.01659, 0.7665, 0.4681, respectively. The function F_1 is written as

$$F_1 = \frac{\nu_e \rho_e u_e d M_P}{\nu^* \mu_e M_e}\sqrt{\frac{1 + \frac{\gamma-1}{2} M_e^2}{1 + \frac{\gamma-1}{2} M_P^2}} \tag{12}$$

The reference value of viscosities and density were computed from the reference temperature method employed by Sommer and Short [7].

$$T^* = T_e\left(0.55 + 0.035 M_e^2 + 0.45\frac{T_w}{T_e}\right) \tag{13}$$

The corresponding density was computed as

$$\rho^* = \frac{P_w}{RT^*} \tag{14}$$

where P_w is the static wall pressure. The coefficient of viscosity is computed using Keyes' viscosity relationship [8].

$$\mu = \frac{1.113 \times 10^{-8}\sqrt{1.8T}}{1 + \frac{122.22}{T(10^{5/T})}} \tag{15}$$

The reference value of viscosity (μ^*) is computed by substituting the reference temperature (T^*) for the static temperature (T) in Equation 15. Equation 15 is in the form where T is in degrees Kelvin. The Preston Mach number used throughout Equations 9–12 is computed by substitution of the total pressure measured by the Preston tube device for the probe total pressure (P_{t2}) in Equation 1.

The rms value of skin friction coefficient is defined as

$$C_f = \sqrt{\frac{1}{3}\left(C_{f_Y}^2 + C_{f_{HK}}^2 + C_{f_A}^2\right)} \tag{16}$$

A second method of skin friction measurement was obtained using a floating element force balance device where the shear force was measured directly. Using the measured shear force, the shear stress (τ_w) is computed by dividing by the surface area of the force balance sensor. The skin friction coefficient is computed as

$$C_f = \frac{2\tau_w}{\rho_e u_e^2} \tag{17}$$

Surface heat transfer distributions were measured using coaxial heat transfer gauges. The surface and subsurface temperatures were measured over a finite time interval. The heat transfer rate ($\dot{q}$) into the surface was computed using a one-dimensional finite element model developed by Hayes [9] for heat transfer measurements using coaxial heat transfer gauges. The energy balance on the surface is presented as follows:

$$\dot{q} = \dot{q}_{cond} + \dot{q}_{conv} + \dot{q}_{rad} \tag{18}$$

Radiation losses were computed to be on the order of less than one percent of the combined heat losses, hence, neglected in the calculation of the total heat flux.

From Equation 18, a non-dimensional heat transfer coefficient is presented as the Stanton number (St),

$$St = \frac{\dot{q}}{(T_{aw} - T_w)\rho C_p u_e} \tag{19}$$

In Equation 19, T_{aw} is the adiabatic wall temperature, T_w is the surface temperature, and C_p is the specific heat of the air at constant pressure. The adiabatic wall temperature, T_{aw} is computed as

$$T_{aw} = T_\infty + r_c \frac{U_\infty^2}{2C_p} \qquad (20)$$

In Equation 20, r_c is the recovery factor and is computed as $r_c = Pr^{\frac{1}{2}}$ for laminar boundary layers and as $r_c = Pr^{\frac{1}{3}}$ for turbulent boundary layers.

Typical measured and experimental uncertainties are given in Table 1 for a tunnel stagnation pressure of 4.83 MPa. In general, the uncertainties increased for lower stagnation pressures.

Table 1: Calculated and Measured Uncertainties

$P_o = 4.83$ MPa	
parameter	*uncertainty* (%)
Re_x	1.7
C_f	4.5
St	10.0
U_∞	1.0
M	0.9
ρ	5.8
P	5.8
T	0.3

CFD Codes

Experimental results were compared to CFD numerical predictions. The flat plate and the compression ramp were modelled using a two-dimensional full-Navier-Stokes code. This code (FDL2D) was developed in-house by Shang [10], and has a wide range of applicability to hypersonic flows. FDL2D uses a MacCormack predictor-corrector numerical scheme and forms an explicit set of equations which are solved for using a tridiagonal block solver. Both the flat plate and compression ramp models included a finite leading edge in the numerical grid in order to more accurately model the finite thickness of the experimental models' leading edge.

The ogive cylinder was modelled by Byers [11] using a vectorizing version of the parabolized Navier-Stokes (PNS) numerical code developed by Stalnaker, et al., [12]. The PNS code uses an implicit solver to generate a conical starting solution at the nose of the ogive cylinder prior to marching an explicit solution along the body. An implicit conical starting solution was applied at $\frac{x}{L} = 0.016$; thereafter, an explicit Beam-Warming scheme was used to solve for the flow parameters along the body. Both FDL2D and PNS codes use a Baldwin-Lomax numerical scheme to model fully-developed turbulence.

IV. Results and Discussion

Flat Plate Tests and CFD Comparisons

A typical static pressure distribution on the flat plate is presented in Figure 6 for a tunnel stagnation pressure of 4.83 MPa. The corresponding CFD prediction of static pressure on the flat plate is shown for comparison. As indicated by the error bar, the numerical prediction lies within the uncertainty of the data. Although not shown, there was favorable agreement between CFD predictions of the static pressure distribution and measurements for all tunnel stagnation pressures tested. Surface pressure was not measured near the leading edge of the model ($\frac{x}{L} = 0$), however, the CFD code does predict a finite leading edge effect and the static pressure near the weak oblique shock increases noticeably. In general, agreement between data and measurement improved as the tunnel stagnation pressure increased.

Figure 7 shows the non-dimensional boundary layer ($\frac{\delta}{L}$) measured midspan along the chord of the flat plate for three free-stream stagnation pressures, 2.07, 4.83, and 9.65 MPa. Numerical predictions are included for comparison to data. As seen, the boundary layer growth is nearly linear along the length of the plate, and the overall thickness decreases as the free-stream stagnation pressure, hence, Reynolds number increases. CFD predictions of boundary layer growth exhibit the same linear growth trend, however, the CFD models tended to underpredict the growth of the boundary layer along the chord length of the plate. This difference between data and CFD prediction is attributed to the difference in criteria used by the code and measurements to determine the boundary layer edge. For experimental measurements, the boundary layer edge was determined as the location in the boundary layer where a negative gradient in the probe stagnation pressure ($\frac{-dp}{dz}$) was detected. On the other hand, the code used an integral method to measure the increase of axial momentum ($\frac{d(\rho u)}{dz}$) in order to locate the boundary layer edge. The boundary layer edge was determined by the code as the position in the boundary layer where

$$d(\rho u) < 0.01 \sum_{z=0}^{\delta} \rho u \qquad (21)$$

Boundary layer measurements for the flat plate are given in Table 2.

Velocity profiles determined from total pressure and temperature profiles and LDV measurements on the flat plate are shown in Figure 8 for three tunnel stagnation pressures. The increased deviation of LDV velocity measurements from velocity profiles derived from measured stagnation pressure and total temperature probe

Table 2: Flat Plate: Boundary Layer Parameters

$\frac{x}{L}$	Re_x (10^7)	Re_θ	δ (mm)	δ^* (mm)	θ (10^{-2} mm)
$P_o = 2.07$ MPa, $M_\infty = 5.71$					
0.34	0.13473	238.49	3.94	1.13	1.82
0.61	0.25395	224.60	7.49	1.91	1.64
0.82	0.33204	1249.02	9.53	2.87	9.45
0.93	0.38845	2020.66	10.54	3.50	14.78
$P_o = 4.83$ MPa, $M_\infty = 5.77$					
0.34	0.30456	503.73	3.43	0.89	1.70
0.61	0.59880	2868.63	5.97	1.98	8.88
0.82	0.67924	4382.77	6.99	2.91	16.21
0.93	0.84464	4835.04	8.00	3.49	16.27
$P_o = 9.65$ MPa, $M_\infty = 5.78$					
0.34	0.66757	2050.59	3.43	0.97	3.16
0.61	1.16635	6753.99	4.95	2.11	10.73
0.82	1.62145	10003.23	6.53	2.84	15.47
0.93	1.79959	9798.99	7.49	3.07	15.47

near the wall are attributed to the error introduced by a probe-surface effect in a thin (4-6 mm) boundary layer. Correlation of the two methods of measuring velocity improve as the distance from the wall increases. The stagnation pressure and total temperature derived velocity profiles indicate an overshoot of the velocity near 70 percent of the boundary layer thickness which was not observed with LDV measurements. This velocity overshoot is not physical, but results from calculation of velocity from the probe total temperature and stagnation pressure data. Total temperature profiles exhibited a similar overshoot. Although not shown, velocity profiles were compared to 1/7 power laws and Van Driest velocity transformations and found to compare favorably to data for cases where the boundary layer was fully turbulent.

Figure 9 shows the non-dimensional heat transfer rate on the flat plate over a range of Reynolds numbers and free-stream stagnation pressures. Code predictions are shown for comparison with the data. The data corresponding to a 0.69 MPa stagnation pressure indicates the boundary layer transitioned from laminar to a fully-developed turbulent boundary layer. Additionally, the first datum for $P_o = 2.07$ MPa, ($x = 15.875$ cm from the leading edge) suggests the boundary layer was transitional. All remaining data shown in Figure 9 corresponds to a fully-developed turbulent boundary layer.

An attempt was made to obtain the best match of test conditions with the CFD boundary conditions corresponding to the location of the skin friction gauge. As seen in Figure 9, boundary layer transition was not predicted by the code (FDL2D). The code employs either all laminar or all turbulent boundary layer models, but boundary layer transition is not modelled. In the regions corresponding to a fully-developed turbulent boundary layer, the agreement between data and numerical predictions was acceptable. Although agreement between the CFD heat transfer predictions and the measured heat transfer rates decreases as Reynolds number increases, a general trend of decreasing Stanton number for increasing Reynolds number was maintained.

Figure 10 shows the skin friction measured at $x = 43.8$ cm over a range of length Reynolds numbers and free-stream stagnation pressures. The open symbols represent skin friction force balance measurements. The solid symbols represent measurements at the same location and test conditions using a Preston tube device. Numerical predictions are shown for comparison with the data. Generally, there is satisfactory agreement between data and the code skin friction predictions. Larger scatter in the data is exhibited at lower Reynolds numbers. This scatter in data at lower Reynolds numbers may be attributed to the transitional nature of the boundary layer, as demonstrated by the heat transfer rates shown in Figure 9. Numerical predictions compare favorably with the Preston tube data, but tend to overpredict the force balance data by about 7-10 percent. In one case ($P_o = 2.07$ MPa), the CFD code underpredicted the data by about 3 percent. At higher Reynolds numbers, the increase in error between numerical prediction and data suggests the code exhibits some limitations to accurately predict skin friction at higher Reynolds numbers.

Ogive Cylinder Tests and CFD Comparisons

A typical static pressure distribution along the length of an ogive cylinder is shown in Figure 11 for a tunnel stagnation pressure of 4.83 MPa. As evidenced by the heat transfer results shown later, this free-stream stagnation pressure produced a transitional boundary layer along the entire length of the ogive cylinder. The datum at $\frac{x}{L} = 0.6$ seems to be an anomaly and is attributed to instrumentation error.

Comparison to the Parabolized Navier Stokes (PNS) numerical prediction is indicated with a solid line. Along the forebody of the ogive cylinder, the PNS code over-predicted the static surface pressure distribution. This trend continued throughout all static pressure distributions on the ogive cylinder. The PNS code over-predicts the initial static pressure because a conical starting solution was used to start the space-marching solution over the remainder of the body. Since cones experience higher surface pressures for a given flow condition than ogive cylinders, the initial solution over-predicts the measured pressure. The error may have been further compounded with the use of a Vigneron sublayer model in the PNS code. The Vigneron sublayer model uses a split pressure term in its formulation and any numerical error introduced is not easily dissipated with the Beam-Warming solver used in the PNS code. As seen, error in the pressure distribution does not dissipate until reaching the shoulder of the ogive cylinder. Thereafter, correlation of CFD predictions with data is excellent.

Figure 12 presents the non-dimensional boundary layer thickness measured at two positions on the ogive cylinder for two tunnel stagnation pressures. No CFD comparisons are shown. At $P_o = 4.83$ MPa, the boundary layer exhibited very little growth which suggests a laminar boundary layer existed over much of the ogive cylinder surface. At $P_o = 9.65$ MPa, and $\frac{x}{L} = 0.53$, the boundary layer was turbulent and is fifty percent thicker than the laminar boundary layer present at $P_o = 4.83$ MPa.

Velocity profiles on the ogive cylinder at two positions were calculated from stagnation pressure and total temperature profiles and by assuming a constant static pressure through the boundary layer. Figure 13 shows the velocity profiles for both tunnel stagnation pressures of 4.83 and 9.65 MPa. Similar to the velocity profiles shown for the flat plate, the velocity overshoots the edge value by about seven percent due to the influence of the measured total temperature overshoot. LDV measurements were attempted on the model, however, the seeded flow was not able to negotiate the relatively large curvature of the ogive section of the model, thus, prevented effective LDV measurements. An investigation on the seed particle dynamics for this model was conducted by Maurice[13]. Particle dynamics were combined with CFD predicted flow fields in order to study the flow path of the seed at hypersonic conditions. Results of the study are indicated in Figure 14. The majority of the seed is deflected by the ogive nose outside of the boundary layer while the few remaining seed particles within the boundary layer impacted the surface of the ogive section. Analysis by Maurice[14] into seed velocity biasing as seed passes through an oblique shock confirms velocity biasing occurs with silicon oil seed. From Figure 15, silicon oil seed on the order of 5.0 microns (the average size of the seed used during the ogive cylinder LDV tests), experiences significant biasing. In Figure 15, $V_{N-SHOCK}$ and $X_{N-SHOCK}$ are components of the velocity and distance normal to the shock. In order to obtain LDV measurements in the boundary layer of the ogive cylinder, a seed material on the order of 1.0 micron would be required to negotiate the curvature of the ogive section and eliminate seed particle velocity bias as the seed material passes through the oblique shock and into the boundary layer.

Figure 16 presents the non-dimensional heat transfer rate, the Stanton number, for the ogive cylinder surface over a range of tunnel free-stream stagnation pressures from 0.69–13.79 MPa and length Reynolds numbers. Heat transfer measurements were conducted only along the cylinder section of the ogive cylinder. Both Stanton numbers and Reynolds numbers are shown in Figure 16 plotted on log-log axes. Similarly, PNS numerical solutions are shown for comparison to the measurements.

Two distinct levels of heating rate are indicated by the data in Figure 16. The lower Stanton numbers correspond to a laminar boundary layer present for tunnel free-stream stagnation pressures of 0.69–2.07 MPa. A transition from laminar to a turbulent boundary layer is clearly indicated by heat transfer measurements corresponding to a 4.83 MPa free-stream stagnation pressure and a length Reynolds number of $8(10^6)$. The boundary layer remained turbulent for the higher stagnation pressures, 9.65 and 13.79 MPa, as indicated by the higher heat transfer rates. Compared to previous data shown for the flat plate, the favorable pressure gradient along the ogive cylinder surface significantly delayed boundary layer transition from laminar to turbulent until higher tunnel reservoir pressures were reached.

PNS numerical predictions of the Stanton number indicate the code under-predicts the heat transfer rate near the intersection of the ogive and cylinder portion of the model. In the area near the shoulder of the ogive cylinder, code predictions of a large drop in heat transfer rate suggest boundary layer separation, however, no separation was detected during the actual wind tunnel tests. Conversely, the code over-predicted the static pressure near the shoulder of the ogive cylinder as seen in Figure 11.

The PNS code under-predicted the heat transfer rate measurements made at 9.65 MPa. This under-prediction was due to a ten degree (Kelvin) mismatch of wall temperature boundary conditions for the PNS code with the measurements. This indicates the overall sensitivity of the code to the wall temperature boundary condition. Heat transfer measurements made at 13.79 MPa compare favorably to the PNS code predictions. In the area where skin friction was measured, the heat transfer rate matched the code predictions well. In all cases, numerous iterations were required in order to match wall boundary conditions and grid spacing for the PNS code prior to obtaining a satisfactory solution. An in-depth explanation of the application of the PNS code is given by Byers[11].

From the PNS solutions used to predict experimental heat transfer rates, the skin friction coefficient is compared for both the data and PNS code prediction in Figure 17. Similar to Figure 16, this figure is shown with log-log axes, over the same range of free-stream stagnation pressures and for the same range of length Reynolds numbers. The overall variation of skin friction with Reynolds number is predicted by the PNS code, however, in general, the code predicted the skin friction only to within 10 percent of the measured values. The very large velocity and temperature gradients present in a hypersonic boundary layer pose a challenging problem for CFD models. The actual application of the PNS code required refinement of numerous grids prior to obtaining a converged solution. General trends were predicted by the PNS code, including transition of the boundary layer from laminar to turbulent and the associated rise in skin friction values. Due to the limited amount of experimental data, further speculation as to the overall agreement of predictions with data is withheld until further experimental testing is completed.

Compression Ramp Tests and CFD Comparisons

The static pressure distribution on the compression ramp is shown in Figure 18 for a 9.65 MPa free-stream stagnation pressure along with the corresponding CFD prediction of static surface pressure distribution. Although not shown, for all test conditions, there was excellent agreement between data and CFD predictions of the static pressure distributions.

Figure 19 shows the measured boundary layer thickness as determined from stagnation pressure and total temperature profiles as compared to the numerical predictions for 2.07, 4.83, and 9.65 MPa stagnation pressures. Measurements indicate a relatively constant growth of the boundary layer was present for all free-stream stagnation pressures tested, independent of Reynolds number. The compressive nature of the boundary layer tended to control the boundary layer growth to a greater extent than that observed with a zero pressure gradient (flat plate) boundary layer; this suggests a more complete energy exchange existed between the fluid entrained in the boundary layer and the free-stream. CFD results predict a thinner boundary layer over the compression ramp surface than what was measured. However, due to the intrusive effects associated with probe measurements in thin hypersonic boundary layers, close agreement between the probe measured boundary layer thickness and the CFD predictions is not expected.

Boundary layer profiles were measured on the compression ramp at four stations along the upper surface using stagnation pressure and total temperature probes and LDV techniques. For the sake of clarity, only velocity profiles at a single location ($\frac{x}{L} = 0.93$), mid-span and for three free-stream stagnation pressures are shown in Figure 20. Velocity profiles deduced from the boundary layer probe measurements are represented by the solid symbols. LDV data is shown as open symbols connected by the solid line. Figure 20 indicates there is poor agreement between the two methods of measurement, except at the boundary layer edge. The poor agreement between LDV measured velocities and deduced velocities from probe data is attributed to the probe measured total temperature profiles. For the ramp, the total temperature overshoot was on the order of 10–20 percent. Thus, a large velocity overshoot, up to 10 percent or more of the edge velocity, results from calculations using the total temperature profile, assuming a constant static pressure profile through the boundary layer. The actual velocity profile is more accurately indicated by the LDV measurements, however, some seed particle velocity biasing has been measured and uncertainties in the LDV data increase near the wall. Although not shown, CFD velocity profiles more closely resemble the LDV velocity profiles without any velocity overshoot.

The total temperature overshoot measured on the compression ramp was 3–4 times that measured on the flat plate or ogive cylinder. Several total temperature probes were used, each carefully calibrated. The results from each probe indicate the same level of temperature overshoot. This large overshoot is attributed to increased viscous interaction that occurs between a compressive boundary layer and the free-steam. Nonetheless, the extent of the total temperature overshoot was unexpected and bares further examination. Unfortunately, very little data on a hypersonic compressive boundary layer exists for a similar model configuration, hence, no comparisons are made.

Heat transfer results are shown for the compression ramp in Figure 21 over a range of free-stream stagnation pressures (0.69–13.79 MPa). Surface heat transfer measurements are indicated by the open symbols and CFD predictions are shown as a solid line for each range of free-stream stagnation pressures. Several trends are noted. First, at 0.69 MPa, the heat transfer results indicate the boundary layer was not fully turbulent until near the aft section of the compression ramp. All other heat transfer measurements, except for one datum at $P_o = 2.07$ MPa, indicate the boundary layer was fully turbulent. Second, the shape of the isentropic compression surface increased the heat transfer rate from the leading edge to the trailing edge of the compression ramp. Increased heat transfer along the surface of the compression ramp supports the earlier discussion of a more complete energy exchange for compressive boundary layers than for favorable or even zero-pressure gradient boundary layers. This increase in heat transfer is seen in Figure 21 as a rapid rise in the Stanton number for each data set at each free-stream stagnation pressure. Lastly, CFD predictions agree very well with the measurements, except where the boundary layer was not fully turbulent. CFD predictions were made using FDL2D, and on the average, 35,000–40,000 iterations were completed for a solution at each pressure.

Skin friction measurements and CFD predictions using FDL2D corresponding to the flow conditions shown in Figure 21 are shown in Figure 22. Skin friction measurements (solid symbols) were made using the skin friction force balance at $\frac{x}{L} = 0.93$, for 0.69–13.79 MPa free-stream stagnation pressures. Skin friction measurements were repeatable, except for measurements made at $P_o = 0.69$ MPa where the boundary layer may have been transitional and the uncertainty of static pressure measurements is increased due to instrumentation limitations. CFD predictions are indicated by the solid line. Although the FDL2D code predicts the proper trends for skin friction, generally, the CFD predictions do not agree with the skin friction force balance measurements. At 0.69 MPa, CFD predictions of C_f are acceptable, however, for increased Reynolds numbers, the agreement between CFD solutions and data degrades, similar to CFD predictions of skin friction for the flat plate shown in Figure 9. Much of the CFD error is attributed to the inability to properly model boundary layer transition. Additionally, since gradients in the axial direction may not be considered negligible for adverse pressure gradients, much larger axial grids than the 250 axial grid points used for this study may be necessary. Such large grids will increase the overall time needed per iteration of the solution. With over 40,000 iterations required per solution, a fully-implicit code may be preferred over the fully-explicit FDL2D code.

V. Conclusions

This study provided an assessment of the ability of two CFD codes to predict heat transfer and skin friction for three generic shapes; a flat plate, an ogive cylinder, and an isentropic compression ramp in Mach 6 flow conditions.

Static pressure distributions were easily predicted by the codes for all configurations tested, although the PNS code over-predicted the static pressure over the ogive section of the ogive cylinder. The discrepency between the data and the PNS code predictions is attributed to the conical starting solution used by the code to model the ogive nose. An ogive starting solution would be more appropriate for favorable pressure gradient configurations.

As a result of the probe-surface interactions, comparisons of probe-measured boundary layer profiles to LDV measurements and CFD numerical predictions involves a large uncertainty in the probe data. Boundary layer probes are relatively large compared to 2–3 mm thick hypersonic boundary layer. Boundary layer measurements were found to be further complicated by LV seed particle biasing, large viscous interactions at the boundary layer edge, and limited probe capabilities. For example, on the compression ramp the total temperature profile measured through the boundary layer exceeded the free-stream stagnation temperature by as much as 20 percent. This suggests a very large viscous interaction occurs near the boundary layer edge. More investigation is needed into this phenomena. A combined temperature-pressure probe, reduced in scale from the probe size used in this investigation is recommended for more accurate probe measurements. Likewise, very low density seed material is needed to overcome seed particle velocity biasing if LDV measurements are to be used to measure hypersonic flow conditions in the presence of large velocity gradients within hypersonic boundary layers.

Heat transfer predictions are possible using either code, alth~~ough a~~ large number of iterations (time steps) and dense numerical grids are required to accurately resolve the temperature gradients and velocity gradients in the boundary layer. For those CFD solutions where the heat transfer was carefully matched to data, skin friction predictions were marginal at best. General trends were predicted, but the discrepancy between prediction and measurement increased as Reynolds number increased. This error is attributed to the inability to model boundary layer transition from laminar to turbulent. The Baldwin-Lomax turbulence model proved insufficient in this respect. The authors recommend the use of a turbulence model which models boundary layer transition, such as the $k-\epsilon$ model.

Acknowledgements

The authors would like to thank the NASP program office for supporting this study under the technical maturation program. We would also like to acknowledge the support of the many individuals throughout the experimental tests. Special thanks are due to John Leugers, Matt Wagner and Hank Baust for their continued support of mechanical instrumentation and data acquisition systems. Additionally, George Siebert, Mark Maurice, Charles Tyler, Linda Smith and Dean Miller provided their expertise in obtaining LDV measurements. The authors would like to thank the numerous technical personnel who were essential in setting up the models and instrumentation, and operation of the facilities; notably, Max Hillsamer, SSgt John Williams (USAF), Rick Allen, and Tom Norris. Special thanks are due to Tony Brigalli who kept us on track by fixing the unfixable problems and facilitated testing.

References

[1] Anthony J. Fiore. Aerodynamic Calibration of the Aerospace Research Laboratories M-6 High Reynolds Number Facility, Final Report. Technical Report ARL-TR-75-0028, Aerospace Research Laboratory, Wright-Patterson AFB, OH, February 1975.

[2] J. H. Preston. The Determination of Turbulent Skin Friction by Means of Pitot Tubes. *Journal of Royal Aeronautical Society*, 58:109–121, 1954.

[3] Eva M. Winkler. Design and Calibration of Stagnation Temperature Probes for Use at High Supersonic Speeds and Elevated Temperatures. *Journal of Applied Physics*, 25:231–233, February 1954.

[4] W. J. Yanta, D. L. Bratt, and R. E. Lee. An Experimental Investigation of the Preston Probe Including Effects of Heat Transfer, Compressibility, and Favorable Pressure Gradient. *AIAA Preprint*, 69-648, June 1969.

[5] E. J. Hopkins and E. R. Keener. Use of Preston Tubes for Measuring Hypersonic Turbulent Friction. *AIAA Preprint*, 69-345, April 1969.

[6] Jerry M. Allen. Evaluation of Compressible-Flow Preston Tube Calibration. Technical Report NASA TN-D-7190, NASA, May 1973.

[7] Simon C. Sommer and Barbara J. Short. Free-Flight Measurement of Turbulent Boundary Layer Skin Friction in the Presence of Severe Aerodynamic Heating at Mach Numbers from 2.8 to 7.0. Technical Report TN3391, NACA, June 1955.

[8] F. G. Keyes. A Summary of Viscosity and Heat-Conduction Data for He, A, H_2, O_2, N_2, CO, CO_2, H_2O, and Air. *Transactions of the American Society of Mechanical Engineers*, 73:589–596, August 1950.

[9] James R. Hayes. Application of Coaxial Heat Transfer Gauges to Wind Tunnel Measurements. Interdivision technical report, Aeromechanics Division, Flight Dynamics Directorate, Wright Laboratory, Wright-Patterson AFB, OH, 1989.

[10] Joseph Shang. A Two-Dimensional Full Navier-Stokes Flow Solver. Code developed by Dr. Joseph Shang and further modifications by D. P. Rizzetta of Wright Laboratory, Wright-Patterson AFB, OH, 1973.

[11] Captain Richard H. Byers. Skin Friction and Heat Transfer Predictions for Hypersonic Turbulent Flow Over an Ogive Cylinder. Master's thesis, Air Force Institute of Technology, Wright-Patterson AFB, OH, 1990.

[12] J. F. Stalnaker, et. al. Improvements To The AFWAL Parabolized Navier-Stokes Flow Code Formulation. Technical Report AFWAL-TR-86-3076, Flight Dynamics Laboratory, Air Force Wright Aeronautical Laboratories, Wright-Patterson AFB, OH, September 1986.

[13] Maurice, Mark S. Fluid Measurement And Instrumentation Forum. ASME-SED-108, June 1991. Paper title - "The Effect of High Speed Expansion Turns on LV Measurement Bias".

[14] Maurice, Mark S. A Particle Size Distribution Technique Using Conventional Laser Velocimetry Measurements. July 1992.

Figure 1: Flat plate wind tunnel model

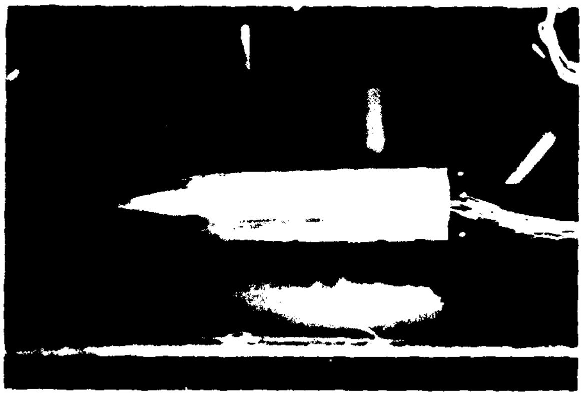

Figure 2: Ogive cylinder wind tunnel model

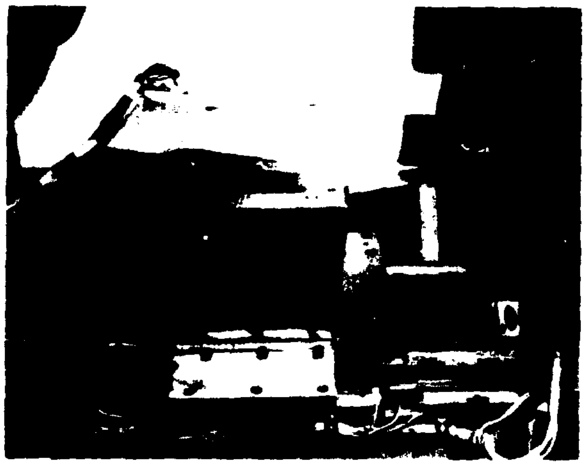

Figure 3. Compression ramp wind tunnel model

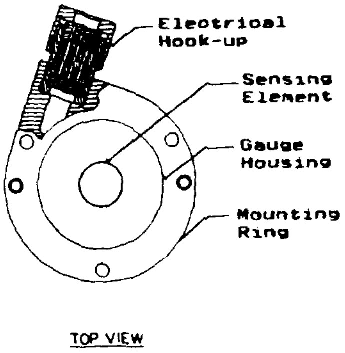
Electrical Hook-up
Sensing Element
Gauge Housing
Mounting Ring
TOP VIEW

Figure 4: Schematic of skin friction force balance

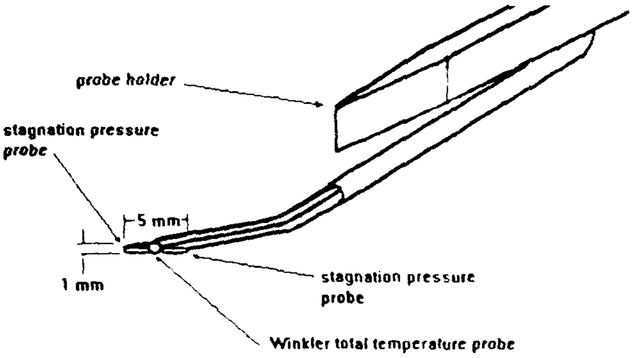
probe holder
stagnation pressure probe
5 mm
1 mm
stagnation pressure probe
Winkler total temperature probe

Figure 5: Schematic of the combined pressure and temperature boundary layer probe

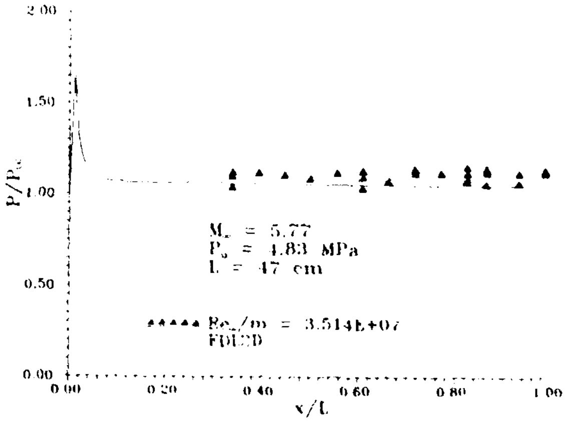

Figure 6: Static pressure distribution on a flat plate

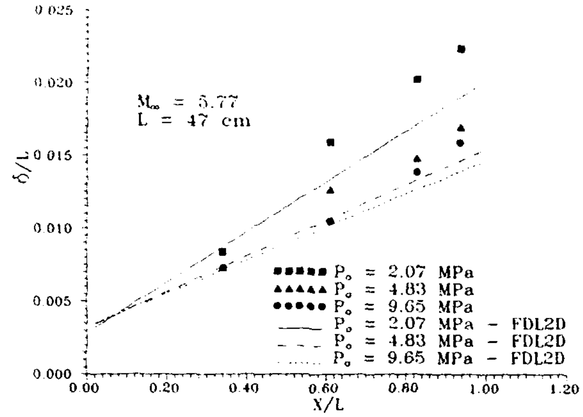

Figure 7: Boundary layer thickness on a flat plate

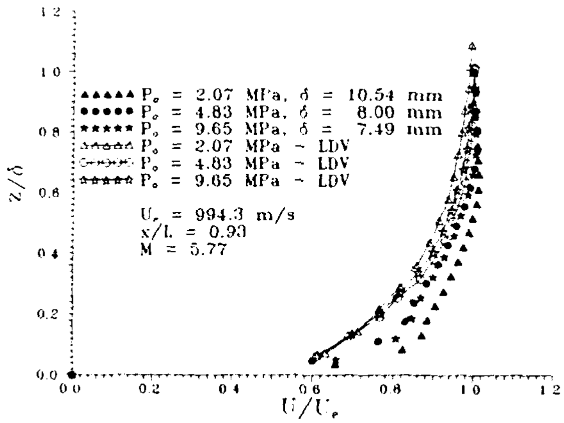

Figure 8: Velocity profiles on a flat plate

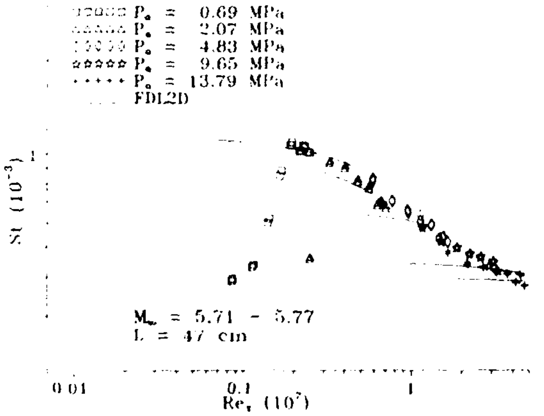

Figure 9: Heat transfer measurements on a flat plate

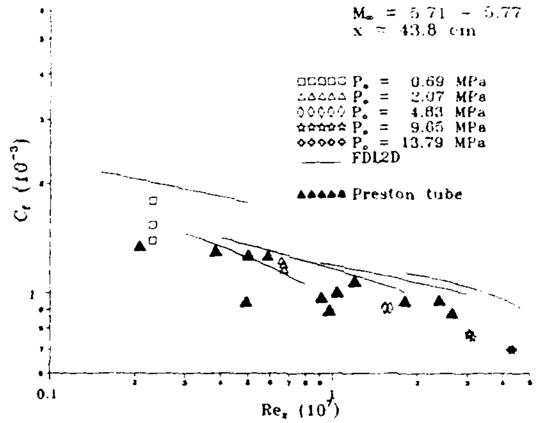

Figure 10: Skin friction measurements on a flat plate

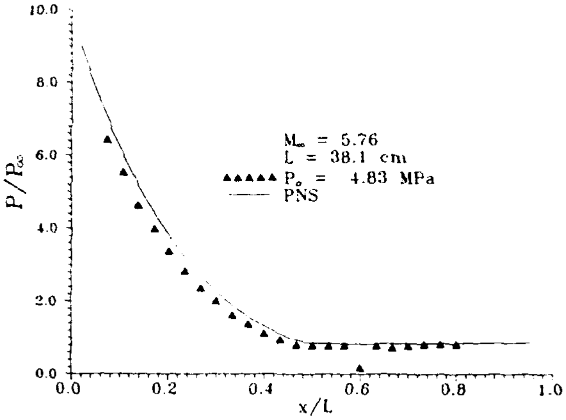

Figure 11: Static pressure distribution on an ogive cylinder

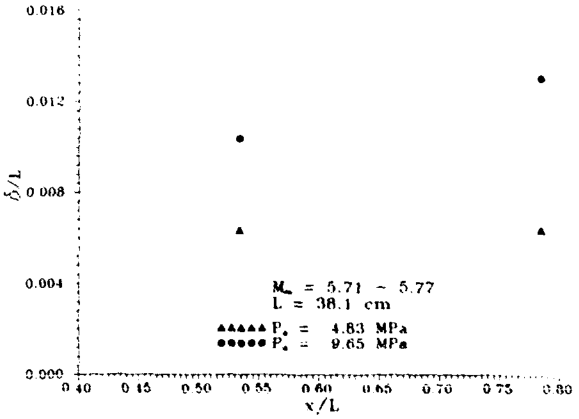

Figure 12: Boundary layer thickness on an ogive cylinder

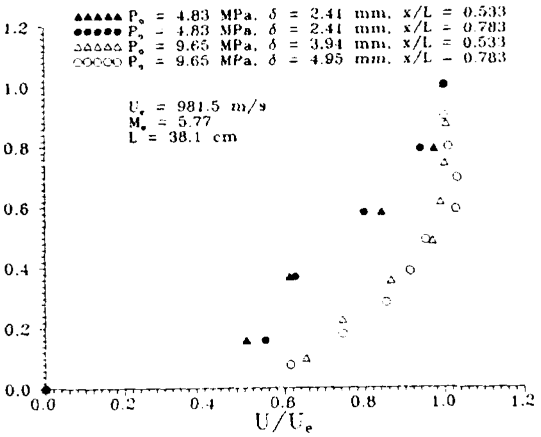

Figure 13: Boundary layer velocity profiles on an ogive cylinder

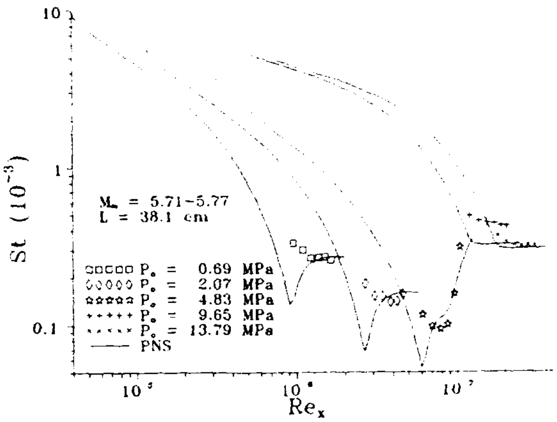

Figure 16: Heat transfer rate on an ogive cylinder

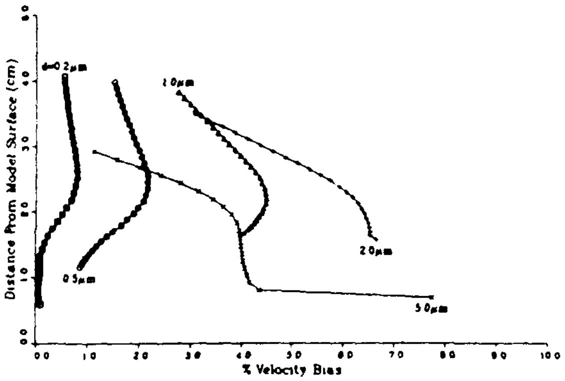

Figure 14: Velocity biasing of LDV seed particles on an ogive cylinder (Maurice[13])

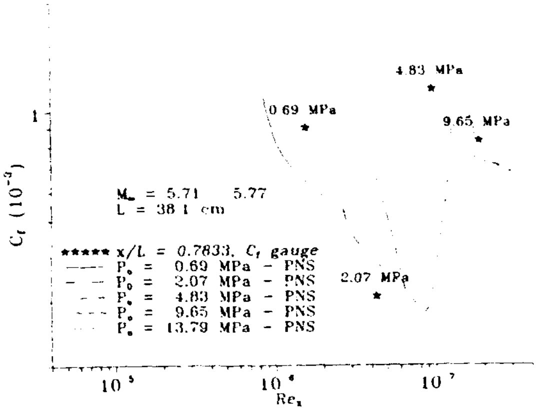

Figure 17: Skin friction on an ogive cylinder

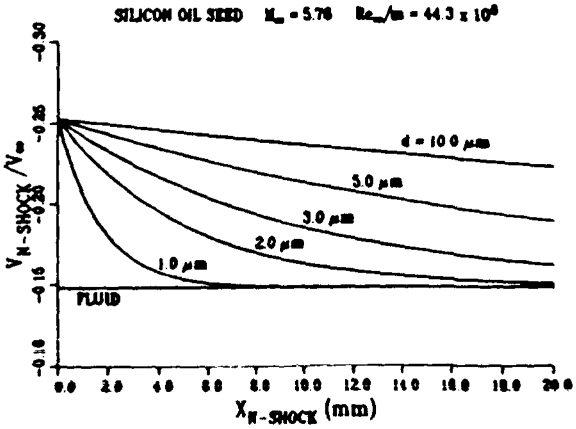

Figure 15: Velocity biasing of silicon oil seed through an oblique shock (Maurice[14])

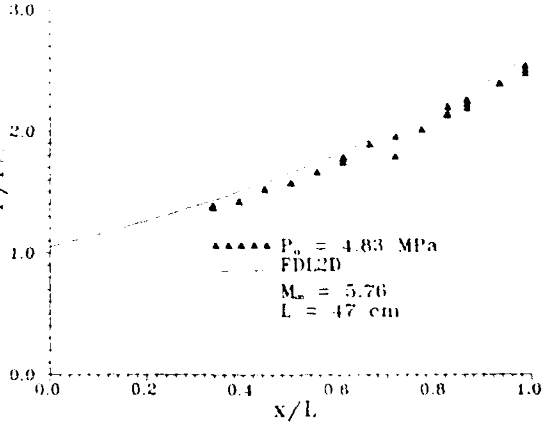

Figure 18: Static surface pressure distribution on a compression ramp

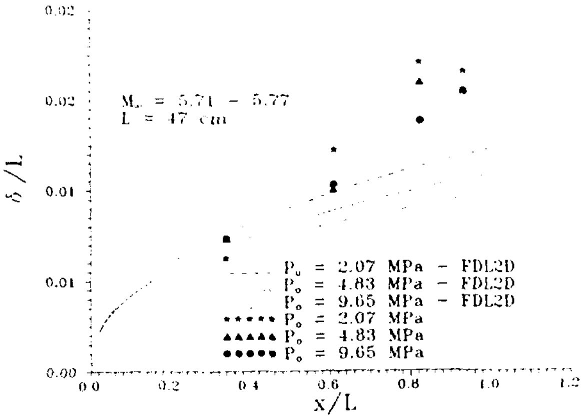

Figure 19: Boundary layer thickness on the compression ramp

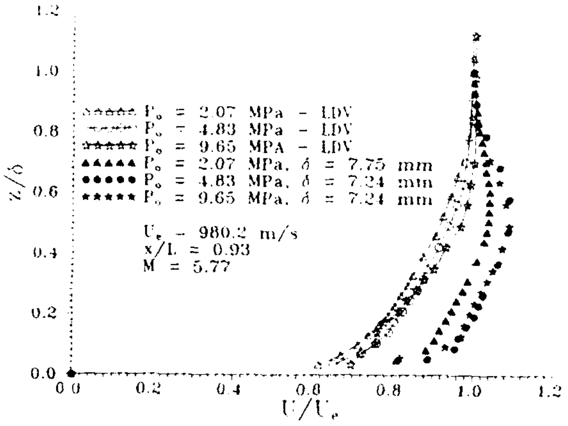

Figure 20: Compression Ramp: Measured velocity profiles

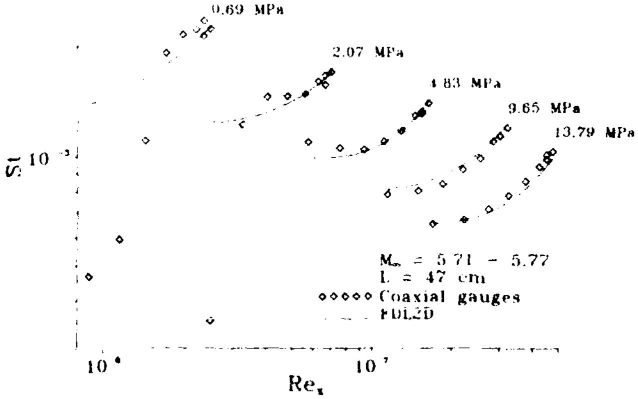

Figure 21: Heat transfer for the compression ramp

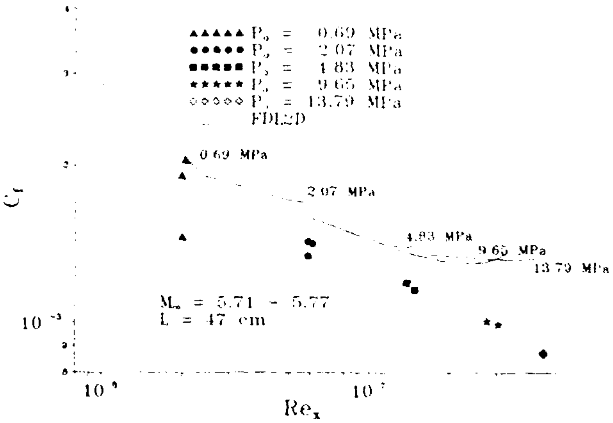

Figure 22: Skin friction for the compression ramp

EXPERIMENTAL, ANALYTICAL AND COMPUTATIONAL METHODS APPLIED TO HYPERSONIC COMPRESSION RAMP FLOWS

G. SIMEONIDES[1], W. HAASE[2] & M. MANNA[1]

[1]von Karman Institute for Fluid Dynamics
Chaussee de Waterloo, 72
B-1640 Rhode St-Genese

[2]Dornier Luftfahrt GmbH
P.O. Box 1303
D-7990 Friedrichshafen 1

SUMMARY

Experimental data on fully laminar and transitional shock wave boundary layer interactions in two-dimensional compression corners are provided and used for the validation of two full Navier-Stokes solvers, as well as for checking the capabilities and limitations of simple analytical prediction methods. Viscous pressure interaction, free interaction and inviscid oblique shock theory are found to predict well the pressure levels on the flat plate upstream of the interaction, within the separated region and downstream of the interaction respectively. The reference temperature theory is found to perform well in attached flow regimes both upstream and downstream of the interaction region, and to provide the basis for a universal peak heating correlation law. Full Navier-Stokes computations are necessary, however, to predict the extent of the interaction region and the associated influence upon the pressure distribution (control effectiveness) as well as the detailed heat transfer distribution. To achieve this, very fine gridding coupled with the use of strict convergence criteria (based on the evolution of the location of the separation point rather than on standard density residuals) is shown to be necessary. It is finally shown that, although sophisticated turbulence models need to be further developed before the detailed characteristics of fully turbulent shock wave boundary layer interactions may be predicted, transitional interactions (where transition typically occurs in the neighbourhood of reattachment) may be adequately handled by algebraic turbulence models "switched on" just downstream of reattachment.

LIST OF SYMBOLS

C	Chapman-Rubesin linear viscosity law constant
c_f	skin friction coefficient (eq. 2.2)
c_H	heat transfer coefficient (eq. 2.3)
c_p	specific heat at constant pressure
K_p	pressure coefficient (eq. 2.1)
L	distance of hinge line from leading edge
L_{pk}	growth length of reattaching boundary layer to location of peak heating
M	Mach number
p	pressure
$\dot{q}_s$	heat transfer rate into model surface
Re	Reynolds number
Re_{unit}	unit Reynolds number (per meter)
T	temperature
u	velocity
x	distance from leading edge
α	ramp deflection angle
α_s	deflection angle of dividing streamline
γ	ratio of specific heats
δ_s	shear layer thickness at reattachment
ρ	density
τ_w	wall shear stress

Subscripts

0	reservoir (total)
∞	freestream
e	at edge of boundary layer
pk	at peak heating
r	recovery (adiabatic wall)
$reat$	at reattachment
ref	reference boundary layer
sep	at separation
w	wall

Superscript

$*$	at Eckert's reference temperature

1. INTRODUCTION

Recent years have seen the development of a number of concepts for novel space transportation systems with widely varying mission requirements which, however, all aim to the optimisation of the performance of such systems and the provision of easy and cost-effective access to space. Many of the proposed systems rely upon the concept of reusability which, effectively, translates to lifting reentry spaceplanes similar to the operational U.S. Space Shuttle Orbiter. Others aim at a lifting ascent as well, with the aid of airbreathing or rocket propulsion, and to an overall operational performance and simplicity similar to that of current commercial airliners.

Among the most critical areas in the design of hypersonic aircraft lies the design of control surfaces

[1,2], where it is well known that strong shock wave boundary layer interactions occur upon their deflection, giving rise to a loss of control effectiveness and high heating rates [3-5]. As a consequence, a significant worldwide research effort has been undertaken to provide a better understanding of the relevant flow processes and reliable prediction techniques, with particular emphasis placed upon the development and validation of Computational Fluid Dynamics (CFD) methods [2,5-8].

Two categories of hypersonic spaceplanes may be distinguished in the modern trends. First, there are lifting reentry vehicles, such as the European Hermes spaceplane and the U.S. HL-20 Personnel Launch System, which are very similar to the Space Shuttle Orbiter, although their small scale poses severe heating problems in nose and leading edge areas, and gives rise to significant uncertainties in the design of control surfaces as the laminar (due to the small scale) oncoming boundary layers are by far more prone to separation in regions of shock wave boundary layer interaction than turbulent boundary layers. Furthermore, transition is often promoted by the process of shock wave laminar boundary layer interaction, a phenomenon that has so far received limited attention (because of its inherent difficulties) despite its relevance to efficient control surface design.

The second category of hypersonic spaceplanes includes lifting ascent/reentry vehicles, such as the U.S. National Aerospace Plane and the German Sänger. The associated high Reynolds numbers encountered during the lifting ascent of such vehicles are expected to yield turbulent flows over many of their wetted surfaces, so that the accurate modelling of turbulence [9] becomes very important in the efficiency of the design.

The present paper addresses the deflected control surface problem, as simulated by flat plate/ two-dimensional compression ramp configurations (Fig.1), at Mach numbers of 6 and 14 with Reynolds numbers to the hinge line in the range $0.3 \times 10^6 - 2.5 \times 10^6$ and wall-to-total temperature ratios between 0.1 and 0.85. The test cases considered involve ramp deflection angles between 7.5° and 25° approached by laminar boundary layers which, in the laboratory, give rise to two-dimensional fully laminar or transitional shock wave boundary layer interactions including cases with extensive separation. Fully turbulent interactions, with the inherent need for turbulence modelling within separated flow regions, are not considered.

In what follows, examples of experimental, analytical and computational results are discussed, emphasising validation issues. A synthesis that may provide useful hints to the designer of control surfaces is also presented.

2. DESCRIPTION OF EXPERIMENTS

Experimentally, the problem has been treated in the two hypersonic wind tunnels of the von Karman Institute (VKI), namely the Mach 6 H-3 blowdown and the Mach 14 Longshot heavy piston gun tunnels [10]. Surface pressure and heat transfer distributions have been measured by a variety of measurement techniques [10] and the data have been complemented by schlieren and surface oil flow and sublimation visualizations. Repeatability and flow establishment (in the Longshot intermittent tunnel) have been demonstrated. Two-dimensionality (in the region of the model centerline) has been checked for the cases chosen for code validation purposes. The uncertainties in the measurements and in the definition of the test conditions have been determined to reflect the current state-of-the-art in hypersonic testing [10-15].

Three test cases are considered for the purposes of code validation, all involving flat plate/ two- dimensional ramp configurations with the flat plate at zero incidence, and a nominally sharp leading edge tested in perfect gas flow conditions. First, a Mach 6 fully laminar test case with a ramp deflected to 7.5° and the hinge line located at 40 mm downstream of the leading edge is considered. The unit Reynolds number is 10×10^6/m, the total temperature of the flow 470 K and the model surface temperature equal to the adiabatic wall temperature. Details of the experiment may be found in [16].

The second and third test cases involve flat plate / 15° ramp configurations at Mach 14 (± 1.5% uncertainty/ non-repeatability), with a unit Reynolds number of 6.5×10^6/m (± 13% uncertainty/ non- repeatability), an equivalent perfect gas total temperature of 2385 K (± 9% uncertainty/ non-repeatability) and a model surface temperature of 295 K. In the second test case the hinge line is located at 70 mm downstream of the model leading edge giving rise to a fully laminar shock wave boundary layer interaction. In the third test case the hinge line is located at 200 mm downstream of the model leading edge and laminar-turbulent transition is exhibited in the close vicinity of reattachment. Details of these experiments may be found in [11-14]. The measurements are characterized by uncertainty levels of ± 15% on the pressure coefficient on the low pressure flat plate part of the model, ± 3% on the pressure coefficient on the ramp, and ± 13% on the heat transfer coefficient over the entire measurement domain.

Three criteria have been employed to detect the occurrence of laminar-turbulent transition:the presence of a granular structure within the boundary or shear layer in schlieren photographs; the noise pattern in 24 kHz surface temperature time traces; and the comparison of the measured heat transfer data downstream of the interaction region to the reference temperature predictions discussed in section 3.

For the comparisons that follow, the data are presented in coefficient form. The pressure coefficient is defined as:

$$K_p = \frac{p - p_\infty}{\frac{1}{2}\gamma p_\infty M_\infty^2} \tag{2.1}$$

The skin friction coefficient is defined as:

$$c_f = \frac{\tau_w}{\frac{1}{2}\rho_\infty u_\infty^2} \tag{2.2}$$

The heat transfer coefficient is defined as a modified Stanton number of the form:

$$c_H = \frac{\dot{q}_s}{\rho_\infty u_\infty c_p (T_0 - T_w)} \tag{2.3}$$

Finally, it is noted that a much larger number of experiments, reported in detail in [13-15], has been conducted at Mach numbers of 6 and 14, and the results have been successfully compared to the analytical predictions discussed in section 3. Although the bulk of this database involves transitional shock wave boundary layer interactions, which are not suitable for code validation purposes for the moment, the data have served the development and validation of a peak heating correlation that is discussed below. In addition, they have provided evidence on the level of striation heating that is often observed in reattaching flows, and have allowed for the determination of an upper limit on the heat transfer rate that is briefly addressed in section 5 [14,15].

3. DESCRIPTION OF THE ANALYTICAL PREDICTIONS

Analytically, it has been found that viscous pressure interaction theory [17], combined with the blast wave theory prediction for the pressure induced by the small leading edge bluntness [18] perform satisfactorily in predicting the pressure distribution over the flat plate part of the models upstream of the onset of the interaction. Free interaction theory [4] has also been found to predict well the plateau pressure level within the separated flow region.

The reference temperature method [19, 20] has been successfully employed to predict the heat transfer distributions over attached flow regions, that is upstream and downstream of the interaction region, including the high heating rates on the deflected ramp downstream of reattachment for both laminar and turbulent reattachment cases. The general reference temperature result is given by:

$$c_H\ (Re_{\infty,x})^n = \frac{A}{s}\left[\frac{u_e p_e}{u_\infty p_\infty}\right]^{1-n}\left[\frac{T_\infty}{T^*}\right]^{1-2n} \times (C^*)^n \left[\frac{T_r - T_w}{T_0 - T_w}\right] \tag{3.1}$$

where n = 0.5, A = 0.332 and s = $\mathrm{Pr}^{2/3}$ for a laminar boundary layer, and n = 0.2, A = 0.0296 and s = 1 for a turbulent boundary layer at high Mach numbers.

Now, application of eq. (3.1) to a reference boundary layer (typically taken as one over a flat plate at zero incidence with freestream edge conditions) with the origin of the boundary layer at the leading edge of the flat plate, gives a reference value for the heat transfer rate (or coefficient) at the location of peak heating on the respective deflected ramp that would occur in the absence of an interaction. An estimate for the heat transfer coefficient at the location of peak heating, corresponding to the peak ramp pressure and with the origin of the ramp boundary layer also taken at the leading edge of the flat plate, may be similarly obtained from eq. (3.1). Finally, if the thinning of the reattaching ramp boundary layer, caused by the reattachment compression, is accounted for by taking its virtual origin in the vicinity of the reattachment point rather than at the leading edge of the flat plate, then the growth length at the location of peak heating used in the Reynolds number term of eq. (3.1) is L_{pk} rather than x_{pk}.

Taking the ratio of the two results yields a theoretically based correlation for peak heating:

$$\frac{\dot{q}_{pk}}{\dot{q}_{ref}} = B[Re^*_{ref,x_{pk}}]^a \left[\frac{p_{pk} u_{pk}}{p_{ref} u_{ref}}\right]^{1-n} \left[\frac{x_{pk}}{L_{pk}}\right]^n \tag{3.2}$$

with
a=0, B=1 and n=0.5 for fully laminar interactions with a laminar reference level,
a=0, B=1 and n=0.2 for fully turbulent interactions with a turbulent reference level, and
a=0.3, B=0.072 and n=0.2 for turbulent peak heating with a laminar reference level.

The length scale L_{pk}, that is the effective growth length of the reattaching boundary layer, has been found [14,15] to be well approximated by the method proposed in [22] as:

$$L_{pk} = \frac{\delta_s}{sin(\alpha - \alpha_s)} \tag{3.3}$$

where the thickness of the shear layer at the reattachment point may be computed by the compressible Blasius result and the deflection angle of the separated shear layer from free interaction theory. The velocity ratio u_{pk}/u_{ref} may often be neglected inducing an error typically of the order of 10%, and the pressure ratio p_{pk}/p_{ref} may be approximated by the inviscid pressure ratio through a single inviscid shock or a two-shock system (separation shock plus reattachment shock) or as the pressure ratio through an isentropic compression. The use of a reference Reynolds number to correlate turbulent ramp data to a laminar flat plate reference heating level is also noted. Details of the development of this correlation law may be found in [14,21].

It is also interesting to note that, for fully laminar or fully turbulent interactions (that is when the reference and ramp boundary layers are both laminar or both turbulent), and neglecting the velocity ratio, eq. (3.2) reduces to:

$$\frac{\dot{q}_{pk}}{\dot{q}_{ref}} = \left[\frac{p_{pk}}{p_{ref}}\right]^{1-n} \left[\frac{x_{pk}}{L_{pk}}\right]^{n} \qquad (3.4)$$

which is equivalent to the numerous pressure interaction semi-empirical peak heating correlations summarized in [23], but includes an additional term that represents the relative growth lengths of the reference and ramp boundary layers. It is recalled that such semi-empirical correlations have been, after [23], very successful for fully turbulent interactions with an exponent $(1-n)$ of close to 0.8 (that is the theoretical reference temperature value), but a complete failure for fully laminar interactions where exponents $(1-n)$ in the range 0.7-1.9 have been determined as opposed to the theoretical value of 0.5. In addition, correlations for peak heating in transitional interactions (with a turbulent ramp peak heating level and a laminar reference level), such as the one proposed in [24], have also presented severe limitations in their performance [15]. Accounting for the thinning of the reattaching boundary layer caused by the interaction process in the form of eq. (3.2) or eq. (3.4), on the other hand, has been found in [14,15,21] to provide *the grounds* for a universal peak heating correlation in regions of both two- and three- dimensional shock wave boundary layer interactions. The results of this improved correlation are presented in section 5.

Finally, what is currently *not* possible with simple semi-empirical and/or analytical methods is the accurate prediction of the extent of the separated region and the location of the separation point, since a universal correlation law has yet to be developed. This, in turn, makes the incorporation of CFD methods in the design process necessary, particularly insofar as the prediction of control effectiveness, which strongly depends on the geometric characteristics of the interaction as opposed to peak heating, is concerned. Clearly, full Navier-Stokes solvers need to be critically validated prior to being relied upon by the designer, and this forms one of the primary objectives of this paper.

4. DESCRIPTION OF COMPUTATIONS

Computationally, the problem of shock wave boundary layer interaction in compression corners has been treated by two Navier-Stokes solvers, one developed at Dornier and one at the VKI. Details on the development of the Dornier code and its performance over a wide range of Mach numbers may be found in [25-29]. The Euler solver on which the currently developed VKI Navier-Stokes code is based is described in [30-32].

In both codes, the two - dimensional unsteady full Navier-Stokes equations are integrated by means of time marching finite volume shock capturing methods based on cell-centered unknowns. The discretization of the convective terms is based on either a central (for the Dornier code) or an upwind (for the VKI code) evaluation of the cell face fluxes. A standard nonlinear blend of second and fourth order artificial dissipation terms is employed to stabilize the central discretizations in the Dornier code. The VKI solver makes use of the flux difference splitting technique to evaluate the cell face fluxes; higher order schemes coupled with TVD properties are implemented on the basis of the MUSCL approach. Both codes employ multi-stage Runge-Kutta integration schemes for the time discretization. The Cebeci-Smith turbulence model [33] is implemented *in the Dornier* code together with a transition "switch" and/or an intermittency function.

The time evolution of the numerical solutions is, in both codes, monitored by means of an L_2 norm of the normalized density residuals. An overall decay of the residuals by approximately four orders of magnitude is generally considered to yield a satisfactory steady state solution. However, the extent of the separated region and the location of the separation point have exhibited a considerable sensitivity to further reduction in the residuals. Therefore, the establishment of the steady state location of the separated point is believed to be a more appropriate convergence criterion, as will be discussed below. Still, it is noted that such an approach is likely to yield significant increases in computational time when noting the asymptotic behaviour of convergence histories.

The Mach 6, 7.5° ramp test case has been computed by both codes. The Dornier computations have been conducted on a series of four meshes in order to check that the solution is independent of further grid refinement. The four mesh levels, employed with two multigrid (V-) cycles, involve a total number of points of 62×12, 124×24, 248×48 and 496×96; in the finer mesh, the normal mesh size at the wall was 5×10^{-6}m. The VKI computation has been performed on 190×60 mesh points, with the normal mesh size at the wall set to 6.7×10^{-5}m. It is noted that the computational domain in the Dornier computations extended to 120 mm downstream of the leading edge as opposed to 80 mm in the VKI computations.

The fully laminar Mach 14, 15° ramp test case has also been computed with both codes. The Dornier computations again include an extensive grid dependence study with computations performed on meshes with 44×20, 88×40, 176×80 and 352×160 points. The wall normal stepsize in the finer mesh was again 5×10^{-6}m. The VKI computations have been performed at two mesh levels, namely with 84×30 and 190×60 mesh points. The first normal stepsize at the wall in the case of the finer grid was 3×10^{-5}m. Indicatively, there were approximately 30 mesh points in the boundary layer at the onset of the interaction (at 50 mm downstream of the leading edge) in the fine VKI mesh and only 15 points in the coarse VKI mesh. The computational domain in the Dornier computations and in the coarse grid VKI computations extended to 250 mm downstream of the model leading edge. The fine grid VKI computations were performed over a length of 210 mm from the model leading edge.

Lastly, the transitional Mach 14 test case, with the hinge line of the 15° ramp located at 200 mm downstream of the model leading edge, has been computed only by the Dornier code. Fully laminar computations have been performed in a mesh series with 61×31, 124×62 and 248×124 mesh points. An additional mesh of 248×64 points has been employed to perform fully laminar and fully turbulent computations, as well as to check the influence of switching on the turbulence model just downstream of the laminar reattachment (note that transition in this experiment was detected to occur in the close vicinity of reattachment). In the latter case, the first wall normal stepsize was 5×10^{-5}m. The computational domain for this test case extended to 400 mm downstream of the model leading edge.

The Dornier meshes were generated by an algebraic grid generation technique in which the outer boundary of the meshes was fitted close to the shock shape in order to optimize the mesh point distribution in the computational domain. The meshes were geometrically stretched. The VKI grids were generated by an analytic technique based on potential theory. In this case, orthogonal and smooth meshes are warranted, but a constant normal mesh size is imposed throughout the computational domain. The meshes were exponentially stretched in the wall normal direction. The grids employed in the present study are illustrated in Figs.2 and 3. Figure 2 shows a coarsened version of the fine 190×60 VKI grid employed in the second test case with the Mach 14 forward 15° ramp. Figure 3 shows a coarsened version of the 248×64 Dornier mesh employed in the third test case with the Mach 14 rear 15° ramp.

5. DISCUSSION OF RESULTS

5.1 Experiments vs. analytical predictions

Typical pressure distributions measured along the centerline of the flat plate and flat plate/ 15° and 25° ramp configurations at Mach 14 are shown in Fig.4. The flat plate data are compared to the combined viscous pressure interaction and blast wave bluntness predictions of [17] and [18], respectively. Also shown are the free interaction predictions for the plateau pressure level of [4] and the inviscid ramp pressure level obtained from oblique shock theory. The "peak" ramp pressure levels, too, have been estimated from oblique shock theory on the assumption of a two-shock system, where the strength of the separation shock gives the predicted plateau pressure level. Clearly, all predictions are in good agreement with the measurements.

Typical measured heat transfer distributions along the centerline of the flat plate and flat plate/ 15° and 25° ramp configurations at Mach 14 are shown in Fig.5. Data with the 15° ramp configuration are shown for two locations of the hinge line. The measurements are compared to the reference temperature predictions of eq. (3.1). The flat plate data, which remain laminar over the entire measurement domain, compare well with the predicted laminar distribution. On the forward 15° ramp, the measurements initially compare well with the laminar reference temperature predictions, but at approximately 120 mm from the leading edge laminar-turbulent transition is occurring and the heat transfer distribution rises from the laminar predictions to the turbulent predictions. The importance of accounting for the thinning of the reattaching boundary layer, caused by the interaction process, by shifting its virtual origin to the vicinity of reattachment is again stressed.

In the rear ramp experiments, laminar-turbulent transition has been detected in the close vicinity of reattachment [14]; hence, the measured data on the ramp compare well with the respective turbulent reference temperature predictions. It is noted that the solid line reference temperature ramp predictions assume the inviscid pressure level on the ramp. However, a pressure overshoot has been measured just downstream of reattachment (Fig.4) which, in the case of the 25° ramp is significant. Evidently, accounting for the actual pressure distribution in the 25° ramp prediction of Fig.5 yields an improvement in the comparison to the measured heat transfer data.

With reference to Fig.5, it is also noted that the predictions of eq. (3.3) for L_{pk} are in good agreement with the measured distance of the location of peak heating from the reattachment point. The latter has been found (from the comparison of the reference temperature predictions to the ramp heat transfer data) to closely represent the location of the virtual origin of the reattaching boundary layer. In other words, eq. (3.3) is seen to provide a good approximation to the effective growth length of the reattaching boundary layer to the location of peak heating.

Furthermore, high resolution spanwise measurements on the rear 15° ramp are shown in Fig.5 to illustrate that significant spanwise heat transfer variations may occur in reattaching flow regions and downstream. These variations have been attributed to the Görtler instability and the associated formation of contra-rotating vortices [34]. However, an extensive parametric study of the resulting heat transfer variations performed in [14,15] has shown that, even in the presence of important steady spanwise heat transfer variations, the local turbulent heating level on the ramp is not significantly exceeded and that, when a fully turbulent boundary layer develops over the entire span of the ramp, the spanwise variations reduce to zero. The conclusion of the work reported in [14,15] has, therefore, been that the local turbulent heating level on the ramp, as given by the reference temperature theory (accounting for the actual conditions at the edge of the ramp boundary layer and for the location of its virtual origin), may provide an adequate estimate for an upper limit of the (time-averaged) heat transfer distribution on the ramp downstream of the region of interaction.

Noting the successful application of the reference temperature method to predicting the heat transfer distribution (in attached flow regions) over a wide variety of geometries [14,15], eq. (3.2) has been employed to correlate laminar and turbulent peak heating data measured in regions of two- and three-dimensional shock wave boundary layer interactions. The result is illustrated in Fig.6, where more than 200 data points from 23 references have been assembled [21], covering a Mach number range of 5-20 and five orders of magnitude variation in Reynolds number, which implies a range of shock wave boundary layer interactions from fully laminar cases in the strong viscous interaction regime to transitional to fully turbulent cases. The geometries considered include two- and three-dimensional flat plate/ramp configurations, flat plates with swept or unswept impinging shocks, regions of glancing shock interaction (flat plates with vertical fins) and a double ellipsoid configuration. A laminar boundary layer developing over a flat plate at freestream conditions has been chosen as the reference case in this correlation.

5.2 Experiments vs. computations

5.2.1 *The Mach 6, 7.5° ramp laminar test case*

The computed pressure distributions for the first test case (section 2) are compared to the measured data in Fig.7. The Dornier computations demonstrate that a grid-independent solution has been attained by the two finest meshes which is in close overall agreement with the measurements. Noting that the experimental data for this test case have been taken in the early 1970's without the strict code validation requirements in mind, the discrepancy observed between the CFD predictions and the measured pressure distribution for a short distance downstream of reattachment remains inexplicable. The VKI computations, performed on a similar mesh to the second finest Dornier mesh (noting the different computational domains and grid stretching), also show good agreement with the measured data as well as with the grid-independent Dornier solution (on the two finer meshes).

The corresponding computed skin friction distributions are shown in Fig.8. Clearly, the coarser Dornier mesh performs well in predicting the skin friction distribution over the attached flow region upstream of the onset of the interaction, indicating that the flat plate boundary layer is adequately resolved and the velocity profile and its gradient at the wall are correctly computed. The correct prediction of the location of the separation point and the extent of the separated region, however, requires the use of highly refined grids.

This is better illustrated in Fig.9, where the evolution of the predicted location of the separation point with mesh refinement and increasing number of iterations is shown. Concerning time convergence, it is noted that the standard engineering convergence criterion of an L_2 norm reduction in the normalized density residuals by four or even five orders of magnitude (on the single VKI mesh level) yields an underpredicted extent of the separated region. and convergence of the location of the separation point (Fig.9) may form a more appropriate criterion in separated flow situations. It is also interesting to note that the multigrid approach employed in the Dornier computations allows to take profit of the coarse grid solutions to accelerate convergence. Indicatively, the normalized density residuals at the end of the Dornier fine grid computation have decreased by three orders of magnitude relative to the initial (coarser grid) solution used to start this fine mesh computation.

5.2.2 *The Mach 14, forward 15° ramp laminar test case*

The computed pressure distributions for the second test case outlined in section 2 are presented in Fig.10. The corresponding comparison between the measured and computed heat transfer distributions is shown in Fig.11. With reference to the Dornier computations, it is noted that a grid-independent solution has again been attained with the two finer meshes of Dornier, which predicts well the location of the separation point (as measured from the schlieren photograph, Fig.12) and is in reasonable agreement with the heat transfer measurements on the ramp up to approximately 0.12 m downstream of the leading edge.

The subsequent discrepancy in Fig.11 is due to the occurrence of laminar-turbulent transition detected in the experiment [14], whereas laminar flow has been assumed throughout the computational domain (see also the comparison of the measured heat transfer data to the reference temperature theory, Fig.5). It is noted that transition in this case is occurring a substantial distance downstream of reattachment and, hence, it is insignificant to the characteristics of the interaction. In addition, the process is taking place in an almost zero pressure gradient region where, at high Mach numbers, it requires a significant length to be completed.

The VKI fine grid computation (190×60 mesh points) is seen to underpredict the extent of the interaction and to be in close agreement with the Dornier solution on the 88×40 mesh. As with the Mach 6 test case discussed in section 5.2.1, it is recalled that the normal mesh resolution of the VKI fine mesh is very similar to the 40 point resolution of the 88×40 Dornier mesh, due to the different normal extents of the computational domain and the different stretching employed in the two cases. Consequently, there are strong indications that normal mesh resolution is significantly more important than streamwise mesh resolution. To be sure, for a computational domain characterized by a length-to-height ratio of about 4, the VKI meshes involved a ratio of number of points in the streamwise direction to the number of points in the wall normal direction of the order of 3, whereas the Dornier meshes involved a ratio of only 2. It follows from Figs.10 and 11 that a mesh point ratio of the order of one half of the length-to-height ratio of the computational domain may be more appropriate for this type of computations. It may also be postulated that the quality of the VKI computations (in terms of the prediction of the extent of the interaction) may be justifiably enhanced if the number of mesh points in the wall normal direction is increased to the detriment of resolution in the streamwise direction.

The importance of grid resolution in the wall normal direction is further manifested by the coarse grid VKI results. Although the pressure distribution in the attached low pressure gradient regions is well predicted by both codes on all meshes, including the 84×30 VKI mesh (Fig.10), clearly the heat transfer distribution in the latter case is underpredicted relative to the finer VKI mesh computation and the Dornier computations (Fig.11). It is also noted that all results but the VKI coarse mesh one are in good agreement with the reference temperature predictions shown in Fig.5. This phenomenon has been encountered in many of the computations in [7,8] and is attributed to an insufficient resolution of the very strong normal temperature gradients in the near wall part of the attached boundary layer.

Finally, a surprising aspect (at first glance) of the comparison between the coarse and fine grid computations of VKI may be that the predicted extent of the interaction is not significantly altered with mesh refinement. This, however, should not be viewed as a grid-independent prediction of the location of the separation point, and the poor performance of the coarse grid computation in the attached flow regions (the flow over which is due to strongly influence the interaction/separation characteristics) should be kept in mind.

5.2.3 *The Mach 14, rear 15° ramp transitional test case*

The measured and computed laminar pressure and heat transfer distributions for the third test case of section 2 are shown in Figs.13 and 14. In this case, a grid-independent solution has not been demonstrated, although, on the basis of the Dornier grid dependence study described in section 5.2.2, the finer grid solution (on the 248×124 mesh) is believed to closely represent the grid-independent solution.

In addition, it is recalled that the shock wave boundary layer interaction in this case is transitional, in the sense that the boundary layer is laminar at separation but transition has been detected to occur in the close vicinity of reattachment [11,14]. Consequently, the finer grid laminar computation is seen to overpredict the measured extent of the separated region, however only by a modest amount. This may be justified as transition is occurring at the very end of the interaction and, hence, it should have a small influence upon its characteristics.

Still, the most significant discrepancy between the laminar computations and the transitional experimental data is that the former strongly underpredict the measured turbulent heat transfer distribution on the ramp. However, with reference to Fig.15, good agreement between experiment and computation on the 248×64 mesh (as well as with the turbulent reference temperature theory, Fig.5) is found when switching on the turbulence model in the computations just downstream of the predicted laminar reattachment point.

In fact, it follows from Figs.13-15 that, for cases with laminar oncoming boundary layers, where the interaction process is expected to promote laminar-turbulent transition (most likely in the highly destabilizing reattachment region), the approach adopted herein, of a laminar computation to the reattachment point and switching to a turbulent computation thereafter, may provide an estimate of the most adverse effects of the interaction. Specifically, a grid independent, fully converged laminar computation is bound to yield the largest possible extent of the interaction and the associated most adverse effect on control effectiveness. Such a laminar computation will also yield the minimum boundary layer thickness in the "neck" (peak heating) region just downstream of the reattachment compression. This minimum boundary layer thickness combined with a turbulent computation (starting from the laminar solution at reattachment) will, in turn, yield an upper limit in heat transfer which, on the basis of the experimental evidence of [14,15], may not be significantly exceeded even in the presence of significant striation heating.

Finally, it is noted that the 1° nose-down angle of attack of the configuration has been employed in the "transitional" computation of Fig.15 only as a crude modelling of the modest (50μm) bluntness of the model leading edge in the experiment. This angle of attack has been chosen because it yields a pressure rise on the flat plate upstream of the interaction similar to the one induced by the leading edge bluntness.

6. CONCLUSIONS

A compression ramp database has been assembled from an extensive series of experiments with laminar boundary layers approaching the deflected ramps in the VKI Mach 6 and 14 hypersonic wind tunnels. Among these experiments, only the Mach 6, 7.5° ramp experiments of [16] and one Mach 14, 15° ramp case [14] have exhibited fully laminar interactions and are, therefore, particularly suitable for code validation purposes. The remaining cases have also demonstrated that the laminar oncoming boundary layers are especially prone to separation, and that laminar-turbulent transition is promoted by the interaction process, notably by the strong destabilizing effects of adverse pressure gradient and concave flow curvature that characterize the reattachment compression. Furthermore, these experiments have provided a profound insight on the phenomenon of striation heating and have demonstrated, as discussed in [14,15], that the time-averaged local turbulent heating level is not significantly exceeded by peaks in the resulting steady spanwise heat transfer variations even when these are of the order of ±50%.

Analytically, viscous pressure interaction combined with blast wave theory has been found to adequately predict the pressure distribution along flat plates (upstream of the onset of the interaction) induced by the growth of the boundary layer and the finite leading edge bluntness. Free interaction theory performs well in predicting the plateau pressure level within the separated flow region, and inviscid oblique shock theory gives satisfactory predictions for the downstream ramp pressure level, as well as for the peak pressure attained at the end of the reattachment compression, provided that the type of flow compression is qualitatively known (isentropic, two-shock or single inviscid shock compression).

The reference temperature method has been shown to be very successful in predicting the heat transfer distribution over attached flow regions, both upstream and downstream of the interaction, on the condition that the effective boundary layer growth length from its virtual origin and the correct flow conditions at the edge of the boundary layer are employed. As a result, a universal correlation law has been developed where, on the basis of the reference temperature theory, more than 200 laminar and turbulent peak heating data, taken over two-dimensional and swept compression ramp and impinging shock configurations at Mach numbers between 5 and 20 and over a wide range of Reynolds numbers, have been successfully correlated.

What is currently not possible by analytical or semi-empirical means is the prediction of the location of the separation point and/or the extent of the separated region. This is largely due to the promotion of laminar-turbulent transition by the interaction process, which implies that the development of a correlation law should account for the parameters relevant to the transition process that are currently not well understood.

Finally, on the computational side it has been demonstrated that, in fully laminar interaction cases, full Navier-Stokes solvers are performing very well and may be safely incorporated in the design process, provided that grid-independent solutions are obtained and attention is given to convergence criteria. It has been shown that monitoring of the evolution of the location of the separation point with computational cycles forms a more appropriate (and strict) convergence criterion than the standard monitoring of normalized density residuals. Although turbulence modelling within separated flow regions is not yet sufficiently mature to be safely incorporated in the design process and moreover so transition modelling, CFD methods may be employed to provide extreme limits for realistic cases where laminar-turbulent transition is promoted by the reattachment process.

Specifically, a fully laminar computation may provide a maximum extent of the interaction and yield the most detrimental effects on control effectiveness. Thereafter, "switching-on" a standard, proven turbulence model in the attached flow region just downstream of reattachment will give an upper limit for the heat transfer distribution on the ramp. It is noted that the (computed) boundary layer thickness in the "neck" region, that occurs at the end of the reattachment compression, will be smaller in the case of a laminar development of the boundary/shear layer to the reattachment point than would be if the flow was already turbulent upstream of the interaction. Consequently, the resulting turbulent peak heating level will again represent an upper limit, as it will correspond to the minimum possible thickness of the reattaching boundary layer in the "neck" region.

ACKNOWLEDGEMENTS

The contribution of J.P. Vermeulen of the VKI towards the development of the peak heating correlation and the striation heating studies is gratefully acknowledged. The Mach 14 ramp experiments and the computations were partially supported by Dassault Aviation under the auspices of the Hermes R&D program monitored by P. Perrier.

eraux aerodynamiques - aerothermique d' Hermes", *in* "Aerodynamics of Hypersonic Lifting Vehicles", AGARD CP 428, November 1987.

2. Neumann, R.D., "Missions and requirements", *in* "Aerothermodynamics of Hypersonic Vehicles", AGARD-FDP-VKI Special Course , May 1988. AGARD Report 761, June 1989.

3. Green, J.E., "Interaction between shock waves and boundary layers", Progress in Aerospace Sciences, *11*, 1970, pp 235-340.

4. Hankey, W.L. Holden, M.S., "Two dimensional shock wave boundary layer interactions in high speed flows", AGARDograph 203, June 1975.

5. Delery, J. and Marvin, J.G., "Shock wave boundary layer interactions", AGARDograph 280, 1986.

6. Bogdonoff, S.M.: Technical evaluation report on the fluid dynamics panel symposium on aerodynamics of hypersonic lifting vehicles, AGARD AR 246, April 1988.

7. Proc. of the "Workshop on Hypersonic Flows for Reentry Problems", Part I, Antibes, France, January 1990. Published by Springer-Verlag, 1992.

8. Proc. of the "Workshop on Hypersonic Flows for Reentry Problems", Part II, *3*, Antibes, France, April 1991.

9. Marvin, J.G., "Progress and challenges in modeling turbulent aerodynamic flows", *in* "Engineering Turbulence Modelling and Experiments", eds. W. Rodi and E.N. Ganić, Elsevier, 1990.

10. Simeonides, G., "The VKI hypersonic wind tunnels and associated measurement techniques", von Karman Institute TM 46, November 1990.

11. Simeonides, G. and Wendt, J.F., "An experimental contribution to the flat plate 2D compression ramp shock wave boundary layer interaction problem at Mach 14: Test case 3.7", *in* Proc. of the Workshop on Hypersonic Flows for Reentry Problems, Part I, Antibes, January 1990. Springer-Verlag, 1992. von Karman Institute PP 1990-12/AR.

12. Simeonides, G. and Wendt, J.F., "Compression corner shock wave boundary layer interactions at Mach 14", *in* Proc. 17th Congress of the International Council of the Aeronautical Sciences, ICAS 90, Stockholm, September 1990; von Karman Institute PP 1990-25/AR.

13. Simeonides, G. and Wendt, J.F., "Fundamental experimental studies of control effectiveness and heating at hypersonic Mach numbers", *in* Proc. 1st European Symposium on Aerothermodynamics for Space Vehicles, ESA SP 318, May 1991, pp 143-148; von Karman Institute PP 1991-22/AR.

14. Simeonides, G., "Hypersonic shock wave boundary layer interactions over compression corners", Ph.D. Thesis, University of Bristol/ von Karman Institute, April 1992.

15. Vermeulen, J.P. and Simeonides, G., "Parametric studies of shock wave boundary layer interactions in two-dimensional compression corners at Mach 6, tions in the reattachment region", von Karman Institute TN in preparation.

16. Gautier, B., "Etude theorique et experimentale des effets du refroidissement parietal sur l'interaction onde de choc- couche limite laminaire en ecoulement plan hypersonique", Ph.D. Thesis, von Karman Institute/ U. Libre de Bruxelles, 1972.

17. Hayes, W.D. and Probstein, R.F., "Hypersonic flow theory", Academic Press, 1959.

18. Lukaciewicz, J., "Hypersonic flow- blast wave analogy", AEDC TR-61-4, 1961.

19. Eckert, E.R.G., "Engineering relations of friction and heat transfer to surfaces in high velocity flow", J. Aero. Sci., *22*, 8, August 1955, pp 585-587.

20. Neumann, R.D. and Hayes, J.R., "Introduction to aerodynamic heating analysis of supersonic missiles", *in* "Tactical Missile Aerodynamics", eds. M.J. Hemsch & J.N. Nielsen, Progress in Astronautics & Aeronautics, *104*, AIAA, 1986.

21. Simeonides, G. and Vermeulen, J.P., "Identification of relevant parameters and revision of peak heating correlations for hypersonic two- and three- dimensional shock wave boundary layer interactions", *in* "Hypersonic Aerodynamics", EuroMech 289, Aachen, April 1992. von Karman Institute PP 1992-16/AR.

22. Bushnell, D.M. and Weinstein, L.M., "Correlation of peak heating for reattachment of separated flows", J. Spacecraft and Rockets, *5*, 9, September 1968, pp 1111-1112.

23. Hung, F.T., "Interference heating due to shock wave impingement on laminar boundary layers", AIAA P 73-678.

24. Hung, F.T. and Barnett, D.O. , "Shock wave boundary layer interference heating analysis", AIAA P 73-237.

25. Haase, W., Wagner, B. and Jameson, A., "Development of a Navier-Stokes method based on a finite volume technique for the unsteady Euler equations", *in* Proc. 5th GAMM Conf. on Numerical Methods in Fluid Mechanics, "Notes on Numerical Fluid Mechanics", *7*, eds. Pandolfi & Piva, Vieweg, 1983.

26. Haase, W., "Solution of the Navier-Stokes equations for subsonic and supersonic flows in rarefied gases", *in* Proc. Numerical Simulation of Compressible Navier- Stokes Flows, "Notes on Numerical Fluid Mechanics", *18*, eds. Bristeau, Glowinski, Periaux, Viviand, Vieweg, 1987.

27. Haase, W. and Echtle, H., "Computational results for viscous transonic flow around airfoils", AIAA P 87-422.

28. Haase, W., "Viscous hypersonic flows over compression ramps", *in* Proc. 8th GAMM Conf. on Numerical Methods in Fluid Mechanics, "Notes on Numerical Fluid Mechanics", *29*, ed. P. Wesseling, Vieweg, 1990.

29. Haase, W., "2D hypersonic ramp flow", *in* Proc. of the Workshop on Hypersonic Flows for Reentry

30. Manna, M, "A 3-D high resolution upwind finite volume Euler solver", von Karman Institute TN 180, April 1992.
31. Manna, M, "Validation of central and upwind 3D compressible flow solvers", *in* "Computational Fluid Dynamics", von Karman Institute LS 1992-04, March 1992.
32. Manna, M., Deconinck, H., Ma, E. and Li, C.P., "A comparison of high resolution upwind solvers on 3D inviscid hypersonic flow", *in* "Theoretical and Experimental Methods in Hypersonic Flows". AGARD CP 514, May 1992.
33. Cebeci, T. and Smith, A.M.O., "Analysis of turbulent boundary layers", Academic Press, 1974.
34. Ginoux, J.J., "On some properties of reattaching laminar and transitional high speed flows", von Karman Institute TN 53, September 1969.

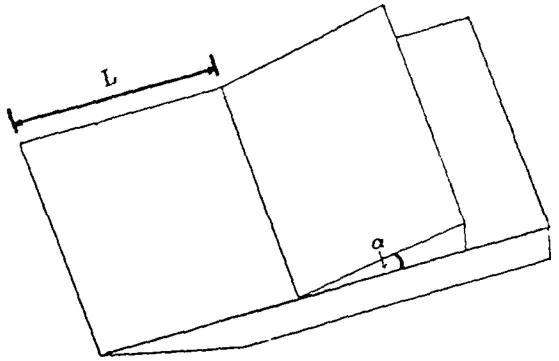

Fig. 1 - Flat plate / two-dimensional ramp geometry

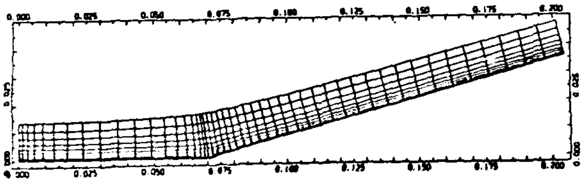

Fig. 2 - Coarsened version of the VKI 190×60 grid employed in the Mach 14 forward ramp computation

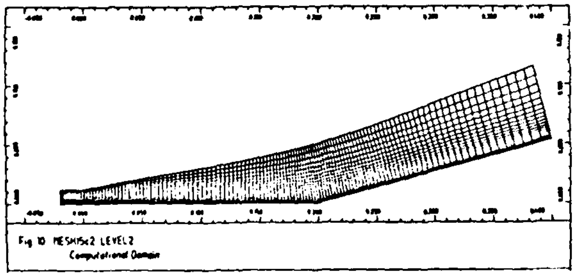

Fig. 3 - Coarsened version of Dornier 248×64 grid employed in the Mach 14 rear ramp computation

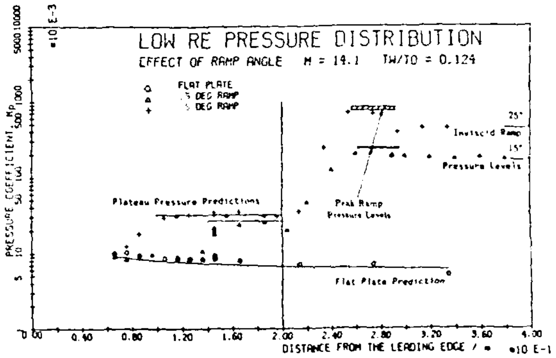

Fig. 4 - Measured pressure distributions over flat plate and flat plate/2D ramp configurations at Mach 14 and $Re_{unit} = 6.5 \times 10^6$/m, and comparison with analytical predictions

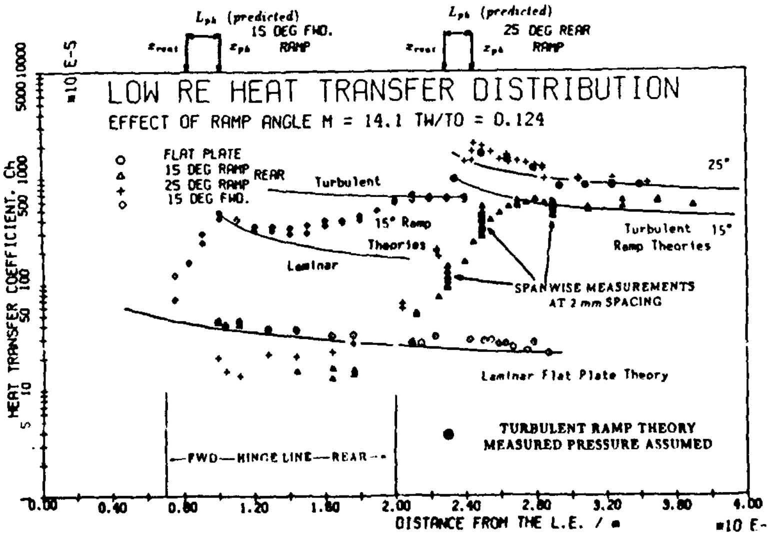

Fig. 5 - Measured heat transfer distributions over flat plate and flat plate/2D configurations at Mach 14 and $Re_{unit} = 6.5 \times 10^6$/m, and comparison

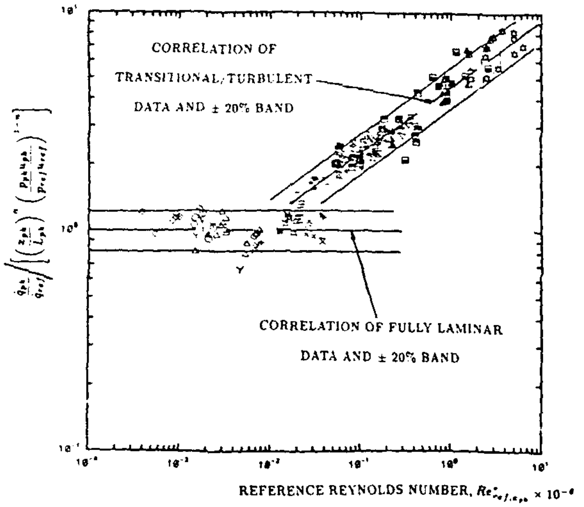

Fig. 6 - Correlation of laminar and turbulent peak heating data referenced to laminar flat plate heating level

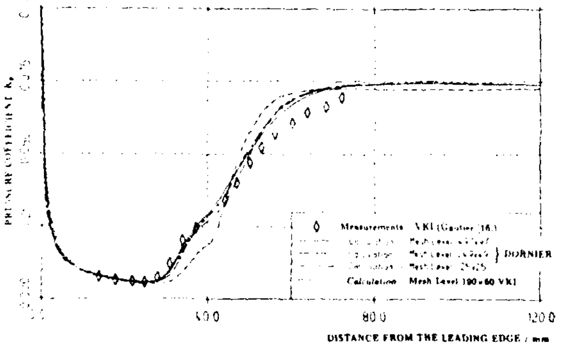

Fig. 7 - Comparison of measured and computed pressure distributions over the flat plate / 7.5° ramp configuration at Mach 6 with $Re_{unit} = 10 \times 10^6$/m and adiabatic wall temperature

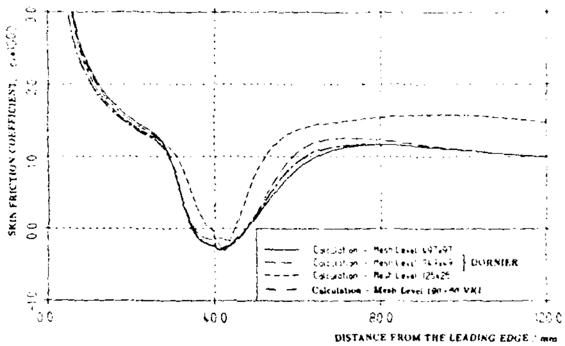

Fig. 8 - Computed skin friction distributions over the flat plate / 7.5° ramp configuration at Mach 6 with $Re_{unit} = 10 \times 10^6$/m and adiabatic wall temperature

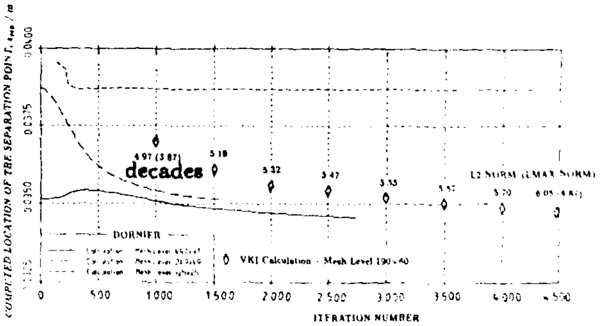

Fig. 9 - Evolution of the computed location of the separation point with number of iterations and grid refinement for the Mach 6, 7.5° ramp test case

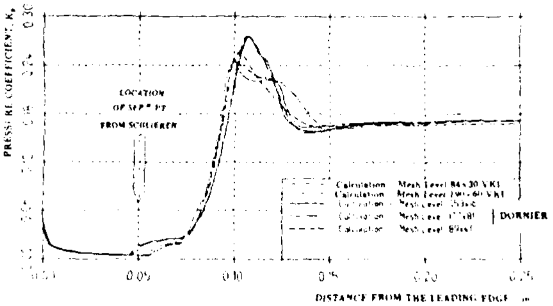

Fig. 10 - Computed (laminar) pressure distributions over the flat plate / forward 15° ramp configuration at Mach 14 with $Re_{unit} = 6.5 \times 10^6$/m and T_w/T_0=0.12

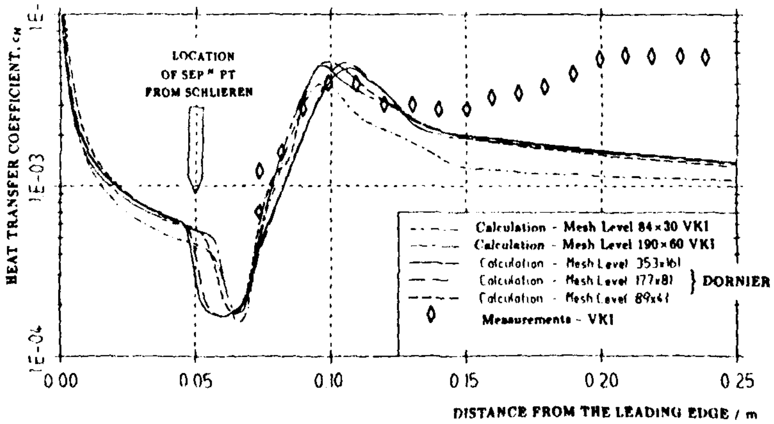

Fig. 11 - Comparison of measured and computed (laminar) heat transfer dis-

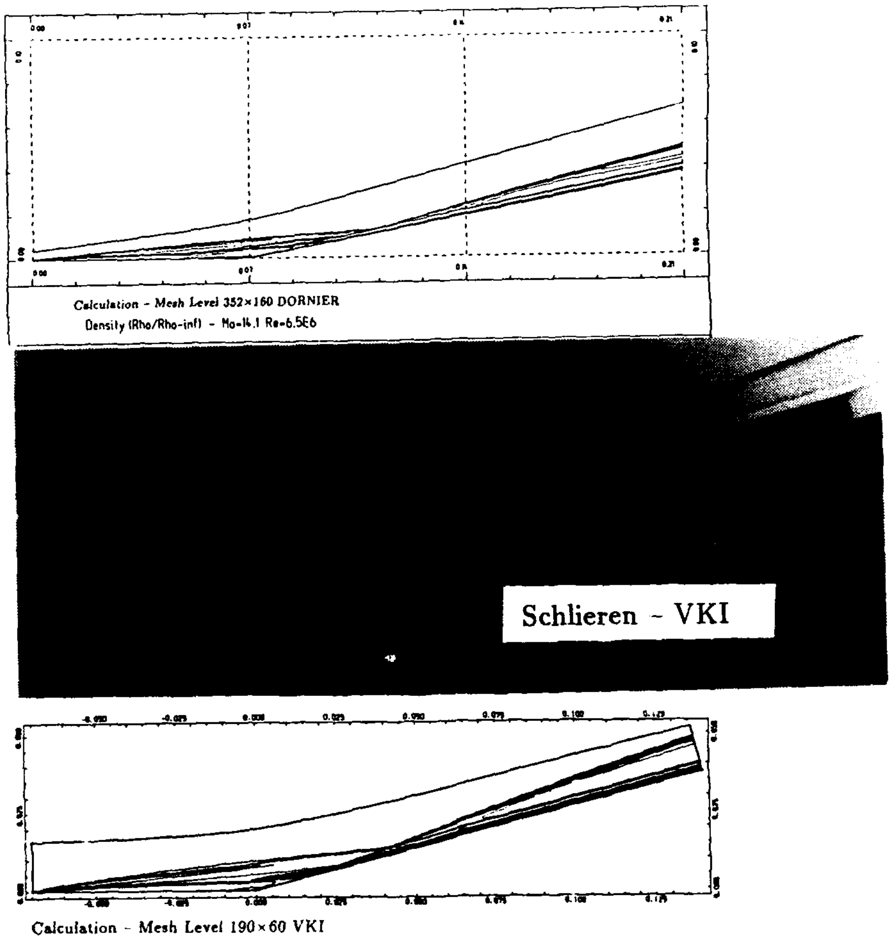
Calculation - Mesh Level 352×160 DORNIER
Density (Rho/Rho-inf) - Mo=14.1 Re=6.5E6
Schlieren - VKI
Calculation - Mesh Level 190×60 VKI

Fig. 12 - Comparison of computed (laminar) density contours with the schlieren photograph for the Mach 14 forward 15° ramp test case

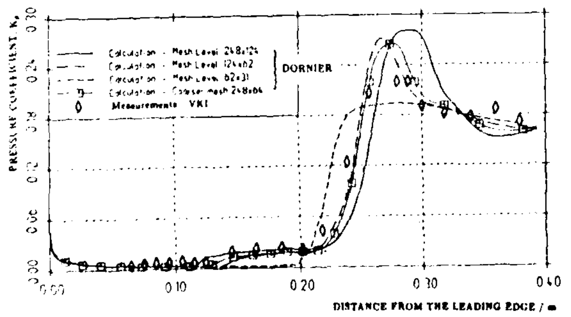

Fig. 13 - Comparison of measured and computed (laminar) pressure distributions over the flat plate / rear 15° ramp configuration at Mach 14 with $Re_{unit} = 6.5 \times 10^6/m$ and T_w/T_0=0.12

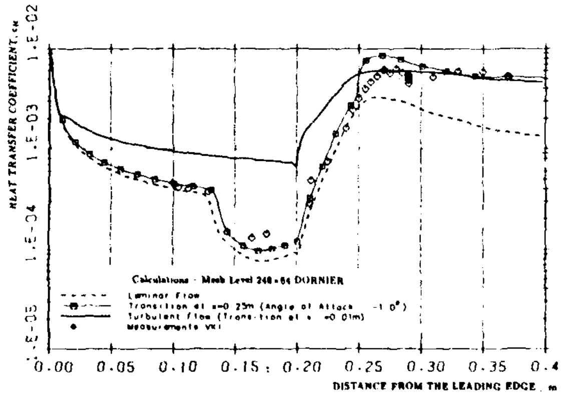

Fig. 15 - Comparison of measured and computed heat transfer distributions over the flat plate / rear 15° ramp configuration at Mach 14 with $Re_{unit} = 6.5 \times 10^6/m$ and T_w/T_0=0.12, with turbulence model "switched-on" at reattachment

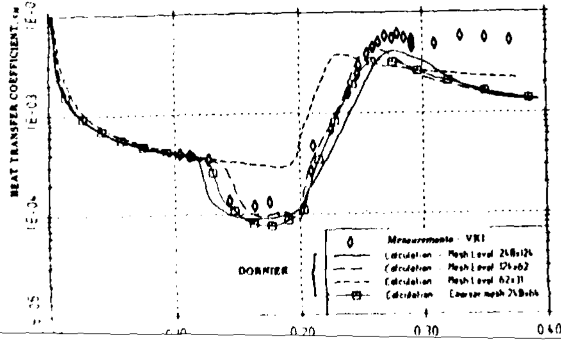

Fig. 14 - Comparison of measured and computed (laminar) heat transfer distributions over the flat plate / rear 15° ramp configuration at Mach 14 with $Re_{unit} = 6.5 \times 10^6/m$ and T_w/T_0=0.12

Joint Computational and Experimental Aerodynamics Research on a Hypersonic Vehicle*

William L. Oberkampf[†]
Daniel P. Aeschliman[††]
Mary (McWherter) Walker[†]
Aerodynamics Department, Org. 1554
Sandia National Laboratories
Albuquerque, New Mexico 87185
United States

SUMMARY

A closely coupled computational and experimental aerodynamics research program was conducted on a hypersonic vehicle configuration at Mach 8. Aerodynamic force and moment measurements and flow visualization results were obtained in the Sandia National Laboratories hypersonic wind tunnel for laminar boundary layer conditions. Parabolized and iterative Navier-Stokes simulations were used to predict flow fields and forces and moments on the hypersonic configuration. The basic vehicle configuration is a spherically blunted 10° cone with a slice parallel with the axis of the vehicle. On the slice portion of the vehicle, a flap can be attached; for this study, flap deflection angles of 10°, 20°, and 30° were used. Comparisons are made between experimental and computational results to evaluate the quality of each and to identify areas where improvements are needed. This extensive set of high-quality experimental force and moment measurements is recommended for use in the calibration and validation of computational aerodynamics codes.

LIST OF SYMBOLS

C_a	Forebody axial force coefficient, $A/(q_\infty S)$
C_m	Pitch moment coefficient, $M/(q_\infty\ S\ D_b)$, referenced about $x/L = 0.5$
C_n	Normal force coefficient, $N/(q_\infty\ S)$
D_b	Diameter of the base
L	Body length
M_∞	Freestream Mach number
p_o	Total pressure
q_∞	Freestream dynamic pressure
R_L	Freestream Reynolds number based on body length
S	Reference area, 11.525 in^2 (7435.9 mm^2)
T_o	Total temperature
T_w	Model wall temperature
x_{cp}	Axial center of pressure measured from the nose
α	Angle of attack, positive when slice on windward side
δ	Flap deflection angle
ϕ	Model roll angle, $\phi = 0°$ for slice on windward side at positive α

1. INTRODUCTION

Although in recent years the design of flight vehicles has been based increasingly upon computational aerodynamics simulation, wind tunnel experimentation continues to play the major role in aerodynamic analysis and design. This role, however, is changing because of significant improvements in the capability of, and confidence in, numerical simulations. For a small class of supersonic and hypersonic flow problems, high-quality numerical solutions are now believed to represent the physics of the problem more accurately than a wind tunnel experiment can simulate the free flight conditions. An example of this is the supersonic or hypersonic, laminar, perfect gas flow over a simple geometry at low angle of attack.

The realization that certain flow fields can be computed more accurately than they can be measured experimentally must begin to change the relationship between computational and experimental aerodynamics. This paper addresses this changing relationship and seeks to improve the synergism between computational aerodynamics and wind tunnel experimentation. The physical and numerical approaches can each gain by using the strengths of one approach to offset the weaknesses of the other, and vice versa. In this project, experiments and computations were jointly conducted for hypersonic, perfect gas, laminar flow over a hypersonic vehicle geometry. The model geometry was designed so that it could easily be modified to produce a range of flow characteristics. For the simplest configuration, we developed higher confidence in the quality of the computational fluid dynamic (CFD) solutions than the experiment. For the more complex configurations, however, the reverse was true.

In experiments designed to validate CFD codes, experimentalists must develop a better understanding of the assumptions made in the numerical simulation so that experiments can be designed that match these assumptions. For example, in choosing a body geometry with which to validate a CFD code, a configuration should be chosen that eliminates unnecessary numerical difficulties. In the present experiment, this is achieved by requiring the body flap to extend to the base plane of the body for all flap deflections. Although this would be unrealistic in actual flight vehicle hardware, it allows a great simplification in body geometry description and outflow boundary conditions in the numerical simulation.

---

* This work performed at Sandia National Laboratories supported by the U. S. Department of Energy under contract No. DE-AC04-76DP00789.

[†] Senior Member Technical Staff.

[††] Distinguished Member Technical Staff.

In this paper, computational and experimental results are presented for a hypersonic vehicle configuration at Mach 8. All of the results were obtained in the Sandia Mach 8 long-duration, blowdown, hypersonic wind tunnel. The basic vehicle configuration is a spherically blunted cone with a slice parallel with the axis of the vehicle. The half-angle of the cone is 10°, and the ratio of spherical nose radius to base radius is 10%. Flaps of various deflection angles can be attached to the slice portion of the vehicle; here, deflection angles of 10°, 20°, and 30° were utilized. An extensive uncertainty analysis was conducted to estimate quantitatively the accuracy of the experimental measurement. The Sandia parabolized Navier-Stokes code is used to generate solutions for the sliced vehicle. For the geometry with the flap deflected, reversed flow occurs, and a time iterative Navier-Stokes code is used to provide comparisons with the data. A detailed study of grid convergence is presented to determine quantitatively the accuracy of the numerical solutions. A comparison of experimental and numerical results for aerodynamic forces and moments is discussed.

2. EXPERIMENTAL INVESTIGATION

2.1 Wind Tunnel and Model Geometry

The Sandia National Laboratories blowdown-to-vacuum hypersonic wind tunnel consists of three contoured axisymmetric nozzles, arranged like a Gatling gun around a common hub. The test section Mach numbers are nominally 5, 8, and 14, respectively. Each nozzle is provided with its own electric resistance heater. Dry nitrogen is used as the test gas for Mach 8 operation, for which the available ranges of p_0 and T_0 provide a unit Reynolds number range of 0.8 to 6.2 million/ft (2.6 to 20.3 million/m). The test section has a diameter of 14 in. (355 mm) and is provided with 8x15 in. (203x381 mm) schlieren-grade windows on the top, bottom, and sides. Usable run times are typically 30-60 seconds, depending on flow Reynolds number, and turnaround time between runs is one hour or less.

A vehicle geometry was carefully chosen for this project that would allow exploration of the strengths and weaknesses of both numerical simulation and physical experiments. The selected geometry is a 10% spherically blunted cone with a slice on the windward side (see Fig. 1). The geometry has two nose tips, a spherically blunted tip and a sharp conical tip, to provide additional flexibility in altering the boundary layer transition point on the model. The slice begins at 0.7 of the length of the body, measured from the spherical nose. The model was designed so that different flaps can be attached to the aft portion of the slice, as noted above. The trailing edge of each flap extended completely to the base of the body.

2.2 Instrumentation

Forces and moments on the model are derived from a six-component, temperature-compensated strain gage balance mounted internal to the model. The axial location of the balance was chosen so that the center of pressure normally lay between the balance gages. A careful calibration of the balance was performed before the start of the experimental program; the resulting matrix of second-order interaction coefficients was then used in all data reduction. Check weights were hung periodically throughout the test series to ensure absence of zero shift or linearity change.

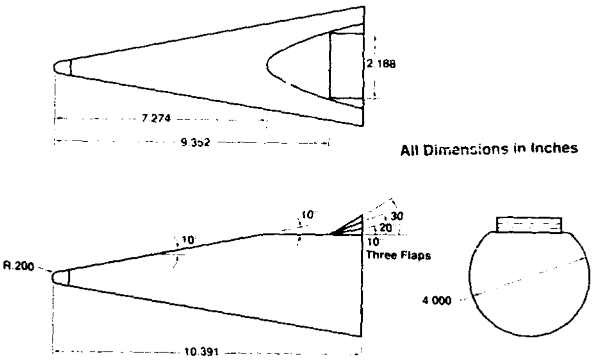

Figure 1: Wind Tunnel Model

It was essential to determine base pressure accurately because of the relatively large contribution of the base pressure to the axial force coefficient. Base pressure was measured at five locations at varying radial and circumferential positions on a base plate attached to the sting just aft of the model. The base plate was a sharp-edged plate set aft 0.065 in. (1.65 mm) from, and parallel to, the model base. The circumferential contour of the plate was 0.2 in. (5.08 mm) radially inward from the edge of the base of the model. Care was taken to ensure it did not contact the model at any point for any flow condition or angle of attack. The five base pressure orifices were located on the base plate so that the pressure measured was actually the pressure in the gap between the model and the base plate. The local pressure on the base plate was assumed to exist at the adjacent point on the base of the model.

To provide thermal boundary conditions of the model surface for the CFD simulations, thermocouples were mounted in the inner surface of the 0.1 in. (2.54 mm) wall, stainless steel, model. Two thermocouples were mounted in the plane of symmetry on the slice side of the model, and two were mounted 180° circumferentially around the model. One pair was located 6 in. (152.4 mm) from the nose, and the other was 7 in. (177.8 mm) from the nose. The wall temperature during a run at these locations varied from 535 to 590 R (297 to 328 K). Because of the very high heat transfer rate near the nose, it is certain that the surface temperature farther forward was higher than temperatures measured with the thermocouples.

Shear-stress-sensitive, temperature-insensitive liquid crystals [1,2] were used in an attempt to help determine the state of the boundary layer (laminar, turbulent, or transitional) and also to visualize surface flow phenomena. Given the proper sensitivity to shear stress, these temperature-insensitive liquid crystals (LCs) change the color of reflected white light as the level of shear stress changes. Quantitative calibration of the reflected colors in terms of shear stress has not been successful; therefore, the technique is entirely qualitative.

2.3 Experimental Conditions and Data Acquisition

As this experiment was designed to be jointly conducted with a numerical simulation, it was important that the state of the boundary layer was known with confidence. Liquid crystals were applied to the surface of the model to determine whether the boundary layer was laminar or turbulent. A Reynolds number of 1.80×10^6, based on model length, was chosen so that laminar flow was assured over the length of the vehicle for all angles of attack (see Section 4.1). The average stagnation conditions were T_o = 1106 R (614 K) and p_o = 340 psia (2.34×10^6 Pa), and freestream Mach number and dynamic pressure were 7.84 and 1.727 psi (1.191×10^4 Pa), respectively. Although the measured wall temperature varied during a run, as mentioned earlier, the numerical simulations used an average wall temperature of 570 R (317 K).

The angle of attack was varied from -10 to 18°. The nominal angles of attack at which forces and moments were measured were -10, -7, -4, -1, 0., 2, 5, 8, 11, 14, 16, and 18°. The roll angle was set at 0 (slice on the windward side), 90, 180, and 270°. The primary purpose for the four roll angles was to quantify the effect on aerodynamic forces and moments of any possible flow field nonuniformities in the wind tunnel. These multiple roll angles were necessary in estimating the uncertainty bounds on the force and moment measurements.

Listed in Table 1 is a run schedule for the experiment. As can be seen from the table, several body geometry and roll angles have multiple runs. This was done to aid in the quantitative uncertainty analysis discussed in the next section. In addition, two different axial locations in the test section were used. This was done so that uncertainty due to possible flow field variations from one tunnel station to another could be evaluated. It is well known that axisymmetric nozzles can be subject to significant variations in flow conditions along the nozzle axis.

During preliminary runs, all five base pressures were recorded at a high data rate and subsequently displayed on a strip chart recorder to assess the pressure lags in the system. The pressure stabilization times required were significant, up to 4 s after a continuous 10° change in angle of attack. These data were then used to pre-set the pitch mechanism pause time between α changes to ensure that all base pressures were stable before data acquisition. (See Ref. 3 for more details.)

Table 1: Run Number Summary

ϕ (deg.)	δ=0°	δ=10°	δ=20°	δ=30°
Tunnel Station 7.6 inches				
0	34,36,37,73	63,72	64,71	65,70
90	39	66,67	69	68
180	40	55	56,57	58
270	41	62	61	59,60
Tunnel Station 4.1 inches				
0	74,75	83	82	81
180	76,77	78	79	80

2.4 Uncertainty of Measurements

In surveying the literature documenting a wide variety of wind tunnel experiments, one rarely finds an analysis conducted to quantify the uncertainty of the measurements. Many times this lack is justified because of the press of time or budget constraints. In experiments designed to validate CFD codes, however, this is strongly believed to be unacceptable. In experiments of this type, special attention should be given to constructing the run schedule to maximize information for an uncertainty analysis and then to quantitatively analyze measurement uncertainty. Typical uncertainty analyses consider the repeatability of individual instrumentation components such as freestream conditions in the test section, strain gages, and pressure transducers [4]. It is clear from using this type of procedure that certain factors contributing to measurement uncertainty are not included: for example, uncertainty due to freestream flow nonuniformities and the interaction of various instrumentation components. An innovative procedure was devised in the current effort that is able to quantify the total uncertainty of force and moment measurements. Further, this procedure is able to delineate the uncertainty into two components; instrumentation uncertainty and test section flow field nonuniformity. This analysis is an experimentally based statistical estimate of variance components of forces and moments.

The instrumentation uncertainty is that uncertainty in body forces and moments caused by all of the following: strain gage hysteresis, nonlinearity, thermal sensitivity shift, and thermal zero shift; the analog data acquisition system; the data reduction software; model pitch, roll, and yaw alignment; run-to-run variations in setting freestream conditions in the test section; and base pressure transducers and instrumentation for eliminating base drag. That is, the instrumentation uncertainty combines all uncertainty components in the entire experiment except those due to test section flow field nonuniformity. To calculate the instrumentation uncertainty, one compares body force and moment measurements for the same physical location in the test section. By examining the run schedule, Table 1, one can choose run pairs that have the same pitch and roll angles and the same location in the test section, and then make comparisons between the measured body force and moment coefficients. Typical run pairs that can be formed are [34,36], [37,73], [56,57], and [74,75]. The total number of run pairs that can be formed for quantifying the instrumentation uncertainty is 14.

Let the difference between an individual force and moment measurement and the average measurement at each angle of attack be defined as the local residual, Δ. For example,

$$(\Delta C_n)_{\alpha_i} = (C_n)_{\alpha_i} - (\overline{C_n})_{\alpha_i} \qquad i=1,2,\ldots I$$

where $(\overline{\ })$ is the average value for each run pair at each angle of attack and I is the maximum number of angles of attack that are in common for the run pairs formed. The total number of instrumentation residuals, i.e., measurements at each pitch angle, is 320 for each quantity:

normal force, pitch moment, center of pressure, and axial force. (See Ref. 3 for more detail.)

The uncertainty in body forces and moments due to a combination of instrumentation uncertainty and test section flow field nonuniformity can be computed by comparison of certain runs. The uncertainty due solely to test section flow field nonuniformity, hereafter referred to as flow nonuniformity, can be calculated by statistical methods. This will be discussed later. Combined instrumentation and flow nonuniformity uncertainty are calculated by comparing force and moment measurements when the model is at physically different locations in the test section. By examining the run schedule, Table 1, one finds two different ways of attaining different locations in the test section. The first method forms run pairs that have the same roll angle and flap angle, but are at different axial stations in the test section. Typical run pairs that can be formed are [34,74], [37,75], [64,82], and [58,80]. The total number of run pairs that can be formed in this way is 20.

The second method forms run pairs based on mirror symmetry between the model at a roll angle of 0° and pitched to a positive angle of attack, and the model at a roll angle of 180° and pitched to the same negative angle of attack. The mirror symmetry pairs are formed for both runs at the same axial station. As the maximum negative angle of attack was -10°, the residuals for individual angles of attack can only be calculated over the range -10 to $+10^o$. Typical run pairs that can be formed are [34,40], [64,56], [74,76], and [81,80]. The total number of run pairs that can be formed in this way is 19. The total number of residuals, from both types of run pairs, that combine instrumentation and flow nonuniformity is 740 for each quantity: normal force, pitch moment, center of pressure, and axial force.

Table 2 gives the estimated standard deviation, $\hat{\sigma}$, (square root of the variance estimate) due to instrumentation, flow nonuniformity, and the total for each quantity measured in the experiment. Also shown in the table is the percent contribution due to each of the components identified. In the calculation for the standard deviation for x_{cp}/L, all residuals for angles of attack of -1, 0, and $+1^o$ were excluded. This was done because it is well known that the uncertainty in x_{cp} becomes infinite as the normal force and pitch moment approach zero. From Table 2 it can be seen that the uncertainty in C_n, C_m, and x_{cp} due to the entire wind tunnel system instrumentation ranges from 9 to 20%, whereas that due to flow nonuniformity is 80 to 91%.

Although this type of uncertainty analysis is new to wind tunnel data analysis, it is suspected that most wind tunnel experiments are dominated by flow field uncertainty and not instrumentation uncertainty. Table 2 shows that the uncertainty in forebody axial force coefficient is 63% due to instrumentation and 37% due to flow. This reversal of uncertainty contributions compared to the other quantities is believed due to instrumentation inaccuracies in removing base drag from the total axial force.

3. COMPUTATIONAL INVESTIGATION

Two types of numerical approaches were used for comparison with, and evaluation of, the experimental measurements: a parabolized Navier-Stokes (PNS) approach and a time iterative Navier-Stokes approach. The PNS approach is able to tightly couple the viscous and inviscid flows and accurately simulate cross-flow separation. The PNS approach can be used for all supersonic flows as long as the axial flow remains in the streamwise direction. Time iterative Navier-Stokes solutions were computed only in regions where the flow is subsonic or axially separated. A summary of the two solution techniques follows.

3.1 Blunt Nose Solution for PNS Calculations

To obtain parabolized Navier-Stokes solutions over a blunt nosed vehicle, the three-dimensional, subsonic and supersonic flow over the spherical nose is calculated first by using the thin layer, time iterative, Navier-Stokes equations. The three-dimensional Navier-Stokes (NS3D) code [5,6] is used to compute the flow field around the nose. The NS3D code provides a starting solution for the parabolized Navier-Stokes code, which is used to advance the flow field solution along the body. The NS3D equations are obtained from the unsteady Navier-Stokes equations by neglecting the viscous derivatives in the streamwise and circumferential directions. The viscous derivatives are retained only in the normal direction. This is referred to as the thin layer model. The same viscous terms that are dropped in boundary layer theory are also dropped in the thin layer model. However, the vertical momentum equation is retained, and a constant pressure is not imposed through the viscous layer. Unlike boundary layer theory, the thin layer model avoids the difficulty of matching an inviscid layer with a viscous layer.

NS3D solves the continuity, momentum, and energy equations in a body-fitted, shock-fitted transformed space. The equations are solved by approximating all partial derivatives by finite difference expressions. The difference

Table 2: Summary of Results for Uncertainty Analysis

Uncertainty Type	C_n		C_m		x_{cp}/L		C_a	
	$\hat{\sigma}$	%	$\hat{\sigma}$	%	$\hat{\sigma}$	%	$\hat{\sigma}$	%
Instrument	0.474×10^{-3}	20	0.406×10^{-3}	19	0.413×10^{-3}	9	0.426×10^{-3}	63
Flow	0.941×10^{-3}	80	0.851×10^{-3}	81	1.322×10^{-3}	91	0.324×10^{-3}	37
Total	1.054×10^{-3}	100	0.943×10^{-3}	100	1.385×10^{-3}	100	0.535×10^{-3}	100

equations are solved by an unsteady, implicit algorithm. Block tridiagonal systems are inverted in each space coordinate at each time step. The solution is advanced in time until a steady-state, i.e., converged, solution is reached.

3.2 Parabolized Navier-Stokes Solution

The PNS equations are thin layer Navier-Stokes equations with an approximation for the convective flux vector. These assumptions permit stable time-like marching of the equations downstream from initial data. The latter assumption does not permit calculation of flows that have separation in the axial direction. Three-dimensional cross-flow separation, however, is permitted. The stated approximations are physically justified for high to moderate Reynolds number flow past bodies with mild axial geometry changes.

The PNS equations are also solved in a body-fitted, shock-fitted transformed space. The finite difference form of the PNS equations are formulated into an approximately factored, locally linearized form. The numerical solution is a noniterative, implicit, finite-difference algorithm. The difference equations are treated in vector form, and their solution requires a factored sequence of block-tridiagonal equations. The equations are solved by inverting the block-tridiagonal systems in the two cross-flow plane coordinates at each location of the marching coordinate. The flow is solved by marching the finite difference equations in planes normal to the axis of the vehicle. Two initial planes of supersonic flow data to start the PNS code are provided by the NS3D code. The afterbody portion is then solved by marching the PNS equations along the body up to the base of the vehicle.

The Sandia PaRabolized Improved Navier-Stokes Technique (SPRINT) code [7], currently in use at Sandia, is an extensively modified version of the Air Force Wright Aeronautical Laboratory parabolized Navier-Stokes code [8]. It is based upon the work of Schiff and Steger [9] and others [10-12]. Sandia has spent several years developing and verifying the SPRINT code by comparing it with experimental data. The code has predicted forces and moments, surface pressure, and heat transfer for different reentry vehicles and flow conditions [13-16].

3.3 Continuation Navier-Stokes Solution

It was anticipated that the sliced vehicle with a large flap deflection would generate a reversed flow region upstream of the flap. To calculate the flow in this region, the SPRINT code was marched to a point ahead of the reversed flow region, and a time iterative Navier-Stokes solution was used to provide the solution over the separated region. The separated region was solved using the F3D code, which was developed by Steger [17] and others [18,19]. It solves the same set of thin layer Navier-Stokes equations described for NS3D, but using a different numerical scheme. The F3D code uses an implicit approximately factored scheme that uses central differences in the circumferential and normal directions and upwinding in the streamwise direction. The streamwise flux vector has been eigen split, allowing the use of backward and forward difference operators.

The F3D code was used to obtain the flow field solutions for the 10°, 20°, and 30° flap deflections. The F3D code was used in the continuation mode with an ideal gas assumed. The flow field grid was provided using the parabolic grid generator in the SPRINT code. The SPRINT solution just ahead of the start of the vehicle slice was imposed over the entire flow field grid to be used as a starting condition for F3D. The F3D code was then marched in time until a steady-state solution was reached. Convergence was assumed when the normalized residuals reached values of 10^{-6} or less.

3.4 Evaluation of Accuracy of Numerical Simulation

To verify quantitatively the accuracy of the computational results, a detailed grid refinement study was performed. Since the force and moment coefficients were compared with experimental data, they were used as the representative parameters in the study. In addition, smoothing and stabilizing parameters were kept to a minimum (zero in some cases) during the grid refinement studies. The grid refinement study presented in this paper is an extension of the work presented by Blottner [20]. The grid is refined in each direction of the three dimensions while holding the other two dimensions fixed. Richardson extrapolation [21] is used to obtain an estimated "exact" solution as the number of grid points approaches infinity. When the parameter of interest, for example axial force coefficient, is less than 1% in error from the estimated exact solution, the grid is considered to be adequately refined for accurate predictions of the given parameter.

The grid study was performed for three cases. First, for the forecone of the sliced vehicle (forward of x/L = 0.7) at α = 0°; second, for the forecone of the sliced vehicle at α = 16°; and third, for the sliced portion of the vehicle (aft of x/L = 0.7) at α = 16°. The forecone solutions were refined separately from the aft portion of the vehicle. This was done because the two portions of the SPRINT solutions were obtained separately. The sliced portion of the vehicle solution was obtained by restarting the SPRINT code just ahead of the slice and respacing the flow field grid to march on the slice. (See Ref. 22 for details on error analysis.)

Table 3: Grid Convergence Study

Case	JMAX (axial)	KMAX (circum.)	LMAX (radial)	Selected Grid J x K x L
$\alpha = 0^{\circ}$	769	3	97	
Forecone	385	3	49	385 x 3 x 49
	193	3	25	
$\alpha = 16^{\circ}$	769	97	97	
Forecone	385	49	49	385 x 49 x 49
	193	25	25	
$\alpha = 16^{\circ}$	769	193	97	
Sliced	385	97	49	193 x 49 x 49
Portion	193	49	25	

Table 3 shows the selected values for JMAX, KMAX, and LMAX for the grid study. Solutions were obtained for all three values of JMAX while using fixed values of KMAX and LMAX. Solutions were obtained while varying KMAX and LMAX in a similar manner. As shown in Figs. 2-4, the fixed values were always twice the converged grid values shown in Table 3 for each case. The value for KMAX was held constant at 3 for the α = 0° solutions because the solution is axisymmetric and the SPRINT code uses cylindrical coordinates.

3.5 Grid Refinement Results

The percent errors for each case and force and moment coefficient are plotted in Figs. 2 through 4. The validity of Richardson extrapolation for the grid sizes used is demonstrated by noting that the slope of the lines in the figures should be the same as the order of the solution. For the lines shown in Fig. 2, the slope should be -1. For the lines shown in Figs. 3 and 4, the slope should be -2. The points shown in Fig. 2 exhibit the expected behavior except for the normal force and pitch moment curves for the forecone at α = 16°. It is felt that any nonlinearity is probably due to required values of smoothing and stabilizing parameters in the SPRINT solutions. Similar results are shown in Figs. 3 and 4 for the refinement in KMAX and LMAX. The accepted values for JMAX, KMAX, and LMAX for each portion of the body are shown in the last column of Table 3.

In addition to computing the exact solution in each direction as if it were a one-dimensional problem, the exact solution was computed using Richardson extrapolation. The percent error from the three-dimensional "exact" solution was computed to determine if the selected grid parameters produced answers that fell within the accepted error. For all three cases, the solutions using the selected grid sizes shown in Table 3 fell within the 1% bound for the fully three-dimensional error estimate.

To anticipate the more complex flow when the flap was deflected, the number of circumferential grid points was arbitrarily increased from 49 to 91 (in the half-plane). Figure 5 shows the vehicle surface grid used for the δ = 30° SPRINT/F3D solutions. It was felt that 91 circumferential grid points would adequately resolve the flow in the region of the flap, but, as opposed to the previous quantitative error analysis, this was purely intuitive. Grid refinement studies were not performed using the F3D code due to the large computing costs. The number of axial points was thinned (SPRINT used 193) because of computer memory limitations. The number of points selected for the axial direction for F3D was 93 (from the start of the slice to the end of the flap). To capture the outer bow shock in F3D, 10 additional radial grid points were added, yielding 59.

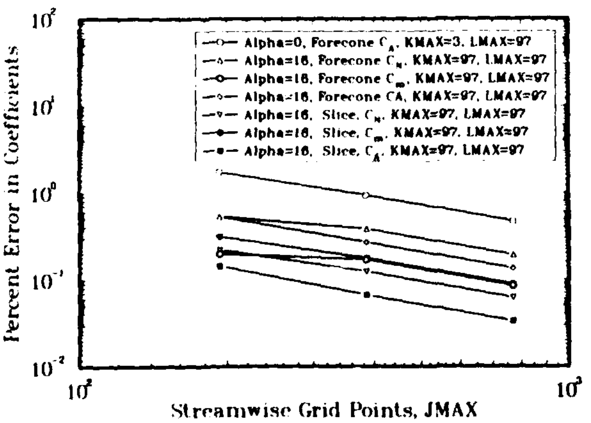

Figure 2: Error in Numerical Force and Moment Coefficients vs. JMAX

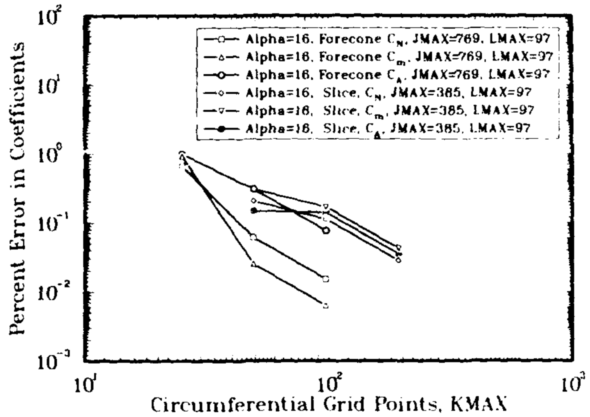

Figure 3: Error in Numerical Force and Moment Coefficients vs. KMAX

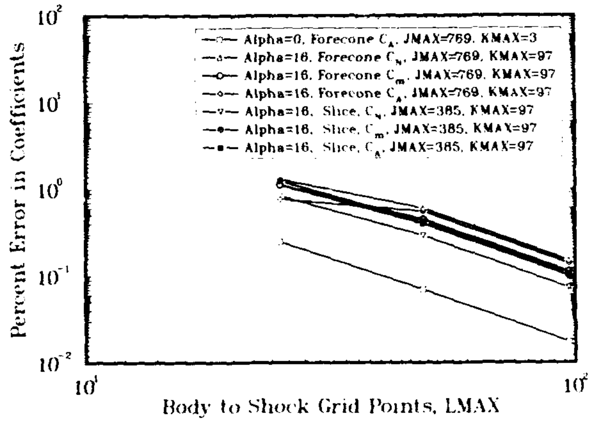

Figure 4: Error in Numerical Force and Moment Coefficients vs. LMAX

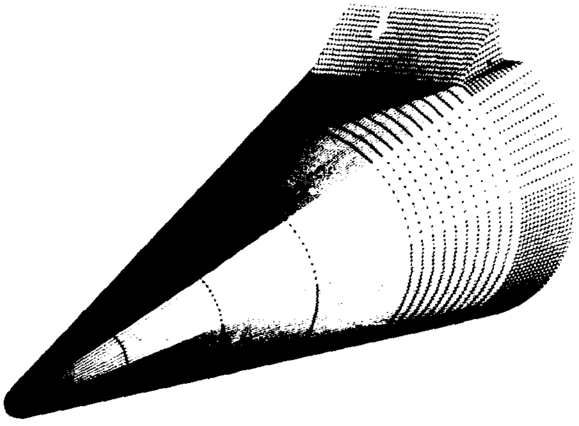

Figure 5: Surface Grid for 30° Flap Deflection, KMAX = 91 in half-plane

4. DISCUSSION OF RESULTS

4.1 Laminar Flow Determination

As this experiment was designed to be a CFD validation experiment for laminar flow, it was crucial to choose the proper Reynolds number. It was hoped that the liquid crystal color change diagnostic technique would provide this information, but a satisfactory color change due to shear stress alone was not achieved. The two most sensitive liquid crystals available were used, but they did not produce the color range desired because of the low surface shear stress at the test conditions. They were, however, still very useful in determining laminar and turbulent flow because of their surface flow visualization capability.

Initial boundary layer determination runs were made with a freestream Reynolds number (based on model length) of 5.0×10^6. Boundary layer studies were made at both 0 and 15° angle of attack as it is known that transition can be triggered by crossflow [23]. At this Reynolds number the surface flow pattern of the liquid crystals showed a distinct surface flow wave pattern at $\alpha = 15^o$. These waves were first distinguishable at about $x/L = 0.45$ and extended to the base of the model. They were standing waves at an angle of roughly 35° to the local surface shear stress. These waves have been observed previously by McDevitt and Mellenthin [24] and Adams [25] in transition studies on hypersonic cones. They are actually stationary vortices near the model surface that occur during the initial instability of the boundary layer before transition. This inflectional instability has been analyzed by Tobak [26] and others. At a Reynolds number of 3.5×10^6, these waves again appeared, but they began at $x/L = 0.6$ and continued to the base of the body. To attain fully laminar flow, even at the highest angle of attack, the Reynolds number was again reduced, this time to 1.8×10^6. At this condition, these stationary vortices could be only faintly seen near the base of the body at $\alpha = 15^o$. Therefore, this Reynolds number was used for all force and moment measurements.

4.2 Slice-Only Configuration

As discussed earlier, the slice-only configuration represents a sufficiently simple geometry, with a laminar boundary layer and only attached flow at low angle of attack. This allows the CFD solution to be computed more accurately than the complete wind tunnel instrumentation system can measure the forces and moments. Therefore, this case actually represents a validation of the physical experiment. For the slice-only configuration, the numerical simulations were shown to contain an absolute error of less than 1% for all force and moment quantities for this configuration.

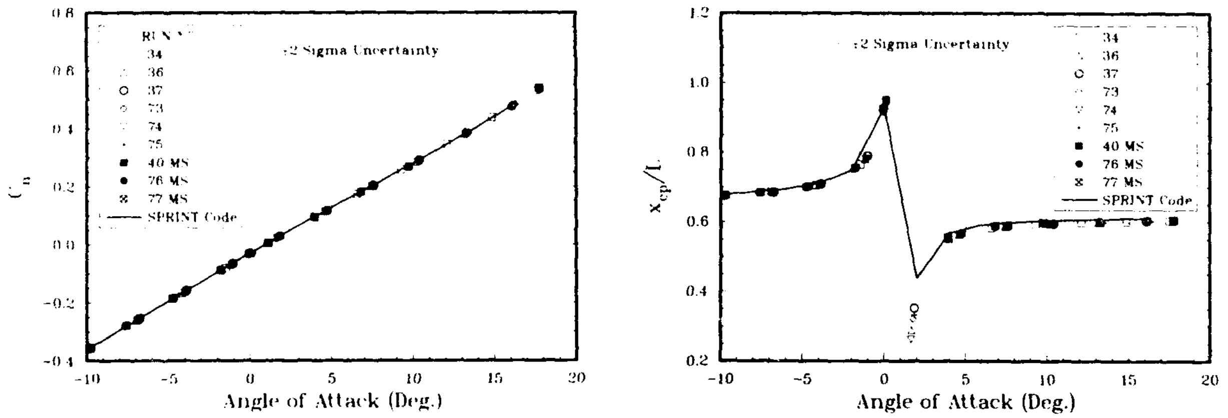

a) Normal Force Coefficient

c) Axial Center of Pressure

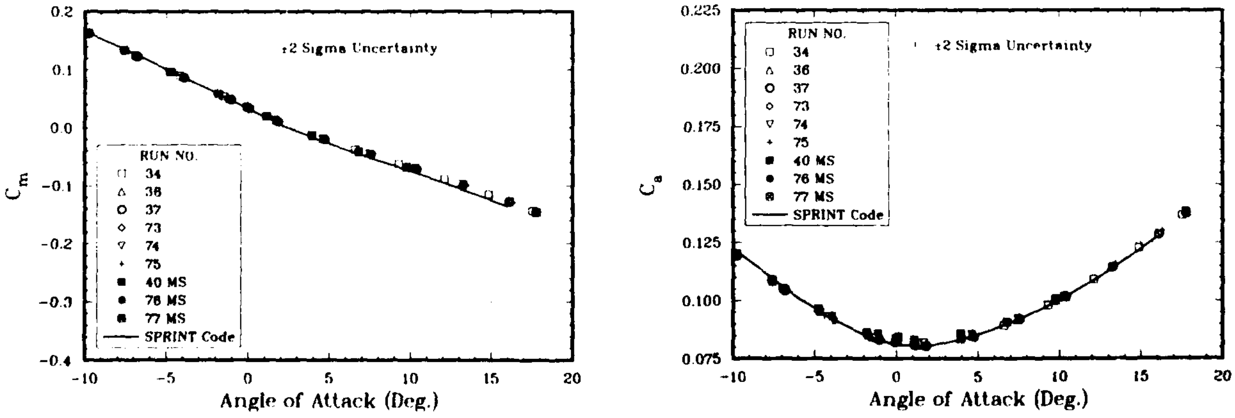

b) Pitch Moment Coefficient

d) Forebody Axial Force Coefficient

Figure 6: Force and Moment Coefficients for Slice-Only Configuration

Figure 6 shows the comparisons between the experimental and numerical results for the slice-only configuration. Figure 6, and every figure showing force and moment measurements, shows data from every run having the same model configuration (see Table 1). That is, plotted in each figure are data from runs that have the same configuration, but at both tunnel axial stations and at a roll angle of 180°. The $\phi = 180^{\circ}$ are referred to as mirror symmetry (MS) runs in the figures. For example, runs 40, 76, and 77 in Fig. 6 are plotted with the $\phi = 0$ runs by setting $\alpha = -\alpha$, $C_n = -C_n$, and $C_m = -C_m$. The slice was located on the windward side of the vehicle for positive angles of attack and on the leeward side of the vehicle for negative angles of attack. The solid line in the figures is a parabolized Navier-Stokes (PNS) calculation using the Sandia code SPRINT. Figure 6a shows excellent agreement between computations and experiment for the normal force coefficient over the entire range of angle of attack.

Figures 6b and 6c show computations and experiment for the pitch moment coefficient and center of pressure, respectively.* It is noted from Fig. 6b that the PNS solution is in excellent agreement with the measurements for low angle of attack, but at large angle of attack, the computations are up to 8% larger (negatively) than the measurements. This disagreement could be due to either slight flow nonuniformities across the test section or inaccuracies in the computations for separated flow on the leeside of the body. If the disagreement is due to nonuniformities in the test section flow field, this could be verified, and eliminated, by inserting the actual measured flow field from the wind tunnel into the computations. Future plans for this joint computational/experimental program call for a detailed recalibration of the test section which will include accurate measurements of the Mach number, pressure, and flow angularity. The actual flow field of the wind tunnel could then be used as nonuniform shock boundary conditions in the computational simulations.

Figure 6d shows computational and experimental results for the forebody ($p_{base} = p_{\infty}$) axial force coefficient. Theory and experiment are in very good agreement over the entire angle of attack range. Note that the $\pm 2\sigma$ uncertainty bound calculated from the uncertainty analysis is larger for C_a than for the other aerodynamic parameters. This is believed to be primarily due to uncertainty in measuring base pressure. In preliminary experimental work, not allowing adequate time for all the base pressure readings to stabilize during the pitch sweep was found to be the dominant contributor to axial force measurement uncertainty. The model pitch timing sequence was then adjusted to minimize this source of error. For hypersonic wind tunnels that use a continuous pitch sweep technique or have very short run times, base pressure stabilization through any tubing length may not be possible. This may require miniature, fast response, surface mounted, base pressure transducers with very high sensitivity for conditions existing in the

4.3 Flap Deflection of 10°

The sliced vehicle with a 10° flap deflection represents a geometry where the SPRINT solutions begin to come into question. For a 10° flap deflection, the laminar boundary layer may axially separate ahead of the flap, and there will certainly be cross-flow separation in the corner formed by the side of the flap and the slice. For this reason, the F3D code was also used to obtain the flow field solutions over the deflected flaps.

Figures 7 and 8 show the comparisons between the experiment and the NS3D/SPRINT and NS3D/SPRINT/F3D codes for the body with 10° flap deflection. In these figures the NS3D/SPRINT combination is referred to as SPRINT, and the NS3D/SPRINT/F3D is referred to as F3D. Agreement between the SPRINT and F3D codes and the experimental data for normal force is quite good and similar to that for the vehicle with no flap. For the axial force coefficient, Fig. 8, the F3D code shows noticeably better agreement with the data than SPRINT. This is expected because of the reversed flow region ahead of the flap. The SPRINT code overpredicts the pressure on the flap, which results in a high prediction for axial force coefficient. The SPRINT solutions were harder to obtain with the flap deflection as compared to the sliced body and required additional numerical damping and stabilizing parameters. SPRINT obviously could not predict the

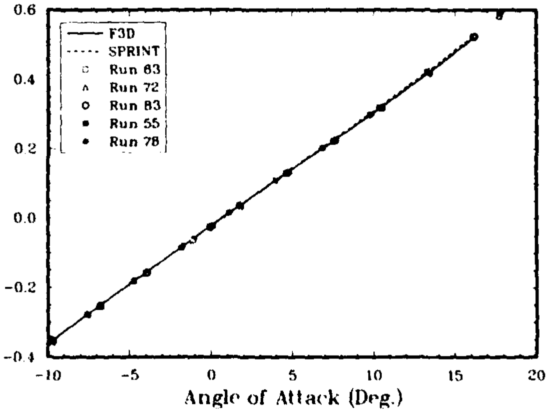

Figure 7: Normal Force Coefficient for 10° Flap Deflection

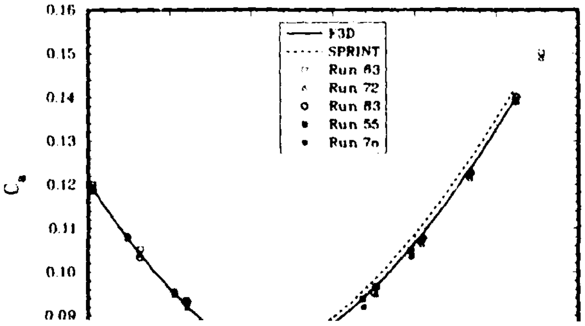

axially separated flow in front of the flap, but it did predict an attached flow. Users of PNS codes are cautioned that a solution may be attainable even though physically there is a thin reversed flow region.

Figure 9 shows a comparison of the experimental oil flow and particle trace lines predicted by the F3D code for zero angle of attack and a 10° flap deflection. The experimental surface flow visualization shows an axially separated flow region ahead of and onto the flap. Comparing the experimental oil flow and the computational traces, it is seen that the code accurately predicts the forward extent of the separated flow region, but the lateral (spanwise) extent is under predicted. The F3D code predicts a thin layer of negative axial velocities at the last axial solution plane. This implies that the flow never reattaches onto the flap and flow is moving onto the flap from the base of the vehicle. The F3D code does not solve the region on the base and, therefore, the solutions become questionable. The code uses an outflow boundary condition which dictates that the last plane of data be the same as the next to last plane. This is a first order boundary condition that could be improved.

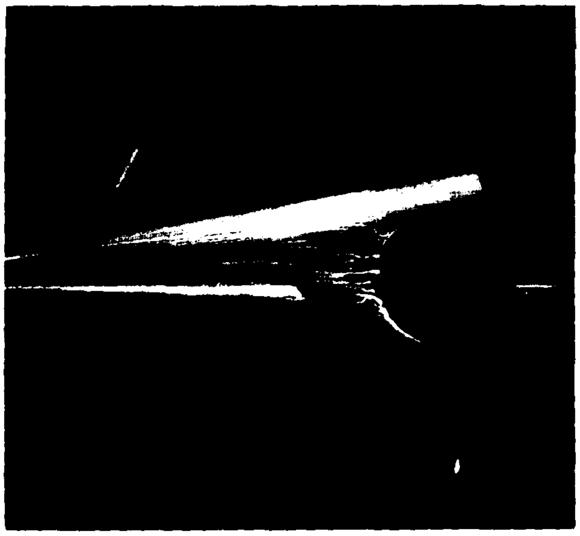

a) Experimental Surface Flow

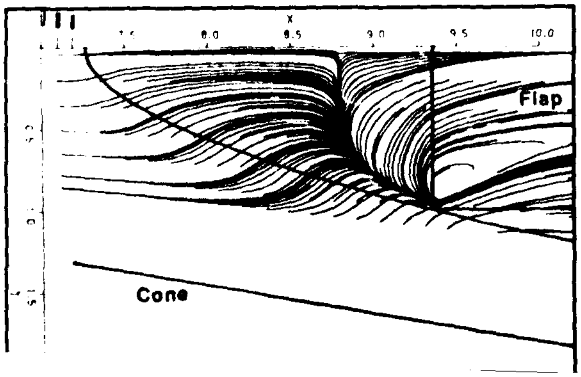

4.4 Flap Deflections of 20° and 30°

Figure 10 presents computational and experimental results for axial force coefficient for a flap deflection of δ = 20°. The comparisons at positive angles of attack disagree by as much as 10%. The axial force comparisons are in good agreement for the negative angles of attack. This is only fortuitous, however, because the low pressure on the leeward side of the vehicle causes a loss in effectiveness of the flap. The F3D solutions have been carefully examined, and shortcomings in neither the numerical approximations nor the grid structure can be found. It is possible that the flow from the base needs to be coupled with the solution over the rest of the vehicle. If this is true, this could significantly increase the complexity and cost of CFD solutions that have this type of flow.

Figures 11 and 12 show results for the center of pressure and axial force coefficient for the 30° flap deflection. It is seen from Fig. 11 that the computational results for the center of pressure are in error up to 0.07L for positive angles of attack. The F3D code also disagrees with the axial force coefficient measurements, Fig. 12, by as much as 20% at positive angles of attack. The F3D surface grid definition used 91 points in the circumferential half-plane, but this may not be sufficient to accurately compute the three-dimensional flow off the sides of the slice and flap. The spanwise pressure variation was inspected in the region of the flap, and it appears reasonable for this type of flow. The magnitude of the pressure is seriously questioned, however, because the computational results for axial force are much larger than the experiment. Another factor that may enter into the disagreement between computations and experiment is that reattachment of the free-shear layer onto the flap is probably turbulent. Transition and turbulent flow are not in the present numerical simulation.

In an attempt to identify the computational shortcomings, two additional computations were made. First, the F3D solution at α = 8° and δ = 30° was allowed to converge an additional 800 time steps beyond the typical 800 time steps required to achieve the previously stated convergence. This had no appreciable effect on center of pressure or axial force coefficient predictions. An additional calculation was made with 151 grid points circumferentially in the half-plane for α = 8° and δ = 30°, but this did not significantly affect the

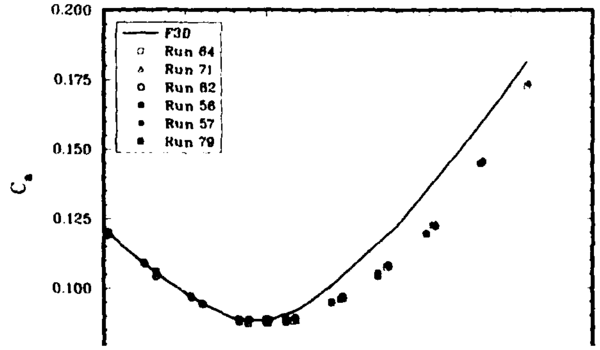

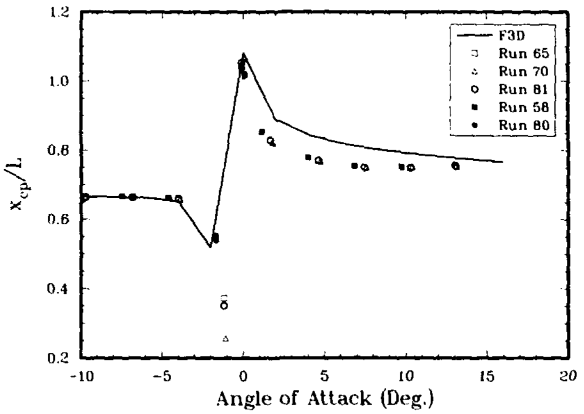

Figure 11: Center of Pressure for 30° Flap Deflection

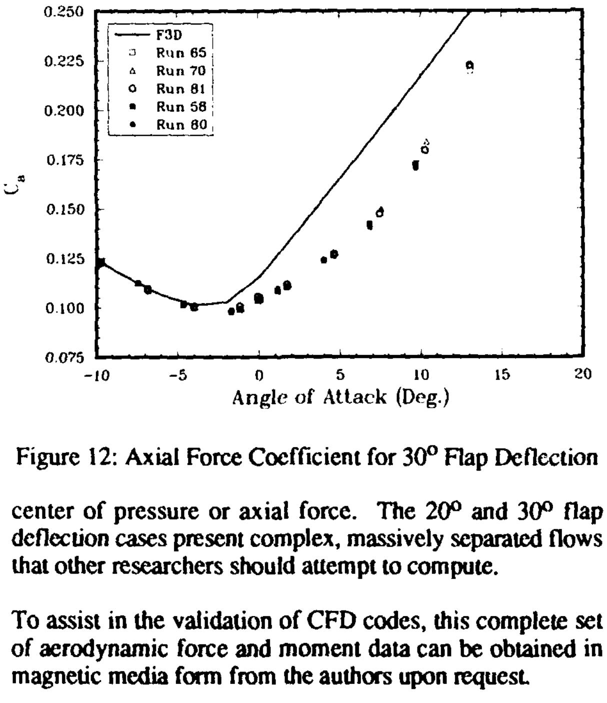

Figure 12: Axial Force Coefficient for 30° Flap Deflection

center of pressure or axial force. The 20° and 30° flap deflection cases present complex, massively separated flows that other researchers should attempt to compute.

To assist in the validation of CFD codes, this complete set of aerodynamic force and moment data can be obtained in magnetic media form from the authors upon request.

5. CONCLUSIONS AND RECOMMENDATIONS

Very good agreement between experimental and computational results were obtained for the slice-only model geometry for all force and moment coefficients. The high accuracy of the numerical solutions for flow over this simple geometry suggest areas where the experimental measurements might be improved. The PNS code attained only fair agreement with the measurements for the 10° flap deflection. For this case, the F3D code agreed very well with the experimental data and it also predicted a small axially separated region ahead of the flap. For flap deflections of 20° and 30°, F3D solutions were seriously in error. Although different numerical improvements were investigated for the 20° and 30° flap deflections, none were shock/boundary layer/separated flow interaction. Other CFD researchers are encouraged to predict these flow fields and compare with the experimental data.

Experimental investigators should take a more constructively critical view toward their measurements, particularly for CFD validation experiments. They should identify and quantify components of uncertainty through detailed uncertainty analyses. Likewise, numerical simulations should routinely include error analyses. With the strengths and weaknesses of each approach openly discussed, a more beneficial and productive relationship can be developed in the future.

6. ACKNOWLEDGEMENTS

The help of Roger Tate, Robert Croll, Ken Harmon, John Henfling, and Don Larson, members of the Aerodynamics Department, is greatly appreciated. In addition, the authors thank Daniel Barnette for his help in running the F3D code and Fred Blottner for his help in executing the grid study.

7. REFERENCES

1. Reda, D. C., "Observations of Dynamic Stall Phenomena on an Oscillating Airfoil with Shear-Stress-Sensitive Liquid Crystal Coatings," Proceedings of the 17th International Council of the Aeronautical Sciences, Stockholm, Sweden, Sept. 1990.

2. Reda, D. C. and Aeschliman, D. P., "Liquid Crystal Coatings for Surface Shear Stress Visualization in Hypersonic Flows," *Journal of Spacecraft and Rockets*, Vol. 29, No. 2, Mar-Apr 1992, pp. 155-158.

3. Oberkampf, W. L., Aeschliman, D. P. and Tate, R. E., "Experimental Aerodynamics Research on a Hypersonic Vehicle," Sandia National Labs. Report in preparation, 1992.

4. "Aerodynamic Data Analysis and Quality: Requirements and Capabilities in Wind Tunnel Testing," AGARD CP-429, 1987.

5. Blottner, F. G. and Larson, D. E., "Navier-Stokes Code NS3D for Blunt Bodies, Part I: Analysis, Results, and Verification," Sandia National Labs Report, SAND88-0504/1, March 1988.

6. Blottner, F. G. and Larson, D. E., "Navier-Stokes Code NS3D for Blunt Bodies, Part II: User's Manual," Sandia National Labs Report, SAND88-0504/2, March 1988.

7. Walker, M. A., "SPRINTRUN: A User Friendly Input Processor for the SPRINT Code," Sandia National Labs Report, SAND89-0625, March 1990.

8. Stalnaker, J. F., Nicholson, L. A., Hanline, D. S., and McGraw, E. H., "Improvements to the AFWAL Parabolized Navier-Stokes Code Formulation," AFWAL-TR-86-3076, September 1986.

10. Chaussee, D. S., Patterson, J. L., Kutler, P., Pulliam, T. H., and Steger, J. L., "A Numerical Simulation of Hypersonic Viscous Flows over Arbitrary Geometries at High Angle of Attack," AIAA Aerospace Sciences Conference, Paper No. 81-0050, 1981.

11. Rizk, Y. M., Chaussee, D. S., and McRae, D. S., "Computation of Hypersonic Viscous Flow Around Three-Dimensional Bodies at High Angles of Attack," AIAA Fluid and Plasma Dynamics Conference, Paper No. 81-1261, 1981.

12. Nicolet, W. E., Shanks, S., and Srinivasan, G., "Flowfield Predictions About Lifting Entry Vehicles," AIAA Aerospace Sciences Conference, Paper No. 82-0026, 1982.

13. McWherter, M., Noack, R. W., and Oberkampf, W. L., "Evaluation of Boundary- Layer and Parabolized Navier-Stokes Solutions for Re-entry Vehicles," *Journal of Spacecraft and Rockets*, Vol. 23, No. 1, Jan-Feb 1986, pp. 70-78.

14. Walker, M. M. and McBride, D. D., "Comparisons of CFD Flow Field Solutions with Experimental Data at Mach 14," AIAA Aerodynamic Testing Conference, Paper No. 86-0742-CP, March 1986.

15. Bartel, T. J., Homicz, G. F., and Walker, M. A., "Comparisons of Monte-Carlo and PNS Calculations for Rarefied Flow Over Reentry Vehicle Configurations," AIAA Aerospace Sciences Meeting, Paper No. 88-0465, Jan. 1988.

16. Hudson, M., "Evaluation of PNS-Computed Heating and Hypersonic Shock Tunnel Data on Sharp and Inclined Blunt Cones," AIAA Aerospace Sciences Meeting, Paper No. 89-0310, Jan. 1989.

17. Steger, J. L., Ying, S. X., and Schiff, L. B., "A Partially Flux-Split Algorithm for Numerical Simulation of Compressible Inviscid and Viscous Flow," Proceedings of the Workshop on Computational Fluid Dynamics, Institute of Nonlinear Sciences, University of California, Davis, California, 1986.

18. Ying, S. X., Steger, J. L., Schiff, L. B., and Baganoff, D., "Numerical Simulation of Unsteady, Viscous, High Angle of Attack Flows Using a Partially Flux-Split Algorithm," AIAA Atmospheric Flight Mechanics Conference, Paper No. 86-2179, August 1986.

19. Srinivasan, G. R., and McCroskey, W. J., "Navier-Stokes Calculations of Hovering Rotor Flowfields," *Journal of Aircraft*, Vol. 25, No. 10, Oct. 1988, pp. 865-874.

20. Blottner, F. G., "Accurate Navier-Stokes Results for the Hypersonic Flow Over a Spherical Nosetip," *Journal of Spacecraft and Rockets*, Vol. 27, No. 2, March-April 1990, pp. 113-122.

21. Richardson, L. F. and Gaunt, J. A., "The deferred approach to the limit," *Trans. Royal Soc.*, London, Series A, Vol. 226, 1927, pp. 229-361.

22. Walker, M. A. and Oberkampf, W. L., "Joint Computational/Experimental Aerodynamics Research on a Hypersonic Vehicle: Part 2, Computational Results," AIAA Aerospace Sciences Meeting, Paper No. 91-0321, Jan. 1991.

23. Balachandar, S., Streett, C. L., and Malik, M. R., "Secondary Instability in Rotating Disk Flow," AIAA Fluid Dynamics, Plasma Dynamics and Lasers Conference, Paper No. 90-1527, June 1990.

24. McDevitt, J. B. and Mellenthin, J. A., "Upwash Patterns on Ablating and Nonablating Cones at Hypersonic Speeds," NASA-TN D-5346, July 1969.

25. Adams, J. C., Jr., "Three-Dimensional Laminar Boundary Layer Analysis of Upwash Patterns and Entrained Vortex Formation on Sharp Cones at Angle of Attack," AEDC-TR-71-215, 1971.

26. Tobak, M., "On Local Inflexional Instability in Boundary-Layer Flows," *Zeitschrift für angewandte Mathematik und Physik*, Vol. 24, 1973, pp. 330-354.

Issues and Approach to Develop Validated Analysis Tools for Hypersonic Flows: One Perspective

George S. Deiwert
Chief, Aerothermodynamics Branch
NASA Ames Research Center
Moffett Field, California 94035
USA

1. SUMMARY

Critical issues concerning the modeling of low density hypervelocity flows where thermochemical nonequilibrium effects are pronounced are discussed. Emphasis is on the development of validated analysis tools, and the activity in the NASA Ames Research Center's Aerothermodynamics Branch is described. Inherent in the process is a strong synergism between ground test and real gas CFD. Approaches to develop and/or enhance phenomenological models and incorporate them into computational flow field simulation codes are discussed. These models have been partially validated with experimental data for flows where the gas temperature is raised (compressive flows). Expanding flows, where temperatures drop, however, exhibit somewhat different behavior. Experimental data for these expanding flow conditions is sparse and reliance must be made on intuition and guidance from computational chemistry to model transport processes under these conditions. Ground based experimental studies used to provide necessary data for model development and validation are described. Included are the performance characteristics of high enthalpy flow facilities, such as shock tubes, ballistic ranges

2. INTRODUCTION

The development of validated analysis tools for hypersonic flows involves a process in which real-gas CFD development and application and experimental testing are performed hand-in-hand, synergistically, until the validation is complete. Hypersonic flows inherently involve real gas phenomena. The validation of CFD tools requires considerations associated with perfect gas CFD validation plus consideration of additional complexities associated with real gas phenomena. These complexities include thermal and chemical time scales, multiple gas species, internal energy flow variables and properties, and coupled fluid/chemical processes.

That it is not possible to fully simulate real gas hypersonic flight conditions in ground test facilities is axiomatic. Ground test experiments must be carefully selected to validate basic principles and concepts in CFD codes. It is necessary to use CFD in the design of experiments, in the definition of the test environment, in the development, application and interpretation of diagnostics, and in the analysis of the test results as a whole. The resulting test data will then form a basis for validating the process and the CFD tools. The CFD codes can be used to extrapolate to flight conditions. And, finally, flight experiments are required to confirm the process as a whole.

These concepts will be developed, in part, in this paper and illustrative examples will be presented. First, the problem will be characterized in terms of aspects of real gas behavior and features associated with high enthalpy, hypervelocity ground test facilities. Next, the importance of real gas phenomena will be discussed as it relates to both aerodynamic

Finally, the process of developing validated analysis tools will be described as represented by selected examples of the ongoing research program in the Aerothermodynamics Branch of the NASA Ames Research Center.

3. CHARACTERISTICS OF REAL GAS

The character of a real gas is described by the internal degrees of freedom and state of constituent molecules; nitrogen and oxygen for air. The internal energy states, rotation, vibration and electronic, of the molecules are excited and, in the limit, the molecular bonds are exceeded and the gas dissociated into atomic and, possibly, ionic constituents. The process of energy transfer causing excitation, dissociation and recombination is a rate process controlled by particle collisions. Binary, two-body, collisions are sufficient to cause internal excitation, dissociation and ionization while three-body collisions are required to recombine the particles into molecular constituents. If the rates of energy transfer are fast with respect to the local fluid dynamic time scale the gas is in, or nearly in, equilibrium. If the energy transfer rates are very slow the gas can be described as frozen. In all other instances, wherein any of the energy exchange rates are comparable to the local fluid time scale, the gas will be thermally or chemically reacting and out of equilibrium.

Each of these definitive states of a real gas, equilibrium, frozen, reacting, can be applied to a gas undergoing compression and heating, such as the gas flowing through a strong shock ahead of a bluff body, or to an expanding and cooling gas, such as a gas flowing away from a stagnation region of a bluff body or a gas expanding into a base region. In the first case the gas will be thermally excited and dissociate and ionize; in the second, the atomic constituents will recombine and internal energy states will relax to lower energy levels.

A real gas implies the existence of any, or all, of the above states. This includes the possibility that a real gas can look identical to a perfect gas or a chemically frozen gas. In a real gas flow the model scale is a primary test variable. The possibility exists to generate a spectrum of "real gas" test conditions at a single geometrically similar test point. These flows can vary from frozen to equilibrium flow.

For chemically frozen flow there is little value to "real gas" experimentation on the nose region; if the flow is frozen at the stagnation point it will remain frozen as it expands about the blunt nose and over the afterbody where it may equilibrate. Nose region information for such a flow will be identical to perfect gas wind tunnel results and can be predicted reliably within the limits of our knowledge of thermodynamic and transport properties. Afterbody data, however, may be of somewhat greater interest, particularly data describing flow over secondary surfaces which may

Similarly for chemical equilibrium flow, "real gas" experiments are not required. In this case, the extrapolation from a perfect gas to a real gas is straightforward, involving appropriate thermodynamic and transport properties for the reacting gas species.

Between the two limits, in the region of reacting gas flows, is the greatest uncertainty and the greatest need for test data. Facilities required for CFD validation of high enthalpy flows are devices capable of generating a reacting gas flow over configurations of interest and must have sufficient diagnostics to describe the character and behavior of the flow.

4. REAL GAS TEST FACILITIES

In principle, there are two ways to create relative motion between the test article and the air; accelerate the air as in a shock tunnel or accelerate the model as in a ballistic range. Both techniques are being employed at present and both are needed to give insight into real gas phenomena. The two concepts have also been combined to create even higher relative speeds as in the NASA Ames Hypersonic Free Flight Aerodynamic Facility (HFFAF) wherein a large shock tunnel is utilized to provide counterflow to an aeroballistic range.

Ballistic ranges represent a unique capability for real gas testing of configurations. They present the only experimental technique by which real gas viscous interaction effects can be observed. Shock tunnels, because of the nature of their expansion process, do not generate sufficiently high test Mach numbers where viscous interaction phenomena would be important.

To date, most data presented from ballistic range facilities have been integrated aerodynamic data on simple geometric configurations Early efforts by Welch[1] demonstrated a significant real gas effect on the center-of-pressure and moment data. More recent data by Strawa[2-4] continue these studies. Validation requires not only such overall aerodynamic data but also distributions of local flow field quantities within the shock and boundary layer of the tested configuration. Aerodynamic coefficient data are determined through the motions of the model down the length of the tube. Drag and static moment can be determined in about half a period of motion, lift coefficient requires 1.5 to 2 cycles, and damping coefficients require even more. Recent advances (Yates[5]) in automated data taking and data reduction techniques have resulted in significant improvements in the accuracy of aerodynamics coefficients and in the efficiency through which they are determined.

In-stream flow field data can be determined from in-flight shadowgraphs and laser holographic interferometry[6,7]. These data provide quantitative information on shock shape and position, turbulence onset, and instream density distribution and provide complementary data to the integrated aerodynamics coefficients to provide data for CFD validation purposes. An obvious advantage of ballistic range testing is that the free stream is accurately characterized and can precisely simulate the flight environment.

Shock tunnels currently offer the only means of producing both the total enthalpy and pressure levels representative of flight beyond Mach 10. Shock tubes and shock tunnels do not precisely simulate flight environment, however, and flow accelerated test facilities require the freestream to be defined. In supersonic test facilities this has been accomplished through the use of isentropic flow expansion models. Real gas accelerations are not isentropic. Realistic CFD models of the expansion process must be used in conjunction with critical (but not exhaustive) instrumentation to fully define the free stream. The fluid-dynamic and thermodynamic state of chemically reacting air (including the species N, O, N_2, O_2, and NO) in the HFFAF 16-inch shock tunnel were characterized accounting for viscous effects in an axisymmetric nozzle. These results are compared in fig. 1 with conventional quasi one-dimensional real gas simulations to identify the magnitude of viscous and geometric effects in a real-gas environment. Complete calibration of a real gas nozzle expansion process can only be achieved through this collaboration between inciteful, limited measurements and increasingly accurate CFD models of the expansion process. Complex real gas flows require the use of full test section calibrations with the key measurements being the free stream density and static temperature. CFD validation must include facility simulation; we must not pretend to simulate flight with flow accelerated ground tests.

5. REAL GAS EFFECTS

5.1 Aerodynamic Performance

Real gas effects are important in the determination of vehicle aerodynamic performance, e.g. aerodynamics coefficients, control surface behavior, onset of transition and relaminarization. One example that illustrates this is the aerodynamic performance of the Space Shuttle during entry.

The Space Shuttle orbiter flight test program has required the aerodynamicist to take a new approach in determining flight characteristics. The initial series of flights of the orbiter were heavily instrumented for the purpose of obtaining accurate aerodynamic data. The flight data derived from the entry Mach range provided for comparisons between flight and wind tunnel derived predicted data in the areas of both aerodynamic performance and longitudinal trim. Romere and Whitnah[8] examined these data and showed that, in the continuum flight regime (altitudes below about 85 km), lift and drag were smaller during the orbiter flights than predictions based on ground test in perfect gas wind tunnels. The center of pressure (CP) is displaced forward by as much as 0.7% of the overall fuselage length compared with predictions based on perfect gas observations. This result, which is attributed to real gas effects, is quite large considering the fact that the full deflection of the control surfaces were expected to produce a CP shift of, at most, about 1% of the overall length. A plot showing the comparison of CP location determined from flight data with preflight predictions is shown in fig. 2. Griffith and Maus[9] show that the observed discrepancy is due, at least in part, to the high temperature real gas effects.

Rakich et al[10] explain this phenomenon by performing a computational study of real gas flows over simple wedges and cones and the flow over the orbiter forebody. The nonequilibrium flow behavior over a pointed cone at zero incidence is described in a qualitative manner as shown in fig. 3 which illustrates the variation in bow shock shape and a typical species, i.e. atomic oxygen, distribution over the conical forebody. Even though the body is conical, the flow has a scale that depends on the time constant for pertinent species reactions. Near the apex of the cone there is a region where time is insufficient for reactions to occur. Here the flow is conical and the species concentrations are nearly frozen at their free stream values. As the fluid moves downstream of the apex the species begin to thermalize and the flow is out of equilibrium. Far downstream all of the reactions have equilibrated, and even those reactions induced locally by the bow shock equilibrate in a short distance relative to the larger shock standoff distance. A quantitative description is shown in fig. 4 where the computed variation of bow shock angle is shown for a 30 degree half angle wedge at conditions corresponding to an altitude of 65.5 km and a flight speed of 6.7 km/s. These conditions are typical of the high laminar heating portion of the orbiter entry trajectory. And finally, in fig. 5 is shown the computed shock shapes for the orbiter forebody for both a perfect gas and reacting gas. These computations correspond to a flight speed of 6.7 km/s, and altitude of 65.5 km, and an angle of incidence of 30 degrees.

Recently, Park and Yoon[11] performed a computational study of real-gas effects on airfoil aerodynamic characteristics. The results of this study showed that the aerodynamic lift and drag coefficients are consistently reduced by thermochemical real gas phenomena, and that, for air, the behavior can be represented by a value of g less than the perfect gas value of 1.4. The computed center of pressures were observed to shift forward due to the thermochemical phenomena, but the extent of the shift is also sensitive to geometry and angle of attack, and cannot be represented by a fixed value for g. The calculated results are illustrated in fig. 6 for an airfoil of chord length 10 m, at an altitude of 74 km/ a speed of 7 km.s, and an angle of incidence of 40 degrees. These results are in qualitative agreement with the data obtained during the entry flights of the Space Shuttle orbiter. Included are results for a reacting air gas, and results for perfect gas at constant g values of 1.4 and 1.2. It can be seen that the constant g of 1.2 solution agrees well with real gas predictions for lift and drag but fails to adequately represent the CP shift between a real gas solution and g of 1.4 solution.

5.2 Aerothermal Heating

Real gas thermochemical nonequilibrium processes are also important in the determination of aerodynamic heating; both convective (including wall catalytic effects) and radiative heating. To illustrate this we consider the hypervelocity flow over a bluff body typical of an atmospheric entry vehicle or an aerospace transfer vehicle (ASTV.)

The qualitative aspects of a hypersonic flowfield over a bluff body are discussed in two parts, forebody and afterbody, with attention to which particular physical effects must be included in an analysis. This will indicate what type of numerical modeling will be adequate in each region of the flow.

5.2.1 *Forebody Flowfield*

A bluff forebody flowfield, illustrated schematically in Fig. 7, is dominated by the presence of the strong bow shock wave and the consequent heating, and chemical reaction of the gas. At high altitude hypersonic flight conditions the thermal excitation and chemical reaction of the gas occur slowly enough that a significant portion of the flowfield is in a state of thermo-chemical nonequilibrium. A second important effect is the presence of the thick boundary layer along the forebody surface. In this region there are large thermal and chemical species gradients due to the interaction of the gas with the wall. Also at high altitudes the shock wave and the boundary layer may become so thick that they merge; in this case the entire shock layer is dominated by viscous effects.

A gas is in thermal nonequilibrium if, for a given density and internal energy, it is in a thermodynamic state where the internal energy modes cannot be characterized by a unique temperature, and is in chemical nonequilibrium if its chemical state does not satisfy chemical equilibrium conditions. As was asserted above, a portion of the forebody flowfield is in thermo-chemical nonequilibrium. This can be seen by considering the trajectory of a control volume of air that enters the shock layer. The translational modes of this volume of gas are heated strongly as it passes through the bow shock wave. The translational modes transfer their energy to the other internal energy modes of the molecules through inter-molecular collisions. Also chemical reaction of the gas species occur such as dissociation and ionization. These processes require a series of intermolecular collisions for equilibrium to be reached. Thus as the volume element of gas is convected through the shock layer, these energy exchanges and chemical reactions occur at a finite rate until, at some point on the streamline, equilibrium is achieved. Therefore, there will be significant thermo-chemical nonequilibrium near the bow shock wave and equilibrium will be approached a large distance along the fluid element's streamline. The rate at which equilibration is realized is dependent on the free-stream density and speed, or altitude and Mach number. A parameter that quantifies the degree of chemical nonequilibrium for a particular condition is the Damkohler number, the ratio of the fluid time scale to the chemical time scale; a similar parameter may be derived for the relaxation of energy modes.

The second important effect in the forebody region is the interaction of the wall with the thermally excited and reacted gas in the boundary layer. At the high altitudes the Reynolds number is relatively small (typically on the order of 10^4 based on free-stream conditions and nose radius). Thus the boundary layer will be thick and viscous effects will dominate much of the flowfield. Also, as the boundary layer is influenced by the cool wall, chemical reactions can be slowed or halted in the vicinity of the wall. The wall can also interact chemically with the flowfield due to catalytic effects that promote the recombination of reacted species at the wall. Thus the inclusion of viscous effects for hypersonic bluff forebody flowfield analyses is mandatory. At high altitudes, the usual assumption of perfect thermal accommodation and no-slip at the wall breaks down. Therefore, for some conditions, temperature and velocity slip effects must also be included.

Another effect related to the low density regime in which ASTV's would operate is the thickening of the bow shock wave to encompass a large volume of the flowfield. The bow shock wave is several mean-free-paths thick and at high altitudes, this implies that the bow shock thickness is an appreciable fraction of the shock standoff distance and can merge with the thick boundary layer. For these thick shock waves, relaxation of internal modes occurs within the shock wave; this effect must be included in any analysis where rarefaction occurs. Also it has been shown that the Navier-Stokes equations under-predict the shock thickness and misrepresent the separation between the density and temperature profiles within a shock wave (Fiscko and Chapman[12]). Thus for some regimes the predicted shock thickness using Navier-Stokes solvers is suspect.

5.2.2 *Afterbody Flowfield*

The flow about an afterbody, illustrated in Fig. 8, is dominated by two phenomena; the presence of the rapid expansion as the highly compressed gas flows around the shoulder of the vehicle and the related initiation of separation of the gas near the vehicle corner. These two effects require specific modeling approaches and capabilities.

The expansion, which is dominated by inviscid effects, has the effect of rapidly lowering the translational temperature, density and pressure of the gas. However, the chemical state of the gas and the temperatures that characterize the energy in the internal modes will tend to remain constant, or frozen. This results in a flow where the vibrational and electronic temperatures of the gas are far higher than the translational temperature and where the gas is more dissociated and excited than predicted by equilibrium conditions. As the gas flows downstream, recombination occurs slowly and the vibrational temperature rises still higher; a result of a portion of the chemical energy of recombination being put into the vibrational modes of the gas. This can cause the gas to radiate significantly in the afterbody region. Another important effect present in the inviscid, expanded region is the presence of species gradients across the wake. This is caused by some portion of the gas having passed through a relatively weak oblique shock wave where reactions are weak, and another part of the gas having passed through the strong forebody shock where reactions are strong. Thus the gas near the center of the wake tends to be more dissociated than that in its extremities and consequently g, the ratio of specific heats, varies across the wake.

A second inviscid effect associated with the wake structure is the presence of a wake shock. As the flow expands around the shoulder of the vehicle, some of it is directed toward the centerline of the body. However, this supersonic flow must change direction and a reflecting shock and an oblique shock wave is formed. The gas becomes compressed in this region, yet the vibrational and electronic temperatures remain high due to freezing, and the gas may radiate significantly.

The location of the separation on the back face of the bluff body is affected by: the state of the boundary layer on the shoulder, the Reynolds number, whether the flow is turbulent or laminar, the ratio of specific heats, and the body geometry. For many cases of interest, particularly at high altitude, the flow can remain attached over a significant portion of the vehicle's afterbody. The location of separation influences the dimension of the recirculation zone and the strength of the shear-layer that forms between the recirculating gas and the external, rapidly expanding, supersonic flow. The recirculation zone entrains gas that was in the forebody boundary layer which is relatively cool but highly dissociated. This recirculation zone will be unsteady, the magnitude of which depending on how the shear-layer behaves and the feedback between the body motion and the state of the gas in the separated region.

The modeling of the free shear-layer must account for large gradients of velocity, temperature, density and species concentration across it, and for the possibility that the flow may be turbulent and unsteady. The numerical treatment of the problem is particularly difficult because of these effects and also due to the uncertain location of this structure.

The afterbody flowfield is characterized by the presence of thermo-chemical nonequilibrium, large gradients in thermodynamic quantities and chemical state, and a large separated region. The combination of these factors stretches computational fluid dynamics beyond it current capabilities.

6. ILLUSTRATIVE EXAMPLES

6.1 Aerodynamic Trim

To acquire data necessary to validate and/or calibrate real gas code capability to predict aerodynamic performance, the aeroballistic range is proposed. Ballistic range data will include visual flowfield data indicating shock shape and location relative to the body (i.e. by way of shadowgraphs) and density distribution (i.e. by holographic interferograms) as well as quantitative information in the form of aerodynamic coefficients including lift, drag and pitching moment. The use of a combination of CFD with experiment has proven most effective in the interpretation of free-flight data. For example, in a recent study on trim angle for the NASA Aeroassist Flight Experiment (AFE) vehicle[5], there was insufficient free-flight data for determining high order terms for series expansion representation of aerodynamic coefficients . In order to extract information from the experimental data, the curvature of the function describing the moment coefficient was required. This curvature was developed using CFD. For the analysis of data from the NASA Ames HFFAF aeroballistic range the higher order terms in the aerodynamic coefficient expansion were determined from CFD simulations; only the lower order terms were found using a six-degree-of-freedom, weighted, least squares procedure. The resulting experimental aerodynamic coefficients and trim angles agree with those computed by CFD. The effective specific heat ratio for the HFFAF was determined by matching the bow shock shape and stand-off distance with CFD perfect gas, constant effective γ, flowfield simulations at the HFFAF test conditions. Results of these comparisons are shown in fig. 9 in which the CFD simulation bow shock is identified by a coalescence of isobars.

AFE model moment coefficient data from the HFFAF are compared with data from two NASA Langley hypersonic cold flow facilities, the 31-inch Mach 10 tunnel and the CF_4 tunnel , in fig. 10. Each of the three facilities can be identified by an effective γ: 1.2 for HFFAF, 1.34 for the Mach 10 tunnel, and 1.11 for the CF_4 tunnel. The measured trim angles are 14.7, 17 and 12 degrees, respectively.

By minimizing the uncertainty in trim angle, design tolerances can be tightened and vehicle configurations can be optimized for specific mission requirements. By using a combination of CFD analysis and ground-based experiments, the real-gas effects can be simulated, analysis tools validated, and flight conditions can be estimated with some confidence. In many cases the aeroballistic range can be used to simulate actual flight conditions and reasonable estimates of aerodynamic trim angle and pitching moment for flight can be determined directly. The agreement shown herein between experimental and computed results for the blunt AFE configuration at the ground test conditions indicate that, at these test conditions, the moment coefficients and trim angles can be computed using efficient ideal gas solvers with an appropriate choice for g; the appropriate value of this parameter can be determined by shock shape comparison. This is not necessarily the case, however, for slender or high lift vehicles. In cases where actual flight conditions cannot be replicated in ground test facilities, real gas solvers must be used to determine if constant effective g approximations are appropriate. As mentioned previously, the variations in g at flight conditions can have a sizable influence on aerodynamic moment coefficient and trim angle.

6.2 Aerothermodynamic Heating

6.2.1 *Compressive flows*

To study the nonequilibrium processes in compressing flow typical of the stagnation region of a bluff forebody, we are looking in some detail at a gas relaxing after being heated by an incident shock wave. By acquiring normal shock in a spectrally clean facility, we are able to quantify the thermochemical state of the gas as a function of time or position. By this means, we can study such processes as vibration-dissociation coupling, vibration-translation exchange, vibration-rotation coupling, etc.[13-15]

The dominant real gas phenomena is the relaxation process occurring in the flow around hypersonic vehicles. Considerable effort has been expended in recent years to model and numerically compute this behavior (e.g. refs. 16-19). The accuracy of such calculations needs further improvement and there are still many physical parameters that are unknown for high temperature real gases. Three types of experimental data are needed in this model development process: 1) data which will enhance our phenomenological understanding of the relaxation process, 2) data on rates for the relevant reactions, and 3) data on bulk properties, such as spectral radiation emitted by the gas, for a given set of aerodynamic conditions. We are in a process of collecting such data by simulating the required aerothermochemical conditions in an electric arc driven shock tube[20-21]. NASA Ames' electric arc driven shock tube facility is powered by a 0.6 MJ 40 kV capacitor bank and is capable of producing shock velocities in the range of 2-50 km/sec. The radiation diagnostic system available at the facility, consists of 1) a linear intensified 700 element diode array and a 2-D intensified CCD array with 576 x 384 active elements, both gateable within a time range of 30 ns - 2.5 ms and both with a 2000-8000 A spectral response. A photomuliplier tube (PMT) is used to record the total radiation from the test gas as well as from the driver gas as they pass through the test section. The signal from the PMT is used to estimate the test time and to trigger the diode array system at a given moment during the test history. A Nd:YAG laser based, double exposure, single plate interferometer is also available at the facility. A schematic of the experimental test setup is shown in fig. 11.

A one-dimensional real-gas flow code for thermo-chemical nonequilibrium (Park[22-23]) is used to predict the thermochemical state of the shock heated gas behind the incident shock. This code uses a multiple temperature description to model the nonequilibrium behavior of the internal state of the gas and to describe the rate processes. From the predicted thermochemical state of the gas synthetic emission spectra can be generated. For this we use the computer code NEQAIR[24,25]. Several modeling steps are involved in this process. First are the chemical rate expressions themselves in which there is always some uncertainty in the Arrenius rate constants, second is the multiple temperature model used to describe both the internal energy states of the gas and the reaction rates, and third is the quasi-steady state model and peripheral approximations used to generate the synthetic spectra in the NEQAIR code. By maintaining a coordinated effort between the modeling activity and the experimental effort it is possible both to improve and refine the phenomenological models as well as validate them. These models will then, in turn, be used in multidimensional flow codes to predict and analyze real gas behavior in more complex flow environments.

To data two sets of experiments have been conducted: 1) measurements at a shock velocity of 6.20 km/sec in 1 Torr nitrogen[26] and 2) measurements at a shock velocity of 10.2 km/sec in 0.1 Torr air[27]. In both the sets, using the linear diode array, the equilibrium and nonequilibrium spectra covering the 3050-5500 A range were recorded.

Measurements in Nitrogen (6.2 km/sec,1.0 Torr): For the nitrogen case, the equilibrium temperature of the test gas based on $N_2(2^+)$ band system was found to be 6500 K. The rotational temperature at the point of peak radiation in the nonequilibrium region, based on the intensities at 3143.7 A and 3159.1 A, was found to be about 8800 K. The vibrational temperature, based on the first vibrational level and the ground state of the $N_2(2^+)$ band system was found to be about 6900 K. The vibrational temperatures of higher vibrational levels were lower than this value.

The equilibrium temperature of the test gas based on the $N_2^+(1^-)$ band system was found to be 7200 K. The rotational temperature at the point of peak radiation in the nonequilibrium region was deduced to be about 8800 K, which is consistent with the value found by using the $N_2(2^+)$ band system. Comparisons of rotational temperature with prediction and with earlier data from Allen et al[28] are shown in fig. 12 The vibrational temperature as measured based on the v(1,2)/v(1,0) levels of the $N_2^+(1^-)$ band system was found to be about 9500 K, with the value decreasing for higher vibrational levels. The temperature based on the v(7,8) vibrational level was about 8500 K. Comparisons of vibrational temperature with prediction and with earlier data are shown in fig. 13.

Measurements in Air(10.2 km/sec, 0.1 Torr): For shock heated air the equilibrium temperature was estimated to be 9620 K. The equilibrium emission spectra observed is shown in fig. 14. By using two different sets of points on the rotational envelope of the $N_2(2^+)$ band system, the rotational temperature, corresponding to the point of peak radiation, was estimated to be about 4400 K and 3990 K respectively, making a mean rotational temperature of 4195 K. Such a low value of rotational temperature was a surprise. The overshoot observed in the nitrogen tests at 6.2 km/sec was absent here. The rotational temperature seems to rise very slowly to reach the equilibrium value. The emission spectra observed at the point of peak radiation is shown in fig. 15.

The vibrational temperature at the point of peak radiation was deduced using the (2,1) and (3,2) bands of $N_2^+(1^-)$ system at 3564.1 and 3548.2 A respectively and was found to be about 9465 K. There were no other vibrational temperature data available for these conditions The measured vibrational temperatures based on $N_2^+(1^-)$ as well as based on $N_2(2^+)$ band systems are in line with the theoretical values as predicted by Park's model[17]. Sharma[20] shows further details and analysis of the experimental data and comparisons with theory.

6.2.2 *Expanding flows*

To study the nonequilibrium processes in an expanding flow as typified by the flow over the shoulder of a bluff body and into the base, or near wake, region, we look at a gas that has been shock heated to high temperature and pressure and allowed to expand rapidly in a two-dimensional nozzle. By using optical diagnostics such as laser holographic interferometry and Raman scattering[29], we can quantify the thermo-chemical state of the gas during the expansion process. We are planning to measure the nonequilibrium vibrational populations for levels up to v=13, in an expanding flow, using spontaneous Raman scattering technique. A nozzle insert has been installed in the driven section operating in a reflected shock mode. However, at first the density flow field is being mapped by laser based holography. The results of this initial test are shown in fig. 16 where good agreement can be observed between computer simulated and experimental fringe interferograms.

In addition to characterizing the thermochemical process in an expanding flow a blunt body base flow test configuration is being developed. Two models will be considered: (1) an uninstrumented free flying model to be used for flow visualization studies without the presence of a sting support, and (2) an instrumented sting mounted model for which both the model and the sting support are instrumented with pressure and heat flux gauges and flow visualization can be realized for comparison with the free flight model. As part of the AGARD FDP WG18 activity it is proposed to test the two configurations in both the NASA Ames 16" combustion driven shock tunnel and the DLR free piston shock tunnel, HEG, at the same enthalpy and the same Mach and Reynolds numbers.

The purpose of the experiment would be to quantify the shear layer separation point, turning angle and wake closure in the presence of flows exhibiting real gas and/or low density behavior. The unsteady character of the near wake will also be characterized, if possible. Body surface instruments will provide data for CFD simulation and calibration/validation. Both sting mounted and free flight models will be necessary to assess and quantify the influence of the sting on the instrumented model.

7. CONCLUDING REMARKS

In summary it has been pointed out that real gas effects are important in hypersonic flows both in terms of their influence on aerodynamic performance and their effect on aerothermdynamic heating. Further, it was pointed out that high enthalpy ground based test facilities cannot fully simulate flight conditions and that they exhibit unique real-gas behavior themselves. Hence, the process for developing validated analysis tools is one where real gas CFD is involved in all aspects of a real-gas ground test program. Only in this manner can sufficient confidence be gained and real gas analysis tools be validated.

Acknowledgements

The staff of the NASA Ames Research Center's Aerothermodynamics Branch are gratefully acknowledged for their substantial contributions to this paper.

References

1. Welch, C. J., Lawrence, W. R. and Watt, R. M., "Real-Gas Effects on the Aerodynamics of Blunt Cones as Measured in a Hypervelocity Range", AEDC TR 79-33.

2. Strawa, A.W., Chapman, G.T., Canning, T.C., and Arnold, J.O., "The Ballistic Range and Aerothermodynamic Testing," AIAA Paper 88-2015.

3. Strawa, A.W. and Prabhu, D. K., "A Comparison of Experimental and Computational Results for 5 and 10 Degree Cones at High Mach Numbers," AIAA Paper 88-2705.

4. Strawa, A. W., Molvik, G., Yates, L., and Cornelison, C., "Experimental and Computational Results for 5 Degree Blunt Cones with Shock Generators at High Velocity," AIAA Paper 89-3377.

5. Yates, L. A. and Venkatapathy, E., "Trim Angle Measurements in Free-Flight Facilities," AIAA Paper 91-1632.

6. Strawa, A. W., and Cavolowsky, J. A., "Development of Non-Intrusive Instrumentation for NASA-Ames' Ballistic Range and Shock Tunnel," AIAA Paper 90-0628.

7. Tam, T. C., Brock, N. J., Cavolowsky, J. A., and Yates, L. A., "Holographic Interferometry at the NASA-Ames Hypervelocity Free-Flight Aerodynamic Facility," AIAA Paper 91-0568.

8. Romere, P. O. and Whitnah, A. M., "Space Shuttle Entry Longitudinal Aerodynamic Comparisons of Flights 1-4 with Preflight Predictions," in Shuttle Performance Lessons Learned, NASA CP 2283, 1983.

9. Griffith, B. J. and Maus, J. R., "Explanation of the Hypersonic Longitudinal Stability Problem - Lessons Learned," in Shuttle Performance Lessons Learned, NASA CP 2283, 1983.

10. Rakich, J. V., Bailey, H. E., and Park, C., "Computations of Nonequilibrium, Supersonic Three-Dimensional Inviscid Flow over Blunt-Nosed Bodies," AIAA J., v 21, No. 6, June 1983, pp 834-841.

11 Park, C., and Yoon, S.,"A Fully-Coupled Implicit Method for Thermo-Chemical Nonequilibrium Air at Sub-Orbital Flight Speeds," AIAA Paper 89-1974.

12. Fiscko, K. A. and Chapman, D. R., "Hypersonic Shock Structure with Burnett Terms in the Viscous Stress and Heat Flux," AIAA Paper 88-2733.

13. Park, C., "Two-Temperature Interpretation of Dissociation Rate Data for N_2 and O_2," AIAA Paper 88-0458

14. Sharma, S., Huo, W., and Park, C., "The Rate Parameters for Coupled Vibration-Dissociation in a Generalized SSH Approximation," AIAA Paper 88-2714.

15. Park, C., "A Review of Reaction Rates in High Temperature Air," AIAA Paper 89-1740.

16. Candler, G. V. and MacCormack, R. W., "The Computation of Hypersonic Ionized Flows in Chemical and Thermal Nonequilibrium," AIAA Paper 88--0511.

17. Candler G. V. and Park C., "The Computation of Radiation from Nonequilibrium Hypersonic Flows," AIAA Paper 88--2678.

18. Gokcen, T. and MacCormack, "Nonequilibrium Effects for Hypersonic Transitional Flows Using Continuum Approach," AIAA Paper 89-0461.

19. Candler, G. V.,"On the Computation of Shock Shapes in Nonequilibrium Hypersonic Flows," AIAA Paper 89--0312.

20. Sharma, S. and Park, C., "A Survey of Simulation and Diagnostic Techniques for Hypersonic Nonequilibrium Flows, " AIAA Paper 87-0406.

21. Sharma, S. and Park, C., "Operating Characteristics of a 60 cm and a 10 cm Electric Arc-Driven Shock Tube, " AIAA Paper 88-0142.

22. Park, C., "Assessment of Two-Temperature Kinetic Model for Dissociating and Weakly Ionizing Nitrogen," J. Thermophysics and Heat Transfer, Vol. 2, No. 1, Jan. 1988, pp 8-16.

23. Park, C., "Assessment of Two-Temperature Kinetic Model for Ionizing Air," J. Thermophysics and Heat Transfer, Vol. 3, No. 3, July 1989, pp 233-244.

24. Park, C., "Nonequilibrium Air Radiation (NEQAIR) Program: User's Manual," NASA TM 86707, July 1985.

25. Whiting, E., and Patterson, J., "Recent Advances at NASA in Calculating The Electronic Spectra of Diatomic Molecules," NASA TM 101034, Oct. 1988.

26. Sharma, S., "Nonequilibrium and Equilibrium Shock Front Radiation Measurements," AIAA Paper 90-0139.

27. Sharma, S., Gillespie, W. D. and Meyer, S. A., "Shock Front Radiation Measurements in Air," AIAA Paper 91-0573.

28. Allen, R. A., Camm, J. C. and Keck, J. C., "Radiation from Hot Nitrogen," AVCO-Everett Research Laboratory Report 102, April 1961.

29. Sharma, S., Ruffin, S., Meyer, S. A., Gillespie, W. D. and Yates, L. A., "Density Measurements in an Expanding Flow Using Holographic Interferometry," AIAA Paper 92-0809.

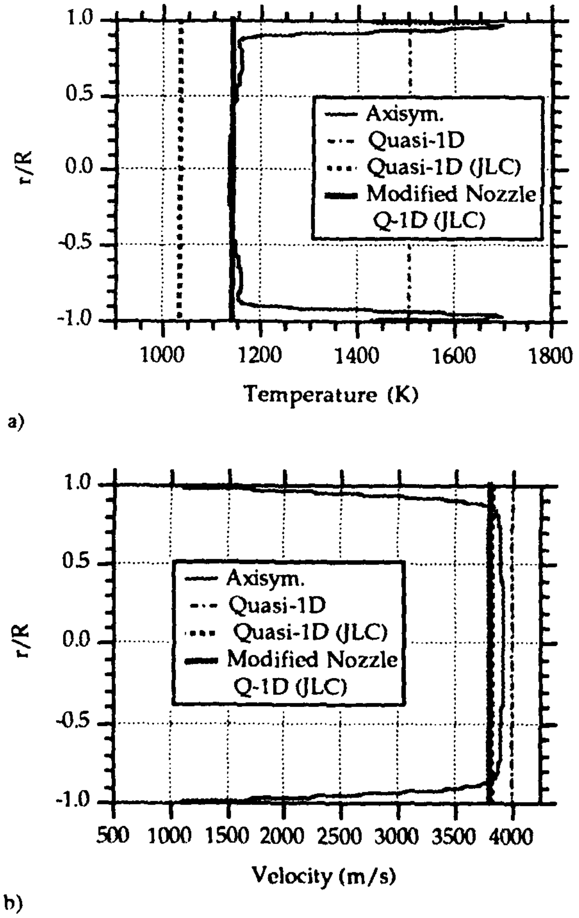

a)

b)

Fig. 1. Ames 16-Inch Shock Tunnel nozzle exit profiles from real-gas CFD prediction: a) Temperature, b) Axial velocity, c) Static pressure, d) Atomic oxygen mole fraction.

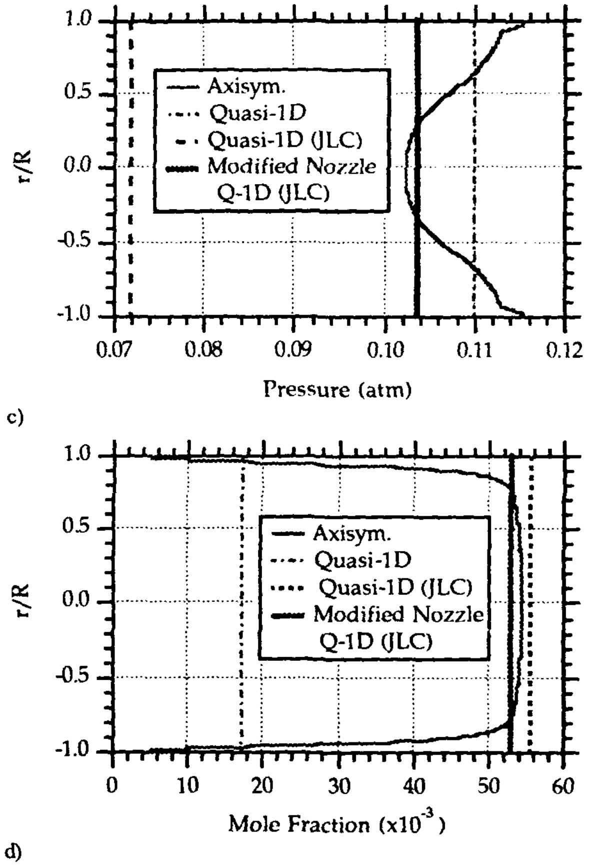

c)

d)

Fig. 1. Concluded

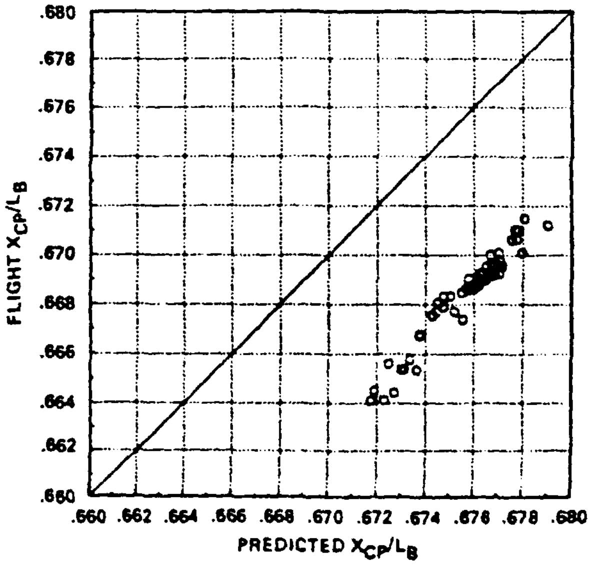

Fig. 2. Hypersonic longitudinal aerodynamic center of pressure correlation of flight with predicted data for pullup/pushover maneuvers: STS-2, M=21.

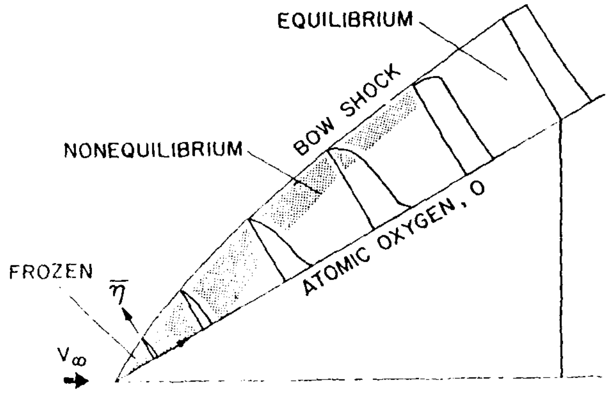
EQUILIBRIUM
BOW SHOCK
NONEQUILIBRIUM
ATOMIC OXYGEN, O
FROZEN
$\bar{\eta}$
V_∞

Fig. 3. Schematic profiles of atomic oxygen between body and shock of a pointed cone.

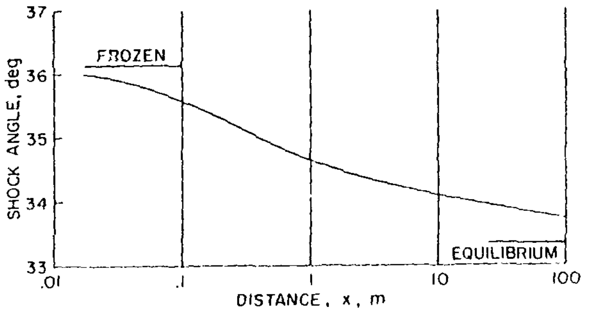

Fig. 4. Shock angle for nonequilibrium flow over a 30 deg. wedge.

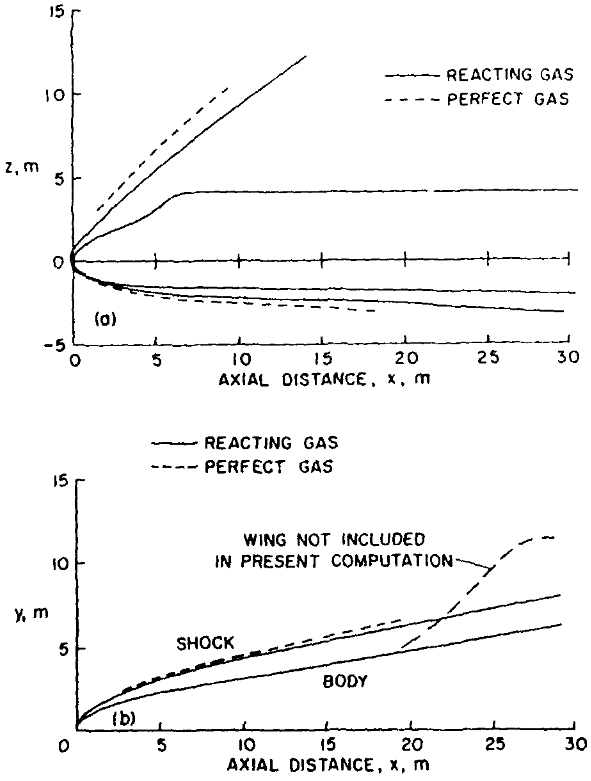

Fig. 5. Shock shape for Shuttle 147 body, a=30 deg, V=6.7 km/s, altitude = 65.5 km: a) side view; b) plan view

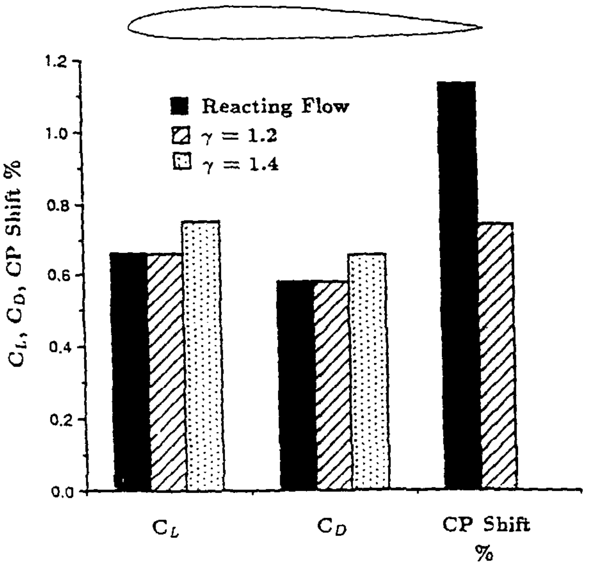

Fig. 6. Lift and drag coefficients and CP shift for airfoil: chord=10 m, alt.=74 km, V=7 k/s,α=40 deg

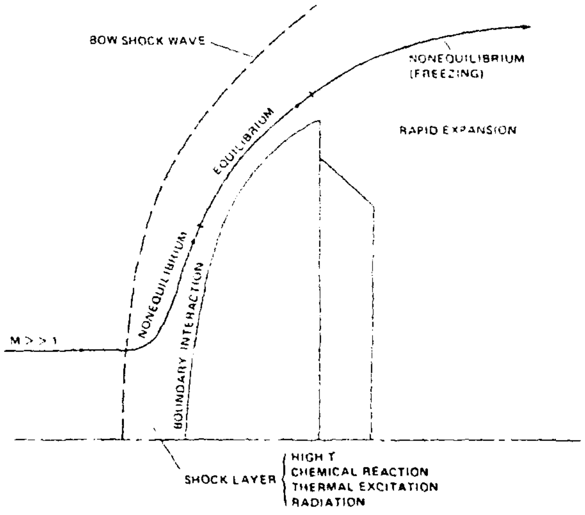
BOW SHOCK WAVE
NONEQUILIBRIUM
(FREEZING)
EQUILIBRIUM
RAPID EXPANSION
NONEQUILIBRIUM
BOUNDARY INTERACTION
M >> 1
SHOCK LAYER
HIGH T
CHEMICAL REACTION
THERMAL EXCITATION
RADIATION

Fig. 7. Schematic of hypervelocity bluff forebody flowfield.

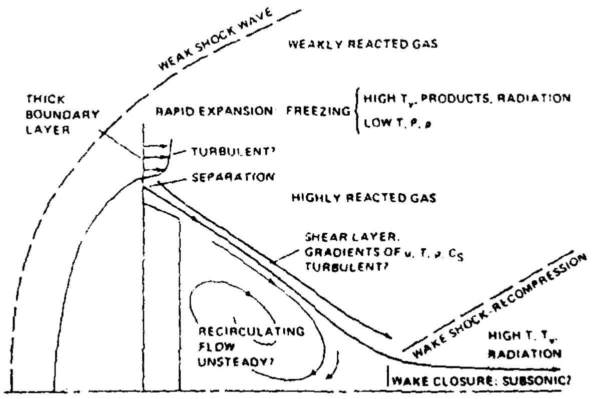
WEAK SHOCK WAVE
WEAKLY REACTED GAS
THICK BOUNDARY LAYER
RAPID EXPANSION
FREEZING
HIGH T_v, PRODUCTS, RADIATION
LOW T, P, ρ
TURBULENT?
SEPARATION
HIGHLY REACTED GAS
SHEAR LAYER,
GRADIENTS OF u, T, ρ, C_S
TURBULENT?
RECIRCULATING FLOW UNSTEADY?
WAKE SHOCK-RECOMPRESSION
HIGH T, T_v,
RADIATION
WAKE CLOSURE: SUBSONIC?

Fig. 8. Schematic of hypervelocity bluffbody near-wake flowfield.

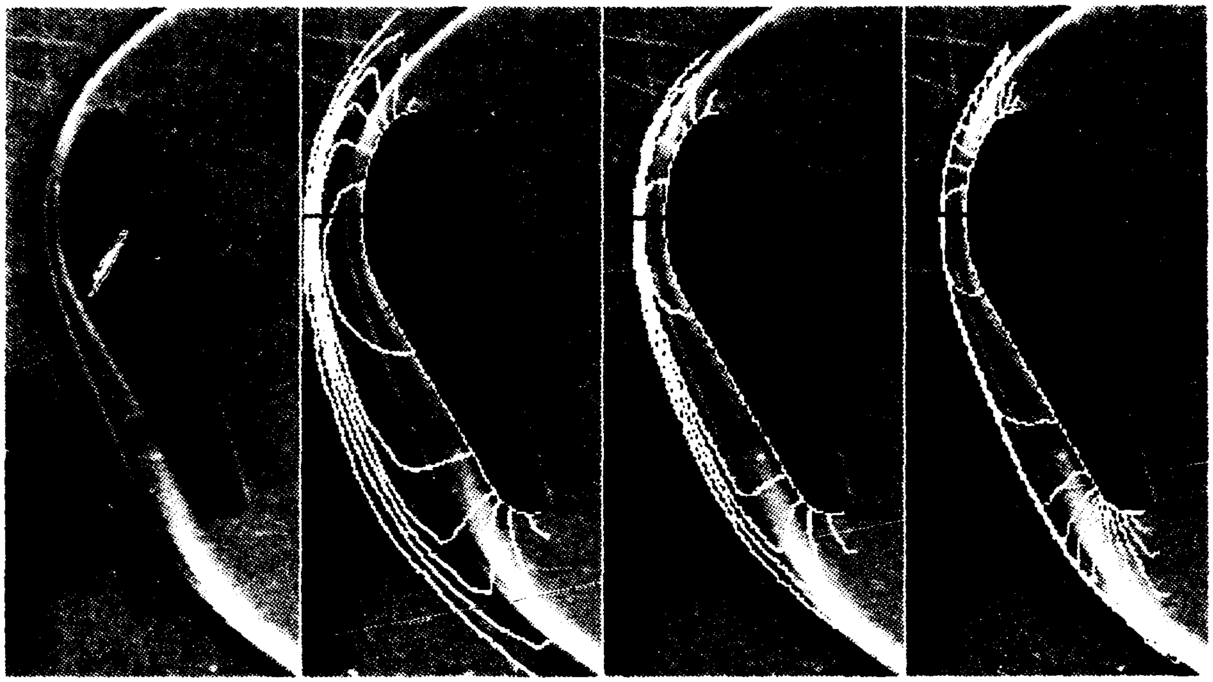

Shadowgraph γ - 1.4, coarse grid solution γ - 1.2, coarse grid solution γ - 1.2, adapted grid solution

Fig. 9. Experimental and computed AFE bow shock

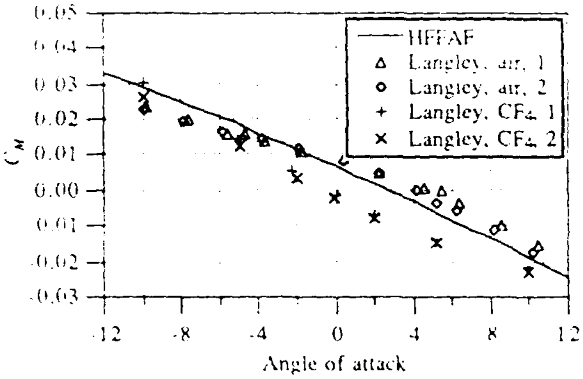

Fig. 10. AFE moment coefficient comparison

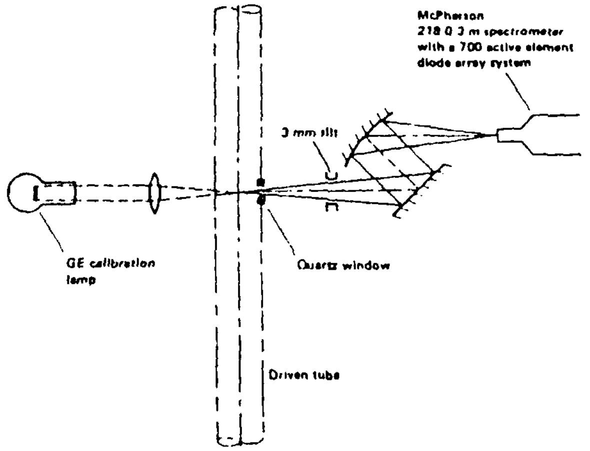
McPherson
218 0.3 m spectrometer
with a 700 active element
diode array system
3 mm slit
GE calibration
lamp
Quartz window
Driven tube

Fig. 11 Schematic of shock tube emission spectra collection optics for diode array system.

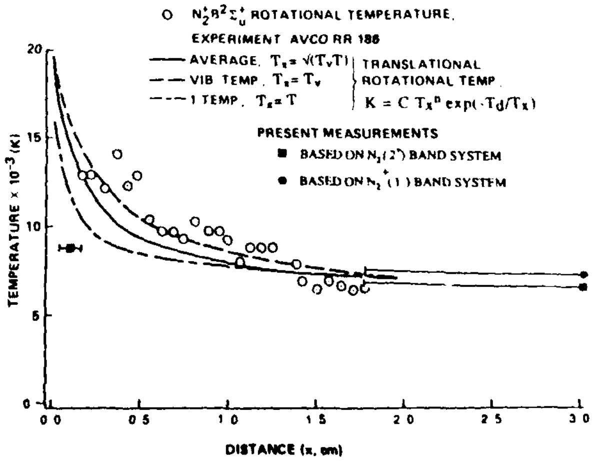

Fig. 12. Rotational temperature behind normal shock in nitrogen: U_S=6.2 k/s, p_1=1.0 torr

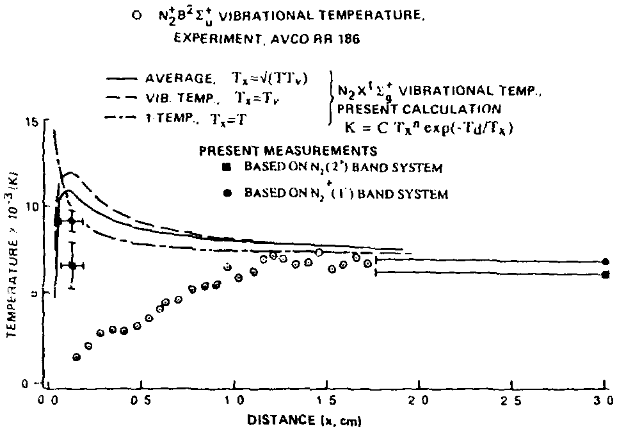

Fig. 13. Vibrational temperature behind normal shock in nitrogen: U_S=6.2 k/s, p_1=1.0 torr.

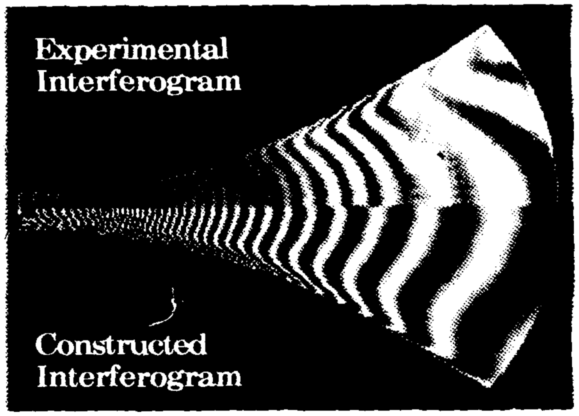
Experimental Interferogram
Constructed Interferogram

Fig. 16. CFD generated synthetic interferogram compared with experimental observation: P_0=1530 PSI, T_0=7200 K.

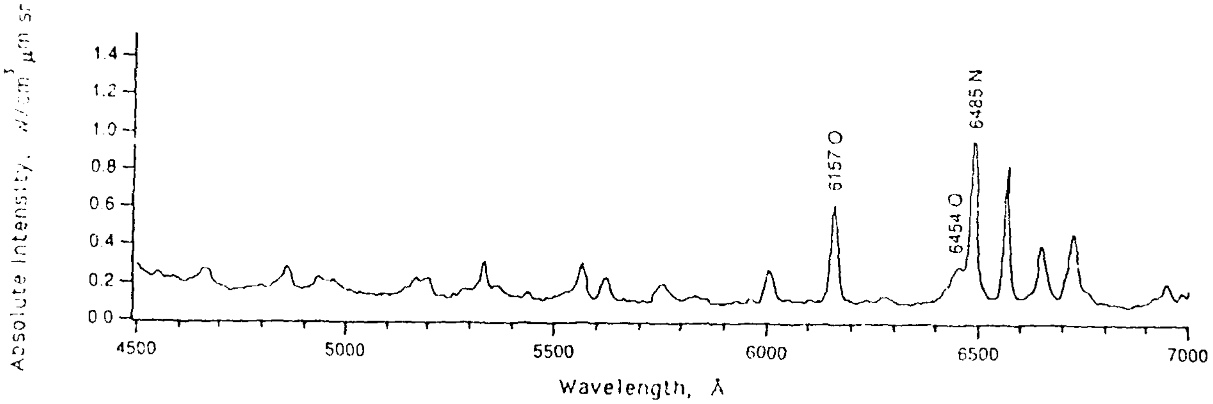

Fig. 14. Equilibrium emission spectra behind normal shock in air: U_S=10.2 k/s, p_1=0.1 torr, gate=1.0 μs, slit=60μm

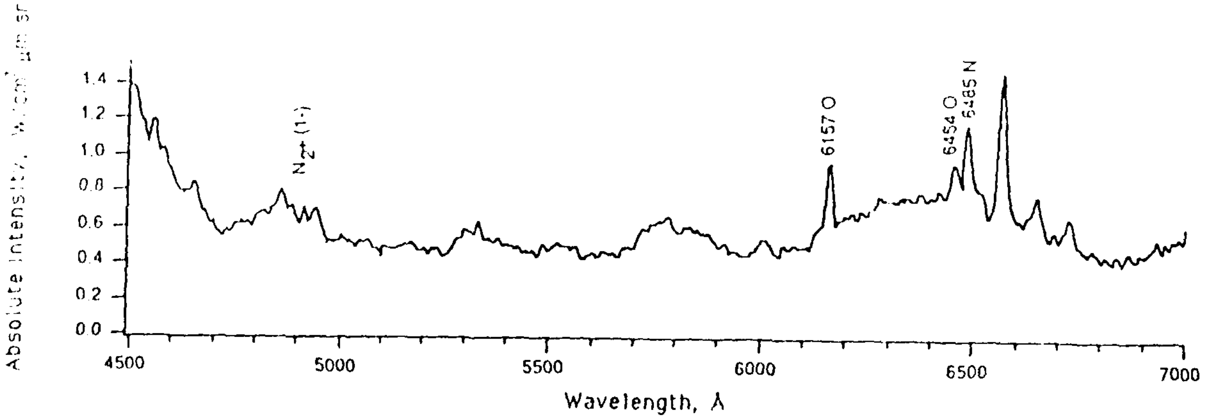

Fig. 15. Nonquilibrium emission spectra behind normal shock in air: U_S=10.2 k/s, p_1=0.1 torr, gate=200 ns, slit=60μm

COMPARISON OF COMPUTATION AND EXPERIMENT FOR A HIGH ENTHALPY, HEATED-DRIVER, SHOCK-TUBE ENVIRONMENT

S. Shahpar, A. Kennaugh, I.M. Hall and D.I.A. Poll
Department of Engineering
University of Manchester
Manchester M13 9PL
UK

1. Summary

A coordinated computational and experimental study has been made of blunt-body flows with non-equilibrium chemistry. The temperature range was such that significant dissociation of oxygen was expected but very little dissociation of nitrogen. Both pure oxygen, O_2 and O, and air, treated computationally using a five species (O_2, N_2, NO, N, O) model, were studied.

Results obtained using different published values of the chemical rate coefficients were compared and assessed for a model problem. The effects of size (i.e. Damköhler number) and freestream velocity were also investigated.

The flow computations used an explicit time-marching method based on a TVD version of the MacCormack predictor-corrector scheme. A point implicit TVD method was developed to deal with the stiffness problems introduced by the finite rate chemistry.

Interferograms of the flow obtained in a shock tunnel are compared with the computational results. The bow shock wave shape and the shock detachment which are dependent on the degree of chemical reaction and thermal excitation of the gas show that the calculation method is promising.

2. Nomenclature

a	Speed of sound
$C_{b,r}$	Pre-exponential term used in evaluating backward reaction rate coefficient
$C_{f,r}$	Pre-exponential term used in evaluating forward reaction rate coefficient
Cp	Pressure coefficient
Da	Damköhler number
E,F,G	Vector fluxes given by equation (4.2)
e	Internal energy per unit mass
$\bar{e}$	Total energy per unit volume
$G_i^{\pm}$	TVD flux "corrector", given by equation (8.5)
H	"Source type" vector flux
h_s	Enthalpy per unit mass of species, s, J/kg
K	Gladstone-Dale constant
K_i	Equilibrium constant for species i
$K_{b,r}$	Backward reaction rate for reaction r, $cm^6/(mol^2.s)$
$K_{f,r}$	Forward reaction rate for reaction r, $cm^3/(mol.s)$
ℓ	Geometrical path
M	Mach number
M_s	Molecular weight of species s, kg/kmol
m	Mass
n_i	Number density
n	Refractive index
p	Pressure
$\Re$	Gas constant
R_{MAX}	Maximum radial distance in the mesh
r	Radial distance
T	Temperature (translational-rotational)
T_v	Vibrational temperature
t	[illegible]
U_∞	Freestream velocity
u_r, u_θ, u_z	Velocity components in cylindrical system
Δ, ∇	Forward and backward operators
γ	Ratio of specific heats
θ	Angle measured in circumferential direction
λ	Wave length
ρ, ρ_s	Complete density, partial density of species
τ	Relaxation time
φ	TVD flux limiter
ω_s	Mass rate of production or depletion of

3. Introduction

Current interest in a vehicle for transatmospheric flight has been the catalyst for renewed research in hypersonic flight. There is also military interest in high kinetic energy missiles which must of necessity travel at hypersonic speeds.

One of the major problems in the laboratory investigation of hypersonic flow is that it is not possible to simulate all the important parameters, such as Reynolds number, stagnation temperature, Mach number and Damköhler number, which are significant during the re-entry phase of a hypersonic flight. It is important, therefore, to choose which parameters are most important, to compare experiment and theory, and then to extend the theory to flight conditions. Since, the real gas effects are essentially dependent on temperature, simulation of high temperature is probably the most important.

It is possible to obtain high temperature flows in a shock tube and work, complementary to the present computations, is in progress in a shock tube at the Goldstein Aeronautical Research Laboratory at the University of Manchester. For temperatures up to about 4000K, the predominant real gas effect is due to the dissociation of oxygen whereas nitrogen dissociation is extremely small. Although high temperatures are attainable in the experiments, the corresponding Mach numbers are relatively low, the maximum shock Mach number attainable to date being about 7. The computations that were carried out were designed to complement the experimental work and, in particular, after validation at the conditions attainable in the experiments, to predict flows at higher Mach numbers. Test cases include typical conditions which can be simulated in the shock tube and typical earth re-entry condition. Two different configurations are being investigated experimentally, a hemi-sphere cylinder and a two-dimensional flat plate with a finite radius leading edge. This leading edge can be modelled by a "circular" cylinder and because of its simplicity, is chosen here as the test model.

Two sets of chemical models were considered: in one the gas is made up of pure oxygen (0_2 and 0) and in the other the gas is made of 5 species (N_2, 0_2, NO, N and 0) and is subject to 17 chemical reactions. The species convection equations are coupled with the Euler equations. The vibrational and electronic degrees of freedom are assumed to remain in thermodynamic equilibrium while the chemical reactions are assumed to proceed at finite reaction rates. The numerical method is explicit for the time integration and is also Total Variation Diminishing. While the basic program computes the high speed chemical reacting flows past a circular cylinder, simple modifications of the program can be made to permit computing other blunt body shapes. The codes were run either on an Amdahl vector processor VP 1100 or on a HP workstation at the University of Manchester.

4. The Euler Equations

The basic equations of inviscid gas dynamics, the Euler equations, are written in terms of four independent variables, the time and the three space dimensions. Under the assumptions of an inviscid, non-heat-conducting gas in local thermochemical equilibrium, these equations can be written in divergence form:

$$\frac{\partial U}{\partial t} = - \nabla.(E(U),F(U),G(U)) \qquad (4.1)$$

With finite rate chemistry and in cylindrical co-ordinates the three-dimensional Euler equations are as follows:

$$\frac{\partial U}{\partial t} + \frac{\partial E}{\partial r} + \frac{\partial F}{\partial \theta} + \frac{\partial G}{\partial Z} + H = 0 \qquad (4.2)$$

where

$$U = \begin{bmatrix} r\rho \\ r\rho u_x \\ r\rho u_y \\ r\rho u_z \\ r\bar{e} \\ r\rho_s \end{bmatrix} \qquad E = \begin{bmatrix} r\rho u_r \\ rp\cos\theta + r\rho u_r u_x \\ rp\cos\theta + r\rho u_r u_y \\ r\rho u_r u_z \\ r(\bar{e}+p)u_r \\ r\rho_s u_r \end{bmatrix}$$

$$F = \begin{bmatrix} \rho u_\theta \\ -p\sin\theta + \rho u_\theta u_x \\ p\cos\theta + \rho u_\theta u_y \\ \rho u_\theta u_z \\ (\bar{e}+p)u_\theta \\ \rho_s u_\theta \end{bmatrix} \quad G = \begin{bmatrix} r\rho u_z \\ r\rho u_z u_x \\ r\rho u_z u_y \\ r(p+u_z^2) \\ r(\bar{e}+p)u_z \\ r\rho_s u_z \end{bmatrix}$$

$$H = \begin{bmatrix} 0 \\ 0 \\ 0 \\ 0 \\ 0 \\ -r\omega_s \end{bmatrix}$$

where r is the radial direction and θ is in the tangential direction. The velocities u_x, u_y and u_z are kept in the original cartesian form. The partial densities of species, s, is denoted by ρ_s and because ionization phenomena are neglected there are only 5 species, N_2, 0_2, NO, O and N, to be considered. Identifying these five species by the subscripts 1 through 5 the global mass conservation condition dictates

$$\rho = \sum_{i=1}^{5} \rho_i \qquad (4.3)$$

5. Chemistry Modelling: Oxygen

The constants in the reaction rate equation are not universally accepted. The effects of using different authors' models have been investigated and the results are included in the discussion section of this paper. The reaction rates used are tabulated in Table (1).

The main chemical reactions for the dissociation of a gas consisting of oxygen only are:

$$R(1): \quad 0_2 + 0 \underset{k_{b,1}}{\overset{k_{f,1}}{\rightleftharpoons}} 20 + 0 \qquad (5.1)$$

$$R(2): \quad 0_2 + 0_2 \underset{k_{b,2}}{\overset{k_{f,2}}{\rightleftharpoons}} 20 + 0_2 \qquad (5.2)$$

The derivation of the reaction rate for oxygen atoms was given in ref [1]. The rate of production ω_0 is

$$\omega_0 = 2M_0\left[k_{f,1}\left(\frac{\rho_{O_2}}{M_{O_2}}\right)\left(\frac{\rho_O}{M_O}\right) - k_{b,1}\left(\frac{\rho_O}{M_O}\right)^3 + k_{f,2}\left(\frac{\rho_{O_2}}{M_{O_2}}\right)^2 - k_{b,2}\left(\frac{\rho_O}{M_O}\right)^2\left(\frac{\rho_{O_2}}{M_{O_2}}\right)\right] \qquad (5.3)$$

where ω_0 has the units of $kg/(m^3s)$.
and,

$$k_{f,r} = c_{f,r} T^{\eta_{f,r}} \exp^{(-E_{f,r}/kT)}$$

$$k_{b,r} = c_{b,r}\, T^{\eta_{b,r}} \exp^{(-E_{b,r}/kT)} \qquad (5.4)$$

where the constant are given in table (1).

Most of the data in the literature for reaction rate coefficients are in cgs units, so the same units are used here. The units for k_f are $cm^3/(mol.s)$ and for k_b $cm^6/(mol^2.s)$, hence these coefficients must be multiplied by 10^{-3} and 10^{-6} respectively to change them to SI units.

Given the forward rate and the equilibrium constant $k_{c,r}$, for each reaction the backward reaction rate constant, $k_{b,r}$, can be found from

$$k_{b,r} = \frac{k_{f,r}}{k_{c,r}} \qquad (5.5)$$

The backward reaction rates for oxygen associations are given in table (2) for the model of Dunn and Kang.

From the above relations the equilibrium constant is

$$k_c = k_{c,1} = k_{c,2} = 1.2x10^3\, T^{-0.5} \exp(-59500/T) \qquad (5.6)$$

The above expression for the equilibrium constant was also used for both Wray's and Gardiner's models.

According to Park [5], the equilibrium constant at temperatures of 1000, 2000, 4000, 8000 and 16000K has been obtained from spectroscopic data. The (natural) logarithms of these $k_{c,r}$ values are fitted by a fourth-order polynomial in $z = 10000/T$, so that $k_{c,r}$ is expressed in the form

$$k_{c,r} = \exp(B_1^r + B_2^r z + B_3^r z^2 + B_4^r z^3 + B_5^r z^4) \tag{5.7}$$

where, $z = (10000/T)$

The coefficients in equation (5.7) for oxygen dissociation given by Park [5] in 1985 are tabulated as model I in table (3). A complete list of reactions for air is given in appendix C.

Later, in 1988, Park [6 and 7] reinterpreted the experimental data and assumed that certain classes of reactions can be described by a single rate-controlling temperature which is an "average" of the local translational and vibrational temperatures. In Park's two-temperature model the effect of nonequilibrium vibrational temperature on the rate coefficient is accounted for by introducing a "geometric" average temperature, T_a, in the form

$$T_a = \sqrt{TT_v} \tag{5.8}$$

The equilibrium constant is given in the form

$$k_{c,r}(T_a) = \exp(B_1^r + B_2^r \ln z + B_3^r z + B_4^r z^2 + B_5^r z^3)$$

The coefficients for the above expression are tabulated in table (2) as model II.

More recently, (in 1990 and 1991), Park [8 to 10] has employed a different curve fit for the equilibrium constant of the form:

$$k_{c,r}(T_a) = \exp(B_1^r + B_2^r/z + B_3^r \ln z + B_4^r z + B_5^r z^2) \tag{5.9}$$

If the density is low the reaction rate could also depend on the particulate nature of the media. Park gives different coefficients for the above curve fit for different number densities n_i and these are tabulated in table (4). The number density of species, n_i is given by

$$n_i = 6.0222 \times 10^{23} \rho \gamma_i \tag{5.10}$$

where ρ is the gas density in g/cm^3 and γ_i is the concentration of species i expressed in the units of moles per gram of mixture. In reference [9] the coefficients in equation (5.9) are taken for a number density of 10^{17} although this is not mentioned in the paper.

6. Chemistry Modelling: Air

For modelling air flows without ionisation effects five species, O_2, N_2, NO, O and N, are commonly used. The chemical reactions considered are

$$\begin{aligned}
&R(1): \quad N_2 + M \underset{k_{b,1}}{\overset{k_{f,1}}{\rightleftharpoons}} 2N + M \\
&R(2): \quad O_2 + M \underset{k_{b,2}}{\overset{k_{f,2}}{\rightleftharpoons}} 2O + M \\
&R(3): \quad NO + M \underset{k_{b,3}}{\overset{k_{f,3}}{\rightleftharpoons}} N + O + M \\
&R(4): \quad N_2 + O \underset{k_{b,4}}{\overset{k_{f,4}}{\rightleftharpoons}} NO + N \\
&R(5): \quad NO + O \underset{k_{b,5}}{\overset{k_{f,5}}{\rightleftharpoons}} O_2 + N
\end{aligned} \tag{6.1}$$

The first three reactions are dissociation-recombination reactions with M denoting a third body given by any of the reactants present. The remaining two reactions are rearrangement reactions involving NO. Thus the total number of elementary reactions is seventeen. Note that reactions are written so that the forward reactions are endothermic which results in a decrease in temperature as the radicals are produced.

The above set of reactions can be complemented by the direct bimolecular reaction

$$R(6): \quad N_2 + O_2 \underset{k_{b,6}}{\overset{k_{f,6}}{\rightleftharpoons}} 2NO \tag{6.2}$$

Although reaction R(6) can be obtained by adding reactions R(4) and R(5), for a non-equilibrium reaction the chemical processes can be independent. However, this reaction is not included in the Dunn and Kang air model and was not considered in the present modelling either.

The corresponding forward-backward reaction rate equations are

$$R1 = \sum_{m=1}^{5} - k_{f,1,m} \frac{\rho_1}{M_1} \frac{\rho_m}{M_m} + k_{b,1,m} \frac{\rho_4}{M_4} \frac{\rho_4}{M_4} \frac{\rho_m}{M_m}$$

$$R2 = \sum_{m=1}^{5} - k_{f,2,m} \frac{\rho_2}{M_2} \frac{\rho_m}{M_m} + k_{b,2,m} \frac{\rho_5}{M_5} \frac{\rho_5}{M_5} \frac{\rho_m}{M_m}$$

$$R3 = \sum_{m=1}^{5} - k_{f,3,m} \frac{\rho_3}{M_3} \frac{\rho_m}{M_m} + k_{b,3,m} \frac{\rho_4}{M_4} \frac{\rho_5}{M_5} \frac{\rho_m}{M_m}$$

$$R4 = - k_{f,4} \frac{\rho_1}{M_1} \frac{\rho_5}{M_5} + k_{b,4} \frac{\rho_3}{M_3} \frac{\rho_4}{M_4}$$

$$R5 = - k_{f,5} \frac{\rho_3}{M_3} \frac{\rho_5}{M_5} + k_{b,5} \frac{\rho_2}{M_2} \frac{\rho_4}{M_4} \qquad (6.3)$$

where the $k_{f,r}$'s and $k_{b,r}$'s are the forward and backward reaction rate coefficients determined as functions of temperature (see appendix A for the kinetic model of Dunn and Kang [2], appendix B for the model of Wray [3] and appendix C for the model of Park [5]).

The source terms that represent the inter-species mass transfer rates may be constructed as

$$\left.\begin{aligned} \omega_1 &= M_1 (R_1 + R_4) \\ \omega_2 &= M_2 (R_2 - R_5) \\ \omega_3 &= M_3 (R_3 - R_4 + R_5) \\ \omega_4 &= M_4 (-2R_1 - R_3 - R_4 - R_5) \\ \omega_5 &= M_5 (-2R_2 - R_3 + R_4 + R_5) \end{aligned}\right\} \qquad (6.4)$$

7. Thermodynamic Model

In the present computation, chemical non-equilibrium is the only rate process considered. Vibrational energy is assumed to be in equilibrium with the translational and rotational energies at the local gas temperature, T_t. Hence, for simplicity, no attempt is made to account for coupling between vibrational and disassociation so it is a "one temperature model". The curve fits for Cp(T), a fourth-order polynomial in temperature, given by Prabhu and Erikson [22] were used for special air model, i.e.

$$C_{p_i}/\Re = \sum_{j=1}^{5} a_{i,j} T^{j-1} \qquad (7.1)$$

and hence H_i, enthalpy per unit mass is

$$H_i = \Re T \sum_{j=1}^{5} a_{i,j} \left(T^{j-1}/j\right) + \Re . a_{i,6} \qquad (7.2)$$

where i refers to species 1 to 5 and $a_{i,j}$ are given for five different temperature ranges (j index). An iterative approach is needed to evaluate the temperature for a given internal energy, e, which is related to the specific enthalpies by:

$$e = \sum_{i=1}^{5} \frac{C_i}{M_i} H_i - \Re T \qquad (7.3)$$

where C_i is the mass fraction of the species i ($C_i = \rho_i/\rho$).

In order to minimise the number of iterations, and thus the cost of computing, the temperature is saved and used as the initial guess for the next time-step. As the solution converges to the steady state, the number of iterations required per time-step should decrease and possibly reduce to one.

8. Numerical Method

As a sequel to Harten's work [11], Davis [12] showed that it is possible to put any second-order classical scheme, such as the Lax-Wendroff scheme, in TVD form. This is accomplished by adding to the basic scheme a non-linear term which gives precisely the correct amount of artificial viscosity needed at each mesh point to limit over-shoots and under-shoots. Following the formulations of Davis [12] and Causon [13], the classical MacCormack scheme is modified for the one-dimensional Euler equations as shown below:

$$U_i^{*} = U_i^{n} - \frac{\Delta t}{\Delta x} \left(F_{i+1}^{n} - F_i^{n}\right) \qquad (8.1)$$

$$U_i^{n+1} = \tfrac{1}{2}\left[U_i^n + U_i^* - \frac{\Delta t}{\Delta x}\left(F_i^* - F_{i-1}^*\right)\right] \tag{8.2}$$

Schemes (8.1) and (8.2) can be updated to become total variation diminishing by adding to the right hand side of the "corrector" step (8.2) the term:

$$\left[G_i^+ + G_{i+1}^-\right].\Delta U_{i+1/2}^n - \left[G_{i-1}^+ + G_i^-\right].\Delta U_{i-1/2}^n \tag{8.3}$$

where,

$$\Delta U_{i+1/2}^n = U_{i+1}^n - U_i^n,\ \Delta U_{i-1/2}^n = U_i^n + U_{i-1}^n \tag{8.4}$$

$$G_i^{\pm} = G\left[r_i^{\pm}\right] = 0.5C(\nu).\left\{1 - \varphi\left[r_i^{\pm}\right]\right\} \tag{8.5}$$

$$C(\upsilon) = \begin{cases} \nu(1-\nu), & \nu \le 0.5 \\ 0.25, & \nu > 0.5 \end{cases} \tag{8.6}$$

$$\nu = \upsilon_i = \max|\lambda| \frac{\Delta t}{\Delta x} \tag{8.7}$$

$$\max|\lambda| = u + a \tag{8.8}$$

where u and a are local flow speed and sound speed respectively, and

$$r_i^+ = \frac{\left[\Delta U_{i-1/2}^n,\ \Delta U_{i+1/2}^n\right]}{\left[\Delta U_{i+1/2}^n,\ \Delta U_{i+1/2}^n\right]},\quad r_i^- = \frac{\left[\Delta U_{i-1/2}^n,\ \Delta U_{i+1/2}^n\right]}{\left[\Delta U_{i-1/2}^n,\ \Delta U_{i-1/2}^n\right]} \tag{8.9}$$

where, [. , .] denotes the inner (i.e. scalar) product of the components of ΔU.

Finally,

$$\varphi(r) = \begin{cases} \min(2r,1), & r > 0 \\ 0, & r \le 0 \end{cases} \tag{8.10}$$

9. Time-Scale for Chemical Non-Equilibrium

Following the approach of Li [14], the chemical time for a species i is defined by

$$\tau_{chem} = \frac{\rho_i}{\omega_i} \tag{9.1}$$

Changes in this relaxation time are given by

$$\Delta\tau_{chem} = \frac{\Delta\rho_i}{\omega_i} = \frac{\Gamma}{\omega_i} \tag{9.2}$$

since ω_i remains nearly constant over a time step. For stability, the chemical time step is chosen such that no change in species density greater than Γ occurs over the time step. For some of the computations that follow Γ has to be as low as 0.002. The fluid dynamic relaxation time step, Δt_{fl}, must satisfy the CFL stability criterion. The internal physical-chemical relaxation time, $\Delta\tau_{chem}$, which involves the finite rate processes of vibrational energy and chemical composition changes also imposes a time step limit. The computational time step, Δt, is therefore taken as the minimum of the fluid and chemical time steps, i.e.

$$\Delta t = \min\left(\Delta t_{fl}, \Delta\tau_{chem}\right) \tag{9.3}$$

If the chemical time steps are much smaller than the fluid times, as occurs near equilibrium, the equations are said to be stiff. This is well characterised by the non-dimensional number known as Damköhler's number:

$$Da = \frac{\text{flow time}}{\text{chemical relaxation time}}$$

for small Da the flow is essentially frozen and the reaction rates, k_f and k_b are very small of order zero. For large Da, where both k_f and k_b tend to infinity and τ_{chem} tends to zero, the flow tends towards its equilibrium state. Significant non-equilibrium processes will occur in a flow in which Da is of order one.

10. Point Implicit Scheme:

For stiff problems, implicit schemes offer large advantages over fully explicit schemes which tend to become unstable as Da tends to large values. However, for multiple space dimensions, the efficiency of this technique can be severely degraded due to the difficulties associated with inversion of large coefficient matrices. Unlike fully implicit methods, point implicit methods do not require the inversion of large matrices. The point implicit MacCormack scheme is, therefore, chosen to integrate the equations when the chemical source terms are stiff. The scheme is mainly adapted from the work of Bussing and Murman [15] and Eklund et al [16] on hydrogen-air combustion problems. Bussing and Murman have shown that if only the steady-state solution is desired, the time history can be modified to remove the stiffness associated with the chemical time scales. The governing equations for one-dimensional flow, equation (4.2), are modified to:

$$SM\left(\frac{\partial U}{\partial t}\right) = -\frac{\partial E}{\partial \xi} + H \qquad (10.1)$$

where SM is a scaling matrix with the purpose of normalising the various time scales to the same order so that the fast processes which usually require small time steps do not hold up the slower processes which can be marched at larger time steps.

The point implicit method can be written as:

$$U_i^{n+1} = U_i^n - \Delta t\left[\left(\frac{\partial E}{\partial \xi}\right)^n + H_i^{n+1}\right] + O(\Delta t)^2 \qquad (10.2)$$

where, n is the old time level and n+1 the new time level. The vector $\mathbf{H}^{n+1}$ is then expanded by a Taylor series.

$$H_i^{n+1} = H_i^n + \Delta t\left(\frac{\partial H}{\partial t}\right)^n + O(\Delta t)^2 \qquad (10.3)$$

$$H_i^{n+1} = H_i^n + K_{i,j}^n\left(U_i^{n+1} - U_i^n\right) + O(\Delta t)^2 \qquad (10.4)$$

where, $k_{i,j}^n$ is the Jacobian of H^n

$$K_{i,j}^n = \left[\frac{\partial H}{\partial U_j}\right]^n \qquad (10.5)$$

Putting equation (10.4) into equation (10.2), simplifying the resulting equation and then rewriting in delta form gives:

$$\left[I + \Delta t K_{i,j}^n\right]\Delta U_i^{n+1} = -\Delta t\left[\left(\frac{\partial E}{\partial \xi}\right)^n + H_i^n\right]$$

$$SM\ \Delta U_i^{n+1} = -\Delta t\left[\left(\frac{\partial E}{\partial \xi}\right)^n + H_i^n\right] \qquad (10.6)$$

where

$$\Delta U_i^{n+1} = U_i^{n+1} - U_i^n$$

and I is the unit vector.

Then the point implicit method becomes:

$$U_i^* = U_i^n - \Delta t.\ SM^{-1}\left(\frac{E_{i+1}^n - E_i^n}{\Delta \xi} + H_i^n\right) \qquad (10.7)$$

$$U_i^{n+1} = ½\left(U_i^n + U_i^*\right) - ½\Delta t.SM^{-1}\left(\frac{E_i^* - E_{i-1}^*}{\Delta \xi} + H_i^*\right) \qquad (10.8)$$

The pre-conditioner submatrix, SM, for air dissociation is detailed in reference [1].

11. Free Stream Flow Conditions used for Test Cases

Test cases include typical conditions which can be simulated in the shock tube and typical re-entry conditions. In order to investigate the effects of using different chemical models on the non-equilibrium flow solutions, the following flow conditions were used:

Test Case I:

$T_\infty = 2577.6$ K
$p_\infty = 8904.3$ Pa
$\rho_\infty = 0.0128$ kg/m^3
$u_\infty = 4.0$ km/s
$x_{ref} = 0.00556$ m
$C_o = 0.0366$

Table (5): Free Stream Flow Conditions for Test Case I.

The above conditions but with the free stream velocity of about 2320 m/s closely represent the conditions that exist in the shock tube experiment. Here u_∞ is taken to be 4 km/s in order to have a high enough temperature to result in more chemically active flows behind the bow shock wave and therefore to be better able to examine the effects of using different chemical models.

The second set of free stream conditions simulate the flows that exist in the shock tube behind the moving shock wave when the driven gas is air rather than pure oxygen, where the air is assumed to consist of 21% O_2 and 79% N_2 by volume. The flow equations in the shock tube, assuming chemical equilibrium conditions, were solved (using the program given in [17]) and the conditions behind the shock wave are given below in test case II. The shock tube program requires the input of the temperature behind the moving shock wave. From that and the initial conditions in the shock tube it calculates everything else including mole fractions of the species. A temperature of 2497 K gives a shock Mach number of 7.03 which is close to the conditions presently attainable in the shock-tube experiments.

Test case II:

$T_\infty = 2497.0$ K
$\rho_\infty = 0.011$ kg/m^3
($p_\infty = 8088.4$ Pa)
$u_\infty = 2075.0$ m/s
$x_{ref} = 0.00556$ m
$C_{N2} = 0.7560$ (77.02% by volume)
$C_{O2} = 0.2082$ (18.56% by volume)
$C_{NO} = 0.2349E-1$ (2.2336% by volume)
$C_O = 0.1226E-1$ (2.186% by volume)
$C_N = 0.4339E-6$ (0.8841E-6% by volume)

Table (6): Free Stream Flow Conditions for Test Case II.

Test case III is similar to test case II but for $u_\infty = 4$ km/s, as it was found that the flows obtained by using test case II conditions was virtually frozen; see the discussion section for more details.

Test case IV simulates the conditions that exist for a typical re-entry flight at an altitude of 75 km. These conditions have also been used by Desideri in ref [18]:

Test case IV:

$T_\infty = 205.3$ K
$\rho_\infty = 0.43E-4$ kg/m^3
($p_\infty = 2.5$ Pa)
$u_\infty = 5152.59$ m/s
($M_\infty = 17.9$)
$x_{ref} = 1.000$ m
$C_{N2} = 0.7670$ (79% by volume)
$C_{O2} = 0.2330$ (21% by volume)
$C_{NO} = 0.1E-7$
$C_N = 0.1E-7$
$C_O = 0.1E-7$

Table (7): Free Stream Flow Conditions for Test Case IV.

12. Convergence Assessments

In order to assess the history of convergence, after a set number of iterations the following variables are monitored and saved in output files for post-processing:

I) The maximum change in the density in the whole flow field between successive iterations and also the location of this maximum change in the grid is recorded after a certain fixed number of iterations, say every 10 iterations.

II) The value of the stagnation temperature, is recorded every 100 iterations.

III) Using the surface pressure distribution, the drag coefficient, Cd, is calculated:

$$Cd = \frac{1.0}{\frac{1}{2}\rho_\infty u_\infty^2} \int_0^{\theta=\pi/2} (P-P_\infty)dy \qquad (12.'$$

The integral is evaluated in the program using Simpson's rule.

In a hypersonic flow a good estimate of the drag coefficient is available. According to Newtonian theory the pressure coefficient is

$$Cp = \frac{P_s - P_\infty}{\frac{1}{2}\rho_\infty u_\infty^2} = 2\sin^2\varphi_b = 2\cos^2\theta \qquad (12.2)$$

giving

$$Cd = (2/3).Cp_{stagnation} \qquad (12.3)$$

13. The Experimental Facility

13.1 The Shock Tube

The shock tube at the University of Manchester Goldstein Aeronautical Engineering Laboratories is divided into three sections; the driver section, the diaphragm section and the test section. The driver section consists of a 1.27m long tube with 70mm internal diameter. The diaphragm section is 0.127m long and is clamped between the driver and test sections. It allows up to two diaphragms to be used and the overall diaphragm pressure ratio to be doubled. The test section is 60mm square and 6.15m long to the working section where there are windows, also 60mm square. Immediately after the working section there is a large dump tank which is used both to stop the main shock being reflected upstream over the model and to reduce the final ambient pressure within the shock tube after each run.

The downstream end of the shock tube is shown as figure 1.1. The square test section can be seen running from left to right. The larger cylindrical sections are the test stations where the timing instrumentation is situated. The large frame either side of the test section, just before the large diameter dump tank, supports the Mach Zehnder interferometer which was used to produce the infinite fringe interferograms shown in this paper. Below the test section is the timing apparatus, amplifiers, triggers and the timer itself, looking from right to left.

The shock tube is used with helium as the driver gas and air, nitrogen, oxygen and (occasionally) nitrous oxide as the test gases. The diaphragms used are either melinex, bursting at 1000 kPa or 2000 kPa with two diaphragms, or aluminium. The aluminium diaphragms are 0.7mm thick and scored to help them petal on bursting. The scoring depth determines the burst pressure and typical pressures are 1340 kPa with a scoring depth of 0.16mm and 1680 kPa with 0.1mm. The diaphragms are annealed after scoring since it was found that the scoring process work hardened them and caused erratic bursting.

When used with two diaphragms the shock tube is set to the desired gas pressures, e.g. 1mmHg test pressure, 1680 kPa between the diaphragms and 3360 kPa in the driver section. The gas between the diaphragms is released and this overpressures the upstream diaphragm which bursts and the flow then bursts the downstream one. This procedure gives generally highly repeatable experiments. The current shock tube generates shock waves with a maximum Mach number of around 7.0 which produce temperatures in the free stream ahead of a model in the working section of around 3000K.

Two timing stations, 300mm apart, immediately ahead of the working section are used to measure the speed of the shock wave and hence its Mach number. The time is used, through a delay generator, to trigger an argon spark when flow visualisation is done.

Interferometry is the most useful visualisation technique for obtaining data about the flow and the methods of analysing the interferograms are relatively simple. When used in the in the infinite fringe mode the interferometer produces fringes which are constant density contours and is, therefore, both a quick and valuable means of analysing a flow and producing data suitable for CFD code validation.

13.2 The Heated-Driver Shock Tube

There are a number of ways to improve the performance of a shock tube. The Mach number of the generated shock depends on the diaphragm pressure ratio and the respective speeds of sound of the driver and test gases. There is an upper limit to the shock Mach number that can be obtained by increasing the pressure ratio, but this can be improved by having a hot light driver gas and a heavy test gas. Given its situation in a large laboratory, it was felt that it would be unsafe to use hydrogen - the lightest gas - as a driver gas in the shock tube so it was decided to use heated helium. Calculations showed that a shock Mach number of 10 would be needed to generate temperatures of above 5000K behind the bow shock, as shown in figure 1.2, and this could be obtained by heating the helium to 300°C using a diaphragm pressure ratio of 26000. Figures 1.3 show the variations, using Horton and Menard's [17] program, of the freestream species concentrations varying with main shock Mach number.

Because the driver gas was being heated it was decided to replace the current driver tube with a longer one (length 3m) and have insulating liners inside. The extra length was necessary to eliminate the effect of heating the gas on the expansion wave, which would travel faster. The new driver tube has an internal diameter of 130mm and accepts cylindrical liners with outside diameter 130mm and internal diameter 70mm. Each liner is 200mm long made from slip cast fused silica. Each one is grooved along the outside and along some of the end faces to allow the passage of thermocouple wires.

The driver section was not ready for testing at the time this paper was written.

14. Fringe Patterns

Recent research has shown that experimental data for shock shape and shock positions are very useful for code validation in chemically reacting air. Prediction of macroscopic quantities such as shock shape and stand-off distance suggests that the chemical and vibrational non-equilibrium kinetics are correctly modelled. However, a better demonstration of the code's validation can be made by a flow field comparison. The density field can be observed using an interferometer and the fringe pattern can be compared with the fringe pattern predicted from the computed density field.

The refractive index, n, of a dissociating biatomic gas is given by

$$n-1 = \rho\,[K_M(1-C_i) + K_A\,C_i] \qquad (14.1)$$

where, C_i is the mass fraction of the atoms in the mixture and K_M and K_A are the Gladstone-Dale constants of the molecular and atomic gases respectively. They are generally believed to be *independent* of the dissociation rate C_i. With this assumption, the ratio of K_M/K_A for oxygen and nitrogen have been determined by Alpher and White [19] from shock tube experiments and are tabulated in table (8).

For temperatures up to 5000K, there can be considerable oxygen dissociation but the ratio of K_M/K_A remains close to one. On the other hand, nitrogen has a value of K_M/K_A appreciably different from 1, although only a small degree of nitrogen dissociation occurs in this temperature range. Therefore, the Gladstone-Dale constant for air can be assumed to be constant and its value at room temperature can be used in order to determine the density for temperatures less than 5000K. However, to minimise the uncertainty of the results, the following expressions were used to relate the density change $\Delta\rho$, to the fringe pattern.

For oxygen, when $\lambda = 440$ nm

$$\Delta\rho_0 = \frac{5263.0\ F}{(1 - 0.0566\ C_0)}\,(\lambda/\ell) \qquad (14.2)$$

$$\Delta\rho_{air} = 4361.93\ F\ (\lambda/\ell) \qquad (14.3)$$

where F is the fringe number, λ is the wave length and ℓ is the experimental geometrical path.

In the present experiments an argon spark source with a green (monochromatic) filter was used with a wave length of $\lambda = 440$ nm. The geometrical path is the width of the working section which is 60 mm. The fringe definition is best when the density is greatest. For the strongest shock wave, $M_s=7$, the attainable free stream density behind the moving shock in the supersonic stream for either oxygen or air is about 0.012 kg/m^3. Computations show that the maximum density, near the stagnation point, is about 5 times the pre-shock value. Re-arranging equation (14.2) for this flow gives:

$$F = (\rho/\rho_\infty - 1.0)/(0.0386/\rho_\infty) = 1.24$$

$$\text{if } \rho_{stag}/\rho_\infty = 5.0 \qquad (14.4)$$

This value has been verified experimentally as only one fringe was visible when the shock Mach number is about 7. However, in order to increase the number of fringes the initial pressure (and therefore density) of the driver gas was increased to about 5 mmHg giving a lower shock Mach number of about 6. The free stream conditions used for these computations are:

Test Case V:

M_s = 6.01
ρ_∞ = 0.048 kg/m^3
T_∞ = 2060 K
u_∞ = 1734.2 m/s
C_{N2} = 0.7624 (0.7850 by volume)
C_{O2} = 0.2273 (0.2048 by volume)
C_{NO} = 9.7681×10^{-3} (0.9387×10^{-2} by volume)
C_O = 4.9394×10^{-4} (0.8900×10^{-3} by volume)
C_N = 1.6904×10^{-9} (0.3481×10^{-8} by volume)

Table (9): Free Stream Flow Conditions for Test Case V

An independent validation can be made using results obtained by Hornung [20] for partially dissociated nitrogen flow around a two-dimensional circular cylinder. The free stream flow conditions for this test case are:

Test Case VI:

The radius of cylinder is 2.54 cm
Nitrogen mass fraction = 0.073
Free stream temperature = 1833 K
Free stream pressure = 2910 Pa
Corresponding to the free stream density of 4.983×10^{-3} kg/m^3
The flow Mach number is 6.14

Table (10): Free Stream Flow Conditions for Test Case VI

The interferometric fringes for this flow have been computed using the following formula

$$F = 0.24 \times 10^{-3}\ \Delta\rho\ (1 + 0.28\ C_N)(\ell/\lambda) \qquad (14.5)$$

where, the wave length, λ, is 533×10^{-9} m and ℓ is taken as 0.1524 m which is the useful diameter of the flow out of the shock tunnel [20].

15. Numerical Results for the Test Cases

15.1 Equilibrium Constant, k_e

Figure (1.4) shows graphically the differences between some of the published values for the oxygen dissociation equilibrium constant. The models compared are Dunn and Kang's, given in table (1), and Park's, outlined in table (3).

Generally, there is little difference between various models for temperatures at less than 6000 K. Above this discrepancies start to show and rise to a maximum of about 23% difference in k_e at a temperature of 10000 K.

Surprisingly, the effect of different number densities, n_i, on Park's model III is negligible, although there are differences between Park's models I, II, and III in the high temperature region. The Dunn and Kang model is similar to Park's model III with a difference of less than 3% in k_e at 10000 K. It should be noted that the existence of only one single exponent term in the Dunn and Kang model make it simpler and cheaper to use compared with the five-term polynomial curve fits of Park's model.

15.2 The Effects of Using Different Chemical Models

The effects of using the different chemical models outlined in section (5) on the computational results are discussed in this section. The test problem is the non-equilibrium flow of partially dissociated oxygen over a circular cylinder with its axis perpendicular to the flow direction. The free stream conditions are given in table (5). The computational mesh consists of 100 radial and 40 tangential grid points and the results are compared after 3101 time-iterations. Note that the equilibrium constants for Park's model I and II are listed in table (3).

Although the curves obtained using different models are not identical, the differences between them are fairly small and probably not significant relative to the numerical uncertainties. However, in the light of the results obtained, the following comments are made.

Figures (2.1) and (2.2) show respectively the pressure and Mach number distribution along the stagnation streamline. As mentioned above the curves are similar, but it is noticeable that the fastest reaction rate, i.e. nearest to the equilibrium condition, occurs using Park's model I. This is not surprising as it was already clear from figure (2.2) that Park's model I had the highest k_e. The fastest reaction model produces the smallest shock stand-off distance and vice versa. The slowest reaction rates, corresponding to results nearest to the frozen flow conditions, was obtained using the Wray's model. The curve obtained using Dunn and Kang's model is almost identical to the one obtained by using Park's model II.

Figure (2.3) shows the mass fraction distribution along the stagnation streamline, it can be seen that the results are almost identical at the stagnation point, although Park's model II has produced slightly higher oxygen atom mass fraction and stagnation pressure than the other models. Figures (2.4) and (2.5) show the surface distribution of pressure and temperature respectively. Although the pressure distribution is very similar for all models, there are distinct differences in the wall temperature distribution. Not surprisingly, the highest temperatures are obtained with Wray's model which is the nearest to the frozen flow conditions and the lowest temperatures were obtained by Gardiner's model and by Park's model II which were closest to the equilibrium conditions. It is interesting to see that the highest temperature does not mean the most oxygen dissociation near the stagnation point. It should also be noted that the differences between various temperature curves are quite small near the stagnation point (about 5%) but become larger as the flow expands and cools round the body (about 10% difference, it can be concluded that the choice of a chemical model is more critical for expanding flows rather than for compressive ones.

15.3 Computations of Non-Equilibrium Air Flows in a Shock-Tube

The first set of non-equilibrium air test cases were done for a flow that exists in a shock tube, behind the moving shock wave when the shock Mach number is about 7. The free stream flow conditions are given in table (6). The computational mesh consists of 100 radial and 40 tangential grid points. R_{MAX} for the flow was set to be 5.0 and the CFL number for the computation was fixed to be 0.8.

The pressure and Mach number 'heights', shown in figures (3.1) and (3.2) indicate that there are no numerical under- or over-shoots anywhere in the flow domain. Figure (3.3) shows the pressure contours which indicate the shock stand-off distance is about 2. Contours of partial density for N_2, shown in figure (3.4), is similar to O_2 which indicates that not much chemical reactions are going on in the flow. However, figures (3.5) and (3.6) which are the contour maps of partial density for NO molecules and O atoms indicate that just behind the shock wave there is some O_2 dissociation which in turn feeds the production mechanism of NO and O with the maximum dissociation occurring near the stagnation point. As the flow expands and cools round the body, NO re-shuffles, N and O atoms re-combine to produce N_2 and O_2 again.

Temperature distributions along the stagnation line and around the body indicate that there is very little variation in the temperature behind the shock-wave and the post-shock temperature value reaches the stagnation point virtually unchanged. This behaviour suggests that there is little chemical reaction occurring in the flow. This is confirmed further by viewing the mass fractions of different species along the stagnation streamline, in figure (3.7), which shows that they are all constant. Although the contours of partial densities of different species change across the bow shock wave and in the flow field, the ratios of different partial densities to the total density are constant. This suggests that the flow is virtually frozen which is due to the small size of the body and also to the relatively low free stream Mach number giving correspondingly low temperatures behind the bow shock wave.

In order to produce non-equilibrium flows with the free stream conditions given in table (6), the free stream velocity was increased to 4 km/s, keeping all other parameters the same. R_{MAX} was taken to be 3 and the CFL number was chosen to be 0.8 as before. During the first hundred time-iterations the drag coefficient, Cd, drops to a minimum and then rises very slowly to a value of 1.253. In a similar way, but more slowly, the stagnation temperature asymptotes to 5500 K but after about 1500 iterations some oscillations develop which could also be seen in the maximum density change for successive iterations. The location of the oscillations was identified to be behind the bow shock wave. However, the residuals have dropped three orders of magnitude in the course of the calculations.

Contour maps of pressure, partial density of N_2, O_2 and NO are shown in figures (3.8) to (3.11). They indicate that the shock stand-off distance is about 1.32 radii and also that there are significant chemical reactions occurring in the flow field. This is best seen in the contour map of partial density of O_2 and NO in figures (3.10) and (3.11) respectively, which indicate a strong reaction front just behind the bow shock wave. The existence of non-equilibrium chemistry is also evident from the temperature contour maps and distribution along the stagnation streamline, (not shown here). The temperature drops immediately behind the shock wave from a high value of 7000 K to 5500 K. The mass fraction profiles along the stagnation streamline indicate that almost all of O_2 has been dissociated while NO peaks to a maximum just behind the shock wave where the minimum value of N_2 mass fractions occurs but then drops back towards zero, therefore the N_2 mass fraction increases back towards its peak pre-shock value.

15.4 Computations of Non-Equilibrium Air Flows for Re-Entry Flight Conditions

In order to validate the computational codes, especially for high Mach number flows, and since the experimental results were not fully available yet, the test conditions previously used by Desideri [18] were used here. The free stream conditions closely simulate a re-entry flight of Mach number 17.9 at an altitude of 75 km. The flow conditions are tabulated in table (7).

Since the code had not been run before for such a high free stream Mach number, the computations were carried out with a CFL number of 0.5. The temperature range and chemical reactions were little different from those tried before, but high Mach numbers result in very low pressures in real life as well as in the non-dimensional computer's world. In this situation an under-shoot in the pressure, e.g. due to the existence of very strong shock waves, could make the pressure become negative leading to unstable computations.

The first set of computations were carried out using the Dunn and Kang air model and on a mesh consisting of 120 radial and 40 tangential grid points. R_{MAX} was set to be 2.3. Figure (4.1) shows the history of convergence which is very similar to test cases II and III. The drag coefficients given by the equation (12.3) is also shown in figure (4.1). It can be seen that initially, up to about 1000 time-iterations, the drag is the same as the perfect gas case but as the real gas chemistry starts to show its effect, the curve asymptotes to a higher Cd value. This is not only due to the face that the stagnation pressure is different from that in the perfect gas case but also that in the real gas case the pressure variation around the body is different from that predicted for a perfect gas using the hypersonic. Newtonian theory. This difference in pressure distribution is the major reason why the pitching moment on a blunt body is so much different from the perfect gas calculations.

Figures (4.2) to (4.4) show the partial densities of different species in the flow field. They all indicate that the shock stand-off distance is about 1.26. The maximum density is about 11.56 which suggests that there is significant dissociation occurring in the flow field. The contour maps of O_2, in figure (4.3), indicate that almost all of the oxygen molecules have been dissociated behind the bow shock wave. Figure (4.4), which is the contour map of NO, indicates that the maximum NO production occurs just behind the shock wave. Temperature contours in figure (4.5) show the reaction front very clearly and how the temperature is reduced behind the shock wave due to the endothermic chemical reactions.

In figure (4.6), the temperature distribution along the stagnation line and around the body, obtained by the present method using the Dunn and Kang air model and by Desideri who used Park's air model. Although it is difficult to read the data from the Desideri's figures, the following comparisons can be made.

The present computational results produce a shock stand-off distance which is about 3.5% larger than Desideri's value of 1.22. The peak temperature, just behind the shock wave, is about 8200 K which is roughly 1.5% smaller than the Desideri's (8310 K). The stagnation temperature was computed here to be 5950 K while Desideri's results indicate a value close to 6450 K (about 8% larger). However, the main discrepancy arises further downstream where the flow is expanded and cooled, eg at $\theta=\pi/2$ on the body the temperature has been predicted to be 3050 K while Desideri's results suggests a temperature of about 3700 K, a difference of 21%. Initially, it was thought that this was due to using a different chemical model, but similar results were obtained when using Park's air model. The real explanation is actually suggested by Desideri who computed the flow using three different schemes, based on the van Leer M.U.S.C.L. approach, namely

(a) the first-order scheme,
(b) the quasi-second-order method with slope-limiters, and
(c) the quasi-second-order method based on the upwind triangle and TVD-averaging.

Obviously, scheme (b) is very similar if not identical to the present results. Desideri concludes that the "quasi-second-order method with slope limiters is more robust than the quasi-second-order method based on the upwind triangle, but the latter is more accurate". This shows the effect of using a symmetric rather than an upwind TVD scheme for computations of very high Mach number hypersonic flows. However, the reader should not conclude that the present code is only first-order accurate, as the resolution of the shock wave indicates that the system is not diffusive like a typical first-order scheme.

It should also be noted that Desideri has used Park's model I (1985) for his computation which is a single-temperature model similar to Dunn and Kang's air model. According to the altitude-velocity map given by Park [21] this may not be justified as the dominant thermochemical phenomena occur in the region where a two-temperature model may be more applicable.

15.5 Fringe Pattern Comparisons

The results of the present calculations are compared with the experimental interferograms in figures (5.1) and (5.2). In figure (5.1), the results are presented for the supersonic flow of hot air, test case V. The calculated stand-off distance (=1.0) and the shock shape is in good agreement with the experiment but the fringe pattern is slightly different from the experimental pattern. The computational results suggest a sharp rise in density behind the shock wave and very gradual increase, shown by the 2nd fringe, towards the surface, but the experimental results indicate a much slower rise through the shock wave and more gradual increase towards the body. The disagreement between the computation and experiment is presently not explained. Possible causes of discrepancies are uncertainties in the experimental results or the limitations of inviscid flow or the one-temperature model used in the computation.

The second interferogram pictures are obtained by Hornung [20] for partially dissociated nitrogen flow in a shock tunnel, given as test case VI. Viscous computations have been carried out for this flow by Candler [23], as well as more recently by Park et al [10]. Both authors have used both one-temperaure and multi-temperature non-equilibrium model. Although Park has made a detailed study and comparisons of his results with Candler, their free stream conditions are not identical as Park has used a free stream density of 5.35×10^{-3} kg/m^3 which would give the same free stream pressure (given in table (10)) if no dissociation was present in the free stream. This might explain the disagreement between their calculations using the one-temperature model.

The present calculation of fringes for this flow using one-temperature model is shown in figure (5.2). The nitrogen flow is calculated using the 5-species air model by setting the mass fractions of O_2, O and NO to be 10^{-7}. As seen in the figure, the calculation reproduces both the shock stand-off distance (0.25) and shock shape. It is also interesting to note that near the body the present inviscid computation appears to be closer to the experimental fringe pattern than the viscous computation. In practice, the boundary layer is extremely thin and two possibilities are that the viscous computations over estimate the boundary layer and that the experimental resolution is insufficient to detect it.

16. Conclusion

The high speed chemical non-equilibrium calculations were performed using the computer codes CYLO2 and CYLAIR. The computations were made using a *VP-1100* computer. The present computational results suggest that the flow solutions were not very sensitive to the choice of a chemical model. However, Dunn and Kang's model is preferred, because it was the easiest to program and the cheapest to run.

The computational results show that the present TVD scheme is satisfactory for simulation of low hypersonic flows with real gas effects, but there is an uncertainty of about 8% in the stagnation temperature for free stream Mach numbers of the order of 20 when compared with previous

Two further non-equilibrium cases were compared with experimental interferograms, good agreement with shock shapes and general fringe patterns were obtained for the low hypersonic, partially dissociated flow of nitrogen. Although, the shock stand-off distance and shock shape are given in good agreement with the experimental results for supersonic flow of hot air in a shock-tube, there are some differences in the fringe pattern that are unexplained at this stage. The present study has demonstrated the valuable information that CFD codes can provide when co-ordinated with suitable experimental work.

Acknowledgement

The authors would like to thank the British Aerospace (Military Aircraft) Ltd., Warton Site, for their financial support during the course of this project.

References

1. Shahpar, S., "Hypersonic Flows Including Real Gas Effects", *PhD Thesis*, University of Manchester, 1990.

2. Dunn, M.G. and Kang, S.W., "Theoretical and Experimental Studies of Re-Entry Plasmas", *NASA CR-2232*, 1973.

3. Wray, K.L., "Chemical Kinetics of High Temperature Air", in "Hypersonic Flow Research", Editor: Riddell, F.R., Academic Press, 1962.

4. Gardiner, W.C. Jr., "Combustion Chemistry", Springer-Verlag, 1984.

5. Park, C., "Convergence of Computation of Chemical Reacting Flows", *Thermophysical Aspects of Re-Entry Flows*, Editor: Moss, J.N. and Scott, C.D., vol. **103**, *Prog. Astronautics & Aeronautics*, AIAA, pp 478-513, 1985. (Available also as *AIAA Paper 85-0247*).

6. Park, C., "Assessment of Two-Temperature Kinetic Model for Ionizing Air", *J of Thermophysics*, vol.**3**, no.3, pp 233-244, July 1989. (Available also as *AIAA Paper 87-1574*).

7. Park, C., "Two-Temperature Interpretation of Dissociation Rate Data for N_2 and O_2", *AIAA Paper 88-0458*, 1988.

8. Park, C. and Yoon, S., "Calculation of Real Gas Effects on Blunt-Body Trim Angles", *AIAA Paper 89-0685*.

9. Park C., "Nonequilibrium Hypersonic Aerothermodynamics", 1990, Wiley.

10. Park, C. and Yoon, S., "Fully Coupled Implicit Method for Thermochemical Nonequilibrium Air at Suborbital Flight Speeds", *J of Spacecraft*, vol.**28**, no.1, pp 31-39, Jan-Feb 91.

11. Harten, A., "High Resolution Schemes for Hyperbolic Conservation Laws", *J Computational Physics*, vol.**49**, pp 357-393, 1983.

12. Davis, S.F., "TVD Finite Difference Schemes and Artificial Viscosity", *NASA CR 172373*, 1984.

13. Causon, D.M., "A Total Variation Diminishing Scheme for Computational Aerodynamics", in *Numerical Methods for Fluid Dynamics III*, Editors: Morton, K.W. and Bains, M.J., Oxford University Press, 1988.

14. Li, C.P., "Time Dependent Solution of Nonequilibrium Air Flow Past a Blunt Body", *AIAA Paper 71-0595*, June 1971.

15. Bussing, T.R.A. and Murman, E.M., "Finite-Volume Method for the Calculation of Compressible Chemically Reacting Flows", *AIAA Journal*, vol.**26**, no.9, pp 1070-1078, September 1988.

16. Eklund, D.R., Hassan, H.A. and Drummond, J.P., "The Efficient Calculation of Chemically Reacting Flow", *AIAA Paper 86-0563*, January 1986.

17. Horton, T.E. and Menard, W.A., "A Program for Computing Shock-Tube Gasdynamic Properties", *NASA Technical Report 32-1350*, January 1969.

18. Desideri, J.A., "Hypersonic Reactive Flow Computations Using Unstructured Meshes", *The Third Joint Europe/US Short Course in Hypersonics*, RWTH Aachen, FRG, October 1990.

19. Alpher, R.A. and White, D.R., "Optical Refractivity of High Temperature Gases. I. Effects Resulting From Dissociation of Diatomic Gases", *Physics of Fluids*, vol.**2**, pp 153-161, 1959.

20. Hornung, H.G., "Nonequilibrium Dissociating Nitrogen Flow Over Spheres and Circular Cylinders", *J Fluid Mechanics*, vol.**53**, Part 1, May 1972, pp 149-176, 1972.

21. Park, C. and Yoon, S., "Calculation of Real Gas Effects on Airfoil Aerodynamic Characteristics", *AIAA Paper 90-1712*, 1990.

22. Prabhu, K. and Erickson, W.D., "A Rapid Method for the Computation of Equilibrium Chemical Composition of Air to 15000K", *NAS TP 2792*, 1988.

23. Candler, G.V., "On the Computation of Shock Shapes in Nonequilibrium Hypersonic Flows", *AIAA Paper 89-0312*, January 1989.

No	References	$c_{f,1}$	$\eta_{f,1}$	$E_{f,1}/k$	$c_{f,2}$	$\eta_{f,2}$	$E_{f,2}/k$
1	Dunn & Kang [2]	9.0×10^{19}	-1.0	59500	3.24×10^{19}	-1.0	59500
2	Wray [3]	6.40×10^{23}	-2.0	59960	1.9×10^{21}	-1.5	59960
3	Gardiner [4]	4.56×10^{19}	-1.0	59400	1.64×10^{19}	-1.0	59400
4	Park I [5]	8.25×10^{19}	-1.0	59500	2.75×10^{19}	-1.0	59500
5	Park II [6]	2.9×10^{23}	-2.0	59750	9.68×10^{22}	-2.0	59750
6	Park III [7]	1.0×10^{22}	-1.5	59500	2.0×10^{21}	-1.5	59500

Table (1): Comparison of Reaction Rates for O_2 Given by Different Authors.

r	Reaction	$c_{f,r}$	$\eta_{f,r}$	$E_{f,r}/k$	$c_{b,r}$	$\eta_{b,r}$	$E_{b,r}/k$
1	$O_2 + O \longleftrightarrow 2O + O$	9.00×10^{19}	-1	5.950×10^{4}	7.5×10^{16}	-0.5	0.0
2	$O_2 + O_2 \longleftrightarrow 2O + O_2$	3.24×10^{19}	-1	5.950×10^{4}	2.7×10^{16}	-0.5	0.0

Table (2): The Kinetic Model of Dunn and Kang.

No	Model No	B_1^r	B_2^r	B_3^r	B_4^r	B_5^r
1	Model I	1.335	-4.127	-0.616	0.093	-0.005
1	Model II	2.855	0.988	-6.181	-0.023	-0.001
2	* Model III	2.460	0.55388	1.7763	-6.572	0.031445

Table (3): Different Curve Fits for the Equilibrium Constant for Oxygen Dissociation According to Park

* For $n_i = 10^{17}$; see table (4) below.

No	Number Density n	B_1^r	B_2^r	B_3^r	B_4^r	B_5^r
1	10^{14}	1.9607	1.8103	3.5716	-7.3623	0.083861
2	10^{15}	2.3160	0.91354	2.2885	-6.7969	0.046338
3	10^{16}	2.4253	0.64183	1.9026	-6.6277	0.035151
4	10^{17}	2.4600	0.55388	1.7763	-6.5720	0.031445
5	10^{18}	2.4715	0.52455	1.7342	-6.5534	0.030209
6	10^{19}	2.4773	0.50989	1.7132	-6.5441	0.029591

Table (4): The Coefficients B_i^r in the Expression for Equilibrium Constant. k_c according to Park (Model III) for Oxygen Dissociation.

	λ = 4800 Å			λ = 5890 Å	λ = 5000 Å	λ = 4400 Å
Species	K_M/K_A	$K_A/(cm^3/gr)$	$K_M/(cm^3/gr)$	$K_M/(cm^3/gr)$	$K_M/(cm^3/gr)$	$K_M/(cm^3/gr)$
Oxygen	1.06	0.18	0.191	0.190	--	--
Nitrogen	0.79	0.31	0.245	0.238	--	--
Air	--	--	0.2281	0.2262	0.2276	0.2293

Table (8): Gladstone-Dale Constants for Different Species for Different Wave Length λ.

Appendix A: Chemical Reactions and Rate Coefficients given by Dunn and Kang:

No	Reaction	Forward Rate Coefficient, K_f $cm^3\ mole^{-1}\ sec^{-1}$	Backward Rate Coefficient, K_b $cm^3\ mole^{-1}\ sec^{-1}$ [*] or $cm^6\ mole^{-2}\ sec^{-1}$	Third Body, M
1	$N_2 + N_2 \leftrightarrow 2N + N_2$	$4.700x10^{17}\ T^{-0.5}\ \exp(-1.13x10^5/T)$	$2.72x10^{16}\ T^{-0.5}$	-
2	$N_2 + M \leftrightarrow 2N + M$	$1.900x10^{17}\ T^{-0.5}\ \exp(-1.13x10^4/T)$	$1.10x10^{16}\ T^{-0.5}$	O_2, NO, O
3	$N_2 + N \leftrightarrow N + N + N$	$4.085x10^{22}\ T^{-1.5}\ \exp(-1.13x10^5/T)$	$2.27x10^{21}$	-
4	$O_2 + N_2 \leftrightarrow 2O + N_2$	$7.200x10^{18}\ T^{-1.0}\ \exp(-5.95x10^4/T)$	$6.00x10^{15}\ T^{-0.5}$	-
5	$O_2 + O_2 \leftrightarrow 2O + O_2$	$3.240x10^{19}\ T^{-1.0}\ \exp(-5.95x10^4/T)$	$2.70x10^{16}\ T^{-0.5}$	-
6	$O_2 + O \leftrightarrow 2O + O$	$9.000x10^{19}\ T^{-1.0}\ \exp(-5.95x10^4/T)$	$7.50x10^{16}\ T^{-0.5}$	-
7	$O_2 + M \leftrightarrow 2O + M$	$3.600x10^{18}\ T^{-1.0}\ \exp(-5.95x10^4/T)$	$3.00x10^{15}\ T^{-0.5}$	NO, N
8	$NO + M \leftrightarrow N + O + M$	$3.900x10^{20}\ T^{-1.5}\ \exp(-7.55x10^4/T)$	$1.00x10^{20}\ T^{-0.5}$	N_2, O_2
9	$NO + M \leftrightarrow N + O + M$	$7.800x10^{20}\ T^{-1.5}\ \exp(-7.55x10^4/T)$	$2.00x10^{20}\ T^{-1.5}$	NO, N, O
10	$N_2 + O \leftrightarrow N + NO$	$7.000x10^{13}\ \exp(-3.80x10^4/T)$	$1.56x10^{13}$ [*]	-
11	$NO + O \leftrightarrow N + O_2$	$3.200x10^9\ T^{1.0}\ \exp(-1.97x10^4/T)$	$1.30x10^{10}\ T^{1.0}$ $\exp(-3.6x10^3/T)$ [*]	-

Appendix B: Chemical Reactions and Rate Coefficients given by Wray:

No	Reaction	Foward Rate Coefficient, K_f $cm^3\ mole^{-1}\ sec^{-1}$	Catalyst, M
1	$N_2 + M \leftrightarrow 2N + M$	$4.20x10^{12}\ T^{0.5}\ (1.133x10^5/T)\ \exp(-1.133x10^5/T)$	N_2
		$1.70x10^{12}\ T^{0.5}\ (1.133x10^5/T)\ \exp(-1.133x10^5/T)$	Ar, O, O_2, NO
		$3.20x10^{12}\ T^{0.5}\ (1.133x10^5/T)^2\ \exp(-1.133x10^5/T)$	N
2	$O_2 + M \leftrightarrow 2O + M$	$5.00x10^{11}\ T^{0.5}\ (5.942x10^4/T)^{1.5}\ \exp(-5.942x10^4/T)$	N_2
		$2.25x10^{12}\ T^{0.5}\ (5.942x10^4/T)^{1.5}\ \exp(-5.942x10^4/T)$	O_2
		$2.50x10^{11}\ T^{0.5}\ (5.942x10^4/T)^{1.5}\ \exp(-5.942x10^4/T)$	Ar, N, NO
		$6.25x10^{12}\ T^{0.5}\ (5.942x10^4/T)^{1.5}\ \exp(-5.942x10^4/T)$	O
3	$NO + M \leftrightarrow N + O + M$	$7.00x10^{10}\ T^{0.5}\ (7.553x10^4/T)^2\ \exp(-7.553x10^4/T)$	Ar, O_2, N_2
		$1.40x10^{12}\ T^{0.5}\ (7.553x10^4/T)^2\ \exp(-7.553x10^4/T)$	NO, O, N
4	$N_2 + O \leftrightarrow NO + N$	$7.00x10^{13}\ \exp(-3.802x10^4/T)$	-
5	$NO + O \leftrightarrow O_2 + N$	$3.20x10^9\ T\ \exp(-1.969x10^4/T)$	-
6	$N_2 + O_2 \leftrightarrow 2NO$	$9.10x10^{24}\ T^{-2.5}\ \exp(-6.471x10^4/T)$	-
7	$N + O \leftrightarrow NO^+ + e$	$6.4x10^9\ T^{0.5}\ \exp(-3.187x10^4/RT)$	-

Appendix C: Chemical Reactions and Rate Coefficients given by Park:

No	Reaction	Forward Rate Coefficient, K_f $cm^3\ mole^{-1}\ sec^{-1}$	Catalyst, M
1	$N_2 + M \leftrightarrow 2N + M$	$3.70x10^{21}\ T^{-1.6}\ \exp(1.132x10^5/T)$	N_2, O_2, NO
		$1.11x10^{22}\ T^{-1.6}\ \exp(1.132x10^5/T)$	N, O
2	$O_2 + M \leftrightarrow 2O + M$	$2.75x10^{19}\ T^{-1.0}\ \exp(5.95x10^4/T)$	N_2, O_2
		$8.25x10^{19}\ T^{-1.0}\ \exp(5.95x10^4/T)$	N, O
3	$NO + M \leftrightarrow N + O + M$	$2.30x10^{17}\ T^{-0.5}\ \exp(7.55x10^4/T)$	N_2, O_2, NO
		$4.60x10^{17}\ T^{-0.5}\ \exp(7.55x10^4/T)$	N, O
4	$O + N_2 \leftrightarrow N + NO$	$3.18x10^{13}\ T^{0.1}\ \exp(3.77x10^4/T)$	-
5	$NO + O \leftrightarrow N + O_2$	$2.16x10^{8}\ T^{1.29}\ \exp(1.92x10^4/T)$	-

No	Reaction	Equilibrium Constant Coefficient , A(i,j)				
		i=1	i=2	i=3	i=4	i=5
1	$N_2 + M \leftrightarrow 2N + M$	3.898	-12.611	0.683	-0.118	0.006
2	$O_2 + M \leftrightarrow 2O + M$	1.335	-4.127	-0.616	0.093	-0.005
3	$NO + M \leftrightarrow N + O + M$	1.549	-7.784	0.228	-0.043	0.002
4	$O + N_2 \leftrightarrow N + NO$	2.349	-4.828	0.455	-0.075	0.004
5	$NO + O \leftrightarrow N + O_2$	0.215	-3.657	0.843	-0.136	0.007

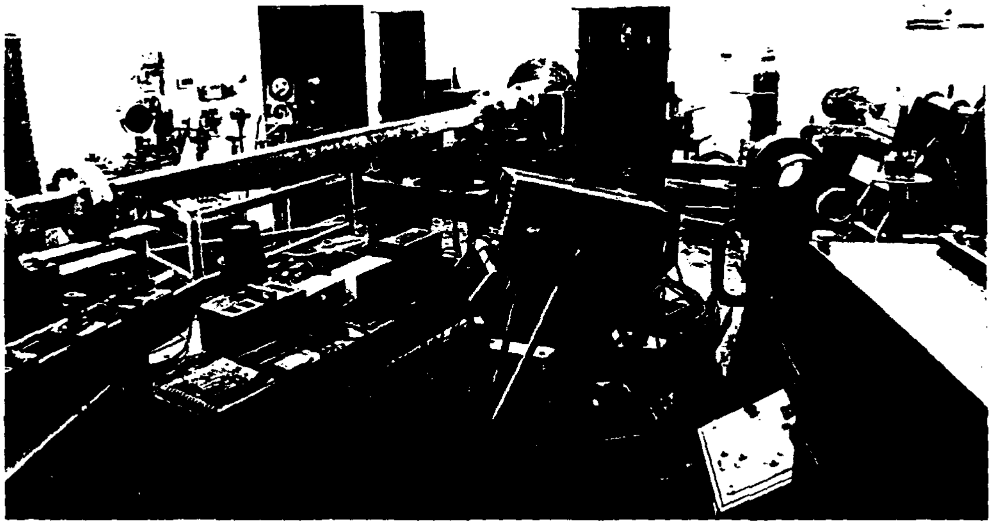

Fig. 1.1 : Shock-tube facility at Goldstein Laboratory.

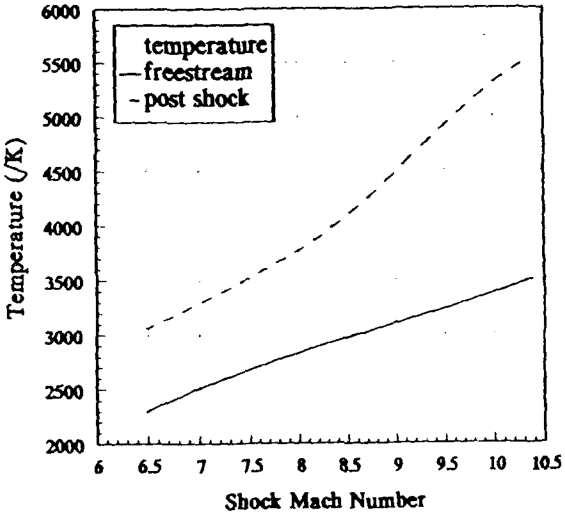

Fig. 1.2 : Attainable Temperatures in a He-Air Shock-tube.

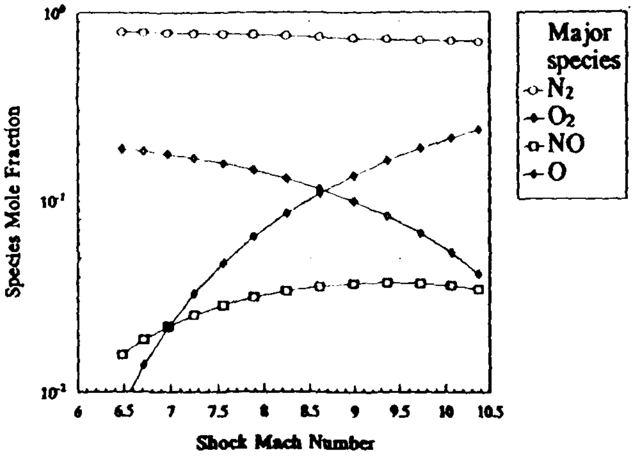

Fig. 1.3 : Variation of Species Mole Fractions with Shock Mach Number.

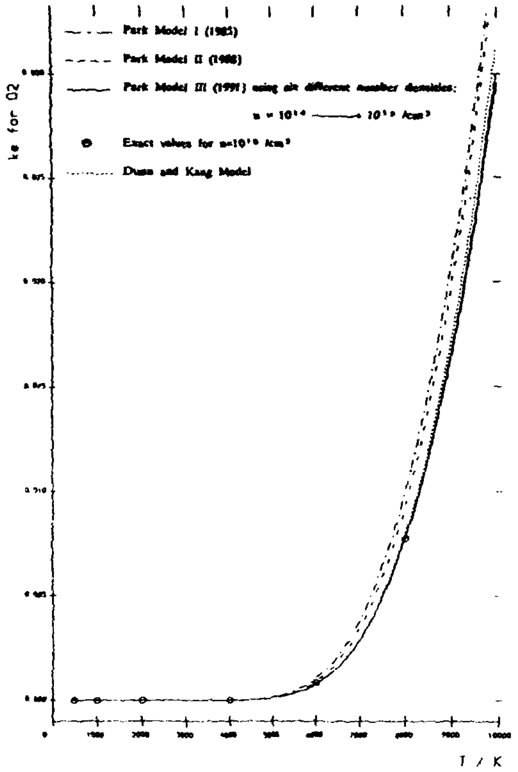

Figure 1.4 : Variation of oxygen equilibrium constant with temperature.

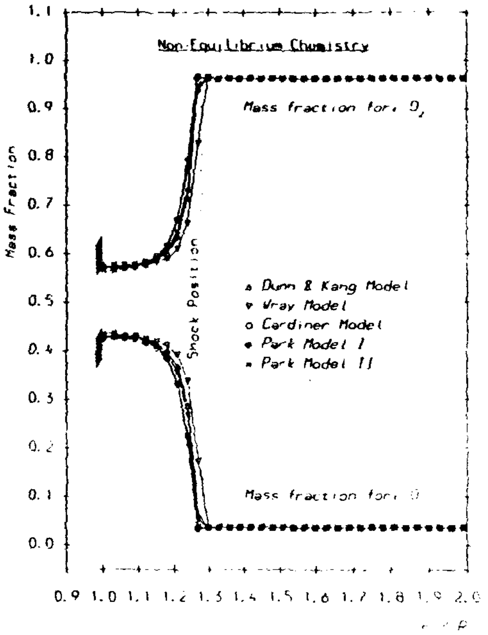

(U=4000. m/s, T=2577.6 K, TVD MacCormack)

Fig. 2.3 : Mass Fraction Profiles Along Stagnation Streamline for Circular Cylinder.

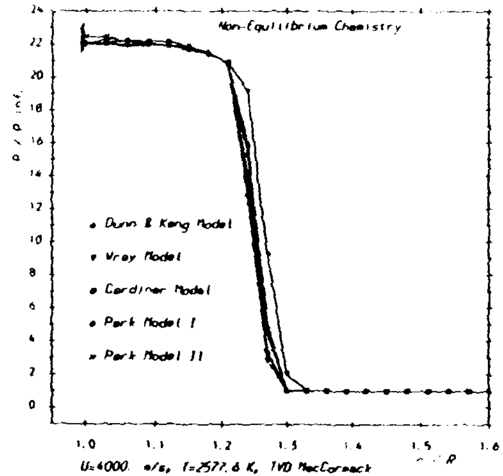

U=4000. m/s, T=2577.6 K, TVD MacCormack

Fig. 2.1 : Pressure distribution Along the Stagnation Streamline.

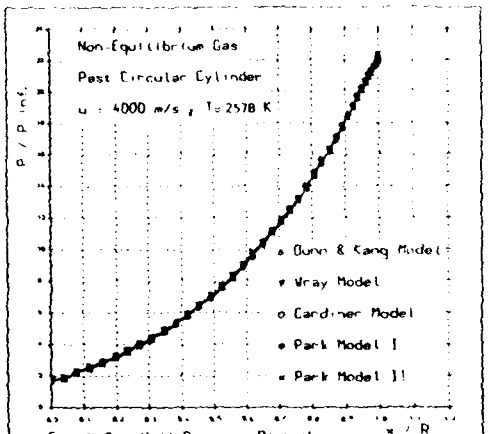

Fig. 2.4 : Wall Pressure Distribution. x / R

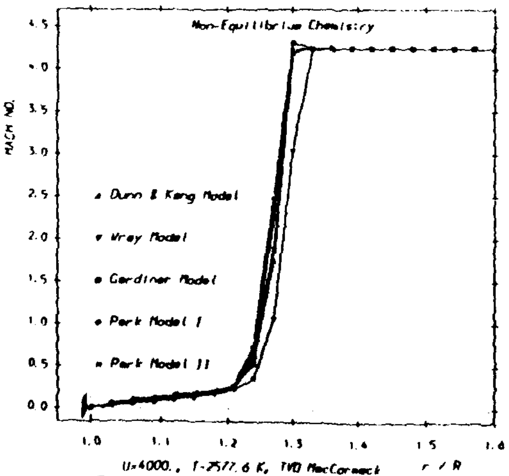

U=4000., T=2577.6 K, TVD MacCormack

Fig. 2.2 : Mach No. distribution Along the Stagnation Streamline.

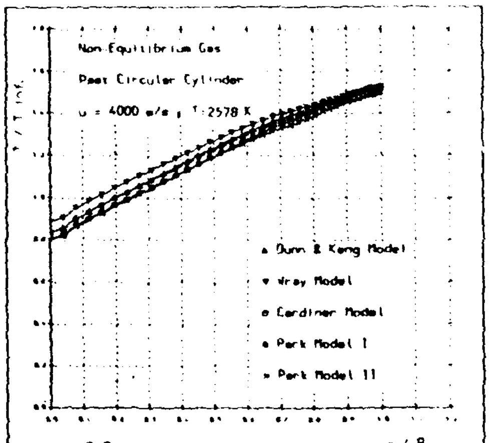

Fig. 2.5 : Wall Temperature Distribution. x / R

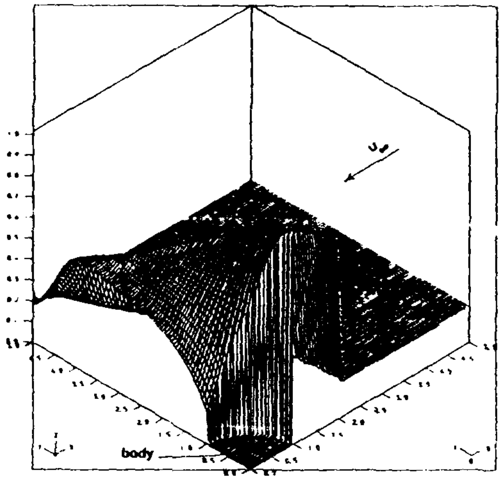

Figure 3.1 : Pressure Heights
U = 2075.0 m/s

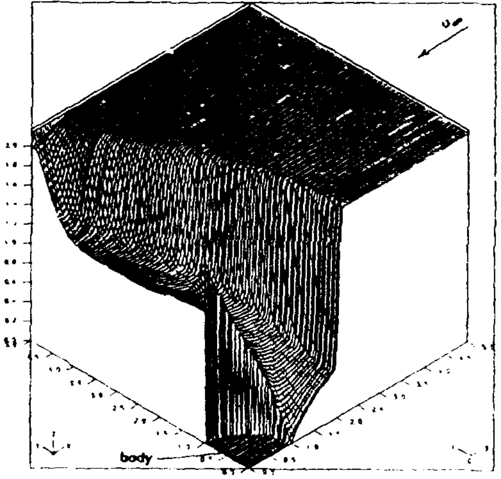

Figure 3.2 : Mach No. Heights
U = 2075.0 m/s

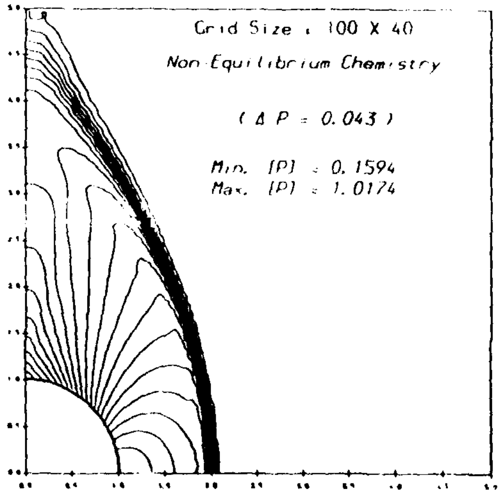

Figure 3.3 : Contours of Complete Pressure
U=2075.0 m/s , T = 2497. K

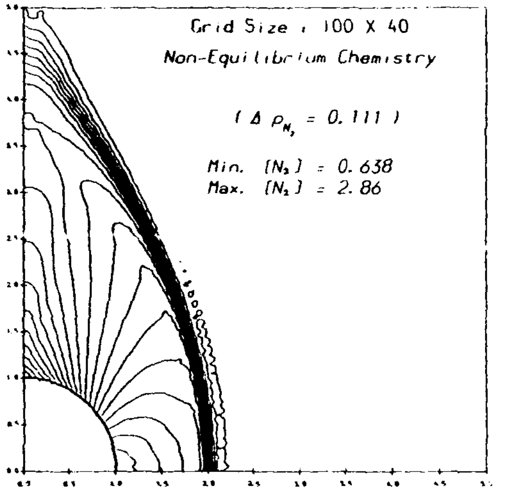

Figure 3.4 : Contours of Partial Density for N_2
U=2075.0 m/s , T = 2497 K

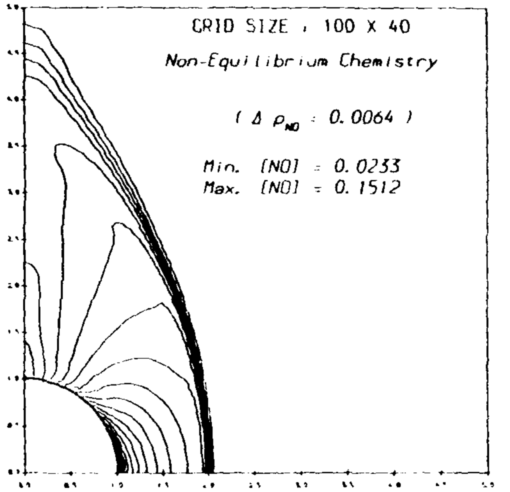

Figure 3.5 : Contours of Partial Density for NO
U=2075.0 m/s , T = 2497. K

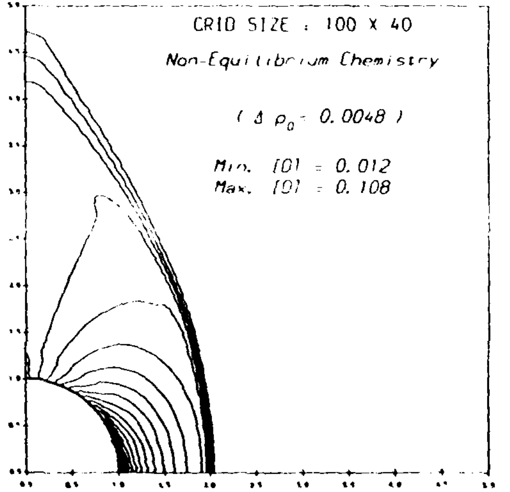

Figure 3.6 : Contours of Density for O Atoms
U=2075.0 m/s , T = 2497.0 K

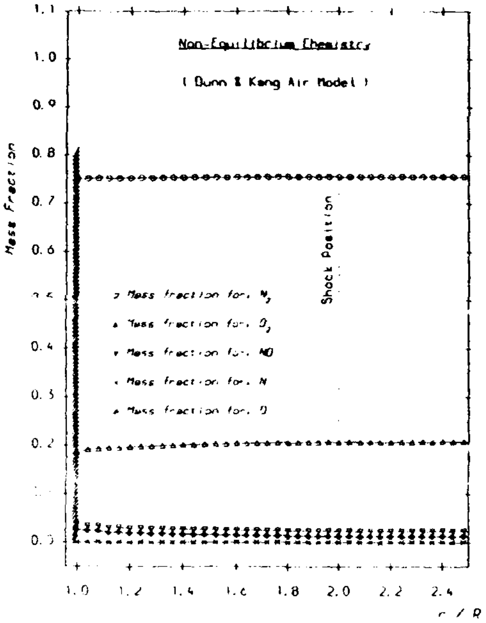

(U=2075.0 m/s, T=2497. K, TVD MacCormack)

Fig. **3.7** Mass Fraction Profiles Along Stagnation Streamline for Circular Cylinder.

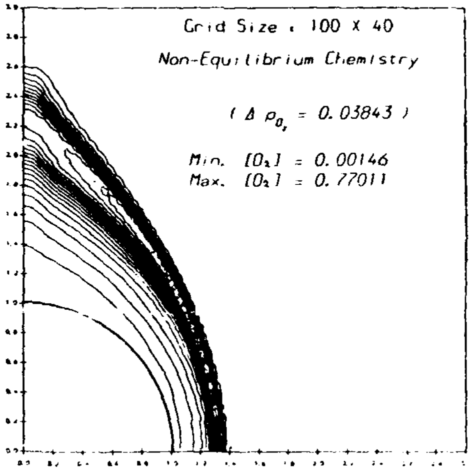

Figure **3.10**: Contours of Partial Density for O_2
U=4000.0 m/s , T = 2497. K

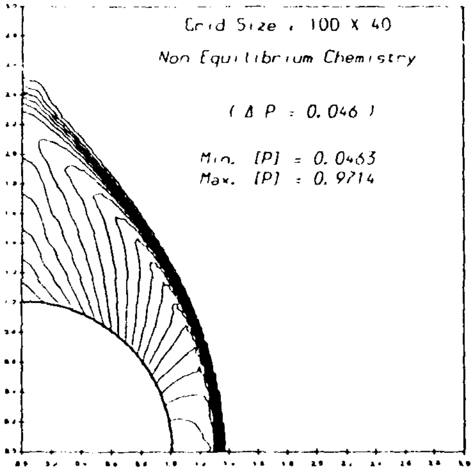

Figure **3.8** : Contours of Complete Pressure
U=4000.0 m/s , T = 2497. K

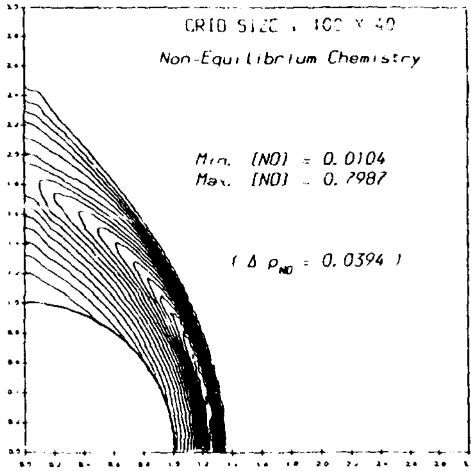

Figure **3.11**: Contours of Partial Density for NO
U=4000.0 m/s , T = 2497. K

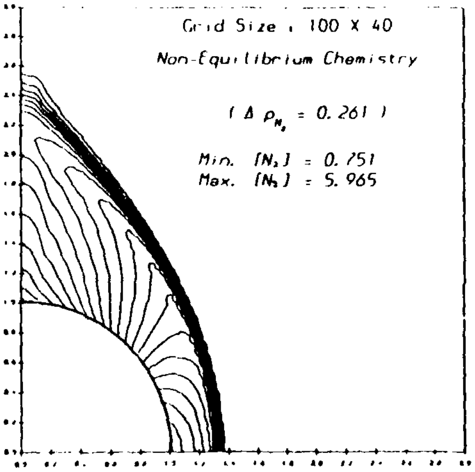

Figure **3.9** : Contours of Partial Density for N_2
U 4000.0 m/s , T = 2497 K

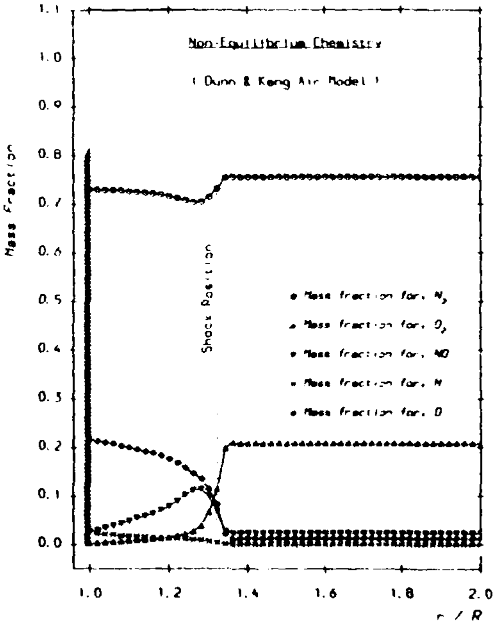

(U=4000.0 m/s, T=2497. K, TVD MacCormack)

Fig. **3.12** Mass Fraction Profiles Along Stagnation Streamline for Circular Cylinder.

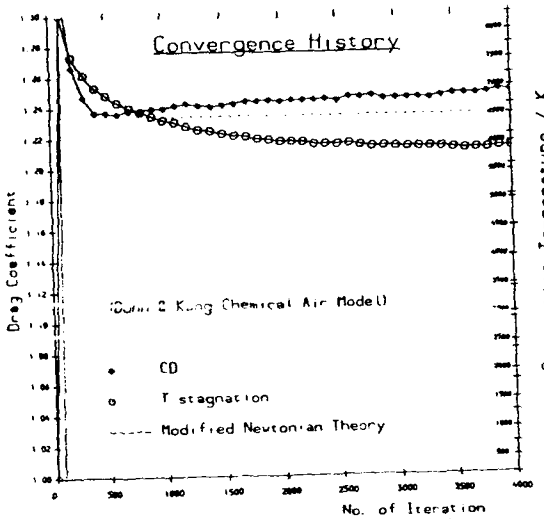

Fig. **4.1** : Convergence History.

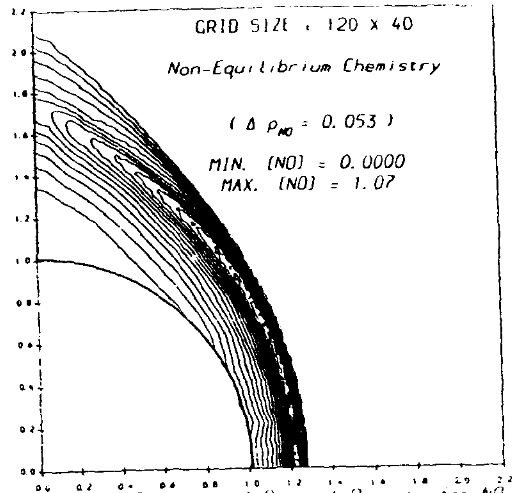

Figure **4.4** : Contours of Partial Density for NO
U=5152.6 m/s ; T = 205.3 K

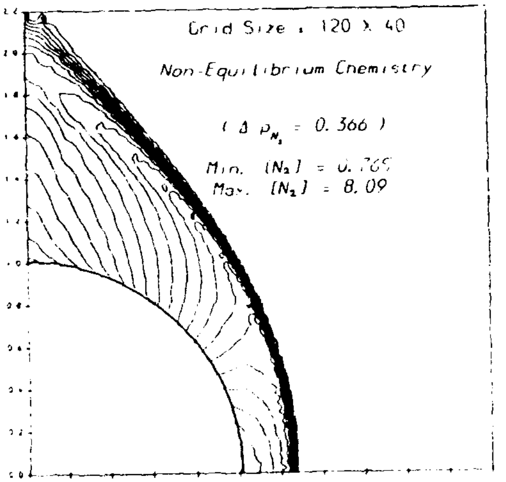

Figure **4.2** : Contours of Partial Density for N_2
U=5152.6 m/s ; T = 205.3

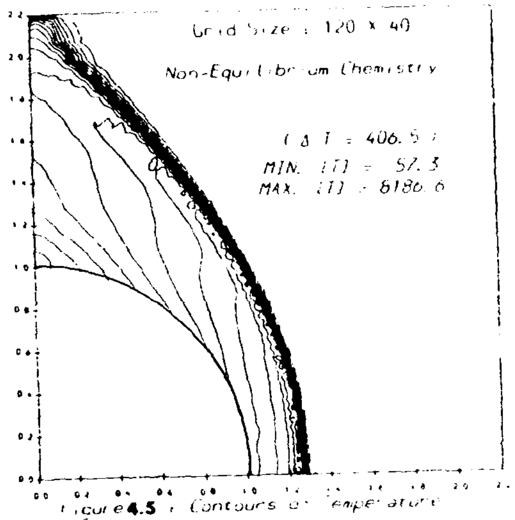

Figure **4.5** : Contours of Temperature

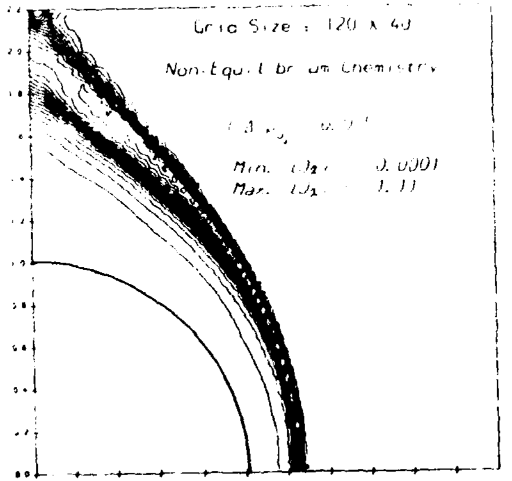

Figure **4.3** : Contours of Partial Density for O_2
U=5152.6 m/s ; T = 205.3 K

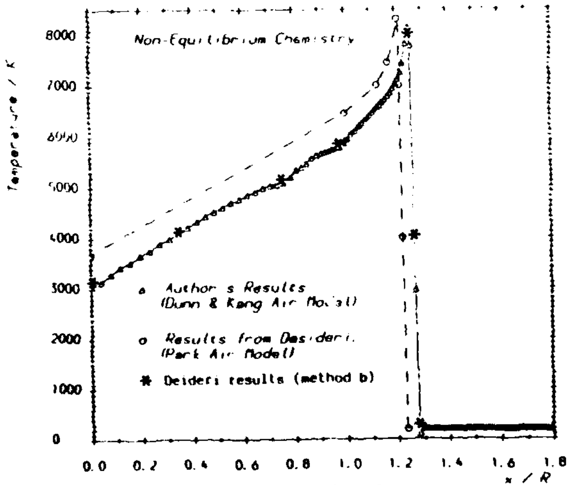

U=5152.6 m/s, T=205.3 K, TVD MacCormack
Figure **4.6** : Temperature Distribution Along the Stagnation Line and Around the Body

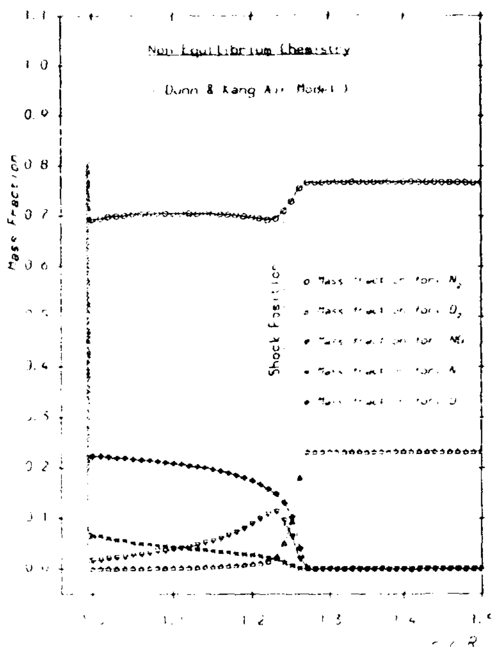

([illegible] m/s, T=205.3 K, [illegible])
Fig. **4.7**: Mass Fraction Profiles Along Stagnation Streamline for Circular Cylinder

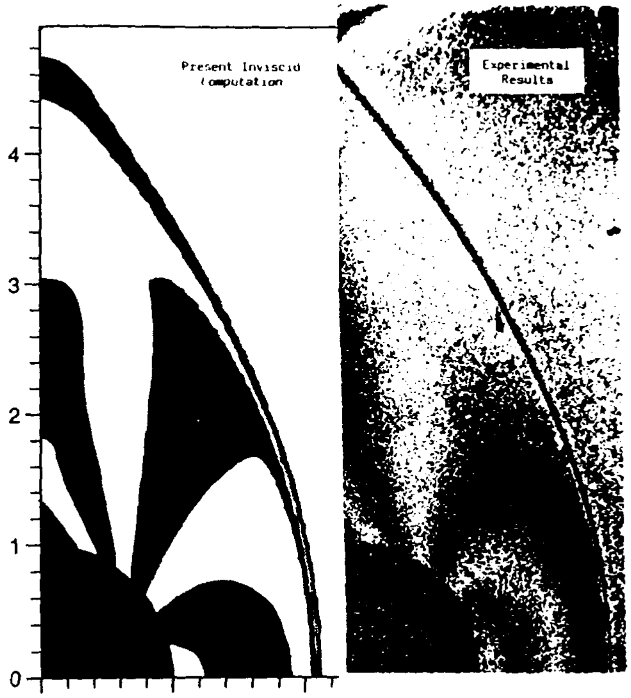
Present Inviscid Computation
Experimental Results
4
3
2
1
0

Fig. 5.1 : Interferograms of Flow Over a Circular Cylinder (r=5.56mm) Tested in a Shock-tube.

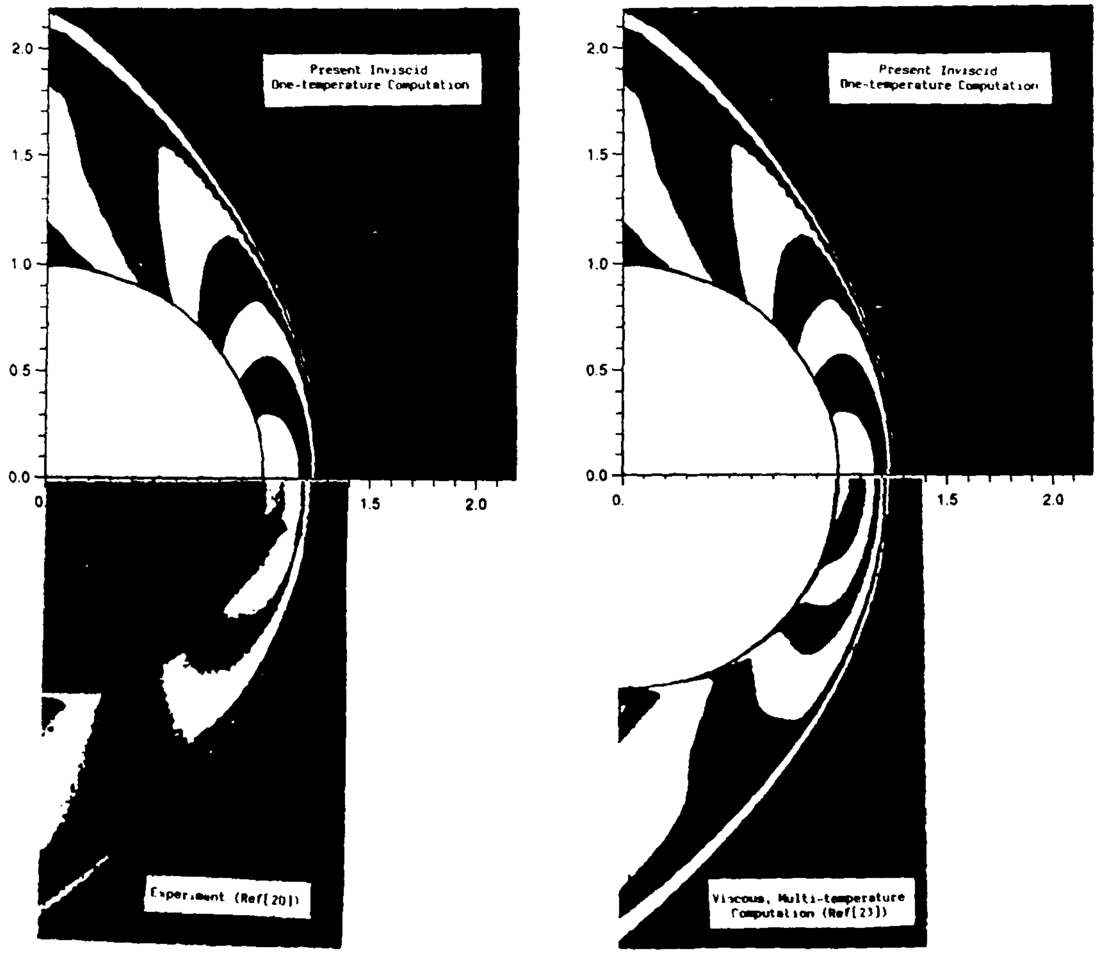
Present Inviscid One-temperature Computation
Present Inviscid One-temperature Computation
Experiment (Ref[20])
Viscous, Multi-temperature Computation (Ref[23])
2.0
1.5
1.0
0.5
0.0
0.
1.5
2.0

Fig. 5.2 : Interferograms of Flow Over a Circular Cylinder (r=25.4mm) Tested in a Shock-Tunnel.

THERMODYNAMIC MODEL OF AIR IN CHEMICAL EQUILIBRIUM

D. Giordano
L. Marraffa
ESA/ESTEC
Propulsion and Aerothermodynamics Division
Aerothermodynamics Section
2200 AG Noordwijk, The Netherlands

1 SUMMARY

A thermodynamic model of air in chemical equilibrium is described. The model includes 13 chemical components, namely $N, O, Ar, e^-, NO, N_2, O_2, N^+, O^+, Ar^+, NO^+, N_2^+, O_2^+$, and is treated as a mixture of perfect gases.

The constant pressure specific heats of the components constitute the basic information to be provided and they are assumed to be specified in the form of interpolating polynomials valid in assigned subranges of a given temperature range; the polynomial expressions have been structured to preserve generality and flexibility with respect to temperature range subdivisions and polynomial coefficient data published by various sources.

The set of the chemical reactions includes 47 reactions, of which only 9 are independent. The equilibrium composition is solved, in terms either of mass fractions or molar fractions, according to *the method* of the equilibrium constants and numerically computed by an iterative scheme which proves fast and accurate.

A FORTRAN program has been written to perform the numerical calculations of the thermodynamic properties and of the equilibrium composition.

Temperature range subdivisions and polynomial coefficient data can be implemented at will. Presently, the program includes data from 3 US sources and 1 Soviet source. *Discrepancies in the constant pressure specific* heats of the components deriving from the choice of different data sources are put in evidence.

The process to validate the program is described and validation evidence is given in the relevant diagrams.

2 CONVENTIONS

The following summation convention is adopted:

- the presence of two or more latin subscripts implies summation

$$\frac{a_i}{b_i}(c_i d_i + e_i) =$$
$$\frac{a_1}{b_1}(c_1 d_1 + e_1) + \frac{a_2}{b_2}(c_2 d_2 + e_2) + \cdots$$

- the presence of one latin subscript or any number of greek subscripts implies no summation

$$a_\epsilon b_\nu(c_\nu + d_j) =$$
$$a_1 b_2(c_2 + d_3) \text{ or } a_3 b_4(c_4 + d_1) \text{ or } \cdots$$

The summation symbol is explicitly indicated when it is not possible to use the above convention.

Superscripts never imply summation but label the symbols for identification purposes.

3 LIST OF SYMBOLS

3.1 Remarks

The mixture enthalpy, entropy, internal energy, Helmholtz potential, Gibbs potential, specific heats are intended per unit total mass of the mixture.

The component enthalpy, formation enthalpy, entropy and its T-dependent part, chemical potential and its T-dependent part, constant pressure specific heat are intended per unit mass of that component.

Running subscripts start from 1; the second column in their list indicates the upper values they can reach.

3.2 Symbols without running subscripts

$a_{L,e}$	equilibrium Laplace characteristic velocity
$a_{L,f}$	frozen Laplace characteristic velocity
$a_{N,e}$	equilibrium Newton characteristic velocity
$a_{N,f}$	frozen Newton characteristic velocity
$c_{p,e}$	equilibrium constant pressure specific heat
$c_{p,f}$	frozen constant pressure specific heat
$c_{v,e}$	equilibrium constant volume specific heat
$c_{v,f}$	frozen constant volume specific heat
f	mixture Helmholtz potential
g	mixture Gibbs potential
h	mixture enthalpy
h'	reference level of h
h''	calculable part of h
$\mathcal{M}$	mixture average molar mass
m_t	total mass
N_t	total mole number
n_{max}	number of A coefficients
p	pressure
p_0	reference pressure
R_G	universal gas constant, 8.31441 $J/mole\,°K$
s	mixture entropy
T	temperature
T_0,T_0'	reference temperatures
u	mixture internal energy
v	specific volume
γ_e	equilibrium specific heat ratio
γ_f	frozen specific heat ratio
θ_{max}	number of temperature subranges
ϑ	dummy integration variable
ν	stoichiometric coefficient matrix
ν^*	stoichiometric coefficient matrix (indep. reac.)
σ	formation matrix
τ	dummy integration variable

3.3 Symbols with running subscripts

A, B	polynomial coefficients
$\mathcal{A}$	chemical affinity
c_p,	component constant pressure specific heat
h	component enthalpy
$(\Delta h)_{T_0}^{f,\circ}$	formation enthalpy at T_0

$\overline{(\Delta h)}^{f,e}_{T_o,T_o'}$	augmented formation enthalpy at T_o, T_o'
$\mathcal{H}^e$	stable element molar enthalpy
K^p	equilibrium constant, partial pressures
K^x	equilibrium constant, molar fractions
K^α	equilibrium constant, mass fractions
M	component molar mass
M^a	atomic species molar mass
N^a	atomic species mole number
p	partial pressure
R	component gas constant
s	component entropy
$\breve{s}$	T-dependent part of s
$\mathcal{T}$	subrange low-bounding temperature
x	component molar fraction
α	component mass fraction
α^a	atomic species mass fraction
λ	stable element stoichiometric coefficient
μ	chemical potential
μ^o	T-dependent part of μ
ν	stoichiometric coefficient
$\Delta\nu$	mole number variation across a reaction
ν^*	stoichiometric coefficient, indep. reac.
ξ^T, ξ^v	equilibrium derivatives
σ	formation coefficient

3.4 Running subscripts

j, φ	4	atomic species
i, k, ϵ	13	components
r, ρ	47	chemical reactions
l	9	independent chemical reactions
n	n_{max}	polynomial coefficients
θ	θ_{max}	temperature subranges

4 STOICHIOMETRY

The air model includes the 13 components listed at the beginning of sec. 1. Consistently, there are 4 atomic species to be taken in account and they are listed in table 1. The formation matrix σ (13×4) corresponding to that combination of atomic species and components is shown, between the double lines, in table 2.

The set of the chemical reactions is shown in table 3 and was generated by processing σ according to the method exposed in [1]. It corresponds to the criterium of excluding the reactions involving more than 2 bodies, exception made for the 3-body reactions which describe the ionization of the neutral components (reac. 4,5,6,12,28,34) and the dissociation of the diatomic components (reac. 1,2,3,41,42,46,47). If this criterium is relaxed and any 3-body reaction is admitted to have non negligible probability of occurrence then the number of the chemical reactions jumps to the order of 100. However, this argument acquires importance when dealing with nonequilibrium circumstances and becomes irrelevant in a chemical equilibrium context, where it suffices to know only the independent chemical reactions. In the present case, there are $13 - 4 = 9$ independent chemical reactions and the mark $\star$ in table 3 indicates those which are conferred such a role. The symbol X stands for any possible catalyst.

The stoichiometric coefficient matrix ν (47×13) corresponding to the set of the chemical reactions is shown in table 4. The rows relative to the independent chemical reactions are extracted to compose the matrix ν^* (9×13), shown in table 5.

The product of ν and σ gives identically the null matrix

$$\nu_{ri}\sigma_{ij} = 0 \tag{1}$$

The conditions (1) with $j = 1, 2, 3$ ensure the mass conservation across the generic reaction; with $j = 4$ they ensure the conservation of the electric charge.

5 FUNDAMENTAL RELATION

The thermodynamic description [2, 3] is accomplished in terms of the fundamental relation $h(s, p, \alpha_1, \ldots, \alpha_{13})$ which, for the case of a mixture of perfect gases, assumes the parametric form

$$h = \alpha_i h_i \tag{2}$$

$$s = \alpha_i s_i \tag{3}$$

with

$$h_\epsilon = h_\epsilon(T_o) + \int_{T_o}^{T} c_{p,\epsilon}(\tau)d\tau \tag{4}$$

$$s_\epsilon = s_\epsilon(T_o, p_o) + \int_{T_o}^{T} \frac{1}{\tau} c_{p,\epsilon}(\tau)d\tau - R_\epsilon \ln \frac{p}{p_o} - R_\epsilon \ln \frac{\mathcal{M}\alpha_\epsilon}{M_\epsilon} \tag{5}$$

The average molar mass of the mixture is defined in terms of the α_k as

$$\mathcal{M} = \left(\frac{\alpha_k}{M_k}\right)^{-1}$$

The last term in the right hand side of (5) represents the part of s_ϵ due to mixing; the argument of the logarithm coincides with x_ϵ, i.e.

$$x_\epsilon = \frac{\mathcal{M}\alpha_\epsilon}{M_\epsilon}$$

The functions $c_{p,\epsilon}(T)$ are supposed to be assigned.

The terms $h_\epsilon(T_o)$ cannot be calculated[1]; they must, therefore, be adapted to allow appearance of the formation enthalpies.

The terms $s_\epsilon(T_o, p_o)$ are not affected by any indeterminateness and are available in tabulated form.

5.1 Constant pressure specific heats of the components

Various publications [4, 5, 6, 7, 8, 9, 10, 11, 12, 13] are available in the literature which provide interpolating polynomials for the $c_{p,\epsilon}$ in assigned subranges of a given temperature range relatively to air components. Some references among those cited do not consider all the components included in the model; therefore, when these references are chosen as data source, some of the components listed in table 2 must be excluded. Accordingly, the corresponding reactions must be excluded from the set in table 3. The polynomials are obtained by curve fitting data listed in tables of thermodynamic properties of individual substances [4, 5, 14, 15, 16].

---

[1] This statement is the standard declaration encountered in the literature. It is the authors' opinion that it may require a careful rethinking. However, we conform to the standard view here and refrain to go deeply into the matter because a discussion about this argument is irrelevant in the context of the present paper for the reasons explained in what follows.

A general expression for the interpolating polynomial of $c_{p,\epsilon}$ consistent with T falling in the θ-th subrange, i.e. $T \in [T_\theta, T_{\theta+1}]$, can be assumed as

$$c_{p,\epsilon} = A_{\epsilon n\theta} T^{n-1} + \frac{B_{\epsilon\theta}}{T^2} \tag{6}$$

All the expressions proposed in the cited references are embedded in the form (6). The summation on n runs from 1 up to a maximum n_{max} which varies according to the author who operates the curve fitting. Readers are referred to [4, 5, 6, 7, 8, 9, 10, 11, 12, 13] for information concerning list of components, temperature range, subrange allocation, A, B coefficients[2] and n_{max}.

With (6) in hand, integrals involving the $c_{p,\epsilon}$ can be performed analytically and readily evaluated.

5.2 Formation enthalpies

There is an arbitrariness in the choice of the reference elements from which a given component is intended to be formed; for example, NO can be thought formed either from the atomic species

$$N + O \rightarrow NO$$

or from the stable elements associated to the atomic species

$$\frac{1}{2}N_2 + \frac{1}{2}O_2 \rightarrow NO$$

Generally, preference is assigned to the stable elements and, therefore, the corresponding formation enthalpies are used in numerical calculations[3].

If the components are meant formed from the stable elements then the corresponding formation enthalpies come in play via the following expressions

$$h_\epsilon(T_\circ) = (\Delta h_\epsilon)^{f,e}_{T_\circ} + \frac{\sigma_{\epsilon j}}{M_\epsilon \lambda_j}\mathcal{H}^e_j(T_\circ) \tag{7}$$

The stoichiometric coefficients λ_j for the *stable elements* associated to the atomic species of the model are shown in table 1.

Values of $M_\epsilon(\Delta h_\epsilon)^{f,e}$ for various substances can be found either tabulated [4, 16] or specified [5, 6, 7, 8, 9, 10, 13, 14, 15] at a given temperature, usually 0 °K or 298.15 °K.

The terms $\mathcal{H}^e_j(T_\circ)$ follow the same fate of the terms $h_\epsilon(T_\circ)$, i.e. they cannot be calculated (see footnote 1).

In (7) it is not convenient to have the $\mathcal{H}^e_j$ evaluated at the same temperature which appears in the left hand side; the reason for that will appear evident in sec. 5.3.2. The inconvenience is avoided by introducing a second arbitrary reference temperature $T'_\circ$ and rearranging (7) to read

$$h_\epsilon(T_\circ) = (\Delta h_\epsilon)^{f,e}_{T_\circ} + \frac{\sigma_{\epsilon j}}{M_\epsilon \lambda_j}\left[\mathcal{H}^e_j(T_\circ) - \mathcal{H}^e_j(T'_\circ)\right] + \frac{\sigma_{\epsilon j}}{M_\epsilon \lambda_j}\mathcal{H}^e_j(T'_\circ) \tag{8}$$

Differences like those in square brackets can be read from the tables and, therefore, the sum of the first two terms in the right hand side of (8) can be calculated without problems. Defining, for short, an augmented formation enthalpy as

$$\overline{(\Delta h_\epsilon)}^{f,e}_{T_\circ,T'_\circ} = (\Delta h_\epsilon)^{f,e}_{T_\circ} + \frac{\sigma_{\epsilon j}}{M_\epsilon \lambda_j}\left[\mathcal{H}^e_j(T_\circ) - \mathcal{H}^e_j(T'_\circ)\right]$$

the (8) can be written in the final form

$$h_\epsilon(T_\circ) = \overline{(\Delta h_\epsilon)}^{f,e}_{T_\circ,T'_\circ} + \frac{\sigma_{\epsilon j}}{M_\epsilon \lambda_j}\mathcal{H}^e_j(T'_\circ) \tag{9}$$

5.3 Adaptation of the expression for h

The substitution of (9) into (4) and of the resulting expression into (2) leads to the following

$$h = \underbrace{\frac{\alpha^a_j \mathcal{H}^e_j(T'_\circ)}{M^a_j \lambda_j}}_{h'} + \underbrace{Y_\iota\left[\overline{(\Delta h_\iota)}^{f,e}_{T_\circ,T'_\circ} + \int_{T_\circ}^{T} c_{p,\iota}(\tau)d\tau\right]}_{h''} \tag{10}$$

In (10) use has been made of the definition

$$\alpha^a_\varphi = \frac{\alpha_\iota \sigma_{\iota\varphi}}{M_\iota} M^a_\varphi$$

There are two main issues to discuss concerning respectively the contributions h' and h'' in (10). The former relates to the reference level of h; the latter to the choice of $T_\circ$.

5.3.1 *Enthalpy reference level*

Whatever $T'_\circ$ may be, the terms $\mathcal{H}^e_j(T'_\circ)$ cannot be calculated and, consequently, the same applies to h'; instead, the calculation of $h'' = h - h'$ does not present any restriction whatsoever. The lack of information about h' becomes irrelevant in the following circumstances:

1. in conditions of chemical equilibrium,
2. in conditions of chemical nonequilibrium when effects of mass diffusion are absent or, better, negligible.

In fact, under those circumstances the α^a_j remain constant and, therefore, such is also h', though it is unknown; consequently, the variations of h and h'' coincide and the term h' can be assumed to play the role of reference level.

When the conditions of chemical nonequilibrium with non negligible effects of mass diffusion prevail, the α^a_j vary and h' is not constant anymore. The (10) is still valid but loses the capability to assess the variations of h. The implications deriving from the presence of a variable

---

[2] The polynomial coefficients given in the cited references might require some minor adaptation and conversion of units before being used in (6). In [5], interpolating expressions are given Gibbs energy $\Phi^\circ(T)$ in the

5.3.2 Choice of $T_\circ$

The reference temperature $T_\circ$ appears only in the quantity between square brackets in (10); this fact implies the invariance of that quantity with respect to $T_\circ$ and explains the reason of the adaptation of (7) to (9). Given the arbitrariness of $T_\circ$ and consistently with the viewpoint[4] that interpolating polynomials for the $c_{p,\epsilon}$ are assigned over the temperature subranges, when T falls in the θ-th subrange it is possible to set $T_\circ = T_\theta$ so that (10) becomes

$$h = \frac{\alpha_j^a \mathcal{H}_j^c(T_\circ')}{M_j^a \lambda_j} + \alpha_i \left[\overline{(\Delta h_i)}^{f,e}_{T_\theta,T_\circ'} + \int_{T_\theta}^{T} c_{p,i}(\tau) d\tau \right] \quad (11)$$

In (11) the invariance of the quantity between square brackets with respect to T_θ implies the independence of the same quantity from the particular subrange allocation in use, i.e. from the chosen data source.

5.3.3 Operative expression of h

Keeping in mind the discussion of sec. 5.3.1 and adhering to the choice made in sec. 5.3.2, the contribution

$$h'' = \alpha_i \left[\overline{(\Delta h_i)}^{f,e}_{T_\theta,T_\circ'} + \int_{T_\theta}^{T} c_{p,i}(\tau) d\tau \right] \quad (12)$$

from (11) is taken as the operative expression of h used to perform the numerical calculations for the model. It applies when T belongs to the θ-th subrange and returns values of the mixture enthalpy with respect to the reference level

$$h' = \frac{\alpha_j^a \mathcal{H}_j^c(T_\circ')}{M_j^a \lambda_j} \quad (13)$$

The reference temperature $T_\circ'$ can still be arbitrarily chosen.

When tabulated values of $M_\epsilon (\Delta h_\epsilon)^{f,e}_{\dots}$ are available, the augmented formation enthalpies in (12) are evaluated from their definition

$$\overline{(\Delta h_\epsilon)}^{f,e}_{T_\theta,T_\circ'} = (\Delta h_\epsilon)^{f,e}_{T_\theta} + \frac{\sigma_{\epsilon j}}{M_\epsilon \lambda_j} \left[\mathcal{H}_j^e(T_\theta) - \mathcal{H}_j^e(T_\circ') \right]$$

When the $M_\epsilon (\Delta h_\epsilon)^{f,e}_{\dots}$ are specified only at a given temperature T_1 one has to calculate first

$$\overline{(\Delta h_\epsilon)}^{f,e}_{T_1,T_\circ'} = (\Delta h_\epsilon)^{f,e}_{T_1} + \frac{\sigma_{\epsilon j}}{M_\epsilon \lambda_j} \left[\mathcal{H}_j^e(T_1) - \mathcal{H}_j^e(T_\circ') \right]$$

and then

$$\overline{(\Delta h_\epsilon)}^{f,e}_{T_\theta,T_\circ'} = \overline{(\Delta h_\epsilon)}^{f,e}_{T_1,T_\circ'} + \left[h_\epsilon(T_\theta) - h_\epsilon(T_1) \right] \quad (14)$$

The difference between square brackets in the right hand side of (14) must be read from the tables.

5.4 Adaptation of the expression for s

In line with the choice made in sec. 5.3.2, when T falls in the θ-th subrange (5) becomes

$$s_\epsilon = s_\epsilon(T_\theta, p_\circ) + \int_{T_\theta}^{T} \frac{1}{\tau} c_{p,\epsilon}(\tau) d\tau - R_\epsilon \ln \frac{p}{p_\circ} - R_\epsilon \ln \frac{\mathcal{M}\alpha_\epsilon}{M_\epsilon} \quad (15)$$

The substitution of (15) into (3) yields

$$s = \alpha_i \left[s_i(T_\theta, p_\circ) + \int_{T_\theta}^{T} \frac{1}{\tau} c_{p,i}(\tau) d\tau - R_i \ln \frac{p}{p_\circ} \right] - R_i \ln \left(\frac{\mathcal{M}\alpha_i}{M_i} \right)^{\alpha_i} \quad (16)$$

The (16) is the operative expression of s used to perform the numerical calculations for the model.

In (16) the mixing part is separated and presented in a form particularly suitable for FORTRAN coding[5].

Values of $M_\epsilon s_\epsilon(T_\theta, p_\circ)$ can be read from the tables. The vast majority of the tables [4, 14, 15, 16] assumes $p_\circ = 1.01325 \cdot 10^5 N/m^2$ but there are also instances [5] which assume $p_\circ = 10^5 N/m^2$.

6 STATE EQUATIONS

The temperature appears as a parameter in (4),(5). The specific volume and the chemical potentials are found from the standard definitions [2, 3] and read

$$\begin{aligned} v &= \frac{T}{p} \alpha_i R_i \\ \mu_\epsilon &= \frac{\sigma_{\epsilon j} \mathcal{H}_j^e(T_\circ')}{M_\epsilon \lambda_j} + \overline{(\Delta h_\epsilon)}^{f,e}_{T_\theta,T_\circ'} - T s_\epsilon(T_\theta, p_\circ) \\ &\quad - \int_{T_\theta}^{T} d\tau \int_{T_\theta}^{\tau} \frac{1}{\vartheta} c_{p,\epsilon}(\vartheta) d\vartheta + R_\epsilon T \ln \frac{p}{p_\circ} \\ &\quad + R_\epsilon T \ln \frac{\mathcal{M}\alpha_\epsilon}{M_\epsilon} \end{aligned} \quad (17)$$

In (17) use has been made of (9); it applies when T belongs to the θ-th subrange.

The μ_ϵ are involved mainly in the calculation of the equilibrium constants and, for that purpose, they are rephrased in the form

$$\mu_\epsilon = \frac{\sigma_{\epsilon j} \mathcal{H}_j^e(T_\circ')}{M_\epsilon \lambda_j} + \mu_\epsilon^\circ(T) + R_\epsilon T \ln \frac{p_\epsilon}{p_\circ} \quad (18)$$

with

$$\begin{aligned} \mu_\epsilon^\circ(T) &= \overline{(\Delta h_\epsilon)}^{f,e}_{T_\theta,T_\circ'} - T s_\epsilon(T_\theta, p_\circ) \\ &\quad - \int_{T_\theta}^{T} d\tau \int_{T_\theta}^{\tau} \frac{1}{\vartheta} c_{p,\epsilon}(\vartheta) d\vartheta \\ p_\epsilon &= p \frac{\mathcal{M}\alpha_\epsilon}{M_\epsilon} \end{aligned}$$

The indeterminateness carried by the μ_ϵ, due to the presence of the terms $\mathcal{H}_j^e(T_\circ')$, disappears when the linear combinations of the chemical affinities are performed; the affinity of a generic reaction is

---

[4] The appropriateness of the choice of $T_\circ$ made here loses its validity when interpolating polynomials are used directly for the integrals appearing in (10). Nevertheless, the concept of augmented formation enthalpy still retains its usefulness.

[5] In fact, the argument of the logarithm tends to 1 when α_ϵ tends to 0 and this can be obtained numerically by replacing the argument with $\left(\mathcal{M}(\alpha_\epsilon + 10^{-50})/M_\epsilon\right)^{\alpha_\epsilon}$. The form $\alpha_\epsilon R_\epsilon \ln(\cdots)$ must be avoided because it cannot be numerically driven to the correct limit.

$$\mathcal{A}_r = \nu_{ri} M_i \mu_i$$

which, after substitution of (18), becomes

$$\mathcal{A}_r = \underbrace{\nu_{ri}\sigma_{ij}\frac{\mathcal{H}_j^c(T_o')}{\lambda_j}}_{0} + \nu_{ri} M_i \left[\mu_i^\circ(T) + R_i T \ln \frac{p_i}{p_o}\right]$$

The contribution containing the terms $\mathcal{H}_j^c(T_o')$ vanishes identically because of the conservation conditions (1) and the affinity is completely determined by the remaining contribution.

7 INTERNAL ENERGY, HELMHOLTZ AND GIBBS POTENTIALS

The mixture internal energy, Helmholtz potential and Gibbs potential are calculated from their relations of definition [2, 3]

$$u = h - pv \tag{19}$$

$$f = h - Ts - pv \tag{20}$$

$$g = h - Ts \tag{21}$$

The (19),(20),(21) return values for u, f, g referred to the level (13) when values from (12) are used for h.

8 EQUILIBRIUM CONSTANTS

Equilibrium constants in terms of partial pressures, mass fractions and molar fractions have been considered for each chemical reaction. They are found respectively from

$$K_\rho^p(T) = p_o^{\Delta\nu_\rho} \exp\left(-\frac{\nu_{\rho i}\mu_i^\circ}{R_i T}\right)$$

$$K_\rho^\alpha(T,v) = K_\rho^p(T)\left(\frac{v}{T}\right)^{\Delta\nu_\rho} \prod\nolimits_\epsilon \left(\frac{1}{R_\epsilon}\right)^{\nu_{\rho\epsilon}}$$

$$K_\rho^x(T,p) = K_\rho^p(T)\left(\frac{1}{p}\right)^{\Delta\nu_\rho}$$

with

$$\Delta\nu_\rho = \sum\nolimits_\epsilon \nu_{\rho\epsilon}$$

9 EQUILIBRIUM COMPOSITION

The equilibrium composition is solved according to the method of the equilibrium constants with the imposition of the atomic species conservation [1].

Allowance is made for the two situations corresponding to the assignment of either T, v or T, p.

9.1 Assignment of T, v

In this case the equilibrium composition is solved directly in terms of the α_i. The equilibrium equations relative to the 9 independent chemical reactions, marked with ⋆ in table 3, read

$$\alpha_1^2/\alpha_6 = K_2^\alpha(T,v) \tag{22}$$
$$\alpha_2^2/\alpha_7 = K_3^\alpha(T,v) \tag{23}$$
$$\alpha_8\alpha_4/\alpha_1 = K_4^\alpha(T,v) \tag{24}$$
$$\alpha_9\alpha_4/\alpha_2 = K_5^\alpha(T,v) \tag{25}$$
$$\alpha_{10}\alpha_4/\alpha_3 = K_6^\alpha(T,v) \tag{26}$$
$$\alpha_{11}\alpha_4/\alpha_5 = K_{12}^\alpha(T,v) \tag{27}$$
$$\alpha_5^2/\alpha_6\alpha_7 = K_{24}^\alpha(T) \tag{28}$$
$$\alpha_{12}\alpha_4/\alpha_6 = K_{28}^\alpha(T,v) \tag{29}$$
$$\alpha_{13}\alpha_4/\alpha_7 = K_{34}^\alpha(T,v) \tag{30}$$

The conservation equations relative to the 4 atomic species read[6]

$$\frac{\alpha_1^a}{M_1^a} = \frac{\alpha_1}{M_1} + \frac{\alpha_5}{M_5} + 2\frac{\alpha_6}{M_6} + \frac{\alpha_8}{M_8} + \frac{\alpha_{11}}{M_{11}} + 2\frac{\alpha_{12}}{M_{12}} \tag{31}$$
$$\frac{\alpha_2^a}{M_2^a} = \frac{\alpha_2}{M_2} + \frac{\alpha_5}{M_5} + 2\frac{\alpha_7}{M_7} + \frac{\alpha_9}{M_9} + \frac{\alpha_{11}}{M_{11}} + 2\frac{\alpha_{13}}{M_{13}} \tag{32}$$
$$\frac{\alpha_3^a}{M_3^a} = \frac{\alpha_3}{M_3} + \frac{\alpha_{10}}{M_{10}} \tag{33}$$
$$\frac{\alpha_4^a}{M_4^a} = \frac{\alpha_4}{M_4} - \frac{\alpha_8}{M_8} - \frac{\alpha_9}{M_9} - \frac{\alpha_{10}}{M_{10}} - \frac{\alpha_{11}}{M_{11}} - \frac{\alpha_{12}}{M_{12}} - \frac{\alpha_{13}}{M_{13}} \tag{34}$$

The α_j^a must be considered assigned.

The numerical method to solve the non linear system (22),…,(34) is based on the following idea: the unknowns $\alpha_1, \alpha_2, \alpha_5, \alpha_8, \ldots, \alpha_{13}$ are eliminated from (31),…,(34) by expressing them in terms of the privileged $\alpha_3, \alpha_4, \alpha_6, \alpha_7$ from the equations (22),…,(30); after the elimination, the resulting equations (31),…,(34) are iterated until convergence to yield the privileged α_i. The remaining α_i are, then, found from the expressions used to eliminate them from (31),…,(34).

9.2 Assignment of T, p

In this case the equilibrium composition is solved in terms of the x_i which are, subsequently, converted to the α_i. The equilibrium equations relative to the 9 independent chemical reactions read formally exactly the same as (22),…,(30); they are obtainable simply replacing the symbol α with the symbol x and the dependence (T, v) with the dependence (T, p).

The conservation equations relative to the 4 atomic species read

$$\frac{N_1^a}{N_t} = x_1 + x_5 + 2x_6 + x_8 + x_{11} + 2x_{12} \tag{35}$$
$$\frac{N_2^a}{N_t} = x_2 + x_5 + 2x_7 + x_9 + x_{11} + 2x_{13} \tag{36}$$
$$\frac{N_3^a}{N_t} = x_3 + x_{10} \tag{37}$$
$$\frac{N_4^a}{N_t} = x_4 - x_8 - x_9 - x_{10} - x_{11} - x_{12} - x_{13} \tag{38}$$

---

[6] The equations (31),…,(34) imply the condition $\sum_e \alpha_e = 1$.

An additional equation is required to close the system because of the presence of N_t, which is another unknown of the problem. It reads[7]

$$\textstyle\sum_\epsilon x_\epsilon = 1 \qquad (39)$$

The N_j^a must be considered assigned.

The numerical method follows the same guidelines described in sec. 9.1.

10 SPECIFIC HEATS & CHARACTERISTIC VELOCITIES

Specific heats and characteristic velocities have been considered relatively to the definitions "frozen" and "chemical equilibrium". The determination of the frozen properties is rather straightforward; the same process relative to the equilibrium properties requires more elaboration. For obvious reasons of space limitations, only final working formulas are discussed and/or given here. Readers interested in the details are referred to [1, 2, 3].

10.1 Frozen properties

The constant pressure and constant volume specific heats are found from

$$\begin{aligned} c_{p,f} &= \alpha_i c_{p,i} \\ c_{v,f} &= c_{p,f} - R_G/\mathcal{M} \end{aligned}$$

Their ratio follows at once

$$\gamma_f = c_{p,f}/c_{v,f}$$

The Newton and Laplace characteristic velocities are found from

$$\begin{aligned} a_{N,f} &= \sqrt{(R_G/\mathcal{M})T} \\ a_{L,f} &= \sqrt{\gamma_f}\, a_{N,f} \end{aligned}$$

10.2 Equilibrium properties

10.2.1 Equilibrium derivatives

The determination of the equilibrium properties presupposes that of the equilibrium composition derivatives $(\partial\alpha_\epsilon/\partial T)_v$ and $(\partial\alpha_\epsilon/\partial v)_T$. General linear systems of equations are available, in principle, but they require some adaptation when particularized to the case of the perfect gases [1].

The system relative to the derivatives $(\partial\alpha_\epsilon/\partial T)_v$ is not the most appropriate from the numerical viewpoint because it involves in the known term array the presence of s_ϵ which carries the numerical troublemaker $\ln(\mathcal{M}\alpha_\epsilon/M_\epsilon)$; this term becomes indefinitely large when $\alpha_\epsilon \to 0$ and blows unavoidably the calculation. The inconvenience is eliminated if recourse is made to the equilibrium derivatives involving the p_ϵ rather then the α_ϵ. These are defined as

$$\xi_\epsilon^T = \left[\frac{\partial}{\partial T}\left(T \ln \frac{p_\epsilon}{p_o}\right)\right]_v$$

and the linear system to evaluate them reads

$$\begin{cases} \nu_{li}^* \xi_i^T = \nu_{lk}^* \dfrac{\tilde{s}_k}{R_k} \\ \xi_i^T \dfrac{\alpha_i \sigma_{ij}}{M_i} = \left[\alpha_k + \ln\left(\dfrac{p_k}{p_o}\right)^{\alpha_k}\right] \dfrac{\sigma_{kj}}{M_k} \end{cases}$$

with

$$\tilde{s}_\epsilon = s_\epsilon(T_\theta, p_o) + \int_{T_\theta}^{T} \frac{1}{\tau} c_{p,\epsilon}(\tau)\, d\tau$$

The system relative to the derivatives $(\partial\alpha_\epsilon/\partial v)_T$ is not affected by any numerical trouble when some α_ϵ tend to 0. It turns out that the terms

$$\xi_\epsilon^v = \frac{v}{\alpha_\epsilon}\left(\frac{\partial\alpha_\epsilon}{\partial v}\right)_T$$

come in play and the system to evaluate them reads

$$\begin{cases} \nu_{li}^* \xi_i^v = \sum_\epsilon \nu_{l\epsilon}^* \\ \xi_i^v \dfrac{\alpha_i \sigma_{ij}}{M_i} = 0 \end{cases}$$

10.2.2 Working formulas

When ξ_ϵ^T and ξ_ϵ^v have been calculated, the constant volume specific heat and the Newton characteristic velocity are found from

$$\begin{aligned} c_{v,e} = c_{v,f} &- R_i(\xi_i^T - 1) \ln\left(\frac{p_i}{p}\right)^{\alpha_i} \\ &-(R_i - \tilde{s}_i)\left[\alpha_i(\xi_i^T - 1) - \ln\left(\frac{p_i}{p}\right)^{\alpha_i}\right] \\ &+R_i\left[\ln\left(\frac{p_i}{p}\right)^{\sqrt{\alpha_i}}\right]^2 \qquad (40) \\ a_{N,e} &= \sqrt{a_{N,f}^2 - \xi_i^v \alpha_i R_i T} \qquad (41) \end{aligned}$$

Then, the equilibrium mixed derivatives follow

$$\begin{aligned} v\left(\frac{\partial s}{\partial v}\right)_{T,ce} &= \alpha_i R_i (1 - \xi_i^v) \\ &\quad +\xi_i^v\left[\alpha_i \tilde{s}_i - R_i \ln\left(\frac{p_i}{p}\right)^{\alpha_i}\right] \qquad (42) \\ v\left(\frac{\partial p}{\partial T}\right)_{v,ce} &= R_i\left[\alpha_i \xi_i^T - \ln\left(\frac{p_i}{p}\right)^{\alpha_i}\right] \qquad (43) \end{aligned}$$

and, finally, the constant pressure specific heat, the specific heat ratio and the Laplace characteristic velocity are found from

$$\begin{aligned} c_{p,e} &= c_{v,e} + \frac{T}{a_{N,e}^2}\left[v\left(\frac{\partial p}{\partial T}\right)_{v,ce}\right]\left[v\left(\frac{\partial s}{\partial v}\right)_{T,ce}\right] \\ \gamma_e &= c_{p,e}/c_{v,e} \\ a_{L,e} &= \sqrt{\gamma_e}\, a_{N,e} \end{aligned}$$

Again, the expressions (40),…,(43) are given in a form suitable for FORTRAN coding (see footnote 5).

11 THE PROGRAM 'AIRETP'

The thermodynamic relations discussed in the preceding sections have been coded in a FORTRAN program. Basically, the program accepts in input an array of thermodynamic points (T, v) or (T, p) and returns the thermodynamic properties of interest, in conditions of chemical equilibrium, according to the selected data source (see sec. 5.1) for a prescribed composition of the atomic species.

---

[7] The equations (35),…,(38) do not imply the equation (39).

Data sources can be implemented at will, provided that their interpolating polynomials of the $c_{p,\epsilon}$ can be brought into the form (6). The data sources presently implemented in the program are [5, 6, 9, 11]. The components marked with * in table 2 are those that cannot be accounted for when the corresponding data-source is selected. Consistently, the chemical reactions which must be excluded are marked with * in table 3.

Values of $M_\epsilon\overline{(\Delta h_\epsilon)}^{f,e}_{T_\theta,T'_0}$ and $M_\epsilon s_\epsilon(T_\theta,p_o)$ relative to the subrange allocations of the implemented data sources are shown[8] in table 6 and table 7. The former quantities are calculated according to the method described in the end of sec. 5.3.3 from the data tabulated in [14, 15] relatively to $T'_0 = 0\,°K$; the latter quantities are read directly from [14, 15] and are relative to $p_o = 1.01325 \cdot 10^5 N/m^2$.

11.1 Constant pressure specific heats of the components

A sample of calculation of the $c_{p,\epsilon}$ is given in fig. 1 and fig. 2; they show the nondimensional constant pressure specific heat of O^+ and O_2, respectively. The solid lines refer to our calculation based on the implemented data sources; values read directly from the tables in [5, 6, 14, 15] are also plotted for comparison.

The fitting of the tabulated data is generally satisfactory, though in some instances the interpolating polynomials do not meet properly at the boundaries of adjacent subranges. The possible existence of discontinuities at the subrange junctions is evidenced by the jump at 6000 °K of the solid line corresponding to [11] in fig. 2. A smoothing procedure to eliminate the discontinuities is described in [11] and, in a better way, in [12]. However, in our opinion smoothing procedures contribute to make clumsy the use of the interpolating polynomials.

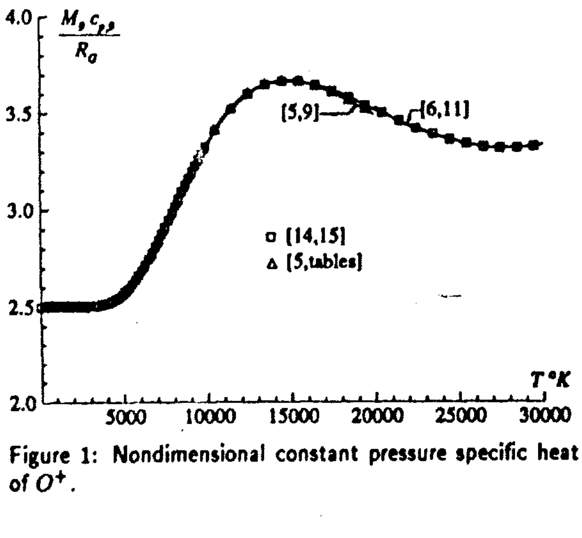

Figure 1: Nondimensional constant pressure specific heat of O^+.

The situation in fig. 1 reveals a satisfactory matching among the tabulated data, though a slight divergence seems to begin at 20000 °K. The same situation exists for N^+, Ar^+ and e^-. The situation in fig. 2 reveals, instead, a heavy disagreement among the tabulated data above 6000 °K. Similar discrepancies exist at high temperatures for the $c_{p,\epsilon}$ of all the remaining components in the model. They should, therefore, be expected to affect also other thermodynamic properties usually listed in the tables. The existence of such a situation remains an open issue and calls for a reconsideration of the methods used to calculate the tables.

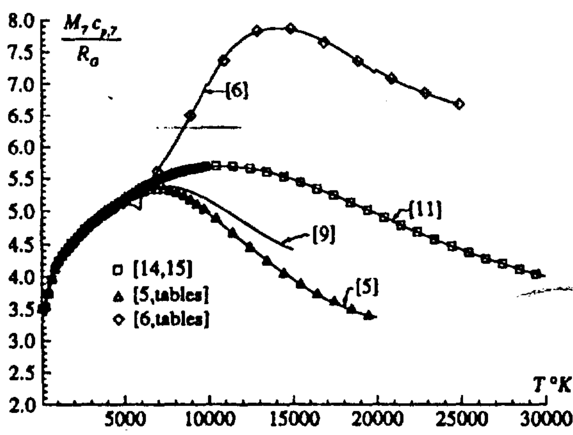

Figure 2: Nondimensional constant pressure specific heat of O_2.

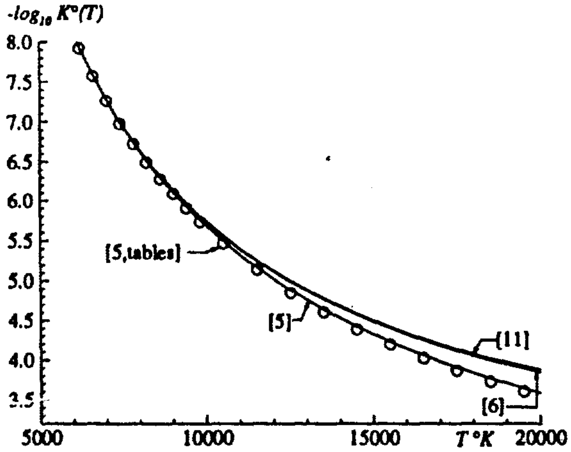

Figure 3: Equilibrium constant, relative to the partial pressures, for the reaction $2N \rightleftharpoons N_2^+ + e^-$.

11.2 Equilibrium constants

The validation of the procedure to calculate the equilibrium constants is based on the reproduction of tabulated data from [5, 17]. The former reference lists the logarithms to the base 10 of the equilibrium constant relative to the partial pressures[9], $\log_{10} K°(T)$ in the notation of the reference, for reac. 1,...,9. The latter reference lists the natural logarithms of the equilibrium constant relative to the molar concentrations, $\ln K_e$ in the notation of the reference, for reac. 1,...,5,7,...,11,22,23,25,33. These data are understood to be the result of calculations from the partition functions.

---

[8] The blank positions in table 6 and table 7 occur when a subrange low-bounding temperature belongs to a data source for which the corresponding component cannot be accounted for.

[9] In [5], that equilibrium constant is defined in terms of the ratios of the partial pressures to $p_o = 10^5 N/m^2$ and, consequently, it is nondimensional.

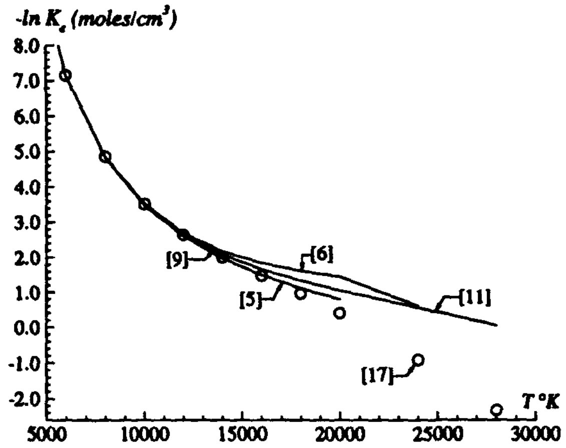

Figure 4: Equilibrium constant, relative to the molar concentrations, for the reaction $O_2 + X \rightleftharpoons 2O + X$.

Our calculations reproduce quite faithfully the tabulated data for all the indicated reactions up to 10000 °K; divergences exist for some reactions above that temperature. Examples are shown in fig. 3 and fig. 4. The discrepancy among the solid lines, which represent our calculation based on the implemented data sources, is an evident consequence of the disagreement among the tables pointed out in sec. 11.1. In fig. 4 it has to be noticed that the trend of the solid lines is appreciably less steep than the trend of the data from [17] above 20000 °K.

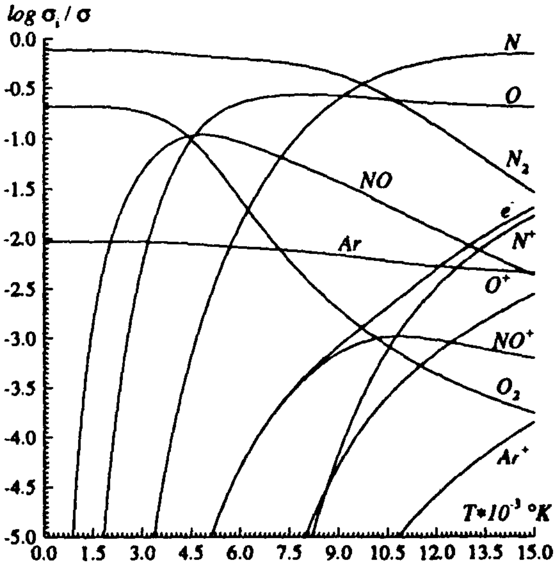

Figure 5: Equilibrium composition of air. Case from [9].

11.3 Equilibrium composition

The validation of the procedure to calculate the equilibrium composition is based on the reproduction of the diagrams from [9, 18, 19, 20, 21, 22]. Two examples are described here; they are relative to a (T, v) and a (T, p) input, respectively.

The first example refers to the case presented in [9, fig. 2c at p. 28] which shows the logarithm to the base 10 of the molar fractions, $\log \sigma_i/\sigma$ in the notation of the reference, versus T at $v = 0.1\, m^3/kg$. The low temperature composition assumed in [9] includes Ar, N_2, O_2 with molar fractions $x_3 = 0.0093, x_6 = 0.7811, x_7 = 0.2096$; the corresponding atomic species composition is $\alpha_1^a = 0.75557, \alpha_2^a = 0.23160, \alpha_3^a = 0.01283, \alpha_4^a = 0.00000$. Our calculation is based, of course, on the selection of [9] among the implemented data sources. The results are shown in fig. 5.

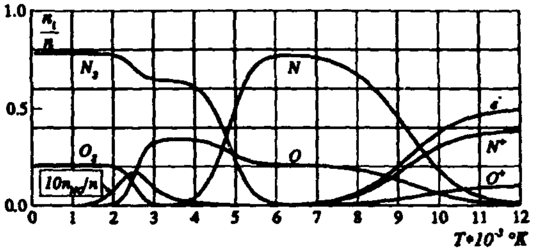

Figure 6: Equilibrium composition of air. Case from [20].

The second example refers to the case presented in [20, fig. 36.a at p. 288] which shows the molar fractions, n_i/n in the notation of the reference, versus T at $p = 0.001\, atm$. The low temperature composition assumed in [20] includes Ar, N_2, O_2 with molar fractions $x_3 = 0.0097, x_6 = 0.7808, x_7 = 0.2095$; the corresponding atomic species composition is $N_1^a = 1.5616, N_2^a = 0.4190, N_3^a = 0.0097, N_4^a = 0.0000$. Our calculation is based on the selection of [5] among the implemented data sources because of the same Soviet origin as [20]. The results are shown in fig. 6.

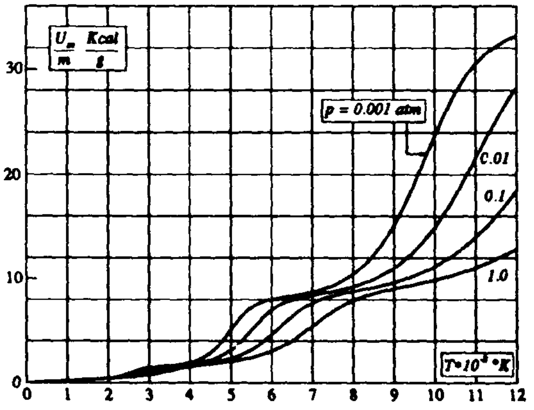

Figure 7: Internal energy of air. Case from [20].

11.4 Enthalpy and entropy

The validation of the procedure to calculate h, s and the other thermodynamic potentials is based on the reproduction of the diagrams from [18, 20, 22]. Two examples are described here.

The first example refers to the case presented in [20, fig. 37b at p. 289, fig. 38b at p. 290]. Those figures show, respectively, the mixture internal energy, U_m/m in the notation of the reference, and the mixture entropy

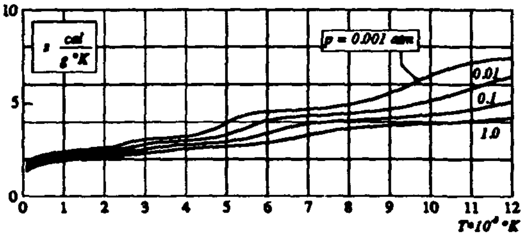

Figure 8: Entropy of air. Case from [20].

of air versus T at $p = 0.001, 0.01, 0.1, 1.0\,atm$. The low temperature composition is the same as described in the second example of sec. 11.3 and, again, [5] was selected as data source for our calculation. The results are shown in fig. 7 and fig. 8.

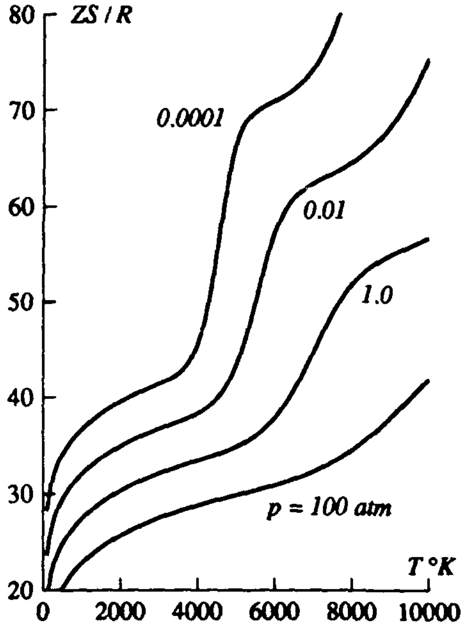

Figure 9: Entropy of dissociating ionizing nitrogen. Case from [22].

The second example refers to the case presented in [22, fig. 9.3 at p. 277, fig. 9.7 at p. 283]. Those figures show, respectively, the dimensionless (molar) entropy and the dimensionless (molar) enthalpy, ZS/R and ZH/RT in the notation[10] of the reference, of dissociating ionizing nitrogen versus T at $p = 0.0001, 0.01, 1.0, 100\,atm$. The atomic species composition for this case is $N_1^a = 1.0, N_2^a = N_3^a = N_4^a = 0.0$. Our calculation is based on the selection of [11] among the implemented data sources because of the same American origin as [22]. The results are shown in fig. 9 and fig. 10.

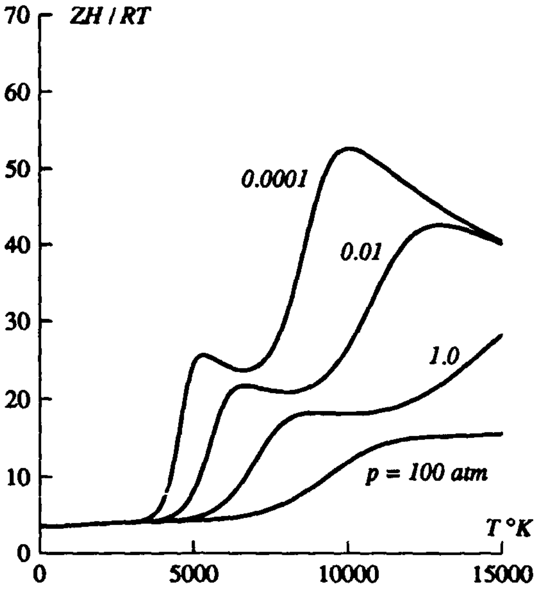

Figure 10: Enthalpy of dissociating ionizing nitrogen. Case from [22].

11.5 Equilibrium specific heats and characteristic velocities

The validation of the procedure to calculate the specific heats, their ratios and the characteristic velocitites is based on the reproduction of the diagrams from [20, 22] and of the tabulated data from [23]. Two examples are described here.

The first example refers to the case presented in [20, fig. 37a at p. 289], which shows the equilibrium constant volume specific heat of air, C_v in the notation of the reference, versus T at $p = 0.001, 0.01, 0.1, 1.0\,atm$. The low temperature composition is the same as described in the second example of sec. 11.3 and, again, [5] was selected as data source for our calculation. The results are shown in fig. 11.

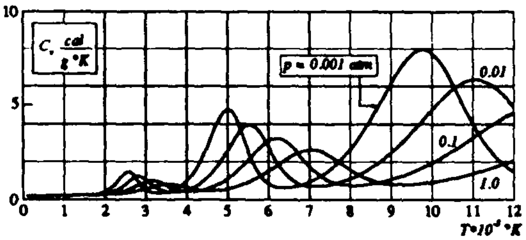

Figure 11: Equilibrium constant volume specific heat of air. Case from [20].

The second example refers to [23]. This reference lists, among other things, tabulated values of γ_e and the ratio of $a_{L,e}^2$ to pv versus T at specified values of p for four nitrogen-oxygen mixtures. Two of them were considered as test case. The former has a low temperature composition constituted by 100% N_2 (pure nitrogen) and a corresponding atomic species composition

---

[10] This notation requires some clarification. R is the universal gas constant and corresponds to R_G. The compressibility factor Z is defined as $\mathcal{M}_{s0}/\mathcal{M}$, where the value at numerator is evaluated at standard T, p conditions, i.e. $273.15\,°K, 1.01325 \cdot 10^5\,N/m^2$. S and H correspond, respectively, to $m_t s/N_t$ and $m_t h/N_t$.

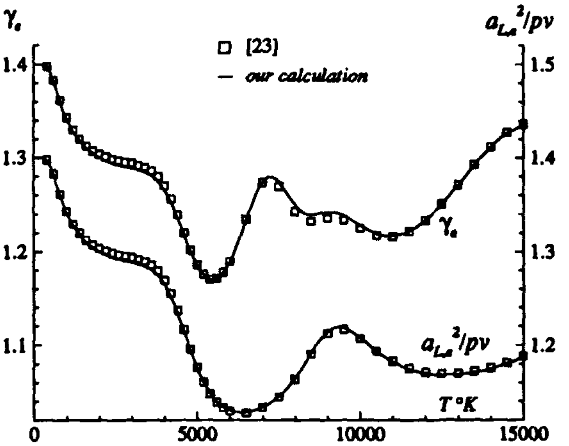

Figure 12: Equilibrium specific heat ratio and Laplace characteristic velocity for the 100% N_2 mixture.

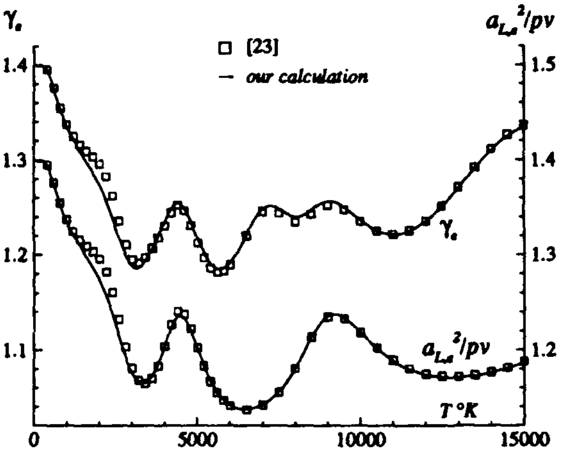

Figure 13: Equilibrium specific heat ratio and Laplace characteristic velocity for the 80% N_2,20% O_2 mixture.

$N_1^a = 1.0, N_2^a = N_3^a = N_4^a = 0.0$. The latter has a low temperature composition constituted by 80% N_2 and 20% O_2, and a corresponding atomic species composition $N_1^a = 1.6, N_2^a = 0.4, N_3^a = N_4^a = 0.0$. The values $p = 0.0001, 1.0, 100\,atm$ were considered for each mixture. Our calculation is based on the selection of [11] among the implemented data sources and reproduces the tabulated data in a satisfactory manner. A complete matching is found for the 100% N_2 mixture regardless of the value assumed for p; instead, slight differences exist for the 80% N_2,20% O_2 mixture between 1000 °K and 4000 °K for increasing p. Evidence of this situation is given in fig. 12 and fig. 13, which are relative to $p = 1.0\,atm$.

12 SENSITIVITY ANALYSIS

An investigation was performed to ascertain possible consequences on the equilibrium composition and on the calculated values of h, s due to the disagreement between the tables [5] and [14, 15] relatively to the $c_{p,\epsilon}$ of some components in the model. A mixture with low temperature composition of 79% N_2 and 21% O_2, and corresponding atomic species composition $N_1^a = 1.58, N_2^a = 0.42, N_3^a = N_4^a = 0.0$, was studied up to 20000 °K for $p = 0.0001, 0.01, 1.0, 100\,atm$. The calculations were performed by selecting [5, 11] among the implemented data sources; [11] was chosen because the authors of that reference operated their curve fitting on the data from [14, 15].

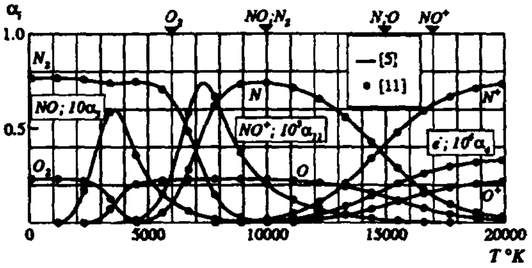

Figure 14: Equilibrium composition of air. Comparison between [5] and [11].

The results of the calculation of the equilibrium composition at $p = 1.0\,atm$ are shown in fig. 14. N_2^+ and O_2^+ are not included because $\alpha_{12}, \alpha_{13} < 10^{-4}$. The black triangles mark the temperatures above which an appreciable divergence begins to exist between [5] and [14, 15] relatively to the $c_{p,\epsilon}$ of the indicated components. The results generated by the two selected data sources match completely. This leads to the conclusion that the incertitudes affecting the $c_{p,\epsilon}$ vanish in the procedure to determine the equilibrium composition.

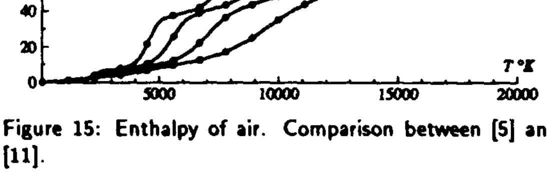

Figure 15: Enthalpy of air. Comparison between [5] and [11].

The results of the calculation of h, s generated by the two selected data sources are shown in fig. 15 and fig. 16 and, again, they match completely. This unexpected matching is explained by the situation in fig. 14: for any given component appearing on top of the diagram, the incertitude about its $c_{p,\epsilon}$ occurs in a temperature zone where its α_ϵ is vanishingly small and makes harmless the terms $h_\epsilon, \tilde{s}_\epsilon$ which are the potential carriers of the incertitude. At high temperatures, the matching of the results is, basically, a direct consequence of the matching in the $c_{p,\epsilon}$ of the monoatomic ionized components N^+, O^+ and e^- (see fig. 1).

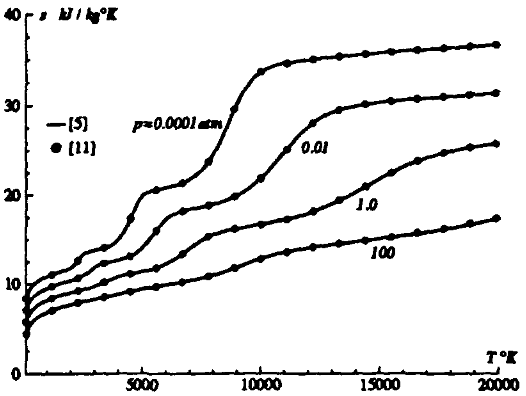

Figure 16: Entropy of air. Comparison between [5] and [11].

13 ACKNOWLEDGEMENTS

This work was carried out in support of the ESA study program for the joint ESA/NASA Comet Nucleus Sample Return mission (ROSETTA).

The authors would like to thank Mr. E. Ludwick, General Electric Co., and Mr. R. A. Thompson, NASA Langley, for their valuable assistance in the procurement of the tables [14, 15].

A special thank goes to Mr. W. Berry, the authors' head of division, without whose support the publication of this paper would have not been possible.

14 REFERENCES

[1] Giordano, D., Marraffa, L., "Thermodynamics of Gas Mixtures in Thermal Equilibrium", *to be published*

[2] Callen, H. B., "Thermodynamics", New York, USA, John Wiley & Sons, 1963.

[3] Napolitano, L. G., "Thermodynamique des Systèmes Composites en Équilibre ou Hors d'Équilibre", Paris, France, Gauthier-Villars Éditeurs, 1971.

[4] McBride, B., Heimel, S., Ehlers, J. G., Gordon, S., "Thermodynamic Properties to 6000 °K for 210 Substances Involving the First 18 Elements", NASA-SP-3001, 1963.

[5] Gurvich, L. V., Veyts, I. V., Alcock, C. B., "Thermodynamic Properties of Individual Substances", New York, USA, Hemisphere Publishing Corporation, 1989 (ISBN 0-89116-760-9), vol. 1, part 2.

[6] Balakrishnan, A., "Correlations for Specific Heats of Air Species to 50000 °K", AIAA-86-1277, June 1986.

[7] Esch, D. D., Siripong, A., Pike, R. W., "Thermodynamic Properties in Polynomial Form for Carbon, Hydrogen, Nitrogen and Oxygen Systems from 300 to 15000 °K", NASA-CR-111989, 1970.

[8] Gordon, S., McBride, B. J., "Computer Program for Calculation of Complex Chemical Equilibrium Compositions, Rocket Performance, Incident and Reflected Shocks and Chapman-Jouguet Detonations", NASA-SP-273 (Interim revision), 1976.

[9] Prabhu, R., Erickson, W. D., "A Rapid Method for the Computation of Equilibrium Chemical Composition of Air to 15000 °K", NASA-TP-2792, 1988.

[10] Gnoffo, P. A., Gupta, R. N., Shinn, J. L., "Conservation Equations and Physical Models for Hypersonic Air Flows in Thermal and Chemical Nonequilibrium", NASA-TP-2867, 1989.

[11] Gupta, R. N., Yos, J. M., Thompson, R. A., "A Review of Reaction Rates and Thermodynamic and Transport Properties for the 11-Species Air Model for Chemical and Thermal Nonequilibrium Calculations to 30000 °K", NASA-TM-101528, 1989.

[12] Thompson, R. A., Lee, K.-P., Gupta, R. N., "Computer Codes for the Evaluation of Thermodynamic Properties, Transport Properties and Equilibrium Constants of an 11-Species Air Model", NASA-TM-102602, 1990.

[13] Gupta, R. N., Yos, J. M., Thompson, R. A., Lee, K.-P., "A Review of Reaction Rates and Thermodynamic and Transport Properties for an 11-Species Air Model for Chemical and Thermal Nonequilibrium Calculations to 30000 °K", NASA-RP-1232, 1990.

[14] Browne, W. G., "Thermodynamic Properties of Some Atoms and Atomic Ions", Eng. Phys. Tech. Memo. #2, Missile & Space Vehicle Dep., General Electric Co., 1962.

[15] Browne, W. G., "Thermodynamic Properties of Some Diatoms and Diatomic Ions", Adv. Aerosp. Phys. Tech. Memo. #8, Missile & Space Vehicle Dep., General Electric Co., 1962.

[16] Stull, D. R., Prophet, H., "JANAF Thermochemical Tables", Dow Chemical Co., NSRDS-NBS 37, 1971.

[17] Park, C., "Nonequilibrium Hypersonic Aerothermodynamics", New York, USA, John Wiley & Sons, 1990 (ISBN 0-471-51093-9).

[18] Peng, T., Pindroh, A. L., "An Improved Calculation of Gas Properties at High Temperatures-Air", *in* "Magnetohydrodynamics", pp 67–88, "4th Gas Dynamics Biennal Symposium of the American Rocket Society and Northwestern University", Evanston, Ill., 1962.

[19] Hilsenrath, J., Klein, M., "Tables of Thermodynamic Properties of Air in Chemical Equilibrium Including Second Virial Corrections from 1500 °K to 15000 °K", AEDC-TR-65-58, 1964.

[20] Sédov, L., "Mécanique des Milieux Continus. Tome I.", Moscou, URSS, Éditions MIR (Traduction française), 1975.

[21] Matsuzaki, R., Hirabayashi, N., "Study of Chemical Reaction Models for High Enthalpy Flow of Air", NAL TR-982, 1988.

[22] Hansen, C. F., "Molecular Physics of Equilibrium Gases. A Handbook for Engineers.", NASA-SP-3096, 1976.

[23] Fowler, B., Brown, R. D., "Charts for Approximate Thermodynamic Properties of Nitrogen-Oxygen Mixtures", NASA-SP-3017, 1965.

j, φ	a. species	M^a $(kg/mole)$	s. element	λ
1	N	$.140067 \cdot 10^{-1}$	N_2	2
2	O	$.159994 \cdot 10^{-1}$	O_2	2
3	Ar	$.399480 \cdot 10^{-1}$	Ar	1
4	e	$.549000 \cdot 10^{-6}$	e	1

Table 1: The atomic species and their respective stable elements.

i, k, ϵ	comp.	N	O	Ar	e	M $(kg/mole)$	[5]	[6]	[9]	[11]
1	N	1	0	0	0	$.140067 \cdot 10^{-1}$				
2	O	0	1	0	0	$.159994 \cdot 10^{-1}$				
3	Ar	0	0	1	0	$.399480 \cdot 10^{-1}$		*		*
4	e^-	0	0	0	1	$.549000 \cdot 10^{-6}$				
5	NO	1	1	0	0	$.300061 \cdot 10^{-1}$				
6	N_2	2	0	0	0	$.280134 \cdot 10^{-1}$				
7	O_2	0	2	0	0	$.319988 \cdot 10^{-1}$				
8	N^+	1	0	0	-1	$.140062 \cdot 10^{-1}$				
9	O^+	0	1	0	-1	$.159989 \cdot 10^{-1}$				
10	Ar^+	0	0	1	-1	$.399475 \cdot 10^{-1}$		*		*
11	NO^+	1	1	0	-1	$.300056 \cdot 10^{-1}$				
12	N_2^+	2	0	0	-1	$.280129 \cdot 10^{-1}$			*	
13	O_2^+	0	2	0	-1	$.319983 \cdot 10^{-1}$			*	

Table 2: The chemical components and their formation matrix σ.

r, ρ		reaction	[5]	[6]	[9]	[11]
1		$NO + X \rightleftharpoons N + O + X$				
2	⋆	$N_2 + X \rightleftharpoons 2N + X$				
3	⋆	$O_2 + X \rightleftharpoons 2O + X$				
4	⋆	$N + X \rightleftharpoons N^+ + e^- + X$				
5	⋆	$O + X \rightleftharpoons O^+ + e^- + X$				
6	⋆	$Ar + X \rightleftharpoons Ar^+ + e^- + X$		*		*
7		$N + O \rightleftharpoons NO^+ + e^-$				
8		$2N \rightleftharpoons N_2^+ + e^-$			*	
9		$2O \rightleftharpoons O_2^+ + e^-$			*	
10		$O + N_2 \rightleftharpoons N + NO$				
11		$O + NO \rightleftharpoons N + O_2$				
12	⋆	$NO + X \rightleftharpoons NO^+ + e^- + X$				
13		$N + NO^+ \rightleftharpoons NO + N^+$				
14		$O + N_2^+ \rightleftharpoons NO + N^+$			*	
15		$O + NO^+ \rightleftharpoons NO + O^+$				
16		$N + O_2^+ \rightleftharpoons NO + O^+$			*	
17		$Ar + NO^+ \rightleftharpoons NO + Ar^+$		*		*
18		$N_2 + O^+ \rightleftharpoons NO + N^+$				
19		$NO + O^+ \rightleftharpoons O_2 + N^+$				
20		$NO + NO^+ \rightleftharpoons N_2 + O_2^+$			*	
21		$NO + NO^+ \rightleftharpoons O_2 + N_2^+$			*	
22		$N_2 + NO^+ \rightleftharpoons NO + N_2^+$			*	
23		$O_2 + NO^+ \rightleftharpoons NO + O_2^+$			*	
24	⋆	$N_2 + O_2 \rightleftharpoons 2NO$				
25		$N + NO^+ \rightleftharpoons O + N_2^+$			*	
26		$O + NO^+ \rightleftharpoons N + O_2^+$			*	
27		$2NO^+ \rightleftharpoons N_2^+ + O_2^+$			*	
28	⋆	$N_2 + X \rightleftharpoons N_2^+ + e^- + X$			*	
29		$N_2 + N^+ \rightleftharpoons N + N_2^+$			*	
30		$N + NO^+ \rightleftharpoons N_2 + O^+$				
31		$N_2 + O^+ \rightleftharpoons O + N_2^+$			*	
32		$Ar + N_2^+ \rightleftharpoons N_2 + Ar^+$		*	*	*
33		$N_2 + O_2^+ \rightleftharpoons O_2 + N_2^+$			*	
34	⋆	$O_2 + X \rightleftharpoons O_2^+ + e^- + X$			*	
35		$O + NO^+ \rightleftharpoons O_2 + N^+$				
36		$N + O_2^+ \rightleftharpoons O_2 + N^+$			*	
37		$O + O_2^+ \rightleftharpoons O_2 + O^+$			*	
38		$Ar + O_2^+ \rightleftharpoons O_2 + Ar^+$		*	*	*
39		$N + O^+ \rightleftharpoons O + N^+$				
40		$Ar + N^+ \rightleftharpoons N + Ar^+$		*		*
41		$NO^+ + X \rightleftharpoons O + N^+ + X$				
42		$N_2^+ + X \rightleftharpoons N + N^+ + X$			*	
43		$N^+ + NO^+ \rightleftharpoons O^+ + N_2^+$			*	
44		$O^+ + NO^+ \rightleftharpoons N^+ + O_2^+$			*	
45		$Ar + O^+ \rightleftharpoons O + Ar^+$		*		*
46		$NO^+ + X \rightleftharpoons N + O^+ + X$				
47		$O_2^+ + X \rightleftharpoons O + O^+ + X$			*	

Table 3: The set of the chemical reactions.

r, ρ	N	O	Ar	e^-	NO	N_2	O_2	N^+	O^+	Ar^+	NO^+	N_2^+	O_2^+
1	1	1	0	0	-1	0	0	0	0	0	0	0	0
2	2	0	0	0	0	-1	0	0	0	0	0	0	0
3	0	2	0	0	0	0	-1	0	0	0	0	0	0
4	-1	0	0	1	0	0	0	1	0	0	0	0	0
5	0	-1	0	1	0	0	0	0	1	0	0	0	0
6	0	0	-1	1	0	0	0	0	0	1	0	0	0
7	-1	-1	0	1	0	0	0	0	0	0	1	0	0
8	-2	0	0	1	0	0	0	0	0	0	0	1	0
9	0	-2	0	1	0	0	0	0	0	0	0	0	1
10	1	-1	0	0	1	-1	0	0	0	0	0	0	0
11	1	-1	0	0	-1	0	1	0	0	0	0	0	0
12	0	0	0	1	-1	0	0	0	0	0	1	0	0
13	-1	0	0	0	1	0	0	1	0	0	-1	0	0
14	0	-1	0	0	1	0	0	1	0	0	0	-1	0
15	0	-1	0	0	1	0	0	0	1	0	-1	0	0
16	-1	0	0	0	1	0	0	0	1	0	0	0	-1
17	0	0	-1	0	1	0	0	0	0	1	-1	0	0
18	0	0	0	0	1	-1	0	1	-1	0	0	0	0
19	0	0	0	0	-1	0	1	1	-1	0	0	0	0
20	0	0	0	0	-1	1	0	0	0	0	-1	0	1
21	0	0	0	0	-1	0	1	0	0	0	-1	1	0
22	0	0	0	0	1	-1	0	0	0	0	-1	1	0
23	0	0	0	0	1	0	-1	0	0	0	-1	0	1
24	0	0	0	0	2	-1	-1	0	0	0	0	0	0
25	-1	1	0	0	0	0	0	0	0	0	-1	1	0
26	1	-1	0	0	0	0	0	0	0	0	-1	0	1
27	0	0	0	0	0	0	0	0	0	0	-2	1	1
28	0	0	0	1	0	-1	0	0	0	0	0	1	0
29	1	0	0	0	0	-1	0	-1	0	0	0	1	0
30	-1	0	0	0	0	1	0	0	1	0	-1	0	0
31	0	1	0	0	0	-1	0	0	-1	0	0	1	0
32	0	0	-1	0	0	1	0	0	0	1	0	-1	0
33	0	0	0	0	0	-1	1	0	0	0	0	1	-1
34	0	0	0	1	0	0	-1	0	0	0	0	0	1
35	0	-1	0	0	0	0	1	1	0	0	-1	0	0
36	-1	0	0	0	0	0	1	1	0	0	0	0	-1
37	0	-1	0	0	0	0	1	0	1	0	0	0	-1
38	0	0	-1	0	0	0	1	0	0	1	0	0	-1
38	-1	1	0	0	0	0	0	1	-1	0	0	0	0
40	1	0	-1	0	0	0	0	-1	0	1	0	0	0
41	0	1	0	0	0	0	0	1	0	0	-1	0	0
42	1	0	0	0	0	0	0	1	0	0	0	-1	0
43	0	0	0	0	0	0	0	-1	1	0	-1	1	0
44	0	0	0	0	0	0	0	1	-1	0	-1	0	1
45	0	1	-1	0	0	0	0	0	-1	1	0	0	0
46	1	0	0	0	0	0	0	0	1	0	-1	0	0
47	0	1	0	0	0	0	0	0	1	0	0	0	-1

Table 4: The stoichiometric coefficient matrix ν.

l	r, ρ	N	O	Ar	e^-	NO	N_2	O_2	N^+	O^+	Ar^+	NO^+	N_2^+	O_2^+
1	2	2	0	0	0	0	-1	0	0	0	0	0	0	0
2	3	0	2	0	0	0	0	-1	0	0	0	0	0	0
3	4	-1	0	0	1	0	0	0	1	0	0	0	0	0
4	5	0	-1	0	1	0	0	0	0	1	0	0	0	0
5	6	0	0	-1	1	0	0	0	0	0	1	0	0	0
6	12	0	0	0	1	-1	0	0	0	0	0	1	0	0
7	24	0	0	0	0	2	-1	-1	0	0	0	0	0	0
8	28	0	0	0	1	0	-1	0	0	0	0	0	1	0
9	34	0	0	0	1	0	0	-1	0	0	0	0	0	1

Table 5: The stoichiometric coefficient matrix ν^* relative to the independent chemical reactions.

i, k, ϵ	comp.	T_e, °K										
		200	300	800	1000	1500	3000	6000	10000	15000	20000	25000
1	N	113500.6	113997.4	116481.5	117475.1	119959.2	127425.1	143767.4	171176.9	208381.1	253938.8	318860.6
2	O	60056.9	60589.2	63130.0	64131.2	66625.7	74101.5	89563.3	111407.6	139919.3	175695.0	229521.9
3	Ar	993.6	1490.4	3974.5		7452.2	14904.4	29808.9	49698.9			
4	e^-	993.6	1490.4	3974.5	4968.1	7452.2	14904.4	29808.9	49681.5	74522.2	99363.0	124203.7
5	NO	22868.3	23564.7	27237.6	28830.8	33008.7	46209.1	73677.0	113502.6	168117.5	225115.0	279964.1
6	N_2	1391.2	2087.1	5670.4	7203.9	11252.9	24227.1	51197.6	89100.0	151626.0	231008.0	309787.3
7	O_2	1391.4	2089.8	5861.8	7503.3	11780.9	25503.2	55867.2	100218.9	156283.5	208392.0	255034.9
8	N^+	448760.5	449275.1	451781.0	452777.3	455264.6	462736.6	478250.2	500212.9	528444.8	557326.4	587380.4
9	O^+	373935.3	374432.1	376916.3	377909.9	380394.0	387846.7	403068.8	426935.5	462381.3	498243.4	532290.5
10	Ar^+	364338.6	364837.4	367469.5		371257.1	379072.3	394225.8	414210.4			
11	NO^+	237227.2	237923.0	241504.4	243036.5	247083.2	260062.5	287145.0	327628.7	399392.8	483900.0	560858.1
12	N_2^+		361393.1		366554.4	370659.0	384531.2	416802.5	460277.8	514159.7	565791.7	613098.1
13	O_2^+		280005.6		285286.1	289476.3	302712.2	330369.4	375432.9	443877.7	507085.7	559500.2

Table 6: Molar augmented formation enthalpies ($cal/mole$). $T_o' = 0\,°K$.

i, k, ϵ	comp.	T_e, °K										
		200	300	800	1000	1500	3000	6000	10000	15000	20000	25000
1	N	34.6308	36.6452	41.5181	42.6268	44.6412	48.0899	51.8221	55.2957	58.3076	60.9069	63.7885
2	C	36.3399	38.5010	43.5016	44.6188	46.6419	50.0957	53.6550	56.4399	58.7458	60.7861	63.1711
3	Ar	34.9994	37.0138	41.8867		45.0098	48.4534	51.8971	54.4368			
4	e^-	3.0048	5.0193	9.8922	11.0008	13.0152	16.4588	19.9025	22.4404	24.4548	25.8840	26.9926
5	NO	47.6479	50.4716	57.6077	59.3840	62.7660	68.8500	75.1747	80.1921	84.6082	87.8876	90.3387
6	N_2	42.9927	45.8140	52.7997	54.5094	57.7859	63.7611	69.9828	74.7900	79.7077	84.2617	87.7847
7	O_2	46.2190	49.0498	56.3619	58.1922	61.6556	67.9651	74.8952	80.5480	85.0998	88.1053	90.1913
8	N^+	36.1098	38.1985	43.1216	44.2331	46.2504	49.7019	53.2723	56.0719	58.3598	60.0204	61.3603
9	O^+	35.0271	37.0415	41.9144	43.0230	45.0374	48.4812	51.9859	55.0043	57.8697	59.9352	61.4561
10	Ar^+	37.7547	39.7769	44.9035		48.3083	51.9286	55.4339	57.9867			
11	NO^+	44.5725	47.3937	54.3763	56.0844	59.3589	65.3361	71.5801	76.7013	82.5830	87.4447	90.8896
12	N_2^+		47.2605		56.0192	59.3400	65.6864	73.1096	78.6960	83.0668	86.0427	88.1577
13	O_2^+		49.3256		58.2594	61.6515	67.7518	74.1198	79.8375	85.3762	89.0282	91.3754

Table 7: Molar entropies ($cal/mole\,°K$). $p_o = 1.01325 \cdot 10^5 N/m^2$.

Three-Dimensional Hypersonic Rarefied Flow Calculations
Using Direct Simulation Monte Carlo Method

M. Cevdet Çelenligil
Department of Aeronautical Engineering
Middle East Technical University
Ankara, 06531 Türkiye

and

James N. Moss
Aerothermodynamics Branch
Space Systems Division
NASA Langley Research Center
Hampton, VA 23665-5225 U.S.A.

1. ABSTRACT

This paper is a summary of the present authors' three-dimensional simulations on the hypersonic rarefied flows in an effort to understand the highly nonequilibrium flows about space vehicles entering the Earth's atmosphere for a realistic estimation of the aerothermal loads. Calculations are performed using the direct simulation Monte Carlo method with a five-species reacting gas model, which accounts for rotational and vibrational internal energies. Results are obtained for the external flows about various bodies in the transitional flow regime. For the cases considered, convective heating, flowfield structure and overall aerodynamic coefficients are presented and comparisons are made with the available experimental data. The agreement between the calculated and measured results are very good.

2. NOMENCLATURE

A_{ref} = reference area
C_i = mass fraction of species i, ρ_i/ρ
C_D = drag coefficient
C_H = overall heat-transfer coefficient
C_L = lift coefficient
d = diameter
Kn = Knudsen number
M = Mach number
p = pressure
$\dot{q}$ = heat flux
R = radius
s_1 = longitudinal coordinate along the surface (measured at the symmetry plane)
T = temperature
T_{int} = internal temperature
T_{tr} = translational temperature
U = velocity in x direction
V = speed
X_i = mole fraction of species i
x,y,z = Cartesian coordinates
α = incidence angle
γ = specific heat ratio
η = distance along the stagnation streamline (measured from the body)
λ = mean free path
ρ = density
τ = shear stress parallel to the grid line in streamwise direction

Subscripts

i = i' th species
s = stagnation
w = wall
ref = reference
∞ = freestream

3. INTRODUCTION

With the development of revitalized interest in hypersonics after 1980's, much interest at the international level has been created for the design of more efficient spacecrafts with improved capabilities. To achieve this goal, new ideas and concepts from the recent technological developments have been introduced to these new generation space vehicles. For instance, today it has been widely accepted that during the deceleration and/or maneuvering of a spacecraft which passes through a planet's atmosphere, the fuel consumption may be substantially reduced by making use of the aerodynamic forces rather than utilizing an all-propulsive system. For aerocapture and orbital transfer applications, aerodynamic drag is the key factor; whereas for synergetic plane change applications, high lift-to-drag becomes important. In other words, aerodynamics can play a major role in today's space technology. Thus, extended knowledge of the aerodynamic characteristics is necessary for proper design.

A spacecraft flies at high altitudes where the gas may be quite rarefied, i.e., the mean free path of the gas molecules are comparable with the size of the vehicle. For instance, the mean free path of the molecules at 115-km altitude is about 1 m, and this approaches the value of 200 m around 200-km altitude. Therefore, estimation of the aerodynamic characteristics in the transitional flow regime, i.e., flow that is bound by continuum and free-molecule limits, is very important. Unfortunately, the present ground-based low-enthalpy facilities cannot simulate the highly nonequilibrium flows about these vehicles and it is necessary to perform these experiments during the flight. Many experiments have already been conducted on the Space Shuttle and also new ones are underway, but this whole process can prove to be quite expensive. Consequently, estimation of aerothermal loads in the transitional regime primarily relies on computer simulations, and the available experimental data are used for code validation.

The flows in the rarefied regime cannot be simulated using the Navier-Stokes equations because the continuum assumptions are violated. On the other hand, application of the Boltzmann equation to such problems appear to have some serious difficulties. For instance, the Boltzmann equation is too cumbersome to apply to relatively complicated two- and three-dimensional flow problems and, more importantly, several important physical phenomena observed in flight (such as chemical reactions, thermal radiation, three-body collisions, etc.) have not yet been formulated in the Boltzmann equation. Hence, as an alternative to directly solving the Boltzmann equation, several particle schemes have been introduced after 1960's.[1,2] These models simulate the rarefied gases at the molecular level by considering the dynamics of the molecules. Among these schemes, the direct simulation Monte Carlo (DSMC) method of Bird[1] has evolved as a powerful physical model and has been applied to a variety of engineering problems many of which are impossible to calculate with other methods. Experimental measurements obtained both in ground-based facilities[3,4,5] and also in flight[6] are found to be in very good agreement with the DSMC results. In the past, the DSMC technique was applied primarily to one- and two-dimensional flow problems due to their smaller requirement for computational time and memory. Application to three-dimensional problems began in earnest in the late 1980's in parallel with the availability of advanced computers, and today capability exists for full-scale flight simulations.[6,7]

At the NASA Langley Research Center, the DSMC method has been applied to a wide range of rarefied flow problems, and this paper is a summary of the present authors' three-dimensional simulation efforts on this subject.

4. IMPLEMENTATION OF DSMC METHOD

The DSMC method ~~is~~ a technique that simulates rarefied flows by keeping track of the positions, velocities and internal energies of some thousands of representative molecules in the flowfield. The motion of the molecules is computed with small time intervals and after each time step the positions of the molecules are updated considering the possible interactions with the domain boundaries. Intermolecular collisions are assumed to be uncoupled from the molecular motion over each time step, and after the collisions the velocities and internal energies of the colliding molecules are updated. Once a stationary-state is achieved in the simulations, computations are carried out and samples are taken to arrive at the time-averaged results.

In this study, the molecular collisions are calculated using the variable-hard-sphere (VHS) model[8] which treats the molecules as hard spheres as far as the scattering angle distribution is concerned, but the collision cross section depend on the relative speed of the colliding partners. The Larsen-Borgnakke phenomenological model[9] is used to control the energy exchange between translational and internal modes. Full thermal accommodation and diffuse reflection are assumed for the gas-surface interaction. The chemical reactions are simulated using a five-species (O_2, N_2, O, N, and NO) nonequilibrium chemical kinetics model. For the conditions investigated, radiation and ionization are negligible and are not considered.

In the present application, the three-dimensional domain is gridded using a body-fitted mesh which is divided into a network of deformed hexahedral (six-faced) cells. The four corners of a cell face may not be coplanar and this makes the generation of body-fitted grids possible on doubly curved surfaces. Each cell is further subdivided into six tetrahedral subcells (which have four well-defined triangular faces) to enable tracking the molecules moving from one cell to another. Also, because it is desirable to choose the collision partners from the nearest candidates (in order to improve the results with regard to the conservation of angular momentum),[2] these partners are selected probabilistically from the same subcells. For all flow problems considered, the adjacent cells and subcells are exactly matched in the whole domain.

The DSMC method is relatively easy to use, flexible and has no stability problems. It is very well suited for the calculations in the transitional flow regime. It should be noted that the computational requirements, in terms of computing time, for the DSMC method increase substantially with increasing gas density. Hence, it can be stated that for a given flow problem there is a lower limit for the selection of the altitude depending on the computing resources. Also, it is necessary to select its computational parameters properly, and only then meaningful results are obtained. (Experience can play an important role in choosing these parameters, in a short time.) For the problems considered in this study, the cell sizes in the body normal direction are less than the local mean free path of the molecules, and the cell lengths in the other two directions are selected such that the change in flow properties across each cell is small. The time increment is less than the mean collision time for a molecule, and the number of simulated molecules in each cell is at least on the order of 10.

5. COMPUTED FLOW PROBLEMS

In this section, computed results are presented for three flow problems.

5.1 Flow About Intersecting Blunt Wedges

Flow around two identical blunt wedges that intersect at a 90-deg angle is investigated in Ref. 10 and the results are summarized in this section. Figure 1 shows the schematic of the body. In the flowfield, there exists four symmetric quadrants around the intersecting wedges, and there is a plane of symmetry within each quadrant, hence, only half of a quadrant needs to be considered in the simulations. Computations are performed for flows encountered at 85- and 100-km altitudes during entry. Naturally, as the altitude increases, the density decreases and the disturbance field in front of the body becomes larger. Therefore, a bigger computational domain with larger cells is used for the 100-km calculations. The domain lies between x= − 0.1-0.2 m, y=0-0.2 m, and z=0-0.3 m for the 85-km altitude case, and between x= − 0.3-0.2 m, y=0-0.35 m, and z=0-0.5 m for the 100-km altitude case. For the 85-km altitude calculations, 16 cells in the streamwise direction, 20 cells in the normal direction, and 16 cells in the spanwise direction are used. For the 100-km case, the domain is divided into 16 cells in the streamwise direction, 11 cells in the normal direction, and 8 cells in the spanwise direction. A total of 82200 simulated molecules are used for the 85-km calculations, whereas this number for the 100-km case is 20800.

At the freestream boundaries of the computational domain, atmospheric conditions[11] (for exospheric temperature of 1200 K) listed in Table 1 are used. The freestream velocity is 7.5 km/s. A symmetry boundary condition is imposed at the far end of the span, assuming the end of the span is sufficiently far from the intersection and the spanwise gradients are negligible. (The results verify this assumption). Again, for the x-z plane at y=0 a symmetry boundary condition is used. The body surface temperature is at a uniform 1000 K. A vacuum boundary condition is stipulated at the downstream exit plane, considering the fact that supersonic velocities prevail in most of the exit section.

Table 1 Freestream Conditions

Altitude, km	$\rho_\infty \times 10^9$, kg/m^3	T_∞, K	X_{O_2}	X_{N_2}	X_O
200	0.3	1026	0.031	0.455	0.514
170	0.9	892	0.044	0.548	0.408
150	2.1	733	0.055	0.616	0.330
140	3.9	625	0.062	0.652	0.286
130	8.2	500	0.071	0.691	0.238
120	22.6	368	0.085	0.733	0.183
110	96.1	247	0.123	0.770	0.106
100	558.2	194	0.177	0.784	0.039
85	7955.0	181	0.237	0.763	0.000

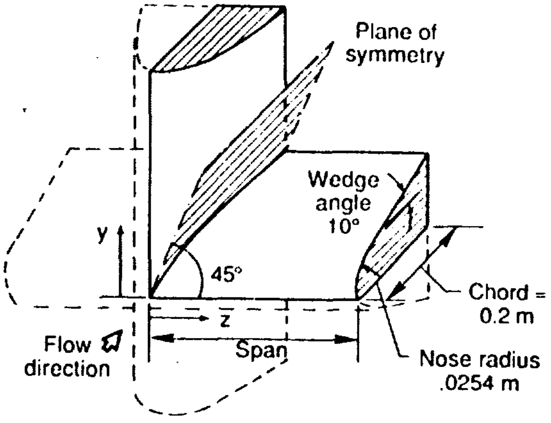

Fig. 1 Schematic of the body.

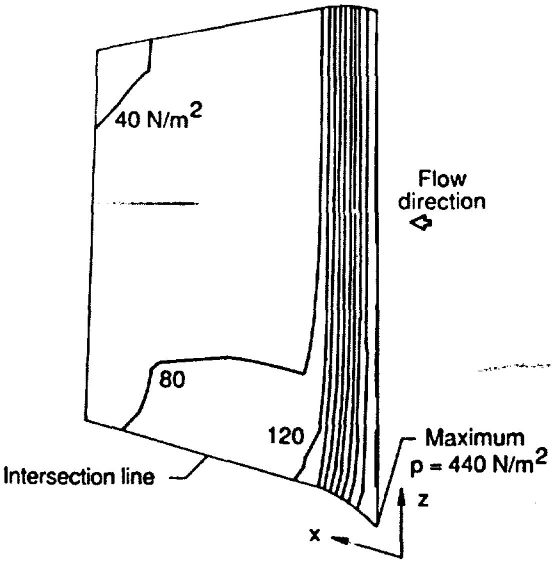

Fig. 2 Surface pressure contours (alt=85 km).

Figures 2-5 show the surface pressure, heat transfer rate, and shear stress (parallel to the grid line in the streamwise direction) distributions for the 85- and 100-km altitude cases. In Figs. 3-5, the results are plotted by perpendicular distances from the body surface; and the streamwise surface strips closest to and farthest from the wedge intersection are denoted as "inner" and "outer" strips, respectively. Figures 6 and 7 present the flowfield density, translational temperature and mass fraction distributions along the stagnation streamlines for 85- and 100-km altitude cases. In these figures, the inner and outer stagnation lines represent the ones closest to and farthest from the wedge intersection, respectively.

In Figs. 3-6, the two-dimensional wedge flow results are plotted for comparison with the three-dimensional outer strip results. The good agreement between them verifies the assumption that the computational domain is extended far enough in the spanwise direction.

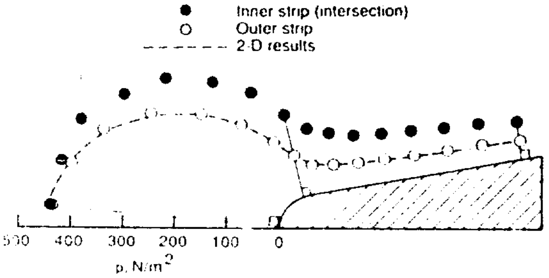

a) Alt = 85 km

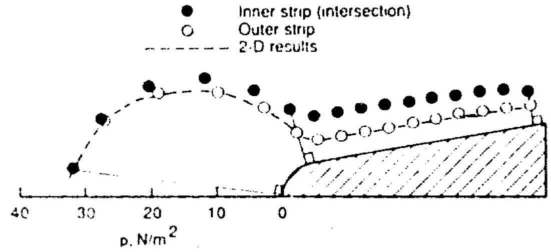

b) Alt = 100 km

Fig. 3 Surface pressure distributions.

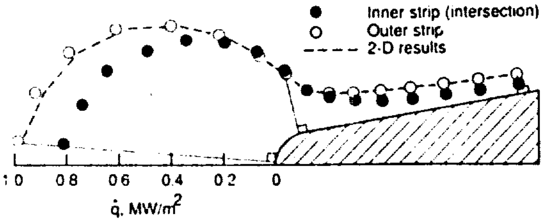

a) Alt = 85 km

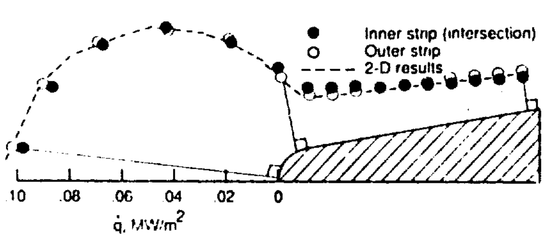

b) Alt = 100 km

Fig. 4 Surface heat-transfer rate distributions.

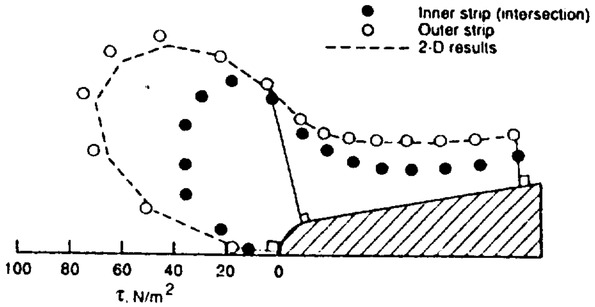

a) Alt = 85 km

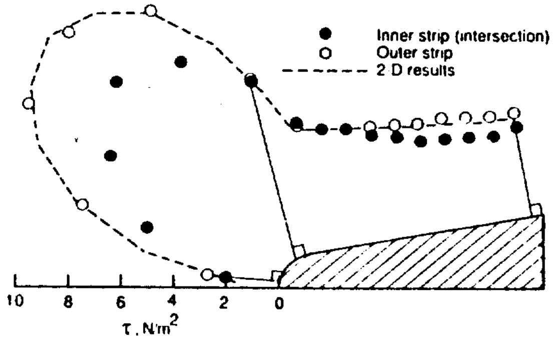

b) Alt = 100 km

Fig. 5 Surface shear stress distributions.

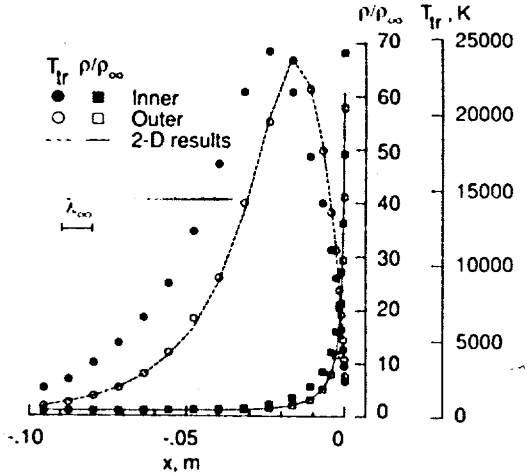

a) Alt = 85 km

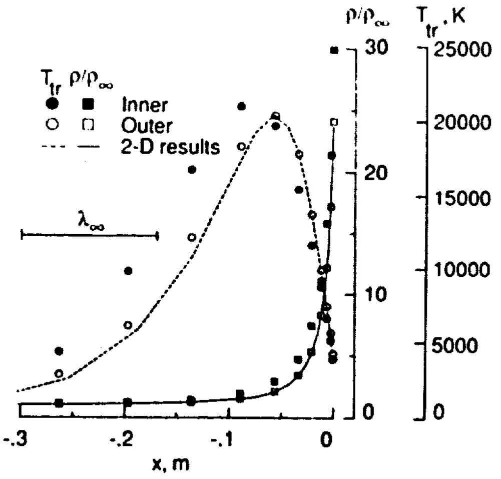

b) Alt = 100 km

Fig. 6 Properties along the stagnation streamline.

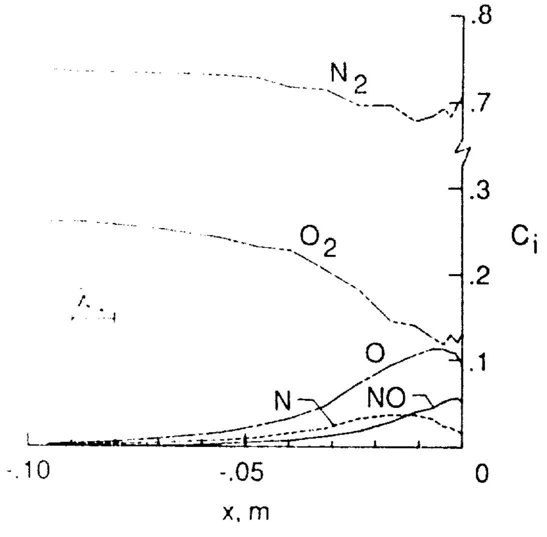

a) Inner stagnation streamline

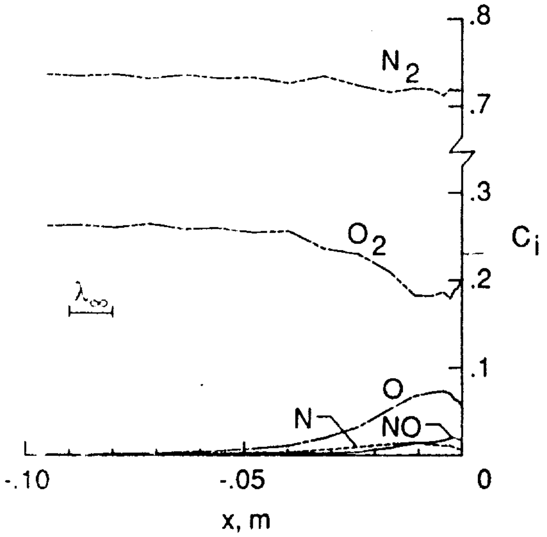

b) Outer stagnation streamline

Fig. 7 Mass fraction distributions along stagnation streamlines (alt=85 km).

5.2 Flow About the AFE Vehicle

In this section, results from References 7 and 12 are summarized. The Aeroassist Flight Experiment (AFE) vehicle (sketched in Fig. 8) is a subscale model vehicle consisting of a forebody aerobrake, a hexagonal experimental carrier, and a solid rocket motor, which is ejected prior to the atmospheric entry. The vehicle's forebody is generated by an elliptic cone that is elliptically blunted in the nose and is raked by a circular skirt at the aft end such that the base length is 4.25 m. The shape of the forebody has been described mathematically in Reference 13. The freestream velocity vector is parallel to the x-axis and makes an angle of 17-deg with the solid rocket motor axis. The origin of the coordinate system is located at the geometric stagnation point, and the x-y plane at z=0 is a plane of symmetry.

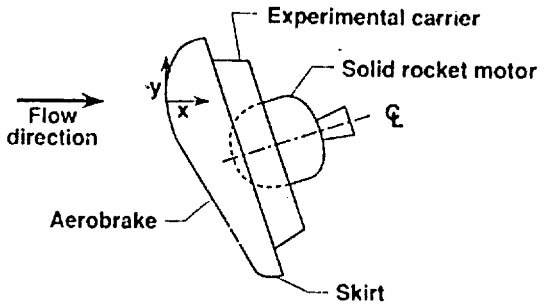

Fig. 8 AFE vehicle.

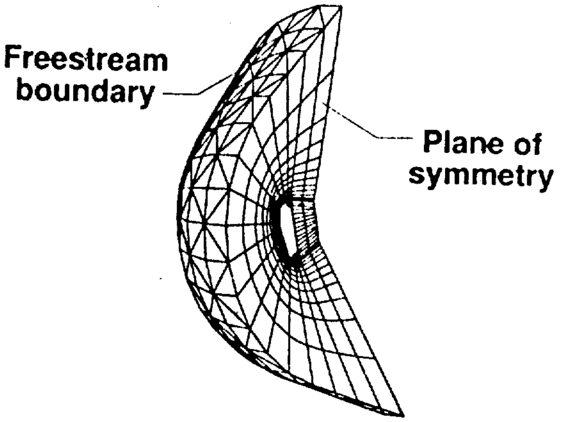

Fig. 9 Computational grid (alt=120 km).

The length of the computational domain in front of the body is chosen as 1 m, 3.7 m, 5 m, 10.6 m, 18.3 m for the 100-, 110-, 120-, 140-, 150-km- and higher-altitude cases, respectively. For the 100- and 110-km-altitude cases, calculations are performed in the forebody portion of the domain and the surface is divided into 200 distorted rectangles with 20 divisions in the longitudinal direction and 10 divisions in the spanwise direction. For the 120- and 130-km-altitude cases both the forebody and afterbody are considered but the calculations show that the afterbody does not affect the results; hence, for the higher altitudes only the forebody domain is used. In the 120- and higher-altitude calculations, the forebody surface consists of 50 distorted rectangles with 10 divisions in the longitudinal direction and 5 divisions in the spanwise direction. The 100-, 110-, 120-, 140-km- and higher-altitude cases are simulated using 5400, 2400, 1820, 600 cells and 68000, 30000, 55000, 20000 molecules, respectively. The computational grid used in the 120-km-altitude calculations is presented in Fig. 9, in which both the cells and the subcells are drawn on the outer freestream boundary, but only the cells are shown on the plane of symmetry for clarity.

At the freestream boundaries, atmospheric conditions listed in Table 1 are used. The entry velocity is 9.9 km/s. The forebody surface temperature (listed in Table 2) is assumed to be uniform and is based on free-molecule radiative equilibrium heat transfer to the stagnation point. For the calculations in which the afterbody is considered, the afterbody wall temperature is assumed to be at a uniform 300 K because the vehicle is insulated with very low conductivity materials.

Table 2 Stagnation Properties and Wall Temperatures for the AFE

Altitude, km	$\dot{q}_s$, W/m^2	p_s, N/m^2	T_w, K
FM	162	0.033	230
200	161	0.033	230
170	414	0.086	300
150	1000	0.211	370
140	1780	0.381	425
130	3720	0.819	500
120	9420	2.220	650
110	31100	9.360	950
100	77300	52.800	1500

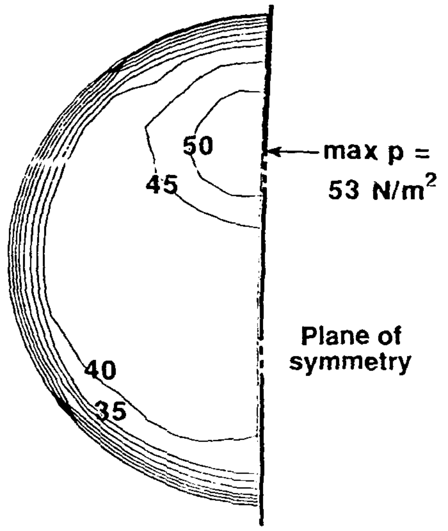

Fig. 11 Surface pressure contours (alt≈100 km).

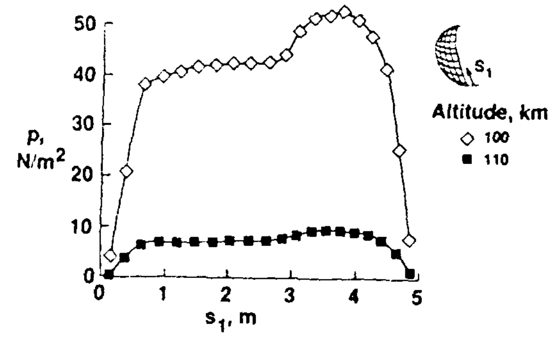

a) Lower altitudes.

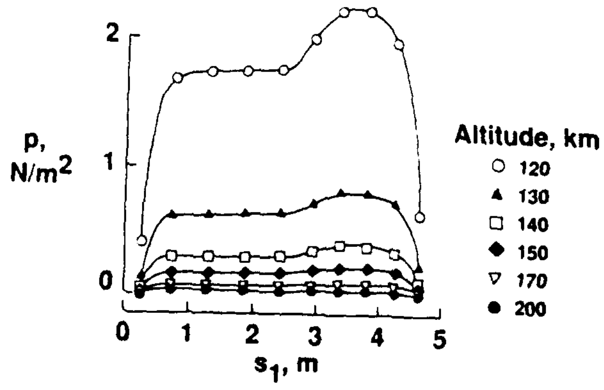

b) Higher altitudes.

Fig. 10 Surface pressure distributions (the small sketch is a perspective view of the forebody surface grid).

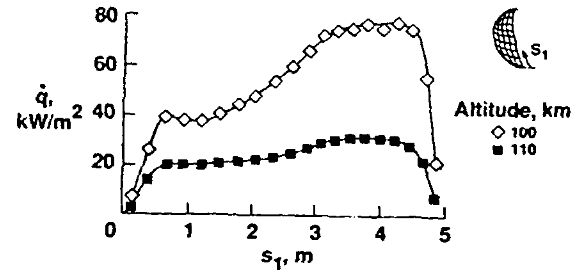

a) Lower altitudes.

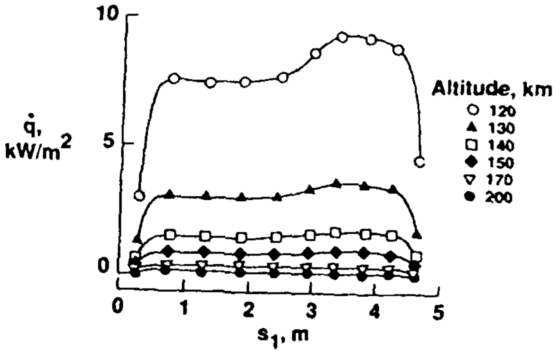

b) Higher altitudes.

Fig. 12 Surface heat-transfer-rate distributions (the small sketch is a perspective view of the forebody surface grid).

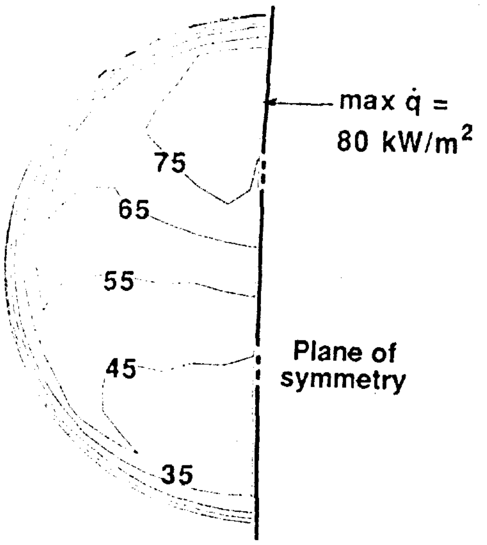

Fig. 13 Surface heat-transfer-rate contours (alt=100 km).

The results presented for this flow problem are based on the samples taken over the 8000 time steps computed after the stationary state. Figures 10-13 show pressure and heat-transfer-rate distributions on the forebody surface. These figures show that both pressure and surface heating have their maxima slightly below the geometric stagnation point, are fairly uniformly distributed along the conical portion of the forebody surface (as per design), and drop rapidly along the skirt. The stagnation pressure and heat-transfer rate results are listed in Table 2 (in which the free-molecule limit is denoted by FM).

Figures 14 and 15 show the density and translational temperature contours in the flowfield. Clearly, the flowfield density increases continuously as the flow approaches the body surface, whereas the translational temperature has its peak value somewhere away from the surface in the upstream direction, and then start decreasing because of the effect of the relatively cooler body surface. Calculations indicate that maximum internal energy occurs further downstream in the lower portion of the computational domain. This is due to the fact that as the molecules move further downstream they experience more molecular collisions during which their high kinetic energies are converted into internal modes. Results show that dissociation is negligible for altitudes of 120 km and higher. But, as the altitude decreases these effects become appreciable. Figure 16 shows the mass fraction distributions along the stagnation streamline for 100-km altitude.

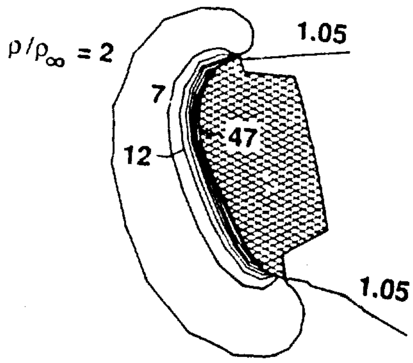

a) Alt=120 km

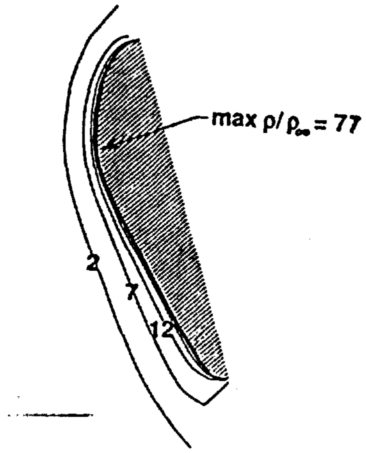

b) Alt=100 km

Fig. 14 Flowfield density contours.

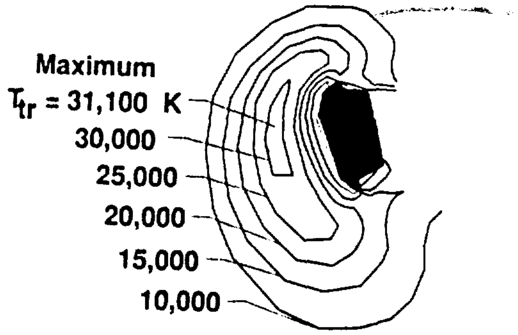

a) Alt=120 km

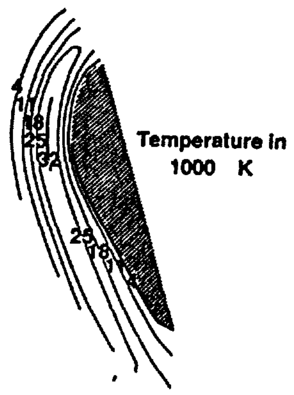

b) Alt=100 km

Fig. 15 Flowfield translational temperature contours.

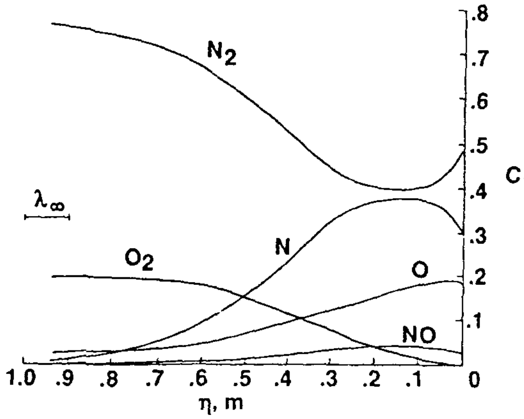

Fig. 16 Mass fraction distributions along the stagnation streamline (alt=100 km).

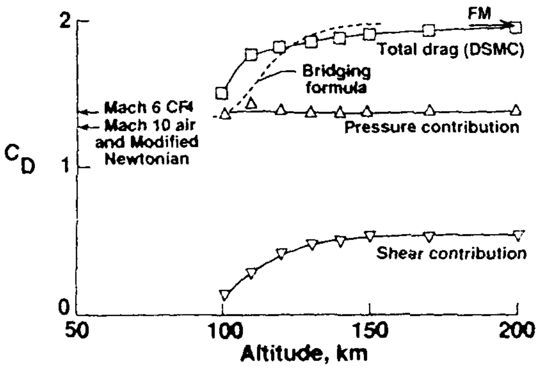

Fig. 17 Drag coefficient variation with altitude.

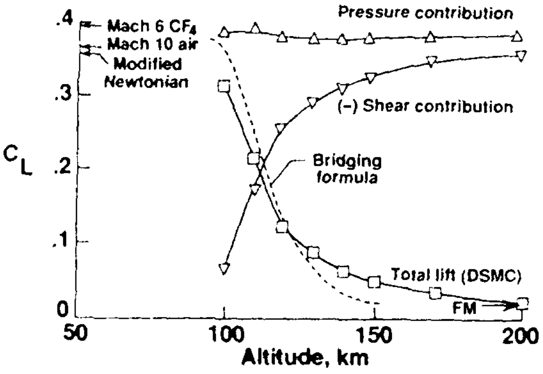

Fig. 18 Lift coefficient variation with altitude.

The overall aerodynamic coefficients (C_D= drag coefficient, and C_L= lift coefficient) are shown in Figures 17 and 18. The forces are normalized with respect to $1/2\ \rho_\infty\ U_\infty^2\ A_{ref}$ where ρ_∞ and U_∞ are the freestream density and velocity, respectively; and A_{ref}, the reference area, equals 14.1 m^2. Also shown in these figures are the calculated free-molecule (denoted by FM) and modified Newtonian results, and experimental wind-tunnel data. These experiments were conducted in the NASA Langley Research Center Mach 10 air and Mach 6 CF_4 (Freon) wind tunnels and are documented in the AFE Aerodynamics Data Base Update II (May 1989). The CF_4 results are believed to be more appropriate as the limiting continuum values because the specific heat ratio γ for air in flight is more closely approximated in wind-tunnel tests by CF_4 (γ=1.2) rather than by low-enthalpy air (γ=1.4). Calculations show that the DSMC results approach the free-molecule limit very slowly as the altitude increases but even at 200-km altitude the flow is not completely collisionless. The results of the Lockheed bridging formula, which empirically connects the axial and normal aerodynamic force coefficients using a sine-square function are also shown in Figs. 17 and 18. This bridging formula relies on the assumption that continuum and free-molecule flows are established at Knudsen numbers of 0.01 and 10, respectively (which corresponds to 95- and 155-km altitudes for the present calculations). These figures also show effects of pressure and shear contributions on the aerodynamic coefficients.

5.3 Flow About a Delta Wing

In this section, results obtained in Reference 5, for the study of a rarefied flow about a delta wing at incidence, are summarized. The aim of this investigation is to compare the computed results with recent experimental measurements of Reference 14. The delta wing considered in this study is highly-swept and is sketched in Fig. 19. It has a flat top, V-shaped bottom, and its edges are rounded with a constant radius. The nose looks elliptical from the side view although it appears sharp from the top view. The origin of the coordinate system is located at the tip of the nose. The x axis is parallel to the top surface and is normal to the base plane. The x-y plane at z=0 is a symmetry plane. The body-fitted grid consists of a total of 7840 cells, and Fig. 20 shows a perspective view for this three-dimensional cell structure.

The flow simulated in this study is a nitrogen wind-tunnel experiment conducted at the DLR in Göttingen, Germany.[14] In this experiment, the flow is produced by a freejet expansion, and gradients exist in the flow. However, the model is very small (4.86 mm) and the experimental data reduction procedures attempted to minimize the effects of the departure from parallel flow on the measured coefficients by using undisturbed freestream properties at the model 2/3-chord location. The freestream conditions used in the calculations are assumed to be uniform and correspond to the undisturbed flow quantities at the 2/3 chord location specified for the experiments. The freestream velocity and temperature are V_∞= 756 m/s and T_∞= 17.4 K, respectively. The body surface temperature is assumed to be at a uniform 293 K. The range of

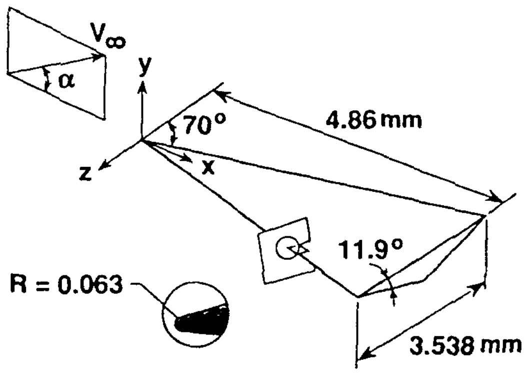

Fig. 19 Schematic of the delta wing (dimensions in mm).

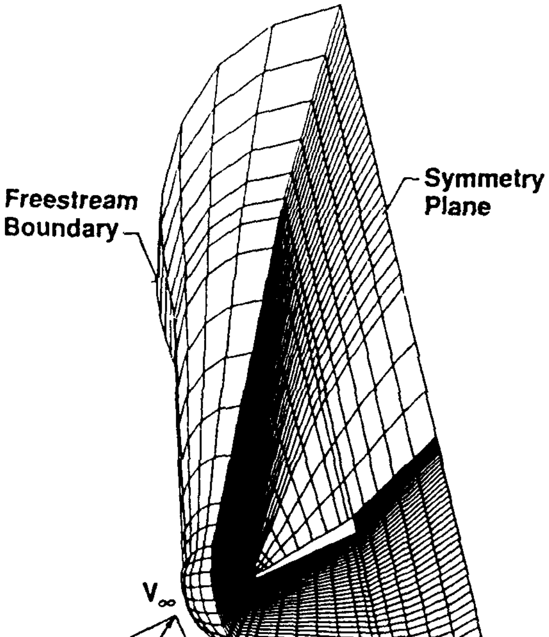

Fig. 20 Perspective view of three-dimensional computational grid.

conditions considered in the present study are such that most of the transitional flow regime is covered ($0.016 \leq Kn_\infty \leq 3.505$). Also, an angle-of-incidence, α, variation is considered for Kn_∞=0.389. The freestream mean free path (used in the definition of the overall Knudsen number) is evaluated using the VHS model with T_{ref}=300 K, d_{ref}=4.07x10^{-10}m, and the temperature exponent of the viscosity coefficient of 0.75. For this problem, a nonreacting gas model with one chemical species (N_2) is used in the simulations and energy exchange between translational and internal modes is considered.

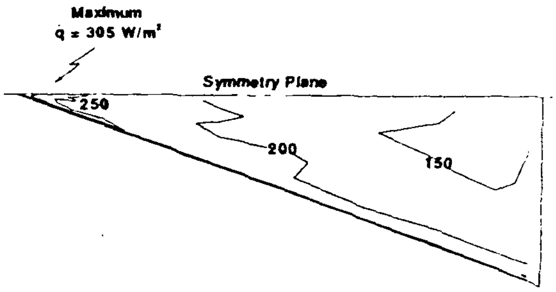

Fig. 21 Surface heat-transfer-rate contours (windward side, Kn_∞=0.389).

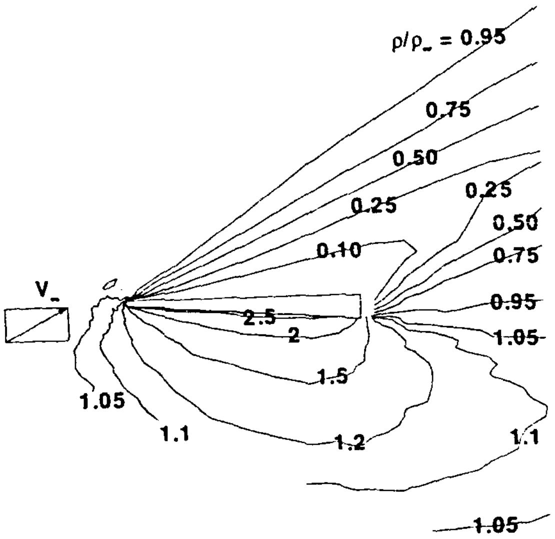

Fig. 22 Flowfield density contours near the symmetry plane (Kn_∞=0.389).

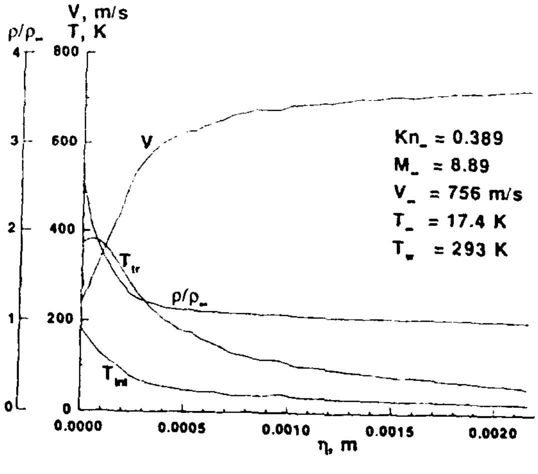

Fig. 23 Flowfield quantities along stagnation streamline.

Figures 21-28 show some of the time-averaged results obtained in this study. Figure 21 shows the surface heat-transfer-rate contours on the windward side. It should be noted that for this problem, the sharp V-shaped bottom and the two sides are

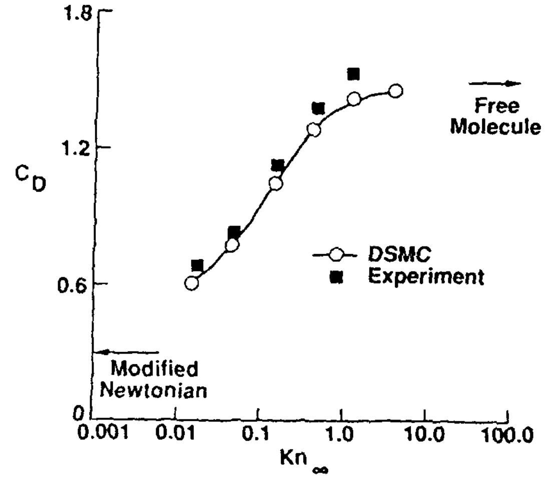

Fig. 24 Drag coefficient (α=30°).

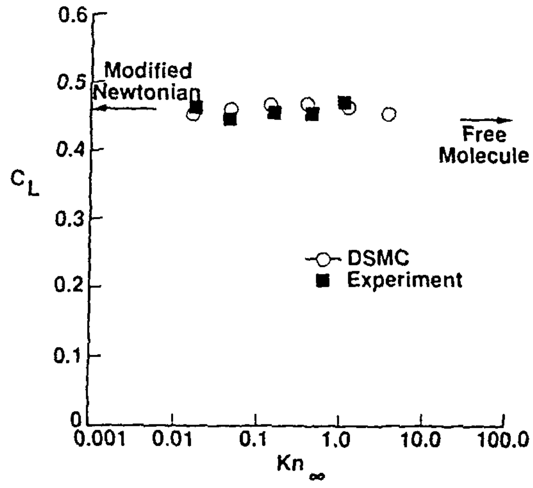

Fig. 25 Lift coefficient (α=30°).

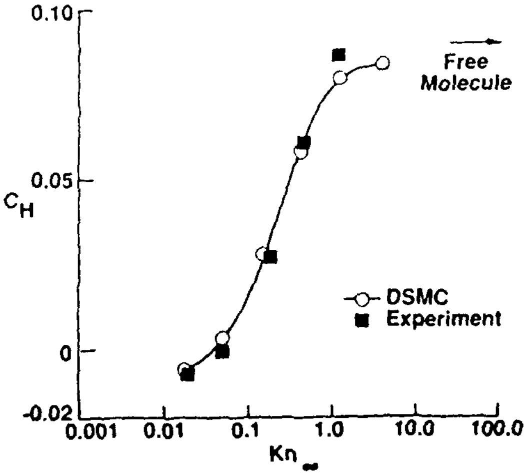

Fig. 26 Heat transfer coefficient (α=30°).

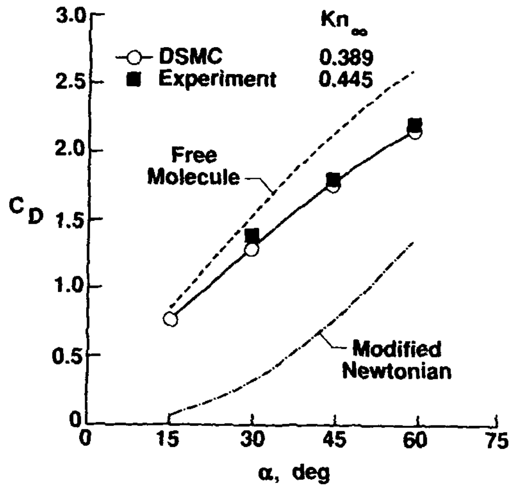

Fig. 27 Drag coefficien. variation with α.

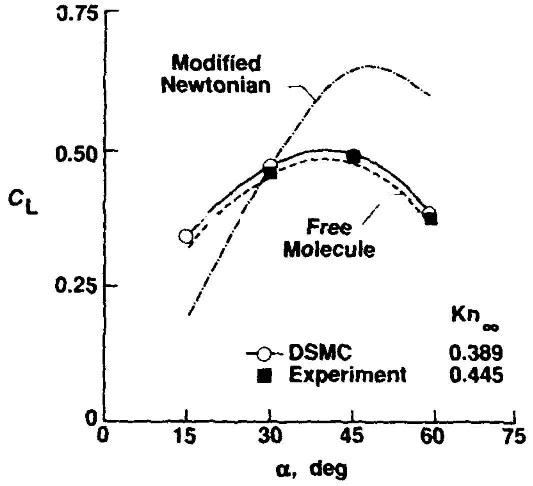

Fig. 28 Lift coefficient variation with α.

leading edges, and the high values for heat-transfer rate (and also pressure) are due to the leading edge effects. Figures 22 and 23 present the flowfield density contours and the distribution of some of the flowfield quantities along the stagnation streamline, respectively. These figures clearly show the characteristic features of rarefied flows, namely, a significant degree of thermal nonequilibrium, velocity slip, temperature jump, and no distinct shock wave structure with abrupt changes in the flowfield properties. The stagnation streamline in this figure is an approximate one in that it is generated by a straight line parallel to the freestream velocity vector passing through the point on the surface where the pressure and heat-transfer rate are maximum.

Figures 24-26 present the effects of the rarefaction on the aerodynamic coefficients. These calculations are performed by varying the freestream density and keeping the other freestream conditions constant. The drag and the lift coefficients are normalized with respect to $1/2\ \rho_\infty U_\infty^2 A_{ref}$ and the heat-transfer coefficient is normalized by $1/2\ \rho_\infty U_\infty^3 A_{ref}$ where A_{ref} is the planview area of the wing with a value of 8.6 mm^2 . In this study, calculations have been performed for various angles of incidence, too. Figures 27 and 28 present some of these results.

6. DISCUSSION

This paper concentrates on the simulation of the transitional flows, and is a part of ongoing research efforts for the application of the DSMC method to complicated three-dimensional configurations. The present computations have been performed using a general three-dimensional DSMC computer program written by G. A. Bird.

The first problem considered in this study, i.e. the flow about intersecting wedges, represents the first application of a general three-dimensional DSMC program at the NASA Langley Research Center. Therefore, in order to build confidence in the computational results, initially several test cases (explained in Reference 10), for which solutions are already known, have been investigated. After verifying the program using these test cases, the program has been applied to the intersecting-wedge problem. This study shows several interesting three-dimensional flow features when comparisons are made with the two-dimensional results. The flowfield structure and surface quantities resulting from the interaction of two wedges (inner streamwise strip) as compared to that well removed from the intersection (outer streamwise strip) have an analogous behavior similar to that observed between the two-dimensional wedge and axisymmetric cone results; i.e., the surface pressures and flow densities are higher, but the surface heat transfer and shear stresses are lower for the inner strip than those calculated for the outer strip. Similarly, the presence of the second wedge effectively increases the overall bluntness of the body, and hence, the disturbance field in front of the intersecting wedges is larger than that in front of a two-dimensional wedge. The calculations indicate that the three-dimensional results approach monotonically the two-dimensional wedge flow results in the spanwise direction. Also, dissociation increases as the altitude decreases and O, N, and NO concentrations are significant near the wedge intersection.

In the second problem, the three-dimensional flow about the AFE vehicle has been investigated. The results show that at high altitudes, distinct classes of molecules are present in the flowfield, namely, freestream molecules, surface-reflected molecules, and the ones that have undergone molecular collisions. Mixing these classes of molecules produces a highly nonequilibrium flow structure. Therefore, it is not possible to interpret properly the kinetic temperatures from the viewpoint of classical thermodynamics because these macroscopic properties are obtained by averaging over various classes of molecules whose distribution functions are separated widely in velocity space. As the altitude decreases, the intermolecular collisions begin to dominate and the nonequilibrium among the energy modes decreases. For example, for the 120-km case the maximum translational temperature is about 10 times the maximum internal temperature in the forebody portion of the domain, and this factor reduces to 3 for the 100-km case. Also, dissociation becomes important at 110-km and lower altitudes.

In the third problem, the calculated results show that, for the range of conditions considered, the flow is quite rarefied and there is no evidence of flow separation. The maximum density occurs downstream of the tip of the wing rather than at the tip. For the flow in the leeside, one finds no evidence of a shock along the symmetry plane for Knudsen numbers greater than 0.045. The density monotonically decreases from the value at the freestream to that adjacent to the top surface. For the cases where Knudsen numbers are less than 0.045, the results show signs of a shock which become stronger with decreasing Knudsen number. The aerodynamic coefficients presented in Figs. 24-26 show some interesting results. For an angle of incidence of 30-deg, the lift coefficient is quite insensitive to Knudsen number. This is due to the fact that the changes in the pressure and shear contributions are comparable in magnitude but opposite in sign. The impact on the drag coefficient is different, since the two contributions are additive. The overall heat transfer coefficient decreases with decreasing Knudsen number, and becomes negative for the smallest Knudsen number case. These results indicate that, as the freestream density increases, the fraction of energy content of the flow that reaches the wing surface decreases due to the collisions in the shock layer that divert molecules away from the body. Figures 27 and 28 indicate that, as the angle of attack decreases, the effective bluntness of the model is reduced (i.e. the flow is actually more rarefied for the lower incidence angles) and the DSMC results become closer to the free-molecular limits. The experimental data for this problem include two-component forces, overall heat-transfer rate and recovery temperature. For the range of conditions for which comparisons have been made, all the calculated results are within the estimated[14] overall experimental uncertainty of ± 8 percent. It is appropriate to note that these calculations were made and presented without prior knowledge of the experimental data as a part of Workshop on Hypersonic Flows for Reentry Problems, Part II, held in Antibes, France, in April 1991.

Finally, it should be mentioned that Bird[6] has recently developed a new set of "fast" general programs for the application of the DSMC method to rarefied flows with complex three-dimensional boundaries. His new programs are efficient in terms of the computational load and also in terms of the effort required to set up particular cases. The power of this new scheme has been illustrated by calculating the flow about the Shuttle Orbiter using a personal computer.[6] Recently further improvements have been implemented into this new scheme and it has been applied to a variety of flow problems.[15]

7. SUMMARY

This paper is a summary of present authors' work presented in more detail in References 5, 7, 10, 12 and references cited in them. The problems investigated in those studies focus on the simulation of three-dimensional rarefied flows using the direct simulation Monte Carlo method. The results obtained indicate the applicability of the DSMC method to complicated three-dimensional problems. The attempt here has been to provide an overview and hope that the reader will turn to those references for more detail.

8. REFERENCES

1. Bird, G.A., "Molecular Gas Dynamics", Clarendon Press, Oxford, England, 1976.
2. Meiburg, E., "Direct Simulation Techniques for the Boltzmann Equation", Rept. DFVLR-FB 85-13, Institut für Theoretische Strömungsmechanik der DFVLR, Göttingen, Germany, 1985.
3. Harvey, J.K., "Direct Simulation Monte Carlo Method and Comparison with Experiment", Progress in Astronautics and Aeronautics: Thermophysical Aspects of Re-entry Flows, Vol. 103, edited by J. N. Moss and C. D. Scott, AIAA, New York, 1986, pp. 25-43.
4. Erwin, D.A., Muntz, E.P., and Pham-Van-Diep, G., "A Review of Detailed Comparisons Between Experiments and DSMC Calculations in Nonequilibrium Flows", AIAA Paper 89-1883, June 1989.
5. Celenligil, M.C. and Moss, J.N., "Hypersonic Rarefied Flow About a Delta Wing – Direct Simulation and Comparison with Experiment", AIAA Paper 91-1315, June 1991.
6. Bird, G.A., "Application of the Direct *Simulation Method* to the Full Shuttle Geometry", AIAA Paper 90-1692, June 1990.
7. Celenligil, M.C., Moss, J.N., and Blanchard, R.C., "Three-Dimensional Rarefied Flow Simulations for the Aeroassist Flight Experiment Vehicle", AIAA Journal, Vol. 29, No. 1, January 1991, pp. 52-57.
8. Bird, G.A., "Monte-Carlo Simulation in an Engineering Context", AIAA Progress in Astronautics and Aeronautics: Rarefied Gas Dynamics, Vol. 74, Pt. 1, edited by Sam S. Fisher, AIAA, New York, 1981, pp. 239-255.
9. Borgnakke, C. and Larsen, P.S., "Statistical Collision Model for Monte Carlo Simulation of Polyatomic Gas Mixture", Journal of Computational Physics, Vol. 18, No. 4, 1975, pp. 405-420.
10. Celenligil, M.C., Bird, G.A., and Moss, J.N., "Direct Simulation of Three-Dimensional Hypersonic Flow About Intersecting Blunt Wedges", AIAA Journal, Vol. 27, No. 11, November 1989, pp. 1536-1542.
11. Jacchia, L.G., "Thermospheric Temperature, Density, and Composition: New Models", Smithsonian Astrophysical Observatory, Cambridge, MA, Special Rept.375, March 1977.
12. Celenligil, M.C., Moss, J.N., and Bird, G.A., "Direct Simulation of Three-Dimensional Flow About the AFE Vehicle at High Altitudes", AIAA Progress in Astronautics and Aeronautics: Rarefied Gas Dynamics: Theoretical and Computational Techniques, Vol. 118, edited by E. P. Muntz, D. P. Weaver, and D. H. Campbell, AIAA, Washington, DC, 1989, pp. 447-461.
13. Cheatwood, M.F., DeJarnette, F.R., and Hamilton, H.H. II, "Geometrical Description for a Proposed Aeroassist Flight Experiment Vehicle", NASA TM-87714, July 1986.
14. Legge, H., "Force and Heat Transfer Measurements on a Disc at 45°-90° Angle of Attack in Free Jet Flow Using Ar, He, N_2, H_2 as Test Gases", DFVLR-AVE Report Number IB 222-89.
15. Rault, D.F.G., "Aerodynamic Characteristics of a Hypersonic Viscous Optimized Waverider at High Altitude", AIAA Paper 92-0306.

Stability of Hypersonic Flow over a Blunt Body

Thorwald Herbert[1]
Department of Mechanical Engineering
The Ohio State University, Columbus, OH 43210-1107, USA

Vahid Esfahanian
DynaFlow, Inc., Columbus, OH 43221-0319, USA

Abstract

A numerical method has been developed to compute the axisymmetric flow over blunt slender bodies with high accuracy to enable reliable analysis of the stability properties. The flow field is obtained using the Beam-Warming method to solve the thin-layer Navier-Stokes equations. The code has been thoroughly validated and applied to compute the laminar flow over a long blunt cone with 7° half-angle at $M_\infty = 8$. The linear stability of this flow has been analyzed with highly accurate finite-difference and spectral methods. The results are compared with previous numerical studies and the experimental data of Stetson et al. [1].

1 Introduction

The projected design of vehicles for flight at hypersonic speeds has revived the interest in stability and transition in compressible boundary layers and shear layers. The stability of boundary layers at high supersonic Mach numbers previously has been studied for easily accessible prototype flows such as similarity solutions of the boundary-layer equations for the flow over a flat plate [2]. Detailed stability experiments have been performed by Stetson et al. [1,3] on sharp and blunt cones with different nose radii. Some of the observations on the effect of bluntness and the associated entropy layer are consistent with theoretical analysis such as the amplification rates of first-mode and second-mode disturbances for the sharp cone [4] and the qualitative effect of the entropy layer on the critical Reynolds number predicted by Khan & Reshotko [5]. Other features, however, such as the broader band of second-mode instability and the general amplification characteristics in the blunt-cone flow at nose radius $R_N = 0.15$ in. have not been explained by theoretical study.

The stability analysis of the flow over blunt, slender bodies at high Mach numbers faces three major problems:

- the computation of the basic flow field and the derivatives of the flow variables with sufficient accuracy,
- the formulation of the stability problem with proper account for the flow physics, and
- the accurate solution of the stability equations.

Traditionally, the flow over an "almost sharp" cone of small nose radius R_N is computed in two parts. The bow shock and the flow field around the nose are computed using the Navier-Stokes equations (NS) or the thin-layer approximation (TLNS). The computational domain typically extends to an arc length up to five times the nose radius, $s = S/R_N \leq 5$. The field downstream of this position is obtained by solving the parabolized Navier-Stokes equations (PNS). One rationale for this split is the high efficiency and low memory demand of marching schemes for parabolized equations. Another reason is the failure of NS and TLNS solvers to converge for larger domains.

Most numerical techniques and flow solvers for realistic configurations have been evaluated on the quality of the pressure and shear stress distributions along the body surface. However, the stability characteristics are governed by the overall flow field, in particular in the neighborhood of critical layers well inside or toward the edge of the boundary layer. PNS codes commonly used have the tendency to produce solutions with slow streamwise oscillations and "wiggles" normal to the surface. The wiggles originate from the need to suppress the negative characteristic speed in the subsonic region adjacent to the wall and are most pronounced in the pressure [6]. Considered that instability and transition occur far downstream, say for $s \geq 100$, the question immediately arises whether the computed solutions are accurate enough to obtain conclusive stability results. This concern has been emphasized by the U.S. Transition Study Group especially in context with the observed discrepancies between experimental and theoretical results for sharp and blunt cones at $M_\infty = 8$ [3,1,4,6] and the potential effects of the entropy layer on the critical Reynolds number and the transition point [5].

---

[1] President, DynaFlow, Inc.

Another important aspect at high Mach numbers is the large displacement thickness of the boundary layer which is $\mathcal{O}(M_\infty^2)$ larger than in incompressible flow and hence may extend over a significant part of the shock layer. It may be necessary to incorporate the boundary conditions at the shock instead of the usual asymptotic conditions at infinity (i.e. far outside the boundary layer) into the stability analysis.

Probably best developed are accurate solvers for the stability equations based on Runge-Kutta methods in combination with shooting techniques [7] or direct solution of the boundary-value problem with 4th-order compact finite difference [8] or spectral methods.

We have conducted an intense effort to clarify some of the open questions. Ironically, the development of an accurate TLNS code and the computation of the basic flow field have consumed an overwhelming share of the total resources, both human labor and computer time. In the following, we give an overview over selected topics.

2 The Benchmark Case

The goal of this study is the accurate computation and stability analysis of the flow over one of the sphere-cone combinations experimentally studied by Stetson et al. [1] with the following characteristics:

spherical nose of radius $R_N = 0.15$ in.
cone with half-angle $\theta_c = 7°$
maximum arc length $s = S/R_N \leq 250$
adiabatic wall
free-stream Mach number $M_\infty = 8.0$
free-stream temperature $T_\infty = 54.3$ K
Reynolds number $Re_\infty = \rho_\infty u_\infty R_N/\mu_\infty = 31250$
ratio of specific heats $\gamma = 1.4$
Sutherland's law of viscosity

We refer to these conditions as the **STDS case**. For comparison we have also analyzed the flow over a sharp cone by solving the Taylor-Maccoll equations with a fourth-order Runge-Kutta method for the same conditions with the following results:

$\theta_{shock} = 10.29649°$ $\quad M_c = 6.8369$
$P_c/P_\infty = 2.6025$ $\quad T_c/T_\infty = 1.3335$
$\rho_c/\rho_\infty = 1.9516$ $\quad (S_c - S_\infty)/R = 0.050864$
$u_c/u_\infty = 0.97953$ $\quad v_c/u_\infty = 0.12027$

where the index c indicates conical conditions, u, v are the velocities along and normal to the axis of the body, respectively, and R is the gas constant. Recently, Simen & Dallmann [9] have presented a TLNS solution for the sharp cone and results on the stability of the flow.

At first glance, one would not expect any significant effect of the small bluntness on the flow field far downstream. However, the detached bow shock of a priori unknown shape makes not only the flowfield computation a more intricate task but causes the shock angle and the strength of the shock to vary from the normal-shock state at the tip to some asymptotic state far downstream. Streamlines that pass through the curved shock in the nose region form a layer of relatively high vorticity, the *entropy layer*, that envelops the body. The viscous boundary layer develops inside this entropy layer which causes a continuous streamwise change of the edge conditions for the boundary layer. Moreover, the gradients $(\partial p/\partial y)_e$ of the pressure and $(\partial u/\partial y)_e$ of the velocity component along the wall do not vanish at the boundary edge (index e) and violate the assumptions of the classical boundary-layer theory. The thickness of the entropy layer increases with the nose radius but decreases along the body as shown in figure 1. Even for small bluntness, the streamlines near the body "remember" the bow shock. Eventually, the entropy layer is swallowed by the boundary at some *swallowing distance* far downstream.

Another important interaction in hypersonic flows is the displacement effect of the boundary layer since the displacement thickness is of the order $\delta/s = \mathcal{O}(M_\infty^2/\sqrt{Re})$ which is by a factor of M_∞^2 larger than its low-speed counterpart. The relatively large outward deflection of the streamlines causes a given body shape to appear much thicker. This new "effective" body shape changes the outer inviscid flow which in turn feeds back on the growth of the boundary layer. This *Mach wave interaction* or *pressure interaction* has been analyzed by Burggraf [10] based on matched asymptotic expansions.

To obtain quantitative information on the various flow features and detailed flow quantities of the benchmark case for a stability analysis, we have employed computational methods.

2.1 Numerical Method for the Basic Flow

The numerical solution of the Navier-Stokes equations at high Reynolds numbers requires a large number of grid points near, as well as along, the body surface to resolve the viscous terms in the boundary layer. For the long body considered here, the narrow spacing along the surface proves to be computationally unnecessarily expensive. At the Reynolds numbers of concern, one can use the thin-layer (TLNS) approximation, i.e. neglect all viscous derivatives in the ξ-direction along the body based on the arguments of the boundary-layer theory. The thin-layer approximation requires high Reynolds number and grid lines to conform to the body. Yet unlike boundary-layer theory, it allows for a normal pressure gradient and requires no matching conditions Unlike the parabolized Navier-Stokes (PNS) approximation, the thin-layer approximation allows for upstream influence in the subsonic region through the pressure term and does not require suppressing the negative characteristic speed in this region as the PNS approximation. As a further advantage over the PNS approach for blunt-body applications, numerical solutions based on the thin-layer concept are self-starting. A disadvantage of the thin-layer model is the higher computational demand that appears acceptable for a small set of benchmark computations.

The implicit factored finite-difference scheme of Beam & Warming [11] is employed to solve the thin-layer Navier-Stokes equations. The detailed derivations of the equations and the numerical algorithms are given in [12,13,14]. A shock fitting procedure is used to obtain an accurate solution in the vicinity of the shock wave. The shock and wall boundary conditions are treated explicitly while the plane of symmetry and outflow conditions are treated implicitly. Billig's correlation [15] is used for an initial shock shape to start the computation.

2.2 Geometry and Grid

With R_N as the reference length, the tangency point of spherical nose and cone frustrum is given by $x_t = 1 - \sin\theta_c$, $y_t = \cos\theta_c$. The Cartesian body coordinates (x_b, y_b) are for $x_b \leq x_t$ given by $x_b = 1 - \cos(s)$, $y_b = \sin(s)$, and for $x_b > x_t$ by $x_b = x_t + (s - \pi/2 + \theta_c)\cos\theta_c$, $y_b = y_t + (x_b - x_t)\tan\theta_c$. where s is the nondimensional arc length along the body. An algebraic grid in the ξ, η plane is used to compute the flow field. The lines of constant ξ are straight lines orthogonal to the body and distributed nearly uniformly along the body surface. The orthogonality is convenient because the solution will be used for the stability analysis. Some adjustment of the grid points in ξ was necessary to match the stations used in the experiments of Stetson et al. For viscous computations, the lines of constant η are clustered near the body surface according to [16,17]

$$\frac{x - x_b}{x_s - x_b} = \frac{y - y_b}{y_s - y_b} = a$$

where (x_s, y_s) are the Cartesian coordinates of the shock, and

$$a = 1 + \beta\frac{1 - \tilde{a}^{(1-\eta/\eta_{max})}}{1 + \tilde{a}^{(1-\eta/\eta_{max})}}, \quad \tilde{a} = \frac{\beta + 1}{\beta - 1}$$

where β is the clustering parameter.

In general the ξ-direction is neither aligned with the streamline direction nor with the body surface. For a flat plate with Cartesian computational grid it can be shown that the thin-layer equations contain the boundary-layer equations. Blottner [18] pursued this issue for an axisymmetric body with orthogonal surface coordinates. He concluded that the thin-layer Navier-Stokes equations neglect longitudinal curvature terms that occur in the second-order boundary-layer theory. In addition, the thin-layer equations include terms involving the second coefficient of viscosity that are of higher order in the boundary-layer theory and usually unimportant.

2.3 Optimization and Verification

The code has been thoroughly verified by comparison with the Navier-Stokes solution for the flow over a hemisphere-cylinder at $M_\infty = 2.94$ by Viviand & Ghazzi [19], a standard case for code verification [12,20,21]. This test case was utilized to analyze the sensitivity of the solution to the number of grid points, the choice of the clustering parameter β at fixed CFL, and the explicit numerical dissipation ϵ_E which was usually set equal to the time step $\Delta\tau$. Details of this comparison have been reported elsewhere [14,22]. Small deviations from the Navier-Stokes solution were observed at the nose and in the immediate neighborhood of the junction where longitudinal curvature terms are important. No undesirable oscillations of the flow field could be detected by use of sensitive visualization techniques.

Comparative studies were also performed for the nose region $s \leq 12$ of the benchmark case. The cases analyzed are listed in table 1. The benchmark case is considerably less sensitive to grid resolution and clustering parameter than the hemisphere-cylinder at lower M_∞ even near the sphere-cone junction, as shown by the temperature distributions for cases III and V in figure 2. At $s = 12$, between 45 and 105 grid points are located inside the boundary layer.

The code is fully vectorized for high performance on the Cray Y-MP. Vectorization, however, increases the memory demand considerably. Since large runs require all the available 64Mwords of memory which are normally shared by eight processors, an autotasking version was produced to exploit parallel processors. In comparison to the single-processor version, the use of four and eight processors reduced the wall-clock time to 62% and 50%, respectively.

2.4 Results and Comparisons with Experiment

Two major cases are considered for the Stetson et al. experiment [1], one with 1300×100 grid points (grid I) and the other with 1300×200 grid points (grid II). For both grids, the clustering parameter β is equal to 1.01. The run histories for these two cases are given in Ref. [14]. The total computation time on a single processor is about 60 hours for Grid I and 260 hours for Grid II on the CRAY Y-MP of the Ohio Supercomputer Center.

Figure 3 shows the sonic line near the nose region for the benchmark case. The shape of the sonic line is very important in blunt-body problems. It is evident from the figure that in the absence of a boundary layer the sonic-line slope is in the upstream direction at the body surface. In general, its slope can be in either direction depending on the free-stream Mach number [23,25]. For large Mach numbers, the slope is upstream which implies that left-running characteristics emanating from the body surface downstream of the sonic point cannot intersect the sonic line, and therefore, cannot influence the upstream flow. Physically, this means for a given large M_∞, the forebody pressure cannot be influenced by body changes downstream of the sonic point.

The comparison of the surface pressure with experimental data and the Taylor-Maccoll solution for an equivalent sharp cone is shown in Figure 4. The blunt-cone wall pressure is slightly higher than that of the inviscid sharp cone because of the displacement effect of the boundary layer. It is important to notice that the pressure initially overexpands with respect to the asymptotic afterbody pressure and very slowly approaches the pressure of the conical flow from below.

Figure 5 shows the comparison of the wall temperature with the experiment. The maximum discrepancy between the computed absolute wall temperature and the measured one is about 15%. It seems the adiabatic wall condition is not a good approximation to the experimental wall condition. Stetson described the wall to be in equilibrium conditions and close to adiabatic [1]. Taking the actual wall temperature to be 85% of the adiabatic wall temperature as a boundary condition appears more realistic. In general, surface pressure, shock shape, and velocity profile are not very sensitive to wall temperature conditions. However, this may not be true for the stability characteristics of these profiles.

Velocity profiles at station 228 are given in Figures 6. The solid lines correspond to the component of velocity parallel to the wall. The comparison is fairly good, especially near the edge of the boundary layer. The probe for measuring the velocities in the experiment was relatively large and caused significant interference near the surface[1].

The variation of pressure, velocity, temperature, and Mach number profiles at different stations have been investigated in detail (see Ref. [14]). We found that at stations upstream of $s = 74$ the velocity and temperature profiles are not typical supersonic profiles even though the Mach number outside of the boundary layer exceeds 5. The entropy layer produced by the curved shock is still thick enough to envelop the boundary layer, as shown by the pressure profiles in figures 7 and 8. Downstream of station 74 all the profiles are similar to the corresponding sharp cone profiles, though not the same.

Figure 9 shows the computed shock shape to compare very well with the experimental shock shape which was obtained from a schlieren picture provided by K. F. Stetson. Also shown is Billig's correlation which compares well only near the nose of the body and diverges widely far downstream from both computed and measured values. Although Billig's correlation requires the shock to approach the correct slope far downstream, this requirement does not necessarily place the shock wave at the correct distance from the wall. The poor quality of this correlation as an initial guess for computations s is in fact one of the reasons for the failure of TLNS codes at larger s.

The effect of grid refinement on the Mach number profile at station $s = 175$ is illustrated in Figure 10. At these far-downstream stations where the shock-layer thickness is relatively large, the solutions for the two grids I and II are basically the same except the coarse grid (Grid I) produces an overshoot in most of the profiles at the boundary-layer edge for the stations above $s \geq 121$. The overshoot at the boundary-layer edge seems to be caused by a small numerical shock oscillation due to the lack of grid resolution near the shock. In addition, the sharp changes of the flow properties at the boundary-layer edge which are typical of hypersonic boundary layers, require a fine grid near the edge. The computational results suggest that a clustering parameter of 1.015 or 1.02 may be a better choice for both grids.

2.5 Shock-Shape Inflection

A significant difference between the shock wave on sharp and blunt cones, aside from the expected detached shock wave at the nose of the blunt cone, is the inflection in the shock shape which occurs several tip diameters downstream from the blunted nose. Bertram [24] has shown the inflection in the shock shape for a truncated cone experimentally. Because of the existence of compression waves arising from the overexpanded type of pressure distribution one would expect to find inflection points in the main shock over a blunted cone [25]. Figure 11 shows the shock angle versus s together with the corresponding inviscid sharp-cone shock angle. The inflection point in the shock shape is at station 66. The shock angle at this station is 9.4313°.

---

[1] K. F. Stetson, personal communication.

2.6 Derivatives

Since the stability characteristics of a flow are not only governed by the natural flow variables but also their derivatives, especially in the neighborhood of critical layers, we have verified that the derivatives appearing in the stability equations are accurately resolved. The fourth-order compact finite-difference method suggested by Malik [8] introduces additional differentiation. Therefore, derivatives up to the third have been checked and found satisfactory as shown in figures 12 for M. An exception is the pressure which shows some inaccuracy of the second and higher derivatives near the wall and the edge of the boundary-layer, as shown in figure 13. These derivatives are originally absent from the stability equations that are directly solved by spectral methods but are introduced by the compact finite-difference formulation.

3 Linear Stability Analysis

The linear stability equations were developed in the traditional way referring to the same coordinate system as the basic-flow computation. In contrast to previous work, we maintained all terms, including those arising from longitudinal and transverse curvature. Careful attention has been paid to the slight difference of the coordinate system and associated velocity components from the usual streamwise coordinate parallel to the wall. The flow angularity, the orientation of the velocity vector with respect to the cone, is less than 4°, and its maximum occurs near the shock. The flow angularity is negative near the wall on the cone frustrum. The streamwise variation of the basic flow has been neglected under the parallel-flow assumption.

3.1 Outer Boundary Conditions

We have considered three types of boundary conditions:

- homogeneous boundary conditions as $\eta \rightarrow \infty$,
- asymptotic boundary conditions at some finite distance from the wall, and
- boundary conditions at the shock based on the linearized Rankine-Hugoniot conditions.

Detailed studies on the implementation of shock boundary conditions into the traditional local stability analysis have been conducted for the flow over a 5° wedge (similarity solution). A typical result for the temporal growth rate is shown in figure 14. The effect of different boundary conditions has been found to be small, except at very small wave numbers. In the region of significant amplification, the growth rates of both oblique first modes and two-dimensional second modes is unaffected by the choice of the outer boundary conditions. Similar results have been obtained for the flow over the blunt cone. It is clear, however, that the local stability analysis cannot accommodate the disturbance propagation along characteristics and hence may not capture the correct physics.

3.2 Numerical Stability Analysis

The stability equations have been solved with both spectral and compact methods for prototype flows to validate the stability codes. For the spectral method, the physical domain $\eta \in [0, \eta_s]$ is mapped to the spectral domain $z \in [1, -1]$ by the transformation $z = (a - b\eta)/(a + b\eta)$ while various grid-point distributions have been applied with the finite-difference method. The programs provide for analysis of temporal or spatial growth. Some of our conclusions as to the utility of various methods at high Mach numbers disagree with those of Malik [8]. We have repeated his spatial eigenvalue calculation for an adiabatic flat plate at $M_e = 4.5$, $Re = 1500$, $T_e = 121°K$ with $\omega = 0.23$ and $\beta = 0$. The results in table 2 show excellent convergence of our spectral method.

3.3 Stability Results

The systematic stability analysis of the benchmark flow is at this time still incomplete, especially the critical Reynolds number has not yet been calculated. We restrict the discussion to the results for the second mode at station 175 where $Re = 2338.53$, $\eta_s = 152.3$. The basic-flow conditions before and after the shock are obtained from the numerical solution. The results for the spatial amplification rate versus the frequency of the second mode is shown in figure 15 together with the experimental results [1] and numerical results of Malik et al. [6]. The wave number $\alpha_r = 0.21$ at the frequency of maximum amplification corresponds to a wavelength twice that of the boundary-layer thickness, $\lambda \approx 2\delta$, as observed by Stetson et al. The maximum growth rate, however, is significantly different from the observed value, and the band width of instability is much narrower, similar to that observed in the sharp-cone experiments [3].

The discrepancy between our numerical results and those of Ref. [8] is significant and of the same order as the difference to sharp-cone results [4]. The disagreement is both in the maximum amplification and the associated frequency. It is unclear whether the discrepancy arises from inaccuracies of the PNS approach in providing the basic flow or in the truncated stability equations . Traditional transition criteria like the e^N method integrate these amplification rates to arrive at a transition Reynolds number [26]. The accumulation of differences leads to results unacceptable for the design of advanced flight vehicles.

4 Conclusions

The thin-layer Navier-Stokes equations were numerically solved for flow at Mach 8 past a 7° half-angle blunted cone. Some conclusions regarding these computations are as follows:

- In the current state, CFD is capable of producing numerical solutions of the Navier-Stokes equations suitable as basic flow for stability analysis.
- The present method of solution for the basic flow is not feasible for practical use in engineering, because of the computational resources required. Our computations establish a benchmark solution to measure the quality of codes currently in use or in development with regard to flow field and stability analysis. Such a code comparison has been proposed as a high priority task by the U.S. Transition Study Group.
- The computational demand is caused by the large number of grid points required for accurate results in combination with slow convergence which arises from two main sources. First, the shock shape is not known prior to the computation, requiring that one of the boundary conditions be found as part of the computation. This can be improved by solving the shock wave boundary conditions implicitly rather than explicitly. Second, we noticed that after the shock wave reaches a "reasonable shape", the maximum error occurs at the outflow boundary where linear extrapolation was used. Linear extrapolation is not valid below the sonic line where the flow is subsonic. Improved convergence might result if the pressure is assumed constant in the subsonic region of the boundary layer at the outflow boundary and is equal to the pressure where the flow is sonic. This assumption is consistent with boundary-layer and characteristic theory.
- Computational results indicate that the flow field becomes qualitatively similar to that of the sharp cone after station $s = 74$. The quantitative differences may affect the flow stability characteristic.
- For routine calculations, it appears necessary to replace the low-order methods currently in use by higher-order, e.g. Hermitean, methods that would improve both the approximation to the flow field as well as the derivatives needed.
- The methods of stability analysis (under the parallel-flow assumption) seem to converge to a picture that is different from that experimentally observed. It is highly desirable to compare in detail the high-accuracy studies for blunt and sharp cones with respect to basic flow and disturbance properties to establish a sound base of stability results.
- In spite of the improved accuracy of the basic flow, stability formulation, and solution of the stability problem, we have not yet found the key to the observed differences in the stability characteristics of the flow over sharp and blunt cones.

It appears all to easy to blame the disagreement on experimental conditions such as the wind tunnel noise (which was present in both sharp and blunt cone experiments). The deviation of the thermodynamic properties in the experiment from those assumed in the computation may contribute some differences. The receptivity of the flow in the two geometries may be drastically different yet is completely ignored in the stability analysis. Moreover, the locally parallel stability theory does not properly account for the propagation of information at high supersonic speeds where the boundary layer occupies a significant part of the shock layer. Since the physical mechanism of the second-mode instability is insufficiently known, the effect of approximations is difficult to estimate.

Independent experiments on the same configuration, perhaps in a "quiet" wind tunnel, would be valuable. On the analytical side, we are in the process of applying the parabolized stability equations (PSE) [27,28,29,30] to model flows at high Mach number. The PSE approach accounts correctly for the propagation of information in convectively unstable flows and permits studies of linear stability characteristics, secondary instabilities, nonlinear mode interaction, and breakdown in streamwise varying flows. Even if the mystery of the blunt-cone results of Stetson et al. may be hidden in the experimental procedures or in some unknown receptivity phenomenon associated with the detached shock, the highly accurate basic flow in combination with the PSE analysis of stability will provide a measure for our capabilities to quantitatively analyze stability and transition at high Mach numbers.

5 Acknowledgment

We acknowledge helpful discussions and suggestions by T. H. Pulliam, J. L. Steger, D. Chaussee and L. B. Schiff at NASA Ames, T. Hsieh at the Naval Surface Weapons Center, and K. F. Stetson at the WPAFB Flight Dynamics Laboratory. This work has been supported by the Air Force Office of Scientific Research under Contracts F49620-87-K-0005 and F49620-88-C-0082. The basic-flow computations have been performed with the Cray Y-MP8/864 of the Ohio Supercomputer Center.

References

[1] Stetson K. F., Thompson, E. R., Donaldson, J. C., and Siler, L. G., "Laminar boundary layer stability experiments on a cone at Mach 8. Part 2 : blunt cone," AIAA Paper 84-0006, January 1984.

[2] Mack, L. M., "Boundary-layer linear stability theory" AGARD Report No. 709, Paper 3, 1984.

[3] Stetson, K. F., Thompson, E. R., and Donaldson. J. C. "Laminar boundary layer stability experiments on a cone at Mach 8. Part 1: Sharp cone," AIAA Paper No. 83-1761, 1983.

[4] Mack, L. M., "Boundary-layer stability analysis for sharp cones at zero angle of attack," AFWAL TR-86-3022, 1986.

[5] Khan, M. M. S. and Reshotko, E., "Stability of the laminar boundary layer on a blunted plate in supersonic flow," in: *Laminar-Turbulent Transition*, Eds. R. Eppler and H. Fasel, Springer-Verlag 1980.

[6] Malik, M. R., Spall, R. E., and Chang, C.-L. "Effect of nose bluntness on boundary layer stability and transition," AIAA Paper No. 90-0112, 1990.

[7] Mack, L. M., "Computation of the stability of the laminar boundary layer" in: *Methods in Computational Physics*, Eds. B. Alder, S. Fernbach, and M. Rotenberg, Vol. 4, 1965, pp. 247-299, Academic Press.

[8] Malik, M. R., "Numerical methods for hypersonic boundary layer stability," *J. Comp. Phys.*, Vol. 86, pp. 376-413, 1990.

[9] Simen, M. and Dallmann, U., "On the instability of hypersonic flow past a pointed cone - comparison of theoretical and experimental results at Mach 8," DLR-FB 92-02, 1992.

[10] Burggraf O. R. "Choice of boundary conditions in viscous interaction theory," *AIAA J.*, vol. 4, 1966, pp. 1145–1146.

[11] Beam R. M. and Warming R. F. "An implicit factored scheme for the compressible Navier-Stokes equations," *AIAA J.*, vol. 16, 1978, pp. 393–402.

[12] Kutler P., Chakravarthy S. R., and Lombard C. D., "Supersonic flow over ablated nosetip using an unsteady implicit numerical procedure," AIAA Paper 78-213, January 1978.

[13] Hsieh T., "Heat transfer calculation for hypersonic flow over a spherical blunt noses using an unsteady implicit scheme," In *Proceedings of the Second National Symposium on the Numerical Methods in Heat Transfer*, Hemisphere, Washington D.C., 1982, pp. 375–401.

[14] Esfahanian, V., "Computation and stability analysis of laminar flow over a blunted cone in hypersonic flow," *Ph.D. Thesis*, The Ohio State University, Columbus, Ohio, March 1991.

[15] Billig F. S. "Shock-wave shapes around spherical and cylindrical nosed bodies," *J. Spacecraft*, vol. 4, 1967, pp. 822–823.

[16] Tannehill J. C., Holst T. L., and Rakich J. V., "Numerical computation of two-dimensional viscous blunt body flows with an impinging shock," AIAA Paper 75-154, January 1975.

[17] Anderson, D. A., Tannehill, J. C., and Pletcher, R. H., *Computational Fluid Mechanics and Heat Transfer*, Hemisphere Publishing, New York, 1984.

[18] Blottner, F. G., "Significance of the thin-layer Navier-Stokes approximation," In *Proceedings of a Symposium on Numerical and Physical Aspect of Aerodynamic Flows III*, Editor: T. Cebeci, Springer-Verlag, New York, 1985, pp. 184-197.

[19] Viviand, H. and Ghazzi, W., "Numerical solution of the navier-stokes equations at high reynolds numbers with application to the blunt body problem," In *Lecture Notes in Physics, No. 59, Proceedings of the Fifth International Conference on Numerical Methods in Fluid Dynamics*, Springer-Verlag, 1976, pp. 434-439.

[20] Hsieh, T., "Calculation of viscous hypersonic flow over a severely indented nosetip," *AIAA J.*, vol. 7, 1984, pp. 935-941.

[21] Müller, B., "Vectorization of the implicit Beam and Warming scheme," in: "Notes on Numerical Fluid Mechanics," vol. 8, Vectorization of Computer Program with Applications to Computational Fluid Dynamics, ed. by W. Gentzsch, Vieweg Verlag, 1984, pp. 172-194.

[22] Esfahanian, V., Herbert, Th., and Burggraf, O. R., "Computation of laminar flow over a long slender axisymmetric blunted cone in hypersonic flow," AIAA Paper No. 92-0756, 1992.

[23] Hayes, W. D. and Probstein, R. F., *Hypersonic Flow Theory*, Academic Press, New York, 1959.

[24] Bertram, M. H., "The bluntness effects on cone pressure at $M = 6.85$," *J. Aero. Sci.*, vol. 23, 1956, pp. 898-900.

[25] Traugott, S. C., "Some features of supersonic and hypersonic flow about blunted cones," *J. Aero. Sci.*, vol. 29, 1962, pp. 389-399.

[26] Malik, M. R., "Stability for laminar flow control design," in: *Viscous Drag Reduction in Boundary Layers*, Progress in Astronautics and Aeronautics, Vol. 123, pp. 3-46, 1990.

[27] Herbert, Th. and Bertolotti, F. P., "Stability analysis of nonparallel boundary layers," *Bull. Am. Phys. Soc.*, Vol. 32, 1987, p. 2079.

[28] Bertolotti, F. P., Herbert, Th., and Spalart, P. R., "Linear and nonlinear stability of the Blasius boundary layer," *J. Fluid Mech.*, 1990, to appear.

[29] Herbert, Th., "Boundary-layer transition – analysis and prediction revisited," AIAA Paper No. 91-0737, 1991.

[30] Bertolotti, F. P. and Herbert, Th., "Analysis of the linear stability of compressible boundary layers using the PSE," *J. Theor. Comp. Fluid Mech.*, Vol. 3, 1991, pp. 117-124.

[31] Singh, D. J., Kumar, A., and Tiwari, S. N., "Effect of nose bluntness on flow field over slender bodies in hypersonic flows," AIAA Paper 89-0270, January 1989.

Case	I	II	II	IV	V
I_{max}	100	100	100	100	100
J_{max}	100	150	200	150	200
s_{max}	12	12	12	12	12
CFL	33.37	33.34	33.33	66.20	66.17
β	1.01	1.01	1.01	1.005	1.005
$10^6\Delta\tau$	590	395	296	444	333
$10^9\max(u_s)$	1.12	2.95	2.23	5.13	5.16
Iterations	14432	19956	28848	19890	26589
CPU Time	1496s	3072s	5858s	3016s	5408s

Table 1. Case descriptions.

J	Spectral Method		Compact Method	
	α_r	α_i	α_r	α_i
60 [8]	0.2534048	-0.0024921	0.2534120	-0.0024933
60	0.253441608	-0.00277438	0.253442014	-0.00277439
70	0.253441660	-0.00277439	0.253441795	-0.00277439
80	0.253441660	-0.00277439	0.253441702	-0.00277439

Table 2. Eigenvalues α obtained with different numbers $J+1$ of collocation points.

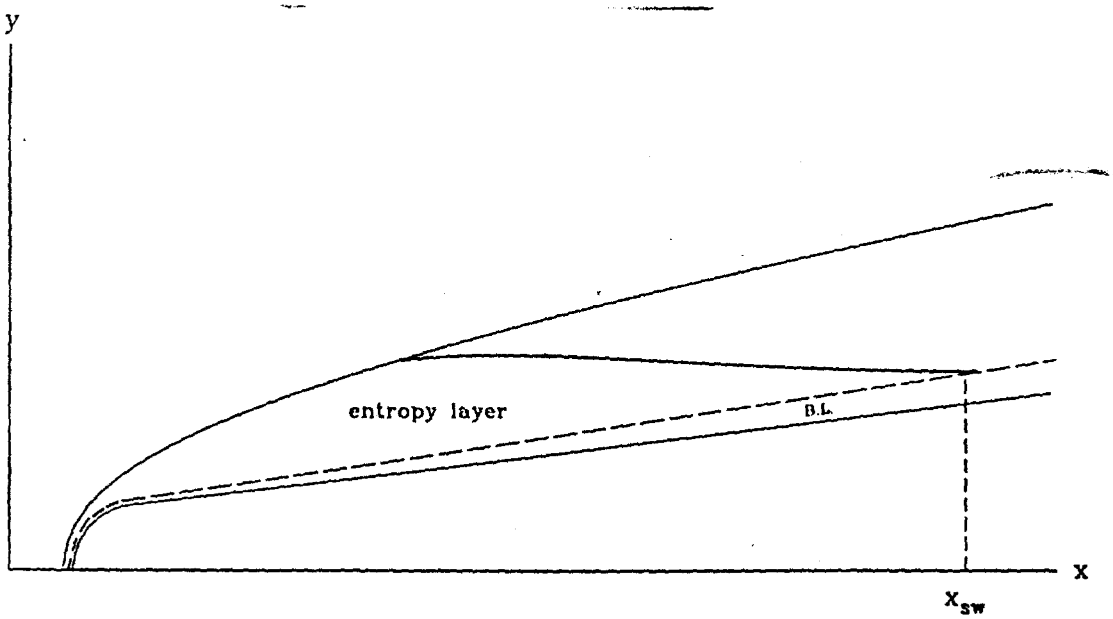
y
entropy layer
B.L.
x
X_{sw}

Figure 1: Physical model for hypersonic flow past a blunted cone (After Ref. [31])

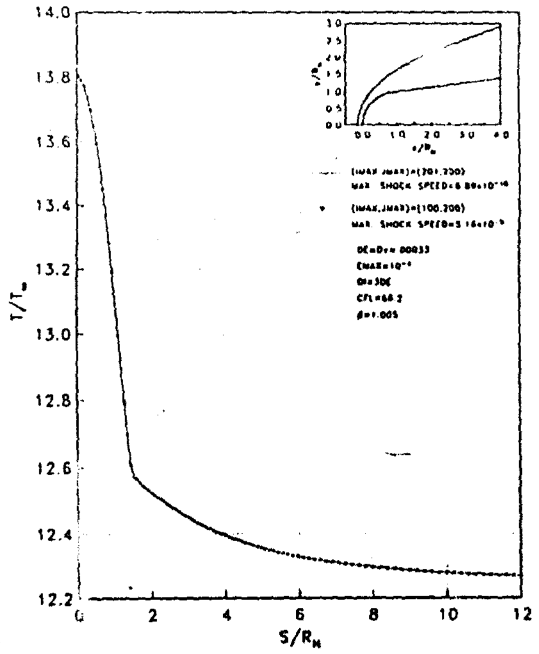

Figure 2. Surface temperature distribution.

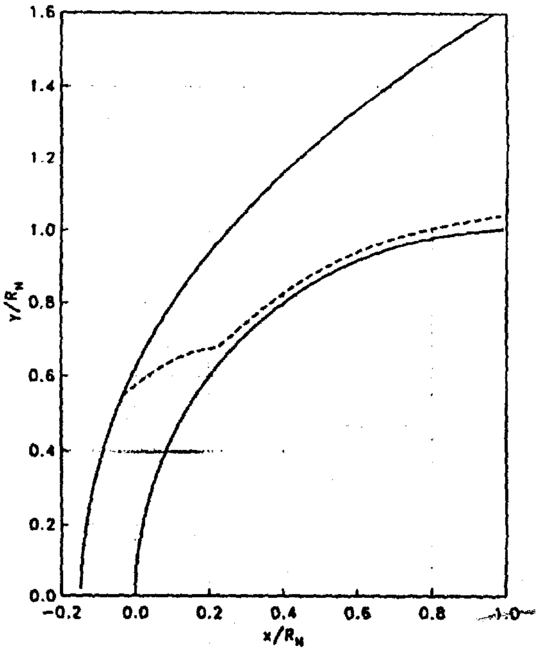

Figure 3. Sonic line between bow shock and body.

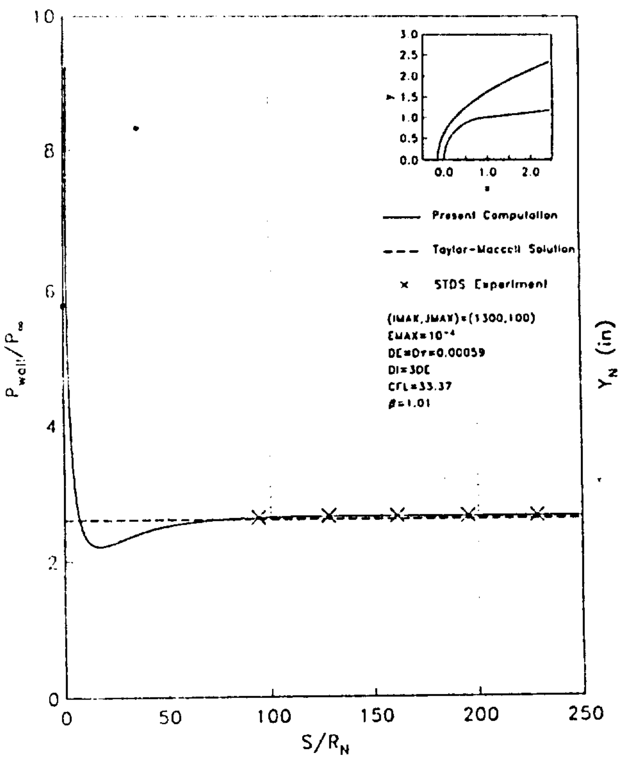

Figure 4: Comparison of surface pressure distributions.

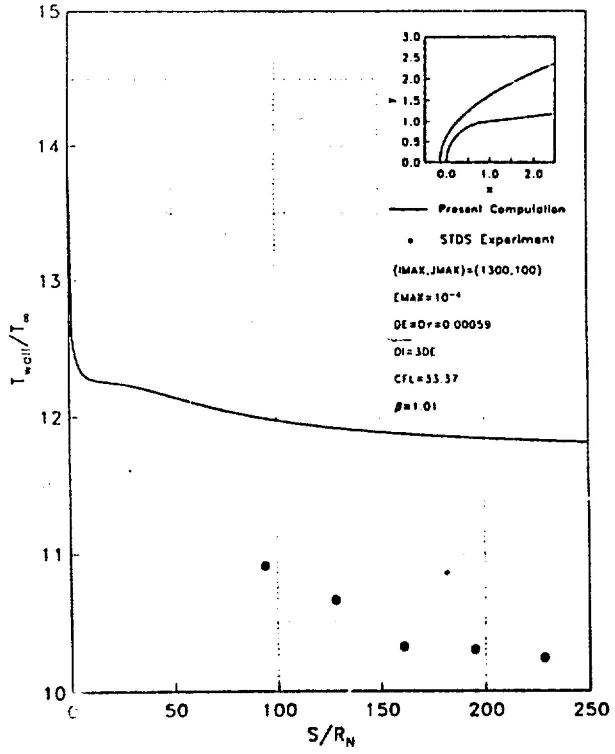

Figure 5: Comparison of surface temperature distribution.

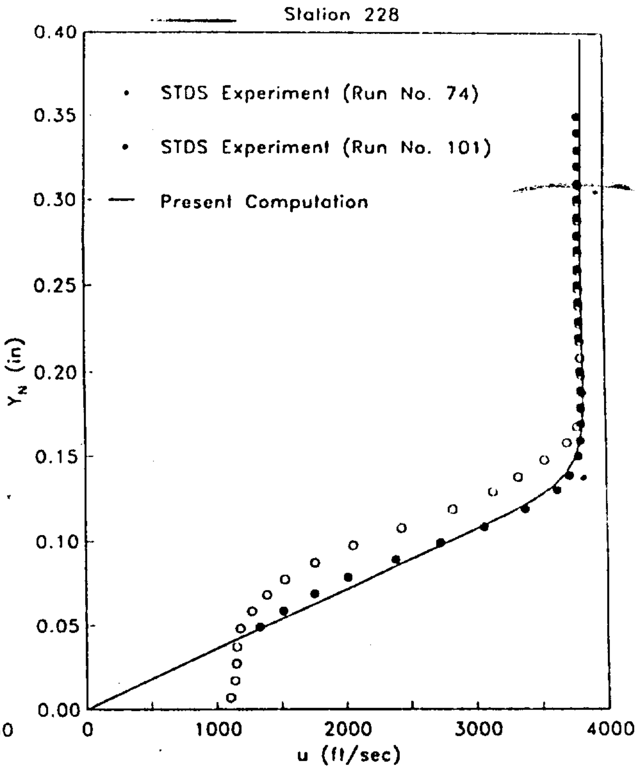

Figure 6: Measured and computed velocity profiles.

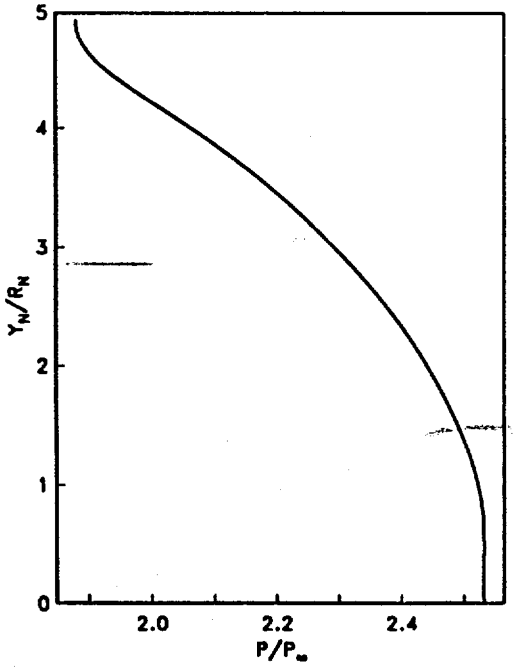

Figure 7: Pressure profile for stations $s = 54$.

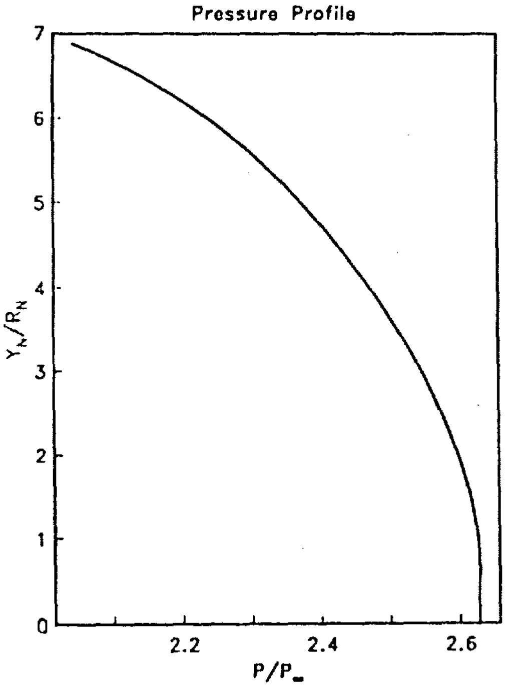

Figure 8: Pressure profile for stations $s = 94$.

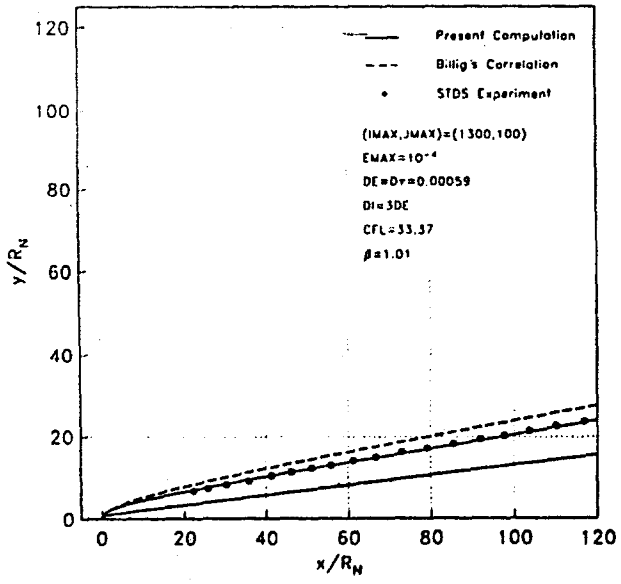

Figure 9: Shock shape comparison with the experiment and Billig's correlation.

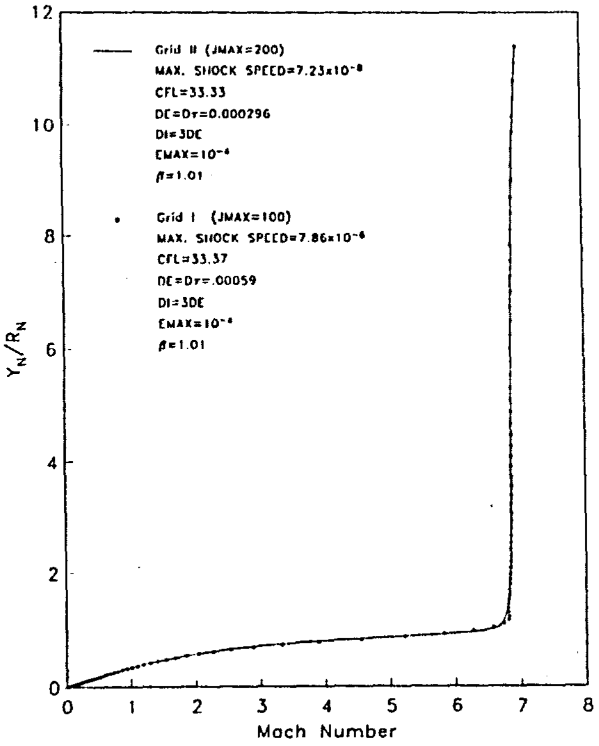

Figure 10: Effect of grid refinement on the Mach number profile at $s = 175$.

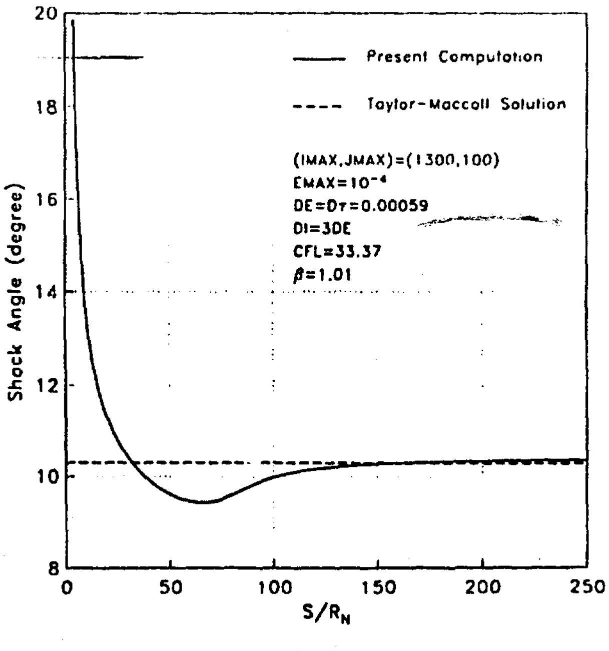

Figure 11: The shock angle along the arc length s.

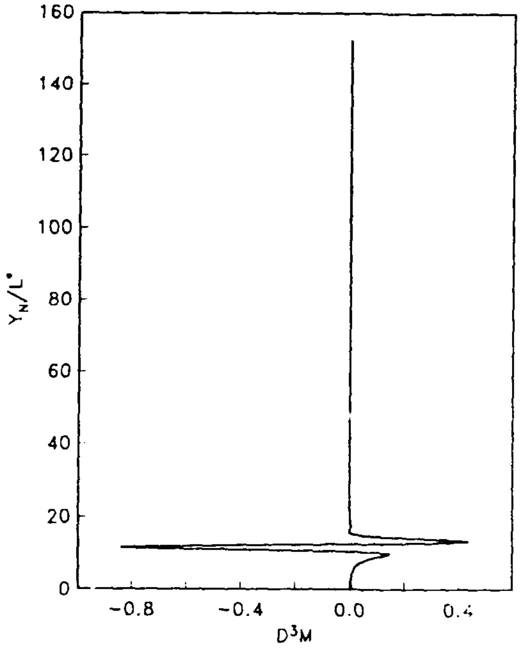

Figure 12: Third derivative of the Mach number profile.

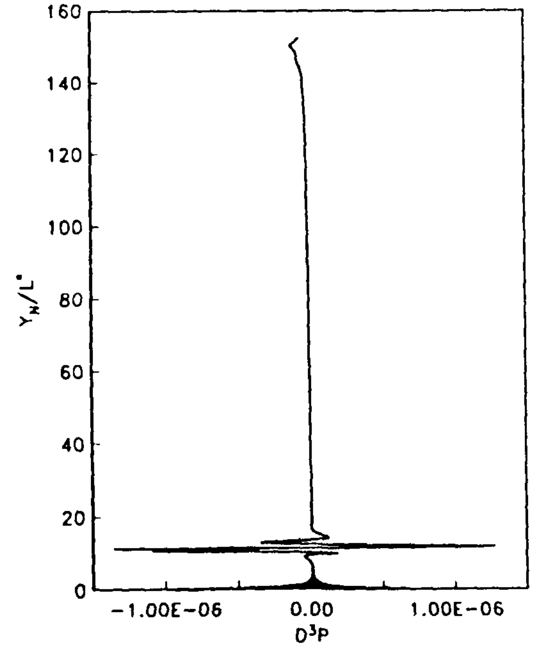

Figure 13: Third derivative of the pressure profile.

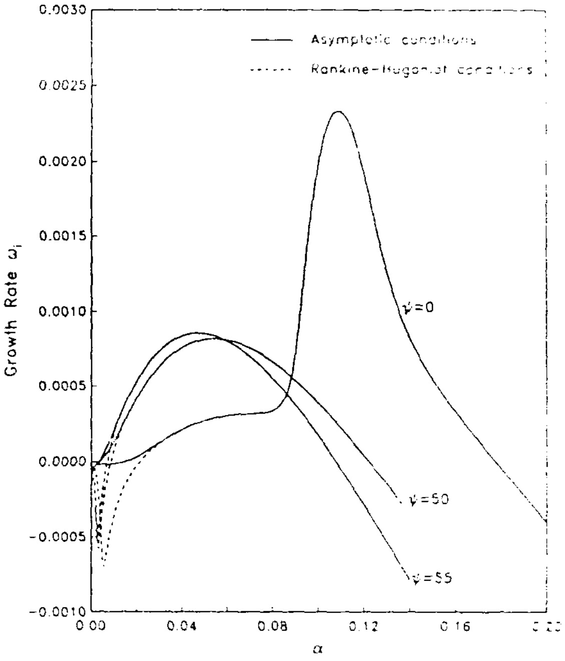

Figure 14: Temperal growth rate vs. wavenumber for a 5° wedge (adiabatic) at $M_\infty = 8$, $Re = 1558$. $T_\infty = 54.3°$, and $y_s = 159.5$.

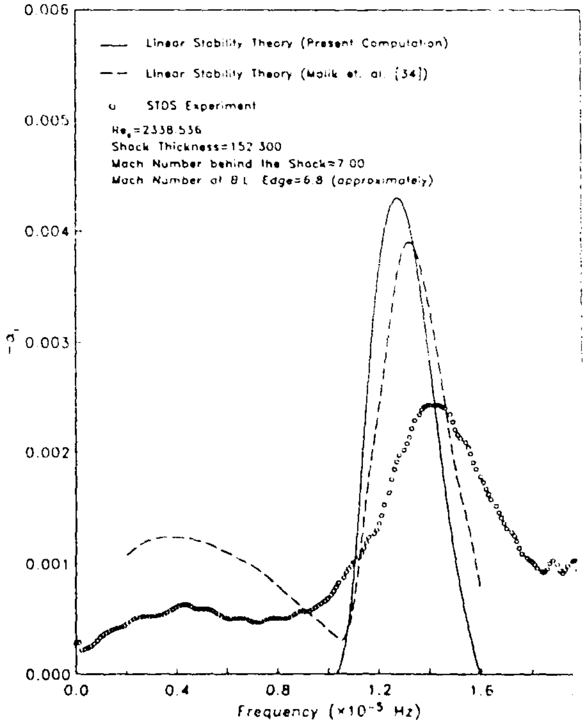

Figure 15: Comparison of measured and computed spatial growth rates at $s = 175$.

STABILITY OF HYPERSONIC BOUNDARY-LAYER FLOWS WITH CHEMISTRY

Helen L. Reed, Gregory K. Stuckert*, and Timothy S. Haynes
Mechanical and Aerospace Engineering
Arizona State University
Tempe, Arizona 85287-6106 U.S.A.

1. SUMMARY

The effects of nonequilibrium chemistry and three-dimensionality on the stability characteristics of hypersonic flows are discussed. In two-dimensional (2-D) and axisymmetric flows, the inclusion of chemistry causes a shift of the second mode of Mack to lower frequencies. This is found to be due to the increase in size of the region of relative supersonic flow because of the lower speeds of sound in the relatively cooler boundary layers. Although this shift in frequency is present in both the equilibrium and nonequilibrium air results, the equilibrium approximation predicts modes which are not observed in the nonequilibrium calculations (for the flight conditions considered). These modes are superpositions of incoming and outgoing unstable disturbances which travel supersonically relative to the boundary-layer edge velocity. Such solutions are possible because of the finite shock stand-off distance. Their corresponding wall-normal profiles exhibit an oscillatory behavior in the inviscid region between the boundary-layer edge and the bow shock.

For the examination of three-dimensional (3-D) effects, a rotating cone is used as a model of a swept wing. An increase of stagnation temperature is found to be only slightly stabilizing. The correlation of transition location (N = 9) with parameters describing the crossflow profile is discussed. Transition location does not correlate with the traditional crossflow Reynolds number. A new parameter that appears to correlate for boundary-layer flow has been found. A verification with experiments on a yawed cone is provided.

2. LIST OF SYMBOLS

A	$= Pr^{1/2} (\gamma - 1) M_e^2 / 2$
C^*	Chapman-Rubesin parameter based on T^*
C^*_{ad}	Chapman-Rubesin parameter based on T^*_{ad}
E_t	total energy of mixture per unit volume
h_1	$=1 + \kappa y$
h_3	$=(r + y \cos\theta)^m$
H	factor in R_{cf}(new) including compressibility
H_{cf}	$= \delta_{10} / y_{max}$; crossflow shape factor
i	square root of -1
J_i	molar flux of species *i*
L	factor in R_{cf}(new) including cooling
m	=0 for 2-D flow; =1 for axisymmetric flow
M	freestream Mach number
M_e	local edge Mach number with respect to a reference frame fixed to surface of rotating cone
M_r	local Mach number of basic state relative to velocity at generalized inflection points
M_∞	pre-shock Mach number
N	amplification factor
p	pressure; mixture pressure
Pr	Prandtl number at reference temperature T^*
q	general basic-state quantity
q_x, q_y, q_z	heat flux
q_0	general disturbance-amplitude distribution
q_1	general disturbance quantity
r	distance from body axis to surface
r	$= T_{w0} / T_{a0}$
R	Reynolds number based on local edge conditions and reference boundary-layer thickness
R_{cf}	$= W_{max}\delta_{10}/\nu$; crossflow Reynolds number
R_{cf}(new)	new crossflow Reynolds number, Eq. (1)
Re_L	Reynolds number based on a reference length
R_t	R at transition according to linear stability theory
R_0	R at x_0
S, S_{ij}	stress tensor
t	time
T	temperature
T_{ad}	local adiabatic wall temperature
T_{a0}	adiabatic wall temperature at upstream point x_0
T_e	edge temperature
T_{w0}	specified wall temperature at upstream point x_0
T_w	local wall temperature
T^*	~~referen~~ce temperature
T^*_{ad}	reference temperature for adiabatic wall
u,v,w	streamwise, normal-to-wall, spanwise velocity
U_e	local inviscid flow speed; for rotating cone, reference frame is fixed to the surface
W_{max}	maximum crossflow velocity, that is, velocity in direction perpendicular to local inviscid flow; for rotating cone, reference frame is fixed to surface
x,y,z	streamwise, normal-to-wall, spanwise coordinates
x_0	initial streamwise position for calculation of N; or upstream position for marching
y_{max}	height of W_{max} above wall
y_1	height of relative sonic point above wall
α	streamwise component of wavenumber
$-\alpha_I$	negative of imaginary part of α; spatial growth rate
β	spanwise component of wavenumber
β_I	imaginary part of β
δ	boundary-layer thickness
δ_{ad}	boundary-layer thickness for adiabatic wall
δ_{cool}	boundary-layer thickness for cooled wall
δ_{incomp}	boundary-layer thickness for incompressible constant-temperature flow
δ_r	$= (\mu_e x/\rho_e U_e)^{1/2}$; reference boundary-layer thickness
δ_{10}	height above y_{max} where crossflow is 10% W_{max}
γ	edge ratio of specific heats
γ_∞	pre-shock ratio of frozen specific heats
η	either a similarity or computational variable in

---

*Present address: DynaFlow, Inc., P.O. Box 21-319, Columbus, Ohio, 43221, U.S.A.

	normal-to-wall direction
κ	$= -d\theta / dx$
μ_e	edge dynamic viscosity
ν_e	edge kinematic viscosity
θ	angle between body surface and body axis
ρ	mixture mass density
ρ_e	edge density
σ_i	species *i* concentration to mixture mass density
τ	time variable in computational domain
ω	frequency of disturbance
Ω	cone rotational speed
ξ, η, ζ	streamwise, normal-to-wall, spanwise computational coordinates

3. INTRODUCTION

The skin-friction drag and heat-transfer rates of hypersonic vehicles can be reduced by delaying transition from laminar to turbulent flow. But the characteristics of transition at these speeds are not well known. Transition *is* known, however, to be highly dependent on the details of the flowfield.

Hypersonic flows are more complicated than incompressible flows for some of the following reasons. 1) At hypersonic speeds, the gas often cannot be modeled as perfect because the molecular species begin to dissociate due to aerodynamic heating. In fact, sometimes there are not enough intermolecular collisions to support local chemical equilibrium and a nonequilibrium-chemistry model must be used. 2) The bow shock is very close to the edge of the boundary layer and must be included in the calculations. 3) The wings are highly swept at hypersonic speeds in order to reduce wave drag. The boundary layers on these wings are consequently highly 3-D. All of these effects must be included in studies of transition.

Linear stability theory proves useful in determining the important effects and their trends. Here, the resultant growth or decay of small disturbances in the boundary layer which lead to transition is the measure of transition enhancement or delay. This paper reports the results of linear stability theory applied to chemically reacting flows with finite shock stand-off distance in Section 4 and 3-D flows in Section 5.

4. CHEMICALLY REACTING TWO-DIMENSIONAL BOUNDARY LAYERS (STUCKERT AND REED)

4.1 Numerical Approach

Qualitative as well as quantitative differences in the linear stability of the shock layer on a sharp cone can be observed when the effects of finite-rate chemical reactions are included. Here a five-component model for dissociated air is used: O_2, N_2, NO, N, and O. Only the effects of dissociation are considered; those of ionization are not. The mixture is also assumed to be one of ideal gases in thermal equilibrium.

The equations governing the flow of this reacting-gas mixture are originally expressed in the body-intrinsic coordinate system (i.e., Anderson et al., 1984). However, since the boundary layer occupies a substantial fraction of the shock layer at hypersonic speeds, these equations are transformed into a coordinate system where the basic-state bow shock is a boundary of the computational domain:

$$\partial(y_\eta Q)/\partial\tau + \partial(y_\eta E)/\partial\xi + \partial(-y_\tau Q - y_\xi E + F - y_\zeta G)/\partial\eta + \\ \partial(y_\eta G)/\partial\zeta + y_\eta H - y_\eta R = 0$$

where

$$Q = h_1 h_3 \{\rho, \rho u, \rho v, \rho w, E_t, \rho\sigma_i\}$$

$$E = E_I - E_V$$

$$E_I = h_3 \{\rho u, \rho u^2 + p/\gamma_\infty M_\infty^2, \rho uv, \rho uw, (E_t + p)u, \rho\sigma_i u\}$$

$$E_V = (h_3/Re_L)\{0, S_{xx}, S_{yx}, S_{zx}, \\ \gamma_\infty M_\infty^2 (uS_{xx} + vS_{yx} + wS_{zx}) - q_x, -j_{ix}\}$$

$$F = F_I - F_V$$

$$F_I = h_1 h_3 \{\rho v, \rho uv, \rho v^2 + p/\gamma_\infty M_\infty^2, \rho vw, (E_t + p)v, \rho\sigma_i v\}$$

$$F_V = (h_1 h_3/Re_L)\{0, S_{xy}, S_{yy}, S_{zy}, \\ \gamma_\infty M_\infty^2 (uS_{xy} + vS_{yy} + wS_{zy}) - q_y, -j_{iy}\}$$

$$G = G_I - G_V$$

$$G_I = h_1 \{\rho w, \rho uw, \rho vw, \rho w^2 + p/\gamma_\infty M_\infty^2, (E_t + p)w, \rho\sigma_i w\}$$

$$G_V = (h_1/Re_L)\{0, S_{xz}, S_{yz}, S_{zz}, \\ \gamma_\infty M_\infty^2 (uS_{xz} + vS_{yz} + wS_{zz}) - q_z, -j_{iz}\}$$

$$H = H_I - H_V$$

$$H_I = \{0, \kappa h_3 \rho uv - mh_1 (\rho w^2 + p/\gamma_\infty M_\infty^2)\sin\theta, \\ -\kappa h_3 (\rho u^2 + p/\gamma_\infty M_\infty^2) - mh_1 (\rho w^2 + p/\gamma_\infty M_\infty^2)\cos\theta, \\ mh_1 \rho w (u\sin\theta + v\cos\theta), 0, 0\}$$

$$H_V = \{0, \kappa h_3 S_{xy} - mh_1 S_{zz}\sin\theta, -\kappa h_3 S_{xx} - mh_1 S_{zz}\cos\theta, \\ mh_1 (S_{xz}\sin\theta + S_{yz}\cos\theta), 0, 0\}$$

$$R = h_1 h_3 \{0, 0, 0, 0, 0, \text{Molar rate of production of species } i\}$$

(Note: E, F, G, H, Q, R are not in the List of Symbols.) The viscosity used to determine the viscous stress tensor S is computed using the mixture laws of Brokaw (1958). The translational thermal conductivity is computed similarly, whereas the internal thermal conductivity is determined as described in Hirschfelder (1957). The molar fluxes j_i are computed using the multicomponent diffusion model described by Curtiss & Hirschfelder (1949), but only diffusion due to concentration gradients is included - diffusion due to pressure and temperature gradients and body forces is not. Finally, the law of mass action is used to compute the molar rate of production of each species assuming that they participate in the elementary reactions:

$$O_2 + M \leftrightarrow O + O + M$$

$$N_2 + M \leftrightarrow N + N + M$$

$$N_2 + O \leftrightarrow NO + N$$

$$O + NO \leftrightarrow N + O_2$$

where M is a collision partner (any of the species present in the mixture) which transfers energy in a reaction.

The thermophysical data needed for the analysis have been taken from a variety of sources. Collision cross section data for the transport properties can be found in Biolsi & Biolsi (1983), Biolsi (1988), Capitelli & Devoto (1973), Capitelli &

Ficocelli (1972), Cubley & Mason (1975), Levin et al. (1987, 1988), Monchick (1959), and Yun & Mason (1962). Thermodynamic data have been taken from Blottner et al. (1971) and Jaffe (1987). Reaction-rate data can be found in Camac & Vaughan (1961), Wray (1962), Thielen & Roth (1986), Monat et al. (1978), and Hanson & Salimian (1984). Reverse reaction-rate constants are computed using the law of detailed balance to express them in terms of the forward-rate and equilibrium constants. For a complete description of the constitutive equations as well as detailed references for the thermophysical data, refer to Stuckert (1991).

4.1.1 Basic State

The basic state is computed using the Parabolized Navier-Stokes equations, which are obtained from those given above by neglecting viscous terms involving derivatives tangent to the body. (To simplify the analysis, this approximation is made in the body-intrinsic coordinate system before the equations are transformed into the shock-fit coordinate system.) The Beam-Warming algorithm (Beam & Warming, 1978) is used in conjunction with a shock-fitting scheme and the Vigneron technique (to suppress *departure* solutions) to solve these equations. This is an efficient implicit algorithm used to march the solution downstream from initial conditions generated here by assuming that the flow is approximately conical near the apex of a sharply pointed body. A stretching function is used to cluster grid points near the edge of the boundary layer - a location where the basic state varies rapidly and which also lies in the vicinity of the critical point of the disturbance state at hypersonic Mach numbers. No artificial dissipation is required for the simple geometry investigated here because there are no discontinuities embedded in the shock layer.

4.1.2 Linear Stability Theory

The linear stability analysis is performed by linearizing the complete Navier-Stokes equations about the basic state. The same basic-state shock-fit coordinate system is used (which is almost conical) and linearized inviscid shock jump conditions are imposed at the basic-state shock location. For a cone, $\kappa \equiv 0$, and so $h_1 \equiv 1$. Normal modes are assumed for the disturbance state variables q_1:

$$q_1 = q_0(\eta)\exp\{i(\alpha\xi + \beta\zeta - \omega\tau)\}$$

and the basic-state flow is assumed to satisfy $\partial q/\partial\xi \equiv 0$. (Note that the basic-state normal-velocity component is *not* set to zero; it is not zero in a conical flow.) The disturbances in velocity and temperature as well as species mass fluxes (i.e., noncatalytic wall) are zero at the surface. (For equilibrium air analyses, the disturbances are assumed to be in chemical equilibrium at the surface.) These homogeneous equations and boundary conditions represent an eigenvalue problem for the eigenvector $q_0(\eta)$. When α and β are specified, the eigenvalue is ω (temporal problem), and when β and ω are specified, the eigenvalue is α (spatial problem). In either case, the governing equations are first discretized using second-order central differences. The temporal problem is easy to analyze because it is linear in ω and hence can be solved using a globally convergent scheme such as the QZ algorithm (e.g., Golub & VanLoan, 1985). Inverse iteration and the Newton-Raphson method can be used to compute the eigenvector and solve the spatial eigenvalue problem.

4.2 Results

The particular case investigated is that of a 10° half-angle cone flying at 8100 m/s and zero angle of attack at an altitude of 60.96 km where the ambient temperature and pressure are 252.6K and $2.008\text{X}10^{-4}$ atmospheres, respectively. The Reynolds number based upon a reference length of 1m and these freestream conditions is 139,900. The atmosphere is considered to be 21% O_2 and 79% N_2 by volume, and the noncatalytic surface of the cone is kept at a constant temperature of 1200K. This is essentially the case considered by Prabhu et al. (1988) except that they assumed a different freestream composition of air. Also, there is no crossflow.

Due to the lack of space, only a couple of basic-state results pertinent to the stability analysis are presented here. It should be mentioned, though, that the boundary-layer edge Mach number is approximately 10 for the given pre-shock conditions. It is slightly lower for the perfect-gas analysis, and slightly higher for the equilibrium- and nonequilibrium-air analyses because the hotter perfect-gas boundary layer is more rarefied and hence thicker, displacing and compressing the external flow the greatest. For the same reason, the perfect-gas edge temperature is approximately 6.5 times the freestream temperature, whereas the equilibrium- and nonequilibrium-air edge temperatures are 6 times the freestream value.

One feature of the boundary layer important to linear stability is the *size* of the region where the disturbance is supersonic relative to the local basic state. A measure of this is

$$\int_0^{y_1} (M_r^2-1)^{1/2}\,dy$$

where M_r is the local Mach number of the basic state relative to the velocity at the generalized inflection points (those points where $\partial(\rho\partial u/\partial y)/\partial y = 0$). This integral is shown in Figure 1 (where x is measured in meters). Corresponding results from a perfect-gas boundary-layer similarity solution are shown for comparison. One can see from this figure that the perfect-gas similarity and PNS solutions yield very comparable results and that in both cases the values of the integrals are substantially less than the corresponding values for the equilibrium- and nonequilibrium-air boundary layers. As Mack (1969) has shown, this integral is closely related to the spacing between his higher inviscid modes; as an approximation, it is inversely proportional to it. The shift to lower frequencies of the most unstable second-mode disturbance when the effects of equilibrium-air chemistry are included has been seen by both Malik (1989) and Stuckert (1991). See Figure 2. The same shift in frequency is observed in the nonequilibrium case for precisely the same reason: the local relative Mach number is in general higher for the reacting-gas cases because the local velocity is almost the same, but the local speed of sound is lower in the colder boundary layers. These reacting-gas boundary layers are colder because some of the heat generated by viscous dissipation is used to dissociate the molecular oxygen and nitrogen.

The equilibrium-air boundary layer also exhibits a feature which is not seen in the perfect gas or the nonequilibrium-air boundary layer (at least for the present flight conditions). In particular, an equilibrium-air mode exists which is supersonic relative to the inviscid region of the shock layer. The eigenfunction for this disturbance is shown in Figure 3. The oscillatory behavior of the magnitude of the disturbance is due in part to the fact that the character of the disturbance-state equations changes when the Mach number of the disturbance is supersonic relative to the boundary-layer edge. It is also due to the fact that the shock stand-off distance is finite, so that solutions to the disturbance-state equations in the inviscid region of the shock layer are possible which do not decay as y becomes large. This is discussed in greater detail by Stuckert & Reed (1992).

5. THREE - DIMENSIONAL HIGH - SPEED BOUNDARY LAYERS (REED AND HAYNES)

5.1 Use of Simple Geometries to Model Three-Dimensional Boundary Layers

At hypersonic speeds, the wings of the vehicles are highly swept and the flow is highly 3-D. When a boundary-layer flow is fully 3-D, the stability and transition behavior is quite different from 2-D flows. Of particular interest are the stability characteristics of these 3-D flows where inviscid criteria may produce a stronger instability (crossflow instability) than the usual Tollmien-Schlichting waves. For a recent review of this subject, see Reed & Saric (1989).

Examples of other 3-D flows of practical interest include rotating cones, yawed cylinders and cones, corners, inlets, and rotating disks. It appears that all of these flows (including swept wings) exhibit the same rich variety of stability behavior that is generic to 3-D boundary layers. A consistent characteristic of the instabilities is the presence of streamwise vorticity within the shear layer.

In fact, in incompressible flow, for example, the experimental and analytical results of Kobayashi et al. (1983) on rotating cones have demonstrated that one can even *model* a swept wing or other more complicated geometry exhibiting crossflow instability by a simpler geometry and study the stability characteristics. Results obtained can thus be directly applied to other 3-D boundary layers. From simpler geometries such as the rotating cone, much of what is known about the flow over the swept wing has been learned.

5.2 Numerical Approach

To evaluate parameters quantifying stability characteristics, the linear stability of the flow over a rotating cone at zero incidence is examined (Figure 4). As mentioned above, this is a simple geometry that is often used very successfully in incompressible flow as a model for a swept wing. At very high speeds, where even the basic-state calculations are a problem, the simple geometry of the rotating cone becomes a suitable and valuable model to study the crossflow instability (Balakumar & Reed, 1991).

The governing boundary-layer equations for a compressible ideal-gas flow are solved in a body-oriented coordinate system. By varying the freestream Mach number, rotational speed, cone angle, and position on the cone, a wide parameter range of possible 3-D boundary layers can be studied and the various non-dimensional parameters associated with the crossflow profile are easily fixed (R, R_{cf}, H_{cf}, . . .). The details of the basic-state formulation and linear stability analysis are available in Balakumar & Reed (1991).

5.3 Previous Linear Stability Theory Results

Calculations were completed at different edge Mach numbers $M = 5.0$ and 8.0 and Reynolds numbers $R = 600, 1000, 2000, 3000$ for a cone of half angle 15° at a non-dimensional rotational speed of 0.375 by Balakumar & Reed (1991). To summarize, they ~~find~~ at all Mach numbers that the maximum amplified crossflow is nonstationary. There exist neutral and unstable stationary waves but the amplification rate is very small compared to the positive frequency.

At $M = 5.0$, for which the 2-D second mode has been observed to clearly dominate the first mode in the ~~flat-plate~~ boundary layer, they find a competition between the crossflow and second mode. At $R = 600$, the maximum amplification rate of the crossflow is higher than the maximum amplification rate of the 2-D second mode; see Figure 5 (from Balakumar & Reed, 1991). As Reynolds number increases, even though the amplification rate of the crossflow increases, it is eventually less than the maximum amplification of the second mode. As Mach number is increased, the second mode dominates earlier.

Further results show that the most unstable second mode in a 3-D boundary layer is actually oblique whereas the second mode in a 2-D boundary layer is 2-D; this is also shown in Figure 5 where the *2-D* direction is -16.2°. The most unstable second mode is inclined at 5° to the inviscid flow direction at $M = 5$ and is inclined at 9° at $M = 8$. However, the difference between the amplification rates in the most amplified direction and in the inviscid flow direction is small, on the order of 2%.

Cooling the wall does not affect the crossflow instability. For $M = 5$, Figure 6 (from Balakumar & Reed, 1991) shows the variation of the critical Reynolds number (at which an instability first appears) versus crossflow Reynolds number (achieved by varying rotational speed, a larger value corresponds to stronger three-dimensionality) for different wall conditions $r = T_{w0}/T_{a0} = 1.0, 0.8,$ and 0.5. As expected, the critical Reynolds number of the first mode increases and the critical Reynolds number of the second mode decreases with wall cooling and confirms the result that wall cooling stabilizes the first mode and destabilizes the second mode. However, for the first mode, it is seen that the critical Reynolds number decreases with increasing crossflow Reynolds number and at large crossflow Reynolds number, the critical Reynolds numbers all approach the same value regardless of the status of the boundary layer. This is observed for all Mach numbers and Reynolds numbers tested.

Similar results have been seen by Lekoudis (1980), Mack (1980), and Bushnell & Malik (1987).

5.4 Transition Prediction and Correlation Parameters

The state-of-the-art transition-prediction method still involves linear stability theory coupled with an e^N transition-prediction scheme (Mack, 1984; Poll, 1984) and is applied at all speeds (Bushnell et al., 1989). N is the result of the integration of the linear growth rate from the first neutral-stability point to a location somewhere downstream on the body. Thus e^N is the ratio of the amplitudes at the two points and the method correlates the transition Reynolds number with N.

Aside from the e^N method along with various modifications (e.g., Cebeci et al., 1988), several past investigators have identified non-dimensional parameters quantifying the characteristics of the crossflow instability for boundary-layer profiles and, in some cases, attempted to correlate these numbers with transition location. Some examples follow.

In subsonic flow, Owen & Randall (1952) introduced a crossflow Reynolds number $R_{cf} = W_{max}\delta_{10}/\nu_e$ as the governing parameter and suggested that transition occurs when the crossflow Reynolds number becomes equal to 175. Pfenninger (1977) used crossflow shape factor $H_{cf} = y_{max}/\delta_{10}$ and crossflow Reynolds number in the design of supercritical airfoils. Dagenhart (1981) then considered stationary crossflow vortices and, instead of solving the linear-stability equations each time, he used a table lookup of growth rates based on the profile characteristics: crossflow shape factor and crossflow Reynolds number. He reported that he could adequately reproduce the results of the more complicated stability codes while using less than 2% of the computer time.

In supersonic flow, Chapman (1961) and Pate (1978) made similar conclusions that crossflow Reynolds number correlates well with transition location. On a yawed cone, King (1991) found that there was no correlation with the traditional crossflow Reynolds number. However, when he reformulated this parameter to include both compressibility and yawed-cone geometry effects, he found a good correlation for both his and Stetson's (1982) data.

5.4.1 Numerical Approach

With the current interest in high-speed flight, there is also a keen desire to determine correlating parameters, *based purely on basic-state profiles*, that can be easily incorporated into existing basic-state codes and will *accurately* predict transition location (or trends) for crossflow-dominated problems. To evaluate parameters quantifying stability characteristics, the linear stability of the flow over a rotating cone at zero incidence is again examined. Results are then applied to available experimental data on other geometries.

Locally, for a given frequency, the maximum growth rate $-\alpha_I$ is found and β_I=0. Then, the amplification factor N is determined by integrating the growth rate in the streamwise direction x from the Branch I location x_0. With the Reynolds numbers at x_0 and x being R_0 and R, respectively,

$$N = -2\int_{R_0}^{R} \alpha_I \, dR.$$

To evaluate transition location, all possible frequencies are sampled to determine where each individual disturbance achieves N = 9. The most upstream of this locus of streamwise locations is deemed the estimated transition location. The values of other parameters characterizing crossflow may then be evaluated against the results of N = 9.

5.4.2 Compressibility Effects

White (1974) points out that to estimate the boundary-layer thickness for a flat plate, one should consider the similarity variable so that

$$\delta R / x = \int_0^{\eta(\delta)} (T/T_e)\, d\eta$$

Extending this to a more general situation, a 3-D compressible boundary layer, δ, should thicken with respect to the corresponding incompressible layer, δ_{incomp}, as

$$\delta / \delta_{incomp} = \int_0^{\eta(\delta)} (T/T_e)\, d\eta \,/\, \eta$$

The quantity, δ_{incomp}, is a constant-temperature incompressible value. The estimated thickness then of a cooled-wall boundary layer, δ_{cool}, to that of an adiabatic wall, δ_{ad}, is (White 1974, Reed & Haynes 1992).

$$\delta_{cool} / \delta_{ad} = (C^* / C^*_{ad})^{1/2}\,(3.279 + 1.721\,[T_w / T_{ad}]\,[1 + A] + 0.664\,A) / (5 + 2.385\,A)$$

where

$$A = Pr^{1/2}\,(\gamma - 1)\,M_e^2/2$$

$$C^* = (T^* / T_e)^{1/2}\,(1 + 110.4 / T_e) / ([T^* / T_e] + 110.4 / T_e)$$

$$C^*_{ad} = (T^*_{ad} / T_e)^{1/2}\,(1 + 110.4 / T_e) / ([T^*_{ad} / T_e] + 110.4 / T_e)$$

$$T^* / T_e = 0.5 + 0.5\,T_w / T_e + A / 6$$

$$T^*_{ad} / T_e = 0.5 + 0.5\,(1 + A) + A / 6$$

and the Chapman-Rubesin parameter is approximated as a constant C* across the boundary layer. Because the incompressible crossflow Reynolds number correlates reasonably well for incompressible flows, a new general definition for R_{cf}, then, is

$$R_{cf}(new) = H\,L\,R_{cf} = H\,L\,W_{max}\,\delta_{10} / \nu_e \qquad (1)$$

where

$$H = \eta(\delta_{10}) \Big/ \int_0^{\eta(\delta_{10})} (T/T_e)\, d\eta$$

$$L = (C^* / C^*_{ad})^{1/2}\,(3.279 + 1.721\,[T_w / T_{ad}]\,[1 + A] + 0.664\,A) / (5 + 2.385\,A)$$

and all temperatures are in K and $\eta(\delta_{10})$ is the value of η at δ_{10}. The quantity δ_{10} has been scaled back to an incompressible value with the inclusion of the new factor H.

To compensate for a cooled wall, then, the factor L is used. Note that, because one is taking the ratio of two normal-to-the-wall lengths, the new factor H is easily computed no matter what the scaling is for the normal-to-the-wall coordinate. Note also that $R_{cf}(\text{new})$ reduces to R_{cf} for incompressible, adiabatic-wall flows.

5.4.3 Results

Using the traditional crossflow Reynolds number and shape factor

$$R_{cf} = W_{max}\, \delta_{10} / \nu \qquad (2)$$

$$H_{cf} = y_{max} / \delta_{10},$$

Figure 7 shows the attempt at transition correlations for an upstream Mach number of M = 3 and various cone angles θ, rotational speeds Ω, and wall and freestream temperatures T_w and T_e. The various flow conditions represented are documented in Table 1. The spread in R_{cf} is on the order of 200% and is therefore not useful for design. Figure 8 shows the same data plotted considering transition Reynolds number R_t versus rotational speed Ω (with increasing Ω implying increasing 3-D effects). Cooling is only slightly stabilizing (see also Lekoudis 1980, Mack 1980, Bushnell & Malik 1987, and Balakumar & Reed 1991) and an increase of stagnation temperature has an even smaller stabilizing effect. Even so, these temperature effects produce large changes in R_{cf}.

Table 1 Rotating-cone configurations for M = 3

Set	Fixed Parameters	Varied Parameters and Range
I	Ω=0.375 T_e=70K adiabatic wall	θ from 10° to 35°
II	Ω=0.25 T_e=70K adiabatic wall	θ from 10° to 20°
III	θ=15° T_e=70K adiabatic wall	Ω from 0.1 to 0.8
IV	θ=15° T_e=260K adiabatic wall	Ω from 0.1 to 0.8
V	Ω=0.375 T_e=260K adiabatic wall	θ from 10° to 35°
VI	θ=15° T_e=70K cooled wall	Ω from 0.1 to 0.8
VII	θ=15° T_e=260K cooled wall	Ω from 0.4 to 0.8

Table 2 shows comparative results for upstream freestream Mach numbers of M = 0.01, 3, and 6 for different freestream-temperature (T_e) and surface-temperature (T_w/T_e) conditions and a wide variety of rotating-cone geometries. The Mach 3 (M = 3) conditions correspond to those in Figure 7 and Table 1. The results of the new definition for crossflow Reynolds number with compressibility effects included, $R_{cf}(\text{new})$ [Eq. (1)], are contrasted with those obtained from the traditional definition, R_{cf} [Eq. (2)]. Also included is the maximum crossflow velocity in $\%U_e$; the significance of this should become apparent in the subsequent discussion.

Figure 9 shows all the rotating-cone data from Table 2 for M = 0 and 3 plotted. There appears to be a relationship between maximum crossflow velocity and the new crossflow Reynolds number, Eq. (1), proposed above. Also, the new compressible values are consistent with the incompressible value.

Table 2

M	M_e	T_e(K)	T_w/T_e	R_{cf}	R_{cf}(new)	W_{max}/U_e(%)
.01	.01	300	1	165	165	5.9
3	3.1	70	2.6	241	119	3.2
3	3.2	70	2.7	311	149	4.5
3	3.4	70	2.9	373	170	5.7
3	3.6	70	3.2	409	175	6.1
3	3.8	70	3.5	428	171	6.1
3	3.1	260	2.5	210	107	2.6
3	3.1	260	2.6	263	132	3.6
3	3.2	260	2.7	316	154	4.8
3	3.4	260	2.9	366	168	5.9
3	3.7	260	3.2	388	166	6.1
3	3.9	260	3.5	400	161	6.0
3	3.2	70	1.5	339	177	4.6
3	3.3	70	1.5	354	179	5.5
3	3.6	70	1.5	354	168	6.1
3	3.8	70	1.5	344	155	6.1
3	4.1	70	1.5	332	140	5.8
3	4.2	260	1.5	448	201	5.6
3	3.8	260	1.5	323	156	6.0
3	4.1	260	1.5	310	142	5.7
6	9.2	70	14.8	2483	255	5.0
6	9.2	260	17.1	2176	217	5.0
6	7.4	70	9.7	2101	309	6.1
6	7.3	70	4.4	1442	247	6.1

Because linear stability theory with N = 9 applied to a rotating cone was used to find this trend, it is important to verify it against experimental data. The most reliable, available, high-speed 3-D transition data to these authors' knowledge is that of King (1991) on the yawed cone in the Mach 3.5 Quiet Tunnel at NASA/Langley. The King experiment was on a 5° half-angle cone yawed at 0.6°, 2°, and 4°. The data of transition locations for various freestream conditions, both quiet and noisy, are documented in King (1991).

Later, King provided the present authors with the computational mean-flow profiles he used in the analysis of his experimental results. Applying the traditional crossflow Reynolds number, Eq. (2), gives values ranging from 80 to 640 for quiet conditions and 60 to 560 for noisy conditions. King found a correlation for his data when both a geometry and compressibility correction were applied. The new parameter proposed in the present paper contains no geometry factor explicitly. Applying the new crossflow Reynolds number, Eq. (1), to these same profiles results in Figure 10.

King (1991) also considered the M = 5.9 experiments of Stetson (1982) on a 8° half-angle cone yawed at 1°, 2°, and 4° and again provided the present authors with the mean-flow profiles he used in the evaluation of this experiment. Considering what Stetson terms as the beginning of transition and applying Eq. (2) gives values ranging from 140 to 780. The results, then, of applying the new crossflow Reynolds number, Eq. (1), to these profiles are also found in Figure 10. The surface of Stetson's cone was cooled, the wall of King's cone was adiabatic. The Stetson data were taken with a noisy freestream.

The trends of the three sets of data in Figure 10 suggest a least squares fit for the correlation of $R_{cf}(\text{new})$ and W_{max}:

Quiet (M=3.5)

$$R_{cf}(\text{new}) = 26.7 + 38.0\, W_{max}/U_e$$

Noisy (M=3.5)

$$R_{cf}(\text{new}) = 14.7 + 33.9\, W_{max}/U_e$$

Noisy (M=5.9)

$$R_{cf}(\text{new}) = 26.5 + 25.2\, W_{max}/U_e$$

where W_{max}/U_e is in %. The three curves are plotted in Figure 11. Below the curves, the flow has not undergone transition. The values of $R_{cf}(\text{new})$ are consistent with the incompressible values found in the literature. It is also surprising that the Stetson data agrees so well with the King noisy data.

6. CONCLUSIONS

The effects of nonequilibrium chemistry and three-dimensionality on the stability characteristics of hypersonic flows have been discussed.

In 2-D and axisymmetric flows, the inclusion of chemistry causes a shift of the second mode of Mack to lower frequencies. This is found to be due to the increase in size of the region of relative supersonic flow because of the lower speeds of sound in the relatively cooler boundary layers.

It is also found that equilibrium and nonequilibrium solutions can be very different depending on the rates of the reactions relative to the time scales of convection and diffusion. In particular, in equilibrium-air calculations, modes which travel supersonically relative to the inviscid region are shown to exist. These modes are a superposition of incoming and outgoing disturbances which exhibit oscillatory behavior because of the finite shock stand-off distance.

For the examination of 3-D effects, a rotating cone is successfully used as a model of a swept wing. A large parameter range of flow conditions can be studied and trends observed. The value of this should become more apparent from the next two paragraphs.

Considering a perfect gas, increasing freestream stagnation temperature only slightly stabilizes the crossflow instability.

For the rotating cone, transition location (N = 9) does not correlate with the traditional crossflow Reynolds number. When compressibility and cooling effects are included, Eq. (1), a relationship exists between the new crossflow Reynolds number and the maximum crossflow velocity at transition. This result has been verified with the yawed-cone data of King (1991) and Stetson (1982). The new crossflow Reynolds number is calculated solely from the basic-state profiles and, as such, it can aid in transition prediction and design for 3-D boundary layers. This formula contains no geometry explicitly and applies for flows with Prandtl number different from unity.

7. ACKNOWLEDGMENTS

The first author especially thanks Rudy King and Dennis Bushnell of NASA/Langley Research Center for supplying the basic-state profiles for the yawed-cone experiments of both King (1991) and Stetson (1982).

This work was previously supported at various stages by the Air Force Office of Scientific Research under Contract No. F49620-88-C-0076, the National Science Foundation under the Presidential Young Investigator Award, McDonnell/Douglas in St. Louis, and General Dynamics/Fort Worth and is currently supported by NASA/Ames Research Center under the Graduate Student Researchers Program.

The first author acknowledges her support by the Institute of Fluid Science, Tohoku University, Sendai, Japan, while on sabbatical there.

8. REFERENCES

Anderson, D.A., Tannehill, J.C., Pletcher, R.H. (1984) *Comput. Fluid Mech. and Heat Transfer*, McGraw-Hill.

Balakumar, P., Reed, H.L. (1991) "Stability of 3-D supersonic boundary layers," *Phys. Fluids A*, 3, 4, 617.

Beam, R.M., Warming, R.F. (1978) "An implicit factored scheme for the compressible Navier-Stokes equations," *AIAA J.*, 16, 4, 393.

Biolsi, L., Biolsi, D.S. (1983) "Transport properties for the nitrogen system: N_2, N, N^+, and e," *AIAA-83-1474*.

Biolsi, L. (1988) "Transport properties for the oxygen system: O_2, O, O^+, and e," *AIAA-88-2657*.

Blottner, F.G., Johnson, M., Ellis, M. (1971) "Chemically reacting viscous flow program for multi-component gas mixtures," *Rep.No.SC-RR-70-754*, Sandia Labs., Albuquerque.

Brokaw, R.S. (1958) "Approximate formulas for the viscosity and thermal conductivity of gas mixtures," *J. Chem. Phys.*, 29, 2, 391.

Bushnell, D.M., Malik, M.R., Harvey, W.D. (1989) "Transition prediction in external flows via linear stability theory," *Symp. Transs. III*, eds.: J. Zierep, H. Oertel, Springer.

Bushnell, D.M., Malik, M.R. (1987) "Supersonic laminar flow control," *NASA-CP-2487.*

Camac, M., Vaughan, A. (1961) "O_2 dissociation rates in O_2-Ar mixtures," *J. Chem. Phys.*, 34, 460.

Capitelli, M., Devoto, R.S. (1973) "Transport coefficients of high-temperature nitrogen," *Phys. Fluids*, 16, 11, 1835.

Capitelli, M., Ficocelli, V.E. (1972) "Collision integrals of oxygen atoms in different electronic states," *J. Phys. B: Atom. Molec. Phys.*, 5, 2066.

Cebeci, T., Chen, H.H., Arnal, D. (1988) "A three dimensional linear stability approach to transition on wings at incidence," Fluid Dyn. Three-Dim. Turb. Shear Flows Transit., *AGARD-CP-438.*

Chapman, G.T. (1961) "Some effects of leading edge sweep on boundary-layer transition at supersonic speeds," *NASA TM D-1075.*

Cubley, S.J., Mason, E.A. (1975) "Atom-atom and molecule-molecule potentials and transport collision integrals for high-temperature air species," *Phys. Fluids*, 18, 9, 1109.

Curtiss, Hirschfelder (1949) "Transport properties of multicomponent gas mixtures," *J. Chem. Phys.*, 17, 6, 550.

Dagenhart, J.R. (1981) "Amplified crossflow disturbances in the laminar boundary layer on swept wings with suction," *NASA TP 1902.*

Golub, G.H., Van Loan, C.F. (1983) *Matrix Computations*, Johns Hopkins Univ. Press, Baltimore; 4th Print., 1985.

Hanson, R.K., Salimian, S. (1984) "Chapter 6: Survey of rate constants in the N/H/O system," in *Combust. Chem.*, ed. W.C. Gardiner, Springer-Verlag.

Hirschfelder, J.O. (1957) "Heat conductivity in polyatomic, electronically excited, or chemically reacting mixtures. III", *6th Symp. (Internat.) Combust.*, Reinhold, 351.

Jaffe, R.L. (1987) "The calculation of high-temperature equilibrium and nonequilibrium specific heat data for N_2, O_2, and NO, *AIAA-87-1633.*

King, R.A. (1991) "Mach 3.5 boundary-layer transition on a cone at angle of attack," *AIAA-91-1804.*

Kobayashi, R., Izumi, H. (1983) "Boundary-layer transition on a rotating cone in still fluid," *JFM*, 127, 353.

Kobayashi, R., Kohama, Y., Kurosawa, M. (1983) "Boundary-layer transition on a rotating cone in axial flow," *JFM*, 127, 341.

Lekoudis, S.G. (1980) "Stability of the boundary layer on a swept wing with wall cooling," *AIAA J.*, 18, 1029.

Levin, E., Partridge, H., Stallcop, J.R. (1987) "High temperature transport properties of air," *AIAA-87-1632.*

Levin, E., Partridge, H., Stallcop, J.R. (1988) "High temperature transport properties of air: N-O interaction energies and collision integrals," *AIAA-88-2660.*

Mack, L.M. (1969) *Boundary-Layer Stability Theory, Jet Propulsion Laboratory Doc. 900-277 (Rev. A)*, JPL, Pasadena.

Mack, L.M. (1980) "On the stabilization of three-dimensional boundary layers by suction and cooling," *Lam.-Turb. Transit.*, eds. R. Eppler, H. Fasel, Springer-Verlag.

Mack, L.M. (1984) "Boundary-layer linear stability theory," Spec. Course: Stab. Transit. Lam. Flows, *AGARD-709.*

Malik, M.R. (1989) "Transition in hypersonic boundary layers,"*4th Symp. Num. Phys. Aspects Aerodyn. Flows*, Long Beach.

Monat, J.P., Hanson, R.K., Kruger, C.H. (1978) "Shock tube determination of the rate coefficient for the reaction $N_2 + O \rightarrow NO + N$," *17th Symp. (Internat.) Combust.*, Combust. Inst., Pittsburgh, 543.

Monchick, L. (1959) "Collision integrals for the exponential repulsive potential," *Phys. Fluids*, 2, 6, 695.

Owen, P.R., Randall, D.J. (1952) "Boundary layer transition on the swept wing," *RAE TM Aero 277.*

Pate, S.R. (1978) "Dominance of radiated aerodynamic noise on boundary-layer transition in supersonic-hypersonic wind tunnels - theory and application," *AEDC TR-77-107.*

Pfenninger, W. (1977) "Laminar flow control laminarization," Spec. Course: Concepts Drag Reduct., *AGARD-R-654.*

Poll, D.I.A. (1984) "Transition description and prediction in three-dimensional flows," Spec. Course: Stab. Transit. Lam. Flows, *AGARD-709.*

Prabhu,D.K., Tannehill,J.C., Marvin,J.G. (1988) "A new PNS code for chemical nonequilibrium flows,"*AIAA J.*, 26, 7, 808.

Reed, H.L., Haynes, T.S. (1992) "Transition correlation in 3-D supersonic boundary layers," submit. *AIAA J.*

Reed, H.L., Saric, W.S. (1989) "Stability of three-dimensional boundary layers," *Ann. Rev. Fluid Mech.*, 21, 235.

Stetson, K.F. (1982) "Mach 6 experiments of transition on a cone at angle of attack," *J. Spacecraft*, 19, 5, 397.

Stuckert, G.K. (1991) "Linear stability theory of hypersonic, chemically reacting viscous flows," Ph.D. Dissert., Ariz. State Univ., Tempe.

Stuckert, G.K., Reed, H.L. (1992) "Linear disturbances in hypersonic, chemically reacting shock layers," submit. *J. Comp. Phys.*

Thielen, K., Roth, P. (1986) "N atom measurements in high-temperature N_2 dissociation kinetics," *AIAA J.*, 24, 7, 1102.

White, F.M. (1974) *Viscous Fluid Flow*, McGraw-Hill.

Wray, K.L. (1962) "Chemical kinetics of high temperature air," *ARS Prog. Astronaut. Rocketry: Hypersonic Flow Res.*, ed. F.R. Ridell, Acad. Press, 7, 181.

Yun, K.S., Mason, E.A. (1962) "Collision integrals for the transport properties of dissociating air at high temperatures," *Phys. Fluids*, 5, 4, 380.

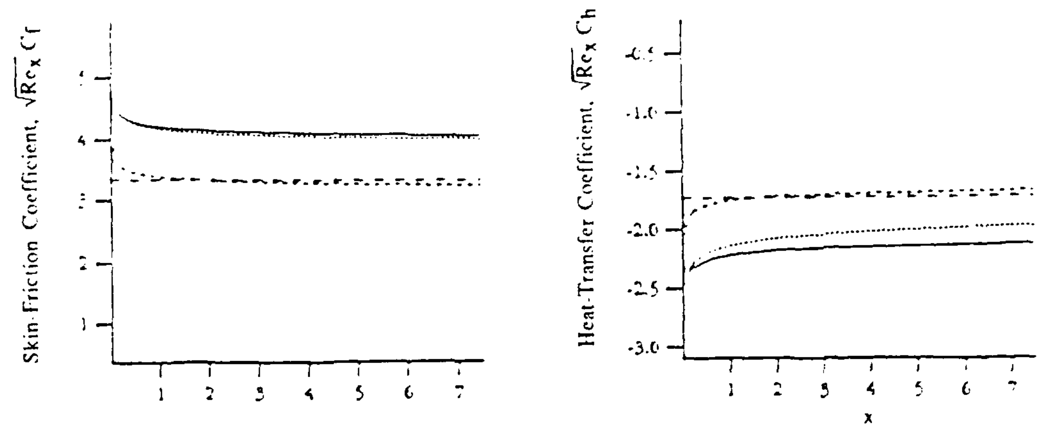

a) Skin-friction coefficient versus x

b) Heat-transfer coefficient versus x

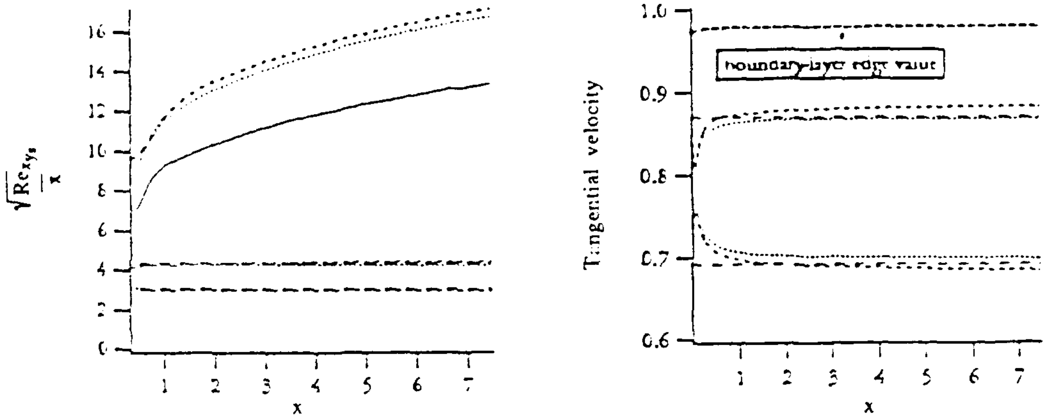

c) Locations of generalized inflection points

d) Tangential velocity at generalized inflection points

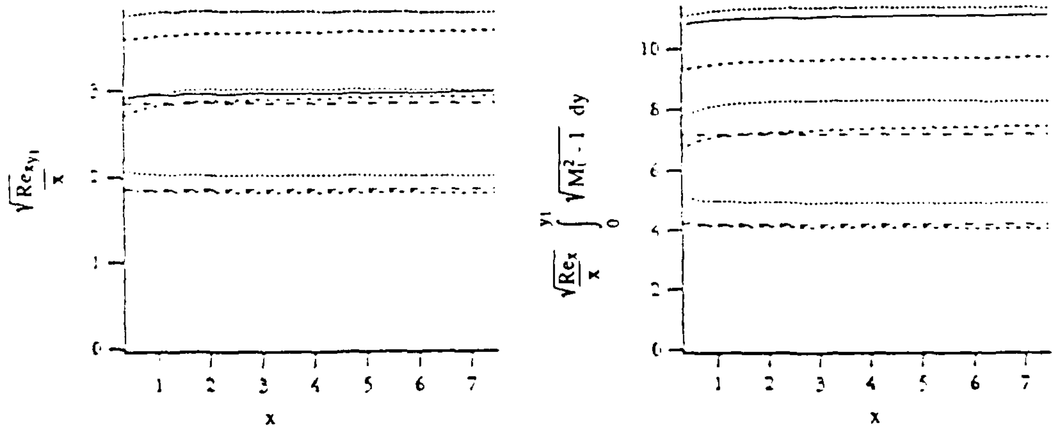

e) Location of relative sonic points for neutral disturbances

f) Neutral-disturbance wavenumber spacing integrals

Figure 1. Basic-state variations with respect to x

- - - Ideal Gas (Similarity Solution), ---- Ideal Gas (PNS),

— Equilibrium, ····· Nonequilibrium

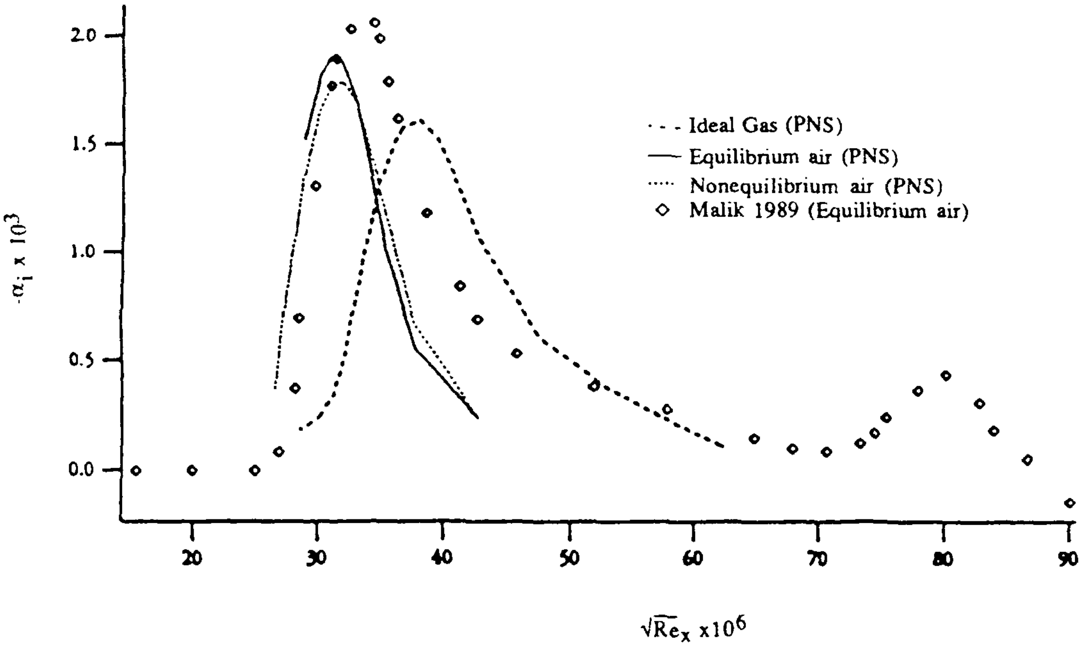

Figure 2. Adiabatic flat-plate boundary-layer disturbance-state amplification rates $\sqrt{Re_x}$ = 2000, Edge Mach number = 10.

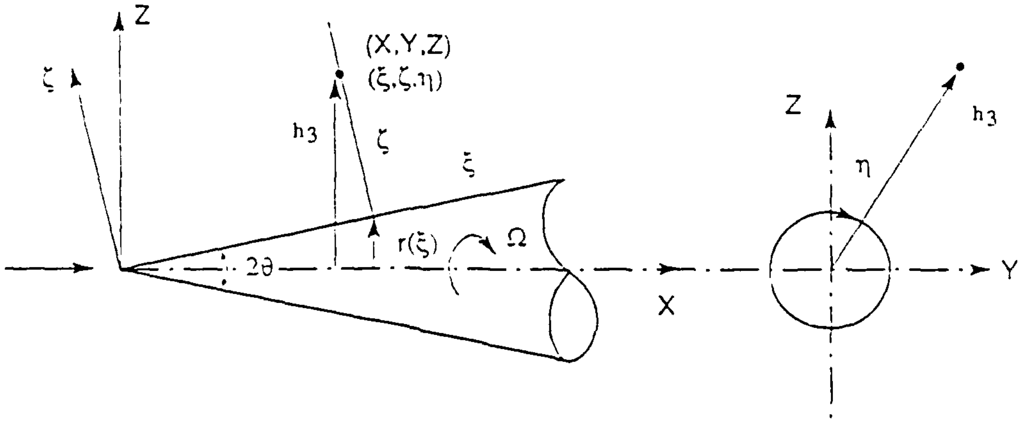
Z
ζ
(X,Y,Z)
(ξ,ζ,η)
h3
ζ
ξ
r(ξ)
Ω
2θ
X
Z
η
h3
Y

Figure 4. Rotating cone in supersonic axial flow and coordinate system.

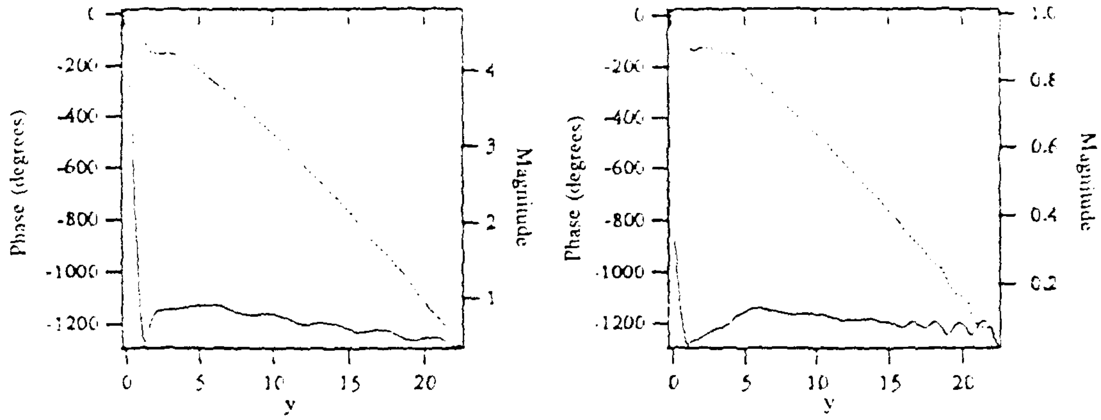

a) Pressure

b) Mixture Density

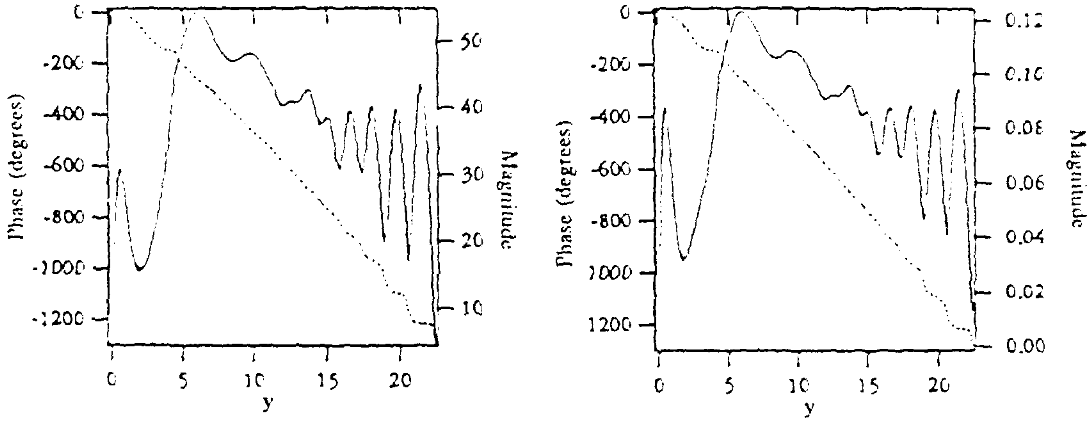

c) Total energy per unit volume, E_t

d) ρu

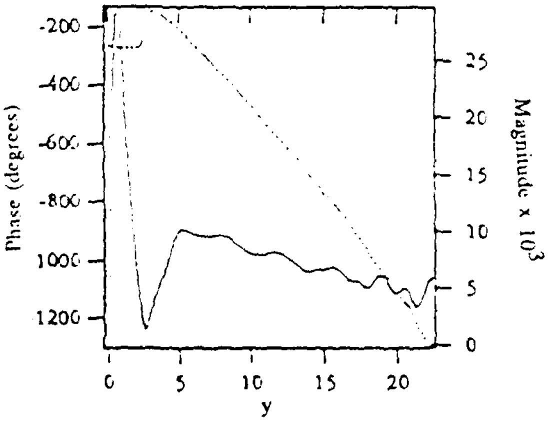

e) ρv

Figure 3. Equilibrium-air shock-layer disturbance-state eigenvector: —— magnitude, ······ phase; $\alpha = (0.364, -0.00415)$, $\beta = (0,0)$, $\omega = (0.279, 0)$; $\sqrt{Re_x} = 1022.3$.

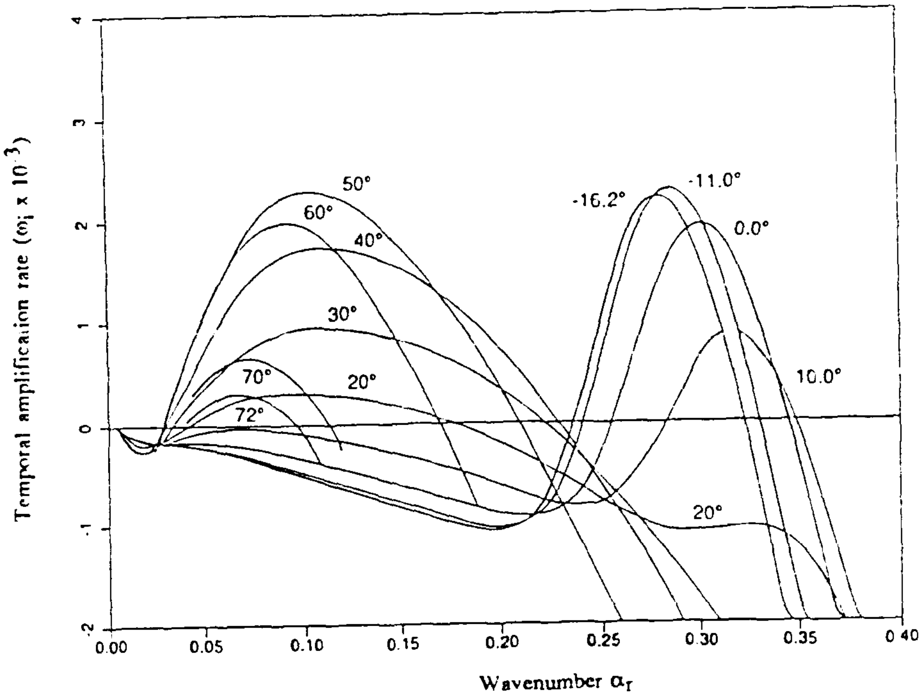

Figure 5. Distribution of amplification rate with wavenumber at M = 5, Re = 600 for different wave angles and with crossflow.

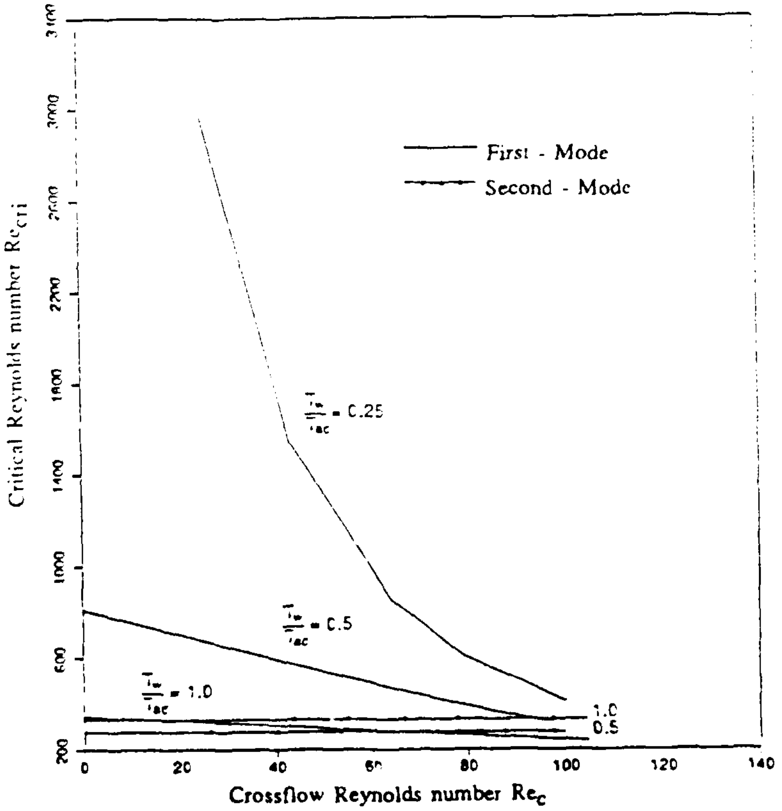

Figure 6. Variation of the critical Reynolds number Re_{cri} with the crossflow Reynolds number Re_c at M = 5.

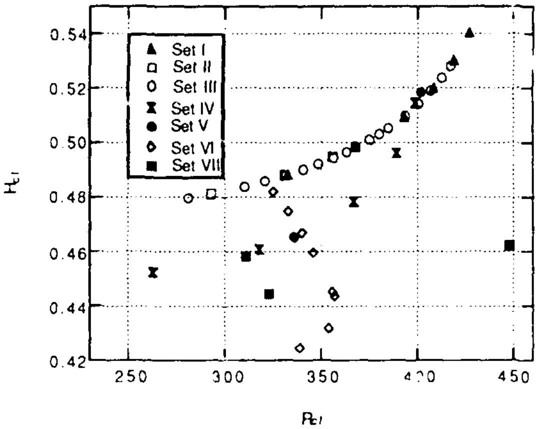

Figure 7. Traditional crossflow Reynolds number vs. shape factor at transition for various wall- and freestream- temperature conditions at M = 3.

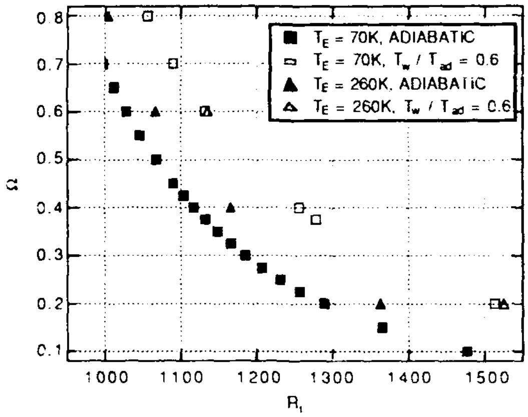

Figure 8. Transition Reynolds number vs. cone rotational speed for various wall- and freestream-temperature conditions at M = 3.

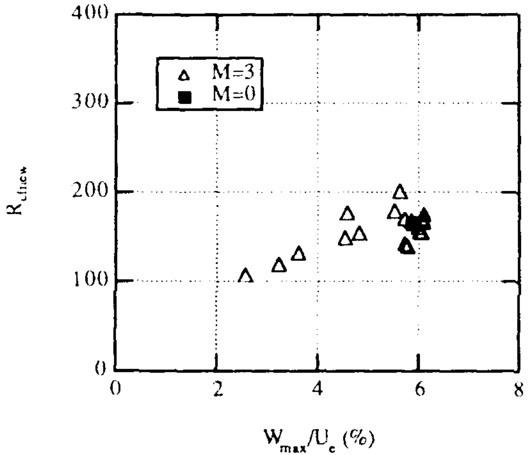

Figure 9. New definition of crossflow Reynolds number (including compressibility effects) versus maximum crossflow velocity for computational rotating-cone data assuming a transition location of N=9. Various freestream- and wall-temperature conditions as well as cone geometries are represented.

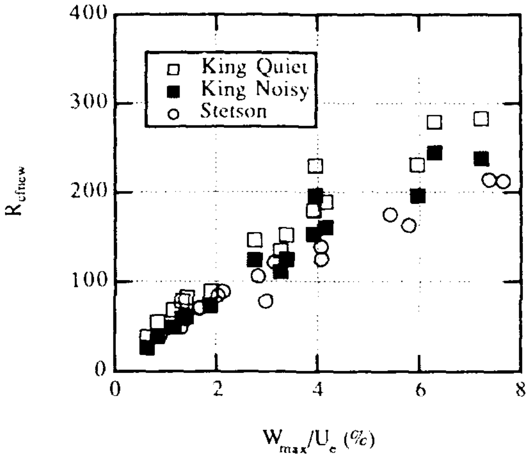

Figure 10. New definition of crossflow Reynolds number (including compressibility effects) versus maximum crossflow velocity for experimental yawed-cone data of King (1991) at M=3.5 and Stetson (1982) at M=5.9.

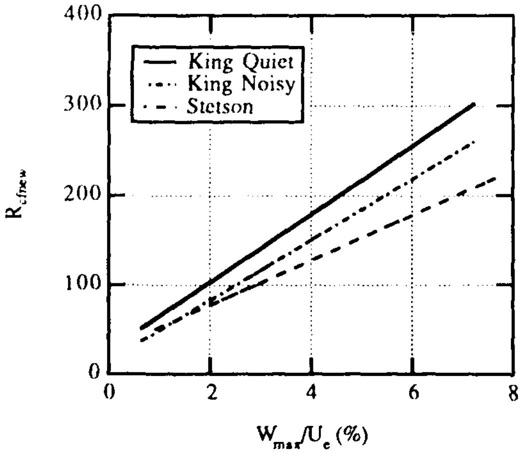

Figure 11. Linear least-squares approximation of new definition of crossflow Reynolds number (including compressibility effects) as a function of maximum crossflow velocity for experimental yawed-cone data of King (1991) at M=3.5 and Stetson (1982) at M=5.9.

REAL GAS AND SURFACE TRANSPIRATION EFFECTS UPON SWEPT LEADING EDGE HIGH SPEED FLOW INCLUDING TRANSITION

D.I.A. Poll
Department of Engineering
University of Manchester
Manchester, M13 9PL
England, U.K.

1. Abstract

This paper considers the extension of simple methods for the prediction of skin friction and heat transfer at an infinite-swept attachment line to cover the hypervelocity flight regime including the effects of surface transpiration. The analysis is limited to the situation where the flow is in thermochemical equilibrium everywhere. Real gas effects are identified and their influence is quantified. The importance of freestream conditions and attachment-line inclination are assessed. Consideration is also given to the issue of boundary layer transition.

2. Notation

a	local sound speed
b	blowing parameter - see equations (12a) and (12b)
C	reference length
C_A	mass concentration of atoms
C_f	skin friction coefficient
Cp	specific heat at constant pressure
D	leading edge diameter or binary diffusion coefficient
f	blowing function - see equation (13)
H	local total enthalpy
h	local static enthalpy
K	leading edge parameter ($2\sqrt{2}$ (C/D))
k	thermal conductivity
Le	Lewis number $(\rho\frac{CpD}{k})$
M	Mach number
Pr	Prandtl number $(\frac{\mu Cp}{k})$
p	pressure
Q	freestream velocity
q	local heat transfer rate per unit area
R	gas constant
$\bar{R}$	attachment-line Reynolds number
r	recovery factor
St	Stanton number
s	constant in Sutherlands viscosity law (110 K)
T	temperature
U,V	velocity components in x and y directions outside the boundary layer
U_1	non-dimensional chordwise velocity gradient $\frac{C}{U_\infty}\left[\frac{dU_e}{dx}\right]_{x=0}$
u,v,w	velocity components in x, y and z directions in the boundary layer
x,y,z	orthogonal, curvilinear coordinate system with origin at the attachment line - see figure 1
Z	compressibility factor in equation of state
γ	ratio of specific heats
η	real gas factor in Sutherlands viscosity law
μ	dynamic viscosity
ν	kinematic viscosity
ρ	density
ϕ	leading edge sweepback or inclination angle
Ψ_e	real gas parameter
Ω	atmospheric constant $\frac{\mu_{ref}}{a_{ref}}\left[1+\frac{s}{T_{ref}}\right]$

Subscripts

A	of atoms
e	at the edge of the boundary layer
f	frozen value
m	of molecules
r	recovery value
T	at transition onset
w	at the wall
∞	in the undisturbed freestream
*	evaluated at the reference enthalpy

3. Introduction

All winged vehicles have leading edges and, in a high speed flight environment, there can be a problem with heat transfer. This is particularly true for transatmospheric vehicles since, in order to have good lift generating characteristics, the wings must have small leading edge radii and they must operate at relatively low angles of attack. Under these conditions the leading edge temperatures may be the highest experienced anywhere on the airframe.

For an unswept leading edge the flow in the immediate vicinity of the attachment line is laminar and the local heating rates are given by solutions of the two-dimensional stagnation point problem. However, at zero sweep the heating rates are very large and the classical method for reducing them is to employ sweep. Provided that the attachment-line flow remains laminar, sweep has a dramatic, beneficial effect upon leading edge heating. However, it is now well established that a swept leading-edge, boundary layer can undergo a transition to turbulence by turbulent contamination of the attachment-line flow - see Poll[1,2]. Therefore, there is the possibility that sweep may result in a transition process which produces heating rates which are greater than those experienced in the unswept laminar case.

A second mechanism which has been proposed for the alleviation of severe leading edge heating is surface transpiration. Once again it is well known that blowing can reduce the thermal loading. However, if, as is often the case, a combination of surface blowing and sweep is to be used then it is necessary to take into account the possibility of transition. Here, not only are the effects of sweep likely to produce transition but blowing also reduces the free-stream Reynolds numbers for transition. Once again the proposed 'remedy' may well produce a situation which is actually worse!

In order to assess the implications of these conflicting effects it is useful to have accurate, yet simple, relations for heat transfer rate and skin friction in terms of 'primitive' variables such as free-stream speed, leading edge radius and leading edge sweep angle. They must also include the effects of surface transpiration. In addition, the conditions under which transition could occur must also be expressed in terms of the same parameters in order that critical boundaries can be readily identified. The objective of this paper is to provide these relations.

4. Basic Concepts

In order to simplify the arguments, we begin by assuming that, because the atomic weights and transport properties of nitrogen and oxygen are similar, we may, to a sufficiently accurate approximation, treat high temperature air as a binary mixture of 'air molecules' and 'air atoms' - see Lees[3]. The effects of ionisation are not considered. Furthermore, it is assumed that, at all points in the flow, including the boundary layer, the mixture is in complete thermal equilibrium i.e the local gas properties and the concentrations of atoms and molecules are determined by the local static enthalpy and pressure only. This implies that the chemical reaction rates are very much faster than rates of convection along streamlines and rates of diffusion across streamlines

Under these conditions the boundary layer equations for steady, laminar flow over an infinite-swept cylinder, as shown in figure 1, have been given by Cohen[4] -

continuity

$$\frac{\partial}{\partial x}(\rho u) + \frac{\partial}{\partial z}(\rho w) = 0$$

x-momentum

$$\rho u\frac{\partial u}{\partial x} + \rho w\frac{\partial u}{\partial z} = \rho_e U_e \frac{dU_e}{dx} + \frac{\partial}{\partial z}(\mu\frac{\partial u}{\partial z})$$

y-momentum

$$\rho u\frac{\partial v}{\partial x} + \rho w\frac{\partial v}{\partial z} = \frac{\partial}{\partial z}(\mu\frac{\partial v}{\partial z}) \qquad (1)$$

z-momentum

$$\frac{\partial p}{\partial z} = 0$$

energy (total enthalpy form)

$$\rho u\frac{\partial H}{\partial x} + \rho w\frac{\partial H}{\partial z} = \frac{\partial}{\partial z}\left[\frac{\mu}{Pr_f}(1+F)\frac{\partial H}{\partial x}\right.$$

$$\left. + \frac{\mu}{Pr_f}(Pr_f - 1 - F)(u\frac{\partial u}{\partial z} + v\frac{\partial v}{\partial z})\right]$$

where

$$F(p,h) = (Le - 1)(h_A - h_m)\left[\frac{\partial C_A}{\partial h}\right]_{p=constant}$$

$$Pr_f = \text{frozen Prandtl number} = \left[\frac{\mu Cp}{k}\right]_f$$

and

$$Le = \text{Lewis number} = \left[\frac{\rho DCp}{k}\right]_f$$

The boundary conditions for the current problem are

$z = 0$ $u = v = 0$
$w = w_w$ = constant
$H = H_w$ = constant
$z \rightarrow \infty$ $u \rightarrow U_e(x)$
$v \rightarrow V_e$ = constant
$H \rightarrow H_e$

For the special case of unit Prandtl number and unit Lewis number we note the existence of a "Crocco relation" between the total enthalpy and the spanwise velocity profile (attachment-line velocity profile) i.e.if $Pr_f = 1$ and $Le = 1$ then

$$\frac{H - H_w}{H_e - H_w} = \frac{v}{V_e} \qquad (2)$$

If the gas consists of a single species then the heat transfer rate in the z direction at any point in the flow is determined by the local temperature gradient and the thermal conductivity i.e.

$$\dot{q} = - k\frac{\partial T}{\partial z}$$

However, when chemical reactions are taking place within the flow, heat is also transferred by mass diffusion of the reacting species. According to Cohen[4] the total heat flux becomes -

$$\dot{q} = -\left[k_f\frac{\partial T}{\partial z} + \rho D_{AM}(h_A - h_m)\frac{\partial h}{\partial z}\left[\frac{\partial C_A}{\partial h}\right]_{p=const}\right]$$

or

$$\dot{q} = - \frac{\mu}{Pr_f}\frac{\partial h}{\partial z}(1 + F(p,h))$$

Therefore, at the wall, *it follows that if* Le = 1 (F = 0) then -

$$\dot{q}_w = -\left(\left[\frac{\mu}{Pr_f}\right]_w\frac{\partial h}{\partial z}\right)_{z=0} = -\left(\left[\frac{\mu}{Pr_f}\right]_w \cdot \frac{\partial H}{\partial z}\right)_{z=0} \qquad (3)$$

If, in addition, the frozen Prandtl number is unity, we may combine the results from equations (2) and (3) to give -

$$St_e = \frac{(-\dot{q}_w)}{\rho_e V_e(H_e - H_w)} = \frac{Cf_e}{2} \qquad (4)$$

This result is identical to the simple Reynolds analogy used in reference 2 for the thermally perfect gas, except that total enthalpy has replaced the product of total temperature and the (invariant) specific heat at constant pressure. Therefore, the problem of determining the heat transfer rate at the wall is reduced to one of finding the surface shear stress. If an accurate approximate method exists for the determination of skin friction then this can be extended, via equation (4), to give correspondingly accurate estimates for surface heating.

In the less complex case of the zero pressure-gradient, flat-plate boundary layer with no wall transpiration, Van Driest[5] and Eckert[6] have proposed that for hypervelocity flows the surface shear stress may be obtained from the incompressible skin friction-Reynolds number relation by using values for density and viscosity which are appropriate for the local static pressure and a 'reference' enthalpy within the boundary layer i.e.

$$C_f = \frac{\tau_w}{\frac{1}{2}\rho_* U_e^2} = 0.664\left(\frac{\mu_*}{U_e\rho_* x}\right)^{\frac{1}{2}}$$

where $\rho_* = \rho_*(p_e, h_*)$

$$\mu_* = \mu_*(p_e, h_*)$$

The reference enthalpy, h., corresponds to some average condition occurring within the boundary layer and its value depends upon conditions at the wall and at the boundary layer edge. According to Eckert[6]

$$h_* = h_e + 0.50(H_w - h_e) + 0.22\ (H_r - h_e)$$

The surface heat transfer rate is then obtained by applying a modified Reynolds analogy i.e.

$$St_e = \frac{(-\dot{q}_w)}{\rho_e U_e (H_r - H_w)} = [Pr_*]_f^{-2/3} \cdot \frac{Cf_e}{2} \qquad (5)$$

where

$$\frac{H_r - h_e}{H_e - h_e} = r = (Pr_*)_f^{1/2} \qquad (6)$$

This is the same as the Colburn[7] form of the Reynolds analogy except that the Prandtl number is taken to be the frozen (no-chemical reaction effects) value appropriate to p_e and h.. In the case of a flow in local thermodynamic equilibrium and unit Lewis number, Cohen[4] has compared exact boundary layer solutions with the corresponding predictions from the reference enthalpy method. For the wide range of conditions considered the simple method is always within 10% of the exact solution for both skin friction and heat transfer rate.

In view of the strong similarity between the infinite-swept, attachment-line boundary layer and the zero pressure-gradient, flat plate boundary layer, we might expect that the adoption of reference enthalpy and a Reynolds analogy of the form given in equation (5) could provide a satisfactory means of extending the relations developed in references 1 and 2 to hypervelocity flow conditions.

5. Laminar Flow over an Impervious Surface

For incompressible flow with no heat transfer - see Poll[2].

$$C_f = \frac{\tau_w}{\frac{1}{2}\rho V_e^2} = \frac{1.141}{\bar{R}} = 1.141\left(\frac{\nu U_\infty U_1}{V_e^2 C}\right)^{1/2}$$

Therefore, in a general compressible flow, we have

$$C_{f_e} = \frac{\tau_w}{\frac{1}{2}\rho_e V_e^2} = 1.141\left(\frac{\nu_e U_\infty U_1}{V_e^2 C}\right)^{1/2}\left(\frac{\rho_* \mu_*}{\rho_e \mu_e}\right)^{1/2}$$

According to Poll[2], the reference temperature for the laminar attachment-line flow is equal to the temperature at the edge of the boundary layer and so for the reference enthalpy approach -

$$h_* = h_e$$

It follows that

$$C_{f_e} = 1.141\left(\frac{\nu_e U_\infty U_1}{V_e^2 C}\right)^{1/2} = \frac{1.141}{\bar{R}} \qquad (7)$$

This is identical to the thermally perfect gas result given in reference 2 and the validity for the case of a flow in chemical equilibrium with unit Lewis number is demonstrated in figure 2 where predictions from equation (7) are compared with Cohen's solutions for the laminar boundary layer equations for a wide range of freestream conditions and sweep angles. In all cases the agreement is better than ± 8%.

Having obtained a relation for skin friction the corresponding expression for the heat transfer rate may be obtained directly from equations (5) and (6) i.e.

$$St_e = 0.571(Pr_e)_f^{-2/3}(\bar{R})^{-1} \qquad (8)$$

Predictions from equation (8) may also be compared with Cohen's exact solutions and the results are presented in figure 3. Once again the agreement is better than ± 8%. Moreover, we note that equation (8) gives a fit which is as good as the two correlating functions which Cohen proposes. In fact, if the constant (1.141) of equation (7) is increased to 1.175 then the modified equation (8) is much better than Cohen's functions since the single relation fits all the data to better than ± 6%.

6. Turbulent Flow over an Impervious Surface

The turbulent flow situation is much more difficult to treat than that for laminar flow. For 'steady' conditions, the usual approach begins with the assumption that the Navier-Stokes equations provide an adequate description at any instant in time. The instantaneous values for the velocities, temperature, density and pressure are then split into a 'mean' component and a fluctuating component whose long time average is, by definition, zero. Having separated the mean and fluctuating components the equations of motion are time averaged and the boundary layer approximations are applied. A set of equations for the mean flow then emerge which can only be solved if appropriate closure relations (turbulence models) are introduced. For a hypersonic boundary layer flow the above process is complex and some of the approximations which are available in subsonic and even supersonic flows cannot be readily justified. A more complete description of the problem is provided by the review paper by Bradshaw[8].

Despite the problems, it is a matter of experimental observation that, for the two-dimensional, zero pressure-gradient, turbulent boundary layer, the Reynolds analogy between heat transfer rate and wall shear stress (equation 5) still holds - at least to a first approximation. Moreover, Eckert and many others have repeatedly demonstrated that the reference enthalpy concept also works reasonably well for flat plate flow. Therefore, in view of this, and, in view of the fact that the perfect gas relations for the laminar attachment-line flow have been successfully extended to cover the high speed flow of a real gas in chemical dissociation equilibrium, it will be assumed that a similar technique will suffice for the turbulent flow situation.

It follows from reference[1] that, for fully turbulent flow, the skin friction is given by

$$C_{f_e} = 0.0689\left(\frac{\rho_*\mu_*}{\rho_e\mu_e}\right)^{0.21}\cdot\left(\frac{\rho_*}{\rho_e}\right)^{0.58}(\bar{R})^{-0.42} \tag{9}$$

where

$$\rho_* = \rho_*(p_e, h_*)$$

$$\mu_* = \mu_*(p_e, h_*) \tag{10}$$

$$\text{and } h_* = h_e + 0.10(H_w - h_e) + 0.60(H_r - h_e)$$

For the surface heat transfer rate we combine equations (9) and (10) with equation (5) i.e.

$$St_e = 0.0345(Pr_*)_f^{-2/3}\left(\frac{\rho_*\mu_*}{\rho_e\mu_e}\right)^{0.21}\left(\frac{\rho_*}{\rho_e}\right)^{0.58}(\bar{R})^{-0.42}$$

(11)

and

$$\frac{H_r - h_e}{H_e - h_e} = r = (Pr_*)_f^{1/3}$$

7. The effect of wall transpiration

In the past it was universally assumed that the attachment-line boundary layer could only exist in the laminar state and that blowing was the "natural" means for reducing heat transfer. A limited number of solutions for laminar flows of a perfect gas with a Sutherland viscosity temperature law are presented by Beckwith[9] and an asymptotic solution for massive blowing has been provided by Libby and Kassoy[10]. Unfortunately, neither of these sources presents sufficient information to enable approximate relations to be deduced, neither considers the issue of suction and no one has considered the problem of transpiration under a turbulent flow.

To rectify this situation a series of computations was performed using a modified version of the fully compressible attachment line boundary layer code given by Adams and Martindale[11]. The principal modification was to change the wall boundary condition so that transpiration could be considered. This proved to be a trivial task and no significant numerical problems were encountered. Preliminary checks were carried out by re-calculating all the cases considered by Beckwith.

In order to present the results in a compact form we introduce a blowing parameter, b, where

$$b = \frac{\rho_w w_w}{\rho_e V_e}\left(\frac{2}{Cf_e}\right)_{w_w=0} \qquad (12a)$$

when effects on wall shear are being considered and

$$b = \frac{\rho_w w_w}{\rho_e V_e}\left(\frac{1}{St_e}\right)_{w_w=0} \qquad (12b)$$

when heat transfer is the issue. Figure 4 shows data covering a very wide range of conditions presented in the form

$$\frac{Cf_e}{(Cf_e)_{w_w=0}} \quad \text{versus} \quad \left(\frac{\rho_w w_w}{\rho_e V_e}\right)\left(\frac{2}{Cf_e}\right)_{w_w=0}$$

and

$$\frac{St_e}{(St_e)_{w_w=0}} \quad \text{versus} \quad \left(\frac{\rho_w w_w}{\rho_e V_e}\right)\left(\frac{1}{St_e}\right)_{w_w=0}$$

We note that all the data effectively collapses onto a single line which is well represented by the relation

$$f = \frac{b}{(\exp(b)\ -1)} \qquad (13)$$

This remarkable result allows us to estimate the effects of transpiration directly from the predictions for zero transpiration under identical free stream and wall conditions.

8. The Effect of Sweep Angle and Freestream Conditions upon Heating Rates

Having obtained expressions for heat transfer rates in terms of conditions at the wall and at the edge of the boundary layer, it is possible to investigate the influence of sweep angle and freestream conditions. In addition, it is possible to assess the direct effect of thermal imperfections in the gas.

We begin by noting that the relations for laminar and turbulent heating rates (equations (8) and (11)) are very similar in form i.e.

$$St_e = A[Pr_*]_f^{-2/3}\left(\frac{\rho_*\mu_*}{\rho_e\mu_e}\right)^{\frac{B}{2}}\left(\frac{\rho_*}{\rho_e}\right)^{1-B}(\bar{R})^{-B} \qquad (14)$$

where A = 0.571, B = 1 and * = e for laminar flow

and A = 0.0345 and B = 0.42 for turbulent flow.

Recalling that

$$\bar{R} = \left[\frac{V_e^2\, C}{\nu_e U_\infty U_1}\right]^{1/2} ,$$

and that for an infinite inclined cylinder

$$U_\infty = Q_\infty \cos ø, V_e = V_\infty = Q_\infty \sin ø$$

equation (14) may be rearranged to give

$$\frac{(-\dot{q}_w)}{(1\ -\ H_w/H_r)} = \pi\left(\frac{\rho_e}{\rho_\infty}\right)^{(1-B)}\left(\frac{\rho_e\mu_e}{\rho_\infty\mu_\infty}\ .\ U_1\right)^{\frac{B}{2}} .$$

$$\left(\frac{Q_\infty\rho_\infty C}{\mu_\infty}\right)^{1-\frac{B}{2}}\ \frac{\mu_\infty}{C}(\sin ø)^{1-B}(\cos ø)^{\frac{B}{2}}H_r$$

where

$$\pi = A\ (Pr_*)_f^{-2/3}\left(\frac{\rho_*\mu_*}{\rho_e\mu_e}\right)^{\frac{B}{2}}\left(\frac{\rho_*}{\rho_e}\right)^{(1-B)}$$

If we now introduce a real gas equation of state

$$p = \rho(ZR)T \qquad (Z = Z\ (T,p))$$

where Z is the compressibility factor and a modified Sutherlands Law for viscosity i.e.

$$\frac{\mu}{\mu_{ref}} = \eta\left(\frac{T}{T_{ref}}\right)^{1/2}\frac{(1\ +\ s/T_{ref})}{(1\ +\ s/T)}\ (\eta\ =\ \eta\ (T,p))$$

then, after some manipulation

$$\frac{(-\dot{q}_w)}{(1\ -\ H_w/H_r)} = \pi\left(\eta_e^B Z_e^{(B-2)}\left(\frac{h_e/T_e}{Cp}\right)^{\left(\frac{4-3B}{2}\right)}\right)^{1/2} .$$

$$\left(\frac{\mu_\infty}{a_\infty}\left[1+\frac{s}{T_\infty}\right]\right)^{\frac{B}{2}}\left(\frac{P_e}{p_\infty}\right)^{(1-B)}\left(\frac{P_e}{p_\infty}.U_1\right)^{\frac{B}{2}}\left(\frac{\cos ø}{C(1\ +\ s/T_e)}\right)^{\frac{B}{2}} .$$

$$\frac{a_\infty H_r(\sin\phi)^{(1-B)}}{\left[\left(1+\left(\frac{\gamma-1}{2}\right)M_\infty^2\cos^2\phi\right)^{\left(\frac{4-3B}{4}\right)}\right]}\left[M_\infty\rho_\infty\right]^{\left(\frac{2-B}{2}\right)} \qquad (15)$$

where $H_r = \frac{a_\infty^2}{(\gamma-1)}\left[1+\left(\frac{\gamma-1}{2}\right)M_\infty^2(\cos^2\phi + r\sin^2\phi)\right]$

and $h_e = CpT_\infty[1+\left(\frac{\gamma-1}{2}\right)M_\infty^2\cos^2\phi]$

Some additional simplification can be achieved through consideration of the atmospheric characteristics, since

$$\frac{\mu_\infty}{a_\infty}[1+s/T_\infty] = \frac{\mu_{ref}}{a_{ref}}\left[1+\frac{s}{T_{ref}}\right] = \text{constant} = \Omega$$

Furthermore, if we let

$$\left[\eta_e^B . Z_e^{(B-2)}\left(\frac{h_e/T_e}{Cp}\right)^{\left(\frac{4-3B}{2}\right)}\right]^{1/2} = \Psi_e\ ,$$

where $\Psi_e = \Psi_e(T_e, p_e)$

(N.B. Ψ' also depends upon the state of the boundary layer) then equation (15) becomes

$$\frac{(-\dot{q}_w)}{(1-H_w/H_r)} = \left\{\pi\Psi_e\left(\frac{p_e}{p_\infty}\right)^{(1-B)}\left(\frac{U_1p_e/p_\infty}{(1+s/T_e)}\right)^{\frac{B}{2}}\right\} .$$

$$\frac{a_\infty^3}{(\gamma-1)}\left(\frac{\Omega}{C}\right)^{\frac{B}{2}}(M_\infty\rho_\infty)^{\left(\frac{2-B}{2}\right)} .$$

$$\left[\frac{\left(1+\left(\frac{\gamma-1}{2}\right)M_\infty^2(\cos^2\phi+r\sin^2\phi)\right)}{\left(1+\left(\frac{\gamma-1}{2}\right)M_\infty^2\cos^2\phi\right)^{\left(\frac{4-3B}{4}\right)}}\right].(\sin\phi)^{(1-B)}.(\cos\phi)^{\frac{B}{2}}$$

The term in { } brackets has been evaluated for a real gas in chemical equilibrium. It should also be noted that this term has some sweep dependence. The relevant real gas information may be obtained from references (9)-(13).

Laminar Flow

In the case of laminar flow, the constant B is equal to unity and a considerable simplification occurs i.e.

$$\frac{(-\dot{q}_w)}{(1-H_w/H_r)} = \pi(\Psi_e)_L\left(U_1\frac{p_e}{p_\infty}\right)^{1/4}\frac{a_\infty^3}{(\gamma-1)}\left(\frac{\Omega M_\infty\rho_\infty}{(1+s/T_e)C}\right)^{1/4} .$$

$$\frac{\left(1+\left(\frac{\gamma-1}{2}\right)M_\infty^2(\cos^2\phi + r\sin^2\phi)\right)}{\left(1+\left(\frac{\gamma-1}{2}\right)M_\infty^2\cos^2\phi\right)^{1/4}} . (\cos\phi)^{1/4}$$

where $(\Psi_e)_L = \left[\frac{\eta_e}{Z_e}\left(\frac{h_e/T_e}{Cp}\right)^{1/2}\right]^{1/2}$

Moreover, since the reference enthalpy is equal to the enthalpy at the edge of the boundary layer,

$$\pi = 0.571\ (Pr_e)_t^{-2/3}$$

and, for flight in the Earth's atmosphere[17],

$$\Omega = 7.273 \times 10^{-8}\ \text{kg/m}^2 \text{ and } \gamma = 1.4$$

Finally, a major simplification is provided by Topham's observation (ref. 18) that for air in thermochemical equilibrium,

$$\frac{p_e}{p_\infty} . \frac{U_1}{K} \approx \sqrt{2}\left(\frac{1+M_\infty\cos\phi}{2}\right)^2$$

where K† is a constant which depends upon the leading edge geometry. Topham suggests that this expression is accurate to within 8% provided that

$2 < M_\infty\cos\phi < 18$

and $6\ \text{km} < \text{altitude} < 60\ \text{km}$

This result is shown in figure 5 where it can be seen that at the higher altitudes and higher Mach numbers a better fit is produced by

$$\frac{p_e}{p_\infty} . \frac{U_1}{K} \approx 0.322\ (1+M_\infty\cos\phi)^2$$

for $6 < M_\infty\cos\phi < 24$

and $37\ \text{km} < \text{altitude} < 76\ \text{km}$

However, the difference between these two relations is only 6.5%.

---

†If the attachment line is established on a circular cylinder of diameter D then

$$K = 2\sqrt{2}\frac{C}{D}$$

Under the above circumstances

$$\frac{(-\dot{q}_w)}{(1-H_w/H_r)} = 0.849(Pr_e)_f^{-2/3}.(\Psi_e)_L a_\infty^3\left(\frac{\Omega K M_\infty \rho_\infty}{(1+s/T_e)C}\right)^{1/2} \times$$

$$\left[\frac{(1+M_\infty\cos\o)\left(1+0.2M_\infty^2(\cos^2\o+r\sin^2\o)\right)(\cos\o)^{1/2}}{(1+0.2M_\infty^2\cos^2\o)^{1/4}}\right]$$

or, if ρ_∞ has dimensions (kg/m^3), a_∞ is in (m/sec) and C is in (m) then

$$\frac{(-\dot{q}_w)}{(1-H_w/H_r)} \approx 0.229(Pr_e)_f^{-2/3}.(\Psi_e)_L a_\infty^3\left(\frac{K M_\infty \rho_\infty}{(1+s/T_e)C}\right)^{1/2}.$$

$$\left[\frac{(1+M_\infty\cos\o)\left(1+0.2M_\infty^2(\cos^2\o+r\sin^2\o)\right)(\cos\o)^{1/2}}{(1+0.2M_\infty^2\cos^2\o)^{1/4}}\right].10^{-6}$$

kwatts/m^2

The only remaining unknown in the above relation is the real gas parameter $(\Psi_e)_L$. For air in thermodynamic equilibrium, this quantity may be obtained from a Mollier diagram (reference 19) or from Feldman's charts (reference 13). However, for altitudes in the range 36km to 80km and normal-to-leading edge speeds below about 8000 m/sec, it can be seen from figure 6 that $(\Psi_e)_L$ exhibits very little dependence upon altitude. In fact, for normal-to-leading-edge speeds between 1200 m/sec and 8000 m/sec,

$$(\Psi_e)_L = 0.96\left[1+0.036\left(\frac{Q_\infty\cos\o}{1000}\right)\right] \quad (\pm\ 3\%)$$

where $Q_\infty\cos\o$ is in (m/sec).

A final simplification may be made by considering the flow at very high Mach number i.e. $M_\infty\cos\o > 10$. In this case

$$\frac{(-\dot{q}_w)}{(1-H_w/H_r)} \approx 0.082Q_\infty^3\left(\frac{K\rho_\infty}{C}\right)^{1/2}\left[1+0.036\left(\frac{Q_\infty\cos\o}{1000}\right)\right]$$

$$(\cos^2\o + r\sin^2\o)\cos\o\ .\ 10^{-6}\ \text{kwatts/m}^2 \qquad (16)$$

where the edge Prandtl number has been assumed constant with a value of 0.72.

Turbulent Flow

For turbulent flow B is equal to 0.42 and consequently

$$\frac{(-\dot{q}_w)}{(1-H_w/H_r)} = \pi\Psi_e\left(\frac{p_e}{p_\infty}\right)^{0.58}\left(\frac{\Omega U_1 p_e/p_\infty}{(1+s/T_e)C}\right)^{0.21}.$$

$$\frac{a_\infty^3}{(\gamma-1)}(M_\infty\rho_\infty)^{0.79}.$$

$$\left[\frac{\left(1+(\frac{\gamma-1}{2})M_\infty^2(\cos^2\o+r\sin^2\o)\right)}{\left(1+(\frac{\gamma-1}{2})M_\infty^2\cos^2\o\right)^{0.685}}(\sin\o)^{0.58}(\cos\o)^{0.21}\right],$$

where

$$\pi = 0.0345(Pr_*)_f^{-2/3}\left(\frac{\rho_*\mu_*}{\rho_e\mu_e}\right)^{0.21}\left(\frac{\rho_*}{\rho_e}\right)^{0.58}$$

$$\text{and}\quad \Psi_e = \left[\frac{\eta_e^{0.21}}{Z_e^{0.79}}\left(\frac{h_e/T_e}{C_p}\right)^{0.685}\right]$$

This may be simplified by introducing a pressure ratio P which is the value of p_e/p_∞ which would be achieved in the ideal gas case (γ = constant = 1.4) i.e.

$$P = \left(\frac{(\gamma+1)(M_\infty\cos\o)^2}{2}\right)^{\frac{\gamma}{\gamma-1}}\left(\frac{\gamma+1}{2\gamma(M_\infty\cos\o)^2-(\gamma-1)}\right)^{\frac{1}{\gamma-1}}$$

the familiar Rayleigh Pitot formula. If, in addition, we define $(\Psi_e)_T$ to be

$$(\Psi_e)_T = \Psi_e\ .\left(\frac{p_e/p_\infty}{P}\right)^{0.58}$$

and introduce Tcpham's approximation, then, for the flight through the earth's atmosphere,

$$\frac{(-\dot{q}_w)}{(1-H_w/H_r)} \approx 0.0693(Pr_*)_f^{-2/3}\left(\left[\frac{\rho_*\mu_*}{\rho_e\mu_e}\right]\frac{K\Omega}{(1+s/T_e)C}\right)^{0.21}.$$

$$\left(\frac{\rho_*}{\rho_e}P\right)^{0.58}(\Psi_e)_T a_\infty^3(M_\infty\rho_\infty)^{0.79}.$$

$$\left[\frac{(1+M_\infty\cos\o)^{0.42}\left(1+0.2M_\infty^2(\cos^2\o+r\sin^2\o)\right)(\sin\o)^{0.58}(\cos\o)^{0.21}}{(1+0.2M_\infty^2\cos^2\o)^{0.685}}\right]$$

or, if ρ_∞ is in (kg/m^3), a_∞ in (m/sec) and C is in (m) then

$$\frac{(-\dot{q}_w)}{(1 - H_w/H_r)} \approx 2.20(Pr_*)_t^{-2/3}\left(\left[\frac{\rho_*\mu_*}{\rho_e\mu_e}\right]\frac{K}{(1 + s/T_e)C}\right)^{0.21} .$$

$$\left(\frac{\rho_*}{\rho_e}\,p\right)^{0.58}(\Psi_e)_T a_\infty^3(M_\infty\rho_\infty)^{0.79} .$$

$$\left[\frac{(1+M_\infty\cos\phi)^{0.42}\left(1+0.2M_\infty^2(\cos^2\phi+r\sin^2\phi)\right)(\sin\phi)^{0.58}(\cos\phi)^{0.21}}{(1+0.2M_\infty^2\cos2\phi)^{0.685}}\right]$$

$$.\ 10^{-6}\ \text{kwatts/m}^2$$

In this final relation there are three unknown quantitites

$$(\Psi_e)_T = F_1(Q_\infty\cos\phi,\ \text{altitude})$$

$$\left(\frac{\rho_*\mu_*}{\rho_e\mu_e}\right) = F_2(h_*,\ h_e,\ p_e)$$

$$\text{and}\ \left(\frac{\rho_*}{\rho_e}\right) = F_3(h_*,\ h_e,\ p_e),$$

$$\text{where}\ h_* = h_*(h_e,\ H_w,\ H_r).$$

The first is a real gas parameter which can be obtained from a Mollier chart or Feldman's charts. However, as in the case of laminar flow, the real gas parameter is much more sensitive to speed than it is to changes in altitude. This is clearly demonstrated in figure 7 which has been obtained from the data presented in reference 13. To a reasonably good approximation.

$$(\Psi_e)_T \approx 0.815\left(1 + 0.190\left(\frac{Q_\infty\cos\phi}{1000}\right)\right)(\pm\ 10\%)$$

$$\text{for}\quad 1200\ \text{m/sec} < Q_\infty\cos\phi < 8000\ \text{m/sec}$$

We note, in passing, that $(\psi_e)_T$ exhibits a much greater dependence upon speed than did $(\psi_e)_L$. The second and third relations are also available from the Mollier chart. However, various authors, for example Cohen[12] and Viegas and Howe[20], have attempted to find correlating formulae for F_2 and F_3. The simplest are probably those proposed by Cohen[12] i.e.

$$\frac{\rho_*\mu_*}{\rho_e\mu_e} = \frac{1 - 1.0213\left(1 - \left(\frac{h_e}{h_E}\right)^{0.3329}\right)}{1 - 1.0213\left(1 - \left(\frac{h_*}{h_E}\right)^{0.3329}\right)}$$

$$\frac{\rho_*}{\rho_e} = \frac{1 - 1.0477\left(1 - \left(\frac{h_e}{h_E}\right)^{0.6123}\right)}{1 - 1.0477\left(1 - \left(\frac{h_*}{h_E}\right)^{0.6123}\right)}$$

In these expressions h_E is a reference enthalpy defined as

$$h_E = 250\ R\ T_{ref}$$

where R is the gas constant for undissociated air, i.e. 287 Joules/kg/K, and T_{ref} is 273.16 K. The correlations are valid for enthalpy ratios (h/h_E) in the range 0.015 to 2.

As in the case of laminar flow, considerable simplification occurs if we consider the high Mach number limit ($M_\infty\cos\phi > 10$) i.e.

$$\frac{(-\dot{q}_w)}{(1-H_w/H_r)} \approx 1.56\left(\frac{\rho_*\mu_*}{\rho_e\mu_e}\right)^{0.21}\left(\frac{\rho_*}{\rho_e}\right)^{0.58}\left(\frac{K}{C}\right)^{0.21} .$$

$$\left(1 + 0.190\left(\frac{Q_\infty\cos\phi}{1000}\right)\right)Q_\infty^3\rho_\infty^{0.79}$$

$$(\cos^2\phi + r\ \sin^2\phi)(\sin\phi)^{0.58}(\cos\phi)^{0.42}\ .\ 10^{-6}\ \text{kwatts/m}^2 \qquad (17)$$

9. Transition

In the case of the infinite-swept, attachment line it is firmly established that, when transition is caused by a large source of disturbance e.g. surface roughness or turbulence convecting out of a wing body junction, the conditions necessary for the first appearance of turbulent bursts on a surface without transpiration is

$$\bar{R}_{*_T} = \left(\frac{V_e^2}{\nu_*(dU_e/dx)_{x=0}} \right)^{1/2} = 245$$

where

$$\frac{T_*}{T_e} = 1 + 0.10\left(\frac{T_w}{T_e} - 1\right) + 0.60\left(\frac{T_r}{T_e} - 1\right)$$

- see Poll[1].

This can be translated into a boundary layer Reynolds number by noting that the laminar momentum thickness Reynolds number is given by the relation

$$R_\theta = \bar{R}\left(\frac{\mu_w}{\mu_e} \cdot \frac{T_e}{T_w}\right)^{1/2} . I$$

where I is a weak function of the edge Mach number and the wall-to-total temperature ratio. For the present purposes we note that for

$$0 < M_e < 6$$

$$I \approx 0.455\left(1 - 0.11\left(\frac{T_w}{T_o}\right)\right)\left(1 - 0.006M_e^2\right)$$

Moreover, when surface suction is applied R_θ is affected directly and we may represent this by a simple linear correction i.e.

$$R_\theta \approx \bar{R}\left(\frac{\mu_w}{\mu_e} \cdot \frac{T_e}{T_w}\right)^{1/2} .I.\left(1 + 0.35\left[\frac{\rho_w w_w}{\rho_e V_e} .\bar{R}\right]\right)$$

$$\text{for} \quad -1.4 < \left[\frac{\rho_w w_w}{\rho_e V_e}\bar{R}\right] < 1.4$$

It follows that, for a surface without transpiration, the value of the laminar momentum thickness Reynolds number at the onset of transition by gross contamination is -

$$R_{\theta_T} = 245\left(\frac{\mu_* \rho_e}{\mu_e\ \rho_*}\right)^{1/2} \left(\frac{\mu_w T_e}{\mu_e T_w}\right)^{1/2} . I \qquad (18)$$

In the case of transition in the presence of surface transpiration, there is no direct evidence to suggest what the role of transpiration might be. However, there is indirect evidence in the form of a direct numerical simulation of incompressible turbulent flow at an attachment line - see Spalart[21]. This study indicates that to a first approximation the value of the laminar momentum thickness Reynolds number at transition onset is constant i.e. not affected by the transpiration. Therefore, in the absence of any evidence to the contrary, it is proposed that the criterion given in equation (18) is valid for flows with transpiration. In terms of the R. criterion this becomes

$$\left[\bar{R}\left\{1 + 0.35\left(\frac{\rho_w w_w}{\rho_e V_e}\right)\bar{R}\right\}\right]_T = 245\left(\frac{\nu_*}{\nu_e}\right)^{1/2} \qquad (19)$$

Provided that

$$-1.0 < \left[\frac{\rho_e w_w}{\rho_e V_e}\right]\bar{R} < 1.0$$

This has an approximate solution

$$\bar{R}_T \approx 245\left[\frac{\left(\frac{\nu_*}{\nu_e}\right)^{1/2} + 86\left(\frac{\rho_w w_w}{\rho_e V_e}\right)}{1 + 172\left(\frac{\rho_w w_w}{\rho_e V_e}\right)}\right] \qquad (20)$$

which is valid over a slightly reduced range

$$-0.5 < \left[\frac{\rho_e w_w}{\rho_e V_e}\right]\bar{R} < 1.0$$

It is clear from equation (20) that blowing reduces the critical value whilst suction increases it. However, the effect of the transpiration is not particularly strong.

In the high speed limit the dynamic viscosity ratio tends to the following limit, in the case of the perfect gas -

$$\frac{\nu_*}{\nu_e} \rightarrow (0.90 + 0.60r\ \tan^2\phi)^{3/2}$$

whilst the suction coefficient

$$\frac{\rho_w w_w}{\rho_e V_e} \rightarrow \frac{\cos\phi}{\tan\phi}\left(\frac{w_w}{Q_\infty}\right)\left(\frac{T_o}{T_w}\right)$$

It follows that equation (20) reduces to

$$D\rho_\infty = \frac{3.24\times10^{-4}}{\tan^2\phi} \cdot \left[\frac{(0.90+0.60r\tan^2\phi)^{3/4} + 86\dfrac{\cos\phi}{\tan\phi}\left(\dfrac{w_w}{Q_\infty}\right)\left(\dfrac{T_o}{T_w}\right)}{1 + 172\dfrac{\cos\phi}{\tan\phi}\left(\dfrac{w_w}{Q_\infty}\right)\left(\dfrac{T_o}{T_w}\right)}\right]^2$$

The interesting feature of this relation is that, in the case of no transpiration, it does not depend upon the free-stream velocity, Q_∞, (although this quantity must be high). A plot of the variation of $D\rho_\infty$ with sweep angle for zero transpiration, one value of blowing and one value of suction are given in figure 8.

It is evident that sweep angle is an important parameter and that transition occurs at the highest altitude (minimum density) when the sweep angle is about 60°. In the case with no transpiration, the earliest possible transition occurs when

$$\rho_\infty = 4.2 \times 10^{-4}/D \quad (\mathrm{kg/m^3})$$

We may also note that, at the high sweep angles, transpiration has little effect upon transition altitude. However, the influence of both sweep and transpiration becomes stronger as the sweep angle decreases.

10. Summary and Conclusions

A series of very simple relationships has been developed for heat transfer at an inclined attachment line in the hypervelocity flight regime.

The results may be summaried as follows

a) laminar flow

$$\frac{(-\dot{q}_w)}{(1 - H_w/H_r)} \approx 0.14(\Psi_e)_L \frac{Q_\infty^3 \rho_\infty^{1/2}}{D^{1/2}} \cdot$$

$$(\cos^2\phi + 0.85\sin^2\phi)\cos\phi \times 10^{-6} \quad \mathrm{kwatts/m^2}$$

with $(\Psi_e)_L \approx 0.96\left[1 + 0.036\left(\dfrac{Q_\infty\cos\phi}{1000}\right)\right]$

for $1200\ \mathrm{m/sec} < Q_\infty\cos\phi < 8000\ \mathrm{m/sec}$

and, with surface transpiration,

$$\frac{(-\dot{q}_w)}{(-\dot{q}_w)_{w=0}} \approx \frac{b}{[\exp(b)-1]}$$

where $b = 2\rho_w w_w H_r \dfrac{(1 - H_w/H_r)}{(-\dot{q}_w)_{w=0}}$

b. turbulent flow

$$\frac{(-\dot{q}_w)}{(1-h_w/H_r)} \approx 2.38(\Psi_e)_T\left(\frac{\rho_*\mu_*}{\rho_e\mu_e}\right)^{0.21}\left(\frac{\rho_*}{\rho_e}\right)^{0.58}\frac{Q_\infty^3\rho_\infty^{0.79}}{D^{0.21}} \cdot$$

$$(\cos^2\phi + 0.90\sin^2\phi)(\sin\phi)^{0.58}(\cos\phi)^{0.42} \times 10^{-6}$$

kwatts/m²

with $(\Psi_e)_T \approx 0.815\left(1 + 0.190\left(\dfrac{Q_\infty\cos\phi}{1000}\right)\right)$

for $1200\ \mathrm{m/sec} < Q_\infty\cos\phi < 8000\ \mathrm{m/sec}$

and, with surface transpiration,

$$\frac{(-\dot{q}_w)}{(-\dot{q}_w)_{w=0}} \approx \frac{b}{[\exp(b)-1]}$$

where $b = 2\rho_w w_w H_r \dfrac{(1 - H_w/H_r)}{(-\dot{q}_w)_{w=0}}$

c. transition

$$D\rho_\infty \approx \frac{3.24\times10^{-4}}{\tan^2\phi} \cdot \left[\frac{(0.90+0.53\tan^2\phi)^{3/4} + 86\dfrac{\cos\phi}{\tan\phi}\left(\dfrac{w_w}{Q_\infty}\right)\left(\dfrac{T_o}{T_w}\right)}{1 + 172\dfrac{\cos\phi}{\tan\phi}\left(\dfrac{w_w}{Q_\infty}\right)\left(\dfrac{T_o}{T_w}\right)}\right]^2$$

Finally, as an illustrative example, the effects of sweep angle upon attachment-line heat transfer rate for a leading edge of diameter 0.2m, flying at 6 km/sec at an altitude of about 30 kms (density = 1.2×10^{-2} kg/m^3) are demonstrated in figure 9. It is apparent that, for laminar flow, the real gas effects are modest and that increasing the sweep angle produces the expected monotonic decrease in heating rate. In the case of turbulent flow the situation is very different. Firstly the real gas effects are large and amount to an increase of over 60% in the heating rate. Secondly, the heating rate itself exhibits a very severe peak, with a maximum value which is three times the laminar level for the same sweep angle, and, thirdly, the transition criterion indicates that the turbulent flow is to be expected under these conditions.

11. References

1. Poll, D.I.A. The development of intermittent turbulence on a swept attachment line including the effects of compressibility. The Aeronautical Quarterly, Vol XXXIV, Feb. 1983.

2. Poll, D.I.A. Skin friction and heat transfer at an infinite-swept attachment line. The Aeronautical Journal, Vol. XXXII, pp 299-318, Nov. 1981.

3. Lees, L. Laminar heat transfer over blunt-nosed bodies at hypersonic flight speeds. Jet Propulsion, Vol. 26, No. 4, April 1956, pp 259-269.

4. Cohen, N.B. Boundary layer similarity solutions and correlation equations for laminar heat-transfer distribution in equilibrium air at velocities up to 41,000 feet per second. NASA Technical Report R-18, May 1961.

5. Van Driest, E.R. The laminar boundary layer with variable fluid properties. Procs of the Heat Transfer and Fluid Mechanics Institute, University of California, Berkeley 1954.

6. Eckert, E.R.G. Engineering relations for friction and heat transfer to surfaces in high velocity flows. Journal of the Aeronautical Sciences, Vol. 22, August 1955, pp 585-587.

7. Colburn, A.P. A method of correlating forced convection heat transfer data and a comparison with fluid friction. Transactions of the American Institute of Chemical Engineers, Vol. 29, 1933, pp 174-210.

8. Bradshaw, P. Compressible turbulent shear layers. Annual Review of Fluid Mechanics, Vol.m 9, 1977, pp 33-54.

9. Beckwith, I.E. Similar solutions for the compressible boundary layer on a yawed cylinder with transpiration cooling. NASA Technical Report R-42, 1958.

10. Libby, P.A. and Kassoy, D.R. Laminar boundary layer at an infinite swept stagnation line with large rate of injection. AIAA Journal, Vol. 8, No. 10, pp 1846-, 1970.

11. Adams, J.C. and Martindale, W.R. Hypersonic lifting body windward surface flow-field analysis for high angles of attack. AEDC-TR-73-2, February 1973.

12. Cohen, N.B. Correlation formulas and tables of density and some transport properties of equilibrium dissociating air for use in solutions of the boundary layer equations. NASA TN D-194, October 1959.

13. Feldman, S. Hypersonic gas dynamic charts for equilibrium air. AVCO Research Laboratory Report 40, January 1957.

14. Hansen, C.F. Approximation for the thermodynamic and transport properties of high-temperature air. NASA Technical Report R-50, November 1957.

15. Tannehill, J.C. and Mohling, R.A. Development of equilibrium air computer programs suitable for numerical computations using time-dependent or shock-capturing methods. NASA CR-2134, Sept. 1972.

16. Tannehill, J.C. and Mugge, P.H. Improved curve fits for the thermodynamic properties of equilibrium air suitable for numerical computation using time-dependent or shock-capturing methods. NASA CR-2470, Oct. 1974.

17. E.S.D.U. Properties of a standard atmosphere. Item number 77021, Oct. 1977 (amended June 1986).

18. Topham, D.R. An empirical formula for stagnation point velocity gradient for spheres and circular cylinders in hypersonic flow. Journal of the Royal Aeronautical Society, Vol. 69, June 1965, pp 407-408.

19. Moeckel, W.E. and Weston, K.C. Composition and thermochemical properties of air in chemical equilibrium. NASA TN 4265, Feb. 1958.

20. Viegas, J.R. and Howe, J.T. Thermodynamic and transport property correlation formulas for equilibrium air from 1000°K to 15000°K. NASA TN D-1429, June 1962.

21. Spalart, P. Direct numerical study of leading-edge contamination. AGARD CP 438 "Fluid Dynamics of Three-Dimensional Turbulent Shear Flow and Transition".

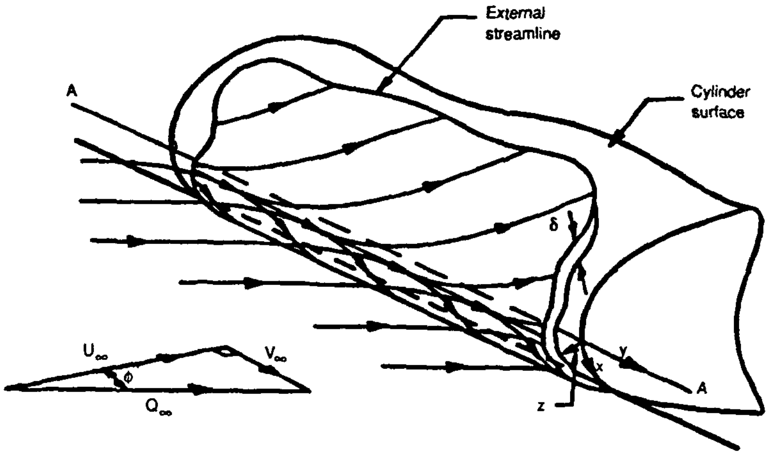

Figure 1. Flow near the leading edge of a long swept cylinder.

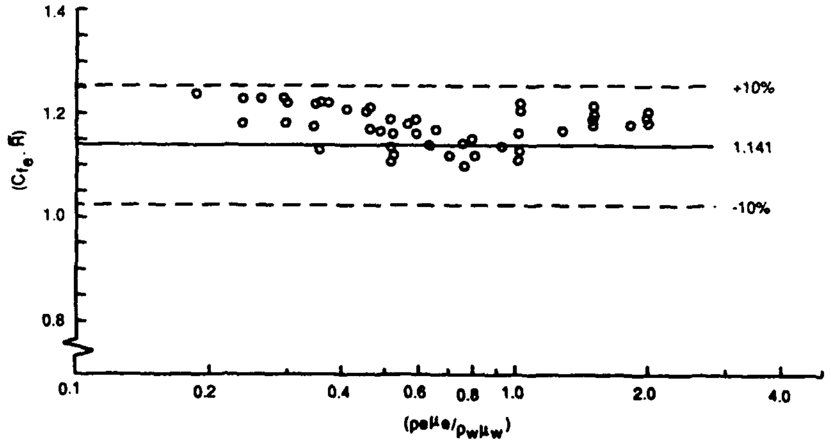

Figure 2. Comparison between the approximate relation for skin friction and Cohen's "exact" solutions. (ref.4)

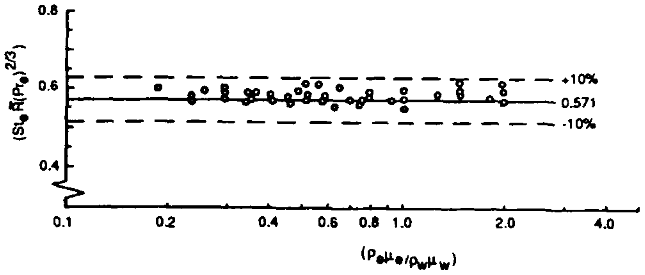

Figure 3. Comparison between the approximate value for heat transfer rate and Cohen's "exact" solutions. (ref.4)

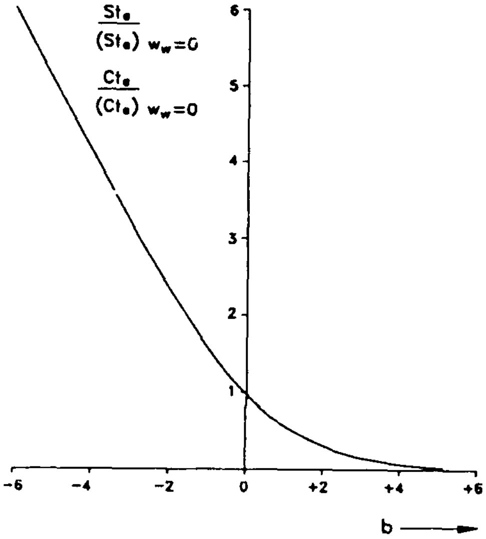

Figure 4. The effect of surface transpiration on skin friction and heat transfer.

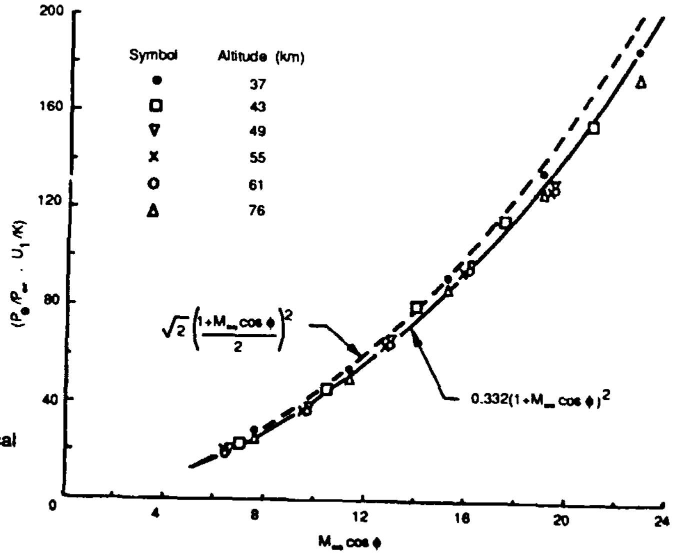

Figure 5. Attachment-line velocity gradient as a function of Mach number and altitude for air in thermochemical equilibrium, after Feldman. (ref.13)

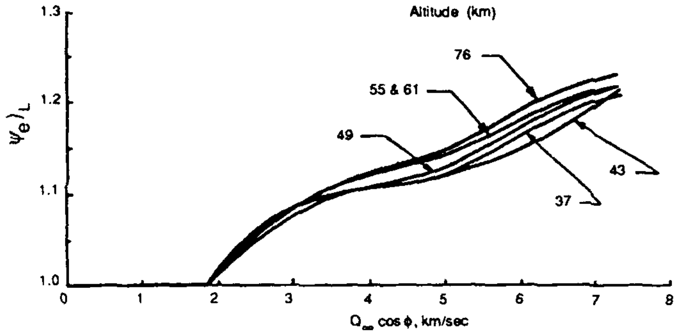

Figure 6. The variation of the laminar real gas parameter $\psi_e)_L$ with speed and altitude, after Feldman. (ref.13)

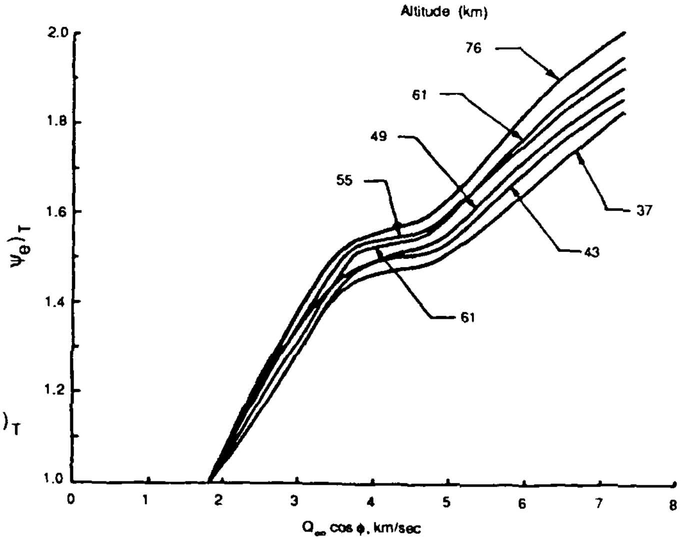

Figure 7. The variation of the turbulent real gas parameter $\psi_e)_T$ with speed and altitude, after Feldman. (ref.13)

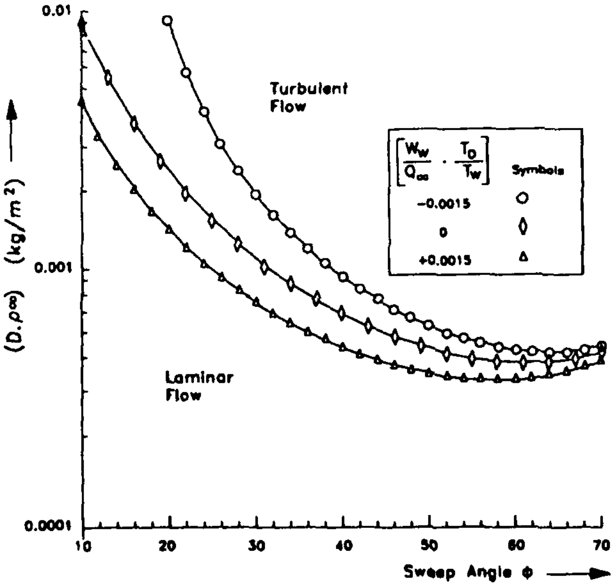

Figure 8. The influence of wall transpiration on transition in the limit of hyper velocity flight.

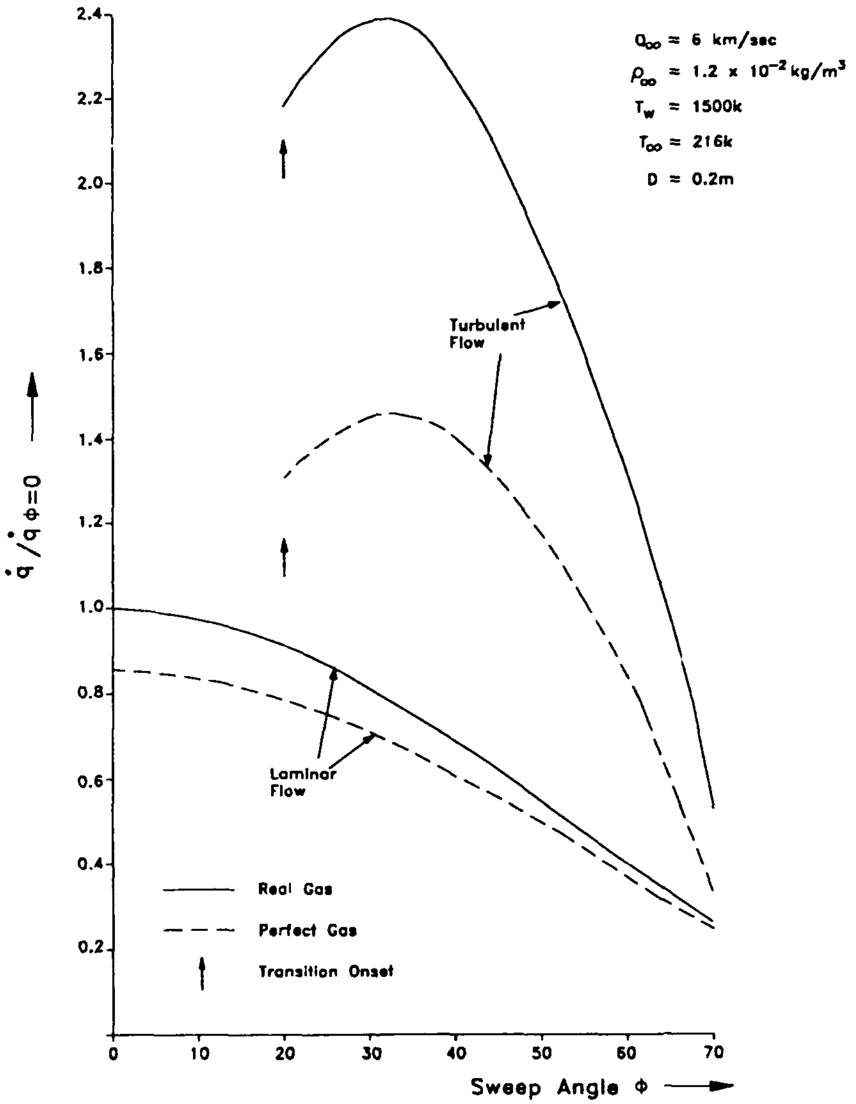

Figure 9. Effect of sweep angle on attachment line heat transfer rates.

On the Instability of Hypersonic Flow Past a Pointed Cone
- Comparison of Theoretical and Experimental Results at Mach 8 -

Martin Simen* and Uwe Dallmann
DLR Institute of Theoretical Fluid Mechanics
Bunsenstrasse 10, D-3400 Göttingen
Germany
*delegated from Dornier Luftfahrt GmbH / Deutsche Aerospace to the DLR
and partly supported by the BMFT

SUMMARY

In view of the prevailing discrepancies between experiment and theory with regard to instabilities in hypersonic flow an extended theoretical approach is studied. For hypersonic flow past a pointed cone Thin Layer Navier Stokes solutions are compared to similarity solutions with different modelling of viscosity-temperature laws. The formulation of the stability equations in curvilinear coordinates allows a discussion of various representations of the local body metric. A systematic sensitivity study of basic state profiles and spatial amplification rates is performed. It is found that the improved agreement with the experiment in the viscous first mode region is equally due to the extended stability analysis, where cone metric is specified, and the extended mean flow solution as well. In the second mode region the major improvement results from the more complete basic state formulation, however, the close agreement with measured growth rates is only achieved when the stability analysis is based on conical metric.

1. INTRODUCTION

For a physical understanding of the initial stages of laminar-turbulent transition of hypersonic flow it is now generally agreed that the best approach is to measure characteristics of instability waves experimentally and to compare these directly to results from stability theory. Effects considered to be relevant for the flow type and configuration under investigation which might influence stability results are taken into account by successive generalizations of the classical, local, linear stability theory.

This approach allows direct comparison of experimental and theoretical data. As opposed to transition experiments, where only mean quantities like wall heat transfer rates are measured, in the so-called instability experiments hot wire anemometer signals are recorded at selected locations within the boundary layer in the form of time series and transformed into power spectra via standard data reduction techniques. The hot wire probe is moved downstream and e.g. placed at a distance from the wall where the disturbance energy signal reaches a maximum. Amplification rates are obtained from the power spectra by determining the change in amplitude in streamwise direction at a certain frequency. Thereby direct comparison to spatial amplification rates from linear stability theory is possible. Such experiments were carried out on flat plates at supersonic Mach numbers by Laufer & Vrebalovich [17], Demetriades [6], Kendall [13], [14], Kosinov, Maslov & Shevelkov [15] and for pointed cones at hypersonic Mach numbers by Kendall [14], Demetriades [7] and Stetson [30].

Kendall's experiments [13] for the first time confirmed the existence and dominance of second mode disturbances in a high Mach number boundary-layer flow. The largest and most detailed data base which allows direct comparison between theory and experiment was given by Stetson [30] [31], [32]. This was the main reason for taking his results as a reference for our computations. The pointed cone as a generic body was also chosen because of its closer geometrical similarity to practical configurations than the flat plate. In addition it is a major outcome of our present work that for improved agreement between theory and experiment the formulation of both the basic state and the stability equations for cone flow should be carried out differently than for flow along a flat plate. Hence, results obtained for a flat plate should not directly be transferred to those for a cone as for example by employing Mangler transformation. The blunt cone case is not considered in the present study because of the additional difficulties associated with the modelling of the nose tip flow region. Our intention is to resolve some discrepancies between theory and experiment for the most simple case where they have been prominent. We analyze a generic hypersonic flow field along a pointed cone. Also this investigation is aimed at clarifying features of linear instability wave propagation. Extension to the non-linear regime should only be performed after generic discrepancies between theoretical and experimental results have been identified.

Stetson's measurements [30] were carried out for a pointed cone of 7 degree half angle, placed in a free stream flow of Mach number eight, stagnation point temperature $T_0 = 728°K$ and a unit Reynolds number $Re/ft = 1 \cdot 10^6\ 1/ft$. A comprehensive representation of data obtained by Stetson is given in **fig. 1**. The figure shows the fluctuation spectra of peak disturbance energy in wall normal direction, obtained at different streamwise locations. The frequencies at which these curves have a maximum are in the range where second mode disturbances are dominant, as demonstrated by Mack [19].

The change in amplitude distribution in streamwise direction for individual frequencies yields spatial amplification rates, directly comparable to stability theory. Such a comparison was carried out by Mack [19].

[20] based on compressible, linear stability equations formulated in Cartesian coordinates and using Mangler transformation to obtain cone boundary layer flow profiles from flat plate similarity solutions. A typical result is given in **fig. 2.** Only qualitative agreement could be achieved between stability calculations and measurements, whereas experimental data from three different authors (Kendall [14], Demetriades [7] and Stetson [30]) obtained in different wind tunnels with similar free stream conditions show close quantitative agreement. **Fig. 2** therefore can be considered as a benchmark for stability calculations since a narrow experimental error bar is given. The quantitative disagreement with the results obtained by Mack [20] has led him to some criticism towards the experimental set up. His main point is that the free stream disturbance field, triggering instability waves within the boundary layer, is not controlled. In fact, the only experiments in supersonic flow using controlled disturbances of specified frequency and amplitude are those of Kendall [13] and Kosinov, Maslov & Shevelkov [15]. In both, at a line or point source, periodic fluctuations were produced within the boundary layer by means of electric glow-discharge. In Kendall's case plane waves were produced by placing electrode pairs within the plate surface at various obliqueness angles. In Kosinov's case pointed electrodes were placed inside the plate in contact with the flow through a small hole. The pulsating flow-discharge here generated wave packets. Mack argued that in an uncontrolled disturbance environment the fluctuation spectra obtained may not neccessarily be due to instability waves but may also represent effects of continuous receptivity, secondary instabilities and non-linear processes. The latter is indicated by the appearance of another amplified frequency range at approximately twice the second mode frequency as shown in **fig. 1.** Also, according to Mack, 'amplification rates obtained from the spectra at the wall normal locations of the peak wideband response are not neccessarily the locations of the peaks of the individual frequency components'. For uncontrolled disturbances the wave motion is determined by a superposition of normal modes of unknown spanwise wave number spectrum. On the other hand the theory considers only single normal modes of specified spanwise wave numbers. Finally, for the wind tunnel used the unknown initial disturbance amplitude at the location of neutral growth may be at such a level that already after a short region of linear amplification non-linear amplification and finally non-linear saturation phenomena may take place.

On the other hand, one can argue that the assumptions under which Mack's stability analysis has been performed do not capture some relevant flow features present in the experiment as discussed in the following: The interaction between an oscillating shock wave and an instability wave originating from the boundary layer was studied by Chang & Malik [3] using linearized Rankine-Hugoniot conditions as outer boundary conditions of the stability problem. However, it was found that only in the hypersonic limit not for the flow conditions of Stetson's experiment, first and second mode disturbances were noticably stabilized. In the same paper by Chang & Malik it was also checked whether a very small nose bluntness as is always present on a real, pointed cone would have an impact on the growth rate, as it was known from both experiments by Stetson et al. [31] and computations by Malik [22], Reshotko & Khan [27] that small nose bluntness significantly stabilizes the flow. However, no effect was found for the case of very small nose radius.

It can be well assumed that under the experimental condition of free stream Mach number eight and wall temperature of 611°K the perfect gas assumption is still valid. A typical case where chemical reactions appear in the flow would be at a Mach number of 25 and a wall temperature of 1200°K, as considered by Stuckert & Reed [35].

Instead we believe that results from stability theory concerning the growth rates of instability waves in the flow past a pointed cone, under the conditions of Stetson's experiment [30], are mainly sensitive towards

- ***non-parallel flow effects***
According to Bertolotti [2], El Hady [9] these effects become pronounced with increasing Mach number and wave obliqueness and closer agreement with the flat plate experiment of Kendall [13] is found when terms due to nonparallelism of the flow are included in the analysis. The same trend is observed when comparing measurements of Kosinov, Maslov & Shevelkov [15] to results from non-parallel theory as pointed out by Maslov [24].

- ***temperature distribution***
Both the stagnation temperature and the wall temperature (cooling) have a strong influence on growth rates for high Mach numbers as demonstrated by Mack [20], [21] and therefore should be specified according to the experiment. The stabilizing influence of wall cooling on first mode disturbances and the destabilizing influence on second mode disturbances has been confirmed experimentally by Lysenko & Maslov [18]. In addition the form in which the temperature dependence of the thermodynamic properties is specified can markedly alter stability results (see Bertolotti [2]). In this investigation we will discuss the effect of different viscosity-temperature laws on spatial amplification rates.

- ***viscous / inviscid interaction***
Several attempts (Gasperas [10], Mack [20], Chang & Malik [3]) have been made to obtain basic state solutions that account for viscous/inviscid interaction which can be expected to be present under the given flow conditions, as the shock distance from the wall, in a range where instability waves grow, is only about three to seven times the boundary layer edge distance from the wall. All of these authors computed solutions of parabolized Navier Stokes equations (PNS) and experienced difficulties to obtain a converged solution. However Chang & Malik [3] reported enhanced agreement with Stetson's experimentally obtained growth rates in **fig. 2,** when about 200 grid points from the wall to the shock were used in the PNS computations.

- ***surface curvatures***
The effect of transverse curvature on the instability of axisymmetric supersonic boundary layer flow has been studied by Malik & Spall [23]. They found that axisymmetric first and second mode disturbances were stabilized but oblique first mode waves were destabilized. Gasperas [11] included cone divergence terms in the stability analysis by introducing body-oriented coordinates and found the effect on axisymmetric disturbances to be stabilizing. Enhanced agreement to Stetson's experimental results in **fig. 2** was obtained. Kosinov & Maslov [16] found in an experiment with

controlled disturbances at free stream Mach number two that cone amplification rates were smaller than those of a flat plate after Mangler transformation.

In this paper we discuss in how far a more complete formulation of both the basic state equations and the stability equations, accounting for viscous/inviscid interaction and complete body geometry, leads to an improved agreement between spatial growth rates of instability waves obtained from linear stability theory and stability experiment. For that purpose we investigate various basic state computation methods. Thin Layer Navier Stokes solutions are compared to similarity solutions with different modelling of viscosity-temperature properties. A systematic sensitivity study of these approaches towards both basic state profiles and spatial amplification rates of two- and three-dimensional instability waves is performed. Special emphasis is layed on identifying relevant parameters that influence the convergence of the numerical solutions of the Thin Layer Navier Stokes equations. The formulation of the stability equations in curvilinear coordinates allows a discussion of various representations of the local body metric. Inviscid stability features of the cone flow solutions are investigated. The present study concentrates on local stability investigations. However, our formulation of the stability equations allows us to outline that non-local stability equations can be derived by generalizing our approach in a straight forward manner.

2. PROBLEM FORMULATION

2.1 Basic State Solutions

2.1.1 Similarity Solutions of the Boundary Layer Equations

The similarity solutions are obtained from the classical boundary-layer equations of compressible, zero pressure gradient, two dimensional, planar boundary layer flow for conservation of mass, momentum and energy. All flow and material quantities are non-dimensionalized by their corresponding (local) inviscid free stream values. The material quantities are treated such that the specific heats c_p^*, c_v^* at constant pressure and volume, are assumed constant along with the Prandtl number $Pr = c_p^* \mu^*/\kappa^*$, (*: dimensional quantity, μ^*: dynamic viscosity, κ^*: thermal conductivity) according to the results which will be discussed in chapter 3.2.2. Dynamic viscosity is assumed to be a function of temperature T^* only, given as a linear function for the Chapman Rubesin similarity solution (see [4]) and given by Sutherland's formula for similarity solutions as obtained by Mack [20]. After introduction of appropriate similarity transformations (see Stewartson [34], p.35) the ordinary differential equations obtained are solved by a fourth order Runge Kutta IMSL-routine for the formulation provided by Chapman-Rubesin [4] and by a variable order Adams-Moulton integration subroutine for the formulation by Mack [20]. The pointed cone boundary layer flow solutions are obtained by introducing Mangler-Stepanov transformation (see Stewartson [34], p.105) which yields (c: cone, fp: flat plate x^1: wall-tangential coordinate, x^3: wall-normal coordinate, $f_{,i}$: covariant derivative in direction i)

$$x_c^1 = 3x_{fp}^1 \, , \quad x_c^3 = x_{fp}^3/\sqrt{3}$$

and

$$f(x_c^3)_{,3} = f(x_{fp}^3)_{,3}/\sqrt{3}$$

The function $f(x^3)$ represents either the velocity or temperature profile. We note that cone similarity profiles obtained from Mangler-Stepanov transformation of the axisymmetric boundary layer equations are identical to flat plate profiles obtained from planar boundary layer equations apart from the constants given above. Cone similarity solutions are obtained only if transverse curvature is neglected in the momentum equations. A discussion of this can be found in Malik & Spall [23] and Mack [20].

2.1.2 Solution of the Thin Layer Navier Stokes Equations

The Thin Layer approximation to the Navier Stokes equations (TLNS) stems from the observation that in high Reynolds number flows the viscous derivatives in the streamwise and circumferential directions are in general numerically not resolved, because they are usually of order of magnitude $O(Re^{-1})$ as opposed to the viscous derivatives in the wall normal direction, which are usually of $O(1)$. (Reynolds number based on free stream quantities and characteristic streamwise length). The latter are in general resolved by clustering grid lines in the boundary layer. Thus the approximation is employed by neglecting the viscous streamwise and circumferential derivatives while retaining those in wall normal direction. As opposed to the Parabolized Navier Stokes (PNS) equations the basic state flow field is obtained by iterating the TLNS solution in time to a steady state. As opposed to PNS computations it is therefore possible to iterate the residual to arbitrary low levels without a constraint on the step size in streamwise direction. Both the PNS and our TLNS are space marching methods, i.e. the mixed hyperbolic-parabolic character of the equations allows that the solution is marched downstream starting from specified initial conditions. In the TLNS space marching method the upstream influence in the subsonic part of the boundary layer is suppressed. Both methods produce departure solutions if the inviscid flow field becomes locally subsonic. For the PNS such exponentially growing solutions additionally can occur for small marching step sizes through the elliptic character introduced into the steady equations if a streamwise pressure gradient is present within the subsonic part of the boundary layer. Hence, the TLNS space marching method is more accurate and more robust but less efficient - due to the additional iteration in time - than conventional implicit parabolized Navier Stokes methods.

Within the Thin Layer Approximation the equations for conservation of mass, momentum and energy are non-dimensionalized with their corresponding free stream values, pressure with twice the free stream dynamic pressure and coordinates with a characteristic length L in streamwise direction. The Prandtl number is assumed constant (see chapter 3.2.2) along with the specific heats. Dynamic viscosity is described by Sutherland's law. Compared to the boundary layer equations the cone flow field is now described by additionally taking into account of pressure gradients via $p_{,i}$ and surface curvature. The TLNS equations include the Euler equations for inviscid flow. Hence, the computation can be extended beyond the shock into the inviscid free stream flow field. Also, complete inviscid flow field solutions can be obtained by neglecting the terms containing Reynolds number.

The computer program utilized to solve the TLNS equations has been written by Müller [26]. Therein the farfield boundary conditions are the free stream conditions (shock capturing). At the surface no-slip conditions for the velocities and isothermal or adiabatic boundary conditions for the wall temperature are specified and zero wall-normal pressure gradient is assumed. Conical conditions are assumed at the singularity for pointed bodies and at the outflow surface the slope of the conservative variables in streamwise direction is assumed constant. The computational mesh is set up such that the grid points are distributed at equal increments in the streamwise direction and clustered near the body in wall normal direction by the function

$$x^3(\lambda) = 1 + b\,\frac{1 - \left(\frac{b+1}{b-1}\right)^{1-\lambda}}{1 + \left(\frac{b+1}{b-1}\right)^{1-\lambda}}\ ; \qquad (1)$$

$$0 \le \lambda \le 1\ ,\ b > 1$$

where $\lambda = (k-1)/k_{\max}$; $k = 1(1)k_{\max}$ and $b = 1\,001$ typically. The governing equations in conservation law form are discretized by approximating the time derivative by the first-order Euler implicit formula, the inviscid spatial derivatives by the second order accurate upwind method of Harten and Yee [12] which has total variation diminishing (TVD) properties by flux modification, and by second order finite differences for the viscous terms. Numerical damping of linear waves is introduced through an entropy function [12], [26] controlled by an entropy parameter E usually of $O(10^{-1})$.The obtained linear system is solved by the diagonally dominant alternating direction implicit (DD-ADI) method using underrelaxation.

2.2 Solution of the Linear Stability Equations

2.2.1 Linear Stability Equations

In linear stability theory the total flow is decomposed into a steady basic flow, whose instability is investigated, plus an unsteady perturbation flow with infinitesimally small amplitudes so that the resulting perturbation equations can be linearized, meaning that no interaction between fluctuation quantities is considered.

The total flow is supposed to satisfy the equations of conservation of mass, momentum and energy in the case considered here of compressible flow along curved surfaces, given in tensor notation as $(i,j,k,m,n = 1,(1),3)$

$$\frac{\partial\rho}{\partial t} + (\rho\, v^j)_{,j} = 0\ . \qquad (2)\text{a}$$

$$\rho\left(\frac{\partial v^i}{\partial t} + v^j v^i_{\ ,j}\right) = -p_{,j}g^{ij} +$$

$$\frac{1}{Re}\left[\,(\lambda v^k_{\ ,k} g^{ij})_{,j} + \{\mu(g^{im}v^j_{\ ,m} + g^{jn}v^i_{\ ,n})\}_{,j}\,\right]\ . \qquad (2)b$$

$$\rho\left(\frac{\partial T}{\partial t} + v^j T_{,j}\right) - (\gamma - 1)M^2\left(\frac{\partial p}{\partial t} + v^j p_{,j}\right) =$$

$$\frac{1}{RePr}\,(\kappa g^{ij}T_{,j})_{,i} + \frac{(\gamma - 1)M^2}{Re}\,g_{ik} \qquad (2)c$$

$$\left[\,\lambda v^m_{\ ,m} g^{kj} + \mu(g^{km}v^j_{\ ,m} + g^{jn}v^k_{\ ,n})\,\right] v^i_{\ ,j}$$

plus the equation of state

$$p = \frac{\rho T}{\gamma M^2}\ .$$

g^{ij}, g_{ij} are the contravariant, covariant metric tensors. The dependent variables ρ, v^i, p, T stand for density, contravariant velocity component in direction i, pressure and temperature. The independent variables are the curvilinear coordinates x^i and time t. M, Re, Pr stands for Mach number, Reynolds number, Prandtl number λ, γ for second viscosity coefficient and ratio of specific heats. All flow and material quantities are nondimensionalized in the same way as for the Thin Layer Navier Stokes equations discussed in chapter 2.1.2. Also Prandtl number and specific heats are again assumed constant. All flow- and non-constant material-quantities are now decomposed into a steady basic and an unsteady perturbation flow quantity.

$$q = \bar{q}(x^i) + \tilde{q}(x^i, t)\ . \qquad (3)$$

The covariant derivatives are evaluated by

$$q^i_{\ ,j} = \frac{\partial q^i}{\partial x^j} + \Gamma^i_{kj} q^k\ ,$$

$$q_{,j} = \frac{\partial q}{\partial x^j}\ . \qquad (4)$$

Γ^i_{kj} is the Christoffel-symbol, as defined e.g. in Aris [1], p. 165. Orthogonal, curvilinear coordinates are introduced so that only diagonal metric tensor elements g^{ii}, g_{ii} remain. In addition the assumption of so-called locally parallel flow*) is imposed, i.e.

$$\bar{q} = \bar{q}(x^3)\ ,$$

$$\bar{v}^i = (\bar{v}^1, \bar{v}^2, 0)\ ,\ \bar{p}(x^3) = const. \qquad (5)$$

Hence, with this formulation non-parallel flow effects on flow instability are a priori not taken into account. In (5) the indices 1, 2 represent coordinate directions locally tangent and 3 locally normal to the body surface. For the perturbation flow quantities, we seek particular solutions of the form

$$\tilde{q}^i = \hat{q}^i(x^3)e^{i\theta} + \text{c.c.}\ ,\ \theta = k^i x^i g_{ii} - \omega t \qquad (6)$$

where $\hat{q}^i$ is the complex amplitude function, ω the frequency and k^i the wave number vector

$$k^i = \frac{1}{h_i}(k(1), k(2), 0) = \frac{1}{h_i}(\alpha/h_1, \beta/h_2, 0)\ . \qquad (7)$$

We also define

$$k_w(i) := (\alpha, \beta, 0)$$

and hence obtain

$$\frac{\partial\theta}{\partial x^i} = k_w(i)\ . \qquad (8)$$

The particular solutions (6) physically represent individual instability waves also termed normal mode solutions. We now introduce the ratio of characteristic lengths in wall-normal and streamwise direction $l/L = 1/\sqrt{Re}$, where l stands for the Blasius length $l = (\nu^*_\infty L/U^*_\infty)^{1/2}$, based on freestream conditions and streamwise characteristic length. With this ratio we assume the following orders of magnitude for a defined norm of the basic and perturbation flow quantities, the coordinates x^i, the frequency ω, the wave number components $k_w(i)$, the Lamé-parameters h_i (see Aris [1], p. 143) and the metric gradients:

---

*) The so-called local parallel flow assumption has the usual meaning that one neglects wall-normal velocity components $\bar{v}^3$. Nevertheless, divergence or convergence of stream lines in planes $x^3 = const$ may still occur (e.g. on a cone).

$$\|\bar{q}\| = 0(1)\ ,\ \ \|\hat{q}\| = A \cdot 0(1)\ , \tag{9)a}$$

$$\|x^1\| = \|x_2\| = 0(1)\ ,\ \ \|x^3\| = 0\left(Re^{-1/2}\right)\ , \tag{9)b}$$

$$\|\omega\| = 0\left(Re^{1/2}\right)\ , \tag{9)c}$$

$$\|k_w(i)\| = 0\left(Re^{1/2}\right)\ . \tag{9)d}$$

$$\|h_i\| = 0(1)\ ,\ \ \left\|\frac{\partial h_i}{\partial x^j}\right\| = 0\left(Re^{-1/2}\right)\ , \tag{9)e}$$

where for the perturbation amplitude $A \ll 1$ is assumed. We note that dimensionless wave number and frequency based on Blasius length is typically of $O(1)$. Then eqs. (9c, 9d) follow from $l/L = Re^{-1/2}$. In addition eq. (9) restricts metric gradients to be of $O(Re^{-1/2})$ in all coordinate directions.

We insert eqs.(3)-(8) into the total flow equations (2) and rewrite each non-constant quantity as product of norm times normalized form. Considering (9) we keep only terms that are linear in A and among these neglect all terms of $O(Re^{-1})$ and smaller. By this procedure we obtain the linear, local stability equations of compressible, three-dimensional, parallel flow along curved surfaces, given in Simen & Dallmann [29].

We note that all dependent variables $\bar{q}^i$, $\hat{q}^i$ are functions of the wall normal coordinate x^3 only. However, we allow for small metric gradients $\partial h_i/\partial x^j$ in all three directions. Therefore we have to point out that by applying for stability analysis of flows where flow divergence in wall-parallel and wall-normal directions or stream line curvature provides terms of $O(Re^{-1/2})$ (or even larger terms), so-called non-parallel flow effects on flow instability are not taken into account. To include such effects a non-local theory (briefly discussed below) would be required. Supposedly small wall tangential gradients in $\bar{q}^i$, $\hat{q}^i$, h_i, $k(i)$, which result in a system of partial differential equations to be solved, can be treated e.g. by the method of multiple scales or by a marching scheme as in Bertolotti [2].

Let us briefly describe how the local approach discussed above can be extended to a non-local theory in a straight forward manner. We replace equations (5) by

$$\bar{q} = \bar{q}(x^j)\ ,\ \ \bar{v}^i(x^j) = (\bar{v}^1, \bar{v}^2, \bar{v}^3)\ ,\ \ \bar{p} = \bar{p}(x^j)$$

and equations (6), (7) by

$$\tilde{q}^j = \hat{q}^j(x^i)e^{i\theta} + c.c.\ ,\ \ \theta = \int k^j dx^j g_{jj} - \omega t\ ,$$

$$k^i(x^1, x^2) = \frac{1}{h_i}\left(\alpha(x^1, x^2)/h_1, \beta(x^1, x^2)/h_2, 0\right)\ ,$$

and we add to equations (9)

$$\|\bar{v}^3\| = 0\left(Re^{-1/2}\right)\ ,$$

$$\|\hat{p}\| = A \cdot 0\left(Re^{-1}\right)\ .$$

$\|\hat{p}\| = A \cdot 0(Re^{-1})$ is introduced to suppress wall tangential gradients of pressure fluctuations, similar to the procedure taken for solving the TLNS equations. (see Müller [26]. With the same procedure as described above, we now obtain an eighth order system of stability equations, which are parabolic in the wall tangential directions. Equations of this type can then be solved via a marching procedure as outlined e.g. in Bertolotti [2]. The benefit of this non-local theory is that the effect of body surface curvature, stream line curvature and curvilinear wave propagation can be studied simultaneously in a consistent way. Terms in the non-local stability equations containing metric gradients $\partial h_i/\partial x^j$ appear because of body surface curvature. Terms with $\partial\bar{v}^i/\partial x^j$ ($l = 1,2$) are due to flow divergence with or without stream line curvature (apart from the body curvature effect). Terms with wave vector derivatives $\partial\alpha/\partial x^i$, $\partial\beta/\partial x^i$ appear for curvilinear wave propagation. Details of such a non-local stability theory in general tensor notation will be given in a different paper. In this paper we concentrate on results obtainable from a local stability theory.

2.2.2 Numerical Method

Due to space limitations the reader is referred to Simen [28], Simen & Dallmann [29] for a detailed description of the numerical method. The local stability equations are discretized by spectral-collocation. The obtained linear system is formulated as a boundary-value problem. As freestream boundary condition we prescribe exponential decay for the eigenfunctions at about 1.5 times the boundary layer thickness. Spatial or temporal stability theory is employed by iterating on the according eigenvalue until all boundary conditions are satisfied to a specified numerical limit. Also local inviscid flow quantities at the wall (index e) and local Blasius length $l = (\nu_e x^1/U_e)^{1/2}$ are introduced for nondimensionalization.

3. RESULTS

As pointed out in the introductory chapter we base our comparison between theoretical and experimental results on the stability experiments carried out by Stetson [30]. The test facility was a closed circuit hypersonic windtunnel operated at a free stream Mach number $M_\infty = 8$ in the test section, a stagnation temperature $T_0 = 728°K$ and a free stream unit Reynolds number $Re/ft = 10^6\ /\ ft = 3.2808 \cdot 10^6/m$. The test article was a 7 degree half angle pointed cone with a nose radius of $3.81 \cdot 10^{-5}m$ which was considered small enough for inviscid entropy layer effects not to play any role. Under these conditions the Mach number of inviscid flow at the wall is 6.83 and the angle between the shock and the cone axis is approximately 11 degrees as given by a solution of the Taylor-Maccoll equation. According to Stetson the flow field surveys were obtained only after the model had reached equilibrium temperature, i.e. adiabatic wall conditions had been obtained.

3.1 Sensitivity Study of Basic State Solutions

For the flow conditions given by the experiment we investigate parametric effects on flow field solutions obtained from the Thin Layer Navier Stokes (TLNS) equations and from similarity transformed boundary layer (SBL) equations. The main parameters affecting the TLNS solutions are identified as number of grid points, grid point distribution and amount of numerical damping. The convergence behaviour of the solution is discussed. The SBL solutions are shown to be sensitive towards the form of the viscosity-temperature law specified.

For the TLNS computations the following flow parameters are held constant: $M_\infty = 8.0$, $T_\infty = 52.75°K$, $Pr = 0.72$, $Re_\infty = 6.525 \cdot 10^6$. The free stream temperature is obtained from

$$T_\infty = T_0 / \left(1 + \frac{\gamma - 1}{2} M^2 \right) .$$

To determine the free stream Reynolds number Re_∞ we proceed as follows: We fix the local Reynolds number $Re = U_e l / \nu_e$ at which according to the experiment turbulent flow is fully developed, $Re_{max} = 3000$. Re_{max} yields the characteristic length in streamwise direction via $L = Re_{max}^2 \cdot \nu_e / U_e$. From $Re_\infty = U_\infty L / \nu_\infty$ we then obtain

$$Re_\infty = Re_{max}^2 \quad (\nu_e / \nu_\infty) / (U_e / U_\infty) ,$$

where dimensionless kinematic viscosity and velocity is given by the inviscid flow solution at the wall together with the dimensionless form of Sutherland's law. Adiabatic wall boundary conditions are chosen. The streamwise grid point distribution was equidistant with 101 grid points resulting in a quadratic increase of the local Reynolds number along streamwise grid points. **Fig.** 3 schematically shows the computational mesh used for the TLNS computation and a surface oriented coordinate system, whose coordinate lines x^2, x^3 in transverse and wall normal direction are shown at a typical location $x^1 (Re = 1731)$ in longitudinal direction. The angle between cone axes and far field boundary is chosen to be 14 degrees to capture the shock located at an angle of 12 degrees.

The grid points are clustered towards the cone surface which is shown in more detail in **fig. 4.** Here the grid point distribution in the near wall region (approximately 1.5 boundary layer thicknesses) is represented dependent on the total number points N between the surface and the outer boundary or dependent on the parameter b in the clustering function of eq. (1). If not specified otherwise the stability analysis presented in the following chapter is based on profiles obtained from $N = 97$, $b = 1.001$. Hence, these were resolved with approximately 60 grid points in the wall near region.

For stability analysis the quality of the basic state solution cannot be evaluated from global flow field data like Mach number or pressure contours. Instead local mean flow profiles near the surface and their first and second derivatives are relevant as they appear as coefficients in the stability equations. **Figs. 5, 6** therefore show velocity and temperature profiles on which the stability analysis in the following chapter is based. In **fig.** 5 with increasing number of grid points the Thin Layer Navier Stokes solutions converge to the case of highest resolution, however, the overall agreement is already close even between the case $N = 97$ and $N = 49$ where the latter has only half the resolution (see **fig. 4**). For example the location of the inflection point in the velocity profile remains almost fixed for all three cases. The derivatives of the Thin Layer Navier Stokes solution were obtained from piecewise third order Lagrange polynomial fits to the original basic flow profiles. No oscillations were observed. We take this, together with the insensitivity of the results with regard to the number of grid points specified, as a hint towards the good quality of our TLNS solutions.

In **fig. 6** it can be seen that numerical damping, controlled via the entropy parameter E as introduced in chapter 2.1.2, has a noticeable impact on both velocity and temperature profiles. $E = 0.3$ represents a case of high numerical damping. For axisymmetric flow around a pointed cone, to obtain a numerically stable solution, practically zero numerical damping is required. This case is represented by $E = 0.025$. A further decrease of E had no more substantial effect on the profile shapes. Also in **fig. 6** the profiles obtained from Thin Layer Navier Stokes solutions are compared to those from boundary layer similarity solutions. It is interesting to note that deviations among the similarity solutions can be larger than those between similarity profiles based on Sutherland law and Thin Layer Navier Stokes profiles.

A rough expectation with respect to the stability characteristics of the various profiles can be formulated from **fig. 6**. The velocity profile of the Chapman-Rubesin solution is the least convex, with the inflection point furthest away from the wall, and can therefore be expected to be the least unstable to so-called first mode waves whereas the high resolution, low numerical damping Thin Layer Navier Stokes profile is the most convex with the inflection point closest to the wall and therefore can be expected to be the most stable.

In **fig. 7** basic state profiles obtained from similarity solutions based on Sutherland's law and from TLNS solutions ($N = 97$, $E = 0.025$, $b = 1.001$) are compared to velocity and temperature profiles measured by Stetson [30] at two different local Reynolds numbers. As discussed in Stetson [30] due to probe interference with the wall the measurements can only be assumed to be accurate in the outer region of the boundary layer, i.e. for $x^{3*}/l > 8$. In this region however it can be seen that the more complete basic state solution yields closer agreement to the experimentally obtained values. As this improved agreement, in the region less affected by interference of the probe and the wall, can be observed for both velocity and temperature profiles at different Reynolds numbers we take this as a confirmation towards the accuracy of the measured and computed values. Only for high local Reynolds numbers the similarity solution based on Sutherland's law can be expected to approach the TLNS solution as the former does not take into account both transverse curvature in the momentum equation (see chapter 2.1.1) and viscous/inviscid interaction which can be present in hypersonic flow at finite Reynolds number. **Fig. 9** shows pressure distributions between the wall and the free stream at several locations along the cone. The inviscid Euler solution is compared to the viscous Thin Layer Navier Stokes solution. The inviscid solution shows conical behaviour, i.e. the wall pressure is constant in streamwise direction. This is not the case for the viscous solutions. There is a negative pressure gradient in streamwise direction with the viscous pressure distribution approaching the inviscid with increasing local Reynolds number. Also the increased distance of the shock from the wall for viscous flow, due to the displacement of fluid within the boundary layer, decreases in this direction. This displacement for a cone flow field solution, accounting for the full cone metric is smaller than for a Mangler-transformed flat plate solution as the effect of transverse surface curvature is not included in the Mangler-transformed boundary layer equations. Both the negative pressure gradient due to interaction and the reduced fluid displacement when full cone metric is taken into account is responsible for the more convex velocity profile of the TLNS solution as compared to the similarity solutions. A first order, marching boundary layer scheme to compute cone flow profiles also would not take into account the streamwise pressure gradient. It therefore should not be expected that the Navier Stokes solutions reproduce first order boundary layer solutions at finite Reynolds numbers.

3.2 Stability Analysis

3.2.1 Inviscid Stability Characteristics

We apply compressible inviscid theory characteristics (see e.g. Mack [21]) to the basic state solutions to obtain a priori information on which profile can be expected to be the least unstable to first and second mode disturbances. The theorems from inviscid theory are also used ot check if phase velocities' conditions for unstable modes are met by selected instability waves. To do so we introduce the following definitions:

The relative Mach number

$$M_r = \frac{(\alpha U + \beta W - \omega) M_e}{\bar{k}_w T^{1/2}}$$

represents the difference between the local mean flow velocity in direction of the wave and the phase velocity, over the local speed of sound.

The generalized inflection point x_s^3 is a point in the boundary layer of two-dimensional, planar flow where

$$\frac{d}{dx^3}\left(\frac{1}{T}\frac{dU}{dx^3}\right)\Bigg|_{x_s^3} = 0$$

holds. Duck [8] found that for axisymmetric boundary layer flow past a pointed cone the so-called "triply generalized inflection point" is relevant, given by

$$\frac{d}{dr}\left[\frac{dU/dr}{Tr\left(1 + \beta^2/(\alpha^2 r^2)\right)}\right]\Bigg|_{r=r_s} = 0 \ .$$

where $r = r_c + x^3 \cos\theta_c$. For large radiuses r, r_c the planar inflection point condition is recovered.

The theorems of Lees and Lin which give conditions for neutral stability or instability of first mode waves can be interpreted such that the profile with the generalized inflection point closest to the wall will be the least unstable to first modes waves. From **fig. 10** this is the case for the TLNS mean flow profile. The wave considered has a wave number $|k_w| = 0.14893$, a wave angle $\psi = 58{,}88°$ and a reduced frequency $F = 0.4 \cdot 10^{-4}$, the local Reynolds number is again $Re = 1731$. **Fig. 10** also shows that the phase velocity condition for unstable, first mode waves

$$c_0 < c < c_s \quad or \quad x^3(c_0^\rho) < x^3(c) < x_s^3$$

is satisfied. $x^3(c_0^\rho)$, $x^3(c)$, x_s^3 are locations where

$$c_0/\cos\psi = 1 - 1/(M_e \cos\psi) \ ,$$

$$c/\cos\psi = U \quad \text{(critical point)} \ ,$$

and

$$c_s/\cos\psi = U(x_s^3) \quad \text{(generalized inflection point)} \ .$$

$c_s - c_0$ was 0.1254 for the Chapman-Rubesin, 0.1249 for the Mack and 0.1074 for the TLNS profile, again indicating that the latter is the least inviscidly unstable (see Mack [21]). x_s^3 for the planar generalized inflection point condition was only slightly different ($\Delta x_s^3 \approx 1$). The additional condition that the relative Mach number be subsonic throughout the boundary layer was verified by computation for all three profiles. A second generalized inflection point appears for the TLNS profile. However, with $c_{s2} = U(x_{s2}^3) < c_0$ this mode is not expected to be unstable.

It was shown by Mack [21] that for unstable second mode waves there exists are region of supersonic relative Mach number in the boundary layer. **Fig. 11** shows that this is the case for all three mean flow solutions at $Re = 1731$ with respect to a two-dimensional wave with $|k_w| = 0.1839$, $F = 1 \cdot 10^{-4}$. For the TLNS profile this region is extended the least into the boundary layer. Hence this profile can be expected to be the least unstable to second mode waves. **Fig. 11** also shows that the phase velocity condition (see Mack [21]) for unstable second mode waves

$$c < U(x^3 = \delta/l) = 1$$

is satisfied.

3.2.2 Sensitivity Study Based on Stability Analysis

Stetson [30] presented the results of his stability experiments in the form of frequency spectra of the spatial amplification rate at a specified Reynolds number and in the form of spatial amplification rates versus Reynolds number for specified frequencies. In the following we adopt the same form of representation. The specified Reynolds number is again $Re = 1731$ and the specified frequency is $F = 1 \cdot 10^{-4}$. The sensitivity study is carried out for two-dimensional waves of the second mode, which are dominant under the given flow conditions, using spatial theory.

Fig. 12, 13 show results concerning parameters that affect the TLNS solution. In **fig. 12** with increasing number of grid points the amplification rates obtained converge to the case of highest resolution, however, the results are less sensitive than may be expected to this parameter. Another indication of the good quality of the TLNS solutions is the independance of amplification rates with respect to the grid point clustering parameter b as shown in **fig. 13.** Numerical damping, however, as seen from **fig. 14** is a spoiler of stability results and therefore must be set to an as low value as possible. The amplification rates obtained from the TLNS solutions do not converge to those obtained from the similarity solutions but to those from the experiment. For the similarity solutions the stability equations with Cartesian metric were solved.

We note that Mack's similarity profiles based on Sutherland's law and constant Prandl number yield very similar amplification rates compared to those obtained for variable Prandtl number which are given in [20]. For the latter heat conductivity was additionally specified as a function of temperature. Hence, it is concluded that the assumption of constant Prandtl number is appropriate under the given flow conditions, where the temperature at the boundary layer edge $T_e = 70°K$. The effect of variable Prandtl number becomes noticable only for $T_e > 100°K$ as discussed in Bertolotti [2].

3.2.3 Comparison between Theoretical and Experimental Results

In this paper we intend to provide some answers to the following problem: Can the prevailing quantitative descrepancy between experimental and theoretical results on the instability of hypersonic flow be resolved by a more complete formulation of both the equations governing the steady mean flow and the evolution of instability waves? Fig. 15 shows that if we do so the descrepancy is quite markedly reduced. We investigate spatial growth rates of three-dimensional waves. At each frequency the wave angle is determined which yields the maximum growth rates. These angles vary from about 70 degree at the lowest frequency to about 40 degree at the frequency where the second mode instability begins to dominate. In this region two-dimensional waves are most amplified. This search for locally maximum growth rates is based on the assumption that in an uncontrolled experiment instability waves travelling in various directions are present and for a certain frequency the wave travelling in the direction where disturbances yield maximum amplification rates will determine the measured growth rate. In **fig. 15** two effects are discussed:

a) The effect of different approximations to the basic state solution

In the stability equations for this discussion in all cases Cartesian metric is specified. The growth rates based on Chapman-Rubesin similarity solutions with linear viscosity-temperature law specified in both boundary layer and stability equations, strongly overpredict the measured values. Results based on Mack's similarity profiles with Sutherland's law specified in both boundary layer and stability equations also are only in qualitative agreement to the experiment. Closer agreement is found if the stability calculations are based on mean flow solutions obtained from the Thin Layer Navier Stokes equations, where viscous/inviscid interaction and the complete cone geometry is taken into account. Here Sutherland's viscosity-temperature law is specified for both the basic state and the stability computations.

b) The effect of surface curvature and flow divergence on cone flow instability

A theoretical value that almost exactly matches the measured maximum growth rate along with a close overall agreement in the second mode region and markedly improved agreement in the first mode region is obtained when together with the more complete basic state solution conical geometry is specified in the stability equations. Cone metric is given by ($m_{ij} = \partial h_i/\partial x^j/h_i/h_j$)

$$h_2 = 1 + x^3 \cos\theta_c/r_c \; ,$$

$$m_{23} = \frac{\cos\theta_c}{r_c}\left(1 + \frac{\cos\theta_c x^3}{r_c}\right)^{-1} \; ,$$

$$m_{21} = \frac{\sin\theta_c}{r_c}\left(1 + \frac{\cos\theta_c x^3}{r_c}\right)^{-1} \; ,$$

$$h_1 = h_3 = 1 \; , \quad m_{12} = m_{13} = 0 \; .$$

Introducing cone metric leads to a 40 % reduction in the maximum growth *rate of the first mode and a* 13 % reduction of this quantity for the second mode. Conical metric can further be split up into the cylindrical metric of the local osculating cylinder with radius $r_{cl} = r_c/\cos\theta_c$ and the conical divergence. Specifying cylindrical metric in the stability equations allows to study the effect of transverse curvature. **Fig. 16** shows the effect to be slightly destabilizing oblique first mode and stabilizing for the second mode with respect to the solution where no surface curvature is specified (Cartesian metric). This behaviour can be observed for basic state solutions with transverse curvature included (TLNS) as well as for those without (Mack's similarity solution) and is in agreement with the results from a parametric study carried out by Malik & Spall [23] for a different free stream Mach number, temperature and cone half angle.

In **fig. 18** we finally compare computed *spatial amplification rates* of two-dimensional instability waves, based on the solution of the Thin Layer Navier Stokes equations and stability equations with cone metric, to experimental values at three different reduced frequencies. Compared to Mack's results in [20] and the results based on Chapman-Rubesin similarity profiles in **fig. 17,** agreement is markedly improved for all three frequencies. Especially close agreement is found for $F = 1.16 \cdot 10^{-4}$, whereas for the highest frequency the experiment predicts somewhat higher spatial amplification rates.

3.3 Inclined Cone Flow Instability and Non-Local Stability Analysis

In this paper we concentrate on describing extended methods for stability analysis of axisymmetric hypersonic flow past a pointed cone. The procedure for analyzing the instability of hypersonic flow past a pointed cone at angle of attack as well as our non-local method of stability analysis will be described in a future paper. In the following we will only discuss some major results. Following Stetson [32] the cone is inclined by $\alpha = 2°$ and placed into a freestream of Mach number $M_\infty = 8$ and temperature $T_\infty = 52.75°K$. At a local Reynolds number of $Re = 1817$ sensitivity studies of the basic flow profiles in the wall near region were performed. One result concerning second derivatives of the velocity profile is shown in **fig. 19.** Monotonic convergence to the case of highest resolution in wall normal direction can be observed. For both the attachment (windward symmetry) and separation (leeward symmetry) line profile $K = 97$ grid points in wall-normal direction yields close agreement to the case of highest resolution. However, for the case $K = 49$ major discrepancies can be observed at the separation line profile. Hence, for basic flow computations 51×53×97 grid points were specified in longitudinal, transverse (half-cone) and wall normal direction. Grid points were distributed at constant length increments in longitudinal and at constant angle increments in transverse direction. The wall normal clustering parameter was chosen as $b = 1.001$ and low numerical damping was specified by setting the entropy parameter $E = 0.01$.

A comparison of amplification rate spectra obtained from our extended methods for basic flow computation and stability analysis with experimental results for attachment line flow at a local Reynolds number $Re = 1817$ is presented in **fig. 20.** The results resemble those for axisymmetric cone flow, i.e. close agreement is found in the frequency band of second mode instability, and better but still unsatisfactory agreement is found in the first mode region. As can be inferred from **fig. 19**, the basic flow characteristics are qualitatively different for attachment and separation line profiles. It therefore is of great interest to investigate the local stability characteristics of the latter. This is presented in **fig. 21** for a local Reynolds number $Re = 1049$. Surprisingly close agreement with experimental results by Stetson [32] for both amplification rate and unstable frequency band is obtained. Also the effect of conical divergence and streamline curvature becomes even more pronounced.

To our knowledge, in the literature instability characteristics of three-dimensional hypersonic flow on an inclined cone have so far not been investigated. This, however, is an interesting subject as in this flow two different instability modes can be expected having comparably large amplification rates. In **fig. 22** for both first and second mode instability, three-dimensional waves are the most amplified with growth rates that are of the same order of magnitude. It therefore cannot be determined which mode will dominate the transition process, as opposed to axisymmetric cone flow, where second mode instability clearly yields the highest growth rates.

The wave number vector components α_s, β_s are defined in direction and perpendicular to the local streamline of inviscid flow at the wall. The stationary vortex line (line perpendicular to the zero frequency line), as can be seen from **fig. 22**, is approximately parallel to this streamline. This is in agreement with experimental measurements by Mc Devitt & Mellenthin [25]. Applying oil-film techniques they found that in a transitional boundary layer on a inclined, ten degree half angle cone in $M_\infty = 7.4$ flow, the vortex path at the wall, on the cone side meridian, is approximately along the direction of the inviscid stream line.

We conclude our investigation by a very brief discussion of non-local effects on amplification rate spectra. By non-local effects we mean that the streamwise evolution of basic flow and disturbance flow is included in the stability analysis. We intend to clarify in how far a non-local stability theory can resolve the remaining discrepancies between amplification rates obtained from theory and experiment in the first mode region of cone flow instability. **Fig. 23** shows non-local amplification rates obtained from cone flow similarity profiles. The destabilizing effect in the low frequency region does not correspond to the experimental observation (see **fig. 15**). The stabilizing effect for reduced frequencies greater than $0.5 \cdot 10^{-4}$ however shifts theoretical values in direction of experimental data. Further details on comparison between local and non-local theory will be given elsewhere.

4. CONCLUSIONS

1. An attempt has been made to resolve decrepancies between experiment and theory with regard to instabilities in hypersonic flow. Markedly improved agreement between linear stability theory and experiment, especially in the second mode region, is found via
   - ***a)*** a more complete formulation of the basic-state equations accounting for viscous/inviscid interaction and complete configuration geometry
   - ***b)*** a more complete formulation of the local stability equations in surface-oriented, generalized coordinates.

   The improved agreement to experiment in the first mode region is equally due to the extended stability analysis and the more complete basic state computation. In the second mode region the major improvement results from the more complete basic state formulation, however, the close agreement to measured values is only achieved when the stability analysis is based on conical metric.
2. A sensitivity study was performed for basic state solutions obtained from Thin Layer Navier Stokes equations. This was based on both mean flow profiles and stability analysis. The results are shown to converge and to be quite insensitive to the resolution of the profiles but sensitive towards the amount of numerical damping specified to maintain numerical stability.
3. It was found that for the given flow conditions, due to the presence of viscous/inviscid interaction, which causes a negative pressure gradient in streamwise direction, and due to the effect of transverse curvature, which leads to reduced fluid displacement within the boundary layer, converged Thin Layer Navier Stokes solutions yield basic flow modeling superior to first order boundary layer or similarity solutions.
   In addition, both mean flow profiles and spatial growth rates from stability analysis based on similarity solutions are sensitive towards the viscosity-temperature law specified.
4. Inviscid instability criteria extended to the flow past a pointed cone were found to explain qualitatively why the mean flow profile obtained from the Thin Layer Navier Stokes solution should be the least unstable to first and second mode waves.
5. The effect of transverse curvature is shown to be weakly destabilizing to oblique first mode waves whereas such waves are markedly stabilized by conical divergence. For a smaller cone angle the orders may be reverse. The two-dimensional second mode is stabilized by both transverse curvature and conical divergence.
6. For the case of an $\alpha = 2°$ inclined cone, stability analysis via extended formulation of basic flow and local stability equations yields close agreement between experimental and theoretical values of amplification rate spectra in the second mode region for both hypersonic attachment and separation line flow. For the latter very close agreement is also found in the first mode region. Three-dimensional, hypersonic cone flow is shown to be equally unstable to three-dimensional first and second mode waves. Stationary vortices are found to align themselves in direction of the streamline of inviscid flow at the surface.
7. Non-local effects on amplification rate spectra, based on axisymmetric cone flow similarity profiles, are shown to be destabilizing in the lower frequency band of first mode waves and stabilizing at higher frequencies. However, final conclusions about the non-local effects should be based on Thin Layer Navier Stokes rather than similarity boundary layer profiles.
8. There are still differences between growth rates obtained from theory and experiment in the first mode region. This may be a reflection of what was pointed out by Stetson [33] that "a conventional,

hypersonic wind tunnel can be quiet for second mode disturbances and noisy for first mode disturbances". Measurements show that freestream disturbance energy amplitudes, as a source for exciting instability waves, are high in the low, first mode frequency band and low in the high, second mode frequency band. Large amplitude freestream noise, however, is known to lead to early non-linear saturation and thus reduced measured growth rates of instability waves. Hence, our results may add some confidence that at least the second mode amplification rates measured by Stetson can be described by primary, linear instability theory. Nevertheless, we agree to Mack [20] that the best "way to verify spatial normal-mode calculations, ..., is by introducing controlled disturbances into the boundary layer" in a controlled, low disturbance wind tunnel environment. This, however, is a task for the experimentalist.

Acknowledgements

The support by Dr. L.M. Mack who kindly provided mean flow profiles and results from stability analysis is greatly appreciated. Dr. B. Müller kindly assisted in the use of his TLNS code. The authors gained considerable benefit from the TLNS-code experiences of E. Kufner. We also thank Dr. G. Schneider and E. Kufner for providing postprocessing routines. Computations for the inclined cone case were carried out by C. Thiedemann. The authors are also indebted to D. Welke for typing the manuscript and to T. Grimm for data plotting.

REFERENCES

[1] Aris, R., *Vectors, Tensors, and the Basic Equations of Fluid Mechanics*. Prentice-Hall, Inc., 1962.

[2] Bertolotti, F.P., *Linear and Nonlinear Stability of Boundary Layers with Streamwise Varying Properties*. Ph.D.Thesis, The Ohio State University, Columbus, Ohio, USA, 1991.

[3] Chang, C.L., Malik, M.R., *Effects of Shock on the Stability of Hypersonic Boundary Layers*. AIAA-90-1448 (1990).

[4] Chapman, D.R., Rubesin, M.W., *Temperature and Velocity Profiles in the Compressible Laminar Boundary Layer with Arbitrary Distribution of Surface Temperature*. J. Aero. Sci., Vol. 16 (1949), pp. 547 - 565..

[5] Cowley, S., Hall, P., *On the Stability of Hypersonic Flow Past a Wedge*. ICASE Report 88-72 (1988), NASA Langley Research Center, Hampton, Virginia, USA.

[6] Demetriades, A., *An Experiment on the Stability of Hypersonic Boundary Layers*. J. Fluid Mech., Vol. 7 (1960), pp. 385 - 396.

[7] Demetriades, A., *Laminar Boundary Layer Stability Measurements at Mach 7 Including Wall Temperature Effects*. AFOSR TR-77-1311 (1977), Air Force Office of Scientific Research, Bolling Air Force Base, Washington, D.C., USA.

[8] Duck, P.W., Shaw, S.J., *The Inviscid Stability of Supersonic Flow Past a Sharp Cone*. ICASE Report No. 90-14 (1990), NASA Langley Research Center, Hampton, Virginia, USA.

[9] El-Hady, N.M., *Nonparallel Instability of Supersonic and Hypersonic Boundary Layers*. AIAA-91-0324 (1991).

[10] Gasperas, G., *Instability of Compressible Laminar Boundary Layers*. AIAA-85-1699 (1985).

[11] Gasperas, G., *The Stability of the Compressible Boundary Layer on a Sharp Cone at Zero Angle of Attack*. AIAA-87-0494 (1987).

[12] Harten, A., *High Resolution Schemes for Hyperbolic Conservation Laws*. J. Comp. Physics, Vol. 49 (1983), pp. 357 - 393.

[13] Kendall, J.M., *Supersonic Boundary Layer Stability Experiments*. Boundary Layer Transition Study Group Meeting (W.D. McCauley, ed.), Vol. II, BSD-TR-67-213, US Air Force (1967) pp. 10-1 – 10-8.

[14] Kendall, J.M., *Wind Tunnel Experiments Relating to Supersonic and Hypesonic Boundary-Layer Transition*. AIAA J., Vol. 13 (1975), pp. 290 - 299.

[15] Kosinov, A.D., Maslov, A.A., Shevelkov, S.G., *Experiments on the Stability of Supersonic Laminar Boundary Layers*. J. Fluid Mech., Vol. 219 (1990), pp. 621 - 633.

[16] Kosinov, A.D., Maslov, A.A., Shevelkov, S.G., *Experimantal Study of the Supersonic Boundary Layer Stability on the Cone Cylinder Model*. In: Laminar-Turbulent-Transition (D. Arnal, R. Michel, eds.), Proc. of the IUTAM Symp., Toulouse, France, 1989, Springer 1990

[17] Laufer, J., Vrebalovich, T., *Stability and Transition of a Supersonic Laminar Boundary Layer on an Insulated Flat Plate*. J. Fluid Mech., Vol. 9 (1960), pp. 257 - 299.

[18] Lysenko, V.I., Maslov, A.A., *The Effect of Cooling on Supersonic Boundary-Layer Stability*. J. Fluid Mech., Vol. 147 (1984), pp.39-52.

[19] Mack, L.M., *Stability of Axisymmetric Boundary Layers on Sharp Cones at Hypersonic Mach Numbers*. AIAA-87-1413 (1987).

[20] Mack, L.M., *Boundary Layer Stability Analysis for Sharp Cones at Zero Angle-of-Attack*. AFWAL-TR-86-3022 (1986). Flight Dynamics Labatory, Air Force Wright Aeronautical Labatories, Wright-Patterson-Air Force Base, Ohio, USA.

[21] Mack, L.M., *Boundary Layer Stability Theory, Special Course on Stability and Transition of Laminar Flow*. AGARD Report No. 709, Paris, France, 1984.

[22] Malik, M.R., *Stability Theory for NASP Transition Prediction*. Fifth National Aero-Space Plane Symposium, Paper No.57 (1988), USA

[23] Malik, M.R., Spall, R.E., *On the Stability of Compressible Flow Past Axisymmetric Bodies*. J. Fluid Mech., Vol. 228 (1991), pp. 443 - 463.

[24] Maslov, A.A., *private Communication*, 1991.

[25] Mc Devitt, J.B., Mellenthin, J.A., *Upwind Patterns on Ablating and Nonablating Cones at Hypersonic Speeds*. NASA TN D-5346 (1969).

[26] Müller, B., *Upwind Relaxation Method for Hypersonic Flow Simulation*. DLR-FB 91-36 (1991), DLR Göttingen, Germany.

[27] Reshotko, E., Khan, M.M.S., *Stability of the Laminar Boundary Layer on a Blunted Plate in Supersonic Flow*. In: Laminar-Turbulent Transition (R.Eppler, H.Fasel, eds.), Proc. of IUTAM Symposium, Stuttgart, 1979, Springer 1980.

[28] Simen, M., *COSMET, a DLR-Dornier Computer Program for Compressible Stability Analysis with local Metric*. DLR-IB 221-91 A 09 (1991), DLR Göttingen, Germany.

[29] Simen, M., Dallmann, U., *On the Instability Hypersonic Flow Past a Pointed Cone - Comparison of Theoretical and Experimental Results at Mach 8 -*. DLR-FB 92-02 (1992), DLR Göttingen, Germany.

[30] Stetson, K.F., Thompson, E.R., Donaldson, J.L., Siler, L.G., *Laminar Boundary Layer Stability Experiments on a Cone at Mach 8, Part 1: Sharp Cone*. AIAA-83-1761 (1983).

[31] Stetson, K.F., Thompson, E.R., Donaldson, J.L., Siler, L.G., *Laminar Boundary Layer Stability Experiments on a Cone at Mach 8, Part 2: Blunt Cone*. AIAA 84-0006 (1984).

[32] Stetson, K.F., Donaldson, J.L., Siler, L.G., *Laminar Boundary Layer Stability Experiments on a Cone at Mach 8, Part 3: Sharp Cone at Angle of Attack*. AIAA-85-0492 (1985).

[33] Stetson, K.F., Kimmel, R.L., *On Hypersonic Boundary Layer Stability*. AIAA-92-0737 (1992).

[34] Stewartson, K., *Theory of Laminar Boundary Layers in Compressible Fluids*. Oxford University Press, 1964.

[35] Stuckert, G.K., Reed, H.L., *Stability of Hypersonic, Chemically Reacting Viscous Flows*. AIAA 90-1529 (1990).

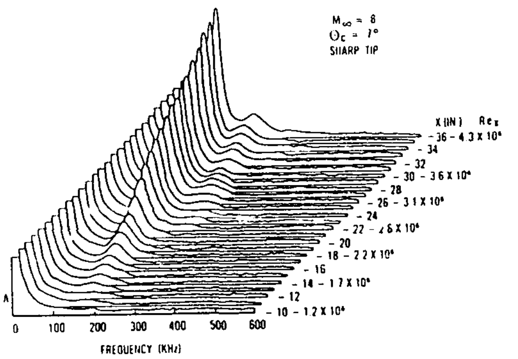

Fig. 1 Amplitude spectra of peak energy fluctuations as a function of local Reynolds number (Stetson [30]).

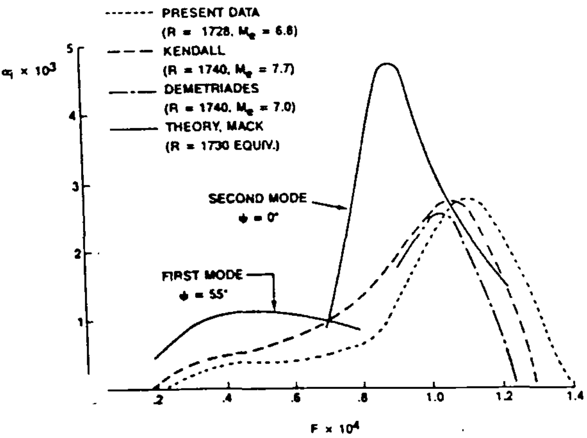

Fig. 2 Spectra of spatial amplification rates; comparison between theory and experiment (Stetson [30]).

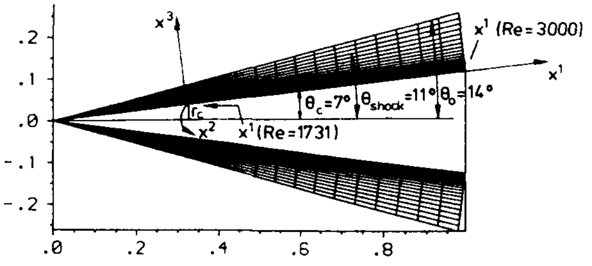

Fig. 3 Schematic *representation* of computational mesh and coordinates.
$M_\infty = 8$, $T_\infty = 53°K$, $Re_\infty = 6.53 \cdot 10^6$.

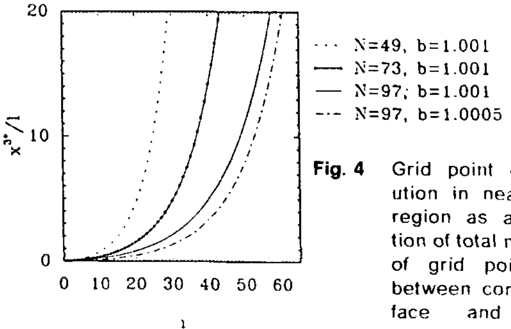

Fig. 4 Grid point distribution in near wall region as a function of total number of grid points *N* between cone surface and free stream boundary, and as a function of clustering parameter *b*.

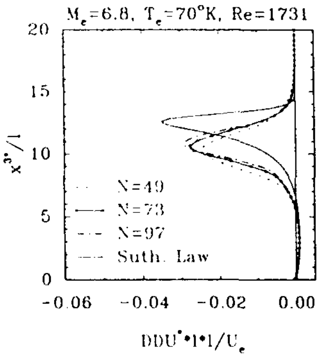

g. 5 Second derivative of velocity profiles as a function of number of grid points *N* between the cone surface and the free stream boundary.

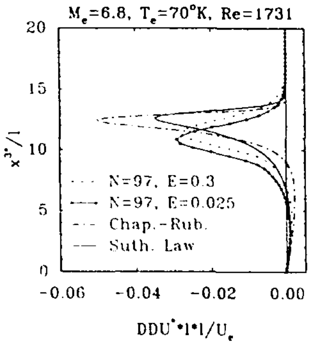

Fig. 6 Second derivative velocity profiles as a function of entropy parameter *E* (numerical damping); comparison to similarity profiles.

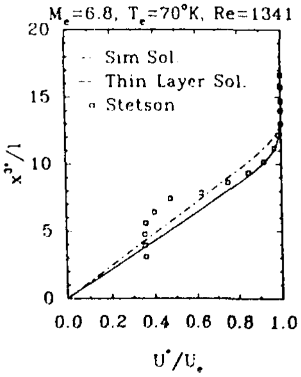

g. 7 Comparison of numerically and experimentally obtained velocity profiles.

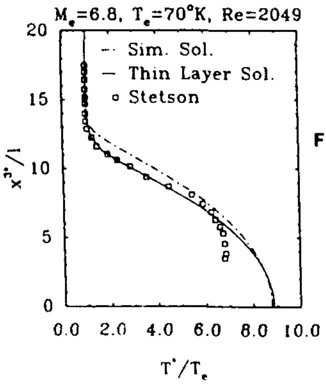

Fig. 8 Comparison of numerically and experimentally obtained temperature profiles.

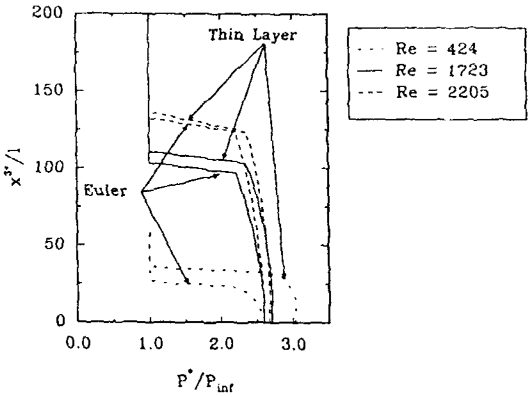

Fig. 9 Viscous-inviscid interaction based on pressure distribution, $M_\infty = 8$, $T_\infty = 53°K$, $Re_\infty = 5.53 \cdot 10^6$.

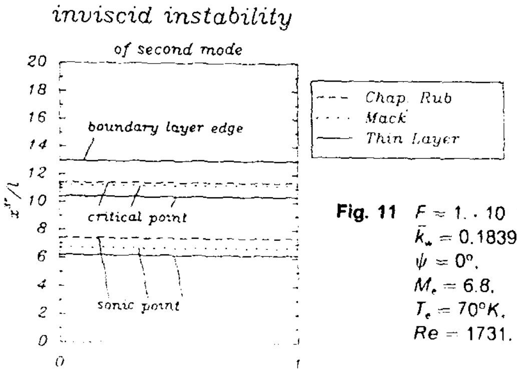

Fig. 11 $F = 1. \cdot 10^{-4}$, $\bar{k}_* = 0.1839$, $\psi = 0°$, $M_e = 6.8$, $T_e = 70°K$, $Re = 1731$.

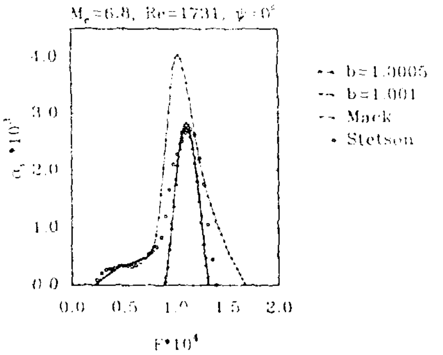

Fig. 13 Effect of grid point clustering parameter b on spatial amplification rate.

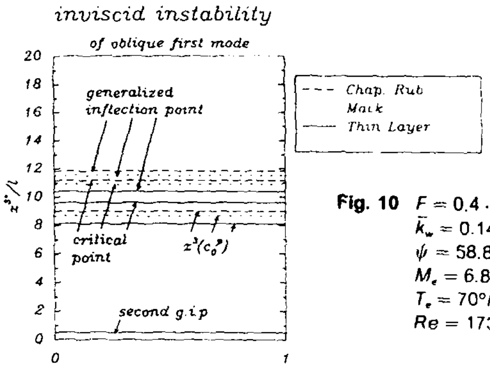

Fig. 10 $F = 0.4 \cdot 10^{-4}$, $\bar{k}_* = 0.149$, $\psi = 58.88°$, $M_e = 6.8$, $T_e = 70°K$, $Re = 1731$.

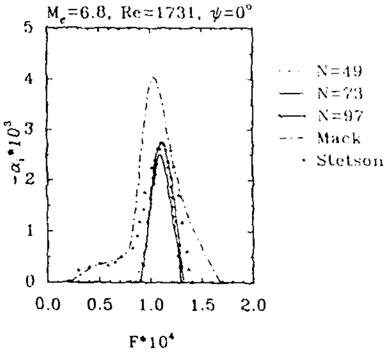

Fig. 12 Effect of total number of grid points N in wall-normal direction of the TLNS-solution on the spatial amplification rate.

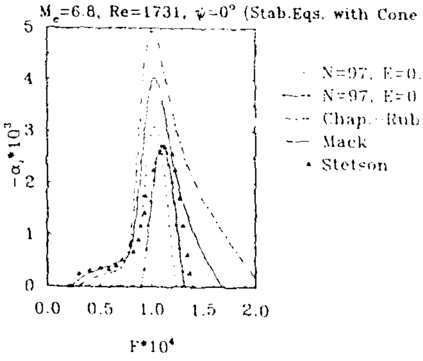

Fig. 14 Effect of entropy parameter E (numerical damping) on the spatial amplification rate; comparison with results from similarity solutions.

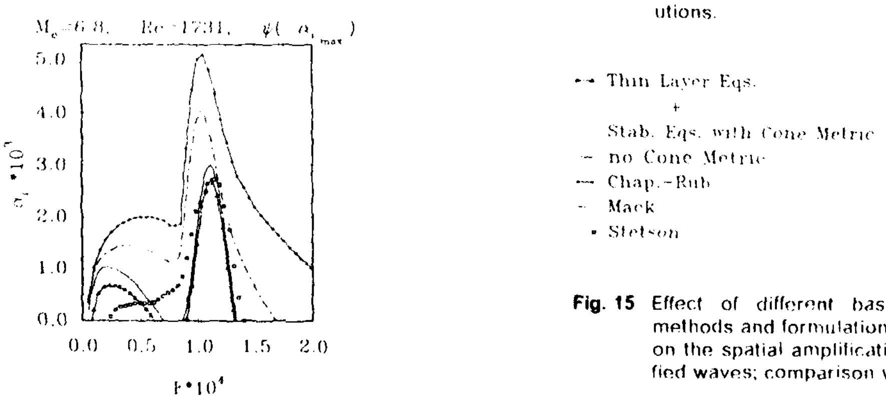

Fig. 15 Effect of different basic state computation methods and formulations of stability equations on the spatial amplification rate of most amplified waves; comparison with experimental data.

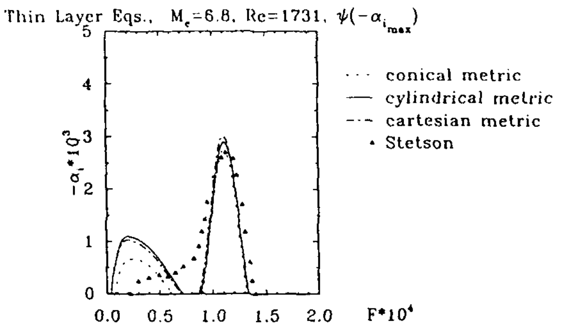

Fig. 16 Effect of different forms of metric on the spatial amplification rate of most amplified waves.

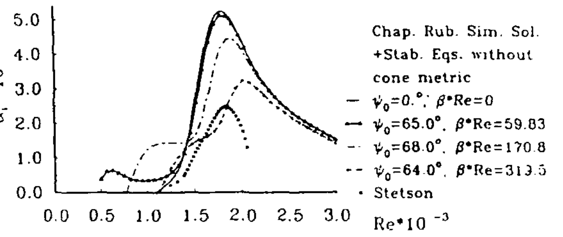

Fig. 17 Comparison of spatial amplification rates from classical stability theory (two- and three-dimensional waves) and experiment.

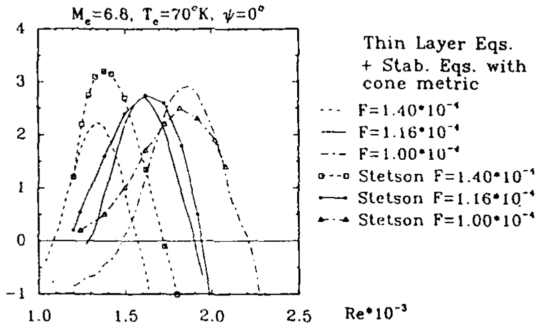

Fig. 18 Comparison of spatial amplification rates obtained from theory and experiment for various reduced frequencies.

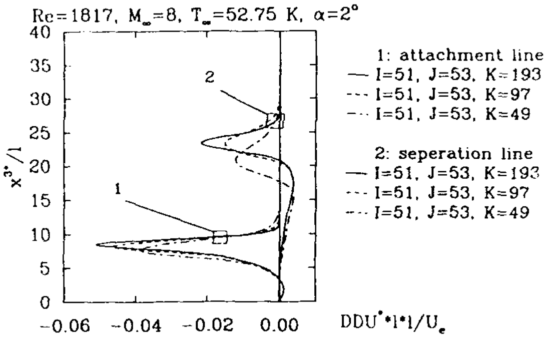

Fig. 19 Second derivatives of velocity profiles as a function of number of grid points K between the cone surface and the free stream boundary.

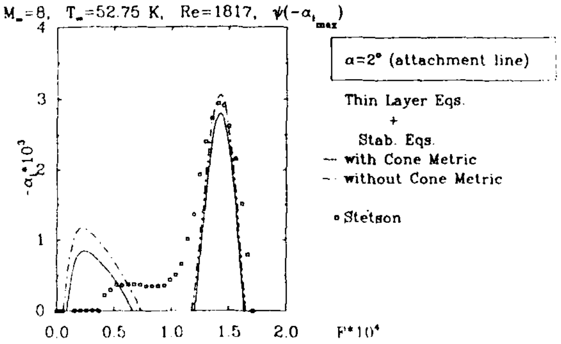

Fig. 20 Comparison of theoretical and experimental spatial amplification rates of most amplified waves in hypersonic attachment line flow on a cone.

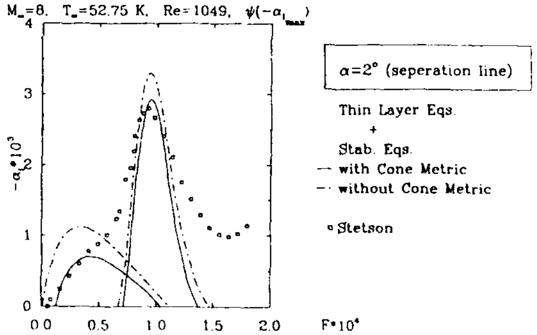

Fig. 21 Comparison of theoretical and experimental spatial amplification rates of most amplified waves in hypersonic separation line flow on a cone.

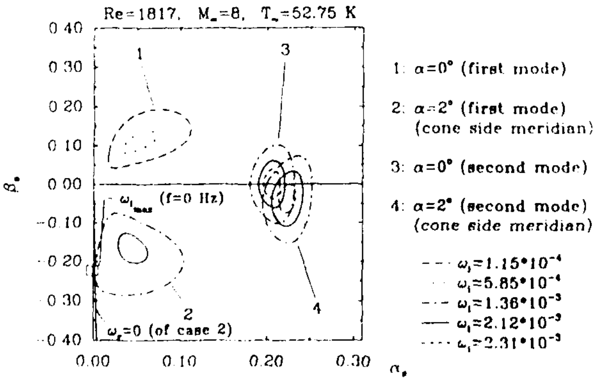

Fig. 22 Three-dimensional first and second mode instability waves in three-dimensional hypersonic flow along cone side meridian; comparison of temporal amplification rates

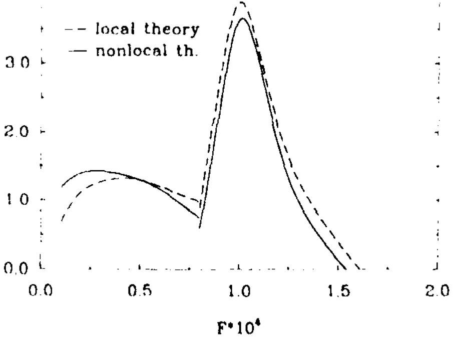

Fig. 23 Non-local effects on hypersonic, axisymmetric cone flow instability; similarity solutions based on Sutherland's law and stability equations with cone metric.

Studies of Hypersonic Viscous Flows

R.Hillier, D.C. Kirk, M.Sell and S.Soltani
Department of Aeronautics,
Imperial College of Science,Technology and Medicine,
London, U.K.

SUMMARY

This paper presents results from current studies on slender bodies of revolution tested at a nominal Mach number of 9. It concentrates on the case of a spherically-blunted cone, providing kinetic heating data for laminar, turbulent and transitional flow regimes. Nose blunting exerts a powerful control on the location of transition, and the quantitative measurements of this location using thin film gauge techniques are supported by flow visualisation using liquid crystal thermography. We also discuss work and plans for two other studies which are in their early stages: these are a cavity-induced separation and the development of turbulent boundary layers under controlled pressure gradients. Preliminary computations using a high resolution Navier-Stokes code are also presented.

INTRODUCTION

Hypersonic flows present particularly difficult problems both for experimentation and computation, so that there is a clear need for well defined experiments which will simultaneously explore the flow physics and provide suitable cases for CFD validation/evaluation. Our work has been directed to these objectives, with a particular interest in providing experimental and computational data on kinetic heating. For simplicity, in both experiment and computation, we attempt to establish two-dimensional flow fields, and we consider that this is best achieved by use of bodies of revolution (i.e. two-dimensional axisymmetric flows) rather than by planar configurations, since the latter will be subjected to three-dimensional or side-wall effects of uncertain magnitude, particularly for separated flows. An additional reason is that the main flow non-uniformities with an axisymmetric nozzle (such as axial Mach number gradients) will also be axisymmetric so that two-dimensionality can be preserved with the body of revolution whereas it would induce secondary flows in the boundary layer of a planar configuration.

The three configurations of interest to us at present (all axisymmetric) are shown schematically in Figure 1. Configuration A, a spherically blunted cone, is used for a study of the effect of nose blunting on the boundary layer development, particularly on transition. Configuration B is designed to provide a test configuration for an extensive study of the behaviour of turbulent boundary layers in pressure gradients of controlled but variable severity. The main experimental surface is the central hollow cylinder, so chosen that pressure gradient effects can be investigated without (in the first instance) the additional effects of dilatation (e.g. for cone flows) and streamline curvature (as with use of a profiled flare). The pressure gradient is generated by the concentric cowl. Although the initial design and manufacture of this model is difficult, it provides enormous flexibility and scope for future developments. The third configuration C, is a recently commenced project on flow separation. It was intended to investigate a new class of separation which had received relatively little attention at hypersonic speeds, and exhibits some simplifying features so that it can provide a hierarchy of increasingly severe problems for CFD code evaluation. Thus separation is fixed at the leading lip (at least initially), and the first stage of the work is a low Reynolds number laminar separation leading finally to a fully turbulent separated flow.

EXPERIMENTAL APPARATUS AND MODELS

The experiments are performed in the Imperial College Aeronautics Department Gun Tunnel. The facility operates with a total run time of 25 ms and a steady flow window of about 5 ms. The operating conditions given in Table 1 represent the maximum achievable.

M_∞	$\Delta M_\infty/m$	$p_{0\infty}(N/m^2)$	Re_∞/m	$T_\infty(K)$	$T_W(K)$
9.16	0.14	6.67×10^7	5.5×10^7	59.8	290

Table 1. Typical operating conditions

Slender models of up to 0.9 m chord can be accommodated in the test section providing total Reynolds numbers of order 40 million to 50 million. The axisymmetric nozzle is contoured, but with a slight axial Mach number variation along the centreline. Here we approximate it at present with the linear gradient given in the Table. This could be readily incorporated into any CFD simulation by setting inflow boundary conditions appropriate to a weak source flow. Experimental techniques available include schlieren visualisation, surface pressure with the possibility of resolving fluctuations up to 50-100 kHz (sufficient for gross movement of separated regions for example but still an order of magnitude less than the highest frequencies in a turbulent boundary layer); pitot profiles using rapid response pitot probes with fine entry heights of order 0.2 mm. and fine wire thermocouple probes for total temperature measurements. Heat transfer measurements are made using thin film platinum sensors hand-painted onto machinable glass ceramic (MACOR) substrates. Figure 2 shows a typical module of 15 gauges, mountable in the instrumentation slot of the blunt cone model. The temperature-time traces for the sensors are integrated digitally with the Cook-Felderman (Ref.1) method to give heat transfer rates. The combination of random and consistent errors give an expected variation of the "true" value in the range -5% to +15% about that measured. Thermal visualisation of the models is made using micro-encapsulated liquid crystal paints (on a black model) and illuminated during the run by a 30 μs white light strobe flash unit. Several paints are used, the main having a lower transition (red) temperature of 25°C and an upper transition (green-blue to colourless) at 35°C

All models have (at least) three pressure tappings around the circumference at one or more specified chordwise locations; these are used for alignment and generally this is achieved within an accuracy of ±1% in pressure. As a final observation the models are all constructed on a modular basis, with the intention of providing flexibility in both use and positioning of instrumentation and adaptability to potential future projects.

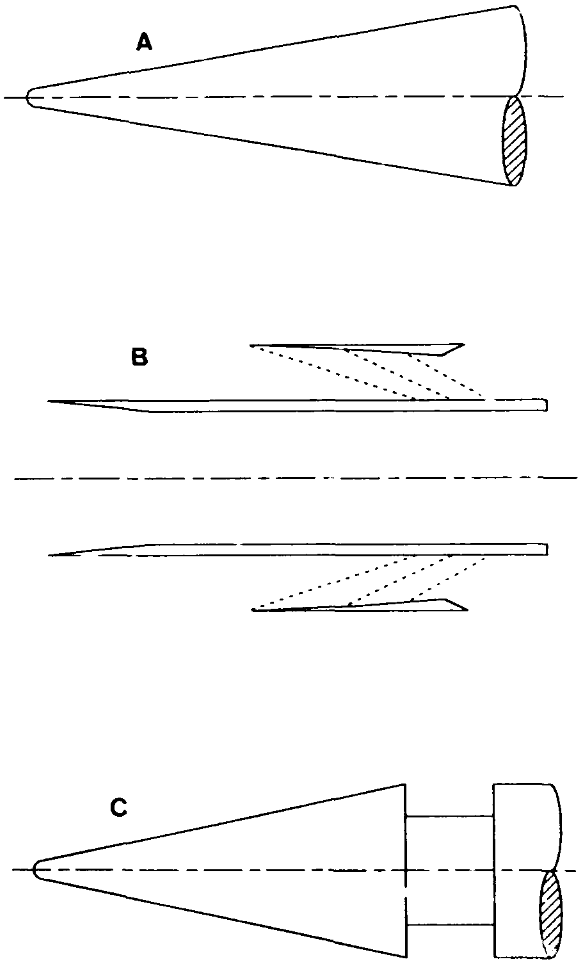

Figure 1 Model Configurations

THE COMPUTATIONAL METHOD

The numerical method is a two-dimensional axisymmetric time-marching scheme, with the calculation time-split between separate inviscid and viscous solvers. The inviscid solver is based upon a second-order Godunov-type algorithm which evaluates cell interface fluxes using a generalised Riemann problem(GRP) based on the method of Ben-Artzi and Falcovitz (Ref.2). In turn the inviscid calculation is split into separate sweeps in the I- and J- directions. In this GRP approach, the initial flow properties in cells (at the commencement of a time step) are established as piecewise linear distributions(in I- or J-), so that at cell interfaces there are possible discontinuities in both the flow variables and their spatial gradients, and the GRP produces a time-dependent flux consistent with this distribution. This requires a 'first-order' Riemann solver to compute the effect of the discontinuity in variables, and a second order correction which takes account of the initial gradients. Exact solution of this latter part is expensive, but also unnecessary, and here we use a very simple acoustic correction. In turn the strategy for solving the basic Riemann problem is firstly to solve the initial value problem acoustically, which is trivial, and only if the subsequent 'contact surface' pressure differs by more than a certain margin (typically 1%) from the initial 'left' and 'right' values is the full iterative solver entered. Typically, for the calculations presented here, this occurs for only 5% of the inviscid flux calculations. The viscous solver utilises a thin layer Navier Stokes formulation, either with a laminar viscosity model or the simple two layer algebraic eddy viscosity model of Baldwin-Lomax (Ref.3) (assuming Prandtl numbers of 0.72 and 0.9 in the laminar and turblent regions respectively); in the transition region a simple linear (with distance) variation from laminar to turbulent viscosity is used. The Sutherland law is used for the molecular viscosity and the Nitrogen gas is treated as perfect with a specific heat ratio of 1.4.

The present code is explicit, but the splitting between I- and J-inviscid sweeps, and the separate viscous solver, provides an efficient formulation. Two further features have been added which greatly enhance the usefulness of the code. Firstly, consistent with the high Mach number, the calculation is advanced in a 'block-marching' procedure, whereby a restricted window of cells in the I- (effective flow) direction are time-iterated to convergence, the block then shifting one cell in the flow direction and the process repeated. Secondly, in parallel with the block marching, the mesh required is constructed as the calculation proceeds. In particular for the cone calculations we could specify (say) that we maintain 60 cells between the body and the shock and 35 (say) between the body and some appropriately defined boundary layer edge. The advantages of this are self evident and are an essential requirement in any systematic study of mesh convergence.

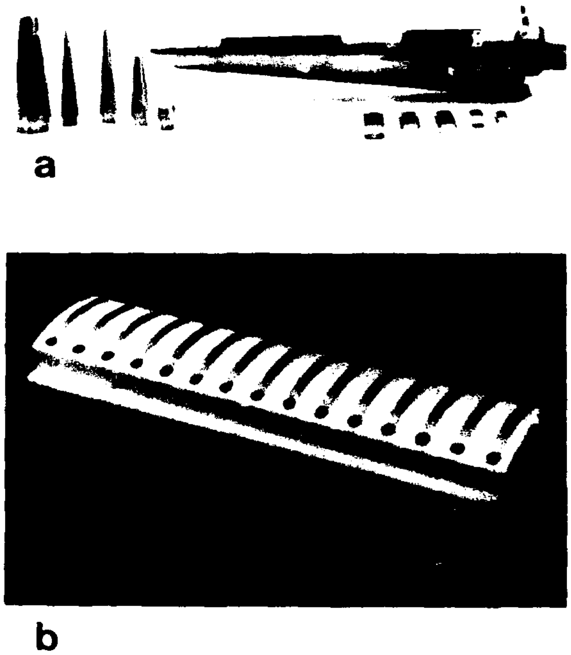

Figure 2. (a) Modular construction of blunt cone model, (b) platinum thin film gauges on machinable ceramic.

THE SHARP AND BLUNTED CONE

General Comments

Nose blunting of hypersonic vehicles causes substantial perturbation of the downstream flow field and boundary layer, both through the alteration in pressure field (Stetson, Ref. 4) but more particularly through the entropy layer associated with the highly curved portion of the bow shock

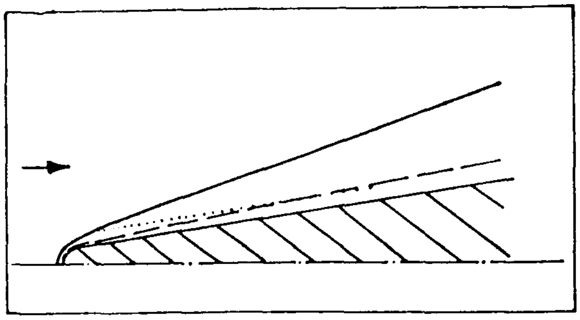

Figure 3. Flow field schematic. —— shock; , entropy layer, - - - , boundary layer

wave (Dolling and Gray, (Ref.5); Softley, Graber and Zempel,(Ref.6); Stetson and Rushton,(Ref.7); Ericsson, (Ref.8); Morkovin, Ref.9)). The effect is illustrated in Figure 3, where a schematic for the blunted cone is shown. In this sketch the initial entropy layer is thicker than the viscous layer, and the downstream development of the interaction between the two is complex, since the 'inviscid' parts of the flow field, which include the entropy layer and the surface pressure distribution, scale upon X/R (distance normalised by the nose radius, say), whereas the boundary layer development is Reynolds number dependent. Given enough streamwise development the boundary layer will always grow to 'swallow' the entropy layer, so that the boundary layer will eventually asymptote to some equivalent sharp cone structure. Before this occurs the boundary layer development will have been controlled by radically different edge conditions. For example, in our study the surface pressure asymptotes to the sharp cone value by some 100 nose radii (see Figure 4). If, at this stage, the boundary layer thickness is still very much less than that of the entropy layer, then the edge Mach number and unit Reynolds number would be about 3.2 and 5.25x10^6/m respectively compared with the aerodynamically sharp cone values of 8.05 and 74.5x10^6/m. In addition, the entropy layer provides a rotational edge condition to the boundary layer.

Thus boundary layer development under an entropy layer is of great practical interest, be it laminar, transitional or turbulent, and the present study encompasses this full range. One interest here is in transition, as it is well known (for example Stetson, (Ref.4); Ericsson, (Ref.8)) that nose blunting has a profound influence, initial slight blunting delaying transition until a trend reversal occurs.

Pressure and Heat Transfer Data

A composite set of pressure data (normalised by the sharp cone value) for a wide range of nose radius Reynolds numbers is shown in Figure 4. For high Reynolds number flows we expect only weak viscous interaction effects and the main cause of scatter in the data is random experimental errors. The data show a pressure undershoot, with a minimum at about 25 nose radii, after which there is a monotonic recovery to the sharp cone value. In boundary layer terms this recovery is only a weak adverse pressure gradient, and is not expected to have a significant effect upon transition (Stetson (Ref.4)). The figure includes the CFD modelling of the pressure distribution.

A large amount of heat transfer data have been collected and there is space to present only a small part of this here. Before discussing them a few points should be noted. Firstly some figures reference models 1 and 2. This simply refers to the fact that on occasion it was necessary to use two models to provide as extensive a data coverage as possible, and the generally small mismatch between them emphasises the high quality of model and instrumentation manufacture. Secondly there are a range of options in defining appropriate Stanton numbers and Reynolds numbers. For the latter we always will use here $Re_{\infty s}$ which is based upon free stream conditions and the wetted length of model. For the Stanton number we define both

$$St_\infty = q/\rho_\infty U_\infty C_p(T_{0\infty} - T_w)$$

and

$$St_c = q/\rho_c U_c C_p(T_r - T_w)$$

the former based purely upon free stream conditions and total temperature and the latter upon 'asymptotic sharp cone' edge conditions with a recovery factor r set to the laminar value of $Pr^{1/2}$.

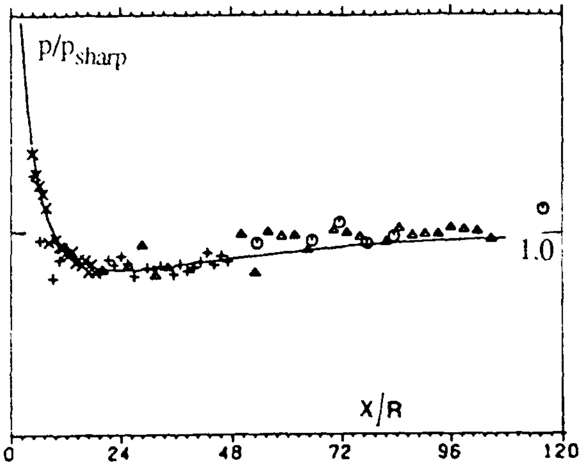

Figure 4. Surface Pressure on blunt cone, normalised by sharp cone value. A range of nose radii are shown. computations. ——

Figure 5 presents data for the basic sharp cone with transition, which is upstream of the first measurement location, expected to occur in the range approximately $3.2 \times 10^6 < Re_{\infty S} < 5.0 \times 10^6$. We have no measure of the basic tunnel background disturbance field. The figure also includes our initial computational modelling of the flow (laminar and turbulent Prandtl numbers of 0.72 and 0.9 respectively). The computations were performed with 120 cells in the laminar zone from the cone apex up to the onset of transition, 22 cells through transition and a further 68 cells in the turbulent zone up to the cone trailing edge. With the adaptive mesh routine employed, 62 cells were maintained between the body surface and the shock wave and, in the boundary layer, 38 cells between the body surface and a boundary layer "edge" defined as the location of 0.5% of the wall vorticity. A mesh stretching was employed in both the chordwise and normal direction, the latter providing a value y^+ at the first cell centre from the body of order 1.0.

The agreement with experiment appears to be good, but it should be recollected that the tolerance on the experimental data is expected to be in the range -5% to +15%. A full mesh convergence assessment of the computations has not yet been completed, but doubling of the cell sizes in the critical wall region (where the temperature peak is located) reduces the predicted levels of heat transfer by only 2%. Probably the most sensitive CFD factor (other than the appropriateness or otherwise of the turbulence model) is the simulation and location of the transition process. It should also be noted that the computations do not include the axial flow gradients, which we anticipate would cause a depression in predicted values by the cone base of about 4%. As a final observation we should note that in data for a 7 degree semi-angle cone presented at the Antibes Workshop on Hypersonic Re-entry Flows (Denman, Harvey and Hiller, (Ref.10)) experimental values for the turbulent boundary layer were some 25% below predictions, by other workers, using the same algebraic turbulence model. The resolution of these discrepancies has to be a combination of reducing the error band on the experimental data, and a better understanding of the CFD modelling of transition and turbulent flow.

In total 9 different nose radii have been tested, each at two unit Reynolds number operating conditions, and provide nose radius Reynolds numbers Re_N ($= \rho_\infty U_\infty R_N/\mu_\infty$), based upon nose radius and free stream conditions, ranging from 15.5×10^3 to 1.375×10^6. The precise range is tabulated in Table 2. A limited selection of these (as asterisked) are represented in Figures 6a to 6e, as typical of a range of interesting conditions based upon St_e versus $Re_{\infty S}$. In some cases the data coverage is more modest than others, and it should be noted that the chordwise Reynolds numbers are limited to 9 million and 30 million for the low and high unit Reynolds number operating conditions respectively. Figure 6a shows the lowest nose Reynolds number case,

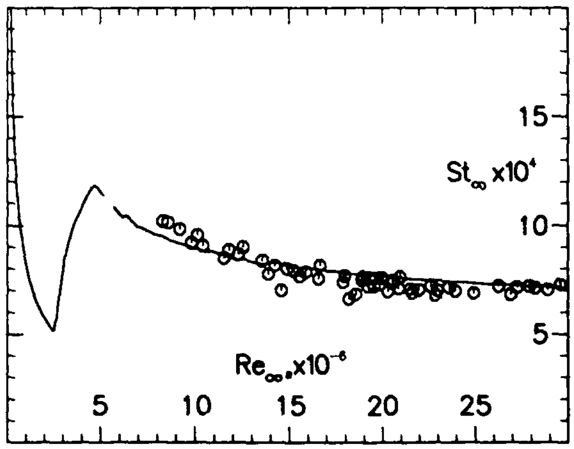

Figure 5. Heat transfer data for sharp cone. o, experiment; —computations.

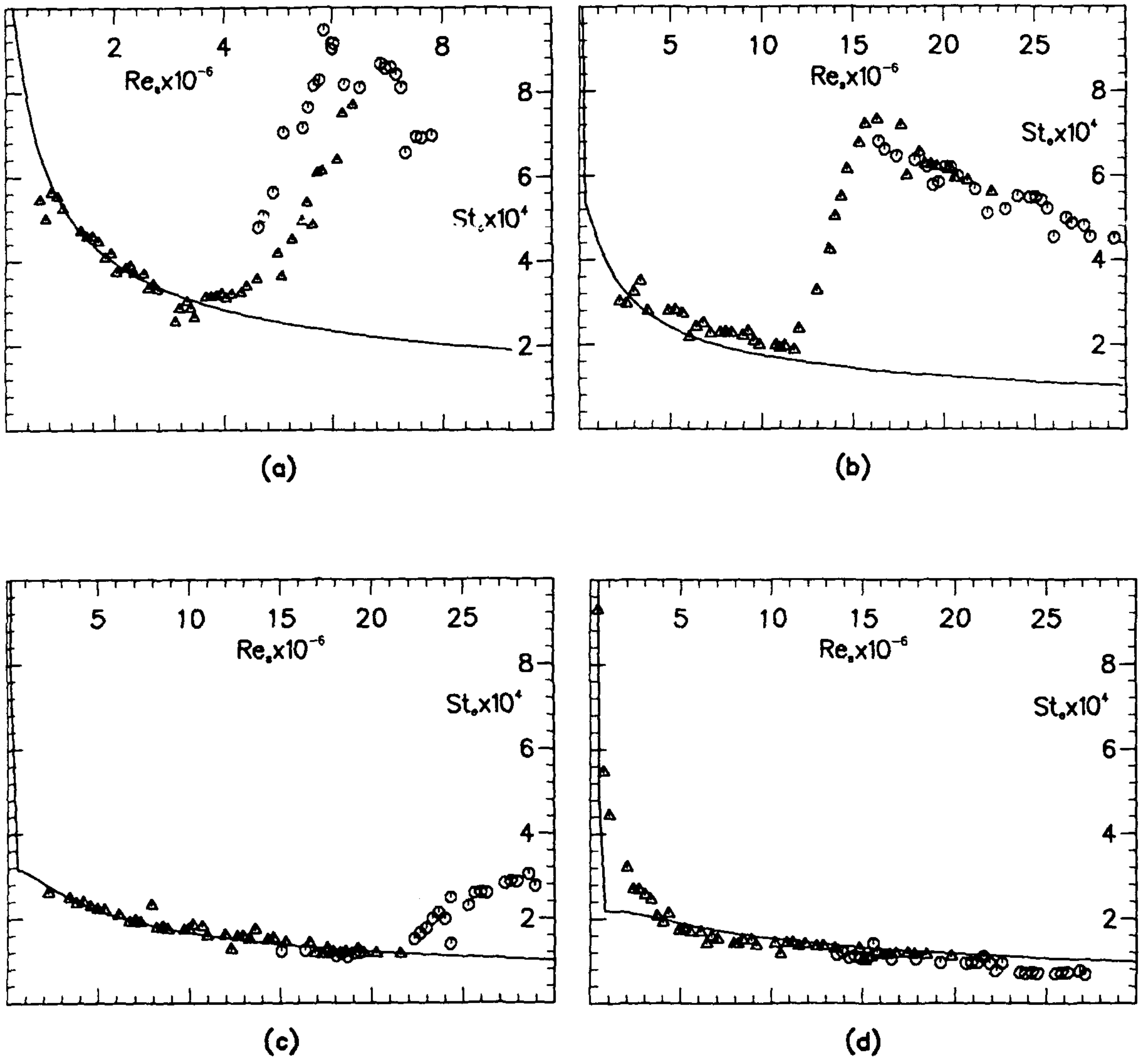

(a) (b)

(c) (d)

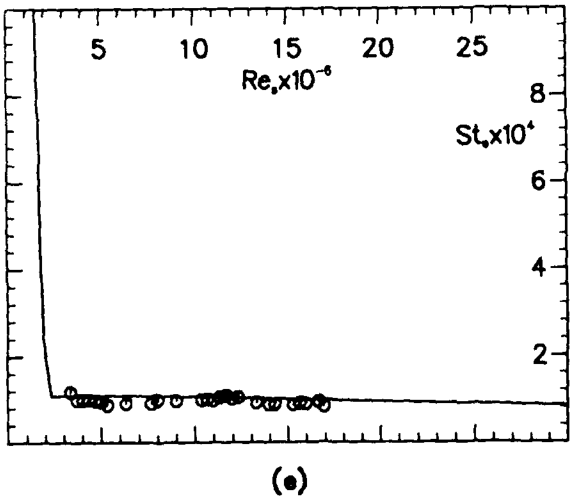

(e)

Figure 6 Heat transfer data for the blunt cone. (a) 1 mm radius cone, $Re_\infty = 1.55 \times 10^7$/m, $Re_N = 15{,}500$; (b) 1 mm cone, $Re_\infty = 5.5 \times 10^7$/m, $Re_N = 55{,}000$; (c) 3 mm cone, $Re_\infty = 5.5 \times 10^7$/m, $Re_N = 165{,}000$; (d) 6.25 mm cone, $Re_\infty = 5.5 \times 10^7$/m, $Re_N = 343{,}750$; (e) 25 mm cone, $Re_\infty = 5.5 \times 10^7$/m, $Re_N = 1{,}375{,}000$. o, model 1; Δ, model 2. —— Prediction by method of Fay and Riddell (Ref 11) and Lees (Ref. 12)

Radius (mm)	Re_N for low Re_∞	Re_N for high Re_∞
1 mm	15,500*	55,000*
1.25 mm	19,375	68,750
1.5 mm	23,250	82,500
1.75 mm	27,125	96,500
2.0 mm	31,000	110,000
3 mm	46,500	165,000*
6.25 mm	96,875 (L)	343,750* (L)
12.5 mm	193,250 (L)	687,500 (L?)
25.4 mm	387,500 (L)	1,375,000*

Table 2. Blunted Cone Test Conditions (L) refers to fully laminar flow over model

indicating a classical laminar-transitional-turbulent heat transfer distribution, with a very satisfactory agreement between models 1 and 2 in what is a particularly difficult region of measurement. Figure 6b likewise shows a typical transitional distribution, with a pronounced rearwards shifting of transition already evident. In Figure 6c transition has been delayed to a chordwise Reynolds number of 20 million and probably is only completed by the rearmost measurement station. Figure 6d is considered to be fully laminar. In Figure 6e, with the highest nose Reynolds number, the position is less clear. On first inspection the data appear almost constant with distance, though close inspection shows a very slight increase between chord Reynolds numbers of 5.5 million and 11.5 million. More significantly, the temperature time traces in this region show the large fluctuations which we associate with transition so that we regard this, possibly, as a reversal of the previous transition trend. Figures 6a to 6e include laminar predictions using the theories due to Fay and Riddell (Ref.11) for the stagnation point heating rates and Lees (Ref.12) for the remaining distribution, showing very close agreement with the measurements on the frustrum.

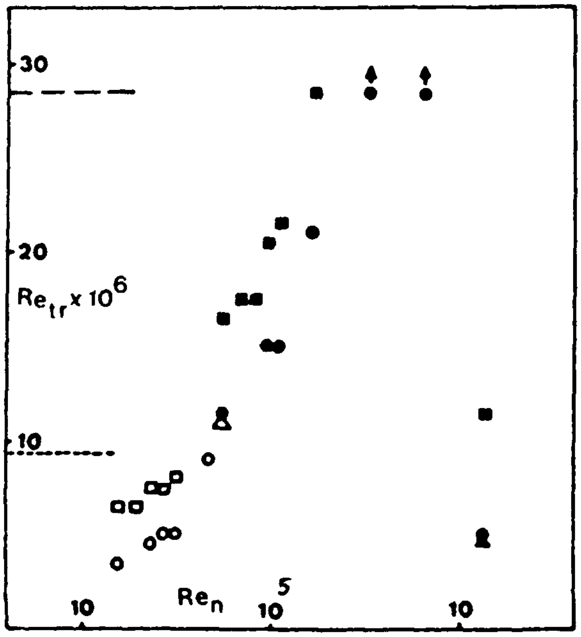

Figure 7. Transition Reynolds number versus nose radius Reynolds number. Onset of transition, o; end of transition, ◻. Open symbols for $\mathrm{Re}_\infty = 1.55 \times 10^7$/m; closed for $\mathrm{Re}_\infty = 5.5 \times 10^7$/m. Estimate from the thermochromic liquid crystal visualisation. △ Maximum chord Reynolds number available.— — . $\mathrm{Re}_\infty = 5.5 \times 10^7$/m. - - - - $\mathrm{Re}_\infty = 1.55 \times 10^7$/m.

Our transition data for all configurations are collected in Figure 7, and are generally unambiguous apart from the interpretation of Figure 6e. Figure 7 shows the 'onset' and 'completion' of transition, and demarcates between the high and low unit Reynolds number conditions. For some cases it was only possible to define an onset or completion value, because of model or instrumentation constraints, and in some the flow appeared to be laminar over the whole model chord (indicated as 'L' in Table 2). For the nose Reynolds numbers of 343750 and 687000 we consider that the onset of transition is for $\mathrm{Re}_{\infty s}$ greater than 28 million, delayed by more than a factor of nine compared with the sharp cone data. One question that concerned us considerably was whether the transition front was axisymmetric or not, since the heat transfer measurements were made along a single chordwise line along the model surface. We did find that rotating the model about its axis produced little noticeable effect on the data (which is a valid exercise since we know from the use of two models that transition does not appear to be provoked by model surface imperfections). We also made some surface thermal visualisations using thermochromic liquid crystal paints. Although these coloured photographs are not good enough quality to reproduce here the conclusions can be stated quite precisely. Three tests were performed. At the low unit Reynolds number condition for the sharp cone, and at high Reynolds number for the 1 mm cone (Re_N=55,000), visual estimates of transition agreed closely with the surface heat flux data (these points are included in Figure 7), with only slight circumferential variations in the location of the front. For the 25.4 mm. nose at the highest unit Reynolds number (Re_N =1,375,000) the visualisations were different showing high temperature streaks trailing downstream from the hemispherical nose, initially parallel but forming a wedge-like spread at a chord Reynolds number of 5 million. This is close to our heat transfer estimates for transition onset and clearly supports our observations on transition reversal.

Various workers have demonstrated the importance of the entropy swallowing length, x_{sw}, in controlling transition. From Stetson (Ref.13) and Rotta (Ref.14) we have for a 5 degree cone at a Mach number of 9.0 that

$$\frac{x_{sw}}{R_N} \approx 26\ (Re_N)^{1/3}$$

which very approximately defines a location where the boundary layer edge condition has recovered to the appropriate sharp cone value. To relate this to our data we can take as an example the 3 mm. nose at the highest unit Reynolds number (Re_N =165,000). In this case the ratio of the measured transition location to the swallowing distance calculated above is approximately 0.1, that is transition expected before full swallowing of the entropy layer. Figure 8 shows a measured Mach number profile for this case (at $Re_{\infty s}$ = 24 million, roughly 80% of the way through transition). We believe that the boundary layer edge lies at the location indicated, giving an edge Mach number of 6.0 compared with a fully swallowed value of 7.8, consistent therefore with the above suggestion. For conditions close to ours (7 degree half angle cone at Mach 9.3) Stetson (Ref.13) showed that when x_{sw}/x_{tr} was of the order 10, there was a maximum delay in transition relative to the sharp cone case, by a factor between 7.0 and 9.0. This again compares very favourably with our observations for the 3 mm radius data. For nose radius Reynolds numbers greater than this value of 165,000 transition should then occur well before entropy swallowing. Indeed, for the 'transition reversal' case the viscous layer will be so thin compared with the entropy layer that the boundary layer edge conditions will be virtually identical to the appropriate inviscid flow local wall conditions. Conversely, with Re_N less than 160,000 we can assume that transition has occurred with entropy layer swallowing more-or-less complete.

HOLLOW CYLINDER MODEL AND CAVITY SEPARATION

Both projects are at a relatively early stage and this section serves as a progress report. Considering the hollow cylinder model first the general design is illustrated in Figure 1 and Figure 9 shows a photograph of the model separated into sections, including pressure and heat transfer inserts. The pressure field is to be radiated onto the centrebody, which is the instrumented surface, from the outer concentrically aligned cowl. The model design has been controlled by some challenging design

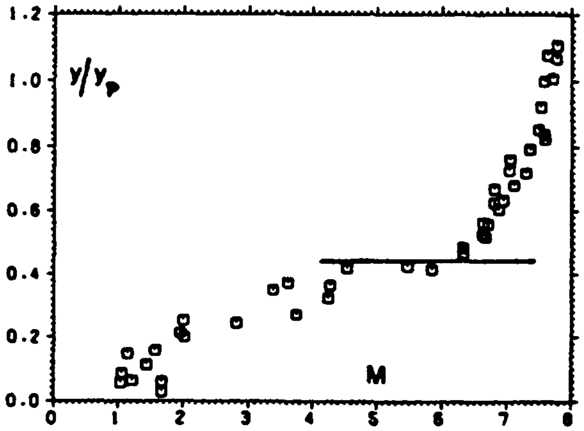

Figure 8. Mach number profile for transitional boundary layer and entropy layer. 3 mm radius cone, $Re_\infty = 5.5 \times 10^7$/m, Re_N = 165,000, $Re_s = 24 \times 10^6$.

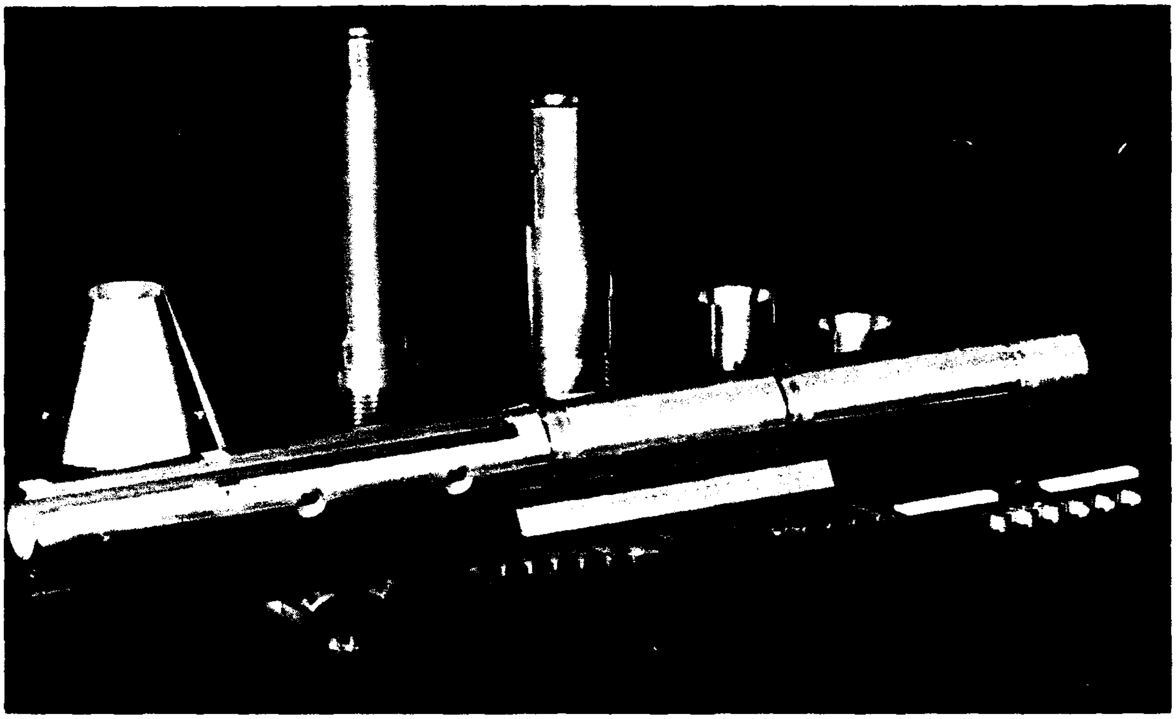

Figure 9 Main cylindrical model including extension pieces and pressure and heat transfer inserts

constraints such as: fitting the total assembly into the uniform test 'diamond'; structural rigidity; flexibility in interchange of instrumentation modules; provision to add a pressure gradient generating flare to the centrebody in addition to the use of the cowl; avoiding choking of the flow through the centrebody whilst maintaining sufficient wall thickness for instrumentation and strength. The initial design problem of avoiding choking was assessed at the beginning by testing a 900 mm chord section of stock tubing of 50 mm inner diameter, provided with a sharp leading edge intake with various outer diameters. Figures 10a and 10b respectively show a stalled flow case and the final design case of a ratio of inner to outer diameter of 0.67. The final model provides a measurement length of 800mm, or maximum chordwise Reynolds number of 44 x 10^6, and is constructed from several cylindrical portions which are interchangeable. Only one of these is machined with an instrumentation slot, and the final arrangement provides the possibility of measurements of pressure or heat transfer at a minimum pitch of 1 mm if required. Figure 11 presents measured pressure data on the centrebody (no cowl) and shows the low scatter of data produced,and also indicates the effect of the weak background tunnel pressure gradient. The first cowl design, which is under manufacture, is intended to impose a 5:1 linear pressure rise over a distance of 100 mm commencing at the chord location of 500mm. This interaction distance is of order several hundred initial momentum thicknesses. Inviscid calculations, using the method of characteristics and the Euler code, are in close agreement and the resultant prediction of surface (inviscid) pressure distribution is given in Figure 12.

The cavity induced separation project has only just commenced and we are currently considering configuration options. One requirement, however, is a fully laminar study, which requires both a reduction in our usual tunnel operating conditions and careful consideration of the likely behaviour of the separated shear layer.

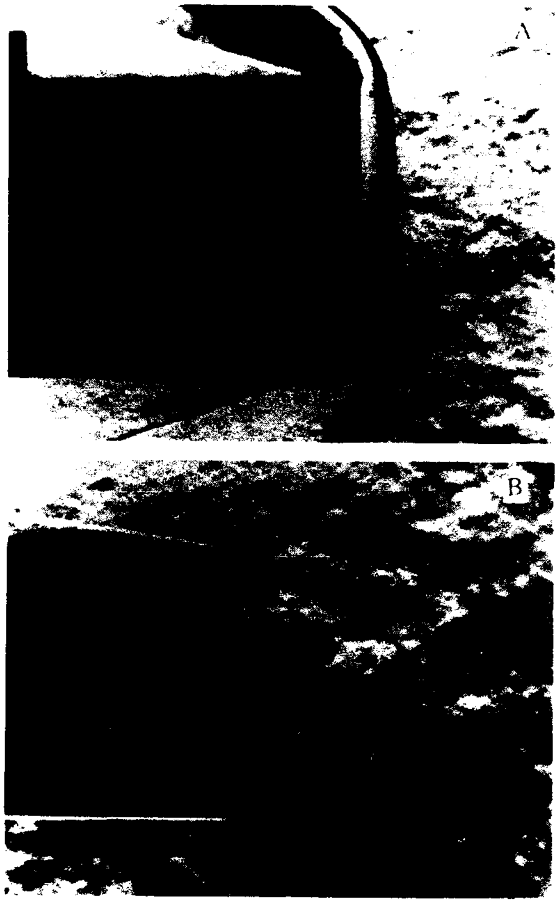

Figure 10 Schlieren photo for hollow cylinder model (a) Choked inlet conditions, (b) design conditions.

CONCLUDING REMARKS

This paper presents results, some preliminary, for current experiments on hypersonic viscous flows. Our general objective is to utilise simple two-dimensional configurations to produce a series of flows which are both of practical interest and also will provide reliable data for CFD code validation. The intention behind the use of axisymmetric configurations is to eliminate the end-effect errors which can contaminate 2-D planar experiments. Our immediate and future plans include: concentration mainly on the pressure gradient and cavity separation model; improvement in the calibration of the test section flow conditions; further development in parallel with the experiments of our CFD capability.

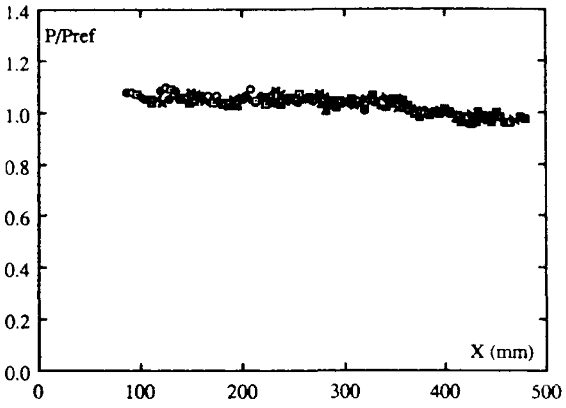

Figure 11 Experimentally measured static pressures along generator of hollow cylinder

ACKNOWLEDGEMENTS

This work was carried out with support from the Defence Research Agency under Agreements 2037/318/XR/AW; 2037/357/XR/AW and the Science and Engineering Research Council/Defence Research Agency Joint Grant GR/G57277. This support is gratefully acknowledged. The authors would like to thank the contracts' monitors Dr. T.A. Holbeche, Dr. P. Street, Mr. J. Woodley and Dr. W. Lester for their continued encouragement and helpful discussions. The views expressed are those of the authors alone.

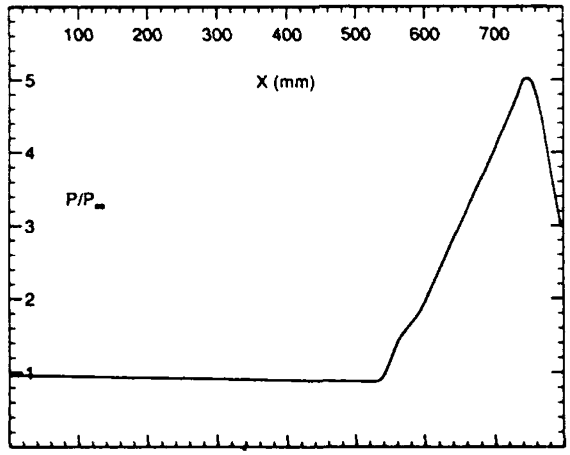

Figure 12 CFD modelling of cowl-induced pressure gradient on centrebody.

REFERENCES

1. Cook, W. J. and Felderman, E. J., "Reduction of Data from Thin-Film Heat-Transfer Gages: A Concise Numerical Technique", AIAA J., Vol. 4, pp 561-562, 1966.

2. Ben-Artzi, M. and Falcovitz, J., "A Second-Order Godunov-Type Scheme for Compressible Fluid Dynamics", J. Comp. Phys., Vol. 55, pp 1-32, 1984.

3. Baldwin, B. S. and Lomax, H., "Thin-Layer Approximation and Algebraic Model for Separated Turbulent Flows", AIAA Paper 78-257, 1978.

4. Stetson, K. F., "On Cone Frustum Pressure Gradient Effects on Transition", AIAA J., Vol. 26, pp 500-502, 1988.

5. Dolling, D. S. and Gray, W. K., "Experimental Study of Supersonic Turbulent Flow on a Blunted Axisymmetric Body", AIAA J., Vol. 24, pp 793-799, 1986.

6. Softley, E. J., Graber, B. C. and Zempel, R. E., "Experimental Observation of Transition of the Hypersonic Boundary Layer", AIAA J., Vol. 7, pp 257-263, 1969.

7. Stetson, K. F. and Rushton, G. H., "Shock Tunnel Investigation of Boundary-Layer Transition at M = 5.5", AIAA J., Vol. 5, pp 899-906, 1967.

8. Ericsson, L. E., "Effect of Nose Bluntness and Cone Angle on Slender-Vehicle Transition", AIAA J., Vol. 26, pp 1168-1174, 1988.

9. Morkovin, M. V., "Transition at Hypersonic Speeds", NASA CR-178315, 1987.

10. Denman, P.A. Harvey, J.K. and Hillier R., "Experimental Study of Attached Boundary Layer and Turbulent Base Flows", 2nd INRIA Workshop on Hypersonic Flows for Re-entry Problems, 1991.

11. Fay J. A. and Riddell, F. R., "Theory of Stagnation Point Heat Transfer in Dissociated Air", J. Aero. Sciences, Vol. 25, pp 73-85, 1958.

12. Lees L., "Laminar Heat Transfer Over Blunt-Nosed Bodies at Hypersonic Flight Speeds", Jet Propulsion, Vol. 26, pp 259-269, 1956.

13. Stetson, K. F., "Nosetip Bluntness Effects on Cone Frustum Boundary Layer Transition in Hypersonic Flow", AIAA Paper 83-1763, 1983.

14. Rotta, N. R., "Effects of Nose Bluntness on the Boundary Layer Characteristics of Conical Bodies at Hypersonic Speeds", Report NYU-AA-66-66, Dept. of Aeronautics and Astronautics, New York University, 1966.

CALCULS D'ECOULEMENTS VISQUEUX EN DESEQUILIBRE DANS DES TUYERES

par

C. Marmignon, V. Joly et **F. Coquel**
ONERA
BP72, 92322 Châtillon Cedex
France

Résumé

Une méthode implicite de volumes finis permettant de déterminer les écoulements visqueux en déséquilibre chimique et vibrationnel dans des tuyères est présentée.
Les termes de flux de fluide parfait sont calculés par un schéma décentré de type Roe du deuxième ordre en espace et les flux visqueux sont déterminés à l'aide d'un schéma centré. Les flux numériques et les termes source sont totalement couplés à l'étape implicite.
Afin d'illustrer la méthode numérique, deux configurations d'écoulements ont été calculées. La première configuration a été proposée en tant que cas test lors du dernier Workshop d'Antibes sur les écoulements hypersoniques (deuxième partie). La deuxième configuration correspond au calcul dans une tuyère de la soufflerie F4 de l'ONERA.

1 Introduction

Dans le cadre du programme Hermes, plusieurs souffleries spécifiques sont développées en Europe, notamment la soufflerie à arc F4 de l'ONERA . Ces souffleries doivent simuler des conditions d'écoulements hypersoniques afin d'effectuer des mesures autour de maquettes de formes réalistes, ces mesures étant par la suite extrapolées aux conditions de vol réel. Ces outils sont aussi d'un grand intérêt pour valider les codes.
En régime hyperenthalpique, un ensemble complet de paramètres de similitude tels que le nombre de Reynolds et le nombre de Mach pour les gaz parfaits n'existe pas. Même si les écoulements internes vérifient le paramètre ρL qui est le plus approprié pour les écoulements dissociés, les résultats d'expériences ne peuvent reproduire les conditions de vol réel. L'écoulement dans une tuyère hyperenthalpique peut se décomposer en trois parties: une zone d'écoulement à l'équilibre dans le convergent suivie d'une zone en déséquilibre chimique et vibrationnel près du col et d'une région d'écoulement figé dans le divergent. L'écoulement en sortie de tuyère sera donc figé avec des températures de vibration plus grandes que la température de translation.
Même si les conditions de vol réel ne peuvent être reproduites, la prédiction des états thermodynamiques et chimiques en amont de la maquette est nécessaire à la comparaison des résultats expérimentaux et numériques sur cette maquette. Par la suite, les calculs permettront la simulation de l'écoulement dans les conditions de vol réel.
Dans ce papier, nous rappelons les principales caractéristiques d'une méthode déjà appliquée au calcul d'écoulements bidimensionnels externes. Cette méthode résout les équations de bilan décrivant les écoulements visqueux en déséquilibre chimique et vibrationnel. Des applications à des tuyères utilisées à Marseille et à l'ONERA sont présentées.

2 Equations de bilan

2.1 Hypothèses de base et modélisation physique

Pour les conditions génératrices considérées, l'ionisation est négligée et l'air peut être modélisé par un mélange idéal de gaz parfaits comprenant les cinq espèces principales, à savoir N2, O2, NO, N et O. La pression du gaz est alors donnée par la loi de Dalton

$$(1) \quad p = \sum_{\alpha} \frac{\rho_\alpha}{M_\alpha} R_{gp} T ,$$

où R_{gp} désigne la constante universelle des gaz parfaits et M_α est la masse atomique de l'espèce α.
Les modes de translation et de rotation, et le mode électronique sont toujours considérés à l'équilibre et sont donc caractérisés par une température unique T alors que les modes de vibration peuvent s'écarter de l'équilibre. Chacune des espèces diatomiques N2, O2 et éventuellement NO est supposée avoir une température de vibration particulière, distincte de la température du mélange . Dans ce papier, le mode de vibration pour le monoxyde d'azote NO est supposé être à l'équilibre avec le mode de translation.
La température du mélange vérifie :

$$(2) \; T = \Big(\sum_{\alpha} \rho_\alpha c_{v,t,r,\alpha}\Big)^{-1} \Big\{ \rho E - \frac{1}{2}\rho U^2 - \sum_{\alpha} \rho_\alpha e_{el,\alpha} - \sum_{\beta} \rho_\beta e_{v,\beta} - \sum_{\alpha} \rho_\alpha h_\alpha^o \Big\}$$

où E est l'énergie totale du mélange par unité de masse et $\vec{U}$ la vitesse barycentrique du mélange. $c_{v,t,r,\alpha}$ est la chaleur spécifique de l'espèce α par unité de masse. Pour l'espèce β, $e_{t,\beta}$, $e_{r,\beta}$, $e_{el,\beta}$, $e_{v,\beta}$ désignent respectivement les énergies de translation, de rotation, électronique et de vibration par unité de masse et h_α^o est la chaleur de formation de l'espèce α par unité de masse. L'énergie $e_{v,\alpha}$ comprend les modes de vibration harmoniques et anharmoniques, ainsi que le couplage rotation-vibration. La température de vibration $T_{v,\beta}$ de l'espèce moléculaire β est donnée par la relation implicite suivante : $e_{v,\beta}(T_{v,\beta}) = \rho_\beta e_{v,\beta}/\rho_\beta$.

Dans les calculs présentés ici, aucun couplage Vibration-Vibration (V-V) ou Vibration-Dissociation (V-D) n'a été pris en compte. Les équations pour les énergies de vibration ne comprennent que les échanges d'énergie Translation-Vibration (T-V) . Le taux d'échange d'énergie Translation-Vibration $\dot{E}_{t-v,\beta}$ est modélisé par :

$$(3) \quad \dot{E}_{t-v,\beta} = \rho_\beta \frac{e_{v,\beta}(T) - e_{v,\beta}}{\tau_{vib,\beta}}$$

où $e_{v,\beta}(T)$ représente l'énergie de vibration par unité de masse de l'espèce β évaluée pour la température locale du mélange. $\tau_{vib,\beta}$ est le temps de relaxation donné par :

$$(4)\quad \frac{1}{\tau_{vib;\beta}} = \sum_{\gamma} \frac{X_\gamma}{\tau_{v;\beta,\gamma}}$$

où X_γ est la concentration molaire de l'espèce γ. Les temps de relaxation entre espèces $\tau_{v;\beta;\gamma}$ sont donnés par la règle semi-empirique de Millikan et White [2].

Le modèle de chimie choisi est celui de Gardiner [3]. Il met en oeuvre dix-sept réactions comprenant quinze réactions de dissociation et deux réactions d'échange.

2.2 Equations de bilan

La forme intégrale des équations de bilan instationnaires pour des écoulements visqueux en déséquilibre peut s'écrire dans des coordonnées cylindriques de la manière suivante :

$$(5a)\quad \iint_S \Big[x_2 W_t - (H - Hs) \Big]\, dS + \int_{\delta S} \Big[x_2 (F_s - Fv_s) - G_s \Big] N_s\, dl = \\ = \iint_S x_2 \hat{\Omega}\, dS$$

où S désigne un domaine de contrôle fixe dans un plan méridien quelconque, δS sa frontière et $\vec{N} = (N_s),(s = 1{,}2)$ la normale unité extérieure à δS. Nous avons :

$$(5b)\quad W = \Big([\,\rho_\alpha\,], \rho\, u_1, \rho\, u_2, \rho\, E, [\,\rho_\beta e_{v;\beta}\,] \Big)^t$$

$$(5c)\quad H = \Big([\,0_\alpha\,], 0, p - (2\mu + \lambda)\, u_2/x_2, 0, [\,0_\beta\,] \Big)^t$$

$$(5d)\quad Hs = \lambda \Big([\,0_\alpha\,], 0, div\vec{U}, 0, [0_\beta\,] \Big)^t$$

$$(5e)\quad F_s = u_s W + p\, \Big([0_\alpha], \delta_{1s}, \delta_{2s}, u_s, [0_\beta] \Big)^t$$

$$(5f)\quad Fv_s = \Big([\,-\rho_\alpha V_{\alpha s}\,], \tau_{s1}, \tau_{s2}, u_1\tau_{1s} + u_2\tau_{2s} \\ - q_s - \sum_\alpha \rho_\alpha h_\alpha V_{\alpha s}, [\,-\rho_\beta\, e_{v,\beta}\, V_{\beta s} - q_{v,\beta s}\,] \Big)^t$$

$$(5g)\quad G_s = \lambda u_2 \Big([\,0_\alpha\,], \delta_{1s}, \delta_{2s}, u_s, [\,0_\beta\,] \Big)^t$$

$$(5h)\quad \hat{\Omega} = \Big([\,\hat{m}_\alpha\,], 0, 0, 0, [\,\hat{E}_{t-v,\beta} + \hat{m}_\beta e_{v;\beta} + \hat{E}_{d-v,\beta}] \Big)^t$$

où $\alpha = 1{,}2{,}3{,}4{,}5$ se rapporte aux espèces N2, O2, NO, N et O, $\beta = 1{,}2{,}3$ aux espèces diatomiques N2, O2 et NO, $s = 1{,}2$ aux directions d'espace. u_1 et u_2 désignent les deux composantes de la vitesse barycentrique $\vec{U}$, λ et μ sont les coefficients de viscosité du mélange, $V_{\alpha s}$ est la vitesse de diffusion de l'espèce α dans la direction x_s, τ_{1s}, τ_{2s} sont les composantes du tenseur des contraintes visqueuses, $\vec{q}_s$ est le vecteur de flux de chaleur du mélange dans la direction x_s, h_α est l'enthalpie par unité de masse de l'espèce α, $\vec{q}_{v,\beta s}$ est le vecteur de flux de chaleur de vibration dans la direction x_s pour l'espèce diatomique β, $\hat{m}_\alpha$ est la production de masse de l'espèce α par unité de volume.

2.3 Coefficients de transport

Le tenseur des contraintes visqueuses τ_{ij} s'écrit:

$$(6)\quad \tau_{ij} = \lambda\, div\vec{U}\, \delta_{ij} + \mu\, \Big(\frac{\partial u_i}{\partial x_j} + \frac{\partial u_j}{\partial x_i}\Big).$$

On fait l'hypothèse de Stokes pour les coefficients de viscosité du mélange : $\lambda + \frac{2}{3}\mu = 0$. Chaque viscosité μ_α d'une espèce est déterminée par la relation de Blottner [4], la viscosité du mélange μ est alors calculée au moyen du modèle d'Armaly et Sutton [5]:

$$(7a)\quad \mu = \sum_\alpha \frac{\mu_\alpha}{1 + \sum_{\gamma \neq \alpha} \frac{X_\gamma}{X_\alpha} \Phi_{\alpha\gamma} \frac{M_\alpha}{(M_\alpha + M_\gamma)} \Big(\frac{5}{3A^{*}_{\alpha\gamma}} + \frac{M_\gamma}{M_\alpha}\Big)}$$

$$(7b)\quad \Phi_{\alpha\gamma} = \Big(\frac{M_\gamma}{8(M_\alpha + M_\gamma)}\Big)^{1/2} \Big(F_{\alpha\gamma} + \Big(\frac{\mu_\alpha}{\mu_\gamma} \frac{M_\gamma^{1/2}}{M_\alpha^{1/2}}\Big)^{1/2} B_{\alpha\gamma}\Big)^2$$

où les coefficients $A^{*}_{\alpha\gamma}$, $F_{\alpha\gamma}$ et $B_{\alpha\gamma}$ vérifient les relations suivantes :

$$(7c)\quad A^{*}_{\alpha\gamma} = \frac{\Omega^{(2,2)*}_{\alpha\gamma}}{\Omega^{(1,1)*}_{\alpha\gamma}} = A^{*}_{\gamma\alpha} = 1.25$$

$$(7d)\quad F_{\alpha\gamma} = \Big(\frac{\Omega^{(2,2)*}_{\alpha\gamma}}{\Omega^{(2,2)*}_{\alpha\alpha}}\Big)^2 = F_{\gamma\alpha} = 1.00$$

$$(7e)\quad B_{\alpha\gamma} = \Big(\frac{\Omega^{(2,2)*}_{\alpha\gamma}}{\Omega^{(2,2)*}_{\gamma\gamma}}\Big)^2 = B_{\gamma\alpha} = 0.78$$

$\Omega^{(2,2)*}_{\alpha\gamma}$ désigne une intégrale de collision pour les collisions entre les molécules α et γ.

La vitesse de diffusion $\vec{V}_\alpha$ est supposée vérifier les lois de Fick suivantes :

$$(8)\quad \vec{V}_\alpha = -D_D \vec{\nabla} Y_\alpha / Y_\alpha \text{ avec } Y_\alpha = \rho_\alpha/\rho.$$

D_D est calculé en supposant un nombre de Lewis constant.

Les vecteurs de flux de chaleur du mélange et de vibration $\vec{q}$ et $\vec{q}_{v;\beta}$ sont supposés suivre les lois de Fourier :

$$(9a)\quad \vec{q} = -(K_t + K_r + K_{el})\vec{\nabla} T + \sum_\beta \vec{q}_{v,\beta}$$

avec

$$(9b)\quad \vec{q}_{v;\beta} = -K_{v,\beta} \vec{\nabla} T_{v;\beta}$$

Le coefficient de conductivité thermique de translation K_t est calculé à partir de la relation d'Armaly et Sutton [6]:

$$(10a)\quad K_t = \\ \sum_\alpha \frac{k_{t,\alpha}}{1 + \sum_{\gamma\neq\alpha} \frac{X_\gamma}{X_\alpha} \Phi_{\alpha\gamma} \frac{M_\alpha M_\gamma}{4(M_\alpha + M_\gamma)^2} \frac{1}{A^{*}_{\alpha\gamma}} \Big(\frac{15 M_\alpha}{M_\gamma} + 5\frac{M_\gamma}{M_\alpha} + 8A^{*}_{\alpha\gamma}\Big)}$$

Les coefficients de conductivité thermiques de rotation et électroniques K_{im} $(im = r, el)$ et les coefficients de conductivité thermiques de vibration $K_{v;\beta}$ dans le mélange sont donnés par l'approche de Monchick, Yun et Mason [7].

$$(10b)\quad K_{im;\alpha} = \frac{k_{im,\alpha}}{\sum_\gamma \frac{X_\gamma}{X_\alpha} \frac{D^{bi}_{\alpha\alpha}}{D^{bi}_{\alpha\gamma}}} \qquad (im = r, el, v)$$

$$(10c)\quad K_{im} = \sum_\alpha K_{im,\alpha} \qquad (im = r, el).$$

En utilisant l'hypothèse d'Armaly et Sutton, les coefficients de diffusion binaire $D^{bi}_{\alpha\epsilon}$ et $D^{bi}_{\alpha\gamma}$ vérifient la relation:

(10d) $$\frac{D^{bi}_{\alpha\epsilon}}{D^{bi}_{\epsilon\gamma}} = \Phi_{\epsilon\gamma}.$$

Le coefficient de conductivité $k_{im,\alpha}$ $(im = t, r, el, v)$ pour chaque espèce α est obtenu par une relation d'Eucken [8]:

(10e) $$k_{im,\alpha} = \frac{6}{5}A^{*}_{\alpha\epsilon}\mu_\alpha c_{v,im,\alpha} \quad \text{avec} \quad im \neq translation$$

(10f) $$k_{t,\alpha} = \frac{5}{2}\mu_\alpha c_{v,t,\alpha}$$

où $c_{v,im,\alpha}$ dans (10e) désigne la chaleur spécifique de l'espèce α par unité de masse correspondant au mode interne im.

3 Méthode numérique

Les équations de bilan (5) sont résolues par une méthode de volumes finis implicite écrite pour des maillages curvilignes structurés. Les flux de fluide visqueux sont discrétisés au moyen d'un schéma aux différences centrées de type Crank-Nicolson alors que les flux de fluide parfait sont approchés par une méthode décentrée de type Roe, le second ordre d'approximation en espace étant obtenu en adoptant l'approche de flux modifié due à Harten [9].

A chaque date $t_n = n\,\Delta t$ où Δt désigne le pas de temps, la méthode de volumes finis permet de construire une solution approchée dont la valeur constante sur chaque cellule de calcul $S_{i,j}$ est notée $W^n_{i,j}$. La solution est avancée en temps selon l'algorithme suivant :

(11) $$\left[x_2\frac{W^{n+1}-W^n}{\Delta t}\Delta S\right]_{i,j} + \lambda^n_{i,j}\int_{\delta S_{i,j}} U_s^{n+1}N_s\,dl$$
$$+\int_{\delta S_{i,j}}\left[x_2(\tilde{F}_s - Fv_s) - G_s\right]^{n+1}N_s\,dl = (H^n\Delta S)_{i,j} + (x_2\hat{\Omega}^{n+1}\Delta S)_{i,j}$$

où $\Delta S_{i,j}$ désigne la surface de la cellule considérée, l'intégrale curviligne le long de la frontière $\delta S_{i,j}$ pouvant alors être décomposée en une somme de quatre flux respectivement associés aux arêtes $i\pm1/2,j$ et $i,j\pm1/2$. Dans la formule (11), $\lambda^n_{i,j}$ représente une valeur moyenne de λ sur $S_{i,j}$ choisie de sorte que l'intégrale portant sur Hs dans (5d) puisse être exprimée en terme de flux :

(12) $$\iint_{S_{i,j}} Hs\; dS = \lambda_{i,j}\int_{\delta S_{i,j}} U_s N_s\,dl$$

$$U_s N_s = ([0_\alpha], 0, u_s, 0, [0_\beta])^t.$$

3.1 Discrétisation en espace des termes de flux

Par souci de simplicité, nous limiterons le présent exposé à la présentation de la méthode d'approximation associée aux termes de flux sur l'arête $i+1/2,j$:

(13) $$\left\{\begin{aligned} P^{n+1}_{i+1/2,j} &= (U_s^{n+1}N_s\Delta l)_{i+1/2,j} \\ Q^{n+1}_{i+1/2,j} &= \left[\,[x_2(\tilde{F}_s - Fv_s) - G_s]^{n+1}N_s\Delta l\right]_{i+1/2,j} \end{aligned}\right.$$

Approximation des flux de fluide parfait

Dans la relation (13), $\tilde{F}_s N_s$ désigne une approximation du flux de fluide parfait $F_s N_{s;i+1/2,j}$ obtenue en adoptant l'approche de flux modifié due à Harten [9]. Ce flux numérique est construit à partir de la méthode de Roe proposée par Abgrall [10] pour les équations d'Euler multi-espèces et multi-températures.

Soit $A_{i+1/2,j}$ une linéarisée de Roe [10] associée au flux $F_s N_{s;i+1/2,j}$, $a^m_{i+1/2,j}$, (m=1,...11) les valeurs propres correspondantes et $R_{i+1/2,j}$ une matrice de vecteurs propres à droite associés. Le flux numérique $\tilde{F}_s N_s$ s'écrit:

(14) $$(\tilde{F}_s N_s)_{i+1/2,j} = \frac{(F_s)_{i,j}+(F_s)_{i+1,j}}{2}(N_s)_{i+1/2,j} + \frac{1}{2}(R\Phi)_{i+1/2,j}$$

où le dernier terme du membre de droite désigne l'opérateur de correction de flux. Afin de simplifier l'implémentation de cet opérateur dans la méthode de volumes finis, nous supposerons que la direction normale à l'arête $i+1/2,j$ reste parallèle à une ligne de maillage $j=Cste$, ce qui permet en conséquence d'écrire $\Phi_{i+1/2,j} = (\Phi^m_{i+1/2,j})_{(m=1,\dots,11)}$ sous la forme :

(15a) $$\Phi^m_{i+1/2,j} = \frac{1}{2}\psi(a^m_{i+1/2,j})(g^m_{i,j} + g^m_{i+1,j})$$
$$-\psi(a^m_{i+1/2,j} + \gamma^m_{i+1/2,j})\,\alpha^m_{i+1/2,j}$$

(15b) $$\alpha^m_{i+1/2,j} = (R^{-1}_{ml})_{i+1/2}[(W_l)_{i+1,j} - (W_l)_{i,j}],$$

où $g^m_{i,j}$ est un limiteur operant sur les variables caractéristiques $\alpha_{i+1/2,j}$. Dans cette étude, nous avons utilise le limiteur classique suivant [11]:

(16) $$g^m_{i,j} = minmod(\alpha^m_{i+1/2,j}\,;\alpha^m_{i-1/2,j})$$

Le terme associé $\gamma^m_{i+1/2,j}$ est défini par :

(17)
$$\gamma^m_{i+1/2,j} = \begin{cases} \psi(a^m_{i+1/2,j})(g^m_{i+1,j} - g^m_{i,j})/(2\alpha^m_{i+1/2,j}) & si \quad \alpha^m_{i+1/2,j} \neq 0 \\ 0 & si \quad \alpha^m_{i+1/2,j} = 0 \end{cases}$$

Dans (17), ψ représente une application, qualifiée de correction d'entropie d'après Harten, définie par :

(18) $$\psi(z) = \begin{cases} |z| & si \quad |z| \geq \delta_1 \\ (z^2 + \delta_1^2)/2\delta_1 & si \quad |z| < \delta_1 \end{cases}$$

où δ_1 est un paramètre devant être choisi nul dans les couches limites.

Discrétisation des flux de fluide visqueux

La linéarisation des flux de fluide visqueux à la date $(n+1)\Delta t$ conduit aux expressions suivantes :

(19a) $$U_s^{n+1} = U_s^n + \left[\frac{\partial U_s}{\partial W}\Delta W\right]^n,$$

(19b) $$G_s^{n+1} = G_s^n + \left[\frac{\partial G_s}{\partial W}\Delta W\right]^n$$

(19c)
$$F_{vs}^{n+1} = F_{vs}^n + \left[\left[\frac{\partial F_{vs}}{\partial W} - \frac{\partial^2 F_{vs}}{\partial q_\varepsilon \partial x_\varepsilon}\right]\Delta W\right]^n + \Delta t\frac{\partial}{\partial x_\varepsilon}\left[\frac{\partial F_{vs}}{\partial q_\varepsilon}\frac{\Delta W}{\Delta t}\right]^n$$

où $q_\varepsilon = \partial W/\partial x_\varepsilon$, $(\varepsilon = 1,2)$. En utilisant (19a), la discrétisation en espace de (13) conduit à :

(20a) $$P^{n+1}_{i+1/2,j} = P^n_{i+1/2,j} +$$
$$\left[\,\overline{(\partial U_s/\partial W)}^{\,n}_{i+1/2,j}\,\frac{[(\Delta W)_{i,j} + (\Delta W)_{i+1,j}]^n}{2}\right](N_s\Delta l)_{i+1/2,j}\,.$$

$$(20b)\quad P^{n}_{i+1/2,j} = \frac{1}{2}[(U_s)_{i,j} + (U_s)_{i+1,j}]^{n}(N_s\Delta l)_{i+1/2,j},$$

où la matrice Jacobienne associée à U_s est évaluée à l'arête $i+1/2,j$. Des expressions similaires à (20) sont utilisées pour le traitement de la contribution de G_s à la discrétisation en espace de (13).

La discrétisation en espace de F_{vs} à la date $n\Delta t$ demande l'évaluation des dérivées en espace apparaissant dans le tenseur des contraintes ainsi que dans les termes de flux de chaleur. Les dérivées en espace sont directement approchées dans le domaine physique par une méthode aux différences centrées mettant en oeuvre la métrique et la solution approchée W^n aux six barycentres (i,j), $(i+1,j)$, $(i,j+1)$, $(i,j-1)$, $(i+1,j+1)$ et $(i+1,j-1)$. Plus précisément, soit Φ une grandeur définie aux quatres noeuds E,W,N et S, dont le barycentre est M ; son gradient au point M est alors donné par :

$$(21)\quad \nabla\Phi_M = (\partial\Phi/\partial x_1\,,\,\partial\Phi/\partial x_2)^{t}_{M} = \frac{[(\Phi_E-\Phi_W)\vec{SN} - (\Phi_N-\Phi_S)\vec{WE}]\times\vec{z}}{(\vec{WE}\times\vec{SN})\,\vec{z}},$$

ou $\vec{z} = \vec{x}\times\vec{y}$. Par exemple, si M correspond au centre de l'arête référencée par $(i+1/2,j)$, la formule (21) utilise les points $E\ (i+1,j)$, $W\ (i,j)$, $S\ (i+1/2,j-1/2)$ et $N\ (i+1/2,j+1/2)$.

De plus, la discrétisation en espace du dernier terme de (5f) demande l'évaluation des dérivées en espace de l'inconnue ΔW. Cette évaluation est menée par une méthode aux différences centrées semblable à la précédente, excepté que seules les contributions de ΔW aux noeuds (i,j) et $(i+1,j)$ sont utilisées.

3.2 Discrétisation en temps

L'implicitation des flux numériques subit une linéarisation conservative, les termes source recoivent également une implicitation par linéarisation obtenue à l'aide de développements de Taylor. Toutefois, afin d'éviter une complexité inutile dans l'expression de l'opérateur implicite, la linéarisation du flux numérique de fluide parfait suit la demarche proposée par Yee [11] selon laquelle la matrice de Roe fait office de linéarisée du flux numérique. De même, les termes de dérivées croisées sont négligées dans l'étape de linéarisation des flux de fluide visqueux.

L'étape implicite couple totalement les termes source et les flux numériques de maniere à pouvoir traiter la raideur du problème.

L'operateur implicite ainsi obtenu est linéaire et peut être inversé de plusieurs facons. Une première facon repose sur une factorisation ADI de l'opérateur implicite, la matrice Jacobienne des termes source intervenant pour une moitié dans chacune des deux directions du maillage. Le système résultant est de structure tridiagonale par blocs de taille 11x11 dans chaque direction du maillage et est inversé à l'aide d'une décomposition LU classique. Une autre façon est de résoudre l'opérateur implicite par une méthode itérative. Cette technique présente l'avantage d'être bien moins sensible au choix du pas de temps que ne le sont les méthodes par factorisation approchées. Elle permet également d'éviter la décomposition parfois inadéquate de la matrice Jacobienne des termes source. La méthode itérative mise en oeuvre est basée sur une stratégie de minimisation des résidus telle que la méthode GMRES préconditionnée par un opérateur de factorisation incomplète [12].

3.3 Conditions aux limites

3.3.1 Frontière paroi

Les conditions à la limite pour la paroi dépendent du comportement de cette même paroi. Dans ce travail, une condition de non glissement est appliquée :

$$(22)\quad (u_s)_W = 0.$$

Nous supposons également que le gradient de pression normal à la paroi est nul :

$$(23)\quad (\partial p/\partial\xi_2)_W = 0.$$

La valeur de la température de paroi est imposée $(T)_W = T_{wall}$ et les températures de vibration sont supposées être à l'équilibre avec la température de paroi $(T_{v,\beta})_W = T_{wall}$.

Dans cet article, la paroi est supposée être soit non catalytique soit complètement catalytique. Cette dernière condition favorise les réactions chimiques et le gaz atteint rapidement une composition d'équilibre correspondant aux conditions locales de pression et de température.

3.3.2 Frontière d'entrée

L'utilisation d'une méthode de volumes finis conduit à traiter la condition d'entrée en terme de flux numérique. Par souci de simplicité, l'analyse que nous donnons ici est menée pour un problème monodimensionnel mais elle peut être aisément étendue à des problèmes multidimensionnels en considérant leur projection sur la normale à la frontière. Considérons une condition d'entrée subsonique.

A gauche de cette frontière, le gaz est décrit par ses propriétés thermodynamiques statiques que sont l'enthalpie totale du réservoir H_{res} et l'entropie S_{res} sous l'hypothèse de l'équilibre chimique et thermique. Ces conditions permettent de définir une courbe dans l'espace des phases constituée des états $W_{B,L}$ qui peuvent être connectés du réservoir à la gauche de la frontière d'entrée.

A droite de cette frontière, l'écoulement est supposé être régulier ainsi qu'à l'équilibre, de telle manière qu'une onde de détente peut être utilisée pour connecter la droite de la frontière d'entrée $W_{B,R}$ à l'écoulement dans le domaine W_R ce qui définit une courbe de raréfaction dans l'espace des phases. Cette courbe est aisément construite en utilisant les invariants de Riemann associés au problème.

Les deux courbes précédentes possèdent sous des hypothèses physiques générales [13] un unique point d'intersection dans l'espace des phases qui définit une discontinuité de contact connectant l'état gauche à l'état droit. Ce problème d'intersection conduit au système suivant dont la résolution nécessite la mise en oeuvre d'une procédure itérative de type Newton :

$$(24a)\quad H(T_{B,L}, Y_{\alpha\,B,L}, u_{B,L}) = H_{res}$$

$$(24b)\quad S(T_{B,L}, Y_{\alpha\,B,L}, p_{B,L}) = S_{res}$$

$$(24c)\quad Y_{\alpha\,B,L} = Y_{\alpha}(T_{B,L}, p_{B,L})$$

$$(24d)\quad T_{v,\alpha\,B,L} = T_{B,L}$$

$$(24e)\quad u_{B,R} = u_{B,L}$$

(24f) $p_{B,R} = p_{B,L}$

(24g) $Y_{\alpha\ B,R} = Y_{\alpha\ R}$

(24h) $T_{v,\alpha\ B,R} = T_{v,\alpha\ R}$

(24i) $u_{B,R} - \dfrac{2}{\gamma_f - 1} a_{B,R} = u_R - \dfrac{2}{\gamma_f - 1} a_R$

(24j) $p_{B,R}\ \rho_{B,R}^{-\gamma_f} = p_R\ \rho_R^{-\gamma_f}$

Remarquons que les relations (24g) à (24j) sont en fait des approximations des invariants de Riemann exacts.

3.3.3 Frontière de sortie

Une condition d'extrapolation d'ordre 1 est appliquée au champ W.

4 Applications

4.1 Résultats pour la soufflerie de Marseille

4.1.1 Description de l'écoulement

Nous présentons un calcul d'écoulement de tuyère correspondant au cas test (problème 8.2) proposé au "Workshop on Hypersonic Flows for Reentry Problems, part II", qui s'est tenu à Antibes en Avril 1991 [14]. Il s'agit d'un écoulement dans une tuyère axisymétrique. L'angle du convergent est de 45°, celui du divergent de 10°. Le diamètre du col et la longueur totale du divergent sont respectivement 0.006 m et 1.13 m. La paroi, supposée non-catalytique, est maintenue à une température de $600K$. Les conditions du réservoir sont $T_0 = 6500\,K$, $P_0 = 1530$ bars.

4.1.3 Résultats

Le domaine de calcul comprend trois parties. Dans une première étape, l'écoulement dans le convergent et au voisinage du col est calculé. On calcule ensuite l'écoulement supersonique en aval du col, en utilisant les résultats de la première étape. Cette stratégie nous permet d'utiliser des maillages adaptés dans chacun des domaines de calcul. Les maillages des trois domaines contiennent respectivement 61x71, 59x71 et 51x71 points. La figure 1 montre les deux premiers domaines ainsi que le maillage du second. Remarquons le recouvrement important des deux domaines.

Les champs de nombre de Mach et de températures de vibration de l'oxygène et de l'azote sont représentés sur les figures 2 et 3. La distribution des températures sur l'axe de la tuyère est représentée sur la figure 4. Dans le convergent, les températures de vibration et de translation sont en équilibre. La température de vibration de O_2 est "gelée" à une valeur de $1670K$ à partir de 0.13 m en aval du col. La température de vibration de N_2 est "gelée" à une valeur de $3000K$ à partir de 0.25 m en aval du col. Les profils des températures au col (Fig.5) montrent que la couche limite est très mince. Sur la figure 6, où sont représentées les fractions massiques calculées sur l'axe, on constate que celles-ci sont gelées pour une distance au col inférieure à celles observées pour les températures de vibration. Ceci est dû aux temps caractéristiques différents pour les phénomènes chimiques et vibrationnels.

Les figures 7 et 8 donnent respectivement les profils de températures et de nombre de Mach en sortie. La couche limite représente environ 10% du rayon de la section de sortie.

4.2 Résultats pour la soufflerie ONERA F4

4.1.1 Description de l'écoulement

Cette soufflerie peut être équipée de quatre tuyères différentes, chacune permettant de simuler un régime d'écoulement différent. En particulier, la tuyère n ° 4 est dédiée à la simulation des effets visqueux et respecte le paramètre $\dfrac{Mach}{\sqrt{Re}}$. Les quatre tuyères ont été conçues grâce à une méthode numérique utilisant un couplage faible entre l'écoulement non visqueux et la couche limite [15]. L'épaisseur de la couche limite est déterminée en utilisant les corrélations de Edenfield [16].

La géométrie réelle de la tuyère est utilisée pour la simulation de l'écoulement. Le rayon du col est 0.0026 m et la longueur totale est d'environ 4.0 m. Les conditions d'arrêt sont données par une enthalpie totale réduite de 200, une pression et une température résultantes dans le réservoir respectivement de 1000 bars et 8315 K. La température de paroi est de 300 K, et la paroi est supposée catalytique. On utilise la même stratégie de division du domaine de calcul, décrite au paragraphe 4.1. L'ensemble des domaines est représenté sur la figure 9 et comprend 517x79 points.

4.2.3 Résultats

Sur la figure 10, qui représente le champ de nombre de Mach, on constate que la géométrie entraîne une légère recompression de l'écoulement près de la sortie. La figure 11 montre la distribution du nombre de Mach sur l'axe de la tuyère. On note sur la figure 12 les valeurs gelées des fractions massiques dans le noyau de l'écoulement ainsi que la couche limite réactive. La figure 13 présente les températures de translation et de vibration de O_2 près de la sortie (à une distance $X = 3.78m$ du col). Les profils de sortie de la vitesse et du nombre de Mach pour la même section sont donnés par les figures 14 et 15. L'épaisseur de la couche limite est supérieure à 20% du rayon de cette section. En fait, la couche limite semble plus mince qu'escomptée, la turbulence n'ayant pas été prise en compte dans cette étude.

Sur la figure 11, on observe l'uniformité de la vitesse dans le noyau de l'écoulement, alors que le nombre de Mach présente des variations importantes dans la même section (Fig.12).

5 Conclusion

Nous avons présenté une méthode implicite de volumes finis développée pour le calcul d'écoulements visqueux laminaires en déséquilibre thermique et chimique. Cette méthode a été appliquée au calcul de l'écoulement dans deux tuyères. Elle s' est avérée bien adaptée au calcul de l'écoulement dans la région du col. Elle prend en compte une modélisation physique réaliste qui peut néanmoins être améliorée par la prise en compte de couplages V-D et V-V. D'autre part, le calcul du divergent pourrait être effectué à l'aide d'un code PNS afin de réduire le temps de calcul.

[1] **C. Flament, F. Coquel, C. Marmignon et H. Hollanders**: "Viscous nonequilibrium flow calculations by an implicit finite volume method", AIAA-91-0702, 1991.

[2] **R. C. Millikan et D. R. White**: "Systematics of vibrational relaxation", J.Chem.Phys., Vol.36, No.12, pp 3209-3213, 1963.

[3] **W. C. Gardiner Jr.**: "*Combustion chemistry*", Springer Verlag, 1984.

[4] **F. G. Blottner, M. Johnson et M. Ellis**: "Chemically reacting viscous flow program for multi component gas mixtures": Sandia Laboratories Report 87115, 1971.

[5] **B. F. Armaly et K. Sutton**: "Viscosity of multicomponent partially ionized gas mixtures", AIAA-80-1495, 1980.

[6] **B. F. Armaly et K. Sutton**: "Thermal conductivity of partially ionized gas", AIAA-81-1174, 1981.

[7] **L. Monchick, K. S. Yun et E. A. Mason**: "Formal kinetic theory of transport phenomena in polyatomic gas mixtures", J. Chem. Phys., Vol.39, No.3, pp 654-669, 1963.

[8] **G. Candler**: "The computation of weakly ionized hypersonic flows in thermo-chemical nonequilibrium", These, 1988.

[9] **H. C. Yee et A. Harten**: "Implicit TVD schemes for hyperbolic conservation laws in curvilinear coordinates", AIAA-85-1513, 1985.

[10] **R. Abgrall**: "Extension of Roe's approximate Riemann solver to equilibrium and non equilibrium flows", Rapport INRIA, 1989.

[11] **H. C. Yee**: "Upwind and symmetric shock-capturing schemes", NASA TM 89464, 1987.

[12] **H. A. Van Der Vorst**: "High performance preconditioning", SIAM J. Sci. Stat. Comput., Vol 10, No 6, pp 1174-1185, Nov. 1989.

[13] **F. Dubois**: "Boundary conditions and the Osher scheme for the Euler equations of gas dynamics", Rapport No. 170, Centre de Mathématiques Appliquées de l'Ecole Polytechnique, 1987.

[14] Proceedings of the Workshop on Hypersonic Flows for Reentry Problems, Antibes (France), Avril 1991.

[15] **C. Flament, G. Rollin**: "Conception d'une tuyère hypersonique", ONERA RT 24/1123 AN, Jan. 1991.

[16] **E. E. Edenfield**: "Contoured nozzle design and evaluation for hotshot windtunnels", AIAA-68-0369, 1968.

TUYERE DE MARSEILLE

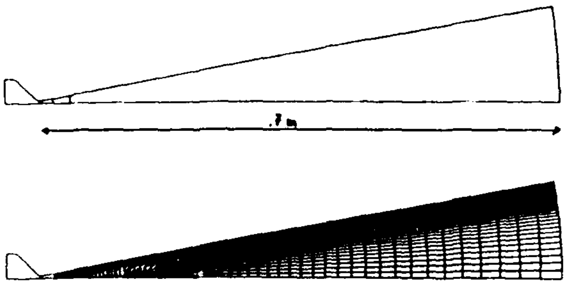

Fig. 1: Maillage 59x71

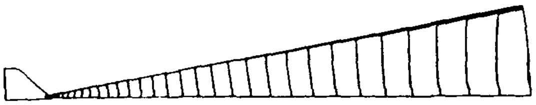

Fig. 2: Champ du nombre de Mach ($\Delta M = 0.25$)

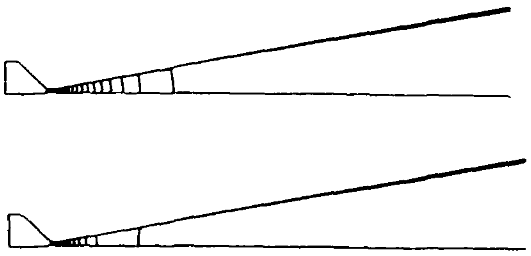

Fig. 3: Champs des températures de vibration de O2 puis N2

($\Delta Tv = 200\ K$)

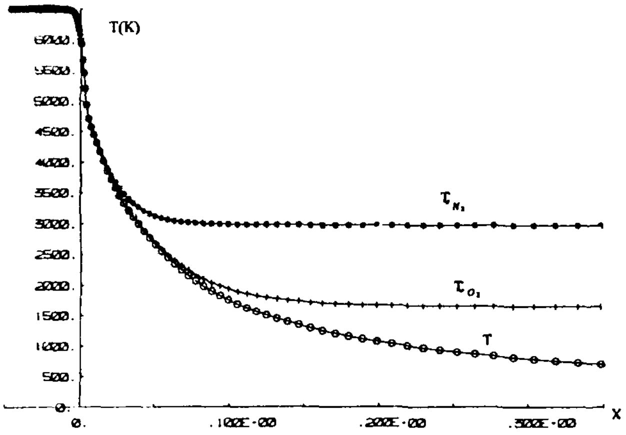

Fig. 4: Distributions des températures le long de l'axe de la tuyère

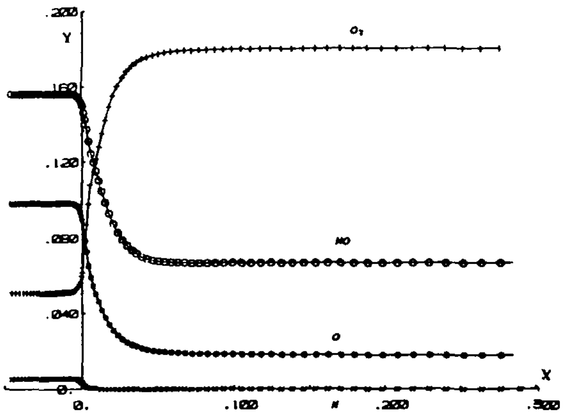

Fig. 6: Distributions des fractions massiques le long de l'axe

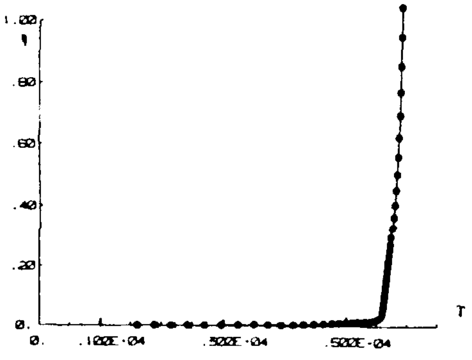

Fig. 5: Profils des températures à travers le col

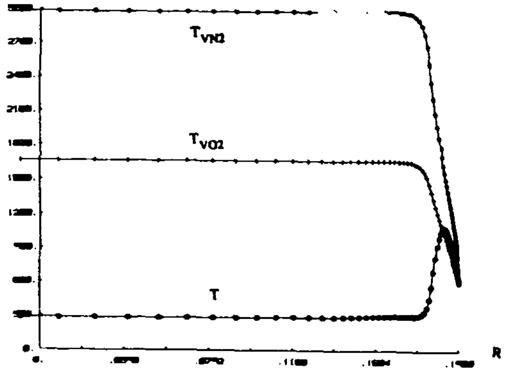

Fig. 7: Profils des températures en sortie de tuyère

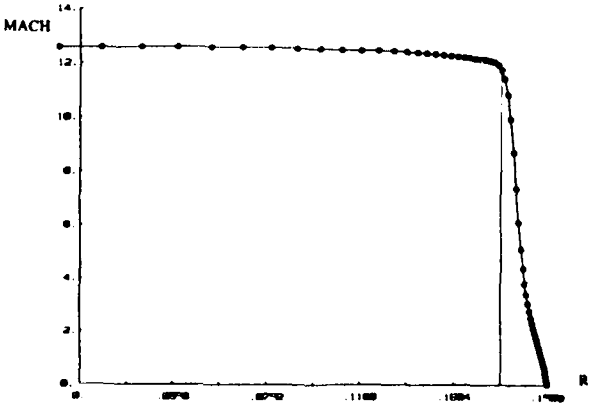

Fig. 8: Profil du nombre de Mach en sortie de tuyère

TUYERE ONERA F4

Fig. 9: Maillage 517x79

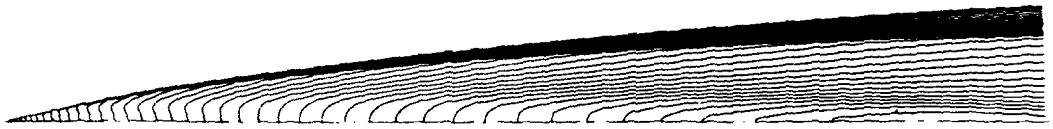

Fig. 10: Champ du nombre de Mach ($\Delta M = 0.25$)

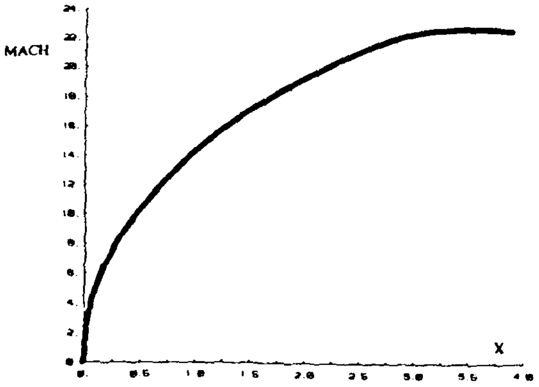

Fig. 11: Distribution du nombre de Mach le long de l'axe

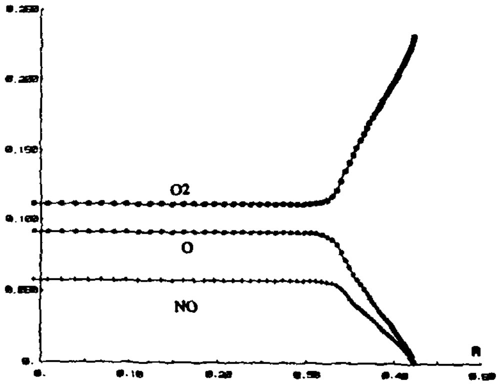

Fig. 12: Profils des fractions massiques à $x = 3.78m$

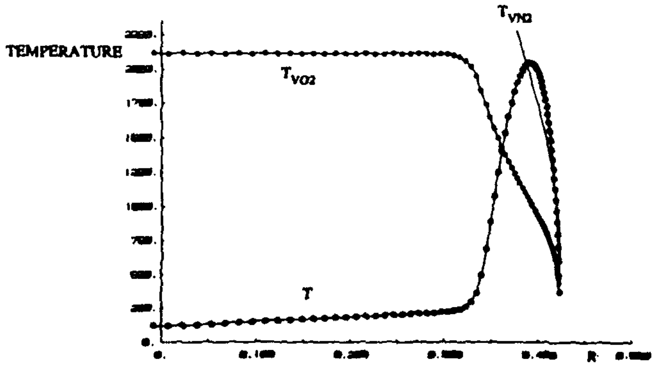

Fig. 13: Profils des températures à $x = 3.78m$

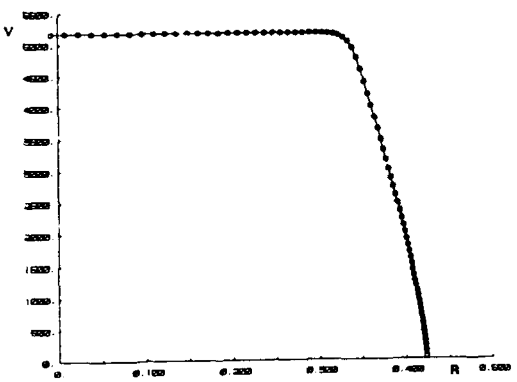

Fig. 14: Profil de vitesse axiale à $x = 3.78m$

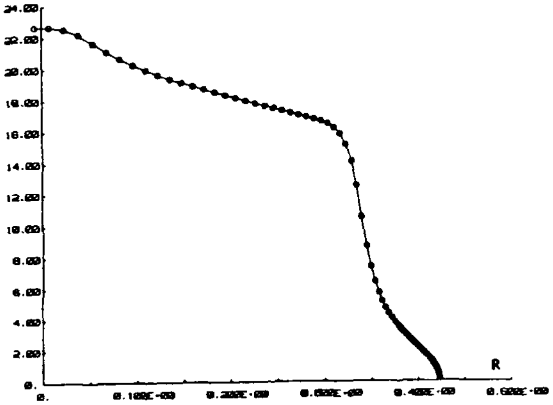

Fig. 15: Profil du nombre de Mach à $x = 3.78m$

NONEQUILIBRIUM HYPERSONIC FLOW IN A WIND-TUNNEL NOZZLE

D. Zeitoun
E. Boccaccio
M. C. Druguet
M. Imbert
R. Brun
Lab. I.U.S.T.I./S.E.T.T. (U.R.A CNRS 1168), Dept. M.H.E.Q
Université de Provence - St Jérôme13397 Marseille Cedex 13
France

ABSTRACT

The interest in hypersonic flow has been renewed through the Hermes European program. A better knowledge of chemical and thermodynamical nonequilibrium processes connected with aerodynamic aspects is needed to study the reentry phase of the shuttle Hermes. Around this research aera, many numerical approaches, taking into account more or less complicated nonequilibrium models, have been developped. In order to validate these computations, different hypersonic facilities have been built or are being designed. In these facilities, the hypersonic air flow is obtained at the exit of a convergent-divergent nozzle in which the reservoir enthalpy level is such that dissociation of diatomic molecules occurs. It is of upmost importance to be able to compute the flowfield in these nozzles, in order to ascertain the upstream conditions in front of the model being studied. The aim of this paper is a numerical study of hypersonic laminar inviscid/viscous flows, taking into account, on one hand, a complete description of chemical and thermodynamical nonequilibrium processes in an inviscid flow and on the other hand, the viscous effects through solving the Navier-Stokes equations for a real gas mixture with a simplified model for the vibrational nonequilibrium effects of diatomic species.

INTRODUCTION

Nowadays, allmost all experimental work in hypersonic flow is performed at the exit of convergent-divergent nozzles, at high enthalpy reservoir conditions, produced in a free piston shock tunnel. The development of the Hermes project has reactived old hypersonic facilities and has brought about new ones, such as the TCM2 at the University of Provence in Marseille (ref 1). The test section is located at the nozzle exit; in order to know the exit flow values it is necessary to compute the flowfield in the nozzle before the experiments, and this for two main reasons :

First, contrary to the real flight, the flow around the model can be found to be spatially non-uniform due to the shape of the divergent part of the nozzle and to the boundary-layer effects. Second, the thermodynamical and chemical states of the flow are typically in nonequilibrium due to the freezing resulting from the rapid expansion in the nozzle. Thus, the knowledge of this upstream flowfield of the simulation model is essential.

The flow regimes in a convergent-divergent nozzle go successively from subsonic, transonic and supersonic, to hypersonic. At the same time, energy exchanges take place, which give rise to physico-chemical processes, like the vibrational excitation of diatomic molecules, dissociation and ionization. Successively, equilibrium, nonequilibrium and frozen zones are present, depending on the local ratio between the characteristic relaxation time of each process and the flow time (ref 2). The flow parameters depend on the concentration of each gas mixture component and on the vibrational energy distribution of diatomic molecules. The continuous interaction between the chemical and thermodynamical processes and the flow is taken into account by the coupling between the equations which describe these processes.

The present work consists in a physical and chemical modelization and a numerical simulation of an inviscid/viscous hypersonic flow in an axisymmetric wind tunnel nozzle. In high enthalpy reservoir conditions, the air is dissociated and may be considered as a mixture of the five species N_2, O_2, NO, N and O, in an equilibrium state. In the axisymmetric nozzle, the hypersonic air flow is supposed to be in a chemical and thermal nonequilibrium state.The diatomic molecule NO is taken to be in a thermal equilibrium state. The chemical kinetics include 17 reactions and the corresponding rate constants are those given by the Park model (ref 3). As concerns the source terms in the vibrational energy equations, two approaches have been used : a Landau-Teller formulation for the dissipative flow (ref 4) and a complete one which includes the Coupled

Vibration Dissociation Vibration model (CVDV) for the inviscid flow (ref 5). This last formulation also modifies the forward rate constants of the chemical kinetics.

The system of equations, which describes the inviscid hypersonic flow, contains the four Euler equations completed by three chemical equations for N, O and NO and two vibrational ones for N_2 and O_2. The system is solved by a semi-implicit finite volume method, in which the convective flux terms are treated explicitly and the source terms implicitly. The solver is based on Van-Leer flux splitting technique using the notion of the "equivalent gamma" (ref 6).

As concerns the viscous case, the system of equations consists of the Navier-Stokes equations with, in addition, mass conservation equations for each chemical species and two vibrational energy conservation equations for N_2 and O_2. This system of ten equations is solved by a non-iterative implicit finite difference scheme with a flux splitting technique in the implicit operator (ref 7). This method is chosen in order to overcome two principal difficulties. The first one is the stiffness of the problem due to the chemical and vibrational processes, and the second one is the need for using fine meshes near the wall in order to capture correctly the boundary layer effects. After discretization, the linear system with a block-pentadiagonal matrix is solved by the Gauss-Seidel line relaxation method. This implicit approach also allows to use a larger intregration time step than that imposed by the CFL condition and so to reduce CPU time for reaching the steady state.

These two numerical methods will be used in order to describe the flow in a hypersonic (45°-10°) convergent-divergent nozzle, with an exit area ratio equal to 4444 over 1.12 m length. The pressure and temperature reservoir conditions are, respectively 1530 bars and 6500 K.The results show :

- the relatively weak influence of the coupling between the chemical and vibrational processes on the freezing level, in the divergent part of this nozzle ;
- the influence of the development of the boundary layer on the core flow, through a comparison between the inviscid and viscous calculations, particularly on the evolution of the vibrational temperatures of the diatomic species.

GOVERNING EQUATIONS

In a cylindrical coordinate system, the axisymmetric conservative equations for an air mixture in a thermal and chemical nonequilibrium state can be expressed in vector form as:

$$\partial_t U + \partial_x(F_e + F_v) + \partial_y(G_e + G_v) + H_a + H_s = 0 \qquad (1)$$

The vector of conservative quantities is given by

$$U = \left(\rho_s (s=1,..,5), \rho u, \rho v, \rho E, \rho_i e_{v_i} (i=1,2)\right)^t \qquad (2)$$

where ρ_s is the density of each species, the subcript s represents the five species N, O, NO, N_2, O_2 of the air mixture and i=1, 2 refers to the diatomic species N_2, O_2 (NO is supposed to be in a thermal equilibrium state), ρ is the density of the mixture, u and v the components of the velocity V and ρE is the total energy per unit volume which contains translational, rotational and vibrational energies, the latent chemical energy of the species and the kinetic energy of directed motion; ρE is given by :

$$\rho E = \sum_{s=1}^{5} \rho_s c_{v_s} T + \sum_{i=i}^{2} \rho_i e_{v_i} + \rho_{NO} e_{vNO} + \sum_{s=1}^{5} \rho_s h_s^{for} + \frac{1}{2}\rho V^2 \qquad (3)$$

In the equation (1) the vectors F_e and G_e represent the Eulerian convective fluxes, the viscous terms F_v and G_v contain the transport term expressions, such as diffusion velocity of each species, stress tensor and heat flux, while the vector H_a includes the axisymmetric terms of the equations. As concern the vector $Hs=(\omega_s, 0, 0, 0, \omega_i)^t$, it contains the chemical source terms ω_s due to the net rate production of each species and the vibrational source terms ω_i of the species N_2 and O_2. These source terms are the result of the chemical and vibrational nonequilibrium modelling and are described hereafter.

Chemical nonequilibrium modelling

In the air mixture, each species is considered as a perfect gas. The chemical source terms are derived from the reactions that occur between these species and are given by the following 17 reactions scheme :

$$\begin{aligned} N_2 + M &\rightleftharpoons 2N + M \\ O_2 + M &\rightleftharpoons 2O + M \\ NO + M &\rightleftharpoons N + O + M \\ N_2 + O &\rightleftharpoons NO + N \\ NO + O &\rightleftharpoons N + O_2 \end{aligned} \qquad (4)$$

with M= N, O, NO, N_2, O_2.

The magnitude of the mass production or removal is obtained from:

$$\omega_s = M_s \sum_r \left(\nu''_{sr} - \nu'_{sr}\right) \left\{ k_{f_r} \prod_s \left(\frac{\rho_s}{M_s}\right)^{\nu'_{sr}} - k_{b_r} \prod_s \left(\frac{\rho_s}{M_s}\right)^{\nu''_{sr}} \right\} \qquad (5)$$

ν'_{sr}, ν''_{sr} refer to the stœchiometric coefficients, k_f and k_b are the forward and backward reaction rates and are given by the Park model (ref 3). If one takes into account the coupling between chemical and vibrational processes, the forward reaction rate k_f of the dissociation equations is modified as following :

$$k_f^c = k_f \, V \tag{6}$$

where V represents the coupling factor which depends on the vibrational modelling through the ratio of partition functions Q (ref 8) :

$$V = \frac{Q(T)}{Q(T_{V_i})} \frac{Q(T_{F_i})}{Q(-U_i)} \tag{7}$$

T is the translational-rotational temperature, T_{V_i} is the vibrational temperature deduced from the vibrational energy of the diatomic species i ; T_{F_i} is an average temperature defined by the following expression :

$$\frac{1}{T_{F_i}} = \frac{1}{T_{V_i}} - \frac{1}{T} - \frac{1}{U_i} \tag{8}$$

where ($-U_i$) can be considered as a temperature corresponding to the probability of dissociation from a vibrational level ; its value depends on the model being considered. In the case of a non-preferential model, the probability of dissociation is the same whatever the vibrational level and $U_i = \infty$. But with the preferential model, the diatomic molecules dissociate preferentially from the upper levels, and the value of U_i is of the order of magnitude of the dissociation characteristic temperature θ_{D_i} (ref 8).

Vibrational non-equilibrium state

The coupling between chemical and vibrational processes also modifies the source terms ω_i of vibrational equations of the diatomic species, which can be written as the sum of different exchanges :

$$\omega_i = \omega_{i\,(T\text{-}V)} + \omega_{i\,(V\text{-}V)} + \omega_{i\,(C\text{-}V)} \tag{9}$$

In this expression $\omega_{i\,(T\text{-}V)}$ represents the internal energy exchanges between the translational and vibrational modes and is classically described by the Landau-Teller formulation :

$$\omega_{i\,(T\text{-}V)} = \frac{\rho_i e^0_{V_i} - \rho_i e_{V_i}}{\tau_i^{VT}} + e_{V_i} \omega_{s=i} \tag{10}$$

with $e^0_{V_i}$ the vibrational energy at equilibrium; since $\omega_{i\,(T\text{-}V)}$ takes into account all the vibrational-translational exchanges, the global relaxation time τ_i^{VT} is expressed as:

$$\frac{1}{\tau_i^{VT}} = \sum_{s=1}^{5} \frac{\xi_s}{\tau_{i\,s}^{VT}} \tag{11}$$

where ξ_s is the molecular fraction of each species s, and $\tau_{i\,s}^{VT}$ is the relaxation time for the exchanges between the diatomic molecules i and any species s ; $\tau_{i\,s}^{VT}$ has the following general form :

$$p\tau_{is}^{VT} = a_{is} \, T^{b_{is}} \exp\left(- \frac{c_{is}}{T^{\frac{1}{3}}} + d_{is} \right) \tag{12}$$

where a_{is}, b_{is}, c_{is} and d_{is} are constants depending on the colliding species and p is the pressure (ref 5).

$\omega_{i\,(V\text{-}V)}$ *refers to the vibrational-vibrational modes of diatomic species :*

$$\omega_{i\,(V\text{-}V)} = \frac{1}{\tau_{i\,j}^{VV}} \times \frac{1}{\rho R \theta_{V_j}} \times \left(\rho_j e_{V_j} \left(\rho_i e_{V_i} + \rho_i R_i \theta_{V_i} \right) \exp\left(\frac{\theta_{V_j} - \theta_{V_i}}{T} \right) - \rho_i e_{V_i} \left(\rho_j e_{V_j} + \rho_j R_j \theta_{V_j} \right) \right) \tag{13}$$

R_i is the molar gas constant, θ_{V_i} is the vibrational characteristic temperature and $\tau_{i\,j}^{VV}$ the relaxation time for V-V exchanges (ref 11).

The last term, $\omega_{i\,(C\text{-}V)}$, corresponds to the dissociation-vibration coupling and is due to the fact that the average vibrational energy of the molecule is partly determined by the chemical relaxation : a recombination or a dissociation of a molecule leads to a gain or a loss ot the average vibrational energy :

$$\begin{aligned} \omega_{i\,(C\text{-}V)} = & - \left(\overline{e_{V_i}} (T_{F_i}) - e_{V_i} (T_{V_i}) \right) \left(\frac{d[\rho_i]}{dt} \right)_f \\ & + \left(\overline{e_{V_i}} (-U_i) - e_{V_i} (T_{V_i}) \right) \left(\frac{d[\rho_i]}{dt} \right)_b \end{aligned} \tag{14}$$

where $\overline{e_{V_i}}(T_{F_i})$ is the average value of the vibrational energy lost in one dissociation and $\overline{e_{V_i}}(-U_i)$ is the one gained with each recombination. Because of the equilibrium conditions, $\overline{e_{V_i}}(-U_i)$ is the limit of $\overline{e_{V_i}}(T_{F_i})$ when T_{V_i} tends to T ; $\overline{e_{V_i}}(T_{F_i})$ can be written as :

$$\overline{e_{V_i}} (T_{F_i}) = \frac{R_i \theta_{V_i}}{\exp\left(\frac{\theta_{V_i}}{T_{F_i}} \right) - 1} - \frac{N_i R_i \theta_{V_i}}{\exp\left(\frac{N_i \theta_{V_i}}{T_{F_i}} \right) - 1} \tag{15}$$

where N_i *is the number of vibrational levels* corresponding to the dissociation energy of the molecule i.

COMPUTATION PROCEDURE

The unsteady governing equations (1) have to be integrated in the convergent divergent axisymmetric hypersonic nozzle, with given reservoir conditions, from an initial solution to yield a time-evolving solution. The complete physico-chemical model has been used with an inviscid flow assumption in order to evaluate the influence of the various processes on the flow parameters and to deduce some simplications. After that the viscous effects are taken into account so as to obtain more realistic values along the axis and at the exit section of the nozzle.

Inviscid flow

In the system of equations (1), the mass mixture conservation equation is introduced and only three species equations (N, O, NO) are written ; the other species N_2 and O_2 are deduced from the atom conservation law. This system is solved by a first order finite volume method (ref 5)

$$\frac{\partial}{\partial t}\int_{Vd} U^n \, dVol + \int_{\partial Vd} \left(F_e^n n_i + G_e^n n_j\right) dS + \int_{Vd} \left(H_a^{n+1} + H_s^{n+1}\right) dVol = 0 \tag{16}$$

In each control volume m of the grid system, the volume-average value of U is updated by the following numerical scheme :

$$\left(I + \frac{\partial H_s}{\partial U}\right)^n \delta U^n = - \frac{\Delta t}{Vol_m} \sum_{k=1}^{4} \left(F_k^n i + G_k^n j\right) \eta_k + \left(\frac{Aera(m)}{Vol(m)} H_a^n + H_s^n\right) \Delta t \tag{17}$$
$$U^{n+1} = U^n + \delta U^n$$

On each cell interface k, the convective flux vector F_k (respectively G_k) is written as the sum of positive F^+ (resp. G^+) and negative F^- (resp. G^-) fluxes. These fluxes are given by a Van-Leer decomposition where the notion of "equivalent gamma" is used (ref 9). The first order time and space integration is explicit for these convective fluxes and implicit for the chemical and vibrational source terms. At each time step, the numerical approach is split in three parts. The first one concerns the classical Euler variables (ρ, ρu, ρv, ρE), the second one the density of the species and, finally, the third takes into account the vibrational energies of the diatomic species. After that, the translational temperature is deduced by the non-linear equation giving the total energy (3) and then the pressure is deduced from the equation of state for the mixture. With this numerical procedure the steady state is obtained after about 5000 iterations with an integration time step equal to 0.1 Δt_{CFL} .

Dissipative flow

To correctly describe the dissipative effects in the wall boundary layer which develops along the nozzle, the mesh distribution must be quite stretched and consequently the explicite step time integration is very small. To overcome this difficulty and those due to the stiffness of the chemical and vibrational equations, the system of ten governing equations (1) is solved by a strongly implicit finite difference scheme (ref 7). For each node (i,j) of the transformed rectangular domain (ξ, η) and at the time step (n + 1)Δt the system is written as :

$$\frac{U^{n+1}-U^n}{\Delta t} + \frac{D}{D\xi}\left(F_e + F_v\right)^{n+1} + \frac{D}{D\eta}\left(G_e + G_v\right)^{n+1} + H_a^{n+1} + H_s^{n+1} = 0 \tag{18}$$

If Φ represents one of the vectors of this equation, it is linearized to yield the expression

$$\Phi^{n+1} = \Phi^n + \left(\frac{\partial \Phi}{\partial U}\right)^n \delta U^n \tag{19}$$

where $\left(\frac{\partial \Phi}{\partial U}\right)$ is the jacobian matrix and $\delta U^n = U^{n+1} - U^n$.

Under these conditions and after having splitted the vector F_e and G_e in a positive and a negative part, the system (18) is equivalent to :

$$\left\{I + \Delta t\left(\frac{D_+A_-}{\Delta\xi} + \frac{D_-A_+}{\Delta\xi} + \frac{D^2S_v}{\Delta\xi^2} + \frac{D_+B_-}{\Delta\eta} + \frac{D_-B_+}{\Delta\eta} + \frac{D^2R_v}{\Delta\eta^2} + C_a + C_s\right)\right\} \delta U^n = \Delta U^n \tag{20}$$

In this equation , D, D_+, D_- are respectively central, forward and backward difference operators, while A_-, A_+, S_v, B_-, B_+, R_v, C_a, C_s are the jacobian matrices of F_e^-, F_e^+ , F_v, G_e^-, G_e^+, G_v, H_a, H_s.

After discretization,the system (20) may be written as a pentadiagonal matrix linear system :

$$\widehat{B}_{i,j}\delta U^n_{i,j+1} + \widehat{A}_{i,j}\delta U^n_{i,j} + \widehat{C}_{i,j}\delta U^n_{i,j-1} + \widehat{D}_{i,j}\delta U^n_{i+1,j} + \widehat{E}_{i,j}\delta U^n_{i-1,j} = \Delta U^n_{i,j} \tag{21}$$

At each time step, a predictor-corrector scheme is used and the system (21) is solved by a Gauss-Seidel line relaxation method with alterning sweeps in backward and forward ξ direction. The conservated vector U is updated by

$$U^{n+1}_{i,j} = U^n_{i,j} + \delta U^n_{i,j} \tag{22}$$

Knowledge of the vector U allows us to obtain the following variables : ρ_s (s=1,...,5), ρ, u, v, e_{v_i} (i=1,2). After that the temperature and pressure are deduced in the same maner as the case of inviscid flow.

Associated to this algorithm, the boundary conditions of the computational domain are the following :

- at the wall nozzle : the translational and vibrational temperatures are given, u=v=0, $\partial P/\partial n=0$ and the concentrations of monatomic species are equal to zero (fully catalytic wall);
- at the symmetry axis : the reflecting image principle is used ;

- at the exit boundary : all flow variables are extrapolated from the computed values ;
- at the inlet boundary : a detailed description is given in a previous paper (ref 10).

During the iterative procedure for obtaining the steady state, the integration step time Δt increases from 5 to 5.10^3 Δt_{CFL}.

RESULTS AND DISCUSSION

The first application of these numerical approaches has been made in order to obtain the flow description in the convergent-divergent conical hypersonic nozzle of the free piston shock tunnel facility of Marseille (TCM2). This nozzle has been chosen as test case at the Antibes I and II Workshops on "Hypersonic Flows for Reentry Problems". The caracteristic dimensions of this nozzle are respectively (45°,10°) for convergent and divergent angles, 0.3 cm - 20 cm for the throat and exit radii, 112 cm for the length of the divergent part. The reservoir conditions are Po = 1530 bars and To = 6500 K and correspond to a reduced total enthalpy H_0/RT_0 equal to 145. With these reservoir conditions and assuming equilibrium, the mass fractions of species in the reservoir are given in Table I.

Y_O	Y_N	Y_{NO}	Y_{O2}	Y_{N2}
$9.64\ 10^{-2}$	$5.46\ 10^{-3}$	0.156	$5.35\ 10^{-2}$	0.689

Table I : Mass fractions of the species in the reservoir

For a better understanding of the physico-chemical modelling on the flow parameters along the nozzle, and for an eventual simplification of these models, the inviscid flow is first numerically studied, with (171*16) mesh points in the nozzle. Fig. 1 shows the temperature evolution along the symmetry axis of the nozzle, and Fig. 2 its isovalues in the nozzle. It can be noted that the CVDV preferential model does not sensibly modify theses evolutions. The discrepancy between the vibrational temperatures of O_2 and N_2 with different models is about 5% and 1%.

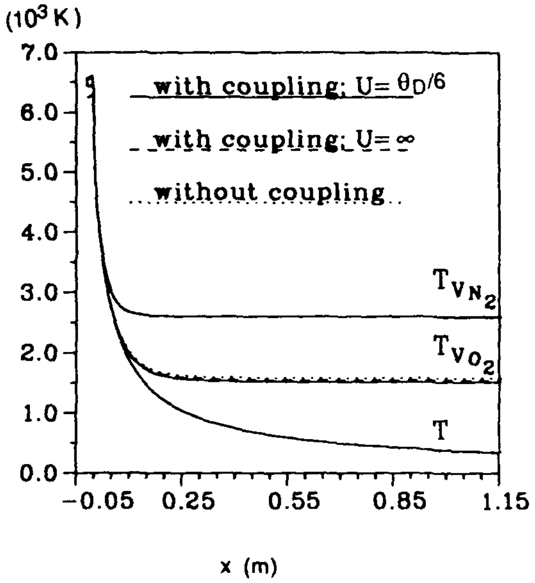

Fig. 1 : Evolution of temperatures along the nozzle axis.

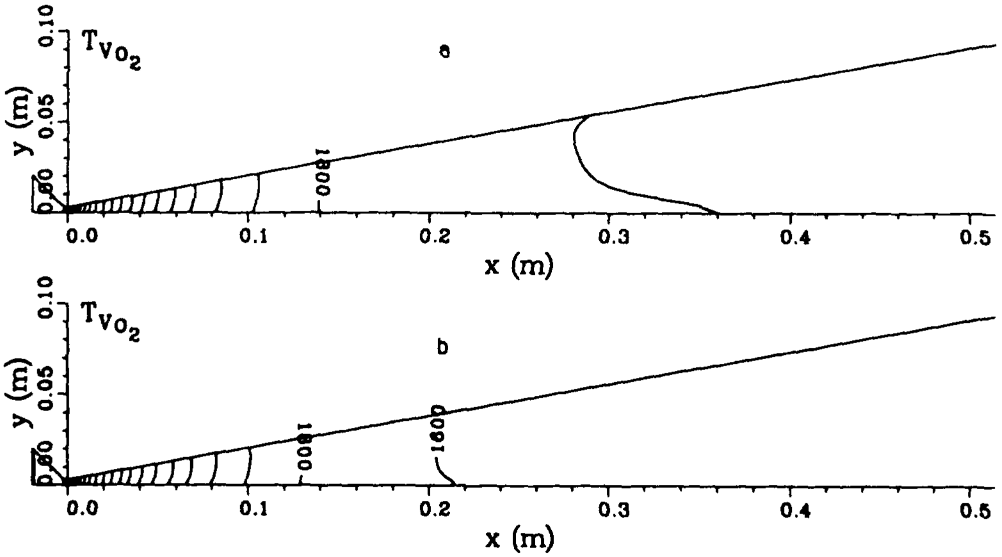

Fig. 2 : Distribution of the vibrational temperature of O_2 in the first part of the nozzle. (a : without coupling ; b : with coupling)

The same conclusion can be reached, regarding the evolutions of the species concentrations expected for the species N where the CVDV approach leads to a frozen value in the divergent part of the nozzle but this concentration (10^{-7}) is however very low as shown Fig. 3.

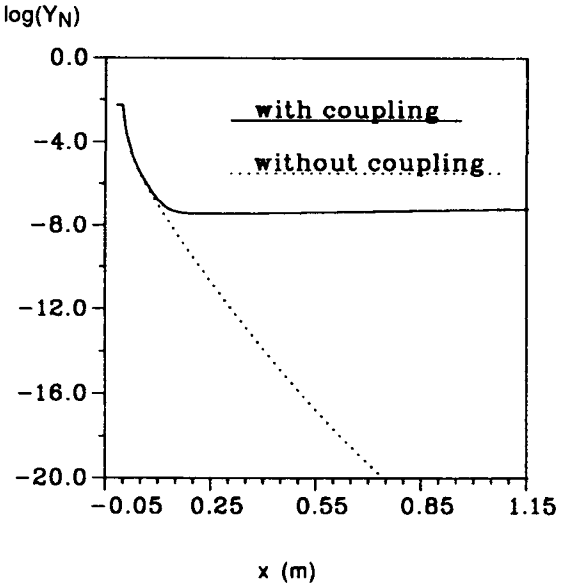

Fig. 3 : Evolution of the mass fraction of N along the nozzle axis.

From these results and due to the very fast freezing of the physico-chemical processes and the decrease of the translational temperature in the nozzle, the coupling between thermal and chemical nonequilibrium can be neglected and only the first term (translational-vibrational exchanges) has to be taken into account in the vibrational modelling. These conclusions, which are not certainly true for higher reservoir enthalpy conditions, have been used in order to simplify the system of equations (1) for the viscous flow.

In this case, the computational domain is meshed with (64x72) grid points in x and y directions with a stretching around the throat and the nozzle wall for capturing the flow gradients. A constant wall temperature is chosen equal to 600 K. The steady state is obtained after about 7000 time iterations in the whole nozzle. This number may seem to be important for an implicit method but one can notice that the steady state is reached after only 700 iterations in the throat region and the difference is due to the propagation of the steady state in the divergent part of the nozzle (ref 4).

Fig. 4 shows the development of the viscous and thermal boundary layers from the chart of Mach number and temperature isovalues. At the exit section of the nozzle their thickness is about equal to 10% of the radius.

The radial evolution of vibrational temperature, by comparison with the temperature T is drawn accross the boundary layer and for three different sections of the nozzle (Fig.5a and 5b). One may remark a nonequilibrium behavior in the boundary layer while the core flow is vibrationally frozen ; also, this behavior starts later for O_2 than for N_2. At the section x = 4 cm, O_2 is still in thermal equilibrium $T_{v_{O_2}} = T$.

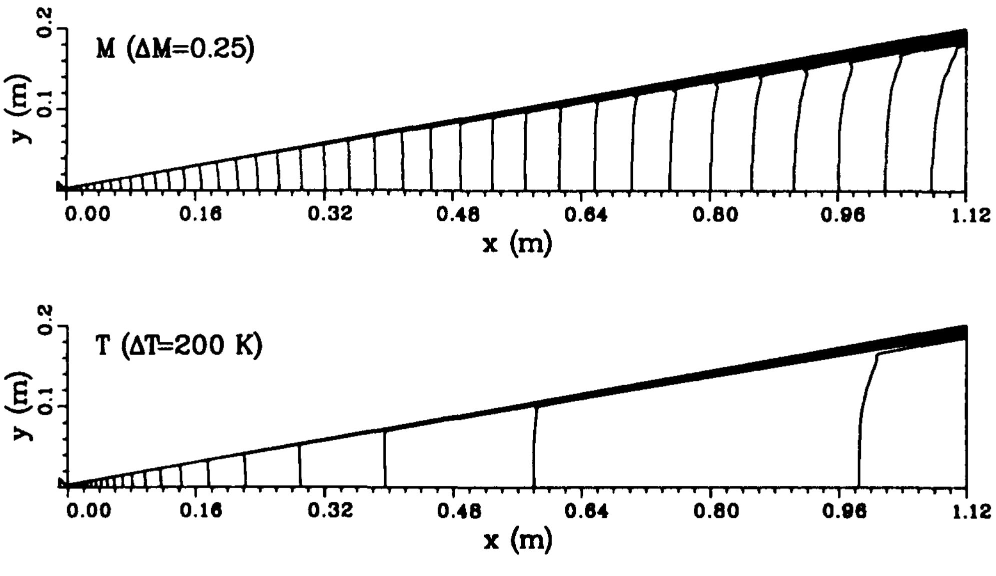

Fig. 4 : Isovalues in the whole nozzle.

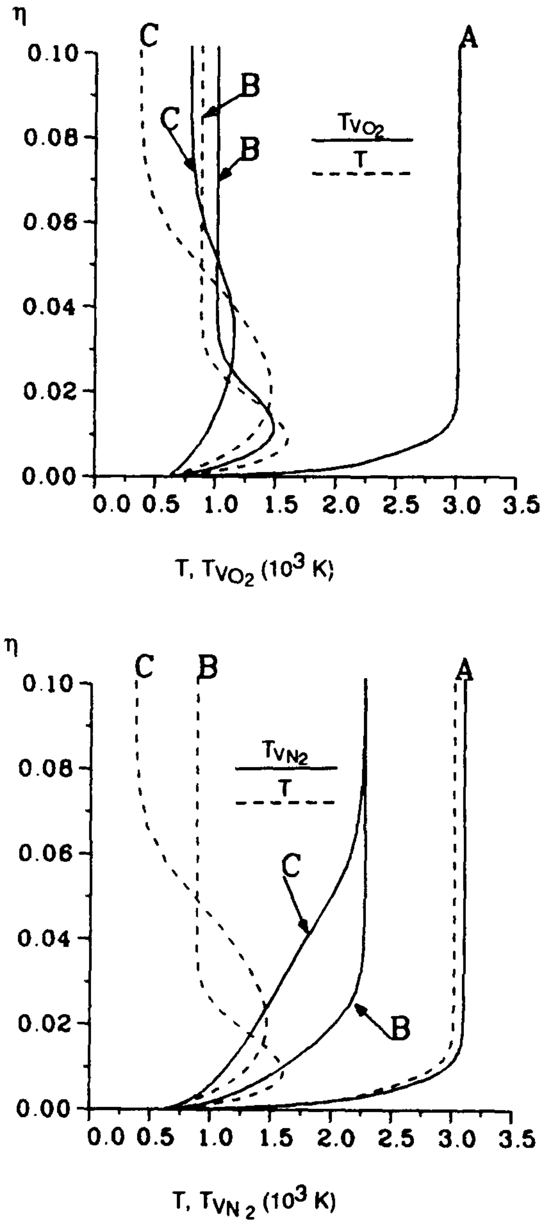

Fig. 5 : Temperature profiles across different sections.
(A : x=0.04m ; B : x=0.34m ; C : x=1.12m)

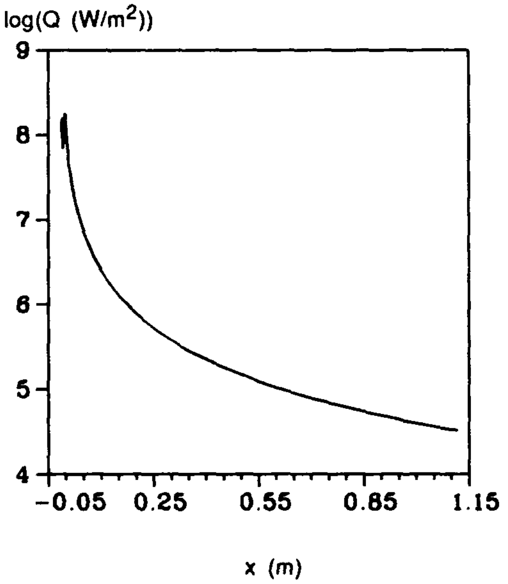

Fig. 6 : Evolution of the wall heat flux Q.

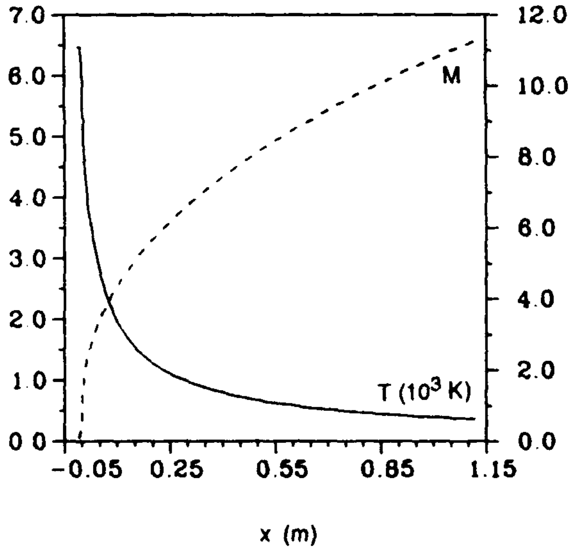

Fig. 7 : Evolution of the temperature and Mach number along the nozzle axis.

The evolution of the wall heat flux Q is represented on the Fig.6 and shows a maximum value equal to 2×10^8 W/m^2 at the throat section and a very fast decrease along the divergent part of the nozzle.

Comparisons with inviscid flow results are made through the evolution of the flow parameters along the symmetry axis. The Mach number and translational temperature evolutions are plotted on Fig.7 and only the viscous case is drawn. This is due to the fact that, curiously, the Euler and Navier-Stokes calculations give nearly the same axial distributions concerning these two parameters. The discrepancy is lower than 1% at the nozzle exit section ; the values are equal to M=11.2 and T=360 K.

On the other hand the effect of the growth of the wall boundary layer, which leads to a reduction of the expanding area ratio in the nozzle, modifies the level of vibrational freezing (Fig. 8). This last one is lower and is established farther in the divergent part of the nozzle for the viscous case ; the discrepancy is about 12% for $T_{V_{N_2}}$ and 48% for

$T_{V_{O2}}$, with exit values respectively equal to 2280 K and 800 K.

In the same way, the evolution of the species mass concentrations along the symmetry axis is plotted on Fig. 9. One can notice a weak increase in the level of chemical freezing and therefore a slightly more important recombination of diatomic species O_2 and N_2 in the viscous case. The exit values are respectively $Y_{N_2}=0.73$, $Y_{O_2}=0.18$, $Y_{NO}=0.07$, $Y_O=0.02$.

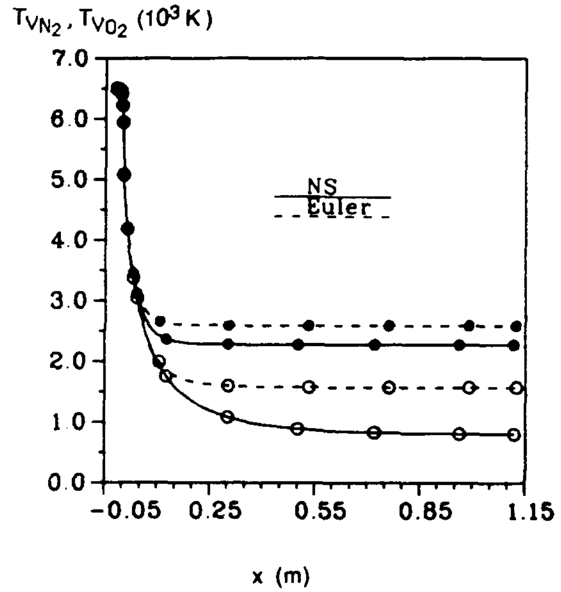

Fig. 8 : Evolution of vibrational Temperatures along the nozzle axis.
(● : T_{VN_2} ; o : T_{VO_2})

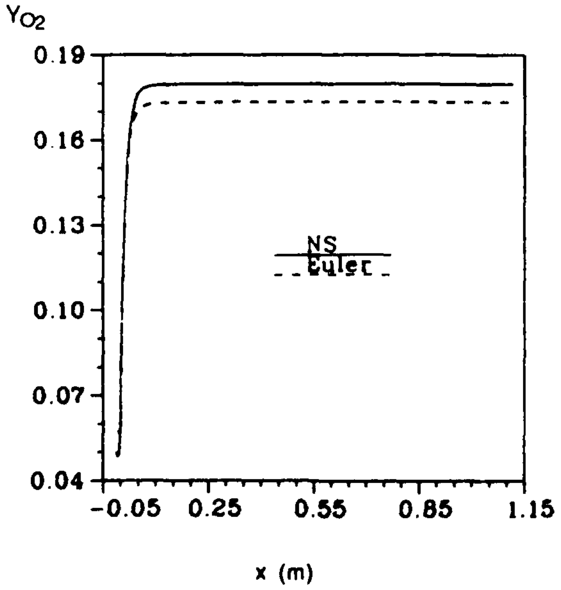

Fig. 9 : Evolution of mass fraction of O_2 along the nozzle axis.

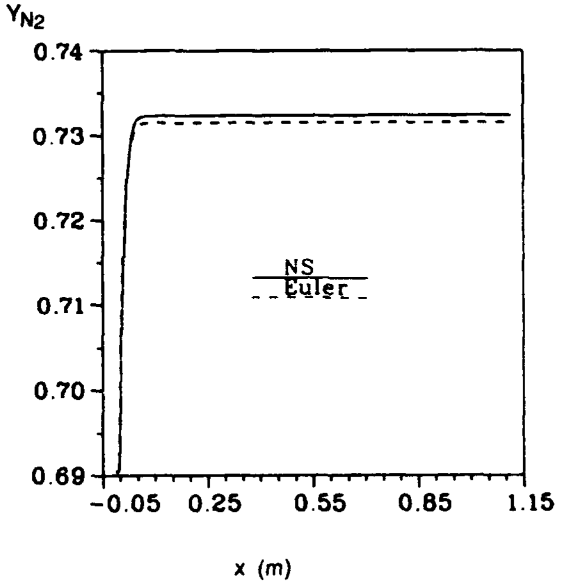

Fig. 10 : Evolution of mass fraction of N_2 along the nozzle axis.

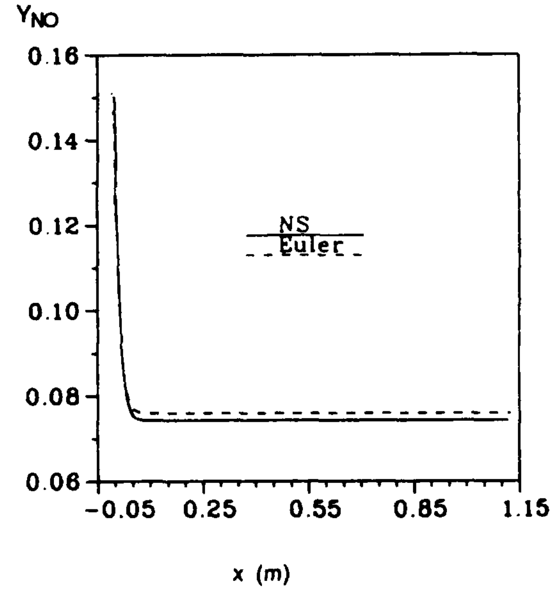

Fig. 11 : Evolution of mass fraction of NO along the nozzle axis.

CONCLUSION

A numerical simulation of a hypersonic flow in the conical nozzle of the TCM2 facility of the University of Provence has been carried out by the solving of Euler and Navier-Stokes equations, taking into account the thermal and chemical nonequilibrium processes which occur in the flowfield.

It has been shown that using a simplified modelling of the vibrational nonequilibrium is adequate in order to describe this hypersonic flow, at least for the reservoir conditions being considered.

It has been also shown that the Euler and Navier-Stokes calculations lead to a very slight discrepancy on the axial distributions of the translational temperature, Mach number and species mass concentrations on the nozzle length. However this discrepancy is more important for the evolution of vibrational temperatures and the levels of vibrational freezing are sensibly lower. Finally the Navier-Stokes calculations allows us to obtain the useful nozzle exit section and the tranverse profiles of the flow parameters in this section.

While this paper is being completed, these numerical codes are still running in order to describe the flow in the same conical nozzle with others reservoirs conditions and in a contoured nozzle with a higher reduced total enthalpy.

ACKNOWLEDGMENTS

The authors would like to thank the "Centre de Calcul Vectoriel de la Recherche" for allowing to access the Cray 2.

REFERENCES

1. Burstchell Y., Brun R. and Zeitoun D., "Two Dimensional Numerical Simulation of the Marseille University Free Piston Shock Tunnel-TCM2", in 18th "Shock Wave" May 1992, to be published.
2. Bray, B.N.C., "Atomic Recombinaison in a hypersonic Wind Tunnel Nozzle", J. Fluid Mech., 6, 1959, pp 1-32.
3. Park C., "On Convergence of Computation of Chemically Reacting Flows", AIAA paper 1985-0247.
4. Boccaccio E., Zeitoun D. and Imbert M., "Navier-Stokes Computation for Nonequilibrium Hypersonic Flows", in "Computing Methods in Applied Sciences and Eng." ed. by R. Glowinski, February 1992, pp 321-330.
5. Druguet M.C., Zeitoun D., and Brun R., "Inviscid Hypersonic Nozzle Flows in Chemical and Vibrational Nonequilibrium State", in "Computing Methods in Applied Sciences and Eng." ed. by R. Glowinski, February 1992, pp 729-738.
6. Zeitoun D., "Chemical and Vibrational Nonequilibrium Flowfields", J. Comp. Methods in Applied Mechanics and Eng., 90, 1991, pp 687-692.
7. Candler G. and MacCormack R. W., "The Computational of Hypersonic Ionized Flows in Thermal and Chemical Nonequilibrium", AIAA paper 88-0511.
8. Marrone P. V. and Treanor C. E., "Chemical Relaxation with Preferential Dissociation from Excited Vibrational Levels", J. Phys. of Fluids, 6, 9, September 1963, pp 1215-1221.
9. Anderson W. K., Thomas J. L. and Van-leer B., "Comparison of Finite Volume Flux Splitting for Euler Equations", AIAA journal 24, September 1986, pp 1453-1460.
10. Nebbache A. and Zeitoun D., "Application of an Implicit Numerical Method to the Computations of Laminar and Turbulent Flows", in "Numerical Method in Laminar and Turbulent Flow", Vol. 6, part 2, Pineridge Press, pp 1399-1409.
11. Colas. P," Ecoulements Hypersoniques Euleriens", Thèse de Doctorat, Université de Provence, juillet 1989.

SOME EXPERIMENTAL STUDY AND NUMERICAL SIMULATION IN WIND TUNNEL FLOW

S.Borrelli[1] and E.Hettena[2]
[1] Centro Italiano Ricerche Aerospaziali, Via Maiorise, I-81043 CAPUA (CE)
[2] Alenia Aeronautica, C.so Marche 41, I-10146 TORINO

ABSTRACT

This paper describes some studies made during a collaboration between the Italian Aerospace Research Center (CIRA) and Alenia D.V.D., whose aim is to provide proper validation of CFD codes in hypersonic flow regime.

In fact, in our opinion, the combination of numerical and experimental tools should give a better theoretical understanding of such type of flow.

Numerical methods able to give accurate prediction of hypersonic flows in Hypersonic Wind Tunnels have been developed and the results obtained by calculations are compared with experimental data gathered by CIRA. Alenia equilibrium three-dimensional Euler solver, originally developed to solve transonic flows and now extended to hypersonic ones, and a non-equilibrium two-dimensional Euler solver, developed by CIRA for the Hermes program, have been used to get test chamber predictions.

1. INTRODUCTION

Recently, much interest has been focused on hypersonic flows and interesting vehicle concepts have been developed which, if implemented, will further increase the interest in hypersonic aerodynamics.

The prediction of highly energized flow about a body moving at hypersonic speed, for either design or detection purposes, is a difficult task. Consideration must be given to solving not only the equations governing fluid flow, but also the ones describing the chemical reactions of high temperature gases.

When a gas composed of polyatomic molecules is heated to high temperatures, its composition changes as a result of chemical reactions. Such a situation typically arises behind the shock wave which envelops a vehicle entering the Earth atmosphere and can be simulated in a high enthalpy facility using energized flows.

As a result of the change in chemical composition, the thermodynamic properties of the gas also change. When the temperature of air is raised above room temperature, deviations from perfect-gas behavior occur: the vibrational mode of the molecules becomes excited, then oxygen and nitrogen dissociate (although at different temperatures), nitric oxide is formed, and so forth.

The chemical composition of air for densities lying between 10^{-2} and 10 times normal air density can be approximately subdivided into the following regimes:

1. $T < 2500\,K$. The chemical composition is substantially that at room temperature.
2. $2500 < T < 4000\,K$. This is the oxygen dissociation regime; no significant nitrogen dissociation occurs; some NO is formed.
3. $4000 < T < 8000\,K$. This is the nitrogen dissociation regime; oxygen fully dissociates.
4. $T > 8000\,K$. Ionization of the atomic constituents occurs.

Ground-based simulation facilities such as wind-tunnels, shock tubes, ballistic ranges, etc $\cdots$ provided in the past, despite several large disagreements with flight data valuable information for designing space vehicles. Main shortcomings of ground facilities are the limited size of the test section and the magnitude of total enthalpy that can be reached. Moreover, both facility and test preparation are very costly. In view of the experience in shuttle reentry aerodynamics, numerical simulations have the potential to provide design data that can complement those obtained in wind tunnels.

In Alenia Aeronautica and CIRA, models for 2-D chemically reacting flows has been previously developed [1,2,3,4]. A first approach of three dimensional hypersonic flows has been realized by Alenia [5] using a code based on equilibrium-air modelization. The present paper will show some developments based upon an extension of such code, comparing the results with the one obtained by CIRA using 2-D non-equilibrium chemistry.

2. TEST-CASES DESCRIPTION

CIRA has been identified as the appropriate organization to design a full scale test facility for the Thermal Protection System (T.P.S.) of the European space vehicle Hermes. E.S.A. has promoted and cofinanced with the Italian Research Ministry (MURST) its development and construction. The design of this facility, called "Scirocco", required deep studies and proper testing programs, some of which were performed at the French wind tunnel Simoun, that can be seen as a scaled down Scirocco. In particular, according to the type of flow around the Hermes vehicle, there are basically two types of simulation to be performed: stagnation flow and flow along the body. Two representative test-models were identified:

1. Semi sphere, in a free flow, to simulate the nose and the wing leading edge.
2. Flat plate in the nozzle boundary layer flow, to simulate flat or curved panels of space vehicles or control surfaces. For such a flow two different conditions have to be tested: turbulent induced flow or natural flow.

The tests at the Simoun facility had the following major objectives:

1. evaluation of the distribution of thermodynamic properties over flat plate as a function of pitching angle.
2. attempt to simulate the PWT conditions over sphere, cylinder and flat plate.

In this work, we have made the assumption of inviscid, adiabatic flow (Eulerian flow) as we wish to isolate the effects of chemical dissociation on pressure distribution. We have, therefore, considered only tests over the flat plate, which provide pressure measurements.

Of the planned series of tests [6], we report in table A those which we have selected for our validation activity. The test conditions there reported are those illustrated in Table D.

Test Conditions	Pitching angle	Objectives
A, B, C'	16°30'	Pressure Measurement
A, B	0°	"
C	0°	"
B	11°30'	"

Table A: test-cases comparison

A sketch of the test chamber with the model, and the used flat plate with the pressure probe distribution, is shown in Figs. 2 3.

3. THE SIMOUN WIND TUNNEL

In order to simulate the severe conditions encountered during Hermes reentry, Aerospatiale has designed and built the SIMOUN plasma-wind tunnel. The major objective of this tunnel is to test materials to be used for the T.P.S. of reentry vehicle at specified levels of pressure and heat fluxes.

In order to provide high temperature air, an high power arc heater plasma generator is used, placed just before the nozzle. The hot gas is generally modelled by two parameters that characterize the flow: the total pressure and the stagnation enthalpy.

Two type of nozzles are available for SIMOUN:

- a circular conical nozzle usually used for testing stagnation region models.
- an hyperelliptic conical nozzle for testing flat plate models.

The nozzle ends into a freejet test chamber where the model is mounted. The flow into this test chamber is tuned by a diffuser connected with a vacuum system. This vacuum system represents also a first level of a heat exchanging system, producing air at just $100°C$.

A schematic representation of this facility is shown in Fig. 4. The hyperelliptic nozzle, which was used for CIRA test campaign, is characterized by:

- $\frac{A}{A_*} = 44$
- $L = 1.051$ m

The throat area of this nozzle is of 7 cm^2. The design criteria on which SIMOUN is based are listed in table B.

Power Supply System	5 MW
Stagnation Pressure	1 to 14 bar
Stagnation Enthalpy	3 to 11 MJ/Kg
Mass Flow Rate	0.04 to 1 Kg/s
Run Duration	1500 s

Table B: SIMOUN design criteria

Operating envelop is shown in Fig.5.

4. FLOW EQUATIONS

Since we are interested in developing a procedure that allows a correct numerical capturing of discontinuities, we write the governing equations in conservation form.

We have,

$$\frac{\partial}{\partial t}\int_{Vol}\rho_i\, d\,Vol + \int_{\partial Vol}\rho_i\,\mathbf{V}\cdot d\mathbf{S} = \int_{Vol}\Omega_i\, d\,Vol \qquad i = 1, NS$$

$$\frac{\partial}{\partial t}\int_{Vol} \rho \, d\, Vol + \int_{\partial Vol} \rho \mathbf{V} \cdot d\mathbf{S} = 0$$

$$\frac{\partial}{\partial t}\int_{Vol} \rho \mathbf{V} \, d\, Vol + \int_{\partial Vol} \rho \mathbf{V} (\mathbf{V} \cdot d\mathbf{S}) + \int_{\partial Vol} p \, d\mathbf{S} = 0 \qquad (1)$$

$$\frac{\partial}{\partial t}\int_{Vol} e \, d\, Vol + \int_{\partial Vol} (p+e) \mathbf{V} \cdot d\mathbf{S} = 0$$

$$\frac{\partial}{\partial t}\int_{Vol} \rho E_{v_j} \, d\, Vol + \int_{\partial Vol} \rho E_{v_j} \mathbf{V} \cdot d\mathbf{S} = \int_{Vol} \rho \dot{E}_{v_j} \, d\, Vol \qquad j = NS, NV_S$$

The first equation of system (1) refer to the production of the species O, N, NO, $\cdots$ denoted in the following respectively by $i = 1, 2, \cdots, NS$. Species diffusion is neglected, only convection and production are considered. Quantity Ω_i/ρ represents the species production rate, and the partial density ρ_i can be computed from the mixture density ρ and the mass concentration Y_i:

$$\rho_i = \rho Y_i$$

Concentrations Y_{O_2} *and* Y_{N_2} *of molecular oxygen* O_2 and molecular nitrogen N_2 respectively, are deduced using the conservation law for atomic species.

The second group of equations of system (1) represents the conservation of mass, impulse and energy.

Last equation of system (1) evaluates the conservation of vibrational energy of the various species (NO, O_2 and N_2, $\cdots$) denoted in the following by the suffix $j = 3, 4, NV_S$. The quantities $\dot{E}_{v_j}$ represents the rate of *production of the vibrational energy* with obviously $NE = NS + 4 + NV_S$ number of equations, where NS is the number of created species, and NV_S the number of vibrating species.

4.1 Equation of State

In order to close system (1), it is necessary to model the air which is considered as a mixture of perfect gases [7]. The equation of state is then

$$p = \sum_{i=1}^{NS} \rho_i R_i T = \rho R T \sum_{i=1}^{NS} \frac{Y_i}{\mu_i}$$

and the enthalpy of such a mixture is defined as:

$$h = \sum_{s=1}^{NE} Y_i C_{p_i} T + \sum_{i=1}^{NS} Y_i h_i^{for} + \sum_{j=NS}^{NS+NV_S} Y_i E_{v_j}$$

In the case of an ideal gas NS=1 and C_p and C_v are constants, and these equations can be rewritten as:

$$p = \rho(\gamma - 1)\left[e - \frac{1}{2}V^2\right] \qquad (2)$$

$$h = C_p T$$

For a real gas in equilibrium conditions C_p and C_v become functions of temperature and pressure. Equation (2) is no more convenient, consequently, a real gas analogy has been introduced:

$$p = \rho(\tilde{\gamma} - 1)\left[e - \frac{1}{2}V^2\right] \qquad (3)$$

and the equilibrium model will provide $\tilde{\gamma}$ which is defined as the ratio of static enthalpy to internal energy.

System (1) can now be reduced to a simpler set by eliminating the first NS and the last NV_S equations. In the more complex case of non-equilibrium, the whole system has to be solved and a thermokinetic model is required.

Chemistry and gasdynamics can be considered as separate systems continuously exchanging information between them. The equilibrium state of the gas at each node point is determined by solving the equilibrium system described on the previous section.

Pressure and static enthalpy, held constant through the chemical process, are obtained from gasdynamics and supplied to the chemistry model which returns equilibrium values of temperature, molar mass, density and $\tilde{\gamma}$.

The value of $\tilde{\gamma}$ can either be directly looked-up from a table as in [8], or analytically computed as follows.

The equation

$$\tilde{\gamma} = \frac{h_{st}}{e_{int}} = \frac{h_{st}}{h_{st} - \frac{p}{\rho}} \qquad (4)$$

can be rewritten as

$$h_{st} = \frac{\tilde{\gamma}}{\tilde{\gamma} - 1}\frac{p}{\rho} \qquad (5)$$

Combining Eq. (5) with the expression for internal energy per unit volume.

$$e_{int} = h_{st} - \frac{p}{\rho} = \frac{e}{\rho} - \frac{1}{2}(V^2) \qquad (6)$$

yields the equation of state, Eq. (3). All that is needed to evaluate $\tilde{\gamma}$ from Eq. (4) is the updated density, which is obtained from Eq. (2) using the equilibrium temperature and molar mass. This approach relies on the relation

$$e_{int} = \int c_v \, dT = \int c_p \, dT - \int \frac{R}{M} \, dT = h_{st} - \frac{p}{\rho} \qquad (7)$$

The final step assumes that the molar mass is not a function of temperature, which is the ideal gas assumption. Alternatively, $\tilde{\gamma}$ could be evaluated from

$$\tilde{\gamma} = 1 + \frac{p}{\rho e_{int}} \qquad (8)$$

where the internal energy is computed in the chemistry model directly. Equation (8) would then be the logical way to evaluate $\tilde{\gamma}$ using the updated pressure.

The values of $\tilde{\gamma}$ and molar mass are held constant between chemistry updates. This imply that $\tilde{\gamma}$ does not vary with the conservation variables. It has been shown that $\tilde{\gamma}$ is only a slow function of internal energy, and for steady state calculations the constant $\tilde{\gamma}$ assumption is acceptable [9].

4.2 Thermokinetic Models

We have used two different chemical models: Park '85 [10] and Evans-Huber-Schexnayder [11].

4.2.1 *Park model*

This model is characterized by 17 reactions involving 5 species (O_2, N_2, O, N, NO). The reaction constants are

$$K_{fr} = c_r T^{n_f} \exp\left(-\frac{D_r}{kT}\right)$$

$$K_{er} = \exp\left(A_1 + A_2 Z + A_3 Z^2 + A_4 Z^3 + A_5 Z^4\right)$$

$$K_{br} = \frac{K_{fr}}{K_{er}} \qquad r = 1, \ldots, 17$$

in which $Z = 10000/T$, and the constants A_1, A_2, A_3, A_4, A_5, c_r and n_f are given in ref. [10].

4.2.2 *Evans-Huber-Schexnayder model*

18 reactions that involve 6 species (O_2, N_2, O, N, NO, NO^+) characterize this model. Forward, backward and equilibrium constants are given by the relations

$$\begin{aligned} K_{fr} &= c_{fr} T^{n_f} \exp\left(-\frac{D_{fr}}{kT}\right) \\ K_{br} &= c_{br} T^{n_b} \exp\left(-\frac{D_{br}}{kT}\right) \qquad r = 1, \ldots, 18 \\ K_{er} &= \frac{K_{fr}}{K_{br}} \end{aligned}$$

in which c_{fr}, c_{br}, D_{fr}/K, D_{br}/K, n_f, n_b are constants given in ref. [11].

In both cases the expressions used for c_{pi} are

$$\begin{aligned} c_{pi} &= \left(\frac{5}{2} + vibr\right) R_i \quad i = 1, 2 \\ c_{pi} &= \left(\frac{7}{2} + vibr\right) R_i \quad i = 3, \cdots, NS \end{aligned}$$

where $vibr$ depends on the vibrational model.

4.2.3 *Non equilibrium vibrational model*

As a vibrational non equilibrium model we have used the one of Landau-Teller [12-13]. In this model, equilibrium vibrational energy is written as

$$E^*_{vj} = \frac{q_j R \theta^v_j}{\exp\left(\frac{\theta_j}{T}\right) - 1} \qquad j = NS, \cdots, NS + NV_S$$

where θ^v_j are the characteristic temperatures of vibration

$$\begin{aligned} \theta^v_{NO} &= 2740 \quad K \\ \theta^v_{O_2} &= 2270 \quad K \\ \theta^v_{N_2} &= 3390 \quad K \end{aligned}$$

We model for both case (Park '85 and EHS) only the vibration of O_2, N_2 and NO. The vibration of NO^+ is neglected because of its little amount.

The production of E_{vj} is given by the relation

$$\frac{dE_{vj}}{dt} = \frac{E^*_{vj} - E_{vj}}{\tau_j} \qquad j = NS, \cdots, NS + NV_S$$

where

$$\tau_j = c_j \frac{\exp\left(\frac{D_j}{T}\right)}{\gamma} \qquad j = NS, \cdots, NS + NS + NV_S$$

The values of the constants c_j and τ_j can be found in ref. [13]. In this case obviously:

$$vibr = 0.$$

4.2.4 *Equilibrium vibrational model*

As a simplification, we can model vibrational level of energy assuming equilibrium conditions (as suggested in basic Park '85 model) i.e.:

$$E_{v_j} = \left(\frac{\theta^v_j}{T}\right)^2 \frac{\exp\left(\frac{\theta^v_j}{T}\right)}{\left(\exp\frac{\theta^v_j}{T} - 1\right)^2} \quad j = NS, \cdots, NS + NV_S$$

In this case,

$$vibr = E_{v_j}$$

and E_{v_j} is computed without solving a differential equation.

5. NUMERICAL APPROXIMATIONS

In order to discretize the continuous problem, the disturbed flow region is embedded into a bounded polygonal domain $\Omega \subset \mathbb{R}^3$. The domain boundary will be denoted by Γ.

Let us write the integral form of the equations over the computational domain Ω.

$$\int_\Omega (W_t + F_x(W) + G_y(W) + H_z(W))\,\phi\, dx\, dy\, dz = 0 \tag{9}$$

where ϕ is a *test-function*.

Let us consider a partition of Ω into a given number N_{cell} of finite volume cells C_i

$$\Omega = \bigcup_{i=1}^{N_{cell}} C_i\,, \tag{10}$$

and let take the following values for the *test-functions*

$$\varphi_i(x,y,z) = \begin{cases} 1, & \text{if}(x,y,z) \in C_i\ , \\ 0, & \text{elsewhere}\ . \end{cases} \qquad (11)$$

After integration per part, equation (9) can be rewritten, for each finite volume cell C_i, as

$$\frac{d}{dt}\int_{C_i} W\,dx\,dy\,dz + \int_{\partial C_i} [F(W)\nu_i^x + G(W)\nu_i^y + H(W)\nu_i^z]\,d\sigma = 0 \qquad (12)$$

where,

$$\vec{\nu_i} = \begin{pmatrix} \nu_i^x \\ \nu_i^y \\ \nu_i^z \end{pmatrix},$$

is the unit outward normal to the cell.

At this point, we have a set of equations for each finite volume cell of the domain. We have then to choose a way to discretize our domain and the time integration scheme.

5.1 Unstructured mesh

In order to use a flexible spatial discretization, we have decided to use unstructured tetrahedrical meshes for Ω. Then, we have to partition this mesh into finite volumes cells. This is accomplish by building a dual mesh as follows. Every element having node i as a vertex is subdivided into 24 subelements delimited by the medians planes. The control volume C_i is made up of the union of all the subelements which have i as a vertex. Fig. 1 shows the way used to build the finite volume mesh.

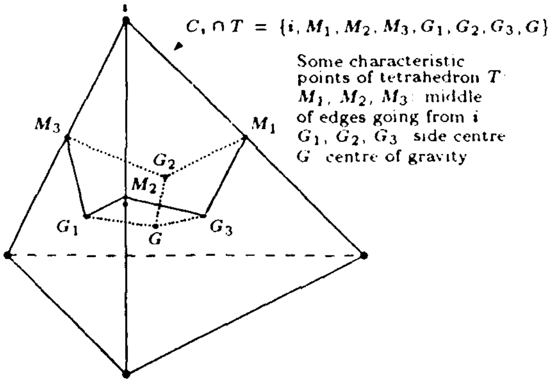
i
$C_i \cap T = \{i, M_1, M_2, M_3, G_1, G_2, G_3, G\}$
Some characteristic points of tetrahedron T
M_1, M_2, M_3: middle of edges going from i
G_1, G_2, G_3 side centre
G centre of gravity
M_3
M_1
G_2
M_2
G_1
G
G_3

Figure 1: Control volume: construction of $\partial C_i \cap T$

5.2 Finite Volume approximation

Refering to equation (12), we have to compute the fluxes over the boundary of each finite volume cell C_i. Our finite volume volume mesh is made of cells with polyedric boundaries. We will note the integrated normal over the interface between two adjacent cells as

$$\vec{\eta_{ij}} = \int_{\partial C_i \cap \partial C_j} \vec{\nu_i}\,d\sigma = \begin{pmatrix} \eta_{ij}^x \\ \eta_{ij}^y \\ \eta_{ij}^z \end{pmatrix} \qquad (13)$$

Thus, the total flux passing through the cell interface ∂C_i can be decomposed in a sum over the contribution coming from the set $K(i)$ of adjacent volumes as follows

$$\begin{aligned} \int_{\partial C_i} [F(W)\nu_i^x + G(W)\nu_i^y + H(W)\nu_i^z]\,d\sigma = \\ \sum_{j\in K(i)} \Bigg[\int_{\partial C_i \cap \partial C_j} F(W)\,\nu_{ij}^x\,d\sigma \\ + \int_{\partial C_i \cap \partial C_j} G(W)\,\nu_{ij}^y\,d\sigma \\ + \int_{\partial C_i \cap \partial C_j} H(W)\,\nu_{ij}^z\,d\sigma\Bigg] \end{aligned} \qquad (14)$$

Denoting the numerical flux function by Φ, the flux passing through the cell interface is approximate by

$$\int_{\partial C_i} [F(W)\nu_i^x + G(W)\nu_i^y + H(W)\nu_i^z]\,d\sigma \approx \sum_{j\in K(i)} \Phi\left(W_i, W_j; \vec{\eta_{ij}}\right) \qquad (15)$$

5.2 Spatial differencing

For the computation of the numerical fluxes, we will use the flux vector splitting technique of B. van Leer [14]. This technique splits the inviscid fluxes according to the direction of signal propagation. It is a first-order accurate scheme which is good for stability, but it is highly dissipative.

5.3 Integration to steady-state

The spatial discretization described previously leads to a semi-discrete set of ordinary differential equations which can be written as

$$Vol(C_i)\,\frac{dW_i}{dt} + R_i(W_i) = 0 \qquad (16)$$

where $R_i(W_i)$ represent the total flux amount applied to cell C_i.

In order to advance in time we have used a four step, linearized Runge-Kutta type alogithm, which can be expressed in the following manner

$$\begin{cases} W_i^{(0)} = W_i^n \\ W_i^{(k)} = W_i^{(0)} - \alpha_k \dfrac{\Delta t}{Vol(C_i)} R(W^{(k-1)}) \quad k = 1,\cdots,4 \\ W_i^{n+1} = W_i^{(4)} \end{cases}$$

where $W_i^{(k-1)}$ is the total fluxes at step $k-1$.

5.3 Computation of the time-step

We use a local time stepping in order to increase the iterative convergence of our numerical scheme. We have to define a C.F.L. like formula [15] to compute local time step

$$\Delta t(i) = \frac{2\,Vol(C_i)}{\sum\limits_{j\in K(i)} \left(\mathbf{V}_{ij}\cdot\vec{\eta_{ij}} + a_{ij}\left\|\vec{\eta_{ij}}\right\|\right)}$$

where a_{ij} is the average of the frozen speed of sound between cells i and j.

6. NUMERICAL EXPERIMENTS

6.1 Nozzle

Simoun nozzle has been computed using quasi 1-D non equilibrium flow with three chemical and two vibrational models and with a full 3-D equilibrium code. The thermokinetic models that has been used are listed on table C.

Model	Dissociation	Vibration
1	E.H.S.	non equil.
2	Park '85	non equil.
3	Park '85	equil.
4	Rakich '83[16]	equil. 1/2

Table C: Thermokinetic models

For 3-D calculations only point A of the operating envelop is available, however in this case the convergent part of the nozzle has been modelled as shown in Fig. 12.

Model	p_{th} (bar)	$Y_{O_{th}}$	$Y_{N_{th}}$	$Y_{NO_{th}}$	T_{th} (K)
CASE A					
1	1.69	0.137	0.45E-3	0.64E-1	3918
2	1.69	0.143	0.47E-3	0.58E-1	3866
3	1.69	0.143	0.47E-3	0.58E-1	3871
4	1.72	0.145	0.55E-3	0.57E-1	3964
CASE B					
1	2.4	0.211	0.11E-1	0.31E-1	4946
2	2.4	0.214	0.11E-1	0.27E-1	4904
3	2.9	0.214	0.11E-1	0.27E-1	4911
4	3.2	0.214	0.13E-1	0.27E-1	5039
CASE C					
1	3.77	0.129	0.55E-3	0.72E-1	4086
2	3.76	0.135	0.57E-3	0.66E-1	4031
3	3.78	0.135	0.57E-3	0.66E-1	4031
4	3.84	0.137	0.68E-3	0.66E-1	4139

Table D: throat conditions

In all quasi 1-D cases, throat inflow conditions are assumed to be in uniform thermokinetic equilibrium. Reservoir condition corresponding to points A, B, and C of Simoun operating envelop (see Fig.5) has been used as described in Table D.

The small differences in throat conditions are mainly due to different vibrational model, and in a small part to differences in the curve fit model adopted to compute the equilibrium constants. All results are listed in Table E.

Model	p (mb)	Mach
CASE A		
Experimental	5.7	
Equilibrium	5.5	5.34
1	2.6	5.76
2	2.6	5.75
3	3.4	5.14
4	3.2	5.39
CASE B		
Experimental	5.5	
1	2.4	5.89
2	2.4	5.59
3	2.9	5.22
4	3.2	5.52
CASE C		
Experimental	12.6	
1	6.6	5.49
2	6.8	5.45
3	8.4	4.93
4	7.8	5.19

Table E: test case comparison

The use of the different non equilibrium chemical modelization has shown to have a small influence in the solution. This is confirmed in the results shown in Table E and Figs. 6 to 11, and has been illustrated in a previous work [17]. On the contrary, larger differences, has been found by the adoption of different vibrational model. While the change in the chemical model causes a variation in the solution, which is confirmed to a small fraction (approximately 0.1 % in Mach number), changing the vibrational model generates variations up to 30 %. Even more sensible variations in the results are present between the non equilibrium and equilibrium solutions, which confirms that a good modelization is suited for this class of flow condition.

We always use as reference value the one obtained with model 1.i. Only results regarding point A are taken into account. All other results are reported on Table E.

Comparing these results with experimental data, a big difference between non equilibrium level of approximation and pressure recorded in the test chamber can be seen. Moreover, the pressure computed with the simpler equilibrium model seems to be in good accordance with experimental data. This effect, that, in a first analysis can be debit to a bad evaluation of non equilibrium, can be explains as follows.

When non equilibrium effect are not taken into account, exchanges between internal and kinetic level are poorly described. These are, because of energy absorbed in chemical reactions, a lower exit Mach number and an higher pressure. In fact, due to the high expansion through the nozzle a large part of energy is serving to accelerate the flow and consequently chemistry cannot develop as fast as the fluidynamics. The final effect is, therefore, an higher exit velocity and a lower pressure.

One must still have in mind that this was only the eulerian part of the phenomena. Let us now take into account some viscous effects. One of the major effect of viscosity in a nozzle expansion flow is to reduce the effective area ratio of the nozzle. Taking into account the displacement thickness, computed with a very simple model, due to Edenfield [18], the reduction of area ratio is of a certain small percentual. This reduction causes a Mach number increment. In such a way we can get an exit pressure level very similar to experimental data. The good accordance between equilibrium model and experimental data is due to those two counterbalanced errors. Exit values obtained with Edenfield model are given in Table F.

Model	p (mb)	Mach
CASE A		
Experimental	5.7	
1 + B.L.	4.9	5.14
3 + B.L.	5.9	4.67
CASE B		
Experimental	5.5	
1 + B.L.	4.9	5.16
3 + B.L.	5.8	4.68
CASE C		
Experimental	12.6	
1 + B.L.	10.6	5.04
3 + B.L.	12.7	4.59

Table F: Boundary layer corrections

6.2 Test Chamber + Model

Two different meshes has been used to compute test condition A with two different flat plate position as indicated in Table G.

Mesh	Flat Plate Pitch. angle	Elements number	Nodes number	Boundary Sides
1	0 deg	577761	104136	23465
2	16 deg. 30	571523	103003	23533

Table G: 3-D mesh characteristic

Those meshes model the entire nozzle (Fig. 12) and the test chamber as shown on Figs. 13,14,15,16. The Flat plate region has been refined in order to ensure a good capture of physical phenomena.

Reservoir conditions has been applied to the nozzle inlet as given in Table D. Figure 17 shows Iso-Mach number lines on the nozzle, the sonic line has been found near the nozzle throat as theoretically expected. Iso lines are perpendicular to the flow propagation which guarantee a constant value of the flow at any point of the nozzle exit.

Comparison with flat plate experimental data are shown on Figs. 18,19 and 20,21 fo. both cases. In the first case (0 deg.) a good agreement with experimental data is found up to three quarter of the plate. On the edge opposite to the nozzle, as well as along the lateral ones, the numerical results are affected by a strong expansion generated by the way the plate was connected to the testing chamber walls. In the 16 deg. 30 case we note that the shock is attached to the inge line in the numerical case while a gradient, indicating a separation bubble, is detectable on the experimental iso lines. Around 50 % of the plate the pressure rises, but this phenomenon is not found by the numerical simulation. A closest look at the pressure values (see Fig. 22 below) shows both the phenomena: in the first 50 % of the plate, out of the separation bubble, the theoretical values well agree with experiments, then a weak shock is visible while the numerical accuracy of the scheme probably smeared out the numerical one. The expansion following the shock is driven differently in experiments and calculations, due to various exit flow conditions from the testing chamber.

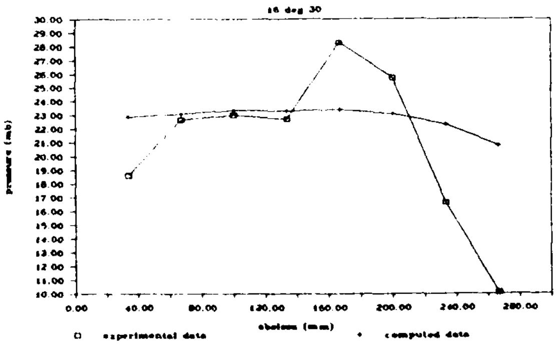

Figure 22: Pressure along the 16 deg. 30 flat plate symmetry axis for both experimental data and numerical experiment.

7. CONCLUSION

Various chemical and vibrational models has been tested for the simulation of hypersonic nozzle flow. In order to have a good numerical accuracy in such kind of flow, not only dissociation but also vibration must be taken into account. Viscosity effects cannot be neglected.

ACKNOWLEDGMENTS

We would like to thank Luca Formaggia for having provided the 3-D unstructured meshes and Sebastiano Caristia for his help with experimental data.

REFERENCES

[1] FORMAGGIA L. and SELMIN V., "Numerical Simulation of High Speed Compressible Flows with Upwind Schemes on Adapted Unstructured Grids", *in* "ICAS Proceedings 1990, 17th Congress of the International Council of the Aeronautical Sciences", September 1990, PAPER ICAS-90-6.10.2.

[2] SELMIN V. and FORMAGGIA L., "Inviscid Calculations by an Upwind Finite Element Method of Hypersonic Flows over a Double (Simple) Ellipse", *in* "Workshop on Hypersonic Flows for Reentry Problems, Part I", January 1990.

[3] SELMIN V. and FORMAGGIA L., "Simulation of Hypersonic Flows on Unstructured Grids", Int. J. Num. Meth. Eng., *34*, 1992, pp 569—606.

[4] BORRELLI S. and SCHETTINO A., "Influence of Chemical Modelling on Hypersonic Flow", *in* "1st European Symposium on Aerothermodynamics for Space Vehicles", ESA/ESTEC May 1991.

[5] HETTENA E., FORMAGGIA L. and SELMIN V., "Inviscid Flow over an Hypersonic Delta Wing", *in* "Workshop on Hypersonic Flows for Reentry Problems, Part II", April 1991.

[6] LEROUX R., "Tuyères sur Moyens d'Essais à Génération Plasma", L'Aéronautique et L'Astronautique, *134*, 1989.

[7] DESIDERI J.-A., GLINSKY N. and HETTENA E., "Hypersonic reactive flow computations", Comput. Fluids, *18*, 1990, pp 151—182.

[8] SRINIVASAN S., TANNEHILL J.C., WEILMUENSTER K.J., "Simplified Curve Fits for the Thermodynamic Properties of Equilibrium Air", ISU-ERI-Ames-86401, ERI Project 1626, CFD 15, Iowa State University, 1986.

[9] GNOFFO P.A., "Hypersonic Flows Over Biconics Using a Variable-Effective-Gamma, Parabolized-Navier-Stokes Code", AIAA Paper 83-1666, July 1983.

[10] PARK C., "On Convergence of Computation of Chemically Reacting Flows", AIAA Paper 85-0247, January 1985.

[11] EVANS J.S., SCHEXNAYDER C.J. and HUBER P.W., "Boundary Layer Electron Profile for Entry of Blunt Slender Body at High Altitude", NASA TN D 7332, 1973.

[12] VINCENTI W.G. and KRUGER C.H., "Introduction to Physical Gas Dynamics", Robert E. Krieger Publishing Co., Inc., Malabar, Florida, reprint 1986.

[13] LANDAU L. and TELLER E., "Zur Theorie der Schalldispersion", Physic Z. Sowjetunion, 1936.

[14] van LEER B., "Flux-Vector Splitting for the Euler Equations", Lecture Notes in Physics, *170*, 1982, pp 507—512.

[15] GILES M., "Energy Stability Analysis of Multi-Step Methods on Unstructured and Structured Grids", CFDL-TR-87-1, Dept. of Aeronautics and Astronautics, M.I.T., 1987.

[16] RAKICH J.V., BAILEY H.E. and PARK C., "Computation of Nonequilibrium Supersonic 3-D Inviscid Flow over Blunt-Nosed Bodies", AIAA Journal, *21*, N. 6, 1983.

[17] "Scirocco Final detailled design report, Part II", Research and Technological Series, *1*, CIRA Int. Rep., 1991.

[18] EDENFIELD E., "Contoured nozzle Design and Evaluation for Hotshot Wind Tunnels", AIAA Paper 68-369, January 1968.

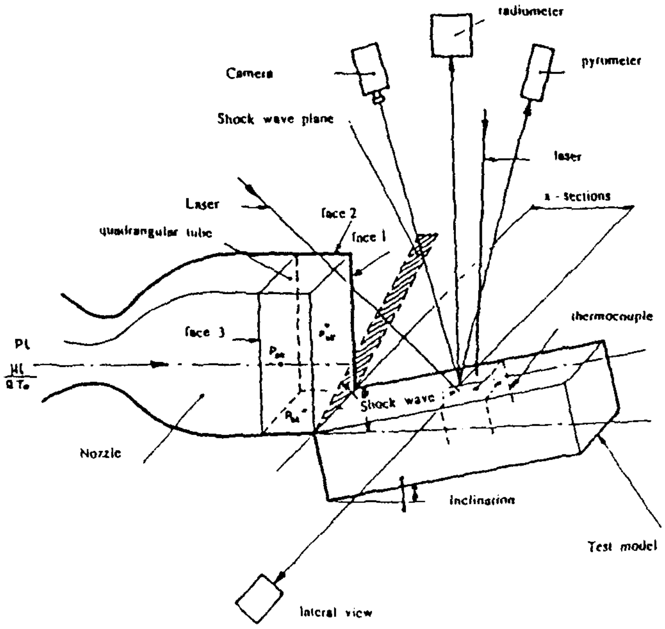
radiometer
Camera
pyrometer
Shock wave plane
laser
Laser
x - sections
face 2
quadrangular tube
face 1
thermocouple
face 3
Pi
P_{st}^{*}
P_{st}
Hi
R To
Shock wave
P_{st}
Nozzle
inclination
Test model
lateral view

Figure 2: Sketch model of Test chamber

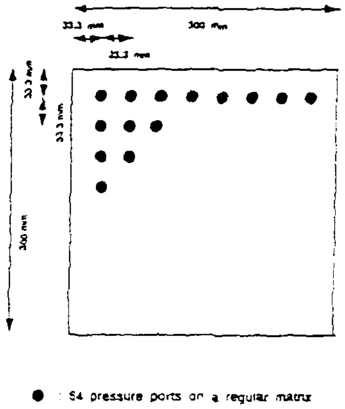
33.3 mm
300 mm
33.3 mm
33.3 mm
33.3 mm
300 mm
● : 54 pressure ports on a regular matrix

Figure 3: Flat plate model and probe distribution

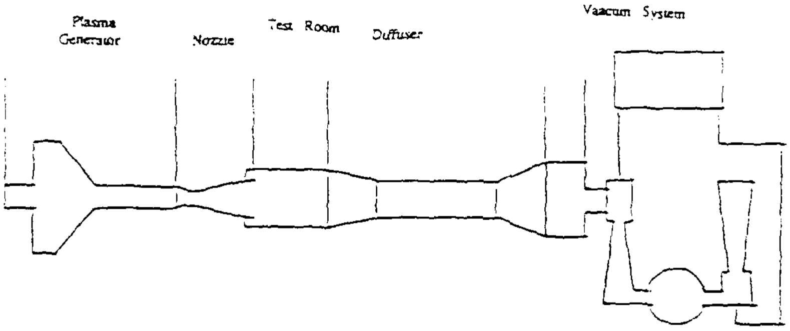
Plasma Generator
Nozzle
Test Room
Diffuser
Vaacum System

Figure 4: Schematic represtentation of Simoun

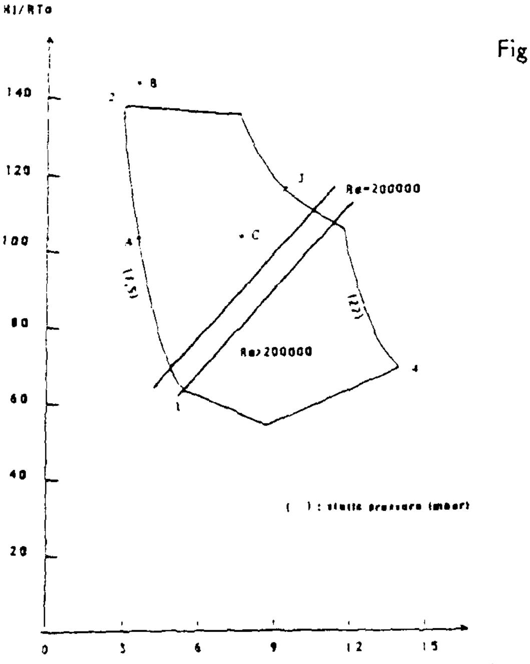

Figure 5: Simoun operating envelop

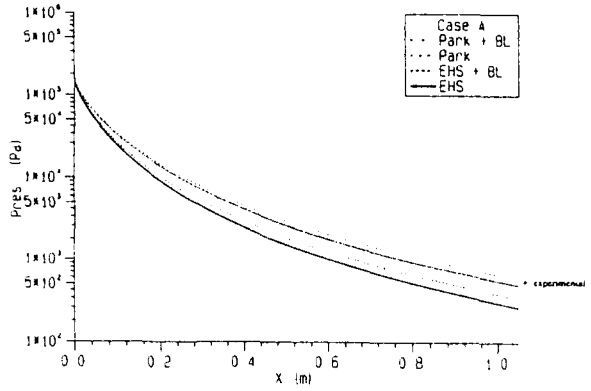

Figure 6: Pressure behaviour through Simoun nozzle. Point A

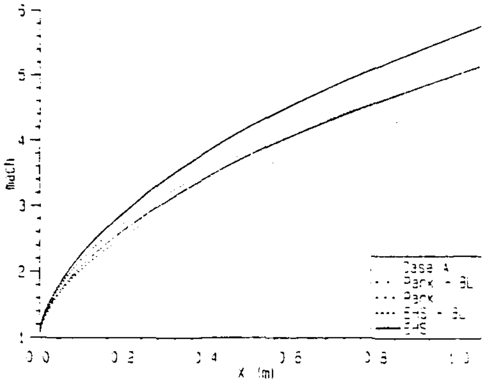

Figure 7: Mach number behaviour through Simoun nozzle. Point A

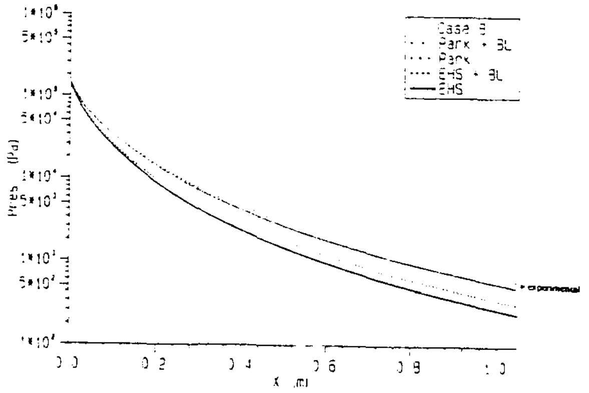

Figure 8: Pressure behaviour through Simoun nozzle. Point B

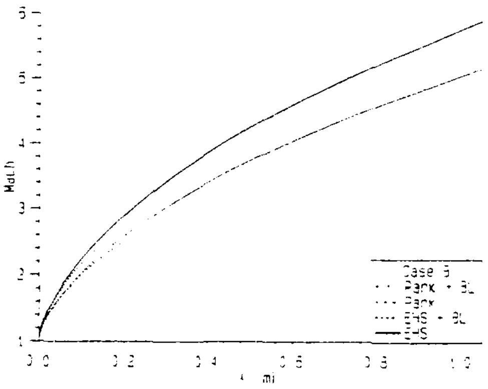

Figure 9: Mach number behaviour through Simoun nozzle. Point B

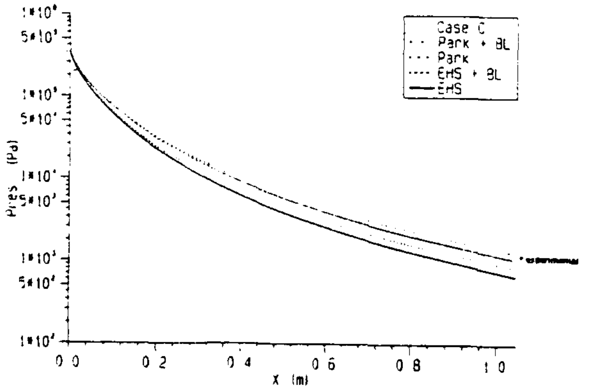

Figure 10: Pressure behaviour through Simoun nozzle. Point C

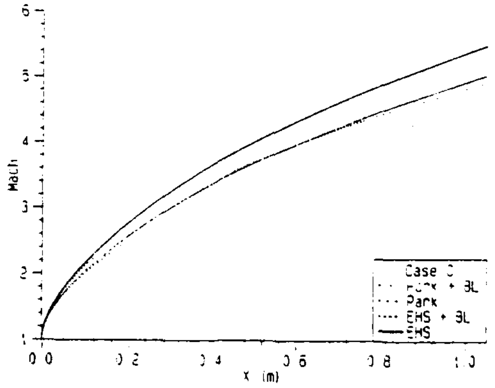

Figure 11: Mach number behaviour through Simoun nozzle. Point C

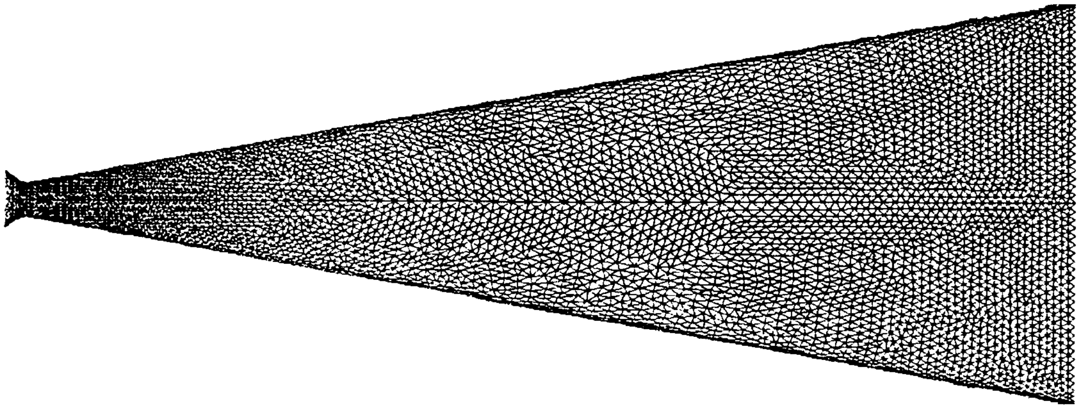

Figure 12: 3-D Mesh. Nozzle.

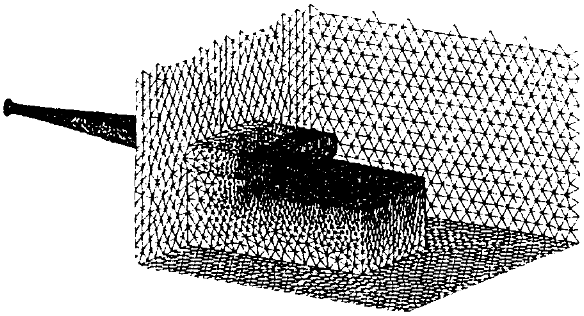

Figure 13: 3-D Mesh. Global view
(flat plate at 0 deg.)

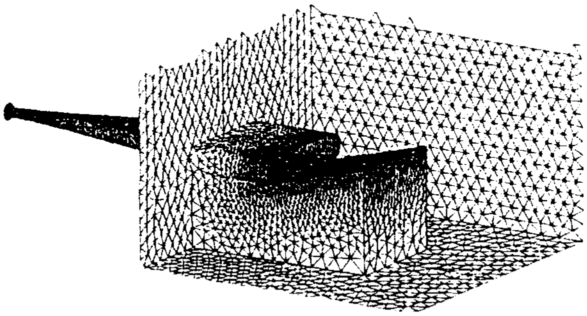

Figure 14: 3-D Mesh. Global view
(flat plate at 16 deg. 30)

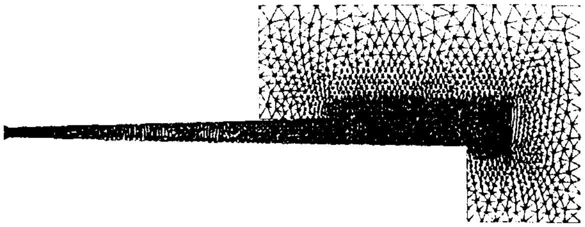

Figure 15: 3-D Mesh. Symmetry plane
(0 deg. flat plate)

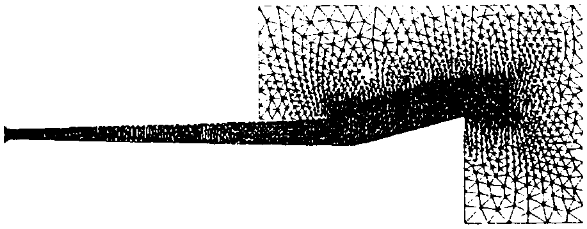

Figure 16: 3-D Mesh. Symmetry plane
(16 deg. 30 flat plate)

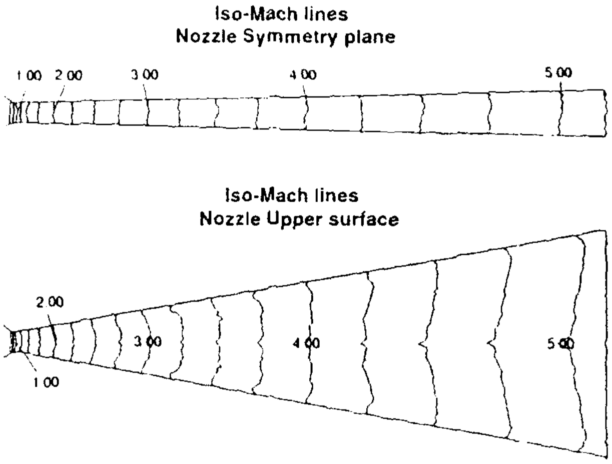

Figure 17: Nozzle Iso-Mach values

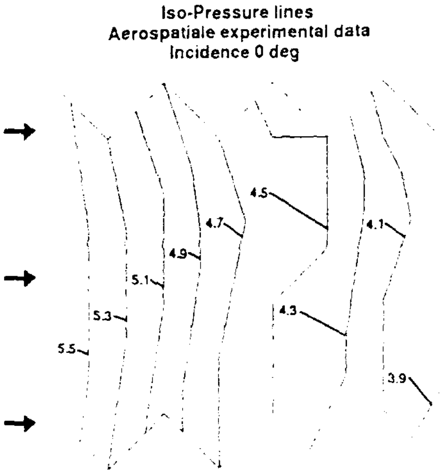

Pres. min = 3.7 mbar ; Pres. max = 5.7 mbar
Delta Pres. = 0.2 mbar

Figure 18

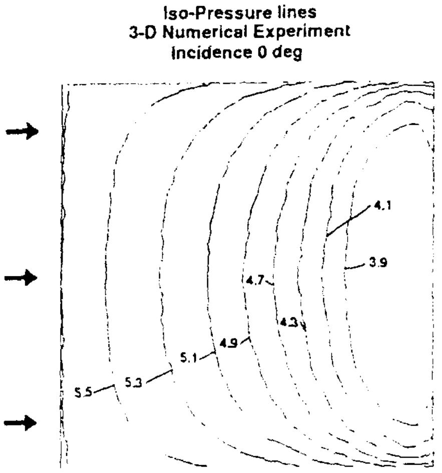

Pres. min = 3.7 mbar ; Pres. max = 5.7 mbar
Delta Pres. = 0.2 mbar

Figure 19

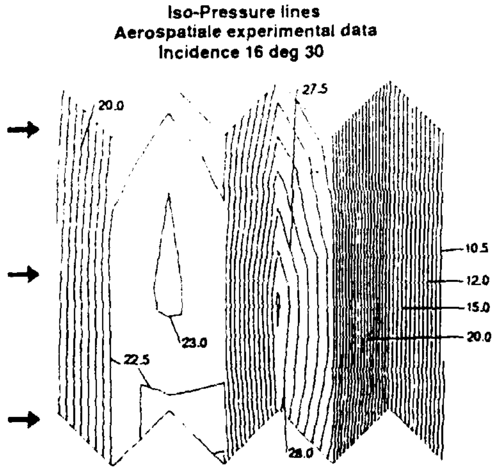

Pres. min = 9.7 mbar ; Pres. max = 28.6 mbar
Delta Pres. = 0.5 mbar

Figure 20

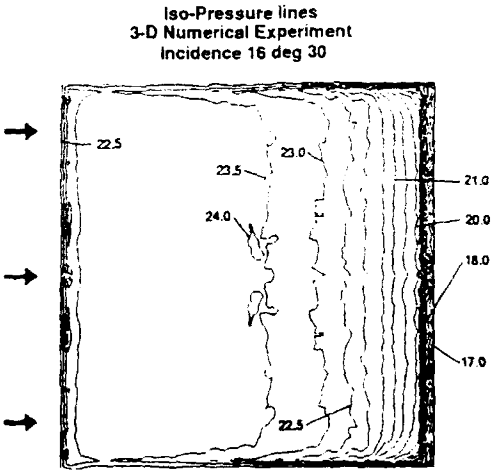

Pres. min = 16.3 mbar ; Pres. max = 24.4 mbar
Delta Pres. = 0.5 mbar

Figure 21

A CFD-BASED AERODYNAMIC DESIGN PROCEDURE FOR HYPERSONIC WIND-TUNNEL NOZZLES

JOHN J. KORTE
Fluid Mechanics Division, MS 156,
NASA Langley Research Center,
Hampton, Virginia 23665 USA

SUMMARY

A new procedure, which unifies the best of current classical design practices, computational fluid dynamics (CFD), and optimization procedures, is demonstrated for designing the aerodynamic lines of hypersonic wind-tunnel nozzles. The new procedure can be used to design hypersonic wind-tunnel nozzles with thick boundary layers where the classical design procedure has been shown to break down. An efficient CFD code, which solves the parabolized Navier-Stokes (PNS) equations using an explicit upwind algorithm, is coupled to a least-squares (LS) optimization procedure. A LS problem is formulated to minimize the difference between the computed flow field and the objective function, consisting of the centerline Mach number distribution and the exit Mach number and flow angle profiles. The aerodynamic lines of the nozzle are defined using a cubic spline, the slopes of which are optimized with the design procedure. The advantages of the new procedure are that it allows full use of powerful CFD codes in the design process, solves an optimization problem to determine the new contour, can be used to design new nozzles or improve sections of existing nozzles, and automatically compensates the nozzle contour for viscous effects as part of the unified design procedure. The new procedure is demonstrated by designing two Mach 15, a Mach 12 and a Mach 18 helium nozzles. The flexibility of the procedure is demonstrated by designing the two Mach 15 nozzles using different constraints, the first nozzle for a fixed length and exit diameter and the second nozzle for a fixed length and throat diameter. The computed flow field for the Mach 15 least squares-parabolized Navier-Stokes (LS/PNS) designed nozzle is compared with the classically designed nozzle and demonstrates a significant improvement in the flow expansion process and uniform core region.

LIST OF SYMBOLS

a_i = coefficients of cubic spline
f = least squares error vector
f_l = component of f
l = index of f
i = grid index, axial direction
$imax$ = total grid points, axial direction
J = Jacobian matrix
j = grid index, radial direction
k = least squares iteration index
M_{axis} = design axis Mach distribution
M_{design} = test section design Mach number
M_x = computed axial Mach number
m = total number of components in f
n = total number of components in X
N = total knots on the cubic spline
Obj = objective function
r_t = original throat radius
X = design parameter vector
X_i = component of X
x = axial coordinate
x_{1-N} = axial coordinate of spline knots
y = radial coordinate
y_w = nozzle wall radius
θ = flow angle, radians
$\omega_M, \omega_{MA}, \omega_\theta$ = weighing factors

INTRODUCTION

Axisymmetric wind tunnels have been used for the last 30 to 40 years for simulating the hypersonic flight enviroment. However, the flow quality of many of these nozzles is not adequate for current research requirements, which now include validating computational fluid dynamic (CFD) computer codes. Efforts have been made to build and update existing hypersonic facilities with new and improved nozzle aerodynamic lines[1,2]. The state of the art in the aerodynamic design of wind-tunnel nozzles is still based on the procedure proposed by Prandtl and Buseman[3] in 1929. This classical procedure requires that the inviscid contour be designed using the method of characteristics (MOC) and corrected with a displacement thickness obtained from a boundary-layer (BL) solution. Recent computational analysis[4] of hypersonic wind-tunnel nozzles designed with the method of characteristic/boundary-layer (MOC/BL) procedure, using solutions to the Navier-Stokes (NS) equations, have shown severe limitations in obtaining the desired flow quality and test conditions when the boundary layer becomes a large percentage of the nozzle's diameter. The MOC/BL design procedure assumes that the characteristics reflect at the location of the inviscid contour. For large boundary layers, typical of hypersonic wind-tunnel nozzles, Candler and Perkins[5] showed that the characteristics reflect between the wall and the location of the inviscid contour. Therefore, the actual characteristics of the nozzle *lag* the characteristics used in the design procedure. In thick boundary layers, the actual characteristics are no longer properly *cancelled*, and the flow quality of the nozzle deteriorates. In this paper, we will present a design procedure which automatically avoids this effect.

The classical theory used in the design procedure of supersonic wind tunnels can be found in a number of reports[6,7,8,9,10] and books[11,12,13]. The basic assumption made is that the boundary layer is small, compared to the characteristic length (nozzle radius), so that the nozzle flow field can be treated as inviscid for designing the aerodynamic lines. Once the aerodynamic lines are determined, a correction is made to account for the displacement thickness of the boundary layer. This basic procedure has been applied successfully to both supersonic and low Mach number hypersonic nozzles.

The inviscid design procedure requires the position of the sonic line at the throat, a prescribed centerline Mach number or pressure distribution, and the condition of uniform flow at the nozzle exit. Once a centerline Mach number distribution has been specified, the MOC can be used to determine an inviscid contour. This inviscid contour can be scaled to any particular size. The design contour for one operating condition is determined by computing the displacement thickness using a boundary-layer code and adding it to the inviscid contour. Modern implementations of the MOC/BL design procedure usually differ only on how the sonic line and centerline Mach number distribution are specified and which numerical technique is used to compute the inviscid flow field and the boundary-layer solution.

Recent designs of hypersonic wind-tunnel nozzles made with the MOC/BL procedure have been evaluated using CFD codes solving the NS equations[2,4,5,14]. Attempts to improve the resulting nozzle design using the CFD codes are difficult because of the computational time required to solve the NS equations and the trial and error process of changing the contour. A mathematical procedure for correcting an existing contour is given by Meyer and Holt[15], but we are not aware of any application of this procedure to a wind-tunnel nozzle design.

For modifying existing wind-tunnel complexes, special design procedures may also be necessary for the newly designed nozzle to mate with existing components. A special CFD procedure[1] was recently developed to design a Mach 4 and a Mach 5 nozzle for the NASA Langley 8-Foot High Temperature Tunnel. The new nozzles were designed in reverse, so that they would match with the exit portion of the existing Mach 7 nozzle.

From the discussion above, it is clear that a new procedure is needed for designing hypersonic nozzles which will produce high quality, uniform flow fields in the test section. To accurately design the hypersonic nozzles for a uniform flow field, the procedure must include the effects of the thick boundary layer on the inviscid flow field. In addition, it may be necessary to include the effects of intermolecular forces, vibrational, and chemical nonequilibruim on the test gas. These effects will be included if the design procedure is based on the solution of the parabolized Navier-Stokes (PNS) equations with the appropriate thermodynamic/chemical model for the gas.

The PNS equations are a subset of the NS equations, which can be integrated using efficient space marching procedures. These equations are obtained from the NS equations by neglecting streamwise diffusion effects and a portion of the subsonic streamwise pressure gradient. For many practical flow fields, such as hypersonic nozzles, these approximations are valid as long as streamwise separation does not occur. To accurately model the curvature of the nozzle contour, a large number of streamwise stations need to be computed, especially in the throat region. Previously, the cost associated with using even a PNS solver in a design procedure would have been prohibitive. With the increased use of supercomputers, efficient and fast CFD solvers have been developed for the PNS equations[16,17]. The explicit upwind noniterative algorithm for solving the PNS equations of Ref. 17 has been modified to solve internal axisymmetric flow fields. A typical Mach 15 nozzle of 130 inches in length can be simulated using over 90,000 streamwise stations in under 90 seconds of Cray 2 CPU time. A typical Mach 6 nozzle can be computed in 10 seconds of Cray 2 CPU time. Using this solver for the PNS equations, it has become practical to consider implementation of an iterative CFD-based design procedure.

The use of CFD codes in design has usually been to provide a direct analysis of the performance of existing or proposed designs. Coupling CFD codes with design procedures has been done for a number of limited applications. The majority of these applications have been to improve a surface pressure distribution over a wing or other simple surface. However, these procedures were not general enough to handle a design which would produce a desired flow field away from the surface. Recently, Huddleston[18] developed a CFD optimization method which is flexible enough to be used for designing nozzles and other flow components. Huddleston's optimization method is based on minimizing an objective function by solving a nonlinear least-squares (LS) problem which will result in an optimal solution for a parametric description of a flow surface. He has applied this method to both two- and three-dimensional nozzles and airfoils, coupled with both Euler and NS flow solvers. However, he did not apply the method to a flow field which included a thick boundary-layer region or a PNS flow solver. The disadvantage of this method is the expense associated with computing sensitivity derivatives necessary to solve the LS minimization problem. The advantage of the method is that it is not limited to a particular configuration or objective function.

In a previous paper, we coupled the LS optimization procedure of Huddleston to an efficient PNS solver and used it for optimizing existing hypersonic wind-tunnel contours[19]. In the LS/PNS procedure, the aerodynamic contour was modeled using a cubic spline. The design parameters were the radii at fixed locations along the nozzle length. The objective function was the error of Mach number and radial velocity in the inviscid region of the nozzle exit. It was necessary to define the initial value of the radii by matching as closely as possible the original MOC/BL designed contour. Newton's method was then used to solve the LS problem. The results demonstrated that an improved exit plane profile could be obtained. However, it was difficult to obtain good initial values of the design parameters and to reach a strong minimum of the objective function. Additional work is needed to improve the method so that it can also be applied for designing wind-tunnel nozzles with specified physical characteristics.

The LS/PNS procedure has now been extended for use in designing complete hypersonic wind-tunnel nozzles[20]. A new form of the objective function was given which defines the shape of the nozzle by specifying the centerline Mach number distribution and the uniform flow exit condition. The design parameters were modified to be the coefficients of the spline associated with the local nozzle wall slope. The motivation for these two modifications came from an attempt to be consistent with the constraints and design methodology used in the MOC/BL design procedures. These two modifications greatly improved the convergence of the optimization problem. This new procedure is presented and demonstrated herein by designing four helium nozzles. The flexibility of the procedure is first demonstrated by designing two Mach 15 nozzles using different constraints, the first nozzle for a fixed length and exit diameter and the second nozzle for a fixed length and throat diameter. The computed flow field for the Mach 15 least-squares/parabolized Navier-Stokes (LS/PNS) designed nozzles is then compared with a MOC/BL designed nozzle. The robustness of the procedure is demonstrated by designing a Mach 12 and a Mach 18 nozzle using the same starting contour used in the Mach 15 designs.

AERODYNAMIC DESIGN PROCEDURE FOR HYPERSONIC NOZZLES

We will assume that the shape of the subsonic and transonic contours of the nozzle have been specified and that a NS solution exists for these sections. A LS/PNS optimization procedure[19] is extended for designing the supersonic/hypersonic portion of the nozzle. The details of the PNS solver can be found in Ref. 17. In this section, we will present a brief review of the LS/PNS optimization procedure used in Ref. 19, emphasizing the changes developed for the application to the design of hypersonic nozzles.

OBJECTIVE FUNCTION

A nonlinear optimization problem is solved for a set of design parameters by minimization of an objective function. We consider the minimization of an objective function, *Obj*, which is dependent on a set of design parameters, *X*, and is constructed from a series of functions, f_l, of the nonlinear LS form[21]

$$Obj(X) = \sum_{l=1}^{m} f_l^2(X) \qquad (1)$$

It is convenient to define vectors *f* and *X*

$$f = [f_1, f_2, \ldots, f_m]^T \qquad (2)$$

$$X = [X_1, X_2, \ldots, X_n]^T \qquad (3)$$

so that the objective function can be written as

$$Obj(X) = f^T(X) f(X) \qquad (4)$$

For each particular minimization problem, there are a number of different possibilities for the definition of *f*. It is desirable that *f* be selected so that *Obj* has a strong minimum and satisfies the design criteria. Recall that the MOC design procedure requires the centerline Mach number, M_{axis}, and the condition of parallel flow at the design Mach number, M_{design}, at the nozzle exit. The same requirements are used here to form an objective function. The components of *f* at the nozzle exit associated with the error in axial Mach number, M_x, and flow angle, θ, are

$$f_l = \omega_M (M_{x_{imax,j}} - M_{design}) \qquad (5)$$

$$f_{l+1} = \omega_\theta (\theta_{imax,j} - 0) \qquad (6)$$

and along the centerline

$$f_{l+2} = \omega_{MA} (M_{x_{i,1}} - M_{axis}) \qquad (7)$$

where ω_M, ω_{MA}, and ω_θ are weighting functions used to adjust the relative tolerances between the different types of error terms. The *imax,j* index identifies one of the grid points used to evaluate *f* at the exit of the nozzle and the *i,1* index a point on the nozzle centerline.

The selection of a centerline Mach number distribution determines the overall length of the nozzle and the contour for the initial expansion, which is somewhat arbitrary. However, from a practical view point, the initial expansion should smoothly blend into the turning contour. If this is done, it is more likely that the contours can be accurately machined. Sivells[8] specified a Mach number distribution which matches theoretical transonic conditions at the throat, conical-source flow conditions through an intermediate region, and design flow conditions at the nozzle exit. The advantage of Sivells's centerline distribution is that it smoothly matches the different flow regions, eliminating discontinuous changes in contour curvature. In our design procedure, the centerline Mach number distribution is specified using the method proposed by Sivells. In Sivells' method, the centerline distribution consisted of four sections: (1) a fourth-order polynomial between the transonic section and the conical-source flow regime, (2) source-flow region, (3) fifth-order polynomial between the source-flow region and the parallel flow regime, and (4) the parallel flow region at the design Mach number (Fig. 1). The coefficients of the polynomials are determined by matching the Mach number and its derivatives with respect to nozzle length at the beginning and end of each section. Sivells gave equations for the derivatives of the source-flow regime, the derivatives at the nozzle sonic line using a transonic series solution, nozzle length, and expressions for determining the transition Mach number where the different sections should start. Unfortunately, these relationships are limited to an ideal gas. We will use Sivells' equations directly for the centerline Mach number distribution since our current nozzle design is for helium, which can be accurately modeled as an ideal gas over the temperature and pressure ranges used herein. However, since we are using a NS solution in the transonic section, these derivatives could be calculated directly from the numerical results. The derivatives necessary for the source-flow region could also be easily computed directly, using the same gas model used in the CFD code.

DESIGN PARAMETERS

Like the objective function, the selection of the design parameters depends on the problem being solved. The ideal set would contain the minimum number of elements and be strongly coupled to the objective function. The design parameters are usually coefficients used to define a wall boundary or quantities which define the flow field conditions. For the design of a nozzle, the flow conditions are usually given, and the wall contour needs to be determined.

WALL CONTOUR

For a contoured nozzle, there is no obvious choice of a function to describe the geometry which would minimize the number of design parameters. A contoured nozzle can have an arbitrary expansion up to the inflection point. After the inflection point, the nozzle contour is determined so that the proper wave cancellation occurs and parallel flow is obtained at the exit of the nozzle. Many contoured nozzles have a curvature discontinuity at the inflection point, i.e. the second derivative is not continuous. In Ref. 19, we used a cubic spline with five knots to model the contoured nozzle. The total number of knots on the spline and the design parameters necessary for defining the contoured nozzle are dependent on how accurately the design problem is to be determined. We will discuss the selection of the number of knots and design parameters later in this section. The nozzle contour is specified using N cubic polynomial equations

$$0 < x \le x_1 \qquad \{ r = a_0 + a_1 x + a_2 x^2 + a_3 x^3$$
$$x_1 < x \le x_2 \qquad \{ r = a_4 + a_5 x + a_6 x^2 + a_7 x^3$$

$$x_{N-1} < x \le x_N$$
$$\{ r = a_{4N-4} + a_{4N-3} x + a_{4N-2} x^2 + a_{4N-1} x^3 \qquad (8)$$

The N cubic equations result in $4N$ coefficients, assuming that the locations x_1 through x_N are known. The requirement of continuity of the surface, slope, and curvature at x_1 through x_N specifies $3(N-1)$ of the coefficients. The remaining $N+3$ coefficients are specified by using the inlet and exit radii and slopes and by specifying the slope at $N-1$ locations. Once the above constants are defined, a linear system of equations is solved to determine the value of the coefficients a_0-a_{4N-1}.

SELECTION OF DESIGN PARAMETERS

Previously[19], we had used selected radii at locations x_i to be used as design parameters. Recall that in the MOC procedure, the wall is determined by the *slope* necessary to turn the flow in the correct direction. The use of wall slopes as design parameters instead of radii is more consistent with the physics of supersonic flow fields. The adoption of a slope-based design parameter greatly improved the convergence of the design procedure. The design parameters used are the coefficients in Eq.(8) for a_5, a_9, ..., a_{4N-3}, which represent the slopes at points x_1, x_2, ..., x_{N-1}. In addition to these, other control parameters were used, depending on the constraints necessary for a particular nozzle design. Typical constraints may be fixed length, nozzle throat, or nozzle exit diameter.

NUMBER OF KNOTS ON THE CUBIC SPLINE

Determining the number of knots on the cubic spline and the location of the control points, x_1-x_N, is an ad hoc process. The procedure adopted is that a preliminary design is made using the predetermined centerline Mach number distribution and then knots and design parameters are added until a converged solution is obtained which satisfies the design requirements.

NONLINEAR OPTIMIZATION BY SOLVING A LS PROBLEM

Now that an objective function and the design parameters have been defined, we turn to addressing the problem of minimizing Eq. (4). Recall that $Obj(X)$ will have a minimum value when its gradient is zero. Newton's method for nonlinear least squares can be written directly as

$$J_k^T J_k \Delta X_k = -J_k^T f_k \qquad (9)$$

where the design parameters are updated by

$$X_{k+1} = X_k + \Delta X_k \qquad (10)$$

This is the small residual problem form of the LS problem. For additional information on methods for solving Eq. (9) for both small and large residual problems, see the text by Scales[21].

SENSITIVITY DERIVATIVES

The elements of the Jacobian matrix, J, are the sensitivity derivatives. Each element of the Jacobian matrix requires a separate flow-field solution. The sensitivity derivatives are approximated using forward finite-differences

$$\partial f_i / \partial X_j = (f_i(X + \Delta X_j) - f_i(X)) / \Delta X_j \qquad (11)$$

The accuracy of the difference approximation is dependent on both the size of ΔX_j and the flow-field solution. The Jacobian elements in this study were computed by specifying ΔX_j to be $X_j * 10^{-6}$. The calculation of the sensitivity derivatives is the most expensive part of the optimization procedure.

UPDATING THE JACOBIAN MATRIX

The expensive portion of the above algorithm is the determination of the elements of the Jacobian matrix. One evaluation of the objective function, $Obj(X)$, is needed for each element of X. If X contains n elements, then each iteration requires $n+1$ functional evaluations or flow-field solutions. An alternate method to explicitly computing the Jacobian matrix is to use an updated formula such as Broyden's[21]. Previously, our attempts to use Broyden's update formula when the design parameters were the radii were unsuccessful[19]. However, after switching to the slope-based design parameters, Broyden's update formula was successfully used.

APPLICATION OF LS/PNS DESIGN PROCEDURE

To demonstrate the procedure, four h[illegible] nozzle aerolines are designed. Two different cases will be considered. For the first case, the nozzle is required to have an exit radius of 10.44 inches and a total length of 125 inches. The design contour is to be computed for a stagnation flow condition of 1,500 psi and 530 degrees R. The wall temperature can be assumed to be constant at 530 degrees R, and the flow to be turbulent. The design exit conditions for the Mach 15 flow field are a 47 percent core flow, with a goal of less than ±2 percent variation in static pressure, and less than ±0.287 degrees variation in flow angle. This particular nozzle was selected because a MOC/BL design had been made for Mach 15 which failed to meet these design requirements (when evaluated with a NS code). The same starting contour will then be used to design a Mach 12 and a Mach 18 nozzle using the same constraints to demonstrate the robustness of the method. The second case will demonstrate the flexibility of the procedure by using the same design conditions as the first case except that the nozzle throat radius, 0.61324 inches, will be held constant, and the exit radius will be determined by the procedure.

The hypersonic portion of the nozzle flow field is computed using an axisymmetric version of the explicit upwind PNS solver of Ref. 17. The subsonic and transonic flow field of the nozzle is computed only once with the Navier-Stokes equations using an axisymmetric version of NASCRIN[22]. The flow field is assumed to be turbulent and is simulated using the Baldwin and Lomax[23] eddy viscosity model. The radial direction is discretized using 50 points, with point clustering at both the wall and the nozzle axis.

The total number of streamwise stations was approximately 90,000. The computer runs were made on Langley's Cray 2 supercomputer.

The first iteration of the design procedure is started by forming the elements of the Jacobian matrix numerically and then solving the nonlinear LS problem. For the second iteration, the elements are updated with Broyden's method. Broyden's update procedure is used until there is no longer any improvement in the convergence of the objective function towards a minimum. The elements are then recomputed numerically, and the procedure continues until either the desired design performance or a minimum is obtained.

DESIGN PARAMETERS

The aerodynamic lines are modeled using 15 knots on a cubic spline. The initial values of the spline coefficients are obtained from evaluating the slope at the selected locations of the MOC/BL designed nozzle contour and are shown in Table 1. The number and location of the knots was selected so that changes in the slope of the aerodynamic lines would be accurately represented (Fig. 2).

Table 1 Initial values of cubic spline for helium nozzle

Index	x(in.)	y_w(in.)	dy_w / dx
1	0.00000	0.61324†	0.00000
2	0.57757	-	0.08062*
3	1.17757	-	0.13214*
4	1.67757	-	0.16226*
5	2.47757	-	0.18155*
6	3.57757	-	0.19470*
7	7.87757	-	0.19810*
8	10.0777	-	0.18444*
9	13.0776	-	0.16740*
10	19.0776	-	0.14000*
11	31.0776	-	0.10530*
12	55.0776	-	0.06850*
13	80.0776	-	0.04810*
14	102.0776	-	0.03590*
15	125.6600	10.44 ‡	0.02683*

*,† are Case 1 design variables.

*,‡ are Case 2 design variables.

A total of 15 design parameters are used in the optimization procedure. The wall slopes dy_w/dx at indexes 2-15, are 14 of the design parameters. For the first case, the 15th design parameter is the inlet radius (at index 1), and for the second case, it is the exit radius (at index 15). The locations of the knots are held constant.

OBJECTIVE FUNCTION

The objective function consists of an array of 148 elements. The first 100 elements are the centerline Mach number errors, evenly spaced over the nozzle length, the next 24 elements are the exit core Mach number profile errors, and the final 24 elements are the exit core flow angle errors. The 24 elements used in the exit core are from the nozzle centerline to halfway across the exit radius. The weighting factors used are

$$\omega_M = 1/M_{design}, \qquad \omega_{MA} = 1/M_{axis(x)}, \qquad \omega_\theta = 1/0.2$$

The centerline Mach number distribution is computed using Sivells' formula by fixing the Mach number at points E, B, and C to be 2.3, 12., and 15, respectively (see Fig. 1) for the Mach 15 design cases. The source-flow region is computed for a conical half-angle equal to 12 degrees. The ratio of the radius of curvature to the nozzle radius at the throat is 9 (used in computing the transonic Mach number distribution). This centerline distribution will result in a uniform flow region of approximately 4.9 inches at the nozzle exit. Note that this is a cut-off contour, in that the nozzle is smaller in length than it would be if the flow had to be fully expanded to the design Mach number. This is common practice in hypersonic nozzles, where so much of the profile is part of the boundary layer[11].

DESIGN LOGIC

Since the significant viscous effects occur in the supersonic/hypersonic section of the nozzle, an approximate procedure is used at the throat for the first case. When the throat radius is a design parameter, the initial Navier-Stokes solution is scaled to a new throat radius after each iteration. Once the design parameters have converged, a new Navier-Stokes solution is computed in the upstream subsonic and transonic section. Since the boundary layer is extremely thin at the throat, we would expect only small differences between the approximate procedure and the new NS solution for the subsonic and transonic section in the inviscid core. The accuracy of this approximation will be investigated in the future by rerunning the subsonic and transonic section with the newly designed contour and recomputing the supersonic/hypersonic region with the new initial conditions. In the second case, this would not be necessary since the throat radius is held constant.

CASE I, FIXED LENGTH AND EXIT RADIUS

In this case, the nozzle throat and the slope at 14 points are used as the design parameters. The objective function for the Mach 15 design is reduced two orders of magnitude (Fig. 3) from the initial guess. The change in the contour over the MOC/BL design is hardly noticeable (Fig. 4). However, significant differences are demonstrated between their flow-field solutions. The centerline Mach number almost exactly follows the specified centerline distribution (Fig. 5). To obtain a uniform profile with less than ±2% error in static pressure, the error in Mach number should be less than ±0.06 Mach. The centerline variation of Mach number for the MOC/BL design in the uniform core region is excessive, greater than ±1.0 Mach (±30% static pressure variation). The LS/PNS variation of centerline Mach number was less than ±0.06 for most of the uniform core region, with a small region almost reaching a variation of ±0.10 Mach (±3% variation in static pressure). The LS/PNS design exit profiles for Mach number (Fig. 6), static pressure (Fig. 7, pressure nondimensionized by the dynamic pressure at Mach 1), and flow angle (Fig. 8) show very good agreement with the design conditions and demonstrate that the flow is much better than the design goal at the nozzle exit. The advantage of the LS/PNS design can clearly be seen in the Mach number contour plot (Fig. 9). Each contour level represents an increment of 0.2 Mach number (±3% static pressure variation). A constant uniform core flow region and a smooth expansion region are demonstrated by the LS/PNS design, which is not obtainable with the MOC/BL design.

These results clearly demonstrate the capability of the new procedure. However, the LS/PNS design could still be improved on by using more design parameters and knots on the cubic spline, a better distribution of the location of the knots, or a different distribution and weight functions used in defining the objective function.

To demonstrate the robustness of the procedure, Mach 12 and Mach 18 nozzles were designed using the same starting contour defined by the coefficients in Table 1. This was accomplished by redefining the objective function for the expansion region and nozzle exit. For the Mach 12 case, the centerline Mach number distribution was modified so that the Mach numbers at points B and C of Fig. 1 were 9 and 12, respectively. The source-flow region for the Mach 12 nozzle design was generated assuming 8° source flow. The centerline Mach number distribution and the exit Mach number profile are shown in Figs. 10 and 11. Excellent agreement is obtained with the design Mach numbers. The slight drop off of Mach number shown in the Mach number profile is because the uniform core region only extends to $y/r_t=8.3$ at this location.

For the Mach 18 case, only the centerline Mach number distribution was modified so that the Mach numbers at points B and C of Fig. 1 were 15 and 18, respectively. The centerline Mach number distribution and the exit Mach number profile are shown in Figs. 12 and 13. In this case, the centerline Mach number distribution has a slight oscillation at the beginning of the uniform core region. An improved solution could be obtained by adding or moving the location of the design parameters or by decreasing the angle at which the flow is expanded in the source-flow region. The uniform core region extends to approximately $y/r_t=7.2$ at the exit of the nozzle. The Mach number profile in this region, again, agrees with the design Mach number. It is obvious that the domain of the objective function could be extended at the exit to include more of the inviscid core. This would force a smaller throat to be used, resulting in a larger uniform core region for the same nozzle length.

CASE II, FIXED LENGTH AND THROAT RADIUS

In this case, the throat radius is held constant and the exit radius and the slope at 14 points are the design parameters. The change in the aerodynamic lines over the MOC/BL design is slightly more noticeable than in the first case (Fig. 14). A small oscillation of the centerline Mach number can be observed in Fig. 15. Due to the fact that the throat region was not permitted to change, a fixed error always occurs between the control centerline Mach number distribution and the computed one near the throat. However, good agreement is, again, obtained with the exit design conditions for the Mach number profile (Fig. 16), pressure profile (Fig. 17), and flow angle (Fig. 18). The uniform core region and the region of optimization extends to approximately $y/r_t=7.5$, which can be seen in the drop in Mach number in Fig. 16.

CONCLUDING REMARKS

A new procedure, which unifies the best of current classical design practices, computational fluid dynamics (CFD), and optimization procedures, has been demonstrated for designing the aerodynamic lines of hypersonic wind-tunnel nozzles. An efficient CFD code, which solves the parabolized Navier-Stokes (PNS) equations, was coupled to a least-squares (LS) optimization procedure. A LS problem was formulated to minimize the difference between the computed flow field and the objective function. The objective function consists of the centerline Mach number distribution and the exit Mach number and radial velocity profiles. The aerodynamic lines of the nozzle were defined using cubic splines, the slopes of which were optimized with the design procedure. The use of slopes at the specified control points as the design parameters improved the convergence characteristics of the design procedure and is consistent with design methods used with the MOC. The new procedure can be used to design hypersonic wind-tunnel nozzles where the classical procedure has been shown to break down. An advantage of the new procedure is that it automatically compensates the nozzle contour for viscous effects as part of the unified design procedure. The new procedure was demonstrated by designing four different helium nozzles. Mach 15, Mach 12, and Mach 18 nozzles were designed for a fixed length and exit radius, and a second Mach 15 nozzle for a fixed length and nozzle throat. The two Mach 15 nozzle designs showed the flexibility of the procedure to easily handle different types of design constraints. The computed flow field for the Mach 15 LS/PNS-designed nozzles demonstrated a significant improvement over the classical MOC/BL designed nozzle. The design of the Mach 12 and Mach 18 nozzles demonstrated the robustness of the procedure by using the same starting contour as the Mach 15 designs.

The new design procedure makes it practical to design high Mach number hypersonic wind-tunnel nozzles using CFD codes. The nozzle designer will have to specify initial and boundary conditions, centerline Mach number distribution, number and location of cubic splines, design constraints, and select a turbulence model for use in the calculations. However, once these conditions are specified, a design can be made with this procedure to satisfy most practical requirements.

ACKNOWLEDGMENT

The author would like to thank Ms. Anne Edwards of Experimental Hypersonics Branch, Space Systems Division, for providing the Navier-Stokes solution used as the initial condition in the calculations.

REFERENCES

[1] Erlebacher, G.; Kumar, A.; Anderson, E. C.; Rogers, R. C.; Dwoyer, D. L.; Salas, M.; and Harris, J. E., "A Computational Design Procedure for Actively Cooled Hypersonic Wind-Tunnel Nozzles Subject to Wall Shape Constraints." Paper presented at the CFD in Aerospace Design Workshop (Tullahoma, Tennessee), Univ. of Tennessee Space Inst., June 4-6, 1985.

[2] Benton, J. R., "Design and Navier-Stokes Analysis of Hypersonic Wind Tunnel Nozzles," M. S. thesis, North Carolina State University, Raleigh, 1989.

[3] Anderson, J. D., *Modern Compressible Flow*, 1st ed., McGraw-Hill, New York, 1982, pp. 303-305.

[4] Benton, J.; Perkins, J.; and Edwards, A., "Limitations of the Method of Characteristics When Applied to Axisymmetric Hypersonic Nozzle Design," AIAA Paper 90-0192, January 1990.

[5] Candler, G. and Perkins, J., "Effects of Vibrational Nonequilibrium on Axisymmetric Hypersonic Nozzle Design," AIAA Paper 91-0297, January 1991.

[6] Armstrong, A. H. and Smith, M. G., "Two-Dimensional Supersonic Nozzle Design, Part I: Theory," Armament Research Establishment, Report No. 5/51, October 1951.

[7] Ruptash, J., "Supersonic Wind Tunnels - Theory, Design and Performance," University of Toronto, Institute of Aerophysics, June 1952.

[8] Sivells, J. C., "Aerodynamic Design of Axisymmetric Hypersonic Wind Tunnel Nozzles," *Journal of Spacecraft and Rockets*, Vol. 7, November 1970, pp.1292-1299.

[9] Beckwith, I. E. and Moore, J. A., "An Accurate and Rapid Method for the Design of Supersonic Nozzles," NACA TN 3322, February 1955.

[10] Johnson, C. B., "Real-Gas Effects on Hypersonic Nozzle Contours With a Method of Calculation," NASA TN D-1622, April 1963.

[11] Lukasiewicz, J., *Experimental Methods of Hypersonics*, Gasdynamics, Vol. 3, Part I., Dekker, New York, 1973, pp80-86.

[12] Zucrow, M. J. and Hoffman, J. D., *Gas Dynamics*, Volume 2: Multidimensional Flow, John Wiley & Sons, Inc., 1977.

[13] Shapiro, A. H., *The Dynamics and Thermodynamics of Compressible Fluid Flow*, Vol. 1, The Ronald Press Company, New York, 1953.

[14] Yang, J. Y.; Lombard, C. K.; Luh, R. C.-C.; Nagaraj, N.; and Codding, W. H., "Aerodynamic Design Modification of A Hypersonic Wind Tunnel Nozzle by CSCM with High Order Accuracy," AIAA Paper 87-1896.

[15] Meyer, R. E. and Holt, M., "The Correction of Wind Tunnel Nozzles for Two-Dimensional, *Supersonic Flow*," The Aeronautical Quarterly, Vol. II, November 1950, pp. 195-208.

[16] Gielda, T. and McRae, D., "An Accurate, Stable, Explicit, Parabolized Navier-Stokes Solver for High Speed Flows," AIAA Paper 86-1116, May 1986.

[17] Korte, J. J., "An Explicit Upwind Algorithm for Solving the Parabolized Navier-Stokes Equations," NASA TP 3050, February 1991.

[18] Huddleston, D. H.,"Aerodynamic Design Optimization Using Computational Fluid Dynamics," Ph. D. dissertation, University of Tennessee, Knoxville, 1989.

[19] Korte, J. J.; Kumar, A.; Singh, D. J.; and Grossman, B., "Least Squares/Parabolized Navier-Stokes Procedure for Optimizing Hypersonic Wind-Tunnel Nozzles," AIAA Paper 91-2273, June 1991.

[20] Korte, J. J., "Aerodynamic Design of Axisymmetric Hypersonic Wind-Tunnel Nozzles Using Least-Squares/Parabolized Navier-Stokes Procedure," AIAA Paper 92-0332, January 1992.

[21] Scales, L. E., *Introduction to Non-Linear Optimization*, Macmillan Publishers LTD, London, 1985, pp. 110-136.

[22] Kumar, A., "Numerical Analysis of the Scramjet-Inlet Flow Field by Using Two-Dimensional Navier-Stokes Equations," NASA TP-1940, May 1981.

[23] Baldwin, B. S. and Lomax, H., "Thin Layer Approximation and Algebraic Model for Separated Turbulent Flows," AIAA Paper 78-0257, Jan. 1978.

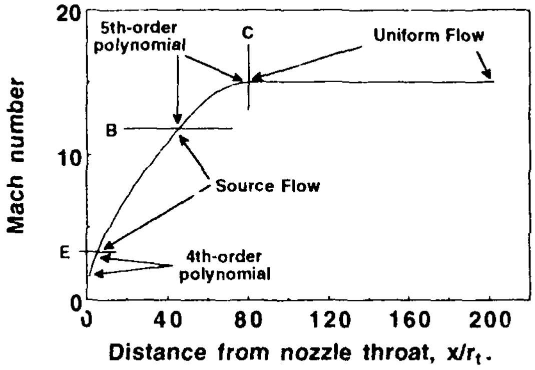

Fig. 1 Design centerline Mach number distribution.

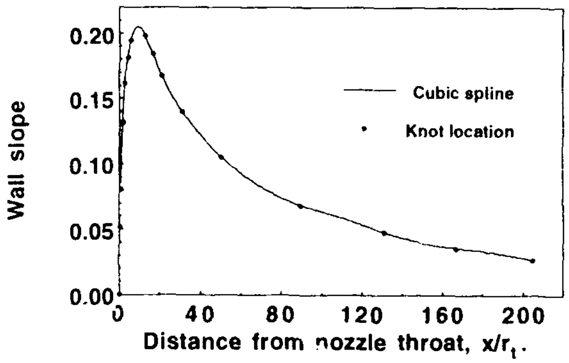

Fig. 2 Wall slope computed using a cubic spline.

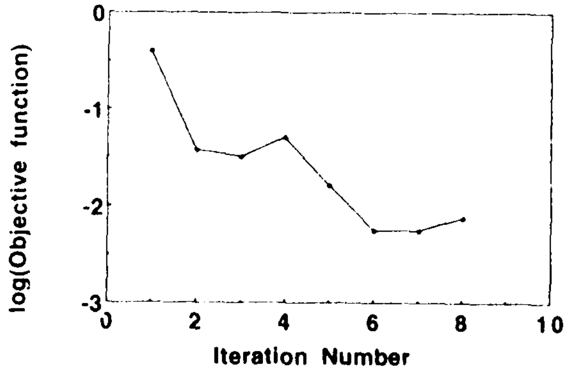

Fig. 3 Reduction of objective function for case 1.

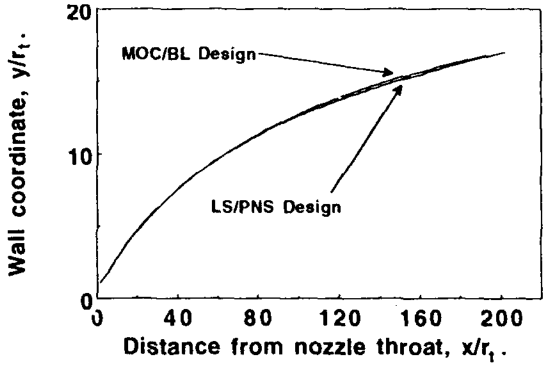

Fig. 4 Comparison of wall contours for case 1.

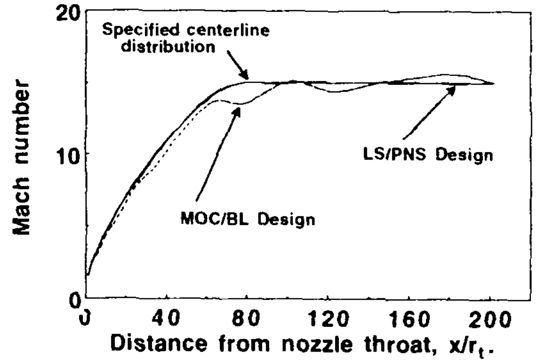

Fig. 5 Centerline Mach number distribution, case 1.

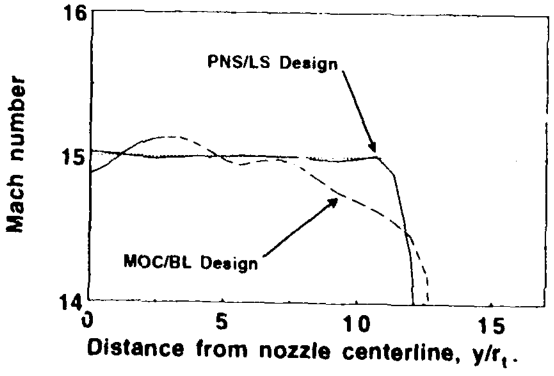

Fig. 6 Nozzle exit Mach number profiles for case 1.

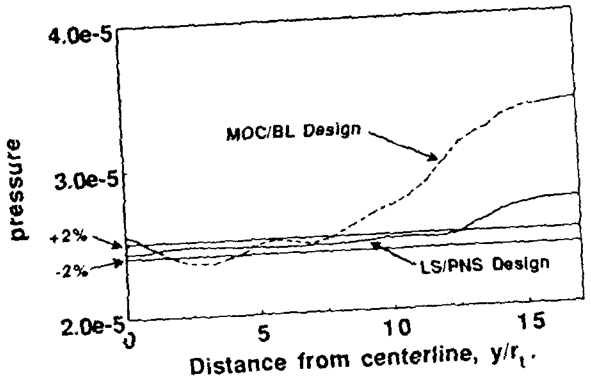

Fig. 7 Nozzle exit pressure profiles for case 1.

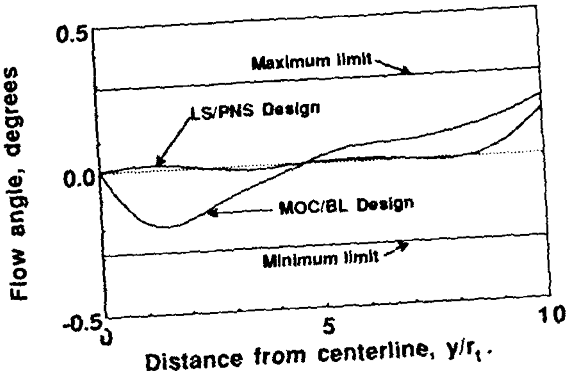

Fig. 8 Flow angle for case 1.

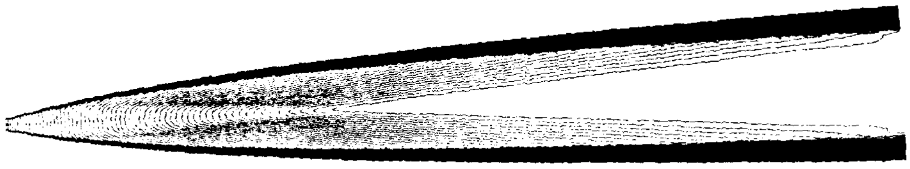

LEAST-SQUARES/PARABOLIZED NAVIER-STOKES DESIGN

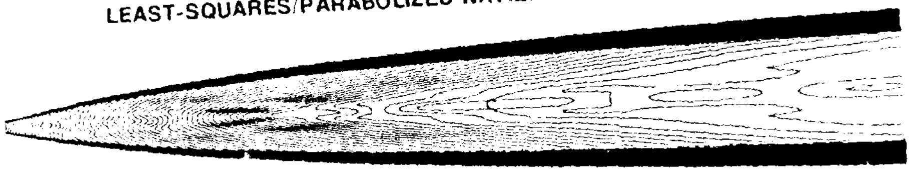

METHOD-OF-CHARACTERISTICS/BOUNDARY LAYER DESIGN

Fig. 9 Comparison of Mach number contours for LS/PNS and MOC/BL designed nozzles, 0.2 Mach increment.

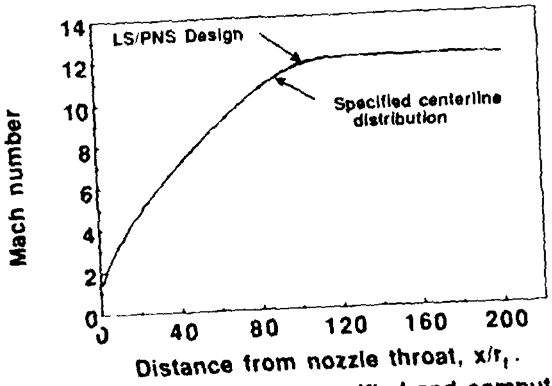

Fig. 10 Comparison of specified and computed centerline Mach number distribution.

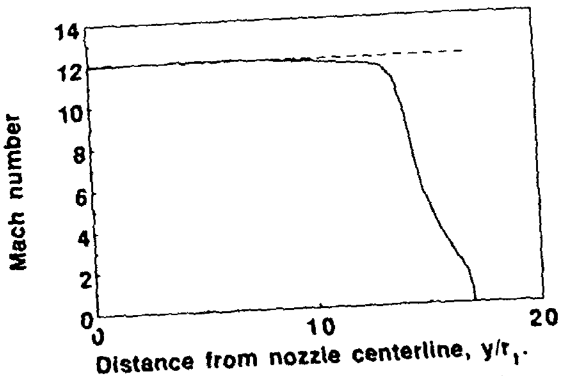

Fig. 11 Comparison of Mach exit profile with design Mach number.

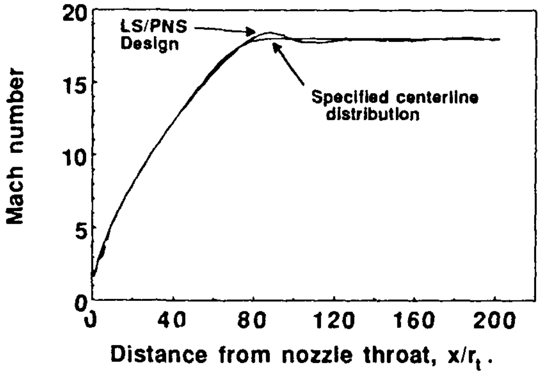

Fig. 12 Comparison of specified and computed centerline Mach number distribution.

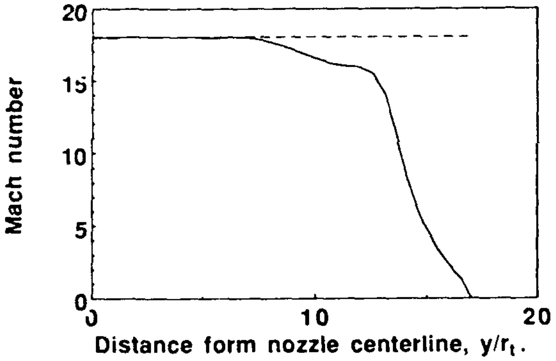

Fig. 13 Comparison of Mach exit profile with design Mach number.

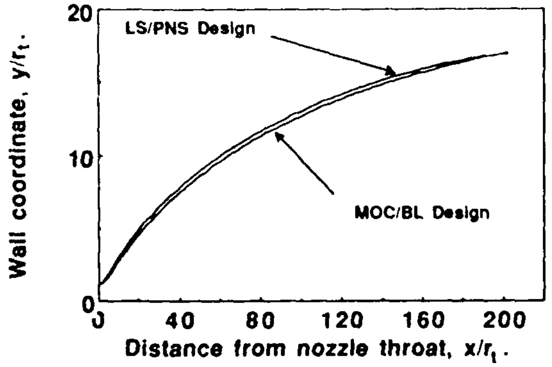

Fig. 14 Comparison of wall contours for case 2.

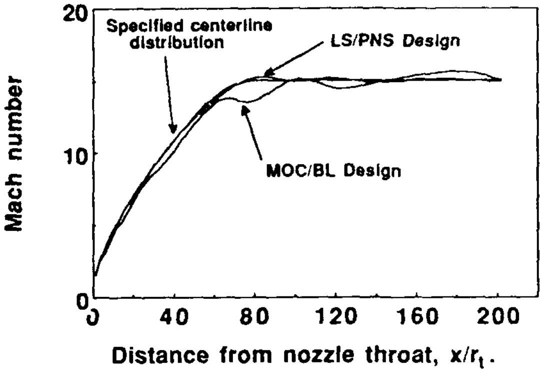

Fig. 15 Centerline Mach number, case 2.

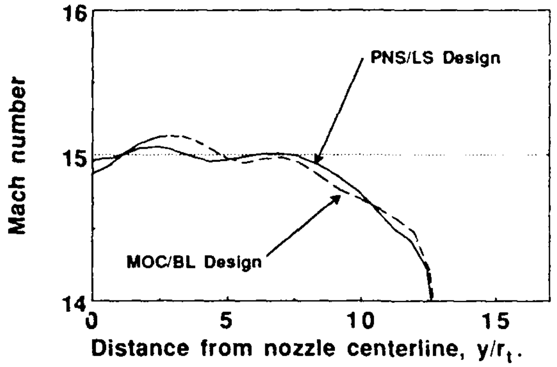

Fig. 16 Exit Mach number profiles, case 2.

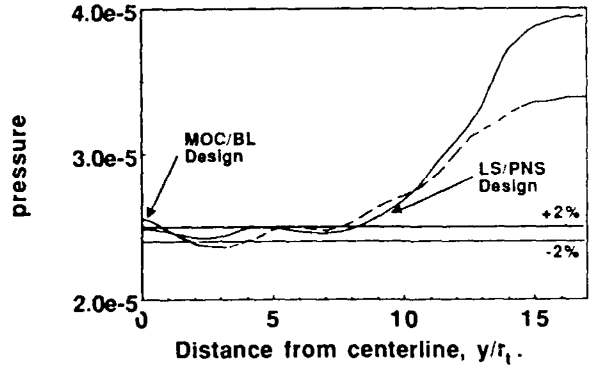

Fig. 17 Nozzle exit pressure profiles for case 2.

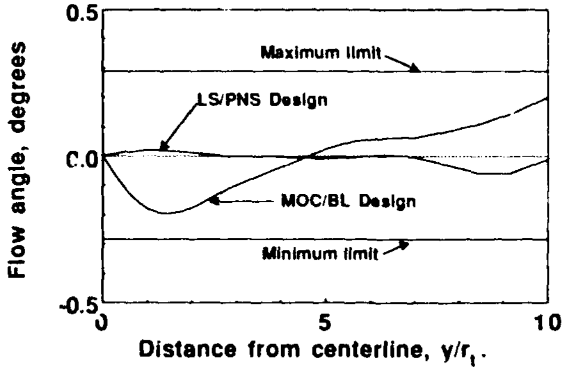

Fig. 18 Flow angle for case 2.

NUMERICAL METHODS FOR AEROTHERMODYNAMIC DESIGN OF HYPERSONIC SPACE TRANSPORT VEHICLES

K.M. Wanie, A. Brenneis, A. Eberle, S. Heiss
Messerschmitt-Bölkow-Blohm AG, Military Aircraft Division, FE211,
P.O. Box 80 11 60, W-8000 München 80

SUMMARY

The requirement of the design process of hypersonic vehicles to predict flow past entire configurations with wings, fins, flaps and propulsion system represents one of the major challenges for aerothermodynamics. In this context computational fluid dynamics has come up as a powerful tool to support the experimental work. The present paper describes a couple of numerical methods developed at MBB designed to fulfil the needs of the design process. The governing equations and fundamental details of the the solution methods are shortly reviewed. Results are given for both geometrically simple test cases and realistic hypersonic configurations. Since there is still a considerable lack of experience for hypersonic flow calculations an extensive testing and verification is essential. This verification is done by comparison of results with experimental data and other numerical methods. The results presented prove that the methods used are robust, flexible and accurate enough to fulfil the strong needs of the design process.

1 INTRODUCTION

The development of airbreathing hypersonic cruise vehicles covers a wide range of new problems in the field of aerodynamics, aerothermodynamics and propulsion integration (Fig. 1, [1]). Completely new aerodynamic shapes have to be found in order to meet the requirements of the whole flight mission. The configuration has to be stable and controlable in a region ranging from very low speed during horizontal take off and landing up to high Mach numbers during cruise. The flow at cruise conditions is mainly dominated by viscous effects and the Reynolds numbers are very high. Due to the long flight times aerodynamic drag and heating have to be minimized in order to reduce weight of fuel and insulation. In this context transition laminar-turbulent, turbulence and solid wall radiation play a major role. Furthermore a good integration of the propulsion system is essential in order to get a suitable precompression of the flow entering the intake and to keep the drag as small as possible. For these reasons it is necessary to predict hypersonic external and internal flows precisely to get detailed knowledge of aerodynamic coefficients, thermal loads, mass flow rates and other physical properties.

With the advent of modern-high speed computers computational fluid dynamics (CFD) is more and more applicable for these investigations and has become an important tool of design aerodynamics. It is commonly used today to support the experimental work. Advantages of CFD as compared to experiments are lower cost and lower turn-around times. This holds especially in hypersonics since due to the high free-stream enthalpy of the flow windtunnel experiments are very expensive. A tremendous technical effort is necessary to simulate effects like radiation, catalytic walls or chemical reactions correctly. CFD is in principle suited to overcome these problems, provided a proper mathematical modelling for the particular effects is available. The development of these models can, of course, be a very difficult task and an extensive testing and verification of both the fundamental numerical method and the physical modelling is necessary.

Since the development of new hypersonic configurations is usually starting from scratch today, a variety of numerical methods is necessary to satisfy the requirements of the particular design phases. In the predesign phase approximate methods and inviscid methods (potential or Euler methods) are used to get a quick survey of the aerodynamic behaviour of the new configuration. For the subsequent verification of the design potential and Euler methods and in some cases also viscous methods are employed. The investigation of flow details (separation, thermal loads) finally is performed by means of viscous methods (coupling of Euler and boundary-layer equations, Navier-Stokes equations). For each method, of course, a flexible, fast grid generation procedure, which is closely linked to the CAD system used for the geometric design, is mandatory.

To cope with these demands a group of numerical methods was developed at MBB (Fig. 2). The capabilities of these methods are ranging from grid generation via viscous and inviscid flow calculation to postprocessing. The present paper focuses on the practical application of these tools in the design cycle. In Chapter 2 a survey of the different levels of modelling real flow is given together with the particular governing equations. In Chapter 3 a description of the computational methods and some fundamental details can be found. In Chapter 4 the numerical methods are first verified by means of simple test cases and comparison with experimental data to ensure the quality of the solutions. Subsequently a sample of results is shown from applications within a design cycle.

2. LEVELS OF MODELLING REAL FLOW

As was mentioned in Chapter 1 various mathematical models for real flow exist, each of them having particular advantages with regard to specific design phases.

The probably best representation of real flow can be expected from a solution of the Navier Stokes equations, provided problems of turbulence modelling are kept apart. The most important drawback of solving the Navier Stokes equations for project applications is the high demand of computer time and storage due to the fine spatial resolution required near solid walls. For this reason a solution of the Navier Stokes equations is usually limited nowadays to investigation of detail problems and simplifications of the Navier Stokes equations are to be used in the design process.

One simplification is to drop the viscous terms to get the inviscid Euler equations. Since in an inviscid calculation no large gradients in the boundary layer have to be resolved a relatively course grid can be used near solid walls, resulting in considerably less effort of computer time and storage. If in addition irrotationality is assumed, the potential equations are obtained which can be solved by even less expensive panel methods. The disadvantage of using inviscid equations is, of course, that it is not possible to calculate thermal loads and skin friction. This can be overcome to a certain extent by a coupling of a solution of the boundary layer equations to the inviscid solution, which is possible in regions where the flow remains attached.

For each design phase suitable methods have to be selected from the above range in order to keep cost and development time as small as possible while retaining the desired accuracy. It should be mentioned, however, that even the solution of inviscid equations can be too expensive for early stages of design. Therefore approximate methods such as the Newtonian like methods or shock expansion methods have to be available as well. These allow to get a very quick and inexpensive coarse survey of the aerodynamic behaviour of new configurations.

In the following the governing equations, the Navier Stokes, the Euler and the boundary layer equations are shortly reviewed. The description of the potential equations is omitted for sake of conciseness. At the end of the chapter the modelling of thermodynamic and transport properties for hypersonic flow is addressed. These can be of major importance for the flow field due to high temperatures and enthalpies involved.

2.1 Navier Stokes and Euler equations

The general governing equations for the present investigations are the time dependent Reynolds-averaged compressible Navier-Stokes equations in conservation law form. In terms of body-fitted arbitrary coordinates ξ, η, ζ using Cartesian velocity components u, v, w they read

$$\frac{\partial}{\partial t}\vec{U} + \frac{\partial}{\partial \xi}\vec{E} + \frac{\partial}{\partial \eta}\vec{F} + \frac{\partial}{\partial \zeta}\vec{G} = 0, \tag{1}$$

where

$$\vec{U} = (\rho, \rho u, \rho v, \rho w, e)^T \tag{2}$$

is the solution vector of the conservative variables and

$$\vec{E} = J\left(\tilde{\vec{E}}\xi_x + \tilde{\vec{F}}\xi_y + \tilde{\vec{G}}\xi_z\right), \tag{3}$$

$$\vec{F} = J\left(\tilde{\vec{E}}\eta_x + \tilde{\vec{F}}\eta_y + \tilde{\vec{G}}\eta_z\right), \tag{4}$$

$$\vec{G} = J\left(\tilde{\vec{E}}\zeta_x + \tilde{\vec{F}}\zeta_y + \tilde{\vec{G}}\zeta_z\right) \tag{5}$$

are the flux vectors normal to the $\xi = const.$, $\eta = const.$, $\zeta = const.$ faces. The Cartesian fluxes therein are

$$\tilde{\vec{E}} = \begin{pmatrix} \rho u \\ \rho u^2 - \sigma_{xx} \\ \rho u v - \sigma_{xy} \\ \rho u w - \sigma_{xz} \\ (e - \sigma_{xx})u - \sigma_{xy} v - \sigma_{xz} w + q_x \end{pmatrix}, \tag{6}$$

$$\tilde{\vec{F}} = \begin{pmatrix} \rho v \\ \rho u v - \sigma_{yx} \\ \rho v^2 - \sigma_{yy} \\ \rho v w - \sigma_{yz} \\ -\sigma_{yx} u + (e - \sigma_{yy})v - \sigma_{yz} w + q_y \end{pmatrix}, \tag{7}$$

$$\tilde{\vec{G}} = \begin{pmatrix} \rho w \\ \rho u w - \sigma_{zx} \\ \rho v w - \sigma_{zy} \\ \rho w^2 - \sigma_{zz} \\ -\sigma_{zx} u - \sigma_{zy} v + (e - \sigma_{zz})w + q_z \end{pmatrix}. \tag{8}$$

Accepting Stokes' hypothesis for Newtonian fluids, $3\lambda + 2\mu = 0$, the stress tensor reads

$$\sigma_{xx} = -p - \frac{2}{3}\mu\left(-2\frac{\partial u}{\partial x} + \frac{\partial v}{\partial y} + \frac{\partial w}{\partial z}\right), \tag{9}$$

$$\sigma_{xy} = \sigma_{yx} = \mu\left(\frac{\partial u}{\partial y} + \frac{\partial v}{\partial x}\right), \tag{10}$$

$$\sigma_{xz} = \sigma_{zx} = \mu\left(\frac{\partial u}{\partial z} + \frac{\partial w}{\partial x}\right), \tag{11}$$

$$\sigma_{yy} = -p - \frac{2}{3}\mu\left(\frac{\partial u}{\partial x} - 2\frac{\partial v}{\partial y} + \frac{\partial w}{\partial z}\right), \tag{12}$$

$$\sigma_{yz} = \sigma_{zy} = \mu\left(\frac{\partial v}{\partial z} + \frac{\partial w}{\partial y}\right), \tag{13}$$

$$\sigma_{zz} = -p - \frac{2}{3}\mu\left(\frac{\partial u}{\partial x} + \frac{\partial v}{\partial y} - 2\frac{\partial w}{\partial z}\right). \tag{14}$$

For the heat flux vector Fourier's law

$$q_x = -k\frac{\partial T}{\partial x}, \quad q_y = -k\frac{\partial T}{\partial y}, \quad q_z = -k\frac{\partial T}{\partial z} \tag{15}$$

is valid.

The letters ρ, p, T, μ, k denote density, pressure, temperature, viscosity and heat conductivity. e is the total inner energy (inner energy + kinetic energy) per unit volume. The indices $()_\xi, ()_\eta, ()_\zeta$ denote partial derivatives with respect to ξ, η, ζ except for the stress tensor σ and the heat flux vector $\vec{q}$. The definition of the metric can be found for example in [2].

The boundary conditions at the wall are the usual no-slip and impermeable wall conditions for the velocity and one condition for the wall temperature (e.g. fixed wall heat flux, adiabatic wall, prescribed wall temperature). At higher Mach numbers it is important to take wall radiation into account since it is an essential process for the reduction of the wall heat fluxes on hypersonic vehicles. For radiating walls the heat-flux vector at the surface is calculated with

$$q = -k\frac{\partial T}{\partial n} + \epsilon\sigma T_w^4, \tag{16}$$

where n is the wall normal direction. The second term in Eq. 16 is the radiation term. σ is the Stephan-Boltzmann constant with $\sigma = 5.67 \cdot 10^{-8} W/(m^2 K^4)$, ϵ is the emissivity factor of the surface material ($0 \leq \epsilon \leq 1$) and T_w is the temperature at the wall.

The Euler equations are obtained from the Navier-Stokes equations by simply neglecting all viscous terms. For the inviscid case slip conditions have to be prescribed at the wall and it is, of course, impossible to specify a boundary condition for the temperature.

2.2 Boundary layer equations

For hypersonic problems classical boundary-layer theory tends to fail to properly model the viscous flow [3,4]. This is due to the fact that typical hypersonic flows of interest are in most cases characterized by relatively thick boundary layers compared to the local curvature of the surface. Furthermore, strong vorticity and an entropy layer are generated by the curved bow shock in front of blunt bodies, which has to be taken into account in a boundary layer calculation. For these reasons a second order boundary layer model has to be used.

The second order, three dimensional, compressible boundary layer equations are derived by an order of magnitude analysis of the terms of the nondimensionalized Navier-Stokes equations transformed to locally monoclinic surface oriented coordinates. Using tensorial notation including the Einstein summation convention they read [5]

$$\left(\sqrt{g}\rho v^\alpha\right)_{,\alpha} + \left(\sqrt{g}\rho v^3\right)_{,3} = 0, \tag{17}$$

$$\begin{aligned} \rho\left(v^\alpha_{,\beta} v^\beta + v^\alpha_{,3} v^3 + \Gamma^\alpha_{\beta\gamma}\, v^\gamma v^\beta + \underline{2\Gamma^\alpha_{\beta 3}\, v^\beta v^3}\right) &= \\ = \frac{1}{Re}\left[\left(\mu v^\alpha_{,3}\right)_{,3} + \underline{2\Gamma^\alpha_{\beta 3}\, \mu v^\beta_{,3}} + \underline{\Gamma^\beta_{\beta 3}\, \mu v^\alpha_{,3}}\right] &- \\ - g^{\alpha\beta} p_{,\beta}, \qquad \alpha = 1, 2, & \end{aligned} \tag{18}$$

$$\underline{\Gamma^3_{\beta\gamma}\, \rho v^\beta v^\gamma} = -p_{,3}, \tag{19}$$

$$\begin{aligned} \rho c_p \left(v^\alpha T_{,\alpha} + v^3 T_{,3}\right) &= \\ = Ec\left(v^\alpha p_{,\alpha} + \underline{v^3 p_{,3}}\right) + \frac{Ec}{Re} g_{\alpha\beta}\, \mu v^\alpha_{,3} v^\beta_{,3} &+ \\ + \frac{1}{Pr\, Re}\left[\left(k T_{,3}\right)_{,3} + \underline{\Gamma^\beta_{\beta 3}\, k T_{,3}}\right]. & \end{aligned} \tag{20}$$

These are the continuity equation, the momentum equations in the directions parallel to the wall, the normal momentum equation and the energy equation. Greek sub- and superscripts take the value one or two and refer to the directions tangential to the wall. $\rho, v^\alpha, v^3, p, T$ are density, contravariant components of the velocity vector, pressure and temperature. Re, Pr, Ec, c_p, μ and k are the Reynolds-, Prandtl- and Eckert-number, specific heat at constant pressure, viscosity and heat conductivity. $\sqrt{g}, \Gamma^\alpha_{\beta\gamma}, g^{\alpha\beta}, g_{\alpha\beta}$ are metric and curvature properties [5]. The terms underlined in the above equations are curvature terms which vanish in first order theory.

At solid walls the same boundary conditions have to be imposed as for the Navier Stokes equations. At the outer edge, the boundary layer has to be matched with the inviscid flow such that second-order effects are included. The only way to achieve this second-order matching is to merge the boundary layer and the external flow at the boundary-layer outer edge, i.e. the velocity coordinates, the pressure and the temperature are set equal to those of the external flow there. This is in contrast to first order theory, where the inviscid flow variables are taken from the wall.

In addition to curvature, the displacement effect of the boundary layer is an important second-order effect. The effective thickening of the body due to the mass flow deficit resulting from viscous effects can be modelled either by modifying the original surface by the displacement thickness or by imposing a distribution of equivalent sources on the original surface to make the displaced surface a stream surface of the equivalent inviscid flow [6]. When the boundary layer flow is known, the corresponding inviscid sources can be calculated [5].

Coupling the inviscid and the boundary layer calculation is thus performed in the following sequence [5]:

- purely inviscid flow calculation with slip at the wall
- boundary layer calculation, including the effect of surface curvature
- calculation of the inviscid sources distribution
- inviscid flow calculation with wall outflow condition
- second boundary-layer calculation with new outer edge boundary conditions matched with the new inviscid flow solution.

2.3 Thermodynamic and transport properties

To close the equations presented in the preceeding chapters the thermodynamic and transport properties of the fluid have to be specified.

For air at moderate Mach numbers the equation of state for perfect gas can be used. In addition, the Sutherland law expresses the viscosity as a function of the temperature and the assumption of constant Prandtl number for the heat conductivity can be employed.

In many cases of practical interest, however, the assumption of perfect gas does not hold due to high temperatures at least in some regions of the flow field [4]. In the general case different degrees of freedom of the molecules can be excited and chemical reactions may occur. These effects lead to an energy consumption decreasing the temperatures and thus the heat loads at the vehicle. For estimating the importance of these effects, the first Damköhler number [7],

$$Da_1 = \frac{t_{flow}}{\tau_{reac}} , \tag{21}$$

can be used, where t_{flow} is a typical residence time of the flow and τ_{reac} is a typical relaxation time of a process. The influence of the reactions on the flow can be classified as follows:

$$\begin{array}{cccll} Da_1 & \rightarrow & 0 & \forall Da_1 & : \text{frozen flow}, \\ 10^{-3} & < & Da_1 & < 10^3 & : \text{non-equilibrium flow}, \\ Da_1 & \rightarrow & \infty & \forall Da_1 & : \text{equilibrium flow}. \end{array}$$

For frozen flow, the influence of chemical reactions and excitation of internal degrees of freedom is vanishing. Thus, a usual perfect gas method can be applied. If necessary, the thermodynamic and transport properties have to be adapted for frozen flow where the gas is not air.

For the calculation of non equilibrium flow a variety of models exist depending on the type of gas in consideration, the chemical reactions involved and other parameters. The description of this modelling is beyond the scope of this paper. Details and further references can be found in [4].

Considering equilibrium flow both the composition of the mixture and the thermodynamic and transport properties are determined by two independent thermodynamic variables. This is the consequence of the fact, that the chemical reactions are so fast, that typical relaxation times are orders of magnitude smaller than typical residence times. Thus, equilibrium is reached at each point and the composition is described by the equilibrium constants. For the calculation of the composition, a procedure minimizing the Gibbs free energy is appropriate. To determine the thermodynamic properties an interpolation procedure is used for the state surfaces based on a bicubic polynomial as basis function [4].

The piecewise bicubic representation is necessary to obtain the required accuracy, because the state surfaces in general show complex shapes. Using appropriate boundary conditions at the edge of each of the intervals, a smooth, twice differentiable state surface is obtained which is of great importance especially for the evaluation of the partial derivatives needed in most viscous and inviscid methods. They are calculated easily by the analytic derivative with respect to the parameters chosen. In order to achieve a high vectorization degree the location points for the surfaces to be build are spaced equidistantly in the computational domain. For several thermodynamic quantities the coefficients have been determined for the parameters internal energy and density (e, ρ) and temperature and pressure (T, p), see [8]. The same approach is used for the interpolation of the transport properties. For the viscosity and the heat conductivity, there are two sets of coefficients, again for the parameters (e, ρ) and (T, p) [8].

For turbulent flows the Boussinesq approximation is used and effective transport coefficients are introduced. The equations are closed with a model for the turbulent viscosity and the turbulent Prandtl number. For the present investigations the algebraic model of Baldwin and Lomax [9] is used.

3. NUMERICAL METHODS

To solve the equations given in Chapter 2 a group of numerical methods was developed at MBB (Fig. 2). The geometry definition is received from the CAD-system CATIA. The program AEMESH is used for the surface grid generation. The surface grids generated can be used as input for the panel method HISSS or for the space grid generation procedures EUGRID and DOGRID. EUGRID generates H-type grids for the Euler solver EUFLEX. DOGRID, developed by Dornier [10], generates multiblock grids and is used together with the Navier-Stokes solver NSFLEX. For postprocessing both a number of special purpose routines and commercial programs are available.

3.1 Grid generation

Starting point for the grid generation process is the geometry definition received from the CAD-system CATIA. As a first step to generate the surface grid the topology of the space grid (e.g. H-type grid, multiblock grid etc.) has to be defined, since this influences the generation of the surface grid. For this purpose singular lines, lost corners, edges of block boundaries etc. situated on the surface are constructed in CATIA. They separate single parts of the surface grid which represent e.g. one block or coordinate face adjacent to a solid wall and which are referred to further on as patches.

The surface grid definition is then done in the interactive program AEMESH (Fig. 2), which is closely linked to CATIA. It uses exactly the same mathematical representation of surfaces and curves as CATIA since the spline coefficients of the CATIA surface and curve representation are transfered to AEMESH. To generate one patch the desired number of points is distributed along the four sides of it using a suitable clustering. Note that a side of a grid patch can also be degenerated to a point, resulting in a singularity in the metrics there. Between the points an approximate grid is generated by means of different techniques (3D interpolation, 3D Laplace equations, 3D Poisson equations). Since this grid will usually deviate from the input geometry the points are then projected to the original surface. This technique guarantees that the original CATIA geometry is used for the flow calculation. The single patches of the surface grid are then stored together as input for EUGRID, DOGRID or for the panel method HISSS (Fig. 2).

For the generation of the space grid two codes are applied at MBB. EUGRID creates H-type grids for Euler calculations by solution of the Poisson equations and supports the Euler solver EUFLEX. Once the surface grid is defined the generation of the space grid is performed almost automatically. Only few input parameters are necessary to fix the shape of the farfield boundary and the grid spacing near solid walls. Due to the blanking technique applied, see [11], even very complex geometries can be handled without difficulties. The second code, DOGRID [10], was developed by Dornier. It is an interactive program for the generation of multiblock grids and is used together with the NSFLEX Navier Stokes solver. Further details can be found in [10].

3.2 Navier-Stokes code NSFLEX

The method used for the solution of the Navier-Stokes equations is called NSFLEX (Navier-Stokes solver using characteristic flux extrapolation) [12,13]. It is written in finite-volume formulation and solves the time-dependent equations to reach the steady state solution asymtotically. For the time integration an implicit relaxation procedure for the unfactored equations is employed which allows large time steps [13]. In the following only a survey of the method is given. A detailed description can be found for example in [2,12].

Starting point for the time integration is the first order in time discretized implicit form of the Navier-Stokes equations. A Newton method can be constructed for the solution vector at the new time level by linearizing the fluxes about the known time level. The resulting system of equations is discretized and solved approximately at every time step by a point Gauss-Seidel relaxation, see [2]. The *CFL* number is typically about 150 to 200 for moderate Mach numbers and may reduce to lower ones for hypersonic applications. The point Gauss Seidel technique is fully vectorized. The speed-up factor on a Siemens/Fujitsu vector computer is about 25 compared to a scalar run on the same processor.

To evaluate the inviscid fluxes a linear locally one dimensional Riemann problem is solved at each finite-volume face up to third order accurate in the computational space. A hybrid local characteristic (*LC*) and Steger-Warming (*SW*) type scheme is employed, which allows the code to work for a wide range of Mach numbers [14]. Van Albada type sensors are used to detect discontinuities in the solution. Diffusive fluxes at the cell faces are calculated with central differences [13].

At solid walls the boundary conditions described earlier are implemented. At the farfield boundaries non-reflecting boundary conditions are inherent in the code since the code extracts only such information from the boundary which is allowed by the characteristic theory. At outflow boundaries, as long as the flow is supersonic, the code does not need information from downstream. In the part of the viscous regime where the flow is subsonic the solution vector is extrapolated constantly. No unphysical upstream effect of this extrapelation has been observed up to now.

A simple approach to account for equilibrium real gas effects is incorporated which allows the Riemann solver and the left-hand side of the flow solver to stay unchanged. In the inviscid fluxes the ratio of the specific heats appears only in the energy equation. A new total energy e is defined with a reference ratio of specific heats γ which is the freestream γ [14]. Introducing this definition into the energy equation a new source term is obtained. If only steady state solutions are of interest the time derivative of the source term can be set identically to zero. This means that the left-hand side of the energy equation is the perfect gas equation and the real gas influence can be formulated as a source term on the right-hand side. Only a few operations are necessary to calculate the source terms. To account for equilibrium real gas effects in the viscous fluxes additional thermodynamic subroutines for the temperature $T = T(p, \rho)$ and the transport coefficients $\mu = \mu(p, \rho)$, $k = k(p, \rho)$ are necessary. The vectorized curve fits [8] described in Chapter 2 are used for the calculation of these properties. For this reason the computer time for real gas simulations is only about 20 % higher than for perfect gas runs.

NSFLEX is designed to allow the use of arbitrary multiblock meshes. All around each block two dummy cell rows are used. In these cells boundary indicators generated in the grid generation system are stored which control the boundary condition for each cell of the block boundaries separately. It is possible either to specify an adjacent cell in the same or another block or to prescribe solid body, symmetry, singular lines and various inflow and outflow conditions by an identification code. Due to this general treatment of the block boundaries a high amount of flexibility is achieved. For an optimum use of storage a one-dimensional storage technique is employed including indirect addressing, see [15]. A two-dimensional and a quasi-two-dimensional version of the code are inherent in the three-dimensional one, which is achieved by a special technique described in [15].

3.3 Euler code EUFLEX

The Euler code EUFLEX provides in principle similar features for the Euler equations as NSFLEX does for the Navier–Stokes equations except that it supports H-type grids instead of multiblock grid topology. A detailed description of the fundamental numerical procedure can be found in [14,16].

3.4 Boundary-layer code SOBOL

SOBOL (second order boundary layers) is a finite-difference method for the solution of the second-order boundary-layer equations. It includes features specific for hypersonic flows (e.g. air as equilibrium real gas, wall radiation, external vorticity and surface curvature effects [3,17]).

The boundary-layer equations are parabolic and can therefore be numerically solved by a space-marching integration process. The method is based on the use of a set of five numerical schemes with different numerical stability properties. At each sweep in the main marching direction, the sequence of calculation in the crossflow direction is selected by choosing the most appropriate scheme at each normal in order to fulfil the local CFL condition and to optimize the crossflow marching process. The difference schemes used are the second-order accurate zig-zag and rectangular schemes described in [18]. The "double zig-zag" scheme is employed to start the solution in a new plane in the main marching direction. The "left" zig-zag and rectangular schemes are used for marching in the positive crossflow direction. Negative crossflow marching is performed with corresponding "right" schemes.

Along the normals, an implicit discretization procedure is applied. The momentum equations in the directions parallel to the wall and the energy equation are solved simultaneously. The discretized nonlinear algebraic equations are iteratively solved with a Newton method, providing tangential velocity and temperature distributions across the boundary layer. At each iteration, the continuity and normal momentum equations as well as the equations for the properties of the gas are solved to provide the remaining flow variables. The control of the local boundary layer growth is also part of the iterative process. For more details about the solution method see [3].

4. VERIFICATION AND APPLICATIONS

4.1 Euler solutions

As a first verification test case for the EUFLEX code the flow past the NACA 0012 airfoil at free stream conditions $M_\infty = 30$, $\alpha = 20°$ is presented (Fig. 3, [16]). For the calculation a H-type grid was used. Due to the very low numerical viscosity of the Euler method the shock inevitably follows the grid lines (Fig. 3a). Nevertheless the c_p-distribution is very smooth (Fig. 3b) and the total temperature preserving feature of the code is very good (Fig. 3c).

As a second test case the Euler solution for the lower stage of a hypersonic space transport system is compared with windtunnel results. Again a H type grid was used with a total number of 388 000 points for the complete configuration and half of it for symmetric flow conditions. The surface grid used is given in Fig. 4a, [19]. Quite good agreement is achieved between experimental and numerical results with regard to the coefficients of the longitudinal motion (Fig. 4b). For more details see [19].

In Fig. 5 an Euler solution is given for a complete test configuration at subsonic freestream Mach number $M_\infty = 0.4$ and relatively high angle of attack $\alpha = 13.5°$. As can be seen from the streamlines given in Fig. 5a the flow separates at the sharp leading edges, resulting in a region of increased-total pressure loss above the wings (Fig. 5b). Note that separation for the present case is not in contradiction to the inviscid flow model, since the sharp leading edge provides a Kutta condition forcing the flow to leave the surface.

Two samples of internal flow calculation conclude the presentation of the Euler results. Fig. 6, [20], shows the surface grid and the isobars of a symmetry-wall-mounted plug nozzle. Again a H type grid was used. The isobars exhibit considerable deviations from axisymmetric flow. The 2D-twin nozzle Mach number isoplots Fig. 7, [20], reveal good capturing of all major flow phenomena. Sliplines, shocks and expansions are clearly visible.

4.2 Navier-Stokes solutions

To assess the accuracy of the viscous methods for hypersonic conditions the flow past a hyperbola at free stream Mach number $M_\infty = 10.0$ was calculated. Both perfect gas and real gas assumptions were used to verify the pseudo-unsteady real gas ansatz in NSFLEX. In Fig. 8a the upper half of the grid is shown. The mesh is adapted to the solution in the boundary-layer regime and at the bow shock position. The stagnation temperature for perfect gas assumption ($T_{0,analytic} = 4620K$) is recovered quite well in the NSFLEX computation ($T_{0,computed} = 4618.98K$) (Fig. 8b). The real gas body temperature (adiabatic wall) is about half the temperature of the perfect gas calculation for this case. The Mach contours (Fig. 8c) demonstrate the smoothness of the solution, the good shock capturing feature of the method and the considerable differences in the shock standoff distance between the perfect and real gas calculation. Fig. 8d gives results for a computation obtained by a coupling of a completely different shock fitting inviscid method [21] with the second-order boundary-layer method SOBOL [17], see also [22]. The comparison with the NSFLEX results shows quite good agreement.

The viscous hypersonic flow past an analytically defined generic cruise vehicle forebody was numerically analysed in [23,24]. On the grid displayed in Fig. 9a a laminar three-dimensional calculation was performed. The skin friction lines in Fig. 9b indicate an attachment line on the lower side and a primary separation on the upper side. In Fig. 9c the temperature distributions along the lower side found from two-dimensional computations for laminar and turbulent flow, perfect and real gas, adiabatic and radiation adiabatic wall are compared. For all turbulent cases transition was fixed at 10 per cent of the body length. For the cases with radiation the emissivity factor in the radiation boundary condition was set to $\epsilon = 0.85$. Compared to the laminar flow the turbulent case without real gas and radiation yields somewhat higher temperatures. If real gas effects are included a significant reduction of the overall wall temperature is observed. The application of radiation boundary conditions finally reduces the temperatures again considerably. A more detailed description of the results including c_p– and c_f–distributions can be found in [23].

Results for a shock impinging on a circular cylinder are presented in Fig. 10, [25]. This situation can be present for example at the lip of an intake. Due to the shock/shock–interaction extremely high heat and pressure loads can appear at the surface. According to [26] six types of shock/shock–interaction can be classified, where Type III (Fig. 10a) and IV (Fig. 10b) result in the highest heat and pressure loads. A detailed analysis of the influence of perfect or real gas assumption and heat radiation on the wall temperature and pressure for these two test problems can be found in [25].

An internal viscous flow result is presented for the NASA P8 intake, see [27]. Fig. 11a and b show a sketch of the geometry and the computational grid, which consists of three blocks. In the isobars (Fig. 11c) the reflection of the cowl shock is clearly vissible. The pressure distributions along the centerline of the ramp calculated with different grids and different numerical viscosity are compared with experimental data in Fig. 11d. For a more detailed analysis of the present results with experimental data see [27].

4.3 Boundary–layer solution

Finally a coupled Euler/boundary–layer solution is presented for hypersonic flow past the nose of the Orbiter reentry vehicle (Fig. 12). The surface grid for this calculation is given in Fig. 12a. To generate the inviscid solution the shock fitting method [21] was used. Based on this solution both first and second-order calculations were performed using SOPOL. Fig. 12b shows temperature contours of the second-order boundary–layer solution. The wall temperatures and the skin friction coefficients of the first and second-order calculation are compared in Fig. 12c and d. Due to the improper coupling of the first-order solution to the inviscid flow considerable discrepancies are observed.

5. CONCLUSIONS

A couple of numerical methods developed at MBB were presented, each of them having particular advantages with regard to specific design phases. The importance of a proper choice of the numerical method in order to keep cost and development time as low as possible while retaining the desired accuracy was emphasised. The governing equations were shortly reviewed and the fundamental numerical methods were described. The results selected from industrial applications demonstrate the capabilities of the methods with regard to external and internal flow calculations. Verification of the methods was done by comparison of the results to experimental data and other numerical methods and by analyzing the results with regard to physical considerations.

References

[1] Hirschel, E.H.: *Aerothermodynamics and propulsion integration in the SÄNGER Technology Programme.* AIAA-Paper 91-5041, 1991.

[2] Schmatz, M.A.: *Hypersonic three-dimensional Navier-Stokes calculations for equilibrium air.* AIAA-Paper 89-2183, 1989.

[3] Monnoyer, F., Mundt, Ch., Pfitzner, M.: *Calculation of the hypersonic viscous flow past reentry vehicles with an Euler-boundary layer coupling method.* AIAA-Paper 90-0417, 1990.

[4] Schmatz, M.A., Höld, R.K., Monnoyer, F., Mundt, Ch., Wanie,K.M.: *Numerical methods for aerodynamic design II.* Space Course, Paper No. 62, Aachen, 1991.

[5] Monnoyer, F.: *The effect of surface curvature on three-dimensional, laminar boundary layers.* PhD Thesis, Université libre de Bruxelles, 1985.

[6] Lighthill, M.J.: *On displacement thickness.* J. Fluid Mech. Vol. 4, 1958, pp. 383-392.

[7] Damköhler, G.: Zeitschrift f. Elektrochemie, vol.42., p.846, 1936.

[8] Mundt, Ch., Keraus, R., Fischer, J.: *New, accurate, vectorized approximations of state surfaces for the thermodynamic and transport properties of equilibrium air.* Z. Flugwiss. Weltraumforsch. 15, 1991, pp. 179-184.

[9] Baldwin, B.S., Lomax, H.: *Thin layer approximation and algebraic model for separated flow.* AIAA-Paper 78-257, 1987.

[10] Seibert, W.: *A graphic-interactive program-system to generate composit grids for general configurations.* The Second International Conference on Numerical Grid Generation in Computational Fluid Dynamics, Florida, 1988.

[11] Heiß, S., Eberle, A., Paul, W.: *Application of the Euler method EUFLEX to a fighter–type airplane configuration at transonic speeds.* AIAA-Paper 92–2620, 1992.

[12] Schmatz, M.A.: *NSFLEX - An implicit relaxation method for the Navier- Stokes equations for a wide range of Mach numbers.* Hackbusch, W., Rannacher, R. (eds): Proc. 5th GAMM-Seminar 'Numerical treatment of the Navier-Stokes equations', NNFM Vol. 30, Vieweg, 1989.

[13] Schmatz, M.A.: *Three-dimensional viscous flow simulations using an implicit relaxation scheme.* Kordulla, W. (ed.): Numerical simulation of compressible viscous-flow aerodynamics. NNFM Vol. 22, Vieweg, 1988, pp. 226-242.

[14] Eberle, A.: *Characteristic flux averaging approach to the solution of Euler's equations.* VKI lecture series, Computational fluid dynamics, 1987-04, 1987.

[15] Wanie, K.M., Schmatz, M.A.: *Implementation and application of the multiblock NSFLEX Navier-Stokes solver* 2nd Int. Conf. ASE 1991, Boston, 1991.

[16] Eberle, A., Schmatz, M.A., Bissinger, N.: *Generalized fluxvectors for hypersonic shock capturing.* AIAA-paper 90-0390, 1990.

[17] Monnoyer, F.: *Calculation of three-dimensional attached viscous flow on general configurations using second-order boundary layer theory.* Z. Flugwiss. Weltraumforsch. 14, 1990, pp. 95-108.

[18] Krause, E., Hirschel, E.H., Bothmann, T.: *Die numerische Integration der Bewegungsgleichungen dreidimensionaler laminarer kompressibler Grenzschichten.* DGLR-Fachbuchreihe, Bd. 3, Braunschweig, 1969, pp. 3-1 to 3-49.

[19] Heiß, S.: *Computation of the aerodynamic forces and moment coefficients for the SÄNGER windtunnel model.* MBB-HYPAC-TN-2080, 1991.

[20] Eberle, A: *Enhanced numerical inviscid and viscous fluxes for cell centered finite volume schemes.* Fourth International Symosium on Computational Fluid Dynamics, Davis, 1991.

[21] Pfitzner, M., Weiland, C.: *3D Euler solutions for hypersonic Mach numbers.* AGARD-CP 428, Paper 22, 1987.

[22] Mundt, Ch., Pfitzner, M., Schmatz, M.A.: *Calculation of viscous hypersonic flows using a close coupled Euler, second-order boundary layer method.* Proc. 8th GAMM-Conf. Num. Meth. in Fl. Mech., NNFM, Vieweg, Braunschweig, 1989.

[23] Wanie, K.M., Schmatz, M.A.: *Numerical analysis of viscous hypersonic flow past a generic forebody.* ICAS-Paper 90-6.7.2, 1990.

[24] Wanie, K.M., Schmatz, M.A.: *Verification and application of the NSFLEX method for hypersonic flow conditions.* 1st European Symposium Aerothermodynamics, ESTEC, 1991.

[25] Hainfellner, M.: *Numerische Untersuchung zur Wechselwirkung eines einfallenden schrägen Verdichtungsstoßes mit dem abgehobenen Stoß eines stumpfen Körpers.* Lehrstuhl für Strömungsmechanik, TU München, LSM 91/73, 1991.

[26] Edney, B.E.: *Anomalous heat transfer and pressure distributions on blunt bodies at hypersonic speeds in the presence of an impinging shock.* The Aeronautical Research Institute of Sweeden, FFA Rept. 115, 1968.

[27] Brenneis, A., Wanie, K.M: *Navier-Stokes results for hypersonic inlet flows.* AIAA-Paper 91-2472, 1991.

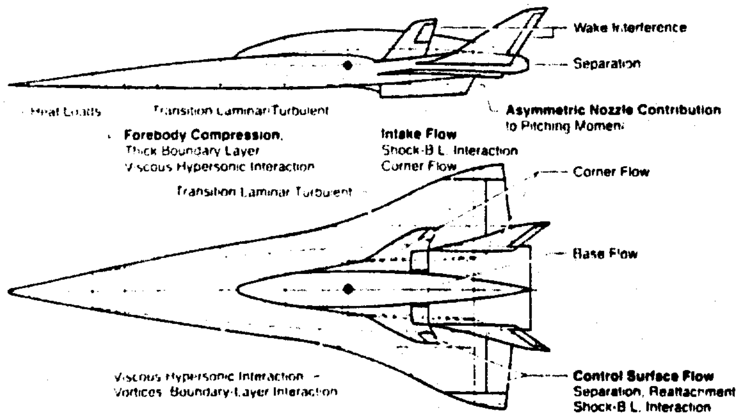
Wake Interference
Separation
Heat Loads
Transition Laminar/Turbulent
Asymmetric Nozzle Contribution
to Pitching Moment
Forebody Compression,
Thick Boundary Layer
Viscous Hypersonic Interaction
Intake Flow
Shock-B L. Interaction
Corner Flow
Corner Flow
Transition Laminar Turbulent
Base Flow
Viscous Hypersonic Interaction
Vortices Boundary-Layer Interaction
Control Surface Flow
Separation, Reattachment
Shock-B L. Interaction

Figure 1: Major aerothermodynamic features of a space-transporation system (schematically)

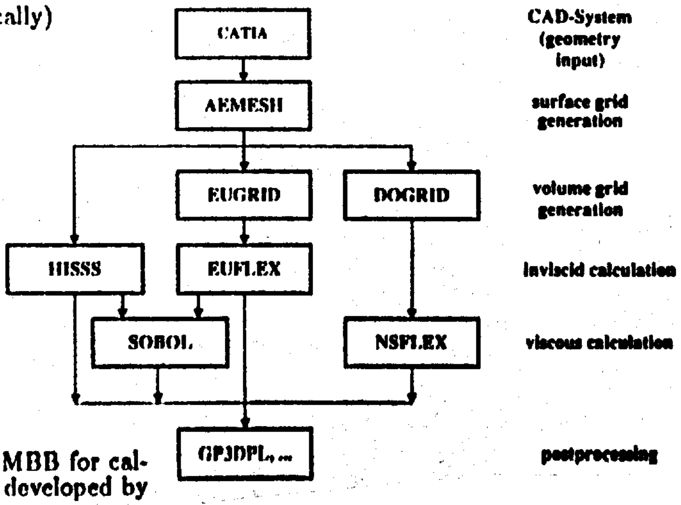
CATIA
CAD-System (geometry input)
AEMESH
surface grid generation
EUGRID
DOGRID
volume grid generation
HISSS
EUFLEX
inviscid calculation
SOBOL
NSFLEX
viscous calculation
GP3DPL,...
postprocessing

Figure 2: Numerical methods used at MBB for calculation of hypersonic flow (DOGRID developed by Dornier)

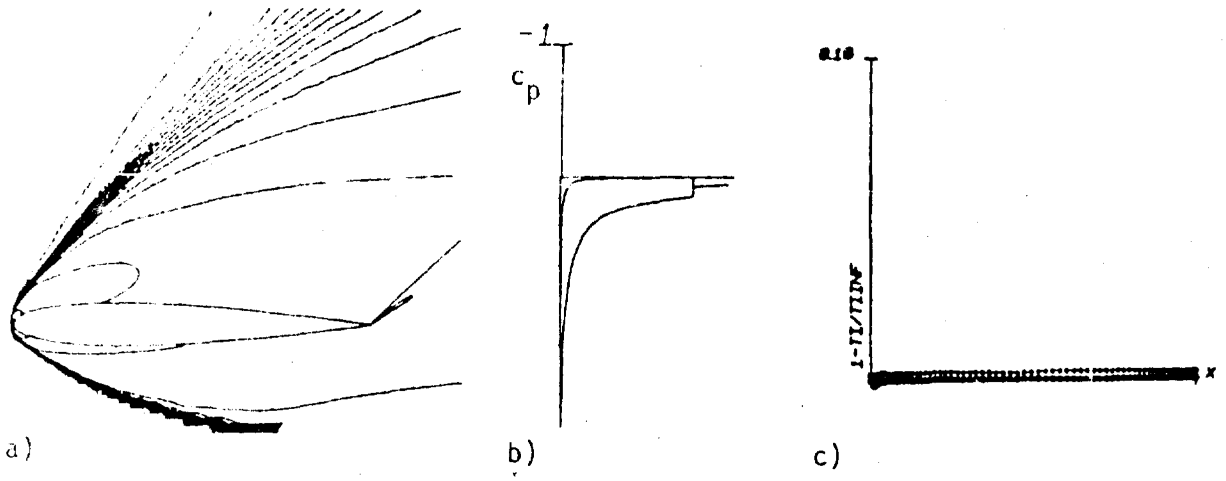

Figure 3: Euler solution for hypersonic flow past the NACA 0012 airfoil ($M_\infty = 30$, $\alpha = 20°$, perfect gas); a) Mach contours; b) c_p-distribution; c) total temperature loss

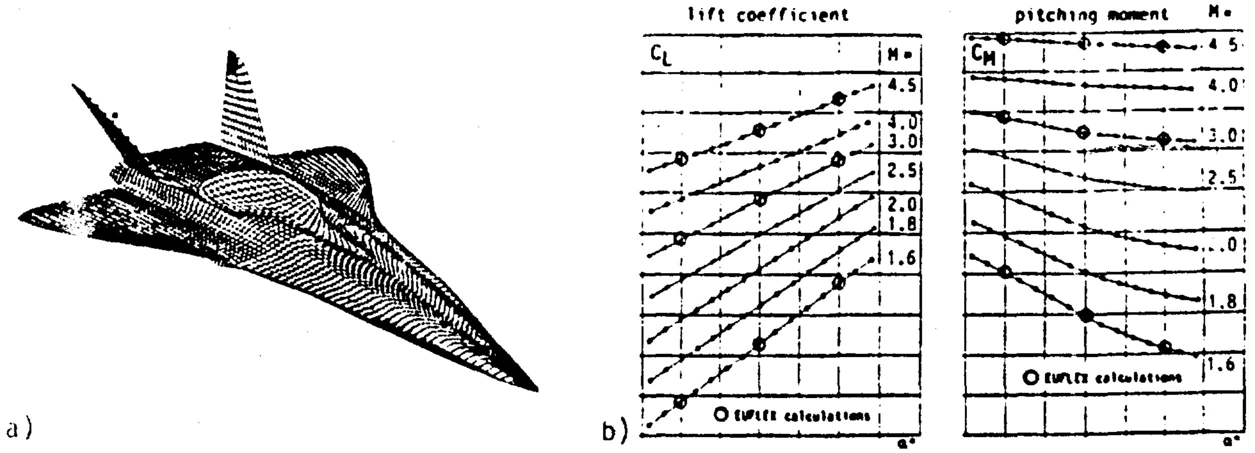

Figure 4: Comparison of Euler solution for lower stage of hypersonic cruise vehicle with windtunnel results; a) surface grid; b) lift coefficient and pitching moment

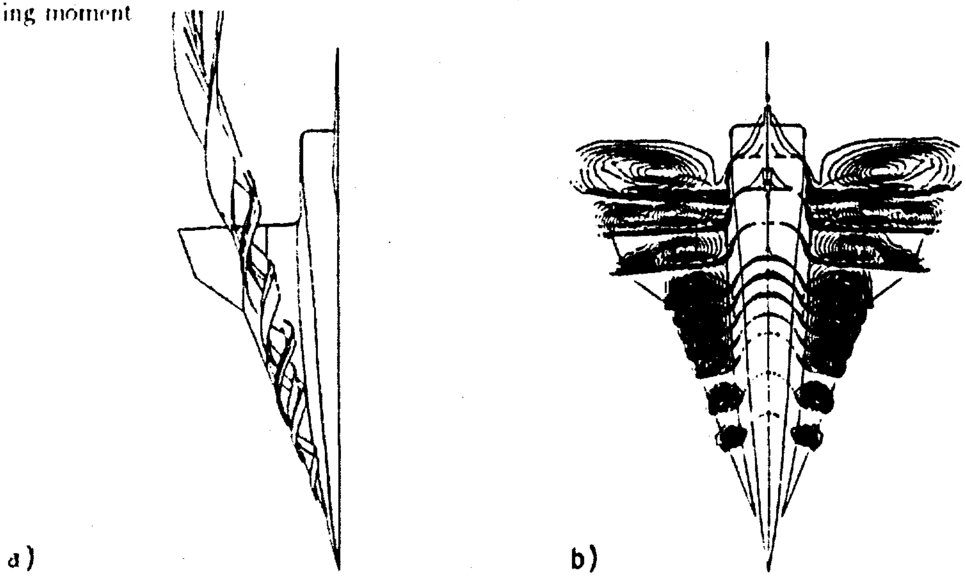

Figure 5: Euler solution for the determination of aerodynamic properties and loads; a) inviscid streamlines emanating from the sharp wing leading edges; b) total-pressure loss contours

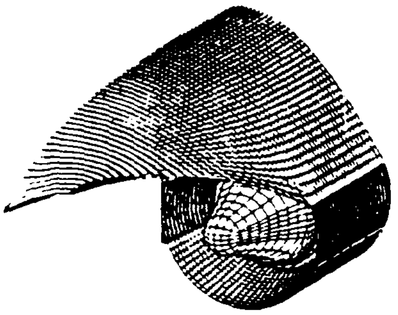

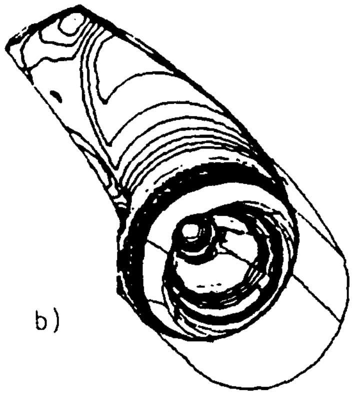

Figure 6: Euler solution for a symmetry-wall-mounted plug nozzle; a) surface grid; b) isobars

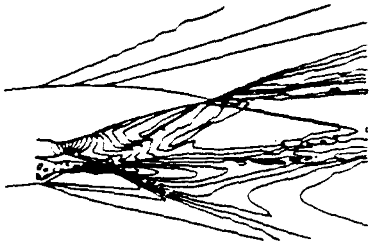

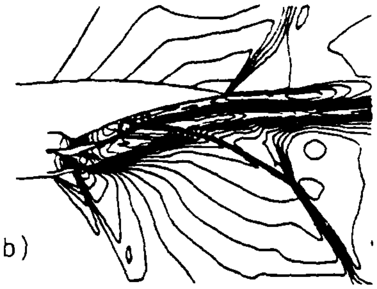

Figure 7: Euler solution for a 2D-twin-nozzle, Mach contours; a) $M_\infty = 3.5$; b) $M_\infty = 1.2$

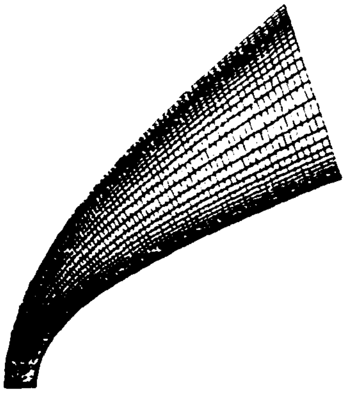

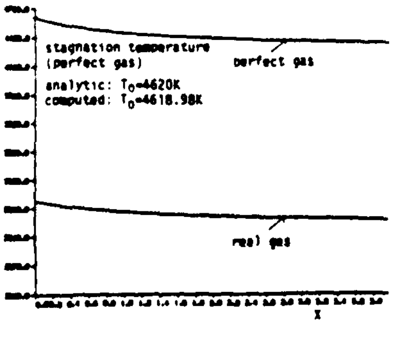

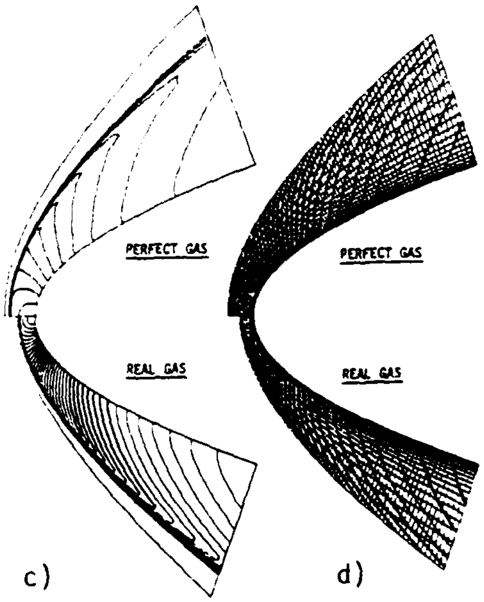

Figure 8: Viscous calculation, hyperbola flow (M_∞ = 10, Re/m = 1,600,000, α = 0°, perfect gas); a) computational grid, Navier-Stokes solution (240 x 50 cells); b) temperature distribution along body, NSFLEX; c) isobars, NSFLEX; d) isobars, coupled Euler/boundary-layer method

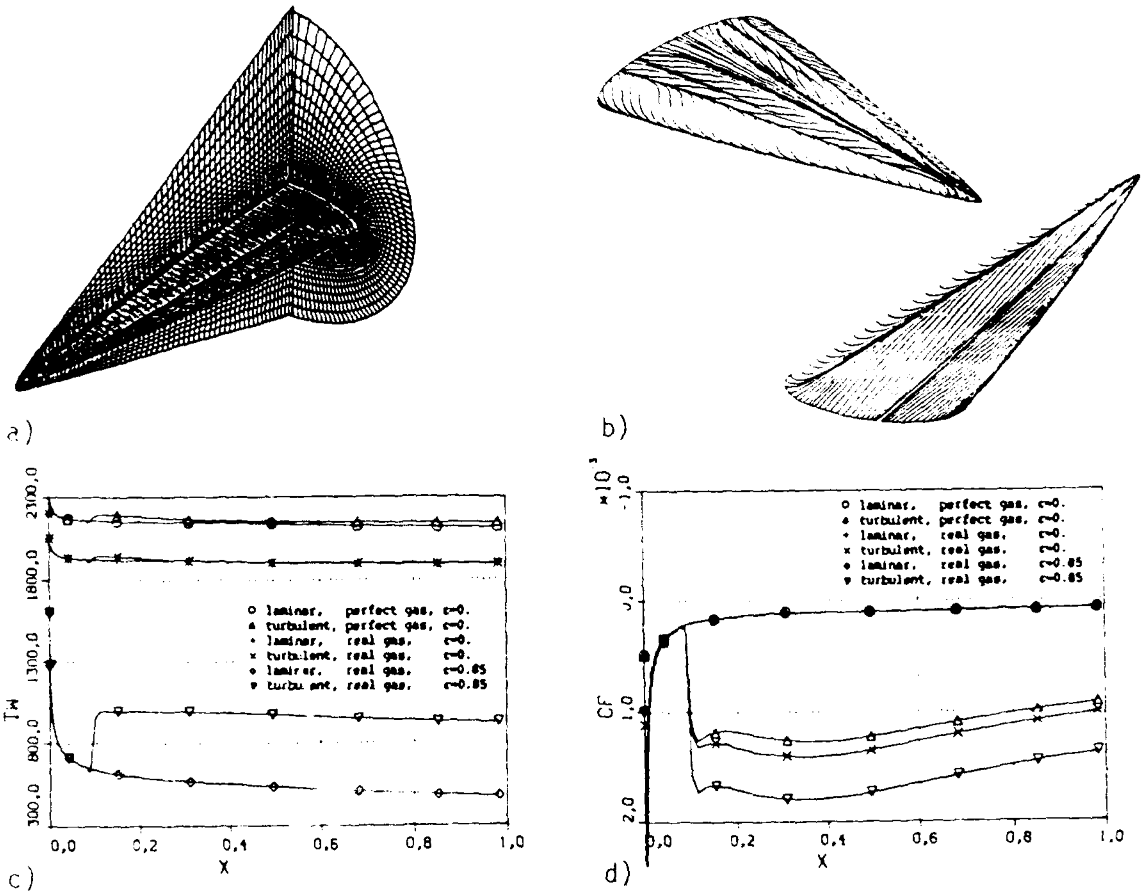

Figure 9: Generic hypersonic forebody calculation ($M_\infty = 6.8$, $\alpha = 6°$, $Re = 1.22\times10^8$, $T_\infty = 227.65K$, laminar) a) computational grid ($75\times70\times64$ cells); b) skin friction lines, lower and upper side; c) temperature distributions (2D calculation); d) skin friction distributions (2D calculation)

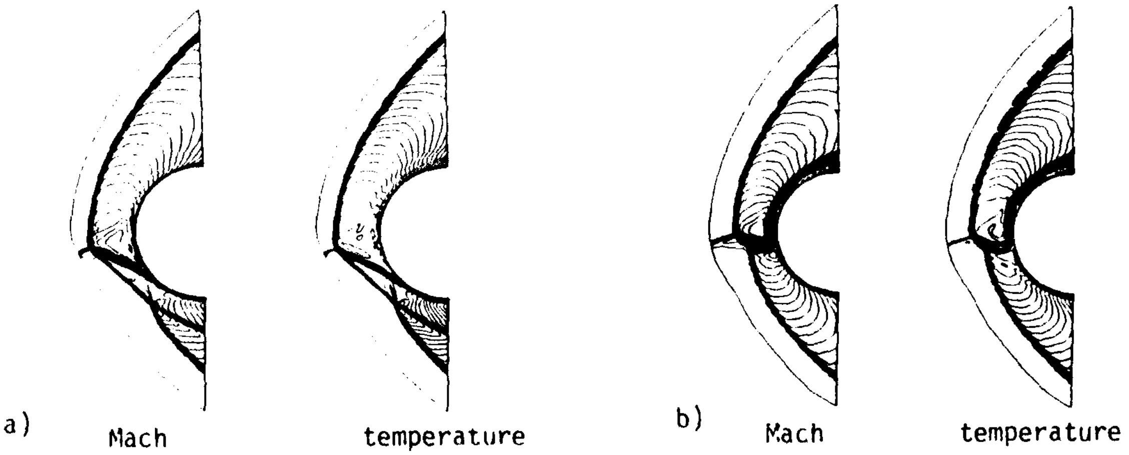

Figure 10: Navier-Stokes calculation of hypersonic flow past a circular cylinder with impinging shock ($M_\infty = 4.6$, $Re/m = 4.4 \times 10^6$, $\epsilon = 0.85$ real gas, laminar) a) interaction type III; b) interaction type IV

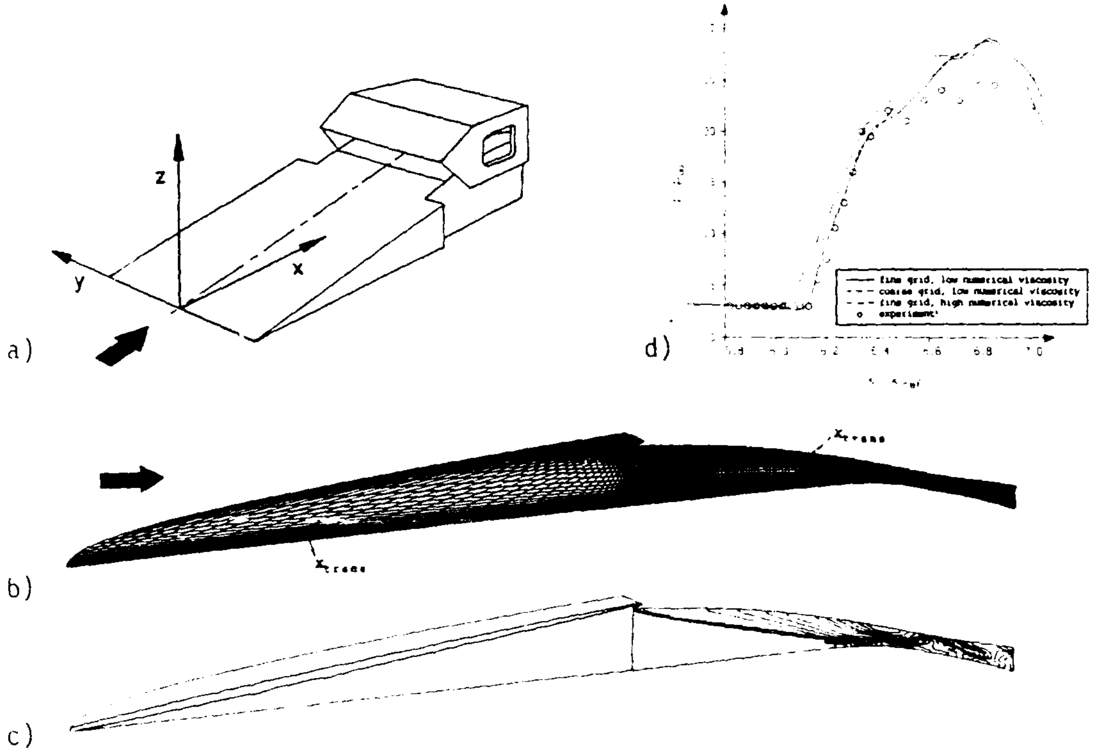
z
y
x
a)
d)
fine grid, low numerical viscosity
coarse grid, low numerical viscosity
fine grid, high numerical viscosity
experiment
x_{trans}
b)
c)

Figure 11: Navier-Stokes calculation. NASA P8 intake ($M_\infty = 7.4$, $Re/m = 8.86 \times 10^6$); a) sketch of geometry; b) computational grid; c) isobars; d) pressure distribution along centerline of the ramp

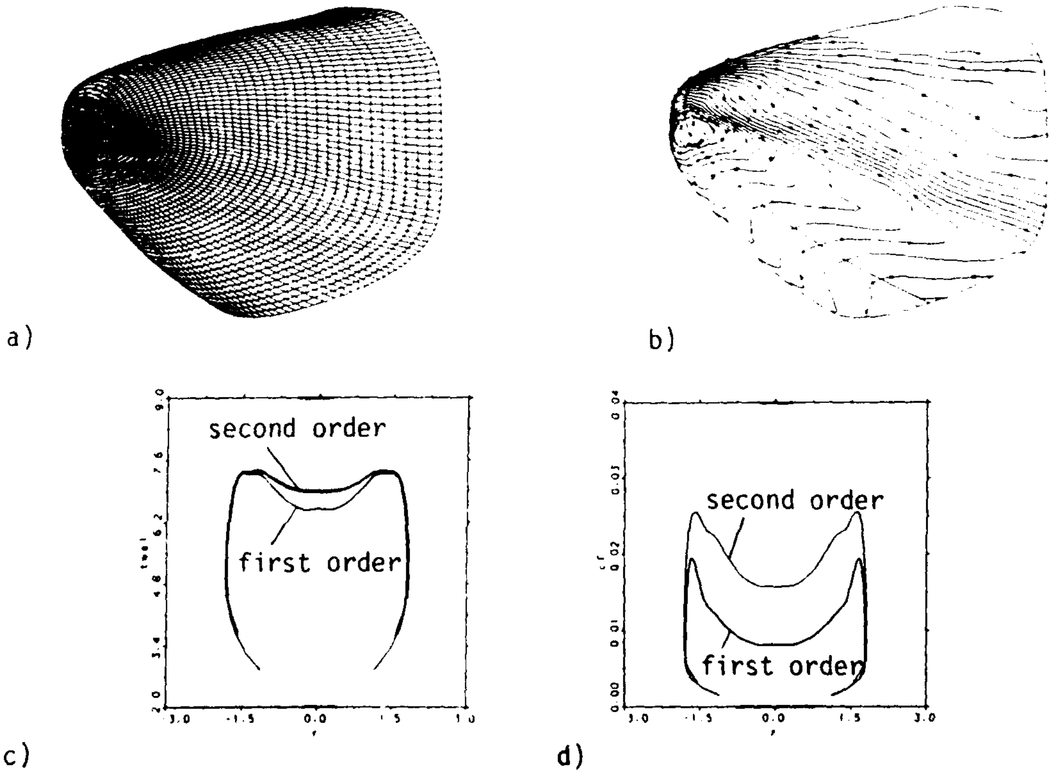

Figure 12. Coupled Euler/boundary-layer calculation, reentry vehicle ($M_\infty = 25.6$, $h = 75km$) a) computational grid; b) temperature contours; c) wall temperature distribution d) skin friction distribution

Hypersonic Multi Block Flow Simulations Around Space Vehicles including Non-Equilibrium Chemistry.

J.B. Vos
Hydraulic Machines and Fluid Mechanics Institute (IMHEF), Swiss Federal Institute of Technology - Lausanne (EPFL),
1015 Lausanne, Switzerland

A.W. Rizzi
The Aeronautical Research Institute of Sweden (FFA), P.O. Box 11021, 16111 Bromma, Sweden

C.M. Bergman
Centre for Computational Mathematics and Mechanics (C2M2), The Royal Institute of Technology (KTH),
10044 Stockholm, Sweden

1. SUMMARY.

An international collaboration on the development of multi block flow solvers using structured grids is presented. The flow equations are solved by the finite volume method using a space centered, explicit time marching scheme augmented by artificial dissipation terms. Implicit residual smoothing is used to accelerate convergence to steady state.

The multi block flow solvers are written on top of the MEM-COM data base system which provides the data structure, and use a Dynamic Memory Manager to allocate the necessary storage for each block. The Euler solver EULMB can be used to simulate hypersonic flows including equilibrium and non-equilibrium air chemistry. Recently the Euler solver has been extended to solve the Navier Stokes equations for laminar caloric perfect gas flows (NSMB flow solver).

Calculated results for the calculation of the flow over a double ellipsoid and over the HERMES space shuttle are presented. The inviscid calculations around HERMES showed that if one is only interested in the aerodynamic coefficients, equilibrium air calculations are sufficient.

Parallel computations showed that the communication overhead between blocks is less than 0.5%, showing that the multi block concept is very promising for using parallel computers efficiently.

2. INTRODUCTION.

Hypersonic flows are characterized as high speed flows in which physical processes, like the dissociation of air and radiative heat transfer, are important. These processes are triggered by strong shock waves present in the flow field around vehicles flying at hypersonic speeds.

The aerothermodynamics design of modern and efficient space planes like HERMES, NASP and SÄNGER must use the most advanced computational and experimental techniques currently available. This is particularly true at flight conditions when air chemistry becomes important, because the ground based testing is difficult and the designer is forced to rely even more on his computational tools. To be really useful these tools must: 1) represent the geometry of a realistic configuration, 2) predict shock wave positions and interactions, vortex phenomena, flow separation, and local heating effects, 3) model the air chemistry, either equilibrium or non-equilibrium, and its effects on item 2, and 4) have reasonable run times on either a supercomputer or a parallel computer.

IMHEF/EPFL, FFA and C2M2/KTH carry out a joint project on the development of multi block flow solvers that meets the four above requirements. It is multi block to treat complex geometries, it incorporates equilibrium and non-equilibrium air chemistry, and it uses efficiently parallel computers. The principal interest of IMHEF/EPFL and FFA in this project is the simulation of complex flows around realistic configurations. The main interest of C2M2/KTH is to develop and explore algorithms for parallel computers.

3. GOVERNING EQUATIONS.

The Navier Stokes equations written in Cartesian coordinates for chemical non-equilibrium flows are written in conservative form as

$$\frac{\partial}{\partial t}\mathbf{w}+\frac{\partial}{\partial x}\left(\mathbf{F}(\mathbf{w})-\mathbf{F}_v(\mathbf{w})\right)+\frac{\partial}{\partial y}\left(\mathbf{G}(\mathbf{w})-\mathbf{G}_v(\mathbf{w})\right)+$$

$$\frac{\partial}{\partial z}\left(\mathbf{H}(\mathbf{w})-\mathbf{H}_v(\mathbf{w})\right)=\mathbf{S}(\mathbf{w}) \qquad (1)$$

The state vector **w** is given by

$$\mathbf{w}=\begin{pmatrix}\rho\\ \rho u\\ \rho v\\ \rho w\\ \rho E\\ \rho_s\end{pmatrix} \qquad (2)$$

and the inviscid flux vectors **F**, **G** and **H** are calculated from

$$\mathbf{F}(\mathbf{w})=\begin{pmatrix}\rho u\\ \rho u^2+p\\ \rho uv\\ \rho uw\\ u(\rho E+p)\\ \rho_s u\end{pmatrix},\ \mathbf{G}(\mathbf{w})=\begin{pmatrix}\rho v\\ \rho uv\\ \rho v^2+p\\ \rho vw\\ v(\rho E+p)\\ \rho_s v\end{pmatrix},\ \mathbf{H}(\mathbf{w})=\begin{pmatrix}\rho w\\ \rho uw\\ \rho vw\\ \rho w^2+p\\ w(\rho E+p)\\ \rho_s w\end{pmatrix} \qquad (3)$$

In the equations above, ρ denotes the density, u, v and w the cartesian velocity components, E the total energy, p the pressure and ρ_s the partial density of species s. The equations for the partial densities are only solved for inviscid chemical non-equilibrium flows.

For caloric perfect gas flows, the viscous flux vectors $\mathbf{F_v}$, $\mathbf{G_v}$ and $\mathbf{H_v}$ state

$$\mathbf{F_v(w)} = \begin{pmatrix} 0 \\ \tau_{xx} \\ \tau_{xy} \\ \tau_{xz} \\ \phi_x - q_x \end{pmatrix}, \mathbf{G_v(w)} = \begin{pmatrix} 0 \\ \tau_{yx} \\ \tau_{yy} \\ \tau_{yz} \\ \phi_y - q_y \end{pmatrix}, \mathbf{H_v(w)} = \begin{pmatrix} 0 \\ \tau_{zx} \\ \tau_{zy} \\ \tau_{zz} \\ \phi_z - q_z \end{pmatrix} \quad (4)$$

where the components of the *shear stress tensor* τ, the heat flux vector q and the viscous dissipation ϕ equal

$$\tau_{xx} = \frac{2}{3}\mu\left(2\frac{\partial u}{\partial x} - \frac{\partial v}{\partial y} - \frac{\partial w}{\partial z}\right) \qquad \tau_{xy} = \tau_{yx} = \mu\left(\frac{\partial u}{\partial y} + \frac{\partial v}{\partial x}\right)$$

$$\tau_{yy} = \frac{2}{3}\mu\left(-\frac{\partial u}{\partial x} + 2\frac{\partial v}{\partial y} - \frac{\partial w}{\partial z}\right) \qquad \tau_{xz} = \tau_{zx} = \mu\left(\frac{\partial u}{\partial z} + \frac{\partial w}{\partial x}\right)$$

$$\tau_{yy} = \frac{2}{3}\mu\left(-\frac{\partial u}{\partial x} - \frac{\partial v}{\partial y} + 2\frac{\partial w}{\partial z}\right) \qquad \tau_{yz} = \tau_{zy} = \mu\left(\frac{\partial v}{\partial z} + \frac{\partial w}{\partial y}\right)$$

$$q_x = -k\frac{\partial T}{\partial x} \qquad q_y = -k\frac{\partial T}{\partial y} \qquad q_z = -k\frac{\partial T}{\partial z}$$

$$\phi_x = \tau_{xx}u + \tau_{xy}v + \tau_{xz}w \qquad \phi_y = \tau_{yx}u + \tau_{yy}v + \tau_{yz}w$$

$$\phi_z = \tau_{zx}u + \tau_{zy}v + \tau_{zz}w$$

where T represents the temperature. The viscosity μ is assumed to be constant or is calculated from Sutherland's law; the thermal conductivity k is in both cases calculated from the *Prandtl number* Pr,

$$k = \frac{\mu c_p}{Pr}$$

where c_p is the specific heat at constant pressure.

The chemical source term $S(\mathbf{w})$ is written as

$$\mathbf{S(w)} = \begin{pmatrix} 0 \\ 0 \\ 0 \\ 0 \\ 0 \\ \dot{\omega}_s \end{pmatrix} \quad (5)$$

where the source term $\dot{\omega}_s$ *represents* the net production rate of species s by chemical reactions, see Section 4.

The system of equations is closed by the relation between the total energy E and the internal energy e,

$$e(\rho_s, T) = E - \frac{1}{2}\left(u^2 + v^2 + w^2\right) \quad (6)$$

and by the *equation of state*, which relates the pressure to the temperature and partial densities

$$p = R^\circ T \sum_s \frac{\rho_s}{M_s} \quad (7)$$

In this equation R° is the universal gas constant and M_s the molar mass of species s. Note that the sum of the partial densities equals the density ρ.

4. AIR CHEMISTRY MODELLING.

4.1. Introduction.

Both equilibrium and non-equilibrium air chemistry have been implemented in the Euler solver EULMB. It has been assumed that air consists of 5 chemical species, respectively the molecules N_2, O_2 and NO and the atoms O and N. This assumption is valid for temperatures below 9000 K, where ionization processes have not become important yet. A second assumption is that air can be treated as a mixture of perfect gases. This implies that intermolecular forces between the particles are neglected, which is a valid assumption when simulating hypersonic flows with a continuum approximation.

4.2. Equilibrium Chemistry.

For flows in chemical equilibrium, no partial differential equations for the partial densities need to be solved, and the Euler equations are the same as for caloric perfect gas flows. The effects of equilibrium chemistry appear in the equation of state, which relates the pressure to the internal energy and the density.

There exist several methods to account for the effects of equilibrium air chemistry, and in a previous study (ref. 1) it was found that a method based on the calculation of the equilibrium composition and equilibrium temperature was computationally the most efficient.

The calculation of the equilibrium air composition for the five species air model requires the solution of five algebraic equations. Of the five species, two are elements (N_2 and O_2) which are conserved under chemical reactions. This means that only three equilibrium reaction equations need to be considered, and these are the reactions in which a chemical species (NO, N and O) is formed from its elements. These *equations, often* called the "laws of mass action" (ref. 2) state:

$$\frac{1}{2}O_2 \leftrightarrow O: \qquad \left(\frac{\rho_O}{M_O}\right)\left(\frac{\rho_{O_2}}{M_{O_2}}\right)^{-\frac{1}{2}} = K_{C,1}$$

$$\frac{1}{2}N_2 \leftrightarrow N: \qquad \left(\frac{\rho_N}{M_N}\right)\left(\frac{\rho_{N_2}}{M_{N_2}}\right)^{-\frac{1}{2}} = K_{C,2} \quad (8)$$

$$\frac{1}{2}O_2 + \frac{1}{2}N_2 \leftrightarrow NO: \quad \left(\frac{\rho_{NO}}{M_{NO}}\right)\left(\frac{\rho_{O_2}}{M_{O_2}}\right)^{-\frac{1}{2}}\left(\frac{\rho_{N_2}}{M_{N_2}}\right)^{-\frac{1}{2}} = K_{C,3}$$

The equilibrium constants K_C are in general exponential functions of the temperature, the latter property related to the internal energy and composition by

$$e = \frac{1}{\rho}\left(\sum_s \rho_s h_s(T) - p\right) \tag{9}$$

The enthalpy of a species, h_s, is a function of the temperature. The equations for the conservation of the elements O_2 and N_2 state respectively

$$\rho_{O_2} + \rho_O + \frac{1}{2}\frac{M_{O_2}}{M_{NO}}\rho_{NO} = \rho Z_{O_2}$$

$$\rho_{N_2} + \rho_N + \frac{1}{2}\frac{M_{N_2}}{M_{NO}}\rho_{NO} = \rho Z_{N_2} \tag{10}$$

where Z is the elemental mass fraction, which for inviscid flows is a constant, equal to its freestream value.

The data given by Park (ref. 3) are used to calculate the equilibrium constants K_C and the enthalpies of the five chemical species.

The system of equations (8)-(10) can be solved by iteration to yield the equilibrium composition and temperature. To save computational costs, an equivalent gamma has been defined as

$$\hat{\gamma} = 1 + \frac{p}{\rho e} = 1 + \frac{R^\circ T}{\rho e}\sum_s \frac{\rho_s}{M_s}$$

and in the computations the pressure is calculated from

$$p = \left(\hat{\gamma} - 1\right)\rho e = \left(\hat{\gamma} - 1\right)\rho\left[E - \frac{1}{2}\left(u^2 + v^2 + w^2\right)\right]$$

This equivalent gamma needs to be recalculated only once per 100 time steps.

4.3. Non-Equilibrium Chemistry.

For flows in chemical non-equilibrium partial density equations describing the mass balance of the different chemical species in the mixture need to be solved. For inviscid flows, the number of partial density equations in Eq. (1) equals the number of species minus the number of elements among these species. For the five species air model, this yields three equations; Eq.(10) is used to find the partial densities of the molecules O_2 and N_2.

The net chemical production rate of a species by chemical reactions, $\dot{\omega}_s$ is calculated as follows. Consider the general system of m reversible reactions,

$$\sum_s \nu^a_{s,k} A_s \overset{k_{b,k}}{\underset{k_{f,k}}{\leftrightarrow}} \sum_s \nu^b_{s,k} A_s \qquad k = 1,\dots,m$$

where $k_{f,k}$ and $k_{b,k}$ are respectively the forward and backward reaction rates, and where A_s denotes the chemical symbol of species s. $\nu_{s,k}$ is the stoichiometric coefficient, and the superscripts a and b refer to reactants and products respectively. In standard text books on combustion (ref. 4) it can be found that for this system of chemical reactions, the chemical production rate term can be calculated from

$$\dot{\omega}_s = M_s \sum_{k=1}^{m} (\nu^b_{s,k} - \nu^a_{s,k})\, J_k$$

$$J_k = k_{f,k} \prod_r \left[\frac{\rho_r}{M_r}\right]^{\nu^a_{r,k}} - k_{b,k} \prod_r \left[\frac{\rho_r}{M_r}\right]^{\nu^b_{r,k}}$$

The forward reaction rates are in general given by an Arrhenius equation,

$$k_{f,k} = B_k T^{\alpha_k} \exp\left(-E_k / T\right)$$

where E_k is the activation temperature, and B_k and α_k are constants. The backward reaction rates are often calculated from the equilibrium constant,

$$k_{b,k} = \frac{k_{f,k}}{K_{C,k}}$$

The five species, seventeen reaction model is used to describe the chemistry. This model consists of three dissociation reactions (dissociation of O_2, N_2 and NO) using each of the five chemical species as third body, and of two exchange reactions. Park's data are used to compute the forward reaction rates and the equilibrium constants (ref. 3).

5. NUMERICAL METHOD.

Equation (1) is discretized in space using the finite volume method (ref. 5), resulting in the following system of ordinary differential equations,

$$\frac{d}{dt}(V_{i,j,k}\, w_{i,j,k}) + Q_{i,j,k} - S_{i,j,k} = 0 \tag{11}$$

where $V_{i,j,k}$ is the volume of the cell (i,j,k), and $w_{i,j,k}$ and $S_{i,j,k}$ are approximations of respectively w and S in this cell. $Q_{i,j,k}$ represents the residue of the inviscid and viscous fluxes leaving or entering the cell, which is calculated from

$$\begin{aligned} Q_{i,j,k} = {} & h_{i+1/2,j,k} - h_{i-1/2,j,k} + h_{i,j+1/2,k} - \\ & h_{i,j-1/2,k} + h_{i,j,k+1/2} - h_{i,j,k-1/2} \end{aligned} \tag{12}$$

where

$$h_{i-1/2,j,k} = \int_{i-1/2,j,k} \boldsymbol{H} \cdot \mathbf{n}\, dS = \boldsymbol{H}_{i-1/2,j,k} \cdot \int_{i-1/2,j,k} \mathbf{n}\, dS$$

In this equation, **n** is the surface normal, dS is the surface area and ***H*** the flux tensor $\boldsymbol{H}$=($\mathbf{F}$-$\mathbf{F}_v$, $\mathbf{G}$-$\mathbf{G}_v$, $\mathbf{H}$-$\mathbf{H}_v$). The value of this tensor at the surface i-1/2,j,k is calculated from Eqs. (3) and (4) using the average of the state vectors having this side in common. On a cartesian grid, this results in a scheme that is second order accurate in space.

The velocity and temperature gradients in the shear stress tensor and the heat flux vector respectively, are calculated at a surface using the gradient theorem on a shifted volume.

$$\nabla\phi = \int \nabla\phi \, dV \Big/ \int dV = \frac{1}{Vol}\int \phi \, dS \qquad (13)$$

Figure 1 shows the 2D layout of a part of the grid used for the calculation of the gradients at surfaces in the direction 1,

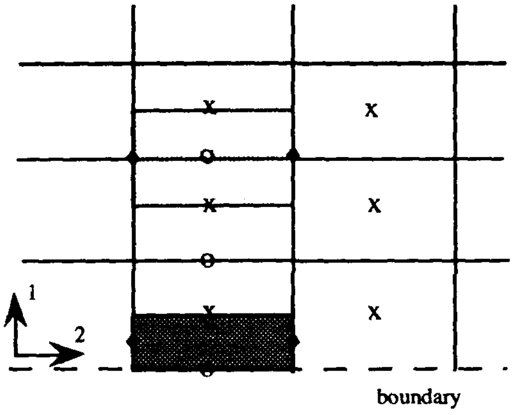

x = cell centers

o = surface center where gradients are calculated

◆ = interpolated value at corners

☐ shifted control volume

▨ half volume at boundary

Figure 1. Layout of a 2D grid system used for the calculation of the gradients in the direction 1.

When integrating Eq. (13) along the shifted control volume, the cell center values are directly available for the direction 1, while for the direction 2, the value of ϕ at the corner points are obtained by averaging the cell center values.

Near boundaries, the shifted volume is reduced to a half volume along which Eq. (13) is integrated. In this way, Dirichlet boundary conditions are imposed directly when calculating the gradients.

Second order accurate schemes permit solutions in the form of a sinus wave, so called spurious or odd/even oscillations, which have to be suppressed by adding a higher order dissipation term. Moreover, second order accurate schemes produce oscillations near shock waves. A second order dissipation term is added to the scheme in the regions of shock waves, making the scheme locally first order. A fourth order dissipation term is added to suppress the odd/even oscillations. After addition of the dissipative terms, Eq. (11) can be written as

$$\frac{d}{dt}(V_{i,j,k}\, w_{i,j,k}) + Q_{i,j,k} - D_{i,j,k} - S_{i,j,k} = 0 \qquad (14)$$

where $D_{i,j,k}$ is the net artificial dissipative flux in cell (i,j,k), which is calculated in a similar way as $Q_{i,j,k}$ by considering fluxes at cell boundaries,

$$D_{i,j,k} = d_{i+1/2,j,k} - d_{i-1/2,j,k} + d_{i,j+1/2,k} - d_{i,j-1/2,k} + d_{i,j,k+1/2} - d_{i,j,k-1/2}$$

The artificial dissipative flux at the cell side (i-1/2,j,k) can be calculated from

$$d_{i-1/2,j,k} = r_{i-1/2,j,k}\, \varepsilon^{(2)}_{i-1/2,j,k} \left(w_{i,j,k} - w_{i-1,j,k} \right) - r_{i-1/2,j,k}\, \varepsilon^{(4)}_{i-1/2,j,k} \left(w_{i+1,j,k} - 3w_{i,j,k} + 3w_{i-1,j,k} - w_{i-2,j,k} \right) \qquad (15)$$

In this equation, r is a scaling factor which relates the dissipative flux to the magnitude of the convective flux through this cell side. This factor is calculated by evaluating the spectral radius of the Jacobian Matrix for the inviscid flux across a cell face (ref. 6). The coefficients $\varepsilon^{(2)}$ and $\varepsilon^{(4)}$ are used to adapt locally the dissipative fluxes, and are calculated as follows. Regions with large pressure gradients are found by calculating the normalized second order pressure gradient,

$$\psi_{i,j,k} = \left| \frac{p_{i+1,j,k} - 2p_{i,j,k} + p_{i-1,j,k}}{p_{i+1,j,k} + 2p_{i,j,k} + p_{i-1,j,k}} \right|$$

From this coefficient, a switch is calculated at the surface of the finite volume cell as the maximum value of ψ at the neighboring cell centers,

$$\nu_{i-1/2,j,k} = \max\left(\psi_{i-1,j,k} , \psi_{i,j,k} \right)$$

From this, the coefficients ε are calculated as

$$\varepsilon^{(2)}_{i-1/2,j,k} = c^{(2)}\, \nu_{i-1/2,j,k}$$

$$\varepsilon^{(4)}_{i-1/2,j,k} = \max\left(0.0 \, , c^{(4)} - \varepsilon^{(2)}_{i-1/2,j,k} \right)$$

where $c^{(2)}$ and $c^{(4)}$ are constants. Typical values used in the calculations presented here are $c^{(2)} = 2.0$, and $c^{(4)} = 0.05$. Note that near shock waves the fourth order dissipation term is switched off, since it generates oscillations in these regions.

Equation (14) is integrated in time using the explicit Runge Kutta scheme (ref. 5). This class of multi stage schemes has proven to give good stability and damping properties. The four and five stage standard Runge Kutta schemes were used here. For the four stage Runge Kutta scheme, the contributions of the viscous and artificial dissipation terms were frozen after the first stage. For the five stage scheme, they were frozen after the second stage.

Since the interest here is only in the steady state solution of Eq. (10), convergence is accelerated by using local time stepping, and by using implicit residual smoothing (ref. 7).

Implementation of non-equilibrium chemistry in the Euler solver was straightforward. Experiences with a 2D Euler solver (ref. 1) have shown that for freestream conditions typical for hypersonic flows, the chemical source term could be treated using the standard Runge Kutta scheme. The (local) time step in the Runge Kutta time integration is now taken as the minimum of the fluid dynamics step and the chemical time step (ref. 8),

$$\Delta t_{chem} = \min \left[\frac{\partial \dot{\omega}_s}{\partial \rho_s}\right]^{-1} \qquad s=1,...,n$$

where n denotes the partial differential equations solved for the partial densities. For the calculations discussed in this paper, it was found that the fluid dynamic's time step always was the smallest.

Test calculations carried out solving partial differential equations for all five species showed that in this case the chemical time step for the O_2 molecules was the smallest, and smaller than the fluid dynamics time step. From this it was concluded that solving partial differential equations only for the species NO, N and O and using the elemental conservation equations for the species O_2 and N_2 reduces the stiffness of the system.

The following boundary conditions were prescribed. At solid walls, the no-slip condition for the velocity field together with an isothermal wall condition for the temperature were applied for viscous flows, while for inviscid flows, the tangency condition was imposed on the velocity field and the pressure at the wall was obtained using linear extrapolation. At outflow and free stream boundaries Riemann invariants were used, and at symmetry boundaries the flux into the computational domain was set to zero. For the block connectivity boundary condition the value of the state vector in the adjacent block was used.

6. PROGRAMME STRUCTURE.

6.1. The MEM-COM data base system.

A flow simulation can be split into several different processes. First, the geometry and the computational domain need to be defined, followed by the generation of the surface meshes. Using these surface meshes, the mesh generator creates a grid. The third process is the solution of the flow equations, and finally, the mesh(es) and the calculated results are visualized and analyzed.

From this description, it is easy to see that output from one process serves as input for other processes, for example the output of the mesh generator is used as input for the flow solver. Data transfer between the processes is in most CFD codes done by means of files. For example, there is a file with the grid system, a file with the flow solution, etc.. With the development of the EULMB and NSMB multi block flow solvers, another strategy has been adopted based on the use of the MEM-COM data base system (ref. 9). MEM-COM is a data management system for memory and memory-to-disk data handling, and offers an easy way to store and retrieve large amounts of data. Data is stored in MEM-COM in two different ways. First, the grid and calculated results are stored block by block in the data base file as long vectors. Second, MEM-COM offers the possibility to store relational tables containing entries in the form keyword + value. The multi block solvers described here use this possibility to describe for each block the mesh and to describe each calculation made (ref. 10).

The main advantage of using the MEM-COM data base system is that all data required for a flow simulation is stored in one single data base file. Exchange of data between the different processes in a flow simulation is done through the data base file. Accessing or modifying data and/or relational tables is simple, and does not require the need to access other data stored. Owing to the possibility to store relational tables, the MEM-COM database file can be saved directly on an archival system since all information necessary to describe the calculation is stored in the data base file.

Finally, MEM-COM incorporates a Dynamic Memory Manager (DMM), which offers the possibility to allocate dynamically the necessary storage of arrays in Fortran programs, and to transfer data from MEM-COM to the flow solver.

6.2. Multi Block Implementation.

From a mathematical point of view and for the numerical scheme used here, there is no difference between a single block and a multi block solver. It is on the level of the incorporation of the boundary conditions that there appears a difference due to the introduction of a block connectivity boundary condition. It should be remarked that in the present version of the multi block solvers, it is assumed that grid lines are continuous across a block interface.

The boundary conditions implementation in the multi block solvers has received special attention to combine a high flexibility and a high computational efficiency. To obtain a high flexibility, each side of a block can be divided into an arbitrary number of windows, each window having a different boundary condition type. To obtain a high computational efficiency, the implementation of the boundary conditions (including the block connectivity boundary condition) is uncoupled from the algorithm used to update the interior points. The concept of boundary arrays and ghost cells (ref. 11) is used to transfer the boundary condition information to the algorithm for the interior points. Two ghost cells are required at each side of the computational domain.

The block connectivity boundary condition is updated only once per time step, while all other boundary conditions are updated each Runge Kutta stage. In this way, it is possible to treat each block in a multi block simulation as if it was a single block calculation (a multi block calculation is seen as multiple single block calculations). Moreover, the communication overhead between blocks is reduced.

Variable storage is allocated block by block using the DMM, which is very suitable for parallel computations on local memory computers, since a block can be directly connected to a processor. On shared memory computers the DMM provides the pointers pointing to the first address of each array.

For multi block calculations using a single processor, EULMB and NSMB contain an option to allocate workspace for the largest block size only. In this way memory is saved and finer grids can be used.

7. CALCULATED RESULTS FOR INVISCID FLOWS.

7.1. The flow around the double ellipsoid.

To test the multi block implementation, the chemical non-equilibrium flow over a double ellipsoid was calculated using a six block mesh having in total 315400 grid cells. The advantage of using a multi block mesh for this type of geometry is that for a single block grid the singular line at the nose may cause numerical problems. This problem is removed when using a multi block grid. The calculation was made with a freestream mach number of 25, and Fig. 2 shows the Mach

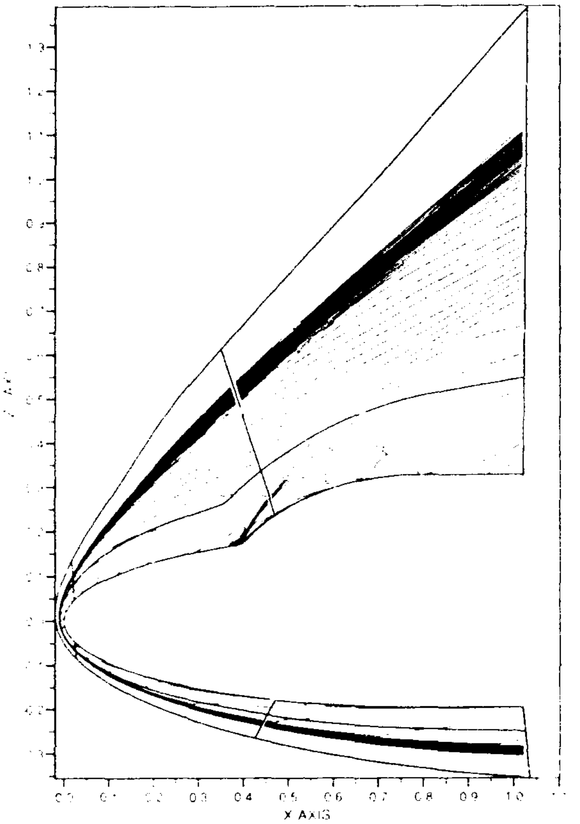

Figure 2. Iso Mach lines in the symmetry plane for the calculation of the chemical non-equilibrium flow over a double ellipoid. $M_\infty = 25$, $p_\infty = 2.52$ Pa, $T_\infty = 205$ K, $\alpha = 30°$.

number isolines in the symmetry plane. As can be seen in this figure, the solver doesn't have problems to treat strong shock waves crossing block boundaries. At the nose of the double ellipsoid, the shock is almost aligned with the block boundary which did not prohibit convergence.

7.2. *The flow over the HERMES space shuttle.*

Single block calculations were carried out for the flow over the HERMES space shuttle with 12° body flap at 76 km. altitude. The freestream Mach number was equal to 25, and calculations were made for a caloric perfect gas, for air at chemical equilibrium, and for air at chemical non-equilibrium.

Three different grid systems were used, and Fig. 3 shows the calculated temperature contours along the body in the symmetry plane for the non-equilibrium calculation on these grids. As can be seen in this figure, the temperatures for the three grids are the same at the windward side of the body, except close to the body flap where the jump in temperature for the coarsest grid is smeared out compared to the other two grids. At the leeward side of the body, the temperature for the coarsest grid differs considerably from the temperatures obtained with the other two grids, and it is concluded that the medium and fine grid give similar results.

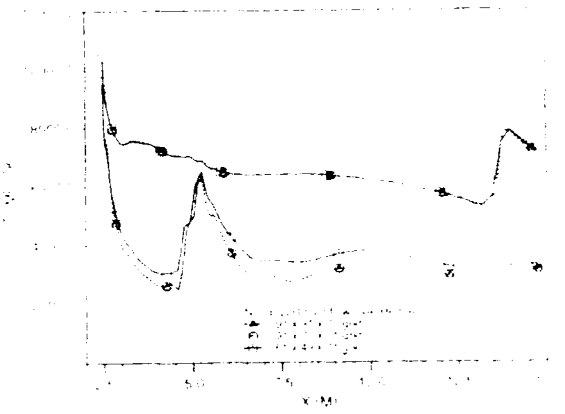

Figure 3. Temperature along the body in the symmetry plane for the chemical non-equilibrium calculation of the flow around HERMES. $M_\infty = 25$, $p_\infty = 2.14$ Pa, $T_\infty = 202$ K, $\alpha = 30°$.

Figure 4 shows the convergence history for the chemical non-equilibrium calculation on the 91x75x71 grid. This calculation was started from an interpolated solution of the 61x49x71 grid. Both the L2-residue and the maximum residue are normalized with the residue at the first step. As can be seen in Fig. 4, the L2-residue drops three orders of magnitude before it reaches an asymptotic value. The drop in maximum residue is only 1.5 orders. Maximum residues were found in the outflow plane, and are for a great past caused by the grid quality in this region, see Fig. 5. Comparing the solution after 1600 steps with that after 2000 steps did not show differences, and it was concluded that the calculation was converged.

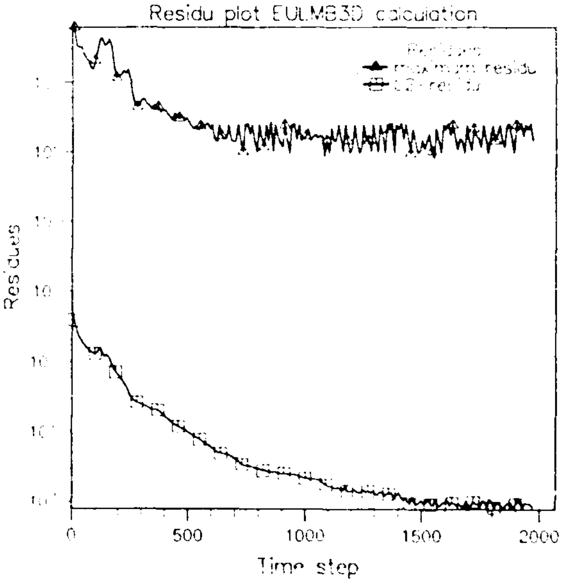

Figure 4. Convergence history for the chemical non-equilibrium calculation of the flow around the HERMES space shuttle, 91x75x71 grid. $M_\infty = 25$, $p_\infty = 2.14$ Pa, $T_\infty = 202$ K, $\alpha = 30°$.

As can be seen in Fig. 5, to mesh the region between the body and the winglet, grid lines were moved down creating a gradient in the mesh. These highly distorted grid cells are responsable for the high maximum residues in the outflow plane.

Figures 6 and 7 show the temperature iso lines in the symmetry plane for the chemical equilibrium and non-equilibrium calculation respectively. The maximum temperature found in the flow field was 5729 K for the equilibrium, and 13832 K for the non-equilibrium calculation, indicating that non equilibrium effects are important.

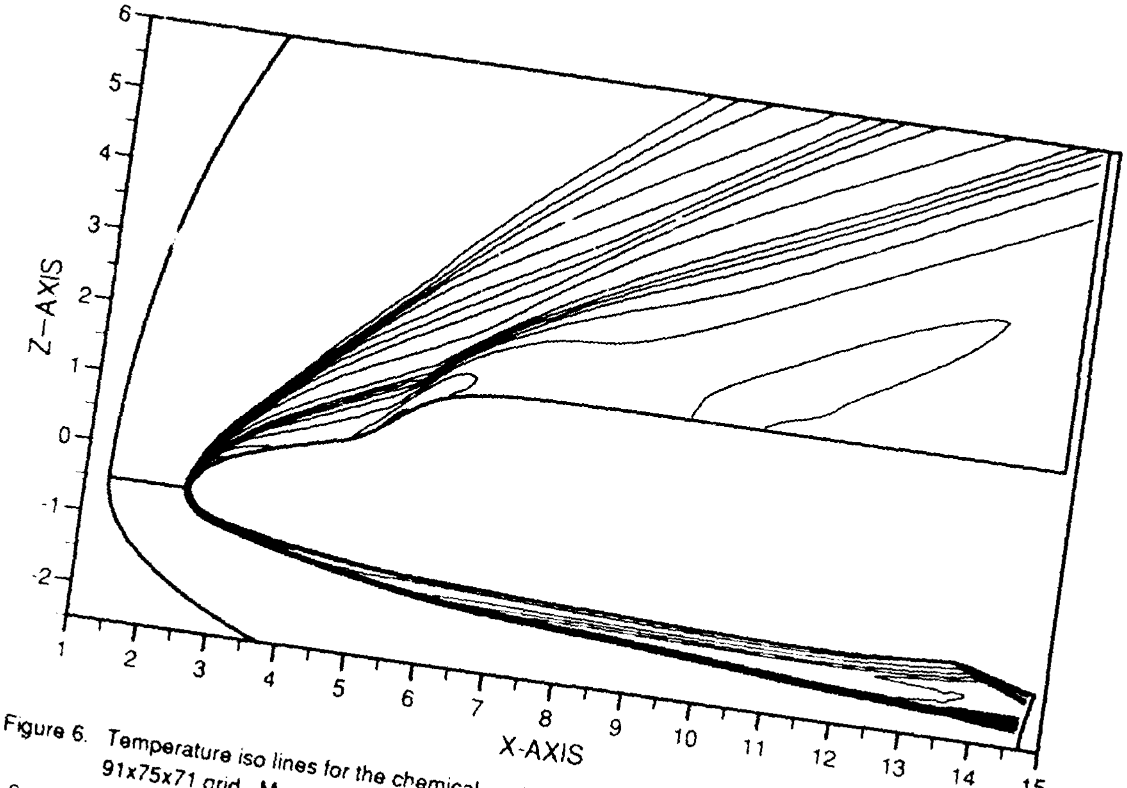

Figure 6. Temperature iso lines for the chemical equilibruim flow around the HERMES space shuttle. 91x75x71 grid, $M_\infty = 25$, $p_\infty = 2.14$ Pa, $T_\infty = 202$ K, $\alpha = 30°$.

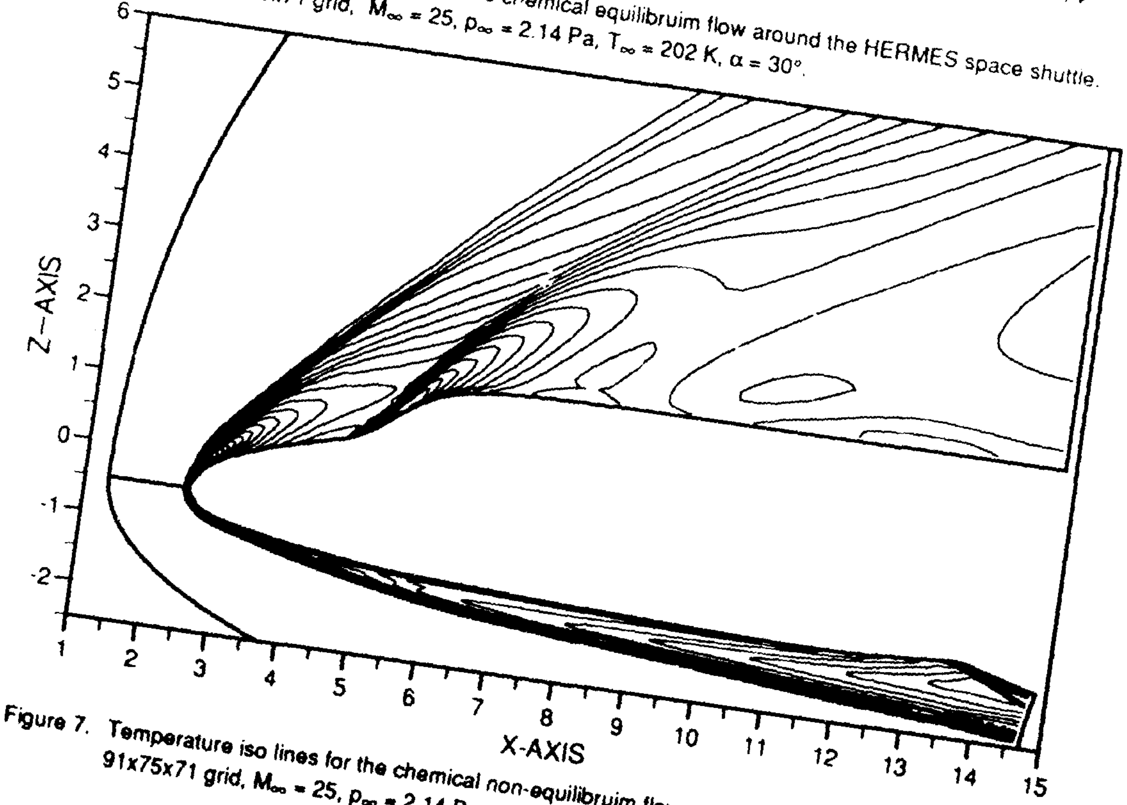

Figure 7. Temperature iso lines for the chemical non-equilibruim flow around the HERMES space shuttle. 91x75x71 grid, $M_\infty = 25$, $p_\infty = 2.14$ Pa, $T_\infty = 202$ K, $\alpha = 30°$.

As can be seen by comparing Figs. 6 and 7, the bow shock is for the equilibrium calculation closer to the body. Temperatures in the flow field are lower when assuming equilibrium chemistry, and because the chemistry has only a small effect on the pressure, this will mean that densities are higher. Since the shock stand off distance is inversely proportional to the density ratio across the shock wave (ref. 12), this implies that the shock is closer to the body.

For the equilibrium calculation, there is a region with high temperature gradients visible at the leeward side of the body. This region corresponds to the region where the O_2 molecules are completely dissociated, but temperatures are too low to start the N_2 dissociation.

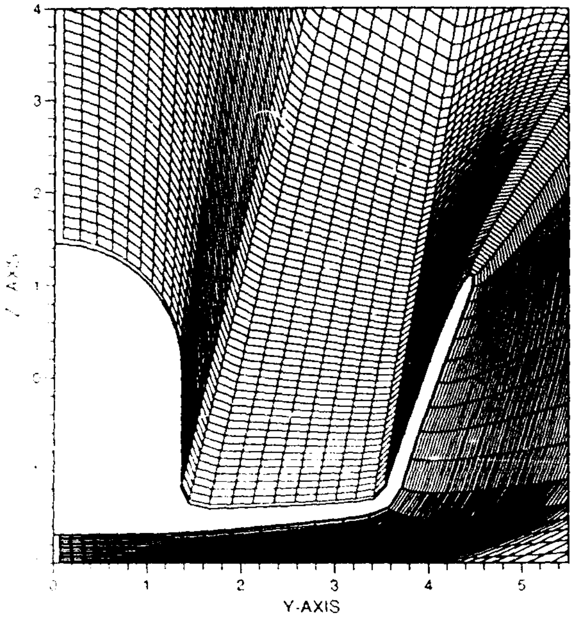

Figure 5. The grid in the outflow plane of the HERMES space shuttle, 91x75x71 grid.

In the non-equilibrium calculation, large temperature gradients are present in the flow field near the bow shock. This is a typical non-equilibrium effect, caused by the fact that the chemistry needs a certain time before it has an influence on the temperature field. Across the shock the flow is frozen, and as soon as the dissociation process has started the temperature decreases rapidly. Note that for the non-equilibrium calculation, the maximum temperature was found close to the bow shock, while for the for the equilibrium calculation it was found at the stagnation point.

The canopy shock is much more pronounced in the chemical non-equilibrium calculation and temperature gradients behind the canopy shock are large due to the recombination of N-atoms. Across the shock N-atoms have been formed which did not have had time to recombine. Much energy is stored in these N-atoms, and this energy is liberated at the canopy shock creating a large jump in temperature here. For the equilibrium calculation, the shock at the canopy forces N_2 molecules to dissociate, absorbing the increase in potential energy at the shock, and only a small jump in temperature is visible.

Table 1 lists the aerodynamic coefficients for the calculations on the 91x91x71 grid for the three thermodynamic models, together with the computational costs. All calculations were carried out on the Cray 2/4-256 of the Swiss Federal Institute of Technology - Lausanne.

thermodynamic model	CD	CL	CM x100	costs CPU s/step
caloric perfect gas	0.381	0.468	-1.54	8.22
equilibrium air	0.400	0.480	-2.61	8.27
non equilibrium air	0.396	0.478	-2.32	36.19

Table 1. Aerodynamic coefficients of the HERMES space shuttle for different thermodynamic models. 91x91x71 grid, 76 km altitude, $M_\infty = 25$, $p_\infty = 2.14$ Pa, $T_\infty = 202$ K, $\alpha = 30°$.

As can be seen from this Table, the effect of equilibrium and non-equilibrium chemistry on the drag and lift is small. The chemistry has a much larger influence on the CM (pitch up moment), and the difference in CM between the caloric perfect gas and equilibrium chemistry calculation is about 70%. This large difference in pitch up moment between caloric perfect gas and equilibrium air computations corresponds with experiences with the American Space Shuttle (ref. 13). It was found that, especially at high Mach numbers, a large difference in predicted (using simplified models) and measured pitch up moment was found.

The aerodynamic coefficients for the non-equilibrium calculation fall in between those of the equilibrium and caloric perfect gas calculation, and they differ at maximum 13% from the equilibrium results.

Comparing the computational costs for the three calculations shows that the costs per time step for the caloric perfect gas and equilibrium calculation are almost the same. The cost of the chemical non-equilibrium calculation is about 4.4 times higher than that of the other two calculations.

8. CALCULATED RESULTS FOR VISCOUS FLOWS.

8.1. The flow around a double ellipsoid.

The isothermal flow around a double ellipsoid was calculated using a two block mesh. Two grids were used, a coarse grid containing 93600 cells, and a fine grid having 250868 cells. The Reynolds number per meter was taken as 10^5, the wall temperature was set to 290 K, and the viscosity and thermal conductivity assumed to be constant.

Figure 8 shows the convergence history for the calculation on the coarse grid, and as can be seen, after an initial 400 steps, both the L2 and maximum residue decrease linearly eight orders of magnitude.

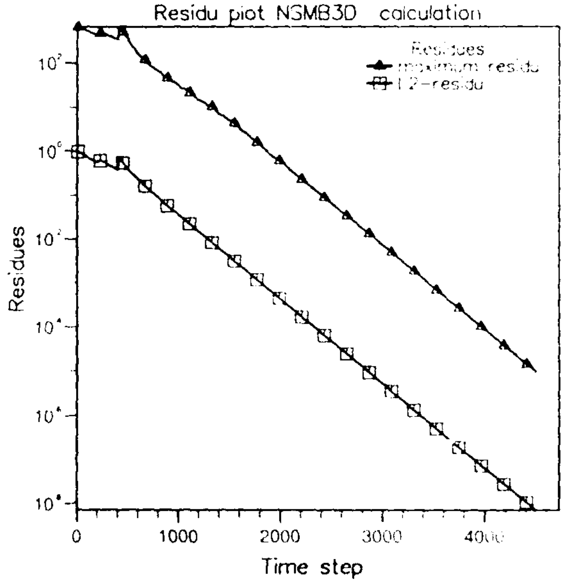

Figure 8. Convergence history for the calculation of the flow around a double ellipsoid. 93600 points, $M_\infty = 8.15$, $Re = 10^5$/m, $T_\infty = 56$ K, $\alpha = 30°$.

Figure 9 shows the iso mach lines in the symmetry plane for the calculation on the fine grid. At the leeward side of the body, the boundary layer region is clearly visible, especially

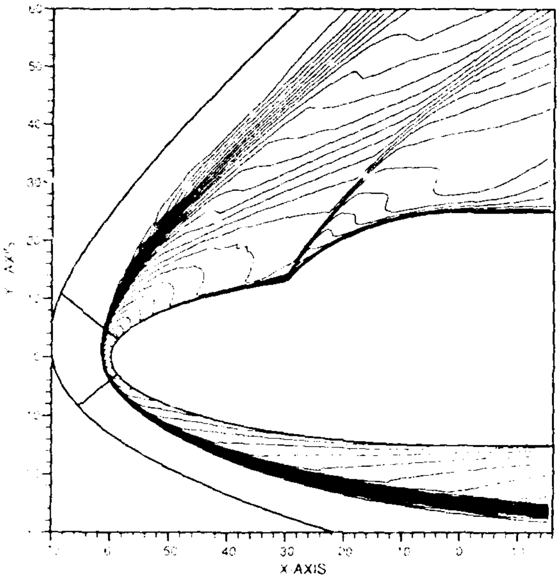

Figure 9. Iso Mach number contours in the symmetry plane, flow around a double ellipsoid. 250868 cells, M_∞ = 8.15, Re=10^5/m, T_∞ = 56 K, α = 30°.

just before and after the canopy. At the canopy, there is a small separated region. This separated region was not found on the coarse grid, due to insufficient resolution of the boundary layer. For the fine grid, about 10-15 grid points were located in the boundary layer at the leeward side of the body. At the leeward side of the double ellipsoid, the bow shock is smeared out due to insufficient grid resolution here.

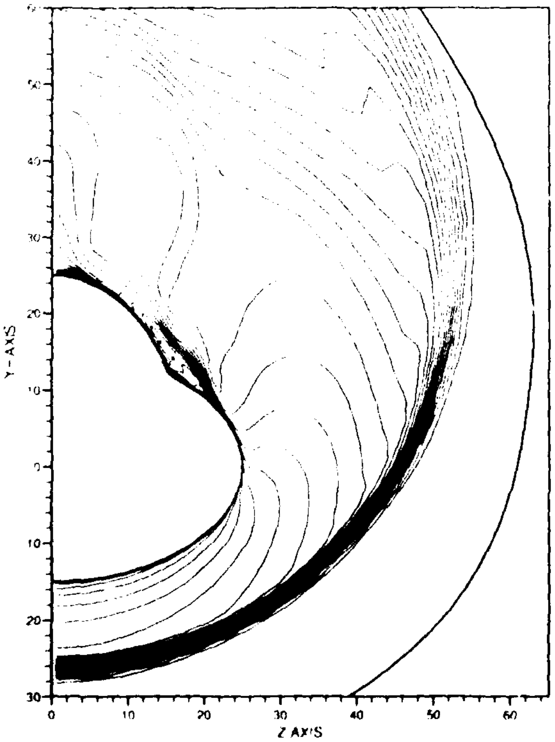

Figure 10. Iso Mach number contours in the outflow plane, flow around a double ellipsoid. 250868 cells, M_∞ = 8.15, Re=10^5/m.

The canopy shock is captured oscillation free, and is not smeared out. Figure 10 shows the iso Mach numbers in the outflow plane. A large region of flow seperation is visible at the intersection of the two ellipsoids, and this region influences the flow field up to the symmetry line.

8.2. The flow around the HERMES space shuttle.

Single block calculations were carried out for the laminar flow around the HERMES space shuttle. The freestream Mach number was equal to 10, the Reynolds number 1.2 10^6, and the angle of attack 30°. The solid wall was assumed to be isothermal, with a wall temperature of 290 K. The transport coefficients were taken to be constant.

Four different grids were used, ranging from a coarse grid of 52x40x52 until a fine grid of 79x119x99 volumes. Between the coarse and fine grid, the number of cells normal to the wall was tripled, while the number of cells in the cross flow direction was almost doubled. Figures 11 and 12 show the iso Mach lines in the symmetry plane for the coarse and fine grid respectively, and the effect of grid refinement is clearly visible.

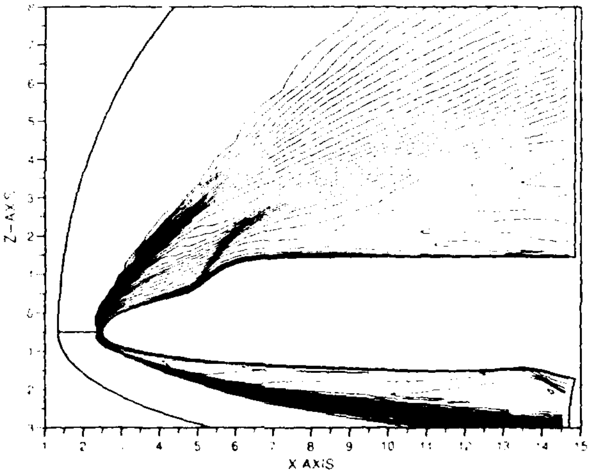

Figure 11. Iso Mach number contours in the symmetry plane, flow around HERMES, 52x40x52 grid M_∞ = 10, Re=1.2$10^6$, T_∞ = 53 K, α = 30°.

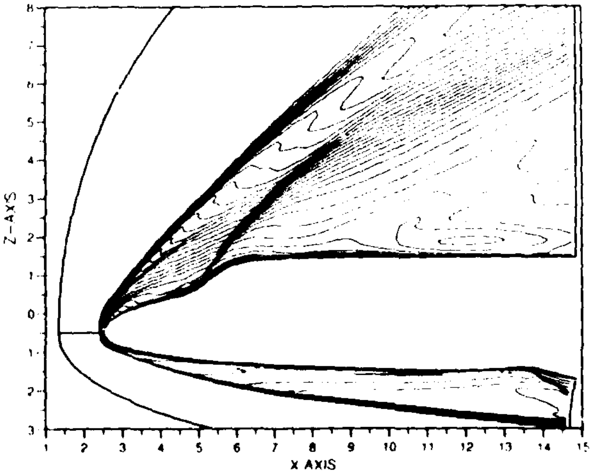

Figure 12. Iso Mach number contours in the symmetry plane, flow around HERMES, 79x119x99

For the fine grid the bow shock is sharp and oscillation free, and the canopy shock is clearly visible. At the canopy the flow is separated, but at the upper body downstream of the canopy the flow remains attached. At the nose of the body, it can be seen that the solution near the singular line is slightly distorted. This is a numerical problem related to the very fine grid spacing in this region. This problem could be avoided by using a multi block mesh. At the windward side of the body, there is a shock wave visible at the bodyflap.

Maximum residues were for all calculations found in the outflow plane due to the highly distorted mesh here, see also Section 7.2 and Fig. 5.

Figures 13-15 show the iso Mach lines in three different cross sections along the body. Figure 13 shows a cross section just before the winglet. As can be seen a separated region is visible close to the intersection between the body and the wing, and another separated region can be observed close to the symmetry plane. The cross flow shock which is visible between these two regions appears almost to be attached to the body. This cross flow shock is similar to that on the deltawing of the Antibes workshop (ref. 14)

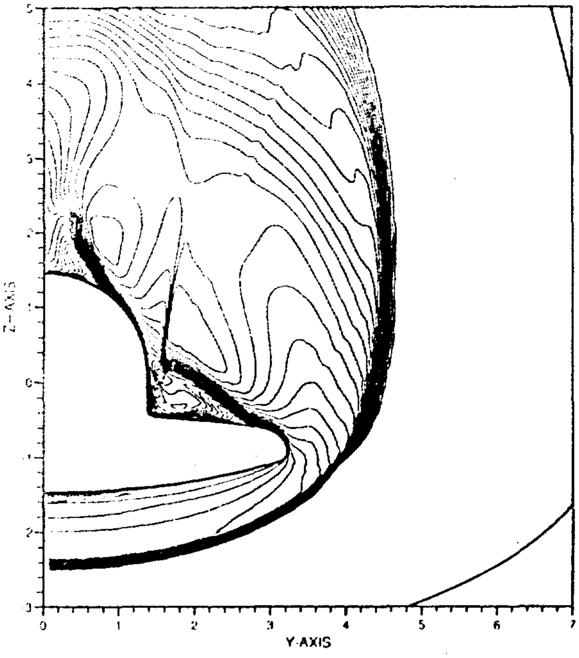

Figure 13. Iso Mach number contours in the cross section x=10, flow around the HERMES space shuttle, 79x119x99 grid, $M_\infty=10$, $Re=1.2\,10^{6}$, $T_\infty=53$ K, $\alpha=30°$.

Figure 14 shows a cross section further downstream, and the influence of the winglet on the flow field is clearly visible. The region between winglet and body is almost one separated region which extends to the symmetry plane. This behavior is even more pronounced at the outflow plane, see Fig. 15.

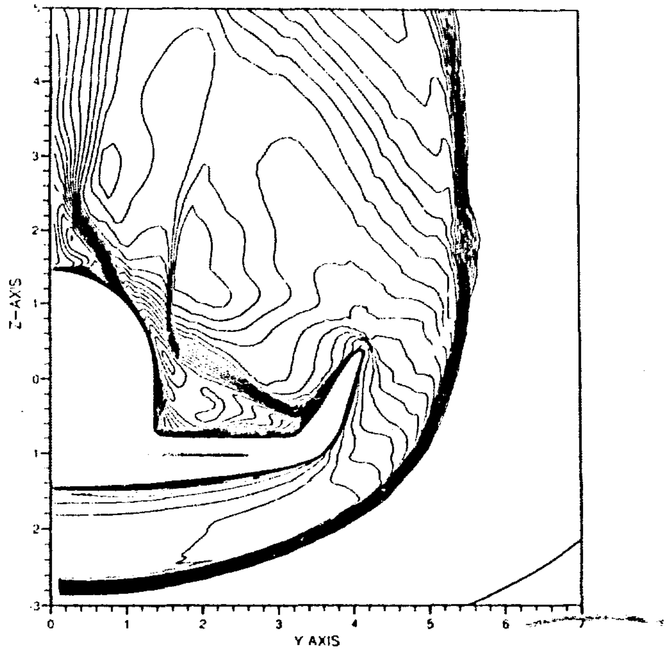

Figure 14. Iso Mach number contours in the cross section x=13, flow around the HERMES space shuttle, 79x119x99 grid, $M_\infty=10$, $Re=1.2\,10^{6}$, $T_\infty=53$ K, $\alpha=30°$.

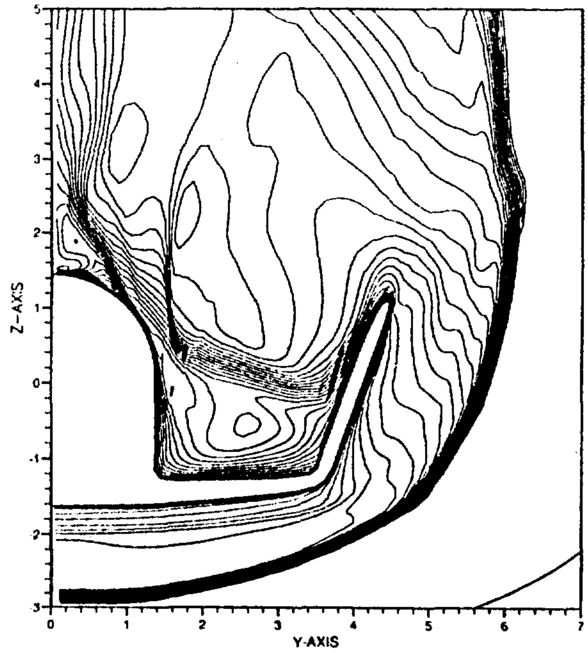

Figure 15. Iso Mach number contours in the cross section x=14.5, flow around the HERMES space shuttle, 79x119x99 grid, $M_\infty=10$, $Re=1.2\,10^{6}$, $T_\infty=53$ K, $\alpha=30°$.

9. RESULTS OF PARALLEL COMPUTATIONS.

Parallel computations were carried out for the inviscid flow over a wedge. A single block grid was split into eight blocks of the same size, and calculations were carried out on the Cray 2/4-256 of the Computing Centre of the Swiss Federal Institute of Technology in Lausanne in dedicated mode. These calculations showed that EULMB was running on 3.982 processors, indicating that the communication overhead between the blocks was about 0.5%. Comparing the convergence histories between the eight block calculation and the corresponding single block calculation showed that the number of steps required to reach convergence was the same.

This means that updating the block connectivity boundary condition only once per time step does not influence the convergence rate.

As a second, more realistic test case, a parallel computation was made for the flow over a double ellipsoid using a six block mesh. In this case, the block sizes varied between 11000 and 85000 points, and it was found EULMB was running on 3.35 processors.

10. CONCLUSIONS.

A project on the development of multi block flow solvers has been presented. Calculated results for the flow around a double ellipsoid using a six block mesh were presented, and showed that strong shock waves crossing block boundaries could be successfully treated with a multi block approach.

Inviscid flow calculations for the flow around the HERMES space shuttle using different models to describe the the thermodynamic properties of air showed that air dissociation has a large influence on the pitch up moment. If one is only interested in the aerodynamic coefficients, it can be concluded that equilibrium air chemistry calculations are sufficient, and it is not necessary to make more expensive non-equilibrium chemistry calculations.

Viscous flow calculations around the double ellipsoid and HERMES space shuttle were presented, and showed that at the leeward side of the body large regions of separation are present.

Calculations carried out on a parallel computer showed that for a well balanced problem the communication overhead between the blocks is small.

11. ACKNOWLEDGMENTS.

Dr. H. Wong from ESTEC, Noordwijk, The Netherlands is acknowledged for making available the six block double ellipsoid mesh used in the inviscid calculations. Dr. Jerome Lordon from Control Data Corporation, Toulouse, France is acknowledged for providing two block Navier Stokes meshes around the double ellipsoid.

The research at the Swiss Federal Institute of Technology was performed with financial support from the Commission Suisse d'Encouragement des Recherches Scientifiques.

12. REFERENCES.

1. Vos, J.B. and Bergman, C.M., "Chemical Equilibrium and Non-Equilibrium Inviscid Flow Simulations using an Explicit Scheme", Computer Physics Communications, Vol. 65, 1991.
2. Vincenti, W.G. and Kruger, C.H., "Introduction to Physical Gas Dynamics", Wiley, New York, 1986.
3. Park, C., "On Convergence of Chemical Reacting Flows", AIAA 85 - 0427.
4. Williams, F.A., "Combustion Theory, 2nd Ed.", Benjamin/Cunnings, Menlo Park, CA, 1985.
5. Jameson, A., "Numerical Solution of the Euler Equations for Compressible Inviscid Fluids", *in* "Numerical Methods for the Euler Equations of Fluid Dynamics", Ed.: Angrand F.,, e.a., SIAM, Philidelphia 1985.
6. Martinelli, L., "Calculation of Viscous Flows with a Multigrid Method", Ph.D thesis, Princeton, 1987.
7. Martinelli, L. and Jameson, A., "Validation of a Multigrid Method for the Reynolds Averaged Equations", AIAA 88-0414.
8. Krispin, J. and Anderson Jr., J.D., "Accelerating the Computation of Steady State Solutions for Non-Equilibrium, Chemically Reacting Flow Fields", AIAA 88-0513.
9. Merazzi, S.M., "MEM-COM An Integrated Memory and Data Management System, MEM-COM User manual Version 5.6", SMR TR-5056 1988, SMR Corporation, P.O. Box 41, CH-2500 Bienne.
10. Vos, J.B. and Bergman, C.M., "EULMB: A Multi Block Euler Solver for 3D Compressible and Chemical Equilibrium Flows." EULMB Handbook Version 2.0, IMHEF Report, 1991.
11. Bergman, C.M., "Development of Numerical Techniques for Inviscid Hypersonic Flows around Re-entry Vehicles". Thesis #341, INP Toulouse, France.
12. Hayes, W.D. and Probstein, R.F., "Hypersonic Flow Theory", Academic Press, New York, 1959.
13. Arrington, J.D. and Jones, J.J., "Shuttle Performance: Lessons Learned", NASA CP 2283, 1983.
14. Desideri, J.A. and Periaux, J., "Proceedings of the Workshop on Hypersonic Flows Part 1", Springer Verlag, 1992.

HYPERSONIC FLOW COMPUTATIONS AROUND RE-ENTRY VEHICLES

J. Peraire[†], J. Peiró[†], K. Morgan[*], M. Vahdati[†] and R.C. Molina[**]

[†] Department of Aeronautics, Imperial College, London SW7 2BY, U.K.
[*] Department of Civil Engineering, University of Wales, Swansea SA2 8PP, U.K.
[**] WMA, ESA-ESTEC, Noordwijk 2200 AG, The Netherlands

1. SUMMARY

The development of an algorithm for the solution of the compressible Euler equations at high Mach numbers on unstructured tetrahedral meshes is described. The basic algorithm is constructed in the form of a central difference scheme plus an explicit added artificial viscosity based upon fourth order differences of the solution. The stability of the solution in the vicinity of strong gradients is preserved by the incorporation of an additional artificial viscosity based upon a second order difference. Higher order accuracy is regained by using the ideas of flux corrected transport to limit the amount of added viscosity. The solution is advanced to steady state by means of an explicit multi-stage time-stepping method. The computational efficiency of the complete process is improved by incorporating an unstructured multigrid acceleration procedure. A number of flows of practical interest are analysed to demonstrate the numerical performance of the proposed approach.

2. INTRODUCTION

Major progress has been made in recent years on the development of unstructured mesh methods for the solution of compressible aerodynamic flows of industrial interest. A variety of flow algorithms have been produced which are suitable for implementation on such meshes and significant achievements have been made in the area of mesh generation and adaptivity. It is now possible to produce solutions, with a high level of precision, for inviscid transonic flows involving geometries which can be as complex as a complete aircraft [1]. In addition, the speed with which such solutions can be obtained has been markedly improved by the adoption of new methods of storing unstructured mesh data and by the incorporation of multigrid acceleration procedures [2]. The unstructured approach is therefore becoming increasingly attractive to the analyst involved in the design of aerodynamic components.

In this paper, we consider the application of unstructured mesh techniques to the modelling of hypersonic inviscid flows. A basic Euler flow solver is constructed from a Galerkin finite element method. The resulting scheme is essentially a central difference type method. A practically useful procedure for smooth flows is produced by replacing the actual fluxes by appropriately defined consistent numerical fluxes. This results in the modification of the original scheme by the addition of an artificial viscosity based upon fourth differences of the solution. This is defined as being our 'high order' algorithm. A stable procedure for the simulation of flows involving strong discontinuities may be produced by adding to the original scheme an artificial viscosity which is based upon second differences of the solution. This is defined as being our 'low order' solution algorithm. The high and low order algorithms are combined, using the ideas [3-5] of flux corrected transport (FCT), to produce a stable monotonic algorithm for shocked flows with the minimum amount of added artificial viscosity. The steady state flow conditions of interest are computed by advancing the transient form of the equations using a multi-stage explicit time stepping process. An edge based data structure is employed for the three dimensional mesh and this has the effect of reducing the memory demands over those made by the more traditional element based data structure of the type familiar to finite element practitioners. This data structure has many features in common with that which has been proposed recently by others [6,7].

Although the edge based data structure is found to reduce the computer time requirements of the flow solver, the total CPU time necessary to produce a converged solution to a problem involving steady inviscid flow past an aerodynamic component can still be considerable. In the structured grid context, solution algorithms equivalent to that proposed here have been effectively accelerated by the use of multigrid methods [8], employing a sequence of successively coarser nested meshes. When the grid which is to be employed for the analysis is unstructured, the multigrid concept has to be extended [2,7,9-12] as the grids which are employed are now not nested i.e. the nodes on one grid do not necessarily coincide with nodes on the next coarsest or the next finest grid. The use of such grids may be incorporated within a multigrid solution procedure provided that appropriate inter-grid transfer procedures are developed. The unstructured multigrid procedure therefore requires a close coupling between an automatic unstructured mesh generation procedure [13] and the flow solver. In [2] it was shown that, for 3D transonic flow computations using unstructured meshes, the computational performance of the flow solver can be dramatically improved when the multigrid procedure is utilised. The multigrid procedure presented in [2] is currently being extended to hypersonic flows and in this paper we report on our initial experiences and present the results of the multigrid computation of the inviscid hypersonic flow over the HERMES 1.0 space shuttle using our 'low order' solution algorithm.

3. THE GOVERNING EQUATIONS

The equations governing three dimensional compressible unsteady inviscid flow are considered in the conservation form

$$\frac{\partial U}{\partial t} + \sum_{j=1}^{3} \frac{\partial F^j}{\partial x_j} = 0 \qquad (1)$$

where U, the unknown vector of conserved variables, and F^j, the corresponding inviscid flux vectors, are defined by

$$U = \begin{bmatrix} \rho \\ \rho u_1 \\ \rho u_2 \\ \rho u_3 \\ \rho \varepsilon \end{bmatrix} \qquad F^j(U) = \begin{bmatrix} \rho u_j \\ \rho u_1 u_j + p\delta_{1j} \\ \rho u_2 u_j + p\delta_{2j} \\ \rho u_3 u_j + p\delta_{3j} \\ (\rho\varepsilon + p)u_j \end{bmatrix} \qquad (2)$$

Here δ_{ij} is the Kronecker delta, ρ, p and ε denote the density, pressure and total specific energy of the fluid respectively and u_j; $j = 1, 2, 3$ are the components of the fluid velocity in the directions x_j; $j = 1, 2, 3$ of a cartesian coordinate system. The set of equations is completed by the addition of the perfect gas equation of state

$$p = (\gamma - 1)\,\rho\,(\,\varepsilon - 0.5\sum_{j=1}^{3} u_j u_j\,) \qquad (3)$$

where γ (= 1.4) is the ratio of the specific heats.

Steady state solutions of these equations are produced by advancing the solution in time until stationary conditions are obtained.

4. AN UNSTRUCTURED MESH FLOW ALGORITHM

4.1 Variational Formulation

The identification of an appropriate variational formulation of the governing equation is the starting point in the construction of a finite element approximation in the spatial domain, Ω, for all $t > 0$. A suitable weak formulation for the problem defined in equation (1) would be : find $U(x,t)$ such that

$$\int_\Omega \frac{\partial U}{\partial t} W \, d\Omega = \sum_{j=1}^{3} \int_\Omega F^j \frac{\partial W}{\partial x_j} \, d\Omega - \sum_{j=1}^{3} \int_\Gamma F^{nb} \, W \, d\Gamma \qquad (4)$$

for every suitable weighting function $W(x)$ and for all $t > 0$. In this equation, the prescribed value of the normal flux on Γ, which will be a function of the solution U, is denoted by F^{nb}. With the spatial domain Ω represented by an unstructured assembly of four noded tetrahedral elements, a piecewise linear approximate solution U^* is sought in the form

$$U^*(x,t) = \sum_J U_J(t)\, N_J(x) \qquad (5)$$

where the summation extends over each node J $(1 \le J \le n_p)$ in the mesh, $U_J(t)$ denotes the value of the approximation U^* at node J at time t, and $N_J(x)$ is the standard linear finite element shape function associated with node J. Using the variational statement of equation (4), the Galerkin approximate solution is constructed as the function U^* which is such that

$$\int_\Omega \frac{\partial U^*}{\partial t} N_I \, d\Omega = \sum_{j=1}^{3} \int_\Omega F^j(U^*) \frac{\partial N_I}{\partial x_j} \, d\Omega - \sum_{j=1}^{3} \int_\Gamma F^{nb}(U^*) N_I \, d\Gamma \qquad (6)$$

for each N_I $(1 \le I \le n_p)$ and for all $t > 0$. These integrals are evaluated by summing individual element contributions. The compact support of the shape function N_I means that equation (6) can then be written as

$$\sum_{e \in I} \int_{\Omega_e} \frac{\partial U^*}{\partial t} N_I \, d\Omega = \sum_{j=1}^{3} \sum_{e \in I} \int_{\Omega_e} F^j(U^*) \frac{\partial N_I}{\partial x_j} \, d\Omega + \sum_{j=1}^{3} \sum_{e \in I} \int_{\Gamma_e} F^{nb}(U^*) N_I \, d\Gamma \qquad (7)$$

where the summation extends only over those elements Ω_e which contain node I. Inserting the assumed form for U^* into this equation, the left hand side integrals may be evaluated exactly, to give

$$\sum_{e \in I} \int_{\Omega_e} \frac{\partial U^*}{\partial t} N_I \, d\Omega = \sum_{e \in I} [\int_{\Omega_e} N_I N_J \, d\Omega\,] \frac{dU_J}{dt} = \sum_J [M]_{IJ} \frac{dU_J}{dt} \qquad (8)$$

where M denotes the finite element consistent mass matrix. The entries in this matrix for a general tetrahedral element can be evaluated explicitly. In the development of the algorithm, M is actually replaced by the lumped (diagonal) mass matrix M_L which is obtained form M by adding all the non zero elements in a row to the diagonal term. The integrals appearing on the right hand side of equation (7) are evaluated approximately, by using a finite element interpolation (similar to equation (5)) to express the fluxes in terms of their nodal values. Thus, for an element e, with nodes I, J, K and L, the domain integral is approximated as

$$\int_{\Omega_e} F^j \frac{\partial N_I}{\partial x_j} \, d\Omega \approx \frac{\Omega_e}{4} \left. \frac{\partial N_I}{\partial x_j} \right|_e \{\, F^j_I + F^j_J + F^j_K + F^j_L \,\} \qquad (9)$$

A standard finite element code would be organised in this fashion and would produce the discrete form of equation (7), at each node I in the mesh, by looping over the individual elements and sending element contributions to the appropriate nodes, according to equation (9). The associated data structure in this case would consist of the list of the nodes I, J, K and L belonging to each element e in the mesh.

However, the terms in equation (7) can be evaluated differently. Suppose that node I in the mesh is directly connected, by edges of the mesh, to the mI nodes $J1$, $J2$, ..., JmI. For present purposes, it will be assumed that node I is an interior node, so that the procedure presented here will need to be modified slightly for nodes which lie on the computational boundary. By using the results of equations (8) and (9) it is readily shown that equation (7) can be written in the form

$$[M_L]_I \left. \frac{dU}{dt} \right|_I = \sum_{j=1}^{3} \sum_{s=1}^{mI} C^j_{IJ_s} (F^j_I + F^j_{J_s}) \qquad (10)$$

where $C^j_{IJ_s}$ denotes the weight for node I for the contribution from edge IJ_s. These weights are computed as

$$C^j_{IJ_s} = \sum_{e \in IJ_s} \frac{\Omega_e}{4} \left. \frac{\partial N_I}{\partial x_j} \right|_e \qquad (11a)$$

and possess the properties

$$\sum_{s=1}^{mI} C^j_{IJs} = 0 \qquad \text{for all } j \qquad (11b)$$

$$C^j_{IJs} = - C^j_{JsI} \qquad \text{for all } j \text{ and } Js \qquad (11c)$$

It is convenient to introduce the vector C_{IJs} which is defined according to

$$C_{IJs} = (C^1_{IJs}, C^2_{IJs}, C^3_{IJs}) \qquad (12)$$

Now let $\mathcal{L}_{IJs}$ denote the modulus of C_{IJs} and let $\mathcal{S}_{IJs}$ denote the unit vector in the direction of C_{IJs}. With this notation, equation (10) can be written as

$$[M_L]_I \left.\frac{dU}{dt}\right|_I = \sum_{s=1}^{mI} \mathcal{L}_{IJs} (\mathcal{F}_{Is} + \mathcal{F}_{JS}) \qquad (13)$$

where

$$\begin{aligned} \mathcal{F}_{Is} &= (F_I^1, F_I^2, F_I^3) \cdot \mathcal{S}_{IJs} \\ \mathcal{F}_{Js} &= (F_{Js}^1, F_{Js}^2, F_{Js}^3) \cdot \mathcal{S}_{IJs} \end{aligned} \qquad (14)$$

Thus the discrete form of equation (7) can be obtained by the alternative approach of looping over each edge in the mesh and sending edge contributions to the appropriate nodes according to equation (13). The property of conservation in the numerical scheme is guaranteed by the asymmetry of the edge coefficients as expressed in *equation (11c)*. The associated data structure required in this case would consist of a list of the edges in the mesh and the numbers of the two nodes associated with that edge. It is apparent that such an edge based data structure is the most compact of all the various possible alternatives which can be used for unstructured meshes [6,7].

The condition of equation (11b) means that the flux at an interior node I does not appear in the discrete equation at node I. Thus a time stepping scheme in the form of equation (13) is central difference in character and allows for the appearance of chequerboarding modes. Thus, to obtain a practically useful scheme the procedure requires an extra ingredient and one remedy is to replace the actual fluxes in equation (13) by suitably defined consistent numerical fluxes. The different forms which may be adopted for the numerical fluxes result in a variety of different numerical schemes.

4.2 Choice of the Numerical Flux

The discretisation of equation (13) may be stabilised, for application to the solution of smooth flows, by the addition of a high order diffusion term. The method generally adopted for constructing a suitable approximation to such an operator, is the recycling of edge differences [14,15]. It is readily observed that this is not a highly accurate method on a general unstructured mesh, as it results in the addition of diffusion even if the solution U varies linearly in space. Therefore, we employ an alternative construction for this diffusion operator, which has beneficial improved accuracy properties and adds no diffusion to a linear field.

An approximation to the gradient of U at the nodes of the mesh can be determined directly, by looping over the edges, as

$$[M_L]_I \left.\frac{\partial U}{\partial x_j}\right|_I = - \sum_{s=1}^{mI} C^j_{IJs} (U_I + U_{Js}) \qquad (15)$$

This expression is exact if the solution U is linear. If σ denotes a coordinate along the edge between nodes I and Js of the mesh, as shown in figure 1, the expression

$$\sum_{s=1}^{mI} \mathcal{L}_{IJs} \left\{ U_{Js} - U_I - \left[\frac{\partial U}{\partial \sigma} \Delta \sigma\right]_{IJs} \right\} \qquad (16)$$

may be interpreted as an approximation, at node I, to a high order derivative operator acting on U. In fact it is readily shown that, on a mesh of equal elements in one dimension, expression (16) is proportional to the standard finite difference discretisation of a fourth derivative, when the approximation

$$\left[\frac{\partial U}{\partial \sigma} \Delta \sigma\right]_{IJs} = 0.5 \left\{ \left[\frac{\partial U}{\partial \sigma}\right]_I + \left[\frac{\partial U}{\partial \sigma}\right]_{Js} \right\} \Delta\sigma_{IJs} \qquad (17)$$

is employed and where $\Delta\sigma_{IJs}$ denotes the distance between node I and node Js. Thus, a stable algorithm for smooth flows may be constructed as

$$\begin{aligned} [M_L]_I \left.\frac{dU}{dt}\right|_I = \sum_{s=1}^{mI} \mathcal{L}_{IJs} [\mathcal{F}_{Is} + \mathcal{G}_{Js} \\ - d_4 |\lambda_{IJs}| \{U_{Js} - U_I - \left[\frac{\partial U}{\partial \sigma} \Delta \sigma\right]_{IJs} \}] \end{aligned} \qquad (18)$$

where d_4 is a user specified constant, λ_{IJs} is the maximum wave speed in the direction $\mathcal{S}_{IJs}$ which is computed as

$$\lambda_{IJs} = | u_{IJs} \cdot \mathcal{S}_{IJs} | + a_{IJs} \qquad (19)$$

with a denoting the speed of sound. A further enhancement here could be to replace $|\lambda_{IJs}|$ in (18) by the Roe matrix [17] evaluated in the direction $\mathcal{S}_{IJs}$, thus

$$\begin{aligned} [M_L]_I \left.\frac{dU}{dt}\right|_I = \sum_{s=1}^{mI} \mathcal{L}_{IJs} [\mathcal{F}_{Is} + \mathcal{F}_{Js} \\ - d_4 |A_{IJs}| \{U_{Js} - U_I - \left[\frac{\partial U}{\partial \sigma} \Delta \sigma\right]_{IJs} \}] \end{aligned} \qquad (20)$$

The above above matrix dissipation form is analogous to that proposed in [16]. In fact this scheme, with $d_4=1$, bears a strong resemblance to a cell vertex upwind solution method [18], in which higher order accuracy is achieved, using the MUSCL approach [19], by linear reconstruction of the solution. In MUSCL, however, the fluxes $\mathcal{F}_{Is}$ and $\mathcal{F}_{Js}$ are evaluated using the linearly reconstructed interface values of U and not just the nodal values.

We investigate the numerical performance of these various possibilities by considering the solution of an inviscid flow over a NACA0012 aerofoil at a free stream Mach number of 0.63 and at two degrees angle of attack. A detail of the grid which is employed for the simulation is shown in figure 2a. This grid has a structured triangular region, of the type suitable for a viscous flow analysis, in the vicinity of the aerofoil surface. In figure 2b the contours of Mach number in the vicinity of the aerofoil obtained using the MUSCL scheme are compared with those obtained using the matrix and scalar dissipation schemes. A comparison of the steady state distribution of entropy deviation over the aerofoil computed using a cell vertex MUSCL scheme and the centered scheme with matrix dissipation of equation (20) is shown in figure 2c. The entropy deviation computed with the centered scheme is seen to be significantly lower. In figure 2d, the computed entropy deviation produced by the centered scheme with the scalar diffusion of equation (18) is shown and it can be observed that the accuracy levels of the matrix dissipation method may be regained by appropriate choice of the user specified coefficient d_4. Thus, for computational convenience, the method of equation (18) is employed as the basis for further development.

Further development is necessary as the scheme does not remain stable when it is used in the analysis of flows involving strong discontinuities. A first order algorithm, which will remain stable for such flows, can be constructed from equation (13) as

$$[M_L]_I \left.\frac{dU}{dt}\right|_I = \sum_{s=1}^{mI} \mathcal{L}_{IJs} \{ \mathcal{F}_{Is} + \mathcal{F}_{Js} - d_2 |\lambda_{IJs}| \; \{ U_{Js} - U_I \} \} \quad (21)$$

where d_2 is a user specified constant. However, the accuracy of this scheme can be expected to be poor because of the indiscriminate manner in which the diffusion is added. It is apparent from equation (21) that the diffusion added here takes the form of an approximation to a second order difference operator. To produce a practically useful scheme we attempt to devise an appropriate procedure for selectively removing the excessive artificial viscosity which is present in equation (21), while maintaining the accuracy of equation (18) over the major portion of the computational domain. Before describing how this requirement can be achieved, we describe the time stepping method which will be employed for advancing either equation (18) or equation (21) towards steady state.

4.3 An Explicit Time Stepping Scheme

We begin by defining

$$Q_I\,(U) = \sum_{s=1}^{mI} \mathcal{L}_{IJs} \{ \mathcal{F}_{Is} + \mathcal{F}_{Js} \} \qquad (22)$$

and we let

$$\mathbf{R}_I\,(U) = Q_I\,(U) + D_I\,(U) \qquad (23)$$

denote the right hand side of either equation (18) or equation (21), with appropriate definition of the artificial viscosity term $D_I\,(U)$. In this form, the contributions made to the right hand side vector **R** by the terms arising from the basic Galerkin formulation and by the explicitly added diffusion can be clearly identified. Assuming that the nodal values U_I^n are known at time t_n, the solution may be advanced over the time step Δt, to time t_{n+1}, by an explicit hybrid multi-stage time stepping scheme [8] e.g. with ΔU_I defined to be equal to the change in the value of the solution U at node I over a time step, an m-stage version of the scheme is written as

$$U_I^{(0)} = U_I^n$$

$$U_I^{(p)} = U_I^{(0)} + \alpha_p \Delta t \; [M_L]_I^{-1} \, \mathbf{R}_I \, (U_I^{(p-1)}) \quad p=1,2,\ldots,m \qquad (24)$$

$$U_I^{n+1} = U_I^{(m)}$$

with the parameters α_p assigned appropriate values. In the interests of computational efficiency, the diffusion contribution **D** to the right hand side vector **R** need not recalculated at every stage of this process. Since the correct modelling of the transient development of the flow is not of interest here, local time stepping is employed to accelerate the convergence behaviour. This is implemented by specifying a constant Courant number, CFL, throughout the mesh and computing the local time step Δt_I for node I in the mesh, according to an energy stability analysis [20], using the relation

$$\Delta t_I = 2 \; \mathrm{CFL} \, [M_L]_I \left[\sum_{s=1}^{mI} \mathcal{L}_{IJs} \, |\lambda_{IJs}| \right]^{-1} \qquad (25)$$

Residual smoothing is also employed to increase the size of the allowable value of the CFL parameter [14,21].

4.4 A Higher Order Procedure for Hypersonics

We attempt to produce an algorithm which behaves as the scheme of equation (18) in smooth regions of the flow and as the scheme of equation (21) in the vicinity of discontinuities. A possible approach involves the determination of an appropriate sensor, π, for detecting the high gradient regions in the flow. For an edge s, connecting nodes I and Js, the sensor for node I can be based on the pressure field, p, and computed as [22]

$$\pi_{Is} = \left| \frac{p_{Js} - p_I - \dfrac{\partial p}{\partial \sigma} \Delta\sigma_{IJs}}{|p_{Js} - p_I| + \left|\dfrac{\partial p}{\partial \sigma}\right| \Delta\sigma_{IJs}} \right| \qquad (26)$$

where the pressure gradient in this expression is evaluated at node I using an expression similar to that employed in equation (15). A sensor constructed in this way has the property that $\pi_{Is} \approx 1$ in the vicinity of strong gradients and $\pi_{Is} \approx 0$ in smooth regions of the flow. By incorporating this pressure sensor into the algorithm of equation (18) in the form

$$[M_L]_I \left.\frac{dU}{dt}\right|_I = \sum_{s=1}^{mI} \mathcal{L}_{IJs} \{ \mathcal{F}_{Is} + \mathcal{F}_{Js} - |\lambda_{IJs}| \, \{ d_2 (U_{Js} - U_I)$$

$$- (1 - \pi_{IJs}) \; [(d_2 - d_4)(U_{Js} - U_I) - d_4 \left[\frac{\partial U}{\partial \sigma} \Delta\sigma \right]_{IJs} \;] \} \} \qquad (27)$$

an algorithm with the desired properties is constructed. Although this algorithm works very well for transonic flow simulations [2], for hypersonic flow analysis it has been found that in order to preserve the stability of the computation very large values of the dissipation constant d_2 need to be used. This results in a considerable smearing of the solution.

An alternative approach is to attempt to improve the accuracy of the solution scheme of equation (21) by the addition of a flux corrected transport (FCT) procedure [3-5]. In the FCT nomenclature, the solution of equation (21) is termed the low order solution, $U^{(L)}$, while the solution of equation (18) is the high order solution, $U^{(H)}$. Then, at any stage in the time stepping procedure, we have that

$$U^{(H)(p)} = U^{(L)(p)} - \alpha_p \Delta t_I [M_L]_I^{-1} \sum_{s=1}^{mI} \mathcal{L}_{IJs} |\lambda_{IJs}| \{ \quad (d_2 - d_4)(U_{Js}^{(p-1)} - U_I^{(p-1)}) - d_4 \left[\frac{\partial U^{(p-1)}}{\partial \sigma} \Delta \sigma \right]_{IJs} \} \tag{28}$$

The idea behind FCT is to limit the amount of artificial diffusion which is removed, from the low order solution to produce the high order solution, by imposing the requirement that the high order solution should remain monotone. Following the standard FCT approach, we first identify, for each node I, the maximum and minimum values that the high order solution be allowed to take at that node. These values are computed according to

$$\begin{aligned} U_I^{(p)max} &= \max \{ U_I^{(L)(p)}, U_{Js}^{(L)(p)}, U_I^{(H)(p-1)}, U_{Js}^{(H)(p-1)} \} \\ U_I^{(p)min} &= \min \{ U_I^{(L)(p)}, U_{Js}^{(L)(p)}, U_I^{(H)(p-1)}, U_{Js}^{(H)(p-1)} \} \end{aligned} \tag{29}$$

where the maximum and minimum in these expressions is sought by considering all the points J_s which are directly connected to node I by edges in the mesh, i.e. for $s = 1, 2, ..., mI$. An edge limiter χ_s is applied to the contributions made by each edge and the value of this limiter is determined so as to ensure that the computed $U_I^{(p)}$, at each node I, lies within the range specified by the maximum and minimum values defined in equation (29). The solution at node I at this stage is thus determined from

$$U^{(p)} = U^{(L)(p)} - \alpha_p \Delta t_I \{M_L\}_I^{-1} \sum_{s=1}^{mI} \chi_s \mathcal{L}_{IJs} |\lambda_{IJs}| \{ \quad (d_4 - d_2)(U_{Js}^{(p-1)} - U_I^{(p-1)}) - d_4 \left[\frac{\partial U^{(p-1)}}{\partial \sigma} \Delta \sigma \right]_{IJs} \} \tag{30}$$

In practice, the limiting procedure is not applied to the set of conservation variables but is applied to the density, the pressure and Mach number separately. The limiter for each edge is computed so that the density, the pressure and the Mach number remain monotone. Further details on the application of the FCT procedure can be found in [5].

The performance of the pressure sensor approach versus the FCT limiting procedure is compared for the computation of the two dimensional hypersonic flow over a double ellipse geometry. The free stream conditions correspond to a Mach number of 8.15 at an angle of attack of 30 degrees. The unstructured mesh of tetrahedral elements employed for the computation is shown in figure 3a. Figures 3b and 3c show the solutions obtained using a pressure sensor and the FCT limiting procedure. The higher resolution obtained with the FCT procedure is readily observed. It should be noted here that although both solutions have monotone pressure fields, the Mach number distribution of the pressure sensor solution has some small overshoots in the bow shock region whilst the FCT solution remains monotone.

4.5 Mesh Generation

The discretisation of the computational domain, Ω, into tetrahedral elements is accomplished by means of an advancing front based mesh generation system [23]. The first stage in this process consists in using a two dimensional advancing front method to produce a triangulation of the boundary, Γ, of the computational domain and the resulting set of triangular faces forms the initial front for the three dimensional generator. The interior of the domain is then filled with tetrahedral elements by using the three dimensional advancing front method. An essential feature of the adopted approach is the manner in which the size and shape of the generated elements is controlled by user specified distribution functions. The generation process is fully automatic and computational domains of general geometric shape can be rapidly meshed [13,24]. The mesh generator assumes an element based data structure, but the elements can be discarded, before the flow computation starts, when the edge coefficients, defined in equation (11), and the lumped mass matrix entries have been computed and stored. For a general tetrahedral mesh, the number of elements (NE), the number of vertices(NP), the number of edges (NS) and the number of boundary triangles (NBF) are related by the expression

$$2*NS + \psi = 2*NE + 2*NP + NBF \tag{31}$$

where ψ denotes a constant which depends upon the Euler number of the boundary surface of the computational domain. For a typical unstructured mesh, the ratio of elements to points is approximately equal to 6 and hence, from the above expression, the ratio of edges to points is approximately equal to 7. Thus, the mesh connectivity information with an element based data structure will require 24 storage locations per node whereas the edge based data structure requires only 14.

5. MULTIGRID EXTENSION

It is well known that the use of an explicit multistage time stepping solution procedure for the Euler equations provides an attractive environment for the effective implementation of multigrid acceleration [8]. The basic idea behind the use of multigrid for the solution of a hyperbolic equation system is to use a sequence of successively coarser grids to compute corrections to the fine mesh solution. The coarse grid equations are also advanced with an explicit multistage scheme, making use of the fact that the allowable time step is now larger than that which can be used on the finest mesh. For example, when two meshes are employed, the fine grid solution U_{If}^{n+1} and the corresponding residual $R_{If}(U^{n+1})$, computed as in equation (23), are transferred onto the coarse mesh as U_{Ic}^n and R_{Ic}^n and the time stepping scheme

$$\begin{aligned} U_{Ic}^{(0)} &= U_{Ic}^n \\ U_{Ic}^{(p)} &= U_{Ic}^{(0)} - \beta_p \Delta t_{Ic} [M_L]_{Ic}^{-1} \{ R(U_{Ic}^{(p-1)}) \\ &\qquad + R_{Ic}^n - R(U_{Ic}^n) \} \quad p=1,2,...,q \\ U_{Ic}^{n+1} &= U_{Ic}^{(m)} \end{aligned} \tag{32}$$

is employed to transport the corrections on this grid. When the coarse mesh steps are completed, the corrections are interpolated back to the fine mesh and used to update the fine mesh solution. It is important to observe that the coarse mesh algorithm of equation (32) ensures that the converged solution on the fine mesh is unaltered by the multigrid process i.e. the coarse mesh correction is zero if $R_{If}(U^{n+1})$ is zero. This algorithm can be extended to more than two meshes and different cycling strategies can be devised.

The restriction operation requires the values of the unknowns and residuals to be transferred from one mesh to a coarser mesh, whereas the prolongation operation requires only the transfer of the computed corrections in the reverse direction. This transfer of information from a grid A to a grid

B may be accomplished in a variety of different ways. It is apparent that appropriate procedures are readily devised when the meshes A and B are structured and nested. However, these operations are not easily accomplished when they are being performed between two general tetrahedral meshes. To illustrate the way in which such operations may be accomplished, consider the transfer of a function f. If we let I_A and I_B denote general nodes on mesh A and mesh B respectively, then a direct interpolation requires a knowledge of the element in mesh A within which node I_B is located together with the values of the shape functions on mesh A at node I_B (see figure 4). With this information, a direct interpolation can then be represented by the formula

$$f_{IB} = \sum_{IA} f_{IA} \left[N_{IA}\right]_{IB} \qquad (33)$$

A possible method of achieving a conservative transfer requires the knowledge of the element in mesh B which contains node I_A together with the values of the shape functions on mesh B at node I_A. The transfer is accomplished as

$$f_{IB} = [M_L]_{IB}^{-1} \sum_{IA} [M_L]_{IA} f_{IA} [N_{IB}]_{IA} \qquad (34)$$

In the present implementation, the fine to coarse mesh transfer of the unknowns is performed by direct interpolation, whereas conservative transfer is used for the residuals. The coarse to fine mesh transfer of the updates is accomplished by direct interpolation.

The sequence of unstructured meshes required for such a multigrid algorithm is readily generated using the mesh generator described above by simply altering the scaling of the user specified distribution functions. The process of determining the information required to accomplish the inter-grid transfers is found by using the same alternate digital tree [25] which is employed in the process of three dimensional unstructured mesh generation.

6. COMPUTATION OF THE FLOW PAST THE HERMES SPACE SHUTTLE

To illustrate the application of the multigrid acceleration procedure we consider the inviscid hypersonic flow about the HERMES 1.0 space shuttle. The free stream flow conditions correspond to a Mach number of 10 and the angle of attack is 30 degrees. Due to the symmetry of the problem only half spacecraft is modelled. The geometrical definition of the spacecraft surface and the outer computational boundary is shown in figure 5a and consists of 5 surface components and 11 segments as described in [13]. Using this geometrical definition, three meshes were generated, consisting 30 558 (6 094), 122 921 (23 539) and 749 070 (137 080) elements (points) respectively. The surface triangulations for the three meshes are shown in figure 5b. The three meshes were used in the multigrid computation. The algorithm employed in the three meshes was the 'low order' scheme of equation (21). A three stage time-stepping scheme was employed with a V multigrid cycle with one pre-smoothing iteration and zero post-smoothing iterations. The Mach number distribution on the surface of the spacecraft and on the computational boundaries is shown in figure 5c. The convergence history showing the number of evaluations of the right hand side of equation (21) versus the logarithm of the maximum density change for the the full approximation scheme is shown in figure 5d. It can be observed how rate of convergence is nearly constant and independent of the finest grid being used. The generation of the three meshes required about 420 minutes CPU time on an IBM RISC 6000/530H workstation and the multigrid solution required about 450 minutes CPU time on the same computer. The memory required for this computation was less than 12 Mbytes.

The solution shown in figure 5d was interpolated onto a finer grid consisting of 1,462 189 elements and 269 780 points. The surface triangulation of this mesh for the complete model is shown in figure 6a. The Flux Corrected Transport algorithm described in section 4.4 was applied using the three stage multi-stepping scheme. The solution was advanced for 500 timesteps using a local CFL number of 2.0. The FCT algorithm was applied at every stage and monotonicity was imposed on Density, Pressure and Mach number. The Mach number and pressure distributions on the surface of the spacecraft and computational boundaries are shown in figures 6b and 6c. The variation of the local Mach number at three different cross sections is plotted in figure 6d. The computed aerodynamic coefficients are $C_L = 0.44$, $C_D = 0.31$ and $C_M = 0.01$ which are in good agreement with those reported in [26].

7. CONCLUSIONS

We have presented an extension of our numerical scheme, originally developed for transonic flows, to the computation of hypersonic flows. The amount of added artificial viscosity is controlled by a FCT algorithm. For hypersonic flows, the FCT algorithm is found to produce more stable and accurate solutions than those obtained using a pressure sensor. The use of the FCT algorithm however, increases the computational cost by a factor of 2.5. The overall unstructured mesh approach appears to be a very efficient technique for modelling hypersonic flows about the complete spacecraft. Specially, if more realistic geometries e.g. including control surfaces, are to be considered. The multigrid algorithm, although used here only in conjunction with the 'low order' scheme, has proven to be an efficient way of accelerating the convergence of the iterative procedure. Future work will concentrate on the use of adaptivity to more accurately resolve localised flow features and on extending the multigrid approach to be used in conjunction with the 'high order' algorithm.

8. ACKNOWLEDGEMENTS

We acknowledge the partial support received from the Aerothermal Loads Branch, NASA Langley Research Center, under NASA Research Grant Number NAGW-1809, fr[illegible] Dassault Aviation and from British Aerospace, Military Aircraft Ltd, Warton. We would also like to acknowledge the support of IBM UK for allowing access to an IBM RISC 6000/530H workstation.

9. REFERENCES

1. J. Peiró, J. Peraire, K. Morgan, O. Hassan and N. Birch, 'The numerical simulation of flow about installed aero-engine nacelles using a finite element solver on unstructured meshes', accepted for publication in Aero. J., 1992
2. J. Peraire, J. Peiró and K. Morgan, 'A 3D finite element multigrid solver for the Euler equations', AIAA Paper 92-0449, 1992
3. J.P. Boris and D.L. Book, 'SHASTA - a fluid transport algorithm that works', J. Comp. Phys. 11, 38- 47, 1973

4. S.T. Zalesak, 'Fully multidimensional flux-corrected transport algorithms for fluids', J. Comp. Phys. 31, 335-349, 1979

5 K. Morgan, J. Peraire and R. Löhner , 'Adaptive finite element flux corrected transport techniques for CFD', in Finite Elements - Theory and Application, D.L. Dwoyer et al (Editors), Springer Verlag, 165-175, 1988

6. T.J. Barth, 'Numerical aspects of computing viscous high Reynolds number flows on unstructured meshes', AIAA Paper 91-0721, 1991

7. D.J. Mavriplis, 'Three dimensional unstructured multigrid for the Euler equations', AIAA Paper 91-1549, 1991

8. A. Jameson, 'Transonic flow calculations', Princeton University Report MAE 1751, 1984

9. E. Perez, 'Finite Element and multigrid solution of the two-dimensional Euler Equations on a non-structured mesh', INRIA Report No.442, 1985

10. R. Löhner and K. Morgan, 'Unstructured multigrid methods for elliptic problems', Int.J.Num.Meth.Engng. 24, 101-115, 1987

11. D.J. Mavriplis, 'Multigrid solution of the two-dimensional Euler equations on unstructured triangular meshes', AIAA J. 26, 824-831, 1988

12. M.-P. Leclercq, J. Periaux and B. Stoufflet, 'Multigrid methods with unstructured methods', Proc. 7th Int. Conf. on Finite Elements in Flow Problems, Huntsville, Alabama, 1989

13. J. Peraire, K. Morgan and J. Peiró, 'Unstructured finite element mesh generation and adaptive procedures for CFD', in Application of Mesh Generation to Complex 3-D Configurations, AGARD Publication No. 464, 18.1-18.12, AGARD Paris, 1990

14. A. Jameson, T.J. Baker and N.P. Weatherill, 'Calculation of inviscid transonic flow over complete aircraft', AIAA Paper 86-0103, 1986

15. J. Peraire, K. Morgan, J. Peiró and O.C. Zienkiewicz, 'An adaptive finite element method for high speed flows', AIAA Paper 87-0559, 1987

16. R.C. Swanson and E. Turkel, 'On central-difference and upwind schemes', ICASE Report 90-44, NASA Langley Research Center, 1990

17. P. Roe, 'Approximate Riemann solvers, parameter vectors and difference schemes', J.Comp. Phys. 43, 357-372, 1981

18. M. Vahdati, K. Morgan and J. Peraire, 'The computation of viscous compressible flows using an upwind algorithm and unstructured meshes', in Computational Nonlinear Mechanics in Aerospace Engineering, S.N. Atluri (Editor), AIAA Progress in Aeronautics and Astronautics Series, 1992 (to appear)

19. B. van Leer, 'Upwind difference methods for aerodynamic problems governed by the Euler equations', in Proc. 15th AMS-SIAM Summer Seminar on Applied Mathematics, B.E. Engquist et al (Editors), Scripps Institution of Oceanography, 1983.

20. M. Giles, 'Energy stability analysis of multi-step methods on unstructured meshes', M.I.T. CFD Laboratory Report CFDL-TR-87-1, 1987

21. A. Jameson and W. Schmidt, 'Some recent developments in numerical methods for transonic flows', Comp.Meth.Appl.Mech.Engng. 51, 467-493, 1985

22. K.Morgan, J.Peraire, R.R. Thareja and J.R. Stewart, 'An adaptive finite element scheme for the Euler and Navier-Stokes equations', AIAA 8th Computational Fluid Dynamics Conference, Honolulu, Hawaii, 1987

23. J. Peraire, K. Morgan and J. Peiró, 'Unstructured mesh methods for CFD', von Karman Institute for Fluid Dynamics Lecture Series, Brussels, 1990

24. K. Morgan, J. Peraire, J. Peiró and O. Hassan, 'The computation of three dimensional flows using unstructured grids', Comp. Meth. Appl. Mech. Engng. 87, 335-352, 1991

25. J. Bonet and J. Peraire, 'An alternate digital tree algorithm for geometric searching and intersection problems', Int.J.Num.Meth.Engng. 31, 1-17, 1991

26. R.-C. Molina, 'Finite Element Computations of Hypersonic Flows', ESA-ESTEC/WMA Report 1992

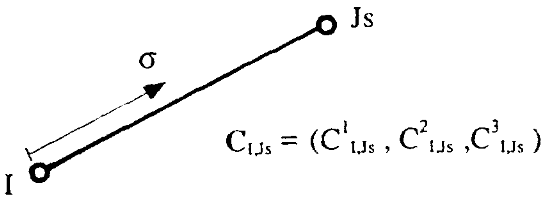

Figure 1.- Local coordinate σ along side between nodes I and J_s.

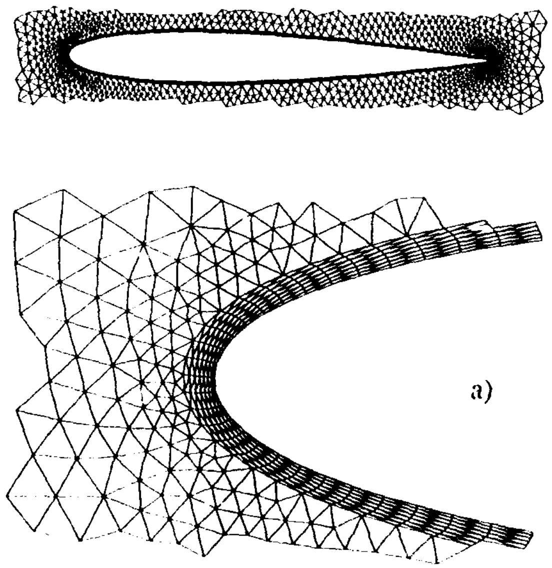

Figure 2.- Inviscid subsonic flow over a NACA0012. $M = 0.63$, $\alpha = 2^{0}$.

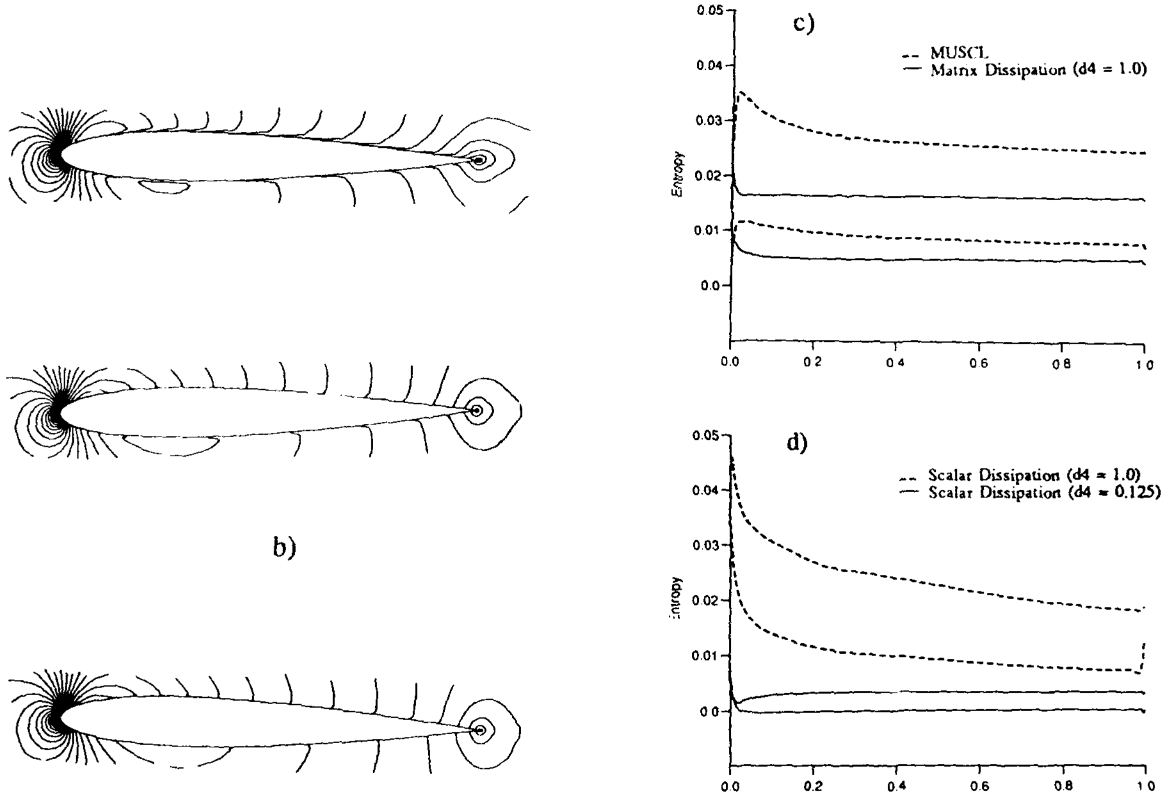

Figure 2.- Inviscid subsonic flow over a NACA0012. M = 0.63, $\alpha = 2^0$. a) Viscous mesh employed, b) Mach number contours using MUSCL, matrix dissipation and scalar dissipation schemes, c) Entropy deviation for MUSCL and matrix dissipation schemes and d) Entropy deviation for scalar dissipation scheme.

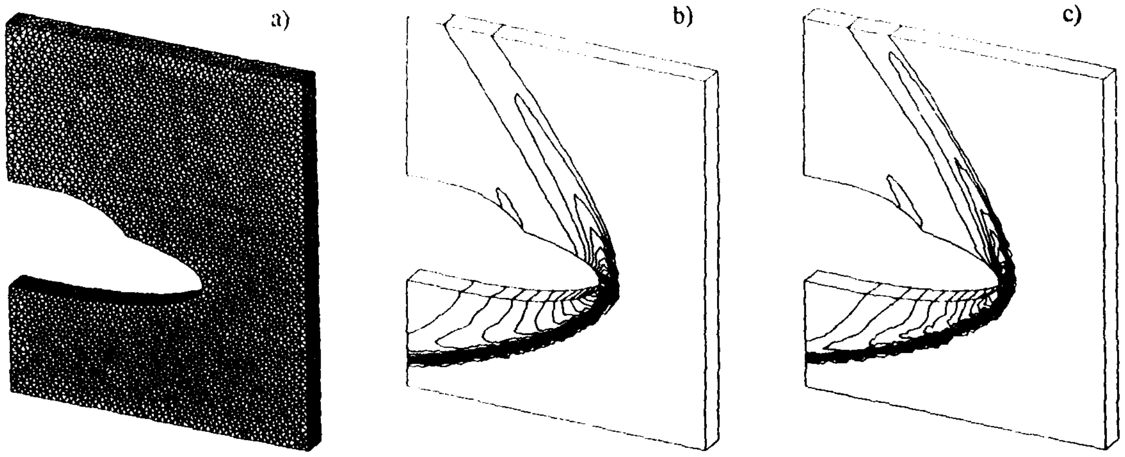

Figure 3.- Hypersonic flow over a double ellipse configuration. M = 8.15, $\alpha = 30^0$. a) Mesh employed, b) Pressure contours using pressure sensor and c) Pressure contours using FCT algorithm.

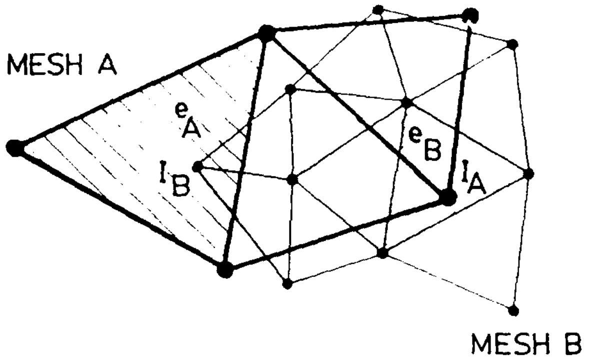
MESH A
e_A
I_B
e_B
I_A
MESH B

Figure 4.- Information transfer between two unnested meshes.

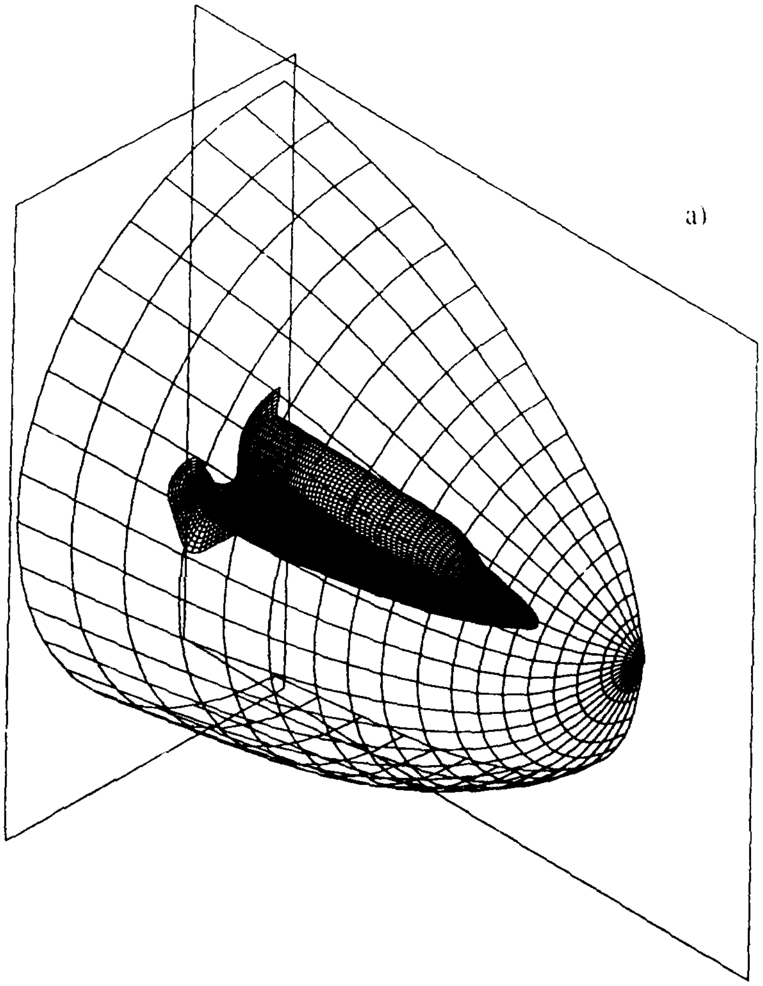

Figure 5.- Multigrid solution of the flow about the HERMES 1.0 space shuttle. $M = 10.0$, $\alpha = 30^0$.

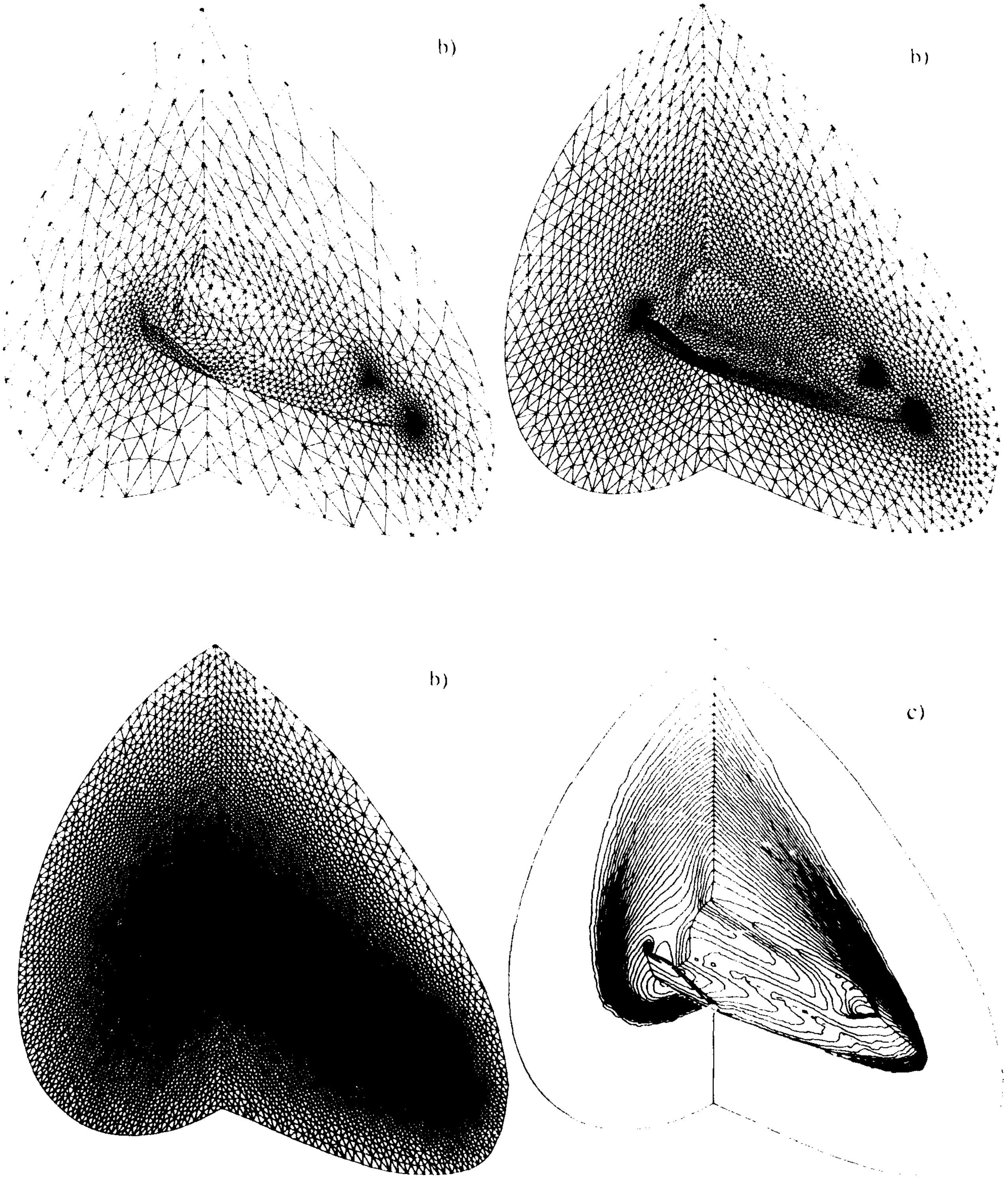

Figure 5.- Multigrid solution of the flow about the HERMES 1.0 space shuttle. $M = 10.0$, $\alpha = 30^0$.

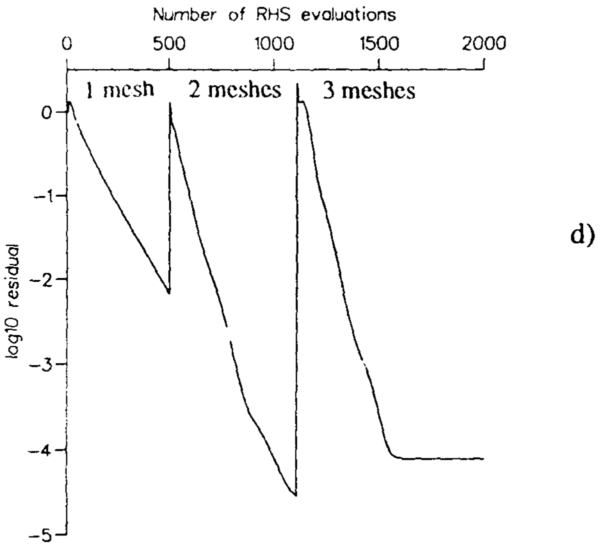

Figure 5.- Multigrid solution of the flow about the HERMES 1.0 space shuttle. M = 10.0, $\alpha = 30^0$. a) Geometry definition, b) Sequence of three meshes employed for the multigrid algorithm, c) Mach number contours using the 'low order' scheme, $\Delta M = 0.2$ and d) Convergence history.

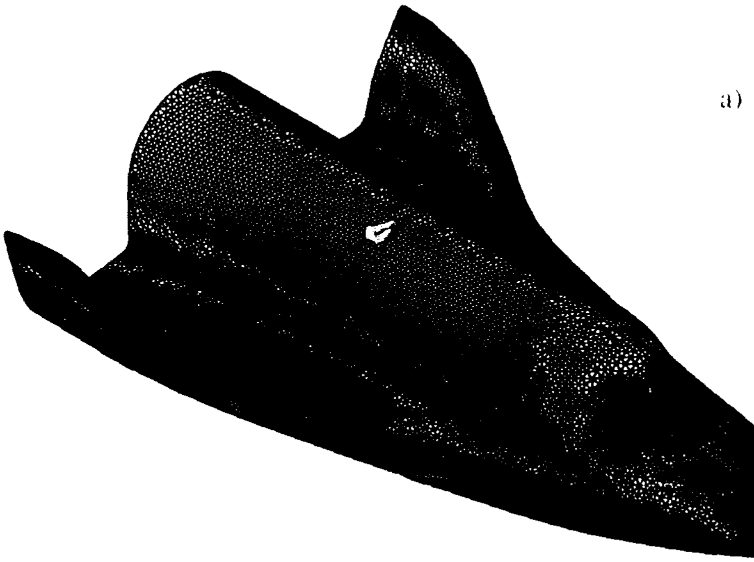

Figure 6.- Hypersonic flow around HERMES 1.0 space shuttle. M = 10.0, $\alpha = 30^0$.

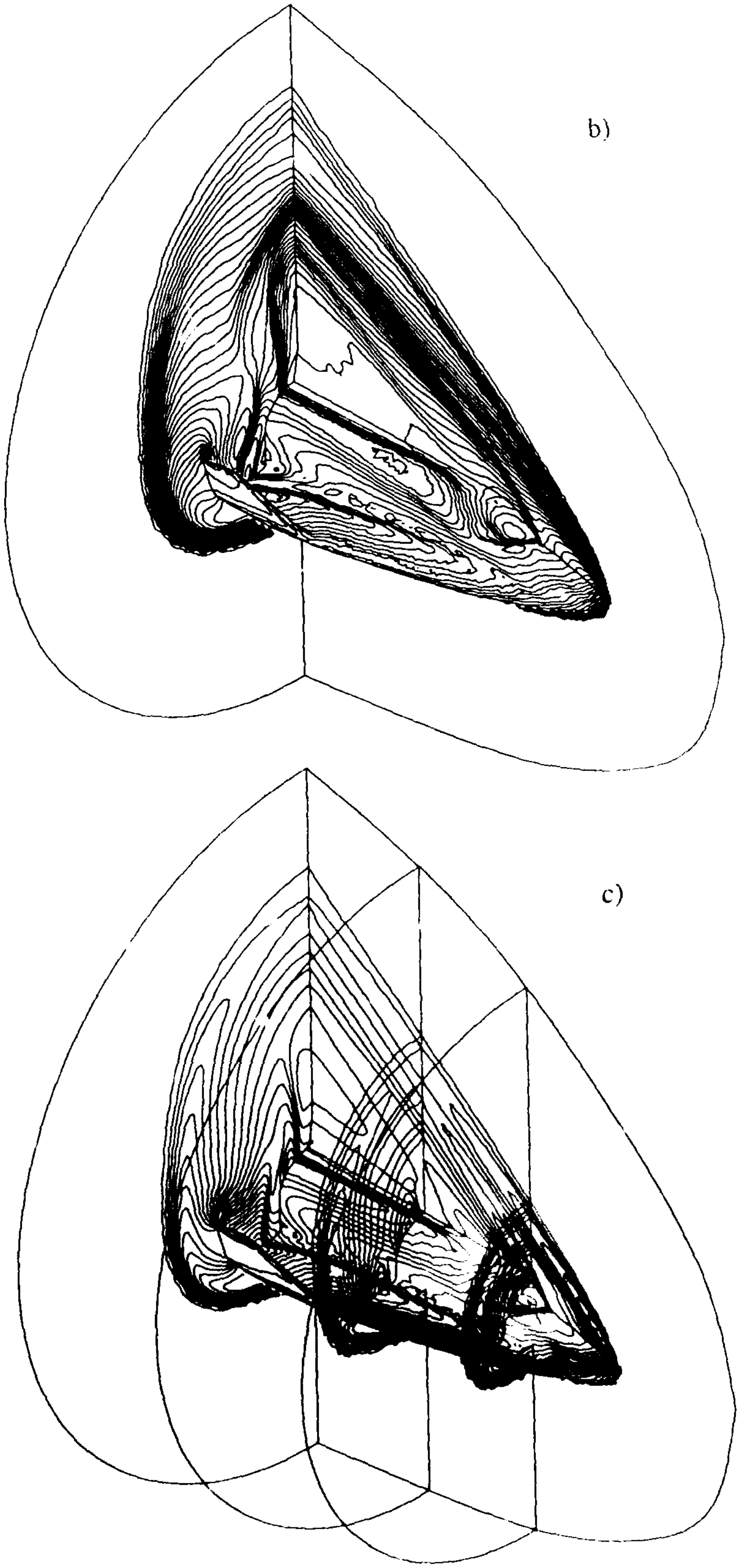

Figure 6.- Hypersonic flow around HERMES 1.0 space shuttle. $M = 10.0$, $\alpha = 30^0$.

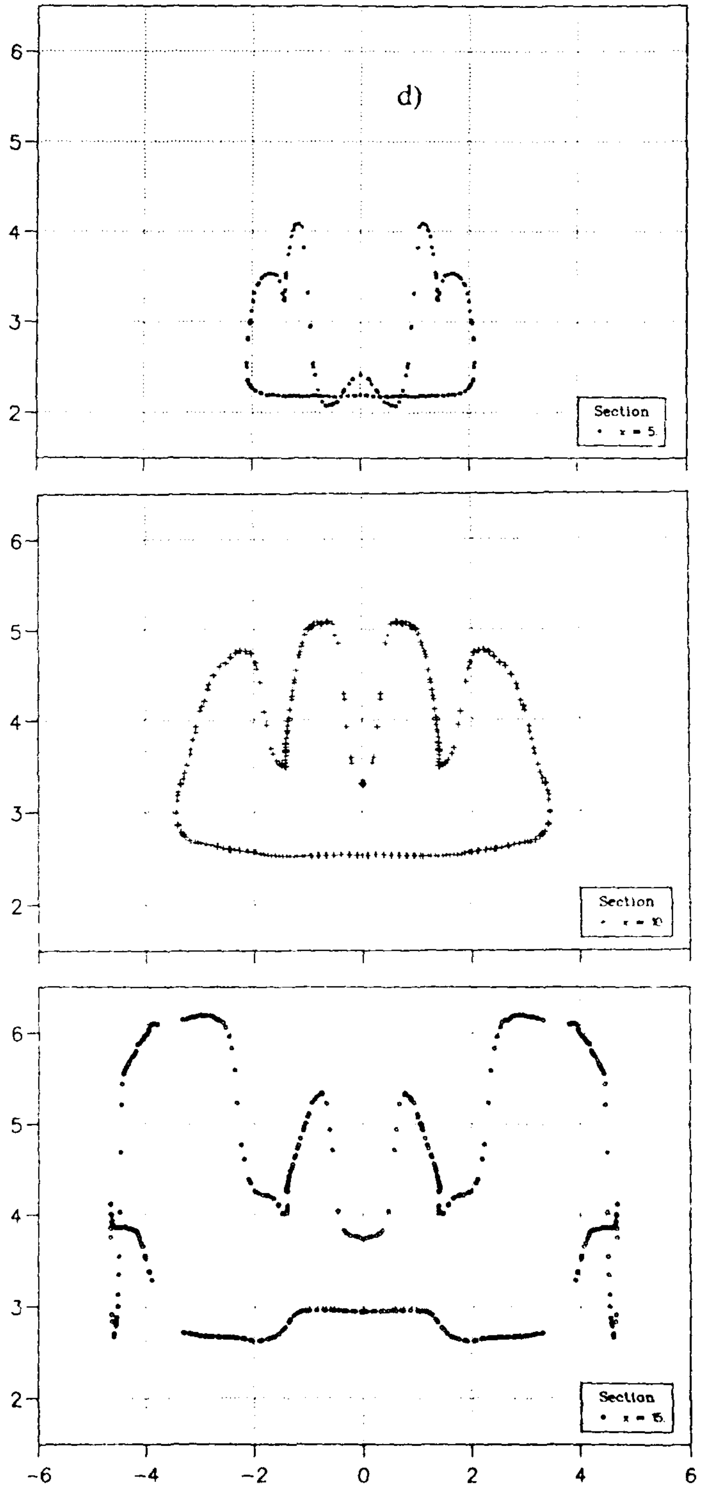

Figure 6.- Hypersonic flow around HERMES 1.0 space shuttle. $M = 10.0$, $\alpha = 30^0$. a) Surface triangulation, b) Mach number distribution $\Delta M = 0.2$, c) Pressure distribution $\Delta \log 10(p/p_\infty) = 0.15$ and d) variation of the Mach number at $x=5$, $x=10$ and $x=15$ m.

ON THE ACCURACY AND EFFICIENCY OF CFD METHODS IN REAL GAS HYPERSONICS

D. Drikakis
Lehrstuhl für Strömungsmechanik, Cauerstrasse 4
D-8520, Erlangen, Germany

and

S. Tsangaris
National Technical University of Athens,
P.O. Box 640 70, 157 10 Zografou-Athens, Greece

SUMMARY

A study of viscous and inviscid hypersonic flows, using generalized upwind methods, is presented. A new family of hybrid flux splitting methods is examined for hypersonic flows. A hybrid method is constructed by the superposition of the Flux Vector Splitting (FVS) method and second order artificial dissipation in the regions of the strong shock waves. The conservative variables on the cell faces are calculated by an upwind extrapolation scheme third order of accuracy. A second order accurate scheme is used for the discretization of the viscous terms. The solution of the system of equations is succeeded by an implicit unfactored method. In order to reduce the computational time a Local Adaptive Mesh Solution (LAMS) method is proposed. LAMS method combines the mesh sequencing technique and the local solution of the equations. Local solution of either Euler or Navier-Stokes equations is applied in the region of the flow field where numerical disturbances are died out slowly. Validation of the Euler and Navier-Stokes codes is obtained for hypersonic flows around blunt bodies. Real gas effects are introduced via a generalized equation of state. Extension of numerical methods in real gas hypersonics is presented for the hybrid FVS method and a Riemann solver.

1. INTRODUCTION

The development of computational methods for hypersonic flows is of increasing interest the last years. CFD is expected to play an important role in hypersonic vehicle design because of the difficulties to produce data from experimental facilities. The purpose of CFD methods is focused in the accurate simulation of flows with strong shock waves, capturing complex flow phenomena and variations of the variables in hypersonic flows. The term "strong shock waves" indicates shock waves with a substantial entropy production (Ref. 1). In the case of air such shocks are referred for Mach numbers greater than three. The study of hypersonic shock waves around a blunt body constists one of the major problem of the hypersonic aerodynamics, because blunt shape is used for the decrease of the heat transfer, especially in the nose of the body. The shock wave is stronger in front of the body while large variations of the flow variables occur across this.

Numerical methods must capture these variations into the thin shock and entropy layer as well as the thick boundary layers and the viscous interaction (Ref. 2, Ref. 3). During the last 15 years many upwind methods have been developed for transonic and supersonic flows These methods have improved the accuracy of the numerical solution for both inviscid and viscous flows (Ref. 4-9). Despite the reliability of these methods, problems have arisen in their applications to flows with strong shock waves, such as blunt body hypersonic flows. Hypersonic flows are dominated by strong shock waves, producing high strength jumps on the flow values. From the numerical point of view the essential problem is the development of numerical schemes which can capture the strong shocks. The numerical methods must produce enough dissipation in order to capture shocks of any strength.

Because of the high speed in hypersonic computations numerical errors cause negative values in flow variables, such as negative pressures or densities. Moreover numerical schemes can not capture strong shocks without spurious oscillations if the mesh lines are not aligned with the shock wave (Ref. 10). For this reason adaptive mesh procedures or low shock fitting methods are used. The bow shock fitting method can be applied successfully around simple geometries but can not be easily generalized around complex geometries and thus it can not be considered as a general method for the capturing of the strong shock waves.

Many researchers have presented the last year modifications of previous numerical methods for applications in hypersonic flows. Yee (Ref. 7) have modified her upwind TVD method scaling properly the arguments of the minmod limiter and making them proportional to the pressure differences. Collela and Woodward (Ref. 11) add numerical dissipation to their method in large discontinuities. MacCarmack and Candler (Ref. 9) use also a combination of two methods in hypersonic calculations adding the original Flux Vector Splitting (FVS) method by Steger-Warming (Ref. 4) in regions where the pressure changes by 25%. Eberle (Ref. 12) has also used a Riemann solver and the original (FVS) method by Steger-Warming in regions with strong shock when the Mach number is greater than three. A combination of TVD method with added dissipation for Navier-Stokes calculations has also been presented by Müller (Ref. 20).

Inspite of the above modifications certain numerical problems arise in hypersonic flow simulation (Ref. 10). Such problems are the spurius non physical oscillations of the numerical solution in the region of the strong shocks, the errors in the conservation of the total temperature as well as the development of accurate thermodynamic models in order to include real gas effects in the numerical simulation. The numerical scheme must be diffusive enough to capture the strong shock waves but at the same time the numerical diffusion must not destroy the physical picture of the flow field. In the present work a new family of hybrid flux splitting methods is examined (Ref. 39) for hypersonic flows. The hybrid methods construct the fluxes as a superposition of the splitting schemes and a second order artificial dissipation model especially constructed for hypersonic flow fields. The conservative variables on the cell faces can be calculated either by a five point upwind scheme (Ref. 12) or by the well known MUSCL scheme (Ref. 13). Thus hybrid FVS methods are created up to fourth order of accuracy for the inviscid fluxes discretization. A second order accurate model is used for the discretization of the viscous fluxes (Ref. 14).

One of the major problems during the numerical solution in hypersonic flows is the slow rates of convergence of the numerical algorithms. In hypersonic flows, small CFL numbers are required for the capturing of slowly moving shock waves. It is know from the experience in transonic and supersonic flows that unfactored solution methods including Gauss-Seidel relaxation allow the use of high CFL numbers. Numerical experiments have shown that high CFL numbers can not be used in hypersonic flows even in the case, where modern unfactored-Newton type mehtods (Ref. 15, Ref. 16) are used for the inversion of the system of equations. In order to reduce the computational time a Local Solution Method (LSM) is presented. This method was developed in the past for the acceleration of the convergence of the Euler and Navier-Stokes codes in transonic and supersonic flows obtaining a significant reduction of the computational time (Ref. 29, 17, 18). Numerical experiments have shown that this method can also be extended under certain modifications in the case of hypersonic flows. The solution of the system of equations is obtained by an unfactored Newton-type method using also a Gauss-Seidel relaxation technique.

Validation of the Euler and Navier-Stokes codes is obtained for supersonic flows around blunt bodies, because these geometries are particularly important shapes in hypersonic aerodynamics.

2. GOVERNING EQUATIONS

The governing equations are the time dependent Navier-Stokes equations for a compressible fluid. The equations can be written in conservation dimensionless form and for a generalized coordinate system as :

$$JU_t + (E_{inv})_\xi + (G_{inv})_\zeta = \frac{1}{Re}\left[(E_{vis})_\xi + (G_{vis})_\zeta\right] \qquad (1)$$

where Re is the Reynolds number, $U = (\varrho, \varrho u, \varrho w, e)^T$ is the conservative solution unknown vector, ϱ, u, w, e are the density, velocity in the x-direction, velocity in the z-direction and total energy per unit volume respectively. E_{inv}, G_{inv} are the inviscid flux vectors while E_{vis}, G_{vis} are the viscous flux vectors. $J = x_\xi z_\zeta - z_\xi x_\zeta$ is the Jacobian of the transformation from the Cartesian coordinates (x, z) to generalized coordinates (ξ, ζ). The inviscid and viscous fluxes are defined as :

$$E_{inv} = J(\tilde{E}\xi_x + \tilde{G}\xi_z)$$

$$G_{inv} = J(\tilde{E}\zeta_x + \tilde{G}\zeta_z)$$

$$E_{vis} = J(\tilde{R}\xi_x + \tilde{S}\xi_z)$$

$$G_{vis} = J(\tilde{R}\zeta_x + \tilde{S}\zeta_z)$$

with

$$\tilde{E} = \begin{bmatrix} \rho u \\ \rho u^2 + p \\ \rho uw \\ (e+p)u \end{bmatrix} , \qquad \tilde{G} = \begin{bmatrix} \rho w \\ \rho uw \\ \rho w^2 + p \\ (e+p)w \end{bmatrix}$$

$$\tilde{R} = \begin{bmatrix} 0 \\ \tau_{xx} \\ \tau_{xz} \\ u\tau_{xx} + w\tau_{xz} - q_x \end{bmatrix} , \qquad \tilde{S} = \begin{bmatrix} 0 \\ \tau_{xz} \\ \tau_{zz} \\ u\tau_{xz} + w\tau_{zz} - q_x \end{bmatrix}$$

The indices ξ, ζ denote partial derivatives, except for the stresses τ_{xx}, τ_{xz}, τ_{zz} and the heat terms q_x, q_z. The stresses and the heat terms are given as :

$$\tau_{xx} = -p - \frac{2}{3}\mu(-2u_x - w_z)$$

$$\tau_{zz} = -p - \frac{2}{3}\mu(u_x - 2w_z)$$

$$\tau_{xz} = \tau_{zx} = \mu(w_x + u_z)$$

$$q_x = -\frac{\gamma\mu}{Pr}T_x , \quad q_z = -\frac{\gamma\mu}{Pr}T_z$$

where *Pr is the Prandtl number.* μ, k are the viscosity and the heat conductivity coefficients while T is the gas temperature. The dimensionless viscosity μ can be defined for a real gas as a function of the density and the specific internal energy :

$$\mu = \mu(\rho, i) \qquad (2)$$

while the Pr number as a function of the temperature and the density :

$$Pr = Pr(T, \varrho) \qquad (3)$$

The formulation of the governing equations is completed by an equation governing of state :

$$p = p(\rho, i) \qquad (4)$$

The implementation of the real gas properties into the numerical algorithm will be presented in another section of the paper.

3. GENERALIZED FVS METHOD FOR HYPERSONIC FLOWS

Almost all of the upwind methods make use of the operator splitting for the discretization of the inviscid fluxes. The use of the high accurate multi-dimensional upwind methods (Ref. 19) is difficult for the development code as well as very expensive in computational time. Because of the use of the operator splitting the solvers find difficult to recognize strong variations which are not aligned with the mesh lines. This problem has also been observed from other authors (Ref. 10, Ref. 20) in flows with strong shock waves. In such flows many of the parameters take very small values and if the solution is not accurate negative squort arguments will blow up the solution. The latest is much stronger in the transient phase that shock wave is moved.

This problem can be overcome increasing the artificial dissipation of the algorithm. In the present study the discretization of the inviscid fluxes is carried out by a modified Steger-Warming FVS method (Ref. 21). The FVS method decomposes the inviscid flux into two parts positive and negative in accordance with the sign of the eigenvalues

$$\left(E_{inv}\right)_{i+\frac{1}{2}} = \left(T\Lambda^{+}T^{-1}\right)_{i+\frac{1}{2}} U^{-}_{i+\frac{1}{2}} + \left(T\Lambda^{-}T^{-1}\right)_{i+\frac{1}{2}} U^{+}_{i+\frac{1}{2}} \qquad (5)$$

where T, T^{-1} are the left and right eigenvector matrices respectively while Λ^{+} and Λ^{-} are the positive and negative eigenvalue matrices. The splitted fluxes are defined on the cell faces of the computational volume instead of the center of the volume because the first formulation improves the results into the boundary layer.

The eigenvalues of the positive and negative eigenvalue matrices are splitted as

$$\lambda_0^{\pm} = \frac{\lambda_1^{\pm} + \lambda_2^{\pm}}{2} \qquad (6a)$$

$$\lambda_j^{\pm} = \frac{\lambda_j + |\lambda_j|}{2} \quad , \quad j = 1, 2 \qquad (6b)$$

where

$$\lambda_0 = u\xi_x + w\xi_z \quad , \quad \lambda_1 = \lambda_0 + S \quad , \quad \lambda_2 = \lambda_0 - S$$

s represents the speed of sound. The splitting of the zeroth eigenvalue in accordance with the equation (6a) reduces the errors concerning the preservation of the total temperature (Ref. 21, 22). The splitted convective fluxes can be defined finally as :

$$\left(E^{FVS}_{inv}\right)^{+}_{i+\frac{1}{2}} = \rho\,\nabla\xi \begin{vmatrix} \frac{1}{2}\,(\lambda_1^{\pm} + \lambda_2^{\pm}) \\ (u + \frac{S\xi_x}{\gamma})\frac{\lambda_1^{+}}{2} + (u - \frac{S\xi_x}{\gamma})\frac{\lambda_2^{+}}{2} \\ (w + \frac{d\xi_z}{\gamma})\frac{\lambda_1^{+}}{2} + (w - \frac{S\xi_z}{\gamma})\frac{\lambda_2^{+}}{2} \\ \frac{1}{2}\,H^{+}\,(\lambda_1^{+} + \lambda_2^{\pm}) \end{vmatrix} \qquad (7)$$

with

$$\xi_x = \frac{\xi_x}{\sqrt{\xi_x^2 + \xi_z^2}} \quad , \quad \xi_z = \frac{\xi_z}{\sqrt{\xi_x^2 + \xi_z^2}}$$

As we mentioned above, in order to overcome the numerical problems in hypersonic flow computations artificial dissipation is added in the FVS method. Because the dissipation terms are not desirable in the smoothed flow regions, an accurate treatment of these is necessary. Two different models have been tested in the numerical experiments. The *first model is known from the* central discretization algorithms (Ref. 23). The added second order artificial dissipation is written as follows :

$$D^2_{\xi}U = \mu_{\xi}(\lambda_{i+\frac{1}{2}} \cdot \varepsilon_{i+\frac{1}{2},j})\,\Delta_{\xi}\,U_{i,j} \qquad (8)$$

where the operators μ_ξ and Δ_ξ are defined as follows :

$$\Delta_{\xi} f = f_{i+1} - f_i \quad , \quad \mu_{\xi} f = f_{i+\frac{1}{2}} - f_{i-\frac{1}{2}}$$

The mean values of the eigenvalues are calculated from the artithmetic average of the neighbouring cells. The coefficient ε is defined as follows :

$$\varepsilon_{i+\frac{1}{2},j} = K_{max}(v_{i+1,j}, v_{i,j}) \qquad (9a)$$

$$v_{i,j} = \frac{|P_{i+1,j} - 2P_{i,j} + P_{i-1,j}|}{P_{i+1,j} + 2P_{i,j} + P_{i-1,j}} \qquad (9b)$$

P is the pressure and K is constant. Because in hypersonic flow around bodies the bow shock is captured close to the body, there is a small number of cells between the shock and the body in the stagnation region. The high pressure values in the stagnation region cause uniform variation of the sensor v and artificial dissipation is added not only in *the shock* but on the whole flow field, in the stagnation region. Thus errors on the preservation of the total enthalpy and less of the accuracy are presented. Control of the added dissipation using the pressure values in fewer cells did not improve the accuracy of the scheme.

Because the zeroth eigenvalue takes value close to zero and the first, second eigenvalues have not large variations in the stagnation regions, they are good indicators for the second order *damping terms.* Thus, the following model is constructed :

$$D^2_{\xi}U = \mu_{\xi}\left(c \cdot r_{i+\frac{1}{2}}\right)\Delta_{\xi}U_{i,j} \qquad (10a)$$

$$r_{i+\frac{1}{2}} = \max\left(\Delta_{\xi}L_0, \Delta_{\xi}L_1, \Delta_{\xi}L_2, \varepsilon\right) \qquad (10b)$$

The terms L_0, L_1, L_2 are defined as :

$$L_j = \frac{\lambda_j}{\sum_j |\lambda_j|} \qquad j = 0, 1, 2 \qquad (11)$$

The parameter c is a constant with typical values between 0.05 and 0.18 while ε is a very small, positive constant number ($\varepsilon = 10^{-5}$). The above model adds only a very small amount of second order artificial dissipation in the shock region.

The generalized flux for hypersonic flows can be defined as :

$$\left(E_{inv}\right)_{i+\frac{1}{2}} = \left(E^{FVS}_{inv}\right)_{i+\frac{1}{2}} + \left(D^2_{\xi}U\right)_{i+\frac{1}{2}} \qquad (12)$$

The above flux can also be used in transonic and supersonic flows putting the constant c in the expression (10a) equals zero.

4. HIGH ORDER EXTRAPOLATION SCHEMES

The conservative variables on the cell faces can be calculated either by a hybrid five point upwind extrapolation scheme (Ref. 12) or by the well known MUSCL scheme (Ref. 13). The hybrid five point upwind scheme is constructed by the superposition of the first, second, third and fourth order extrapolation schemes :

$$U^{\pm}_{i+\frac{1}{2}} = A\,U^{1,\pm} + (1-A)\left[BU^{2,\pm} + (1-B)\left[CU^{3,\pm} + (1-C)U^{4,\pm}\right]\right] \qquad (13)$$

The superscripts 1, 2, 3, 4 *denote the several* order of the extrapolation. For instance the third and fourth order extrapolations are defined as :

Third order :

$$\left(U^3_{i+\frac{1}{2}}\right)^{-} = \frac{1}{6}\left(5U_i - U_{i-1} + 2U_{i+1}\right)$$

$$\left(U^3_{i+\frac{1}{2}}\right)^{+} = \frac{1}{6}\left(5U_{i+1} - U_{i+2} + 2U_i\right)$$

Fourth order :

$$\left(U^4_{i+\frac{1}{2}}\right)^{-} = \left(U^4_{i+\frac{1}{2}}\right)^{+} = \frac{1}{2}\left(7U_i + 7U_{i+1} - U_{i-1} - U_{i+2}\right)$$

The terms A, B are limiter functions and are defined by the second order derivatives of the pressure (Ref. 12) :

$$A = \min\left(1, d\left|P^2_{\xi\xi,i+1} - P^2_{\xi\xi,i}\right|\right) \qquad (14a)$$

$$B = \min\left(1, b\left|P^2_{\xi\xi,i+1} - P^2_{\xi\xi,i}\right|\right) \qquad (14b)$$

The values of the constants d, b and C are d = 4.5, b = 2.5, C = 2.25.

A second approach for the calculation of the conservative variables on the cell faces is the MUSCL scheme :

$$U^{-}_{i+\frac{1}{2}} = U_{i,j} + \frac{S_{i,j}}{4}\left[\left(1 - kS_{i,j}\right)\nabla + (1+kS)\Delta\right]U_{i,j} \qquad (15a)$$

$$U^{+}_{i+\frac{1}{2}} = U_{i+1,j} - \frac{S_{i+1,j}}{4}\left[\left(1 + kS_{i+1,j}\right)\nabla + \left(1 + kS_{i+1,j}\right)\Delta\right]U_{i+1,j} \qquad (15b)$$

where $\Delta U_{i,j} = U_{i+1,j} - U_{i,j}$, $\nabla U_{i,j} = U_{i,j} - U_{i-1,j}$. S is the van Albada limiter function (Ref. 24) for the detection of discontinuities. The spatial accuracy of the MUSCL scheme depends on the parameter k. For k = -1 it produces a fully upwinded scheme, for k = 0 a symmetric, for k = 1/3 a third order biased one and for k = 1 a centered one. MUSCL scheme is second order accurate for two dimensional flows while the third order upwind biased formulation of this scheme is strictly third order for one dimensional calculations. Stability analysis has shown (Ref. 11) that the contribution of the third order dissipation is similar for the third order hybrid upwind and the MUSCL scheme in the fully upwinded formulation (k = -1). The fourth order hybrid upwind as well as the other formulations of the MUSCL scheme do not contribute in the third order derivatives of the truncation error analysis of the scalar one dimensional convection-diffusion equation.

Thus, third order hybrid upwind as well as fully upwinded are prefered for hypersonic calculations because contribute in the diminishing of the numerical oscillations known as "odd-even decoupling". It is also obvious that the hybrid upwind scheme is third order in smoothed *flow regions and it is switched on* first order of accuracy in the regions of discontinuities.

Numerical experiments (Ref. 11, Ref. 21) have shown that hybrid upwind and MUSCL scheme present similar behaviour in inviscid flows but it does not happen in viscous flows. MUSCL scheme in combination with the FVS method causes inaccuracies into the boundary layers while third order hybrid scheme capture the skin friction and the velocity distribution in boundary layes with satisfactory accuracy (Ref. 21). The generation of numerical errors, in boundary layers calculations has also been observed by other authors in the past (Ref. 24, Ref. 26). In accordance with the above hybrid upwind is used for the viscous flows.

5. UNFACTORED IMPLICIT RELAXATION SOLUTION

An unfactored implicit method is used in combination with the generalized FVS method for the solution of the system of equations. The implicit method is first order accurate in time. The unfactored equations are solved by a Newton-type method constructing a sequence of approximation q^{v} such that

$$\lim_{v>1} q^{v} \rightarrow U^{n+1}$$

where v is the sub iteration state. A Newton form is obtained by the linearization of the equation (1), around the known subiteration state v, as follows :

$$J \cdot \frac{\Delta q^{v+1}}{\Delta t} + \left(A^{v}_{inv}\Delta q^{v+1}\right)_{\xi} + \left(C^{v}_{inv}\Delta q^{v+1}\right)_{\zeta} + \left(C^{v}_{vis.th}\Delta q^{v+1}\right)_{\zeta} =$$

$$J \cdot \frac{U^{n} - q^{v}}{\Delta t} - RHS \qquad (16a)$$

where

$$RHS = \left(E^{v}_{inv}\right)_{\xi} + \left(G^{v}_{inv}\right)_{\zeta} - \frac{1}{Re}\left(E^{v}_{vis}\right)_{\xi} - \frac{1}{Re}\left(G^{v}_{vis}\right)_{\zeta} \qquad (16b)$$

q^{v}, q^{v+1} are the solution vectors at the subiteration states v, v+1 respectively. Gauss-Seidel relaxation using 4 subiteration states is applied on the left hand side (LHS) of equation (16a) while the RHS is held constant (Ref. 22). On the LHS the thin layer viscous Jacobian C^{th}_{vis} is used for steady state calculations, saving computational time. The inviscid fluxes on the (LHS) of equation (16a) are splitted :

$$\left(A^{v}_{inv}\Delta q^{v+1}\right)_{\xi} = \left(A^{v}_{inv}\Delta q^{v+1}\right)_{i+\frac{1}{2}} - \left(A^{v}_{inv}\Delta q^{v+1}\right)_{i-\frac{1}{2}}$$

$$\left(A^{v}_{inv}\Delta q^{v+1}\right)_{i+\frac{1}{2}} = \left(T\Lambda^{+}T^{-1}\right)^{+}_{i+\frac{1}{2}}\left(\Delta q^{v+1}\right)^{+}_{i+\frac{1}{2}} + \left(T\Lambda^{-}T^{-1}\right)^{v}_{i+\frac{1}{2}}\left(\Delta q^{v+1}\right)^{-}_{i+\frac{1}{2}}$$

with

$$\left(\Delta q^{v+1}\right)^{+}_{i-\frac{1}{2}} = b\Delta q^{v+1}_{i} + \frac{1}{2}(1-b)\left(3\Delta q^{v+1}_{i} - \Delta q^{v+1}_{i-1}\right)$$

$$\left(\Delta q^{v+1}\right)^{+}_{i+\frac{1}{2}} = \left(\Delta q^{v+1}\right)_{i+1}$$

The parameter b is a function, defined from the values of the RHS in order to decrease the accuracy of the extrapolation in the regions of the discontinuities. In order to retain the stability of the implict solution, the splitted eigenvalue matrices are defined as :

$$\Lambda^{+} = \max(F, \Lambda) \quad , \quad \Lambda^{-} = \min(-F, \Lambda)$$

where

$$F = B \quad h\max\left[\lambda_{1}, \lambda_{2}\right]$$

The sensor B is defined by the equation (14b) if the hybrid upwind is used for the discretization of the inviscid fluxes. If the FVS method is used with the MUSCL upwind the sensor B is better to be defined by the squares of the Mach number on the left and right states of the cell face. The constant h is 0.5.

6. LOCAL SOLUTION METHOD

As we mentioned in the introduction of the present work slow rates of convergence have been observed in numerical simulation of hypersonic flow fields. In order to reduce the computational time a combination of the mesh sequencing technique with a local solution method is applied. In the mesh sequencing technique (Ref. 17, Ref. 28) an initial guess on the fine mesh is obtained by first iterating the solution of the equations on a sequance of coarser grids and then interpolating the solution to the next finer grid.
The coarse mesh is constructed by eliminating every second line of the fine mesh in each direction. The refining grid criterion for the interpolation of the solution from the coarse to the fine mesh is the maximum variation max($\Delta\varrho$, $\Delta(\varrho u)$, $\Delta(\varrho w)$, Δe) of the conservative variables during the iterations. Because in the mesh sequencing procedure the center of the volumes of the fine mesh are not a subset of the volumes of the coarse mesh, bilinear interpolation is used for the calculation of the conservative variables from the corresponding variables on the coarse mesh. In the present calculations two levels (coarse and fine mesh) have been used.

Panaras (Ref. 29) has observed for first time that the solution of the equations is not necessary to be obtained in the whole flow field during the iterations. This fact originates from the non-uniformities of the flow variation towards a steady or unsteady solution. An analytical study of the numerical disturbances has been presented by Panaras (Ref. 29) using an implicit approximately factored scheme for the thin layer Navier-Stokes equations. In accordance with the non-uniform propagation of the disturbances the solution of the equations can be obtained only in the regions of the flow field where the disturbances are large (exceed a prescribed value) while the rest flow field is considered to be converged. Drikakis et. al. (Ref. 18) has also observed that the numerical disturbances are decreased rapidly away from the solid boundary and the regions of shock wave, in transonic and supersonic flows. In the case of hypersonic flow around a blunt body the shock wave is formed near the solid boundary and thus interaction between solid boundary and shock wave in inviscid flows as well as between the shock wave and the thick boundary layer in viscous flows occurs. The behaviour of the numerical disturbances has been studied separately for the inviscid and the viscous flow cases. The basic conclusions from this study have as follows : In inviscid hypersonic flows the numerical disturbances are diminisched faster from the solid boundary region (except of the stagnation region), than the region of the slowly moving shock wave. During the numerical solution the shock wave is moved until its final steady state position is achieved. After the steady state position of the shock, numerical disturbances continue to exist in the region of the large variations until the achievement of the final steady state values of the variables across the shock wave. In accordance with the above local solution can be achieved in a region around the shock wave and in front of the body nose, during the numerical iterations.

In viscous hypersonic flows large values of the numerical disturbances are presented (after a number of iterations) into the boundary layer and around the shock wave. Thus two local solution zones are constructed. The first overlaps the bow shock wave while the second overlaps a part of the boundary layer around the body. A region between the two zones is freezed until the steady state solution is achieved in the whole flow field. The local solution regions are generated by an adaptation procedure (Ref. 18).

7. INCORPORATION OF REAL GAS EFFECTS

The introduction of a real gas model for equilibrium conditions required minimum modifications of the generalized FVS method. Extensions of FVS methods with real gas effects have also been presented in the past by other authors (Ref. 30-33).

The incorporation of the equilibrium gas model is consisted from two parts. The first part concerns the flux splitting formulas on the right hand side of equation (16a). It is known that if we consider the pressure as a function of the density and the specific internal energy the present FVS method does not satisfy the homogeneous property of the Euler equations. Thus the incorporation of the real gas model is succeeded by a parametrization, introducting an equivalent ratio of specific heats $\tilde{\gamma}$, defined as :

$$\tilde{\gamma}(\rho, i) = 1 + \frac{P(\rho, i)}{\rho i} \qquad (17)$$

The generalized equation of state as well as the equations for the transport properties (viscosity, thermal conductivity, Prandtl number) have been developed by Srinivasan et. al. (Ref. 34-35). The "true" speed of sound can be expressed by the introduction of the pressure derivatives as :

$$S^2 = P_\rho + P\frac{P_i}{\rho 2} \qquad (18a)$$

where P_ρ and P_i are the pressure derivatives with respect to the density and the specific internal energy, respectively. In FVS method it is not necessary the speed of sound to be defined by equaation (18a) because the parametrization using the equivalent ratio $\tilde{\gamma}$ (eq. 17) has already been used in generalized form. Thus in order to save computational time the speed of sound is defined as :

$$S^2 = \tilde{\gamma}(\rho, i)\,\frac{P}{\rho} \qquad (18b)$$

Although the splitted fluxes on the right hand side have not significant modifications for the real gas model, a different approach on the left hand side of equation (16a) can be used by the derivation of the Jacobian matrices and the eigenvectors for a general equation of state (Ref. 33). The above derivation make the Jacobians and the eigenvectors as fucntions of the pressure derivatives. Numerical experiments for the present steady hypersonic flows showed that the above procedure increase the computational time while has not any influence in the numerical results. Thus the equivalent $\tilde{\gamma}$ ratio is used in all the parts of the method.

In order to save computational time the γ ratio and the transport properties of the air are updated every fiftieth iteration. This process does not affect the stability of the numerical solution.

8. RESULTS

Validation of the Euler and Navier-Stokes codes is obtained for hypersonic flows around blunt bodies, because these geometrics are particularly important shapes in hypersonic aerodynamics.

Initially the efficiency of the Local Solution Method (LSM) has been tested for the hypersonic inviscid flow $M_\infty = 6.3$ around a cylinder. A physical picture of the flow field is shown in Figure (1a) plotting the iso-density lines around the cylinder. For this flow case the influence of the mesh sequencing and the LSM as well as the influence of the relaxation factor (in the Gauss-Seidel relaxation sweeps) in the convergence has been studied. In transonic and supersonic flows ($M_\infty \leq 2$) the relaxation factor (RL) has the value 0.2. For the present flow the mesh sequencing procedure has been tested using the relaxation factor with the values RL = 0.2, RL = 0.6. From figure (1b) it is obvious that the value RL = 0.6 improves the convergence. In the same figure it is also shown that the mesh sequencing procedure reduces the computational work in comparison with the fine mesh. The mesh sequencing method has also been used in combination with the LSM. After the convergence of the solution on the coarse mesh (Residual ≈ 10^{-6}) the iterations are continued on the fine mesh. The local solution is applied when the residual reaches the value of about 10^{-3}. The convergence of the equations on the partial meshes is faster than the convergence on the fine mesh (using mesh sequences). Thus, after 450 iterations the convergence has been achieved. by the LSM while using only the mesh sequencing procedure 720 iterations are required. Hence the combination of the mesh sequencing method and the LSM is used for the calculation of the present hypersonic flow fields.

The first test case for the validation of the Euler code, is the hypersonic flow $M_\infty = 8$ around a circular cylinder. Two different meshes have been used. The lines of the first mesh (Figure 2a) are not aligned with the bow shock wave, while the lines of the second mesh are fitted in the shock. The mesh size for the meshes is 1200 cells (30x40). The first mesh is used in order to show that the above hybrid flux splitting method produces only minimum oscillations in the bow shock, although the shock intersects the mesh lines. In Figures (3a, b) the iso-pressure lines using the meshes of Figure (2a) and (2b) respectively, are plotted. The bow shock is captured without spurious oscillations. In the second mesh (Fig. 2b) the mesh lines in the radial direction have clustered in the bow shock, and thus the thin structure of the shock wave is obtained. The satisfactory resolution of the shock (Fig. 3a) inspite of the use of a non-adaptive mesh, is due to the minimum second order artificial dissipation which is added to the shock wave. The present hyprid method preserves also satisfactory the total temperature. The error in the total temperature along the symmetry line is shown in Figure 4. The analytic solution for the temperature on the stagnation point is 4071 °K while the corresponding computed is 4111.7 °K (error about 1%).

The second test case is considered for validation both of the perfect and of the real gas versions of the Euler code. This flow case is the hypersonic flow with free stream Mach number 15 over a blunt body. The above flow field was also calculated by Grossman and Walters (Ref. 36) using Roe's flux difference splitting method both for perfect and real gas model. In figure (5) the computational mesh 81x41 is shown. Reference conditions were chosen to correspond with atmospheric conditions at an altitude of 45 km : $p = 170\ \mathrm{N/m^2}$, $\varrho = 0.002\ \mathrm{kg/m^3}$, T = 295 °K.

For real gas calculations the thermodynamic subroutines of Srinivasan et. al. (Ref. 34) have been used. The iso-pressure lines for the perfect gas and the real gas calculations are shown in Figure (6). The resolution of the shock waves is very good. The pressure contours show the large differences, in the stand-off distance, between the perfect and equilibrium air. In Figures (7a, b, c) the distributions of the pressure, temperature and density along the symmetry line are presented. The present results are compared with the corresponding results by Grossman and Walters (Ref. 36). The jump of the flow values across the shock wave is also compared with the analytic solution. The calculated stand-off distance d = 0.401 R is in good agreement with the corresponding experimental value d = 0.3941 R by Billig (Ref. 37). In figures (8a, b, c) the distribution of the pressure, temperature and density along the body surface both for perfect and equilibrium air are presented. The distributions of the pressure temperature and density along the symmetry line for the equilibrium air are shown in figures (9a, b, c). All the above resuts are in good agreement with the corresponding results from the literature.

The validation of the Navier-Stokes code in hypersonic flows has been obtained for the flow with free stream Mach number $M_\infty = 10$, $Re = 1.2 \times 10^4$ around a hyperbola with equation :

$$\left(\frac{x}{500\ \mathrm{mm}}+1\right)^2-\left(\frac{y}{88\ \mathrm{mm}}\right)^2=1$$

This hypersonic flow has also been studied by other authors (Ref. 22-38). Reference conditions were chosen to correspond to atmospheric conditions at an altitude 52 km : $p = 48.67\ N/m^2$, $T = 220\ ^oK$, $\rho = 7.7 \times 10^{-4}\ kg/m^3$.
The wall of hyperbola is considered adiabatic. The computational mesh is 60 x 60 (fig. 10). Iso-Mach lines for the perfect air are shown in figure (11) while comparison of the flow field for the perfect and equilibrium air is shown in figure (12) plotting the iso-temperature lines. The resolution of the shocks is satisfactory. The code preserves the symmetry of the solution (fig. 11). It is noted that the calculations have been obtained in the whole flow field although the flow is symmetrical. The abrupt change of the flow direction in the region of the strong variations is shown in fig. (13) for the real gas case. Comparisons between present results and Ref. 38, 39 for the pressure coefficient, temperature and skin friction are shown in figures (14-18).

The real gas effects are not significant in the pressure distribution (fig. 15) but in the temperature field (fig. 16). The results for the pressure and skin friction distribution (figs. 14, 17) are in good agreement with the corresponding results from the literature (Ref. 38, 39). In figure 19 the variation of the equivalent ratio of specific heats $\tilde{\gamma}$ is plotted for the hypersonic flow field. Lower values than $\tilde{\gamma} = 1.4$ (perfect air) are observed in the case of equilibrium air. Finally the convergence histories for the perfect gas as well as for the real gas calculations are shown in figures (20a, b). The number of iterations is the same but the thermodynamic subroutines of the equilibrium air increase the total computational time about 20%.

9. CONCLUSIONS

The accuracy and the efficiency of upwind hybrid FVS methods have been discussed while results for inviscid and viscous hypersonic flows have been presented. The conclusions are as follows :

1. The efficiency of the unfactored solution can be improved by using the mesh sequencing and the local solution method.

2. The hybrid FVS method can capture strong shock waves with satisfactory accuracy either the mesh lines are fitted in the shock wave or not.

3. The results of Euler and Navier-Stokes codes are in satisfactory agreement with the corresponding results from the literature.

10. REFERENCES

1. Woodward, P., Colella, P., "The Numerical Simulation of Two-Dimensional Fluid Flow with Strong Shocks", J. Comput. Phys., Vol. 54, 1984, pp. 115-173.

2. Hayes, W.D., Probstein, R.F., "Hypersonic Flow Theory", Academic Press, New York, 1959.

3. Anderson, J.D., Jr., "Hypersonic and High Temperature Gas Dynamics", Int. ed. McGraw Hill, 1982.

4. Steger, J.L., Warming, R.F., "Flux Vector Splitting of the Inviscid Gasdynamic Equations with Application to Finite-Difference Methods", J. Comp. Phys., Vol. 40, 1981, pp. 263-293

5. Roe, P.L., "Approximate Riemann Solvers, Parameters Vectors, and Difference Schemes", J. of Comp. Phys., Vol. 43, 1981, pp. 357-372.

6. Van Leer, B., "Towards the Ultimate Conservative Difference Scheme. II. Monotonicity and Conservation Combined in a Second-Order Scheme", J. Comp. Phys., Vol. 14, 1974, pp. 361-370.

7. Yee, H.C., "Upwind and Symmetric Shock Capturing Schemes", NASA - TM - 89464, 1987.

8. Chakravarthy, S.R., "High Resolution Upwind Formulations for the Navier-Stokes Equations", VKI Lecture Series, Comp. Fluid Dynamics, 1988-05, 1988.

9. MacCormack, R.W., Candler, G.V., "The Solution of the Navier-Stokes Equations Using Gauss-Seidel Line Relaxation", Comp. and Fluids, Vol. 17, No. 1, 1989, pp. 135-150.

10. Kordulla, W., "Computational Techniques for Hypersonic Flows", AGARD, No. 761, 1988.

11. Colella, P., Woodward, P.R., "The Piecewise Parabolic Method (RPM) for Gas Dynamical Simulations", J. Comput. Phys., Vol. 54, 1984, pp. 174-201.

12. Eberle, A., "Characteristic Flux Averaging Approach to the Solution of Euler's Equations", VKI Lecture Series, Comp. Fluid Dynamics, 1987-04, 1987.

13. Van Leer, B., "Flux-Vector Splitting for the Euler Equations", Proc. 8th Int. Conf. on Numerical Methods in Fluid Dynamics, Aachen, 1982, Lecture Notes in Physics, Vol. 170, Springer, Berlin, 1982, pp. 507-512.

14. Chakravarthy, S.R., Szema, K.Y., Goldberg, U.C., Gorski, J.J., "Application of a New Class of High Accuracy TVD Schemes to the Navier-Stokes Equations", AIAA-Paper 85-0165, 1985.

15. Chakravarthy, S.R., "Relaxation Methods for Unfactored Implicit Upwind Schemes", AIAA-84-0165, AIAA 22nd Aerospace Sciences Meeting, Reno, Nevada, Jan. 9-12, 1984.

16. Schmatz, M.A., Brenneis, A., Eberle, A., "Verification of an Implicit Relaxation Method for Steady and Unsteady Viscous and Inviscid Flow Problems", AGARD CP 437, 1988, pp. 15-1 ÷ 15-33.

17. Drikakis, D., Tsangaris, S., "Improved Mesh Sequencing Method for the Accelarated Solution of the Compressible Euler and Navier-Stokes Equations", 17th ICAS Congress, Stockholm, Sweden, 9-14 September, 1990.

18. Drikakis, D., Tsangaris, S., "Local Solution Acceleration Method for the Euler and Navier-Stokes Equations" AIAA Journal, vol 30/2, 1992, pp 340-348.

19. Colella, P., "Multidimensional Upwind Mehtods for Hyperbolic Conservation Laws", J. Comput. Phys., Vol. 87, 1990, pp. 171-200.

20. Müller, B., "Simple Improvements of an Upwind Scheme for Hypersonic Flows", AIAA-paper, 89-1977, 9th CFD Conference, Buffalo, New York, 1989.

21. Drikakis, D., Tsangaris, S., "Laminar and Turbulent Viscous Compressible Flows Using Improved Flux Vector Splittings", 9th GAMM Conference on Numerical Methods in Fluid Mechanics, 25-27 September 1991, Lausanne, Switzerland.

22. Schmatz, M.A., "Hypersonic Three-Dimensional Navier-Stokes Calculations for Equilibrium Gas", AIAA-paper, 89-2183, 7th Applied Aerodyn. Conf., Seattle, July 31, 1989.

23. Jameson, A., Schmidt, W., Turkel, E., "Numerical Solutions of the Euler Equations by Finite Volume Methods Using Runge-Kutta Time-Stepping Schemes" AIAA - 81 - 1259, 1981.

24. Van Albada, G.D., Van Leer, B., Roberts, W.W., "A Comparative Study of Computational Methods in Cosmic Gas Dynamics", Astron. Astrophys., Vol. 108, 1982, pp. 76-84.

25. Hänel, D., Schwane, R., Seider, G., "On the Accuracy of Upwind Schemes for the Solution of the Navier-Stokes Equations", AIAA-Paper 87-1105, 1987.

26. Van Leer, B., Thomas, J.L., Roe, P.L., Newsome, R.W., "A Comparison of Numerical Flux-Formulas for the Euler and Navier-Stokes Equations", AIAA-Paper 87-1104-CP, AIAA 8th Computational Fluid Dynamics Conference, Honolulu, Hawaii, June 9-11, 1987.

27. Drikakis, D., Tsangaris, S., "A Multi-Zonal Local Solution Methodology for the Accelerated Solution of the Turbulent Navier/Stokes Equations", 18th ICAS Congress, 20-25 September, 1992, Beijing, People's Republic of China.

28. Pulliam, T.H., Steger, J.L., "Recent Improvements in Efficiency Accuracy and Convergence for Implicit Approximate Factorisation Algorithm", AIAA-Paper, 5-0360, 1985.

29. Panaras, A.G., "The Spatially Non-Uniform Convergence of the Numerical Solution of Flows", J. of Comp. Phys., Vol. 82, 1989, pp. 429-453.

30. Grossman, B., Walters, R.N., "Flux-Split Algorithms for the Multi-Dimensional Euler Equations with Real Gases", Computer and Fluids, Vol. 17, No. 1, 1989, pp. 99-112.

31. Liou, M. S., Van Leer, B., Shuen, J.S., "Splitting of Inviscid Fluxes for Real Gases", J. Comput. Phys., Vol. 87, 1990, pp. 1-24.

32. Glaister, P., "An Aproximate Linearised Riemann Solver for the Three Dimensional Euler Equations for Real Gases Using Operator Splitting", J. Comput. Phys., Vol. 77, 1988, pp. 361-383.

33. Drikakis, D., Tsangaris, S., "An Implicit Characteristic-Flux-Averaging Method for the Euler Equations for Real Gases", Int. J. for Numerical Methods in Fluids, Vol. 11, 1990.

34. Srinivasan, S., Tannehill, J.C., "Simplified Curve Fits for the Transport Properties of Equilibrium Air", NASA CR-178411, 1987.

35. Srinivasan, S., Tannehill, J.C., Weilmuenster, K.J., "Simplified Curve Fits for the Thermodynamic Properties of Equilibrium Air", NASA RP-1181, 1987.

36. Grossman, B., Walters, R.W., "Analysis of Flux-Split Algorithms for the Euler's Equations with Real Gases", AIAA J., Vol. 27, No. 5, 1989, pp. 524.

37. Billig, F.S., "Shock-Wave Shapes Around Spherical - and Cylindrical - Nosed Bodies", J. of Spacecraft and Rockets, Vol. 4, No. 6, 1967, pp. 822-823.

38. Mundt, CH., Pfintzer, M., Schmatz, M.A., "Calculation of Viscous Hypersonic Flows Using a Coupled Euler/2nd Order Boundary Layer Method", MBB-FE122-S-PUB-387, 1989.

39. Drikakis, D., "Development of Upwind Numerical Methods for High Speed Aerodynamics", Ph.D. dissertation, NTUA, 1991.

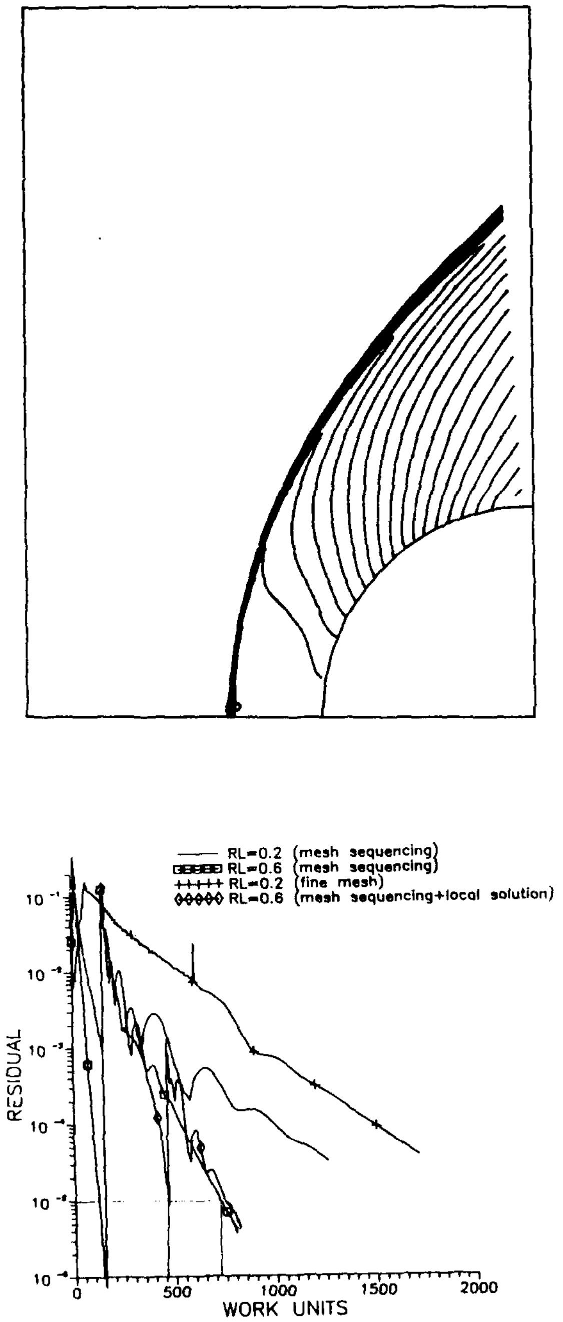

Figures 1a,b : Hypersonic flow M∞ = 6.3 around a cylinder a. Iso-density lines b. Convergence histories.

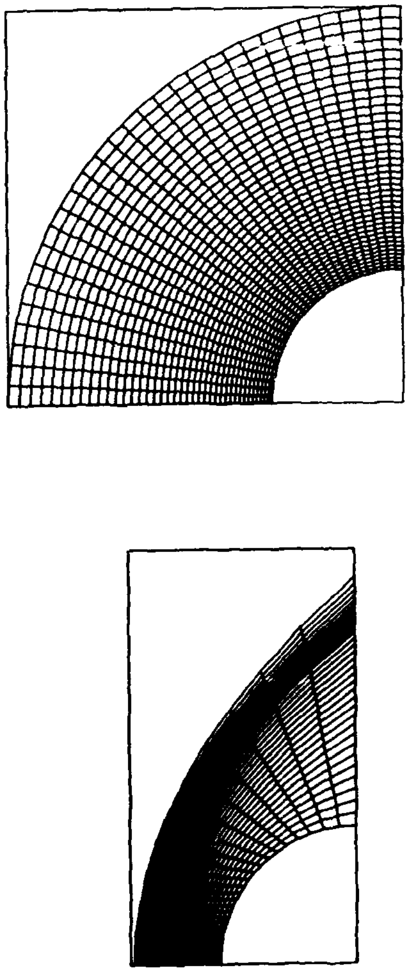

Figures 2a,b : Computational meshes for the hypersonic flow M_∞ = 8 around a cylinder a. Non-adaptive mesh b. Adaptive mesh.

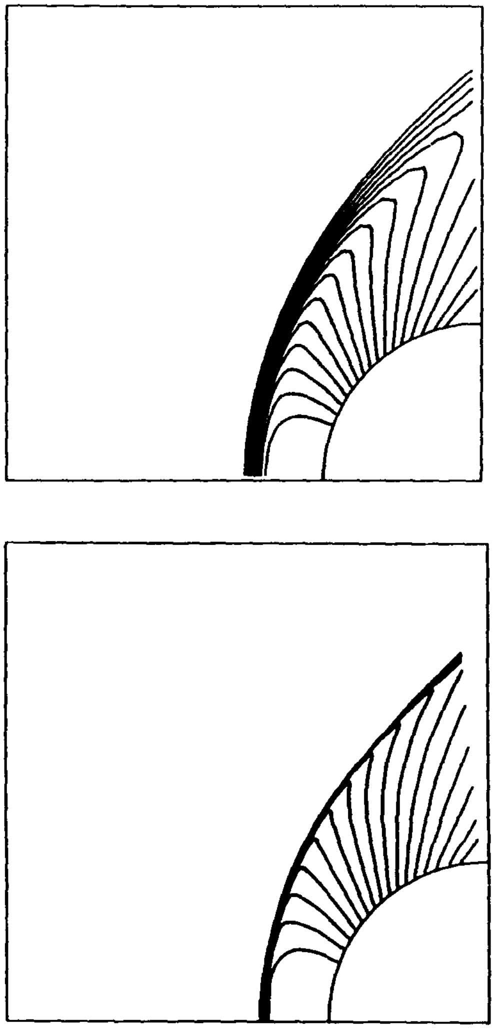

Figures 3a,b : Iso-pressure lines for the hypersonic flow M_∞ = 8 a. Non- adaptive mesh solution b. Adaptive mesh solution.

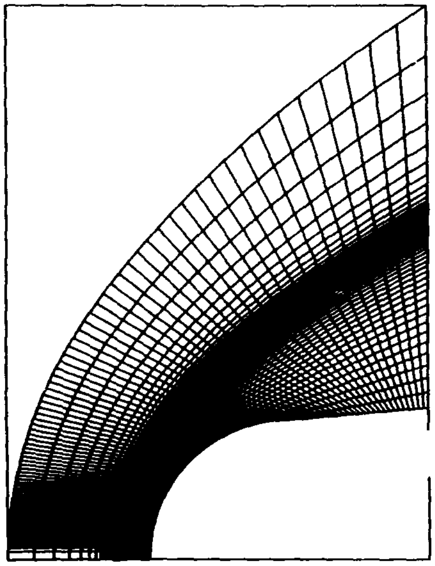

Figure 5 : Computational mesh (81x41) for the inviscid hypersonic flow M_∞ = 15.

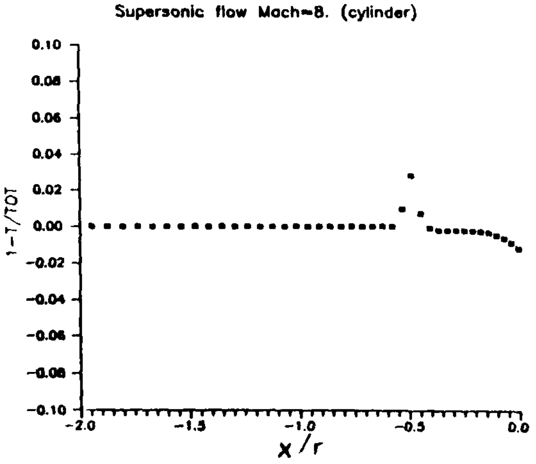

Figure 4 : Total temperature error along the symmetry line.

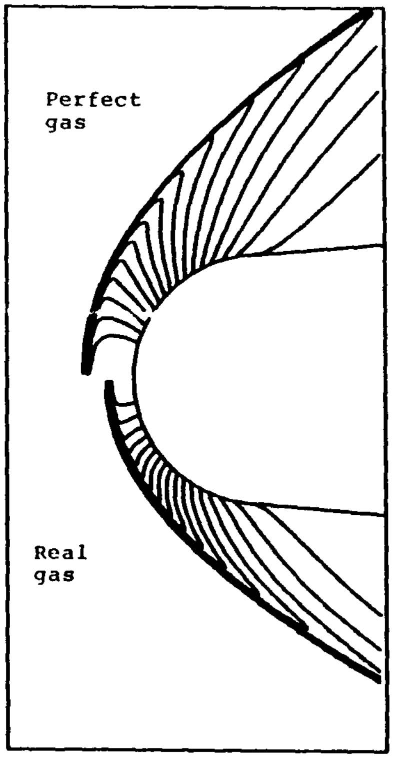

Figure 6 : Iso-pressure lines for perfect and equilibrium air.

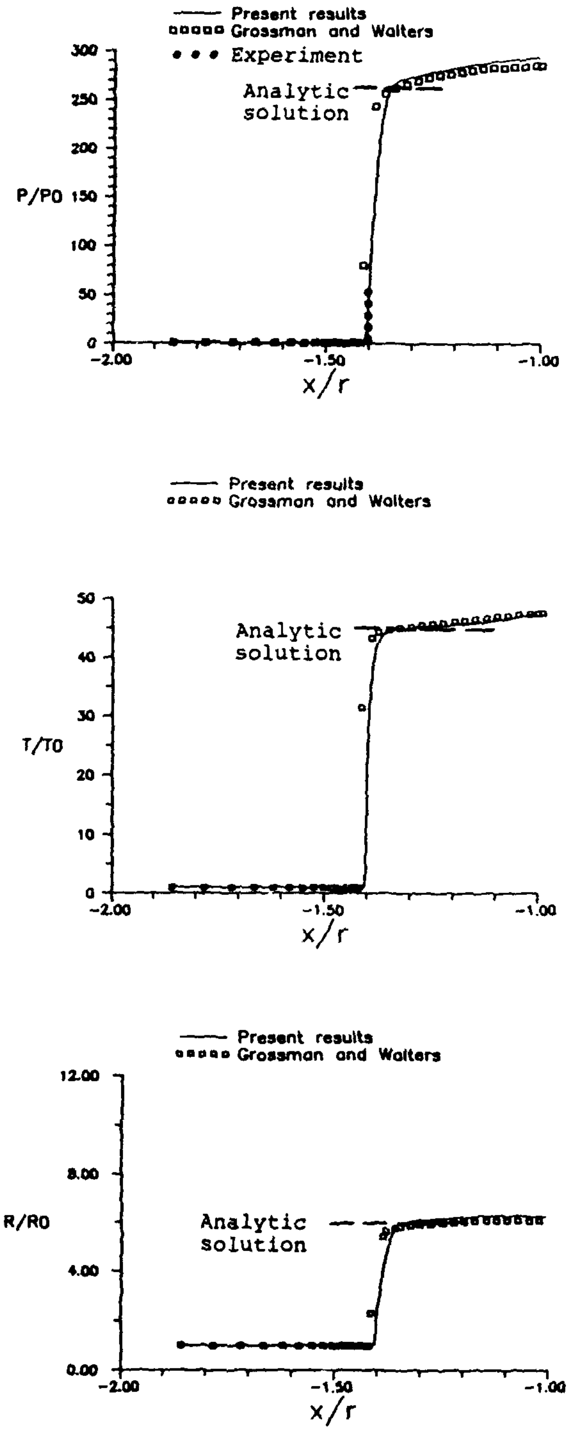

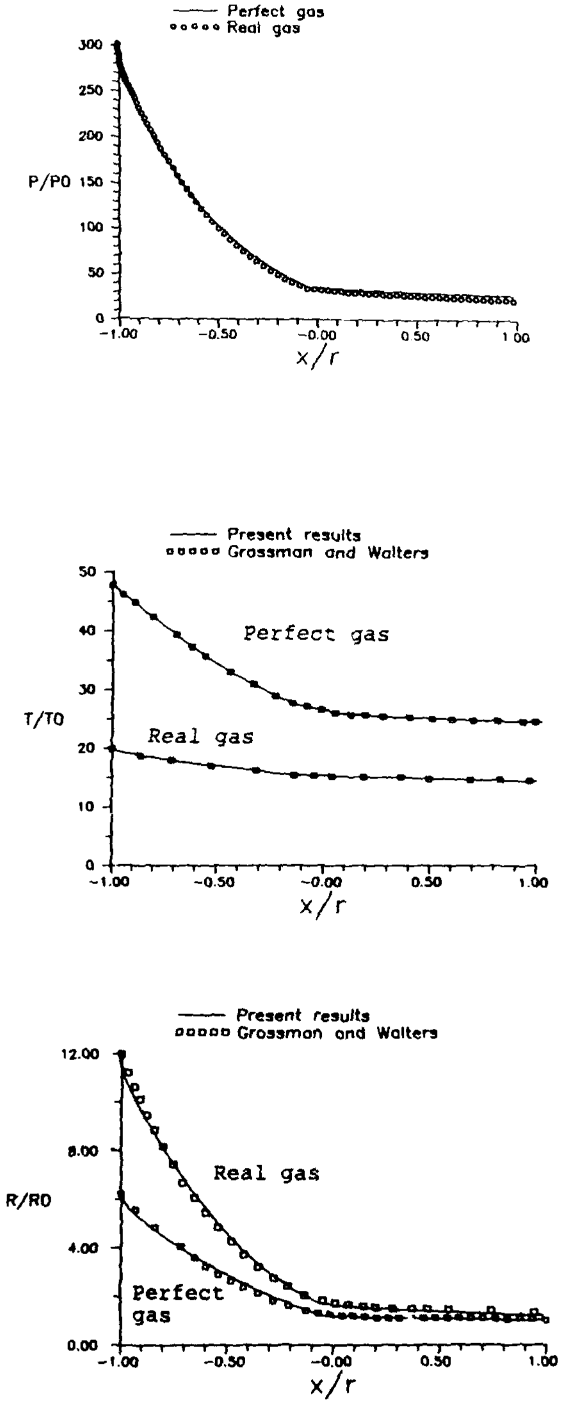

Figures 7a,b,c : Distributions along the symmetry line for the perfect air a. pressure b. temperature c. density.

Figures 8a,b,c : Distributions along the body surface. Comparisons between perfect and equilibrium air a. pressure b. temperature c. density.

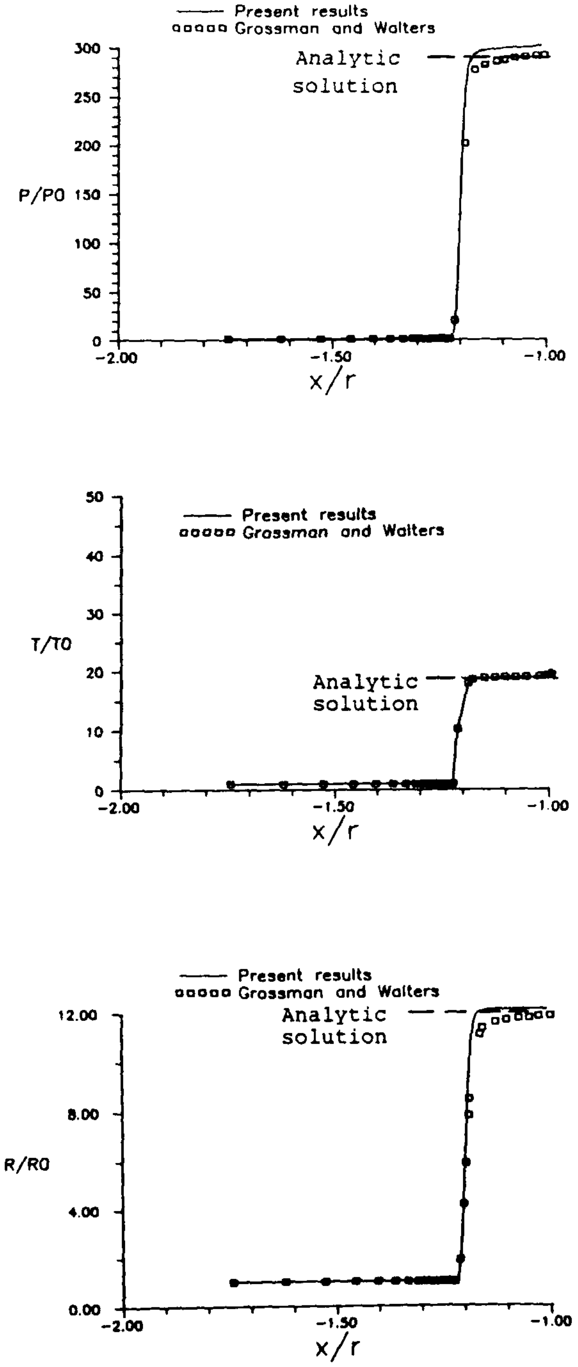

Figures 9a,b,c : Distributions along the symmetry line for the equilibrium air a. pressure b. temperature c. density.

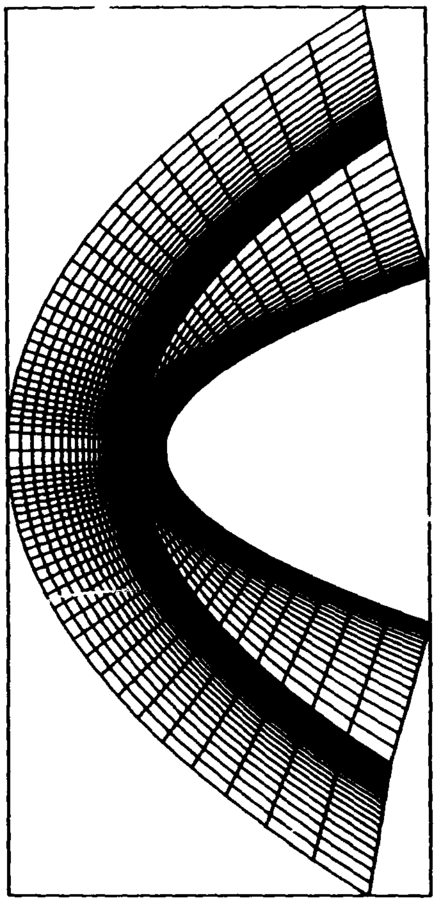

Figure 10 : Computational mesh (60x60) for the viscous hypersonic flow (M_{∞} = 10. Re = 1.2 x 10^4) around the hyperbola.

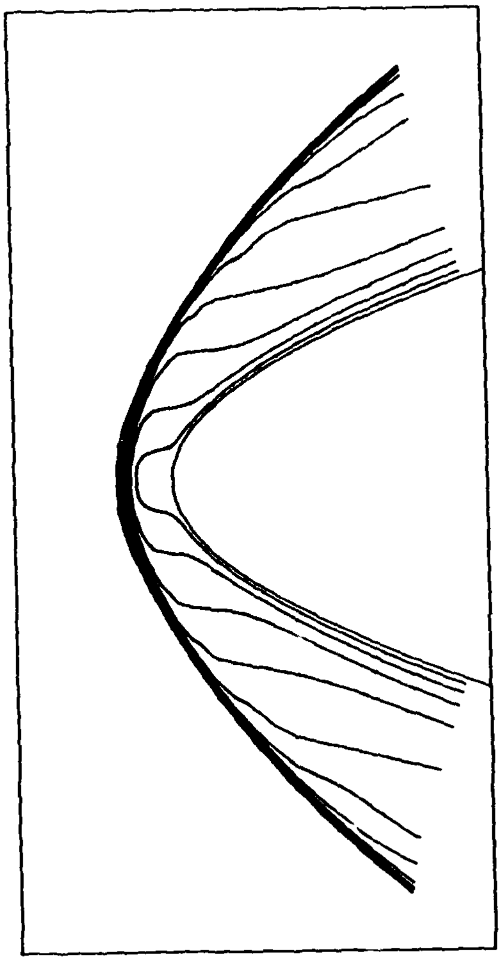

Figure 11 : Iso-Mach lines on the whole flow field (perfect air).

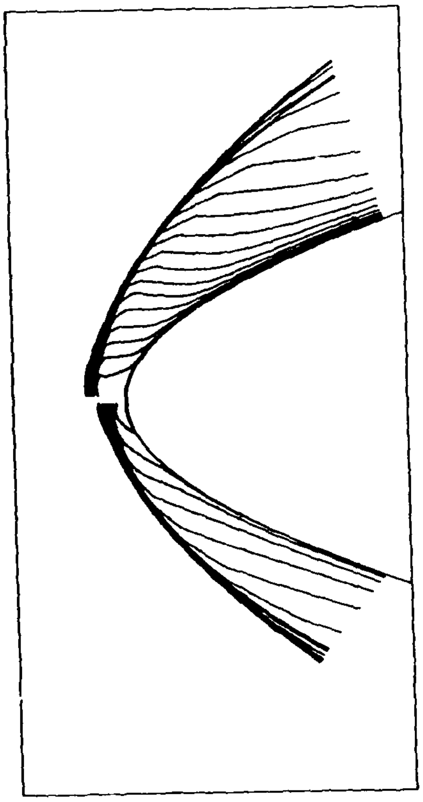

Figure 12 : Iso-temperature lines for the perfect and equilibrium air (Viscous hypersonic flow $M_\infty = 10$, $Re = 1.2 \times 10^4$).

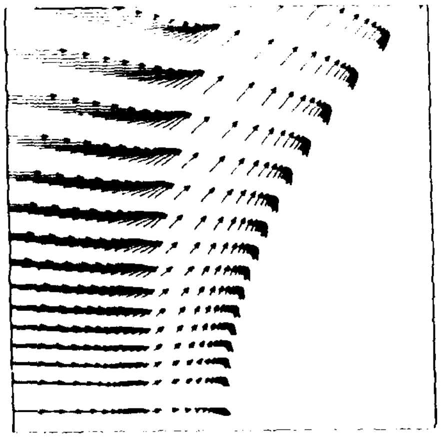

Figure 13 : Velocity vectors in the stagnation region of hyperbola (equilibrium air).

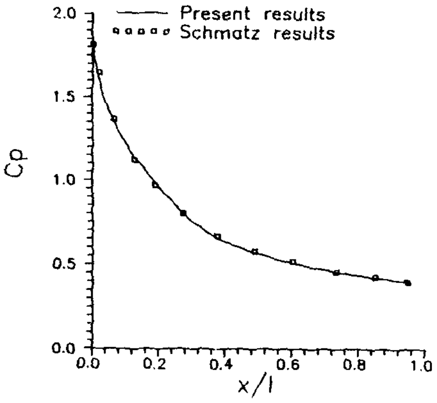

Figure 14 : Pressure coefficient distribution (Cp) along the hyperbola wall (perfect air).

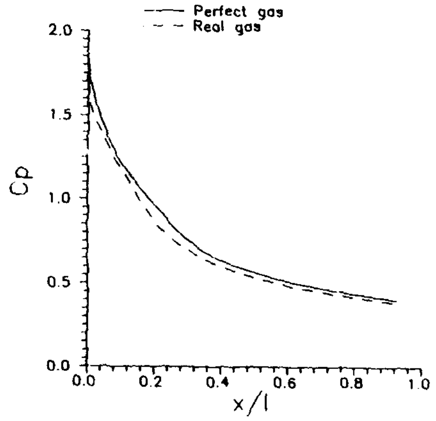

Figure 15 : Comparison of Cp between perfect and equilibrium air.

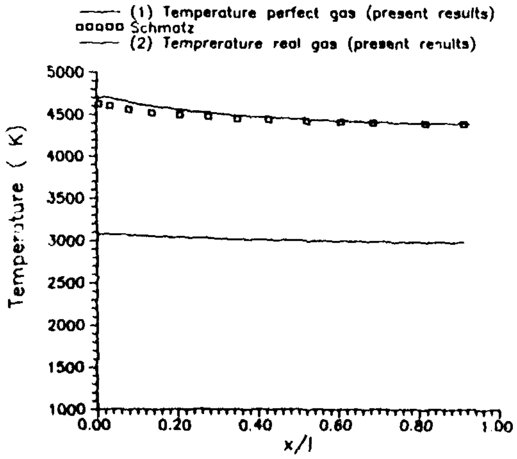

Figure 16 : Temperature distributions along the hyperbola wall.

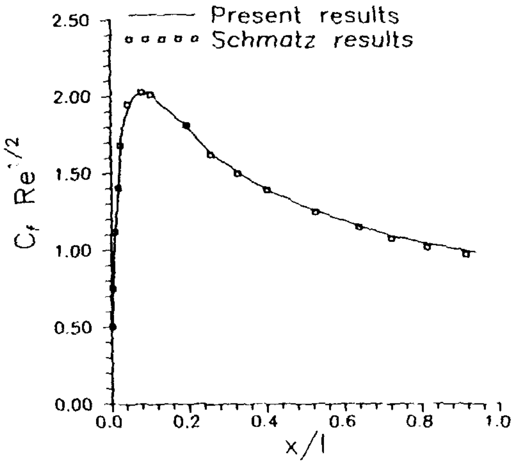

Figure 17 : Skin friction distribution (C_f) along the hyperbola wall (perfect air).

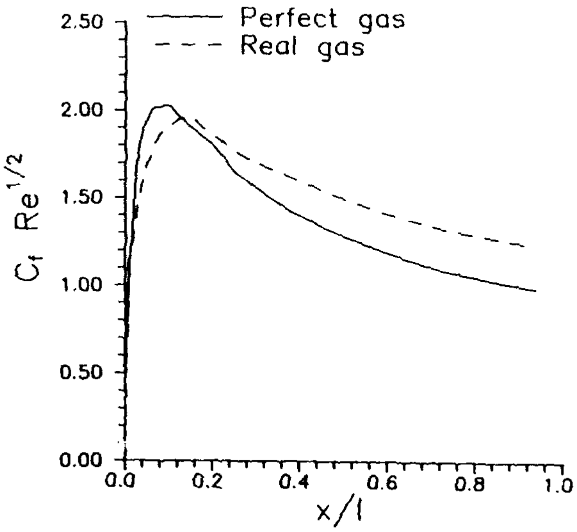

Figure 18 : Comparison of C_f between perfect and equilibrium air.

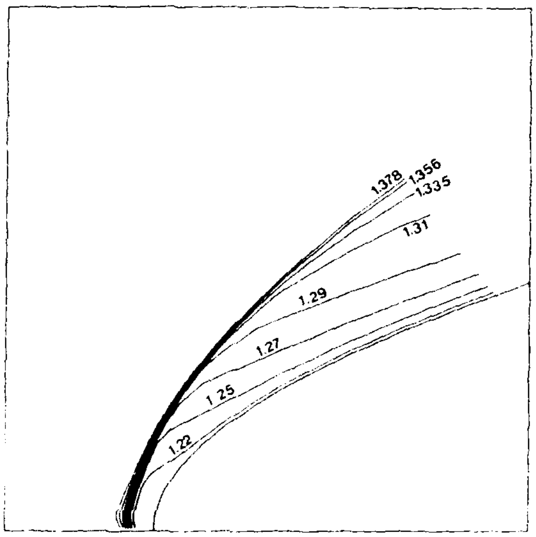

Figure 19 : Variation of γ in the viscous hypersonic flow field.

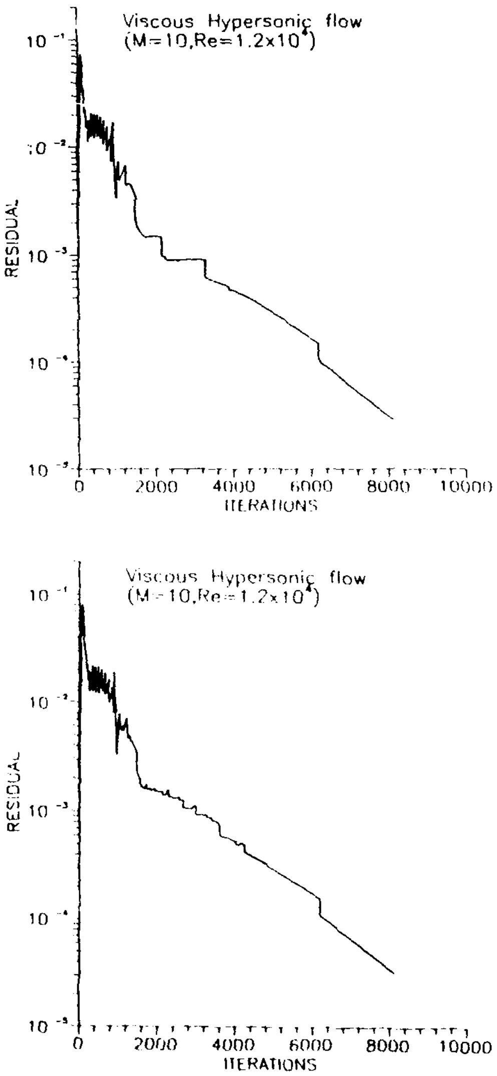

Figure 20a,b : Convergence histories for the viscous hypersonic flow a. Pefect air b. Equilibrium air.=

A COMPARISON OF HIGH RESOLUTION UPWIND SOLVERS ON 3-D INVISCID HYPERSONIC FLOWS

M. Manna & H. Deconinck[*]
C.P. Li & E. Ma[†]
von Karman Institute for Fluid Dynamics
Chaussée de Waterloo 72 - 1640 Rhode S. Génèse, Belgium
Nasa Johnson Space Center
EG3 Houston - Texas 77058, USA

1 Summary

The paper presents a detailed comparison of numerical results obtained by solving the Euler equations for the inviscid flow over delta wings in reentry configurations. The investigation involves a side-by-side comparison between independently developed upwind Euler solvers at VKI (M3D) and NASA Johnson Space Center (E3D) using identical grids.

In both solvers the governing equations are integrated by means of time marching finite volume shock capturing methods, based on a cell centered upwind evaluation of the cell face fluxes and non linear limiters. High resolution schemes are obtained via MUSCL characteristic variable extrapolation to ensure TVD properties and therefore monotonic discontinuity capturing.

Further comparisons are made with several published results by other authors based on both upwind and central discretizations.

The present results contribute in asserting the high resolution upwind TVD schemes as the most reliable numerical technique to handle the strong discontinuities typical of high speed flows. The performances of the two upwind solvers are satisfactory and the numerical results in good agreement. However, the important issue of reaching a grid converged solution for the present complex three-dimensional inviscid flow problems, has not been achieved.

2 Introduction

The design of space vehicles like the HERMES space shuttle heavily relies upon an accurate prediction of the hypersonic flight regime encountered during the reentry in the atmosphere. In this paper a related model problem is studied, namely the inviscid hypersonic flow past delta wings at high angle of attack. Although less complex than the real reentry configuration, it is representative for some of the typical difficulties to be dealt with, namely a strong bow shock very near to the windward side of the wing, a subsonic stagnation region around the nose and a very strong expansion around the leading edge which terminates in a vortical region on the leeward side of the wing.

The main objective of this work is to shed some light over the difficult task of the choice of a numerical method which can accurately and efficiently solve the Euler equations, well aware of the fact that the practical importance of the Euler equations to investigate real flows is limited, although not negligible. Accurate inviscid solutions are of paramount importance in order to construct reliable viscous solvers. In fact, for high Reynolds number flows, and in general for convection dominated problems, a correct treatment of the nonlinear convective terms is crucial, so that the conflicting issues of numerical dissipation (stability) and accuracy can be best accomplished.

Further, the present work aims to contribute to a database for numerical validations, by providing extensive numerical and algorithm details on the basis of well defined test cases. An effort is made to compare solutions obtained with different solvers on identical grids. A detailed description of the inviscid mechanism responsible for the leeside vortex formation arising from the expansion around the blunt leading edge of the wing is also given.

In the following sections the governing equations are briefly reviewed, while the space and time discretizations techniques as implemented in the VKI and JSC solvers are extensively discussed. Numerical results are compared on the basis of both qualitative and quantitative criteria.

Further, comparisons are made with several published results by other authors [1, 2], based on both upwind and central discretizations.

3 Governing equations

The governing equations are the three dimensional time dependent Euler equations, describing the conservation laws of mass, momentum and energy. Choosing a Cartesian system they can be written in divergence form in terms of the conservative variables vector Q as:

$$\frac{\partial Q}{\partial t} + \frac{\partial F(Q)}{\partial x} + \frac{\partial G(Q)}{\partial y} + \frac{\partial K(Q)}{\partial z} = 0 \qquad (1)$$

where the vector $Q = (\rho, \rho u, \rho v, \rho w, \rho e_t)^T$, contains the density ρ, the three velocity components u,v,w and the total energy per unit mass e_t.

The flux vectors F, G and K are given by:

$$F = \begin{pmatrix} \rho u \\ \rho u^2 + p \\ \rho uv \\ \rho uw \\ \rho u h_t \end{pmatrix} \qquad (2)$$

$$G = \begin{pmatrix} \rho v \\ \rho uv \\ \rho v^2 + p \\ \rho vw \\ \rho v h_t \end{pmatrix} \qquad (3)$$

---

[*] von Karman Institute

[†] NASA Johnson

$$K = \begin{pmatrix} \rho w \\ \rho u w \\ \rho v w \\ \rho w^2 + p \\ \rho w h_t \end{pmatrix} \tag{4}$$

where h_t is the total or stagnation enthalpy defined as $h_t = e_t + p/\rho$. Using the perfect gas assumption $p = \rho R_g T$, where R_g is the perfect gas constant, the static pressure p is evaluated as:

$$p = (\gamma - 1)\rho\left[e_t - \frac{1}{2}(u^2 + v^2 + w^2)\right] \tag{5}$$

where γ is the specific heat ratio, which ensures the closure of the system of equations.

System (1) can be written in compact form introducing the operator $\vec{\mathcal{H}}$ as:

$$\vec{\mathcal{H}} = F\vec{1}_x + G\vec{1}_y + K\vec{1}_z \tag{6}$$

$$\frac{\partial Q}{\partial t} + \vec{\nabla} \cdot \vec{\mathcal{H}}(Q) = 0 \tag{7}$$

Integrating (7) over a control volume $\mathcal{V}$, with surface $\mathcal{S}$, and applying the Gauss divergence theorem, one gets:

$$\frac{\partial}{\partial t}\iiint_{\mathcal{V}} Q\, d\mathcal{V} + \iint_{\mathcal{S}} \vec{\mathcal{H}} \cdot \vec{n}\, d\mathcal{S} = \vec{0} \tag{8}$$

where $\vec{n} = (n_x, n_y, n_z)^T$ is the outward pointing normal of the surface.

By defining the total flux normal to the surfaces of the elementary control volumes $\mathcal{V}$ is terms of the normal component of the velocity $V_n = \vec{V} \cdot \vec{n} = un_x + vn_y + wn_z$ as:

$$\mathcal{H}_n = \vec{\mathcal{H}} \cdot \vec{n} = \begin{pmatrix} \rho V_n \\ \rho u V_n + p\, n_x \\ \rho v V_n + p\, n_y \\ \rho w V_n + p\, n_z \\ \rho V_n h_t \end{pmatrix} \tag{9}$$

then equation (8) can be rewritten as:

$$\frac{\partial}{\partial t}\iiint_{\mathcal{V}} Q\, d\mathcal{V} + \iint_{\mathcal{S}} \mathcal{H}_n\, d\mathcal{S} = 0 \tag{10}$$

With the usual cell centered approach, the finite volume approximation of equation (10) yields to the following semi-discrete form:

$$\frac{\partial}{\partial t}Q_j = -\frac{1}{\mathcal{V}_j}\sum_{k=1}^{N_f}[\mathcal{H}_n]_{j,k}\Delta\mathcal{S}_{j,k} \tag{11}$$

where $[\mathcal{H}_n]_{j,k}$ is the total flux normal to the surface $\Delta\mathcal{S}_{j,k}$ exchanged between points j and k. The quantity $[\mathcal{H}_n]_{j,k}$ will be referred in the following as the numerical flux function $\tilde{\mathcal{H}}$ or $\left[\tilde{\mathcal{H}}_n\left(Q^L, Q^R\right)\right]$, which is evaluated as a function of the left and right extrapolated values to the cell face (denoted by Q^L and Q^R).

The VKI code makes use of general hexahedra as control volumes (and therefore $N_f = 6$). The surface vectors are evaluated through the cross product of the face diagonals. For the cell volume the hexahedron is subdivided in in three five sided pyramids pointing at the same vertex and sharing the same main diagonal (Figure 1). Following the approach proposed in [3] the resulting stencil, which is kept all over the domain, reduces to:

$$\begin{aligned} \mathcal{V}_{1234} &= \frac{1}{3}\vec{r}_{17} \cdot \left(\vec{\mathcal{S}}_{1584} + \vec{\mathcal{S}}_{1265} + \vec{\mathcal{S}}_{1432}\right) &(12) \\ &= \frac{1}{3}\vec{r}_{17} \cdot \left[(\vec{r}_{18} \wedge \vec{r}_{45}) + (\vec{r}_{16} \wedge \vec{r}_{25}) + (\vec{r}_{13} \wedge \vec{r}_{24})\right] \end{aligned}$$

In the JSC code a different approach is followed. The volume of the generic hexahedron is taken to be the average of two triple scalar products of the position vectors of eight centroids surrounding the node. The surface vectors are obtained from two sets of cross products of the edge vectors.

4 Numerical method

In the following both the space and time discretization techniques as implemented in the VKI and JSC codes are described.

4.1 Space discretization

In both codes the numerical flux function $\tilde{\mathcal{H}}$ is evaluated by means of upwind techniques, which take into account the signs of the eigenvalues of the Jacobian matrices. Both the flux vector splitting method (FVS) of Van Leer and the flux difference splitting method (FDS) of Roe have been implemented.

For the FVS technique the numerical flux function is split in backward and forward contributions, according to the component of the Mach number normal to the cell interface. For subsonic normal Mach number ($-1 < M_n < 1$), one obtains [4]:

$$\mathcal{H}_n(Q^L, Q^R) = \mathcal{H}_n^+(Q^L) + \mathcal{H}_n^-(Q^R) \tag{13}$$

where:

$$\mathcal{H}_n^{\pm} = \mathcal{H}_n^m \begin{pmatrix} 1 \\ u \pm (2 - M_n)\frac{c}{\gamma}n_x \\ v \pm (2 - M_n)\frac{c}{\gamma}n_y \\ w \pm (2 - M_n)\frac{c}{\gamma}n_z \\ \frac{c^2}{\gamma+1}\left(\frac{2}{\gamma-1} \pm 2M_n - M_n^2\right) + \frac{V}{2}^2 \end{pmatrix} \tag{14}$$

where $\mathcal{H}_n^m$ is the mass flux given by:

$$\mathcal{H}_n^m = \pm\frac{\rho c(1 \pm M_n)^2}{4} \tag{15}$$

On the other hand, if the flow in the normal direction is supersonic, the Van Leer splitter reduces to the full upwind flux:

$$\begin{array}{llll} \text{for} \quad M_n \geq 1 & \text{then}: & \mathcal{H}_n^+ = \mathcal{H}_n & \mathcal{H}_n^- = 0 \\ \text{for} \quad M_n \leq 1 & \text{then}: & \mathcal{H}_n^+ = 0 & \mathcal{H}_n^- = \mathcal{H}_n \end{array}$$

The Roe flux difference splitting method is also implemented in both codes, but since it has not been employed for the present results will not be described herein. The reader can refer to [5, 6] for details about the implementation of the Roe scheme in 3-D solvers.

4.2 Higher order schemes

Higher order schemes, coupled with TVD (Total Variation Diminishing) properties are implemented following the MUSCL approach [7]. Spatially second order accurate results are obtained by replacing the piecewise constant initial data of the Riemann problem with piecewise linear initial data. This is achieved by evaluating the numerical flux function at the cell interface[1] by means of discontinuous left and right extrapolated values. The evaluation of the numerical flux functions is based upon new left and right states, which corresponds to second and third order spatial differencing:

---

[1] In the following the subscript referring, for instance, to the cell interface between node i, j, k and $i, j+1, k$ will be denoted as $j + \frac{1}{2}$

$$\overline{Q}^R_{j+\frac{1}{2}} = Q_{j+1} - \frac{1}{4}\left[(1-\eta)\Delta_{j+\frac{3}{2}} + (1+\eta)\Delta_{j+\frac{1}{2}}\right] \quad (16)$$

$$\overline{Q}^L_{j+\frac{1}{2}} = Q_j + \frac{1}{4}\left[(1-\eta)\Delta_{j-\frac{1}{2}} + (1+\eta)\Delta_{j+\frac{1}{2}}\right] \quad (17)$$

where $\Delta_{j+\frac{1}{2}} = Q_{j+1} - Q_j$, and the parameter η determines the spatial accuracy.

The numerical flux function $\tilde{\mathcal{H}}_{j+\frac{1}{2}}$ for the Van Leer splitting then becomes:

$$\tilde{\mathcal{H}}_{j+\frac{1}{2}} = \mathcal{H}^+\left(\overline{Q}^L_{j+\frac{1}{2}}\right) + \mathcal{H}^-\left(\overline{Q}^R_{j+\frac{1}{2}}\right) \quad (18)$$

where $\overline{Q}^L$ and $\overline{Q}^R$ are MUSCL extrapolated values.

In order to preserve TVD properties limiting functions are applied on the differences in characteristic variables defined as:

$$\delta W = \mathbf{L}\,\delta Q = \mathbf{R}^{-1}\delta Q \quad (19)$$

$$\delta Q = Q^R - Q^L$$

which have been found truly superior compared to the primitive or conservative variables, although the computational cost is higher [5]. Matrices $\mathbf{L}$ and $\mathbf{R}$ are the left and right eigenvectors of the flux Jacobian $\mathbf{D}_n$ of the vector $\mathcal{H}_n$. They have been selected[2] so that the resulting characteristic variables are composed of one entropy wave, two shear waves corresponding to two orthogonal directions $\vec{s}$ and $\vec{t}$ in the plane of the cell face, and two acoustic waves:

$$\delta\vec{W} = \begin{pmatrix} \delta\rho - \frac{\delta p}{c^2} \\ \delta\vec{V}\cdot\vec{s} \\ \delta\vec{V}\cdot\vec{t} \\ \delta\vec{V}\cdot\vec{n} + \frac{\delta p}{\rho c} \\ \delta\vec{V}\cdot\vec{n} - \frac{\delta p}{\rho c} \end{pmatrix} \quad (20)$$

The upwind biased interpolation is modified as follows [8]:

$$\begin{aligned} \overline{Q}^R_{j+\frac{1}{2}} &= Q_{j+1} - \tfrac{1}{4}\mathbf{R}\psi^R & \Big[&\left(1-\eta\psi^R\right)\mathbf{L}\Delta_{j+\frac{3}{2}} + \\ & & &\left(1+\eta\psi^R\right)\mathbf{L}\Delta_{j+\frac{1}{2}}\Big] \\ \overline{Q}^L_{j+\frac{1}{2}} &= Q_j \ + \tfrac{1}{4}\mathbf{R}\psi^L & \Big[&\left(1-\eta\psi^L\right)\mathbf{L}\Delta_{j-\frac{1}{2}} + \\ & & &\left(1+\eta\psi^L\right)\mathbf{L}\Delta_{j+\frac{1}{2}}\Big] \end{aligned}$$

where:

$$\psi^R = \frac{2\mathbf{L}\Delta_{j+\frac{1}{2}}\,\mathbf{L}\Delta_{j+\frac{3}{2}} + \epsilon}{\mathbf{L}\Delta^2_{j+\frac{1}{2}} + \mathbf{L}\Delta^2_{j+\frac{3}{2}} + \epsilon} \quad (21)$$

$$\psi^L = \frac{2\mathbf{L}\Delta_{j-\frac{1}{2}}\,\mathbf{L}\Delta_{j+\frac{1}{2}} + \epsilon}{\mathbf{L}\Delta^2_{j-\frac{1}{2}} + \mathbf{L}\Delta^2_{j+\frac{1}{2}} + \epsilon} \quad (22)$$

The parameter ϵ is a small bias to prevent division by zero in uniform flow regions which was set to 10^{-7} in the present calculation. Note that primitive variables are used in the JSC code.

4.3 Boundary conditions

A consistent boundary condition approach, as proposed in [9], is adopted in the VKI solver. A consistency condition is imposed on the numerical flux function so that the computed boundary unknowns lead to fluxes that satisfy the physical boundary conditions: the total flux normal to the cell interface is set equal to the total flux with imposed boundary conditions:

$$\mathcal{H}_n(Q^B, Q^I) = \mathcal{H}^\bullet_n(Q^B) \quad (23)$$

In the case of Van Leer flux vector splitting one obtains:

$$\mathcal{H}^+_n(Q^B) + \mathcal{H}^-_n(Q^I) = \mathcal{H}^\bullet_n(Q^B) \quad (24)$$

where for a solid wall $\mathcal{H}^\bullet_n$ is given by
$\vec{Q} = (0, p\,n_x, p\,n_y, p\,n_z, 0)^T$.

In general the LHS of equation (23) depends on the particular choice of the Riemann solver. Equation (24) is a set of non linear algebraic equations between the interior unknown Q^I and the boundary unknown Q^B. These additional equations for the boundary unknowns complete the system of flux balance equations.

The JSC solver uses one-sided differences to compute unknowns on the wall and readjust the velocity components to satisfy the tangency condition.

4.4 Time integration

Equation (11), obtained after the space discretization is a system of ordinary differential equations, which is solved through an explicit procedure.

A four stage Runge-Kutta scheme ($m = 4$) applied to equation (11) yields[3]:

$$\begin{aligned} Q^{(0)} &\overset{\text{def}}{=} Q^n \\ Q^{(k)} &= Q^{(0)} - \alpha_k \tfrac{\Delta t}{V}\mathcal{R}\left(Q^{(k-1)}\right) \qquad k = 1, m \\ Q^{(n+1)} &\overset{\text{def}}{=} Q^m \end{aligned} \quad (25)$$

where $\Delta t = t^{n+1} - t^n$, and $\mathcal{R}$ denotes the contour integral of the fluxes as described in the previous section, or equivalently the RHS of equation (11). To enhance the stability region the Runge-Kutta scheme, when used in conjunction with upwind space discretization, non standard coefficients ($\alpha_1 = 0.12$, $\alpha_2 = 0.26$, $\alpha_3 = 0.5$, $\alpha_2 = 1$) have been used [10]. The local time step is evaluated as:

$$\Delta t \leq \frac{V_j}{\sum_{k=1}^{6} \lambda^+_{max}\,\Delta S_{j,k}} \quad (26)$$

where λ^+_{max} is the maximum eigenvalue of $\mathbf{D}_n$.

The JSC code solves equation (11) by means of a forward Euler scheme.

5 Numerical results

Numerical results are presented for two test cases on delta wing geometries defined on the occasion of two workshops on hypersonic flows [11, 12]. The model problem investigated is indeed less complex compared to the real wing in reentry configuration. However, the general flow features of delta wings in hypersonic regime are well represented by the simplified geometries which are investigated in the present work.

At high Mach number and high incidence the overall flow features are dominated by a strong bow shock which is responsible for the peak heating in the nose region and along the leading edges of the wing. In these conditions the flow which undergoes the bow shock cannot remain attached to the leeside wing, and generally during the expansion from windward to leeward side separates and develops into vortical regions. The locations of the separation points depend upon many parameters such as the Mach number normal to the leading edge, the angle of attack, the thickness and *the sweep angle of the wing*. The reader can refer to the classical work of Squire [13] for a qualitative analysis of the flow over flat wings. However, for wings of finite thickness with round leading edges, no theoretical conclusion can be drawn (at least at the best knowledge of the authors) and there is no other real means of investigation except experimental and numerical testing.

---

[2] A detailed description of the construction strategy employed for the eigenvectors and the characteristic variables can be found in [5]

[3] Omitting the subscript denoting the cell index

The importance of accurate Euler solutions for these type of flows is related to the fact that mechanism of formation of the leeside primary vortical region is essentially inviscid. During the expansion process from windward side to leeward side of the wing, the flow quickly becomes supersonic. It follows that the continuous flow turning which takes place during the expansion has to be compensated by a cross flow shock in order to recover the freestream direction. The cross flow shock foot, which is generally curved and therefore responsible of local vorticity production, according to Crocco's theorem, embeds a vortical region.

Although the above mentioned features take place in a near vacuum environment, and therefore their influence upon the overall lift and drag of the entire wing is small, if not negligible, they can still have important impacts on local flight components, and hence their understanding needs to be deepened.

5.1 Hypersonic flow over sharp nose delta wing

The first model problem which is investigated deals with a 70° swept blunt delta wing, at 30° angle of attack and Mach number of 7.15 [11]. The geometry of the wing is shown in Figure (2). The leading edges are portions of cylinders of constant radius, which implies that a cross section of the leading edge plane by a vertical plane perpendicular to it, is a portion of a circle. Consequently, in the base plane, which is instead perpendicular to the axis, the rounded tip is a small portion of an ellipse. It is worth mentioning that the finite thickness of the wing in the streamwise direction inhibits the conical flow approximation.

An O-O type of grid of $121 \times 61 \times 61$ points, (121×61 points in the cross plane) provided by KTH [14], is employed for the simulation (Figure (3)). Due to the high density of the grid ($\approx 400{,}000$ points) and the limited storage capability of the available machine (Alliant FX60, 8 Mwords of 32 bits) a domain decomposition technique is adopted in the VKI solver. The original grid is decomposed into 5 blocks of about 80 thousand points along the streamwise direction. Starting from the nose region, the blocks are sequentially solved, the coupling of the solution being guaranteed by a special boundary treatment. The extrapolated[4] MUSCL values in the last plane of the upstream block are stored after application of the limiting procedure. They are later read as inflow boundary conditions for the downstream block and are not updated anymore, since the flow, as seen from the downstream block, is supersonic in the inlet plane.

This test problem has been solved by many authors. Present results are compared with the solutions by Rizzi et al. [14] (KTH), Guillen et al. [2, 15] (ONERA) and Murman et al. [16] (MIT).

The ONERA code is an implicit multi-domain solver (FLU3M) based upon an upwind MUSCL type of scheme (virtually identical to the present ones). The solution is carried out on C-H grid of $121 \times 64 \times 60$ points, later refined through a multi-domain decomposition up to two million points.

The KTH and the MIT codes use a finite volume discretization based upon a symmetric evaluation of the convective terms, in conjunction with a nonlinear blend of second and fourth order artificial dissipation terms.

The MIT solution is obtained on H-O type of grid of $33 \times 49 \times 97$ points, whose outer boundary is adjusted to the shock shape in order to efficiently use the grid points in high gradient regions.

The present solutions, as well as the KTH one, are carried out on a symmetric grid (Figure (3)), and therefore do not take advantage of the vicinity of the bow shock to the leeward side of the wing.

A first comparison of the present solutions with the one from ONERA, KTH and MIT is respectively presented in Figures (4), (5), (6) and (7). In all figures the iso-Mach lines are shown with an increment of 0.2 (0.5 in the comparison with MIT) in a plane at 50% of the root chord ($X/C_r = 0.5$, C_r being the root chord of the wing from its apex), normal to the longitudinal axis of the wing.

The VKI and the JSC solutions show a very good qualitative agreement (Figure (4)). The same remark applies to the ONERA solution (Figure (5)) and to a smaller extend to the KTH one (Figure (6)). Substantial differences are indicated in Figure (7) by the comparison with the MIT solver.

All the computations mostly agree both in terms of position and resolution of the bow shock, although the upwind codes indicate their superiority compared to the central ones (note that the VKI, JSC and KTH solutions are obtained on the same grid).

As far as the comparison of the leeward side features is concerned, several issues need to be *clarified before* drawing any conclusion.

Firstly, all the results indicate that the cross flow shock is located at about 25% span position. The shock foot is curved and embeds a vortical region (Figure (8)). As already mentioned the curvature of the cross flow shock, together with the different entropy level of adjacent particles which have undergone the bow shock in different positions are the cause of the local vorticity generation. Indeed, the flow is subject to a sudden change in direction (via a shock) during the expansion from windward to leeward side, as confirmed by the surface streamlines of Figure (9).

All *the computations* indicate a fairly good agreement from a qualitative point of view. However, in the symmetry plane it appears that in general the grid resolution is insufficient to properly resolve the gradients in the direction normal to the wing surface.

The MIT solution shows substantial discrepancies with all the other calculations. An oblique cross flow shock which meets a shear layer travelling inboard and upward, is generated at about mid span (Figure (7)). One might presume that these features are more close to the real viscous phenomena, and therefore the solution method is overdissipative. This is surprising, since the same numerical method applied by KTH produces a solution with the proper amount of added dissipation.

Rizzi and Murman, in order to justify the large discrepancies in the leeward side features, argued that the flow over a blunt and smooth body does not admit a unique solution, unless a geometric Kutta condition is somehow specified [1]. It is a personal opinion of the authors that the argument is not valid for this specific test case. In the expansion process, in fact the flow remains supersonic and can go around the blunt leading edge through a continuous series of Prandtl-Meyer expansions. In addition, there is no essential role played by the artificial dissipation terms when a grid converged solution is reached. In ref. [14] Rizzi showed that no significant change in the overall flow field features is obtained either coarsening the grid, or doubling the dissipation coefficients. The ONERA group refined the 400,000 point initial grid up to two million, and although some flow details are better resolved, the essential flow features, such as the cross flow shock position, do not change at all. This is best demonstrated by the surface Mach number distribution, relative to the cross section $X/C_r = 0.5$ shown in Figure (10a). The present solutions are practically identical to the ONERA single domain solution obtained on a grid of equal density (curve a). The multi-domain ONERA computation (curve b) agrees better with the KTH one. One is tempted to conclude that, due to the high grid resolution, the multi-domain ONERA solution has to be considered as the ultimate one. However, the response of the other solvers, as well as the Mach number level on the leeward side[5] might indicate that the expansion is somehow overpredicted.

---

[4] Only fully upwind scheme ($\eta = -1$) can be employed in order to decouple two adjacent blocks.

The total pressure coefficient $C_{p_0} = 1 - p_0/p_{0\infty}$, shown in Figure (11a), demonstrates that almost 90% of the total pressure is lost through the strong bow shock (normal Mach number of about 4.5). A considerable additional loss takes place during the expansion of the flow around the leading edge. The nature of such a loss is easily explained recalling that the visualized surface data refer to different particles which carry different entropy levels. The further loss due to the cross flow shock is clearly visible at about 25% span position. The pressure coefficient distribution $C_p = (p - p_\infty)/2\rho_\infty V_\infty^2$ on the leeside is shown in Figure (10c) with a very enlarged scale (note that the overall range for the surface data is $-0.027 \leq C_p \leq 0.6$). All the computations show an expansion almost down to vacuum (which corresponds to a pressure coefficient of 0.28). The typical vortex pressure distribution is found between the symmetry plane and the foot location of the cross flow shock. The ONERA fine grid computation shows a new phenomenon occurring within the vortical region, namely a weak shock on the body itself.

Many surface distributions shown above are characterized by a small overshoot at the leading edge of the wing, whose origin is unclear to the authors (more about this in the next section).

5.2 Hypersonic flow over blunt nose delta wing

This test problem deals with a geometry similar to previous one. The sharp nose is replaced by a blunt one, and the windward side is curved and not flat anymore. The geometry of the wing (shown in Figure (11)) cannot be defined analytically and a surface grid was provided by Weiland [12]. The flow conditions are again typical of a reentry configuration, namely freestream Mach number of 8.7 and angle of attack of 30°.

Numerical results have been obtained on two C-H type grids (Figure (12)) of 73 × 41 × 37 and 37 × 79 × 125 points generated at JSC [6]. In contrast to the KTH grid employed for the previous problem, the grid lines are nicely clustered at the windward side so that an excellent capturing of the bow shock structure is already possible with a small number of points in the cross plane.

As for the previous test case, the VKI solution is carried out via a multi-block domain decomposition, while the JSC solution is performed in single block.

Present results are compared with the one from ONERA [17] obtained on an adapted grid. The final refined solution refers to a multi-domain decomposition on a grid of about one million points.

Although the geometries of the wings are quite similar the overall flow structures are substantially different. Firstly, due to blunt nose, the bow shock is detached and therefore a subsonic pocket exists. A detailed view of the nose region in the symmetry plane is given in Figure (13) where the iso-Mach lines are shown with an increment of 0.5. Both the sonic line and the stagnation point are clearly visible.

On the leeward side the flow, which has undergone the bow shock, rapidly expands and ends up into a strong vortical motion. Note that, conversely to the previous wing whose flow features show a quasi-conical structure[6], a fully three dimensional flow field characterizes the blunt nose wing. In fact, different patterns are indicated by the iso-Mach (Figure (14)) and iso-pressure (Figure (15)) lines of four different cross flow planes, located at about 20%, 40%, 60% and 80% of the root cord. A curved shear layer travelling inboard and upward, and terminating in a cross flow shock, is opening up and developing in streamwise direction. The vortical region is embedded by the shear layer in a constant pressure field shown in Figure (15). In Figure (16) the iso-Mach lines (increment of 0.2) relative to a cross flow plane at 50% of the root chord ($X/C_r = 0.5$) as resolved by the present codes are compared. A very close qualitative agreement is obtained.

In Figure (17) the VKI solution is compared with the one from ONERA. Again a good qualitative agreement is reached, although, thanks to the algebraic adaptive grid generator and to the very high density of the grid, the bow shock is resolved in greater detail by the ONERA code.

As for the previous test case all the solutions agree well quantitatively for the windward side features. On the leeward side, instead, considerable differences exist as shown by the surface distributions of Figures (18a), (18b) and (18c). The largest difference among the computations occurs on the wing body, between the leading edge and the cross flow shear layer, where a strong discontinuity is predicted by the ONERA computation. Surprisingly, the VKI solution reveals everywhere else the same surface data. The JSC solution is somewhere in between the two; a slightly different cross flow discontinuity position is also visible.

Despite the very fine grid, the leading edge discontinuity predicted by the ONERA code remains, in the author's opinion, questionable, since all the solutions carried out on coarser grids showed a even larger (!) magnitude of the discontinuity itself [12]. It is interesting to note that the ONERA solution looses all its total pressure at the discontinuity location, whereas the present computations don't (Figure (18c)). The leading edge discontinuity might be related to a local loss of accuracy determined by hexahedra with an extremely high aspect ratio in regions of very strong gradients. This is definetely the case of the JSC grid which has been refined by doubling the number of grid points only in the cross flow planes.

Code performances

In Figure (19) the convergence history relative to the second test case is presented for the VKI solver. The $\mathcal{L}_2$ norm of the normalized density residuals is shown in logarithmic scale. Curve denoted by (1) refers to a first order calculation for one of the two blocks in which the whole domain is decomposed. The converged solution is used as initial guess for the second order run (curve (2)). Overall about 4,000 iterations per block have been performed. A cell wise constant local C.F.L. number of 1 has been used. The JSC solution (not shown) is terminated after 1,500 iterations on a Cray XMP/460. The VKI code is designed in order to exploit the capability of the Alliant FX50 multiple vector concurrent machine (5 processors 5 pipelines). The CPU time in seconds per node per iteration is given below for the VKI and JSC solvers:

---

[5] Note that the freestream Mach number is 7.15

[6] The surface streamlines of Figure (10) show a self similar behaviour in the axial direction.

Code	Machine	CPU/Node/Iter.
M3D (VKI)	Alliant FX50	1.9×10^{-3}
E3D (JSC)	Cray XMP/460	6.0×10^{-5}

6 Conclusions

No final conclusion can be drawn at this moment since the ultimate solution for these complex flow problems has not been reached yet. In particular the leading edge features are not fully clarified.

However, the comparison of the high resolution upwind schemes with the standard central type of discretization (on the same grid) suggests a number of remarks.

Firstly, for high speed flows and in general in presence of strong discontinuities the upwind evaluation of the cell face flux is superior to the central one. In these conditions the proper tuning of the dissipation parameters can be very hard if not impossible. The natural consequence is that an over-dissipative solution is likely to be obtained, as is believed to be the case for the MIT results. Therefore extreme care has to be exercised when using central schemes for viscous hypersonic computations, especially for high Reynolds number flows.

On the other hand, the evaluation of a high resolution flux function is substantially more expensive compared to a central one in terms of operation costs. Therefore, the computational saving could be translated in an increased grid density for a given computer power.

A key point is doubtless the necessity of a grid converged solution. Although with the actual machines this seems feasible, the effort needed to significantly increase the grid density (to several million points) cannot be afforded yet. As an example the sharp nose wing, whose features are quasi-conical, mainly requires a good resolution in the cross flow planes. The blunt nose wing, instead, is characterized by a fully three dimensional flow field and, hence, needs a sufficient resolution in all the coordinate directions.

Therefore for complex three dimensional (even) inviscid flow problems, the capabilities of the numerical solution to correctly represent the real physical phenomena are considerably more limited compared to two dimensional flows, the limit being more related to the storage constraints rather than to CPU performances.

As a possible way out for the future one may hope that the accuracy of the spatial discretization will be significantly increased (ENO schemes, spectral methods) and that massive parallel computers will become largely available.

Acknowledgments

The authors wish to acknowledge Dr. A. Rizzi for providing the sharp delta wing grid.

References

[1] RIZZI A., MURMAN E.M., ELIASSON P. and LEE K.M. 'Calculation of hypersonic leeside vortices over blunt wings'. In *Vortex Flow Aerodynamics*, pages 8.1-8.17, Neuilly Sur Seine, France, October 1990. AGARD. Conference Proceedings No. 494.

[2] GUILLEN P. and BORREL M. 'Contribution to test problem VII.1'. In *Workshop on hypersonic flow for reentry problems*, pages 103-107, Antibes, France, January 1990. INRIA. Part I, Volume 5.

[3] KORDULLA W. and VINOKUR M. 'Efficient computation of volume in flow predictions'. *AIAA Journal*, 21(6):917-918, June 1983.

[4] VAN LEER B. 'Flux vector splitting for the Euler equations'. In *Proceedings 8th International Conference on Numerical Methods in Fluid Dynamics*, 1982. Berlin: Springer Verlag.

[5] MANNA M. 'A 3-D high resolution upwind finite volume Euler solver'. Von Karman Institute for fluid dynamics, April 1992. *Technical Note 180*.

[6] LI C.P. and MA E. 'Inviscid flow over a delta wing'. In *Workshop on hypersonic flow for reentry problems*, pages 95-120, Antibes, France, April 1991. INRIA. Part II, Volume 7.

[7] VAN LEER B. 'Towards the ultimate conservative difference scheme V, A second order sequel to Godunov's method'. *Journal of Computational Physics*, 32:101-136, 1979.

[8] MULDER W.A. and VAN LEER B. 'Implicit upwind methods for the Euler equations'. *AIAA paper 83-1930*, July 1983.

[9] DECONINCK H. and STRUYS R. 'A consistent boundary condition for cell centered upwind finite volume Euler solvers'. *Numerical methods for fluid dynamic III*, Clarendon Press, Oxford. April 1988.

[10] LALLEMAND M.H. 'Dissipative properties of Runge-Kutta schemes with upwind spatial approximation'. *INRIA Rapports de Recherche*, March 1990. No. 1173.

[11] DESIDERI J.A., GLOWINSKI R. and PERIAUX J. . *'Hypersonic flows for reentry problems'*. Springer Verlag, January 1992. Proceedings of a workshop held at Antibes, France, 22-25 January 1990.

[12] DESIDERI J.A., GLOWINSKI R. and PERIAUX J. . *'Hypersonic flows for reentry problems'*. Springer Verlag. Proceedings of a workshop held at Antibes, France, 15-19 April 1991 ,to appear.

[13] SQUIRE L.C. 'Regimes over delta wings at supersonic and hypersonic speeds'. *Aero Quart*, pages 1-14, February 1976.

[14] ELIASSON P. and RIZZI A. 'Hypersonic leeside flow computations using centered schemes for delta wing problem VII'. In *Workshop on hypersonic flow for reentry problems*, pages 167-180, Antibes, France, January 1990. INRIA. Part I, Volume 5.

[15] DA COSTA J.L., HACHEMIN J.V. and GUILLEN P. 'A multi-domain Euler code applied to hypersonic flows'. In *AIAA 22th Fluid Dynamics, Plasma Dynamics and Lasers Conference proceedings*, 1991. AIAA paper 91-1699.

[16] MURMAN E.M. and LEE K.M. 'Inviscid flow over a delta wing'. In *Workshop on hypersonic flow for reentry problems*, pages 109-118, Antibes, France, January 1990. INRIA. Part I, Volume 5.

[17] LE TOULLEC L. and GUILLEN P. 'Hypersonic delta wing flow calculations using a multi-domain MUSCL Euler solver'. In *Workshop on hypersonic flow for reentry problems*, pages 1-19, Antibes, France, April 1991. INRIA. Part II, Volume 5.

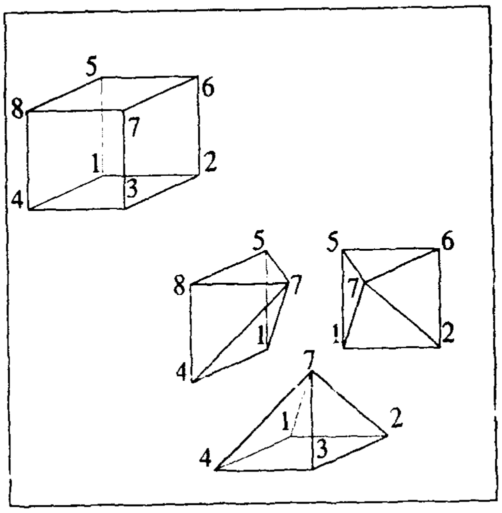
5
6
8
7
1
2
4
3
5
8
7
1
4
5
6
7
1
2
7
1
2
4
3

Figure 1

Sub-division of the hexaedron into three pyramids.

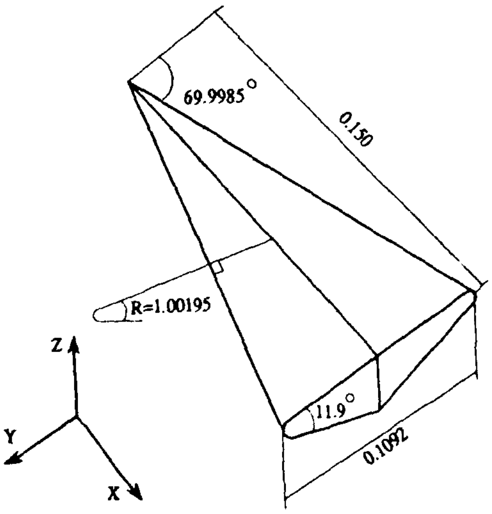
69.9985°
0.150
R=1.00195
Z
Y
X
11.9°
0.1092

Figure 2

Geometry of the sharp nose wing.

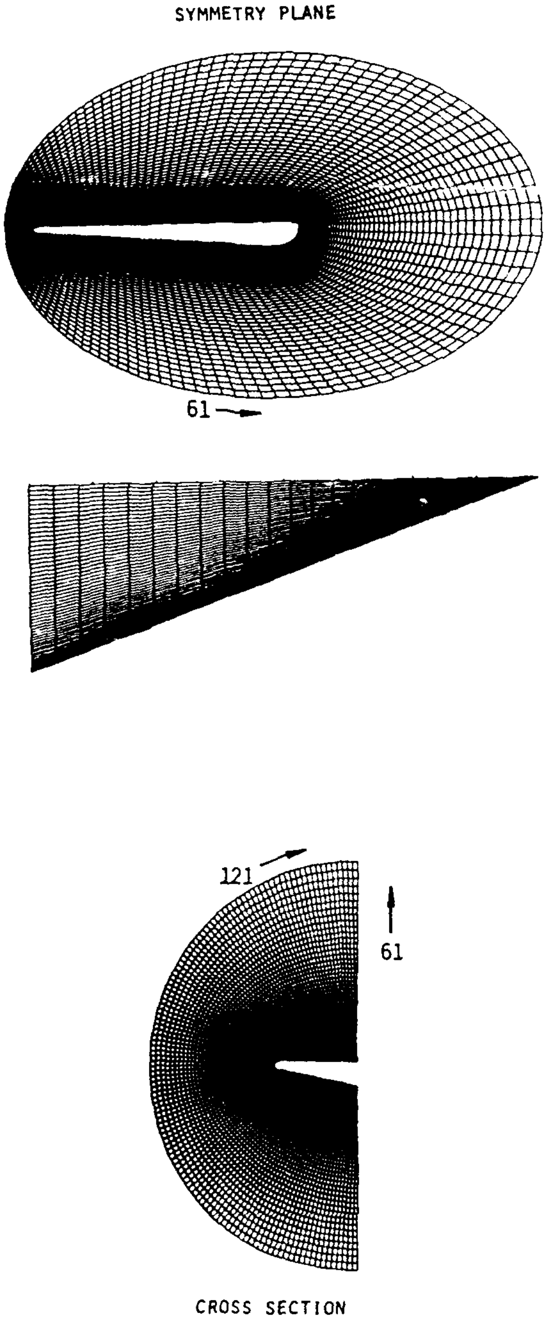
SYMMETRY PLANE
61
121
61
CROSS SECTION

Figure 3

O-O grid, 121 × 61 × 61 points.

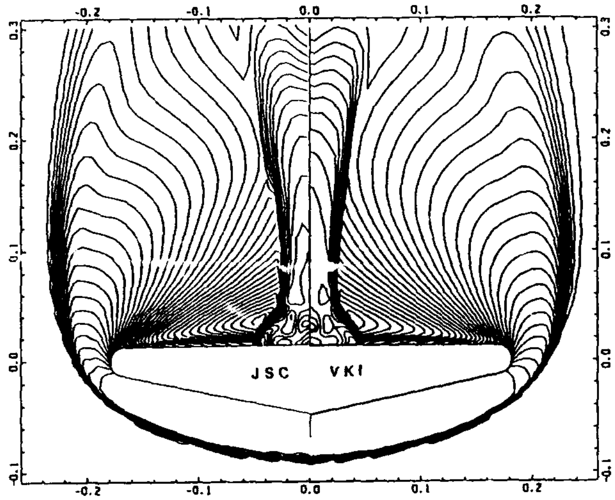

Figure 4

Comparison of VKI-JSC iso-Mach lines in a cross flow plane at $X/C_r = 0.5$.

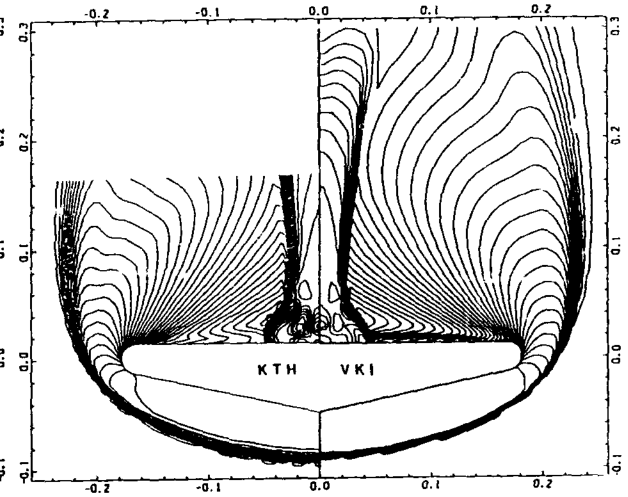

Figure 6

Comparison of VKI-KTH iso-Mach lines in a cross flow plane at $X/C_r = 0.5$.

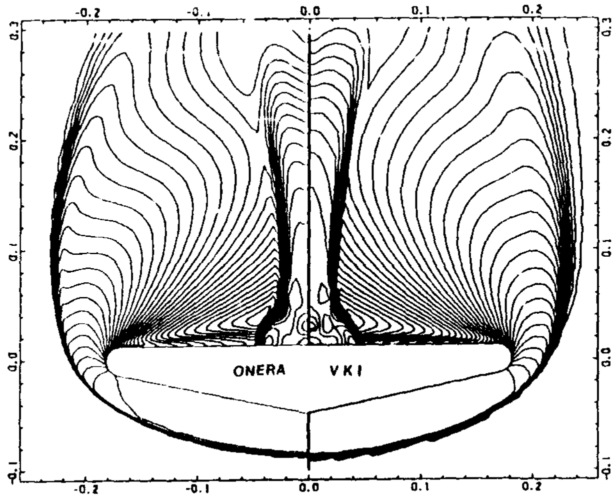

Figure 5

Comparison of VKI-ONERA iso-Mach lines in a cross flow plane at $X/C_r = 0.5$.

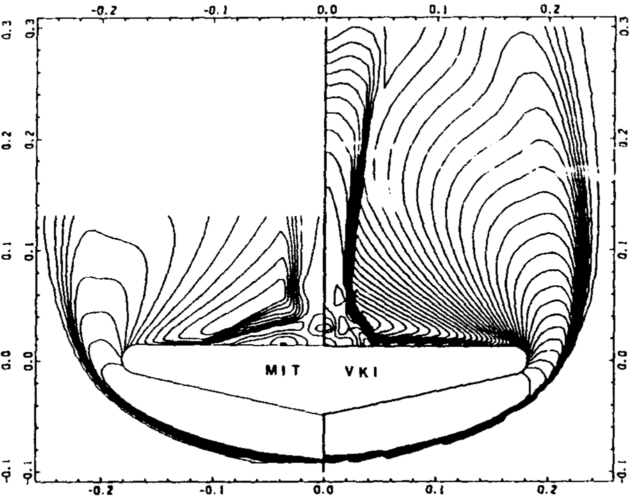

Figure 7

Comparison of VKI-MIT iso-Mach lines in a cross flow plane at $X/C_r = 0.5$.

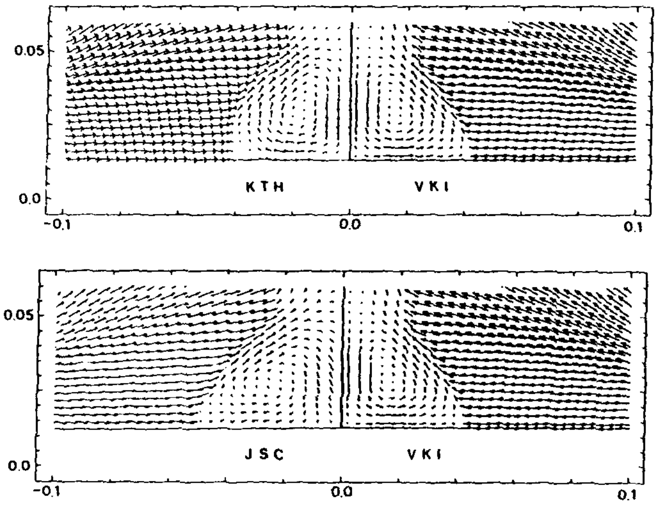

Figure 8
Comparison of VKI-KTH (top) and VKI-JSC (bottom) vortical regions in a cross flow plane at $X/C_r = 0.5$.

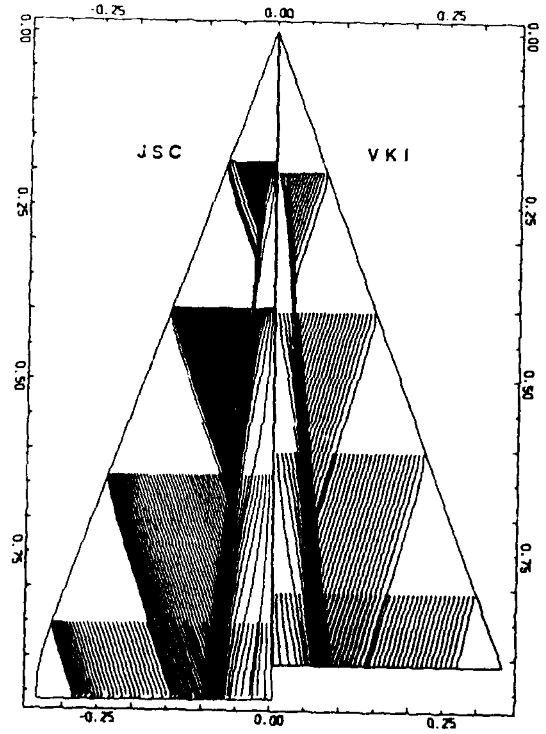
-0.25
0.00
0.25
0.00
0.25
0.50
0.75
JSC
VKI

Figure 9
Comparison of VKI-JSC surface streamlines.

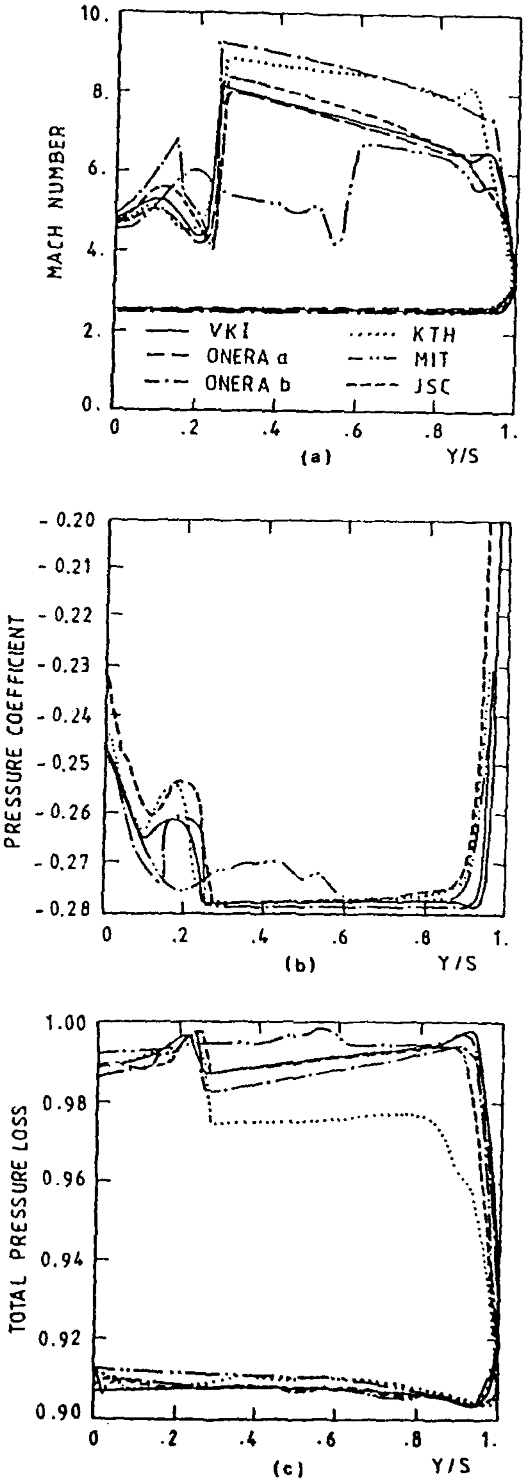

Figure 10
Surface data in a cross flow plane at $X/C_r = 0.5$.

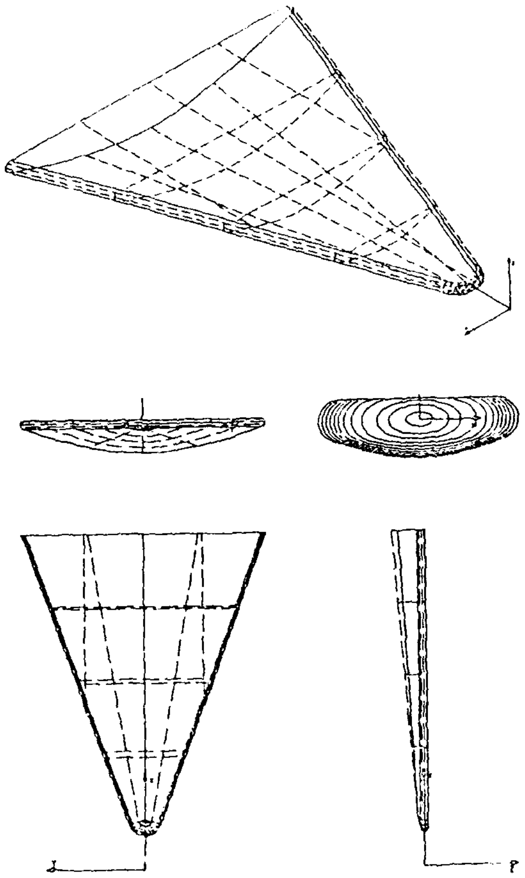

Figure 11
Geometry of the blunt nose wing.

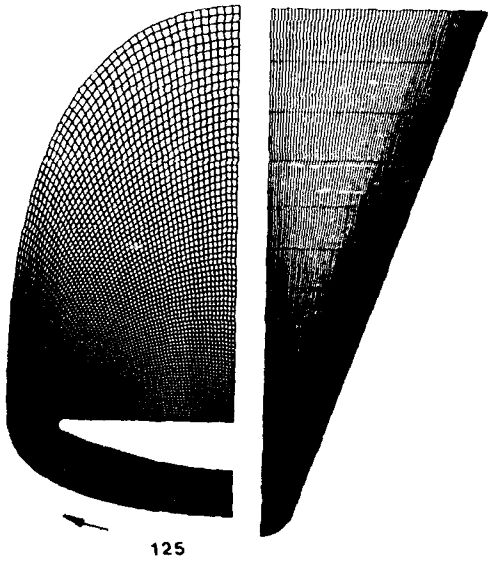

Figure 12
C-H grid, 73 × 41 × 37 points.

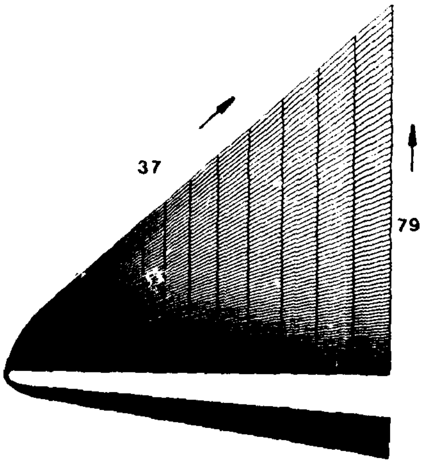

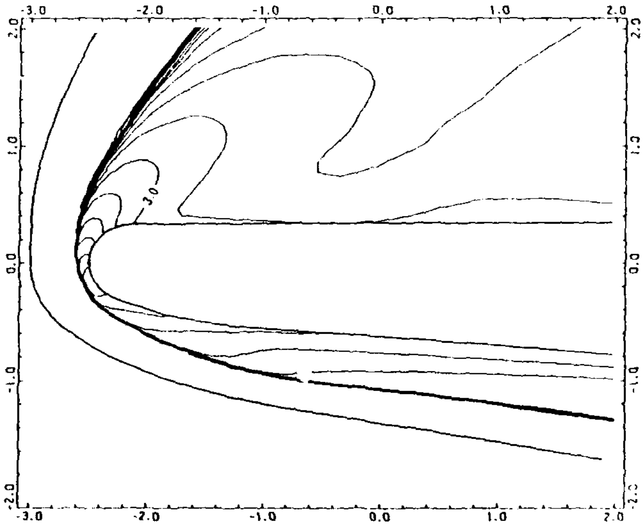

Figure 13
Iso-Mach lines in the symmetry plane, detailed view of the nose region.

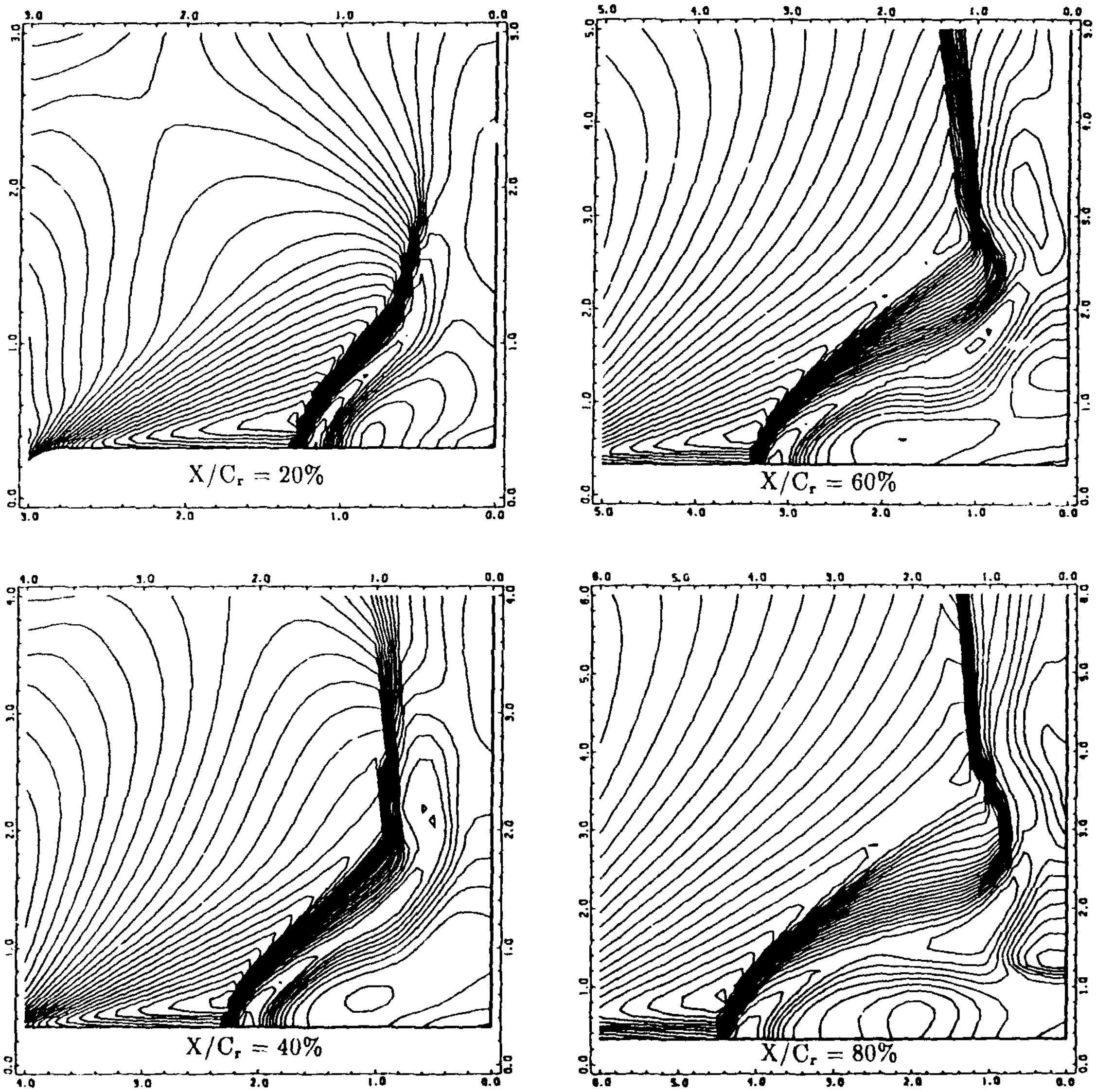

Figure 14

Iso-Mach lines in four cross flow planes.

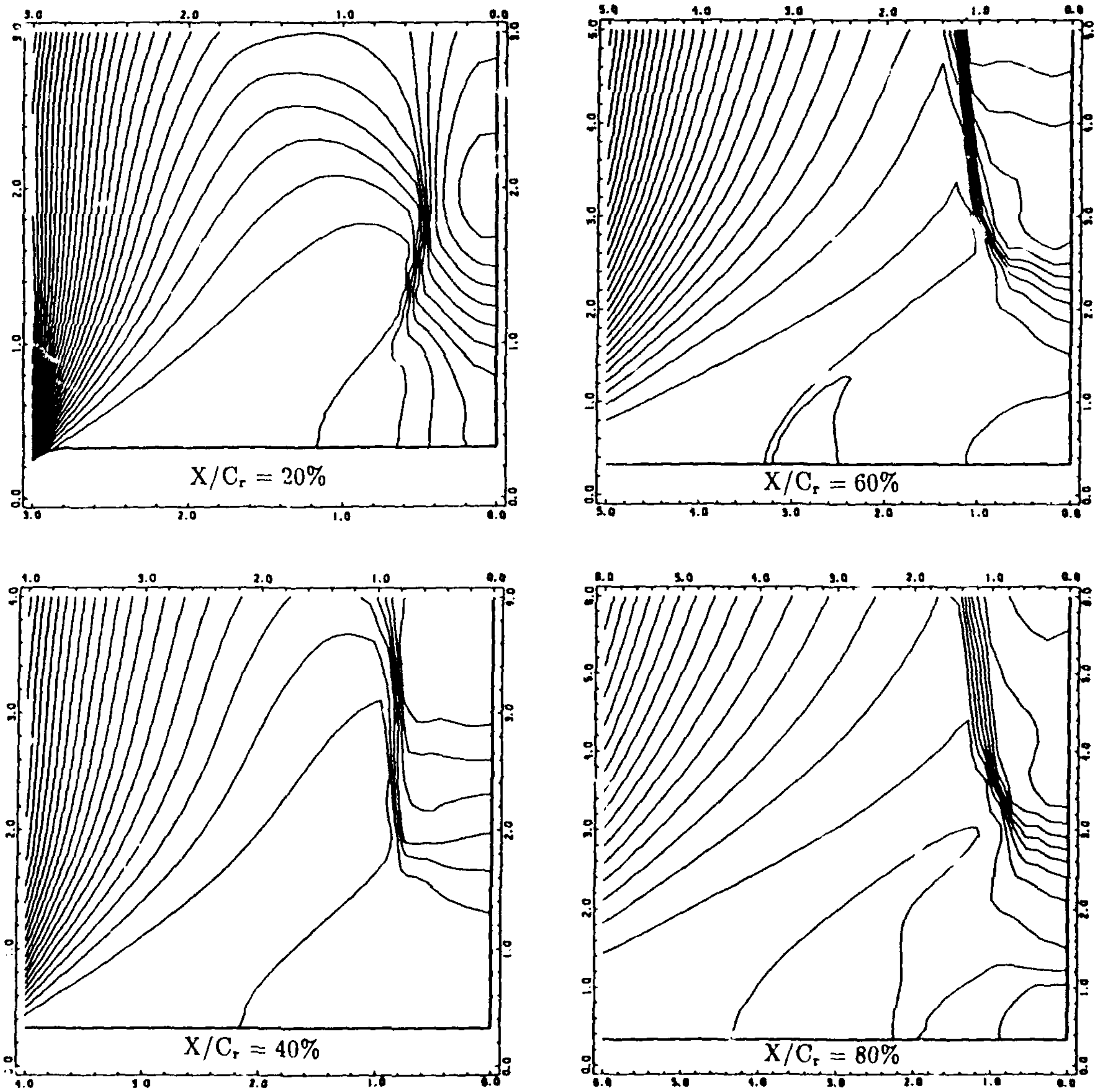

Figure 15
Pressure lines in four cross flow planes.

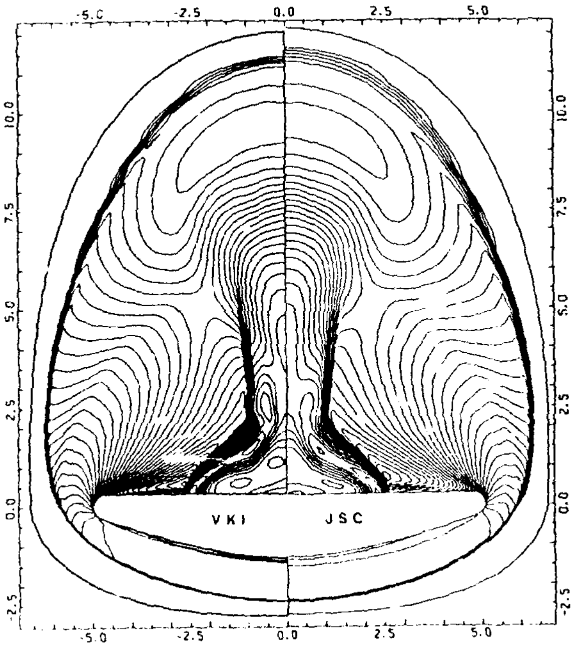

Figure 16

Comparison of VKI-JSC iso-Mach lines in a cross flow plane at $X/C_r = 0.5$.

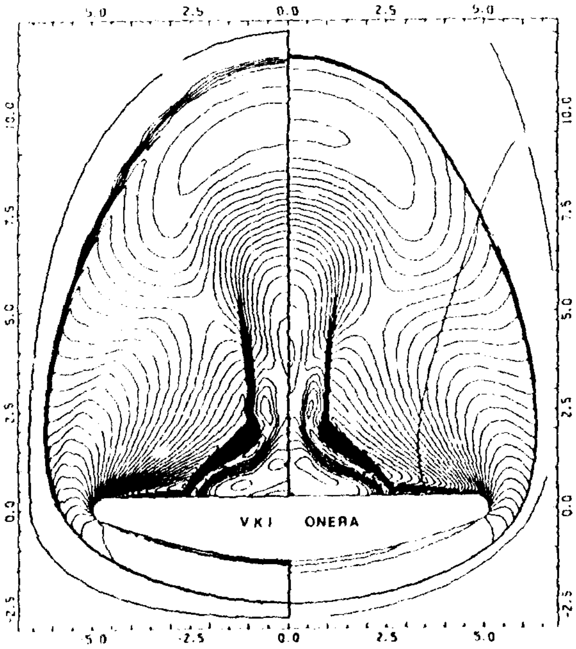

Figure 17

Comparison of VKI-ONERA iso-Mach lines in a cross flow plane at $X/C_r = 0.5$.

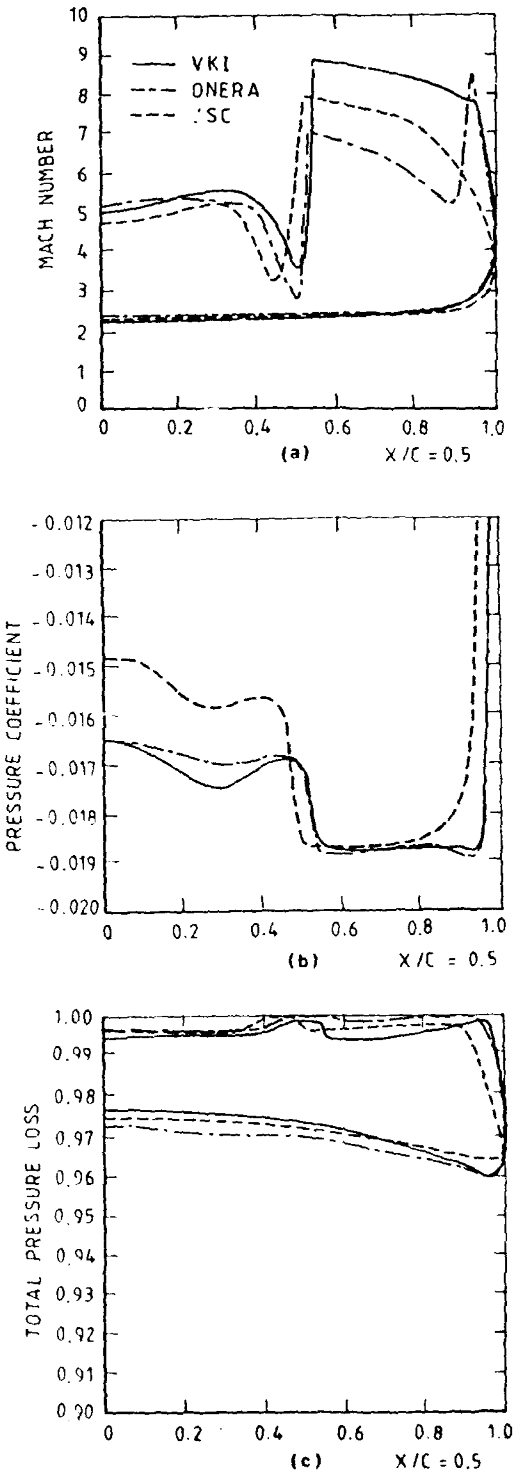

Figure 18

Surface data in a cross flow plane at $X/C_r = 0.5$.

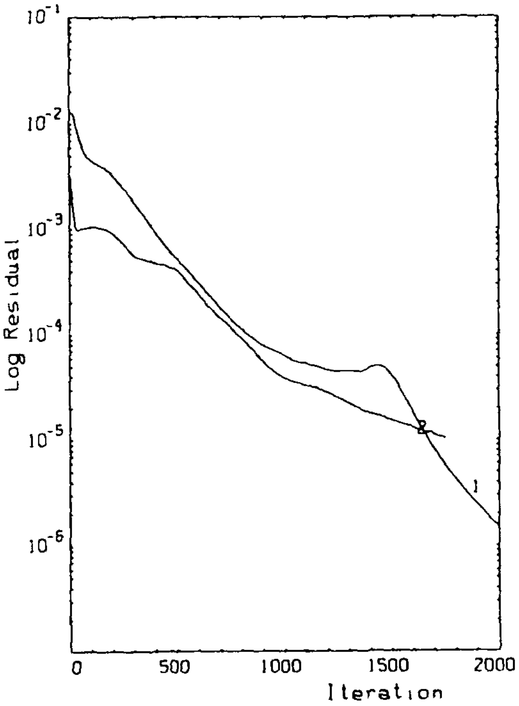

Figure 19
Convergence history.

Local Aerothermal problems during HERMES Re-entry

A. Naïm, M. Mallet, P. Rostand, J.M. Hasholder
78, Quai Marcel Dassault 92214 St Cloud

I-Résumé

L'exposé suivant présente les résultats obtenus par le code de calcul Navier Stokes utilisé à Dassault-Aviation dans le cadre de calculs aérothermiques sur HERMES.

L'objectif est de définir la stratégie employée, seules les grandes lignes des outils utilisés seront décrites. Cette méthode a été pensée de façon à être utilisable dans un maximum de cas possibles. Il s'agit d'une véritable chaîne de calculs qui est, non seulement multi-codes mais aussi multi-sites.

La préparation des prédicteurs Navier-Stokes s'est faite sur IBM ES 9000/820 MVS ESA et les calculs par eux mêmes sur NEC SX3 (supercomputer du NLR aux Pays Bas) ainsi que sur CRAY YMP (du C.I.R.A. en Italie) sous UNIX.

Cette particularité implique d'autres contraintes qui nous amènent à écrire des codes de calculs totalement portables sur des machines qui sont d'architectures très différentes.

Nous allons présenter un cas de validation de la chaîne complète, puis un certain nombre de résultats préliminaires sur des cabines de l'avion spatial HERMES (A.S.H.), ainsi que des points importants pour la définition des détails de la protection thermique de cet avion.

Le cas de validation est une cabine HERMES forme 0.0. La maquette correspondante a été essayée dans la soufflerie R3CH de l'ONERA

Les cas réels considérés sont les suivants :

- les différents formes de cabines avec verrières
- le point d'impact sur le nez de l'avion par une météorite
- les joints inter-tuiles (en position première tuile)

Ibis- Abstract

The objective of this paper is to present results obtained with the Navier Stokes code used by *Dassault Aviation for* aerothermal reentry problems.

We will emphasize the strategy employed and only give an outine of the numerical technique developed for each solver involved in the calculation.

The method is designed to have a wide range of application. It involved a sequence of calculations using different modules and interfaces.

This tool is not only multi-codes but also multi-computers.

The preparation of the initial solution sets for computations were performed on our IBM ES 9000/820 with MVS ESA operating system, and most of the computation was done on a NEC SX3 (at NLR in the Nederlands) and on a CRAY YMP (at C.I.R.A in Italy) with UNIX operating system. We shall present a validation case using the complete sequence, and afterwards a number of critical points of micro-aerothermodynamics. The validation test case is a Complete Hermes canopy of the 0.0 geometry (shape number 185 in Dassault catalogue) .A model of this shape was tested in R3CH ONERA wind tunnel yielding experimental results that are used for comparison.

For the flight cases we plan to compute :

- Various canopy shapes
- A meteorite impact on the Hermes noze cap
- Joint between tiles (in first tile position)

II- Moyens employés/ contraintes

L'utilisation du solveur N.S. entraine des coûts de calcul élevés essentiellement liés à la nécessité d'utiliser un maillage extrèmement fin dans la couche limite. Il est donc souhaitable de limiter son utilisation aux zones où les caractéristiques de l' écoulement l'imposent (recirculations). Une stratégie permettant une utilisation locale du solveur N.S a été développée. D'autre part cette utilisation locale permet aussi d'effectuer des calculs dans les situations où la contrainte mémoire limite le nombre de noeuds utilisables.
Le code N.S. requiert environ 150 nombres réels par noeud de maillage, ceci est relativement faible pour un code 3D non structuré implicite.

Pour mener à bien cette étude, une approche optimale tant du point de vue temps CPU que temps de mise en oeuvre a été définie

La procédure employée est la suivante :

- a) Création d'un maillage 2D surfacique triangu -laire avion complet
- b) Construction d'un maillage 3D tétraédrique complet permettant de faire le calcul EULER
- c) Calcul du champ EULER
- d) Calcul de couche limite
- e) Stockage du fichier d'informations pour la construction du maillage N.S. (épaisseurs de couches limites etc.)
- f) Construction du maillage 2D surfacique de la zone N.S.
- g) Construction du maillage de la zone N.S. avec les informations de e)
- f) Prédicteur sur la zone N.S.
- g) Calcul N.S.

Un certain nombre de conditions sont à prendre en compte au cours de la réalisation de l'algorithme précédent :

- Il est important de minimiser la zone de calcul N.S. tout en étant capable de capter les caractéristiques de l'écoulement visqueux. On parlera de 'boîte Navier Stokes'
  En effet, dans la plupart des cas, un calcul EULER + couche limite correspond au bon choix de modélisation, il est par conséquent inutile d'utiliser une modélisation N.S.
  Le code Navier-Stokes est utilisé dans les zones décollées.
- La zone sélectionnée doit être de dimension suffisante pour permettre une bonne initialisation.
  En effet, par exemple dans le cas de la cabine les flancs verticaux parallèles au vent ne doivent pas être trop proches du plan de symétrie par suite de l'importance des décollements.

- Une bonne définition de la couche limite est nécessaire.
  Si les phénomènes de thermique l'imposent, il est possible de fixer le nombre de points dans la couche limite.
- Des études ont montré qu'il est préférable de structurer le maillage dans cette zone.
- Les différents codes utilisés ayant des modes de stockage de données différents,
  le développement d'utilitaires spécifiques pour les faire communiquer a été réalisé.

- De façon à prendre en compte tous les cas de figures possibles, deux initialisations du champ sont disponibles :

(+) Initialisation partielle :
l'espace complet est initialisé par le résultat d'un calcul EULER et les facettes limites seulement par une couche limite.

(+) Initialisation complète :
comporte une initialisation du champ par un calcul EULER plus une couche limite.

On utilise l'initialisation complète uniquement quand cela est possible (les contraintes de cette méthode seront expliquées plus tard).

III- Initialisations par une couche limite (historique et développements)

Le modèle standard d'interface prévoit d'initialiser les facettes limites seulement par un prédicteur EULER et couche limite.

Par la suite il est apparu possible d'initialiser l'ensemble du domaine de calcul (cf cas de validation sur HMS185 R3ch) de la même façon.

La convergence est alors plus rapide en ce qui concerne les résidus en densité.

Les valeurs de frottement et de flux s'établissent aussi très vite.

Une grande précision est nécessaire lors de la définition des limites du domaine, en effet il s'agit de conditions aux limites pour le code N.S.; celles-ci ne seront pas modidiées en cours des itérations et une éventuelle imprécision préviendrait l'établissement d'une solution de bonne qualité.

Pour l'initialisation des facettes limites du domaine, utilise les caractéristiques du champ EULER projeté dans la couche limite.

Une fois ce champ projeté il est possible de choisir le type de prédicteur C.L. à utiliser.

La procédure consiste à passer dans un premier temps un calcul de couche limite par méthode intégrale ou différences finies (suivant la difficulté du cas de calcul) sur la peau de l'avion complet (extraite du maillage pour le calcul EULER) afin de stocker les valeurs d'épaisseurs de couche limite et les grandeurs intervenant dans la construction des profils. Les grandeurs extérieures de pression, température et densité sont également stockées.

Il faut noter que ces calculs sont réalisés avec des codes industriels de couche limite de DASSAULT AVIATION. Ils sont employés aussi bien en bas subsonique qu'en hypersonique et pourront ainsi être utilisés dans tous les cas de figures où la décomposition par blocs est possible (Problème subsonique).

La deuxième étape consiste à identifier les noeuds du maillage Navier-Stokes par leurs valeurs de Y/delta (Y étant la distance à la peau et DELTA , l'épaisseur de couche limite au noeud considéré). Les profils de couche limite étant eux-mêmes définis en Y/DELTA, il est simple d'associer une nouvelle valeur de vitesse et de température en chaque noeud. La pression étant supposée constante dans la couche limite, on peut en déduire, avec la valeur de température, la masse volumique.

L'intitialisation du champ complet repose sur le même principe

Le traitement des régions comportant des concavités très rapprochées est plus délicat, on procède de la façon suivante:

Il faut construire deux maillages de la zone N.S.

- Le premier (maillage support) est prismatique dans la couche limite avec une raison et une épaisseur définies par le calcul de C.L. précédent.
- Le deuxième (maillage calcul) est déduit du précédent par tétraèdrisation dans la zone N.S.

Les deux maillages sont topologiquement identiques en ce qui concerne les numérotations des noeuds. Avec le maillage support on calcule les distances des noeuds à la peau très précisément.

Pour chaque noeud peau une liste de filiation est établie (ensemble des points qui se succèdent dans la direction perpendiculaire à la peau) cette filiation permet de définir le bon profil de couche limite. Par la suite le profil est attribué au noeud homologue du maillage calcul.

IV- Description du code de résolution des équations de Navier-Stokes

La résolution des équations de Navier-Stokes doit permettre une connaissance précise des structures tourbillonnaires et de la couche limite (y compris des profils de température permettant de calculer correctement les flux de chaleur). Cela conduit à des difficultés numériques spécifiques :

- le schéma doit précisément équilibrer les petites valeurs en diffusion physique et la diffusion numérique nécessaire pour préserver la stabilité.
- les performances du code (précision et vitesse de convergence) ne doivent pas subir de dégradation quand le maillage comprend des éléments allongés et de petites dimensions dans la direction perpendiculaire à la peau.
- la capacité de capture des chocs doit être bonne.

Le code de résolution des équations Navier-Stokes tridimensionnel reference [3] s' efforce d'atteindre ces objectifs.

Il utilise une approche de type éléments finis, le système d'équations aux dérivées partielles étant écrit sous forme faible.Ceci permet une grande flexibilité géométrique.

La formulation développée possède de bonnes caractéristiques de stabilité et de précision grâce à l'utilisation des opérateurs 'Galerkin / moindres carrés', qui s'apparente à une formulation de type S.U.P.G. (Streamline Upwind Petrov Galerkin).

La formulation de type Galerkin est une méthode stable. Cependant lorsqu'il y a de forts gradients il peut se produire des oscillations. Pour les corriger, un opérateur destiné à capturer les discontinuités a été ajouté à la formulation.

La convergence du code est accélérée par l'utilisation de méthodes de type GMRES non linéaires reférence [1] péconditionné de manière non symétrique par les blocs diagonaux de la matrice jacobiènne. Une vectorisation complète est obtenue par la mise en oeuvre de techniques de coloriage.

Plus de détails sont disponibles dans les réferences.

Le code N.S. peut prendre en compte les phénomènes de vibration et de dissociation des molécules de l'air.

Le modèle comporte 5 espèces (N2, O2,NO, N et O) pour trois réactions chimiques à l'équilibre cf réference [2]. On peut ainsi avoir une idée de l'influence sur l'écoulement, sur les flux de chaleur, etc .. des effets de la dissociation des molécules d'azote et d'oxygène pour les écoulements hypersoniques qui font l'objet de notre étude.

Le code N.S peut faire des calculs à température peau fixée identique, ou différente sur chaque facette.

Un module de prise en compte de phénomènes radiatifs est également incorporé.

Ce module offre deux possibilités :

La première, utilisée pour les formes convexes (dite à 'système ouvert') ne tient pas compte des facettes parois en vis à vis.

Elle consiste, connaissant le flux de chaleur convectif, à faire un bilan thermique simple entre le flux convectif et le flux radiatif local émis pour une facette.

Ce bilan permet de définir une température d'équilibre radiatif qui devient une nouvelle condition aux limites pour le code N.S.

La deuxième, utilisée pour les formes présentant des parties concaves significatives (dite 'système fermé') est plus globale.

Le bilan thermique est composé de trois termes le flux convectif, le flux radiatif reçu dans la facette et le flux radiatif émis par la facette. On introduit un facteur de configuration Fij entre la facette considérée (indice i) et les autres facettes (indice j) qui ,de par leur proximité et leur position, peuvent influencer le bilan thermique.

Fij ne dépend que de la géométrie des deux surfaces.

Le couplage ainsi défini peut être itératif dans la mesure où la matrice des facteur Fij peut être inversée une fois pour toutes. On allège le calcul par un prétraitement permettant d'isoler les facettes pour lesquelles il y a couplage. Les zones restantes sont traitées en 'système ouvert'

V- Test de validation - cas de soufflerie -

Il s'agit de la cabine de la forme HERMES 0.0 (forme 185 dans la nomenclature DASSAULT/ aérodynamique théorique) .

La maquette correspondante (1/30 ème) a été essayée dans la soufflerie R3Ch de l'ONERA gaz parfait.

La maquette est à température paroi fixée.

Le cas de calcul reconstituant la mesure par les thermocolor se définit de la façon suivante:

MACH = 10
INCIDENCE = 30
DERAPAGE = 0
TEMPERATURE GENERATRICE = 1123 K
PRESSION GENERATRICE= 120 bar
TEMPERATURE CORPS = 290 K

Le support de calcul est un maillage tétraédrique d'environ 87.000 noeuds soit 500.000 éléments (cf figure 1)

Sur la figure 2 on distingue la boite N.S. et le maillage EULER. On peut se rendre compte de la souplesse de la méthode. En effet on a pu, à partir d'une géométrie EULER ne comportant pas de verrières, avoir un prédicteur EULER+CL dans tout le champ sur une géométrie N.S.avec verrières (et leur géométrie complexe de bourrelets).

L'ordinateur utilisé pour les calculs est l'ordinateur du N.L.R. NEC SX3/12, 256 Méga octets de mémoire centrale laissant à l'utilisateur 164 Méga Octets. C'est une machine 32/64 bits dont la performance en crête est de 2.75 Giga Flops.

La convergence a été obtenue après 1000 itérations en implicite La descente des résidus basés sur les densités est de quatre ordres environ après seulement 500 itérations . Mais pour les calculs N.S. une bonne convergence en densité n'est pas suffisante, il faut vérifier la convergence des frottements et flux de chaleurs spécialement dans les zones critiques.

La courbe de convergence (figure 3) rend compte

- De la qualité de l'initialisateur (descente très rapide)
- De la convergence en résidus sur la densité vers 500 itérations.
- De la poursuite des itérations pour obtenir les flux convergés

L'analyse des résultats de soufflerie permettent la comparaison des flux de chaleur donnés par la soufflerie

- coef h défini par :

h = flux /(T de frottement - T(corps))) .

On passe des STANTON donnés par le code N.S. définis par :

STAN = flux / ((densité*vitesse))(inf)*Cp*
(T(inf) - T(corps))

à h dans notre cas de la façon suivante :

h = 33000 * STAN

La comparaison calcul/soufflerie est tracée figure 4

On constate que les localisations des maxima de STAN sont identiques (au dessus du hublot central). En ce qui concerne les valeurs max, la soufflerie donne 0.036 pour 100 fois le flux, alors que le calcul donne 0.0425. Le résultat est acceptable car il correspond à la zone d'incertitude de la méthode expérimentale.

Les formes des ISO STAN sont comparables mais pas tout à fait identiques.

En effet le calcul N.S. donne des iso plus 'ouvertes', ce qui est dû probablement, soit à la prise en compte de la condition de symétrie par le code N.S., soit à l'exploitation des changements de couleur des thermocolor soufflerie (virages) sur la maquette.

VI- Calcul sur la cabine pour un point de vol - comparaison avec le cas de soufflerie à iso-forme -

le cas de calcul cabine en vol choisi est un cas en gaz réels à :

ALTITUDE = 60 Km
MACH = 20
INCIDENCE = 30 degrés
DERAPAGE = 0 degrés
(ce qui correspond à un REYNOLDS par mètre de 120890 à cette altitude)

Le point considéré est plus bas que le point de vol réel pour rendre le résultat dimensionnant.

Contrairement au calcul de soufflerie pour lequel l'hypothèse température de paroi constante est correct, le calcul vol est effectué en imposant l'équilibre radiatif à la paroi.

Les lignes pariétales de frottements (figure 5) permettent d'avoir une représentation globale de l'écoulement

Il apparait de façon claire deux zones, l'une à l'amont du décollement, l'autre à l'aval du recollement.

Les zones de décollement à MACH=10 et MACH=20 ont des topographies trés différentes. En effet, il existe sur le cas à MACH=10 un point près du plan de symétrie qui semble être un point central de recollement. Sur le cas vol MACH=20, l' écoulement passe par un 'arceau' central sans décollement.

En ce qui concerne la zone de recollement le resserrement des lignes de frottement montre que le niveau d'échauffement est plus important sur le cas à MACH 10. Les lignes de frottement divergent après le point de recollement ce qui diminue l'épaisseur de couche limite , donc augmente les flux de chaleur. La zone à protéger est située sur la vitre centrale au niveau du sourcil. La figure 6 des flux de chaleur (CH) le confirme.

De plus l'effet de gaz réel à MACH=20 diminue la zone de décollement. On constate qu'à MACH=20 le choc est plus couché.

On distingue clairement sur cette figure que les flux de chaleur sont plus importants dans les conditions de soufflerie.

Des calculs effectués sur la forme lisse ont prouvé que les échauffements dans cette configuration sont admissibles. Le problème à résoudre a un caractère local certain. Il faut arriver à étudier de façon très précise la nature de l'écoulement 3D dans la zone des verrières. On trace pour cela les lignes isotempératures en même temps que les lignes de frottements pariétales.

Il apparait une zone de recirculation fluide sous le sourcil sur la verrière. En amont de cette zone la densité de lignes isotempératures montrent que le gradient est assez fort.

Pour protéger le plus possible la zone de verrières on montre une étude typique de variation effectuée pour améliorer le dessin et conduisant, pour de petites variations de forme, à des variations notables d'échauffement et de lignes pariétales de frottement.

VII- Deux cas de calcul en aérodynamique locale sur Hermes

Position du problème :

La protection thermique d'Hermes est de trois types :

- Structure chaude (thermostructure:nez bord d'attaque,..)
- Protection souple (F.E.I.)
- Protection thermique rigide (tuiles à jupe à l'intrados et tuiles à pattes à l'extrados) constituant environ 30% de la surface mouillée de l'A.S.H.
  (représentation de la topologie de la protection thermique figure 8)
  La tuile permet une isolation primaire par reradiation du flux thermique, le maintien des formes aérodynamiques, l'étanchéité à l'eau, la protection de l'isolant multi-écran et de l'environnement extérieur direct.

L'isolant multi-écran (I.M.E.) isole la structure primaire en fonctionnement nominal, permettant d'assurer une protection en cas de perte de tuile (isolant multi-écran sous toile. L'isolant semi rigide (I.S.R.) limite la circulation d'air chaud dans les volumes sous les tuiles (cloisonnement), assure une barrière thermique et de pression lors de la perte d'une tuile, forme un appui continu pour les flancs des tuiles.

Il est important de déterminer la tenue de cette protection thermique durant toute la phase d'entrée.

Les échauffements les plus importants se produisant à l'intrados.

On présente ici l'étude des deux problèmes suivants :

a) Influence sur l'écoulement d'un trou sur le nez de l'avion causé par l'impact d'une météorite

b) Résistance à l'échauffement des joints intertuiles

Le point de vol le plus thermiquement dimensionnant a été choisi. Parmi les trajectoires de rentrée possibles, le point de vol le plus critique sur la trajectoire enveloppe permise a été sélectionné.

Il correspond aux caractéristiques suivantes :

ALTITUDE = 59 Km
MACH = 17.8
INCIDENCE = 40 degrés
DERAPAGE = 0 degré

La simulation de ce point de vol doit être la plus précise possible. La possiblité offerte par le code N.S. de prendre en compte les phénomènes de dissociation des molécules de l'air a été employée.

D'autre part, l'importance dans certaines zones des convexités impose de prendre en compte les phénomènes de radiation.

DETAILS DES CALCULS

La stratégie précédemment décrite a été employée. Pour avoir une simulation numérique précise des phénomènes physiques à étudier, deux maillages tétraédriques de 100.000 éléments pour le point d'impact au nez et de

250.000 éléments pour le calcul sur le joint inter-tuiles ont été réalisés.

Les visualisations des limites des maillages des boîtes N.S. se trouvent sur les figures 9 10 et 11. Les maillages sont superposés au maillage peau de l'avion complet ayant servi à la réalisation du EULER.

Les prédicteurs EULER + C.L. sur les plans d'entrée seulement ont été employés

A) IMPACT PAR UNE METEORITE

Le maillage (coupe à Y=Cste figure 12) est composé de trois domaines cylindriques, le premièr dans le fluide , le deuxième dans le matériau de protection avion, le troisième est un cylindre interne pour évacuer le fluide qui passe dans le trou d'impact (le trou d'impact est supposé circulaire).

On a rempli le cylindre interne d'air à pression infinie (très faible) de façon à simuler les conditions de débit. Ce cylindre doit être de volume suffisant dans la mesure où, en se remplisssant de fluide venant de la cavité externe la pression augmente ,donc, peut influencer l'écoulement externe. La convergence des flux de chaleur a été obtenue après environ 1000 itérations.Le calcul a démarré avec un prédicteur ayant une température paroi constante égale à 1100 K.

il a fallu 200 itérations ,dans ces conditions, pour stabiliser les flux de chaleur.

Par la suite, une nouvelle évaluation des températures radiatives (bilan convection reradiation à la peau tenant compte des influences des facettes en vis à vis). Ce bilan impose de nouvelles températures d'équilibre radiatif à la peau pour continuer à itérer. On recommence cette procédure jusqu'à convergence totale des températures.

Les lignes de courant présentées figure 13 représentent l'écoulement final dans une coupe à Y=constante passant par un plan contenant l'axe des trois cylindres. La zone d'impact (resserrement des lignes de courant) est apparente, ainsi que la zone de recirculation dans le domaine externe.La topographie de l'écoulement devient stable en pression après 300 itérations environ (la palette a été choisie de façon à faire apparaître la zone externe). En ce qui concerne la représentation des nombres de MACH figure 14, on constate qu'il se forme une zone transsonique dans le trou. Le point d'échauffement maximal est apparent sur la figure 15 (important gradient de pression et pression locale maxi).

B) ELEMENTS CONCERNANT L'ETUDE DES TUILES

Il est important de choisir la position relative des deux tuiles pour minimiser l' échauffement des joints. Comme point de départ de cette étude nous avons déterminé une position 'en diagonale' pour éviter le plus possible le déclenchement de la transition (cf figures 9 10 et 11 pour configuration).

Le maillage approprié prend en compte en détails les zones entre les tuiles. Elle comporte des points d'inflexions rendant difficile la réalisation d'un maillage régulier. L'initialisation s'est faite uniquement sur le plan d'entrée. Les zones de recirculation dans les cavités comportant des morceaux de joints sont intéressantes à étudier dans la mesure où l'apport en flux de chaleur par frottement est faible mais l'apport radiatif est élevé.

Sur la figure 17 on présente le résultat préliminaire en températures. On remarque la zone d'échauffement par frottement sur la deuxième tuile frontale, mais surtout l'échauffement par réradiation dans les parties concaves.

VIII- Conclusion

Les méthodes de calcul utilisées à Dassault-Aviation ont permis d'obtenir des résultats satisfaisants pour les cas de calculs complexes hypersoniques nécessaires au dessin de l'avion HERMES. Il a fallu modéliser un bilan thermique complet tenant compte d'éléments radiatifs. Cependant les résultats présentés doivent être considérés comme étant encore à valider par d'autres cas d'essais et de calcul. Le même code fournit un recoupement satisfaisant sur les cas du Workshop d'Antibes (1991). Cependant la non linéarité des problèmes thermiques demanderait de rendre encore plus complète la modélisation :

il faudrait prendre en compte les éventuels phénomènes de conduction dans les matériaux. De plus la porosité de certains constituants de la protection thermique modifie les pressions au à la peau, et par conséquent l'écoulement global.

Nous avons affaire à un système très complexe qui ne peut être résolu par des méthodes classiques (simple calcul Navier Stokes sur un champ complet).

Il demande la mise en place d'une structure évolutive et modulaire permettant la prise en compte d'éléments de modélisation de plus en plus fins.

Remerciements

Les auteurs ont à coeur de remercier

MM P.Perrier , Ph Caupenne, D. Alleau, J.C Courty, E. Teupootahiti, J.A. Nicolaï de Dassault Aviation qui ont participé à l'élaboration de ce document.

Références

[1] Z. Johan, T.J.R. Hughes and F Shakib, "A globally convergent matrix-free algorithm for implicit time-marching schemes arising in finite element analysis in fluids", Computers Mehods in applied Mechanics and Engineering, 87 (1991) 281-304

[2] F. Chalot, T.J.R. Hughes, and F. Shakib, "Symmetrization of conservation laws with entropy for high temperature hypersonic computation".Computing Systems in Engineering, 1 495-521,(1990)

[3] M. Mallet "A Finite Element method for computational fluid dynamics" Ph.D. Thesis Stanford University. 1985

[4] F. Huet "application of mesh generation to complex 3D configurations" Agard proceedings N° 464 (1989)

MAILLAGE NAVIER STOKES

HMS 185 CABINE

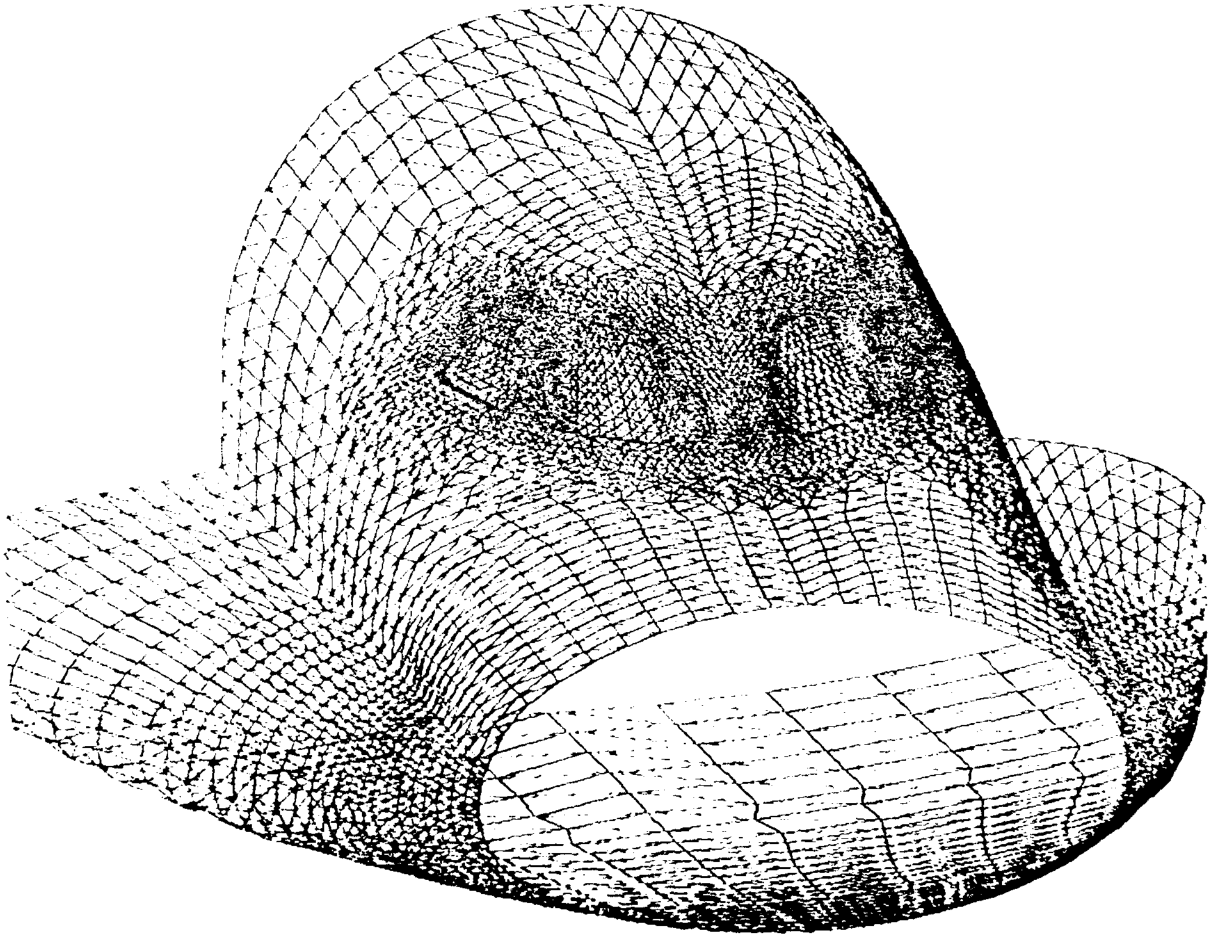

Figure 1

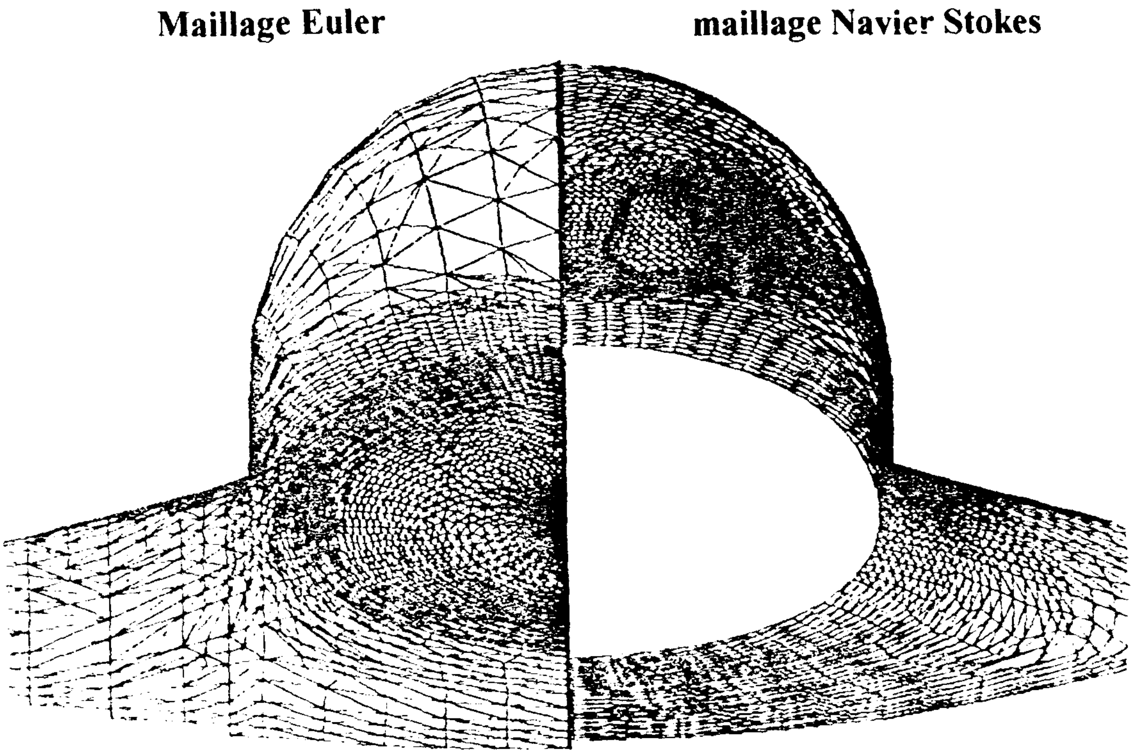
Maillage Euler
maillage Navier Stokes

Figure 2

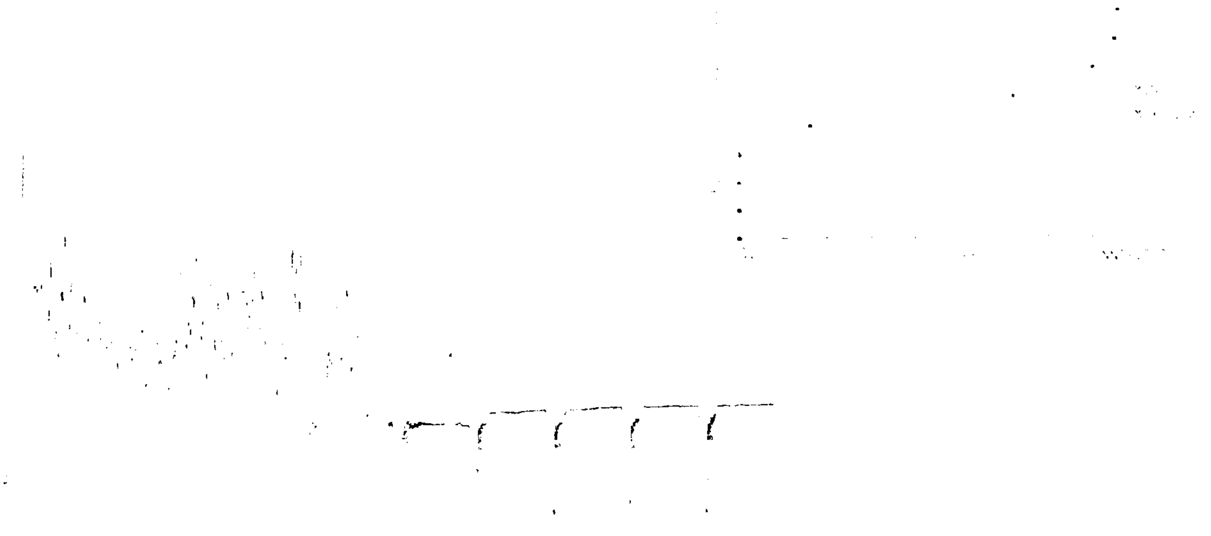

Courbes de convergence des résidus max

Figure 3

Hermes 00 Mach=10 Inci=30
Valeurs à diviser par 100 pour STAN
Soufflerie R3ch transition déclenchée
Navier Stokes 1000 itérations

Valeur maxi 0.36 soufflerie
Valeur maxi 0.425 Navier stokes

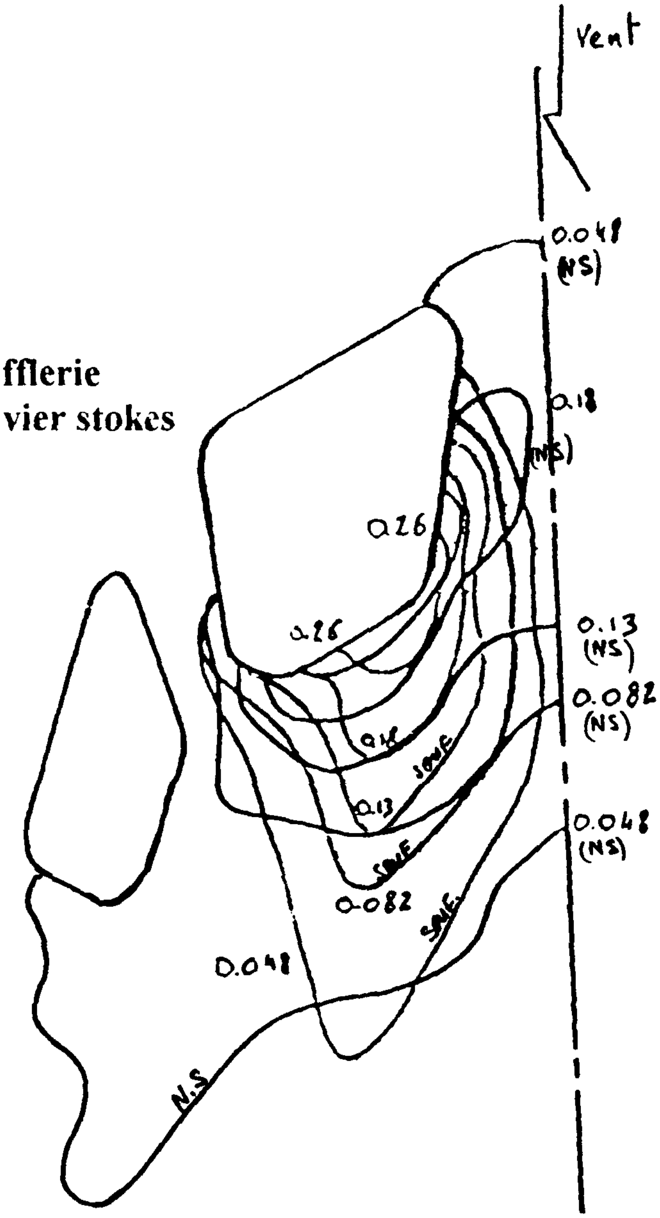

Comparaison des échauffements Navier-Stokes/soufflerie

Figure 4

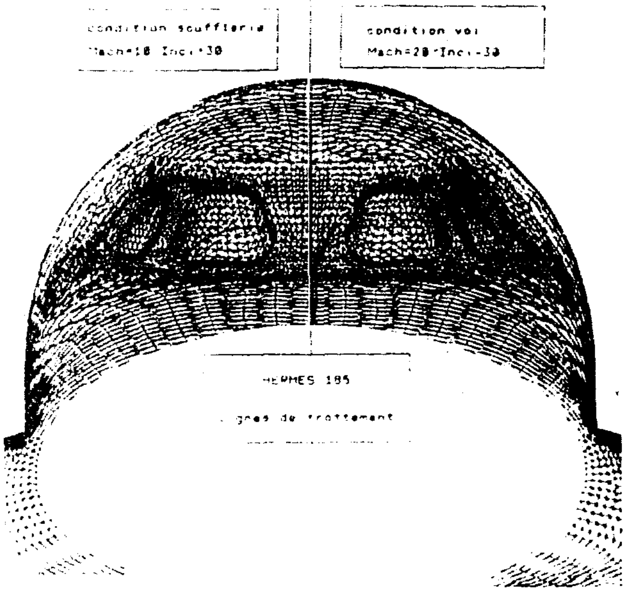
condition soufflerie
Mach=10 Inci=30
condition vol
Mach=20 Inci=30
HERMES 1B5
lignes de frottement

Figure 5

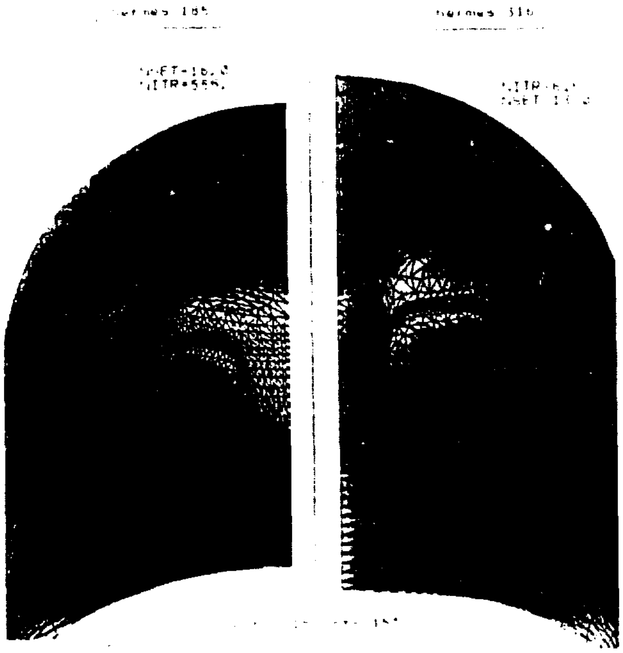
Hermes 1B5
Hermes 31b
NSET=16.0
NITR=555.
NITR=
NSET

Figure 7

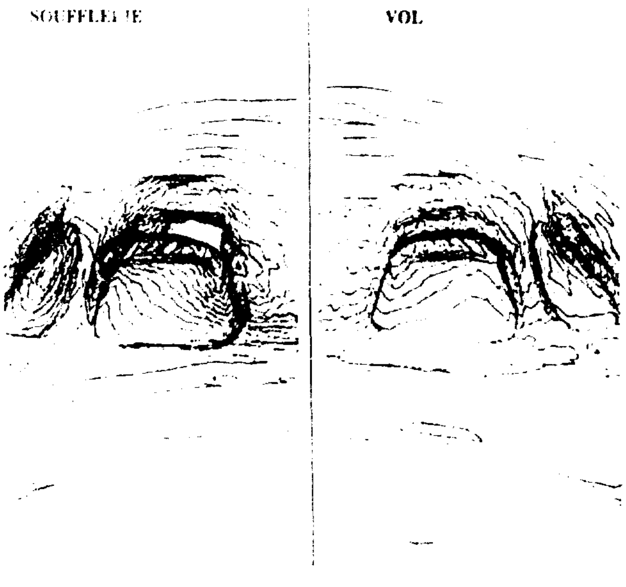
SOUFFLERIE
VOL

Figure 6

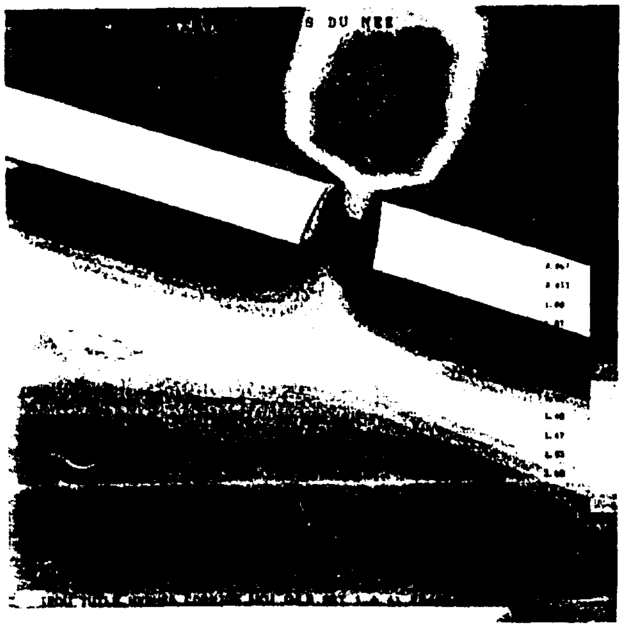

Figure 14

TUILE A JUPE

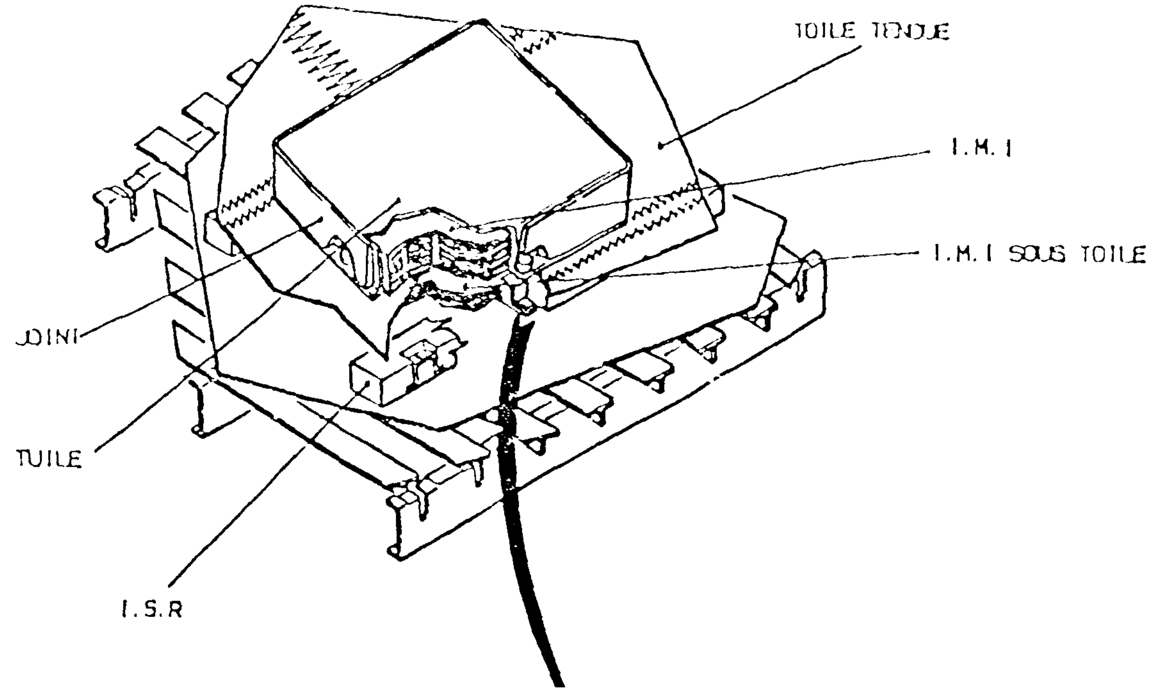
TOILE TENDUE
I.M.I
I.M.I SOUS TOILE
JOINT
TUILE
I.S.R

TOPOLOGIE DU SOUS SYSTEME DE PROTECTION THERMIQUE

Figure 8

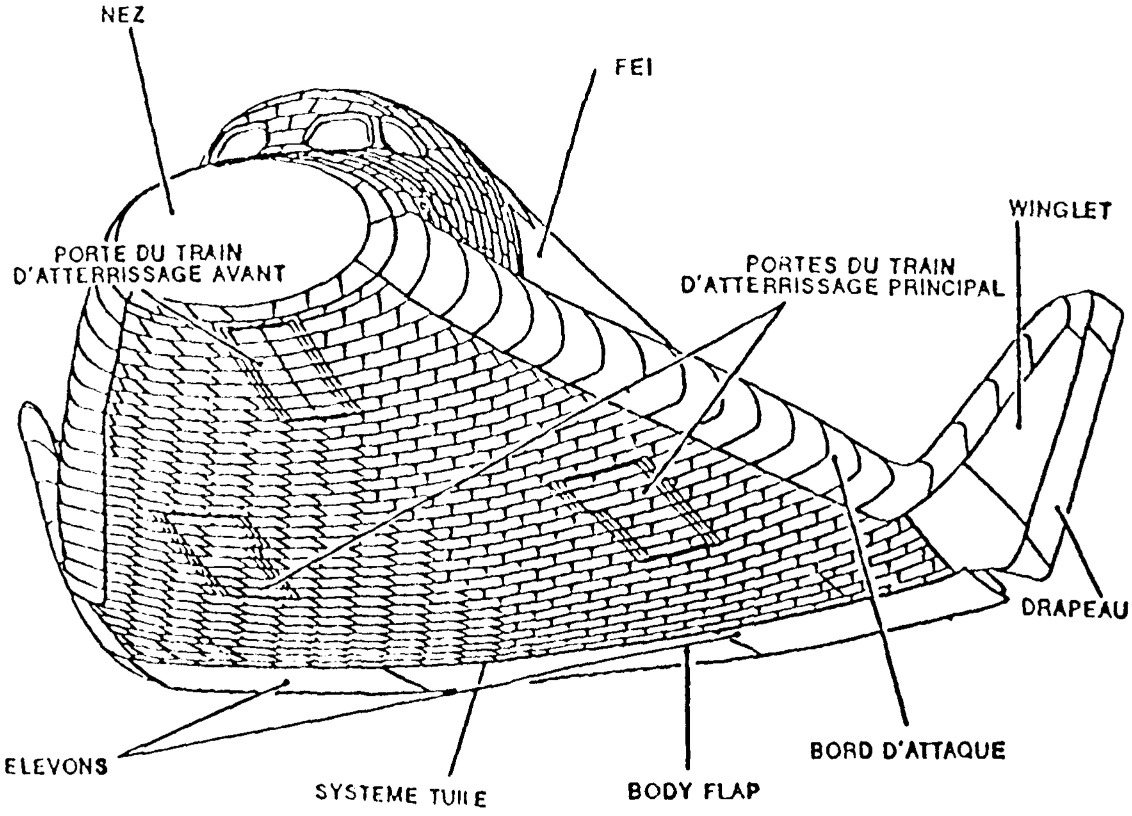
NEZ
FEI
WINGLET
PORTE DU TRAIN D'ATTERRISSAGE AVANT
PORTES DU TRAIN D'ATTERRISSAGE PRINCIPAL
DRAPEAU
ELEVONS
SYSTEME TUILE
BODY FLAP
BORD D'ATTAQUE

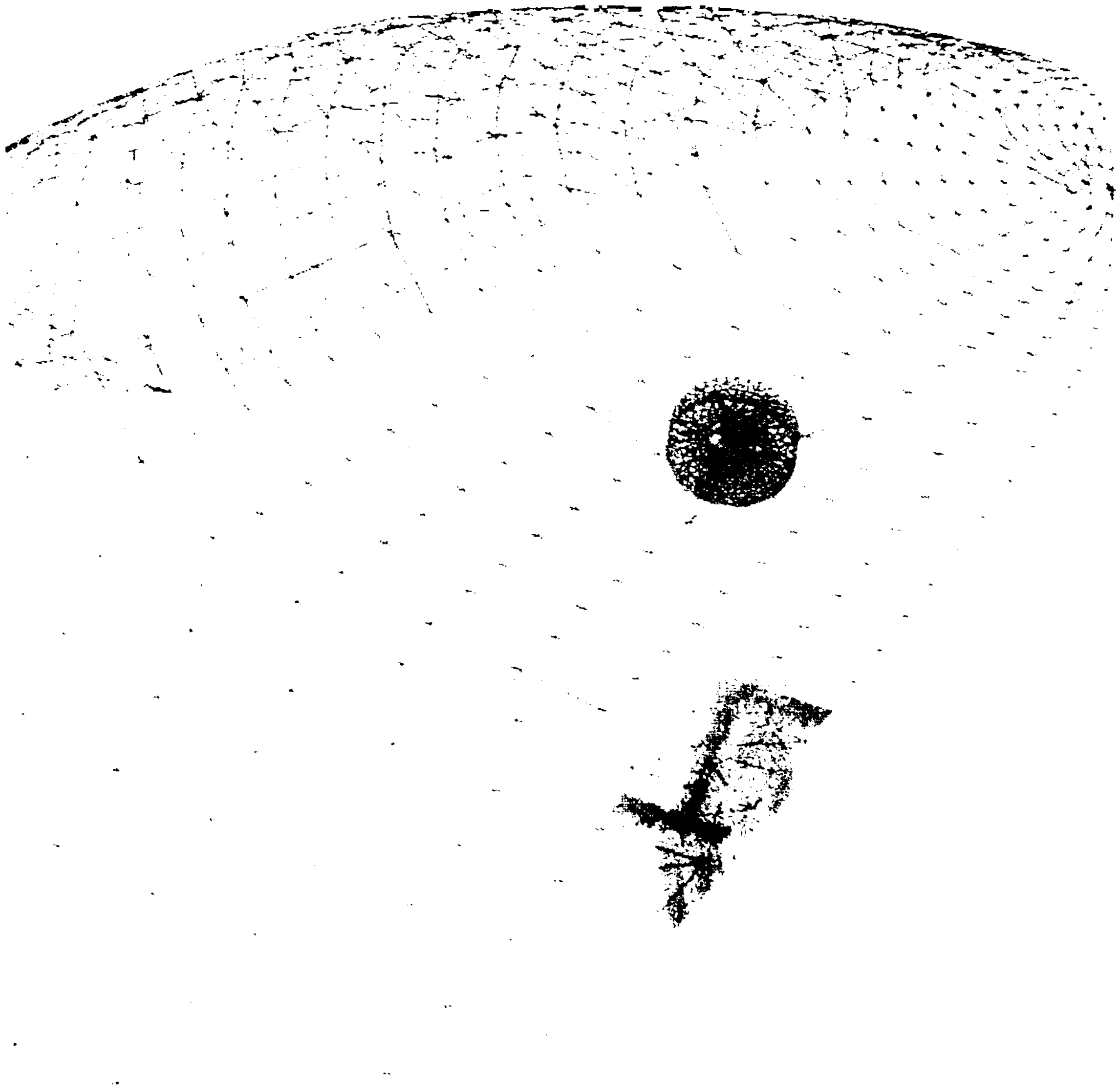

Figure 9

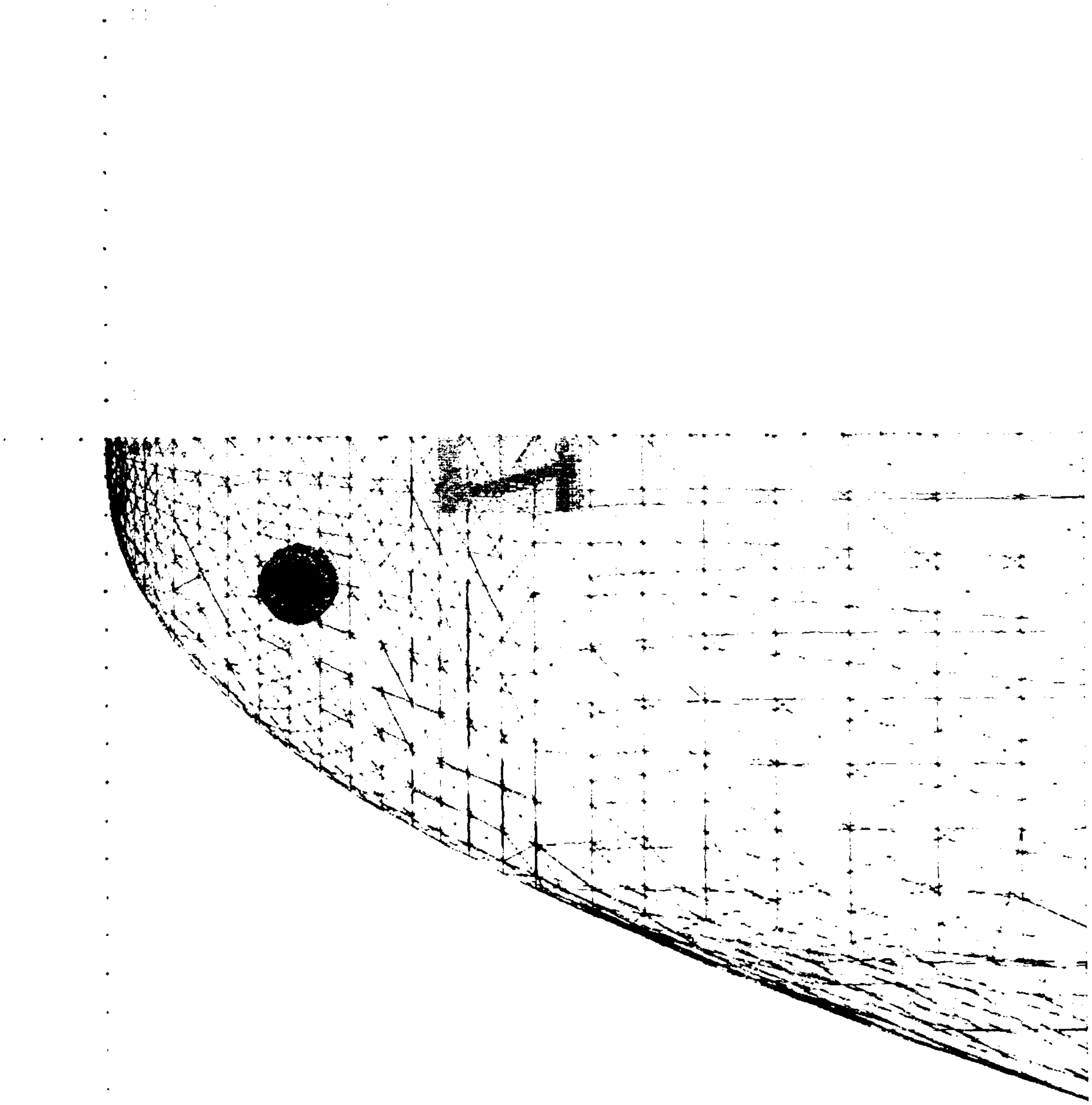

Figure 10

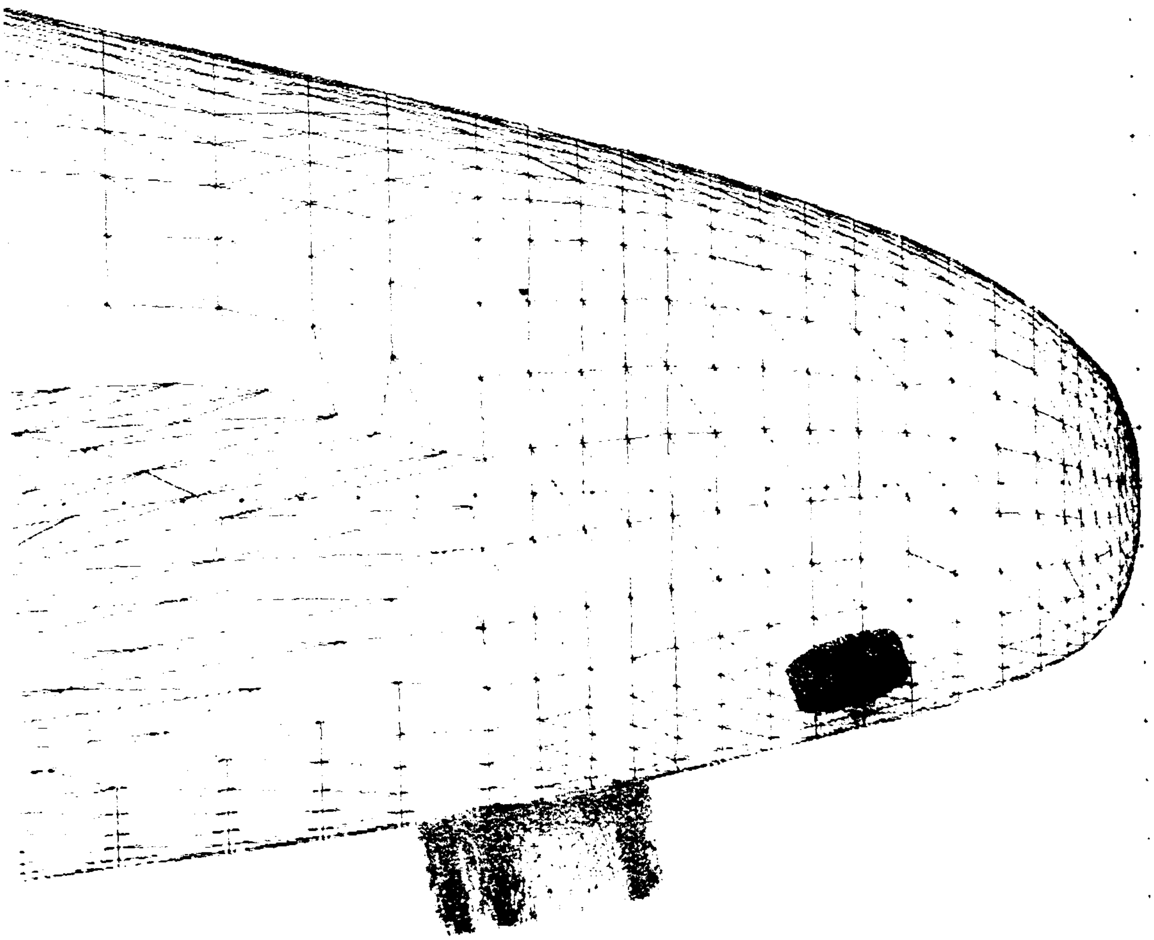

Figure 11

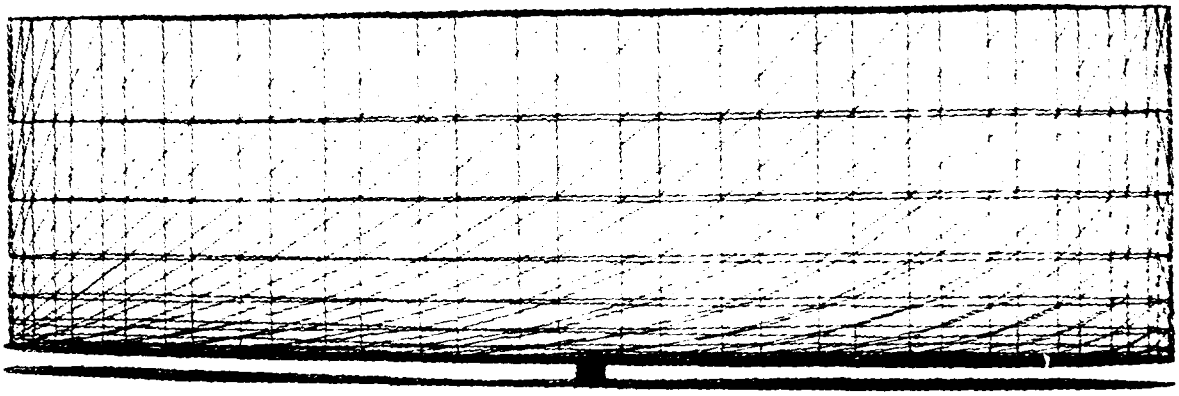

Figure 12

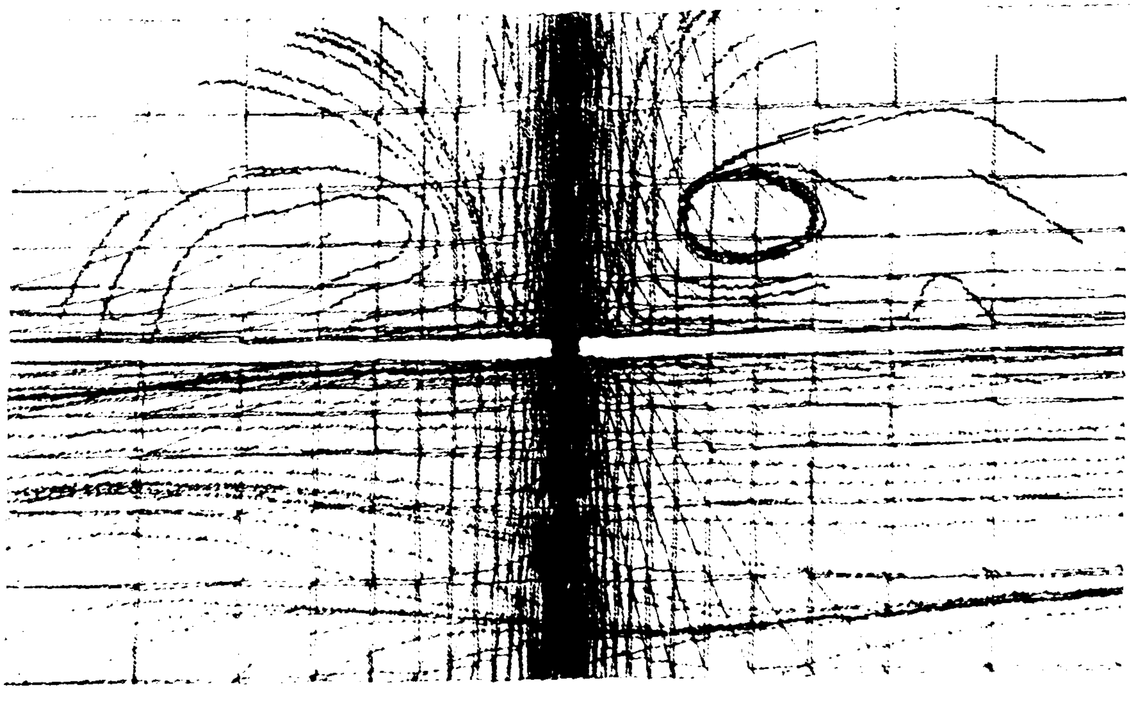

Figure 13

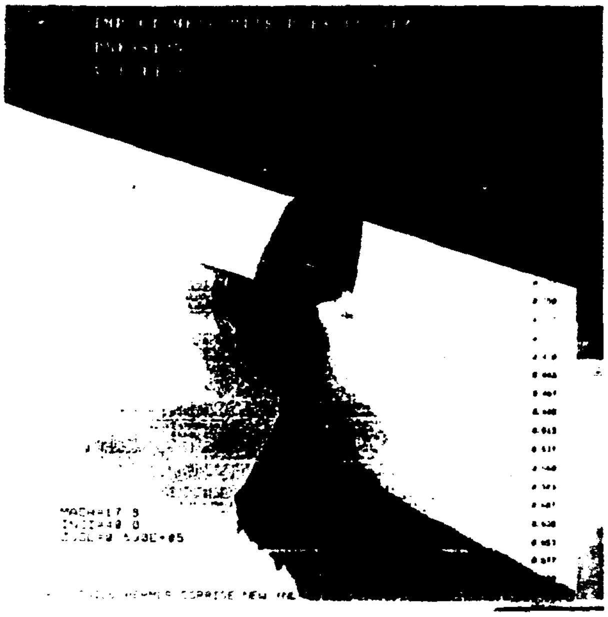

Figure 15

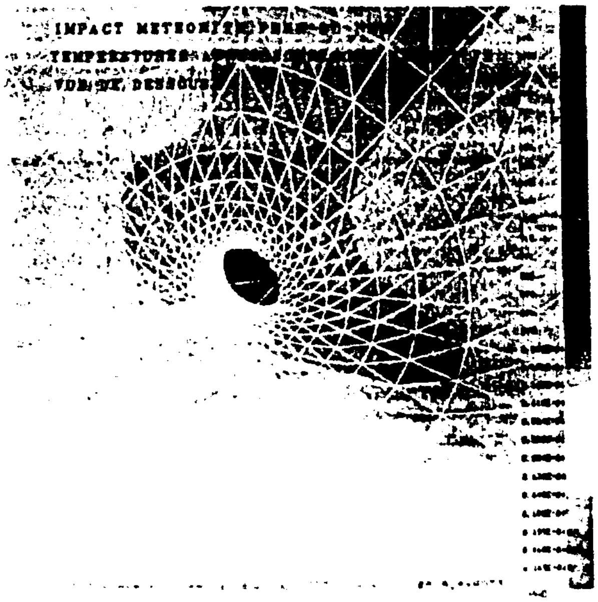

Figure 16

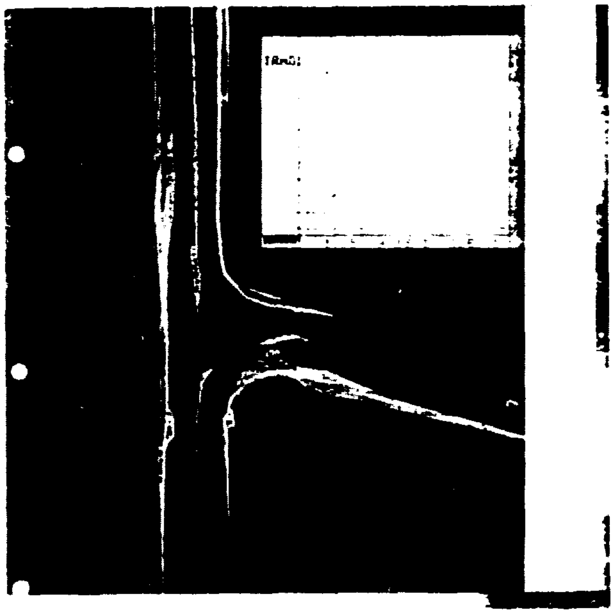

Figure 17

THERMAL AND CHEMICAL NON EQUILIBRIUM HYPERSONIC FLOW COMPUTATIONS

F. Grasso and V. Bellucci

Department of Mechanics and Aeronautics
University of Rome "La Sapienza"
Via Eudossiana, 18 - 00184 - Rome, Italy

ABSTRACT

In the present work a two temperature model has been developed for the description of thermal and chemical nonequilibrium viscous hypersonic flows. The model employs a vibrational coupling factor as proposed by Treanor and Marrone, and it uses a model based on a non preferential removal of vibrational energy. The technique relies on a finite volume approach based on a second order accurate Total Variation Diminishing formulation that accounts for thermal and chemical nonequilibrium effects. The stiffnes due to the disparity in time scales is reduced by introducing a precondition matrix that allows a pointwise implicit solution of the source terms.

Applications of the model to compute viscous hypersonic flows over a wedge and a cylinder have shown that the post-shock temperature plays a fundamental role in the achievement of thermal equilibrium.. and that the boundary layer is the most affected by thermal nonequilibrium.

INTRODUCTION

The analysis of hypersonic flows differs substantially from that of supersonic flows, and the development of advanced space transportation systems requires a detailed simulation of the high temperatures effects (usually referred to as "real gas" effects).

At ambient temperature air can be represented as a perfect gas having only the translational and rotational modes (fully) excited.

High speed flows are characterized by a high kinetic energy content that is converted into translational energy (for example past bow shocks and within the boundary layer due to viscous dissipation), thus increasing the brownian motion of the particles, and, as a consequence, the (translational) temperature of the gas. The high temperature is then responsible for the vibrational and electronic excitation, dissociation of diatomic molecules, and ionization. Therefore, under typical hypersonic conditions air must be considered as a mixture of reacting gases whose thermodynamic state is characterized by: *i)* a translational temperature (identifying the translational and rotational energy modes); *ii)* a vibrational temperature for each of the poliatomic species (identifying the vibrational energy contribution); *iii)* and an electronic temperature (for the electronic energy contribution of the heavy particles and for the translational contribution of the free electrons).

Depending upon the characteristic scales of the thermal and chemical exchange processes, different situations may arise. The flow is said to be in equilibrium if both thermal and chemical time scales are small compared to the fluid-dynamic time scale. A frozen situation arises if thermal and chemical time scales are large compared to the fluid-dynamic time scale. Finite rate processes must be taken into account when all time scales are of the same order.

Two parameters can be defined to characterize the thermal (vibrational) and chemical relaxation processes: the ratio of the fluid-dynamic time to the vibrational relaxation time (Ψ_v), and the ratio of the former to the chemical time (Ψ_c).

The vibrational relaxation time scale (τ_v) can be estimated from the Millikan and White relation

$$\frac{1}{\tau_v} = \frac{p}{C} \exp\left(-\frac{A}{T^{1/3}}\right)$$

In the shock layer, Ψ_v is given by

$$\Psi_v = \frac{L}{U_\infty} \frac{R}{C} \rho_{shk} T_{shk} \exp\left(-\frac{A}{T_{shk}^{1/3}}\right)$$

where ρ_{shk} and T_{shk} are the post-shock density and temperature values, and R is the gas constant. Then, using the hypersonic limit for an estimation of ρ_{shk}/ρ_∞ one obtains:

$$\Psi_v = K_v \exp\left(-\frac{A}{T_{shk}^{1/3}}\right) \frac{\rho_\infty L}{U_\infty} T_{shk} \qquad (1)$$

where K_v is a constant.

For dissociating air, assuming that diatomic oxygen dissociates due to collisions with diatomic oxygen and nitrogen, the chemical time scale (τ_c) can be approximately estimated as follows:

$$\frac{1}{\tau_c} = C\,T^{-1} \exp\left(-\frac{B}{T}\right) \frac{Y_{O_2}}{\overline{W}} \frac{\rho^2}{\rho_\infty}$$

where $\overline{W}$ is the average molecular weight and Y the mass fraction.

In the shock layer, Ψ_c is given by

$$\begin{aligned} \Psi_c &= \frac{L}{U_\infty} C\,T_{shk}^{-1} \exp\left(-\frac{B}{T_{shk}}\right) \frac{Y_{O_2}}{\overline{W}} \frac{\rho_{shk}^2}{\rho_\infty} \\ &= K_c \exp\left(-\frac{B}{T_{shk}}\right) \frac{\rho_\infty L}{U_\infty} T_{shk}^{-1} \qquad (2) \end{aligned}$$

where K_c is a constant.

From Eqns.(1),(2) we observe that both parameters Ψ_v and Ψ_c are most strongly influenced by the post shock translational temperature, and that non equilibrium effects depend upon the flight conditions. Limit situations arise depending upon the values of Ψ_v and Ψ_c.

In the present work we analyze flows characterized by finite rate processes, i.e. flow situations for which both Ψ_v and Ψ_c are of O(1).

The simulation of thermal and chemical non equilibrium hypersonic flows has been investigated by several authors.

Candler [1] assumes: *i)* a rapid energy exchange between the translational and rotational modes; *ii)* a finite energy transfer rate for the vibrational modes of the different diatomic species; *iii)* and the same temperature characterizing electron translation and electronic modes. For the coupling between vibration and dissociation Candler assumes that the vibrational energy lost (gained) due to dissociation (recombination) is the average vibrational energy of the molecules (non preferential removal of vibrational energy). For high temperature ionized air he has developed a six temperatures model to compute AOTV flight experiments, and has shown the influence of thermo-chemical non equilibrium on the flow field.

Palmer [2] has developed a two-temperatures model to compute dissociating, ionizing flows in thermo-chemical non equilibrium. He also assumes a simple model for vibration-dissociation coupling as proposed by Candler. Applications of the model to compute AFE flight experiments show reasonably accurate solutions.

Mitcheltree [3] has investigated the application of several dissociation and ionization models for (very) high velocity entries. The model is based on a two-temperatures model, where the chemical-vibrational coupling is taken into account by means of a weighted dissociation ratio controlling temperature. Applications to sphere-cone bodies show that variations in the reaction rates have little effects on the surface pressure and convective heating.

Gnoffo [4] has developed a rather complete model for thermal and chemical non equilibrium ionizing flows based on either a two- or three-temperatures model. He assumes curve fits for the thermodynamic relations and collision-integrals, preferential dissociation model similar to that of Candler. Applications of the model to compute aeroassist flight experiments show limitations arising from uncertainties in the thermodynamic and collision integrals curve fits, the chemical reaction mechanism and the effects of preferential dissociation modeling.

Grasso and Bellucci [5] have developed a model for thermal equilibrium and chemical non equilibrium flows including gas-surface interactions, and have shown the influence and limitations arising from uncertainties in thermodynamic relations, transport and chemical kinetics mechanisms.

In the present paper we develop a model for thermo-chemical non equilibrium flows, under the assumption of a rapid energy exchange between the vibrational and electronic modes (two temperature model). In the model we account for preferential dissociation and recombination effects by introducing a vibrational coupling factor as proposed by Treanor and Marrone. The diffusional effects on the translational-vibrational energy exchanges are neglected, perfect gas relati~~ons are~~ used to determine the thermodynamic relations and collision integrals curve fits are employed for the transport mechanism. The equations are solved by a finite volume approach based on a total variation diminishing scheme that accounts for (thermal and chemical) real gas effects. The model has been applied to compute dissociating nitrogen flows around circular cylinder, and non equilibrium dissociating air flows over a wedge.

GOVERNING EQUATIONS

In the present work the governing equations are formulated accounting for all species conservation equations. The equations are the conservation equations for a mixture of gases in thermal and chemical non equilibrium under the continuum assumption (i.e. the phenomena associated with large values of the Knudsen number are neglected). The model assumes: *i)* a single translational temperature (T) characterizing the translational modes and the fully excited rotational modes (of the molecular species); *ii)* a single vibrational temperature (T_V) characterizing vibrational and electronic modes (that are assumed to be in equilibrium with each other); *iii)* and the absence of ionization. In vector form the two-dimensional conservation equations are

$$\frac{\partial}{\partial t}\int_S \mathbf{W}\,dS + \oint_{\partial S}\mathbf{F}\,\mathbf{n}\,ds = \int_S \mathbf{H}\,dS \qquad (3)$$

where **W**, **F** and **H** are, respectively, the vector unknown, the sum of the inviscid and viscous fluxes, and the source term **H**, and they are defined as follows

$$\mathbf{W} = [\rho_q, \rho u, \rho v, \rho E, \rho e_V]^T$$

$$\mathbf{F} = (\mathbf{F}_E - \mathbf{F}_V, \mathbf{G}_E - \mathbf{G}_V)$$

$$\mathbf{H} = [\dot{w}_q, 0, 0, 0, \dot{\omega}_V]^T$$

and

$$\mathbf{F}_E = \left[\rho_q u, \rho u^2 + p, \rho u v, \rho u H, \rho u e_V\right]^T$$

$$\mathbf{G}_E = \left[\rho_q v, \rho u v, \rho v^2 + p, \rho v H, \rho v e_V\right]^T$$

$$(\mathbf{F}_V, \mathbf{G}_V) = [-\rho_q \mathbf{u}_q, \sigma, \mathbf{u}\cdot\sigma - \mathbf{Q}, -\mathbf{Q}_V]^T$$

Furthermore

$$\sigma = \mu\left[\nabla\mathbf{u} + (\nabla\mathbf{u})^T\right] - \frac{2}{3}\mu(\nabla\cdot\mathbf{u})\mathbf{I}$$

$$\mathbf{Q} = -(\eta_t + \eta_r)\nabla T - \eta_V \nabla T_V + \sum_q h_q \rho_q \mathbf{u}_q$$

$$\mathbf{Q}_V = -\eta_V \nabla T_V + \sum_q e_{V,q} \rho_q \mathbf{u}_q$$

$$E = \sum_q Y_q e_q + \frac{u^2 + v^2}{2}$$

$$H = E + \frac{p}{\rho}$$

$$\rho = \sum_q \rho_q$$

where $\mathbf{I}$, $\mathbf{u}_q$, Y_q, e_q, $e_{V,q}$ and h_q are, respectively, the unit tensor, the diffusion velocity, the mass fraction, the internal energy, the vibrational-electronic energy and the enthalpy of the q-th species. Moreover, $\dot{w}_q$ and $\dot{\omega}_v$ are the source terms due to finite rate chemistry and the vibrational-electronic energy source term.

Thermodynamic Relations

In general the internal energy and the enthalpy of species q are functions of the translational and vibrational temperatures.

The internal energy of each species is the sum of the translational, rotational, vibrational and electronic contributions (according to the factorization property of the partition function) [15].

For atomic species one has

$$e_q = \frac{3}{2} R_q T + e_{e,q} + \Delta h_q^o \tag{4}$$

For diatomic species, assuming that the rotational modes are fully excited, one obtains

$$e_q = \frac{5}{2} R_q T + e_{v,q} + e_{e,q} + \Delta h_q^o \tag{5}$$

where $e_{v,q}$, $e_{e,q}$ and Δh_q^o are, respectively, the vibrational and electronic energy contributions, and the enthalpy of formation (see Ref [5]).

The expressions for the energy contributions due to the excited vibrational and electronic states are obtained assuming Boltzmann distributions at the vibrational temperature (T_V) and a harmonic oscillator behaviour of the diatomic molecules, thus yielding

$$e_{v,q} = R_q \theta_q^v \frac{1}{\exp\left(\theta_q^v / T_V\right) - 1} \tag{6}$$

$$e_{e,q} = R_q \frac{\sum\limits_{i=1,N_q^e} g_{q,i} \theta_{q,i}^e \exp\left(-\theta_{q,i}^e / T_V\right)}{\sum\limits_{i=1,N_q^e} g_{q,i} \exp\left(-\theta_{q,i}^e / T_V\right)} \tag{7}$$

where θ_q^v, $\theta_{q,i}^e$ and $g_{q,i}$ are, respectively, the characteristic vibrational temperature, the electronic characteristic temperature of state i and its degeneracy [5].

Observe that due to vibration-dissociation coupling, the expression ~~of the~~ vibrational energy is approximated (even under the assumption of thermal equilibrium). Indeed, on account of the fact that dissociation occurs at the higher vibrational levels, only a finite number of such levels should be accounted for. The number of vibrational levels before the occurrence of dissociation depends on the dissociation energy. For nitric oxide, molecular oxygen and molecular nitrogen one obtains $N_{NO}^v = 28$, $N_{O_2}^v = 27$, $N_{N_2}^v = 34$. For temperatures ≤ 10000 K it is found that the maximum value of the percentage error is O(1%). Therefore, the use of the equilibrium (at temperature T_V) expression for vibrational energy is justified even in the presence of chemical non equilibrium [5].

In the present work ionization has been neglected. For the five major species that have been accounted for (O, N, NO, O_2, N_2), the number of electronic states is $N_q^e = 19, 22, 15, 19, 11$, as given in Ref.[16]. However, spectroscopic data for the higher electronic states are uncertain. Moreover, if the temperature is not greater than 10000 K, a reduced number of electronic states can be accounted for. Park [7] argues that the only excited electronic states are those that have an energy exceeding that of the ground state by a factor less than 2 eV, thus obtaining $N_q^e = 2, 2, 0, 3, 0$. Likewise, Palmer [2] neglects the electronic excitation of nitric oxide and diatomic nitrogen, and uses $N_q^e = 3, 3, 0, 3, 0$. Candler [1] accounts for the first two levels of all species.

In the present model the number of electronic states has been determined by imposing that the percentage error of the internal energy of each species computed with a reduced number of states is less than 1% of the value obtained by accounting for all electronic states. This gives $N_q^e = 2, 3, 2, 7, 2$ (see Ref. [5]).

Transport Coefficients

At high temperature the transport properties (viscosity, thermal conductivity and diffusion coefficients) are affected by the dissociation.

In the present work the transport coefficients are based on the Chapman-Enskog theory and on an extension of Yos' formula [4,17,18]. Chapman-Enskog theory amounts to solve Boltzmann's equation for the singlet-velocity distribution function (that coincides with the maxwellian one when the gas is in equilibrium), and strictly holds for monoatomic gases. Yos has extended the approach to account for the effects of momentum and energy transfer between different species by collisions. Based on the relations developed by Yos the mixture viscosity is defined as

$$\mu = \sum_q \frac{m_q \gamma_q}{\sum\limits_r \gamma_r \Delta_{q,r}^{(2)}(T)} \tag{8}$$

where m_q, $\Delta_{qr}^{(2)}$ and γ_q are, respectively, the mass of the species q, the modified collision integral, and the molar concentration, the latter being defined as

$$\gamma_q = \frac{\rho_q}{\rho W_q}$$

For a mixture of gases in thermal non equilibrium, the heat conduction accounts for the contributions of the transport of translational energy and the transport of energy due to the internal structure.

The translational thermal conductivity is defined as follows

$$\eta_t = \frac{15}{4} \kappa \sum_q \frac{\gamma_q}{\sum_r a_{q,r} \gamma_r \Delta_{q,r}^{(2)}(T)} \tag{9}$$

$$a_{q,r} = 1 + \frac{[1-(m_q/m_r)][0.45-2.54(m_q/m_r)]}{[1+(m_q/m_r)]^2}$$

The contributions of the different internal energy modes are accounted for by defining a thermal conductivity for each mode.

For the fully excited rotational mode we have

$$\eta_r = \kappa \sum_q \frac{\gamma_q}{\sum_r a_{q,r} \gamma_r \Delta_{q,r}^{(1)}(T)} \tag{10}$$

where the q summation is over all diatomic species.

For the vibrational-electronic thermal conductivity we have used a simplified expression corresponding to partial excitation of the two modes, thus obtaining:

$$\eta_V = \kappa \sum_q \frac{\gamma_q (C_{v,q}^V / R_q)}{\sum_r \gamma_r \Delta_{q,r}^{(1)}(T)} \tag{11}$$

where $C_{v,q}^V$ is the vibrational specific heat coefficient defined as

$$C_{v,q}^V = \frac{d e_{V,q}}{d T_V}$$

The diffusion coefficient of species q in the mixture and the diffusion flux are given by

$$D_q = \frac{\kappa T}{p} \frac{\gamma_t^2 W_q (1 - W_q \gamma_q)}{\sum_{r \neq q} \gamma_r \Delta_{q,r}^{(1)}(T)} \tag{12}$$

$$\rho_q \mathbf{u}_q = -\rho D_q \nabla X_q$$

X_q is the molar fraction of species q, and $\gamma_t = \sum_q \gamma_q$.

The modified collision integrals $\Delta_{q,r}^{(k)}$ depend upon the dynamics of the collisions between particles of type q and r, and on the energy potential. In particular the same temperature variation as proposed in Ref.[4] has been used.

Chemistry Model

In the absence of ionization only five major species are assumed (O, N, NO, O_2, N_2) and the chemical reaction mechanism is [16]:

$$\begin{aligned} O_2 + M &\rightleftarrows O + O + M \\ NO + M &\rightleftarrows N + O + M \\ N_2 + M &\rightleftarrows N + N + M \\ N_2 + O &\rightleftarrows NO + N \\ NO + O &\rightleftarrows O_2 + N \end{aligned} \tag{13}$$

where M is anyone of the five species.

The first three reactions in Eqn.(13) are heavy particle impact dissociation reactions, the fourth and fifth reactions are exchange reactions.

The forward reaction rate constants are defined as follows:

$$k_{f,r} = C_{f,r} T^{\eta_{f,r}} \exp(-E_{f,r}/\kappa T) \tag{14}$$

where the constants C's, η's and E's are, respectively, the Arrhenius constants, the pre-exponential factors, and the activation energies, and they are determined experimentally.

Observe that the rate constants need to be modified to account for the coupling between vibration and dissociation. Park [16] introduces a weighted dissociation rate-controlling temperature defined as

$$T_d = T^n T_V^{1-n}$$

and defines the forward rate constants of the dissociation reactions as a function of T_d

$$k_{f,r} = k_{f,r}(T_d)$$

Park has originally proposed a value of $n = .5$ which has been found to place too much a weight on T_V. More recently Park [16], and Gnoffo [4], use a value of $n = .7$, thus yielding ~~faster~~ dissociation reactions immediately past the shock. Hansen [19] and Mitcheltree [3] have introduced a dependency on the vibrational temperature by taking $n = .9 - .4\, T_V/T$.

In the present work we have followed the more rigorous approach of Treanor and Marrone [20], that introduce a vibrational coupling factor V and redefine the forward rate constants as follows

$$k_{f,r} = \dot{k}_{f,r}(T)\, V(T, T_V)$$

$$V = \frac{Q^v(T_F)\, Q^v(T)}{Q^v(T_V)\, N^v}$$

where Q^v is the vibrational partition function of the dissociating species and T_F is a temperature defined as

$$\frac{1}{T_F} = \frac{1}{T_V} - \frac{1}{T}$$

The forward reaction rate constants $\tilde{k}_{f,r}$ are given by Eqn.(11), where the coefficients are those of Ref. [16]. The backward reaction rate constants are assumed to be unaffected by the chemical-vibrational coupling, and evaluated as

$$k_{b,r} = \frac{\tilde{k}_{f,r}}{k_{eq,r}}$$

where $k_{eq,r}$ represents the equilibrium constant for the r-th reaction, defined as

$$k_{eq,r} = \exp\left(B_{1,r} + B_{2,r}\ln z + B_{3,r}\,z + B_{4,r}\,z^2 + B_{5,r}\,z^3\right)$$

where $z = 10000/T$, and the values of the parameters $B_{i,r}$ are given in Ref. [21].

Vibrational Energy Exchange

The source term $\dot{\omega}_v$ accounts for the translation-vibration exchange due to collisions and vibrational energy lost (or gained) due to dissipation (or recombination)

$$\dot{\omega}_v = \dot{\omega}_{t-v} + \dot{\omega}_{cv}$$

The translation-vibration energy exchange is modeled according to the Landau Teller theory [15] that assume that vibrational jumps due to collisions take place only between adjacent quantum levels and obtain

$$\dot{\omega}_{t-v} = \sum_q \rho_q\,\frac{e_{v,q}(T) - e_{v,q}(T_v)}{\tau_q}$$

where the summation is over all the diatomic species and τ_q is the vibrational relaxation time defined as

$$\tau_q = \left(\sum_r \frac{X_r}{\tau_{q,r}}\right)^{-1} + \tau'_q$$

where the first term coincides with the expression given by Millikan and White [22], and τ'_q is the collision-limited correction proposed by Park [16]

$$\begin{aligned}
\tau_{q,r} &= \frac{1}{p}\exp\left(A_{q,r}(T^{-1/3} - .015\,W_{qr}^{1/4}) - 18.42\right)\\
A_{q,r} &= 1.16\,10^{-3}\,W_{qr}^{1/2}\,\theta_q^{4/3}\\
\frac{1}{\tau'_q} &= 6.02252\,10^{2}\left(8\,\frac{R_q T}{\pi}\right)^{1/2}\left(\frac{50000}{T}\right)^2\frac{\rho_q}{W_q}
\end{aligned}$$

Observe that we have neglected the diffusional effects and have not introduced the empirical bridging formula of Park [16] that seems to give a better description of the vibrational relaxation for very high post shock temperatures.

Different approaches have been reported for the vibrational energy exchange due to chemical-vibration coupling. Gnoffo [4], Candler [1], Palmer [2] and Park [16] assume that such a term is related to the average vibrational energy. More recently Park [16] has suggested that the reduction (or the increase) of vibrational energy during dissociation (or recombination) is related to the energy available after energetic collisions, and is proportional to dissociation energy diminished by the translational one. These models are based on a simplifying assumption that the vibrational energy removed by dissociation is equal to the energy gained by recombination. As shown by Treanor and Marrone [20] this is strictly true under thermal equilibrium.

In the present work we have also related the chemical-vibration energy exchange to the average vibrational energy on account of the fact that the model of Park neglects thermal non equilibrium effects [1], thus we have

$$\dot{\omega}_{cv} = \sum_q e_{v,q}\,\dot{w}_q$$

NUMERICAL SOLUTION

The solution of the governing equations for high speed flows requires the use of robust and accurate schemes. The flux-difference splitting of Roe [23], and the flux-vector splitting of Steger and Warming [24] and Van Leer [25] have been widely used for (perfect gas) high speed flow computations. Glaister [26] has extended Roe's approximate Riemann solver to (real gas) hypersonic flows in equilibrium. Flux-vector splitting for real gases has been developed by Liou and Van Leer [27], and Grossman and Cinnella [11]. Montagné *et al.* [28] have implemented a second order symmetric total variation diminishing scheme for inviscid flows in chemical equilibrium. A more general methodology for the solution of hypersonic flows in non equilibrium has been presented by Liu and Vinokur [12]. Grasso and Bellucci [5] have followed the approach of Ref.[12] to develop a second order total variation diminishing method to include the effects of non equilibrium chemistry.

In the present work we generalize the approach of Ref.[12] to thermo-chemical non equilibrium flows.

Space and time discretizations are separated by using the method of lines, and a system of ordinary differential equations is obtained for every computational cell. A cell centered finite volume formulation is employed. By approximating surface and boundary integrals by means of the mean value theorem and mid-point rule, the governing equations (Eqn.(3)) are cast in the following discretized form:

$$S_{i,j}\,\frac{d\mathbf{W}_{i,j}}{dt} + \sum_{\beta=1}^{4}(\mathbf{F}_{num}\cdot\mathbf{n}\Delta s)_\beta = S_{i,j}\,\mathbf{H}_{i,j} \qquad (15)$$

where β stands for the generic cell face, **n** is the positive unit normal to cell face whose length is Δs, and $S_{i,j}$ is the cell area.

The numerical flux vector is:

$$\mathbf{F}_{num} \cdot \mathbf{n} = (\mathbf{F}_{E,num} - \mathbf{F}_{V,num})\, n_x + (\mathbf{G}_{E,num} - \mathbf{G}_{V,num})\, n_y \tag{16}$$

Numerical Inviscid Flux Discretization

An upwind biased second order total variation diminishing (TVD) scheme has been used to evaluate the inviscid flux contribution. The scheme is based on the modified Harten-Yee method generalized for multispecies in chemical non equilibrium [29]. The scheme has good properties of monotonicity and conservativity in the presence of discontinuities, and it yields second order accuracy and oscillation free solutions. By enforcing consistency at cell face $(i + 1/2, j)$ one obtains:

$$(\mathbf{F}_{E,num}\, n_x + \mathbf{G}_{E,num}\, n_y)_{i+1/2,j} = \frac{1}{2} \Big[\big(\mathbf{F}_{E_{i,j}} + \mathbf{F}_{E_{i+1,j}}\big) n_x + \big(\mathbf{G}_{E_{i,j}} + \mathbf{G}_{E_{i+1,j}}\big) n_y + \mathbf{R}_{i+1/2,j}\, \mathbf{\Phi}_{i+1/2,j} \Big] \tag{17}$$

The term $\mathbf{\Phi}_{i+1/2,j}$ represents the numerical antidiffusive flux contribution, that modifies the inviscid flux to make the scheme upwind biased TVD and second order accurate, and a *minmod* limiter is selected for its better computational efficiency and speed of convergence [29]. The right eigenvector matrix ($\mathbf{R}$) of the normal inviscid flux jacobian is constructed by characteristic decomposition in the direction normal to cell faces, and its expression is given in Appendix A.

Numerical Viscous Flux Discretization

According to the constitutive equations, the viscous fluxes depend upon the gradients of the primitive variables ($\mathbf{u}$, T, T_V, Y_q). The numerical counterpart is obtained by applying Gauss theorem to a computational cell whose vertices are the two grid nodes (I, J) and $(I, J-1)$ and the centers of the two adjacent cells (i, j) and $(i + 1, j)$. For an arbitrary function φ the numerical derivatives at $(i + 1/2, j)$ are evaluated according to the following formulas:

$$\left(\frac{\partial \varphi}{\partial x}\right)_{i+1/2,j} = \frac{\Delta_i \varphi\, \Delta_j y - \Delta_j \varphi \Delta_i y}{\Delta_i x\, \Delta_j y - \Delta_j x\, \Delta_i y}$$

$$\left(\frac{\partial \varphi}{\partial y}\right)_{i+1/2,j} = -\frac{\Delta_i \varphi\, \Delta_j x - \Delta_j \varphi\, \Delta_i x}{\Delta_i x\, \Delta_j y - \Delta_j x\, \Delta_i y}$$

where

$$\Delta_i(\cdot) = (\cdot)_{i+1,j} - (\cdot)_{i,j} \quad ; \quad \Delta_j(\cdot) = (\cdot)_{I,J} - (\cdot)_{I,J-1}$$

The grid values $\varphi_{I,J}$, $\varphi_{I,J-1}$ are obtained by bilinear interpolation of cell center values. Hence, the discretized viscous flux contribution at cell face $(i + 1/2, j)$ is an algebraic function of grid and cell center values, i.e.

$$(\mathbf{F}_{V,num})_{i+1/2,j} = f\,(\mathbf{W}_{i,j}\,;\, \mathbf{W}_{i+1,j}\,;\, \mathbf{W}_{I,J}\,;\, \mathbf{W}_{I,J-1})$$

Time Integration

In the presence of chemical non equilibrium the system of ordinary differential equations is stiff due to the presence of the production term $\mathbf{H}$. Stiffness arises for the disparity between the characteristic chemical and fluid-dynamic times. Hence, the time integration would require an extremely small time step. However, for steady flows stiffness can be reduced by introducing a precondition matrix P, and the system of ordinary differential equations is modified accordingly

$$\mathbf{P}_{i,j} \frac{d\mathbf{W}_{i,j}}{dt} + \frac{1}{S_{i,j}} \sum_{J=1}^{4} (\mathbf{F}_{num} \cdot \mathbf{n}\, \Delta s)_J = \mathbf{H}_{i,j} \tag{18}$$

The integration in time of Eqn.(18) is performed by a three-stage Runge-Kutta point implicit algorithm [8]:

$$\mathbf{W}_{i,j}^{(0)} = \mathbf{W}_{i,j}^{n}$$

$$\mathbf{P}_{i,j}^{(k-1)} \left(\mathbf{W}_{i,j}^{(k)} - \mathbf{W}_{i,j}^{(0)}\right) =$$

$$\alpha_k \Delta t \left\{ -\frac{1}{S_{i,j}} \sum_{J=1}^{4} \left((\mathbf{F}_{E,num}^{(k-1)} - \mathbf{F}_{V,num}^{(k-1)}) \cdot \mathbf{n}\, \Delta s \right)_J + \mathbf{H}_{i,j}^{(k-1)} \right\}$$

$$\mathbf{W}_{i,j}^{n+1} = \mathbf{W}_{i,j}^{(3)}$$

The precondition matrix scales all the characteristics times to the same order, and it is defined as

$$\mathbf{P}^{(k-1)} = \mathbf{I} - \alpha_k \Delta t \left(\frac{\partial \mathbf{H}}{\partial \mathbf{W}}\right)^{(k-1)} \tag{19}$$

For computational efficiency, a partial jacobian of the source term $(\partial \mathbf{H}/\partial \mathbf{W})$ is used by neglecting the dependency of $\mathbf{H}$ on ρu, ρv, ρE, ρe_V, without affecting the accuracy of the steady-state solution.

Boundary Conditions

The numerical solution of the governing equations requires boundary conditions to be imposed along the boundaries. Referring to Fig. 1 typical boundary conditions are: *i)* outflow; *ii)* freestream; *iii)* solid wall.

Outflow conditions

In general, the outflow conditions along Γ_2 depend on the Mach number. For an exit Mach number greater than one, first order extrapolation conditions are imposed on all variables:

$$\frac{\partial \mathbf{W}}{\partial x} = 0$$

Freestream conditions

At the freestream boundary (Γ_1), depending on the flow direction, different conditions are imposed. If the flow is entering then free stream values are imposed.

$$p = p_\infty \quad ; \quad T = T_V = T_\infty$$

$$Y_i = Y_i^{eq}(T_\infty) \quad ; \quad u = c_\infty M_\infty \quad ; \quad v = 0$$

If the flow is exiting, then first order extrapolation conditions are imposed along Γ_1.

Solid wall

On a solid wall (Γ_4) continuum-type boundary conditions are set and the no-slip condition is enforced on the velocity: $u = v = 0$.

The pressure is obtained by assuming a zero normal pressure gradient, and fixed wall temperature or adiabatic conditions are set. Moreover, it has been assumed that the vibrational temperature of the molecules is equal to the wall temperature.

The surfaces of most hypersonic vehicles are made up of either a metal, a metal oxide, or carbon materials, and gas-surface reactions should be accounted for. However, in the present work the effects of the gas surface interaction have been neglected and the normal (species) diffusion fluxes is zero at the wall, thus yielding

$$\frac{\partial Y_i}{\partial n} = 0$$

RESULTS

Case 1 - 10 deg Wedge

The first test case corresponds to the flow over a 10 deg wedge at free stream velocity of 8100 m/s, an altitude of 61 km and a wall temperature of 1200 K. This test case has been investigated by other authors [6,30] and shows a small degree od non equilibrium in the boundary layer. The test case is *simple* on account of the simplicity of the geometry. However, it contains all of the relevant features of complex hypersonic flows and has been selected to study the sensitivity of the solution upon thermal non equilibrium effects. The computations have been obtained on a 176 × 48 grid with (nondimensional) mesh spacing ranging from .0015 to .069, and cell aspect ratio that varies between .5 and 13. For this test case two computations are reported corresponding to the thermal and chemical non equilibrium model (TCNE), and the thermal equilibrium - chemical non equilibrium model (CNE). Referring to Fig. 1, the boundary (Γ_1) has been positioned half a meter upstream of the wedge leading edge (located at $x = 0$). The outflow boundary (Γ_2) has been set at $x = 4$m, and the freestream boundary has been positioned at $y = 1.35$m. Figure 2 shows the translational and vibrational-electronic temperatures computed with the TCNE model, as well as the temperature obtained with the CNE model vs the nondimensional normal distance from the wall at $x = 3.5$m. Comparison of the two solutions shows that the largest (thermal) non equilibrium effects are confined within the shock layer. The use of TCNE reduces dissociation, thus yielding a larger value of the peak translational temperature (the differences being 550 K). The computed results also show that the inviscid part of the shock layer is approximately vibrationally frozen. Indeed, the vibrational temperature varies significantly only below $y/L \simeq 0.1$ as shown in Fig. 2. Figure 3 shows the oxygen mass fraction distribution vs the (nondimensional) normal distance. This figure indicates that most of the dissociation occurs within the boundary layer, which is the most affected by the thermal non equilibrium.

Case 2 - 2 in. Cylinder

The second test case is that of a 2 in. cylinder in partially dissociated hot nitrogen ($Y_{N_2} = 0.927$, $Y_N = 0.073$, $T_\infty = 1833K$). The freestream velocity is 5590 m/s and the wall is assumed adiabatic. The computations have been performed on a 176 × 74 grid with normal mesh spacing ranging between $0.2 \cdot 10^{-9}$ and 0.2. The temperature, the density and the molecular nitrogen mass fraction distributions along the stagnation streamline are reported in Figs. 4-6. The high value of translational temperature (approximately 12000 K) is responsible for the nitrogen dissociation. As in the previous test case, very small differences are noticeable between the TCNE and CNE solutions, indicating that for this test case the main non equilibrium effects have to be ascribed to the chemical ones. Investigations of the translational and vibrational-electronic temperatures show, indeed, that thermal equilibrium is reached immediately after the shock. Some discrepancies between the two solutions are observed at the stagnation point, where the flow should (asymptotically) reach equilibrium. In Fig. 7 the computed density field is compared with the experiments of Hornung [31], where the interferogram of the flow field is reported. The overall (qualitative) agreement of the computed and measured density is good. However, some differences in the density field (already found with a thermal equilibrium approximation) are observed, which are probably due to finite energy transfer rates for the vibrational modes of the different molecules, as concluded by Candler [30]. The computed stand-off distance (equal to 6 mm, evaluated as the distance at which the density ratio is equal to 6) agrees well with the experimental value reported in Ref. [31].

CONCLUSIONS

In the present work a two-temperature model has been developed for the description of thermal and chemical nonequilibrium viscous hypersonic flows. The model employs a vibrational coupling factor as proposed by Treanor and Marrone, and it uses a model based on a non-preferential removal of vibrational energy. The solution methodology has been developed within a finite volume approach based on a second order accurate Total Variation Diminishing formulation that accounts for thermal and chemical non equilibrium effects. The stiffnes due to the disparity in time scales is reduced by introducing a precondition matrix that allows a pointwise implicit solution of the source terms.

The model has been applied to compute the flows over a 10 deg wedge and on a 2 in. cylinder. Comparisons of the fully non equilibrium solution with that corresponding to a thermal equilibrium assumption show that the post-shock temperature plays a fundamental role in the achievement of thermal equilibrium., and that the boundary layer is the most affected by thermal non equilibrium.

REFERENCES

[1] Deiwert G., Candler G., "Three-Dimensional Supersonic and Hypersonic Flows Including Separation", AGARD Rep. No. 764. 1989.

[2] Palmer G., "The Development of an Explicit Thermochemical Nonequilibrium Algorithm and Its Applications to Compute Three Dimensional AFE Flowfields", AIAA-89-1701.

[3] Mitcheltree R.A., "A Parametric Study of Dissociation and Ionization Models at 12 Km/sec", AIAA-91-1368.

[4] Gnoffo P.A., Gupta R.N., Shinn J.L., "Conservation Equations and Physical Models for Hypersonic Air Flows in Thermal and Chemical Nonequilibrium", NASA Technical Paper 2867, 1989.

[5] Grasso F., Bellucci V., "Modeling of Hypersonic Non Equilibrium Flows", to appear in Advances in Hypersonic Aero/Thermodynamics, 1992.

[6] Prabhu D.K., Tannehill J.C., Marvin J.G., "A New PNS Code for Chemical Nonequilibrium Flows", AIAA J., Vol. 26, 1988.

[7] Park C., Yoon S., "Calculation of Real-Gas Effects on Blunt-Body Trim Angles", AIAA-89-0685.

[8] Bussing T.R.A., Murman E.M., "Finite-Volume Method for the Calculation of Compressible Chemically Reacting Flows", AIAA J., Vol. 26, 1988.

[9] Desideri J.A., Glinsky N., Hettena E., "Hypersonic Reactive Flow Computation", Comp. and Fluids, Vol. 18, n. 2, pp. 151–182, 1990.

[10] Shuen J.S., Yoon S., "Numerical Study of Chemically Reacting Flows Using a Lower-Upper Symmetric Successive Overrelaxation Scheme", AIAA J., Vol. 27, 1989.

[11] Grossman B., Cinnella P., Garrett J., "A Survey of Upwind Methods for Flows with Equilibrium and Non-Equilibrium Chemistry and Thermodinamics", AIAA-89-1653.

[12] Liu Y., Vinokur M., "Upwind Algorithms for General Thermo-Chemical Nonequilibrium Flows", AIAA 89 0201.

[13] Hollanders H., Marraffa L., Montagné J.L., Morice Ph., Viviand H., "Computational Methods for Hypersonic Flows Special Techniques and Real Gas Effects", ONERA.

[14] Yee H.C., Shinn J.L., "Semi-Implicit and Fully Implicit Shock Capturing Methods for Nonequilibrium Flows", AIAA J., Vol. 27, 1989.

[15] Vincenti W.G., Kruger C.H. Jr., *Introduction to Physical Gas Dynamics*, John Wiley and Sons, Inc., New York, 1965.

[16] Park C., *Nonequilibrium Hypersonic Aerothermodynamics*, John Wiley and Sons, Inc., New York, 1990.

[17] Lee J.H., "Basic Governing Equations for the Flight Regimes of Aeroassisted Orbital Transfer Vehicles", *Thermal Design of Aeroassisted Orbital Transfer Vehicles*, Nelson H.F. ed., Volume 96 in Progress in Astronautics and Aeronautics, American Inst. of Aeronautics and Astronautics, Inc., 1985.

[18] Gupta R.N., Yos J.M., Thompson R.A., Lee K.P., "A Review of Reaction Rates and Thermodynamic and Transport Properties for an 11-Species Air Model for Chemical and Thermal Nonequilibrium Calculations to 30 000 K", NASA Reference Publication 1232, 1990.

[19] Hansen C.F., "Collision-Induced Gas Phase Dissociation Rates", Final Report on NASA Grant NAG 1-1046, Aug. 1990.

[20] Marrone P.V., Treanor C.E., "Chemical Relaxation with Preferential Dissociation from Excited Vibrational Levels", The Physics of Fluids, 6, 1963.

[21] Park C., "Convergence of Computation of Chemical Reacting Flows", AIAA-85-0247.

[22] Millikan R.C., White D.R., "Systematics of Vibrational Relaxation", Journal of Computational Physics, 39, 1963.

[23] Roe P.L., "Approximate Riemann Solvers, Parameter Vectors, and Difference Schemes", J. Comp. Phys., 43, 1981.

[24] Steger J.L., Warming R.F., "Flux Vector Splitting of Inviscid Gasdynamics with Application to Finite Difference Methods", J. Comp. Phys., 40, pp. 263–293, 1980.

[25] Van Leer B., "Flux-Vector Splitting for the Euler Equations", ICASE Report 82-30, September 1982.

[26] Glaister P., "An Approximate Linearized Riemann Solver for the Three Dimensional Euler Equations for

Real Gases Using Operator Splitting", J. Comp. Phys., 77, 1990.

[27] Liou M.S., Van Leer B., Shuen J.S., "Splitting of Inviscid Fluxes for Real Gases", J. Comp. Phys., 87, 1990.

[28] Montagné J.L., Yee H.C., Klopfer G.H., Vinokur M., "Hypersonic Blunt Body Computations Including Real Gas Effects", NASA TM 10071, 1988.

[29] Yee H.C., "A Class of High-Resolution Explicit and Implicit Shock-Capturing Methods", NASA Technical Memorandum 101088, 1989.

[30] Candler G., "On the Computation of Shock Shapes in Nonequilibrium Hypersonic Flows", AIAA-89-0312.

[31] Hornung H.G., "Non-equilibrium Dissociating Nitrogen Flow Over Spheres and Circular Cylinders", Journal of Fluid Mechanics, 53, 1972.

APPENDIX A

TVD Terms for Thermal and Chemical non Equilibrium Flows

The expression of the elements ($\varphi'_{i+1/2,j}$) of the numerical antidiffusive flux contribution is obtained by characteristic decomposition in the direction normal to cell face.

To construct linearly independent eigenvectors basis vectors are chosen in such a way as to be orthogonal to the cell face normal. Consequently, the right eigenvector matrix ($\mathbf{R}$) of the normal inviscid flux jacobian is defined as

$$\mathbf{R} = \begin{bmatrix} \delta_{qr} & 0 & 0 & Y_q & Y_q \\ u & -c\,n_y & 0 & u + c\,n_x & u - c\,n_x \\ v & c\,n_x & 0 & v + c\,n_y & v - c\,n_y \\ \dfrac{\mathbf{u}\cdot\mathbf{u}}{2} - \dfrac{\chi_r}{K} & c(\mathbf{u}\cdot\mathbf{b}) & 1 & H + c\,u_n & H - c\,u_n \\ 0 & 0 & 1 & \epsilon_V & \epsilon_V \end{bmatrix} \tag{20}$$

where $\mathbf{b}$ is the span basis vector orthogonal to $\mathbf{n}$, and K and χ_q are the pressure derivatives defined as

$$K = \left(\frac{\partial p}{\partial \rho \epsilon}\right)_{\rho_q} = \frac{\sum \rho_q R_q}{\sum \rho_q C^{tr}_{v,q}} \tag{21}$$

$$\chi_q = \left(\frac{\partial p}{\partial \rho_q}\right)_{\rho e} = R_q T - K\,\epsilon^{tr}_q \tag{22}$$

where $C^{tr}_{v,q}$, ϵ^{tr}_q and c are, respectively, the constant volume specific heat coefficient and the internal energy corresponding to translational and rotational modes, and the frozen speed of sound, which is defined as

$$c = \left[(K+1)\,\frac{p}{\rho}\right]^{1/2} = \sum_q Y_q \chi_q + K\,h - K\,\epsilon_V \tag{23}$$

The values at the interfaces are calculated by using a generalization of Roe's averaging to account for thermal and chemical non equilibrium.

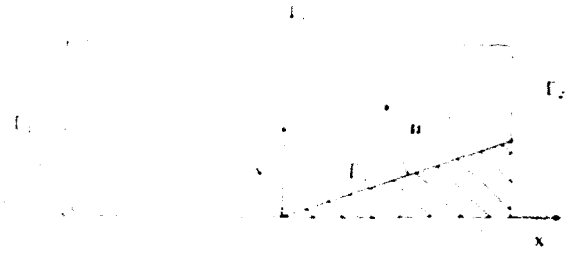

Fig. 1 – Computational domain for Test Case 1.

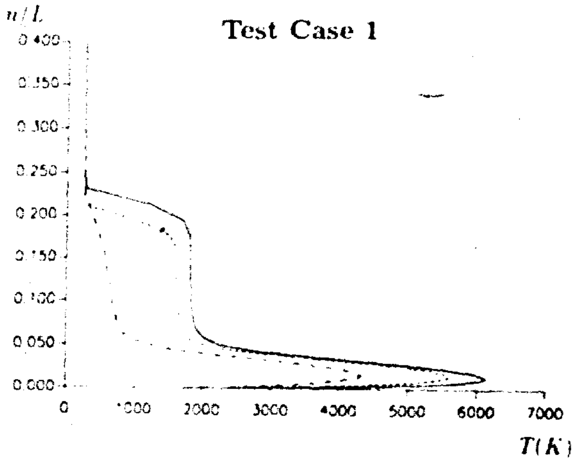

Fig. 2 – Temperature vs normal distance from the wall: ———, translational temperature (TCNE model); – · –, vibrational-electronic temperature; – – –, translational temperature (CNE model).

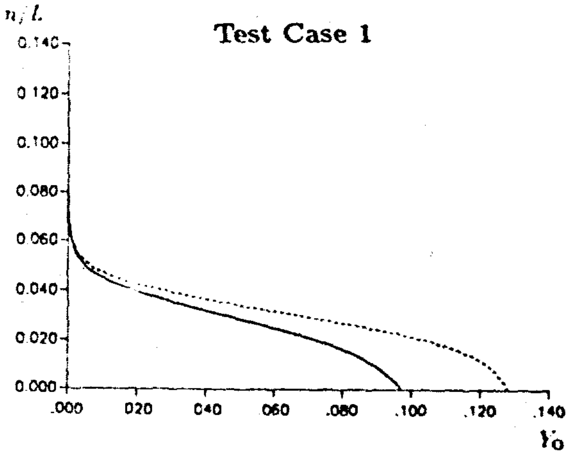

Fig. 3 – Atomic oxygen mass fraction vs normal distance from the wall: ——, TCNE model; – – –, CNE model.

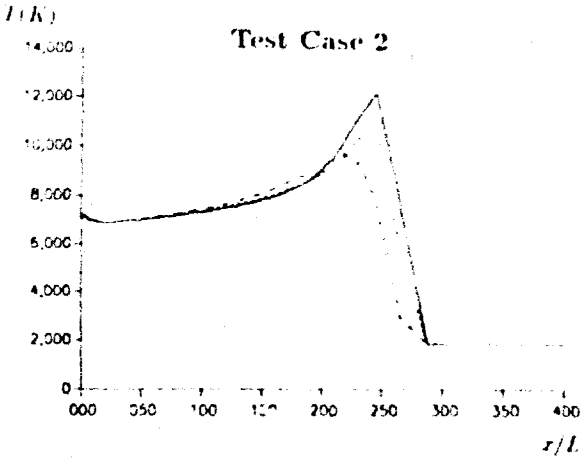

Fig. 4 – Temperature along stagnation line: ———, translational temperature (TCNE model); – · –, vibrational-electronic temperature; – – –, translational temperature (CNE model)

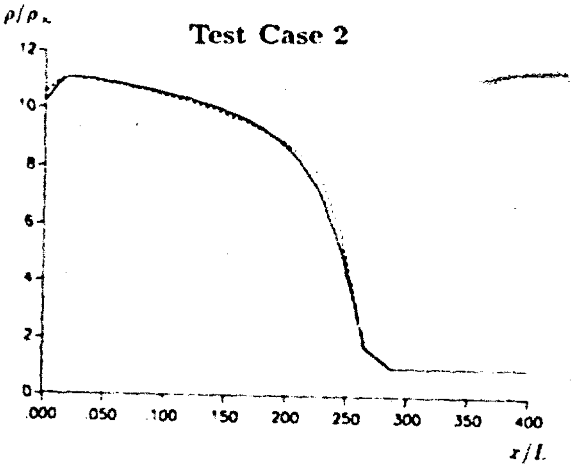

Fig. 5 – Nondimensional density along stagnation line: ——, TCNE model; – – –, CNE model.

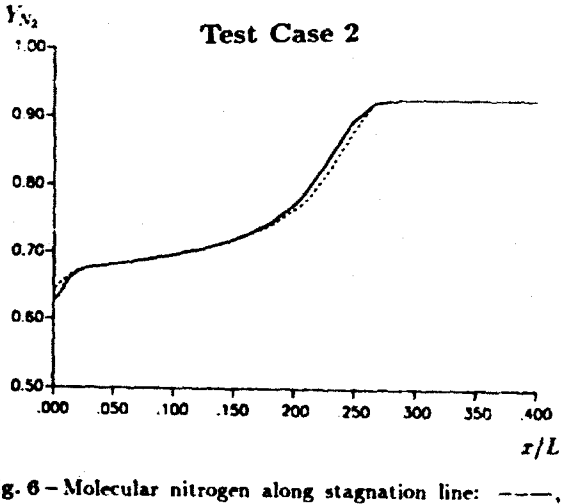

Fig. 6 – Molecular nitrogen along stagnation line: ——, TCNE model; – – –, CNE model.

Test Case 2

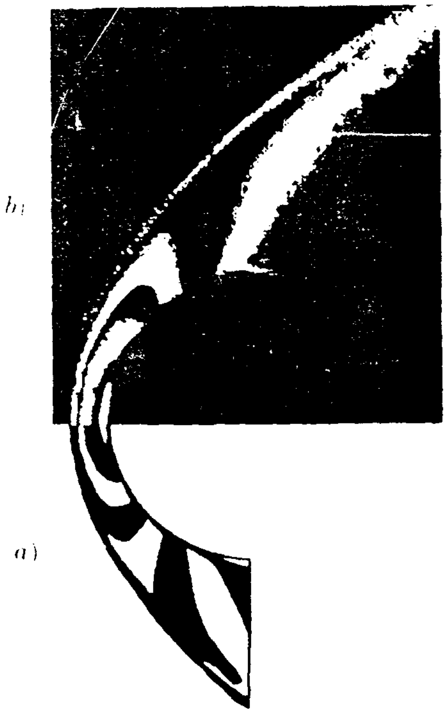

Fig. 7 - Density field: a) computed result, b) experiment Ref. [31].

GENERAL DISCUSSION
THEORETICAL AND EXPERIMENTAL METHODS IN HYPERSONIC FLOWS
7 May 1992

Mr. Bignell, British Aerospace, Sowerby Research Centre

Ladies and Gentlemen: We now come to a very important part of our meeting which is the Technical Evaluation followed by the general discussion. First the Technical Evaluation. It is a particular pleasure for me to be able to welcome Professor Eli Reshotko, our Technical Evaluator. Incidentally, I should say straight away that if I get through the next hour and a half without referring to him as Professor Roshko, it will be a miracle. Just a little bit of background to this meeting on the involvement of Professor Reshotko. I don't know if it was said on Monday morning when the opening ceremony was taking place, but the last time the Fluid Dynamics Panel of AGARD addressed Hypersonics in a symposium was in Bristol in April of 1987. Another aside here is that we are very fortunate that we also have at this meeting, the Technical Evaluator of that meeting, Professor Bogdonoff. We addressed hypersonics in Bristol in 1987. Following that, Professor Reshotko, who was a member of the Fluid Dynamics Panel at the time, made a proposal setting up an Ad Hoc Study Group on Hypersonics Research and Technology which began life in, I think it was the spring of 1988 and it ran for approximately two years. But as a result of that study group, three things have so far emerged. One is an AGARD Working Group on Hypersonics which is just about to hold its first meeting, if it hasn't just had it already, but it is pretty imminent. The work shop which took place last week at Le Fauga-Mauzac certainly had an AGARD background and an AGARD input and this symposium, so those are the three activities. I do believe that Professor Reshotko was the person who initially proposed that this symposium should take place anyway. He was a member of the Fluid Dynamics Panel for about 7 - 8 years and he left in 1989, so he has been a member of the Fluid Dynamics Panel until comparitively recently. There is another good reason that we are fortunate to have Professor Reshotko as our Technical Evaluator, and let me explain what I mean. I guess the basic question posed by this symposium must be how we are doing in the AGARD community in Hypersonics. In other words, have we made real progress since the Bristol meeting in 1987? Are we using wisely our resources, which are fairly limited in this field? What is the way forward? I imagine that Professor Reshotko will thoroughly address all of these questions, and I have absolutely no doubt whatsoever that he will give us plain and honest answers and yet at the same time be technically stimulating. Eli, welcome back, we are delighted to have you here. The FDP members and the delegates of the conference await your evaluation with great interest and anticipation. The floor is yours.

Professor Reshotko, Case Western Reserve University

Ladies and Gentlemen, it is my great pleasure to be with you here and an honor to have been chosen as the Technical Evaluator for this symposium. I entered into this job with some trepidation and humility. However, my task was made even more difficult by the very generous hospitality of our hosts here in Torino. I want to thank all of you here who have commiserated with me in trying to meet the time constraints of this task. As Bob mentioned, many of us were present in Bristol in April 1987 when the Fluid Dynamics Panel sponsored a symposium on the Aerodynamics of Hypersonic Lifting Vehicles. We were then very much engaged in the vehicle development programs such as NASP, HERMES, HOTOL and SANGER. We were furiously relearning hypersonics and reconstructing it using the modern technologies of CFD and advanced experimental techniques. There was excitement and some optimism evident at the Bristol meeting about the future of hypersonic activity. Well, it is now 5 years since Bristol. HOTOL and SANGER have been suspended, if not cancelled. NASP and HERMES continue, but those programs are in much more troubled circumstances than they were then. We began to realize that the ambitions of those programs were beyond our technology base and that the upgrading of the technology base would not be simple or quick. We would have to pay the price for 20 years of neglect in hypersonic research and development. The mood at this symposium is more subdued and perhaps more sober. It is directed more at methodology than at vehicles. I hope that it reflects a constructive effort by our entire community to develop in a more rational and consistent manner, the technology base that we will need for future vehicle development. In these remarks I will not comment on specific papers. I was not particularly bashful about commenting on them during the discussion periods over the past four days, and I shall have the opportunity to be more specific in my formal report which I understand will be included in the symposium proceedings volume. Rather, I will comment now on a number of topics which were triggered by the presentations at this symposium. These comments, of course, will reflect a number of personal opinions and you are free to comment on my opinions when the discussion opens.

A number of philosophies were put before us at this symposium. Philosophies are useful in charting constructive paths for the solution of problems. I like them. Monsieur Perrier offered a design philosophy in which experiment and CFD interacted, which together with some flight tests would provide a finalization of the vehicle design. The methodology that he proposed is very much in line with the simulation methodology that was put forth some years ago for the transonic regime by AGARD FDP Working Group 09. It might be interesting for FDP to consider such an exercise for the hypersonic regime to make sure that no critical issues in hypersonic design are overlooked. The Pegasus vehicle that we heard about at this symposium was designed exclusively analytically and has been successfully flown. It would seem, therefore, to be a very good testbed for the flight evaluation of critical design issues.

I think that we can all agree that validated CFD codes are an essential tool of our design efforts. Joe Marvin presented us with a comprehensive roadmap for the validation activity. It is worth studying and following. But we must keep in mind that validation means that a code not only agrees with experiment but has also captured the essential physics. The physics are important. Analytical tools such as classical boundary layer theory, which are based on the physics, should be used more often to provide credibility checks on both experiments and computational codes.

The session on instrumentation was for me an example of yet another philosophy; that of a cooperative effort by people at the working level toward improving their capabilities through the sharing of information and providing each other with constructive criticism. I have experience with such an activity through my many years as Chairman of the U.S. Transition Study Group. I was very pleased to hear of the advances in the development of the new experimental tools. But some of them have been around for a long time and are regarded as mature by the instrument people. So, I have been wondering why they are not more widely used. Maybe mature means something different to the developers than to the users.

Take CARS, for example. I have been hearing about CARS for abo~~ut 20~~ years, yet it is not widely used. CARS techniques are generally used by the people who developed them, or else by his neighbor who will use the technique only as long as his CARS expert is around. If you don't have a CARS expert locally, you don't have CARS. My theory is that until a technology such as CARS becomes a commercially available turnkey instrument, it will not be widely acceptable to the wind tunnel community. Maybe that is the definition of maturity. Certainly, that was our experience with laser velocimetry. Also, many of the optical techniques that we have heard about have been developed using as examples, free jets, mixing layers, generally flows that are without boundaries. Can they be used in wall bounded flows? ~~After all,~~ boundary layers are a very important aspect of our studies. Can these optical techniques be used in boundary layer flows? It is not clear. If they cannot, they become less interesting. Do existing tunnels have the optical accesses needed for modern optical instrumentation? Is retrofitting possible or do we have to design new tunnels around the optics, such as perhaps is being done with F-4 and other such facilities. Perhaps the instrumentation workshops or study groups should include some wind tunnel people, in order that the user view be represented in the development of the instrumentation.

The next item that I would like to comment on is the question of what is a real gas? We had a variety of real gas papers, but they were not all consistent in their real gas assumptions. Steve Deiwert in his paper gave us quite a complete description of the real gas issues, namely the non-equilibrium species composition, the thermal non-equilibrium and of course, the need to compute thermodynamic and transport properties for the local mixture. I was happy to see that a good number of the papers presented here did consider all these aspects of real gas flows. An issue was raised at the meeting as to whether meaningful testing could be done in a wind tunnel stream that was out of equilibrium. I offered a comment that there might not be a problem for blunt configurations which are equilibrated behind their bow shock waves, but that the problem might in fact exist for slender configurations. This question might be readily addressed computationally by our colleagues who made presentations here at the meeting, for example, Messieurs Marmignon and Zeitoun who presented real gas solutions for high enthalpy wind tunnel flows. If they could continue their calculation over a model in those flows, let us say a blunt model, and a slender model, and then also do equivalent calculations assuming an equilibrium free stream and compare the two results, then we would have some sense as to whether there is sensitivity to the non-equilibrium aspect of these high enthalpy tunnel free streams. The result would certainly be most interesting.

Let me say something about Euler vs Navier Stokes. My whole career has been involved with viscous effects in aerodynamics, so I do have a bias. But I insist that viscous effects must be included in any hypersonic internal flow calculation because of the effect of thick boundary layers taken together with the confinement of a mass flow. An Euler calculation for internal flows can be entirely misleading. I also endorse viscous calculations for the external flows because of the consequences of flow separation and aerodynamic heating which are of paramount importance in hypersonic vehicle design. Regarding stability and transition, I was very pleased to see a critical evaluation at high supersonic speeds of both sharp cone and blunt cone instability as well as cross flow instability. I was disappointed, however, that the issue of transition estimation was almost totally ignored. Indeed, when one author of a paper that assumed laminar flow was asked how he knew that his flow was not turbulent, he could only shrug his shoulders. The computational community should become more familiar with the present state of transition estimations. It is not a simple topic and cannot be dealt with by simple formulas. After all, if the steady Navier Stokes equations require so much effort and care, why should one expect transition, which is the consequence of unsteady phenomena, and best modelled by unsteady Navier Stokes equations, to be addressed by simple formulas.

Let me note also that missing from this symposium was any consideration of radiative gas dynamics or the radiative cooling of vehicle surfaces which can become important in vehicle design as we continue on to higher Mach numbers.

Well, as you can gather, the tasks that remain for us in hypersonics are not simple. Our hypersonic regime after all extends all the way to orbital speed and perh~~aps even~~ beyond, if we consider entry from other planets. For orbital speeds, we are talking about flight Mach numbers of 25 or so. For planetary or re-entry from other planets, we are talking about Mach number 35 and above. Yet, our activity to date seems to be concentrated in the lower portion of the Mach 5 to 15 range, at least as represented at this meeting. Please remember that at Mach number 15, an orbital vehicle has acquired only one-third of its eventual kinetic energy. So, two-thirds of the eventual kinetic energy that is acquired by the vehicle in going into orbit, is above Mach 15. If we envision air-breathing propulsion all the way to orbit, as for example in the NASP program, then we will have to give much more concentrated attention to the development of very efficient scramjet propulsion systems for flight Mach numbers from 15 to 26. We heard very little about such propulsion systems here at this symposium.

We have a lot of work to do. Yet I believe that the interest of our world community and activities in space is permanent. Therefore, there will be a continuing interest in the aerodynamics of vehicles that enable us to exploit the opportunities of space. But, as I said earlier, this will be enabled by a more rational, continuous and sustained effort in developing the proper technology base.

This has now been my second hypersonic FDP symposium. I look forward to participating with all of you in the next FDP hypersonic symposium in the not too distant future.

Mr. Pignell
Thank you very much for that evaluation, Eli. It has given us plenty of food for thought. Essentially, ladies and gentlemen, it is your turn. I must stress that when you are making a comment to the discussion, will you please identify yourself; give your name and affiliation. The reason is quite simple. The discussion is being recorded for inclusion in the Conference Proceedings. The comments will be sent to you before the publication goes out so you can check that what you said is what you meant to say, and if it is not what you meant to say, you can actually change it. Now, we really need to impose some structure, some focus on the discussion. The broad headings that I have written down here, which have all been covered, obviously, in Eli's evaluation are: experimental techniques and facilities, CFD design methods, development, validation, application of such methods, and last but by no means least, flow physics and chemistry modelling.

I think maybe if we have some comment or some discussion on the experimental techniques and facilities, given what the evaluation has come up with, that might be a good starting point.

Dr. Kienappel, DLR Göttingen
A comment and a question. I agree that we need close contact between the users and the people who develop the instrumentation, there is no question about this. But I have to say there have been users in this workshop. I would be interested to hear from Professor Bogdonoff how he is seeing the developments between the Bristol meeting and this meeting.

Mr. Bignell
Would you care to respond? Actually, I have got the best seller here, which is your technical evaluation report from the Bristol meeting. I was going to come to that at some stage.

Professor Bogdonoff, Princeton
I really am not quite prepared to answer such a general question, but let me give you an impression. I think much of what Eli said summarizes my own feelings. Five years is not a long time, maybe for younger people, but it is a long time for me. In a way I was disappointed in what has happened in five years. It is understandable because most of us are driven by our own national programs. In Europe, HERMES is a driver; in the United States, Aerospaceplane is a driver, and so on. At the same time, there has not really been a lot of effort in the fundamentals of hypersonics, at least as I see it. Eli has pointed out a good bit of this. I am pleased to see that there are some facilities that weren't available 5 years ago. I would like to point out that although these facilities look like great steps, and I think significant commitment has been made, there is still no concept of a facility which does, as Eli points out, get to the heart of hypersonics, which is the 15 to 25 range, and perhaps that is because our national programs do not push that way. Facilities are national efforts and perhaps as nations we have not tackled that problem. I think it is going to be really difficult to exploit hypersonics in general if we don't have the capability to talk about the Mach number range, as Eli pointed out, is two-thirds of the energy to go to orbit, the 15 to 25 range or beyond that point. The big differences I see in five years are greatly increased capacity for computation and the continual development of instrumentation. Eli mentioned the lack of use of new instrumentation in critical problems, but maybe the new facilities will be designed for that. Computation still bothers me a great deal because most of it is not validated. I didn't see very much more here than I saw five years ago on a concentrated effort to validate these computations. The computations which the designer needs to design. There are computations for fundamentals which seems to be coming along much better, but the idea of having computations which are validated adequately for design still concerns me. The designers, and fortunately I am not one of them, must not sleep very well if they are going to have to worry about designing a vehicle with computation which has some questions about whether it has the real physics, whether it has the details that he needs for design.

Mr. Bignell
Could I just ask a question of you relative to that point. Are these computations not validated simply because the experimental facilities are not there to provide the data? Is that part of the answer?

Professor Bogdonoff
Well, that is an excuse. That is not an answer. You can validate computations in very poor facilities. If you really know what is in the facility, and you make the right measurements, then the question is whether the computation can take whatever you gave it and get the right answer! You can validate computations without having a facility which simulates, very well, what the flight conditions are. This has not really been done very well. I believe this is because most people are not willing to spend a lot of time and effort to do something which is really for computational validation, rather than solving an important problem of hypersonics. The second point may very well be more critically determined by the facility: I don't think that we spend enough time and money for instrumentation and designing experiments just for CFD calibration or validation; I am sorry that Dick Bradley wasn't here because that is part of his early report, but I don't think I heard very much at this meeting about very carefully designed experiments which were just to find out whether a theory or computation was really good. It is more than just measuring some pressures or some forces or things like that. The details have to be well-enough defined so that the designers can believe that that tool will solve a real problem.

Mr. Bignell
Do we have any further comments on that aspect?

Dr. Eitelberg, DLR-Gottingen
I would like to make two remarks. I for one was present at the Instrumentation Workshop in the role as a user of instrumentation so I think that the accusation that the instrumentation people don't involve facility users is not quite what it seems to be. The second one is that I noticed how two speakers have used the Mach number as a measure of kinetic energy. I can't agree with that. The Mach number is a compressibility number and the kinetic energy is given by the velocity squared and we may form non-dimensional numbers in making a ratio of the velocity squared to some other significant energy, be it dissociation energy, for example. I think that there is, from our side, a concentrated effort to get into the kinetic energy ranges that Professor Reshotko and Professor Bogdonoff have been talking about.

Professor Reshotko
Would you be happy if I amend my statement to say from 15,000 feet per second to 25,000 feet per second and then up to 35,000 feet per second. I simply didn't feel like saying thousands of feet per second every time.

Mr. Bignell
Are there any other comments that people want to make on experimental facilities and instrumentation. Any further comments on the work shop?

Professor Poll, University of Manchester
Yes, I would like to make a comment. It relates to experiments and CFD. It strikes me that, with the present level of development of CFD, its real application is to enhance considerably the data that you can get from experiments. The current position is that you can build a tunnel and create a flow. However, the range of instrumentation that you can get in there is extraordinarily limited. Surface pressures are easy to measure but they are not very good for code validation because even crude methods can compute pressures accurately. You can't determine static temperatures very easily, you are stuck with measuring total temperatures, and really the instrumentation capability, even if we take the current state of the art, is extremely limited. My feeling is that, provided you know some details of the flow that you are trying to compute, CFD can produce a reasonably good prediction. If you can do a reasonably good computation, then you can use the code as a diagnostic tool; a much more effective diagnostic tool than many of the proposed forms of exotic instrumentation. So if you have a pressure distribution and perhaps a few interferometer pictures, you can do a computation which, with enough fiddling about, will reproduce the limited experimental data, then you can use CFD as a very effective 'instrument' for quantities which you cannot measure.

Mr. Bignell
Do we have any comments from the CFD community? Not specifically in relation to that?

Ing. en Chef Masure, STCAN/BA, Paris
A question that has been raised during this symposium is the following: for steady boundary conditions, is the solution of an aerodynamic problem steady or unsteady? I don't think that Professor Reshotko during the closing discussion addressed this querstion which is for me a very important one. Is a flow globally steady or unsteady?

Professor Reshotko
We had one paper that did address that question, that of David Dolling, where he pointed out that a certain flow, namely the shock boundary layer interaction was unsteady. He provided ample evidence that it was unsteady. However, he did not identify a mechanism for that unsteadiness. Without the mechanism, we will have a very hard time modelling the unsteadiness. We have to understand what it is in that flow that leads to the unsteadiness. Is it related to any reattachment singularity that we do not understand. The important point here is that a validated computational effort is needed for this problem that will have to understand the physics. That should be one of our objectives in dealing with the mechanism of that unsteadiness.

Mr. Bignell
Professor Bogdonoff raised an interesting point in talking about the need to provide designers with methods they can use to design their spacecraft, spaceplanes, whatever. Unfortunately, I was unable to attend on Monday when there was a session on design of hypersonic vehicles. It was one of the sessions that I was looking forward to. Perhaps I can ask those people who are involved in design whether any statement was made on the design requirements and the performance requirements; what sort of level of accuracy are you asking for in order to be able to do the calculations that you have to do. What sort of sensitivity studies are you able to do? I come from a missile background and from a design point of view that is the sort of things that one does, fairly early on, i.e., sensitivity studies to see what effect on performance you get with plus or minus 5 % accuracy in being able to compute a particular flow parameter. I just wondered if anybody would like to comment on that?

Professor Reshotko
Monsieur Perrier is not here to defend himself, but he did offer an approach to the issue of design for the hypersonic vehicles. While he did not address the necessary accuracies, I think that in his desire that experiment and CFD together with some flight calibration points be put together into a design technology, he would be sympathetic to your point and adhere to it. He also brought up one other thing, when you think of a design for a flight vehicle you run into some critical issues that are not necessarily the ones that are being investigated in the laboratory. He brought up one that was simply windshield heating. You have to have a windshield, and it is made of a material that is not necessarily a heat resistant material, or the best heat resistant material. How do you handle the issue of windshield heating? That comes up in design, it is not something that we normally investigate. I think that he, in his paper, laid out a fairly complete list of the issues. He did not, of course, address them according to what level of accuracy is needed to resolve them.

Mr. Bignell
Would anybody else like to comment on design and performance requirements for hypersonic vehicles?

Mr. Muylaert, ESTEC
I think the issue of design requirements and instrumentation accuracy requirements for high enthalpy testing was not enough addressed during this conference, nor during last week's hypersonic instrumentation workshop which was held in Toulousse. In fact, computational sensitivity studies should be done on generic forms incorporating the physical phenomenon of interest. These studies should tell us what the most sensitive parameters to be measured are, and to what measurement accuracy the instrumentation specialists should develop them. As an example: the CFD people should provide an answer to the question whether a 1% accuracy in NO mass fractions for electron beam fluorescence or laser induced fluorescence is enough or compatible with a 10% accuracy requirement in heat flux. The instrumentation development people should not be left alone but guided by the CFD people.

Professor Stollery, Cranfield
I was just looking back at the notes I made at the time Bob, on Monday's session. Nearly everybody talked about the need for transition data, which Eli Reshotko has already referred to. It seems to me it is incredibly difficult to design a vehicle if you don't know where transition is. Although all the wind tunnels can tell you what the difference in heat load, pressure distribution and control effectiveness is when you get laminar and turbulent flow, they can't give you the transition Reynolds number. It seems from this meeting, that the only two rays of hope are the quiet wind tunnels and the possibility of flight testing, e.g. using Pegasus.

Professor Poll
I would just like to make a comment on that comment and address the transition issue. There has been an awful lot of time and effort spent in the transition community working on problems which are of little or no relevance to flight vehicles. The amount of money that must have been spent on transition on the sharp cone and blunt cone at zero incidence doesn't bear thinking about. Yet, that is not a flight condition of any interest whatsoever. We have to be very careful that the physicists don't have a field day when it comes to doing experimental and computational work.

We have seen one example where 11 consecutive days had been spent on a CRAY YMP to tell us that we still couldn't explain an experiment that was done 5 years ago - it also wouldn't explain experiments which were done 40 years ago! In the transition field we need to take a more realistic look at precisely what mechanisms are going to be important on the kinds of vehicles that one wants to build and then design your fundamental research program accordingly.

Professor Herbert, Ohio State University
Just on the side: at the time we did this work, our new Cray YMP was 60% idle. Disregarding this, I consider the computer time well spent to obtain benchmark results in an area where accurate data are scarce. Our interest in reliable high-Mach number computations isn't all that old because the original idea was to build NASP with known technology. Since we learned that some research was necessary, we started 3 or 4 years ago to build our computational "stability tunnel", and I reported about how far we got up to this point. Next year, or in three years, our capabilities will be much better. At this time, we just have to evaluate and compare with whatever data are available and accessible. There seems to be sufficient interest in sharp and blunt cones at high speeds to conduct detailed experiments. I don't see anything wrong with computations for the same cases.

Professor Deconinck, von Karman Institute
I wouldn't feel an expert on answering really your question, but I would like to touch a related question. I would like to comment on the fact that Euler computations are extremely important to check to Navier Stokes computations to make sure that you have the inviscid limits correct if you increase Reynolds number. For this reason alone I feel that it is very important to check Euler calculations.

Dr. Ing. Korner, DLR Braunschweig
I would like to comment on our experience with Euler computations for supersonic flow, Mach numbers from 2 to 4. When we have wave drag dominated configurations, as for example with HERMES, all aerodynamic coefficients are given in a rather proper way by Euler computations: lift, pitching moment, the lateral derivatives and also the drag, because the viscous drag is only a small part. The base drag has to be excluded. Secondly, if you have slender configurations then there is a larger part coming from the viscous drag, then it is necessary for the drag and the drag-related derivatives to do a viscous correction or viscous calculation. As to the other aerodynamic coefficient and derivates, results from Euler-calculations are sufficient.

Mr. Bignell
This was one of the messages which emerged in the Missile Aerodynamics Conference in Friedrichshafen, that Euler could be used and it appeared to give good results.

Mr. Mendenhall, Nielsen Engineering
Having been at the Friedrichshafen Conference, I would like to relate something from our paper. In the design of Pegasus, which has come up several times this afternoon, we used both Euler and Navier Stokes methods, but what I have not heard at this conference is the fact that there are other methods available, and the only thing I can imagine that might be against their use is the fact they were developed more than 20 years ago. There are still some very good aerodynamic methods available that the designer must use because he can't afford to design a configuration with Navier Stokes codes alone. It is physically, financially and economically impossible to do this in many cases. What we found in the Pegasus work is that you need a whole "tool box" full of codes. Not only do you need a tool box full of codes at all levels, you need multiple independent codes at similar levels. By that I mean that it was not uncommon for us to use three independent codes and get three completely different answers. Admittedly, Pegasus is an unmanned vehicle, so we could accept more risk and uncertainty, but remember, there were no wind tunnel data to fall back on. That is when the designer starts to lose some sleep at night.

Mr. Bignell
Sorry, Mike. Did you say that there were no wind tunnel data available? It was actually designed completely analytically and flown analytically, was it? That is some achievement really.

Professor Slooff, NLR
This is somewhat of a secondary reaction to one of the remarks that Professor Bogdonoff made. He sort of reproached the CFD community for not paying sufficient attention to validation type of efforts. In a general sense I think that he is completely correct, but I would just like to remind the audience that one of the few papers that I was able to attend, I think that it was the one by Oberkampf from Sandia Labs, was what I consider to be a very thorough study of mesh refinement and by extrapolation to get the zero mesh results, if you like, and then compare them with wind tunnel data. I would like to see more of that kind of exercise in the future.

Professor Reshotko
I heard two things that I would like to talk about. First of all, Dr. Korner mentioned the experience in the Mach 2 to 4 range. I can't disagree about the Mach 2 to 4 range, but I would say that once aerodynamic heating becomes an issue, you have to work with a viscous code. So, maybe it is above Mach 4, but my feeling is that as we get into the hypersonic regime, heating becomes one of the primary issues as much as drag, if not even more than drag and therefore, you need a viscous code. Commenting on Mike Mendenhall's statement, I fully agree. I am very much a proponent of using the full tool box, even with some of the old methods, as I tried to say in my talk. The old methods were really based on the physics.

That is how they were derived. So, they become the credibility checks for other methods or experiments and we have to continually make these credibility checks because we might be embarrassed otherwise. I will cite one experience of the first Antibes Conference where there were three Navier Stokes computations done on the heat transfer to a sharp cone in the laminar regime. They all gave different results. They were not slightly different, they were a lot different. None of the presenters had made a check against simple laminar boundary layer theory for that example. They would have readily seen whether they were right or not. I understand that that was corrected by the second Antibes Conference, but that was a shortcoming of many of the papers in the first Antibes Conference that they did not make credibility checks of their computational results.

Mr. Mallet, Dassault Aviation
I would like to make a comment also on validation. I do agree that we should do more for validation, but I would just like to mention that I think a lot of people here have been involved in organizing and contributing to workshops, so I think the issues have been identified and people are doing efforts to improve on that.

Mr. Vancamberg, Dassault Aviation
I want to comment on the levels of codes and the Euler, Navier Stokes from the designer's point of view. We try to adjust the level of codes to the needs of the design. I quite agree that for hypersonics if you want to solve all the problems the only way is to go Navier Stokes. But for forces and moments, for clean configurations, I think Euler calculations can give you a good idea of what is going on and to make sensitivity analyses I think you can have some good results. I quite agree that the heating problem is one of the major problems of hypersonics and generally speaking, the first main problem is the laminar windward heating. Then you can have boundary layer results. That is quite a good level now to have a sufficient answer. Of course, when you come to flap efficiency or canopy heating or heating between flaps, or things like that, then you have to go to full 3D Navier Stokes solutions.

So from the designer point of view we have to adjust mainly to money constraints, you have to adjust the level of modellization to the level of the problems that you want to tackle. One other thing is that, generally speaking, the scientific community tries to put as much as they can on the physical modelling, and the best physical modelling possible. I think that this is a very good thing to make progress for things to go on. From a designer point of view we might have to take less sophisticated models and give conservative answers and that will allow us to sleep a little better. How do I know when I am conservative? Well I think the answer is obtained by physical thinking. For example, it was stated one of the big problems of HERMES for example is the bow shock;winglet interaction. Do we have it or don't we have it? We generally make calculations at chemical equilibrium and that gives us the closest position of the shock versus the winglet. So in that way we know that we are conservative. For the heat flux for example, we generally take full equilibrium or fully catalytic walls and that gives us some margin there. Generally speaking, we try, due to physical reflection, have a conservative approach.

Professor Ciray, Middle East Technical University
Mr. Chairman, I don't know if I would divert the course of the discussion to a different subject if I dare to mention that one thing that has intrigued me. Until now nobody has said anything about rarefied conditions. I don't know if it was on your agenda. Everything is taken from continuum point of view until now. Does this mean that the problem of rarefied conditions is not important or is it solved or is it not relevant to this discussion?

Mr. Bignell
Would anybody like to respond to that?

Professor Reshotko
I will take a try at that. When we consider airbreathing vehicles to orbital speed, such as the National Aerospace plane, then you are necessarily within the atmosphere because you have to breathe air, so the rarefied problems do not come up. If you have a vehicle that starts in a rarefied environment and then comes in, we already have experience with those vehicles, so that the problems that will arise have arisen already and they have been designed into vehicles such as the Shuttle and the like. They don't present research problems as such, although there may be some research issues yet to be settled. Because of these two extremes, they are not prominent problems.

Professor Bogdonoff
I seldom don't agree with Eli. Usually, when I have, I have been proven wrong, but I would like to make a comment about rarefied flows. Every computation that was presented at this meeting, except one paper, used Navier Stokes or some continuum formulation. One question that one might ask is just how far can you take that computation? I think that Professor Ciray has a question which could be interpreted many ways. There is a limit in altitude perhaps where you can't use the Navier Stokes equation. There is also the question which is not at all clear to me and which has not been addressed here, to the effect of chemistry. I believe all papers were limited to 5 moleculer species and 17 reactions. It is not at all clear that the upper atmosphere is composed of only oxygen and nitrogen alone. One thing that might be done with some of these computations of chemistry is to examine what the real atmosphere might have which might validate or invalidate the use of just 5 species. The upper atmosphere is dissociated, and at least in my mind, will be flown through at very high Mach numbers. It is hard to believe that we are going to be flying at Mach 2 or 4 or 10 in the upper atmosphere. At very high speeds, Mach numbers 20, 25, 35, non-continuum and trace gases may be important factors. It is not clear to me that, just because we haven't had any problems up there with the Shuttle they are not a critical problem. It might very well be when we look at hypersonics in the long term.

Mr. Bignell
Would anyone else like to comment on flow physics chemistry?

Dr. Moss, NASA Langley
Eli mentioned that at lower altitudes rarefaction is not an issue. This is not the case where you have a small characteristic length scale. For example, the shock-on-lip problem is a problem of current interest for NASP where you have relatively high density hypersonic flow (Alt = 35 km), yet the characteristic length is very small and the potential non-continuum effects are exacerbated by the shock-shock interactions. This is a problem that is currently being investigated to examine the importance of non-continuum effects. Hopefully, meaningful comparisons can be made between numerical methods (DSMC and Navier Stokes) and between numerical and experimental results to isolate the relevant physics for this problem.

At higher altitudes, the effects of rarefaction can be very critical in simulating the thermochemical state of hypersonic flows and, consequently, the impact it has on the heating and aerodynamics of vehicles. Two areas of interest are control flap effectiveness and pitching moment. Finally, at orbital conditions there are innumerable problems where rarefaction effects are critical in characterizing both the environment and the performance of space systems ranging from satellite to space platforms. Problems concerning gas-surface interactions, plumes and plume interactions, and contamination are areas of current research.

Mr. Bignell
There was one question I would like to ask in all innocence, and it may well be deemed to be a provocative question, but it is not meant to be that in any sense. As I was looking at the screen this afternoon, I was looking at a vehicle which looked rather like the space shuttle, and here we are 30 years after the shuttle was designed, built and flown successfully. The methodology must have been proved in terms of CFD development, application and experimental techniques and facilities. What sort of methodology was used to design the shuttle which clearly was used successfully? You could hardly do a flight test of the vehicle. I know there were lots of flying lifting bodies, but they may not have contributed an awful lot. I wondered if Dr. Goodrich would comment, having worked on the shuttle.

Dr. Goodrich, AGARD
The methodologies used 25 years ago for the aerothermodynamic design of the shuttle have indeed proven to be successful after some 50 shuttle missions and 10 years of operation. Even without this knowledge, if I were starting the shuttle activities tomorrow, I think that I would start where we did then to get preliminary design information and then take the same attack to validate the design margins with CFD tools - depending on the schedule and costs factors. I don't see anything that has changed dramatically in 25 years except that the CFD codes are more efficient now. One may be able to obtain a useful Navier-Stokes solution for these vehicles now, although based on a recent project that I worked on, it was still difficult to get good Navier-Stokes solutions for relatively simple 3-D blunt bodies under certain conditions. I would still be inclined to start with our design tool box to come out with a preliminary design and then go to Euler/boundary-layer solutions for timely margin-assessment activities. Then, if you have the resources, go to the Navier-Stokes codes. Unfortunately, in 25 years, we haven't made the advances necessary to start, I don't think, at a different point for aerothermodynamic design activities.

This is, however, not the case for aerodynamic analysis. Improvements in the design methodology used for the orbiter aerodynamic pitching moment predictions at hypersonic flight conditions are rather easy to achieve today because these design predictions were based primarily on ideal gas wind tunnel measurements and correlations. Euler-based, real-gas CFD predictions could have been useful then, and should be useful today, in providing good estimates of the aerodynamic forces and moments for shuttle-orbiter-like vehicles at hypersonic flight conditions.

Mr. Bignell
Thank you for that. I find that very interesting. It is now quarter past 5 and we are getting on towards concluding our discussion. The other question that I wanted to ask was that Professor Reshotko in his evaluation raised a number of issues. Could I ask the chairman or a member of the new AGARD Working Group on Hypersonics if any of these issues are being addressed specifically.

Professor Poll
If I can comment on what Dr. Goodrich just said. The space shuttle, viewed from a non-US perspective, is a piece of good, solid, boiler-plate engineering. The criticism is that its payload fraction is microscopic. The real issue is how do you build better vehicles and better vehicles presumably means something with a much better payload fraction. That comes by reducing your design uncertainties, that is you knock down your conservatism. One of the critical large uncertainty areas which has a direct effect on payload, because it has a direct effect on thermal protection, is transition. Yes, transition is part of the brief of Working Group 18, which is the one to which you referred. Heating, either through transition itself or through issues like shock boundary layer interaction is a central issue to WG 18, as is the consideration of improved experimental facilities in order to get better physics information, again in areas for which the uncertainty level has traditionally been high. Also, just for good measure, there are the impliciations of real gas effects which extend up to the rarefied limit. All of these key issues are being studied because, if we make advances, it will reduce the uncertainty levels which in turn will lead to much more efficient vehicles.

Dr. Kienappel
Concerning the task of the Working Group 18 on hypersonics, there is the main aim of this working group which is to validate the codes in turbulence, transition, viscous interaction and rarefied. On the other hand the second task for the Working Group, and I believe that this is one of the issues of this conference, is the calibration of the existing wind tunnel for new experiments.

Mr. Bignell
Are there any other burning issues which anyone wishes to raise?

Dipl. Ing. Sacher, DASA/MBB

I cannot leave this symposium with the somewhat pessimistic view that we have got from Professor Bogdonoff on progress or missing progress since 1987 and now where we stand in 1992. I think our symposium in Bristol has been a 'state of the art' review of what was available at this time. I remember several contributions, lectures on listing up availability of facilities being not any more in a production phase, and plans for new facilities. Since that time I think something was achieved in Europe. We have seen during this week, at least, the reports from France. We have two new facilities now under calibrations having the first tests and further validation tests are planned. We have seen the first exercise in those Antibes workshops on 8 test cases. It was a huge effort and a European data base on hypersonic is going on to be established. I remember the CFD sessions in 1987. We had heard something about Navier Stokes solutions and Euler calculations, but not to such an extent as we have seen during this week. I will refer to some of these papers addressing the 3D Navier Stokes calculations on Hermes. We have seen results on a two-stage to orbit transportation concept also, dealing with potential flow, with Euler codes, with Navier Stokes codes. I agree that those codes in many cases are still not really validated, but there is considerable progress in the last 5 years. The next step must be the validation of these codes, but this takes time, and specifically designed experiments are needed having been mentioned in many of these comments, but these experiments are underway. In addition, the instrumentation now is in progress. In 1987 we hadn't had a session on instrumentation. Everything was gone, because we had worldwide stop in hypersonics. Even the people operating the wind tunnels 20 years ago were gone, so we had to educate a new generation of engineers. I think this is underway and has been undertaken and the first progress could be seen at present. One last example, a completely new experience is that we now know, that we need; for example, HET, the hot experimental technique. It was mentioned by the paper of John Wendt, and this is now progressing. My view on progress during the last five years is not so pessimestic as seen by Professor Bogdonoff.

Mr. Bignell

Thank you for that contribution. I don't see any hands raised, so I think it is appropriate to draw the discussion to a close. Time is moving on anyway. Just before ~~passing~~ over to the FDP chairman, I would obviously like to thank Professor Reshotko for his eloquent evaluation. It was all that I expected it to be. I would like to thank all the speakers, presenters who have performed during the week, especially those who came from the workshop who only had a couple of days to get the material together for the meeting here. It was very commendable. I would like to thank obviously my co-chairman, Christian Dujarric and members of the Program Committee who put this meeting together and finally, I would like to thank all of you who have contributed throughout the week and this afternoon in the general discussions. I will now hand over to Professor Slooff who will close the meeting.

Professor Slooff

Thank you Bob. There is an end to every event, and this is the end of a week of hard work, both in the technical as well as in the social sense, I think. I have myself only been able to attend a small fraction of the meeting, and also I am by no means an expert in hypersonics. What I heard, however, was very interesting. The fact that at this late hour in the afternoon there are still so many attendees illustrates the success of the meeting. I would like to compliment the Program Committee, particularly the co-chairmen, Bob Bignell and Christian Dujarric with this success.

Much credit for the success of this meeting goes to the Politechnico of Torino for the excellent facilities and services that they have provided. In particular, I would like to thank the Dean, Professor Zich, and the local coordinator, Professor Onorato. You will have noticed that Professor Onorato was assisted by a very elegant team consisting of his secretary, Vilma Boaglio, and three of his students, Elisabetta Buscati, Isabella Gonnet and Enrico Cerrato. They also deserve an applause.

Thanks are due also to the people who perhaps had the most difficult job, that is the interpreters, Mrs. Borlat-Rossano, M. Speed and M. de Liffiac. Then we had the people from SHAPE taking care of the audio apparatus, Mr. Gregory Wyatt and Mr. Murray Costellow. We also have to thank Mr. Savorelli of the Polytechnico who took care of the visual aids.

On behalf of all of us, I would also like to thank the Italian National Delegates, in particular Colonel Celegato and his staff, Lt. Spuziani, Maresciallo Rubinato, Muresciallo Zampaglione and Sgt. Moscatelli.

In addition, special thanks go to the Director of Engineering of Alenia, Dr. Ing. Lojawno and the Director of Engineering of Fiat, Dr. Maccagnani. We thank them all for inviting us and for setting up such a fantastic program of technical and social events. You certainly did set a new record for hospitality towards AGARD.

There is one person, a Fluid Dynamics Panel member here from Torino, that has done a tremendous amount of work behind the scenes in putting this all together and I would ask you to follow me in a warm applause for Dr. Bucciantini and his assistant, Paola Turletto.

No AGARD FDP meeting can be run properly without the indispensable help of its Executive Dr. Winston Goodrich and his secretary Anne Marie Rivault. You did a terrific job again and we thank you both for that.

Finally, I would like to draw your attention to some of the future activities of the Fluid Dynamics Panel. In this rapidly changing world the mission and tasks of AGARD are a subject of discussion. I am sure that you agree with me that AGARD has every reason to continue its work in the spirit of this past week. You can help by disseminating the information given on this viewgraph to your colleagues and by sending out the message of AGARD in general.

This finally is the end. Thank you all for your patience and for your personal contributions to the success of this symposium. I wish you a good and interesting trip to Modane tomorrow for those of you who go and, of course, a safe journey back home.

REPORT DOCUMENTATION PAGE

1. Recipient's Reference	2. Originator's Reference	3. Further Reference	4. Security Classification of Document
	AGARD-CP-514	ISBN 92-835-0694-4	UNCLASSIFIED/ UNLIMITED

5. Originator
Advisory Group for Aerospace Research and Development
North Atlantic Treaty Organization
7 Rue Ancelle, 92200 Neuilly sur Seine, France

6. Title
THEORETICAL AND EXPERIMENTAL METHODS IN HYPERSONIC FLOWS

7. Presented at the Fluid Dynamics Panel Symposium held in Torino, Italy, from 4th—8th May 1992.

8. Author(s)/Editor(s)
Various

9. Date
April 1993

10. Author's/Editor's Address
Various

11. Pages
596

12. Distribution Statement There are no restrictions on the distribution of this document. Information about the availability of this and other AGARD unclassified publications is given on the back cover.

13. Keywords/Descriptors

Hypersonic flow
Computerized simulation
Hypersonic vehicles
Design
Computational fluid dynamics
Computer programs
Boundary layer transition
Rarefied gas dynamics
Nozzle flow
Hypersonic nozzles

14. Abstract

The 43 papers prepared for the AGARD Fluid Dynamics Panel (FDP) Symposium on "Theoretical and Experimental Methods in Hypersonic Flows" that was held 4th—8th May 1992 in Torino, Italy are contained in this report. In addition to these papers, the Technical Evaluation Report aimed at assessing the relevance and success of the Symposium in meeting the technical needs of the aerospace community and the transcript of the General Discussion held at the end of the meeting are included in this document.

The objectives of the Symposium were to (1) report and assess the advances being made by the AGARD community on the development and application of theoretical methods and experimental techniques for simulating hypersonic flows over aerospace vehicles, (2) highlight outstanding problem areas, and (3) establish pointers to aid in the planning and implementation of future research programmes. Major topics covered by the Symposium were testing techniques and instrumentation, computational methods and physical modelling, and validation and accuracy assessment.

AGARD Conference Proceedings 514
Advisory Group for Aerospace Research and Development, NATO
THEORETICAL AND EXPERIMENTAL METHODS IN HYPERSONIC FLOWS
Published April 1993
596 pages

The 43 papers prepared for the AGARD Fluid Dynamics Panel (FDP) Symposium on "Theoretical and Experimental Methods in Hypersonic Flows" that was held 4th–8th May 1992 in Torino, Italy are contained in this report. In addition to these papers, the Technical Evaluation Report aimed at assessing the relevance and success of the Symposium in meeting the technical needs of the aerospace community and the transcript of the General Discussion held at the end of the meeting are included in this document.

P.T.O.

AGARD-CP-514

Hypersonic flow
Computerized simulation
Hypersonic vehicles
Design
Computational fluid dynamics
Computer programs
Boundary layer transition
Rarefied gas dynamics
Nozzle flow
Hypersonic nozzles

AGARD Conference Proceedings 514
Advisory Group for Aerospace Research and Development, NATO
THEORETICAL AND EXPERIMENTAL METHODS IN HYPERSONIC FLOWS
Published April 1993
596 pages

The 43 papers prepared for the AGARD Fluid Dynamics Panel (FDP) Symposium on "Theoretical and Experimental Methods in Hypersonic Flows" that was held 4th–8th May 1992 in Torino, Italy are contained in this report. In addition to these papers, the Technical Evaluation Report aimed at assessing the relevance and success of the Symposium in meeting the technical needs of the aerospace community and the transcript of the General Discussion held at the end of the meeting are included in this document.

P.T.O.

AGARD-CP-514

Hypersonic flow
Computerized simulation
Hypersonic vehicles
Design
Computational fluid dynamics
Computer programs
Boundary layer transition
Rarefied gas dynamics
Nozzle flow
Hypersonic nozzles

AGARD Conference Proceedings 514
Advisory Group for Aerospace Research and Development, NATO
THEORETICAL AND EXPERIMENTAL METHODS IN HYPERSONIC FLOWS
Published April 1993
596 pages

The 43 papers prepared for the AGARD Fluid Dynamics Panel (FDP) Symposium on "Theoretical and Experimental Methods in Hypersonic Flows" that was held 4th–8th May 1992 in Torino, Italy are contained in this report. In addition to these papers, the Technical Evaluation Report aimed at assessing the relevance and success of the Symposium in meeting the technical needs of the aerospace community and the transcript of the General Discussion held at the end of the meeting are included in this document.

P.T.O.

AGARD-CP-514

Hypersonic flow
Computerized simulation
Hypersonic vehicles
Design
Computational fluid dynamics
Computer programs
Boundary layer transition
Rarefied gas dynamics
Nozzle flow
Hypersonic nozzles

AGARD Conference Proceedings 514
Advisory Group for Aerospace Research and Development, NATO
THEORETICAL AND EXPERIMENTAL METHODS IN HYPERSONIC FLOWS
Published April 1993
596 pages

The 43 papers prepared for the AGARD Fluid Dynamics Panel (FDP) Symposium on "Theoretical and Experimental Methods in Hypersonic Flows" that was held 4th–8th May 1992 in Torino, Italy are contained in this report. In addition to these papers, the Technical Evaluation Report aimed at assessing the relevance and success of the Symposium in meeting the technical needs of the aerospace community and the transcript of the General Discussion held at the end of the meeting are included in this document.

P.T.O.

AGARD-CP-514

Hypersonic flow
Computerized simulation
Hypersonic vehicles
Design
Computational fluid dynamics
Computer programs
Boundary layer transition
Rarefied gas dynamics
Nozzle flow
Hypersonic nozzles

The objectives of the Symposium were to (1) report and assess the advances being made by the AGARD community on the development and application of theoretical methods and experimental techniques for simulating hypersonic flows over aerospace vehicles, (2) highlight outstanding problem areas, and (3) establish pointers to aid in the planning and implementation of future research programmes. Major topics covered by the Symposium were testing techniques and instrumentation, computational methods and physical modelling, and validation and accuracy assessment.

ISBN 92-835-0694-4

The objectives of the Symposium were to (1) report and assess the advances being made by the AGARD community on the development and application of theoretical methods and experimental techniques for simulating hypersonic flows over aerospace vehicles, (2) highlight outstanding problem areas, and (3) establish pointers to aid in the planning and implementation of future research programmes. Major topics covered by the Symposium were testing techniques and instrumentation, computational methods and physical modelling, and validation and accuracy assessment.

ISBN 92-835-0694-4

The objectives of the Symposium were to (1) report and assess the advances being made by the AGARD community on the development and application of theoretical methods and experimental techniques for simulating hypersonic flows over aerospace vehicles, (2) highlight outstanding problem areas, and (3) establish pointers to aid in the planning and implementation of future research programmes. Major topics covered by the Symposium were testing techniques and instrumentation, computational methods and physical modelling, and validation and accuracy assessment.

ISBN 92-835-0694-4

The objectives of the Symposium were to (1) report and assess the advances being made by the AGARD community on the development and application of theoretical methods and experimental techniques for simulating hypersonic flows over aerospace vehicles, (2) highlight outstanding problem areas, and (3) establish pointers to aid in the planning and implementation of future research programmes. Major topics covered by the Symposium were testing techniques and instrumentation, computational methods and physical modelling, and validation and accuracy assessment.

ISBN 92-835-0694-4